



# PROCEEDINGS VOL I

A large, grainy black and white photograph of a particle accelerator. It shows various cylindrical and rectangular components, some with flanges and bolts, connected by pipes and structural supports. The lighting is dramatic, with strong highlights and deep shadows.

## BEAMS'96

DISTRIBUTION STATEMENT A

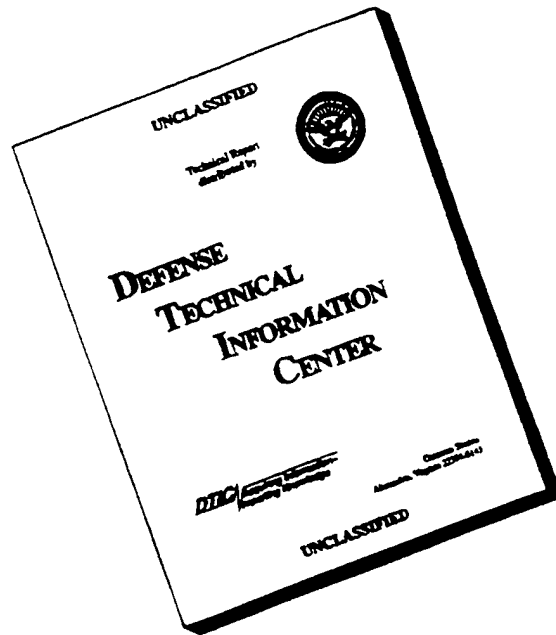
Approved for public release;

Dist. Unlimited

11th International Conference on High Power Particle Beams  
Prague, Czech Republic  
June 10-14, 1996

19961204 015

# DISCLAIMER NOTICE



**THIS DOCUMENT IS BEST  
QUALITY AVAILABLE. THE  
COPY FURNISHED TO DTIC  
CONTAINED A SIGNIFICANT  
NUMBER OF PAGES WHICH DO  
NOT REPRODUCE LEGIBLY.**



# REPORT DOCUMENTATION PAGE

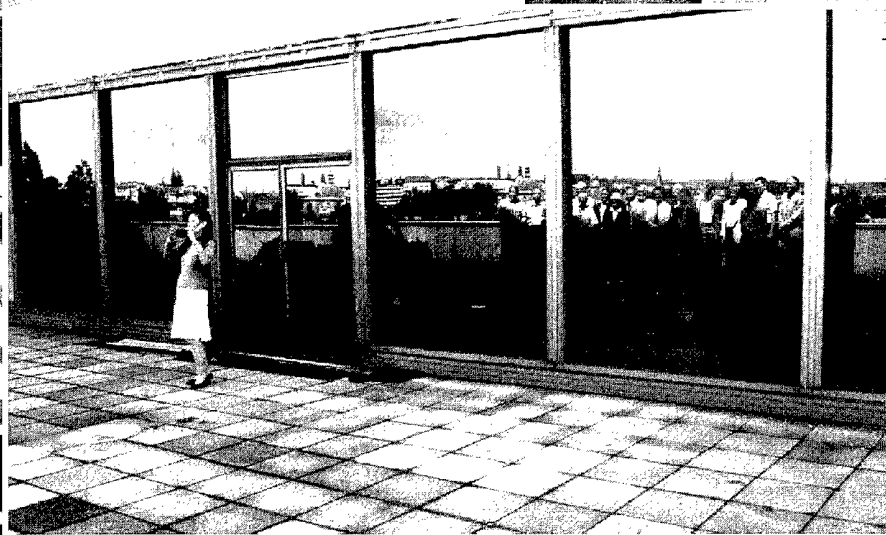
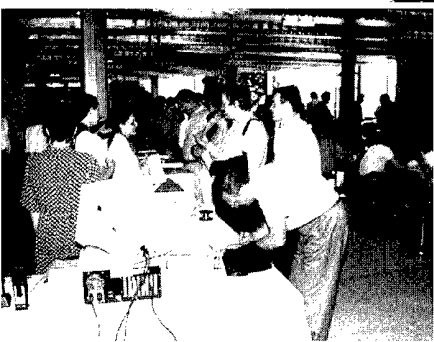
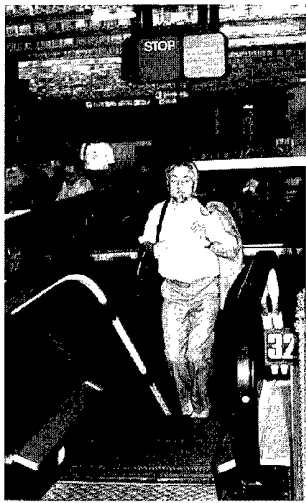
Form Approved OMB No. 0704-0188

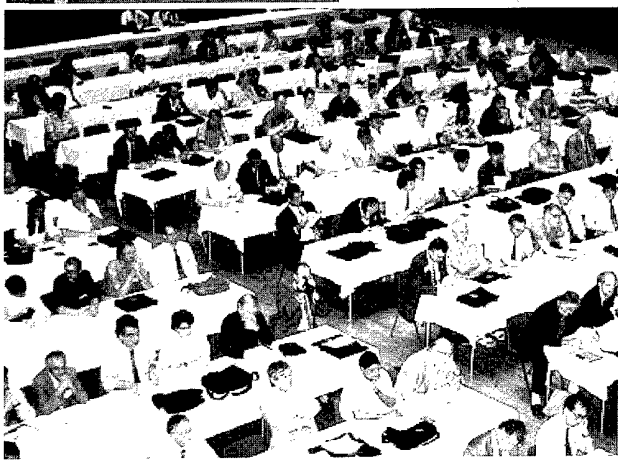
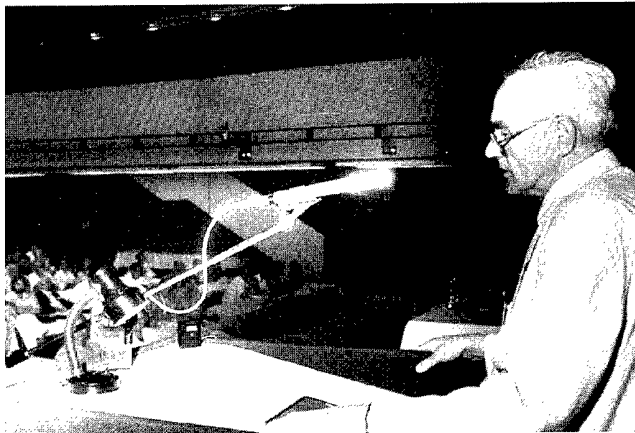
Public reporting burden for this collection of information is estimated to average 1 hour per response, including the time for reviewing instructions, searching existing data sources, gathering and maintaining the data needed, and completing and reviewing the collection of information. Send comments regarding this burden estimate or any other aspect of this collection of information, including suggestions for reducing this burden to Washington Headquarters Services, Directorate for Information Operations and Reports, 1215 Jefferson Davis Highway, Suite 1204, Arlington, VA 22202-4302, and to the Office of Management and Budget, Paperwork Reduction Project (0704-0188), Washington, DC 20503.

1. AGENCY USE ONLY (Leave blank)		2. REPORT DATE July 1996	3. REPORT TYPE AND DATES COVERED Conference Proceedings, 10-14 June 1996	
4. TITLE AND SUBTITLE 11 <sup>th</sup> International Conference on High Power Particle Beams			5. FUNDING NUMBERS F6170895W0273	
6. AUTHOR(S) Karel Jungwirth and Jiří Ullshmiel (Editors)				
7. PERFORMING ORGANIZATION NAME(S) AND ADDRESS(ES) Institute of Plasma Physics Czech Academy of Sciences Za Slovankou 3 182 00 Prague, Czech Republic			8. PERFORMING ORGANIZATION REPORT NUMBER CSP-96-1026	
9. SPONSORING/MONITORING AGENCY NAME(S) AND ADDRESS(ES) EOARD PSC 802 BOX 14 FPO 09499-0200			10. SPONSORING/MONITORING AGENCY REPORT NUMBER CSP-96-1026	
11. SUPPLEMENTARY NOTES				
12a. DISTRIBUTION/AVAILABILITY STATEMENT  Dist "A"			12b. DISTRIBUTION CODE  <div style="border: 1px solid black; padding: 5px; text-align: center;"> <b>DISTRIBUTION STATEMENT A</b>  Approved for public release  Distribution Unlimited </div>	
13. ABSTRACT (Maximum 200 words)  Two volumes of conference proceedings from the 11 <sup>th</sup> International Conference on High Power Particle Beams (BEAMS '96) held in Prague, Czech Republic between 10-14 June 1996.				
14. SUBJECT TERMS			15. NUMBER OF PAGES 1,308	
			16. PRICE CODE	
17. SECURITY CLASSIFICATION OF REPORT  UNCLASSIFIED	18. SECURITY CLASSIFICATION OF THIS PAGE  UNCLASSIFIED	19. SECURITY CLASSIFICATION OF ABSTRACT  UNCLASSIFIED	20. LIMITATION OF ABSTRACT  UL	

NSN 7540-01-280-5500

Standard Form 298 (Rev. 2-89)  
Prescribed by ANSI Std. Z39-18  
298-102





# **BEAMS'96**

**Proceedings of the  
11th International Conference on High Power Particle Beams**

**Prague, Czech Republic  
June 10-14, 1996**

*Edited by*

**Karel Jungwirth and Jiří Ullschmied**  
Institute of Plasma Physics, Prague

**Volume I**

Published by

Committees of the 11th International Conference  
on High Power Particle Beams  
Institute of Plasma Physics  
Academy of Sciences of the Czech Republic  
Za Slovankou 3  
182 00 Prague 8  
Czech Republic

**Proceedings of the 11th International Conference  
on High Power Particle Beams - Vol. I  
First Edition, 1996**

ISBN 80-902250-3-9 (Vol.1)

ISBN 80-902250-4-7 (Vol.2)

ISBN 80-902250-2-0 (set)

---

Printed by Tiskárna „K“, Ltd., Sokolovská 45, 18600 Prague 8, Czech Republic  
Cover designed by Jiří Ullschmied

# CONFERENCE ORGANIZATION

Honorary Chairman:	<b>Pavel Šunka</b>
Conference Chairman:	<b>Karel Jungwirth</b>
Co-Chairman:	<b>Jiří Ullschmied</b>

The Conference was held under the auspices of:

**Council for Research and Development of the Czech Government  
Academy of Sciences of the Czech Republic  
Engineering Academy of the Czech Republic  
Lord Mayor of Prague**

Conference host:

**Institute of Plasma Physics, Academy of Sciences, Czech Republic**

Organizational support:

**Faculty of Electrotechnical Engineering, Czech Technical University  
Faculty of Mathematics and Physics, Charles University, Prague**

## INTERNATIONAL ADVISORY COMMITTEE

<b>Abraham Blaugrund</b>	Weizmann Institute of Science, Israel
<b>Timothy Coffey</b>	Naval Research Laboratory, USA
<b>Donald Cook</b>	Sandia National Laboratory, USA
<b>Gerald Cooperstein</b>	Naval Research Laboratory, USA
<b>Bernard Etlicher</b>	École Polytechnique, France
<b>Karel Jungwirth</b>	Academy of Sciences, Czech Republic
<b>Günther Kessler</b>	Forschungszentrum Karlsruhe, Germany
<b>Alan Kolb</b>	Maxwell Laboratories, Inc., USA
<b>Gennady Mesyats</b>	Academy of Sciences, Russia
<b>Sadao Nakai</b>	Osaka University, Japan
<b>Keishiro Niu</b>	Teikyo Heisei University, Japan
<b>Dmitri Ryutov</b>	INP, Novosibirsk, Russia
<b>Valentin Smirnov</b>	TRINITI, Troitsk, Russia
<b>Charles Stallings</b>	Physics International Co., USA
<b>Ravi Sudan</b>	LPS Cornell University, USA
<b>Kiyoshi Yatsui</b>	Nagaoka Univ. of Technology, Japan

DTIC QUALITY INSPECTED 2

## LOCAL STEERING COMMITTEE

<b>George Bekefi</b>	MIT, Cambridge, USA
<b>Hansjoachim Bluhm</b>	Forschungszentrum Karlsruhe, Germany
<b>David Hammer</b>	LPS Cornell University, Ithaca, USA
<b>Stanislav Hemelík</b>	Energoprojekt a.s., Prague, CR
<b>Petr Karas</b>	ČEZ, a.s., CR
<b>Günther Kessler</b>	Forschungszentrum Karlsruhe, Germany
<b>Vasili Koidan</b>	INP, Novosibirsk, Russia
<b>Jiri Linhart</b>	University of Ferrara, Italy
<b>Václav Lobovský</b>	Škoda Nuclear Machinery, Plzeň, CR
<b>Yitzak Maron</b>	Weizmann Institute of Science, Israel
<b>David Mosher</b>	NRL, Washington, USA
<b>Joan Ma Pierre</b>	Defense Nuclear Agency, USA
<b>Nikolai Popkov</b>	Arzamas-16, Sarov, Russia
<b>Leonid Rudakov</b>	RRC Kurchatov Inst., Moscow, Russia
<b>Dmitri Ryutov</b>	INP, Novosibirsk, Russia
<b>Lubomír Soudek</b>	Škoda, koncern, Plzeň, CR
<b>Regan Stinnett</b>	SNL, Albuquerque, USA
<b>Ravi Sudan</b>	LPS Cornell University, Ithaca, USA
<b>Pavel Šunka</b>	IPP AS, Prague, CR
<b>Jiří Ullschmied</b>	IPP AS, Prague, CR
<b>Roger White</b>	Maxwell Laboratories, San Diego, USA

## TECHNICAL/PROGRAMME COMMITTEE

<b>Walter Bauer</b>	Forschungszentrum Karlsruhe, Germany
<b>Václav Babický</b>	IPP AS, Prague, CR
<b>Hansjoachim Bluhm</b>	Forschungszentrum Karlsruhe, Germany
<b>Ladislav Drška</b>	Czech Technical University, Prague, CR
<b>David Hinshelwood</b>	NRL, Washington, USA
<b>Peter Hoppé</b>	Forschungszentrum Karlsruhe, Germany
<b>Marian Karlický</b>	Astronomical Institute AS, Ondřejov, CR
<b>Karel Koláček</b>	IPP AS, Prague, CR
<b>Aleš Krejčí</b>	World Trend, Prague, CR
<b>Pavel Kubeš</b>	Czech Technical University, Prague, CR
<b>Rostislav Mach</b>	Nuclear Physics Inst. AS, Řež, CR
<b>Joseph Shiloh</b>	FM Technologies, USA
<b>Amanda Ness</b>	Maxwell Laboratories, San Diego, USA
<b>Vojtěch Píffl</b>	IPP AS, Prague, CR
<b>Karel Rohlena</b>	Physical Institute AS, Prague, CR
<b>Tomáš Růžička</b>	Academy of Sciences, CR
<b>Pavel Strelkov</b>	Institute of General Physics, Moscow, Russia
<b>Milan Tichý</b>	Charles University, Prague, CR
<b>Jiří Ullschmied</b>	IPP AS, Prague, CR
<b>Václav Valenta</b>	Škoda Nucl. Machinery, Plzeň, CR
<b>Pavel Vrba</b>	IPP AS, Prague, CR

## ACKNOWLEDGEMENT

We wish to thank the

**European Science Foundation, Strasbourg**  
**Naval Research Laboratory, Washington D.C.**  
**Office of Naval Research, Washington D.C.**  
**Physics International Company, San Leandro CA**  
**Sandia National Laboratory, Albuquerque NM**  
**US Air Force European Office of Aerospace R&D, London**

as well as our domestic sponsors

**ČEZ, a.s., Prague**



**Energoprojekt Praha a.s., Prague**



**Škoda Nuclear Machinery, Ltd., Plzeň**



for their contributions to the success of the Conference, and

**MŠMT - Ministry of Education of the Czech Republic**

for its support of publishing this Proceedings.



EP 1050 MINOLTA COPIER  
by courtesy of

**MINOLTA Ltd., Prague**

has been used at preparing this Book





# TABLE OF CONTENTS

## VOLUME I

<b>Opening Addresses</b> (K. Jungwirth, P. Šunka) .....	<b>VII</b>
<b>PAPER INDEX</b> .....	<b>i-xvi</b>
<b>Invited Papers O-0</b> (J. Quintenz - SNL; V. Chernyshev - VNIIEF Arzamas; B. Goel - FZK, K. Yatsui - LBT Nagaoka) .....	<b>1</b>
<b>Invited Papers O-1</b> (ICF, Accelerators, B&P Diagnostics) .....	<b>37</b>
<b>Invited Papers O-2</b> (Ion Beams, Ion Diodes) .....	<b>72</b>
<b>Invited Papers O-3</b> (PP Technology, POS, BDTT) .....	<b>121</b>
<b>Invited Papers O-4</b> (Liners, Z-pinches, Plasma Foci) .....	<b>140</b>
<b>Invited Papers O-5</b> (Electron Beam Physics, B-P Systems) .....	<b>182</b>
<b>Invited Papers O-6</b> (HP Microwaves, FELs) .....	<b>206</b>
<b>Invited Papers O-7</b> (Industrial Applications of Beams and PP) .....	<b>249</b>
<b>Invited Papers O-8</b> (Radiation Sources) .....	<b>276</b>
<b>Contributed Papers P-1</b> (B-P Interaction, Electron Beam Physics, FELs, H-P Microwaves) .....	<b>319</b>
<b>Contributed Papers P-2</b> (Capillary Discharges, H-C Discharges, Laser Plasma Discharges, Imploding Liners, Plasma Foci, Pseudosparks) .....	<b>501</b>
<b>AUTHOR INDEX</b>	

## VOLUME II

<b>PAPER INDEX</b> .....	<b>i-xvi</b>
<b>Contributed Papers P-2 - continuation</b> (Radiation Sources, Z-Pinches) .....	<b>649</b>
<b>Contributed Papers P-3</b> (Accelerator Related Topics, Electron Beam Applications, Ion Beam Applications, PP-Applications, BDTT, Explosive Generators, Pulsed Power Technology) .....	<b>781</b>
<b>Contributed Papers P-4</b> (Astrophysics, B-P Physics, ICF, Ion Beam Physics, Ion Diodes, Ion Rings, Ion Sources, POS, SOS, Targets) .....	<b>1027</b>
<b>Panel Discussion</b> (G. Cooperstein, H. Bluhm, H. Karow, J. Quintenz, D. Ryutov, G. Mesyats, V. Smirnov, R. Sudan) .....	<b>1273</b>
<b>Closing Ceremony</b> (K. Jungwirth, J. Shiloh, J. Quintenz) .....	<b>1287</b>
<b>BEAMS Statistics</b> (J. Ullschmied) .....	<b>1289</b>
<b>From the BEAMS Pre-history</b> .....	<b>1290</b>
<b>LIST OF PARTICIPANTS</b> .....	<b>1293</b>
<b>AUTHOR INDEX</b>	

# OPENING ADDRESSES

## Chairman's Opening Address

Karel Jungwirth

Ladies and gentlemen, distinguished guests, dear colleagues,

It's a great pleasure and honour for me to have the opportunity to address this distinguished audience on behalf of the Academy of Sciences of the Czech Republic at the occasion of opening our 11th High Power Particle Beams Conference. These Conferences are held regularly each second year at different places all over the world, and Prague is honoured by the right to be the host town strictly speaking for the first time only. Nevertheless, the two ones in 11 - the sequence number of the Conference - seem to have a bit symbolic meaning, since the very first precursor of these Conferences, the First International Symposium on Beam-Plasma Interaction, was organised here already in 1967. And I am really happy that after so many years of enforced isolation which followed we can meet here again with our friends and colleagues and that also your personal presence here confirms that Prague is now a good place where to meet.

This town has actually a long tradition in many fields closely related to science and technology, be it mathematics, physics or astronomy, engineering, chemistry, biology, physiology or medicine. I would like to remind you in this connection that science - or at least the early attempts of it - flourished already at the court of the renaissance Emperor Rudolf II in the 16th century. Among others, he invited to Prague the famous astronomer Tycho de Brahe and thereafter also Johannes Kepler, who discovered here two of his three famous laws of motion of the planets. From many other names may I mention just the physicist and philosopher Ernst Mach who held for 28 years the Chair of Experimental Physics at the University in Prague and who was one of its most distinguished rectors or Christian Doppler who formulated the famous principle bearing his name while being professor of mathematics at the Technical University in Prague.

In this country, the Academy has always served the general literacy and contributed substantially to the progress in science. It is only natural that even this meeting is organised by one of the Institutes of our Academy - the Institute of Plasma Physics. The present Academy of Sciences of the Czech Republic itself has among its predecessors the Royal Bohemian Learned Society established as early as in 1773. Already a century later (in 1861) Jan Evangelista Purkyně, the same scientist who discovered the living cell, suggested in his tractate "Academia" formation of a very progressive type of a scientific institution complementing the learned society with an autonomous assembly of research institutes. As a plasma physicist by profession, I can hardly avoid the temptation to mention at this occasion that Purkyně was also the promoter of the word plasma into the modern science.

But back to the present days. I have no doubts that the work you all have done guarantees that this will be an exciting and rewarding meeting and I sincerely wish you a pleasant stay in Prague!

## Welcome Address of the Host

Pavel Šunka

Good morning to everybody.

It is my great pleasure to welcome all of you here in Prague on the Conference BEAMS'96 on behalf of the hosting Institute of Plasma Physics. The present conference is the 11th one and it starts the third decade in history of such meetings. Twenty years is generally accepted as the age when a human being becomes adult and fully responsible for his own future. It seems to me that the research in high power particle beams and generally, in technology of extremely high pulsed power, reached its adult age even earlier. As a baby of military laboratories it had no problems with funding and so progress in its development was very fast.

At sixties the main effort was directed to multiterawatt single shot electron beam machines as AURORA device and its counterparts in the former Soviet Union. In a short time one could find that the technology of high current REBs is rather simple and so it became accessible for universities and for other laboratories. At early seventies the first results on application of REBs in fusion research were published and at 1975 the first BEAMS conference was organized at Albuquerque.

Since that time many things changed. On the one hand, broad international cooperation was established and progress in pulsed power technology and its applications is tremendous. Among others I mention ion beams for inertial fusion, X-ray radiation sources, microwave generators and FELs. On the other hand, due to the fundamental political changes at the late eighties, interest to military applications of the pulsed power technology decreased and generally speaking, in most countries the present spirit is not very favorable for funding of any long range project.

Nevertheless, I am optimist. On several last meetings we can see that besides reports on progress in traditional topics, there is an increasing number of papers on applications of the pulsed power in new fields and it indicates good future for our meetings.

We did the best in our possibilities for organization of the present one and on this occasion I should like to express my thanks to Jiří Ullschmied who was able to arrange almost impossible things. I wish to all of you to meet here many new, interesting and as most as possible, correct ideas.

Thank you for your attention.

# PAPER INDEX - Volume I

## Invited Papers

O-0-1 • <b>Progress in Pulsed Power Fusion</b> , Quintenz, J.P., Adams, R.G., Bailey, J.E., Bloomquist, D.D., Chandler, G.A., Coats, R.S., Cook, D.L., Cuneo, M.E., Deeney, C., Derzon, M.S., Desjarlais, M.P., Dukart, R.J., Filuk, A.B., Haill, T.A., Hanson, D.L., Johnson, D.J., Kiefer, M.L., Leeper, R.J., Lockner, T.R., Marder, B.M., Matzen, M.K., McDaniel, D.H., McGuire, E.J., Mehlhorn, T.A., Mendel, C.W., Menge, P.R., Renk, T.J., Rosenthal, S.E., Ruiz, C.L., Sanford, T.W.L., Seamen, J.F., Seidel, D.B., Slutz, S.A., Spielman, R.B., Stygar, W.A., Sweeney, M.A., Tisone, G.C. ....	1
O-0-2 • <b>High Power Explosive Magnetic Energy Sources for Thermonuclear and Physical Applications</b> , Chernyshev, V.K. ....	7
O-0-3 • <b>Status of Equation of State for Aluminium in the Light of Beam-Target Interaction Experiments at KALIF</b> , Goel, B., Hoebel, W., Marten, H., Vorobiev, O.Yu., Lomonosov, I.V., Gryaznov, V.K. ....	23
O-0-4 • <b>Pulse-Power Technology and Its Application at LBT, Nagaoka</b> , Yatsui, K., Masuda, W., Grigoriu, C., Masugata, K., Jiang, W., Imada, G., Imanari, K., Sonegawa, T., Chishiro, E. ....	27
O-1-1 • <b>Pulsed Power Driven Hohlräum Research at Sandia National Laboratories</b> , Leeper, R.J., Alberts, T.E., Allshouse, G.A., Aubert, J.H., Baca, P., Baca, P.M., Bailey, J.E., Barber, T.L., Breeze, S.P., Carlson, A.L., Chandler, G.A., Cook, D., Derzon, M.S., Douglas, M.R., Dukart, R.J., Fehl, D.L., Gilliland, T., Hebron, D.E., Hurst, M.J., Jobe, D.O., Johnson, D.J., Kellogg, J.W., Matzen, M.K., Martinez, C., Mehlhorn, T.A., McDaniel, D.H., McGuire, E.J., McGurn, J.S., McNamara, W.F., Moats, A.R., Muron, D.J., Nash, T.J., Noack, D.D., Olsen, R.W., Olson, R.E., Porter, J.L., Quintenz, J.P., Ruggles, L.E., Ruiz, C.L., Sawyer, P.S., Seamen, J.F., Spielman, R.B., Stark, M.A., Torres, J.A., VanDevalde, D.M., Vargas, M., Wenger, D.F., Zagar, D.M. ....	37
O-1-2 • <b>Determination of the Time Dependent Magnetic Field Distribution in Pulsed-Power Systems</b> , Maron, Y., Arad, R., Davara, G., Gregorian, L., Krasik, Ya.E., Kroupp, E., Sarfaty, M., Shpitalnik, R., Weingarten, A. ....	41
O-1-3 • <b>Spectroscopic Techniques for Measuring Ion Diode Space-Charge Distributions and Ion Source Properties</b> , Filuk, A.B., Bailey, J.E., Adams, R.G., Carlson, A.L., Ching, C.H., Desjarlais, M.P., Lake, P., McGuire, E.J., Mehlhorn, T.A., Pointon, T.D., Maron, Y., Stambulchik, E. ....	48
O-1-4 • <b>Recent Experiments towards Production and Diagnostics of Nitrogen Ion Beam for Medium-Mass Ion Beam ICF</b> , Kasuya, K., Yasuike, K., Miyamoto, S., Nakai, S., Kamiya, T., Funatsu, M., Okayama, H., Nishigori, K., Sunami, H., Wu, C., Ido, D., Adachi, T., Watanabe, M., Ebine, T., Niimi, G. ....	52
O-1-5 • <b>Status of Magnetically-Insulated Power Transmission Theory</b> , Mendel Jr., C.W. ....	56
O-1-6 • <b>The Proof-of-Concept Experiment for the Spiral Line Induction Accelerator</b> , Putnam, S.D., Bailey, V.L., Smith, J., Lidestri, J., Thomas, J., Lackner, H., Nishimoto, H. ....	60
O-1-7 • <b>The State of Development of an Intense Resonance Electron-Ion Accelerator Based on Doppler Effect</b> , Yegorov, A.M., Ivanov, B.I., Butenko, V.I., Ognivenko, V.V., Onishchenko, I.N., Prishchepov, V.P. ....	64
O-1-8 • <b>Ion Beam Neutralization with Ferroelectrically Generated Electron Beams</b> , Herleb, U., Riege, H. ....	68
O-2-1 • <b>Target Experiments with High-Power Proton Beams</b> , Baumung, K., Bluhm, H., Hoppe, P., Kanel, G.I., Razorenov, S.V., Rusch, D., Singer, J., Stoltz, O., Utkin, A.V. ....	72
O-2-2 • <b>Field-Reversed Ion Ring Configurations for Fusion</b> , Sudan, R.N., Greenly, J.B., Hammer, D.A., Omelchenko, Yu.A., Podulka, W.J. ....	81

O-2-3 • <b>Plasma Lens Focusing and Plasma Channel Transport for Heavy Ion Fusion,</b> Tauschwitz, A., Yu, S.S., Bangerter, R.O., Barnard, J.J., Eylon, S., Fessenden, T.J., Kwan, J., Leemans, W., Peters, C., Reginato, L., Sharp, W.M. ....	91
O-2-4 • <b>Formation of an Intense Proton Beam of Microsecond Duration,</b> Engelko, V., Giese, H., Schalk, S. ....	95
O-2-5 • <b>Uniform Current Density and Divergence Control in High-Power Extraction Ion Diodes,</b> Desjarlais, M.P., Coats, R.S., Lockner, T.R., Pointon, T.D., Johnson, D.J., Slutz, S.A., Lemke, R.W., Cuneo, M.E., Mehlhorn, T.A. ....	101
O-2-6 • <b>Anode Plasma Dynamics on an Extraction Applied-B Ion Diode: Effects on Divergence, Ion Species and Parasitic Load,</b> Greenly, J.B., Appartaim, R.K., Olson, J.C. ....	111
O-2-8 • <b>Light Ion Beam Transport Research at NRL,</b> Hinshelwood, D.D., Boller, J.R., Cooperstein, G., Fisher, R.C., Greenly, J.M., Jones, T.G., Mosher, D., Neri, J.M., Noonan, W.A., Oliver, B.V., Olson, J.C., Ottinger, P.F., Rose, D.V., Stephanakis, S.J., Welch, D.R., Young, F.C... ..	115
O-3-1 • <b>The DECADE Performance Assessment Program,</b> Weber, B.V., Ottinger, P.F., Commisso, R.J., Goyer, J.R., Kortbawi, D., Thompson, J., Rowley, J.E., Filios, P., Babineau, M.A. ....	121
O-3-2 • <b>Microsecond Plasma Opening Switch Experiments on GIT-4,</b> Bystrickii, V.M., Kim, A.A., Kokshenev, V.A., Koval'chuk, B.M., Lisitsyn, I.V., Sinebryukhov, A.A., Sinebryukhov, V.A. ....	127
O-3-4 • <b>A 3-MA Compact-Toroid-Plasma-Flow-Switched Plasma Focus Demonstration Experiment on SHIVA STAR,</b> Kiuttu, G.F., Graham, J.D., Degnan, J.H., Brzosko, J.S., Coffey, S.K., Gale, D.G., Holmberg, C.D., Kreh, B.B., Meyers, J.W., Outten, C.A., Ruden, E.L., Ware, K.D. ....	131
O-3-5 • <b>New Solid State Opening Switches for Repetitive Pulsed Power Technology,</b> Lyabutin, S.K., Mesyats, G.A., Rukin, S.N., Slovikovskii, B.G., Turov, A.M. ....	135
O-3-7 • <b>Beam Driven Transmutation Technology,</b> Bowman, C.D. ....	139
O-4-1 • <b>ANGARA-5-1 Program Development on Superfast Liner Implosion for ICF Physics Study and Basic Research,</b> Branitski, A.V., Grabovski, E.V., Fedulov, M.V., Frolov, I.N., Kuznetsov, D.V., Mishenski, V.O., Nedoseev, S.L., Oleinik, G.M., Otochin, A.A., Pichugin, V.E., Smirnov, V.P., Volkov, G.S., Zaitsev, V.I., Zajivikhin, V.V., Zakharov, S.V., Zurin, M.V., Velikhov, E.P., Dyabilin, K.E., Fortov, V.E., Lebedev, M.E., Danilenko, K.V., Zakharov, S.V., Gerusov, A.V., Razinkova, T.J., Sasorov, P.V., Nikiforov, A.F., Nikiforov, V.G., Krukovkii, A.Yu. ....	140
O-4-2 • <b>X-Ray Power Increase from Symmetrized Wire-Array Z-Pinch Implosions,</b> Sanford, T.W.L., Nash, T.J., Allshouse, G.O., Marder, B.M., Nash, T.J., Mock, R.C., Douglas, M.R., Spielman, R.B., Seamen, J.F., McGurn, J.S., Jobe, D., Gilliland, T.L., Vargas, M., Struve, K.W., Stygar, W.A., Hammer, J.H., DeGroot, J.S., Eddleman, J.L., Whitney, K.G., Thornhill, J.W., Pulsifer, P.E., Apruzese, J.P., Mosher, D., Peterson, D.L., Maron, Y. ....	146
O-4-3 • <b>PBFA Z: A 20-MA Z-Pinch Driver for Plasma Radiation Sources,</b> Spielman, R.B., Breeze, S.F., Deeney, C., Douglas, M.R., Long, F., Martin, T.H., Matzen, M.K., McDaniel, D.H., McGurn, J.S., Nash, T.J., Porter, J.L., Ruggles, L.E., Sanford, T.W.L., Seamen, J.F., Stygar, W.A., Torres, J.A., Zagar, D.M., Jobe, D.O., Peterson, D.L., Shoup, R.W., Struve, K.W., Mostrom, M., Corcoran, P., Smith, I. ....	150
O-4-4 • <b>S-300, New Pulsed Power Installation in Kurchatov Institute, Investigation of the Stable Liner Implosion,</b> Chernenko, A.S., Gorbunin, Yu.M., Kalinin, Yu.G., Kingsep, A.S., Koba, Yu.V., Korolev, V.D., Mizhiritskii, V.I., Rudakov, L.I. ....	154
O-4-5 • <b>Test of EMG-720 High Explosive Magneto-Cumulative Generator,</b> Popkov, N.F., Pikar', A.S., Ryaslov, E.A., Kargin, V.I., Mironychev, P.V., Nazarenko, S.T., Pavlov, V.S., Makartsev, G.F., Gurin, V.E., Korolev, P.V., Kataev, V.N., Nudikov, V.N., Russkov, A.S., Semyonov, S.I., Chernyshev, V.V., Vorontzov, V.I., Saratov, A.F., Logunov, G.I., Degnan, J.H., Kiuttu, G.F., Coffey, S.K., Summa, W.J., Ware, K.D. ....	158

O-4-6 • <b>Mechanism of Hot Spots Formation in Magnetic Z-Pinch</b> , Kubeš, P., Koláček, K., Krejčí, A., Kravárik, J., Paduch, M., Tomaszewski, K. ....	162
O-4-8 • <b>Ion Beams from High-Current PF Facilities</b> , Sadowski, M. ....	170
O-4-9 • <b>Pinches and Micropinches in the SPEED 2 Plasma Focus</b> , Roewekamp, P., Decker, G., Kies, W., Lucas, B., Schmitz, F., Ziethen, G., Simanovskii, D.M., Bobashev, S.V. ....	174
O-4-10 • <b>Generation of Rotation and Shear Flow in an Imploding Liner</b> , Hammer, J.H., Ryutov, D.D. ....	178
O-5-1 • <b>First Results on the GOL-3-II Facility</b> , Agafonov, M.A., Arzhannikov, A.V., Astrelin, V.T., Bobylev, A.V., Burdakov, A.V., Chagin, M.N., Denisenko, P.V., Deulin, Yu.I., Khilchenko, A.D., Koidan, V.S., Konyukhov, V.V., Kvashnin, A.N., Lee, O.A., Makarov, A.G., Mekler, K.I., Melnikov, P.I., Nikolaev, V.S., Perin, S.S., Postupaev, V.V., Razilov, R.V., Rovenskikh, A.F., Semenov, E.P., Sinitsky, S.L., Tarasov, A.V., Vdovin, S.V., Zotkin, R.P. ....	182
O-5-2 • <b>Multi-Kiloampere, Electron-Beam Generation Using Metal Photo-Cathodes Driven by ArF and KrF Lasers</b> , Carlson, R.L., Moya, S.S., Ridlon, R.N., Seitz, G.J., Shurter, R.P. ....	188
O-5-3 • <b>Numerical Simulation of the High Explosive Magnetic Cumulative Generator EMG-720</b> , Deryugin, Yu.N., Zelenskii, D.K., Kazakova, I.F., Kargin, V.I., Mironychev, P.V., Pikar', A.S., Popkov, N.F., Ryaslov, E.A., Ryzhackova, E.G. ....	192
O-5-4 • <b>Studies of Collective Processes in REB-Plasma Systems</b> , Masuzaki, M. ....	196
O-6-1 • <b>New Developments in Relativistic Klystron Amplifiers</b> , Friedman, M., Colombant, D., Fernsler, R., Hubbard, R., Lampe, M., Serlin, V., Slinker, S. ....	206
O-6-2 • <b>Powerful FEM-Generator Driven by Microsecond Sheet Beam</b> , Agafonov, M.A., Arzhannikov, A.V., Ginzburg, N.S., Peskov, N.Yu., Sinitsky, S.L., Tarasov, A.V. ....	213
O-6-3 • <b>Pulse Shortening in High Power Microwave Sources</b> , Benford, J., Price, D., Benford, G. ....	217
O-6-4 • <b>Generation Efficiency and Radiation Stability of Multiwave Cerenkov Generators</b> , Deichuly, M.F., Koshelev, V.I., Petkun, A.A. ....	221
O-6-5 • <b>High-Power Broad-Band Tunable Microwave Oscillator, Driven by REB in Plasma</b> , Kuzelev, M.V., Loza, O.T., Ponomarev, A.V., Rukhadze, A.A., Strelkov, P.S., Shkvarunets, A.G., Ulyanov, D.K. ....	225
O-6-6 • <b>Beam-Plasma Generators of Stochastic Microwave Oscillations Using for Plasma Heating in Fusion and Plasma-Chemistry Devices and Ionospheric Investigations</b> , Mitin, L.A., Perevodchikov, V.I., Shapiro, A.L., Zavyalov, M.A., Bliokh, Yu.P., Fainberg, Ya.B. ....	229
O-6-7 • <b>Design and Cold-Testing of Two 100 MW Gyrokystron Amplifiers for Collider Applications</b> , Lawson, W., Cheng, J., Castle, M., Saraph, G., Anderson, J., Hogan, B., Granatstein, V.L., Reiser, M. ....	238
O-6-8 • <b>First Experimental Observation of Cyclotron Superradiance</b> , Ginzburg, N.S., Zotova, I.V., Sergeev, A.S., Konoplev, I.V., Shpak, V.G., Yalandin, M.I., Shunailov, S.A., Ulmaskulov, M.R. ..	242
O-6-9 • <b>High-Efficiency FEL with Bragg Resonator Driven by Linear Induction Accelerator</b> , Ginzburg, N.S., Kaminski, A.A., Kaminski, A.K., Peskov, N.Yu., Sedykh, S.N., Sergeev, A.P., Sergeev, A.S. ....	245
O-7-1 • <b>Plasma Technology for Treatment of Waste</b> , Cohn, D. ....	249
O-7-2 • <b>Pulsed Power Systems for Commercial Treatment of Materials Using Short Pulse, Intense Ion Beams</b> , Neau, E., Schneider, L.X., Reed, K.W. ....	255
O-7-3 • <b>Application of Low-Energy High-Current Electron Beams for Surface Modification of Materials</b> , Proskurovsky, D.I., Rotshtein, V.P., Ozur, G.E. ....	259
O-7-5 • <b>Progress Toward a Microsecond Duration, Repetitively Pulsed, Intense-Ion Beam</b> , Davis, H.A., Olson, J.C., Reass, W.A., Coates, D.M., Hunt, J.W., Schleinitz, H.M., Lovberg, R.H., Greenly, J.B. ....	263

O-7-6 • Pulsed Electron Beam Facility GESA for Surface Treatment of Materials, Mueller, G., Schumacher, G., Strauss, D., Engelko, V., Andreev, A., Komarov, O., Schegolikhin, N. ....	267
O-7-7 • Laser Sources of Multiply Charged Heavy Ions, Rohlena, K., Králíková, B., Krása, J., Láská, L., Mašek, K., Mocek, T., Pfeifer, M., Skála, J., Straka, P., Farny, J., Parys, P., Wolovski, J., Woryna, E., Mróz, W., Golubev, A., Sharkov, B., Shumshurov, A., Collier, J., Haseroth, H., Langbein, K. ....	271
O-7-8 • Large-Scale Plasma Source Ion Implantation and Deposition Experiments, Rej, D.J., Faehl, R.J., Henins, I., Mašek, K., Nastasi, M., Scheuer, J.T., Walter, K.C., Wood, B.P. ....	275
O-8-1 • SYRINX - a Research Program for the Pulsed Power Radiation Facility, Etlicher, B., Chuvatin, A.S., Choi, P., Frescaline, L., Aranchuk, L., Cassany, B., Avrillaud, G., Frolov, V., Rouille, C., Auvray, P., Semushin, S., Dumitrescu-Zoita, C., Leon, J.F., Kovack, F., Monjaux, P., Lassalle, F., Bayol, F., Johan, A., Kovalchuk, B., Kim, A. ....	276
O-8-2 • Inductive-Energy Power Flow for X-Ray Sources, Ware, K.D., Filios, P.G., Gullickson, R.L., Hebert, M.P., Rowley, J.E., Schneider, R.F., Summa, W.J., Vitkovitsky, I.M. ....	284
O-8-3 • Excitation of Intense Shock Waves by Soft X-Radiation, Branitski, A.V., Fortov, V.E., Danilenko, K.N., Dyabilin, K.S., Grabovskii, E.V., Vorobiev, O.Yu., Lebedev, M.E., Smirnov, V.P., Zakharov, A.E., Persiansev, I.V. ....	292
O-8-4 • Plasma X-Ray Sources Powered by Megajoule Magnetocumulative Generators, Popkov, N.F., Averchenkov, V.Ya., Pikar', A.S., Ryaslov, E.A., Kargin, V.I., Lazarev, S.A., Borovkov, V.V., Nazarenko, S.T., Makartsev, G.F. ....	296
O-8-5 • RS-20-Type Repetitive Generator with Planar Configuration of Plasma Opening Switch, Agalakov, V.P., Barinov, N.U., Belenki, G.S., Dolgachev, G.I., Zakatov, L.P., Qiu, A.C., Shen, Zh.K., Sun, F.J., Wang, X.H., Xu, R., Zeng, J.T. ....	301
O-8-6 • Studies on Pulsed Hollow Cathode Capillary Discharges, Choi, P., Dumitrescu-Zoita, C., Larour, J., Rous, J., Favre, M., Zambra, M., Moreno, J., Chuaqui, H., Wyndham, E., Wong, C.S. ...	305
O-8-7 • Powerful Accelerators for Bremsstrahlung and Electron Beams Generation on the Basis of Inductive Energy-Storage Elements, Diyankov, V.I., Kovalev, V.P., Kormilitsin, A.I., Lavrentiev, B.N. ....	309

### Contributed Papers P-1

P-1-2 • Experimental Study of Collective Processes in REB, Bogdanov, L.Yu., Sominski, G.G. ....	319
P-1-4 • Theoretical Aspects of the Electronical Devices Operating Due to Interaction between Annular Electron Beams and the Azimuthal Surface Waves, Girka, V.O., Girka, I.O. ....	323
P-1-6 • Spectrum of Plasma Electrons Observed in Strong Langmuir Turbulence Driven by REB, Vyacheslavov, L.N., Gurko, V.F., Kandaurov, I.V., Kruglyakov, E.P., Meshkov, O.I., Sanin, A.L., Zharov, V.F. ....	327
P-1-9 • Energy and Angular Spreads of Beam Electrons and Microwave Radiation Due to Strong Beam-Plasma Turbulence, Koguchi, H., Masuzaki, M., Yoshikawa, M., Takahata, S., Toda, K., Ando, R., Kamada, K. ....	331
P-1-10 • Macroscopic Symptoms of Collapse in REB-Plasma Interaction Experiments in Strong Magnetic Field, Burmasov, V.S., Kandaurov, I.V., Kruglyakov, E.P., Meshkov, O.I., Sanin, A.L., Vyacheslavov, L.N. ....	335
P-1-12 • Broadband mm Radiation from Beam Driven Strong Turbulence, Masuzaki, M., Yoshida, H., Ando, R., Kamada, K., Ikeda, A., Lee, C.Y., Kawada, M. ....	339
P-1-16 • Spectroscopic Measurements of Turbulent HF Fields at the REBEX Machine, Ullschmied, J., Šimek, M., Koláček, K., Řípa, M. ....	343



P-1-19 • <b>High Power Microwave Emission and Diagnostics of Microsecond Electron Beams,</b> Gilgenbach, R., Hochman, J.M., Jayness, R., Rintamaki, J.I., Lau, Y.Y., Luginsland, J., Lash, J.S., Spencer, T.A. ....	347
P-1-20 • <b>Multi-Stage Autoacceleration of an Intense Relativistic Electron Beam,</b> Kamada, K., Hasegawa, D., Igarashi, H., Kusunoki, T., Lee, C.Y., Koguchi, H., Ando, R., Masuzaki, M. ....	351
P-1-21 • <b>Transport Control of Intense Electron Beam Using Undulator Guide,</b> Mori, M., Nishiyama, S., Kawata, S., Hanamori, S., Naito, K., Kato, S., Kawakita, Y., Hakoda, M. ....	355
P-1-23 • <b>Generation and Transportation of Low-Energy, High-Current Electron Beams,</b> Ozur, G.E., Proskurovsky, D.I., Nazarov, D.S. ....	359
P-1-25 • <b>Focusing and Guiding Intense Electron Beams by a Superconductor Tube,</b> Roth, P. ....	363
P-1-26 • <b>Reduction of Angular Spread at Nonadiabatic Electron Motion in Magnetically Insulated Diode,</b> Arzhannikov, A.V., Sinitsky, St.L. ....	367
P-1-27 • <b>Experimental Study of a High-Power TWT Electron Beam,</b> Arkhipov, A.V., Sominski, G.G. ....	371
P-1-28 • <b>Modelling of Electron Stream Discharge,</b> Vrba, P. ....	375
P-1-29 • <b>Chaotic Dynamics of Electron Beam with Virtual Cathode in the Bounded System,</b> Anfinogentov, V.G. ....	381
P-1-32 • <b>Effective Code for Numerical Simulation of the Helical Relativistic Electron Beam,</b> Lygin, V.K., Manuilov, V.N., Tsimring, Sh.E. ....	385
P-1-33 • <b>Electron, Ion, and Atomic Beams Interaction with Solid High-Molecular Dielectrics,</b> Milyavskii, V.V., Skvortsov, V.A. ....	389
P-1-39 • <b>An Experimental Study on Cyclotron-Cherenkov Radiation,</b> Lee, C.Y., Masuzaki, M., Yoshida, H., Toyosugi, N., Kamada, K., Ando, R. ....	393
P-1-40 • <b>Harmonic Millimeter Radiation from a Microwave FEL Amplifier,</b> Liu, Y.-H., Marshall, T.C. ....	397
P-1-43 • <b>High-Harmonic Relativistic Gyrotron as an Alternative to FEL,</b> Bratman, V.I., Kalynov, Yu.K., Kolganov, N.G., Manuilov, V.N., Ofitserov, M.M., Samsonov, S.V., Volkov, A.B. ....	401
P-1-45 • <b>Electromagnetic Properties of Corrugated and Smooth Waveguides Filled with Radially Inhomogeneous Plasma,</b> Shkvarunets, A., Kobayashi, S., Weaver, J., Carmel, Y., Rodgers, J., Granatstein, V.L., Destler, W.W. ....	405
P-1-46 • <b>A 2-Gigawatt, 1- Microsecond, Microwave Source,</b> Caryotakis, G., Jongewaard, E., Phillips, R., Scheitrum, G., Tantawi, S., Luhmann Jr., N.C. ....	406
P-1-53 • <b>High-Selectivity Resonator for Powerful Microwave Sources,</b> Abubakirov, E.B., Fuchs, M.I., Kovalev, N.F. ....	410
P-1-57 • <b>Experimental Investigations of Beam Potential Depression Effect in Gyrotrons,</b> Kuftin, A.N., Zapevalov, V.E. ....	414
P-1-58 • <b>Study of Space Charge Oscillations in Gyrotron,</b> Louksha, O.I., Sominski, G.G. ....	418
P-1-59 • <b>Co-operative High-Power Radiation of Two Beams at the Dual Vircator Complex,</b> Magda, I.I., Prokopenko, Yu.V. ....	422
P-1-61 • <b>Coaxial Plasma Filled Structures,</b> Onishchenko, I.N., Balakirev, V.A., Korostelev, A.M., Markov, P.I., Sidorenko, D.Yu., Sotnikov, G.V. ....	426
P-1-64 • <b>Beam-Plasma Processes Relevant to High-Power Wide-Band Plasma-Filled Microwave Sources,</b> Zavyalov, M.A., Mitin, L.A., Perevodchikov, V.I., Shapiro, A.L. ....	430
P-1-65 • <b>Dependence of Microwave Generation on Beam-Plasma System Length,</b> Krasilnikov, M.A., Kuzelev, M.V., Rukhadze, A.A. ....	431

<b>P-1-66 • Approaches to Achieving High Efficiency, Long Pulse, Vacuum Backward Wave Oscillator Operation,</b> Schamiloglu, E., Gahl, J.M., Grabowski, C.T., Abdallah, C.T. ....	433
<b>P-1-67 • Observations of Electron Bunching in the Micro-Pulse Electron Gun,</b> Shiloh, J., Mako, F., Peter, W., ....	437
<b>P-1-68 • Wide-Bandwidth High-Power Travelling Wave Tube Amplifiers: Comparison of Dielectric and Periodic Slow-Wave Structures,</b> Shlapakovskii, A. S. ....	441
<b>P-1-69 • Reflex Triode with Resonant Cavity as a Load for Inductive Storage,</b> Didenko, A.N., Gorbachev, K.V., Kogutnitskii, A.E., Mikhailov, V.M., Nesterov, E.V., Roschupkin, S.A., Shumilin, V.P., Stroganov, V.A. ....	445
<b>P-1-70 • Experimental Studies of a Generation Delay Time in Reflex Triode with Inductive Storage,</b> Didenko, A.N., Fortov, V.E., Gorbachev, K.V., Nesterov, E.V., Roschupkin, S.A., Shumilin, V.P., Stroganov, V.A. ....	449
<b>P-1-73 • Virtual Cathode Driven by Short Pulse Electron Gun,</b> Spassovski, I.P., Cho, S.O., Lee, J., Lee, B.-Ch., Jeong, Y.-U., Messina, G., Yovchev, I.G., Nikolov, N.A. ....	453
<b>P-1-74 • Accelerator for High Power Microwave Generation,</b> Chernykh, E.V., Fortov, V.E., Gorbachev, K.V., Nesterov, E.V., Stroganov, V.A., Shumilin, V.P. ....	457
<b>P-1-75 • Pulsed Power Microwave Calorimeter,</b> Lisichkin, A.L., Nesterov, E.V., Shumilin, V.P., Stroganov, V.A. ....	461
<b>P-1-76 • Air Breakdown Induced by a High-Power Short-Pulse Microwave,</b> Wakisaka, T., Yatsuzuka, M., Nobuhara, S. ....	465
<b>P-1-77 • Coaxial Vircator Source Development,</b> Woolverton, K., Kristiansen, M., Hatfield, L.L. ....	469
<b>P-1-78 • A 70 Ghz High-Power Repetitive Backward Oscillator with a Permanent-Magnet-Based Electron-Optical System,</b> Shpak, V.G., Shunailov, S.A., Ulmaskulov, M.R., Yalandin, M.I., Ermakov, A.E., Zhakov, S.V., Gass, V.G., Korobeinikov, A.Yu. ....	473
<b>P-1-79 • High Power Microwave Oscillator: Vircator-Klystron,</b> Jiang, W., Masugata, K., Yatsui, K. ..	477
<b>P-1-80 • Effect of Plasma Formation on Electron Pinching and Microwave Emission in Virtual Cathode Oscillator,</b> Yatsuzuka, M., Nakayama, M., Nobuhara, S., Young, D., Ishihara, O. ....	481
<b>P-1-84 • Formation and Diagnostic of Helical Gyrotron Electron Beams,</b> Andronov, A.N., Ilyin, V.N., Khmara, V.A., Kuftin, A.N., Lygin, V.K., Louksha, O.I., Manuilov, V.N., Postnikova, A.S., Robozarov, S.V., Sominsky, G.G., Tsimring, Sh.E., Zapevalov, V.E. ....	485
<b>P-1-85 • Multi-Frequency Microwave Pulses Production in a Vircator,</b> Zherlitsyn, A.G., Lyakshev, A.N., Melnikov, G.V. ....	489
<b>P-1-86 • Research of the Generation of Microsecond Microwave Irradiation in Vircator,</b> Zherlitsyn, A.G., Kotlyarevskii, G.I., Lyakshev, A.N., Tstvetkov, V.I. ....	492
<b>P-1-87 • Generation of Ultrashort Microwave Pulses Based on Cyclotron Superradiance Effect,</b> Ginzburg, N.S., Zotova, I.V., Sergeev, A.S. ....	496

## Contributed Papers P-2

<b>P-2-1 • Dynamics of Capillary Discharge Driven by Fast Pulse Power Generator,</b> Hosokai, T., Nakajima, M., Aoki, T., Horioka, K., Ogawa, M. ....	501
<b>P-2-4 • Time Resolved Observations of Plasma Evolution in the Hollow Cathode Region of a Transient Hollow Discharge,</b> Favre, M., Zambra, M., Moreno, J., Chuaqui, F., Wyndham, E., Choi, P. ....	505
<b>P-2-5 • Improvement on the Physical Description of the Boundary Conditions between the Hollow Cathode Region and the A-K Gap in a Transient Hollow Cathode Discharge,</b> Kaufman, Y., Choi, P. ....	509

P-2-6 • <b>Investigation of Ectons Dynamics in Laser-Induced Breakdowns</b> , Skvortsov, V.A., Vogel, N.I. ....	513
P-2-7 • <b>The Generation of High-Power Charge Particle Micro Beams and Its Interaction with Condensed Matter</b> , Vogel, N.I., Skvortsov, V.A. ....	518
P-2-8 • <b>The Rayleigh-Taylor Instability and the K-Shell Radiation Yield for Imploding Liners</b> , Baksht, R.B., Datsko, I.M., Labetsky, A.Yu., Roussikh, A.G., Fedyunin, A.V. ....	522
P-2-9 • <b>Investigation of Energy and Current Concentration in Composite Z-Pinch through Its Soft X-Ray Emission on ANGARA-5-1</b> , Branitski, A.V., Grabovski, E.V., Zakharov, S.V., Zurin, M.V., Oleinik, G.M., Smirnov, V.P., Frolov, I.N., Borisov, V.V., Slavnov, Yu.K., Usov, Yu.K. ....	526
P-2-10 • <b>Measurements of Soft X-Ray Power and Spectral Features on ANGARA-5-1</b> , Branitski, A.V., Oleinik, G.M. ....	530
P-2-11 • <b>Investigation of Layered Z-Pinches on ANGARA-5-1</b> , Branitski, A.V., Grabovski, E.V., Zakharov, S.V., Zurin, M.V., Nedoseev, S.L., Oleinik, G.M., Smirnov, V.P., Frolov, I.N. ....	548
P-2-12 • <b>Some Features of Liners Convergence Accelerated with the Help of Powerful EMGs</b> , Grinevich, B.E., Chernyshev, V.K., Buzin, V.N., Petrukhin, A.A., Zharinov, E.I. ....	538
P-2-17 • <b>Investigation of Superfast Composite Pinch with Unstable External Liner on ANGARA-5-1</b> , Branitski, A.V., Grabovski, E.V., Fedulov, M.V., Frolov, I.N., Kuznetsov, D.V., Medovshikov, S.F., Mishenski, V.O., Nedoseev, S.L., Oleinik, G.M., Pichugin, V.E., Sasorov, P.V., Smirnov, V.P., Zaitsev, V.I., Zakharov, S.V., Zurin, M.V. ....	542
P-2-18 • <b>New Concentrator of 5 MA on ANGARA-5-1 for Liner Implosion</b> , Grabovski, E.V., Nedoseev, S.L., Oleinik, G.M., Pichugin, V.E., Smirnov, V.P., Zajivikhin, V.V. ....	546
P-2-19 • <b>Liner-Converter Experiment on AMBIORIX</b> , Gasque, A.M., Grua, P., Romary, P., Sajer, J.M., Friart, D., Zenhter, P., Jacquet, L., Pornet, J., Dan'ko, S., Gorbulin, Yu., Kalinin, Yu.G., Kingsep, A. ....	550
P-2-20 • <b>Generation of Rotation and Shear Flow in an Imploding Liner</b> , Hammer, J.H., Ryutov, D.D. ....	554
P-2-25 • <b>Liner-Wall Interaction During the Magnetic Implosion</b> , Chernyshev, V.K., Zharinov, E.I., Mokhov, V.N., Garanin, S.F., Grinevich, B.Ye., Kudelkin, I.D., Buzin, V.N., Ionov, A.I., Sokolova, O.V., Zimakov, S.D., Yegorychev, B.T., Yerichev, V.N., Shaidullin, V.Sh., Degnan, J.H., Hussey, T.W., Kiuttu, G.F. ....	558
P-2-28 • <b>Electrical Characteristics of a Small Plasma Focus Device</b> , Choi, P., Favre, M., Silva, P., Chuaqui, H., Wyndham, E. ....	566
P-2-29 • <b>Studies of Current Sheath Evolution in a Small Plasma Focus Device</b> , Silva, P., Favre, M., Chuaqui, H., Wyndham, E., Choi, P. ....	570
P-2-30 • <b>Characteristics of a Small Plasma Focus Device</b> , Favre, M., Silva, P., Chuaqui, H., Wyndham, E., Choi, P., Dumitrescu-Zoita, C. ....	574
P-2-32 • <b>Influence of Stub Anode on Plasma Motion and Neutron Yield in a 18-kJ Plasma Focus</b> , Lu, M., Yang, T., Han, M., Yang, S. ....	578
P-2-33 • <b>Computer Simulation of a Plasma Focus Device Driven by a Magnetic Pulser</b> , Georgescu, N., Zoita, V., Larour, J. ....	582
P-2-34 • <b>Highly Ionized Copper Contribution to the Soft X-Ray Emission in a Plasma Focus Device</b> , Zoita, V., Patran, A., Larour, J. ....	587
P-2-35 • <b>Magnetic Pulse Compression Circuits for Plasma Devices</b> , Georgescu, N., Zoita, V., Presura, R. ....	591
P-2-36 • <b>Soft X-Ray Spectroscopic Investigation a of a Plasma Focus Operated in Pure Neon</b> , Presura, R., Zoita, V., Paraschiv, I. ....	595

P-2-37 • <b>Working Gas Effects on the X-Ray Emission of a Plasma Focus Device</b> , Cengher, M., Presura, R., Zoita, V. ....	599
P-2-38 • <b>Pseudospark Switches (PSS) for Pulsed Power Applications</b> , Heine, F., Prucker, U., Frank, K., Goertler, A., Schwandner, A., Tkotz, R., Hoffman, D.H.H., Christiansen, J. ....	603
P-2-41 • <b>Nanosecond Breakdown of Liquid Dielectrics</b> , Mankowski, J., Kristiansen, M., Hatfield, L. ...	607
P-2-42 • <b>The EMP Excitation of Radiation by the Pulsed Relativistic Electron Beam</b> , Balakirev, V.A., Sidel'nikov, G.L. ....	611
P-2-43 • <b>High Power Pulsed Neutron Source for Electronuclear Installation</b> , Korenev, S.A., Puzynin, I.V., Samoilov, V.N., Sissakian, A.N. ....	615
P-2-44 • <b>Intensive Neutron Source Based on Powerful Electron Linear Accelerator LIA-30 and Pulsed Nuclear Reactor FR-1</b> , Bossamykin, V.S., Koshelev, A.S., Gerasimov, A.I., Gordeev, V.S., Grishin, A.V., Averchenkov, V.Ya., Lazarev, S.A., Maslov, G.N., Odintsov, Yu.M. ....	619
P-2-45 • <b>Monte Carlo Simulation of High-Flux 14 MeV Neutron Source Based on Muon Catalyzed Fusion Using a High-Power 50 MW Deuteron Beam</b> , Vecchi, M., Karmanov, F.I., Latysheva, L.N., Pshenichnov, I.A. ....	623
P-2-47 • <b>The NIKE Electron Beam-Pumped KrF Laser Amplifiers</b> , Serlin, V., Sethian, J.D., Pawley, C.J., Obenschein, S.P., Gerber, K.A., Deniz, A.V., Lehecka, T., Webster, W. ....	627
P-2-48 • <b>AIRIX at CESTA</b> , Anthouard, P., Bardy, J., Bonnafond, C., Delsart, P., Devin, A., Eyharts, P., Eyl, P., Guilhelm, D., Labrousche, J., Launspach, J., De Mascureau, J., Merle, E., Picon, J.C., Roques, A., Thevenot, M., Villate, D., Voisin, L. ....	628
P-2-50 • <b>Space Power Distribution of Soft X-Ray Source ANGARA-5-1</b> , Dyabilin, K.S., Fortov, V.E., Grabovskii, E.V., Lebedev, M.E., Smirnov, V.P. ....	632
P-2-51 • <b>Dielectric-Filled Radiofrequency Linacs</b> , Faehl, R.J., Keinigs, R.K., Pogue, E.W. ....	636
P-2-52 • <b>Operation of LIA-30 Linear Induction Accelerator in the Mode of Generation of Two Bremsstrahlung Pulses</b> , Bossamykin, V.S., Gerasimov, A.I., Gordeev, V.S., Grishin, A.V., Gritsina, V.P., Tarasov, A.D., Fedotkin, A.S., Lazarev, S.A., Averchenkov, V.Ya. ....	640
P-2-53 • <b>X-Ray Radiation Source Based on a Plasma Filled Diode</b> , Popkov, N.F., Kargin, V.I., Ryaslov, E.A., Pikar', A.S. ....	644

# PAPER INDEX - Volume II

## Contributed Papers P-2 - continuation from Volume I

P-2-54 • <b>Ironless Betatrons - Short Radiation Pulse Generators for Roentgenography of Fast-Going Processes</b> , Pavlovskii, A.P., Zenkov, D.I., Kuropatkin, Yu.P., Mironenko, V.D., Suvorov, V.N. ....	649
P-2-55 • <b>Determination of the Effective Impulse Time Duration of Interaction of Soft X-Radiation with Matter</b> , Dyabilin, K.S., Fortov, V.E., Grabovskii, E.V., Lebedev, M.E., Smirnov, V.P. ....	653
P-2-56 • <b>"INTERRAD" - Inductive Terawatt X-Ray Generator (project)</b> , Popkov, N.F., Pikar', A.S., Kargin, V.I., Ryaslov, E.A., Lyubomirskii, A.G. ....	656
P-2-57 • <b>New Bifocal Pinch Experiment SPEED-3</b> , Raacke, J., Berntien, U., Decker, G., Kies, W., Roewekamp, P. ....	659
P-2-58 • <b>Plasma Flow Discharge Researches at the PIRIT-2000 Facility</b> , Popkov, N.F., Ryaslov, E.A., Kargin, V.I., Pikar', A.S., Vorontsov, V.I., Kotel'nikov, D.V., Melkozerov, A.V. ....	663
P-2-59 • <b>A 10 TW Pulsed Energy Complex 'PIRIT-2000' for Investigation of Short-Wave Radiation</b> , Popkov, N.F., Ryaslov, E.A., Kargin, V.I., Pikar', A.S., Vorontsov, V.I., Kotel'nikov, D.V., Melkozerov, A.V. ....	667
P-2-62 • <b>Focusing of Megaampere Electron Beam in Gas Cell for Production of Flash X-Ray Source</b> , Zinchenko, V.I., Chlenov, A.M., Shijan, V.D. ....	671
P-2-63 • <b>Optimization of the Linear Induction Accelerator Construction for Maximizing the Bremsstrahlung Output</b> , Zinchenko, V.I., Toulisov, E.V., Chlenov, A.M., Shijan, V.D. ....	675
P-2-64 • <b>Space and Time Resolved Observations of Hot Spots Dynamics in a Vacuum Spark Discharge</b> , Chuaqui, H., Favre, M., Saavedra, R., Wyndham, E., Choi, P., Dumitrescu-Zoita, C., Soto, L. ....	679
P-2-65 • <b>Imaging of Exploding Wire Plasmas by High-Luminosity Monochromatic X-Ray Backlighting Using an X-Pinch Radiation Source</b> , Pikuz, S.A., Shelkovenko, T.A., Romanova, V.M., Hammer, D.A., Faenov, A.Ya., Pikuz, T.A. ....	683
P-2-90 • <b>Electron Beam Effects on the Spectroscopy of Satellite Lines in Aluminum X-Pinch Experiments</b> , Abdallah Jr., J., Faenov, A.Ya., Hammer, D.A., Pikuz, S.A., Csanak, G., Clark, R.E.H., Romanova, V.M., Shelkovenko, T.A. ....	687
P-2-66 • <b>Research of Generation Mechanism of Plasma Points in Z-Pinch</b> , Afonin, V.I., Garafov, A.M., Kovalev, V.P., Lazarchuk, V.P., Ostashev, V.I., Petrov, S.I., Potarov, A.V. ....	691
P-2-67 • <b>On the Ionization-Temperature Instability Role in Z-Pinch Hot Spots Generating</b> , Afonin, V.I., Diyankov, O.V., Glazyrin, I.V., Koshelev, S.V. ....	697
P-2-92 • <b>About Possible Mechanism of Generation of Plasma Points in Plasma of Multicharged Ions of Fast Z-Pinch</b> , Afonin, V.I., Voronov, B.F., Zakharov, A.E., Murugov, V.M., Ponomarev, S.V., Senikh, A.V. ....	701
P-2-68 • <b>Suppression of Rayleigh-Taylor Instability in Z-Pinch Loads with Tailored Density Profiles</b> , Cochran, F.L., Velikovich, A.L., Davis, J. ....	705
P-2-69 • <b>Limitations on the K-Shell X-Ray Conversion Efficiency of a Krypton Z-Pinch Plasma</b> , Davis, J., Giuliani Jr., J.L., Rogerson, J., Thornhill, J.W. ....	709
P-2-70 • <b>2.5 D Numerical Method for MHD Equation with Magnetic Diffusion in Arbitrary Moving Coordinate System for Z-Pinch Plasma Simulation</b> , Diyankov, O.V., Glazyrin, I.V., Koshelev, S.V. ....	713
P-2-71 • <b>Numerical Modelling of MHD Instabilities in Z-Pinch Hot Spot</b> , Glazyrin, I.V., Diyankov, O.V., Karlykhanov, N.G., Koshelev, S.V. ....	717

P-2-72 • <b>Sheath Broadening in Imploding Z-Pinches Due to Large-Bandwidth Rayleigh-Taylor Instability</b> , Hammer, J.H., Eddleman, J.L., Tabak, M., Toor, A., Zimmerman, G.B., De Groot, J.S. ....	721
P-2-73 • <b>Numerical Analysis of Cold Core Formation During Wire Electroexplosion</b> , Karlykhanov, N.G., Glazyrin, I.V., Diyankov, O.V. ....	725
P-2-74 • <b>On the Necessary Modification of Z-Pinch MHD-Models</b> , Kingsep, A., Rudakov, L. ....	729
P-2-75 • <b>X-ray Spectroscopic Characterization of Hot Spots in Neon Z-Pinch</b> , Renner, O., Krouský, E., Krejčí, A., Pfeifer, M., Foerster, E. ....	733
P-2-76 • <b>Diagnostics of Low Energy Carbon Fibre Z-Pinch</b> , Kubeš, P., Kravárik, J., Skladnik-Sadowska, E., Baranowski, J., Paduch, M., Tomaszewski, K., Gogolewski, P. ....	737
P-2-77 • <b>Concept and Elementary Theory of a Sandwich Liner</b> , Linhart, J.G., Chittenden, J.P. ....	741
P-2-78 • <b>Optimized Debris Stoppers for Z-Pinches</b> , Gondarenko, N.A., Pereira, N.R. ....	745
P-2-79 • <b>PRS and POS/PRS Coupling Experiments on HAWK</b> , Peterson, G.G., Apruzese, J.P., Comisso, R.J., Fisher, A., Kellogg, J.C., Mosher, D., Stephanakis, S.J., Thornhill, J.W., Weber, B.V., Young, F.C. ....	749
P-2-80 • <b>X-Ray Emission from a High-Atomic-Number Z-Pinch Plasma Created from Compact Wire Arrays</b> , Sanford, T.W.L., Mosher, D., De Groot, J.S., Hammer, J.H., Marder, B.M., Maxon, S., Nash, T.J., Spielman, R.B., Springer, P.T., Struve, K.W., Thoe, R.S., Welch, D.R., Alley, W.E., Bruns, C., Eddleman, J.L., Emic, J., Gilliland, T.L., Hernandez, J., Jobe, D., McGurn, J.S., Mock, R.C., Seamen, J.F., Vargas, M., Zimmerman, G.B. ....	753
P-2-81 • <b>Numerical Simulation of PRS Yields for a Pulsed Power DECADE-QUAD Generator</b> , Giuliani, J.L., Schneider, R.F., Rogerson, J., Davis, J. ....	757
P-2-82 • <b>Optimization of Gas Target Production for Z-Pinch Implosions</b> , Semushin, S., Etlicher, B., Rouille, C. ....	758
P-2-83 • <b>Space and Time Resolved Observations of Plasma Dynamics in a Compressional Gas-Embedded Z-Pinch</b> , Soto, L., Chuaqui, H., Favre, M., Saavedra, R., Wyndham, E., Aliaga-Rossel, R., Mitchell, I. ....	762
P-2-84 • <b>Computer Modelling of a Small Neon Gas-Puff Pinch</b> , Ullschmied, J. ....	766
P-2-86 • <b>Hydrosimulations of Z-Pinch</b> , Benattar, R., Ney, P. ....	771
P-2-87 • <b>Numerical Modelling of High-Temperature Plasma in a Strong Magnetic Field at RFNC-VNIIEF</b> , Diyankov, O.V., Glazyrin, I.V., Karlykhanov, N.G., Zubov, A.D. ....	775
P-2-88 • <b>Current Instability of "Snow Plough"</b> , Rudakov, L.I., Sevastianov, A.A. ....	779
P-2-89 • <b>Radiation from Turbulent Intense Z-Pinches</b> , Rudakov, L.I., Sudan, R.N. ....	780

### Contributed Papers P-3

P-3-2 • <b>Particle Acceleration by Inverse-Weibel Instability</b> , Kawata, S. ....	781
P-3-3 • <b>High Current Pulsed Ion Inductor Accelerator for Destruction of Radioactive Wastes</b> , Korenev, S.A., Puzynin, I.V., Samoilov, V.N., Sissakian, A.N. ....	785
P-3-4 • <b>Processes in a Dense Long-Pulse Electron Beam Focused on a Solid Target</b> , Arkhipov, A.V., Sominski, G.G. ....	789
P-3-6 • <b>Application of an Intense Long Pulse Electron Beam for Investigation of ITER Divertor Material Erosion</b> , Engelko, V., Andreev, A., Komarov, O., Kovalev, V., Lyublin, B. ....	793
P-3-7 • <b>Electron-Beam Sustained Glow Discharge in a N<sub>2</sub>+CO Gas Mixture at Cryogenic Temperature</b> , Azharonok, V.V., Filatova, I.I., Chubrik, N.I., Shimanovich, V.D., Gurashvili, V.A., Kuzmin, V.N., Turkin, N.G., Vaselenok, A.A. ....	797

P-3-8 • Processing of Metals by Powerful Electron Beams, Gofman, Yu.I. ....	801
P-3-9 • Use of Charged Particles Beams for Research of Mechanical Behaviour of Thermonuclear Reactor First Wall Candidate-Materials, Gofman, Yu.I. ....	805
P-3-11 • Modification of Material Surfaces by the Pulsed Electron Beam Facility "GESA", Mueller, G., Schumacher, G., Strauss, D., Engelko, V., Andreev, A., Kovalev, V. ....	809
P-3-12 • Modification of Titanium Alloy Parts Properties by Intensive Current Electron Beam, Nochovnaya, N.A., Shulov, V.A., Proskurovsky, D.I., Rothstein, V.P. ....	813
P-3-17 • High Power Pulse Electron Beam Modification and Ion Implantation of Hg(1-X)CdXTe Crystals, Voitsekhovskii, A.V., Remnev, G.E., Opekunov, M.S., Kokhanenko, A.P., Korotaev, A.G., Denisov, Yu.A., Oucherenko, D.A. ....	817
P-3-18 • Influence of Pulsed Electron and Ion Beams of Energy on the Structural and Mechanical Properties of Metals, Romanov, I.G., Tsareva, I.N., Romanova, G.M. ....	821
P-3-19 • SO <sub>2</sub> , NO <sub>x</sub> and H <sub>2</sub> S Oxidation by Simultaneous Application of Electron Beam and Electric Field in Humid Air, Salnikov, L.I., Nichipor, H., Radjuk, E., Chmielewski, A.G., Zimek, Z. ....	824
P-3-21 • Research of Action of a Pulsing Frequent Electron Beam on Micro-organisms in Water Solutions, Sokovnin, S.Yu., Kotov, Yu.A., Mesyats, G.A. ....	828
P-3-22 • About Transport Current Change in High-Temperature Superconducting Real Wires and Tapes as a Result of Electron Irradiation, Davlatjan, T.A., Kalachnikov, V.V., Kruglov, V.S., Tokarev, A.S. ....	832
P-3-23 • Influence of Electron Irradiation on Current Distribution Process in Granulated High-Temperature Superconducting Real Wires and Tapes, Davlatjan, T.A., Kalachnikov, V.V., Kruglov, V.S., Tokarev, A.S. ....	836
P-3-92 • Mass-Transport in W-Cu System under High Energy Electron Irradiation, Bondarenko, G.G., Tikhonov, A.N., Shlenov, Yu.V., Yakunkin, M.M. ....	840
P-3-25 • Influence of Carbon and Nitrogen Ions on the Structure and Properties of Carbon Fibers, Gavrillov, N.W., Emlin, D.R., Ligachev, A.E., Ligacheva, E.A., Nochovnaya, N.A., Karpova, I.G. .	844
P-3-26 • Metal Surface Characterization by Intense Pulsed Ion Beam Irradiation, Hashimoto, Y., Yatsuzuka, M., Uchida, H., Yamasaki, T. ....	848
P-3-28 • Ion Beam Treatment of PE and PTFE and their Adhesion Abilities, Klyachkin, Yu., Kondyurin, A. ....	852
P-3-29 • Structure of Polymer Surface after Pulse Ion Beam Treatment, Klyachkin, Yu., Kondyurin, A., Tereshatova, E., Yakusheva, D. ....	853
P-3-31 • The Use of Pulsed Power Ion/Electron Beams for Studying of Units of Electronuclear Reactor, Korenev, S.A., Korenev, A.S., Puzynin, I.V., Samoilov, V.N., Sissakian, A.N. ....	854
P-3-33 • Pulsed Metal-Ion Beams for Modifications of Solids, Langner, J., Piekoszewski, J., Stanislawski, J. ....	860
P-3-37 • Chain of Phase Transitions in Metals Subjected to Heavy Inert Gas Ion Bombardment, Panesh, A.M., Lozovskii, A.D. ....	864
P-3-39 • The Nuclear Interaction Analysis Methods for Diagnostics of High Power Ion Beam Technologies, Ryzhkov, V.A., Grushin, I.I., Remnev, G.E. ....	869
P-3-40 • The Deposition of Thin Metal Films at High-Intensity Pulsed-Ion-Beam Influence on the Metals, Remnev, G.E., Zakoutaev, A.N., Grushin, I.I., Matvienko, V.M., Potyomkin, A.V., Ryzhkov, V.A., Ivanov, Yu.F., Chernikov, E.V. ....	873
P-3-41 • The Application of High Power Ion Beams in Aircraft Engine Building for Reconstruction of Refractory Alloy Parts, Shulov, V.A., Nochovnaya, N.A., Remnev, G.E. ....	878

P-3-42 • <b>Modelling of Ion Beam Surface Treatment</b> , Stinnett, R.W., Maenchen, J.E., Renk, T.J., Struve, K.W., Campbell, M.M. ....	882
P-3-43 • <b>Short-Pulsed-Electric Degradation of Aqueous Organics</b> , Bystritskii, Vit.M., Gonzales, A., Olson, T., Puchkarev, V., Rosocha, I., Wessel, F., Yankelevich, Y. ....	886
P-3-44 • <b>Thermal Imaging Experiment on ANACONDA Ion Beam Generator</b> , Jiang, W., Yatsui, K., Olson, J.C., Davis, H.A. ....	890
P-3-45 • <b>Preparation of Thin Films by Ablation with the ANACONDA Ion Beam Generator</b> , Yatsui, K., Jiang, W., Davis, H.A., Olson, J.C., Waganaar, W.J., Rej, D. ....	894
P-3-46 • <b>Study of YBCO Thin Films Deposited by Intense Pulsed Light Ion Beam Evaporation</b> , Grigoriu, C., Chamdani, E.P.A., Miu, D., Masugata, K., Yatsui, K. ....	898
P-3-93 • <b>High Power Ion Beam Influence to Stainless Steels</b> , Remnev, G.E., Struts, V.K. ....	902
P-3-47 • <b>Energy Characteristics of the Process of Air Scrubbing from Hydrocarbon Contaminants in a Barrier-Discharge Reactor</b> , Bugaev, S.P., Kuvshinov, V.A., Sochugov, N.S., Khryapov, P.A. ....	905
P-3-48 • <b>Compact Repetitive Generators for Medical X-Ray Diagnostics</b> , Filatov, A.L., Korzhenevskii, S.R., Kotov, Yu.A., Mesyats, G.A., Motovilov, V.A., Scotnikov, V.A. ....	909
P-3-50 • <b>Compact High-Current, Subnanosecond Electron Accelerator</b> , Shpak, V.G., Shunailov, S.A., Ulmaskulov, M.R., Yalandin, M.I., Pegel, I.V., Tarakanov, V.P. ....	913
P-3-51 • <b>Nuclear Reactions Cross Section Measurement Using Z-Pinch Technology</b> , Bulgakov, T., Bystritskii, Vit.M., Mesyats, G.A., Sinebryukhov, V.A., Sinebryukhov, A.A., Bystrickii, V., Grebenyuk, V., Parzhitskii, S., Sabirov, B., Stolupin, V., Luchinsky, A., Chaikovski, S., Mahrin, V., Ratakhin, N., Sorokin, S., Gula, A., Filipowicz, M., Wozniak, J. ....	917
P-3-52 • <b>About Using of Ion Accelerators in Accelerator Driven Systems</b> , Chigrinov, S., Kievitskaya, A., Petlytski, V., Rutkovskaia, K. ....	921
P-3-58 • <b>The Experimental Investigation of Explosive Opening Switch</b> , Zhang, J., Zhong, H., Li, Ch., Liu, Y., Cheng, D., Peng, X. ....	924
P-3-59 • <b>High Power, Repetitive Stacked Blumlein Pulse Generators</b> , Davanloo, F., Borovina, D.L., Korioth, J.L., Krause, R.K., Collins, C.B., Agee, F.J., Kingsley, L.E. ....	928
P-3-62 • <b>Inductive Line Energy Storage Generator</b> , Choi, P. ....	932
P-3-66 • <b>Schemes of High-Power Pulsed Generators with Inductive Storages on Stepped Lines</b> , Gordeev, V.S., Bossamykin, V.S. ....	938
P-3-67 • <b>The Nanosecond Generator RG-1 with Near-Rectangular Pulse</b> , Bulan, V.V., Grabovski, E.V., Gribov, A.N., Luzhnov, V.G. ....	942
P-3-68 • <b>Protection of Control and Monitoring Equipment from Electromagnetic Noise in the 67 MJ, 50 kV Capacitor Bank</b> , Galakhov, I.V., Gasheev, A.S., Grusin, I.A., Gudov, S.N., Kuz'michev, Yu.P., Murugov, V.M., Osin, V.A., Pankratov, V.I., Pegoev, I.N. ....	946
P-3-69 • <b>Diagnostics of the 67 MJ, 50 kV Pulsed Power Capacitor Bank</b> , Galakhov, I.V., Gasheev, A.S., Grusin, I.A., Gudov, S.N., Murugov, V.M., Osin, V.A., Pankratov, V.I., Pegoev, I.N. ....	950
P-3-70 • <b>PFN-Marx Pulsers for HPM Testing Application</b> , Kekez, M.M. ....	954
P-3-71 • <b>Controlled Multiple Channel Switch</b> , Kormilitsyn, A.I., Diyankov, V.S. ....	958
P-3-72 • <b>Energy Concentration on S-300 Pulsed Power Generator</b> , Bakshaev, Yu.L., Chernenko, A.S., Korolev, V.D., Mishiritskiy, V.I., Zazhivikhin, V.V. ....	962
P-3-73 • <b>High-Voltage Nanosecond Generator with Pulse Repetition Rate of 1,000 p.p.s.</b> , Gubanov, V.P., Korovin, S.D., Stepchenko, A.S. ....	965



P-3-74 • <b>High-Voltage Many-Pulses Generator with Inductive Energy Store and Fuse,</b> Kovalev, V.P., Diyankov, V.S., Kormilitsyn, A.I., Lavrentyev, B.N. ....	969
P-3-75 • <b>Functioning of High-Tc Bulk Superconductor Lenses (Supertrons) for Intense Electron Beams,</b> Matsuzawa, H., Matsushita, A., Ueda, Y., Matsubara, H., Suganomata, S. ....	973
P-3-76 • <b>Synchronization of 67 MJ, 50 kV Pulsed Power Capacitor Banks Operation,</b> Besuglov, V.G., Galakhov, I.V., Gasheev, A.S., Grusin, I.A., Gudov, S.N., Kirillov, G.A., Murugov, V.M., Osin, V.A., Petrakov, V.N. ....	977
P-4-82 • <b>High-Power Semiconductor RSD-Based Switch,</b> Bezuglov, V.G., Galakhov, I.V., Grusin, I.A., Zolotovskiy, V.I., Gudov, S.N., Logutenko, S.L., Murugov, V.M., Osin, V.A., Petrakov, V.N., Grekhov, I.V., Korotkov, S.V., Kovtun, V.I., Martynenko, V.A., Chumakov, G.D. ....	981
P-3-77 • <b>Nanosecond Electron Beams Compact Generator,</b> Konkin, D.V., Nagovitsin, A.Yu., Pavlov, S.S., Popkov, N.F. ....	985
P-3-79 • <b>Design and Analysis of the PBFA-Z Vacuum Insulator Stack,</b> Shoup, R.W., Long, F., Martin, T.H., Stygar, W.A., Ives, H., Spielman, R.B., Struve, K.W., Mostrom, M., Corcoran, P., Smith, I. ....	989
P-3-80 • <b>Characterization of Diamond Film and Bare Metal Photocathodes as a Function of Temperature and Surface Preparation,</b> Shurter, R.P., Moir, D.C., Devlin, D.J. ....	993
P-3-81 • <b>Development Status of Triggered Vacuum Switches at All-Russian Electrotechnical Institute and Prospects of Its Applications,</b> Alfverov, D.F., Vozdvijenskii, V.A., Sidorov, V.A. .	999
P-3-82 • <b>DECADE Design and Testing Status,</b> Sincerny, P., Childers, K., Goyer, J., Kortbawi, D., Roth, I., Stallings, C., Dempsey, J., Schlitt, L. ....	1003
P-3-83 • <b>Explosive Opening Switches with Controlled Time of Current Rising in the Load,</b> Chernyshev, V.K., Volkov, G.I., Ivanov, V.A., Pak, S.V., Skobelev, A.N. ....	1008
P-3-84 • <b>Development of Highly Repetitive Pulse Power System Using Amorphous Metallic Cores,</b> Masugata, K., Yatsui, K. ....	1010
P-3-85 • <b>Printed Board Dipole Trim Magnet Design for 20 MeV LIA,</b> Liu, Ch., Zhu, W., Zhang, K., Zhang, W., Yu, H. ....	1014
P-3-86 • <b>Halo Formation in RMS Matched Intense Ion Beams,</b> Chen, Ch., Fink, Y., Davidson, R.C., Qian, Q. ....	1018
P-3-87 • <b>Equivalent Circuit Modeling of Space Charge Dominated Magnetically Insulated Transmission Lines,</b> Hiraoka, K., Nakajima, M., Horioka, K. ....	1022

### Contributed Papers P-4

P-4-1 • <b>High-Voltage Space Tether for Particle Scattering in Earth's Radiation Belts,</b> Danilov, V.V., Mirnov, V.V., Ucer, D. ....	1027
P-4-2 • <b>Electron Beams in Large Coronal Loops,</b> Karlický, M., Aurass, H., Mann, G. ....	1031
P-4-4 • <b>Relativistic Electron Beam Dynamics in the Pulsar Magnetosphere,</b> Chedia, O.V., Kahniashvili, T.A., Machabeli, G.Z., Nanobashvili, I.S. ....	1035
P-4-6 • <b>Energetic High Current Density Electron/Ion Beam Generation in Plasma Opening Switches,</b> Krasik, Ya.E., Arad, R., Weingarten, A., Maron, Y. ....	1039
P-4-7 • <b>CO Laser Interferometer for REB-Plasma Experiments,</b> Burmasov, V.S., Kruglyakov, E.P. ..	1046
P-4-9 • <b>Measurements of the Initial Density Distribution of Gas Puff Liners by Using Rayleigh Scattering,</b> Kalinin, Yu.G., Shashkov, A.Yu. ....	1050

<b>P-4-10 • Refractive Index Gradient Diagnostics: Analysis of Different Optical Systems and Application to the COBRA Ion Diode</b> , Knyazev, B.A., Greenly, J.B., Hammer, D.A., Krastev, E.G., Cuneo, M.E. ....	1054
<b>P-4-11 • Spectroscopic Determination of the Magnetic Field Distribution in a Gas-Puff Z-Pinch Plasma</b> , Gregorian, L., Davara, G., Kroupp, E., Maron, Y. ....	1058
<b>P-4-12 • Spectroscopic Investigations of the Implosion Dynamics of a Gas-Puff Z-Pinch Plasma</b> , Davara, G., Gregorian, L., Kroupp, E., Peter, B., Fisher, V., Maron, Y. ....	1063
<b>P-4-14 • Application of Charge Coupled Devices as Spatially-Resolved Detectors for X-Ray Spectrograph</b> , Attelan-Langlet, S., Etlicher, B., Mishenski, V.O., Papazian, Yu.V., Smirnov, V.P., Volkov, G.S., Zaitsev, V.I. ....	1064
<b>P-4-15 • CR-39 Nuclear Track Detector Application for the Diagnostics of Low Energy High Power Ion Beams</b> , Opekounov, M.S., Pechenkin, S.A., Remnev, G.E., Ivonin, I.V. ....	1068
<b>P-4-16 • Voltmeter with Compton Electrons</b> , Pereira, N.R., Gorbics, S.G., Weidenheimer, D.M. ....	1071
<b>P-4-17 • The Role of Electron Beams and New Excitation Channels and for Dielectronic Satellites in Dense Plasmas</b> , Rosmej, F.B., Bryunetkin, B.A., Faenov, A.Ya., Skobelev, I.Yu., Kalashnikov, M.P., Nickles, P.V., Schnuerer, M. ....	1075
<b>P-4-18 • Visualisation of the High-Current E-Beams on Solid Surfaces</b> , Solomonov, V.I., Osipov, V.V., Mikhailov, S.G., Lipchak, A.I. ....	1076
<b>P-4-21 • Characteristics of Charge Coupled Devices over X-Ray Spectral Band</b> , Mishenski, V.O., Volkov, G.S., Zaitsev, V.I., Zazhivikhin, V.V. ....	1080
<b>P-4-24 • Study of Plasma in MAGO Chamber by Own Neutron Radiation</b> , Burenkov, O.M., Garanin, S.F., Demin, A.N., Dudin, I.F., Korchagin, V.P., Morozov, I.V., Mokhov, V.N., Pavlovsky, E.S., Chernyshev, V.K., Yakubov, V.B. ....	1084
<b>P-4-25 • Focused Proton Beams Propagating in Reactor of Fusion Power Plant</b> , Niu, K. ....	1091
<b>P-4-26 • Energy Loss of Heavy Ion Beams in Plasma</b> , Okada, T., Hotta, T. ....	1095
<b>P-4-27 • Stable Propagation of Light-Ion Beam in Inertial Confinement Fusion</b> , Okada, T., Murakami, H. ....	1099
<b>P-2-91 • The Interaction Physics of the Fast Ignitor Concept</b> , Deutsch, C., Furukawa, H., Mima, K., Murakami, M., Nishihara, K. ....	1103
<b>P-4-32 • Investigation of the Composition of an Ion Beam Produced Using a Multi Arc Ion Source</b> , Engelko, V., Giese, H., Mischin, M., Schalk, S., Tsibin, O.Y. ....	1107
<b>P-4-33 • Measurement of Extent of Intense Ion Beam Charge Neutralization</b> , Engelko, V., Giese, H., Schalk, S. ....	1111
<b>P-4-97 • Charge Neutralization of Small Ion Beam Clumps</b> , Welch, D.R., Olson, C.L., Hanson, D.L. ..	1115
<b>P-4-35 • Ne Beam-Kr Target Interaction</b> , Fortov, V.E., Kostin, V.V., Vorob'ev, V.S., Kulish, M.I., Mintsev, V.B., Hoffman, D. ....	1119
<b>P-4-39 • Recent Results from Experimental and Numerical Investigations of the Selfmagnetically B<sub>0</sub>-Insulated Ion Diode</b> , Bauer, W., Hoppé, P., Bachmann, H., Bluhm, H., Buth, L., Massier, H., Rusch, D., Stein, E., Stoltz, O., Vaeth, W., Westermann, T. ....	1123
<b>P-4-40 • Ion Diode Diagnostics to Resolve Beam Quality Issues</b> , Bluhm, H., Arzhannikov, A., Buth, L., Hoppé, P., Licht, V., Matveenko, A., Rusch, D., Stoltz, O., Singer, J., Singleton, C., Tauschwitz, A., Vaeth, W., Yoo, S. ....	1127
<b>P-4-42 • Electron Inertia Effects for an Electron Fluid Model by the Applied-B Ion Diode</b> , Gordeev, A.V., Levchenko, S.V. ....	1131
<b>P-4-43 • The Vortex-Like Self-Consistent Electron Fluid Model by the Applied-B Ion Diode: Equilibrium and Instability</b> , Gordeev, A.V. ....	1135

P-4-44 • <b>Electron Sheath Collapse in an Applied-B Ion Diode</b> , Grechikha, A.V. ....	1139
P-4-45 • <b>Ion Diode Optics: Measurement of Divergence and Aiming of Beams for Transport to Light-Ion ICF Targets</b> , Krastelev, E.G., Knyazev, B.A., Lindholm, F., Hammer, D.A., Kusse, B.R., Greenly, J.B. ....	1143
P-4-46 • <b>Modification of Diode Characteristics by Electron Back-Scatter from High-Atomic-Number Anodes</b> , Mosher, D., Cooperstein, G., Rose, D.V., Swanekamp, S.B. ....	1147
P-4-47 • <b>Experimental Observations of Effects of Electron Backscattering from High-Atomic-Number Anodes in Large-Aspect-Ratio, Electron Beam Diodes</b> , Cooperstein, G., Mosher, D., Stephanakis, S.J., Swanekamp, S.B., Weber, B.V., Young, F.C. ....	1151
P-4-48 • <b>Self-Pinch Focusing Experiments Performed on the KALIF Accelerator Using the Bappl Diode</b> , Hoppé, P., Nakagawa, Y., Bauer, W., Bluhm, H., Buth, L., Guth, H., Hellmann, A., Massier, H., Rusch, D., Stoltz, O., Tauschwitz, A., Vaeth, W. ....	1155
P-4-49 • <b>Ion Diode Simulation with a Finite-Volume PIC Approach for the Numerical Solution of the Maxwell-Lorentz System</b> , Munz, C.-D., Schneider, Rud., Stein, E., Voss, U., Westermann, T., Krauss, M. ....	1159
P-4-50 • <b>Characteristics of Magnetically Insulated Diode in a Multi-Shot Operation</b> , Chishiro, E., Masugata, K., Yatsui, K. ....	1163
P-4-51 • <b>Evaluation of the Effect of Anode Groove Pitch to Ion Beam Focusibility on Spherical Plasma Focus Diode</b> , Imanari, K., Jiang, W., Masugata, K., Yatsui, K. ....	1167
P-4-52 • <b>The Cornell Field-Reversed Ion Ring Experiment FIREX: Experimental Design and First Results</b> , Podulka, W.J., Greenly, J.B., Anderson, D.E., Glidden, S.C., Hammer, D.A., Omelchenko, Yu.A., Sudan, R.N. ....	1171
P-4-53 • <b>3-D Studies of the Formation and Stability of Strong Ion Rings</b> , Omelchenko, Yu.A., Sudan, R.N. ....	1175
P-4-57 • <b>High Current Ion Injectors for Long-Pulse Induction Accelerators</b> , Hasegawa, J., Nakai, H., Iwasaki, H., Nakajima, M., Horioka, K., Kawasaki, S. ....	1179
P-4-61 • <b>Microstructured Liquid Metal Electron and Ion Sources (MILMES/MILMIS)</b> , Mitterauer, J. ....	1183
P-4-93 • <b>Generation of High Intensity and High Power Metal Ions by Vacuum Arc TAMEK Sources</b> , Tolopa, A.M. ....	1187
P-4-96 • <b>Experiments on Ion Space-Charge Neutralization with Pulsed Electron Beams</b> , Herleb, U., Riege, H. ....	1191
P-4-99 • <b>Photo-Resonance Anode Plasma Production by a KrF Laser</b> , Knyazev, B.A., Melnikov, P.I., Doroshkin, A.A., Matveenko, A.N., Bluhm, H. ....	1195
P-4-63 • <b>Interaction of a Fast Magnetic Field with Non-Magnetized Plasma for the Plasma Opening Switch Case</b> , Chuvatin, A.S., Rudakov, L.I., Etlicher, B. ....	1199
P-4-64 • <b>Experimental Characteristics of GIT-8 Plasma Opening Switch</b> , Chuvatin, A.S., Rouille, C., Etlicher, B., Bayol, F., Morell, A., Kim, A., Loginov, S.V., Kokshenev, V.A., Koval'chuk, B.M. ....	1203
P-4-65 • <b>Anomalous Resistivity in the Plasma Opening Switch</b> , Dolgachev, G.I., Zakatov, L.P., Kalinin, Yu.G., Kingsep, A.S., Nitishinski, M.S., Ushakov, A.G. ....	1207
P-4-67 • <b>Investigation of a Strip-Line Long-Conduction-Time Plasma Opening Switch on MAG-1'</b> , Frolov, V., Chuvatin, A.S., Semushin, S., Etlicher, B. ....	1211
P-4-68 • <b>Theoretical Modelling of the Magnetic Field-Penetration in a Plasma Opening Switch Experiment</b> , Gomberoff, K., Shpitalnik, R.R., Weingarten, A., Krasik, Ya.E., Maron, Y. ....	1215
P-4-69 • <b>Spectroscopic Investigation of the Time Dependent Magnetic Field Distribution in a Plasma Opening Switch</b> , Shpitalnik, R.R., Weingarten A., Gomberoff, K., Krasik, Ya.E., Arad, R., Sarfaty, M., Maron, Y. ....	1216

P-4-71 • <b>Experimental Investigation of the Ion Current Distribution in Microsecond Plasma Opening Switch</b> , Bystrickii, Vit.M., Grigor'ev, S.V., Kharlov, A.V., Sinebryukhov, A.A. ....	1217
P-4-72 • <b>Experimental Investigation of the Material Surface Modification in Microsecond Plasma Opening Switch</b> , Bystrickii, Vit.M., Grigor'ev, S.V., Kharlov, A.V., Sinebryukhov, A.A., Burkov, P.V., Grigoryev, V.P., Koval, T. ....	1221
P-4-73 • <b>Effect of Anomalous Resistivity on the Dynamics of Plasma Switching</b> , Kingsep, A., Munier, A. ....	1225
P-4-74 • <b>Energetic Ion Emission in a Positive Polarity Nanosecond Plasma Opening Switch</b> , Sarfaty, M., Krasik, Ya.E., Weingarten, A., Fruchtman, A., Maron, Y. ....	1229
P-4-79 • <b>Preliminary Studies on a Plasma Focus Opening Switch</b> , Wong, C.S., Choi, P., Moo, S.P., Singh, J.P. ....	1233
P-4-80 • <b>Two Dimensional Hall MHD Modeling of a Plasma Opening Switch with Density Inhomogeneities</b> , Zabaidullin, O., Chuvatin, A.S., Etlicher, B. ....	1237
P-4-81 • <b>Theoretical Model of the SOS Effect</b> , Darznek, S.A., Mesyats, G.A., Rukin, S.N., Tsiranov, S.N. ....	1241
P-4-85 • <b>Inhomogeneous Mixing Effect of D and T Fuels on ICF Pellet Implosion</b> , Kawata, S., Kurawaki, K., Tuyuki, A., Hirota, K. ....	1245
P-4-86 • <b>Large-Size Pellet in Ion-Beam ICF</b> , Kawata, S., Kurawaki, K., Tuyuki, A., Hirota, K. ....	1249
P-4-87 • <b>Slowing Down of an Ablatively Accelerated Foil after Impact on a Stationary Target</b> , Marten, H., Goel, B., Hoebel, W. ....	1253
P-4-88 • <b>Temperature Diagnostics of KALIF Targets by Soft X-Ray Spectroscopy</b> , Meisel, G., Bluhm, H., Buth, L., Hoppe, P., Huetner, R., Rusch, D., Saenger, E., Schoen, T., Singer, J., Stoltz, O. ....	1257
P-4-89 • <b>Stability of Burning Wave in Practical Size of Target</b> , Niu, K. ....	1261
P-4-90 • <b>Plasma-Beam Interaction Experiment at TIT</b> , Ogawa, M., Neuner, U., Endou, T., Yamauchi, S., Nakajima, M., Horioka, K., Oguri, Y. ....	1265
P-4-92 • <b>Theoretical and Experimental Investigation of REB Interaction with Aerogel Targets</b> , Efremov, V.P., Fortov, V.E., Demidov, B.A., Ivonin, I.A., Vorobiev, O.Yu., Keeler, N. ....	1269

#### **Note**

*Missing code numbers belong to the pre-registered papers not presented at the conference. In a very few cases the full texts of papers were not available even two months after the deadline and, therefore, just the abstracts have been included in the Proceedings.*

# INVITED PAPERS

## **Session O-0**

J. Quintenz - SNL; V. Chernyshev - VNIIEF;  
B. Goel - FZK, K. Yatsui - LBT Nagaoka

## **Session O-1**

ICF, Accelerators, B&P Diagnostics

## **Session O-2**

Ion Beams, Ion Diodes

## **Session O-3**

PP technology, POS, BDTT

## **Session O-4**

Liners, Z-Pinches, Plasma Foci

## **Session O-5**

Electron Beam Physics, Beam-Plasma Systems

## **Session O-6**

HP Microwaves, FELs

## **Session O-7**

Industrial Applications of Beams and PP

## **Session O-8**

Radiation Sources

## PROGRESS IN PULSED POWER FUSION\*

J.P. Quintenz, R.G. Adams, J.E. Bailey, D.D. Bloomquist, G.A. Chandler, R.S. Coats, D.L. Cook, M.E. Cuneo, C. Deeney, M.S. Derzon, M.P. Desjarlais, R.J. Dukart, A.B. Filuk, T.A. Haill, D.L. Hanson, D.J. Johnson, M.L. Kiefer, R.J. Leeper, T.R. Lockner, B.M. Marder, M.K. Matzen, D.H. McDaniel, E.J. McGuire, T.A. Mehlhorn, C.W. Mendel, P.R. Menge, L.P. Mix, A.R. Moats, T.J. Nash, C.L. Olson, R.E. Olson, T.D. Pointon, J.L. Porter, T.J. Renk, S.E. Rosenthal, C.L. Ruiz, T.W.L. Sanford, J.F. Seamen, D.B. Seidel, S.A. Slutz, R.B. Spielman, W.A. Stygar, M.A. Sweeney, and G.C. Tisone.

*Sandia National Laboratories, P.O. Box 5800, Albuquerque, NM 87185-1191, USA*

### Abstract

Pulsed power offers an efficient, high energy, economical source of x-rays for inertial confinement fusion (ICF) research. We are pursuing two main approaches to ICF driven with pulsed power accelerators: intense light ion beams and z-pinches. This paper describes recent progress in each approach and plans for future development.

### Introduction

The United States Department of Energy has been funding research into Inertial Confinement Fusion since early 1970s. The long term goal of this ICF research is the production of high yield in the laboratory for Defense and Energy applications. High yield in this context means thermonuclear yield of 200-1000 MJ. Recently the Department has selected the laser technology to demonstrate ignition in the laboratory. The National Ignition Facility is a project in the United States aimed at building a large laser capable of delivering 1.8 MJ of  $3\omega$  (350 nm) light to a target. The 1.8 MJ of laser energy will result in  $\sim 100 - 150$  kJ of x-ray energy absorbed in the capsule. The predicted thermonuclear yield with this absorbed x-ray energy is 2 - 20 MJ. Ignition demonstration in the NIF would be a major step forward toward obtaining high yield in the laboratory. However, a high-yield target is expected to require approximately 1 MJ of x-rays absorbed in the capsule ablator with radiation symmetry on the surface of the capsule of better than 1%. In order to achieve this radiation symmetry, a large case-to-capsule radius ratio is needed. Consequently, a driver will be required with approximately 10 MJ incident on the target, prohibitively expensive using laser technology. In addition, any energy application of ICF will require a repetitive pulse capability (4 Hz); again, not possible with lasers. Pulsed-power-driven ICF offers an attractive alternative with affordable, high energy, high efficiency drivers and the potential for repetitive pulse operation. The pulsed power ICF program has two main elements: intense light ion beams and z-pinches. This paper provides an overview of recent progress in both of these pulsed power approaches as well as our plans for the future.

### Progress in Light Ion Beam Development

The baseline approach for a light-ion beam-driven high-yield capability (HYC), also called the Laboratory Microfusion Facility (LMF) includes 12 low-power ion beams with an on-target

\*This work was supported by the United States Department of Energy under Contract DE-AC04-94AL85000; work done in collaboration with the NRL, Cornell University, University of Wisconsin, Weizmann Institute, and Mission Research Corporation.

ion power of 5.4 TW each and 12 high-power beams ( $\sim 50$  TW each). For a recent review article on light ion ICF with extensive references see reference [1]. Each high power module would produce a 27 TW lithium beam at voltages ranging from 28 - 35 MV controlled so as to bunch the beam and increase the beam power by a factor of  $\sim 2$  as it travels from the diode to the target, resulting in a  $\sim 50$  TW beam at the target location. The required focal intensity is somewhat in excess of  $50 \text{ TW/cm}^2$ . Lithium ion beams have been focused on the Particle Beam Fusion Accelerator II (PBFA II) to intensities of  $2 \text{ TW/cm}^2$ . The resulting specific deposition in an ion-driven hohlraum was  $1400 \text{ TW/g}$  [2]. This represents the highest specific power deposition created by an ion beam. The achievement of a  $2 \text{ TW/cm}^2$  focal intensity was an improvement of over an order of magnitude in intensity between the period of 1990 through 1993. However, this rapid increase in focal intensity has been difficult to continue.

The available power brightness ( $I$ ) from a focused ion beam is determined principally by the beam microdivergence ( $\Delta\theta$ ) and the lithium beam power ( $P_i$ ) available ( $I \propto P_i/\Delta\theta^2$ ). Progress in understanding and reducing divergence has resulted in lithium beam microdivergence on PBFA II of 20 - 25 mrad. High yield facility microdivergence requirements depend on the mode of transport considered but will be between 6 and 12 mrad. Further improvement in beam divergence will likely rely upon improvements in source divergence, source uniformity, control of electromagnetic instabilities, and two-stage acceleration in which the ion longitudinal momentum is increased while maintaining the transverse momentum imparted in the first stage of acceleration.

Lithium ion power available has been shown, through a series of carefully diagnosed experiments, to be limited by an unwanted ion current flowing in parallel with the desired lithium beam. This parallel current (parallel load) has been designated the parasitic load. The parasitic load is composed of accelerated ions from the bulk and surface contamination in the ion source and surrounding hardware. Recently on the SABRE accelerator [3], through an extensive protocol of RF glow discharge cleaning and heating of the anode-cathode gap and impermeable anode coatings, the peak lithium current density was increased by a factor of 50-100%.

A major effort since Beams '94 has been the design, construction, and implementation of an extraction ion diode of PBFA II. PBFA II recently completed its 10th year of operation, and until late last year, the ion diode on PBFA II was a radially focusing diode in which the ion beam was focused to the cylindrical axis at the midplane of the accelerator. All high-yield facility concepts utilizing light ion beams require that the beam be extracted from the diode region and propagated several meters to the target. The modification to PBFA to allow for extraction-ion-diode experiments has been named PBFA-X (Fig. 1).

The first shot of PBFA-X with an ion beam was taken in September of 1995. In its first experimental series completed in April of 1996, PBFA-X demonstrated a much higher shot rate than achieved with the radial diode. The improved diagnostic access and proximity of vacuum pumping with this hardware were also advantages.

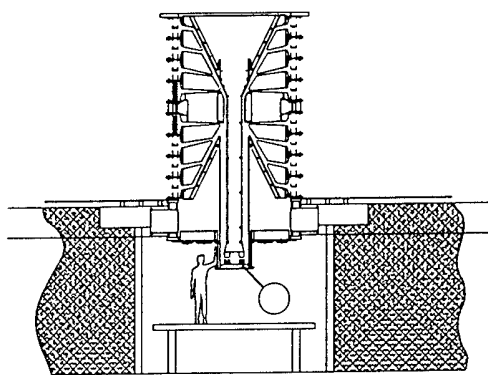


Fig. 1. PBFA-X configuration

With the success of the heating and cleaning experiments on SABRE, an improved protocol was applied to the PBFA-X extraction diode resulting in a dramatic improvement in the diode voltage history. A prematurely shortened voltage pulse is a signature of a falling diode impedance due to dramatically increasing total ion current in the diode. This total ion current is composed of both the desired lithium current and the parasitic current. By application of heating and cleaning techniques on PBFA-X, the diode pulse width was greatly increased. The addition of an active ion source then resulted in a lithium ion power extracted from the diode of  $\sim 4$  TW, the most ever from an extraction ion diode.

This advance in intense ion beam generation and focusing has resulted from careful application of multiple diagnostics, analytic theory, and numerical simulation. As an example of diagnostic improvements, it is now possible to measure on a millimeter spatial scale with nanosecond time resolution, electric fields in excess of 10 MV/cm using visible spectroscopy to measure the Stark shift [4]. Analytic theory, coupled with numerical simulation, has resulted in the ability to rapidly optimize magnetic field profiles for desired ion-beam current-density profile, an effort which in the past has taken about one week of experimentation for each different diode configuration [5].

Once an ion beam with adequate microdivergence and power is achieved, it still must be transported from the diode approximately 4 m to the target in any high-yield facility. This standoff is required to protect the beam generation apparatus from the debris and energy resulting from a high yield explosion, and to provide a drift distance for voltage-ramped pulse compression. Progress in transport physics has also been impressive. Previously, calculations using the IPROP code [6] have been shown to give excellent agreement with gas breakdown transport experiments at the Naval Research Laboratory (NRL) [7]. IPROP now predicts excellent current neutralization (at  $\sim 1$  torr) for the achromatic lens transport system and substantial net currents (up to 50%) for the self-pinch mode of propagation (at  $\leq 100$  mtorr). The baseline approach for a light ion LMF uses the achromatic lens system in which a solenoidal lens is located about 1.5 m from the target; results from the University of Wisconsin show that this is workable for LMF, and even for the LIBRA-LITE power plant concept. However, a more desirable approach is to use self-pinch transport which allows the beam to propagate several meters in gas to the target. Recent IPROP simulations for self-pinch transport are very encouraging. Self-pinch transport experiments have been initiated at NRL using 1 MeV protons, and will be initiated this summer at Sandia National Laboratories using 4 MeV Li ions. Self-pinch transport is very attractive for both high yield and energy options for both light and heavy ions.

Although advances in understanding of the physics of light ion beam generation and focusing have been impressive, the maximum Li intensity has remained at  $2 \text{ TW/cm}^2$  since 1993 while research continued on the separate issues of divergence and parasitic load reduction. Because of the outstanding results recently obtained with pulsed power driven z-pinches described in the next section, the near term emphasis in the pulsed power ICF program is shifting away from light ion beams towards z-pinches. Basic research into the fundamental issues limiting light ion beam focusing will be accomplished on the smaller SABRE accelerator at Sandia, on the Gamble II accelerator at the Naval Research Laboratory, and on the recently completed COBRA accelerator at Cornell. We anticipate that progress during the next two years will justify a second experimental series at the much high power levels available on PBFA-X.



## Progress in Z-pinch Development

Pulsed power accelerators have been used for many years to drive magnetic implosions (z-pinches). The load in these implosions has varied from cylindrical arrays of wires arranged at constant radius, to gas puffs and low density foams. These loads have historically coupled extremely well to pulsed power accelerators with resulting high electrical-to-kinetic energy efficiency. In the application as an x-ray source, the kinetic energy in the imploding system is converted into x-rays when the imploding plasma stagnates on axis. Z-pinches have historically been efficient at coupling electrical energy into kinetic energy in the implosion system, but the x-ray power available from these z-pinches has been limited to less than 20 TW. During the past year, however, breakthroughs in load fabrication (which has allowed in excess of 190 5  $\mu\text{g}/\text{cm}$  Al and W wires to be mounted forming a 1 - 2 cm diameter cylindrical array) and improved understanding of load behavior have resulted in dramatic improvements in x-ray power available from these sources (see [8] and [9] for results and references). Recently the x-ray power available from a tungsten load has exceeded 85 TW, the most power ever generated in a laboratory device. Remarkably, the energy in x-rays has remained nearly constant at 400 - 500 kJ as the power has been increased. These results were obtained on the Saturn accelerator. Saturn delivers 20 TW of electrical power to the load. Therefore, the 85 TW in x-rays represents a factor of four power gain. Such high power and energy x-rays sources have major applications in the ICF program.

Experiments have been performed utilizing these x-ray sources to heat vacuum hohlraums [2]. These hohlraums are complementary to those generated by lasers and offer unique capability in large volumes ( $5 \text{ cm}^3$ ) and long life time ( $>20 \text{ ns}$ ) at moderate temperatures ( $>80 \text{ eV}$ ). These large, long lived hohlraums provide an excellent environment for many different experiments relevant to both ignition and high yield capsule designs. For example, smaller, secondary hohlraums can be mounted on the side of the primary hohlraum (Fig. 2) to simultaneously measure secondary hohlraum drive conditions while performing experiments in which shock waves are driven through samples of ablator materials mounted to the other secondary hohlraum. Besides providing a source of x-rays to study ignition relevant physics, these z-pinches can be used to provide x-rays to drive ICF capsules themselves. Several concepts employing vacuum hohlraums or imploding hohlraums (hohlraums in which the hohlraum case itself implodes thereby increasing the hohlraum temperature) have been investigated with computer modeling. Experiments to explore these concepts have just begun [2, 10].

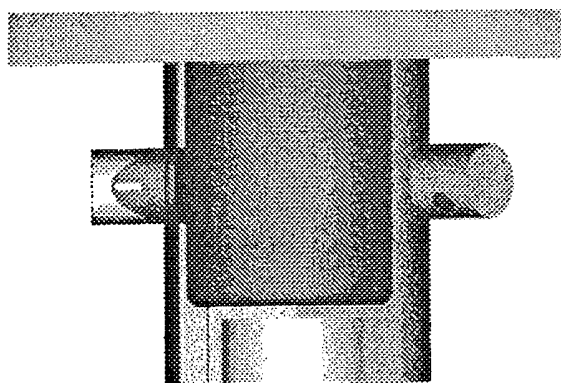


Fig. 2. Z-pinch driven hohlraum experimental configuration: primary hohlraum with secondary hohlraums

A major modification to PBFA to enable z-pinch experiments is underway (PBFA-Z). The Saturn accelerator delivers approximately 7 MA to a z-pinch load resulting in approximately 500 kJ of x-rays being generated. PBFA-Z when used to drive z-pinches will generate approximately 18 MA through a z-pinch load and will result in the production of 1.5 - 2 MJ of x-rays. The 85 TW and  $>80 \text{ eV}$  produced on Saturn are expected to scale to  $>150 \text{ TW}$  of x-

rays and  $>120$  eV in vacuum hohlraums on PBFA-Z. If this scaling can be demonstrated in experiments beginning later this summer, then the way will be clear to the follow on proposed accelerator, X-1, which would be designed to deliver 40 MA to a z-pinch load generating 6 - 8 MJ of x-rays.

## Conclusions

Pulsed Power provides an economical source of x-ray energy for ICF research. In the near term we plan to use energetic, intense z-pinch x-ray sources for ignition-relevant and high-yield capsule physics experiments. Capsule implosions driven by these x-ray sources have been simulated using coupled radiation/hydrodynamics computer codes and indications are that they are worth pursuing with existing and future pulsed-power accelerators. Z-pinchs represent the best means to generate high-energy, high-power x-ray environments for exploring ignition and high-yield relevant capsule physics in the near term. In the far term, light-ion driven ICF will be required for repetitive high yield applications such as energy production. Our plan, therefore, is to utilize z-pinchs in the near term to explore and refine the high-yield capsule designs and requirements, while in parallel developing intense ion-beam technology so that, when high yield is demonstrated in the laboratory, technology for utilizing the high-yield capability for defense applications and energy production will be available.

## Acknowledgments

The pulsed power ICF program is an international effort. Important contributions to the field are being made by scientists and engineers from around the world. This presentation has emphasized activities at Sandia National Laboratories, however, the authors would like to acknowledge our many colleagues who have contributed to the recent progress. Many of these advances are presented elsewhere at this conference.

[1] Quintenz, J.P., Bloomquist, D.D., Leeper R.J., Mehlhorn, T.A., Olson C.L., Olson, R.E., Peterson, R.R., Matzen, M.K., and Cook, D. L.: Progress in Nuclear Energy, 30, 183-242 (1996).

[2] Leeper, R.J., in cooperation with: Alberts, T.E., Allshouse, G.A., Aubert, J.H., Baca, P., Baca, P.M., Bailey, J.E., Barber, T.L., Breeze, S.P., Carlson, A.L., Chandler, G.A., Cook, D., Derzon, M.S., Douglas, M.R., Dukart, R.J., Fehl, D.L., Gilliland, T., Hebron, D.E., Hurst, M.J., Jobe, D.O., Johnson, D.J., Kellogg, J.W., Matzen, M.K., Martinez, C., Mehlhorn, T.A., McDaniel, D.H., McGuire, E.J., McGurn, J.S., McNamara, W.F., Moats, A.R., Muron, D.J., Nash, T.J., Noack, D.D., Olsen, R.W., Olson, R.E., Porter, J.L., Quintenz, J.P., Ruggles, L.E., Ruiz, C.L., Sawyer, P.S., Seamen, J.F., Spielman, R.B., Stark, M.A., Torres, J.A., Vandevalde, D.M., Vargas, M., Wenger, D.F., Zagar, D.M.: Beams '96, June (1996) Paper O-1-1

[3] Cuneo, M.E. et al.: Proc. 10th Pulsed Power Conference, Albuquerque, NM (1995)

[4] Filuk, A.B., Bailey, J.E., Adams, R.G., Carlson, A.L., Ching, C.H., Desjarlais, M.P., Lake, P., McGuire, E.J., Mehlhorn, T.A., Pointon, T.D., Maron, Y., Stambulchik, E.: Beams '96, June (1996) Paper O-1-3

[5] Desjarlais, M.P., Coats, R.S., Lockner, T.R., Pointon, T.D., Johnson, D.J., Slutz, S.A., Lemke, R.W., Cuneo, M.E., Mehlhorn, T.A.: Beams '96, June (1996) Paper O-2-5

[6] Welch, D.R., Olson, C.L., Hanson, D.L.: Beams '96, June (1996) Paper O-2-9

[7] Hinshelwood, D.D., Boller, J.R., Cooperstein, G., Fisher, R.C., Greenly, J.M., Jones, T.G., Mosher, D., Neri, J.M., Noonan, W.A., Oliver, B.V., Olson, C.J., Ottinger, P.F., Rose, D.V., Stephanakis, S.J., Welch, D.R., Young, F.C.,: Beams '96, June (1996) Paper O-2-8

[8] Sanford, Th.W., Nash, T.J., Marder, B.M., Mock, R.C., Douglas, M.R., Spielman, R.B., Seamen, J.F., McGurn, J.S., Jobe, D., Gilliland, T.L., Vargas, M., Humphreys, R., Struve, K.W., Stygar, W.A., Hammer, J.H., DeGroot, J.S., Eddleman, J.L., Whitney, K.G., Thornhill, J.W., Pulsifer, P.E., Apruzese, J.P., Mosher, D., Maron, Y.,: Beams '96, June (1996) Paper O-4-2

[9] Spielman, R.B., Breeze, S.F., Chandler, G.A., Deency, C., Long, F., Martin, T.H., Matzen, M.K., McDaniel, D.H., McGurn, J.S., Nash, T.J., Ruggles, L.E., Sanford, W.L., Seamen, J.F., Stygar, W.A., Torres, J.A., Zagar, D.M., Shoup, R.W., Struve, K.W., Mstrom, M., Corcoran, P., Smith, I.,: Beams '96, June (1996) Paper O-4-3

[10] Derzon, M.S. et al.,: Proc. 11th Topical Conference on High Temperature Plasma Diagnostics, Monterey, California, and the references therein, May (1996)

# HIGH-POWER EXPLOSIVE MAGNETIC ENERGY SOURCES FOR THERMONUCLEAR AND PHYSICAL APPLICATIONS (OVERVIEW)

V.K. Chernyshev

All-Russian Scientific Institute of Experimental Physics  
607190, Sarov, Nizhni Novgorod Region, Russia

## Abstract

High-power energy sources unavailable up to now are needed to carry out any one project on inertially confined controlled thermonuclear fusion (CTF). Considerable advances have been made in the area of explosive magnetic generators (EMG) as for their output characteristics (high-power combined with high energy content).

To evolve the concept of magnetic cumulation proposed by academician A. D. Sakharov in 1951 two new concepts to increase EMG fast-operation by two orders (from tens of microseconds to tenths of microseconds) by increasing at the same time the current pulse amplitude more than by an order were proposed at VNIIEF in the early sixties.

The concept aimed to solve CTF problem due to target magnetic compression (MAGO) under the effect of fast-increasing field was proposed (1972) on the basis of VNIIEF achievements, discussed (1976) at the USSR Academy of Sciences and published (1979).

The key physical questions are analysed, the problems to be solved are posed and the results achieved in the experiments with fast-operating high-power EMGs, fast-opening switches, transmitting lines, insulation systems are discussed in the paper. The results obtained in the experiments on liner acceleration, as well as on preliminary plasma magnetization and heating, carried out at the constructed EMGs are discussed briefly.

The conclusion that MAGO system is the most suitable one to provide the ignition because the designing of high-power energy sources to be used in this system is practically completed and the concept itself does not need any intermediate transformations of one type of energy into another always accompanied by the decrease of the total efficiency.

## 1. Introduction

Feasibility of controlled thermonuclear fusion (CTF) is one of the most attractive problem in modern physics.

Even when high degree of sophistication and high level of scientific and technical safety are inherent in atomic power stations, considerable amounts of fissile materials concentrated in space and time will always worry people from the viewpoint of possible extremist steps and wicked will of anomalous persons.

CTF will entirely eliminate these worries. In reactor thermonuclear fuel delivery is provided gradually and may be stopped at every instant. This is one among the important advantages of CTF.

Stationary systems with magnetic confinement, in particular ITER, are the most advanced in CTF area.

However the scope of works, time and cost necessary to create stationary systems are so high that the alternative "pulse" projects based on inertial confinement are worthy to more attention.

The approach providing two advantages would be of prime interest:

- at the stage of SCIENTIFIC IGNITION the approach should not require enormous expenditures of about 1 billion dollars to construct energy sources usually needed to feed lasers, ion beams, etc;
- at the stage of TECHNICAL IGNITION the approach should not require a great scope of works aimed to remount the surrounding the chamber cumbersome supply facilities when replacing systems with spent radiative capabilities (as in the case of ITER).

Ignition, to be sure, is the nearest principal goal of all inertial confinement projects. The most interesting physical studies providing extended data to answer the key questions may be carried out when approaching the ignition threshold.

So it is evident that high-power energy sources are needed to carry out all inertially confined CTF projects. When minimum start level of basic characteristics provided by such sources is concerned, the compromise between the output energy more than 10 Mj (when the stored energy is more than 30 Mj) and the output power more than 10 TW presents evidently the possibility to begin serious study of targets themselves. Creation of energy sources based on classical principles, having the same or higher characteristics needed to provide the ignition turned to be rather complicated and costly problem.

Academician A. D. Sakharov (1951) was the first who pointed up the possibility to achieve thermonuclear ignition on the basis of magnetic cumulation without resort to fissile materials.

A. D. Sakharov not only put forward the basic concept of magnetic cumulation, but also proposed two remarkable configurations: MC-1 system to produce high-power magnetic fields and MC-2 system, the multisection helical generator with variable step, to produce high-power pulse current and energy [1].

Moreover in 1952 A. D. Sakharov pointed out the possibility to apply magnetic cumulation to "Produce high-power gas discharge in D-T mixture transforming into thermonuclear burst".

He recommended to use MC-1 system to study the feasibility of X-ray or neutron production in the compression of heavy-walled chamber filled with deuterium.

At the same time A. D. Sakharov proposed the idea to use the pressure of magnetic field produced by MC-2 generator to provide the implosion of metal shells. However there was neither validated concept nor, more

importantly, high-power energy sources over long period. The intensive work took fifteen years to achieve the fundamental understanding of various physical peculiarities inherent in magnetic cumulation and of its limitation [2,3].

These generators have permitted to store much electromagnetic energy ( $>10$  Mj), but they were rather slow-operating ( energy storage time was 100 ms and more ) and, most important, they could not deliver much energy into the outer load rapidly (in  $\sim 1$ ms). The problem concerning the reduction of the time down to the microsecond level was not solved even with the transformers described in [3]. Thus the discussed EMGs were unsuitable to provide the ignition.

As follows from the later publication (1968), the American investigators from

J. Shearer's group at Livermore National Laboratory carried out the work [4] much the same from the viewpoint of fast operation.

New ideas were needed on the way to the ignition.

## 2. MAIN IDEAS OF FAST-OPERATING INCREASE

The sudden change has resulted in two new ideas:

- the creation ( V.Chernyshev and A.Korolyov, 1961) of disk generators that enabled to reduce by one order (up to microsecond units) the typical time of EMG operation and the same time to increase, not less than one order (up to 100 MJ and more) the stored energy, as well:

- the creation (V.Chernyshev, E.Zharinov and G.Volkov, 1958) of fast switching the EMG current-carrying contour, that made it possible to reduce the time of energy deliver to a load of up to ten parts of msec. (The first publication of our results on the fast delivery of energy is given in [2]).

These ideas have not come suddenly. By that time, there was an understanding that though such serious applications as a thermonuclear flash, the available MC-2 generators without a principle energy increasing device (from 10 up to 100 MJ and more), and a fast energy delivery device (of 1 ms duration) presented a very useful system, they very suited to be as preamplifier, only. They required to be further equipped with systems that would enable greatly increase the fast-operating, specific energy and energy gain simultaneously.

### 2.1. PLAN OF A 100 MJ - HIGH SPEED DISK ENERGY AMPLIFIER CONSTRUCTION

Let us consider a long coaxial, that as shown in [3], has made it possible to amplify energy (Fig.1). The figure shows that, when a coaxial part is extended, and a charge inside the tube is kept, the time of the EMG operation increases, and the efficiency drops. The growing rate of the magnetic energy generation stops to be equal to the constant energy emission rate of a cylindrical charge inside the tube.

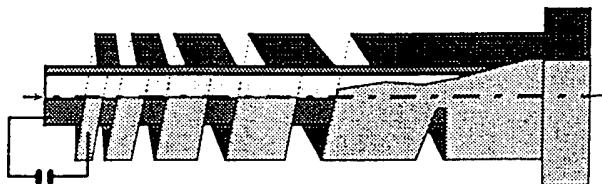


Fig.1 MC-2 GENERATOR

It seems that the time of the EMG operation may be sharply reduced by means of an axial initiation. But since the inductance slightly depends on the coaxial radii ratio,  $L \sim l \cdot \ln(R/r)$ , the energy gain drops sharply, as well.

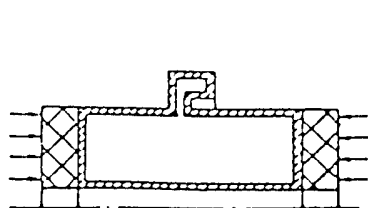
The external location of the high explosive charge along the coaxial outer diameter is effective in time (equals 2), but is low in the efficiency and results in the system complication that provides the initiation on the cylindrical surface.

From the formula one sees that it is the more beneficial to compress the contour along the axis, i.e. from the ends, imparting the side walls a counter motion (see Fig.2a) and to locate the explosive charges in their external (Fig.2b) surfaces instead of the radius to be handled. Once required distance between the end was found, a desired short time could be obtained. For instance, to achieve a fast response of 10  $\mu$ s duration, the end walls must be a 40 mm- distance extended (taking into account the end wall motion velocity equal to 2 km/sec), etc.

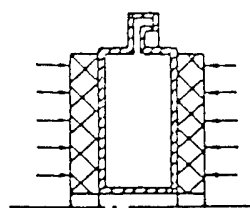
The contraction of a flow inside disk-shaped toroidal contour by the end walls opens a remarkable opportunity to work with fields of substantially different radii that differ from one another by an order. Besides, the magnetic field pressure ( $P \sim 1/r^2$ ) on the small radius of the contour differs by 2 orders from the perimeter pressure.

Having given a small outstripping of the charge detonation of the preaxis zone this enables to obtain a smooth pattern of the magnetic flow displacement from a small radius to the contour perimeter, that results in an effective work in the vicinity of dynamic contact point, where the main action of the explosion products against the field forces with a given high field  $H$  takes place, though the remaining part of the contour is still cold.

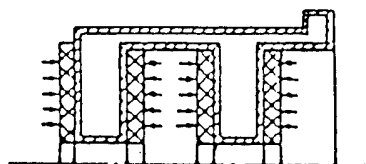
In the long run, the total energy store to be increased, several similar generators are set in series along the common axis (see Fig. 2c).



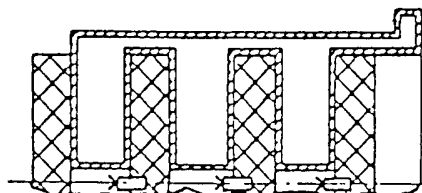
a) LONG TIME, IT IS DIFFICULT TO PROVIDE GOOD CONTACTS & CONTOUR INTEGRITY



b) GOOD TIME, LOW ENERGY

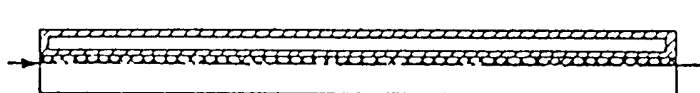


c) GOOD TIME, GOOD ENERGY, LOW EFFICIENCY

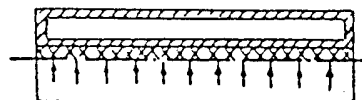


d) GOOD TIME, ENERGY, EFFICIENCY; THE SHARPENING OF PULSE IS DESIRABLE

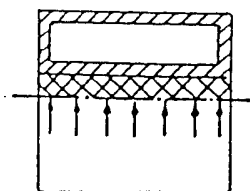
Fig. 2 EMG with short disc HE charge



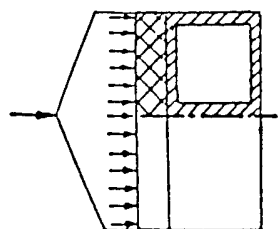
3.1 DETONATION AT ONE SIDE



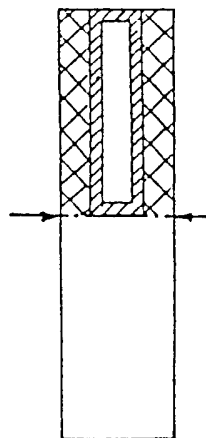
3.2 AXIAL DETONATION



3.3 AXIAL DETONATION



3.4 PLANAR WAVE DETONATION



3.5.DETONATION AT TWO POINTS ON THE AXIS

Fig. 3 Five toroidal configurations

To increase the efficiency, their charges be integrated in "pairs" (see Fig.2d); and for the sake of simplicity the initiation system, the charges detonation is performed by a detonators chain mounted on the axis (see Fig.2d).

5 various toroid configurations different in length to outer diameter ratio, and the way of the contour contraction were investigated (see Fig.3):

1. L-10D; charge inside the tube;  
detonation is observed from the end;
2. L-5D; charge within the tube;  
detonation is observed on the axis;
3. L-D; charge in the tube;  
detonation is observed on the axis;
4. L-D/5; a charge is located on one of the ends;  
detonations takes place from a flat lens;
5. L-D/10; the charges are located on the both ends;  
detonation is on the axis.

As it was expected, the 5th configuration is the best, due to a higher field uniformity.

Now, there remain some ways to increase the disk EMG fast-operation. The first way, as mentioned earlier was the use of the disks counter motion (double gain). The other way was the change of flat disks by shaped ones (gain not less 2.5). In the first experiments (1962) on generators with disk high explosives (hereinafter designated as disk EMG, see Fig.4a and 4b) there were obtained energy gains  $K = 35$  (current gain  $K = 43$ ; and a magnetic flow conservation factor  $\Phi_f/\Phi_0=0.82$ )[5].

In the experiments on shaped DEMG of 400 mm in diameter (see Fig.4d) with the initial current 5.7 mA there was formed a current pulse of amplitude 150 MA with the effective time growth 4 msec. In the experiment there was obtained a current increase rate of  $3.8 \times 10^{13}$  A/sec. In one compression cavity the energy of 3.5 MJ [5] was achieved.

It has become clear, that when one uses 30-element disk EMG (see Fig.5) it is possible to obtain energy of 100 MJ with a typical rise time of 4  $\mu$ ms.

So, the idea of the creation of the disk EMG with a substantially nonuniform field in the compression contour and the counter motion current carrying components has been implemented.

A high value of the energy density in the EMG volume (300 J/sm) has been experimentally confirmed.

## 2.2. ENERGY DELIVERY FROM HELICAL AND DISK EMG INTO THE OUTER LOAD.

In order to transfer the MC-2 generator to a fast-operating device for various physical applications, the idea appeared of quick energy taking out from the compressible volume by rupture of the current carrying contour using HE and by using of extra current of breaking.

A schematic diagram of this idea implementation is shown in Fig.6a. In the first experiments, performed by V.Chernyshev, E.Zharinov, G.Volkov in 1958 there was installed on explosive toroidal charge with a circular cross-section. The HE charge was detonated by a central tube expanded on the final stage of the EMG operation. Along the external side of the HE charge there was stretched a foil, outside of which a ribbed barrier with circular grooves was installed. At that time there were no disk generators yet, and all the tests were carried out with arrangements of MC-2 type, having long working time.

Even in the first tests the use of the described circuit breaking unit allowed to gain excellent results, i.e. to reduce current increase time to 100 and more times and make it independent on flux compression time. Time of bringing the energy out into the load was reduced to 0.3...0.5  $\mu$ sec. This result produced significant influence on further development of all kinds of opening switches in VNIIEF. Later, it became known that the US researchers and (Michigan University) [7] had a trend to fulfill current circuit break with the help of explosive charge. But any foreign publications on the use of explosive or other opening switches in EMG did not appear.

In the first tests with helical EMG of small size and explosive breaking units in flux compression circuit, the current being broken did not exceed 1 million amperes. Breaking unit itself took a very small part of EMG volume (see Fig.6a). At turning to EMG's able to generate large currents, the picture changes greatly. Let's watch this question a little detailed.

At EMG dimensions increase  $m$  times, its output energy increases  $m^3$  times, and output power is proportional  $m^2$  (because proportionally to  $m$  EMG working time also increases). If at the same time one increases breaking unit dimensions also  $m$  times, the energy transmitted through its area unit will increase as  $m^3/m^2$  i.e.  $m$  times. Thus, if in a small model, the original opening switch parameters were selected at the limit of its abilities, then the enlarged breaking unit model will be inefficient. To keep the breaking unit working regime it is necessary to enlarge additionally the surface of breaking foil  $m$  times.

If at the increase of EMG dimensions it is also necessary to keep commutation time at previous level, then opening switch dimensions are needed to be increased much more.

It is seen from Fig.6 that if in small EMG fast operating switch took a small part of volume and was practically invisible, then as EMG enlarges the switch becomes more and more "hypertrophied".

Usually at low currents (to 10 MA) an aluminium foil was used as an explosion ruptured conductor (see Table 1).

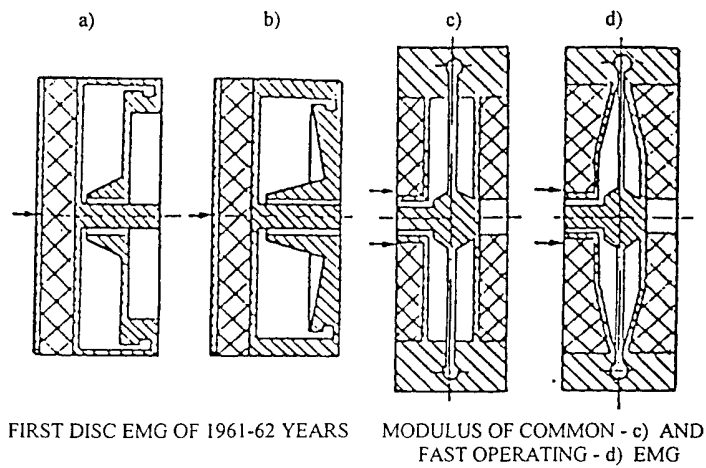


Fig. 4 Disc EMGs

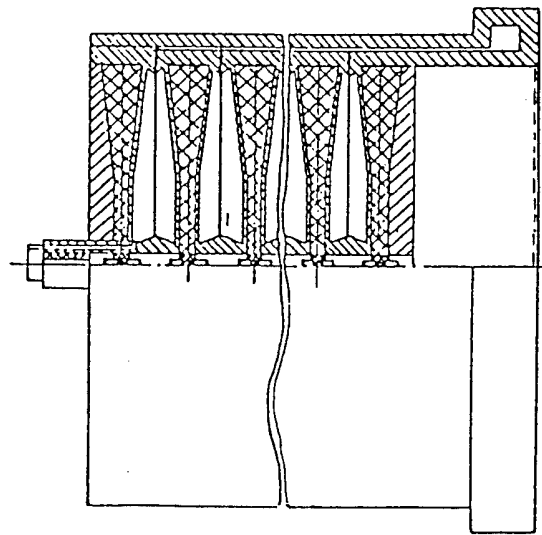


Fig 5. Fast operating multielement DEMG configuration

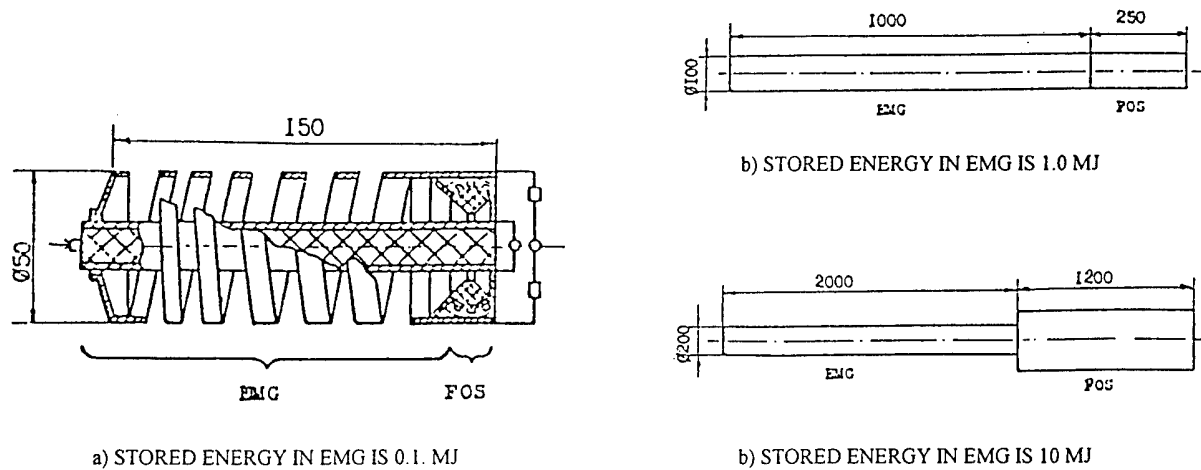


Fig. 6 How do the EMGs of different stored energy look



$\delta_{al}, \text{mm}$	0.15	0.23	0.37
$I_{BMF}, \text{MA}$	1.0	2.8	8.5
$\tau_{0.1-0.9}, \mu\text{sec}$	0.5	1.0	1.5

Modular principle of opening switch construction was researched, which proved itself to be good. In ten-module unit, where each of opening switches worked in the last column of table 1 regime, the EMG circuit break was provided by the current of 85 MA. The current in the load was 50 MA at derivative  $4 \cdot 10^{13}$  A/sec and time of growth  $1,7 \mu\text{sec}$  [6]. Thus in the first approximation the task of developing fast operating keys for helicals EMGs was solved.

To break currents of value 10 MA and more in the cases where it is necessary to use thicker foils (1 mm) and monounit construction of opening switch (which is the simplest way), it is advisable to turn over to cumulative dielectric jets proposed by I.M.Vitkovitski et.al [8].

With the help of single breaker  $\varnothing 200 \times 600$  mm with cumulative jets working in the circuit with 20 MA current at linear current density  $0,4 \text{ MA/cm}$  in inductive load of 35 nH, current pulse with amplitude of 10 MA and rise time of  $2 \mu\text{sec}$  was obtained [9].

The obvious advantage of explosive breakers is that of their ability to produce current pulse sharpening to great number of times (100), makes their use, especially coupled with helical EMG, the most winning.

Their basic disadvantage is the increase of final EMG circuit spurious inductance and also some complication of explosive's initiation at larger area, but though such areas are still not very large ( $\sim 1 \text{ m}^2$ ), it is still tolerable.

Using much more fast operating disk EMGs allowing to store energy of hundreds MJ and capable to form in inductive loads of 10 nH value current pulses of hundreds MJ with characteristic current rise time (e-folding time)  $5-10 \mu\text{sec}$ , there is no need for our purposes to obtain sharpening more than 10 times. So in DEMGs one can use much more simple electroexploding (wire or foil) opening switches.

As a result of detailed experimental research it was shown that at equal initial conditions, the current rise time jitter increase spread for such switches can be reduced to the value not worse than 10%, and the duration of current pulse rise time can be reliably reduced to 15 times [10]. This did not contradict to other authors' works on electrical conductors explosion.

It's impossible not to mention the great impression that was produced on us by the book "Exploding Wives" edited by Chase and Moor in US and published in a number of volumes.

The use of electrically exploding conductor together with DEMG allowed us to realize the delivery of the energy of 10 MJ into outer load of 10 nH for  $1 \mu\text{sec}$  time at the voltage on the switch of 460 kV and solve the task of fast energy bringing out of disk EMGs [11].

### 2.3. THE WAYS OF GENERATOR MC-2 WORK IMPROVEMENT

The main idea of all our works on MK-2 generation improvement is a trend to raise generator fast action. Even in explosive breaking units feeded from helical EMGs, foil is very sensible to current action integral, and in disk EMGs durable starting, current flow from helical preamplifier leads to a number of undesired after-effects. The effective time of the helical EMG operation was necessary to be reduced. Reduction of EMG work effective time has led to the increase of helix wound density, which in its turn sharpened the problem of cut-off ( $2\pi$ -clocking).

Detailed analysis of cut-off mechanism allowed to specify the cut-off absence criterion [13], that finally become:  $d < h \cdot \tan \alpha / 2\pi$ , where  $h$ -pitch,  $\alpha$ -half of tube dispersion angle,  $d$ -utmost permissible tube and wounds bias from nominal. This criterion being fulfilled, the cut-off losses in helical EMGs were practically eliminated.

To eliminate the strong influence of sharp front wound edge form (contacting with tube cone) on the energy increase, right-angled section wound profile was substituted for a round one (1961).

To raise carrying ability to the value of passing current the coefficient of filling pitch with wound's body was increased to 0,9 i.e. nearly twice (1964).

To low the flow losses, instead of single-running spiral multirunning spirals were used with increasing number of runs from 2...3 to 16...36 to the end of a spiral (1961-1962).

Cutting of tube was substituted for wire winding, which simplified the production and raised precision.

The most prominent step of the direction of helical fast-operating EMG was proposed and realized in 1962. The idea was in constructing the helix in which the inductivity speed output in two points being away from each other at a distance equal to spiral diameter, differed 9-16 times, that allowed to raise the helix fast-operation by factor 3.

Helical EMG fast-operation gave rise to terrible problem-electrical break downs in EMG circuit.

The problem was successfully solved due to realization helix construction principle in such a way, that maximum amplitude of voltage between tube cone and spiral winds is being constant during the whole EMG working time. This principle can be satisfied if one changes generator inductively at time according to the law.

$$L(t) = L_0 \exp[\varepsilon / \Phi_0 \alpha \cdot (1 - e^{\alpha t}) - \alpha t]$$

$$\varepsilon = J \cdot L; \quad \alpha = R/L$$

where  $L_0, F_0$  - starting inductivities and magnet flow ;

R- resistance, defining all the losses in the circuit;

t - time [14].

Placing properly selected solid isolation on helix winds allowed to solve the problem of electric strength of helical EMGs, especially important for the work of the starting half of spiral.

At the final half of helix there appears another problem- the problem of magnetic strength of solenoid as a whole.

During the research we managed to watch axial bias of last helix winds under the influence of magnet field radial component [15]. Owing to proper design decisions we also managed to solve this task and provide helical EMGs highly effective work in magnet fields up to 1 million oersteds. As a result of carried out research and proposed improvements we managed several times raise fast-operation, specific energy and energy increase coefficient simultaneously, in comparison to helix part of original MC-2 generator.

In some helical EMG, where it was necessary, energy increase was driven to values of 700-1200. some output data of some EMGs are given in Table 2 as an example.

Diameter mm	$E_f$ MJ	$K_E$ nH	$e$ J/cm <sup>3</sup>
240	3	100	60
240	5,4	340	100
200	6,7	50	130
240	10 (13)	60	190

To differ from the known MC-2 generators, fast operating generators (in which all above mentioned improvements were implemented) characterized with combination of several times higher energy increase coefficients, fast -operation and specific energy [16] the new title "Potok" was awarded (see Table 3).

Technical characteristics of helical explosive magnetic generators "Potok"

Table 3

	"Potok" 1 MA 25 nH	"Potok" 6 MA 25 nH	"Potok" 0,88 MA 3000 nH	"Potok" 18 MA 60 nH	"Potok" 12 MA 110 nH	"Potok C" 34 - 62	"Potok" 35 MA 50 nH
Initial inductance, μH	300	22	250	100	115	34 - 62	160
Initial energy, kJ	2.02	7	36	20	40	90 - 220	50
Load inductance, nH	25	35	3000	60	110	50 - 750	50
Max current in the load, MA	1.0	6.0	0.88	18	12.0	4.6 - 21	35
Magnetic energy in the load, MJ	0.012	0.63	1.0	10	8.0	8 - 11	30
Characteristic (e- folding) risetime, μsec	3	9	45	40	35	35 - 40	30
Inner diameter, cm	5.0	10	16	20	24	24	40
Length, cm	25	60	160	200	160	160	350
HE mass, kg	0.1	1.6	6.3	25	21	21	120
Total mass, kg	1.8	10	40	90	140	140	550

### 3. THE BASIC UNITS OF THE INSTALLATION.

On the basis of the achievements in developing unique considering their power and energy parameters EMGs, it was proposed in VNIIEF the way to solve the problem of ICF on the basis of thermonuclear target pression by fast increasing magnet field, not exceeding during its working time 5...10 million oersteds. Basic scheme of the system and its substantiation were firstly proposed in 1972. In 1976 general concept of ICF problem decision on the basis of magnetgasodinamic cumulation of energy was reported in AS USSR by academician J. B. Khariton, and in 1979 it was published in DAS [18] for the first time.

#### 3.1. SHORT DESCRIPTION OF MAGNET PRESSION CONCEPT ( SHORTLY MAGO ).

The energy supplying element of the system is a ponderomotor unit (PU), being an axially symmetrical construction in which along the thin skin-layer of conducting matter (metal or plasma) fast increasing current is flowing from special source.

Under the influence of magnet field arising during current flow, the conducting matter liner accelerates and presses thermonuclear target.

For one of the PU types at current increase time (5 - 10 msec) and inputted energy of 250 - 500 MJ according to calculations it is managed to obtain spherically-symmetrical target pression and achieve

thermonuclear fuel density (DT-gas) in central part of target  $20 \text{ g/cm}^3$  at temperature of 3-4 keV. Besides, in calculations ignition of thermonuclear reaction is carried out with high enough energy supply. In such a system it is necessary to achieve high rate of target pression symmetry (deviations in pressure along the target surface must not exceed 0,5%). The required value of inputted into PU energy reduces with the reduction of its input time.

For the other PU type, when gas was used as the accelerated matter, at a short current increase time (0,5-1 msec) and inputted energy 30-50 MJ it is managed to obtain ignition.

In numerical calculations, 1D & 2D programs of calculating gasodinamics equations with nonlinear heat conductivity, magnet field diffusion, thermonuclear reactions kinetics, with neutrons spread considering effects related to turbulent mixing and resilient-plastic features [18] of matter, were used.

The scheme of the whole installation is very simple (see Fig.7).

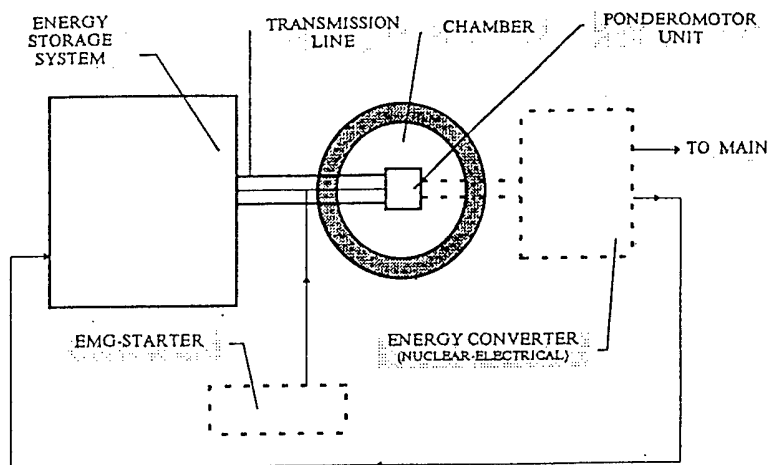


Fig.7 THE PRINCIPAL SCHEME OF MAGO INSTALATION

It contains four principally necessary units:

- powerful energy source (storage)
- chamber for thermonuclear explosions confinement
- ponderomotor unit being inserted into the chamber before the explosion
- transmission line, connecting the energy source with ponderomotor unit placed in the chamber.

Storage and chamber shall be rated for a long use, and ponderomotor units and, at least part of transmission line which is in the chamber, are unretained elements. Possibly at first storage, commutation will also be unretained.

Profitability of such an electric station can be provided, if unretained elements will be cheap enough. Working matter, being heated in the chamber comes into electric power generator with the following chemical processing. Part of produced electric energy comes to the storage to charge it for the next cycle and the main part is used for commercial purposes. Some other transformations of produced energy into other kinds of energy (laser radiation, ion beams, etc, which have small efficiency) is not required here.

### 3.2. BASIC UNITS REQUIREMENTS

It is necessary to note, that requirements to energy source are very high (250-500 MJ for 5-10  $\mu\text{sec}$ ). Being built to the classical principles, it will seem to cost \$10. Though in other projects with inertial confinement the driver is not cheaper.

One of the main advantages of MAGO project is the opportunity to manage without such an expensive energy source. At least at the stage of scientific ignition (so called "breakeven" incomparably more simple and cheap explosive magnetic energy sources mentioned above can be used.

Exploding chamber creation is also very difficult task, but such difficulties seem to be on this side a common sense.

For the first cycle starting, when the storage is not yet charged, EMG-starter with explosion confinement chamber can be needed.

There are also other difficulties (to provide electric energy generators efficiency at the level of 30 %; losses in the storage-at the level of 70%). It is seen that these difficulties can be overcome. But the main obstacle is to gain ignition.

### 4. KEY DIRECTIONS OF PU RESEARCH.

The fulfillment of the above mentioned first test with one pression cavity DEMG 400 mm diameter, in which at current amplitude of 150 MA and stored energy of 3,5 MJ, record fast-operation was achieved of 4 msec, showed the real possibility of obtaining in 30-elements unit the energy of 100 MJ and, became the

strongest stimulus for the beginning of works on development and research of different types of ponderomotor units (PU). The main three questions stirred the researchers minds:

Is it possible in a simple cylinder geometry, being considered yet by A.D. Sakharov, (which, by the way, the most comfortable for diagnostic purposes) without attracting any new two-dimensional effects, to press target with cold D-T mixture to the temperature of thermonuclear ignition?

Is there any hope for possibility of Spherically Symmetric implosion cover intended to press D-T mixture in the target, if the cover acceleration is produced by magnet field, having Axial Symmetry?

How to accomplish the preheating of D-T mixture in the target to kiloelectronvolt temperature, in order to them provide it following adiabatic pressing?

Noone could answer these principle questions before 1970-1972. There were a great number of other very important questions, a large amount of calculative - theoretical and experimental research were needed to be done to answer them:

- how to accomplish thinwall(2...3 mm) transmission line for transmitting of magnet energy from EMG to PU, being capable at up to half a million voltage?

- how to accomplish magnet acceleration of different covers to unusual speeds of 5,10,50 km/sec?

- what asymmetry of shells movement can be achieved? what is the state of covers during their magnet acceleration, when their outer layer is rated to be deliberately fused and often vapoured or is corroded by Ralley-Talor type disturbances.

- how to keep plasma temperature at the level of 0,2...0,3 keV during at least 1...2msec, so that to accomplish its adiabatic pression with a liner, if it is known, for example, that the life-time of hot plasma in the system with plasma focus is 100 times shorter.

At that time noone knew answer to these questions.

## 5. PONDEROMOTOR UNITS RESEARCH RESULTS.

In the frame of MAGO concept a group of theorists V.B.Yakubov, Je.S. Pavlovski, S.F.Garanin, A.M.Bujko headed by B.N.Mokhov, together with a group of experimentators M.S.Protasov, A.A.Petrukhin, V.A.Shevtsov, A.I.Kuziaev, B.E.Grinevich, V.V.Vahrushev, E.I.Zharinov, headed by V.K.Chernyshev researched theoretic, physical and technical questions of the work of different types of energy supplying arrangements-ponderomotor unit of a system based on magnetic pression of a target.

PU is intended for transformation of magnet flux energy into kinetic energy of axial-symmetric covers-liners, that compress and heat of thermonuclear target.

The element, common to researched PUs, is a so-called energy liner. In its simplest case, it is a cylindric conducting cover implosing along the axis and placed between two buff-end walls ("metallic Z-pinch").

The very first calculations have already shown that, having moderated requirements to EMG and to PU cover, with the help of one energy liner it is hard to raise energy liner density to the length unit higher than 5-10 MJ/cm, which is not enough to achieve ignition. So, the answer to the first key question was obtained.

In real case, not only energy insufficiency, but very strict requirements to assymetry make monodimentional cylinder ignition system hardly accomplished.

In VNIIEF it was proposed the new way [19] of energy liner density raise by using magnetcascade PU, the scheme of which is shown at Fig.8.

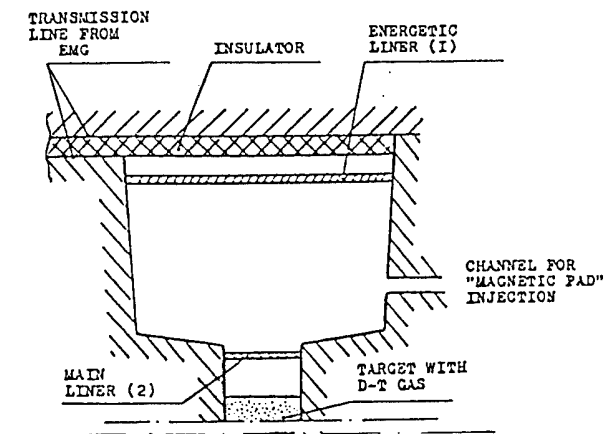


Fig.8 MAGNETO-CASCADE P.U.

Here, besides the energy liner, target liner, called principal is used, and a magnetic pad is quickly inducted between them. Requirements to such, PU are described in the work [19].

But before starting such PU research it was necessary to have at least the following EMG types:

- magnetic pad generator (10 MJ, 1  $\mu$ sec)

- energy acceleratıng generator (250 MJ, 5-10  $\mu$ sec), see Fig.9.

In its turn, to construct magnetic pad generator the helical energy preamplifier (1), disk amplifier (2) and powerful current opening switch (3) (power  $> 10$  TW is required) are needed.

For energy liner acceleration the big disk EMG (4) with more powerful preamplifier (5) was needed. At first we could save using magnetic pad generator without opening switch for energy liner model acceleration. And that was done. But further disk EMG with 250-500 MJ energy storage was necessary.

Besides, it is sharply desirable to have highly inductive EMG with explosive breaking unit (6), which can be used, for example, for the purposes of plasma preheating.

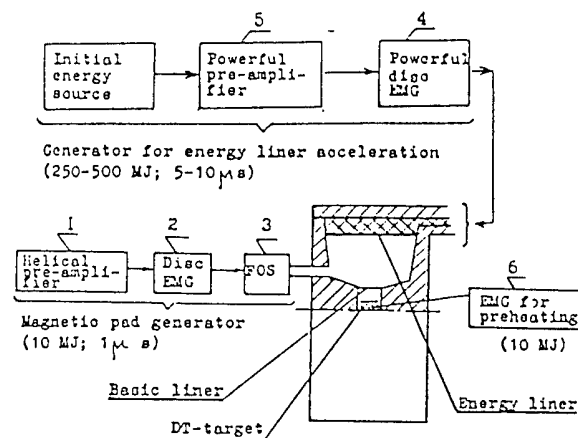


Fig.9 MINIMAL EMG KIT FOR MAGNETO-CASCADE INVESTIGATION

Minimum EMG set containing six units (see Fig.9) is enough for PU research.

Firstly, researches related with EMGs themselves creation were carried out. The results are provided in work [11].

Under finishing the required EMGs development, PU research was started [19]. The tests followed the aim to get the idea of cover acceleration character, coincidence of experiments and calculations, asymmetry implosion character, etc., based on magnetic compression of a target.

PU is intended for transformation of magnet flux energy into kinetic energy of axial-symmetric covers-liners, that fulfill compression and heating of thermonuclear target.

### 5.1. RESULTS OF MAGNETOCASCADE PU STUDIES.

As a result of the analysis of the general magnetocascade PU scheme it was shown by calculations that due to inertialess of the magnetic field it is possible to deliver more than a half of the kinetic energy from the energy liner to the main one and to provide energy contraction per a unit of a liner length, necessary to achieve the ignition.

With the velocity of energy aluminium liner 45 km/sec having the length of 10 sm, mass of 5 g/sm and initial radius of 20 sm, magnetic pad with the initial energy of 10 MJ, delivered for 1 msec, the main liner (which compresses the target) with the length of 2,5 sm, mass of 2 g/cm and initial radius of 4,5 sm, has the velocity of 155 km/s, which corresponds to linear density of the energy liner 20 MJ/sm.

In the experiments on the energy liner going up that were performed on the DEMG of 400 mm in diameter ( $R=186$  mm, aspect ratio=1000, surface mass  $4,3 \times 10$  g/sm, length=1000 mm, and EMG current of 54 mA) the liner velocity prior to its impact to the accepting shell was 25 km/sec.

The experiments have shown that to increase the energy liner velocity up to 45 km/sec, it requires the DEMG energetics to be enhanced only, and that is possible to do.

In the experiments on the cylindrical plasma liner (a model of the basic one) there was used a magnetic pad generator, that had been developed by that time, (15-component DEMG of 400 mm in diameter with a foil opening switch, and a closing switch), which enabled to produce 35 mA current with the time rise of 1 ms in inductance more than 10 nH.

Aluminium liner ( $R_0=300$  mm;  $l=10$  mm; wall thickness tolerance 1%) was gone up to 50 km/sec. In the performed experiments the asymmetry was 60...30 ns, that 5...10 times exceeded the desired value. This asymmetry was caused not so much of the liner wall thickness tolerance, as the current angular asymmetry.

The experiments have indicated that a key problem for the creation of a system with the magnetic cascade PU will be the gain of the required low asymmetry.

The advantage of the plasma (explosive) liners is the dynamic decrease of their aspect ratio  $R/R_{\text{liner}}$  radius  $R$  -effective thickness  $R$  ratio) during the detonation. This will low the asymmetry on the account of the Rayleigh-Taylor instability limitation.

Another way of improving the symmetry is the going up of inexplusive liners (or at least their bulky mass). Here, the strength and viscosity impede the development of Rayleigh-Taylor instability, at least on the part of the going up, where a magnetic pressure does not exceed the strength, that allows to increase  $R_o/R$ .

For the inexplusive liners (imitating an energetic ones) to be gone up, a DEMG of 1000 mm in diameter was used, which supplied 90 mA current to the copper and the 70 mA to aluminium liners.

A liner with  $R_o=225$  mm,  $l=70$  mm;  $R=1.4$  mm (1.9 mm for Al); wall thickness tolerance - 1.4% (2% for Al);  $R_f=100$  mm (56.5 mm for AL) was gone up by a magnetic field to a velocity 6.3 km/sec (15 km/sec for Al).

The kinetic energy both copper and aluminium liner was 25 MJ, that was considered as the highest value for the liners accelerated by a magnetic field.

The results of the performed experiments have shown that the change of the cylindrical liner on the radius of the receiver contacts location does not exceed + 9% for copper and + 14% for aluminium liners.

Besides, the inexplusive liners used for further compression of a thermonuclear target can be employed also as liner-opening switches to intensity the current pulses, when the velocity of energy delivery from the DEMG accumulated inductance to an inductive load is determined by a velocity of the spill valve opening (the liner velocity), and a gas inertness (Alfen sound velocity). Such conduction of the liner-opening switch operations was fulfilled.

In the course of the experiment, the aluminum liner ( $R_o=145$  mm;  $l=50$  mm; thickness - 0.7 mm) was gone up by the DEMG current pulse of amplitude 69 mA up to 10 km/s. Azimuthal nonsymmetry on the radiuses of 115.2; 109.8 and 104.3 mm was respectively 2.1; 3.5 and 4.1 mm.

The experiments that had been performed, enabled to obtain a specific data on various liners capabilities concerning not only magnetic cascade PU, but from the viewpoint of creating high power closing switches, and also of pressing thermonuclear targets with a magnetized plasma.

## 5.2. PU FOR TARGET QUASISPHERICAL COMPRESSION.

As the calculations show, the transition from a cylindrical to spherical (or quasi-spherical) compression geometry allows the ignition conditions to be easily obtained, though the requirements to the symmetry remain high.

However, the analysis of this system both in the calculation and the experimental viewpoints becomes complicated. Firstly, a number more expensive two dimensional calculations is to be conducted. Secondly, the experiment procedure capabilities are greatly limited as it is impossible to penetrate the most interesting target central zone without affecting the characteristics of the spherical convergence [10].

For the key issue to be solved, which attracted the interest of all scientists and engineers (theorists, physicists, specialists in gas dynamics, and designers) on the feasibility and impossibility of obtaining the shell spherical symmetry convergence induced by the magnetic field having an axial symmetry, a special pondermotive unit a schematic diagram of which is shown in Fig.10 (above) has been simulated and developed.

The accelerated shell itself was in the form of an axially flattened body of revolution with a complex profile of generator, and was inserted to the inner conductor also of a specific external surface profile within which a current ran from the high-power disk EMG. To meet the required conditions of acceleration in the zones of the shell, shaped inserts.

The forms of the cavity shell between the internal and external conductors of the coaxial and the inserts geometry obtained as the results of two-dimensional calculating are shown in Fig.10 (in the middle part) to the moment close to the time of the shell rush up to the target imitator.

The results of one of the two experiments most constantly reproducing all two process features, are shown in Fig.10 (below).

The experiment result treatment, has demonstrated that a low asymmetry (some percents in relative values of  $R/R$ ) is observed in polar domains only on the area accounting some percents of the spherical surface as a whole.

Thus, the possibility of obtaining the shell spherical symmetry convergence induced by the magnetic field having the axial symmetry, was theoretically substantiated, and experimentally confirmed [18].

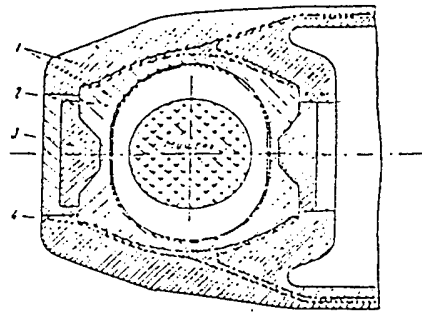
The intensification of simulations and experimental efforts in a target spherical compression will be required on the final stage of investigations under the MAGO project, when there will be important to integrate achievements in all types of PU for the ignition to be obtained.

## 5.3. GAS PONDERMOTIVE UNIT

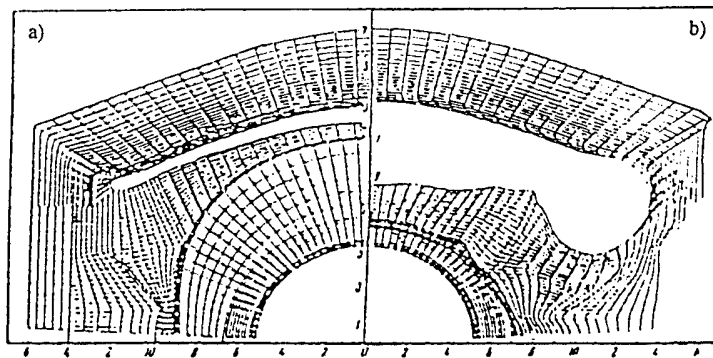
In the works (17,18,19) an opportunity of the DT-gas dynamic energy cumulation in the system consisting of a central thermonuclear target and one or several cylindrical or spherical liners that constrain the target. The liners were gone up by a magnetic field induced by a high-power EMG.

In such systems, for the ignition be achieved, apart from the source with a stored energy of 500...1000 MJ and a fast operation of 5...10 msec it is necessary to provide a high level of the gas compression (not less than 1000) and, thus a high degree of the target compression symmetry.

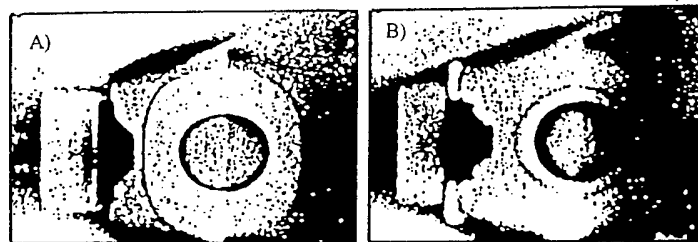
In order to reduce the strict requirements to the symmetry and level of the gas compression it was suggested that a magnetized DT-plasma should be preheated up to the temperature of (20) and the additionally



10.1 P.U. SCHEME: 1 - CONDUCTOR, 2 - SHELL, 3 - INSERT, 4 - INSULATOR



10.2 COMPUTATIONAL RESULT OF SHELL MOVEMENT: A - INITIAL POSITION OF P.U.  
B - POSITION OF P.U. CLOSE TO THE MOMENT OF THE SHELL-TARGET IMPACT



10.3. EXPERIMENTAL RESULTS: A - INITIAL POSITION OF P.U., B - POSITION OF P.U.  
CLOSE TO THE MOMENT OF THE SHELL-TARGET IMPACT

Fig. 10 On the possibility of spherially symmetric implosion of the shell  
under the action of axially symmetric magnetic field

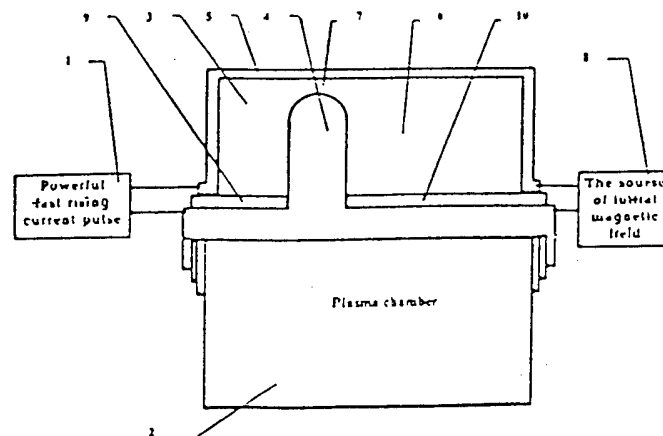


Fig. 11 The scheme of the gas ponderomom unit for magnetized plasma heating

be adiabatically compressed up to a temperature and density satisfying Lawson criterium. Also, the compression is performed by a liner and the heat insulation of the walls is provided by a azimuthal magnetic field frozen in the plasma.

Gas pondermotive unit (GPV) of such type consists of 2 coaxial sections (acceleration and deceleration of plasma) connected by a narrow ring nozzle (Fig.11). GPU is filled with a D-T gas at a small pressure ( 10 Torr). At first, a slowly increasing current is let through the GPU (to avoid the gas discharge at the nozzle), which is used to provide the both sections with a magnetic flux. Then, the EMG that provides a fast increasing current, is attached to the acceleration section in let. The resulting high electric field frozen into the cold plasma by the action of pondermotive forces of a stronger field of the main feeding together with the plasma runs through the supersonic nozzle from the first section to the second one, where a shock wave, that slows down and preheats the plasma is produced.

In response to the transition of the next adiabatic compression and additional heating the plasma by the liner, it has been possible, according to the calculations [20,21], to reduce the liner velocity requirements from 200...300 km/sec; the compression level from 10 to 10<sup>3</sup>, and also the system compression symmetry.

In the course of the experimental investigation on the GPU, a number of experiments have been performed.

Beginning with low energies and moving from an initial level of the neutron yield of 10 neutron per pulse, and little by little analyzing the processes and building up the energy, it has been thus far possible to advance a deep understanding of basic phenomena of the neutron yield increase.

So, in one of the typical series of the experiments on the GPU having an inner radius of 10 cm, the acceleration section in width of 2,7 cm, deceleration section of 3-fold width, nozzle of minimum width 1,2 cm; initial DT- gas pressure of 5 torr, initial magnetizing plasma current 1.7 mA; main current of the plasma acceleration 7.2 mA (at derivative 3.3 mA/ms), that corresponds the total energy 200 kJ admitted to the chamber vacuum volume, the neutron yield at the time of the neutron generation 1...2 ms has accounted for  $N = 2.5 \cdot 10^{12} \pm 20\%$ . (For series of the experiments the scatter in the data is 20%.) The velocity of the plasma flux through the supersonic nozzle is of 1000 km/s.

In subsequent series of the experiments at large energy, the neutron yield is recorded as  $3...5 \cdot 10^{13}$  neutron per pulse as for the temperature, it reaches its kiloelectronvolt level. A specific oscillogram of the relationship between the neutron yield rise velocity and time is shown in Fig. 12, and a photograph of hot zone, obtained in its own neutrons is presented in Fig. 13.

## **6. ON THE SCIENTIFIC AND TECHNICAL BREAK-THROUGH IN THREE KEY FIELDS OF PRESENT-DAY PHYSICS.**

As a result of the described intensive studies of many years the concept of ignition based on MAGO experimental setup was developed. Below is given the description of the concept and setup scheme.

During activities the unique experimental setup was brought into being and the scientific break-through in three key fields of present-day physics was made.

### **Physics of super-power sources.**

- fast-operating EMG of "Potok" family, having an output power of 10 TW and a stored energy of 10 MG, 100 MG or more, have been designed.

### **Physics of magnetized plasma.**

- ionized magnetized DT plasma previously heated to 0,2...1 keV has been produced, whose lifetime is 2  $\mu$ sec and wherein  $4 \cdot 10^{13}$  thermonuclear reactions have been performed.

### **Physics of high energy densities.**

- the liner energy density of  $>1\text{MJ/g}$  has been experimentally achieved, which is 200 times as much as the explosive energy density;

- it has been proved both by calculations and experiments that a quasispherical shell implosion is possible under the magnetic field having an axial symmetry.

## **7. SCHEME OF MAGO EXPERIMENTAL SETUP USED TO PROVIDE IGNITION.**

The basic setup assemblies are schematically shown in Fig. 14.

## **8. WHAT IS MAGO CONCEPT?**

To say it in simplified terms, MAGO concept is the set of fast and powerful energy sources meant first of all to provide ignition, which together with the specified set of ponderomotive assemblies (gas and spherized liner type) makes it possible to carry out the following sequence of physical processes under the below specified conditions:





Fig. 12 Neutron intensity versus time dependence (markers 0.4  $\mu$ s)

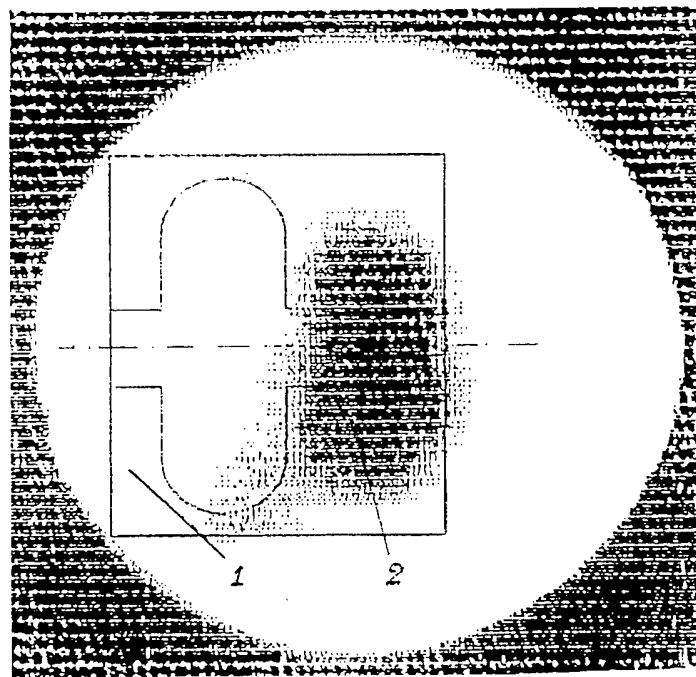


Fig. 13 Hot plasma irradiating region - photograph taken in its own neutrons

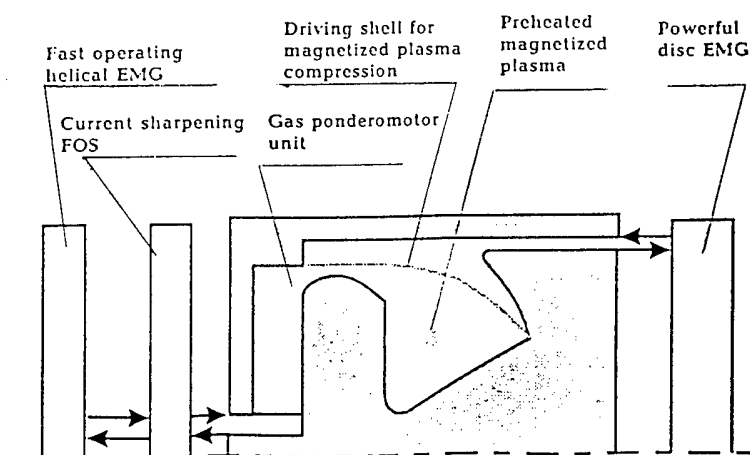


Fig. 14 The scheme of experimental MAGO setup

Process	Conditions
- introduction into deuterium-tritium mixture of the magnetic field from the source of stored energy	0,1...0,2 ME 1...2 MG
- plasma ionization and preheating to the temperature of from the high-speed source of stored energy	0,1...1,0 keV 10...20 MG
- compression of the preheated magnetized plasma with a hemispherical shell accelerated to the veracity of	5...20 km/sec
- fast-growing magnetic field from the powerful stored energy source	100...200 MG

## 9. SUPER-POWER ENERGY SOURCES. LEVEL OF RESULTS OBTAINED USING A PONDEROMOTIVE ASSEMBLY.

These are the results of the studies, which have been carried out:

1. EMGs of "Potok" family have been developed which have an output power of >10TW, the energy taken out into the external load being >10 MG:	2. Ionised and magnetized plasma having a heating temperature of 0,2 - 1 keV has been produced in 1000 cm <sup>3</sup> volume. The lifetime is $\cong 2 \mu\text{sec}$	3. The liner energy density of > 1 MJ/g has been experimentally achieved, which is 200 times as much as the explosive energy density.
1.1. Fast-acting helical EMGs •energy inirease 200, 1000 •specific time 10...40 $\mu\text{sec}$ •specific energy 100 J/cm <sup>3</sup> •output energy 0...40 MJ	2.1. The basis principles have been tested: •plasma magnetization •generation of supermagnetosonic ion fluxes •preheating	3.1. Acceleration has been provided using magnetic fields of different liners. The following has been achieved: Mass Velocity 1 g 50 km/sec 250 g 15 km/sec
1.2. Fast-acting disk EMGs •energy increase 10...30 •specific time 5...12 $\mu\text{sec}$ •specific energy 200...600 J/cm <sup>3</sup> •output energy 60...100 MJ	2.2. A stable generation of 14MeV neutrons having (3-5)·10 <sup>13</sup> n/pulse yield has been provided.	3.2. It has been proved that a quasispherical shell implosion is possible under the magnetic field having an axial symmetry.
1.3. Fast-opening sevitches •current 70...100 MA •specific time 1 $\mu\text{sec}$ •voltage 500 kV	2.3. The hot zone form and dimensions (in centimeters) has been determined by photographing in its own neutrons. 2.4. The lack of heavy ion admixtures from the walls has been experimentally shown.	
<u>Conclusion:</u> the energy sources are ready to operate for the preheated magnetized plasma compression.	<u>Conclusion:</u> the magnetized plasma is ready for compression.	<u>Conclusion:</u> the driver and the compression system are ready for compression experiments.

Thus, the work has come up to the culmination stage of studies, when the final phase, that is an adiabatic compression, is to be tested and the presence of the second temperature peak is to be ascertained.

## 10. MAGO ADVANTAGES.

- magnetized plasma application "locks up" electron and ion thermal conductivities, which enables ignition to be achieved at lower liner velocities and plasma compression level;
- to provide ignition, there is no need to build bulky expensive buildings and facilities costing hundreds of million dollars. Super-power EMGs, having already been developed, can serve as energy sources.
- there are no limitations preventing from the international collaboration on a large scale, since low  $\rho_0$  and  $\rho_{\text{max}}/\rho_0$  as well as the need for a magnetic field make this work advantageously different from all those pertaining to ICF.

## 11. IMMEDIATE OBJECTIVES.

- development and study of a high-temperature (0,3 ... 1,5 keV) chamber making possible further plasma compression;
- investigation of different methods and physical processes of compressing the preheated magnetized plasma in the thermonuclear chamber;
- ignition threshold attainment.

## 12. THE REQUIRED FINANCING LEVEL.

- to approach ignition conditions by the year 2000, 1.06 million dollars per year are needed for performing the work.

## 13. CONCLUSION.

Designers believe that MAGO course is the quickest and most cost-effective way of achieving thermonuclear ignition.

## REFERENCES.

1. А.Д. Сахаров и др. Аннотации докладов, представленных на международную конференцию Мерагаусс-1, Рим, Италия, 1965.
2. А.Д. Сахаров, Р.З. Людаев, Е.Н. Смирнов, Ю.И. Паюшев, А.И. Павловский, В.К. Чернышев, Е.А. Феоктистова, Е.И. Жаринов, Ю.А. Зысин. Магнитная кумуляция, ДАН, том 165, №1, 2, 3; стр.65, 1965г.
3. А.Д. Сахаров Взрывомагнитные генераторы, УФН, том 88, выпуск 4, стр. 725, апрель 1966г.
4. Shearer I.W., Abraham C.M., Benham B.P., Faulkner J.E., Ford F.C., Hill M.M., Stephens W.H., Steinberg D.J., Wilson J.R., J. Appl Phys. 39, 4, 2102 (1968).
5. В.К. Чернышев, М.С. Протасов, В.А. Шевцов. Первые дисковые взрывомагнитные генераторы, в книге "Сверхсильные магнитные поля". Физика. Техника. Применение. Труды третьей международной конференции по генерации мегагауссных магнитных полей и родственным экспериментам, стр. 23, Новосибирск, 13-17 июня 1983. Под ред. В.М. Титова, Г.А. Швецова.
6. V.K. Chernyshev, V.V. Vakhrushev, G.I. Volkov, V.A. Ivanov and I.K. Fetisov. Helical EMG module with explosive current opening switches, Megagauss Fields and Pulsed Power Systems. Edited by V.M. Titov and G.A. Shvetsov, p.433, Nova Science Publishers New York, 1989
7. Эрли, Уолкер. Накопитель индуктивной энергии - средство исследований высокой температуры, в книге "Получение и исследование высокотемпературной плазмы", И.Л., Москва, 1962
8. D.Donte, R.D.Ford, W.A.Lupton, I.M.Vitkovitsky Proceedings of 7-th Symposium Engineering Problems of Fusion Research Knoxville, Tennessee, V.2, № 4, p.p.1066-1070, 1977
9. В. К. Чернышев, В.В. Вахрушев, Г.И. Волков, В.А. Иванов, С.В. Пак. Обострители тока для мощных спиральных ВМГ, см. тезисы 5 Всесоюзной конференции по инженерным проблемам термоядерных реакторов, стр.176, Ленинград, 1990
10. V.K.Chernyshev, G.I.Volkov, V.A.Ivanov and V.V.Vakhrushev. Study of basic regularities of formation of multi-MA-current pulses with short risetime by EMG circuit interruption. Megagauss Physics and technology, Edited by Peter I. Turchi, p.663, 1979
11. V. Chernyshev, M. Protasov, V. Shvetsov, P. Piskarev, E. Zharinov, G. Volkov, V. Vakhrushev, B. Grinevich, V. Ivanov, V. Demidov, S. Pak, N. Bidylo, V. Pogorelov, A. Petrukhin, A. Kuzyaev, V. Yakubov, V. Shpagin. Explosive magnetic generators of "POTOK" family, VIII Int. Pulsed Power Conf. 17-19 June, San-diego, USA, 1991
12. V.K.Chernyshev, E.I.Zharinov, S.A.Kazakov, V.N.Buzin, V.E.Vaneev and M.I.Korotkov. Magnetic flux cutoffs in helical explosive magnetic generators. in Proceedings of MG-4 conference Megagauss Technology and Pulsed Power Applications. Edited by C.Fower, R.Caird and D.Erickson. Plenum Press, New York, London, p.455, 1986
13. Г. Кнопфель. Сверхсильные импульсные магнитные поля. Мир, Москва, 1972
14. В. А. Демидов, Е.И. Жаринов, С.А. Казаков, В.К. Чернышев. Быстроходные спиральные взрывомагнитные генераторы "Сверхсильные магнитные поля". Труды конференции MG-III. Изд. Наука, Москва, 1984
15. В.К. Чернышев, Е.И. Жаринов, О.Д. Михайлов. Влияние осевого смещения витков на возникновение пробоев в спиральных ВМГ. ПМТФ, №1, стр. 3, 1985
16. V.Chernyshev, M.Protasov, V.Shevstov, P.Piskarev, E.Zharinov, G.Volkov, V.Vakhrushev, B.Grinevich, V.Ivanov, V.Demidov, S.Pack, N.Bidylo, V.Pogorelov, A.Petrukhin, A.Kuzyaev, V.Yakubov, V.Shpagin. Explosive magnetic generators of "POTOK" family. VIII Int. Pulsed Power Conf. 17-19 June, San-Diego, USA, 1991
17. Ю.Б. Харитон, В.Н. Мохов, В.К. Чернышев, В.В. Якубов. О работе термоядерных мишеней с магнитным обжатием. УФН, т. 120, 706, 1976
18. В.Н. Мохов, В.К. Чернышев, В.В. Якубов, М.С. Протасов, В.М. Данов, Е.И. Жаринов. О возможности решения проблемы управляемого термоядерного синтеза на основе магнитогазодинамической кумуляции энергии. ДАН СССР, том 247, №1, стр. 83, 1979
19. Investigation of liner pondermotor units, used as drivers in magnetic implosion system. V.Chernyshev, V.Mokhov, M.Protasov, V.Yakubov, A.Petrukhin, A.Kuzyaev, E.Pavlovskii, A.Buyko, B.Grinevitch, V.Mamyshev, V.Vakhrushev, V.Shevstov, V.Demidov. VIII Int. Pulsed Power Conf. 17-19 June, San-Diego, USA, 1991
20. А. Буйко, Г. Волков, С. Гаранин, В. Демидов, Ю. Долин, В. Змушко, В. Иванов, В. Корчагин, М. Ларцев, В. Мамышев, И. Морозов, Н. Москвичев, В. Мохов, А. Мочалов, Е. Павловский, С. Пак, С. Трусилло, В. Чернышев, В. Якубов. Исследование возможности получения термоядерной замкнутой плазмы в системе с магнитным обжатием - МАГО. III Забавихинские Научные чтения. Кыштым, Россия, 14-17 января, 1992. Physics of High Energy Densities.
21. Investigation of possibility of thermonuclear magnetized plasma in the system with magnetic implosion MAGO. A.Buyko, G.Volkov, S.Garanin, V.Demidov, Yu.Dolin, V.Zmushko, V.Ivanov, V.Korchagin, M.Lartsev, V.Mamyshev, I.Morozov, N.Moskvichev, V.Mokhov, A.Mochlov, E.Pavlodckii, S.Pack, S.Trusillo, V.Chernyshev, V.Yakubov IX Int. Pulsed Power Conf. 21-23 June, Albuquerque, USA, 1993

# Status of Equation of State for Aluminum in the Light of Beam-Target Interaction Experiments at KALIF

B.Goel, W.Höbel, H.Marten

*Forschungszentrum Karlsruhe Postfach 3640, 76021 Karlsruhe, Germany*

O.Yu. Vorobiev, I.V. Lomonosov, V.K.Gryaznov

*Institute of Chemical Physics Chernogolovka, Russia*

## Abstract

The present paper contains an investigation of the hydrodynamics of thin Aluminum foil accelerated by light-ion beams at KALIF using  $B_{\theta}$ -diode. The peak power density in these experiments was  $0.15 \pm 0.05$  TW/cm<sup>2</sup>. In an earlier paper we have analysed the experimental data using an analytical equation of state. In the present paper we show that the state of these accelerated foils is sensitive to the equation of state data and use data based on more profound models. We combine EOS models designed for shock wave modelling describing melting, vaporisation and experimental data on compression and unloading of porous matter with those developed for strongly ionised material based on the model of chemical equilibrium.

## Introduction

Due to the bulk character of energy deposition and high specific power density light ion beam is attractive tool for the investigation of the properties of matter in extreme conditions. During the energy deposition the state of the matter changes from initially solid to partially ionised dense plasma and then finally to strongly coupled hot plasma. The response of the target to the beam action depends on the thermodynamical and optical (in the case of high temperatures) properties of the target material in all the states reached in energy deposition zone. So the measurements of the acceleration of the target can be used to check EOS models in a wide range.

In the present work we analyse results of foil acceleration experiments using different EOS models in numerical simulation. Wide-range semiempirical multiphase EOS for aluminum [1] based on available shock-wave experimental data has been combined with a model of chemical equilibrium [2] accounting for multiple ionisation of material. The aim of this work is to investigate how sensitive is velocity profile of accelerated foil to thermodynamical properties i.e. equation of state of material.

## Mathematical Model

The Euler equations of motion are used to describe the dynamics of matter under the impact of an intense ion beam. To describe the dynamic damage of the material we use a continuum-kinetic model obtained on the basis of experimental observation of the velocity profiles of the free surface as the compression pulse reaches the surface and causes a release wave in the target [1]. To close the equations of motion equations of state are used. The details of hydrodynamic calculations have been published previously [3]. The hydrodynamic calculations were performed using the Godunov method with a moving-grid algorithm. The nodes of the grid are moved with contact velocities calculated by

solving the Riemann problems between the neighbouring cells. The numerical procedure employed allows the Riemann problem to be solved for any equation of state.

### Experiments and simulation

Experiments analysed in this paper have been described extensively by Baumung [4]. Thin foils of aluminum of different thickness were irradiated with KALIF beam. The velocity of rear surface was measured by the ORVIS system. In our analysis we assume that the beam characteristics do not change appreciably from shot to shot. This assumption is justified for this analysis, because at present, not all the beam parameters are measured in each shot. The electrical signals on the diodes were measured regularly and showed no major differences for successful shots. The total beam intensity was measured to characterise the beam power by nuclear diagnostics and Faraday cups [5]. Because of the experimental constraints beam diagnostics cannot be performed together with the foil acceleration experiments.

Numerical simulation performed with the measured shape of voltage and power profile [5] showed, that with a reasonable variation of peak power density, between 0.1-0.2 TW/sq.cm we were not able to describe the experiment using the Bushman EOS. The main discrepancy appears when the material is ionised (that corresponds to the time interval between 10-20 ns). In [3] a simple analytical equation of state for aluminum was postulated to describe these experiments. This equation of state also describes shock compression data adequately. In Fig.1 results obtained with analytical EOS are compared with those calculated using SESAME EOS. In the present work, to improve the description we have combined the Bushman EOS with the model of chemical equilibrium [7] using normalised ionisation degree as a switching parameter. This approach has been used in ref.[8] to describe the shock wave generation by intense pulse of soft x rays. In ref.[7] the chemical model [2] of gases has been extended to the region of strongly coupled multicomponent plasma. In a strongly coupled plasma short range forces play an important role. The repulsive forces accounting for the effect of overlapping electrons are taken into account. In addition to the repulsive mechanism bond energies responsible for the existence of condensed states are also introduced into the chemical model. Results of simulations with this unified EOS table are shown in Fig.2. It is seen that accurate accounting for ionisation and for short range forces allows to describe experiments much better. In this paper we compare this unified EOS with the results of our analytical model [3] and investigate the region of discrepancies.

### Comparison of EOS models

In Fig.3-4 different EOS models used in simulation are compared. At high energy densities (curves **D**) all EOS except of the Bushman EOS give very close values for pressure in low density region. Analytic EOS occupies an intermediate place between the Bushman model and the other models. The main reason why the Bushman EOS does not describe the experiment (at 10-20 ns of time interval) seems to be the underestimation of the plasma pressure at moderate energy density (see curve **B**). This is no surprise as in the original Bushman model partial ionisation is not taken into account. The agreement of results calculated with SESAME EOS with experiments is also not satisfactory. The other models, on the contrary, overestimate the pressure at high energy densities. Results of simulation with the Bushman EOS (Fig.1) show not only insufficient amplitude of the

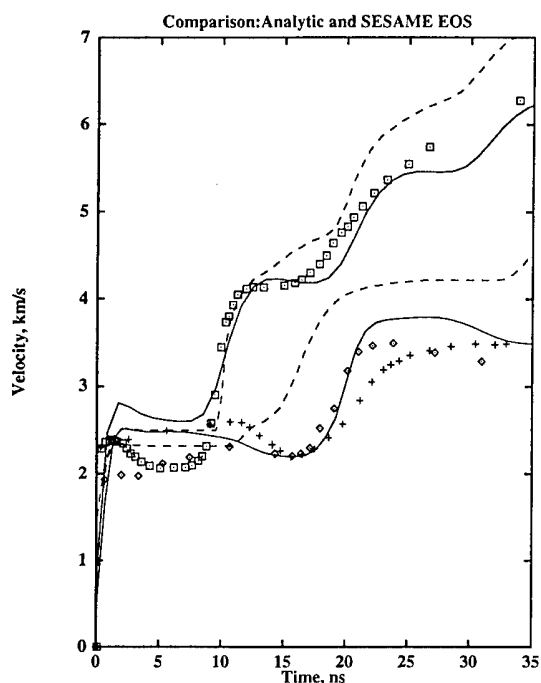


Figure 1: Velocity profiles for 0.075, and 0.05 mm Al foils calculated using the Analytic EOS (solid lines) and SESAME EOS (dashed lines)

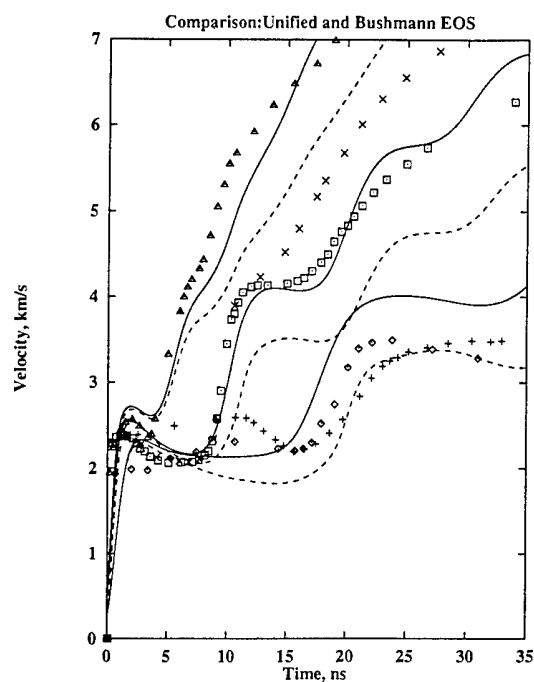


Figure 2: Velocity profiles for 0.075, 0.05, 0.033 mm Al foils calculated using unified tabulated EOS (solid lines) and the Bushman EOS (dashed lines).

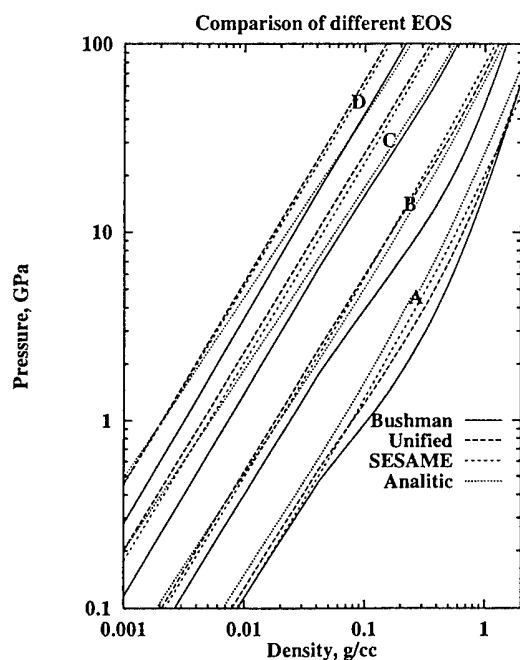


Figure 3: Pressure as a function of density at constant internal energy (A-50 kJ/g, B-200 kJ/g, C-800 kJ/g and D-2 MJ/g) calculated using different EOS models

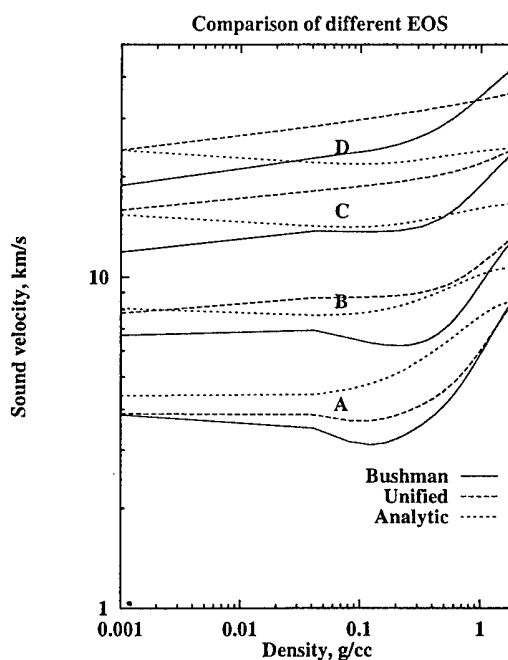


Figure 4: Sound velocity as a function of density at constant internal energy (A-50 kJ/g, B-200 kJ/g, C-800 kJ/g and D-2 MJ/g) calculated using different EOS models

second velocity step (because the pressure calculated is not high enough) but also a slower increase in the second velocity step. This can be partially explained by underestimation of the sound velocity (see Fig.4 curves **A**, **B**) calculated with this EOS. Results obtained with corrected (unified) EOS (see Fig.2) describe experiments better also due to higher sound velocity in comparison with original Bushman EOS.

## Conclusions

On the basis of the analysis of foil acceleration experiments we have compared different equations of state. We have shown that simulation results strongly depend on the used equation of state. In addition to the analytical equation of state in generalised Mie-Grüneisen form [3] that describes experiments well, we have also generated a tabulated unified EOS. This tabulation combines the advantage of condensed matter equation of state, that describes the shock wave experimental data, with chemical equilibrium model accounting for interparticle interactions in strongly coupled dense plasma. The main difference in the analytical equation of state that describe experiments well [3] and other equations of state is in the region of temperatures 5-10 eV and densities 1.-0.1 g/cc. The implication of this deviation on the parameters of chemical model is under investigation.

## Acknowledgements

The authors thank Prof.G.Kessler, director of the Institute of Neutron Physics and Reactor Technology of the Research Center Karlsruhe and Prof. V.E.Fortov of the High Energy Density Research Center, Moscow for their continuous interest and support making this work possible. The work was partly supported by the INTAS agreement No 94-3189.

## References

- [1] Bushman A.V, Kanel G.I., Ni A.L., Fortov V.E. Intense Dynamic Loading of Condensed Matter. Taylor & Francis, London (1993)
- [2] Ebeling, W., Förster, A., Fortov, V.E., Gryaznov, V.K. & Polishchuk, A.Ya. (1991) Thermophysical Properties of Hot Dense Plasmas, Teubner-Texte zur Physik, Bd. 25, Teubner Verlag, Stuttgart-Leipzig
- [3] Goel B., Vorobiev O.Yu. Equation of State Information from Beam-Target Interaction Experiments at KALIF, accepted for publication in *Laser and Particle Beams* (1996)
- [4] Baumung K. et al. Proc. 9th International Conference on High-Power Particle Beams, (ed. D.Mosher, G.Cooperstein) Vol.I (1992) 68
- [5] Hoppé, P. et al. (1995) Characteristics of the ion beam produced by  $B_{\theta}$ -diode, in Physics of Intense Light Ion Beams and Production of High Energy Density in Matter, Annual Report 1994, Report FZKA 5590, Forschungszentrum Karlsruhe
- [6] SESAME Library, Lawrence Livermore National Laboratory, Report UCID-118574-82-2 (1982).
- [7] Gryaznov, V.K, Iosilevski et al, Thermophysical Properties of Working Media of Gas Phase Nuclear Reactor (Atomizdat, Moscow, 1980) in Russian
- [8] Grabovski, E.V., Smirnov V.P. et al JETP 82 (3) (1996)

## Pulse-Power Technology and Its Applications at LBT, Nagaoka

K. Yatsui, W. Masuda, C. Grigoriu, K. Masugata, W. Jiang,  
G. Imada, K. Imanari, T. Sonegawa and E. Chishiro

*Laboratory of Beam Technology, Nagaoka University of Technology, Nagaoka,  
Niigata 940-21, Japan*

Research activities on pulsed power technology and its applications at Laboratory of Beam Technology, Nagaoka University of Technology are reviewed. These activities include 1) development of a high power induction type linear accelerator (8 MV, 5 kA, 50 ns), 2) development of intense ion beam source, and 3) applications of pulsed ion beam in thin film and nanosize powder production.

### 1. Introduction

One of the important applications of the pulsed power technology is generation of intense, pulsed charged particle beam. In our laboratory, we are developing intense ion beam source for producing high temperature, high density plasma which is extensively applied in material processing. We are also developing intense electron beam source as a driver of high power, pulsed electromagnetic radiation.

Our research interests are 1) deposition of thin films by ion beam evaporation, 2) production of nano-size powders by ion beam ablation, 3) materials surface treatment by ion beam bombardment, and 4) generation of high power electromagnetic radiation, from microwave to X-ray, by using relativistic electron beams.

Most of the experimental results presented in this paper were obtained on the pulsed power generator ETIGO-II[1]. Beside ETIGO-II, in our laboratory, there are several other pulsed power modulator in different scales with different levels of power output. We are also developing our next large accelerator, ETIGO-III.

A new accelerator, ETIGO-III, is presently under construction in our laboratory, which is a high power induction type linear accelerator with output electron beam of electron energy 8 MV, beam current 5 kA, and pulse width 50 ns. It is expected to be used in experiments on pulsed microwave generation, pulsed X-ray emission, free electron laser, and other applications.

We have developed a three-dimensionally focusing, self-magnetically insulated ion beam diode, the spherical plasma focus diode (SPFD). With the SPFD, maximum ion beam energy of 360 J was focused on an target area of  $0.07 \text{ cm}^2$ , giving average ion beam energy density as high as  $5 \text{ kJ/cm}^2$ .

We have demonstrated successful preparation of thin films and nanosize powders by using the technique of intense pulsed ion beam evaporation. In this paper, we present the experimental results of thin film deposition of ZnS,  $\text{YBa}_2\text{Cu}_3\text{O}_{7-x}$ ,  $\text{BaTiO}_3$ , cBN,  $\text{ZrO}_2$ , ITO, and apatite, as well as the experimental results of the synthesis of nanosize powders of  $\text{Al}_2\text{O}_3$ . [2-7]

### 2. Induction linear accelerator ETIGO-III

An induction type electron beam accelerator, ETIGO-III, is presently under construction.



Figure 1 shows the schematic diagram of ETIGO-III. It consists of Marx generator, pulse forming line, transmission line, and induction voltage multiplier. The output voltage (670 kV) of the pulse forming line is fed to three cores of each stage, inducing 2 MV across each gap. There are totally four gaps in the induction voltage multiplier that is about 13 meters long. The first stage is an electron injector which produces an annular electron with outer diameter of 6 cm. The other three stages accelerate the injected beam to electron energy of 8 MV with peak current of 5 kA and pulse width of 50 ns.

ETIGO-III is expected to be in full operation by the end of the year 1996. The research activities using ETIGO-III will be mainly on generation of electromagnetic radiation. Experiments on microwave and X-ray generation will be carried out early next year, which will probably be followed by experiments on free electron laser.

We are also planning to add the outputs of other pulsed power generators to the induction voltage multiplier to obtain higher electron energy.

### **3. Development of high power density ion beam source [8,9]**

In order to obtain an ion beam with a large solid angle of irradiation, we have developed a new type of self-magnetically insulated ion-beam diode, the spherical plasma focus diode (SPFD). Figure 2 illustrates the structure of the SPFD. Basically, it consists of two concentric spherical electrodes. The outer electrode is the anode that has an epoxy flashboard (spray with 10  $\mu\text{m}$  in thickness) on the inner surface as the ion source. The inner electrode is the cathode which is made of copper wires (0.1 mm in diameter) with a transparency of  $\sim 95\%$ . The basic principle of ion-beam generation by the SPFD is as follows. Electrons are first accelerated toward the anode from the cathode. The diode current generates an azimuthal magnetic field that turns electrons due to the Lorentz force. The gap is insulated by the self-magnetic field gradually from the upstream side toward the downstream side when the current increases. On the inner surface of the anode, due to electron bombardment and/or surface flashover, a surface plasma is generated from which ions are accelerated toward the cathode. Through the cathode, the ions focus toward the geometric center.

The total ion beam energy generated and focused by the SPFD was measured by using the method of calorimetry. Figure 3 shows the experimental setup. An aluminum cup was set in the cathode. In front of the cup, there is a copper plate on which a centered hole with diameter of 3 mm was opened. The cup was separated from the plate and the cathode by heat insulating material. The temperature of the cup was monitored by a thermal sensor connected with a thermometer.

The experiments were carried out on pulsed power generator ETIGO-II, operated with the output of voltage 1 MV, current 100 kA, and pulse width 50 ns. The maximum ion beam energy calculated from the temperature increase of the aluminum cup was 360 J, giving an ion beam energy efficiency of  $\sim 7.2\%$  and an average ion beam energy density of  $\sim 5 \text{ kJ/cm}^2$ , over the  $\phi 3 \text{ mm}$  hole on the copper plate.

### **4. Applications of intense pulsed ion beam to materials science [2-7]**

#### **4.1 Source of Intense, Pulsed Ion Beam**

In the following experiments, we have used a magnetically insulated ion diode which is driven by the pulsed power generator "ETIGO-II"[1]. Figure 4 shows the experimental setup of the ion beam diode and the film deposition system. The diode gap, where the ions are accelerated, has a geometrically focused configuration. The ions, mostly protons, are

generated by surface flashover from the polyethylene sheet attached on the anode surface. The cathode, working as a one-turn theta-pinch coil, produces a transverse magnetic field, by which electrons emitted from the cathode are prevented from reaching the anode. The radii of anode and cathode curvatures are 160 and 150 mm, respectively. Gap length between the anode and cathode is 10 mm. The vacuum chamber is evacuated to  $\sim 10^{-4}$  Torr.

Figure 5 shows typical waveforms of  $V_d$  (diode voltage),  $I_d$  (diode current),  $P_d (= V_d I_d)$ , and  $J_i$  (ion-current density) at  $z = 140$  mm downstream from the anode. From Fig. 25 we see the peaks to be  $V_d \sim 1$  MV,  $I_d \sim 80$  kA,  $P_d \sim 80$  GW,  $J_i \sim 1$  kA/cm<sup>2</sup> with  $\tau$  (pulse width)  $\sim 70$  ns (FWHM).

## 4.2 Experimental results of thin film preparation

### 4.2.1 ZnS and ZnS:Mn Thin Films

Figure 6 shows the film thickness as a function of the number of shots of the LIB, where a sintered, cubic ZnS (35-mm in diameter, 5-mm thick) and a glass was used as the target and the substrate, respectively. The distance between the target and the substrate was approximately 40 mm. We see that the film thickness is  $\sim 0.3$  mm/shot (over 30 mm in diameter), and that it increases almost linearly with increasing number of shots.

To evaluate the crystallinity of the film prepared above, we have studied an X-ray diffraction (XRD) pattern, a sample of which is presented in Fig. 7. The ASTM (American Standard for Testing Materials) data of cubic and hexagonal ZnS are also plotted for comparison. All the positions of these peaks are seen to be in a good agreement with those of hexagonal ZnS, and the intensity ratio as well. Hence, we find the film prepared is hexagonal with a strong orientation in the (002) direction. Adding Mn as a color center, we have prepared ZnS:Mn thin film and developed double-insulating-layer-structured electroluminescent device, where we have sequentially deposited BaTiO<sub>3</sub>, ZnS:Mn, Ta<sub>2</sub>O<sub>5</sub>, HfO<sub>2</sub>, and Al layers on an indium-tin-oxide (ITO) coated glass. The thickness of ZnS:Mn is  $\sim 200$  nm.

Figure 8 shows the luminance vs. applied voltage of this electroluminescent device (zero to peak, sinusoidal) with the operation frequency as a parameter. The color emitted was observed to be yellow-orange. The threshold voltage ( $V_{th}$ ) is  $\sim 80$  V, above which the luminance of 1 cd/m<sup>2</sup> is obtained. The luminance rapidly increases with increasing voltage in the range of 60  $\sim$  110 V, and also with increasing frequency in the range of 100 Hz to 10 kHz. The maximum luminance of 105 cd/m<sup>2</sup> is obtained at 10 kHz excitation at 144 V.

### 4.2.2 YBaCuO Thin Film

Figure 9 shows the XRD patterns of the film prepared by the IBE, where sintered YBa<sub>2</sub>Cu<sub>3</sub>O<sub>7-x</sub> (20-mm in diameter, 3-mm thick) and MgO (100) is used as the target and the substrate, respectively. Here, a mylar film (3-mm thick) is placed between the diode chamber and the target box so as to exclude carbon ions which are included in the LIB extracted from the MID. As deposition, no crystallinity exists (see Fig. 9(a)). After the annealing, for 2 hours at 985°C and 10 hours at 485°C in oxygen for this particular case, the crystallinity appears. The film is seen to be strongly oriented in the c axis (see Fig. 9(b)).

Figure 10 shows the resistivity of the film prepared by the IBE as a function of temperature with the pressure of oxygen in the target as a parameter. We see  $T_c$  (onset)  $\sim 60$  K and  $T_c$  (zero)  $\sim 25$  K.

### 4.2.3 BaTiO<sub>3</sub> Thin Film

Figure 11 shows the XRD pattern of the film prepared by five shots by the IBE, where cubic BaTiO<sub>3</sub> and Si (100) coated by aluminum is used as the target and the substrate, respectively.

The content of the target is as follows: BaTiO<sub>3</sub> 92.7 mol%, TiO<sub>2</sub> 4.5 mol%, Nd<sub>2</sub>O<sub>3</sub> 2.6%, Bi<sub>2</sub>O<sub>3</sub> 0.1 mol%, and MnCo 0.1 mol%. Since several peaks of (100), (110), (111), (200), (210) and (211) corresponding to BaTiO<sub>3</sub> are clearly obtained, a polycrystalline film of cubic perovskite BaTiO<sub>3</sub> has been prepared. Figure 12 shows the characteristic X-ray intensity ratio of Ti/Ba measured by XMA (or EPMA) as a function of the number of shots. Here, the mark of ● and ○ indicates the characteristic X-ray intensity ratio of Ti(K<sub>α</sub>)/Ba(L<sub>α</sub>) and Ti(K<sub>β</sub>)/Ba(L<sub>β1</sub>) of the film prepared, respectively. Furthermore, the upper and lower line indicates the characteristic X-ray in-tensity ratio of the target, Ti(K<sub>α</sub>)/Ba(L<sub>α</sub>) = 1.25 and back side IBE (IBE/BS), one shot, 25°C. Ti(K<sub>β</sub>)/Ba(L<sub>β1</sub>) = 0.52. We clearly find that the X-ray intensity ratio of the film is almost the same as the target indicating good stoichiometry, and that it does not change if we increase the number of shots.

We compared the characteristics of BaTiO<sub>3</sub> thin films prepared on the front and the rear sides of the substrate. Figure 10 shows the dielectric constant as a function of the frequency for the front side IBE compared with the back side IBE. It is seen from Fig. 13 that, compared with that obtained by the back side IBE, the dielectric constant of the film obtained by the front side IBE is increased at low frequencies.

#### 4.2.4 BN Thin Film

Figure 14 shows the IR transmittance characteristics of the film prepared by the IBE with the diode voltage as a parameter, where hexagonal BN (h-BN) and Si is used as the target and the substrate, respectively. There exists only h-BN at low power density. At high power density, on the other hand, we find clearly an absorption dip corresponding to c-BN in addition to h-BN mentioned above.

#### 4.2.5 ZrO<sub>2</sub> Thin Film

Figures 15 (a) and (b) show the XRD patterns of thin films prepared by the IBE with the percentage of Y<sub>2</sub>O<sub>3</sub> in the target as a parameter, where sintered, monoclinic ZrO<sub>2</sub> and Si(100) is used as the target and the substrate, respectively. At lower percentage of Y<sub>2</sub>O<sub>3</sub>, e.g., 1.1, 2.2, and 4.5 mol% of Y<sub>2</sub>O<sub>3</sub>, tetragonal structure appears, but it changes to cubic at higher percentage of Y<sub>2</sub>O<sub>3</sub>, e.g., 7 and 12 mol% of Y<sub>2</sub>O<sub>3</sub>.

### 4.3 Experimental Results of Nanosize Powder Syntheses

Extending the basic idea of the ion beam evaporation for producing thin films, we have used this method to synthesize powders by cooling the ablation plasma with particles in gases. Reactive LIB-ablation syntheses of nanosize powers of alumina has been succeeded.<sup>5,6)</sup>

Figure 16 shows the experimental setup for power syntheses. The ion beam diode and the target are basically the same with that used in the experiments for thin film deposition. A mylar film (2 μm thick) is placed to separate the target chamber from the diode. The target chamber is filled by oxygen with the pressure of 1 or 10 Torr. The powders are collected on the surface of the cylinder located on top of the target as well as on the meshes (stainless steel, 400 meshes) located at the end of the cylinder. Analysis, including the x-ray diffraction (XRD) and the transmission electron microscopy (TEM), were carried out for the sample made by 20 shots.

Figure 17 shows the XRD patterns of the powders as produced (in the absence of annealing) at 1 Torr (Fig. 14a) and 10 Torr (Fig. 17b) of oxygen. Here, the powders were collected from the inner wall at 270-330 mm downstream from the target (Al) and stuck on the meshes. At 1 Torr of oxygen (see Fig. 17a), we see clearly the presence of Al in addition to stainless steel which originates from the meshes used. Furthermore, the peaks due to γ-alumina can

be seen, although the intensities are weak. At 10 Torr of oxygen (see Fig. 17b), on the other hand, the peaks of  $\gamma$ -alumina are strongly enhanced and become predominant while those of aluminum are weakened. Hence, we find that aluminum tends to react with oxygen at higher pressures.

Figure 18 shows TEM photographs of the powders obtained at (a) 1 Torr and (b) 10 Torr of oxygen, while the electron diffraction pattern of the powders of Fig. 18b is presented in Fig. 18c. Here, the powders were collected by meshes placed at 330 mm downstream from the target. It is clearly found there exist powders in both cases whose diameters are several tens of nm. Furthermore, the shape seems to be spherical. From Fig. 18c, it is clear that the electron diffraction pattern agrees with that of  $\gamma$ -alumina.

Figure 19 shows the distribution of the diameter of the powders prepared at (a) 1 Torr and (b) 10 Torr of oxygen, which were obtained from Figs. 18a and 18b, respectively. At 1 Torr of oxygen (see Fig. 19a), we see that the diameters of the powders distribute from 5 ~ 50 nm, and that the powders of 10 ~ 25 nm in diameter, dominate ~ 75 % of the whole. From Fig. 19b, at 10 Torr of oxygen, they distribute from 5 ~ 65 nm. The powders of 5 ~ 25 nm in diameter dominate, which corresponds to ~ 90 % of the whole.

Figure 20 shows XRD patterns of the powders produced at 10 Torr of oxygen with the annealing temperature in nitrogen as a parameter; (a) 800°C, (b) 1100°C, and (c) 1200°C. At an annealing temperature of 800°C, only  $\gamma$ -alumina can be seen (see Fig. 20a). At 1100°C (Fig. 20b),  $\gamma$ -alumina disappears, and instead of it  $\delta$ -alumina (a little bit strong) and  $\alpha$ -alumina (weak) are seen to be present. At 1200°C, furthermore, we see in Fig. 20c that  $\delta$ -alumina disappears, and that only  $\alpha$ -alumina remains.

## References

- [1] K. Yatsui, Y. Shimotori, Y. Araki, K. Masugata, S. Kawata, and M. Murayama, Nucl. Fusion Suppl. **3** (1987) 177.
- [2] K. Yatsui, Laser and Particle Beams, **7** (1989) 733.
- [3] Y. Shimotori, M. Yokoyama, H. Isobe, S. Harada, K. Masugata, and K. Yatsui, J. Appl. Phys., **63** (1988) 968.
- [4] Y. Shimotori, M. Yokoyama, S. Harada, K. Masugata, and K. Yatsui, Jpn. J. Appl. Phys. **28** (1989) 468.
- [5] K. Yatsui, X. D. Kang, T. Sonegawa, T. Matsuoka, K. Masugata, Y. Shimotori, T. Satoh, S. Furuuchi, Y. Ohuchi, T. Takeshita, and H. Yamamoto, Phys. Plasmas, **1** (1994) 1730.
- [6] K. Yatsui, W. Jiang, G. Imada, T. Sonegawa, E. Chishiro, H. Kubo, K. Masugata, and W. Masuda, in Proceedings of the 10th Int'l Conf. on High Power Particle Beams, edited by W. Rix and R. White (NTIS, 1994), **II**, 913.
- [7] K. Yatsui, C. Grigoriu, H. Kubo, K. Masugata, and Y. Shimotori, Appl. Phys. Lett., **67** (1995) 1214.
- [8] W. Jiang, T. Sakagami, K. Masugata, and K. Yatsui, Physics of Plasmas, **2**, (1995) 325.
- [9] W. Jiang, T. Sakagami, K. Masugata, and K. Yatsui, Laser and Particle Beams, **13**, (1995) 343.

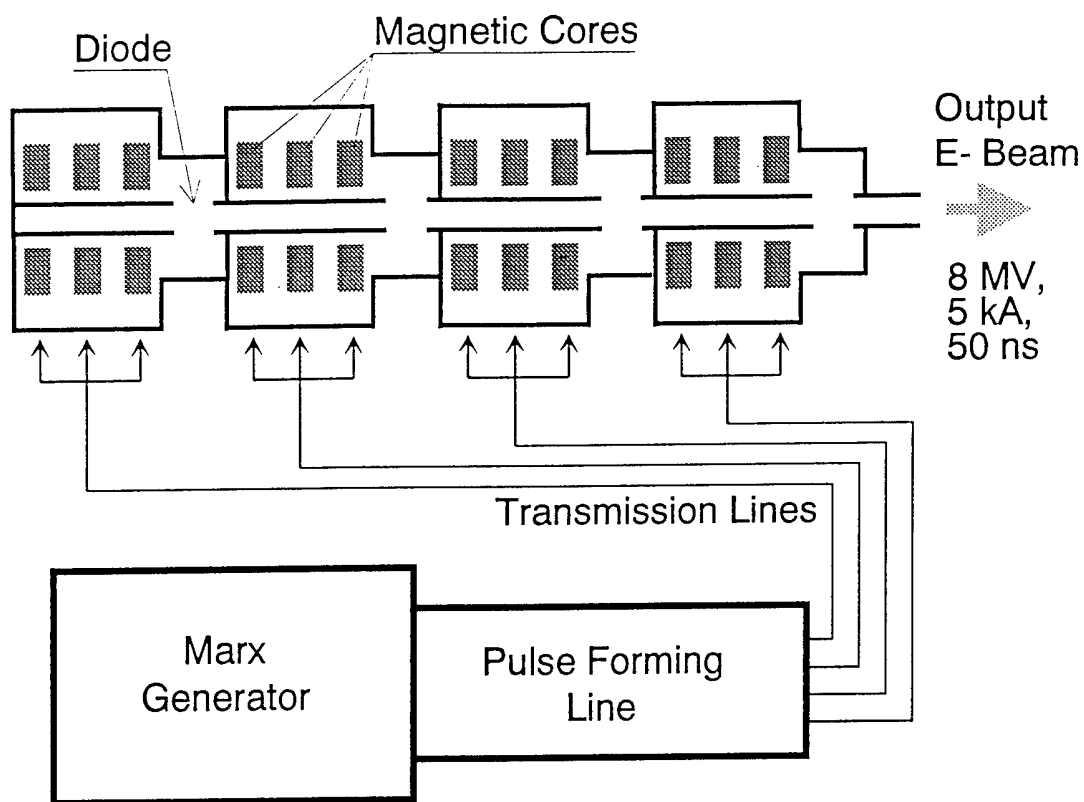


Fig. 1 Schematic of induction linear accelerator ETIGO-III.

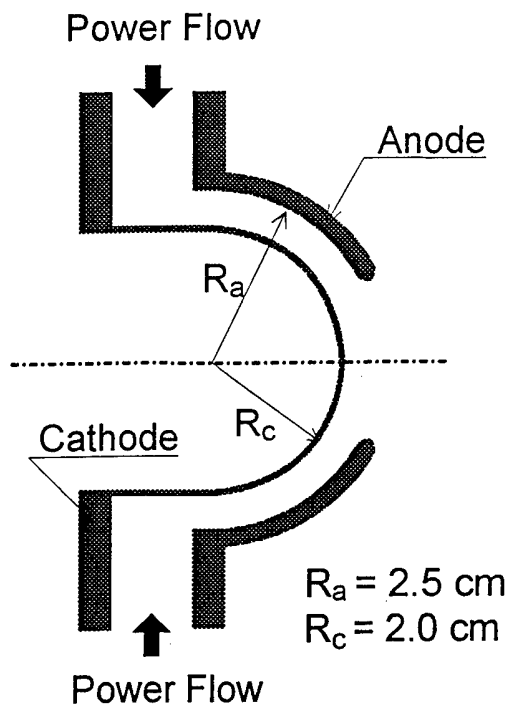


Fig. 2 Structure of spherical plasma focus diode (SPFD).

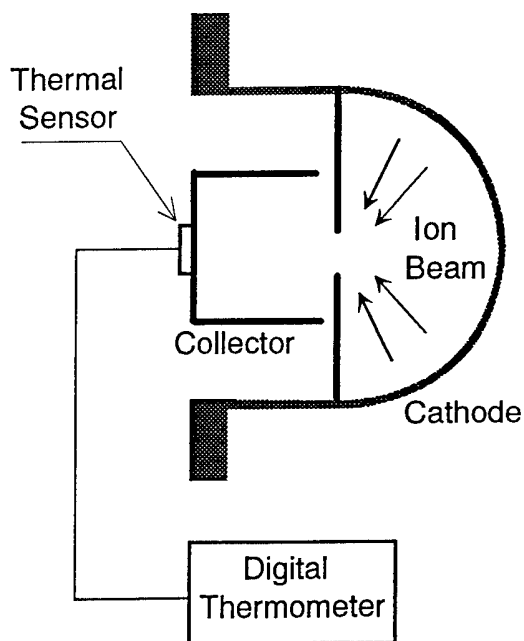


Fig. 3 Experimental setup for ion beam energy measurement.

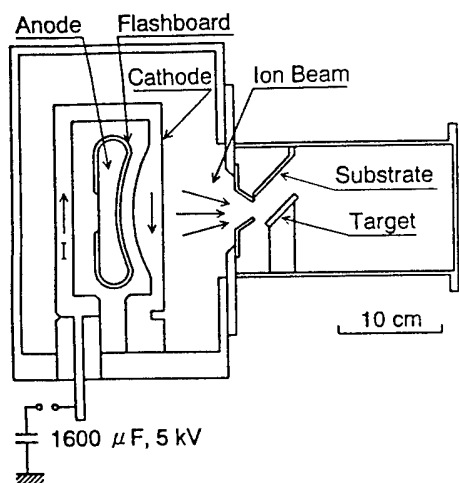


Fig. 4 Experimental setup for thin film deposition.

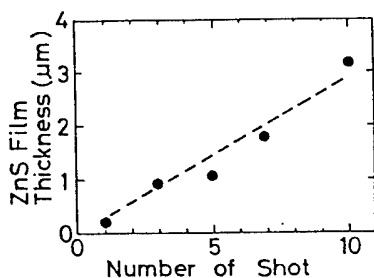


Fig. 6 Film thickness of ZnS vs. number of shots.  $V_d \sim 940$  kV,  $J_i \sim 7$  kA/cm<sup>2</sup>,  $l$  (distance between target and substrate) = 18 mm

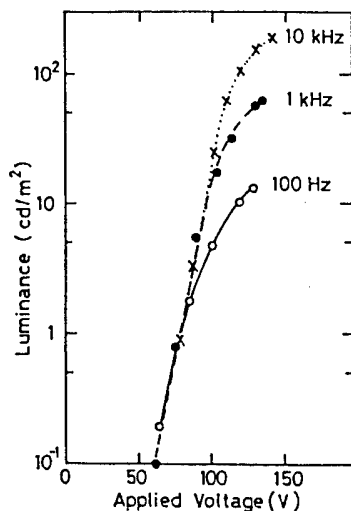


Fig. 8 Luminance of ZnS:Mn EL device vs. applied voltage.

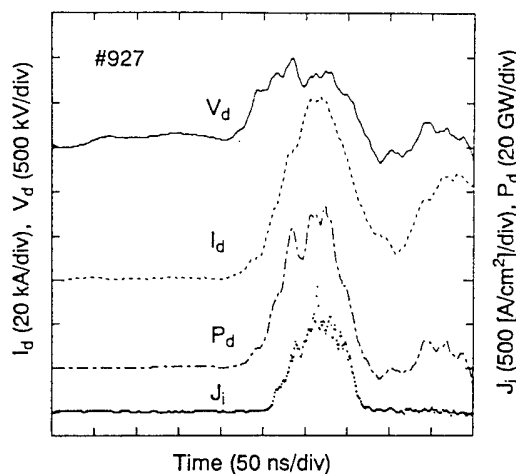


Fig. 5 Typical waveforms of  $V_d$ ,  $I_d$ ,  $P_d$  and  $J_i$ .

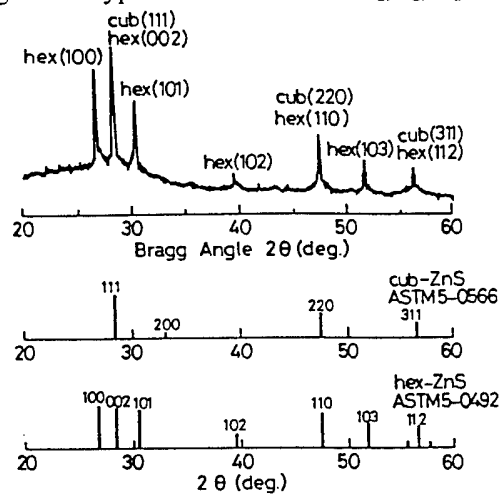


Fig. 7 XRD pattern for ZnS powdered from thin films.

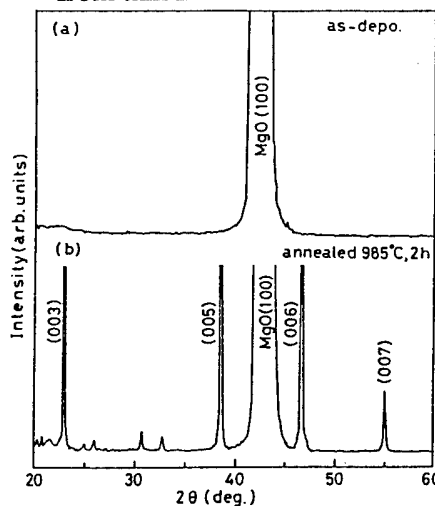


Fig. 9 XRD patterns of the YBaCuO film of (a) as deposition, and (b) after annealing.

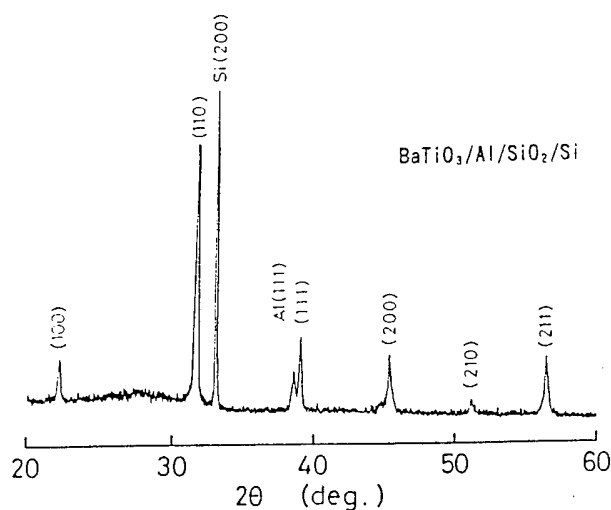


Fig. 11 XRD pattern of the BaTiO<sub>3</sub> film.

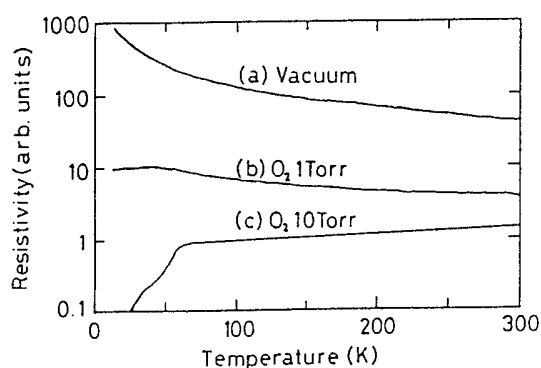


Fig. 10 Resistivity of the YBaCuO film vs. temperature with the oxygen pressure as a parameter (two shots, with Mylar film).

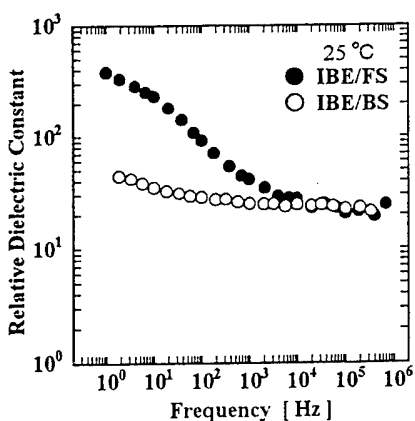


Fig. 13 Dielectric constant as a function of frequency for front side IBE (IBE/FS) and back side IBE (IBE/BS), one shot, 25°C.

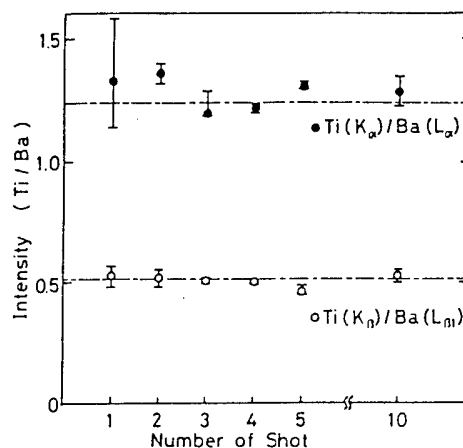


Fig. 12 Characteristic X-ray intensity ratio of Ti/Ba vs. number of shots.

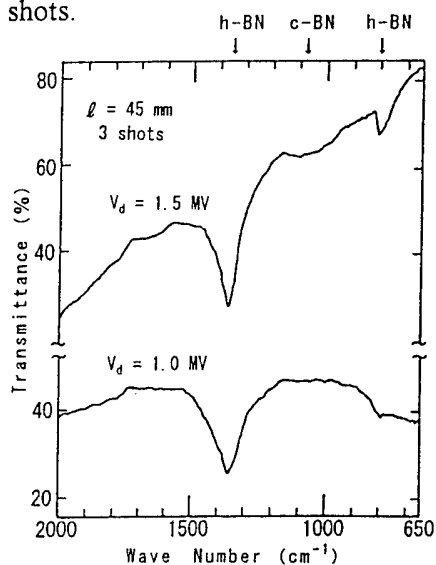


Fig. 14 IR transmission of the BN film.

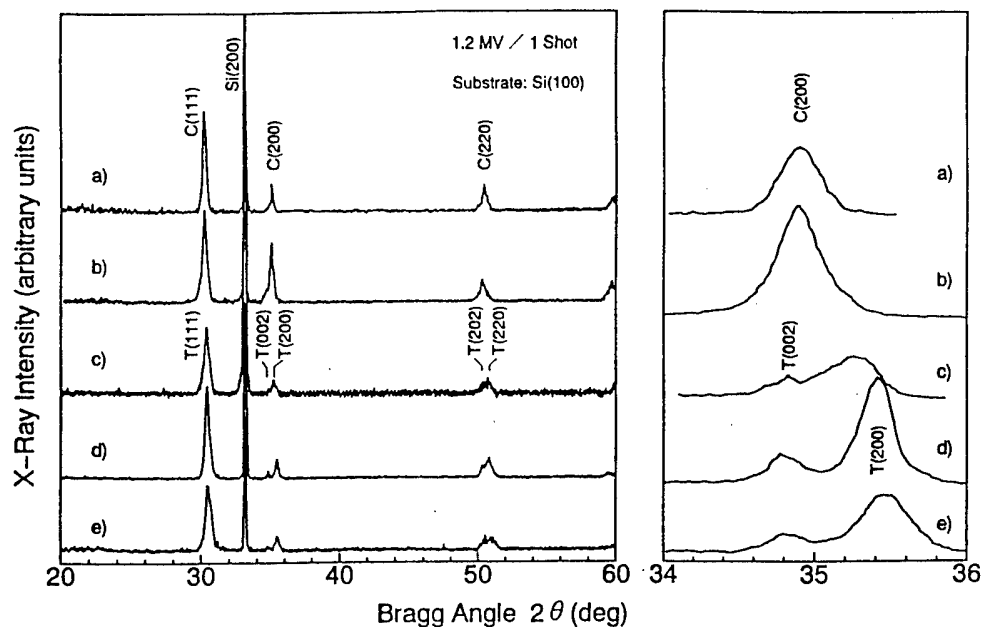


Fig. 15 XRD patterns of  $\text{ZrO}_2$  film (right: its magnified scale) with  $\text{Y}_2\text{O}_3$  (mol%) as a parameter; a) 12, b) 7, c) 4.5, d) 2.2, and e) 1.1.

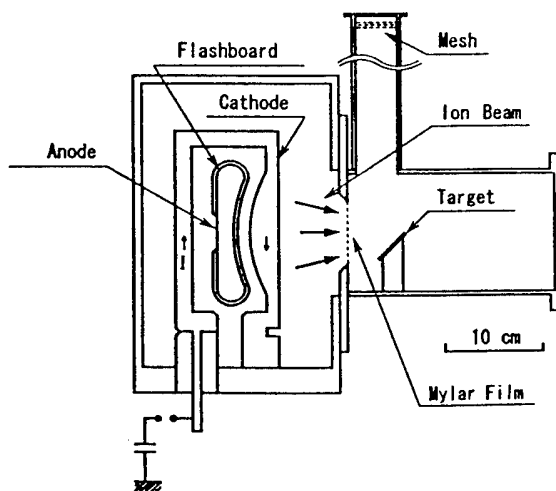


Fig. 16 Experimental setup for powder synthesis

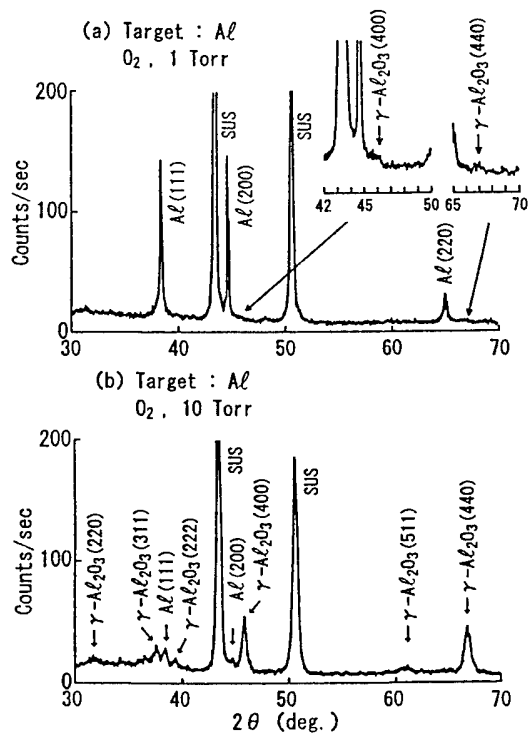


Fig. 17 XRD patterns of powders as produced at (a) 1 Torr and (b) 10 Torr of oxygen.



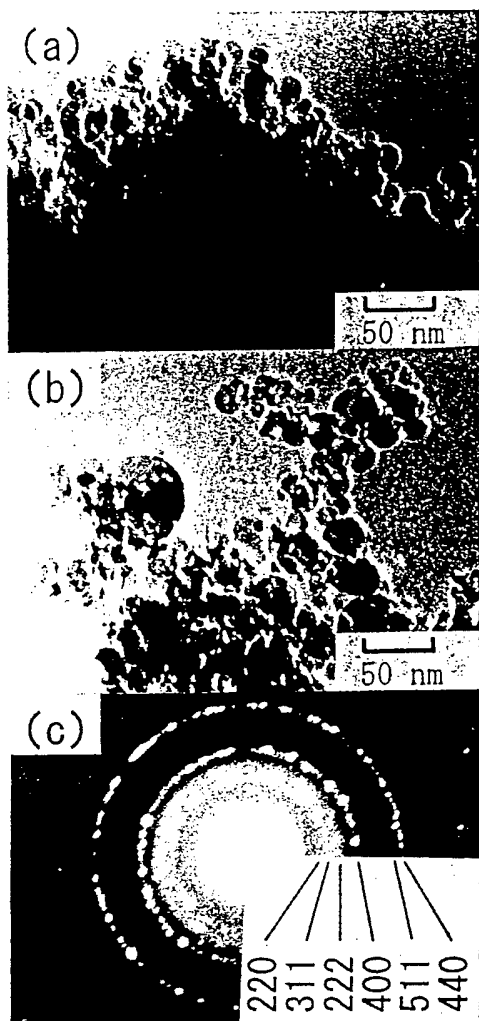


Fig. 18 TEM photographs of powders synthesized at (a) 1 Torr and (b) 10 Torr of oxygen, while electron diffraction pattern of (b) is presented in (c).

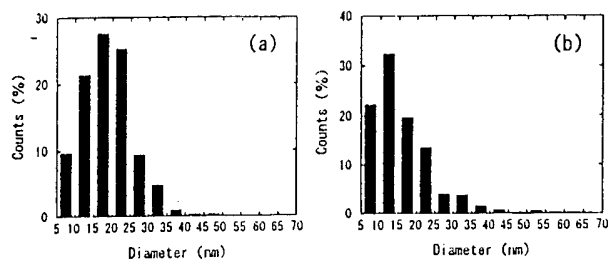


Fig. 19 Distribution of diameter of powders prepared at (a) 1 Torr and (b) 10 Torr of oxygen.

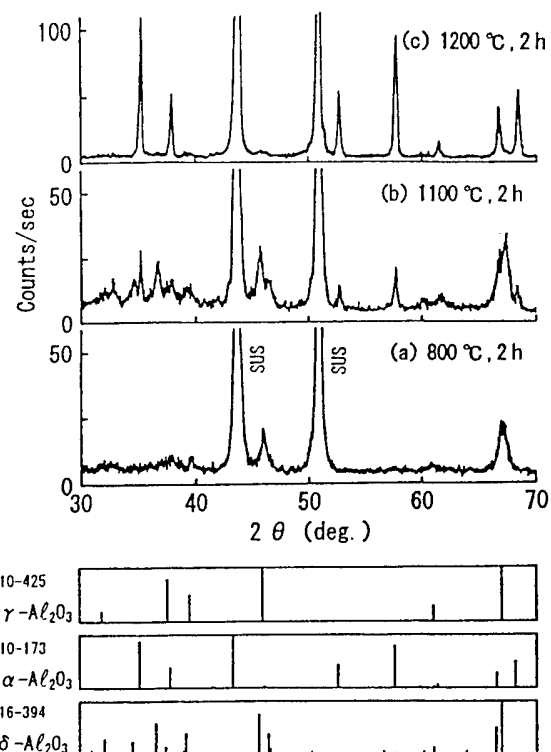


Fig. 20 XRD patterns of powders produced at 10 Torr of oxygen at annealed in nitrogen at (a) 800°C, (b) 1100°C, and (c) 1200°C.

## Pulsed Power Driven Hohlraum Research at Sandia National Laboratories

R. J. Leeper, T. E. Alberts, G. A. Allshouse, J. H. Aubert, P. Baca, P. M. Baca, J. E. Bailey, T. L. Barber, S. P. Breeze, A. L. Carlson, G. A. Chandler, D. L. Cook, M. S. Derzon, M. R. Douglas, R. J. Dukart, D. L. Fehl, T. Gilliland, D. E. Hebron, M. J. Hurst, D. O. Jobe, D. J. Johnson, J. W. Kellogg, M. K. Matzen, C. Martinez, T. A. Mehlhorn, D. H. McDaniel, E. J. McGuire, J. S. McGurn, W. F. McNamara, A. R. Moats, D. J. Muron, T. J. Nash, D. D. Noack, R. W. Olsen, R. E. Olson, J. L. Porter, J. P. Quintenz, L. E. Ruggles, C. L. Ruiz, P. S. Sawyer, J. F. Seamen, R. B. Spielman, M. A. Stark, J. A. Torres, D. M. VanDevalde, M. Vargas, D. F. Wenger, and D. M. Zagar,

*Sandia National Laboratories, Albuquerque, New Mexico 87185 USA*

**Abstract.** Three pulsed power driven hohlraum concepts are being investigated at Sandia National Laboratories. These hohlraums are driven by intense proton and Li ion beams as well as by two different types of z-pinch x-ray sources. This paper will be an overview of the experiments that have been conducted on these hohlraum systems and will discuss several new and novel hohlraum characterization diagnostics that have been developed for this work. These diagnostics include an active shock breakout measurement of hohlraum temperature and a new transmission grating spectrograph for detailed thermal radiation spectral measurements.

### Introduction

Indirect drive inertial confinement fusion (ICF) uses high powered laser beams, particle beams, or z-pinchs to compress and heat capsules containing fusion fuel with the goal of producing thermonuclear energy. In this scheme, the primary high powered radiation sources are used to heat high-Z radiation cavities, or hohlraums, converting the driver energy to x-rays which implode the capsule.<sup>1</sup> The hohlraum enables the capsule to be imploded with a high degree of symmetry since a radiation cavity acts to smooth spatial irregularities of the primary radiation source.

Another property of a hohlraum cavity that makes it useful for indirect drive ICF is its ability to amplify the power of the primary x-ray radiation source. A hohlraum can be described by a simple power balance model.<sup>2</sup> In this model, the x-ray source power driving the hohlraum is balanced by power losses into the hohlraum wall and losses due to any holes in the wall. This relationship may be written as

$$P_{x-ray} = A_{wall}(1-\alpha)\sigma T^4 + A_{hole}\sigma T^4 \quad (1)$$

where  $P_{x-ray}$  is the x-ray source power,  $A_{wall}$  is the hohlraum wall area,  $A_{hole}$  is the area of the hohlraum covered with holes,  $\alpha$  is the albedo of the hohlraum wall (the ratio of the power emitted by the wall to the power incident on the wall),  $\sigma$  is the Stefan-Boltzmann constant, and  $T$  is the hohlraum radiation temperature. A typical value of  $\alpha$  for a Au wall hohlraum at a temperature of 75 eV is 0.8. Neglecting any losses through hohlraum holes, this power amplification for a typical pulsed power driven hohlraum is given by equation (1) as

$$\frac{\sigma T^4}{(P_{x-ray} / A_{wall})} = \frac{1}{(1-\alpha)} = 5 \quad (2)$$

for  $\alpha=0.8$ . As can be appreciated from this simple example, the ability of a hohlraum to amplify the primary x-ray source by a factor approaching five is what makes indirect drive ICF feasible.

This paper will describe three pulsed power driven hohlraum designs that are currently being experimentally investigated at Sandia National Laboratories. The first of these hohlraums is proton or lithium ion beam driven and is configured into either conical or cylindrical geometries. The second hohlraum system that is being studied consists of a central cylindrical hohlraum that has two smaller hohlraums attached to its side. The central hohlraum is driven by the implosion of a tungsten wire array z-pinch plasma radiation source located on its axis. The third hohlraum concept that is being investigated consists of a low density ( $2\text{--}10\text{ mg/cm}^3$ ) foam z-pinch that is imploded. In this design, the energy of the imploding z-pinch is used to directly heat the hohlraum.

## **Ion Heated Hohlraum Experiments**

The light ion ICF program is based upon an x-ray driven or indirect drive target concept.<sup>3</sup> Several target experimental series have been carried out on the PBFA II facility to investigate fundamental physics issues associated with this concept.<sup>4</sup> These issues include ion beam spatial parameters (symmetry, position, and vertical beam height), ion beam energy and power deposition, the conversion of ion-beam energy into soft x-ray thermal radiation, and the conversion of ion-beam energy into hydrodynamic motion. Fig. 1 shows the three classes of targets that have been used in our experiments to study the conversion of ion-beam energy into radiation. For all three classes of targets, the radial ion beam passes through the Au walls of the target and due to  $dE/dx$  energy losses, is finally stopped in the  $3\text{--}6\text{ mg/cm}^3$  CH foam region of the target. The rapid beam heating of the foam causes it to ionize and emit soft x-ray radiation. This soft x-ray emission in turn heats the gold walls of the target which reradiate creating a hohlraum.

The first target experiments on PBFA II employed intense proton beams to study thermal x-ray production in a cylindrical foam target shown in Fig. 1a. Details of these experiments may be found in Ref. 2. A peak brightness temperature of 35 eV was measured in these experiments.

In an effort to increase the ion specific power density in our PBFA II experiments, Li beams were employed that increased the specific power density by over an order of magnitude.<sup>4,5</sup> The hohlraum targets used in the Li experiments are shown in Fig. 1b and Fig. 1c. The parameters of the PBFA II Li beam were a peak voltage of 10 MeV, a peak power density of  $1\text{--}1.5\text{ TW/cm}^2$  averaged over a 6-mm-diameter spherical target, a FWHM of 13-15 ns, and a peak specific power density of 1400 TW/g. The physics issues under study included Li ion coupling into the foam at 1400 TW/g, the opacity of the CH foam, the tamping of the Au wall by the foam, and the thermal x-ray emission. Evidence of radiation smoothing and the hohlraum nature of this target system was obtained from data that demonstrated that a 25% asymmetry in the incident Li beam was smoothed to a 6% asymmetry in the thermal x-rays emitted below 280 eV.<sup>5</sup> The target shown in Fig. 1c was designed to maximize the radiation temperature by minimizing the hohlraum surface to volume ratio. The analysis of this shot series yielded the highest radiation temperature yet achieved in an ion-beam driven hohlraum, 63 eV.

## **Z-pinch Driven Vacuum Hohlraum System**

A z-pinch vacuum hohlraum system that is being studied is shown in Fig. 2. This hohlraum system consists of a central 2 cm diameter by 2 cm tall cylindrical hohlraum that has two 6 mm diameter by 9 mm long cylindrical hohlraums attached to its side. The central hohlraum is

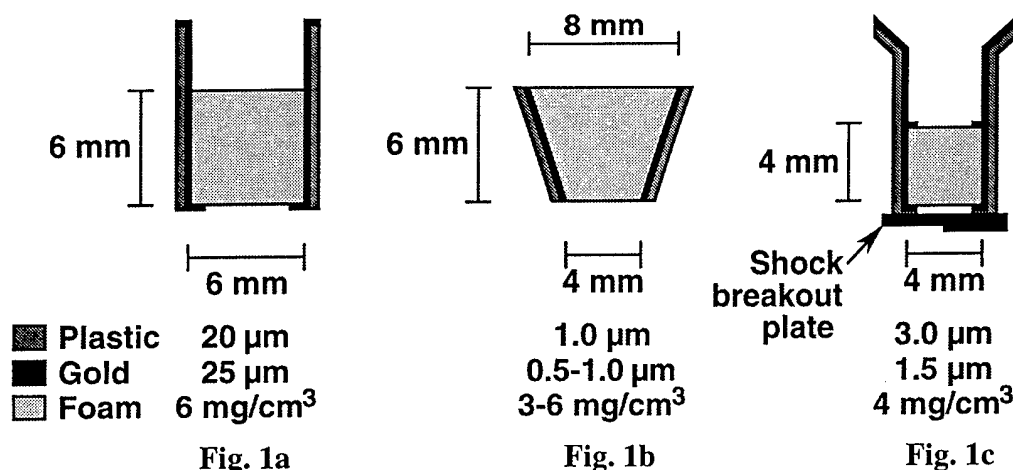


Fig. 1. Conical and cylindrical hohlraum targets designed for hohlraum physics studies on PBFA II. a) Proton cylindrical target. b) Lithium beam conical target. c) Lithium beam cylindrical target.

driven by the implosion of a tungsten wire array z-pinch plasma radiation source located on its axis. Soft x-ray radiation from the imploded z-pinch heats the walls of the central cavity which reradiate. Holes drilled in the central z-pinch hohlraum allow radiation to flow into the smaller side hohlraums. The geometry of the system is arranged to insure a spatially uniform, near Planckian radiation spectrum in the two side hohlraums that can be used to investigate ICF relevant issues associated with ablator physics, material equations of state, and material opacity.

In recent experiments on the Sandia National Laboratories' Saturn accelerator, the radiation drive in the small hohlraums was monitored with an 11 channel x-ray diode (XRD) array; a 16 channel transmission grating spectrometer; and time- and energy-resolved soft x-ray cameras. The shock velocity in polycarbonate step and wedge witness plates was measured by means of a streaked image of laser light reflected from the rear surface of the witness plate. Preshot radiation-hydrodynamic code predictions of shock velocity were within  $\pm 10\%$  of the measured values. The degree of uniformity of shock breakout along the  $\sim 3\text{-mm}$ -long hohlraum slot (corresponding to a theoretical  $\sim 3\text{ eV}$  variation) were consistent with computational predictions. Data from these instruments indicate that radiation temperatures of 82 eV have been reached in the central hohlraum. Measurements of the radiation spectrum and temperature in the side hohlraums show a nearly Planckian spectrum and a shock velocity measured with the active shock breakout technique that is consistent with a prediction of a 65 eV radiation temperature. A key remaining uncertainty is a quantitative understanding of the time-dependent hohlraum radiation drive conditions as measured by the XRD and transmission grating spectrograph. This uncertainty is due to diagnostic hole closure and plasma filling of the hohlraum. Recent experiments utilized CH "tamped" diagnostic apertures, and upcoming experiments will explore the issues further via a direct look at Be-tamped apertures with a higher resolution x-ray imaging diagnostic.

## Dynamic Hohlraum System

In an effort to increase the radiation temperature in a pulsed power driven hohlraum, the concept shown in Fig. 3 is being investigated.<sup>6</sup> In this design, denoted as a dynamic hohlraum, the energy of the imploding z-pinch is used to directly heat the hohlraum. The hohlraum consists of a 10 mm diameter low density (2-10  $\text{mg}/\text{cm}^3$ ) foam z-pinch that is imploded to a diameter of  $\sim 1\text{ mm}$ . The outer region of the foam is

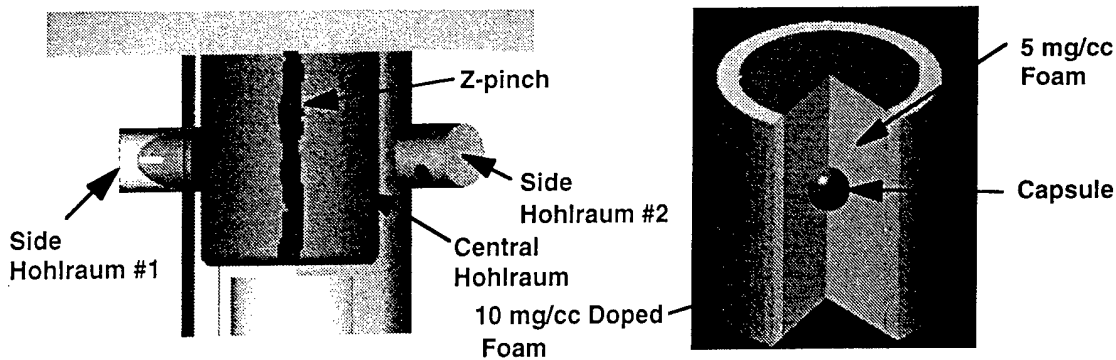


Fig. 2 Schematic of the vacuum hohlraum system. Fig. 3 Dynamic hohlraum concept.

doped with gold such that a large fraction of the thermal radiation generated in the implosion is contained. The radiation trapped in the final imploded state of this hohlraum enable a high radiation temperature to be reached in this system. At a future date, an imploding thermonuclear fuel capsule would be placed in the center of this system.

A recent experimental series fielded on the Saturn accelerator investigated current initiation in these types of foam systems.<sup>6</sup> This series studied the initiation properties of foam targets at peak currents of 6-7 MA. Optical framing cameras and streak optical fiber arrays were used to observe the early sheath formation in the outer regions of the low density foam. Both prepulse and a gold conducting coating were found to be necessary for good coupling to the accelerator source. Electrode contacts and the anode/current return configuration were determined to be limitations in the experimental series. A variant to these experiments was to implode a z-pinch tungsten wire array directly onto a low density cylindrical foam. Good results were obtained in heating a foam system by this method. This technique will be explored in future experiments on Sandia's new 20 MA z-pinch driver facility, PBFA II-Z.

## Conclusion

Three pulsed power driven hohlraum concepts are being investigated at Sandia National Laboratories for application to inertial fusion research. These hohlraums are driven by intense proton and Li ion beams as well as by two different types of z-pinch x-ray sources. Research on these hohlraum systems will continue on Sandia's PBFA II-Z facility.

## Acknowledgment

This work is supported by the US Department of Energy under Contract No. DE-AC04-94AL85000.

## References

- [1] J. Lindl, Phys. Plasmas **2**, 3933 (1995).
- [2] R. L. Kauffman et al., Phys. Rev. Lett. **73**, 2320 (1994).
- [3] R. E. Olson et al., Proc. 15th IEEE Symp. on Fusion Engineering, p. 189 (1993).
- [4] R. J. Leeper et al., Journal of Plasma and Fusion Research **71**, 945 (1995).
- [5] M. S. Derzon et al., Phys. Rev. Lett. **76**, 435 (1996).
- [6] M. S. Derzon et al., Proc. 11th Topical Conference on High Temperature Plasma Diagnostics, Monterey, California, May 12-16, 1996 and the references therein.

# Determination of the time dependent magnetic field distribution in Pulsed-Power Systems

Y. Maron, R. Arad, G. Davara, L. Gregorian, Ya. Krasik, E. Kroupp,  
M. Sarfaty, R. Shpitalnik, and A. Weingarten

Faculty of Physics  
Weizmann Institute of Science  
Rehovot, 76100, Israel

## Abstract

Time-dependent measurements of the magnetic field distributions in diode, plasma opening switch, and Z-pinch plasmas, based on the observation of the Zeeman effect or of the ion acceleration, are reviewed. Relatively high spatial resolution is obtained by locally doping the plasma with the desired species. Besides information on the device properties, the measurements allowed for determining the plasma conductivity and for investigating the field penetration mechanism. Determination of the current density allowed the electron drift velocity to be known.

## I. Introduction

The distribution of magnetic fields in the plasmas or in the non-neutral regions of pulsed power systems significantly affects the current flow, the resultant plasma heating, the plasma motion, and the thermal convection, and thus plays an important role in the overall operation of the devices. Therefore, development of nonintrusive methods for reliably observing the time dependent magnetic field distribution in such configurations, with satisfactory accuracy and spatial resolution, is of major importance. Here, we review measurements of the B-field distribution in Ion diode, Z-pinch, and Plasma Opening Switch (POS) experiments.

The methods used for measuring the magnetic field distributions are the observations of the Zeeman splitting of emission lines<sup>1-4)</sup> and observation of the ion acceleration due to the magnetic field gradients from the emission line Doppler shifts<sup>3,5)</sup>. Together with the electron density determined independently, the latter yields the magnetic field gradient<sup>5)</sup>.

## II. Local plasma doping

For studying the time dependent magnetic field penetration into a plasma, obtaining spatially resolved measurements of the magnetic field along the direction of penetration is a necessity. Since spectroscopic observations of spontaneous emission are integrated along the line of sight, the only way to achieve local measurements is by locally doping the plasma with the species that produces the line emission desired for the diagnostics. In doping the plasma it should be ascertained that the doped material is sufficiently low in density to cause no significant perturbations in the plasma properties, namely, the electron density and temperature, ionic composition, and the ion velocity distribution (this has been systematically examined in our experiments but will not be discussed in this report). The measurement spatial resolution is determined by doping the plasma in a region of the smallest size that allows for the required line intensity.

An additional advantage in employing plasma doping is that it allows for selecting lines of various species, suitable for the determination of the magnetic field under various conditions. For example, one should select heavy ions if the Zeeman splitting is to be

discriminated against the Doppler broadening, light ions if the line Doppler shifts are used to give the ion acceleration, lines from low-lying levels in order to minimize the Stark broadening, and lines from high-lying levels in order to reduce the opacity effect. The opacity can also be reduced by using a sufficiently low density for the doped material.

Various methods are used for the plasma doping. Material that contains the desired species can be deposited on electrodes in the devices. If plasma is formed over the electrode surface, particles originating in that material will be ejected into the plasma, and then ionize to various charge states. In the ion diode experiment<sup>1)</sup> the anode was coated with compounds of barium, which provided enough BaII in the surface-flashover-produced anode plasma. An additional advantage in using BaII in this experiment was that BaII propagated in the plasma relatively slowly and ionized into higher charge states within  $\leq 0.1$  mm from the anode surface. Thus, we could obtain the magnetic field within 0.1 mm from the anode surface, enabling us to determine the value of the B-field that fully penetrates the  $\simeq 2$ -mm-thick anode plasma.

In the 100-ns coaxial POS experiment<sup>2,3,5)</sup>, material was deposited on the inner electrode (the anode) and was evaporated into the anode cathode gap using a  $\simeq 10$  GW/cm<sup>2</sup>, 10 ns laser pulse focused on a spot  $\simeq 200$   $\mu$ m in diameter. The POS current was applied about 3  $\mu$ s after the laser pulse allowing the doped species to propagate over most of the 2.5-cm anode-cathode gap. Here, barium was deposited on the anode for the observation of the Zeeman effect, and magnesium was used for the determination of the magnetic field by the ion-acceleration method.

In this POS experiment a 2D mapping of the magnetic field in the  $r, z$  plane was achieved. In the experiments, the doped column position was varied in the  $z$  direction over the plasma axial dimension. The spatial resolution in the axial (given by the doped-column width) and the radial (determined by the optical arrangement) were  $\simeq 1$  and 0.02 cm, respectively. As yet, the field was measured at a single azimuth.

Another method to dop the plasma, developed in our 0.5  $\mu$ s POS experiment, is by injecting a narrow beam of gas into the anode-cathode gap through a hole in the cathode<sup>6)</sup>. The seeding arrangement consists of an ultrafast gas valve and a skimmer to collimate the beam. It allows for doping the plasma with various gaseous elements including noble gases. Another advantage is that it makes possible doping the plasma with higher-density neutral particles whose motion is unaffected by the magnetic field, which results in little Doppler broadening for the line. Also with this method a spatial resolution better than that obtained by the laser evaporation technique was achieved.

For the Z-pinch experiment no plasma doping was used. The line emission was observed parallel to the pinch axis with the optical arrangement designed to give spatial resolution of  $\simeq 0.4$  and 2 mm in the radial the azimuthal directions, respectively<sup>4)</sup>. In a previous study<sup>7)</sup> we found that during the implosion phase the lower-charge-state ions reside closer to the axis than the higher-charge-states ions. Based on these findings we performed axial observations of the imploding plasma, utilizing line emissions of various charge state ions at different times and radial locations.

### III. Polarization spectroscopy

In the relatively low density plasmas the Zeeman splitting can mainly be obscured by Doppler broadening due to the ion motion under the magnetic field. Therefore, relatively heavy ions should be doped in order to minimize the ion velocities. In the diode measurements the use of BaII ions resulted in a well distinguished Zeeman splitting in the line

profile<sup>1)</sup>. The observation of the Zeeman splitting and the use of repeated shots allowed an accuracy of  $\simeq \pm 2\%$  for the magnetic field measurements to be achieved (this accuracy made possible the observation of the diamagnetic effect of the electron flow in the diode gap see below). In the POS measurements, however, the Zeeman splitting of the BaII line was comparable to the Doppler broadening. In these measurements, therefore, both spectral profiles of the  $\sigma$  and  $\pi$  line components had to be measured (the  $\pi$ -component profile is mainly affected by the Doppler broadening). The Zeeman splitting and Doppler broadening are then obtained self-consistently by comparing a calculation of the profiles of both components to the measured ones<sup>2,3)</sup>.

In the higher density plasmas (the Z-pinch experiment), the line profile can also be affected by Stark broadening and opacity. Therefore, calculations<sup>8)</sup> of line Stark broadening for the time and space varying electron densities were used to select lines with the smallest broadening. Also, collisional radiative calculations were used to obtain the atomic level populations, allowing for calculating the opacity effects and their influence on the line shape. In the measurements reported here for the Z-pinch experiment, the spectral profiles of the lines selected were dominated by Stark broadening, which was about twice the average Zeeman splitting of the various line components<sup>4)</sup>. Nevertheless, the use of polarization spectroscopy as described in the above, allowed for determining the magnetic field with a reasonably good accuracy. This was made possible by using sufficiently intense lines and achieving high accuracy for the line profile measurements.

The diagnostic systems for the various experiments are described in Refs. 1-5. In brief, the systems allow for measuring the time dependent spectral profiles of two emission lines, or the profiles of the  $\sigma$  and  $\pi$  components of a single line, in a single discharge.

## IV. Results

### A) Magnetically insulated ion diode

For the diode experiment we used a planar magnetically insulated diode<sup>1)</sup>. Light was collected from the anode plasma parallel to the lines of the externally applied magnetic field. The measurements were integrated along the anode length and the spatial resolution in the gap direction was  $< 0.1$  mm.

An example of the measured magnetic field in the plasma is shown in Fig. 1. To within the uncertainties, the magnetic field in the anode plasma at early times equals the applied magnetic field ( $7.6 \pm 10\%$  kG). The magnetic field then rises by  $\simeq 0.8$  kG during the pulse, then drops to about the applied field when the diode current  $I$  is zero ( $t \simeq 150$  ns), followed by a decrease below the applied field when  $I < 0$ . The magnetic field rises again above the applied field when  $I$  rises ( $t \geq 250$  ns). This demonstrates the diamagnetic effects of the electron flow in the diode acceleration gap.

The rise in the magnetic field on the anode side due to the electron flow within the first 100 ns of the pulse was found to be much larger than that obtained from a one-dimensional Brillouin-flow model calculation. However, it was consistent with estimates<sup>9)</sup> based on the measured ion current density and on the electric field distribution across the diode acceleration gap observed<sup>10)</sup> for a similar diode configuration. Those observations<sup>10)</sup> showed significant electron flow close to the anode plasma, beyond the calculated electron-sheath region, which should enhance the diamagnetic effect on the anode side.

The penetration into the anode plasma of the diamagnetic signal due to the electron flow in the gap was calculated using the magnetic diffusion equation in which the plasma



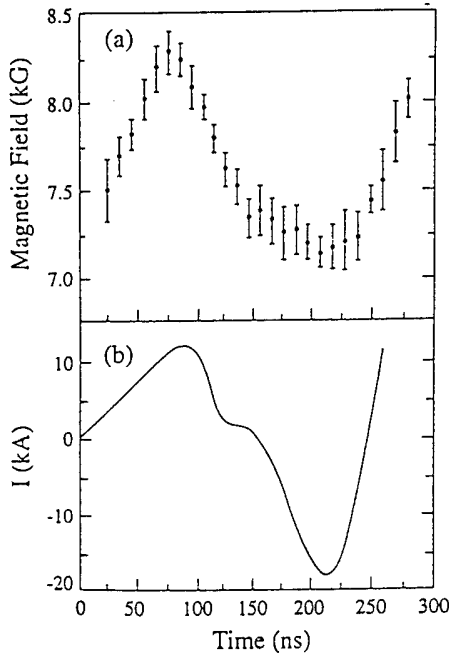


Fig. 1(a) Magnetic field as a function of time, within 0.1 mm from the anode surface of a magnetically insulated ion diode, observed using the BaII 6142 Å line. The data points are averaged over  $N=11$  identical discharges. The error bars shown for each time are the standard deviations divided by  $\sqrt{N-1}$ . Besides these error bars shown there is an uncertainty of  $\pm 6\%$  in the absolute value of the observed magnetic field; (b) The diode total-current waveform.

conductivity is a parameter. The calculated field penetration was found to be consistent with a plasma conductivity  $10\times$  lower than the Spitzer conductivity, known from an experimental determination of the electron temperature and the ionic composition of the plasma<sup>11</sup>). This anomalous conductivity and the observed magnetic field were also found to be in agreement with the observed rate of the plasma expansion against the magnetic field and the uniformity of the electron temperature in the plasma<sup>11</sup>). The latter was examined using an estimate of the thermal convection based on the measured magnetic field<sup>11,12</sup>). Furthermore, together with the pressure-driven current in the plasma, this conductivity yielded a reasonable Ohmic heating rate for the plasma electrons. In addition, the effect of the magnetic field in the plasma on the flow of various ionic species, and thus its influence on the composition of the extracted ion beam, could also be studied<sup>13</sup>).

## B) Plasma Opening Switch

Our POS is coaxial with the inner electrode (the anode) charged positively. The inner and outer electrode radii are 2.5 and 5 cm, respectively, and the peak current is  $\simeq 135$  kA with quarter period of 90 ns. The plasma is produced by a gaseous plasma source, which is mounted inside the anode and injects the plasma radially outward. The plasma axial dimension is  $\simeq 4$  cm. For the Zeeman-splitting observations, two spectrometers were employed to measure the line  $\sigma$  and  $\pi$  components simultaneously in a single discharge.

Results on the magnetic field penetration velocity and the time dependent 2-D structure of the magnetic field are given elsewhere<sup>2,3</sup>). Here, we only mention a few findings. Figure 2 shows the axial  $B$ -field distributions at  $t=20, 30$ , and 50 ns after the beginning of the current at the generator side edge of the plasma, obtained from the Zeeman splitting of a BaII line. The magnetic field was observed to penetrate into the plasma at a velocity of  $\simeq 10^8$  cm/sec, three orders of magnitude higher than the diffusion velocity, and higher than the Alfvén velocity. The high penetration velocity and the sharp gradient of the magnetic field in the axial direction indicate penetration in the form of a shock. At  $t=30$  ns the field also appears at the load side of the plasma, while it is still close to zero at  $z \simeq 0.5$  cm. At

$t = 50$  ns, field is present over the entire plasma. At that time it is found that most of the current flows at the load-side edge of the plasma and between the plasma and the load (see below).

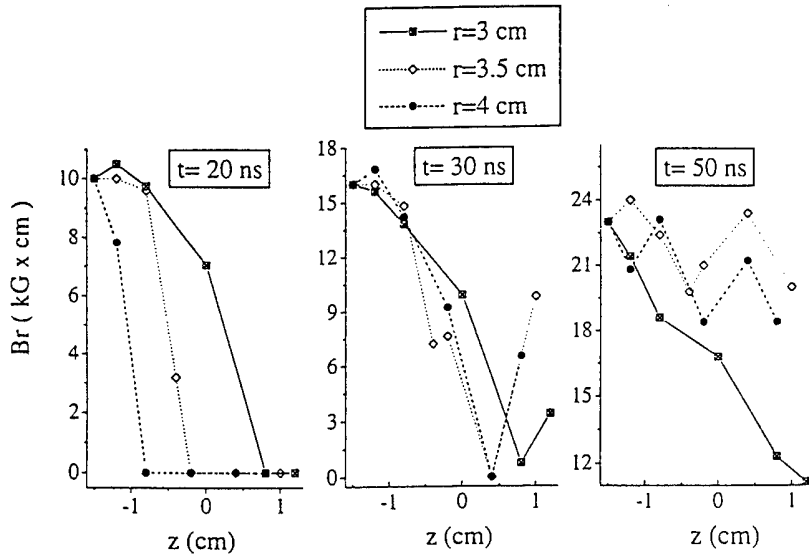


Fig. 2 The magnetic field (multiplied by the radius) as a function of the axial distance in the POS for three radial positions  $r=3$ ,  $3.5$ , and  $4$  cm at (a)  $t=20$  ns, (b)  $t=30$  ns, and (c)  $t=50$  ns after the start of the current pulse.  $z=0$  is the injected plasma axial center with the generator side denoted by a negative  $z$ .

The evolution of the magnetic field distribution was calculated using a model based on the Hall effect<sup>14,15</sup>). In the model we used our measured electron density distribution and assumed fast penetration along the POS electrodes<sup>3</sup>). The results were found to be in good agreement with the data given in the above.

Using the ion-acceleration method, the velocity distributions for various-charge-state ions were observed<sup>2,5</sup>). The magnetic field axial distributions for various times, obtained by measuring the Doppler shifts of line emission of MgII doped in the plasma, are shown in Fig. 3. Here, the magnetic field could also be measured at the load-side edge of the plasma, showing a relatively high current density in this region. This is expected to cause plasma acceleration towards the load, as supported by charge collection measurements. Also, the difference between  $B$  observed in the load-side edge of the plasma and that measured at the load shows a current loss between the switch plasma and the short-current load.

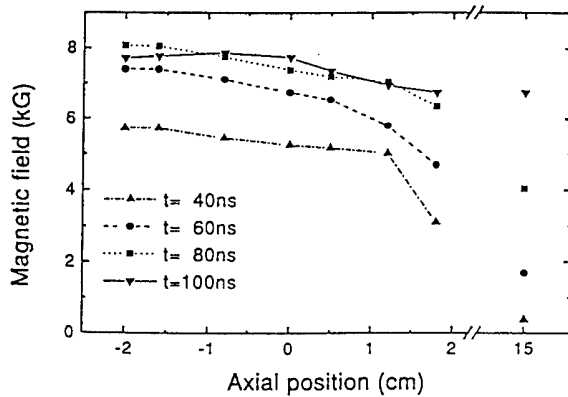


Fig. 3 Axial magnetic field distributions for several times at  $r=3.2$  cm (0.7 cm from the anode surface) obtained from axial time-dependent local velocities of MgII doped in the plasma. In obtaining  $B$ , we used an electron density  $1.3 \times 10^{14} \text{ cm}^{-3}$ , determined from the observed particle ionization times. The data points are connected by straight lines. The points at  $z=15$  cm give the magnetic field measured by the Rogowski coil near the shorted load.

### C) Z-pinch experiment

In the Z-pinch experiment<sup>4)</sup> we employ a gas-puff device for the injection of a hollow cylinder of gas (CO<sub>2</sub> or, argon). The anode-cathode gap is 1.35 cm, and the diameters of both anode and cathode are 4 cm. The plasma pinches at  $\simeq 620$  ns after the start of the current pulse, when the current is  $\simeq 220$  kA.

The dominance of the Stark effect over the line Zeeman splitting as mentioned above, required the observation of the  $\pi$  and  $\sigma$  line components. For each polarization we performed at least 20 discharges, thus obtaining an uncertainty of  $\simeq \pm 2\%$  in the FWHM of the averaged profile. The experimental data points were then fitted to a Lorentzian. The spectral line profiles were calculated for each polarization based on the Zeeman splitting and Stark broadening as input parameters. Comparison to the measured profiles yielded the magnetic field at each radius and time, with an accuracy of 15-20%. Detailed description of the line profiles observed and a discussion on the accuracy is given in a separate report<sup>4)</sup>. Here we only present the radial distribution of the magnetic field obtained for two times during the implosion, as shown in Fig. 4. The fitting curves presented are obtained from solutions of a 1-D magnetic diffusion equation the boundary conditions of which (namely, the outer plasma radius and the magnetic field at this radius) are determined experimentally<sup>4)</sup>, and in which the plasma conductivity is a parameter. The best-fit curves given in Fig. 4, yield plasma conductivity that is close to the Spitzer value. Also given in Fig. 4 are the values of the boundary field  $B_0$ , obtained using the total discharge current in the plasma measured by a Rogowski loop. The good agreement between  $B_0$  and the spectroscopically determined magnetic field at the plasma outer radius indicate that the entire current flows through the plasma. The distributions given in Fig. 4 also show that the  $B$  field penetration depth is about half of the plasma shell thickness.

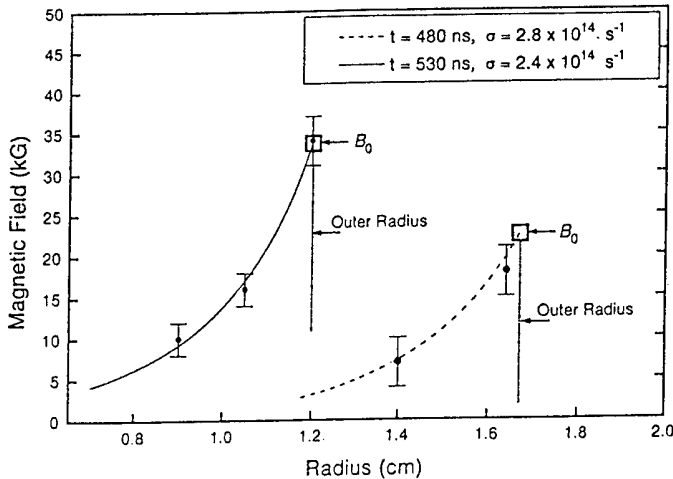


Fig. 4 The magnetic field distribution in the plasma at  $t = 480$  and  $530$  ns (the pinch occurs at  $\simeq 620$  ns). The curves are best-fit solutions of the magnetic field diffusion equation using plasma conductivity  $\sigma$  as indicated. The  $1/e$  decrease of the magnetic field occurs at distances of 0.24 and 0.22 cm from the plasma outer radius for  $t = 480$  and  $t = 530$  ns, respectively.  $B_0$  is the field calculated using the total discharge current measured by a Rogowski loop.

Using these results we calculated the  $J \times B$  forces across the plasma shell and compared it to the radial acceleration of the various charge-state ions obtained from the line-emission Doppler shifts. This comparison yielded the temporal and radial distributions of the contributions of the magnetic field pressure and the thermal pressure to the radial acceleration.

### Summary

The magnetic field distribution can be measured in various pulsed power systems with satisfactory accuracy and spatial resolution. In principle, methods based on laser spectroscopy can also be utilized. For example, the use of laser-induced two-photon processes with the appropriate geometry is expected to allow for measurements of smaller magnetic fields with an improved spatial resolution in all directions<sup>16</sup>). Observation of the magnetic field in higher power z-pinches may be possible using VUV line emission.

### References

1. Y. Maron, E. Sarid, E. Nahshoni, and O. Zahavi, *Phys. Rev.* **A39**, 5856 (1989).
2. M. Sarfaty, R. Shpitalnik, R. Arad, A. Weingarten, Ya.E. Krasik, A. Fruchtman, and Y. Maron, *Phys. Plasmas* **2**(6), 2583 (1995).
3. R. Shpitalnik, A. Weingarten, K. Gomberoff, Ya. Krasik, and Y. Maron, Observations of fast Magnetic Field Penetration in a Plasma Opening Switch, WIS Report, WIS/96/15/Mar.-PH, 11th Int. Conference in High Particle Beams, Prague, Czech Rep., June 10-14, 1996, to be published.
4. G. Davara, L. Gregorian, E. Kroupp, and Y. Maron, 11th Int. Conference in High Particle Beams, Prague, Czech Rep., June 10-14, 1996, WIS-96/16/Feb.-PH Report, to be published; L. Gregorian et al., these proceedings.
5. M. Sarfaty, Y. Maron, Ya. E. Krasik, A. Weingarten, R. Arad, R. Shpitalnik, A. Fruchtman, and Y. Maron, *Phys. Plasmas* **2**(6), 2122 (1995).
6. R. Arad, Ya. Krasik, L. Ding, and Y. Maron, 11th Int. Conference in High Particle Beams, Prague, Czech Rep., June 10-14, 1996, to be published.
7. M.E. Foord, Y. Maron, G. Davara, L. Gregorian, and A. Fisher, *Phys. Rev. Lett.* **72**, 3827 (1994).
8. S. Alexiou, *Phys. Rev. Lett.* **75**, 3406 (1995); S. Alexiou and Y. Maron, *J. Quantitative Spectroscopy and Radiative Transfer*, Vol. 53, pp 109-124 (1995); S. Alexiou and Yu. Ralchenko, *Phys. Rev.* **A49**, 3086 (1994).
9. C.W. Mendel, Jr. and J.P. Quintenz, *Comments Plasma Phys. Controlled Fusion* **8**, 43 (1983).
10. Y. Maron, M.D. Coleman, D.A. Hammer, and H.S. Peng, *Phys. Rev.* **36**, 2818 (1987).
11. Y. Maron, M. Sarfaty, L. Perelmutter, O. Zahavi, M.E. Foord and E. Sarid, Electron temperature and heating processes in a dynamic plasma of a high power diode, *Phys. Rev.* **A40**, 3240 (1989).
12. S.I. Braginskii, in *Review of Plasma Physics*, edited by M.A. Leontovich, Vol. 1, p.205., (1965).
13. Y. Maron, L. Perelmutter, E. Sarid, M.E. Foord, and M. Sarfaty, *Phys. Rev.* **A41**, 1074 (1990).
14. A.S. Kingsep, L.I. Rudakov, and K.V. Chukbar, *Sov. Phys. Dokl.* **27**, 140 (1982); A.S. Kingsep, K.V. Chukbar, and V.V. Yankov, in *Review of Plasma Physics*, edited by B.B. Kadomtsev (Consultants Bureau, New York, 1990), Vol. 16, p.243.
15. A. Fruchtman, *Phys. Rev.* **A45**, 3938 (1992); A. Fruchtman, and K. Gomberoff, *Phys. Fluids* **B5**, 2371 (1993).
16. Y. Maron and C. Litwin, *J. Appl. Phys.* **54** 2086 (1983).

## SPECTROSCOPIC TECHNIQUES FOR MEASURING ION DIODE SPACE-CHARGE DISTRIBUTIONS AND ION SOURCE PROPERTIES

A.B. Filuk, J.E. Bailey, R.G. Adams, A.L. Carlson, C.-H. Ching, M.P. Desjarlais, P. Lake,  
E.J. McGuire, T.A. Mehlhorn, T.D. Pointon

*Sandia National Laboratories, Albuquerque, NM 87185-1187 USA*

Y. Maron and E. Stambulchik

*Weizmann Institute of Science, Rehovot, Israel, 76100*

*We are using time- and space-resolved visible spectroscopy to measure applied-B ion diode dynamics on the 20 TW Particle Beam Fusion Accelerator II. Doppler broadening of fast Li atoms, as viewed parallel to the anode, is used in a charge-exchange model to obtain the  $\text{Li}^+$  ion divergence within 100  $\mu\text{m}$  of the anode surface. The characteristic Stark/Zeeman shifts in spectra of alkali neutrals or singly-ionized alkaline-earths are used to measure the strong electric ( $10^9$  V/m) and magnetic ( $\sim 6$  T) fields in the diode gap. Large Stark shifts within 0.5 mm of the anode indicate the LiF emits with a finite field threshold rather than with Child-Langmuir-type emission, and the small slope in the electric field indicates an unexpected build-up of electrons near the anode. In the diode gap, we aim to unfold fields to quantify the time-dependent ion and electron space-charge distributions that determine the ion beam properties. Observed electric field non-uniformities give local beam deflections that can be comparable to the total beam microdivergence. We are implementing active laser absorption and laser-induced fluorescence spectroscopy on low-density Na atoms injected into the diode gap prior to the power pulse. The small Doppler broadening in the Na spectra should allow simultaneous electric and magnetic field mapping with improved spatial resolution.*

### INTRODUCTION

Driving Inertial Confinement Fusion (ICF) targets with light ions in a pulsed-power accelerator requires efficient electrical power conversion into an appropriate-species ion beam of low divergence. This conversion is under study at Sandia in high-power applied-B ion diodes. We are using spectroscopic techniques to probe the physics of diode anode (A) and cathode (K) processes, and the AK gap space-charge distributions, on a 20 TW PBFA II  $\text{Li}^+$  ion diode. The Stark shift of low-density excited neutrals in the AK gap is used to obtain the time- and 2-D-space-resolved electric field, which can then yield the electron and ion space-charge densities. This powerful non-perturbing technique [1] allows direct study of the diode gap charge dynamics that determine the limiting beam power density that can be delivered to an ICF target.

Previously-reported measurements [2] have described electric field profiles  $E(x,t)$  in a barrel-geometry ion diode as a function of time  $t$  and the distance from the anode  $x$ . These profiles were compared with those generated by a fully-3-D, idealized particle-in-cell (PIC) simulation code [3]. Good agreement between simulation and experiment was seen early in the beam pulse, but a growing discrepancy within  $\sim 10$  ns of the ion

beam start showed that important non-ideal effects were missing from the simulation. Our goal is to measure, understand, and control these non-ideal effects to increase the ion beam brightness and ensure reliable scaling for a high-gain ICF driver.

### MEASUREMENT USING GAP ATOMS

As described in detail elsewhere [4], an array of lens-coupled fiber optics is used to collect AK gap optical emission from  $\sim 2$  mm diameter cylindrical lines-of-sight and transport that light to remote multiplexed spectrographs, where the spectra are streaked and recorded on film. The  $3 \times 6$  fiber arrays can be oriented with the longer dimension across the AK gap ( $x$  direction) to resolve the  $E(x,t)$  profiles, or oriented parallel to the anode surface (the azimuthal direction  $\phi$  in a barrel-geometry or extraction-geometry ion diode) to resolve  $E(\phi,t)$  non-uniformities. An extremely useful feature in the emission spectra is Stark-shifted 2s-2p emission from  $\sim 10^{12} \text{ cm}^{-3}$  Li atoms in the  $\sim 10$  MV/cm AK gap electric field. The calculated and measured Stark shifts of these non-Rydberg transitions offer a previously-untested regime for advancing Stark effect and basic atomic physics calculations [5]. The Li atoms are observed to have several-keV Doppler

broadening energies parallel to the anode surface, and move away from the anode across the AK gap with typically 10 keV energies. The fast Li atom energies and the absolute Li atom density seen appear to be due to Li atom production via charge exchange of the  $\text{Li}^+$  ion beam in a few monolayers of desorbed anode impurities. Only about 5% of the  $\text{Li}^+$  beam ions undergo charge exchange events to make the low-density Li atoms we observe, so this process is not expected to contribute significantly to impedance loss [6].

## SOURCE & NEAR-SOURCE RESULTS

These experiments used a passive LiF-coated anode that emits  $\text{Li}^+$  ions when subjected to ~5-10 MV/cm electric fields. It is important to know the beam microdivergence generated by the ion emission source, since the total  $\text{Li}^+$  beam microdivergence of typically 25 mrad after acceleration to 9 MeV is at least twice what is needed for efficient ICF target drive. It is difficult to spectroscopically observe directly the  $\text{Li}^+$  ions because their closed-shell atomic structure puts populated-transition wavelengths into the extreme vacuum ultra-violet. Instead, we use the charge-exchange model of fast Li atom production to infer the  $\text{Li}^+$  ion beam microdivergence very close to the anode surface.

The small fraction of  $\text{Li}^+$  ions undergoing a charge exchange event in a thin desorbed impurity layer can be modeled. We assume self-consistently that the charge exchange layer thickness is much larger than the few-micron scale size of charge clumping or conductor surface roughness needed even to account for all the final beam microdivergence being acquired near the anode surface. The velocity distribution of the  $\text{Li}^+$  ions at the charge-exchange layer is then essentially transferred to the Li atoms, and the angular spread in  $\text{Li}^+$  ion velocities can be obtained from the Doppler broadening of Li atom emission viewed parallel to the anode surface. Geometrical path length effects in the charge-exchange layer give typically less than 20% correction of the atom velocity full-width-at-half-maximum (FWHM) to obtain the incident ion velocity FWHM. Using this technique, we find that typically at most about half the final beam microdivergence is acquired in the immediate ion source vicinity. The remainder may be due to instabilities [7] or non-uniformities [8].

Another interesting result is the measurement of electric field at ~1/2 mm from the LiF anode, showing field strength much larger than the space-charge-limited (SCL) value [2]. For even moderately-uniform ion emission this result would require the LiF surface has a non-zero field value during intense ion current emission, in contrast with the zero-field SCL condition. Our measurements show that, even allowing for ion space-charge effects, the anode electric field is typically 7-10 MV/cm in the early phase of the ion beam. This field-threshold emission is consistent with earlier theoretical ideas on ion emission from LiF in strong electric fields and intense electron bombardment [9]. Later in the power pulse, Li atom emission is observed with no Stark shift near the anode while the onset of impurity ion lines is seen, indicating plasma does form non-uniformly over the anode at about the time that impurity C, O, and H ions are significantly contaminating the  $\text{Li}^+$  beam [10]. We are investigating electron stimulated and thermal impurity desorption and ionization as a mechanism for this beam purity loss and diode impedance loss.

## AK GAP RESULTS

Further insight has been gained on the surprising observation [2] of approximately-uniform  $E(x)$  in the first few mm away from the anode surface. Previous theoretical ideas and simulation results had the ion space-charge dominating the electron space-charge near the anode, so that from Gauss' law the electric field should have increased sharply with distance from the anode, until the dense part of the electron sheath was encountered some distance across the AK gap. A nearly-flat or falling  $E(x)$  profile near the anode (see Figure 1) implies an electron build-up there comparable to the ion space-charge. However, such extensive electron diffusion across the AK gap is usually intuitively associated with extreme ion currents, which we do not observe. As well, it is difficult to maintain large average electron density in the near-anode region unless most electrons there are moving essentially along the magnetic field.

We have shown that the flat near-anode  $E(x)$  profiles actually give predicted ion current densities very consistent with what is observed. An integral expression obtained by one of us (MPD) using flux conservation and pressure balance gives implicitly the ion (mass  $M$ , charge  $q$ ) cur-

rent density  $J_i$  across a physical AK gap  $d$  that is reduced by virtual cathode motion to a dynamic gap  $g$ , in terms of  $E(x)$ , the normalized electric potential  $\tilde{\Phi}(x) = \Phi(x)/V$  associated with the electric field ( $\tilde{\Phi}(0) = 1$ ,  $\tilde{\Phi}(g) = 0$ ,  $\tilde{\Phi}'(g) = 0$ ), and the magnetic field at the virtual cathode  $B_c$ , as (in Gaussian units)

$$\overline{B}_o d = \int_0^g [B_c^2 + E^2(x) + \alpha J_i (1 - \sqrt{1 - \tilde{\Phi}(x)})]^{1/2} dx,$$

with  $\overline{B}_o d$  the average vacuum magnetic flux in the AK gap and  $\alpha = 8\pi\sqrt{(2MV)/q}$ .

Our  $E(x)$  profiles cannot be measured accurately out near the virtual cathode position because of the Li neutral time-of-flight delay. However, by simply assuming constant electron density beyond our largest- $x$  measurement, where  $E$  is approaching zero, we can continue  $E(x)$  out to  $x=g$  and calculate  $J_i$  and  $g$  self-consistently. Figure 1 illustrates typical  $E(x)$  data and the constant-density extrapolation. The calculated  $J_i$  of

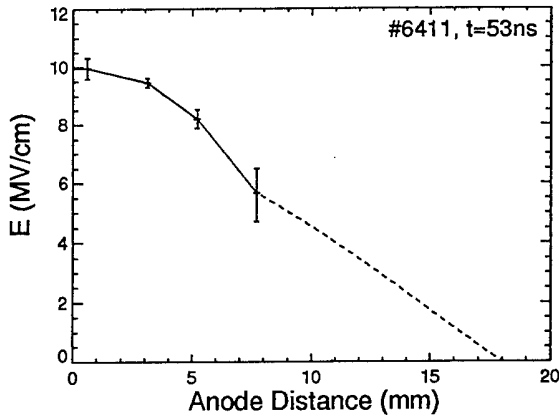


Fig. 1. Measured PBFA II diode electric field profile  $E(x)$  with constant-density extrapolation (dashed).

$0.9 \text{ kA/cm}^2$  agrees well with the average current density measured by filtered Faraday cups and an ion magnetic spectrometer. These results give us confidence in the data interpretation, but the remaining discrepancy with simulation charge distributions indicates additional physics may need to be included in the simulations.

Detailed  $E(x, \phi)$  time evolution has been measured in the diode gap using up to 18 lines-of-sight in the  $3 \times 6$  fiber array. Figure 2 shows a sequence of 2-ns-averaged  $E(x, \phi)$ , illustrating the large variations and non-uniformities as a function of  $\phi$ . In an ideal diode,  $E(\phi)$  at fixed  $x$  would

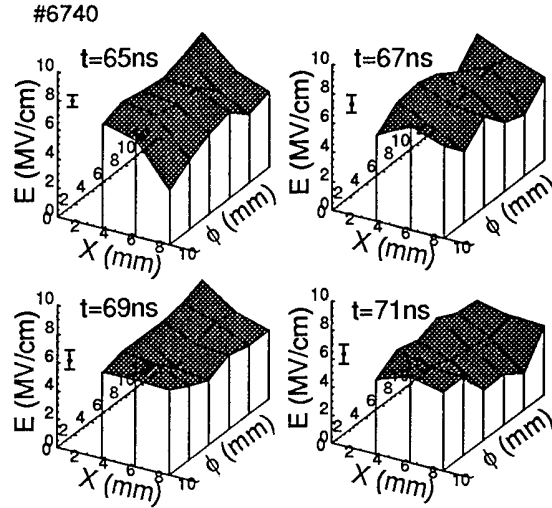


Fig. 2. Measured 2-D-resolved PBFA II diode electric field as a function of distance across ( $x$ ) and along ( $\phi$ ) the AK gap, starting 5 ns after peak  $\text{Li}^+$  beam power. Typical error bars are shown.

be constant during our time-averaging window. The experimental non-uniformities indicate fluctuations of net charge density over space and time, possibly caused by intermittent anode or cathode plasma phenomena.

The non-uniform  $E(\phi)$  implies azimuthal clumping of potential and existence of electric field components  $E_\phi$  transverse to the direction of primary beam acceleration. These  $E_\phi$  components can deflect the beam and impair the final focus quality on target. We have done high-precision  $E(x, \phi)$  measurements as shown in Figure 1 to obtain estimates of  $E_\phi(x)$  and the associated RMS local beam deflection angles.  $E(x)$  at two adjacent azimuths A and B are used to calculate the potentials  $\Phi_{A,B}(x)$  by assuming self-consistently that  $E_x \sim -E$ . Since the anode is a constant-potential conductor and induced  $\frac{\partial B}{\partial t}$  potentials are negligible,  $E_\phi(x)$  between A and B can be estimated as  $-(\Phi_A - \Phi_B)/d_{AB}$  (where is  $d_{AB} \sim 2 \text{ mm}$  is the azimuthal distance between A and B). The  $E$  measurement uncertainty needs to be better than  $\pm 5\%$  to obtain statistically meaningful results for  $E_\phi$ . We have done extensive uncertainty characterization of our  $E$  measurement technique to verify the size of our error bars [11]. Preliminary results of unfolds are shown in Figure 3. Short-lived transverse fields increasing up to several MV/cm with distance from the anode indicate azimuthal charge clumping that can give  $\sim 25 \text{ mrad}$  RMS beam deflections, comparable to the typical total beam microdivergence. The mechanism for these charge nonuniformities

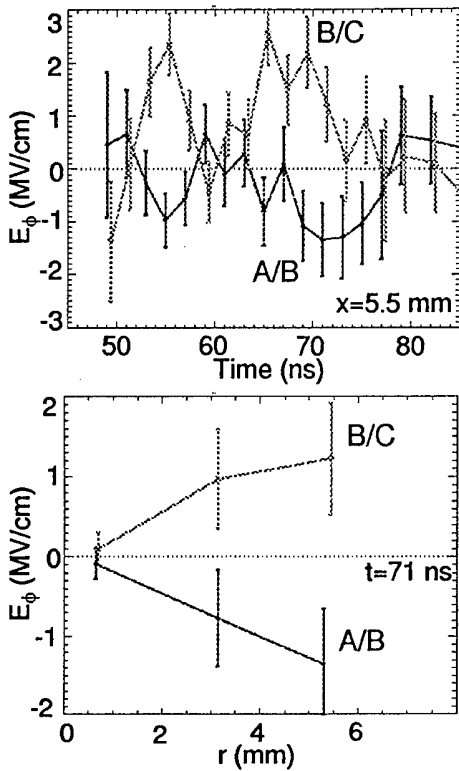


Fig. 3. Preliminary unfolded  $E_\phi$  components from a PBFA II experiment, at azimuths A,B and B,C: a) at fixed position  $x$ , and b) at fixed time  $t$ . Ion beam onset is at  $t=41$  ns.

needs to be understood.

## ACTIVE SPECTROSCOPY

While much has been learned by viewing the conveniently-occurring Li atom emission, this passive spectroscopy is limited by the  $\sim 30$  ns atom time-of-flight across the AK gap, the large Doppler broadening of the fast Li atoms, and the line-of-sight integration. We are implementing an Active Spectroscopy Probe (ASP) by injecting  $\sim 5 \times 10^{12} \text{ cm}^{-3}$  Na atoms into the diode AK gap just prior to the experiment, and using saturated laser-resonance-fluorescence or absorption spectroscopy to obtain a detailed Stark-Zeeman Na I 3s-3p pattern with full 3-D space and time resolution [12]. As shown in Figure 4, the information content in the low-Doppler-broadening Na atom emission pattern can give much better electric and magnetic field measurement than from the fast Li atoms, yielding the charge and magnetic flux information needed for understanding of actual ion diodes. Initial experiments [13] with the laser-driven low-density Na atom source and collection optics are promising.

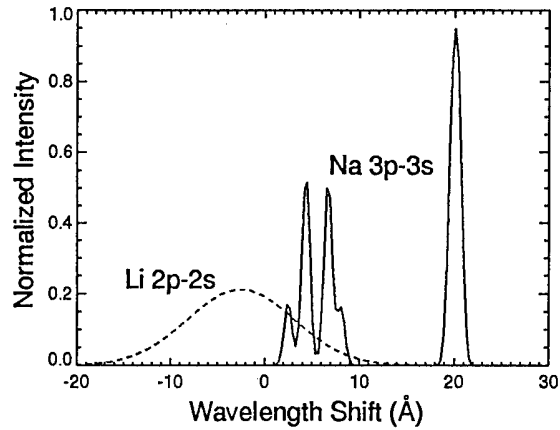


Fig. 4. Comparison of calculated Stark/Zee-man-shifted resonance-line emission for comparable densities of naturally-occurring fast Li atoms (dashed) and actively-injected Na atoms (solid). Calculation used 6 MV/cm and 6 T crossed electric and magnetic fields.

We are grateful to the PBFA II operations crew and D.F. Wenger for technical assistance, and to D.L. Cook, R.J. Leeper, and J.P. Quintenz for support. Funding for this work has been provided by the U. S. Department of Energy under Contract DE-AC04-94-AL85000.

- <sup>1</sup>Y. Maron, et al., Phys. Rev. Lett. **57**, 699 (1986), Phys. Rev. A. **36**, 2818 (1987).
- <sup>2</sup>J.E. Bailey, et al., Phys. Rev. Lett. **74**, 1771 (1995).
- <sup>3</sup>T.D. Pointon et al., Phys. Plasmas **1**, 429 (1994).
- <sup>4</sup>J. Bailey, et al., Rev. Sci. Instr. **61**, 3075 (1990).
- <sup>5</sup>J.E. Bailey, in *Proc. 7th Int. Workshop on Atomic Physics for Ion-Driven Fusion, Madrid, Spain*, October 16-20, 1995. To be published in Laser & Particle Beams.
- <sup>6</sup>M.P. Desjarlais, J. Appl. Phys. **66**, 2888 (1989).
- <sup>7</sup>M. P. Desjarlais et al., Phys. Rev. Lett. **67**, 3094 (1991).
- <sup>8</sup>S.A. Slutz, Phys. Fluids B **4**, 2645 (1992).
- <sup>9</sup>T. A. Green et al., Sandia National Laboratories report SAND95-1794 (available from NTIS).
- <sup>10</sup>T. A. Mehlhorn et al., in *Proc. 10th Int. Conf. on High Power Particle Beams, San Diego, CA, 1994* (NTIS PB95-144317), p. 53.
- <sup>11</sup>J.E. Bailey, et al., in *Proc. 13th Topical Conf. on High-Temperature Plasma Diagnostics, Monterey, CA, May 13-17, 1996*. To be published in Rev. Sci. Instr.
- <sup>12</sup>B.A. Knyazev, et al., in *Proc. 9th Int. Conf. on High Power Particle Beams, Washington, DC, 1992* (NTIS PB92-206168), p. 1043.
- <sup>13</sup>C.-H. Hong, et al., in Ref. 11.



## RECENT EXPERIMENTS TOWARDS PRODUCTION AND DIAGNOSTIC OF NITROGEN ION BEAM FOR MEDIUM-MASS ION BEAM ICF

K. Kasuya\*, K. Yasuike\*\*, S. Miyamoto\*\*,\*\*\* S. Nakai\*\*, T. Kamiya\*, M. Funatsu\*, H. Okayama\*, K. Nishigori\*,  
H. Sunami\*, C. Wu\*, D. Ido\*, T. Adachi\*, M. Watanabe\*, T. Ebine\* and G. Niimi\*

\*Department of Energy Sciences, Interdisciplinary Graduate School of Science and Engineering,  
Tokyo Institute of Technology, Nagatsuta 4259, Midori-ku, Yokohama, 226, Japan

\*\* Institute of Laser Engineering, Osaka University, Yamadaoka 2-6, Suita, Osaka, 565, Japan

\*\*\* Laboratory of Advanced Science and Technology for Industry,  
Himeji Institute of Technology, Shosha 2167, Himeji, Hyogo, 671-22, Japan

### Abstract

To promote the research of medium mass ion beams, associate topics are investigated recently. This is a combined paper of the three groups shown above. These groups are cooperating in recent years. The first group presents new proposals and preliminary results concerning (1) re-operation of cryogenic diode for nitrogen beam, (2) laser plasma production to supply ion source, (3) application of CCD camera element to advanced particle detector, (4) application of cryogenic technique to advanced material production method and (5) reform of UV laser for future diode cleaning or plasma production. On the other hand, the joint group of the second and the third groups presents (6) most recent results of time- and spatial- dependent particle beam diagnostics by an advanced arrayed pin-hole camera.

### The Reason Why We Propose Nitrogen Beam

Under the recent research circumstances around us, it may seem that we need not to propose a medium-mass ion beam as a candidate driver beam for the ICF-oriented research works. Never the less, we are afraid of the fail in enough focusing of the light ion beams by the inherent high charges themselves, and we are also afraid of the fail in enough focusing of the heavy ion beams by the longitudinal beam instabilities. From this point of view, the medium-mass ion beams are attractive, and we propose nitrogen beams as the first candidate to be investigated.

In the cases of the MCF Tokamak apparatuses and also in the cases of big accelerators for fundamental nuclear physics experiments, they use machine cleaning techniques with various methods including DC or RF discharge and cryogenic cooling. Some people in SNL also started to make use of these cleaning techniques to get higher beam intensity [1]. One and half decades ago we proposed a cryogenic anode [2] in the field of intense LIB generation which was tested also in SNL (Sandia National Laboratories) with higher voltage and current [3]. In more recent years, cryogenic cathode is tested separately in SNL to suppress the parasitic loads successfully [4].

Anyhow we must use cryogenic techniques in the future intense ion diode, which suggest that we should try to use both the cryogenic anode and the cryogenic cathode simultaneously. And the first candidate is nitrogen ion beam which is realized without the liquid helium or the alternative refrigerators. We need a moderate refrigerator to cool the anode, and a thermal shield around the anode, but the liquid nitrogen temperature is enough for the shield. With the shield almost all part of the harmful impurities which is water vapor are stopped. The incoming nitrogen as the leakage gas from the outside of the diode chamber is acceptable, because we need to supply nitrogen with any method to the anode surface.

Recently we operated our refrigerator again, and we could cool our diode down to 60K with our refrigerator without thermal shield around the diode. It is planned in a week or so for the anode with the thermal shield to be cooled down to 30K which corresponds to the nitrogen vapor pressure of  $10^{-4}$  Torr for the diode operation.

### **Laser Plasma Production to Supply Ion Source**

If we must supply only plasmas to the anode surface without supplying the neutral particles, we must use plasma injection diode for further good beam quality. We may also need to produce multiply-charged ion beams in some cases. To fulfill these kinds of requirements, we are preparing to get laser-produced plasmas by an e-beam pumped KrF laser of 100 MW output power.

Lithium and Aluminum targets in a vacuum chamber were irradiated by the laser lights of 0.7 J energy and  $3.2 \times 10^4$  J/cm<sup>2</sup> flux. The produced plasmas were measured by a biased ion collector, and the luminosity was observed by a fast frame camera. The plasma surface density for Li and Al were estimated to be  $2.8 \times 10^{16}$  /cm<sup>2</sup> and  $1.6 \times 10^{16}$  /cm<sup>2</sup>. Examples of the luminosity measurements are shown in Fig 1.

### **CCD Camera Element Applied to Direct Particle Detector**

If we use the plastic track detectors to measure the ion tracks, the chemical process to get the tracks after the beam irradiation is troublesome and lengthy. To overcome this, we are proposing that we use a CCD camera element which is directly irradiated by the ion beams to produce electric signals associated with the beams. As we could just suppress the background noise in this method, we hope that the main results will be obtained very soon.

### **Cryogenic Technique Applied to Advanced Material Production Method**

In the field of material processing, laser light is very convenient and is used often to irradiate the targets. This is because we need no special interface between the beam source and the target, when the beam is laser light. Of course there are no problems, if the ion beam target can be installed in a vacuum chamber. On the contrary, if we must put some amount of gas around the target and the pressure is too high for the ion diode to be operated, we can not find a suitable interface under our recent technology.

One of the examples is the process in which we make thin films of high temperature super-conductor materials under the ion beam irradiation of such targets. The target must be placed in a chamber filled with oxygen to get good films. To overcome this problem, we propose to use cryogenic targets on which we put necessary amount of oxygen in the frozen state before the irradiation of the target by the intense ion beams. As we can get enough low temperature to freeze oxygen with the refrigerator mentioned above, this method is easy to be realized for us. Even if we can use only the liquid nitrogen to cool the target, water can be used instead of the oxygen.

Moreover, if the conventional plastic anode of the ion diode can be replaced by a pure anode of a cryogenic diode, more preferable condition for this kind of material processing can be realized. Even if we can use only the liquid nitrogen to cool our anode and the attained temperature of the anode is not so low, we can use the water (ice) also as the anode plasma source.

We built a cryogenic target which was cooled by liquid nitrogen, and we irradiated the ice-covered target by proton beams. We are now also preparing the diagnostics of the ablation process to investigate the fundamental processes.

### **Reform of UV Laser for Diode Cleaning or Plasma Production**

In recent years, we are developing a discharge-pumped KrF laser with high mean output power. More recently we revised the pre-ionization method, where the former conventional UV light was replaced by the X-ray. Although the characteristics must be investigated from now on, we will use this laser to clean our ion diodes. Together with the cryogenic methods applied to our diodes and the conventional methods to purify, the UV laser cleaning will be scheduled to be tested in the near future. The plasma production by this laser is also planned.

### **Two-Dimensional Beam Diagnostics for Two Stage Ion Diode**

Two-dimensional arrayed pinhole camera (APC) is used to measure the two stage ion diode. This is an extension of one-dimensional APC in [5]. Performances of the APC are a spatial resolution of better than 2 mm, angular observation range of 60 mrad, an effective angular resolution of about 7 mrad and a temporal resolution is

about 15 ns. Measured results show that the ion beams accelerated by the two stage magnetically insulated ion diode have an isotropic beam divergence in ExB direction and perpendicular to that direction, where B is the insulating magnetic field in the diode.

Figure 2 shows the schematic of ion diode with two-dimensional beam angular distribution in radial direction  $\Delta\theta_r$  and azimuthal direction  $\Delta\theta_\phi$ . The structure of the 2D-APC is shown in Fig. 3. The APC consists of multiple ion pinhole cameras (shown as the pinhole array in the figure) and an ion detector. Each pinhole camera of the APC observes the same beam area with different observation angle.  $\Delta\theta_r$  and  $\Delta\theta_\phi$  of a point acquired from different observation angles  $\theta_\phi$  and  $\theta_r$  are individually obtained by the corresponding pinhole rows. The beam divergence  $\Delta\theta$  at the position is evaluated by a half-width of the distribution at the half-maximum (HWHM) of the Gaussian fitted curve to the data.

The ion beam, to be measured in the experiments, has an annular symmetry that is generated by the two-stage ion diode [6]. Active area sizes of the beam source are an inner radius of 56 mm and an outer radius of 80 mm, which corresponds to the beam cross section area of 99 cm<sup>2</sup>. A diode aperture, from which the beam is extracted, is larger than the active area. The beam parameters are an ion energy of up to 1.2 MeV, an ion current density of 2-20 A/cm<sup>2</sup>, duration time of ~100 ns and a main ion specie of Proton (H<sup>+</sup>). In order to observe the beam uniformity throughout the beam cross-section, the spatial observation range is required to be set larger than the whole radii of the active area of the beam with spatial resolution of less than 2 mm. The required time resolution is about 10 ns, which corresponds to the transition time from diocotron instability into the ion-mode instability.

The structure of the APC is shown in right side of Fig. 4. We have used a gated MCP as a time resolved ion imaging detector. The APC is consisted by multiple-pinhole plate, micro-channel plate as an ion detector and a CCD camera. A pinhole plate is made from 100 mm thickness Tantalum plate. The pinhole diameter is 100  $\mu$ m. The spatial resolution is mainly determined by the pinhole size, and the spatial resolution on the anode as a result of the design is better than 2 mm. The gate timing is monitored at the terminator located at one end of the line. The gate width can be changed from 15 ns to 300 ns.

Figure 4 shows our experimental set-up. The diode A-K gap of the first and the second stages are 10 and 11 mm, respectively. The diode insulating magnetic field is about 0.5 T that corresponds to diode critical voltage 2.2 MV. The aluminum grooved epoxy filled anode was used for the ion source.

In the experiments, the ion specie is mainly proton with an energy of less than 1 MeV, which was measured by Thomson parabola spectrometer. Typical ion current density was 10 to 20 A/cm<sup>2</sup>, which was lower than the Child-Langmuir current. The pulse width of the MCP gating pulse was 15 ns. The timing of MCP gating pulse was 90 ns later from the beginning of the diode voltage.

Spatial distributions of the divergence in radial and azimuthal directions and intensity are shown in Fig. 5. The position at 0 mm in Fig. 5 corresponds to the beam radius of 70 mm in Fig. 4. The active area of the beam source corresponds to the position from -10 mm to 10 mm on the horizontal axis in Fig. 5. The azimuthal divergence shows radial and intensity dependence. This divergence also shows higher values than that of radials in spite of parallel direction to the grooves on the anode. These results are considered as results of the instabilities in the electron sheath and agree with the tendency predicted by the computational simulations.

[1] J.P. Quintenz, R.G. Adams, G.O. Allshouse, J.H. Aubert, L.D. Bacon, J.E. Bailey, D.D. Bloomquist, J. Boyes, G.A. Chandler, R.S. Coats, D.L. Cook, J.T. Crow, M.E. Cuneo, M.S. Derzon, M.P. Desjarlais, et al., "Progress in the Light Ion Driven Inertial Confinement Fusion Program," 15th Int'l Conf. on Plasma Physics and Controlled Nucl. Fusion Research, Seville, Spain, IAEA-CN-60/B-1-I-6, 1994.

[2] K. Kasuya, K. Horioka, T. Takahashi, A. Urai and M. Hijikawa, Applied Physics Letters, 39, 887 (1981), T. Takahashi, K. Horioka, H. Yoneda, and K. Kasuya, Applied Physics Letters, 46, 249 (1985).

[3] D. Hanson et al., Journal of Applied Physics, 70, 2926 (1991).

- [4] M. Cuneo, P. Menge, D. Hanson, J. Bailey, M. Bernard, M. Desjarlais, A. Filuk, W. Fowler, T. Lockner, S. Sluz and G. Ziska, Bulletin of the American Physical Society, 39, 1644 (1994).
- [5] K. Yasuoka, S. Miyamoto and S. Nakai, Review of Scientific Instruments, 67 437 (1996).
- [6] S. Miyamoto, A. Zakou, S. Yasumura, K. Takitani, T. Akiba, K. Imasaki, C. Yamanaka and S. Nakai, "Two Stage Diode for Light Ion Fusion Driver," IAEA Technical Committee Meeting on Drivers for Inertial Confinement Fusion, 15-19 April 1991 Osaka Japan.



Lithium Plasma



Aluminum Plasma

Fig. 1 Examples of luminosity measurements.

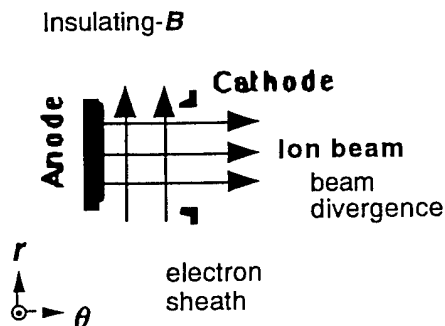


Fig. 2 The schematic of ion diode.

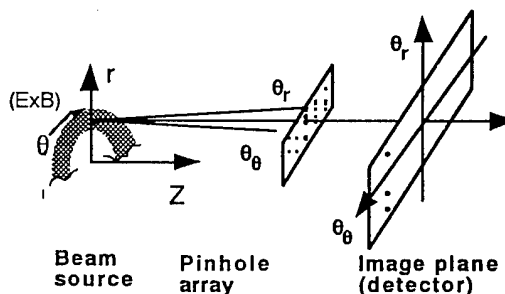


Fig. 3 The structure of the 2D-APC.

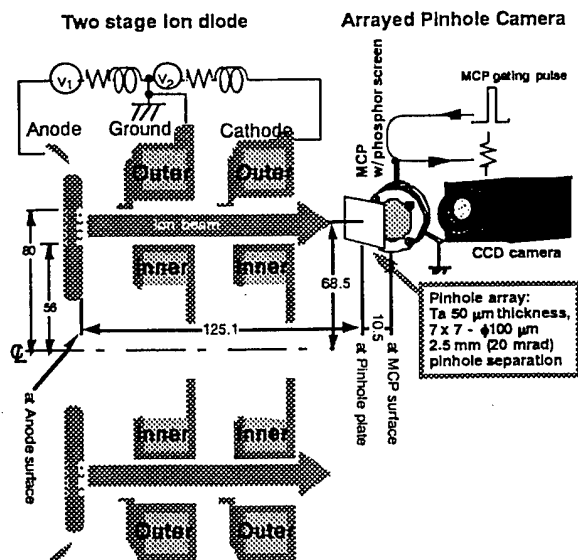


Fig. 4 Experimental set-up with a 2D-APC.

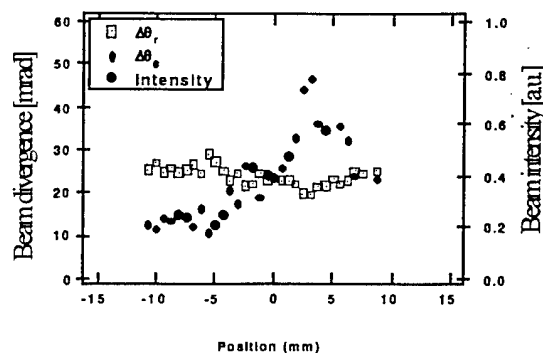


Fig. 5 Spatial distribution of beam divergence and intensity.

## Status of Magnetically-Insulated Power Transmission Theory

C. W. Mendel, Jr.

Sandia National Laboratories, Albuquerque, NM, 87185-1194, USA

**Abstract:** The theory of magnetically-insulated power flow has improved dramatically over the last two decades since the early works of Creedon<sup>1</sup>, Lovelace and Ott,<sup>2</sup> Ron, Mondelli, and Rostoker<sup>3</sup>, and of Bergeron.<sup>4</sup> During the intervening years theoretical improvements included a complete general kinetic theory that involved distributions of electrons based on quasi-conserved canonical variables<sup>5</sup> and was used to study flow stability<sup>6</sup> and to analyze simulations<sup>7</sup> and pulsers with voltage adders.<sup>8,9</sup> The status of theory at this time allowed us to understand many features of these flows, but did not allow detailed analysis for design and data interpretation.

Recent theoretical advances have drastically changed this situation. Two recent static models<sup>10,11</sup> based on layered flows have allowed us to understand and to improve power coupling in voltage adders, current adders, plasma opening switches and in systems where the vacuum impedance varies along the flow. A dynamic model based upon electrons flowing in one or more thin layers has permitted detailed self-consistent time-dependent calculations which include electron flow.<sup>12</sup> This model accurately predicts experimental and simulational data.

**Introduction:** Models of static magnetically-insulated power flow have been studied for many years.<sup>1-4</sup> These are used to calculate voltage from current, and as a basis for stability analysis, but have not been very useful as a design tool. General kinetic theories included general static and dynamic flows.<sup>5,7</sup> These provided much understanding, and can be used for analyzing waves and stability,<sup>6</sup> and used for simulation diagnostics,<sup>7,8</sup> but kinetic theories have been of limited use as a design tool. Generally systems designers have used circuit codes that at most include only direct electron losses across the magnetically-insulated transmission line (MITL). These losses are important for slowing front velocities, but are not as important as electrons flowing parallel to the transmission line axis.

Recently new models have become available which include electron flow and can be useful for system design and data analysis. These include static models that can be used to optimize system components such as vacuum voltage adders and impedance transitions,<sup>9,11</sup> and a dynamic model that includes all important effects that are measured in experiments.<sup>12</sup>

**Static Models:** Illy, Kuntz, and Westermann used a layered model involving stratified, constant density layers to understand the voltage adder in the Kalif-Helia driver.<sup>9</sup> The model calculations were compared to simulations. Church and Sudan<sup>10</sup> used a similar model to study simulated layered flows. They concluded that multiple-layer flows can be modelled with two layers due to a tendency of layers away from the cathode to break into vortices. This had been noticed earlier in simulations done by Rosenthal.<sup>8</sup> Mendel and Rosenthal<sup>11</sup> found a somewhat simpler model with zero-thickness electron layers placed in appropriate positions. Electron layer position is determined by a parameter called flow impedance. Flow impedance was originally introduced for quantifying the performance of plasma-opening switches.<sup>13</sup> It was soon realized that the definition could be generalized so that its value described the position of the centroid of the electron charge in any transmission line.<sup>11</sup>

Most transmission line systems are axially symmetric. For this reason it is convenient to use cylindrical coordinates, and to transform the radius,  $r$ , to a new radial coordinate,  $R$ ,

given by  $R = \pm(\mu_0/\epsilon_0)^{1/2}/(2\pi) \ln(r/r_0)$  where  $r_0$  is an arbitrary positive constant. The sign of this definition is conveniently chosen to be negative for a negative outer conductor and positive for a positive outer conductor MITLs. In this coordinate system vacuum impedance is the distance between the cathode and the anode, and flow impedance is the distance between the centroid of the electronic charge and the anode. By working in this coordinate system, and by using enclosed current in place of the azimuthal magnetic field, and enclosed charge per unit length in place of radial electric field, the cylindrical problem has the same form as a planar problem.<sup>11</sup>

Magnetically-insulated flows at voltages relevant to pulsed-power systems involve important amounts of electron charge and current that should not be neglected. However, the electrons behave more simply than at lower voltages because field pressures dominate the electron pressure.<sup>7</sup> For this reason, models can assume that the net force on the electron cloud is zero. For axial forces this is equivalent to saying that the axial electric field is zero at the centroid of the electron cloud, i.e. at the position of the thin layer in the model. This is the same as saying that the electrons flow on equipotential lines, and is just the parapotential flow assumption that Creedon used to such great advantage.<sup>1</sup> The assumption that the radial force on the electron cloud is zero everywhere yields a pressure balance relationship relating the local values of enclosed current and charge.

An accurate model of these flows can be obtained by replacing the electron cloud by one or more thin layers of charge. The thin-layer model simplifies voltage adder calculations. Using the parapotential and pressure balance relationships, and assuming all input line voltages, vacuum impedance, and flow impedances are the same, the downstream flow impedance is calculated to be as shown in Fig. 1.

**Dynamic Model:** We have developed a dynamic model<sup>12</sup> capable of calculating the voltage, currents, and electrode charges at all points in MITL systems. The model inputs are the forward wave and impedance of the driver, the MITL vacuum and flow impedances at all axial locations, and the load current.

The model uses a single layer of electrons, and since there is one added conductor (the electron layer) there are three Telegrapher equations. These equations describe Faraday's law, continuity at the anode, and continuity at the cathode. When there is no electron flow the latter two equations are identical. Transverse currents are determined from data (experimental or simulational) for frontal velocities of step waves, plus space-charge limited cathode conditions. The frontal velocity data are general, and need to be determined only for one simple system and not repeated for each problem.

Figure 2 shows data taken behind forward and backward wave simulation data. The data are shown as A,V pairs where A is the magnetic flux per unit length and V is the electric voltage, both taken behind the step wave front. These data were used to determine two constants related to the electron losses in forward and reflected waves. These two constants do not change when the problem changes. Also shown in Fig. 2 are the model results taken for the same drive waves and MITL geometry. The load impedances were not the same since the simulation used an electron diode while the model used a resistor.

Figure 3 shows a simulated wave when it is in the transition region of a MITL that begins at 11.9  $\Omega$  and then increases to 24.3  $\Omega$ . The wave into the MITL input has a sine<sup>2</sup> shape with a 6 ns wide base. Figure 4a shows the simulated and modelled line voltage versus axial position at one instant of time. Figure 4b shows the anode and cathode currents, also at 6 ns.

**Three Interesting Observations:** These models have proven valuable in interpreting experimental data, and have been used in the design of new pulsers. They also have been

used to explain experimental data and provide some interesting design rules.

The optimum adder design, shown in Fig. 1 is given by a sequence of vacuum impedances proportional to  $n^{1/2}$ , rather than proportional to  $n$  as in the vacuum case. In such a design flow impedance is never below one-half vacuum impedance (Fig. 1). This reduces overall system inductance, and eliminates losses at adders during wavefronts.

Simulation and experimental data indicate that wave front velocity depends upon Figure 1. Downstream flow impedance versus wave voltage and not geometry. Using vacuum impedance for multiple-line voltage adders. Faraday's law, it can be shown that waves passing increases in vacuum impedance must lose electrons at the impedance transition in the proportion needed so that a MITL does not see a reflection from a vacuum impedance increase. This explains an observation of Rosenthal and Desjarlais.<sup>13</sup> Using simulations they noticed that a MITL seeing a load runs at the forward wave self-limited value until the load impedance is low enough to draw more than the self-limited cathode current.

Perhaps the most interesting prediction relates to flow impedance during forward waves downstream of voltage adders with more than four feed lines. If the line voltage is plotted versus the magnetic flux per unit length for a forward step wave, it must be a straight line in the A,V plane because of Faraday's law. The slope of this line is the frontal velocity. The frontal velocity is always faster than the electron drift velocity behind the front. As a result there is a loss front at the beginning of the wave, where magnetic field is low, followed by a region of emission where electrons are filling in behind the front as it moves away from the drifting electrons. Between these two regions is a point where insulation is marginal. Ahead of it electrons are not insulated, behind it they are.

Figure 5 shows such a wave plotted in the A,V plane. The straight line representing  $V(t)$  plotted versus  $A(t)$  starts at the point 0,0 (i.e. at the front of the wave), goes upward to the point where the electrons begin to be insulated, and finally onward to the final value on the generator side of the front. If this were done for all amplitudes of forward waves there would be two curves; the locus of insulation points and the locus of forward wave points.

For the single layer model these two lines are the same when the flow impedance is half the vacuum impedance. If it is less than half the vacuum impedance the insulation line

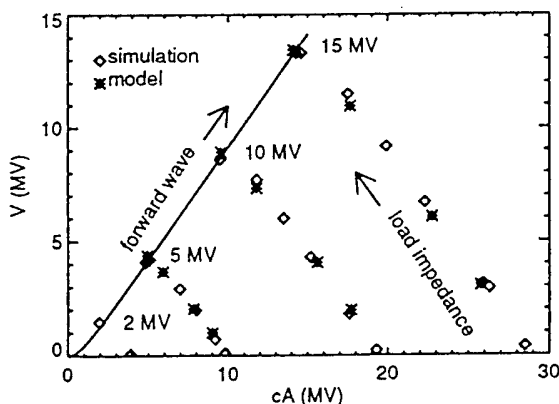
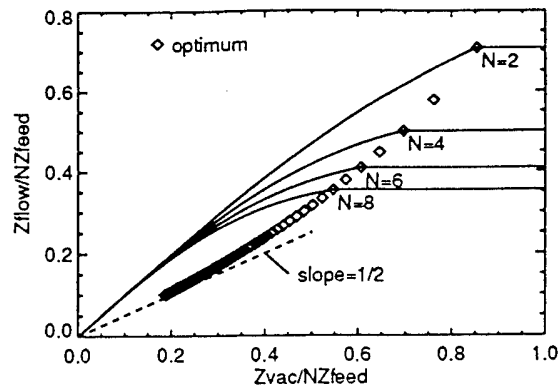


Figure 2. Step wave data taken behind forward a reflected waves from simulations and the model.

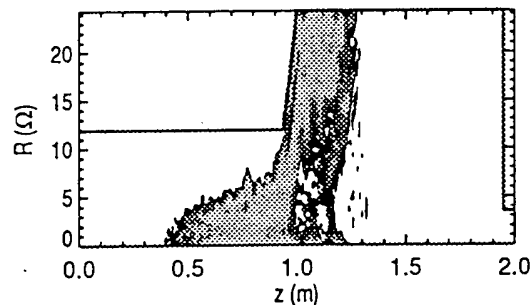


Figure 3. Electronic charge density in a simulated impedance change. The line is the electrode shape.

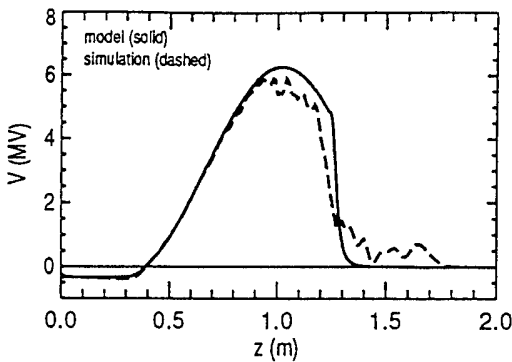


Figure 4a.  $V$ , at the time of Fig. 3.

**Acknowledgements:** The author would like to thank S. E. Rosenthal for providing simulation data, and S. E. Rosenthal and D. B. Seidel for comments on this manuscript.

This work was supported by the United States Department of Energy under contract DE-AC04-94AL85000.

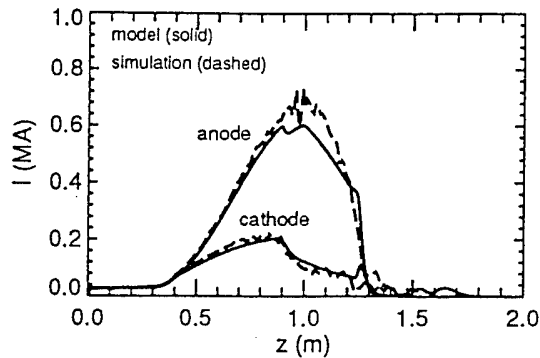


Figure 4b. Current at the anode and cathode at the same time as Fig. 3.

is to the right of the forward wave line, and the front is never insulated. Thus, if a device, for instance a vacuum-matched ten feed-line adder, tries to make the flow impedance less than half the vacuum impedance, electrons will be lost at the adder until the flow impedance is half the vacuum impedance. Thus the importance of using the optimum adder design.

**Conclusions:** The theory of magnetically-insulated electron flow in transmission lines is well understood, and models are now adequate for confident use for data analysis and system design.

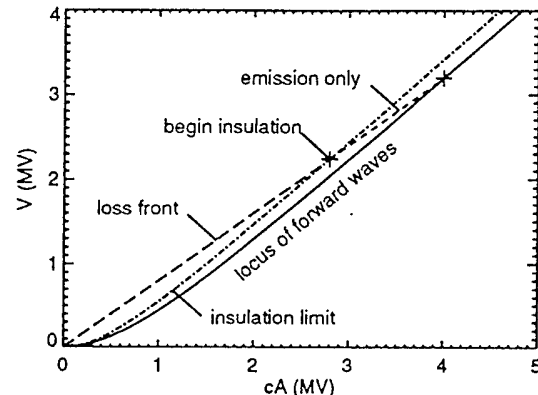


Figure 5. A step-forward wave in the A,V plane. When A,V is above the insulation line electrons can cross from cathode to anode.

- [1] J. Creedon, J. Appl. Phys. **46**, 2946 (1975), J. Appl. Phys., **48**, 1070 (1977).
- [2] R. V. Lovelace and E. Ott, Phys. Fluids **17**, 1263 (1974).
- [3] Ron, A. A. Mondelli, and N. Rostoker, IEEE Trans. Plasma Sci. PS-1, 85 (1973).
- [4] K. D. Bergeron, J. Appl. Phys. **48**, 3065 (1977).
- [5] C. W. Mendel, Jr., J. Appl. Phys. **50**, 3830 (1979), C. W. Mendel, Jr., D. B. Seidel, and S. A. Slutz, Phys. Fluids **26**, 3628 (1983), R. I. Lawconnel and J. Neri, Phys. Fluids B **2**, 629 (1990).
- [6] C. W. Mendel, Jr., J. A. Swegle, and D. B. Seidel, Phys. Rev. A **32**, 1091 (1985).
- [7] C. W. Mendel, Jr., S. E. Rosenthal, and D. B. Seidel, Phys. Rev. A **45**, 5854 (1992).
- [8] S. E. Rosenthal, IEEE Trans. Plasma Sci. PS-19, 822 (1991).
- [9] S. Illy, M. Kuntz, and T. Westermann, Phys. Plasmas **1**, 2748 (1994).
- [10] B. W. Church and R. N. Sudan, Proc. of the 9th Int'l. Conf. on High-Power Particle Beams, Washington, DC May 1992. D. Mosher and G. Cooperstein editors.
- [11] C. W. Mendel, Jr. and S. E. Rosenthal, Phys. Plasmas **2**, 1332 (1995).
- [12] C. W. Mendel, Jr. and S. E. Rosenthal, submitted to Phys. Plasmas.
- [13] C. W. Mendel, Jr., M. E. Savage, D. M. Zagar, W. W. Simpson, T. W. Grasser, and J. P. Quintenz, J. Appl. Phys. **71**, 3731 (1992).
- [14] S. E. Rosenthal and M. P. Desjarlais, private communication.



## THE PROOF-OF-CONCEPT EXPERIMENT FOR THE SPIRAL LINE INDUCTION ACCELERATOR\*

S. Putnam, V. Bailey, J. Smith, J. Lidestri<sup>[a]</sup>, J. Thomas, H. Lackner and H. Nishimoto

*Pulse Sciences, Inc.  
600 McCormick Street  
San Leandro, CA 94577 USA*

### *Abstract*

A proof-of-concept experiment (POCE) for the Spiral Line Induction Accelerator (SLIA) is underway at Pulse Sciences, Inc. to demonstrate a new compact high current ( $\geq$  few kiloamperes) recirculating induction accelerator for high power ( $\geq 100$  kW) commercial processing and other applications. Hardware has been fabricated to generate 9.5 MeV electron beams at 2 and 10 kA by recirculating the beam for two passes through each of two 1.5 MeV accelerating units. Initial experiments have demonstrated acceleration of 2 and 10 kA beams to 5.5 MeV by transport around a complete turn with two passes through a single accelerating unit and work is currently in progress to complete the full POCE. Experimental results to date are reported.

### *Introduction*

Linear induction accelerators (LIAs) such as the Advanced Test Accelerator (ATA) at the Lawrence Livermore National Laboratory (50 MeV, 10 kA) have been used for some time to accelerate high current electron beams. Many applications requiring a more compact accelerator configuration necessitate effective accelerating gradients significantly higher than that of ATA ( $\sim 600$  kV/m). Recirculation of a beam through common accelerating units on each side of a racetrack configuration can effectively increase the gradient of an LIA by nearly twice the number of circulations, thereby allowing gradients  $\geq 10$  MV/m with existing induction driver technology. The SLIA accelerator uses a recirculating spiral beamline geometry for efficient and simple injection and extraction in the presence of the longitudinal magnetic field required to confine the high current beam at low injection energy. Practical considerations limit the number of circulations to  $\sim 10$ , giving an upper bound on the kinetic energy of  $\sim 50$  MeV.

In order to transport high current beams with large energy spread around the SLIA bends, an  $\ell = 2$  stellarator field<sup>[1]</sup> is added to the toroidal and vertical magnetic fields. The SLIA bends are designed<sup>[2]</sup> to be achromats or identity transformations to first-order in  $\Delta p/p$ , the fractional beam momentum mismatch. Since the equations of beam centroid motion in a straight stellarator with a transverse dipole field are identical to those of a stellarator bend with a momentum mismatch, experiments early in the program simulated (stellarator pitch, total length, and beam space charge effects) the 5.0 MeV, 10 kA beam of the first POCE bend in a straight stellarator section for easy diagnostic access using an 850 keV, 250 A beam. These experiments<sup>[3]</sup> demonstrated the existence of the stellarator achromat at the predicted magnetic field levels and verified the increased tolerances of the bends to momentum mismatches. Simulated momentum mismatches of  $\pm 25\%$  were propagated through the "straight bend" without measurable charge loss.

In addition to use of a new strong focussing scheme for the bends, the SLIA incorporates a different accelerating gap design than the pillbox gap structure of LIA's, such as ATA. The SLIA configuration necessitates off-axis accelerating gaps in the cells which would result in strong

[a] Currently at Dept. of Biochemistry and Molecular Biophysics, Columbia University, New York.

\*Work sponsored by the Advanced Research Projects Agency and monitored by Naval Surface Warfare Center.

excitation of transverse beam deflection modes in a pillbox geometry, leading to beam disruption by the collective beam breakup instability. To avoid this problem, SLIA has a shielded gap design wherein the accelerating voltage from the radial power feed of the cavity is applied across the end of a transmission line which is coaxial with the individual beam line. Only asymmetric modes above the coaxial cut-off can couple to the cavity. To decouple centroid motion from bend transport and cavity excitation, this frequency ( $\sim 900$  MHz for SLIA/POCE) is chosen to be above the highest frequency components of the beam current and accelerating voltage profiles. Cold RF characterization tests of a prototype SLIA accelerating cell<sup>[4]</sup> suggest adequate stability for the POCE and higher kinetic energy SLIAs.

Other issues of the high current SLIA include beam envelope matching on/off the stellarator fields of the bends and the three-wave electromagnetic or Hughes-Godfrey (H-G) collective instability.<sup>[5]</sup> Since the beam equilibrium profile is circular in the solenoidal guide field and elliptical in the stellarator, non-adiabatic transitions on/off the stellarator field of the bend cause envelope oscillations which can result in emittance growth and/or loss of charge for larger radii beams as the centroid of off-momentum beam slices oscillates in transport around the bend. Experiments have been conducted with some success to evaluate two different matching schemes.<sup>[6]</sup> From theory, the H-G instability is avoided for the SLIA/POCE parameters when the longitudinal magnetic field is applied in the same direction as the electron velocity, while reversing the guide field direction results in an unstable regime. Experimental results from the SLIA/POCE have not shown evidence of the instability with the reversed guide field which is of interest because at the same guide field level, a stronger focussing stellarator field can be used compared to the stable direction.

#### *SLIA/POCE Experimental Apparatus.*

The SLIA/POCE experimental apparatus shown in Figure 1 consists of the 3.5 MV injector, two 1.5 MV accelerating units, and the vacuum magnetic beam transport system. A schematic of the experiment showing the position of the components and the current and beam position monitors C10-C18 before and after each bend and accelerating unit is given in Figure 2.

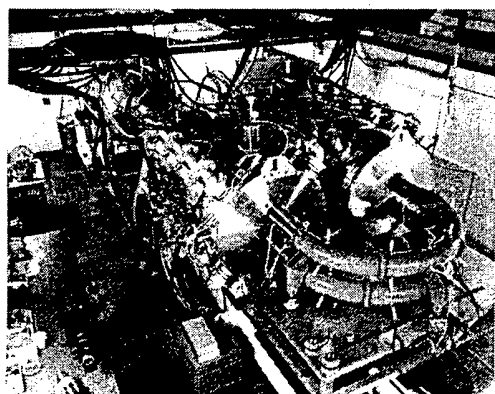


Figure 1. The SLIA/POCE experiment.

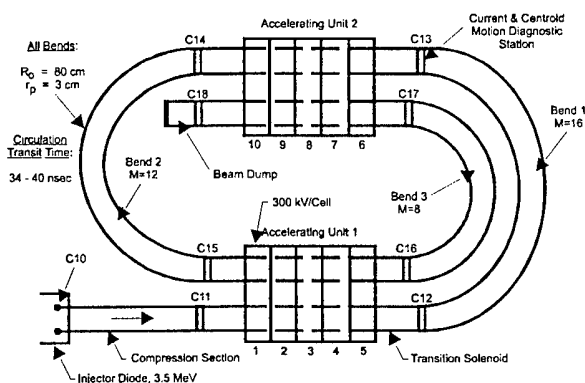


Figure 2. SLIA/POCE layout and diagnostic stations.

The SLIA injector is a lower voltage (3.5 MV) and shorter pulse length (37 ns above 80% of maximum voltage) version of similar devices built by PSI for radiographic applications. The injector has produced diode currents of 2.4 kA to 17.5 kA at an output voltage of 3.5 MV. The diode voltage and current injected into the compression section are shown in Figure 3 for the recent 2.4 kA experiments. The current density of the beam is increased from  $\approx 50$  A/cm<sup>2</sup> at the cathode to  $\approx 5000$  A/cm<sup>2</sup> at the end of the 3 meter compression section.

The two 1.5 MV accelerating units each contain five 300 kV induction cells with two accelerating gaps in each cell. The accelerating cell power supply provides the 300 kV, 83 ns, full-width-at-half-maximum (FWHM), voltage pulse shown in Figure 4 to the accelerating cells. A 12 m single-turn beam line length (40 ns single-turn transit time) was chosen so that, although in different beam pipes, the head and tail of the  $\approx 38$  ns FWHM beam overlap in the accelerating cells thereby keeping the cell loading roughly constant during the voltage pulse.

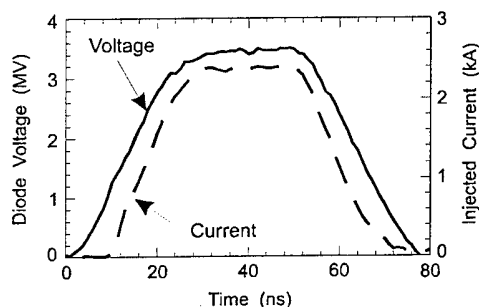


Figure 3. Diode voltage and injected current.

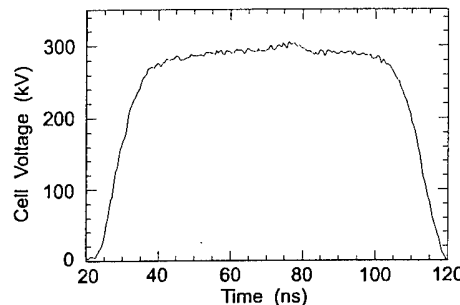


Figure 4. Accelerating cell voltage for the 2.4 kA two-pass experiment.

The transition region between the AUs and the bends have space for adding steering magnets to control the beam position and angle as it enters the bend or AU and quadrupole magnets for matching the beam envelope on/off the stellarator field of the bend. The 80 cm major radius SLIA/POCE bends contain four (toroidal,  $\ell = 2$  stellarator, dipole, and quadrupole correction) magnetic field coils built up radially on top of each other.<sup>[7]</sup> The toroidal M numbers ( $M = 4\pi R_0/L$ , where  $R_0$  is the major radius and  $L$  is the pitch length of the stellarator winding) for the SLIA/POCE bends are  $M = 16, 12$ , and  $8$  for the first through the third bend. The quadrupole correction magnet is used to set the betatron field index,  $n$ , directly. The outside minor diameter of the bend including all four magnets is 17.26 cm while the inside diameter of the beam pipe is 6.02 cm.

The beam current and x,y displacements of the beam centroid are measured during the pulse at diagnostic positions C10 - C18 by an array of  $B_\theta$  loops. Both photographic film and a shielded CCD array are used to record the time integrated Cherenkov image of the beam position and profile.

### Experimental Results

Transport experiments have been conducted at nominal 2, 10 and 15 kA injection current levels using accelerating unit 1 (AU1) and a complete-turn transport line for up to two passes through AU1. With the recent completion of the full POCE hardware the first set of experiments are underway at the 2 kA level with no matching or steering elements in the beam lines.

Experiments to quantify the dispersion of the stellarator bends and compare with theory have been completed for all three bends using the injected beam shown in Figure 3 without acceleration where the beam energy is most accurately known. The energy spread of the injected beam shown in Figure 3 is  $\approx 65\%$  while the POCE design goal is  $\sim 20\%$  total energy bandwidth.

Figure 5(a) compares the current injected into bend one with the transmitted current for no acceleration using a 3.0 kG achromat and the H-G stable configuration. The transmitted charge is  $\sim 88\%$  of the total injected charge which corresponds to 100% current transmission for energies  $> 75\%$  of the peak. The energy bandwidth of this particular achromat is thus  $\sim 25\%$ . A comparison of centroid motions at the exit of the bend with and without an applied stellarator field shows an increase of 10 ns in the transmitted current pulsewidth with the stellarator field for centroid displacements  $< 5$  mm from the axis. This data is in close agreement with theoretical prediction. To

illustrate the stronger focussing properties of reversed field achromats, Figure 5(b) shows an overlay of injected and transmitted current for a 1.5 kG achromat of bend one. At one-half the toroidal field level of the forward field achromat of Figure 5(a), this achromat gives approximately equivalent current bandwidth for an even higher energy 4.7 MeV, 2 kA beam generated from a different diode configuration. Figure 6 shows good current and charge transport around bend one for a 10 kA, 4.3 MeV beam using a reversed field 2.9 kG achromat.

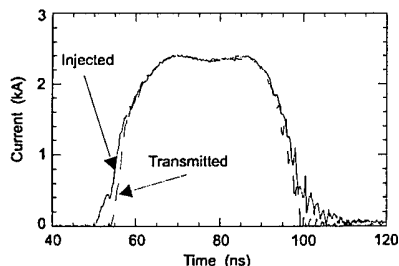


Figure 5a. Injected and transmitted current (bend 1, 3.5 MeV, 3.0 kG).

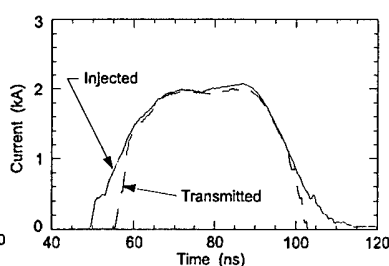


Figure 5b. Injected and transmitted current (bend 1, 4.7 MeV, 1.5 kG).

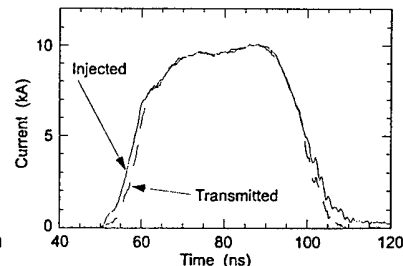


Figure 6. Injected and transmitted current (bend 1, 4.3 MeV, 2.9 kG).

To illustrate the recent transport results with the 2.4 kA beam of Figure 3, the current profile at the end of bend two at 6.5 MeV is shown in Figure 7. The 85% charge transport is the same as at the end of bend one at 5.0 MeV. Since 81% of the total injected beam charge has an initial kinetic energy  $> 80\%$  of the peak injected energy, the experimental charge transport efficiency compares favorably with the 20% design goal for total energy bandwidth. Figure 8 is a Cherenkov image of the beam cross section at the exit of the accelerator at 9.5 MeV.

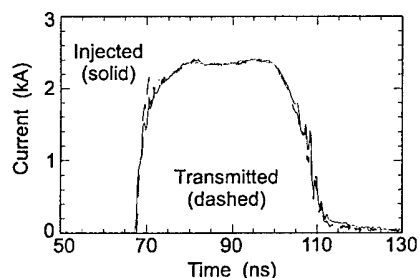


Figure 7. Transmitted and injected current (bend 2, 6.5 MeV, 3.4 kG).

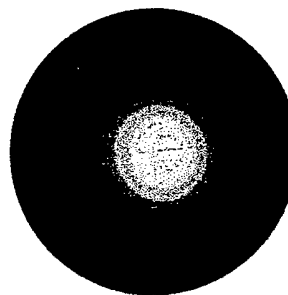


Figure 8. Beam image at exit of accelerator (9.5 MeV, 2.4 kA, beam diam = 17 mm FWHM).

### Acknowledgement

Theoretical support during the early phase of the program by the Naval Research Laboratory, Science Applications International (McLean, VA) and Mission Research Corporation (Albuquerque) is gratefully acknowledged. The guidance and encouragement of Dr. B. Hui of ARPA and Drs. J. Miller and E. Nolting of the Naval Surface Warfare Center, White Oak have been much appreciated.

### References

- [1] C. Roberson, et al., *Particle Accel.*, 17, 79 (1985).
- [2] S. Putnam, Semi-Annual DARPA Charged Particle Beam Review, Washington, DC, April 1989.
- [3] V. Bailey, et al., *Intense Microwave and Particle Beams III*, SPIE Proc., 1629, pg. 490 (1992).
- [4] J. Edighoffer, *IEEE Part. Accel. Conf.*, May 1991, Conference Record 91CH3038-7, 5, pg. 3117.
- [5] T. Hughes and B. Godfrey, *Phys. Fluids*, 29, 1698 (1986); M. Tiefenback, et al., Final Report PSIFR-2543-01, July 1991, Pulse Sciences, Inc. San Leandro, CA 94577.
- [6] M. Tiefenback, et al., *IEEE Part Accel. Conf.*, May 1991, Conf. Record 91CH3038-7, pg. 3195; J. Krall, et al., *J. Appl. Phys.*, Vol. 77, pg. 463 (1995).
- [7] V. Bailey, et al., *IEEE Part. Accel. Conf.*, May 1991, Conf. Record 91CH3038-7, pg. 3123.

# THE STATE OF DEVELOPMENT OF AN INTENSE RESONANCE ELECTRON-ION ACCELERATOR BASED ON DOPPLER EFFECT

A.M. Yegorov, B.I. Ivanov, V.I. Butenko, V.V. Ognivenko,  
I.N. Onishchenko, and V.P. Prishchepov

*National Science Center - Kharkov Institute of Physics and Technology (KFTI)  
Kharkov, 310108, Ukraine*

## Abstract

An intense ion accelerator has been proposed and now is being developed in which accelerating and focusing electric fields in a slow wave structure are excited by an intense electron beam using anomalous and normal Doppler effect. The results of theoretical studies and computer simulations show the advantage of this acceleration method that will allow to obtain acceleration rate of order of 10 - 100 MeV/m, ion beam energy and current of order of 10-100 MeV, 1-10 A. A project and technical documentation of an experimental accelerating installation are worked out. At the moment the accelerator-injector "URAL-5" of energy 5 MeV is in operation; preliminary experiments on a small installation have been carried out; experimental investigations of an accelerating RF resonator model (in 1/2 scaling) are performed; the accelerating test installation is being manufactured.

## Introduction

In a two-beam electron-ion accelerator it is possible for the driver electron beam to excite RF fields in an ion linear accelerator that are accelerating and focusing at the same time. A considerable gain may be obtained in the current of accelerated ions and in the acceleration rate. Refs. [1,2] outlines the concept and theory studies of a two-beam high current ion accelerator based on the Doppler effect. According to this concept an intense electron beam injected along the accelerator axis together with the accelerated ion beam generates accelerating and focusing RF fields in the spatially periodic accelerating structure of a linear accelerator. RF fields are excited by the interaction of E-beam with transverse fields of any spatial harmonic due to cyclotron instability under anomalous Doppler effect (ADE) or normal Doppler effect (NDE) whereas the ions are accelerated by the longitudinal field of the same harmonics or another one corresponding Cherenkov resonance.

Such acceleration schemes are the intermediate or hybrid ones between conventional and collective accelerators (e.g., [3,4]) using well investigated and technologically elaborated electrodynamic structures of the former and accelerating/focusing high gradient RF fields of the latter. The preliminary calculations [1] show the new type of accelerators to be promising due to expected considerable accelerating fields ( $10^5$ - $10^6$  V/cm) and simultaneous phase and radial stability of accelerated ions. (Fields of order of  $10^5$  V/cm were obtained in suitable experiments [5]). This concept may perhaps provide the ground for creation of ion accelerators with 10-100 MeV energy and 1-10 A current. The tolerance system for them may be conceptually similar to one for classic accelerators and powerful electron RF devices (i.e., practically feasible). To begin the realization of such accelerators we provide research and development activities including theoretical and experimental investigations, and construction of an accelerating installation.

### Project of the Experimental Accelerating Stand (EAS)

The Experimental Accelerating Stand (EAS) is intended to prove the workability of a new promising type of ion accelerators and to optimize their parameters. The intense electron beam propagating along the system axis in the resonant magnetic field with the given value and distribution over the length will excite focusing and accelerating fields in EAS due to the anomalous Doppler effect. To save money one intends to use the operating linear proton accelerator (e.g. the "Ural-5" accelerator of 5 MeV energy and 30 mA current) as an injector. If a more powerful injector is available the current in EAS may exceed 1 A. Table 1 gives the main EAS parameters calculated to accelerate protons from 5 MeV initial energy to 8 MeV final energy. Fig.1 shows the EAS scheme. The accelerating section is designed on the basis of the H-type resonator with drift tubes on meeting suspenders (such accelerators are designed successfully at the KFTI). Electron injector utilizes the electron gun with the transverse

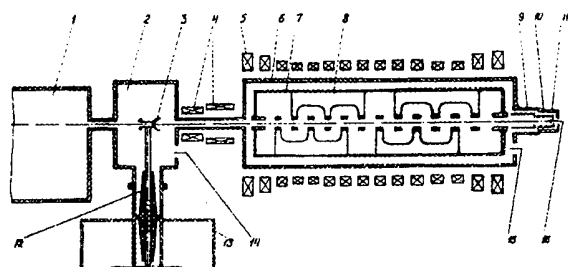


**FIGURE 1.** The EAS setup. 1- accelerator-injector, 2- vacuum chamber, 3- electron gun, 4, 5- magnetic coils, 6- vacuum chamber, 7- H-type resonator, 8- support "combs" with drift tubes, 9- electron collector, 10- ion collector, 11- collector bottom, 12- high-voltage input, 13- high-voltage pulse transformer, 14, 15- vacuum pumping, 16- ion outlet.

**TABLE 1.** The Main Parameters of the Experimental Accelerating Stand (preliminary data)

1	Input proton energy	5 Mev	10	Magnetic field intensity	
2	Output proton energy	8 MeV		for EAS input	609 Oe
3	Proton current	30 mA		for EAS output	439 Oe
4	Electron beam energy	350 keV	11	Resonator length	161 cm
5	Electron beam current	150 A	12	Operating frequency	148.5 MHz
6	Pulse duration	2.5 mksec	13	Accelerating field intensity	56 kV/cm
7	Pulse frequency	1 pps	14	Synchronous phase	60°
8	Electron beam initial radius	1.3 cm	15	Shunt impedance	35 MOhms/m
9	Electron beam final radius	2.4 cm			

compression of the beam and the supply unit of a powerful clystron of industrial production. The H-type resonator 7 is excited by an electron beam created by the electron gun 3. The electron beam is focused by the magnetic coils 4 and the solenoid 5. The electron gun is supplied by high-voltage pulse transformer 13. A proton beam from accelerator 1 is injected along the axis through a central hole in a cathode of the electron gun 3, and pass in the H-type resonator 7 to have an additional acceleration. Accelerating and focusing RF fields are excited by the electron beam upon the anomalous Doppler resonance conditions. The solenoid 5 (consisted of 15 coils) creates a resonance space-changed magnetic field. Vacuum in chambers 2 and 6 is provided by magneto-discharge and turbomolecular pumps at the level of  $10^{-7}$  mm Hg. On the output end of chamber 9 there are located the electron collector 9, the ion collector 10 with a moving bottom 11, and branch pipes 15 for vacuum line coupling.

Energy and current of the electron beam are chosen to be sufficiently large (up to 350 keV and 200 A respectively) to prevent excessive longitudinal deceleration and beam radius increase (due to longitudinal-transverse momentum transformation of beam electrons that is inherent in RF generation due to anomalous Doppler effect [6]). At this stage of research the conditions are chosen when energy losses of the electron beam are small in order to simplify calculations and increase their reliability as well as to simplify the experimental adjustment of the accelerator. Because of that the efficiency of the energy transfer from the electron beam to the ion one is small ( $<1\%$ ). Ref.[1] discusses the ways enhance the efficiency considerably and they will be studied in later developments. The magnitude of the resonant magnetic field  $H(z)$  was determined from the conditions of RF fields excitation due to anomalous Doppler effect [1].

### Results of research and development

The following results are obtained.

1. The physical concept of the two-beam high-current ion accelerator based on Doppler effect is well grounded. This concept may provide the ground for creation of ion accelerators with 10 - 100 MeV energy, 1 - 10 A current, and 10 - 100 MeV/m rate of acceleration.

2. The project of the EAS is developed. The EAS is intended to prove the workability of this type of ion accelerators and to optimize their parameters. The main EAS parameters are calculated to accelerate protons from 5 MeV initial energy to 8 MeV final energy. The accelerating section is designed on the basis of the H-type resonator with drift tubes on meeting suspenders. The operating linear proton accelerator will be used as an injector.

3. The set of nonlinear self-consistent equations has been elaborated for wave excitation by an electron beam in case of anomalous and normal Doppler effects in a H-type accelerating structure both for amplification and generation regimes.

4. The theoretical investigation and computer simulation in the bounds of the obtained set of equations have been fulfilled. It has been shown that for the experimental setup the planned accelerating gradient of order of 60 kV/cm can be achieved. Initial efficiency of order of 1% will become higher with growing phase velocity and keeping resonance by means of specially profiled magnetic field.

5. The method of stationary magnetic field synthesis with required dependence on longitudinal coordinate was realized. Thus it is used the regularization method developed by Acad. A.N. Tikhonov for solution of (so named) incorrect inverse problems. By this method the calculation of a solenoid for creation of a non-uniform resonant magnetic field in the EAS is accomplished.

6. Theoretical investigations and computer simulations of ion acceleration in a two-beam electron-ion accelerator were carried out. Detailed studies of ion acceleration dynamics and its radial focusing have been realized. Computer simulations of ion acceleration and focusing have been accomplished for wide set of parameters including the main EAS parameters. Coulomb interaction of accelerated ions is taking into account by "large particle" simulation method. In this approximation an ion beam (or a bunch) is presented as a set of particles ("clouds") in a form of infinitely thin rings with variable radii and longitudinal positions; the axis of each ring is aligned with the RF structure (main) axis. As a result, we have derived the motion equations for these "clouds" with taking into account all electric fields in a two-beam electron-ion accelerator: electromagnetic wave fields, RF and DC space charge fields of a driving electron beam, space charge fields of accelerating ions. In our studies we use main limitations adopted for linac simulation codes as follows: for describing of beam average properties, including second moments of distribution function and rms emittance,

about one thousand macro-particles are adequate for obtaining reproducible and accurate results with account of space-charge effects; furthermore, ion-ion and ion-neutral collisions can not taken into consideration. It ought to note that unlike analytical considerations longitudinal and transverse motions do not separate in this case, and one does no assumption about form of the ion bunches.

The feature of radial motion of the particles near the synchronous phase is as follows: the bunch collapses here both in radial and phase directions (that corresponds in this case to simultaneous radial and phase focusing), and as a result a part of the ions leave in radial direction to the drift tube. This is explained by that the concentration of the ions increases so much that the radial focusing field can not compensate the Coulomb field of bunch, and a part of the ions is "thrown off". This instability of the accelerated bunch (which can be called as the collective longitudinal-transverse one) did not consider by analytical methods. We found that the collective longitudinal-transverse instability defines the upper limit of ion current to be accelerated. For the parameters of the EAS the ion limit current of order of 3 - 4 A have been determined.

7. We have investigated the problem of field excitation in two sections of a two-beam ion accelerator under consecutive anomalous and normal Doppler effect conditions. It seems reasonable to use an energy stored in electron transverse motion in a first accelerator section excited at anomalous Doppler effect for wave excitation at normal Doppler effect in a second (next) section. We have accounted correlation between sections by solution of a self-consisted equations for consecutive excitation by an electron beam of a first section at ADE, and further excitation of a second one at NDE. For the EAS parameters in the case of two sections we obtain in the 1-st one (at ADE)  $E_z = 60$  kV/cm and in the 2-nd one (at NDE):  $E_z = 40$  kV/cm. Thus these estimations demonstrate the opportunity of using of the 2-nd section for the further acceleration of ions in two-beam ion acceleration.

8. The investigations carried out show this acceleration method to advantage and lead to the expediency of the research and development continuation. At the present the Experimental Accelerating Stand is being manufactured at the KFTI.

### Acknowledgments

It is a pleasure for authors to thank A.M.Sessler (LBL) for attention, valuable comments and support. Work performed under contract with the Lawrence Berkeley Laboratory and supported by the Director, Office of Energy Research, Division of High Energy Physics of the USA Department of Energy under Contract No. DE-AC03-76F00098.

This work is supported as well by the State Committee of Science and Technology of Ukraine (Project No. 9.02.02/059-92, "Doppler").

- [1] Ivanov, B.I., e.a. "On Application of Anomalous and Normal Doppler Effects in Some New Acceleration Methods," XV Intern. Conf. on High Energy Accelerators, Hamburg, Germany, July, 1992.
- [2] Ivanov, B.I., e.a. "Development of a Project and Theoretical Substantiation of a Two-Beam Electron-Ion Accelerator", *ALP Conference Proc.*, **335**, Advanced Accelerator Concepts, pp.429-450, NY, 1995.
- [3] Sloan, M.L., and Drummond, W.E., *Phys. Rev. Lett.*, **31**, 1234 (1973).
- [4] Indykul, V.P., e.a., *Plasma Phys.*, **2**, No.5, 775(1976) (in Russian).
- [5] Gapanovich, V.G., Ivanov, B.I., e.a., *Sov. Phys. Tech. Phys.*, **35**(1), 116 (1990).
- [6] Ivanov, B.I., and Gorozhanin, D.V., *Sov. Phys. JETP*, **71** (3), 567 (1991).



# ION BEAM NEUTRALIZATION WITH FERROELECTRICALLY GENERATED ELECTRON BEAMS

U. Herleb and H. Riege

*CERN, LHC Division, CH-1211 Geneva 23, Switzerland*

## Abstract -

A technique for ion beam space-charge neutralization with pulsed electron beams is described. The intensity of multiply-charged ions produced with a laser ion source can be enhanced or decreased separately with electron beam trains of MHz repetition rate. These are generated with ferroelectric cathodes, which are pulsed in synchronization with the laser ion source. The pulsed electron beams guide the ion beam in a similar way to the alternating gradient focusing of charged particle beams in circular accelerators such as synchrotrons. This new neutralization technology overcomes the Langmuir Child space-charge limit and may in future allow ion beam currents to be transported with intensities by orders of magnitude higher than those which can be accelerated today in a single vacuum tube.

## Introduction

Nowadays high ion beam current intensities are required for all kinds of accelerators. This is also true for heavy-ion (HI) linacs and circular accelerators such as the future LHC at CERN [1]. The intensity is limited by the particle source or the technology of the accelerator system. Space-charge effects cause the most important problems in high-intensity charged particle accelerators. In conventional accelerators the beam travels in vacuum tubes and its space-charge forces are compensated by external magnetic focusing fields in the transverse direction and by electrical accelerating fields in the longitudinal direction. When the particles enter the relativistic regime, the Lorentz transformations for the focusing and accelerating fields show an increasing compensation of the transverse space-charge forces, but not of the longitudinal electric space-charge field components. Hence, the beam intensity in classical accelerators is limited by the technically feasible magnetic focusing ( $<10$  T) and electric accelerating ( $<100$  MV/m) fields. Space-charge forces are especially destructive at very low kinetic particle energy and for HI with high charge states. Nature shows that currents in the MA range and current densities more than  $10^{10}$  A/cm<sup>2</sup> can be transported in lightning and in high pressure gas or vacuum discharges. Such extreme current density values become possible because of the mutual space-charge and current compensation in the counter-moving electron and ion streams of the discharge plasmas. Several neutralization processes and techniques can be envisaged for increasing beam intensities in accelerators beyond the classical regime. In the past, space-charge neutralization has often been applied in high-intensity ion and electron sources and accelerators [2–5]. Passive or active neutralization techniques may be applied. A passive process is the self-neutralization of an intense electron [6], or ion beam [4] passing through a plasma or low-pressure gas. Reference [4] describes an example of the passive neutralization of an ion beam propagating through several accelerating grids, from which electrons are sputtered off and accelerated in the opposite direction. In passive neutralization modes the accelerated beam is the master of the process, attracting charged particles of opposite sign from the environment (for example a plasma or a low-energy electron source [3]). Active neutralization is characterized by external control over the accelerated beam. In this neutralization mode auxiliary beams of opposite charge can ‘guide’ the accelerated beam through different sections of the accelerator system. This paper describes the active space-charge neutralization of a beam of highly-charged HI, to increase selectively the

intensity of the highest charge states compared to the case without neutralization. Pulsed electron beams are used to exert control over the accelerated HI beam.

### **Method, experimental set-up, results and conclusions**

Whereas in the classical accelerator regime space-charge fields are generally equal to or smaller than the external focusing and accelerating fields, in a fully space-charge compensated high-intensity accelerator, space-charge forces would exceed the external electric and magnetic forces if neutralization were absent. Since a direct transition from a conventional scheme to a fully neutralized accelerator system is technically difficult, we envisage the application of space-charge neutralization at first in the critical sections of a classical accelerator system. The low energy sections of a classical accelerator usually form the most critical bottlenecks: the particle source, the initial drift tubes, and the very first accelerating sections. The method considered here aims to neutralize and to enhance a particular charge state from the whole spectrum of an HI beam and to 'suppress' all the other HI charge states. The neutralization, is achieved by intense, high-repetition rate electron beam pulses [5] which move in the same or in the opposite direction with respect to the HI beam, with differing absolute velocities. Intense electron beam pulses are generated in a gun with switched ferroelectric (FE) cathodes [7,8]. Recombination losses in such mutually penetrating beams can be considered negligible [9]. Ionization processes lead to an increase of the high-charge state population of the HI spectrum. By maintaining accurate control over the current intensity, the position, the diameter, the time-sequence and the synchronization of the electron beam pulses with the HI source, part of the HI beam is transferred through the neutralization section with increased intensity. The scheme shown in Fig. 1 exerts alternating gradient forces (focusing by the electron pulses and expansion by the HI space-charge) on the chosen HI beam part. If such a process, which is characterized by partial neutralization, is applied inside an HI source, such as a laser ion source (LIS), the fundamental mechanisms of charge and beam generation and the interaction mechanisms between the HI and electron beam pulses and the source plasma must be known, in order to efficiently control the neutralization. The application of partial neutralization inside a drift tube is easier. A well-suited accelerator section for neutralization is the first acceleration gap after an HI plasma source (LIS). The bunches of highly-charged HI generated inside the source self-neutralize with slow plasma electrons before, during, and after leaving the active source region of the LIS. Inside the first acceleration gap the HI have their accompanying electron cloud partially 'stripped off' because of the accelerating field. If behind that gap the net HI beam current exceeds the Langmuir Child (LC) equivalent limit, the HI blow up. Pulsed, repetitive electron beam neutralization in a critical section can maintain a much higher ion beam current in the transport channel than allowed by the LC limit. Technically the neutralization scheme near an accelerating gap is easier to perform than inside a LIS with its tiny target spot. A detailed description of the whole set-up (Fig. 2) is given in Ref. [10]. The main components are a small LIS with an Nd:YAG laser (5 ns pulse length), an electron gun with an FE cathode (Figs. 2 and 3) generating energetic, pulsed, focused, hollow electron beams, and beam diagnostics comprising an electrostatic ion analyser (EIA), a Faraday cup (FC), and a beam current transformer (BCT). The electron gun shown in Fig. 2 sends electron pulses in the direction of the LIS. The FE cathode has a 3 mm hole in the centre, which allows the ion beam to pass through the FE cathode into the analysing section of the system. The focusing and temporal synchronization conditions for the neutralization encounters of the electron and ion beam pulses near the first accelerating gap can be studied with an off-line electron gun (Fig. 3) which is equipped with a luminescent screen placed at a distance from the FE cathode corresponding to that of the FE cathode and the first accelerating gap.

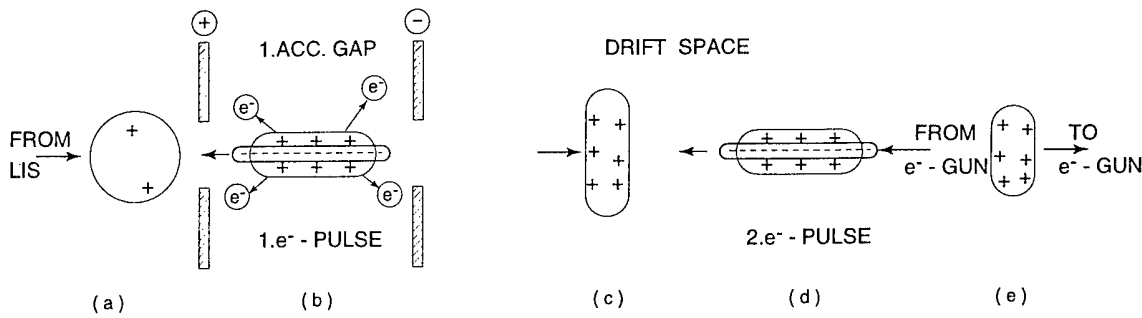


Fig. 1: Principle of ion beam space-charge neutralization with pulsed electron beams

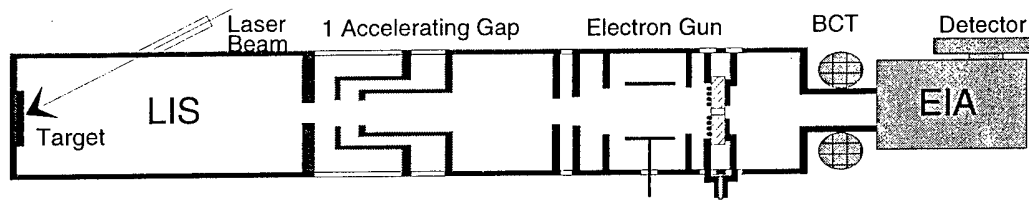


Fig. 2 Main experimental set-up

The LIS, together with the EIA, generate HI spectra in which the different charge states are well separated [10]. Furthermore the FE electron gun can produce high-rep-rate electron bunches which are accurately defined in space and time, and which can be easily synchronized with the laser pulse. Figure 4a shows the focusing of electron beams generated with an annular FE cathode emission grid in the off-line FE gun, and observed with a luminescent screen at the end of the gun. Figure 4b shows a double electron pulse with a spacing of 1  $\mu$ s, the intensity and focal length of which can be varied in a controlled way. Figure 5 shows the intensity increase by a factor of 2 of the  $Al^{2+}$  energy spectrum, neutralized with a single electron pulse and measured with a photomultiplier behind the EIA and compared to the non-neutralized case. The synchronization conditions of the LIS and the FE gun were chosen in this case to cause neutralization to happen in the drift tube between the gun and the accelerating gap. Figure 6 shows the energy spectrum of charge-state  $Al^{7+}$  obtained with the EIA with electron bunches hitting the ions near the acceleration gap and in front of the LIS side of the FE gun.

The neutralization experiments described here and in Ref. [10], in spite of not being carried out in optimal conditions, have resulted in an intensity increase by a factor of two for  $Al^{2+}$  and four for  $Al^{7+}$  ions. For the highest charge states the relative increase can reach one order of magnitude. The accuracy and precision of the electron beam generation will allow a much stronger intensity increase to be obtained. These results could have important consequences not only for accelerators in high energy physics research, but also for inertial fusion oriented accelerator systems, as they show the way out of the dilemma of classical machines: the space charge limitation in an accelerator using vacuum as the transport medium. The application of the neutralization technique is encouraged in a real accelerator source and in the low-energy part of an HI linac. The method described permits d.c., RF and inductive acceleration in the non-neutralized sections, and even inductive acceleration in the neutralized sections, as well as the use of magnetic insulation and plasma lenses for fine-focusing ion beams.

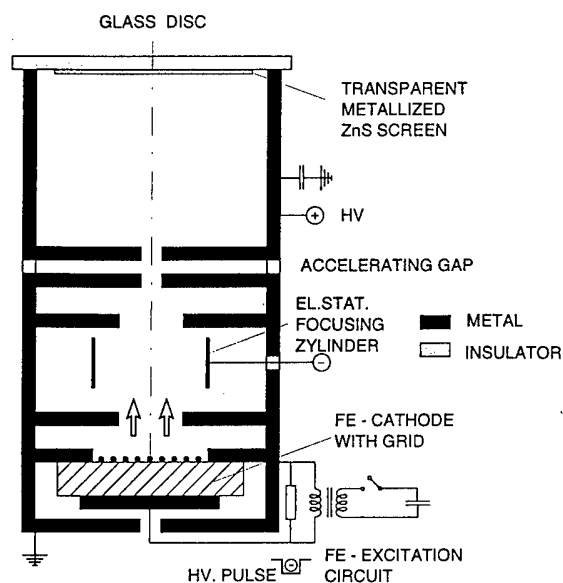


Fig. 3: Electron gun with ferroelectric cathode

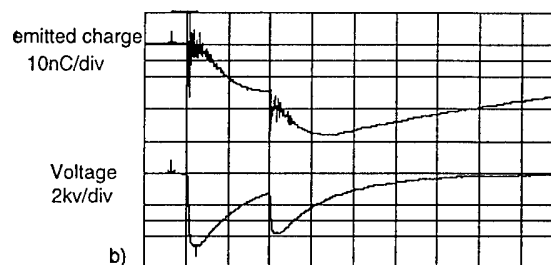
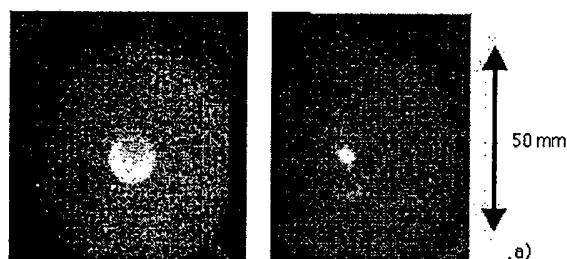


Fig. 4: a) Images from a luminescent screen of the focused and non-focused electron beam pulses. b) High rep-rate electron pulse current waveforms measured in the off-line electron gun

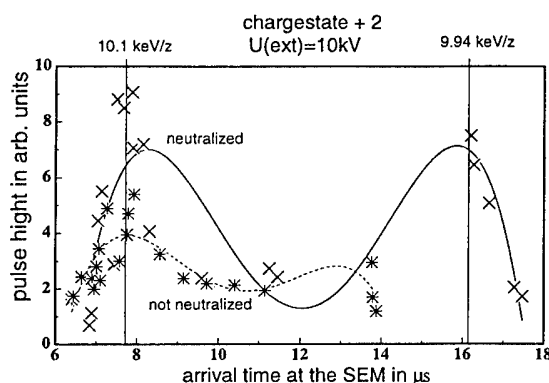


Fig. 5: Low-charge state ion beam enhancement by a factor of 2 with neutralization in the drift tube

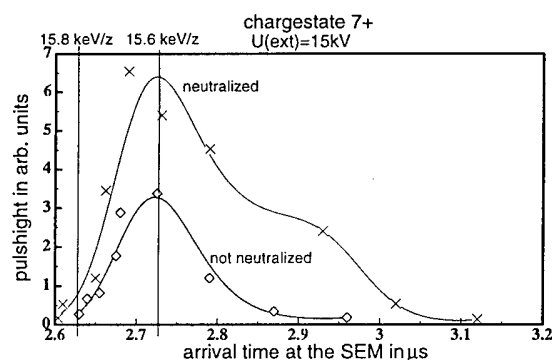


Fig. 6: Energy spectrum of  $\text{Al}^{7+}$  ions with and without space-charge neutralization near the accelerating gap

- [1] H. Haseroth and C. Hill, internal report CERN PS/BI 95-51 (1995).
- [2] S. Humphries, Jr., J. Appl. Phys. 49 (1978) 501.
- [3] S.A. Kondrashev, B. Yu. Sharkov, J. Collier and T.R. Sherwood, internal report ITEP 73-94.
- [4] H. Gundel and H. Riege, Appl. Phys. Lett. 56 (1990) 1532.
- [5] D. Boimond, et. al., Proc. XVth Int. Conf. on High Energy Accelerators, ed. J. Rossbach, Hamburg (1992) p. 185.
- [6] D. Bloess, et. al., Nucl. Instrum. Methods 205 (1983) 173.
- [7] H. Gundel, H. Riege, E.J.N. Wilson, J. Handerek and K. Zioutas, Ferroelectrics 100 (1989) 1.
- [8] H. Riege, Nucl. Instrum. Methods A 340 (1994) 80.
- [9] F. Dothan and H. Riege, internal report CERN PS/BI 92-01 (1992).
- [10] U. Herleb and H. Riege. post-deadline poster P4-96 presented at this Conference.

## TARGET EXPERIMENTS WITH HIGH-POWER PROTON BEAMS

K. Baumung, H. Bluhm, P. Hoppé, G.I. Kanel\*, S.V. Razorenov\*, D. Rusch,  
J. Singer, O. Stoltz, and A.V. Utkin\*

*Forschungszentrum Karlsruhe, P.O. Box 3640, 76021 Karlsruhe, Germany*

*\*Russian Academy of Sciences, Institute of Chemical Physics,  
Chernogolovka 142432, Russia*

### Abstract

At the Karlsruhe Light Ion Facility KALIF a pulsed high-power proton beam ( 50 ns,  $0.15 \text{ TW/cm}^2$ , 8 mm fwhm focus diameter, 1.7 MeV peak proton energy) is used to generate short, intense pressure pulses or to ablatively accelerate 10-100- $\mu\text{m}$ -thick targets to velocities  $>10 \text{ km/s}$ . The velocity history of the rear target surface is recorded by line-imaging laser Doppler velocimetry with high spatial ( $\geq 10 \text{ }\mu\text{m}$ ) and temporal ( $\geq 200 \text{ ps}$ ) resolution, and provides information on proton beam parameters, and on the state of the matter at high energy densities and intense loading. Utilizing the bell-shaped power density profile we have demonstrated a new straight-forward method for measuring the shock pressure that leads to material melting in the rarefaction wave. For the first time, the dynamic tensile strength was measured across a crystal grain boundary, and using targets with a 1D periodic structure, the growth rate of a Rayleigh Taylor instability could be measured for the first time in direct drive experiments with an ion beam.

### Introduction

The Karlsruhe Light Ion Facility KALIF is a 1.7 MV, 600 kA, 50 ns FWHM pulse power accelerator delivering 50kJ of electrical energy to a  $2.25 \text{ }\Omega$  load [1]. The experiments reported here were performed using the self-magnetically insulating  $\text{B}_\theta$ -diode [2] in which the protons are extracted from a plasma layer on the anode surface that is formed by a radial flash-over discharge across an annular polymethyl-methacrylate (PMMA) inlay at the beginning of the power pulse. Current and space-charge neutralization is provided by electrons picked up by the beam when passing between the radial cathode vanes. This process takes place in vacuum which facilitates experimenting with this diode. In addition,  $\sim 10$  successive shots can be performed without replacing hardware. The peak power density in the 8-mm-diameter fwhm focal spot is  $0.15 \pm 0.5 \text{ TW/cm}^2$ . With proton ranges in condensed matter of 10 to 20  $\mu\text{m}$  energy densities in the range of 1 MJ/g at specific power densities of 10 to 20  $\text{TW/g}$  can be achieved with this diode.

The interaction of the proton beam with a solid target is characterized by the high bulk energy deposition in the beginning that is due to a time-of-flight compression or "bunching" of the beam front on the 15-cm- trajectory between the anode and the target. As a result, the first protons hitting the target have intermediate energies of 0.3-1 MeV and consequently a range up to  $>10 \text{ }\mu\text{m}$ . The massive energy deposition leads to a rapid temperature increase that the thermal expansion cannot follow. High pressure builds up – 25-30 GPa in aluminum – that causes the hot, partially ionized material of the energy deposition zone to expand rapidly or "ablate", and a compression wave to progress into the adjacent cold material. On its arrival at the rear free surface, the compressed matter expands and thereby accelerates the surface to a velocity of  $\sim 3 \text{ km/s}$  (with aluminum). The material expansion propagates as a release wave back into the target. On contact with the energy deposition zone the expanded matter is again pressurized, and another compression wave propagates to the rear surface. Reverberations of compression and rarefaction waves "ringing" between the rear free surface and the energy deposition zone "ablatively" accelerate the residual condensed part of the target to velocities  $>10 \text{ km/s}$ .

### Experimental setup

The velocity history of the target surface opposite to the ablation plasma is recorded by the improved line-imaging laser-Doppler velocimeter [3] depicted in fig. 1. This instrument illuminates a vertical measuring line on the target up to  $\sim 10$  mm high and  $300\text{ }\mu\text{m}$  wide by expanding the beam in the vertical direction through a cylindrical lens and focusing it by lens  $L_1$ . This line is imaged onto the mirror planes of an oblique wide-angle Michelson interferometer by lenses  $L_1$  and  $L_2$ . Because the interference fringes are localized in these planes the second imaging by lenses  $L_3$  and  $L_4$  provides a sharp image of the target together with fringes of high contrast and allows to vary the scale in a wide range. The original laser beam has a Gaussian power profile and expanding this profile in one dimension still gives a kind of a bell-shaped intensity distribution. Because the intensity losses of the whole optical system due to vignetting always leads to a decrease at the edges of the field of view, we use a  $1.5\times$  beam expander (not shown in the figure) to slightly detune the laser profile to an annular ("dough nut") shape. This levels the intensity on the illuminated line. For high spatial resolution of  $<10\text{ }\mu\text{m}$  lens  $L_1$  alone is used together with the modified illumination system shown in fig. 1. A 1D beam expander is used to increase the  $f$ -number of the 3-mm-diameter hollow laser beam in the horizontal direction. This results in a diffraction-limited illuminated area on the target that is  $\sim 30\text{ }\mu\text{m}$  wide by  $300\text{ }\mu\text{m}$  high and permits to better utilize the laser power because the slit at the streak camera input cuts off intensity outside a narrow measuring line anyway.

In our paper we present three new experiments that make use of the particular properties of the KALIF beam, and of the capabilities of the line imaging velocimeter, respectively.

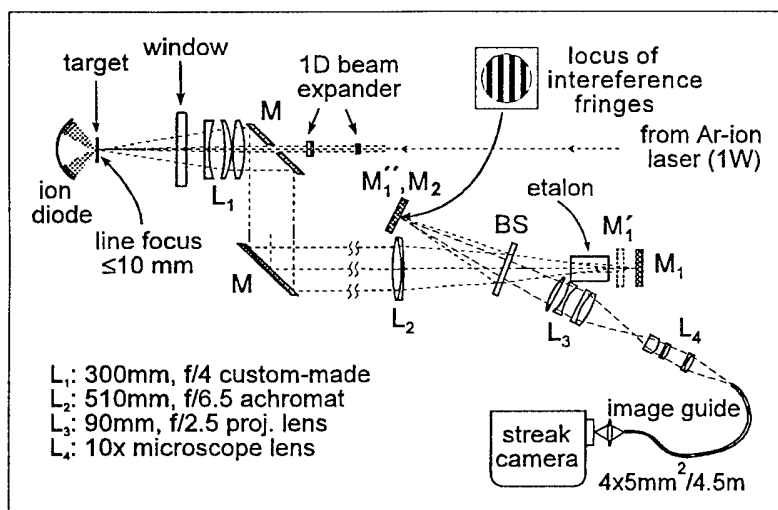


Fig. 1.

The line-imaging laser-Doppler velocimeter with  $<10\text{ }\mu\text{m}$  spatial resolution. Intermediate imaging onto the mirror planes provides optimum contrast of the interference fringes and allows to vary the scale in a wide range

### Dynamic tensile strength measurements

We have used the nanosecond-scale pressure pulses that can be generated with KALIF by either the direct beam interaction or by impacting thin ablatively accelerated flier plates to measure the dynamic tensile strength or "spall strength" of single crystal and polycrystalline samples at strain rates up to  $>10^7\text{ s}^{-1}$  [4,5]. A short shock wave is reflected from a free surface as a stress wave. The superposition of the outward moving decaying tail of the shock wave and the inward moving rarefaction wave results in a stress wave whose amplitude increases with the distance from the surface until the material fails. The relaxation of the stressed material results in a pressure wave whose arrival on the free surface indicates that spalling occurred. With the Hugoniot equation of state (EOS) of the material known, both the spall strength and the strain rate are determined from the same velocity history of the rear target surface. So far, these velocity measurements were performed in the focal spot of the illuminating laser of a few

100  $\mu\text{m}$  diameter, and spatial dependence was not considered. Taking advantage of our experimental capabilities we have investigated for the first time, in analogy to the spatial variation of the micro hardness, the variation of the spall strength of copper samples that were annealed in a  $\text{H}_2$ -atmosphere at  $600^\circ\text{C}$  to increase the grain size to a few  $100\mu\text{m}$ . A result is depicted in fig.2 showing a 10% spatial variation. In order to investigate the spall behavior at a single distinct grain boundary we used magnesium samples grown with grain sizes of a couple of millimeters. The samples were cut to 0.5-1-mm-thick slices, polished, and slightly etched to render the grains visible. From our experiments follows that, at least at high strain rates, the grain boundary is also a boundary for the dynamic rupture process. The individual crystal grains fail independently and show different tensile strengths that depend on the orientation relative to the plane stress wave. This result is interesting because the strength of single crystals normally exceeds that of polycrystalline material because grain boundaries act a failure initiation sites.

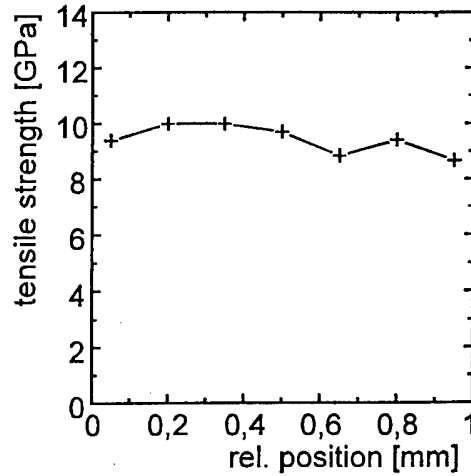


Figure 2:  
Spatial variation of the dynamic tensile strength of a copper sample with a grain size of  $200\text{-}500\mu\text{m}$ .

### First Proton-beam driven Rayleigh-Taylor experiments

The driving motivation for the research and development work on pulsed high-power light ion beams is the potential application in inertial confinement fusion (ICF). The maximum specific power deposition of  $100\text{-}200\text{ TW/g}$  achieved on KALIF so far is not high enough for ICF-relevant radiation physics experiments. However, with ablative accelerations of target foils  $>10^{11}\text{ m/s}^2$  and the performance of our high-resolution line imaging velocimeter we have the possibility to investigate experimentally, for the first time, the ICF-relevant issue [7] of the evolution of Rayleigh-Taylor (RT) instabilities with high-power light-ion beam driven targets. This hydrodynamic instability develops when a layer of dense material ( $\rho_h$ ) is accelerated by a medium of low density ( $\rho_l$ ). For small-scale sinusoidal perturbations on the interface with amplitudes  $\eta_0$  and spatial periods  $\lambda$  ( $\eta_0 \ll \lambda$ ) the classical theory [8] predicts an exponential growth in time

$$\eta(t) = \eta_0 e^{\gamma t}, \quad \text{where } \gamma = \sqrt{Akg} \text{ is the growth rate} \quad (1)$$

$A_k = (\rho_h - \rho_l) / (\rho_h + \rho_l)$  is the Atwood number,  $k = 2\pi/\lambda$  is the perturbation mode wave number, and  $g$  is the acceleration that is assumed constant in this approach.

In ICF, the drive - laser light, x rays, or light ions - heats the outer layer of the fuel capsule wall causing material ablation, the low-density ablation plasma accelerating the high-density capsule wall. Because a uniform implosion is crucial to obtaining fusion conditions, the R-T instability is a serious complication as it couples imperfections of the outer shell to the inner surface and disrupts the symmetry. It occurs twice as the shell implodes: during the initial acceleration phase, and during the final deceleration when the pusher compresses the low-density fuel. However, in 1974 already, Bodner found [7] that for ablatively accelerated layers "fire polishing" that favors the ablation of peaks relative to the valleys, and convective effects in the ablation zone - heat and mass flows across the boundary between the two media - should

stabilize the growth and, for large- $k$  modes (small periods  $\lambda$ ), even suppress the RT instability. This was confirmed in numerous theoretical investigations reviewed in [9] and in laser-driven experiments on Nova at Lawrence Livermore National Laboratory where, depending on  $k$  reductions of the growth rate  $\gamma$  to 20-60% of the classical values were found with planar targets [10]. Different analytical approximations fitted to numerical results were established trying to make an estimation of the Atwood number  $A$  for the case of an ablation layer [9,11] introducing the density gradient scale length  $L = \rho/(d\rho/dx)$  and the ablation velocity  $v_a = \dot{M}/\rho_0$  defined as the mass flow velocity per unit area normalized to the initial density of the ablator. Following ref. [9] the reduced growth rate for ablative acceleration becomes

$$\gamma = \sqrt{\frac{kg}{1 + kL}} - 3kv_a \quad (2).$$

Except for  $L$ , we can determine all other quantities in equ. (2) experimentally. The basic idea is to use the line-imaging velocimeter to measure the velocity distribution on the rear side of a structured target along a measuring line perpendicular to the structure. In a first test, we used a 70- $\mu\text{m}$ -thick target into which grooves of trapezoidal cross section 40  $\mu\text{m}$  deep and 5  $\mu\text{m}$  wide in the valley, and a 30- $\mu\text{m}$ -spacing were cut with a readily available diamond tool. Because of the small acceleration achieved with this relatively thick target and, above all, because of the high wave number  $k$  no instability growth could be observed, but at least a spatial resolution of the velocimeter of <10  $\mu\text{m}$  could be demonstrated. As was mentioned above, the ablative acceleration is due to compression and release waves ringing between the energy deposition zone and the rear free surface. With targets much thicker than the maximum proton range (20-30  $\mu\text{m}$  in aluminum, depending on the peak voltage of the respective KALIF pulse) this leads to a step-like velocity increase and a strongly oscillating acceleration (see fig. 3) the duration of the periods with zero or even negative acceleration increasing with the target thickness. Accordingly, reducing the target thickness smoothens these steps and can result in a nearly constant acceleration. Because of the high blow-off velocity in the ablation zone the energy deposition zone hydrodynamically uncouples from the residual part of the target ("disappears behind the sonic horizon") after the peak proton range is reached. Due to range-shortening effects in the hot ablation plasma [12] that happens even before peak voltage is reached. As a result, the acceleration is highest during the initial 15-20 ns of the voltage rise. This is why, in order to obtain maximum and as constant accelerations as possible, the target thickness should not be much greater than the maximum proton range, that is 20-30  $\mu\text{m}$ .

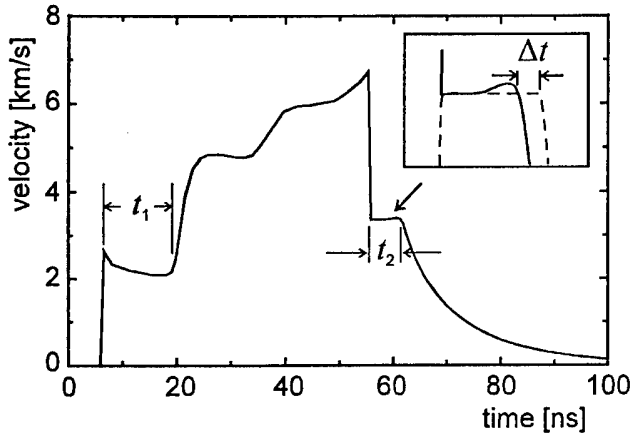


Figure 3:

Ablative acceleration of a 71- $\mu\text{m}$ -thick foil and impact on a LiF-window. Time  $t_1$  corresponds to twice the wave transit time between the rear target surface and the ablation zone at the beginning of the interaction,  $t_2$  is twice the transit time 55 ns later. With the bulk sound velocity known from the Hugoniot EOS, the respective residual thickness of the solid target can be determined. In the inset, the curvature of the measured curve (solid) compared to the calculated one (dashed) indicates a density gradient at the ablation boundary. The calculation is made for the initial thickness minus the maximum proton range.  $\Delta t$  reflects the expansion of the ablation plasma through heat conduction.



Because it is difficult to machine aluminum foils of that thickness we decided to structure the foils by embossing them on a brass die. This is a  $3 \times 3 \times 1$  cm<sup>3</sup> square provided with four slightly protruding 2-mm-wide sections into which periodic grooves with triangular cross section were machined using a diamond tool with a 155° blade. Four different mode wavelengths have been realized (50, 70, 100, and 150 μm) with an aspect ratio  $2\eta_0/\lambda = 0.11$  to satisfy the condition of a "small" perturbation. The target is prepared by cutting a 10-mm-wide strip from an aluminum foil that was previously polished and annealed at 500°C in a Ar-atmosphere to remove the hardness originating from the rolling process. This strip is placed on the die perpendicular to the orientation of the structured zones and covered by a cylindrical PVC-rod of 10 mm diameter placed in the same direction. This assembly is then compressed by parallel jaws. Because the PVC deforms under pressure, the soft aluminum foil is pressed close to the die without a significant change in the thickness and retains a periodic structure with an aspect ratio of 1-3 % depending on  $\lambda$ . While the parts in the valleys show a sine-like shape the part in contact with the tops of the die contains higher order modes. In the experiment this side is facing the ion to reduce a possible influence.

Compared with previous experiments, a recent modification of the B<sub>0</sub>-diode has led to an improved stability of the impedance, and thus to a higher peak voltage and proton range [13]. To avoid early burn-through of the 22-27-μm-thick targets prepared for the RT experiments we decided to put absorption filters of 6-10 μm thickness at a 2-mm-distance in front of the targets. This arrangement attenuates the power density on target but this essentially reduces the amplitude of the first jump of the surface velocity caused by bunching (see fig. 3). This is not a restraint because the acceleration, and not the absolute velocity is essential for the RT experiments. Unfortunately, the reproducibility of the KALIF voltage pulse, and even more of the ion diode performance is rather poor. Together with usual experimental problems this is, why in two out of a series of 18 shots only the experimental conditions were such as to give a clear effect. Figure 4 displays the velocimeter record of an experiment using a target with a 50 μm perturbation wavelength. Shown is the space coordinate on target perpendicular to the embossed structure versus time. The velocity information is contained in the intensity modulation. The horizontal structure in the steady state before the acceleration (up to 6 ns) is due to the different laser light reflection at the flanks, the peaks, and the valleys. The vertical interference fringes after 6 ns are lines of equal velocity. The initial jump of 3 fringes is not

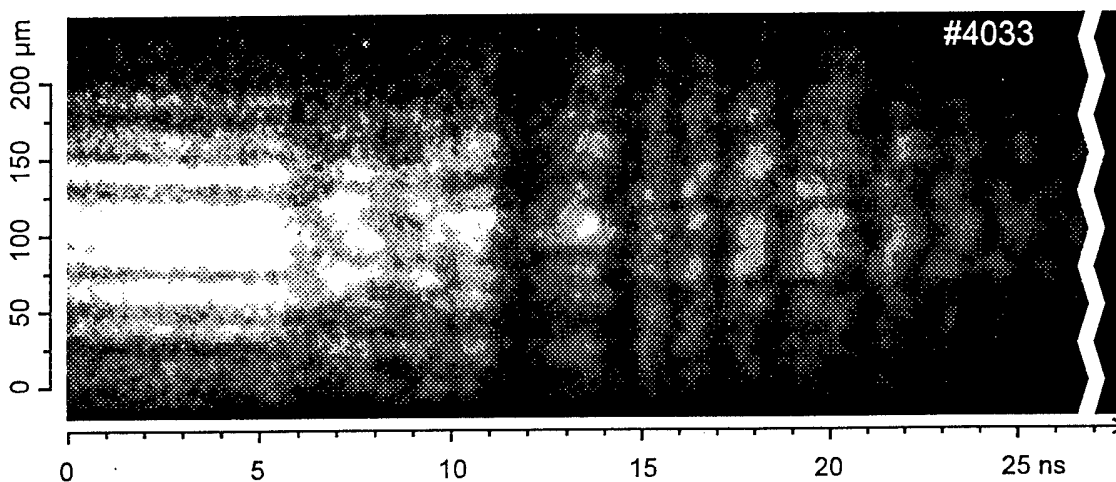


Figure 4:  
Velocimeter interferogram showing the position on target versus time in an RT experiment with a 50 μm wavelength (the target is indicated on the left side). The velocity information is contained in the intensity modulation. The velocity increment between two vertical fringes is  $v_0 = 521$  m/s.

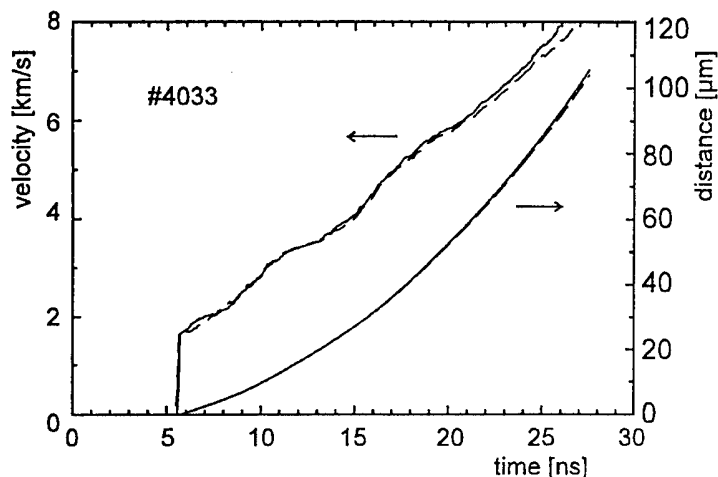


Figure 5:

Velocity histories evaluated from the raw data shown in fig. 4 and integrated flight distances for the peaks (solid) and valleys (dashed) positions of a 50  $\mu\text{m}$  wavelength target. The acceleration is  $g \approx 3 \times 10^{11} \text{ m/s}^2$ . After 22 ns, the peaks advance the valleys by 1.5  $\mu\text{m}$ .

resolved. The fringe constant of the velocimeter, that is the velocity increment between two successive fringes, was  $v_0 = 521 \text{ m/s}$  in this experiment. The target is indicated on the right side. In the first phase, the velocity does not depend on the position but after  $\sim 15 \text{ ns}$  a clear structure appears indicating that the velocity is by  $0.3 v_0$  greater in the positions of the peaks (seen from the rear side) than for the valleys. From figure 5, in which the velocity histories for the peak and valley positions, and the integrated distances covered are displayed follows a fairly constant acceleration of  $g = 3 \times 10^{11} \text{ m/s}^2$ , and a 1.5- $\mu\text{m}$ -advance of the peaks compared with the valleys after 22 ns of acceleration. With an initial peak-to-valley distance of  $\sim 1 \mu\text{m}$  this gives an increase by a factor of 2.5, and a growth rate  $\gamma = 0.029 \text{ ns}^{-1}$ , that is 15 % of the classical value  $\gamma_{cl} = \sqrt{kg} = 0.19 \text{ ns}^{-1}$ . The second experiment with  $\lambda = 70 \mu\text{m}$  and  $g = 10^{11} \text{ m/s}^2$  gives 15% of the classical growth rate, too, compared with 20-60% found in laser-driven experiments [10].

The largest experimental uncertainty - maybe a factor of two - in these first results arises from the initial perturbation amplitude  $\eta_0$  that we took from profilometer measurements of identical specimens assuming that the embossing is reproducible. Nevertheless, it seemed interesting to compare them with the analytical formula (2). For that purpose, we assess the ablation velocity  $v_a$  from measurements of the wave reverberation periods of numerous experiments from which the thickness of the ablated material layer displayed in fig. 6 is

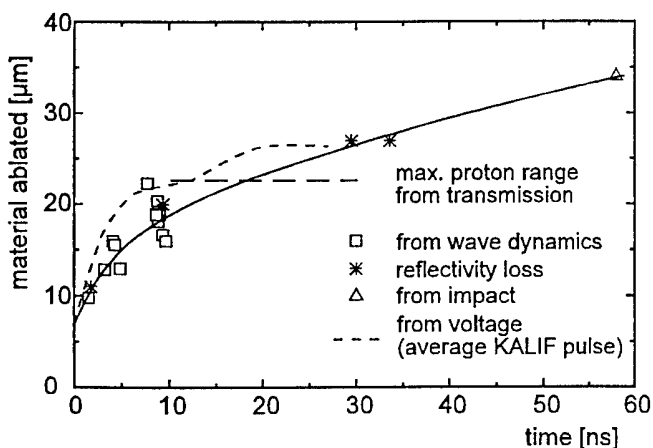
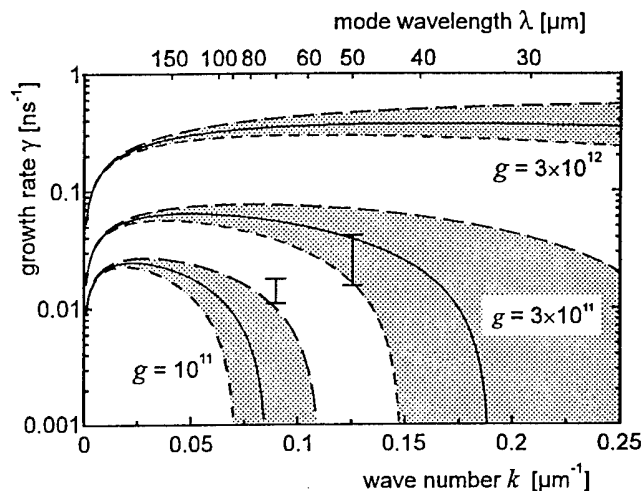


Figure 6:

The average position of the ablation front (solid line) was determined by different methods for different instants in a number of experiments (cf. fig. 3). Due to range shortening effects in the hot ablation plasma the maximum proton range (long dash) determined by transmission experiments is smaller than the range corresponding to the KALIF peak voltage in cold matter (short dash). According to numerical simulations the further propagation of the ablation front is due to radiative heat transfer. The ablation velocity that can be deduced from this figure amounts to  $>2000 \text{ m/s}$  in the beginning (bunching of the beam front) and drops to 250 m/s after peak voltage.

Figure 7:

Comparison of RT growth rates calculated for three different accelerations using equ. (2) and the experimental data for  $g=10^{11}$  m/s<sup>2</sup> and  $3 \times 10^{11}$  m/s<sup>2</sup>. The ablation velocity was taken from fig 6. as  $v_a=300$  m/s for the period up to 30 ns. The shaded zones cover the range of  $L=1$   $\mu$ m (top) and  $L=10$   $\mu$ m (bottom) of the density gradient scale length (solid lines for  $L=5$   $\mu$ m). At higher accelerations –  $3 \times 10^{12}$  m/s<sup>2</sup> is in the scope of our 1 TW/cm<sup>2</sup> B-applied diode - and greater wavelengths the growth rate is significantly greater and less dependent on the ablation front parameters.



deduced. As can be seen in fig. 3, the reverberation period, that of course depends on the target thickness too, decreases with time indicating that the ablation front propagates into the cold material. From the inset in fig. 3 follows that the ablation front propagates beyond the maximum proton range, and that the onset of the velocity drop is smooth if compared with the calculation for an impactor of constant density. Recalculations of the velocity history indicate that radiative heat transport in the ablation front is crucial to properly simulate the smooth decrease of the velocity that in fact is due to a density gradient [14].

For the density gradient scale length the simulations yield a couple of micrometers during the first nanoseconds and  $L=10$   $\mu$ m after 30 ns. Because the acceleration  $g=3 \times 10^{11}$  m/s<sup>2</sup> is relatively small, the corrections in equ. (2), with  $k=0.125$   $\mu$ m<sup>-1</sup> for shot 4033 and  $v_a=300$  m/s for the time period up to 30 ns, become very large. As a consequence, uncertainties in the correction make it difficult to compare the results with equ. (2). This is shown in fig. 7 which displays the growth rate as a function of the wave number. The shaded zones were calculated for three different accelerations using the density gradient scale lengths  $L=1$   $\mu$ m (bottom),  $L=10$   $\mu$ m (top), and  $L=5$   $\mu$ m (solid line) which are in the range of the simulations results for the period up to 30 ns. From fig. 7 follows that with the accelerations realized smaller wave numbers would have been more appropriate for obtaining a larger measuring effect and less dependence on the ablation front parameters. From fig. 7 also follows that at higher accelerations –  $g=3 \times 10^{12}$  m/s<sup>2</sup> is in the scope of our 1 TW/cm<sup>2</sup> B-applied diode – the growth rate is much greater and less dependent on the ablation parameters provided they are in the same range.

### Shock melt pressure measurements on aluminum

Because the shock adiabat, or Hugoniot, of solids crosses the melting region at high pressures, strong shock waves can cause a transition to the molten state. However, this transition can also occur during shock release from a solid state if the release isentropes traverses the melting region [14]. The threshold shock wave pressure that leads to a melting state during shock release at a free surface is of interest not only as a test for wide-range multiphase equations of state models but also for applications like space craft shield design.

We are presenting a straightforward method to measure the threshold pressure utilizing the particular experimental capabilities on KALIF. According to the power density profile that is similar to a somewhat flat-topped Gaussian of  $\sim 8$ -mm-diameter FWHM, the radial velocity distribution of an ablatively accelerated flier foil is bell-shaped with a flattened center [3]. Because the ablation pressure  $p$  scales with the power density  $I$  approximately as  $p \sim I^{0.7}$  the power density profile results in a smoothed velocity profile showing a 25 to 30%-decrease of

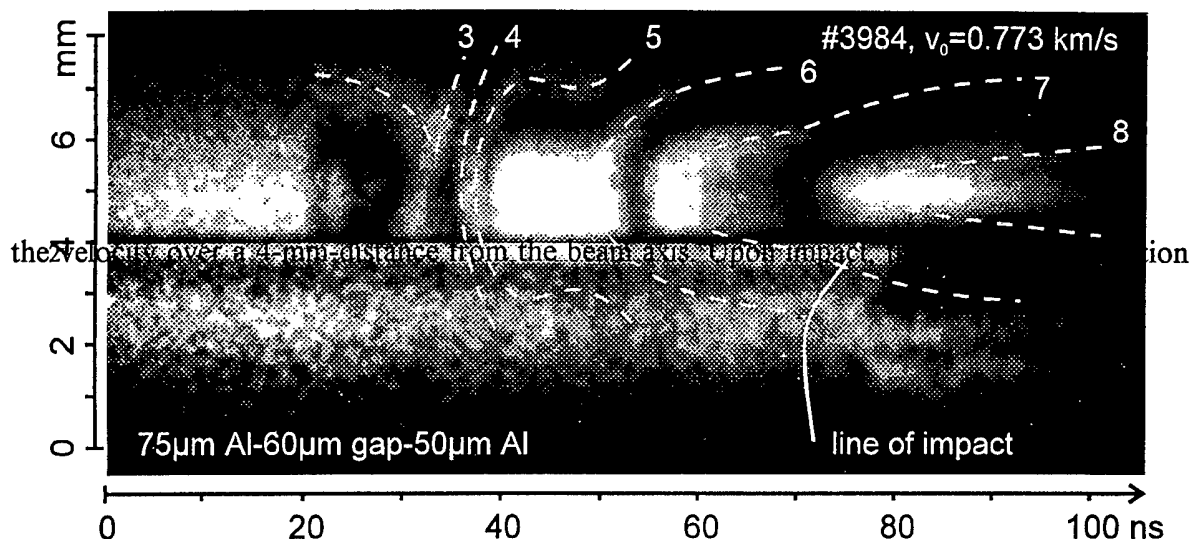


Figure 8:

Velocimeter interferogram showing the position on target versus time in an impact experiment. The velocity information is contained in the intensity modulation, the dashed lines visualize the lines of equal velocity, the first jump of 3 fringes being not resolved. The velocity increment between two fringes is  $v_0 = 773$  m/s. The field of view is split on the 75- $\mu$ m-thick aluminum flier plate (above 4 mm) and the 50- $\mu$ m-thick aluminum target (below 4 mm). The acceleration starts at 19 ns, the impact (on the opposite side of the target) occurs between 71 and 76 ns. The surface facing the velocimeter starts to move  $\sim 6$  ns later. The reflectivity loss which is supposed to be caused by material melting occurs between fringes 6 and 7, at an impact velocity of  $\sim 5.1$  km/s which corresponds to a pressure of 62 GPa.

the velocity over a 4-mm-distance from the beam axis. Upon impact, this velocity distribution causes a pressure profile that decreases by  $\sim 30\%$  over the same distance. This inspired us with the idea to utilize the nonuniformity of the flier velocity, and the line-imaging laser-Doppler velocimeter capabilities to measure the shock melt pressure. Splitting the field of view of the velocimeter on both the flier and the target allows us to measure the impact velocity profile and the response of the target simultaneously. With an appropriate velocity interval chosen, the shock melt pressure threshold is contained in the pressure interval observed. The loss of the velocimeter signal due to a drop of the intensity of the reflected laser light is considered indicative of material spraying that occurs at the free surface upon the shock-wave release from a melting state. The pressure interval can be adjusted by the total flier thickness (mass) and – or the distance of the target. Figure 8 depicts a velocimeter record of an experiment with aluminum in which the target is hit at velocities ranging from 4–5.7 km/s. The curvature of the impact line indicates that the impact was not planar. Probably, the target was deformed by cutting close to the edge located at 4 mm. The onset of intensity loss is located between fringe 6 and 7, at a velocity of 5.1 km/s which corresponds to a pressure of 62 GPa. This compares well with results of the wide-range multiphase EOS model of ref. [14] that predicts melting onset at 61 GPa and a 100% melt fraction at 79 GPa.

We are planning to improve the experimental conditions by a more precise assembly of the flier-target arrangement using micromachining techniques, and an increased field of view of the velocimeter to diminish uncertainties of the impact velocity distribution. The application of thin absorbing foils in front of the flier to control the power density should allow us to realize appropriate velocities using thinner fliers that accelerate in a more steady way in order to reduce uncertainties caused by the ringing of the flier. A numerical analysis of the experiments investigating the influence of the state of the flier is on the way. We are preparing experiments on magnesium, titanium and stainless steel but, given the peak flier velocities of  $>12$  km/s reached on KALIF so far, even high-melting materials like tungsten can be investigated.

## Conclusions

We have presented new results in the investigation of high energy density states of matter using the KALIF high-power proton beam, and a spatially resolving laser-Doppler velocimeter.

For the first time we measured the spatial variation of the dynamic tensile strength and we have shown that for shock wave lengths in the range of the grain size the grain boundary also represents a boundary for the material rupture: particular crystal grains fail independently.

We have presented first results on proton-beam driven Rayleigh-Taylor instability growth rate measurements. At accelerations realized with our  $0.15 \text{ TW/cm}^2$  B<sub>o</sub>-diode of a few times  $10^{11} \text{ m/s}^2$  the growth rate strongly depends on the ablation front parameters. We are planing to perform further experiments using the  $1 \text{ TW/cm}^2$  B-applied diode that should provide accelerations  $>10^{12} \text{ m/s}^2$  at which the measuring effect is expected to be approximately one order of magnitude greater as much less dependent on the ablation front properties.

Finally, we propose a new straight-forward method to determine the threshold shock pressure that leads to a melting state in the shock release wave taking advantage of the experimental capabilities of the KALIF beam and the line-imaging velocimeter. With peak impact velocities  $>12 \text{ km/s}$  realized so far measurements even on high-melting materials are possible.

## Acknowledgment

Part of this work was supported by the Russian-German Cooperation Program, by the NATO Science Programme, and INTAS grants. The authors appreciate the continuous interest and support of their joint work by G. Kessler, director of the Institut für Neutronenphysik und Reaktortechnik, FZK Karlsruhe, and by Academician V.E. Fortov, director of the High Energy Density Research Center, Moscow. They also acknowledge the technical assistance by R. Huber and the KALIF operators.

- [1] H. Bluhm, K. Böhnelt, L. Buth, P. Hoppé, H.U. Karow, A. Klumpp, D. Rusch, T. Scherer, U. Schülken, and J. Singer: *Digest of Technical Papers*, 5th IEEE Pulsed Power Conference, Arlington, VA, June 10-12, 1985 (IEEE, New York, 1985), pp. 114-117.
- [2] W. Schimassek, W. Bauer, and O. Stoltz: *Rev. Sci. Instrum.* **62**, 168 (1991).
- [3] K. Baumung, H. J. Bluhm, P. Hoppé, H. U. Karow, D. Rusch, O. Stoltz, J. Singer G.I. Kanel, A.V. Utkin, and S. V. Razorenov: *Proc. 10<sup>th</sup> Int. Conf. on High-Power Particle Beams*, edited by W. Rix and R. White (NTIS, Springfield, VA, 1995), pp. 211-214.
- [4] S.V. Razorenov, A.V. Utkin, G.I. Kanel, V.E. Fortov, A.S. Yarunichev, K. Baumung, and H.U. Karow, *High Pressure Research* **13**, pp. 367-376 (1995).
- [5] K. Baumung, H. Bluhm, B. Goel, P. Hoppé, H.U. Karow, D. Rusch, V.E. Fortov, G.I. Kanel, S.V. Razorenov, A.V. Utkin, and O.Yu. Vorobjev, to be pub. in *Laser Part. Beams* **14**(2), 1996.
- [6] Z. Henis and Sh. Eliezer: *Phys. Rev. E* **48**, 2094 (1993).
- [7] S. E. Bodner: *Phys. Rev. Lett.* **33**, 761 (1974).
- [8] G. Taylor: *Proc. R. Soc. Lond.* **A201**, 192 (1950).
- [9] J.D. Kilkenny, S.G. Glendinning, S.W. Haan, B.A. Hammel, J.D. Lindl, D. Munro, B.A. Remington, S.V. Weber, J.P. Knauer, and C.P. Verdon: *Phys. Plasmas* **1**, 1379 (1994).
- [10] B.A. Remington, S.V. Weber, M.M. Marinak, S.W. Haan, J.D. Kilkenny, R.J. Wallace and G. Dimonte: *Phys. Plasmas* **2**, 241 (1995).
- [11] H. Takabe, L. Montierth, and R.L. Morse: *Phys. Fluids* **26**, 2299 (1983).
- [12] B. Goel and H. Bluhm, *Journ. de Physique - Coll. C7* **49**, C7-169 (1988).
- [13] W. Bauer, P. Hoppé, H. Bachmann, H. Bluhm, L. Buth, H. Massier, D. Rusch, O. Stoltz, W. Vöth, and Th. Westermann: this conference.
- [14] H. Marten, B. Goel, and W. Höbel, this conference.
- [15] Z. Henis and Sh. Eliezer: *Phys. Rev. E* **48**, 2094 (1993).

# FIELD-REVERSED ION RING CONFIGURATIONS FOR FUSION<sup>1</sup>.

R.N. Sudan, J.B. Greenly, D.A. Hammer,  
Yu.A. Omelchenko, and W.J. Podulka

*Laboratory of Plasma Studies, Cornell University, Ithaca, NY 14853 USA*

## Abstract

A new project to experimentally demonstrate the formation of a field reversed ion ring, FIREX, with  $\sim 1$  MeV protons was launched at Cornell in August 1993. We describe the physical processes and technological constraints that have determined its design and construction which was completed early this year. The nominal parameters of the power supply for generating the proton beam needed for producing the ion ring is 1 MV, 800 kA, 130 ns. The experimental program began in February 1996 and results at 70% full power are presented. Projections to what could be expected at full power are also outlined.

## I. Introduction

The prime candidate for a fusion reactor is based on the Tokamak. However it has become evident from the design phase of the International Tokamak Experimental Reactor (ITER) that it is a very large and costly device that will take a long time to build. There is at present controversy about whether it will even ignite based on our present understanding of plasma heat transport. Thus there is a great premium in favor of compact magnetic configurations for fusion reactors. The field reversed configuration (FRC) [1] is unique in that it is compact, no mechanical structure in the center of the torus is needed, no appreciable toroidal field exists, the engineering beta is near unity, the magnetic system is a straight solenoid and the scrape-off layer exhausts outside the magnetic coils. However magnetohydrodynamic stability of an FRC is not assured in the limit when the plasma radius is many times the ion gyro-radius but the situation improves when both quantities are comparable [2].

The concept of a large-orbit, field reversed ion ring, which is a natural development of the E-layer of Christofilos, was first proposed in 1974 [3]. The influence of the large orbit ions on the low frequency stability of the configuration is very positive [4]. The FRC and Ion Ring Configuration (IRC) have the same magnetic topology but the azimuthal current in the former is carried by the diamagnetic current of small orbit particles while in the latter the orbits of the energetic ions are comparable to the plasma radius. A hybrid configuration in which a significant fraction of the azimuthal current is carried by energetic large orbit ions has also been suggested [5]. A study [6] of an ion ring fusion reactor indicates that it will be a low  $Q$  driven system.

The transport of energetic ions to a  $D - T$  pellet for ICF may also be affected through the transport of ion rings magnetically compressed to high energy [7]. High current accelerators employing ion rings have also been suggested [8].

While field-reversed electron rings have been successfully created since 1971 [9], trapped field-reversed ion rings have yet to be demonstrated. A transient ( $\sim 30$  ns) field reversal was created at NRL by injecting a pulse of ions through a magnetic cusp [10] but the beam was not trapped. Trapped ion rings with a field reversal factor of  $\sim 5\%$  have been routinely produced at Cornell [11,12,13]. The field reversal was limited by the pulsed power supply for the ion source.

<sup>1</sup>Work supported by US DOE Grant No. DE-FG02-93ER54221

The main difficulty is the quantity of charge in ions needed in a single pulse from a source. It can be easily established that the number of non-relativistic protons  $N$  in an ion ring is given by

$$N = R\zeta/r_i \quad (1)$$

where  $R$  is the ring mean radius (cm),  $\zeta = \delta B/B \lesssim 2$  for field reversal,  $\delta B$  is the magnetic field produced by the ring current on axis,  $B$  is the external field, and  $r_i = e^2/m_i c^2$  is the classical ion radius. Thus the proton charge is  $m_i/m_e$  times the electron charge required for field reversed electron rings. For  $R \sim 15$  cm,  $N \sim 2 \cdot 10^{17}$  and  $q = Ne \sim 32$  mC. Since the creation of an ion ring requires a drastic change in the magnetic topology of a solenoid field immersed in a plasma it must be done on as rapid a time scale as possible. In an external field of  $\sim 10$  kG, the proton cyclotron period is  $\sim 66$  ns. If we choose the injection time scale  $\tau \sim 10^2$  ns to be of the same order then the pulse of proton current needed is  $I \sim Ne/\tau \sim 3 \cdot 2 \times 10^5$  A. Given an injection and trapping efficiency of say 60% the required proton current from the source, is  $\sim 600$  kA. The proton energy required is  $\sim 1$  Mev for  $R \sim 15$  cm and  $B \sim 10$  kG.

A new project FIREX (field reversed ion ring experiment) funded by DOE was launched at Cornell in August 1993, with the objective of producing a field reversed ion ring. The basic technique for creating such an ion ring is that previously developed in the Cornell experiments [11,12,13] viz. by injection of an annular beam of ions from a magnetically insulated ion diode through a magnetic cusp into a solenoidal field with mirrors.

In FIREX the solenoidal field has an axial gradient so that the circulating beam particles are slowed down and eventually reflected by the mirror effect. For trapping of an ion ring to succeed the following issues have to be carefully considered:

- (1) Prompt space charge neutralization of the injected positive charge on a time scale  $\lesssim 10$  ns.
- (2) Neutralization of the azimuthal ion current by the charge neutralizing electrons must be reduced in order for the self-magnetic field to appear quickly and provide axial confinement of ring ions.

Prompt space charge neutralization is achieved by rapid ionization of the ambient gas (hydrogen) at a pressure  $50 \sim 100$  mT into which the beam is injected at a current density of  $\lesssim 1$  kA/cm<sup>2</sup> [11,12,13]. Complete current neutralization in the cusp region can be avoided by allowing the injected current to be close to the conducting walls where the tangential electric field vanishes [8]. Analysis [14] reveals that current neutralization is avoided if the electrostatic electric field across magnetic flux surfaces is shorted by whistler waves communicating this boundary condition to the ion beam. Thus the whistler transit time between the conducting walls and the beam should be less than the beam pulse time. Further downstream where the magnetic field is solenoidal the electron current can be cancelled by the background ion  $\mathbf{E} \times \mathbf{B}$  drift. This cancellation occurs on the time scale for the magnetosonic wave that is generated by the head of the ion beam to reach the walls and return to the beam [15].

In order to design the FIREX system with its power supply, a numerical simulation program was put into effect to investigate the detailed physics of the formation and trapping process. We describe the main results from these studies in Sect. II. The design of FIREX and the experimental results to date are given in Sects. III and IV.

## II. Numerical Simulation of Formation and Trapping of Ion Rings

A new, two and half dimensional ( $2\frac{1}{2}$  D), axisymmetric hybrid PIC code FIRE was developed to study the formation of ion rings [16]. This code follows an evolutionary development from previous codes employed at Cornell [17,18,19]. It assumes the existence of a background plasma

into which the beam is injected. Both beam and background ions are treated as particles experiencing slowing-down collisions with bound electrons and neutral atoms respectively. The electrons are treated as an inertialess fluid through the generalized Ohm's law. Quasi-neutrality is assumed throughout. This model is described in detail in Ref. 16. This code has provided deep insight into ring formation dynamics. Figure 1 shows the injected profile of the proton current and energy as a function of time. The evolution of the beam is seen in Fig. 2. The annular beam protons are injected close to the conducting wall. A beam angular divergence of 40 mrad did not interfere with the beam bunching and trapping. Notice that a magnetosonic wave develops at the head of the beam. The beam ions coalesce through the action of  $j_\theta B_r$  Lorentz force at  $t \approx 0.30 \mu\text{sec}$  after injection. The field lines are highly distorted at this stage, the magnetic field increases between the ring and the wall but is reduced on axis. Finally at  $t > 1 \mu\text{sec}$  the closed field lines form and resistive reconnection takes place at  $t \sim 4 \mu\text{sec}$ . Once the ring with closed field lines is formed the trapped cold plasma whose density is about  $10^2$  times the energetic ion density behaves as a coherent object. Thus the protons which would be reflected quickly by the mirror effect of the ramped solenoidal field are obliged to share their momentum with the cold plasma ions. This reduces the reflected velocity of the injected ions by two orders of magnitude. This phenomena provides a very favorable condition for trapping the ring by switching an auxiliary up-stream mirror on a few  $\mu\text{sec}$  timescale.

During the ring formation process almost two-thirds of the injected ions are captured in the ion ring and almost half the initial beam energy is lost to the magnetic field distortion and dissipation through collisional decay of the induced return current. The actual initial coalescence of the ring ions results from an Alfvén like instability driven by the ring current [16].

More recently a three dimensional code FLAME has been developed to study the stability of an ion ring and whether any departures from strict axisymmetry would be deleterious for ring formation. These studies are contained in a companion paper [20]. We have found that a dipole  $m = 2$  distortion of several percent of the radial component of the static magnetic field at the characteristic beam injection radius does not significantly interfere with the beam trapping and formation processes observed with the  $2\frac{1}{2}$  D code FIRE. However the 3-D simulation reveals that the modulation at  $m = 2$  which develops in the formation stage and disappears later due to phase mixing of the large-orbit ions results in an increase in the spread of the radial velocity component with a concomitant increase in the radial thickness.

### III. FIREX System

The FIREX system whose layout is given in Fig. [3] was completed in January 1996. The FIREX system design, and the basic issues addressed in that design, are described in this section.

The numerical simulations described above have been the main design tool for the final choice of parameters for the beam generator and magnetic system for ring formation in the FIREX experiment. The FIRE simulations incorporated temporal profiles of injected ion beam voltage and current, derived from simulations of the electrical design of the pulser combined with experimental data on beam generation in the same parameter range, chiefly from the LION diode [21]. A major extrapolation was made from previous ion diode experience in pulse length, from about 60 ns in LION, to 150 ns for FIREX. This was determined by the amount of charge necessary to produced field reversal, the desire to inject in about one ion cyclotron time scale, and the constraints on magnetic field, minimum pulser impedance, and attainable ion diode impedance profile. Iteration of the pulser, diode and coil system parameters was then carried out to arrive at the final design. Results of the simulations showed a number of important features of field-reversed ring formation that have been taken into consideration in the experimental design. The axisymmetric magnetic system is configured with an axially very short



(12 cm) cusp, coupled closely to the ion diode insulating magnetic field. The annular proton beam crosses the cusp, entering a slowly ramped solenoidal field which rises from 7 kG to 9 kG over about 2 m axial length (Fig. 2(a)). As described above, simulation of this configuration shows the beam crossing the cusp and entering the solenoid during the 150 ns injection time, with significant but not dominant self-magnetic field, so that the perturbation to the cusp field is not extreme and the beam ion orbits produce a well-behaved radially localized rotating layer. The axially short cusp and the shape of the magnetic ramp were optimized using the simulations.

The pulser design and its coupling to the ion diode was carried out using SPICE electrical design code simulations. The diode electrical characteristics were modeled by scaling from experimental data from LION experiments, with extended pulse length, but at the same voltage and current density. The pulser design was implemented in SPICE using a transmission line simulation of capacitive and inductive elements, and standard phenomenological models of switching components. The FIRE simulation shown above uses the ion beam energy (voltage) and current waveforms derived from SPICE simulations of the actual final pulser/diode design.

The FIREX pulser was designed by S. Glidden, D. Anderson and J.B. Greenly, using the circuit developed by the SPICE simulations. The pulser design is detailed in a companion paper [21], and consists of a 300 kJ Marx generator, a water-dielectric intermediate storage capacitor with gas output switch, and a water pulse-forming section using two stages of multiple parallel water gap switches, producing a nominal 1.4 ohm, 150 ns pulse with current up to 800 kA.

The FIREX ion diode was designed by J.B. Greenly and W. Podulka. The design of the diode accelerating gap, its electrode and magnetic field configuration, is constrained strongly by its close coupling to the magnetic cusp. A design was developed that makes the cusp very compact axially, giving well centered injected ion orbits and minimal cross-field propagation length to minimize charge-neutralization concerns. The very strong cusp fields allow proportionally strong diode insulating magnetic field, which we believe to be crucial for allowing the necessary level of diode performance. It was found possible within the strong geometric constraints dictated by the cusp to produce a diode gap configuration very close to the optimum design that has been developed during the last two years in LION diode experiments. The magnetic fields are produced by a superposition of the external solenoid field produced by a 3 s pulse, and the field produced by the diode coil, a 0.5 ms pulse. The field is shaped by resistive components which exclude the fast field, while allowing the slow field to penetrate. A more detailed view of the diode design issues, and operation are given in Ref. [21].

## IV. Experimental Results:

FIREX ring formation experiments have up till now been made at up to 70 kV Marx charge, or about 80% of maximum. The FIREX pulser is now operating reproducibly at the 70% level, and the results are described in this section. Power coupling from the pulser to the ion beam is not yet optimized, but results have already confirmed the important features of the diode design, and show a diode operating regime which should scale to full design output. Ref. [21] shows diode current, voltage and impedance waveforms in this regime. The diode is presently producing about 400 kA peak current, with essentially no damage to an epoxy groove anode. The diode begins to emit ion current as the voltage rises above 300 kV, and the full pulse width is 200 ns. The diode impedance drops to about 1 ohm at about 70 ns into the pulse, and then declines slowly to the end of the pulse.

At this power level, in order to reach the observed ion current density of over 600 A/cm<sup>2</sup>, an enhancement of over 15 times Child-Langmuir current density for protons, the diode must be operated at a relatively low magnetic field so that it is very near  $V^*$ , the voltage at which ion current density diverges and magnetic insulation is lost. A substantial fraction of the pulse time

is required for the diode to evolve to this operating equilibrium. Nevertheless, very stable and reproducible operation is observed, with high ion efficiency and very slow impedance collapse after the diode reaches the 1 ohm operating level. This performance, scaled to full power, will allow a relatively stronger magnetic insulation factor, and should give a faster current rise with better power coupling from the pulser and high ion efficiency.

Ion ring injection experiments have already given several important results. Fig. [4] shows a set of data from injection into different background gas densities, resulting in varied background plasma conditions. We see directly that the self-magnetic field of the ring does not instantaneously appear at the system axis. In fact under these conditions, the diamagnetic signal peaks after the fast-moving ring has passed by a given axial position. The perturbed magnetic field then exhibits a damped oscillation. Both these phenomena are expected to occur; they are consistent with FIRE simulations which show the magnetosonic radial propagation of the ring magnetic perturbation which delays the signal on axis and results in a damped oscillation. These effects are crucial in the ring trapping and field-reversal scenario revealed by the simulations. Simulations with an injected beam similar to the conditions of Fig. [4] produce a diamagnetic signal on axis of about one third to one quarter of that which would have been produced by the unneutralized ion ring current. This is consistent with the experimental beam and ring diagnostics, and gives a benchmark for the background resistivity used in the code. The full diamagnetism of the ring cannot appear during the short time in which these fast-moving, untrapped rings transit the solenoid. When the diode voltage pulse and the magnetic field are adjusted so that the ring moves axially much more slowly (Fig. [5]), the diamagnetic signal on axis coincides much more closely in time with the ring passage, as expected. In this figure, the ring was of much lower current density than those of Fig. [4], but the slow velocity allowed induced background current to decay, and a much larger fraction of the ring diamagnetism to appear.

As the adjustment of fields and voltages continues, the first evidence of the stopping and reflection of part of the ring in the ramped field has also been observed (Fig. [6]). Since the diode insulating field and the cusp and solenoid are so closely coupled, all system parameters including pulser voltage, diode gap and insulating field strength, and solenoid ramp strength must be adjusted together to bring the system to its ultimate performance. This optimization process is under way to achieve field reversal in FIREX.

The following considerations enter in scaling from the present results to predict the expected ion ring strength at full power. First, at full power, the peak voltage will be allowed to rise only slightly above the present 900 kV to about 1 MV. The voltage at peak power will rise from 600 to 800 keV. The peak current can then double, from 400 kA to about 800 kA within the capability of the pulser. The ion ring strength is expected to rise as full power is approached, by the following factors. First, the peak ion current will rise by a factor of two, and will be reached earlier in the pulse. The total amount of injected proton charge with energy above 300 keV, which is presently estimated to be at least 15 mC, should rise to more than 30 mC. The use of EMFAPS ion source should give a nearly pure proton beam instead of the present estimated 60% protons, bringing the charge to more than 50 mC. The ring diamagnetic field is directly proportional to the total charge in the ring, and inversely proportional to the axial length of the ring (until the ring length becomes comparable to its radius). The present rings, injected through the cusp at 60% of full magnetic field, have only about 200 keV energy in rotation, and the remaining large axial velocity makes a long ring (about 1 m length) that does not slow and reflect significantly in the gradual magnetic ramp. At full magnetic field, about 550 keV will go into rotation through the cusp, leaving a short, slow moving ring that is predicted to form an axially compact ring. A charge of 50 mC in a trapped, axially compact ring (about 20 cm length), is more than that required for field reversal. This simple scaling would then predict that with three times the charge, and one-fifth the length, the ring would have fifteen times the

present diamagnetic field. Remembering that the external solenoid field will go up from 60% to full strength, a factor of 1.7, the relative ring diamagnetism should rise by about a factor of ten. We believe that the full diamagnetic field of the present ring is at 15-25% reversal.

### Acknowledgment

We are indebted to Sandia Laboratories for allowing parts of the LION machine to be incorporated into FIREX and to J. Ramirez for reviewing the design of the FIREX pulsed power system.

## References

- [1] L.C. Steinhauer et al., FRC 2001: A White Paper on FRC Development in the Next Five Years, to appear in *Fusion Technology* (1996).
- [2] D.C. Barnes, et al., *Phys. Fluids* **29**, 2616 (1986).
- [3] R.N. Sudan and E. Ott, *Phys. Rev. Lett.* **33**, 354 (1974).
- [4] See for example: J.M. Finn and R.N. Sudan, *Nucl. Fusion* **22**, 1443 (1982).
- [5] R.N. Sudan, "Particle Ring Fusion", in Unconventional Approaches to Fusion, Ettore Majorana Int. Science Series, B. Brunelli and G.G. Leotta, Eds. (Plenum Press, New York, 1982) vol. 13 p. 311.
- [6] H.H. Fleischmann and T. Kammash, *Nucl. Fusion* **15**, 1143 (1975).
- [7] R.N. Sudan, *Lasers and Particle Beams* **11**, 415 (1993).
- [8] R.N. Sudan, *Phys. Rev. Lett.* **70**, 1623 (1993).
- [9] M.L. Andrews et al., in *Plasma Phys. and Controlled Nucl. Fusion Research* (Proc. 4th Int. Conf. Madison 1971) Vol. 1, IAEA Vienna (1971) p. 169.
- [10] C.A. Kapetenakos, et al., *Phys. Rev. Lett.* **44**, 218 (1980).
- [11] P.L. Dreike et al., *Phys. Rev. Lett.* **47**, 225 (1981); *Phys. Fluids* **25**, 59 (1982).
- [12] P.D. Pedrow et al., *Appl. Phys. Lett.* **47**, 225 (1985).
- [13] J.B. Greenly et al., *Phys. Fluids* **29**, 908 (1986).
- [14] B.V. Oliver, D.D. Ryutov and R.N. Sudan, *Phys. Fluids* **1**, 3383 (1994).
- [15] H.L. Berk and L.D. Pearlstein, *Phys. Fluids* **19**, 1831 (1976).
- [16] Yu.A. Omelchenko and R.N. Sudan, *Phys. Plasmas* **2**, 2773 (1995).
- [17] A. Mankofsky, A. Friedman and R.N. Sudan, *Plasma Phys.* **23**, 521 (1981).
- [18] A. Mankofsky, R.N. Sudan and J. Denavit, *J. Comput. Phys.* **70**, 89 (1987).
- [19] P.M. Lyster and R.N. Sudan, *Phys. Fluids B* **2**, 2661 (1990).
- [20] Yu.A. Omelchenko and R.N. Sudan, "3D Studies of the Formation and Stability of Strong Ion Rings", BEAMS 96 Conference.
- [21] W.J. Podulka, J.B. Greenly, D.E. Anderson, S.C. Glidden, D.A. Hammer, Yu.A. Omelchenko and R.N. Sudan, BEAMS 96 Conference.

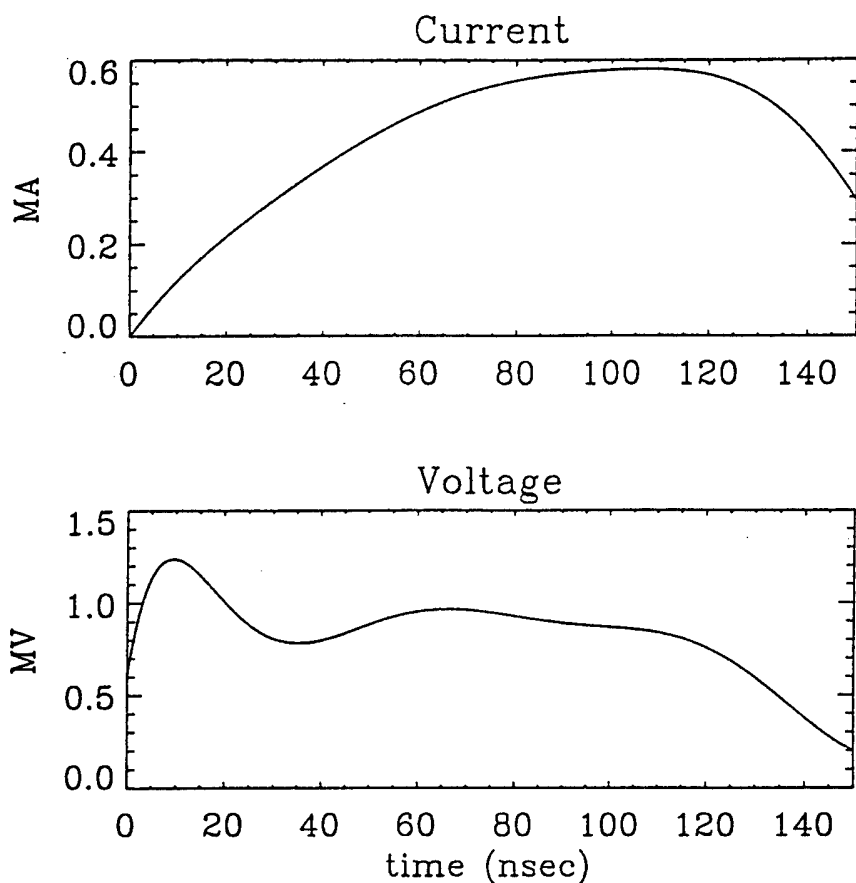


Figure 1: Typical voltage current profiles with time employed in simulations.

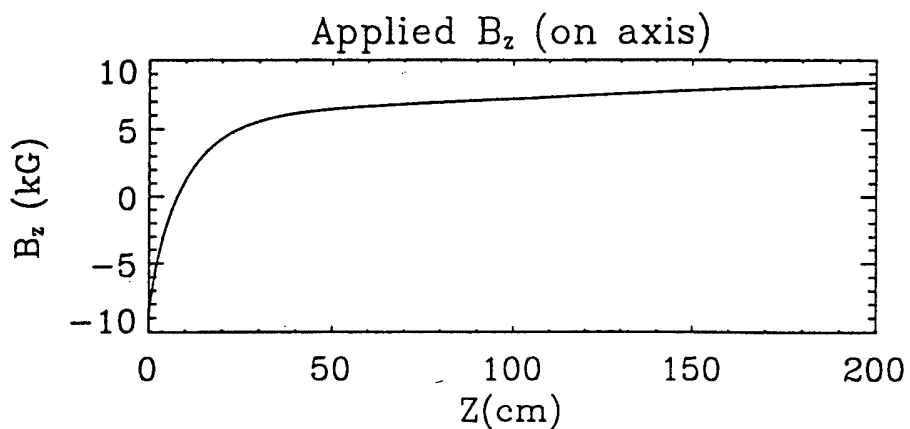


Figure 2(a): The applied  $B_z$  on the axis as a function of distance from the anodes.

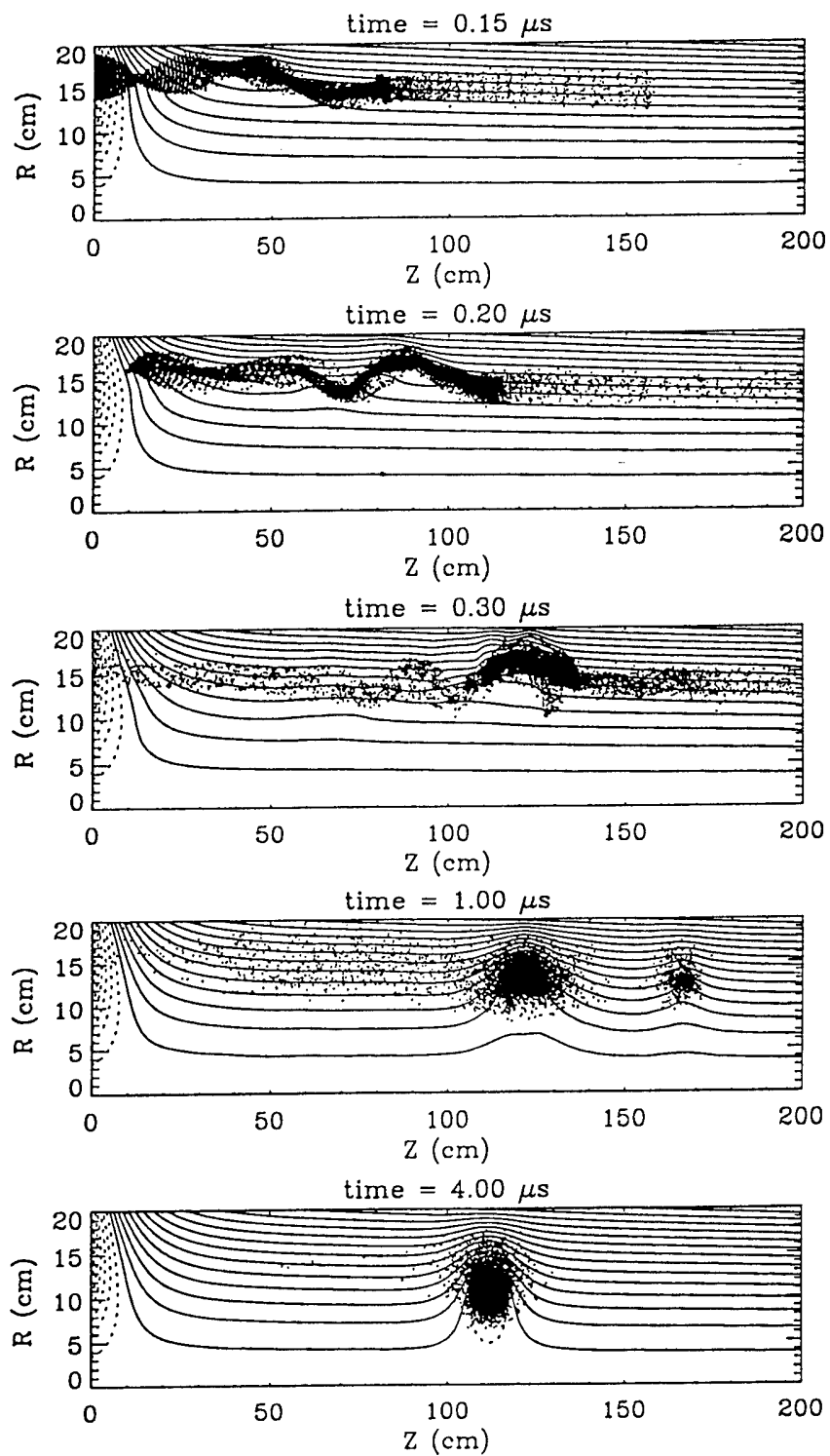


Figure 2(b): Beam evolution after injection with accompanied changes in the magnetic flux;  $N_b = 4 \times 10^{17}$ .

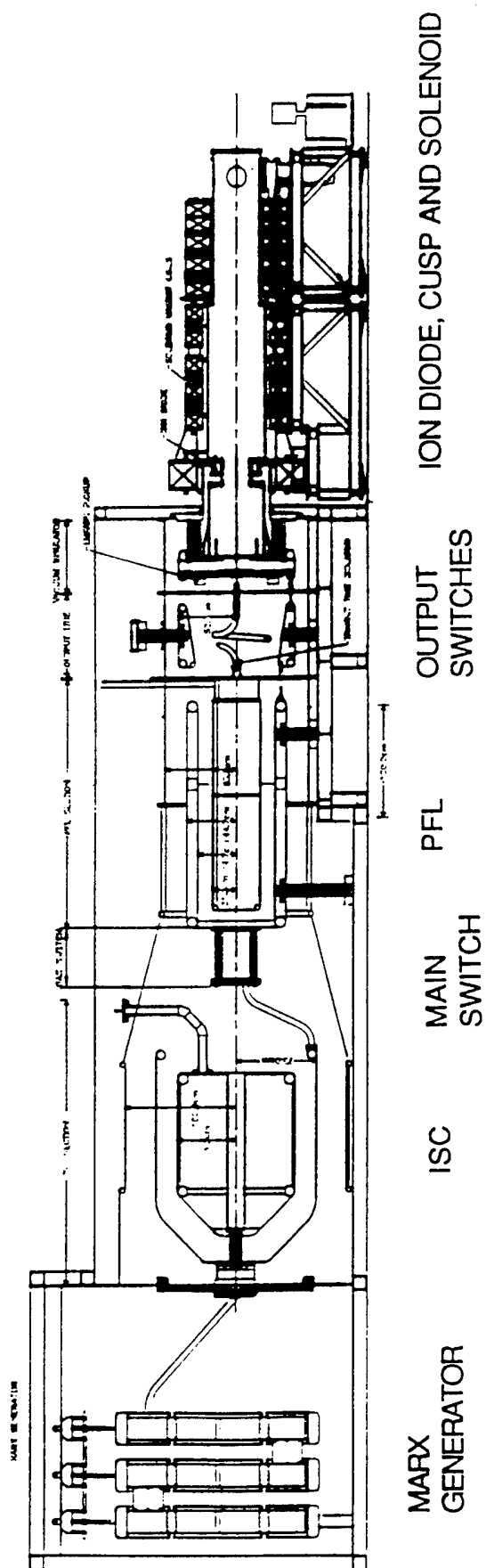


Figure 3: Layout of the FIREX Experiment

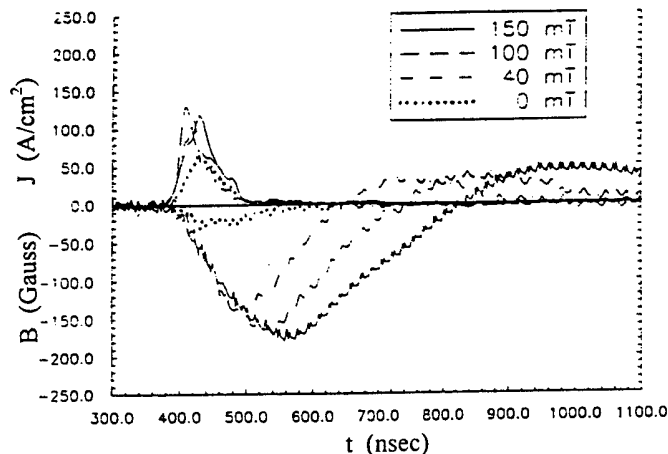


Figure 4. Ion ring injection with high axial velocity ( $E_z < 500 \text{ keV}$ ) into different hydrogen gas pressures. Positive signals are ion ring current density at  $r=16 \text{ cm}$ ,  $z=50 \text{ cm}$  ( $z=0$  is the diode location). Negative signals are on-axis diamagnetic fields at  $z=60 \text{ cm}$  ( $B_z=2.5 \text{ kG}$ ). Note that the magnetic signals peak after the ring current has passed by the probe location, and have long damped oscillatory tails, whose period depends on gas pressure. This is evidence of the magnetosonic velocity in the beam-formed plasma.

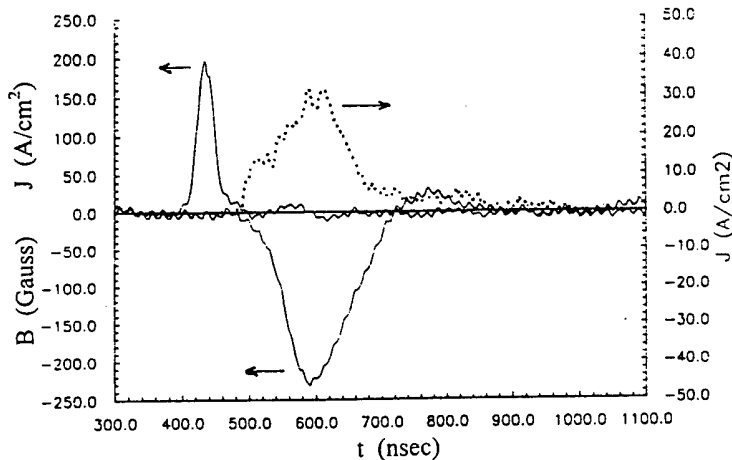


Figure 5. Ion ring injection with lower axial velocity ( $E_z < 200 \text{ keV}$ ) into 80 mTorr hydrogen gas. Positive signals are ion beam current density at the diode (solid), and ion ring current density at  $z=72 \text{ cm}$  (dotted). Negative signal is on-axis diamagnetic field at  $z=82 \text{ cm}$  ( $B_z=4.1 \text{ kG}$ ). Comparing to Fig. 4, note the much later timing of the ring current, and the near-coincidence of ring current and diamagnetism. The diamagnetism is larger than Fig. 4, even though the current density is a factor of three smaller, because the lower ring velocity gives more time for decay of the background current which shields the ring diamagnetism.

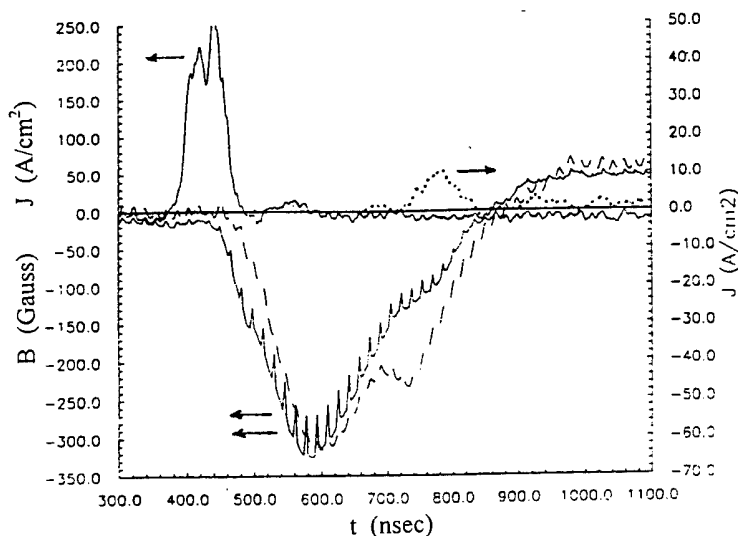


Figure 6. Ion ring injection at low axial velocity ( $E_z < 150 \text{ keV}$ ), showing partial reflection of the ring in the ramped solenoid. Signals are as in Figure 5, but the ion ring current density is collimated to measure only reflected ring, and there are two diamagnetic signals, at 52 cm ( $B_z=4.5 \text{ kG}$ ) (solid) and 82 cm (dashed), with a relative delay of the initial rise showing velocity away from  $z=0$  (the diode), and a reversed delay of the second (reflected) peak that shows velocity backward, toward  $z=0$ . The timing of this peak indicates that the reflection occurred past  $z=150 \text{ cm}$ , near the peak of the ramped mirror field.

## PLASMA LENS FOCUSING AND PLASMA CHANNEL TRANSPORT FOR HEAVY ION FUSION

A. Tauschwitz\*\*, S.S. Yu, R.O. Bangerter, J.J. Barnard\*, S. Eylon, T.J. Fessenden, J. Kwan,  
W. Leemans, C. Peters, L. Reginato, W.M. Sharp\*

*Lawrence Berkeley National Laboratory, 1 Cyclotron Road, Berkeley, CA 94720, USA*

*\*Lawrence Livermore National Laboratory, Livermore, CA 94550, USA*

*\*\*present address: Universität Erlangen, Physikal. Inst., Erwin-Rommel-Str.1, 91058 Erlangen, Germany*

### Abstract

The final focus lens in an ion beam driven inertial confinement fusion reactor is important since it sets limiting requirements for the quality of the driver beam. Improvements of the focusing capabilities can facilitate the construction of the driver significantly. A focusing system that is of interest both for heavy ion and for light ion drivers is an adiabatic, current carrying plasma lens. This lens is characterized by the fact, that it can slowly (adiabatically) reduce the envelope radius of a beam over several betatron oscillations by increasing the focusing magnetic field along a tapered high current discharge. A reduction of the beam diameter by a factor of 3 to 5 seems feasible with this focusing scheme. Such a lens can be used for an ignition test facility where it can be directly coupled to the fusion target. For use in a repetitively working reactor chamber the lens has to be located outside of the reactor and the tightly focused but strongly divergent beam must be confined in a high current transport channel from the end of the lens into the immediate vicinity of the target. Laser preionization of a background gas is an efficient means to direct and stabilize such a channel. Experiments have been started to test both, the principle of adiabatic focusing, and the stability of laser preionized high current discharge channels.

### 1. Adiabatic Plasma Lens Focusing

Active plasma lenses have usually been used as 'thin' lenses [1,2]. 'Thin' in this context means that the beam passage through the lens requires less than a quarter of a betatron oscillation. A thin lens is characterized by the fact that the focal length of the lens depends on the phase of the betatron oscillation that the particles have reached at the end of the lens. Particles of different energy or charge state are focused to different points. If the focal point is close to the end of the lens, the beam diameter inside the discharge plasma changes significantly. In this case the efficiency of the lens can be enhanced by fitting the discharge diameter to the beam envelope. This can be achieved by tapering the discharge tube and does not affect the ion optical properties of the lens [3]. Such a tapered lens with an adiabatically slow increase of the focusing power can be used as a thin or as a thick lens. A thick adiabatic lens is characterized by the fact, that the focusing field extends over a length of several betatron wavelengths. In this type of lens a reduction of the beam envelope can be achieved independent of the betatron phase with which the ions reach the end of the lens, by reducing the amplitude of the betatron oscillations with the increasing focusing field [4,5]. This provides the possibility of focusing beams with a high momentum spread or beams with particles in mixed charge states. The smallest diameter for a beam of high momentum spread is exactly at the end of the lens. The beam diameter increases rapidly behind the lens. In the adiabatic lens the beam envelope is described by Hill's Equation  $d^2/dz^2 = -k^2 r$  with  $k^2(z) = Z(z)2eI / a^2(z)\beta mc^3$ . Here  $Z$  denotes the charge state of the ion,  $I$  is the total discharge current in the lens, and  $a$  is the radius of the focusing discharge. In the adiabatic approximation  $1/k^2 dk/dz \ll 1$  a solution can be written in the form  $r = C \exp(i/k dz) / k^{1/2}$ . If the ratio of the beam radius at the end of the lens  $r_{out}$  and at the entrance of the lens  $r_{in}$  is  $b = r_{out}/r_{in}$  the initial wave number  $k_{in}$  has to be decreased by a factor of  $b^2$  to  $k_{out} = k_{in}/b^2$  at the end of the lens in order to reduce the radius of the beam envelope by a factor of  $b$ . To achieve a beam size reduction of  $b=3$  for typical parameters of a driver beam with  $m=200$  amu,  $\beta=0.3$ , with a discharge current of  $I=100$  kA, and assuming that the beam is stripped from initially  $Z=+16$  to  $Z=+64$  at the end of the lens, the channel has to be tapered down from the entrance radius  $a_{in}=11.25$  mm to



an exit radius  $a_{out} = 2.5$  mm. This yields a reduction of the beam radius from  $r_m = 7.5$  mm to  $r_{out} = 2.5$  mm. The admissible emittance for the beam is determined by the conservation of phase space density over the simple relation  $\varepsilon/r = ka$ , which allows a normalized emittance of 62 mm mrad for the above example.

## 2. Application to an Ignition Test Facility

An application of an adiabatic plasma lens for an ignition test facility is sketched out in fig. 1. The adiabatic lens as the central element of the final focus system is located inside the reactor chamber and directly connected with the fusion target. Depending on the required uniformity of target illumination one or several lenses can be used.

Since the adiabatic lens is not capable of a sufficiently high focusing ratio, a conventional quadrupole lens is necessary to match the ion beams from the accelerator to the entrance of the adiabatic lens. A lens that reduces a beam from a radius of 7.5 mm to a 2.5 mm spot radius on the target needs a length of about 1.7 m to fulfill the adiabaticity condition. This distance is the length of one betatron oscillation at the entrance of the lens or of nine betatron wavelengths at the exit of the lens, for a discharge current of 100 kA, an ion mass of 200 amu, and a velocity of 0.3 c. Such a lens has an acceptance angle of  $\pm 30$  mrad. The large acceptance angle, the space charge neutralization and the insensitivity to beam emittance of the adiabatic lens

make the entrance of the tapered discharge an ideal place to combine several driver beams. The main advantages of this focusing scheme are that it is achromatic and allows therefore a fast drift compression of the ion bunches, and that it can focus beams with very high emittance which allows to reduce the final ion energy. Since this scheme does not depend on ballistic focusing the vacuum requirements for the target chamber are low. The disadvantage, that the lens has to be replaced after every target explosion is relatively minor for an ignition facility with a few shots per day.

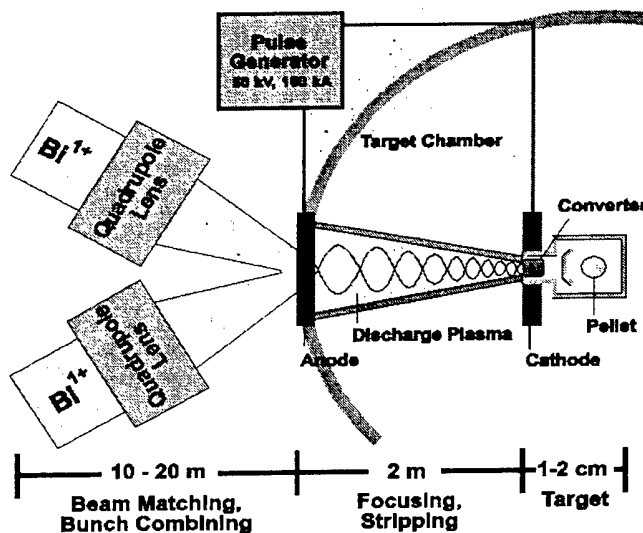


Fig.1 Schematic layout of a target chamber for an ignition facility using adiabatic focusing.

## 3. Experimental Test of an Adiabatic Plasma Lens

One of the most important characteristics of an adiabatic plasma lens is its capability to focus high emittance beams. Therefore the focusing properties and the transmission of the lens for high emittance beams are important topics in an experimental test. An electrostatic quadrupole injector (ESQ) capable of producing a singly charged potassium beam at an energy of up to 2 MeV was used to test the focusing properties. The short ion range in solid matter does not allow windows in the beam path at this energy. Therefore a three stage differential pumping system was used to reduce the pressure in the discharge tube of 1 Torr helium over a distance of 135 mm to  $10^{-6}$  Torr at a free beam aperture of 5 by 15 mm. An electrical diagnostics using a Faraday cup was chosen to measure the intensity of the transmitted beam in spite of problems caused by the electromagnetic noise of the discharge, because this diagnostics provides a good temporal resolution. A spatial resolution of the beam profile behind the discharge can be achieved by a pinhole that can be moved across the exit aperture of the lens. A schematic representation of the plasma lens, the differential pumping system and the diagnostic system is shown in fig. 2. Experiments were performed with beams of 1.1 and 1.5 MeV ion energy. The 360 mA current of the 1.1 MeV potassium beam at the entrance of the differential pumping system is reduced to about 5 mA at the entrance of the discharge. Without discharge gas the pinhole with a diameter of 0.5 mm at the end of the discharge tube with a length of

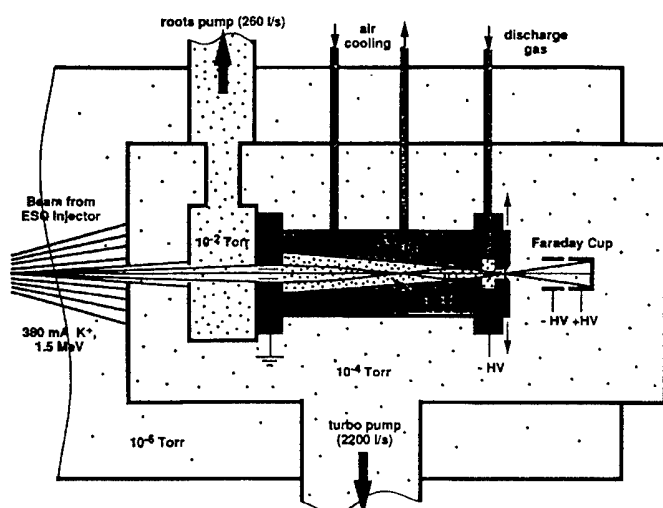


Fig. 2 Set up for a test of adiabatic plasma lens focusing of an 1.5 MeV potassium beam.

from 7.6  $\mu\text{A}$  to 200  $\mu\text{A}$  was found. The experimental results are in good agreement with simulations of the focusing which include the initial beam conditions, stripping, and the emittance increase by scattering. The large intensity increase in spite of the strong scattering of the ions in the discharge gas and the presents of different charge states indicate, that the adiabatic focusing works as expected. Further experiments are planned to measure the transmission trough the lens and the intensity profile of the beam behind the lens.

#### 4. Application to a Fusion Power Reactor

In contrast to an application in an ignition test facility the destruction of the lens with each pellet explosion can not be tolerated for a power reactor. Therefore the adiabatic lens has to be located outside of a reactor chamber. A schematic reactor layout using an adiabatic lens is sketched out in fig. 3. The focused beam is guided from the end of the lens to the target by a high current discharge channel. The envelope radius of the beam in this channel has to be the same as at the end of the lens and determines the spot radius on the target. Since lens and channel require the same discharge current, they can be driven by a single current pulse generator. One or, to reduce the circuit inductance, several current return channels are required from the target back to the generator. Fig. 3 sketches two transport channels from opposite sides and two return current channels perpendicular to the transport channels. Laser preionization of a background gas in the mbar pressure regime inside the reactor chamber is used to stabilize and direct the transport channels. An excimer laser pulse energy of less than 10 J is sufficient for this purpose. Besides the advantages of achromaticity and the possibility to focus high

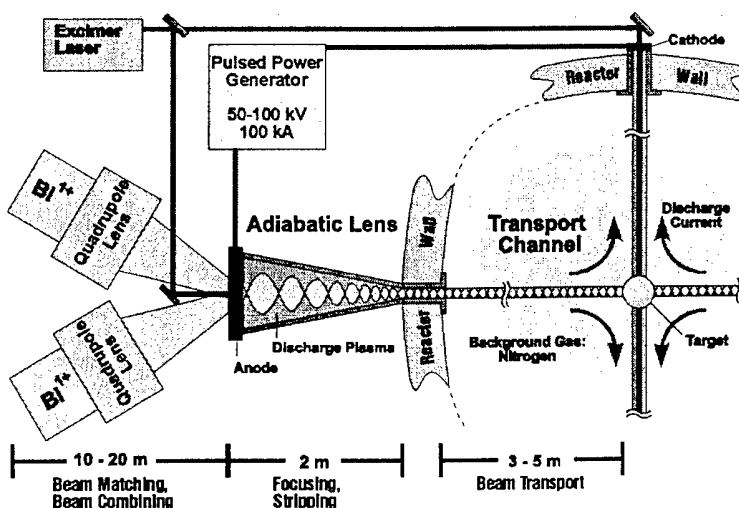


Fig. 3 Schematic layout of a reactor chamber using adiabatic focusing and discharge channel transport.

emittance beams this focusing scheme simplifies the protection of the beamlines from debris in the reactor by reducing the number and area of the entrance ports for the beams to a minimum and, the background gas reduces the stress of the first reactor wall.

### 5. Investigation of Discharge Channel Generation by Laser Preionization

The feasibility of the discharge channel transport of the focused ion beams is crucial for the applicability of the adiabatic focusing to a fusion power reactor. Earlier experiments[6,7] addressing the creation of laser preionized discharge channels, and the ion beam transport in such channels were done using narrow, insulating discharge tubes, which reduce breakdown problems and increase the channel stability. For the experiments

described here a metal discharge chamber with a cross-section of 25 cm by 25 cm and a gap between the electrodes of 40 cm was used. The electrodes were mounted electrically insulated from the chamber on Plexiglas flanges. A KrF laser with a wavelength of 248 nm and a pulse energy of up to 100 mJ in a 20 ns pulse, focused to a parallel beam of 5 by 5 mm cross-section was used for the preionization. The laser ionizes a channel in the discharge gas mixture of 10 Torr N<sub>2</sub> and 0.2 Torr benzene.

The laser light, that is not absorbed in the discharge gas, is used to trigger a sparkgap, which discharges a capacitor of 0.15  $\mu$ F at a voltage of 10 kV into the laser ionized channel. The resulting discharge current of 1 kA improves the conductivity in the plasma channel. With a delay of 10 to 50  $\mu$ s the main capacitor bank of 4.8  $\mu$ F, charged to a voltage of 30 kV, is discharged into this channel. This high current discharge is diagnosed with pickup probes to measure the current distribution in the discharge chamber, and with a gated CCD camera with a time resolution of 2 ns to investigate the stability of the discharge. A typical current wave form of the total discharge current and of the current enclosed in a channel with 36 mm radius are shown in fig. 4. The peak current of the discharge is reached 3.8  $\mu$ s after the ignition of the main discharge and reaches a value of 63 kA out of which 55 kA are flowing in the central channel. Measured from the light distribution the current channel has a half width of 6 mm radius after 3.8  $\mu$ s and is slowly expanding. Pictures with an exposure time of 8 ns, taken at different times of the discharge, show a high reproducibility and no signs of hydrodynamic instabilities. These channels seem to be well suited for heavy ion beam transport.

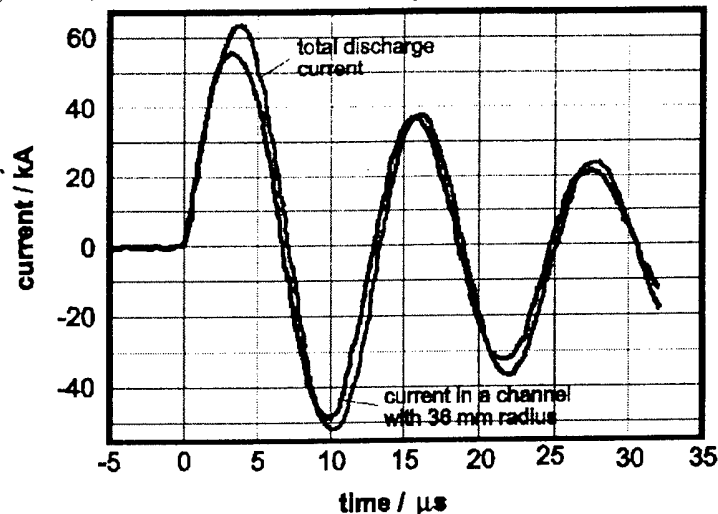


Fig.4 Total discharge current and current enclosed in a laser preionized channel with a radius of 36 mm.

### 6. Acknowledgments

One of the authors (A.T.) was supported by a Feodor-Lynen fellowship granted by the German Humboldt foundation during his work at the Lawrence Berkeley National Laboratory. This work was partially funded by the German ministry for education and research (BMBF).

### References

- [1] E. Boggasch et al., Appl. Phys. Lett. **60** (1992) 2475-2477
- [2] R. Kowalewicz et al., Int. J. Mod. Phys. (Proc. Suppl.), **2A**, (1993) 182-184
- [3] A. Tauschwitz et al., IEEE Trans. on Plasma Sci., **23** (1995) 388-392
- [4] P.F. Ottinger et al., Phys. Fluids **23** (1980) 909-920
- [5] P. Chen et al., Rev. Lett. **64** (1990) 1231-1234
- [6] J.N. Olsen, R. L. Leeper, J. Appl. Phys. **53** (1982) 3397 - 3404
- [7] C.A. Frost et al., Appl. Phys. Lett. **41** (1982) 813-815

# FORMATION OF AN INTENSE PROTON BEAM OF MICROSECOND DURATION

V. Engelko\*, H. Giese, S. Schalk

*Forschungszentrum Karlsruhe, INR, Postfach 3640, D-76021 Karlsruhe, Germany*

*\*Efremov Institute of Electrophysical Apparatus, 189631, St. Petersburg, Russia*

The proton beam facility PROFA serves as a test installation for ion source development and beam transport optimization for an intense pulsed proton beam of low kinetic energy, envisaged for ITER divertor load simulation. We discuss the present state of the investigations with the emphasis on diode operation parameters, beam divergence and beam transport efficiency. Companion papers to this conference [1, 2] describe details of beam composition and space charge neutralization studies.

## 1. INTRODUCTION

One of the tasks presently pursued at FZK/Karlsruhe is the possibility of simulating ITER divertor erosion under plasma disruption conditions by exposing divertor candidate materials to an intense ( $\sim 1$  kA), pulsed ( $\geq 10\mu\text{s}$ ), low kinetic energy (10-30 keV) proton beam with a power density of up to  $10\text{ MW/cm}^2$ . Conceptual numerical studies led to the reference design of a machine 'KANDIS' [3, 4], capable of producing a beam with the required parameters by combining a spherical diode for proton beam production with a two-stage focusing system. At the first stage the beam is focused ballistically in the presence of a magnetic field configuration of which is close to configuration of the beam. At the second stage protons are captured by a magnetic field and then the beam is adiabatically compressed. The main parameters of this reference design KANDIS are the following:

Area of emitting surface	$10\,000\text{ cm}^2$
Current density at this surface	$\geq 0.1\text{ A/cm}^2$
Magnetic field at this surface	$6\text{ mT}$
Source divergence of the beam	$\leq 30\text{ mrad}$
(Permissible value for optimal space charge neutralization [3]: $70\text{ mrad}$ )	
Magnetic field at the target	$4\text{ T}$
Length of ballistic stage	$150\text{ cm}$
Length of compression stage	$50\text{ cm}$

The magnitude of the magnetic field induction at the target location did not only

result from the beam focusing necessities, but was also chosen with a view to perform divertor-material erosion investigations under typical ITER conditions.

Thus for realization of the described reference design, the following problems had to be solved: creation of a large area proton source, producing a low divergence beam with a current density  $\geq 0.1\text{ A/cm}^2$  and pulse duration  $\geq 10\mu\text{s}$ , and development of a method for effective neutralization of the beam space charge in the focusing region. To treat these tasks, the PROFA facility was built in 1994 [5], representing a scaled down version of the reference design conceived for a max. beam current of  $\sim 150\text{ A}$  and serving as a test-bed for vacuum diode development and beam transport optimization.

The paper presents the results obtained up to now at this facility.

## 2. THE PROFA FACILITY

The principal layout of the PROFA facility in its present state is shown in Fig.1. An extraction type ion source of 44cm diameter with concave electrode surfaces for ballistic beam focusing is accommodated in a stepwise tapered vacuum vessel.

The PROFA ion source comprises an anode discharge electrode (ADE) for plasma production and a set of stainless steel grids for ion extraction. The ADE is a perforated concave stainless steel shell containing 750 spark units with an average

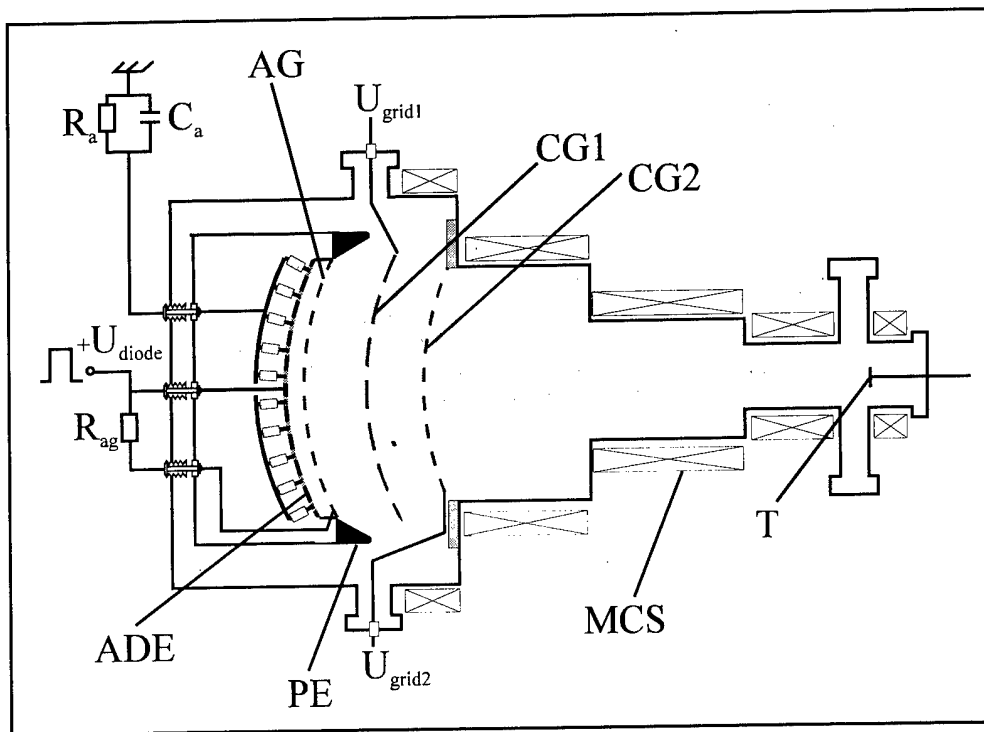


Fig. 1: Schematic layout of the pulsed proton beam facility PROFA.

ADE: anode discharge electrode; AG: anode grid; PE: Pierce electrode;  
CG1, CG2: cathode grids; MCS: magnetic coil system; T: target.

distance of 2cm. Each of these spark units consists of a polyethylene plug of 6 mm diameter and a central needle electrode. All needle electrodes have series resistors  $R_0$  and are jointly connected to ground via an external RC network  $R_a$ ,  $C_a$ .

Applying a positive high voltage pulse to the ADE leads to a surface discharge across each polyethylene plug from the ADE body to the central needle electrode, and to the formation of a hydrogen-rich plasma cushion on the ADE surface. Adequate choice of the components  $R_0$  and  $C_a$  ensures homogeneous firing of the spark units over the ADE surface. After expansion of the plasma cushion to the anode grid AG, ions are extracted under the influence of the diode electric field and accelerated towards an accel-decel configuration consisting of an adequately biased double grid arrangement CG1, CG2. After passing through the ballistic focus at a distance of 60 cm from the diode, the proton beam diameter is further reduced by magnetic compression.

The diagnostic tools employed and the parameters measured with these were:

- (i) *Three electrode collector (TEC)*: [1]  
ion current and current density and spatial density of electrons accompanying the ions.
- (ii) *Capacitive probe (CP)*:  
beam potential
- (iii) *Langmuir probe (LP)*:  
radial space charge distribution.
- (iv) *Calorimeter array*:  
beam profile
- (iv) *Shadow box / movable collimator*:  
beam divergence

All system currents of interest were measured using Rogowsky-coils.

### 3. RESULTS

**Anode plasma.** Photographs of the operating anode show that the discharge units fire rather homogeneously:  $\approx 75\%$  of the total number for a diode voltage of 22 kV.

A simple model of anode plasma dynamics predicts that its density depends on time and anode discharge current  $I_{dis}$  as:

$$n = \frac{\kappa I_{dis} t}{e(\pi R^2 h + v_i A t)} \quad (1)$$

Here  $\kappa$  is a coefficient,  $e$  is the electron charge,  $v_i$  is the ion sound velocity,  $R$  is the radius of ADE,  $h$  is the distance between ADE and AG and  $A=2\pi(R^2+Rh)$ .

From (1) follows

$$j_i = \frac{0.5 \kappa \alpha I_{dis} v_i t}{\pi R^2 h + 2\pi v_i t R (R + h)} \quad (2)$$

where  $\alpha$  is the transparency of AG.

From (2) it follows that during the time interval  $t \approx 2.5h/v_i$  ion current density increases up to its saturation value, which is equal to

$$j_i \approx \frac{0.5 \kappa \alpha I_{dis}}{2\pi R^2}, \quad I_i \approx 0.25 \kappa \alpha I_{dis} \quad (3)$$

So one can expect that the stationary value of the ion current and current density is directly proportional to the discharge current.

The anode plasma parameters were measured by means of Langmuir probes. The results showed, that the predominant ion species are protons. The plasma density reaches a stable value within 5  $\mu$ s. It becomes proportional to  $I_{dis}$ , when  $I_{dis}$  exceeds a certain value. The electron temperature changes in time in the range 10 - 20 eV.

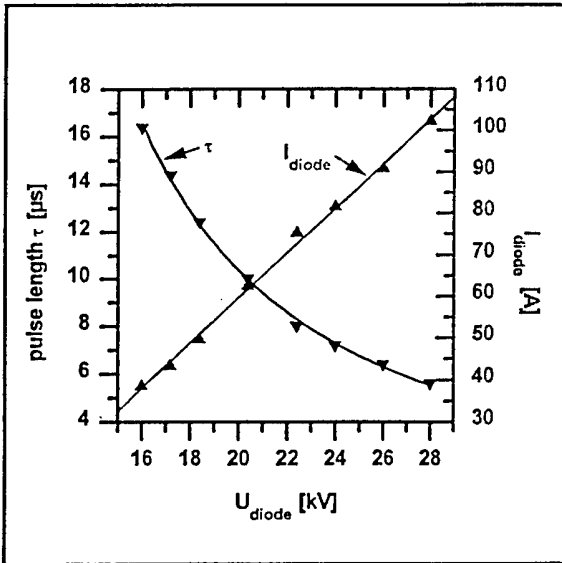


Fig. 2 Pulse length and total diode current as a function of voltage for  $R_a = 8 \Omega$ . A linear fit for  $I_{diode}$  is included.

**Source operation.** The potential of the anode grid AG was found to strongly influence  $I_i$ , which reached a maximum when AG was allowed to adopt anode plasma potential. This was achieved by connecting AG to the anode discharge electrode ADE through a resistor of adequate magnitude. An increase of almost 50% in ion current was observed with respect to the situation when AG was held at the potential of ADE.

The behavior of the ion current was found to be in good agreement with expression (2). The current achieves its stationary value within 5  $\mu$ s. This value is directly proportional to  $I_{dis}$  with  $I_i \approx 0.05 I_{dis}$ .

Two representative examples of the dependence of  $\tau$  and  $I_{diode}$  on  $U_{diode}$  and  $R_a$  are given in Fig. 2 and 3. One can see that  $I_{diode}$  exceeds 100 A at  $U = 28$  kV. Unfortunately  $\tau$  is only about 5.5  $\mu$ s under such conditions. Pulse lengths of up to 40  $\mu$ s were obtained for lower diode currents, limited only by the capability of the pulse power supply.

Fig. 4 shows two measured angular distributions of the maximum ion current density  $j_i$  recorded at a distance of 7 cm below the second cathode grid under the following operating conditions:

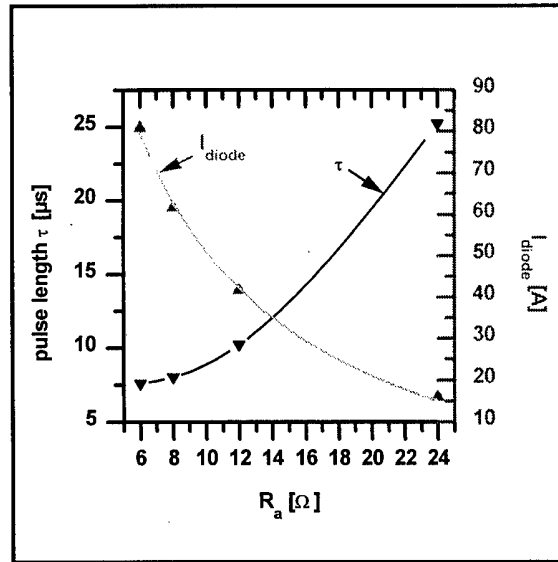


Fig. 3 Pulse length and total diode current against anode resistor  $R_a$  for  $U_{diode} = 20.4$  kV.

$U_{\text{diode}} \approx 20 \text{ kV}$ ,  $R_a = 8 \Omega$ , diode gap  $\approx 1.5 \text{ cm}$ , cathode grid distance  $3 \text{ cm}$ . Both measurements were made using a  $11.5 \text{ mm}$  entrance aperture TEC. While dis. 1 was recorded using the anode configuration shown in Fig. 1, dis. 2 was obtained using an additional grid of 35% transparency installed between the anode discharge electrode and the anode grid. Dis. 1 shows a Gaussian profile, with  $j_i$  near the beam axis exceeding  $0.1 \text{ A/cm}^2$ . Considering the focusing effect and the grid transparencies, this value corresponds to  $0.11 \text{ A/cm}^2$  at the emitting boundary, the AG. The directly measured total diode current was  $55 \text{ A}$ , which agrees well with the current obtained from integration of dis.1.

Dis. 2 shows that the introduction of an additional anode grid has substantially improved homogeneity of the plasma profile, but at the cost of reduced current density.

For comparison, Fig. 4 also shows the ion current density obtained from Child Langmuir theory. The reduction of  $j_i$  at large angles is due to the increase of the diode gap originating from the inadequate curvature of the cathode grids.

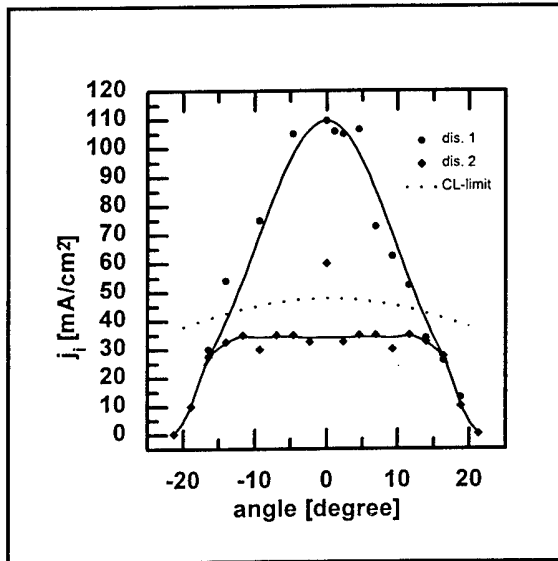


Fig. 4: Maximum ion current density as a function of angle, recorded  $7 \text{ cm}$  below second cathode grid for two conditions. (see text for details).

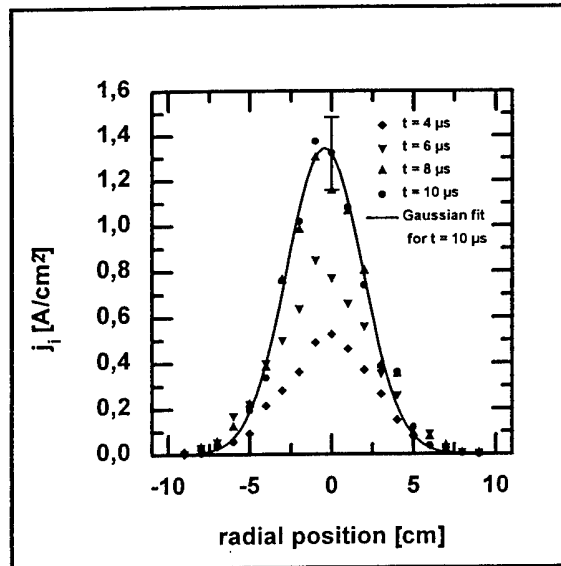


Fig. 5: Radial ion current density profiles in the ballistical focus plane for different times after pulse onset.

**Beam divergence.** This parameter was measured without magnetic field using alternatively 1) a shadow box with ion sensitive film as a detector: 2) a movable collimator sampling a small part of the beam, propagating in a certain angular direction [2], and 3) radial ion current density profiles measured in the ballistic focus.

While due to its limited resolution, the first method did not deliver results of sufficient accuracy, the second method yielded for the protonic part of the beam a divergence value of  $50 \text{ mrad}$ .

The third method will be discussed here in some more detail. The results of a series of radial beam profile measurements in the focal plane, obtained under the same conditions as dis.1 in Fig. 4 for different moments in time are shown in Fig. 5. The centre-axis measurement was repeated 7 times to check the reproducibility of the results. The error bar shown in Fig. 5 indicates the total scatter observed and corresponds to a relative statistical standard variation of  $12\%$ . In principal, a global divergence information could be directly derived from one of the profiles of Fig. 5 (e.g. the Gaussian fit for  $t = 10 \mu\text{s}$ ) and the focal distance of  $60 \text{ cm}$ . It is clear, however, that the value obtained here would not

directly correspond to the parameter of interest, i.e. the source divergence, but would represent a superposition of the source divergence and the effect of beam widening due to insufficient space charge neutralization. (While in normal machine operation the presence of the magnetic compression field provides optimal conditions for space charge neutralisation, and thus minimizes beam widening (see below and [1]), the measurements of Fig. 5 were made without magnetic field and thus beam widening plays a significant role!). It was therefore attempted to split the information that could be extracted from Fig. 5 into the different contributions and thus to obtain the desired value of the source divergence. This was done by running a set of parametric calculations of the radial beam profile in the focal plane, in which the source divergence and the degree of space charge neutralisation were systematically changed in small increments. The calculated result that best fitted the measured 10  $\mu$ s profile of Fig. 5 is shown in Fig. 7. This calculation used a combination of a source divergence of 70 mrad and a degree of the space charge neutralisation of 99.95%. The source divergence found here is in satisfactory agreement with the

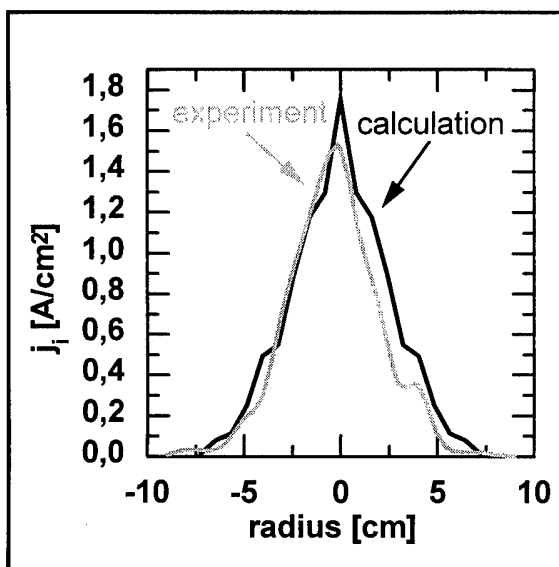


Fig. 6: Comparison of measured and calculated radial beam current density profiles in the ballistic focus

measured anode plasma temperature, if one assumes that the ion temperature is comparable to that of the electrons.

In conclusion it seems to be justified to state that the beam divergence lies in the range 50 - 70 mrad. Although this value exceeds the anticipated design value of 30 mrad by about a factor of 2, the beam transport is nevertheless satisfactory since the mechanism of beam space charge neutralisation has been optimized:

**Beam space charge (BSC) neutralization.** This point is described in detail in companion paper [1].

In the presence of the magnetic compression field, the BSC neutralization is provided by sec. emission electrons from the cathode grids. Provided that the grids are appropriately biased:

$-U_{G1} \geq -1\text{kV}$ ,  $-U_{G2} = -100 \div -300\text{V}$ ,  
sec. electron emission from these is sufficient for full BSC neutralization. Close to the beam axis, electrons expand over the full length of the focusing channel within  $2 \div 2.5 \mu\text{s}$ , creating an electric field of sufficient strength to confine the protons inside the focusing channel. Full neutralization of the BSC is achieved after 5  $\mu\text{s}$ .

**Beam composition.** This point is described in detail in companion paper [2].

The information on beam composition was obtained using time of flight diagnostics. It was found that protons can represent the predominant beam component, if in the beginning and periodically after each 100 shots, the anode polyethylene plugs are mechanically cleaned by cutting off a surface layer of around 0.5 mm thickness. Operation using a discharge current exceeding a certain threshold value ( $\approx 5\text{A}$ ) also increased the proton contents of the beam.

**Efficiency of beam transport and focusing.** The beam transport efficiency  $I_T^i/I_i$ , where  $I_T^i$  is the ion current on the target and  $I_i$  is the beam current penetrating the focusing channel, is found to be close to 100%, after a delay of  $2 \div 2.5 \mu\text{s}$  counted from the beginning of the anode pulse.

Using alternatively a TEC or an array of small calorimeters (Fig. 8), the beam ra-



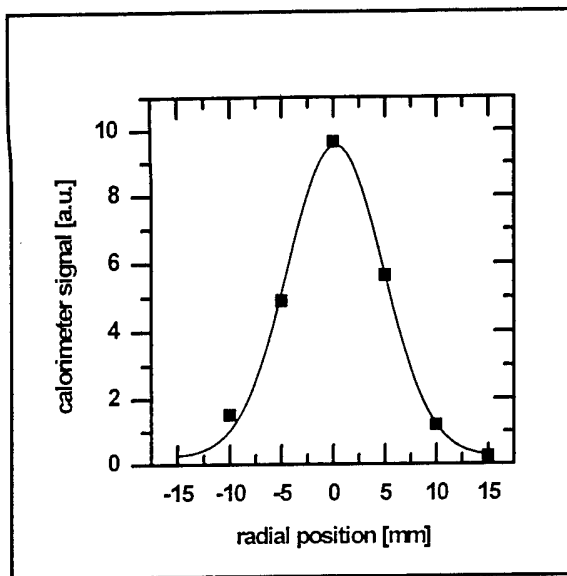


Fig. 7: Radial beam profile in the target plane.

dus in the target plane was found to be in good agreement with calculated predictions. Quantitative measurements of the target current density using the TEC were impeded e.g. by beam induced plasma formation inside the TEC, frequently leading to premature discharge of the intermediate electrode biasing capacitor. The information so far available is therefore of approximate character. Use of  $U_a = 20\text{kV}$  and  $R_a = 8\ \Omega$ , resulted in a diode current of  $\approx 60\text{A}$ , a current penetrating the compression channel of  $\approx 35\text{A}$  and led to ion current densities in the target plane of  $15 \div 25\text{A/cm}^2$ .

**Alternative use of the PROFA ion source.** The described ion source can not only be applied for the production of protons but also for other kinds of ions, in particular carbon and metal ions or even mixed ion species. For this purpose the polyethylene plugs are removed from the ADE and needle electrodes are installed that consist of a material corresponding to the ions of interest.

#### 4. CONCLUSIONS

1) The ion source developed here provides a large area proton beam with a current density  $j_i > 0,1\text{ A/cm}^2$  and a pulse duration  $\tau$  in the microsecond range ( $\tau \leq 10\ \mu\text{s}$  when  $j_i \geq 0,1\text{ A/cm}^2$ ). For lower currents, pulse lengths of up to  $40\ \mu\text{s}$  were obtained,

limited only by the capability of the pulse power supply. The design of the source allows to easily increase the beam cross section to  $10^4\text{cm}^2$ .

2) The total divergence of the beam is still rather high:  $50 \div 70\text{ mrad}$ .

3) The source can be used for obtaining different kinds of ions, in particular, carbon, metal and also mixed ions.

4) Suitable conditions were found for neutralization of the beam space charge in the focusing channel, providing high efficiency of beam transportation and focusing. Apparently, the radial electrical field produced by the ion-accompanying electrons improves beam focusing.

5) The operating conditions that lead to a high content of protons in the beam were identified.

6) Extrapolation of the results found up to now on the PROFA facility to the full scale reference design KANDIS would result in a target power density of  $\approx 7\text{MW/cm}^2$  for a pulse length of  $10\ \mu\text{s}$ .

7) Residual problems that have to be solved are the following:

- Improvement of the homogeneity of the anode (emitting) plasma;
- Increase of the cathode unit transparency;
- Clarification of the mechanism of the pulse duration restriction in the high current density operating regime.

#### 5. REFERENCES

- [1] V. Engelko et al; 'Measurement of extent of intense ion beam charge neutralization', this conference.
- [2] V. Engelko et al; 'Investigation of the composition of an ion beam produced using a multi arc ion source', this conference.
- [3] V. Engelko, V. Kuznetsov, G. Vjazmenova, H. Wuerz, 'Compression of intense proton beams', Proc. Beams '94, San Diego 1994
- [4] V. Engelko, H. Giese, S. Schalk, Ch. Schultheiss, H. Wuerz, 'Pulse intense proton beam facility for ITER disruption simulations', Proc. Beams '94, San Diego 1994
- [5] V. Engelko et al, 'Generation and Focusing of an Intense Long Pulse Proton Beam', IEEE Int. Conf. on Plasma Science ICOPS'95, Madison, Wisconsin, USA, June 5-8, 1995, Book of Abstracts, p. 289.

## Uniform Current Density and Divergence Control in High Power Extraction Ion Diodes\*

M. P. Desjarlais, R. S. Coats, T. R. Lockner,  
T. D. Pointon, D. J. Johnson, S. A. Slutz, R. W. Lemke,  
M. E. Cuneo, and T. A. Mehlhorn

*Sandia National Laboratories  
P. O. Box 5800  
Albuquerque, New Mexico 87185 USA*

### Abstract

A theory of radial beam uniformity in extraction ion diodes is presented. The theory is based on a locally one dimensional analysis of the diamagnetic compression of magnetic streamlines and the self consistent determination of the virtual cathode location. The radial dependence of the applied magnetic field is used to determine the critical parameters of this locally one dimensional treatment. The theory has been incorporated into the ATHETA magnetic field code to allow the rapid evaluation of realistic magnetic field configurations. Comparisons between the theoretical results, simulations with the QUICKSILVER code, and experiments on the PBFA-X accelerator establish the usefulness of this tool for tuning magnetic fields to improve ion beam uniformity. The consequences of poor beam uniformity on the evolution of ion diode instabilities are discussed with supporting evidence from simulations, theory, and experiments.

### Introduction

In recent years our understanding of the mechanisms which generate beam divergence in applied- $B$  ion diodes has greatly improved. Electromagnetic instabilities in the diode gap are recognized to be a primary cause of the beam divergence. The spectrum of fluctuations in the acceleration gap is believed to be dominated by two instabilities, the diocotron instability,<sup>1</sup> and the ion mode instability.<sup>2-7</sup> The diocotron instability has the higher frequency and is less damaging to the ion beam. The ion mode instability locks in on the ion transit time and causes unacceptably large divergences.<sup>3,4</sup> As power is fed to the diode, the diocotron mode generally appears first and generates what can be an acceptably low divergence. If no attempts are made to halt or slow the expansion of the electron sheath towards the anode, the ion mode follows quickly. Two methods of limiting the expansion of electrons are to use very high magnetic fields or to use a small non-emitting, electron collecting protrusion or blade on the anode called a limiter.<sup>8</sup> It has been shown with 3-D QUICKSILVER<sup>9</sup> simulations that the onset of the ion mode may be delayed or prevented by these methods.<sup>3,4</sup> Experiments at FZK in Karlsruhe, Germany and at Cornell University in the United States, have shown that the beam divergence can be reduced with the use of an electron limiter or high fields.<sup>10,11</sup> One striking difference between the ion mode and the diocotron mode is the symmetry of the wave. The ion mode, as observed in simulations and experiments, exhibits strong variations in amplitude along the magnetic field direction and the diocotron is very uniform<sup>12</sup> along the field. Figure 1 shows data from PBFA II shot 6711. Five sets of Faraday cups (top and bottom) were arranged in azimuth over one

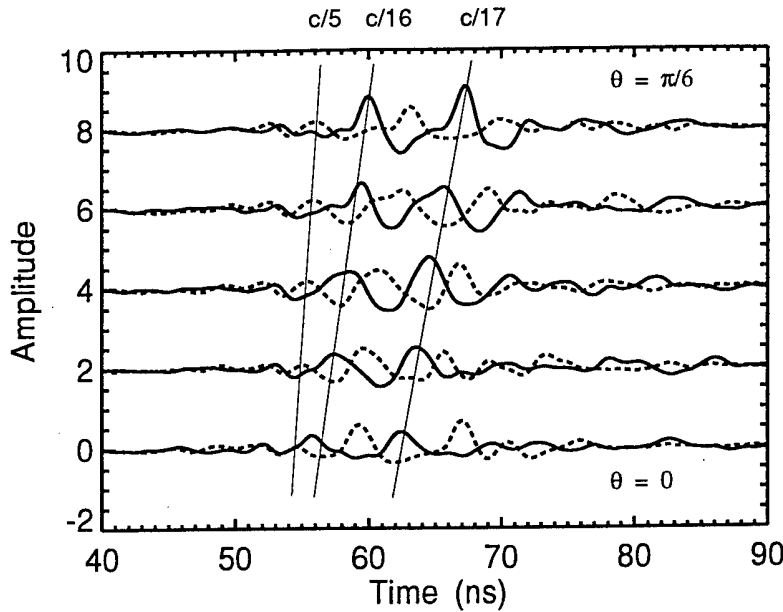


Fig. 1. The Faraday cup oscillations about the mean for PBFA II shot 6711. The solid line is from the top side of the diode, the dotted line is from the bottom. The wave has a phase velocity of approximately  $c/16$  after approximately  $t=55$  ns.

twelfth of the diode circumference. The data indicates an oscillation in the ion beam current density that breaks the symmetry between the top and bottom halves of the diode and has a low phase velocity, consistent with the ion mode. This breaking of the symmetry between the top and bottom halves of the diode has recently been observed in QUICKSILVER simulations<sup>12</sup> in good agreement with the experimental results. These observations are supported by theoretical work that establish the stronger growth of ion mode perturbations with variations along the applied magnetic field.<sup>5-7</sup> Figure 2 shows results from Ref. 7 indicating higher growth rates and lower phase velocities for ion modes with perturbations along the magnetic field. It has been observed in 3-D simulations that if the ion beam profile is not sufficiently uniform in the direction of the applied field, the ion mode is stimulated, grows rapidly, and causes large divergence under conditions that would otherwise favor the diocotron and lower divergences.<sup>12</sup>

The preferred applied- $B$  ion diode configuration for the generation of light ion beams is the extraction geometry; the insulating magnetic field is predominately radial and the ion beam propagates primarily in the axial direction. A critical factor in the performance of applied- $B$  ion diodes is the limiting voltage  $V_*$ , which is proportional to the applied magnetic flux between the virtual cathode and the anode.<sup>13</sup> The prevailing  $1/r$  dependence of the applied magnetic field in the extraction configuration implies a lower  $V_*$  at larger radii. As the voltage is raised,  $V_*$  is approached more closely at larger radii. If the applied field is parallel to the anode when the diode voltage is zero, the diamagnetic compression of the field will be greater at larger radii as the voltage rises, leading to a skewing of the beam to larger radii. This asymmetry of the ion beam profile would favor the development of the ion mode. If progress is going to be made in reducing the divergence of ion beams in extraction diodes, it appears that control of the beam uniformity will be an essential component. The tendency for a purely radial magnetic field to skew the beam to larger radii can be compensated for

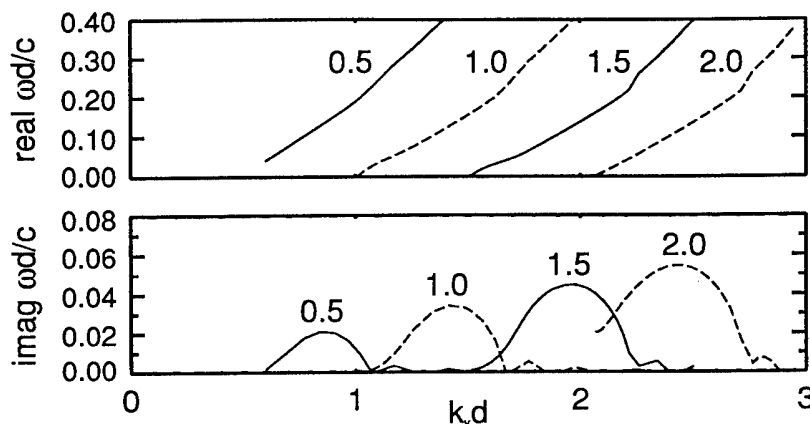


Fig. 2. The real and imaginary frequency components for ion mode perturbations as a function of the wavenumber perpendicular to the applied field  $k_y d$ . The numbers above each curve correspond to the wavenumber along the magnetic field  $k_z d$ .

by the choice of an appropriate tilt of the applied field towards the anode at smaller radii. In essence, the greater diamagnetic compression at larger radii is compensated for by moving the electrons closer to the anode with the applied field at smaller radii.

In the past, we have attempted to produce centered, uniform beams through an often tedious process of trial and error. In this paper we introduce a theoretical treatment of the beam uniformity problem for extraction diodes. Examples of this analysis as employed in the ATHETA<sup>14</sup> magnetic field code using actual diode fields are shown along with comparisons with experiments on the PBFA-X accelerator and simulations with the QUICKSILVER 3-D particle-in-cell simulation code.

### Extraction Diode Geometry

A simple drawing of an extraction diode is shown in Fig. 3. The geometry is cylindrical with the anode at  $z=0$ . The voltage is applied by a TEM pulse in the magnetically insulated transmission line (MITL). An axial electric field develops in the diode and electrons are pulled off the cathode tip. A strong magnetic field is used to inhibit the flow of electrons to the anode. In an extraction diode the magnetic field is predominately radial and this induces the electrons to  $\mathbf{E} \times \mathbf{B}$  drift in the  $\hat{\theta}$  direction. This rotating cloud of electrons forms a virtual cathode that defines the acceleration gap for ions drawn off the anode surface. The virtual cathode surface coincides with the magnetic streamline that passes through the cathode tip. The ions travel in the  $\hat{z}$  direction. The magnetic field is provided by two cathode coils, on both sides of the extraction region, and in some diodes, another pair of coils on the anode side as well. Shown in Fig. 4 are example applied magnetic field streamlines for a diode with anode and cathode coils. In order to focus the ions on the centerline, the angular momentum of the ions must be zero. The anode coils are particularly useful in compensating for the diffusion of magnetic field into the anode surface and any charge stripping considerations in order to satisfy this constraint.

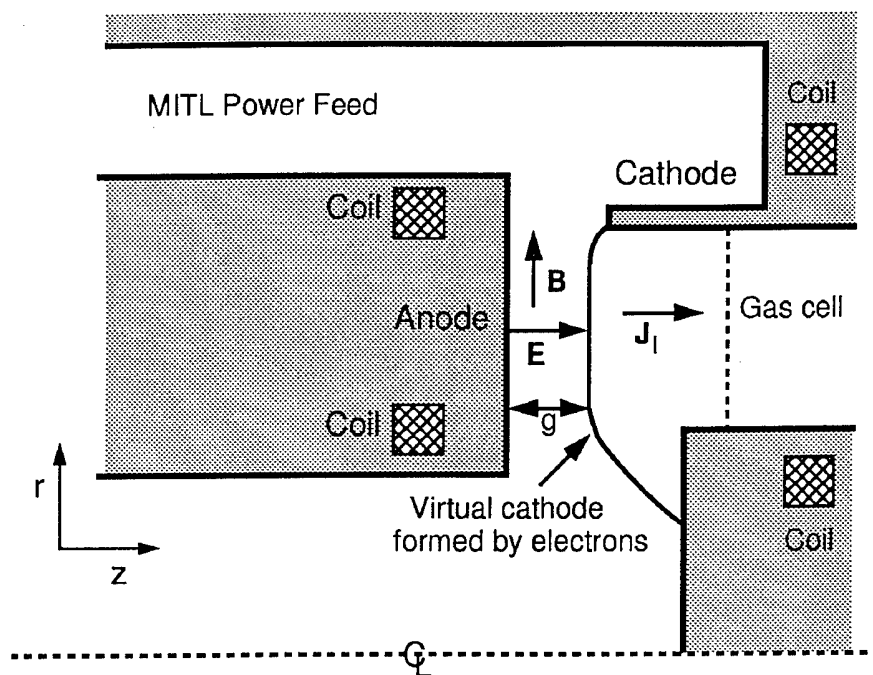


Fig. 3. The extraction diode geometry and coordinate system.

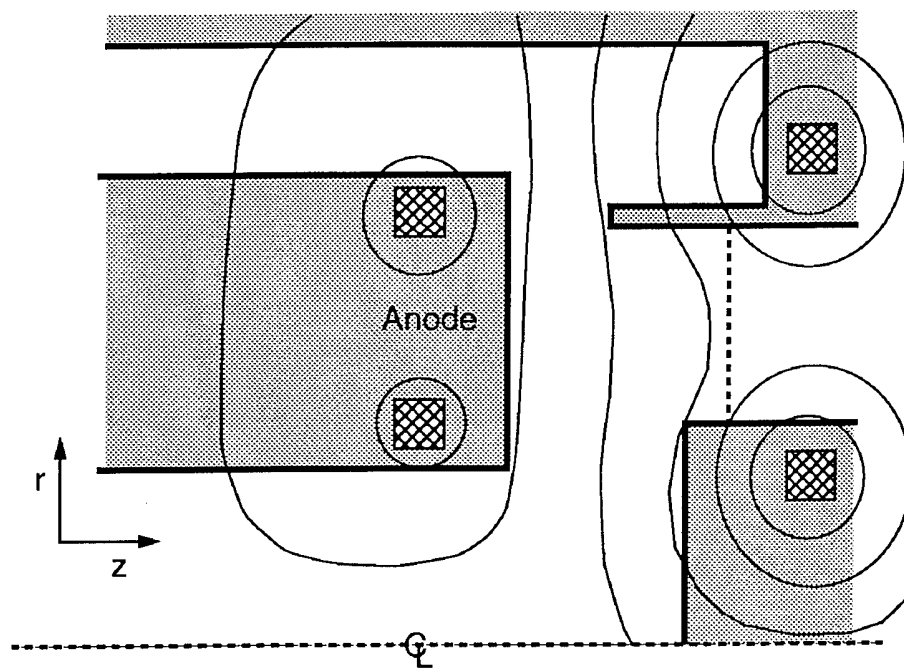


Fig. 4. A representation of the applied magnetic field streamlines for a diode with anode and cathode coils.

### Extraction Diode Theory

A theory of applied- $B$  diode operation is detailed in Ref. 13. In that treatment, the diode parameters are assumed to be uniform over the face of the anode. Here we need to take into account the radial variations inherent in the extraction geometry. The

most significant radial variation is that of the magnetic field.

A brief summary of the results of Ref. 13 may be useful here. The virtual cathode is defined by the magnetic flux surface that passes through the cathode tip. For a given distribution of electrons in the gap and a given magnetic flux between the cathode and anode, there is a limiting voltage  $V_*$  where the self-consistent virtual cathode position approaches the anode. As  $V \rightarrow V_*$  the acceleration gap shrinks to zero and the ion current diverges. This motion of the virtual cathode can be easily understood in terms of the pressure balance in the diode. In steady-state, the total particle and electromagnetic pressure terms must be in balance:

$$\frac{B^2}{2\mu_0} - \epsilon_0 \frac{E^2}{2} + \sum_{e,i} n M v^2 = \text{Constant.}$$

The electron pressure is usually negligible because of the electron's small mass. For space-charge-limited conditions on the anode and cathode, the electric field terms vanish there. Since the ions are born with zero velocity, they contribute zero pressure to the anode side of the gap. Equating the remaining pressure terms on the anode and cathode gives

$$\frac{B_a^2}{2\mu_0} = \frac{B_c^2}{2\mu_0} + J_i \sqrt{\frac{2M}{q}} V, \quad (1)$$

where  $B_a$  is the anode magnetic field,  $B_c$  is the cathode magnetic field (weakly varying),  $J_i$  is the ion current density,  $M/q$  is the ion mass to charge ratio, and  $V$  is the diode voltage. The second term on the right is just the ion stagnation pressure  $n_i M v_i^2$  rewritten in terms of  $J_i$ . The dynamic gap is referred to here as  $g$  and the initial insulating magnetic flux as  $\psi_0$ . The term on the left will scale as  $(\psi_0/g)^2$  because of flux conservation. The ion pressure term will scale as  $(V/g)^2$  because of the Child-Langmuir dependence of current on voltage. Since  $\psi_0$  is fixed, as the voltage increases the gap  $g$  must get smaller to maintain pressure balance, ultimately going to zero at the voltage where the ion pressure term approaches the anode magnetic pressure term. In this fashion the limiting voltage  $V_*$  is proportional to the applied magnetic flux in the diode. At voltages well below the limiting voltage, the diamagnetic effects scale like  $(V/V_*)^2$ . In the limit  $V \rightarrow 0$  the ion current is proportional to the Child-Langmuir current. The proportionality constant depends on the shape of the electron density profile in the gap, 1.0 for a  $\delta$ -function distribution at the virtual cathode and 5.5 for a flat distribution between the virtual cathode and the anode. The limiting voltages are  $0.75c\psi_0$  and  $0.6c\psi_0$  respectively. The critical voltage for electron insulation  $V_{\text{crit}}$  is approximately  $c\psi_0 - 0.5 \text{ MV}$ .

In Ref. 13, the electron distribution is modeled as a flat density profile that encompasses a fraction of the dynamic gap given by  $\rho g$ , with the two limits  $\rho = 0$  and  $\rho = 1$  corresponding to the extremes just described. It has been shown with 3-D QUICKSILVER simulations that the electron sheath generally starts out very thin and is well approximated by the  $\rho = 0$  or superinsulated limit, but that in response to the symmetry breaking instabilities, broadens out until electrons are collected on the anode, behaving more like the  $\rho = 1$  or saturated limit.<sup>4</sup> For the extraction diode we need to specify the corresponding parameters  $\rho(r)$  and  $\psi_0(r)$  to account for the radial variations.

As the electrons are diffusing across the magnetic flux surfaces, they are also moving in and out radially along flux surfaces, often with an energy that is a sizeable fraction of the gap energy  $eV$ . If electrons migrate to a flux surface that intersects the anode at some point, it is likely that those electrons will be lost to the anode. Consider the magnetic field shown in Fig. 4. As electrons diffuse across flux surfaces, they are likely to first encounter the anode at the inner radius. If we model the diode locally using the set of flat electron distributions introduced in Ref. 13, the inner radius would be modeled by  $\rho = 1$  because the electrons would make it all the way to the anode at that point. Other radii would be modeled by a value of  $\rho$  that is close to, but slightly less than 1. This is the basis for our extraction diode theory. At each value of  $r$  the parameter  $\rho(r)$  is taken to be the fraction of the initial gap flux between the virtual cathode streamline and the first streamline to intersect the anode at some point on or near the emission surface. The sheath profile function  $\rho(r)$ , the applied flux between the virtual cathode streamline and the anode  $\psi_0(r)$ , and the location of the virtual cathode streamline (at zero voltage) are all that are needed to apply the analysis from Ref. 13 for each radial position. Note that the diode voltage must be lower than the minimum value of  $V_*(r)$  across the anode.

### ATHETA Modeling

The analysis described above has been incorporated into the ATHETA magnetic field code. Diffusive calculations with the DATHETA<sup>14</sup> code are used to generate the fields for each individual coil as a function of time, providing a basis set of fields that can be read into ATHETA. The amplitudes of each basis field component can be specified independently. Once a complete magnetic field set is chosen, ATHETA finds the virtual cathode streamline position by following the magnetic field from the cathode tip and also finds the function  $\rho(r)$  by finding the first streamline to intersect the anode as approached from the cathode side. ATHETA also finds the critical voltage for electron insulation  $V_{\text{crit}}(r)$ , or equivalently  $\psi_0(r)$ . A subroutine containing the analysis described above rapidly computes the predicted ion beam profile consistent with the total integrated current and accelerator load line. The effects of numerous combinations of anode and cathode coil currents can be quickly evaluated. Examples of predicted beam profiles from ATHETA are shown in Fig. 5. The profile indicated by the solid line corresponds to a zero trim case for a PBFA-X diode. The ions species is lithium and the diode voltage is approximately 6.5 MV. The minimum  $V_{\text{crit}}(r)$  is approximately 10 MV in each case, but the location of the minimum varies with the coil currents. The cathode tip is 1.5 cm from the anode surface. A 6 MV/cm field emission threshold on the anode is used to model emission from LiF. The predicted profiles for space-charge-limited emission are generally much less peaked. The dashed line shows the effect of a 14.8% reduction in the inner coil current (negative trim). The profile indicated by the dot-dashed line shows the effect of an 11.4% reduction in the outer anode coil current (positive trim). The more highly enhanced the ion current density is above the Child-Langmuir current density, the more sensitive the profile is to slight changes in the trim. Figure 6 gives an indication of the degree of uniformity possible, at least within the context of the theory. This profile was obtained by adding an additional anode coil between the inner and outer anode coils. The extra anode coil provided a degree of tuning not possible with just the two existing anode coils. The current in the auxiliary anode coil was about 16% of the current in the outer coil

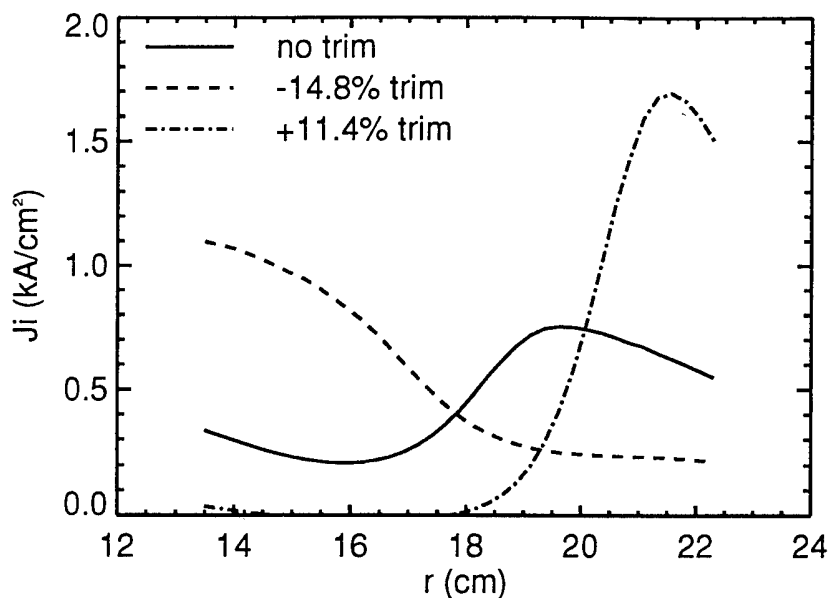


Fig. 5. The predicted beam profile from ATHETA for zero, -14.8 and 11.4 percent trim. The ion species is lithium and the diode voltage is about 6.5 MV. A 6 MV/cm field emission threshold is used to model LiF.

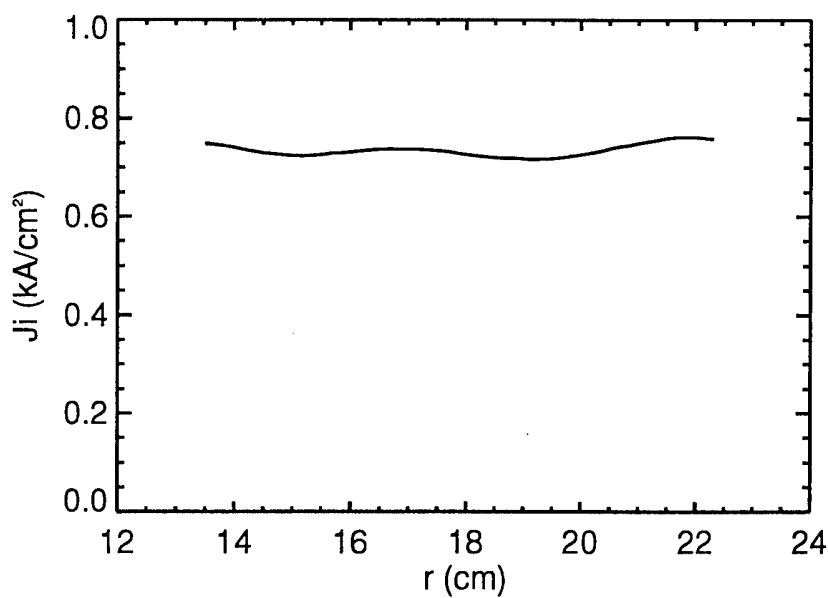


Fig. 6. An example of an optimized field profile for the same diode as modeled in Fig. 5. An auxiliary anode coil carrying 16% of the outer anode current was used to help tune the beam profile. The ion emission is space-charge-limited.

for a comparable number of turns. In addition the ion emission was assumed to be space-charge-limited.



## Comparisons with Experiments and Simulations

As a test of this analysis, we performed experiments on the PBFA-X accelerator. Five operating points were examined with two shots per operating point. In these experiments, each pair of anode and cathode coils were in series. The anode coil currents could be varied from one another by the use of a trim coil in parallel with either the inner or outer anode coil. This relative imbalance is referred to as the trim and is given by  $(I_{inner} - I_{outer})$  divided by the maximum of  $I_{inner}$  and  $I_{outer}$ . If the trim coil is in parallel with the inner coil, the trim is negative. Conversely for the outer coil. This convention is useful because positive trim will tend to move the beam outwards and negative trim will tend to move the beam inwards. In each case, the current in the untrimmed coil is kept at the nominal zero trim level. No attempt was made to keep  $V_{crit}$  constant.

Figure 7 shows the results of these experiments plotted as the mean beam radius relative to the mean anode radius versus the percentage of trim. The experimental radius information was obtained using an array of Faraday cups in the extraction region of the diode. With the exception of one errant data point, the experimental points are well grouped, indicating a good degree of repeatability. Also included in Fig. 7 are results from simulations with the QUICKSILVER 3-D particle-in-cell code and two sets of points from theoretical calculations. The simulations were performed for the zero trim case, the 14.8% negative trim, and the 11.4% positive trim. The simulation results are in good agreement with the experimental results. The theoretical points marked with the crosses are predicted values obtained before the experiments. The predicted points are skewed to the outer radii relative to the experimental points for the zero and negative trim cases. This suggests that the theory underestimates the electron space-charge contribution on field lines close to the anode at smaller radii. The flat electron density profile used in the theory is less weighted towards the anode than the profiles observed in simulations.<sup>4</sup> The theoretical points marked with the circles were obtained after the experiments by normalizing one operating point to the upper experimental point at zero trim. The normalization consisted of a 7.5% increase in the outer anode coil current to shift the beam towards smaller radii and an adjustment to the diode operating point to account for differences between the experiments and the calculations. The rest of the adjusted theoretical points fall into place using the same normalization. This suggests a systematic shortcoming of the theory, most likely in the electron profile model, but also points out the improvement in accuracy if the theory is normalized to experimental points. In practice we have done just that, used the theory to predict initial operating points, and then normalized the theory to predict subsequent operation with very good success. A snapshot of the three simulation beam profiles around the time of peak ion current are shown in Fig. 8. The simulation profiles are rounded at the edges. This is expected from edge effects, such as magnetic tension terms, that are not included in the theory.

We have used this analysis to design a simulation of an extraction diode with a limiter. The fields used are realistic fields as opposed to the idealized fields used in earlier work.<sup>15</sup> Nonuniformities in the ion beam current associated with realistic magnetic fields have made confirmation of the earlier results with idealized magnetic fields very difficult. The beam uniformity algorithm in ATHETA was used to design a magnetic field for very good uniformity. In this particular case, an additional cathode

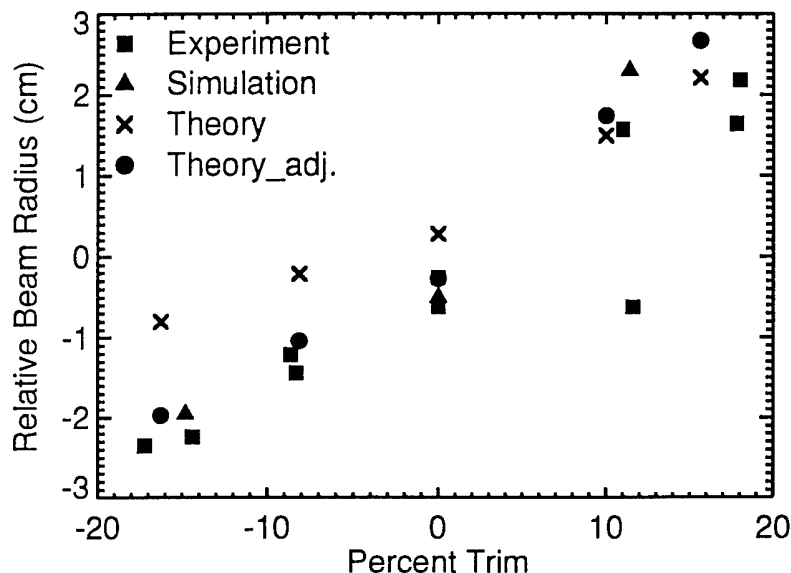


Fig. 7. Data from experiments compared with results from QUICKSILVER simulations and ATHETA calculations.

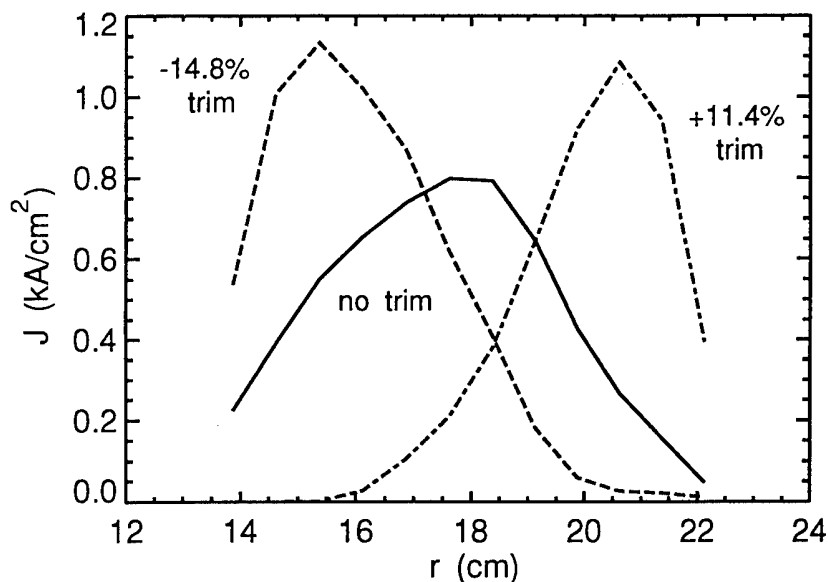


Fig. 8. The beam profile as a function of radius for the three simulation points in Fig. 7.

coil was employed to improve the uniformity. (A limited set of simulations without the auxiliary coil had poorer predicted uniformity and did not show successful suppression of the ion mode.) The predicted beam current density with the extra cathode coil varied by less than  $\pm 10\%$  across the anode and was symmetric. The simulation showed a persistent diocotron oscillation and did not make a transition to the ion mode. The divergence was maintained at about 9 milliradians.

## Conclusion

A theory of extraction diode operation has been developed that uses details of the magnetic field configuration to determine the parameters of a locally one dimensional model for each radial position in the diode. The total current is obtained by integrating over the anode surface and a load line calculation determines the voltage. This analysis provides a radial current density profile for a given magnetic field configuration, ions species, and diode voltage. By including this analysis in the ATHETA magnetic field code, we can rapidly evaluate realistic magnetic field configurations for predicted beam uniformity and tune the magnetic field for improved uniformity. The results of these calculations have been shown to be in good agreement with results from experiments on PBFA-X and simulations with the QUICKSILVER 3-D particle-in-cell code. This tool works best when it can be normalized to experimental data. We have used this analysis to design a magnetic field which allowed the suppression of the ion mode in a simulation of an extraction diode with realistic magnetic fields and an electron limiter. The ion divergence in the simulation remained below 10 milliradians.

## Acknowledgment

This work was supported by the US/DOE under contract No. DE-AC04-94AL85000.

- [1] O. Buneman, R. H. Levy, and L. M. Linson, J. Appl. Phys. **37**, 3203 (1966).
- [2] C. L. Chang, D. P. Chernin, A. T. Drobot, E. Ott, and T. M. Antonsen, Jr., Phys. Fluids **29**, 1258 (1986).
- [3] M. P. Desjarlais, T. D. Pointon, D. B. Seidel, R. S. Coats, M. L. Kiefer, J. P. Quintenz, and S. A. Slutz, Phys. Rev. Lett. **67**, 3094 (1991).
- [4] T. D. Pointon, M. P. Desjarlais, D. B. Seidel, S. A. Slutz, R. S. Coats, M. L. Kiefer, and J. P. Quintenz, Phys. Plasmas **1**, 429 (1994).
- [5] R. N. Sudan and D. W. Longcope, Phys. Fluids B **5**, 1614 (1993).
- [6] R. W. Lemke and S. A. Slutz, Phys. Plasmas **2**, 549 (1995).
- [7] S. A. Slutz, R. W. Lemke, T. D. Pointon, M. P. Desjarlais, D. J. Johnson, T. A. Mehlhorn, A. B. Filuk, J. E. Bailey, Phys. Plasmas **3**, 2175 (1996).
- [8] S. A. Slutz, T. A. Mehlhorn, J. E. Maenchen, C. Ruiz, and J. R. Woodworth, J. Appl. Phys. **62**, 16 (1987).
- [9] D. B. Seidel, M. L. Kiefer, R. S. Coats, T. D. Pointon, J. P. Quintenz, and W. A. Johnson, in *Computational Physics*, edited by A. Tenner (World Scientific, Singapore, 1991), pp. 475-482.
- [10] H. Bluhm, P. Hoppe, H. Bachmann, W. Bauer, K. Baumung, L. Burth, H. U. Karow, H. Laqua, D. Rusch, E. Stein, and O. Stoltz, in *Proceedings of the 9th International Conference on High-Power Particle Beams*, Washington, DC, May 1992, p. 51.
- [11] J. B. Greenly, C. K. Struckman, B. R. Kusse, and W. A. Noonan, in *Proceedings of the 9th International Conference on High-Power Particle Beams*, Washington, DC, May 1992, p. 43.
- [12] T. D. Pointon and M. P. Desjarlais, J. Appl. Phys., to be published 8/96.
- [13] M. P. Desjarlais, Phys. Fluids B **1**, 1709 (1989).
- [14] J. P. Quintenz, D. B. Seidel, M. L. Kiefer, T. D. Pointon, R. S. Coats, S. E. Rosenthal, T. A. Mehlhorn, M. P. Desjarlais, and N. A. Krall, Laser Part. Beams **12**, 283 (1994).
- [15] M. P. Desjarlais and T. D. Pointon, in *Proceedings of the 9th International Conference on High-Power Particle Beams*, Washington, DC, May 1992, p. 775.

## Anode Plasma Dynamics in an Extraction Applied-B Ion Diode: Effects on Divergence, Ion Species and Parasitic Load\*.

J. B. Greenly, R. K. Appartaim, J. C. Olson

*Laboratory of Plasma Studies, Cornell University, Ithaca, N.Y. 14853 USA*

Analysis of data from the LION (1.2MV, 300kA, 40ns) extraction applied-B diode [1] allows a number of inferences regarding the effects of anode plasma dynamics on ion beam divergence, ion species composition, and diode impedance and power coupling. In-gap emission spectroscopy and beam diagnostics [1] have been used to investigate the mechanisms which determine anode plasma dynamics and its effects on diode performance. The two dominant features of anode plasma dynamics observed on LION are (1) expansion away from the solid anode surface and into the accelerating gap during the beam pulse, and (2) evolution of the composition of the plasma during the pulse, with a strong increase of both neutrals and high charge states of heavier ion species during the latter part of the pulse. A previous paper [1] has presented the data that support conclusion (2). In this paper, we present data characterizing the plasma expansion, and suggest a possible picture of the mechanism of the plasma dynamics that could produce these basic features.

Figure 1 shows anode plasma spatial extent as a function of time for typical LION diode regimes, as derived from streak photography of anode plasma light, and diode impedance evolution with time. The model used to relate diode impedance to the effective anode location on the gap is that of Desjarlais [2], assuming that the effective anode surface where the electric field vanishes (space-charge limited emission) is the "edge" of the anode plasma, and that magnetic flux fully penetrates the plasma. A set of diode current-voltage characteristics for LION derived from this model are shown in Figure 2.

The assumption of flux penetration is central to the arguments to follow. The diode characteristic is strongly modified, especially at high ion current density enhancement, and strong heating of the plasma may occur. Flux penetration would occur under a number of scenarios: if the plasma edge moves across the field by motion of neutral particles with subsequent ionization as has often been proposed, or if the effective resistivity is high enough for the rising magnetic field due to compression of the insulating flux toward the anode by the diamagnetic cathode electron flow to penetrate. The necessary resistivity may be supplied by neutral collisions, or by anomalous processes such as fast EMHD penetration. Krall [3] has considered lower hybrid drift turbulence as a dissipation mechanism, and there may be others. Whatever the mechanism, if rising field penetrates on a time scale of a fraction of the diode current risetime, a substantial amount of energy would be dissipated in the plasma. For parameters typical in a LION pulse, penetration of a 1T field on a 10 ns timescale results in  $>10^8$  W dissipated in the plasma. Radiation and conductive and convective loss to the anode surface would absorb most of this power, heating the solid surface. Furthermore, during penetration there will be a magnetic field gradient in the plasma and hence a force on the plasma which will tend to compress it toward the anode during the current rise. On the other hand, if penetration is nearly instantaneous, almost no force and no heating would occur. Thus a measurement of the magnetic field in the anode plasma would be a very valuable input into understanding the dynamics of the plasma and its possible influence on diode performance.

In Fig. 1, we see that the anode motion inferred from the model assuming penetration tracks with but exceeds the motion inferred from plasma light. This is not surprising, since the latter is certainly only a lower limit: if the effective anode occurs at a plasma density which has luminosity below the threshold of streak sensitivity, the streak data will underestimate the plasma thickness. The velocity of compression of flux surfaces toward the anode during current rise is  $\sim 10$ cm/ $\mu$ s, so if the field was strongly excluded by the

plasma, it would be very difficult to explain the plasma expansion during the current rise, yet the impedance model would require even greater expansion if flux was excluded. Thus the similar expansion inferred from both model and streak data gives some degree of confidence that the magnetic field does penetrate the plasma on a time scale shorter than the current risetime. Unfortunately, these considerations do not give enough information to estimate the actual penetration rate or consequent force or power dissipation on the plasma.

Figure 1 shows a characteristic evolution of the plasma thickness that was universally observed on LION. The plasma expands rapidly, at  $>5\text{cm}/\mu\text{s}$  for the first  $\sim 10\text{-}20\text{ns}$  of the beam pulse. Expansion then slows or even stagnates for  $\sim 20\text{ ns}$  through the main current rise to peak beam power. Then, as the diode voltage and current decline, rapid expansion resumes, at a rate that can approach  $10\text{cm}/\mu\text{s}$  in highest current shots with strong parasitic load. This resumption of expansion is coincident with the increase of strong neutral emission lines in the plasma, as well as lines of high charge states of ions such as carbon and oxygen [1]. In the remainder of this paper, we outline a model of, or more properly a set of questions about, the anode plasma dynamics which may explain these observations, and briefly indicate some implications of this model for overall diode performance. To summarize the observations to be explained, the LION data have shown:

- 1) Initial fast expansion of the anode plasma.
- 2) early high energy (cathode) electron loss, which peaks during the interval of fastest current rise, then nearly disappears after peak power. The electron loss is nearly the same in parasitic and nonparasitic regimes.
- 3) a stagnation of plasma expansion during fastest current rise to peak power.
- 4) rapid plasma expansion as current falls to the end of the pulse, somewhat faster in strong parasitic load regime.
- 5) during current fall, rapid increases in neutrals and high ion charge states within  $0.5\text{mm}$  (diagnostic resolution) of the plasma edge, but not beyond into the gap.

The proposed model contains the following elements:

- 1) The initial fast expansion of the plasma is an outstanding question. The initial sources of plasma may be cathode loss electron-induced desorption, dielectric breakdown due to charge deposition, surface flashover driven by the applied electric field, etc. Whatever the source, the rapid expansion requires a strong heating of the vaporized anode material to a velocity of  $5\text{ cm}/\mu\text{s}$ , requiring  $>10\text{eV}$  energy for at least some component of this material. This heating may be due to a combination of previously proposed mechanisms, e.g., by cathode electron bombardment, instability of diamagnetic surface current flow in the plasma[2], or dissipation due to conduction of the ion beam current back to the surface through the plasma. However, it appears difficult to reach the necessary velocity by thermal means. One simple alternative which has not been considered is suggested if one assumes that the initial efflux of plasma from the surface is very weakly ionized. When this material extends  $1\text{ }\mu\text{m}$  above the solid surface, until the electrons exceed  $5 \times 10^{13}/\text{cm}^3$  density and  $1\text{eV}$  temperature, the Debye shielding length is longer than the plasma thickness. This means that the gap electric field penetrates this layer. Even if space-charge limited ion flow is already taking place, reducing the field to zero at the solid surface, the voltage drop across this  $1\text{ }\mu\text{m}$  is  $>10\text{V}$ . If the neutral density is much larger than the ion density, the substantial rate of charge exchange could produce a fast neutral flux that can move into the gap at the observed velocity. Also, if the layer is very nonuniform, localized "blobs" of plasma with ions accelerated in this way could move across the magnetic field by polarization drift. In either case, the acceleration that causes plasma expansion would come not from heating, but from electrostatic force on the plasma ions.

- 2) After the initial fast expansion phase, the plasma does exclude the electric field except in a thin sheath, but neutrals can still be transported from the solid surface through the anode plasma and then ionized at or beyond the effective anode surface in a fraction of the pulse length. Collisional equilibration time of neutrals with plasma ions (including elastic collisions and charge exchange) is short compared to ionization time by the low energy

plasma electrons, and neutrals can acquire the necessary velocity to traverse the  $\sim$ mm thickness of the plasma in times shorter than the pulse length.

3) The key element of this model is that there exists an avalanching ionization mechanism just outside the plasma edge, driven by trapped electrons originating from neutrals ionized as they pass through the edge. When an ionization occurs in the gap near the edge, the resulting ion is extracted in the beam, and the electron is accelerated toward the anode. Electrons originating in this way are well trapped in the electric and magnetic fields of the gap and the magnetic field in the plasma, in orbits which remain in the neighborhood of the plasma edge. The energy of these electrons depends on their point of origin: the further out in the gap, the higher the energy. For example, with  $1\text{ kA/cm}^2$  at  $1\text{ MV}$ , the average energy of electrons born in the first  $0.1\text{ mm}$  away from the plasma edge (assuming that the space charge of these electrons does not strongly perturb the gap electric field) is about  $1.4\text{ keV}$ , and the distribution ranges up to  $15\text{ keV}$ . The CV lines observed in LION late in the pulse confirm the presence of a substantial population of at least  $300\text{ eV}$  electrons. This population has much larger cross section for ionization of neutrals and ions than the  $\text{MeV}$  cathode electrons, and an ionization avalanche can result, limited by the rate of loss of these electrons to the anode. Welch [4] has carried out simulations that show this avalanching.

To understand the dynamics of these electrons, a fundamental condition in the diode must be recognized. The amount of charge extracted in the beam ( $\sim 10^{14}$  electron charge/cm $^2$  in  $30\text{ ns}$ ) is much larger than the amount of net polarization charge ( $\sim 10^{12}/\text{cm}^2$ , positive near the anode, or negative near the cathode) which produces the electric field in the gap. Thus in a time of  $< 1\text{ ns}$ , if a significant fraction of the ion current were being supplied by particles ionized in this avalanche, enough electrons would be left in the trapped layer to neutralize the entire positive anode charge layer. This cannot happen, or the electric field would collapse in the gap. Thus these electrons must be lost rapidly, with sub-ns lifetime. This loss could be driven by collisions with plasma ions and neutrals, but collisions are unlikely to be fast enough to detrapp  $> 100\text{ eV}$  electrons in  $< 1\text{ ns}$ . Field fluctuations due to either instability or static spatial nonuniformity could detrapp these electrons. Even with a short electron trapping time, the net positive space charge layer at the plasma edge would be partially neutralized, which would enhance ion current density. The electron detrapping fluctuations would have further consequences, including enhancement of ion divergence. The LION data indicating suppression of cathode electron loss late in the pulse places some upper limit on the magnitude of these fluctuations, since it appears that these very high-energy electrons remain well trapped in the gap.

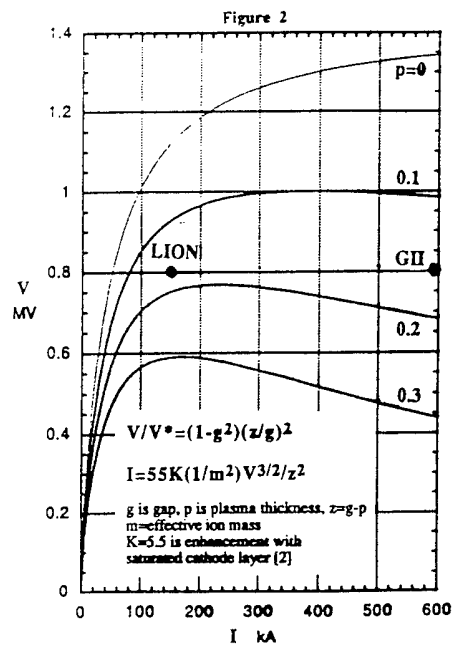
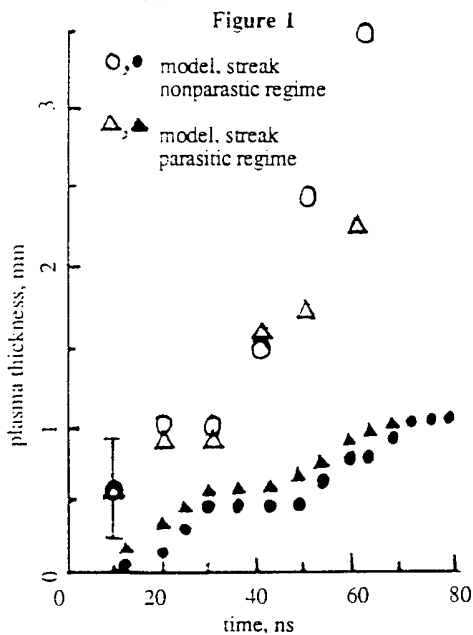
4) The stagnation of plasma motion near peak power could be due to a near balance between the expansion mechanisms and the combination of magnetic compression of the plasma and erosion by ion extraction.

In summary, the basic mechanism of anode plasma expansion which appears consistent with all the LION data is production of particles, mostly neutrals, at the solid surface, which collisionally acquire high enough velocity to arrive at the plasma edge, and which then ionize by avalanche driven by the trapped electrons produced by ionization, resulting in the production of plasma beyond the edge, and the propagation of that edge into the gap. Thus rapid plasma expansion and the simultaneous appearance of lines of both neutrals and highly ionized states could all be consistent.

One of the many open questions related to this scenario is why some diodes exhibit complete impedance collapse at the end of the pulse, and others such as the LION diode do not. Impedance model analysis similar to that for LION, carried out with data from several diodes including the small SABRE diode on GAMBLE II [5] which all tend to collapse to zero voltage and large current at the end of the pulse, all indicate that the diode operating point at peak power falls to the right of the peak of the diode characteristic with finite plasma thickness. Such a point for G(amble)II is indicated on Figure 2. This case is chosen because the diode voltage at peak power, gap and magnetic field were all nearly identical to the LION parameters, while the diode area was half that of LION, so the GII point can be plotted on this figure (with doubled current). It is remarkable that the points

for LION and GII lie on nearly the same characteristic, with a plasma thickness of about 0.15 of the gap, or 1mm, at about the same time in the pulses, but GII produced four times the current density of LION. Within the Desjarlais model [2], this is a simple consequence of finding the intersection of this diode characteristic with the generator load line. The fact that GII then evolves to zero impedance while LION remains nearly constant to the pulse end must be a consequence of plasma dynamics, and the model would suggest that one important factor may dominate. The GII point corresponds to much stronger diamagnetic field compression than LION. For these points, the model gives 25% of the gap magnetic flux within the anode plasma for LION, but 45% for GII. In both cases, the anode plasma expands rapidly after peak power, and the velocity of expansion appears to be similar. However, the larger diamagnetic compression in GII results in 85% of the insulating flux within the anode plasma by the time the plasma thickness has reached 2 mm, and 95% at 2.5 mm near the end of the pulse, whereas in LION the corresponding numbers are 40% at 2mm and 48% at 2.5 mm. A fundamental factor not yet mentioned here is the expansion of the cathode plasma into the gap. On LION this proceeds at about 2-3cm/ $\mu$ s, not enough to collapse the LION gap, but enough at the same velocity after 50 ns to lose the remaining 5% of the flux in GII and short the gap. Thus, assuming the same plasma expansion velocity history for both diodes, by the end of the pulse GII has lost almost all of the insulating flux into the anode plasma and the impedance collapses, while LION maintains insulation. The same plasma expansion histories may result in qualitatively different impedance histories depending upon the degree of ion current density enhancement that can be driven by a pulsed power driver with a particular diode. High enhancements lead naturally to impedance collapse. If penetration of the rising magnetic field into the plasma dissipates substantial energy, the evolution to high enhancement would also drive the ablation of surface material into the plasma and exacerbate impedance collapse and generation of parasitic ions.

\*Work supported by Sandia National Laboratories.



## References

- [1] J. B. Greenly, .K. Appartaim, J.C.Olson and L.Brissette, *Proc. 10th Intl. Conf. on High Power Particle Beams*, June 1994, San Diego, p.398.
- [2] M.P. Desjarlais, *Phys. Fluids B* 1, 1709 (1989).
- [3] N.A.Krall, personal communication.
- [4] D.R. Welch, M.E. Cuneo, C.L. Olson and T.A. Mehlhorn, *Phys. Plasmas* 3, 2113 (1996)
- [5] D. Hinshelwood, personal communication.

## Light Ion Beam Transport Research at NRL

D. D. Hinshelwood, J. R. Boller, G. Cooperstein, R. C. Fisher,<sup>1</sup> J. M. Greenly,<sup>2</sup>  
T. G. Jones, D. Mosher, J. M. Neri, W. A. Noonan,<sup>5</sup> B. V. Oliver, C. L. Olson,<sup>3</sup>  
P. F. Ottinger, D. V. Rose,<sup>1</sup> S. J. Stephanakis, D. R. Welch,<sup>4</sup> and F. C. Young

*Plasma Physics Division, Naval Research Laboratory,  
Washington DC, 20375 USA*

<sup>1</sup>*JAYCOR, Vienna VA, 22181 USA*

<sup>2</sup>*Cornell University, Ithaca NY, 14853 USA*

<sup>3</sup>*Sandia National Laboratories, Albuquerque NM 87185 USA*

<sup>4</sup>*Mission Research Corporation, Albuquerque NM 87106 USA*

<sup>5</sup>*University of Maryland, College Park, MD 20742 USA*

### Abstract

Transport of light ion beams through low-pressure background gas is under investigation at NRL in support of the light-ion ICF program at Sandia National Laboratories. Scaling experiments and the field solver/orbit code ATHETA have been used to design and construct a focusing, extraction applied-B diode for transport experiments. We have developed an active anode source to provide a high proton fraction in the ion beam and a fast ion turn-on time. A very sensitive Zeeman diagnostic is being developed to determine the net current distribution in the beam/transport system. Both analytical and numerical techniques using several codes are being applied to transport modeling, leading to the capability of full system studies.

### Introduction

In a light-ion-beam inertial-confinement-fusion (ICF) reactor, transport over 4 meters from the diode to the target is needed to provide power compression by time-of-flight bunching and for standoff of the diode hardware from the target [1,2]. Two schemes are studied at present, neither of which involves any hardware in the reactor chamber: (1) ballistic transport with solenoidal lens focusing (BTSF), where an auxiliary field just outside the chamber, and the diode field, combine to form an achromatic lens pair that focuses the ion beam onto the target; and (2) self-pinch transport (SPT), where the beam is focused into a region of low-pressure gas, where incomplete current neutralization provides a net current that confines the ion beam in a narrow channel to the target. This approach is particularly exciting because the predicted net currents would allow a shorter focal length than with BTSF, and thus an increased beam microdivergence. Microdivergence reduction is a major, ongoing problem of diode research, and so transport research has great leverage for the ICF program. SPT of ICF-parameter beams requires net currents of at least a few percent, while BTSF of these beams requires net currents of at most a tenth of a percent (larger net currents for BTSF act like a distributed lens which must be accommodated for in the transport system). Therefore, the physics of gas breakdown and conductivity growth is crucial to both schemes. While we are studying both transport schemes, our primary effort at present is directed toward self-pinch transport of proton beams produced by an applied-B diode on the Gamble II generator.

### Self-pinch transport experiment

In designing a self-pinch transport experiment, we want to choose the system parameters to minimize the net current fraction needed to confine the beam. At the same time, we want the



injected proton current to be as large as possible to maximize our relevance to ICF. For a given channel radius, the net current fraction  $I_c/I_p$  and proton current  $I_p$  are given by:

$$\frac{I_c}{I_p} \propto \frac{\Theta_\mu^2 D^2}{\eta V f_p} \quad I_p \propto \frac{V^{3/2} \eta R^2 f_p}{D^2}$$

where  $\Theta_\mu$ ,  $D$ ,  $\eta$ ,  $V$ ,  $f_p$ , and  $R$  refer to the beam microdivergence, diode gap, ion current enhancement in the diode (relative to the Child-Langmuir value), voltage, proton fraction, and diode outer radius, respectively. Thus we want a small microdivergence, high voltage, large radius, high proton fraction, high enhancement, and small gap. Since applied-B diode behavior degrades as the enhancement is raised or the gap reduced, it is necessary to see how far these parameters can be pushed.

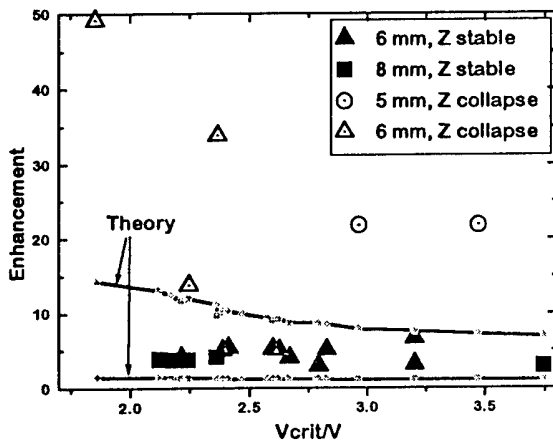


Figure 1: Summary of small-diode data

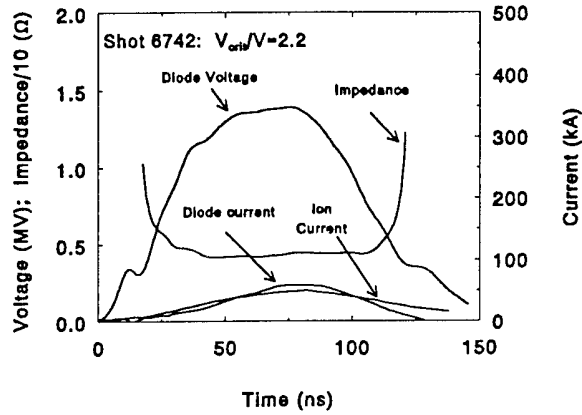


Figure 2: Typical shot at moderate enhancement

Results obtained with a small-area ( $50 \text{ cm}^2$ ) applied-B diode guide our design. In Fig. 1, the observed ion current enhancement is plotted as a function of  $V_{\text{crit}}/V$ , which is a measure of the applied field strength. The shots are divided into those with stable impedance histories and those which exhibit rapid impedance collapse. The lines show the range of enhancement predicted by Desjarlais' theory [3] in the absence of anode plasma expansion. As the applied field is reduced to raise the enhancement, or as the gap is reduced below 6 mm, we observe impedance collapse (there are many more "collapse" points beyond the upper left of this graph) and high enhancement that is indicative of rapid anode plasma expansion.

Figure 2 shows data from a typical shot with moderate enhancement, showing stable impedance and very high ion current efficiency. The microdivergence is about 20 mrad, but the proton fraction is about 50%, and the resulting 25-kA proton current is too low to be interesting. The current can be scaled up by increasing the diode area and voltage.

The small-diode results point to a minimum gap of 6 mm, an enhancement of 5, and a microdivergence of 20 mrad. Gamble II constraints limit the voltage to 1.5 MV and the radius to 10.5 cm. Relevance to ICF dictates a maximum channel radius of 2 cm. This specifies the diode design, with an expected ion current of 200 kA. The 20 mrad microdivergence dictates a 70-cm focal length, and the resulting confinement current is about 40 kA. Therefore, with a 50% proton fraction, a 40% net current fraction will be needed. Numerical simulations predict

this fraction to be achievable, but we would like to decrease it by boosting the proton content of our beam.

Design of this shallow-focusing diode is carried out using the Sandia field-solver and orbit code ATHETA [4]. As seen in Fig. 3a for a simple spherically-focusing anode, the applied and self fields combine to overfocus ions emitted from outer radii and defocus ions emitted from the inner radii. The former can be corrected by shaping the anode, but the latter can only be fixed by moving the emission surface to larger radius and moving the inner coil to smaller radius. Doing so increases the mechanical stress on the inner coil. This is compensated for by doubling the coil width. After iteratively tuning the anode shape, good focusing is recovered, as seen in Fig 3b.

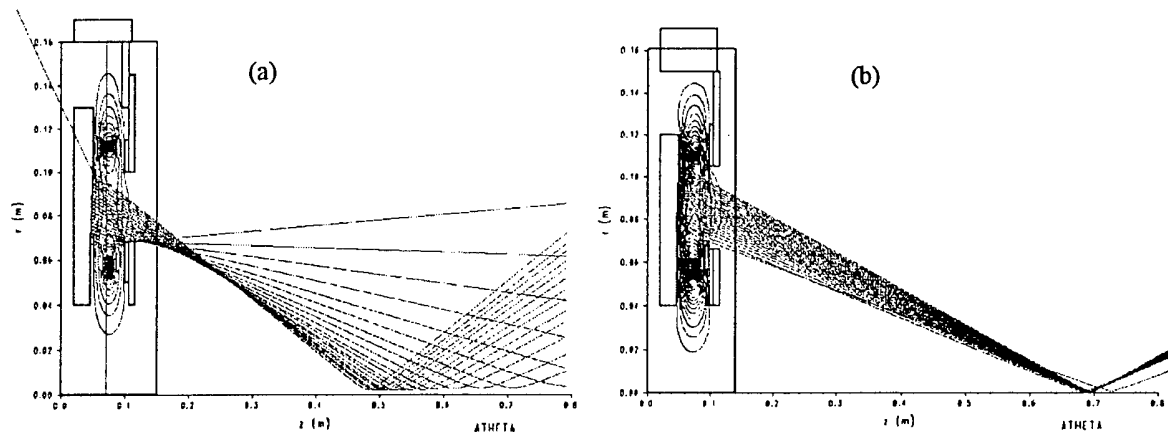


Figure 3: (left) ATHETA predictions for spherical anode; (right) predictions for shaped convex anode.

These calculations neglect field diffusion into the metal, and anode plasma expansion. When both are included, ions are no longer emitted from a zero flux surface. The resulting angular momentum prevents focusing. The solution is to pulse the coils first with a slow, low-amplitude reverse current, producing a field whose diffusion cancels that of the main field. When field diffusion and an assumed 1-mm anode plasma expansion are both taken into account, a proper choice of counterpulse field allows us to recover ATHETA predictions very similar to those in the right of Fig. 3.

A new diode has been constructed based on the above analysis and is being tested on the Gamble II generator. The applied field is 7.5 T in the gap and 12 T at the inner coil surface, giving a large but tolerable mechanical stress. Because the diode operates at a higher impedance than the generator, a parallel, blade load located upstream of the diode is used to shed the excess generator current.

#### Active anode source

An EMFAPS active anode source, based on those used at Cornell and the Karlsruhe Research Center (FZK) [5], will be used to improve the proton fraction and ion turn-on time. This consists of a thin layer of metal deposited on a dielectric substrate. A fast current pulse desorbs and ionizes adsorbed gas, resulting in a thin layer of plasma conformal to the anode. In the Cornell and FZK experiments, an opening switch diverts the early generator current through the foil. To improve controllability, we drive the foil with an external pulser. This

source has increased the proton fraction in our small-diode experiments. The drive system has been upgraded for the new diode. A low-inductance ( $\sim 2$  nH), low-jitter ( $\sim 2$  ns) solid foil switch, triggered by the generator, switches a small water line into six striplines that carry current through the transit-time isolator to the foil. A small surface-flashover switch located just before the foil blocks the water-line prepulse. This system provides a 120-kA, 20-ns foil current pulse with a peak  $dI/dt$  of over 10 kA/ns. Bench testing of the source for the new diode has just begun. We see uniform light emission from the foil breakdown, with no significant arcing or filamentation.

### Beam magnetic field profile measurement

To study beam current neutralization we need to know the magnetic field profile in the beam. Measurement of Zeeman splitting is made difficult by the small shifts involved: for the self-pinched case, the splitting is  $\sim 0.01 \text{ \AA}$ , below the resolution of most stigmatic instruments, and for the ballistic case, it is  $\sim 0.001 \text{ \AA}$ , within the Doppler profile. The solution is to use polarization selection with differential detection [6]. The approaches used for the two transport schemes are shown in Fig. 4. The narrow-band pump beam is directed across a diameter of the ion beam, in an appropriately seeded gas, imaging the transverse fluorescence. This gives spatial resolution and results in always looking along the field, where the two Zeeman components have opposite circular polarization. They are separated and differentially detected. For the low-field case, we tune the pump to the wings of the Doppler profile. For the high-field case, where the splitting exceeds the Doppler width, we plan to pump the  $m=0$  excited state, and then insert a monochromator, tuned so that the lines are at the edge of the response curve. In both cases, the differential signal will be related to the Zeeman splitting. Atomic physics and technological considerations point to the use of barium for the low-field case and samarium for the high-field case. We have demonstrated a proof-of-principle of the low-field technique on the bench, using Helmholtz coils to provide the field. We have achieved 20-Gauss resolution, as shown in Fig. 5. The next step will be to repeat this for the high-field technique, and then address the issues of fielding this diagnostic in the pulsed-power environment.

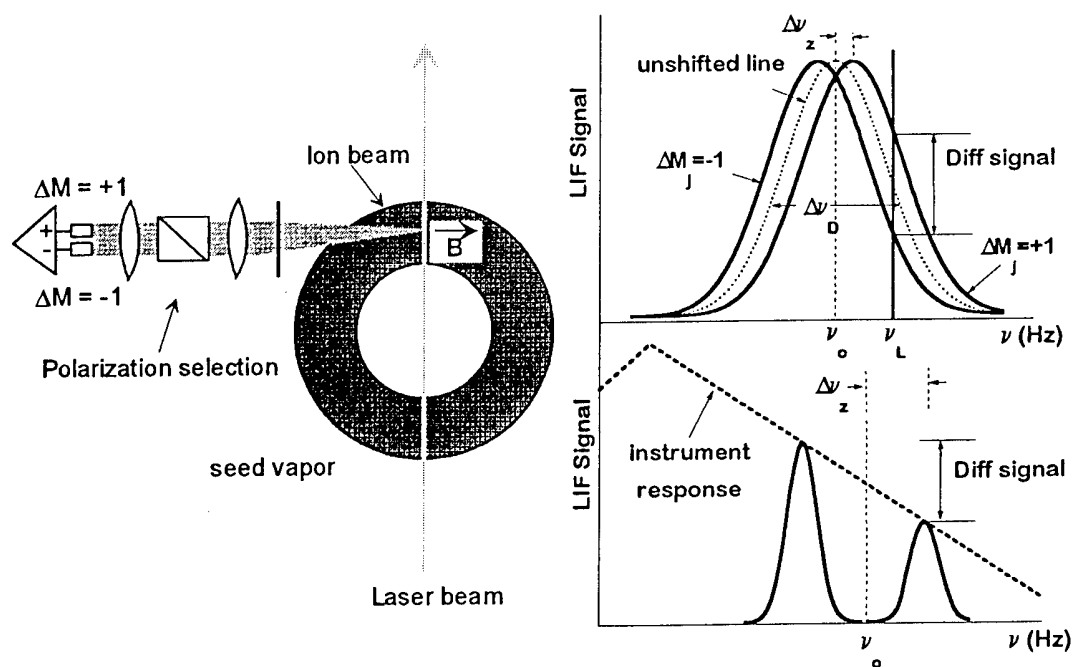


Figure 4: (left) Zeeman diagnostic; (top right) scheme for BTSF; (bottom right) scheme for SPT.

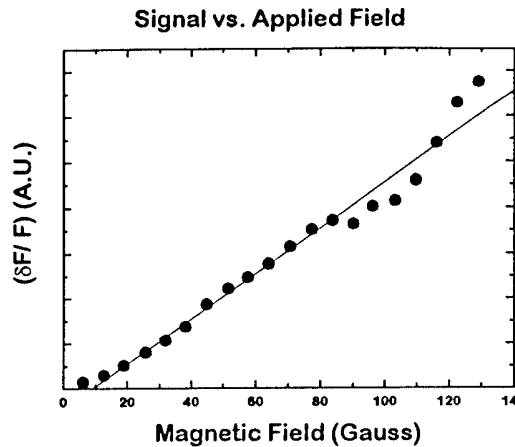


Figure 5: Bench test of Zeeman diagnostic

Gas	$t_{th}$ (ns)	$t_b$ (ns)	$t_r$ (ns)
GII - He	0.23	1.30	85.0
GII - N	0.05	0.50	5.0
GII - Ar	0.03	0.27	4.5
ICF - He	0.04	0.30	9.0

Table 1: Gas breakdown timescales

### Gas breakdown and conductivity growth theory

We are using many theoretical tools to study gas breakdown and conductivity growth: a zero-D code and analytic modeling [7] to get scaling laws; a 1-D PIC code with a detailed atomic physics treatment to model the early-time phenomena, and the multidimensional hybrid codes IPROP (3-D) [8] and Solenz (21/2-D) [9]. The use of these models is contributing to a complete understanding of gas breakdown.

IPROP, with its fluid treatment of cold electrons and PIC treatment of fast particles, has made encouraging predictions for self-pinch transport [8]. For conditions relevant to the Sandia SABRE generator, net current fractions of up to 50% in low-pressure argon are predicted. Zero-D calculations illustrate the relevance of the Gamble II experiments to ICF. Calculation of the energy input to the gas is fairly straightforward; its equipartition between ionization and electron temperature is key to current neutralization. We find 3 important timescales - energy input  $t_{th}$ , impact ionization  $t_b$ , and conductivity growth  $t_r$ . These timescales are given in Table 1 for different gases at Gamble II parameters and for helium at ICF parameters.

There are two questions in evaluating self-pinch transport: (1) can the required net currents be obtained? and (2) given these net currents, how well will the ion beam propagate? The first can be addressed by using the heavier gases, which have timescales similar to those under ICF conditions. The second can be addressed by using helium, which should provide the larger net current fraction needed for confinement under Gamble II conditions.

The zero-D code is being used to model earlier transport experiments on Gamble II, calculating the net current fraction, electron density, and temperature for different gases under these parameters. The electron density was measured interferometrically in the experiment. Theory gives good agreement for He and N but overpredicts the density by over a factor of two for Ar. We speculate that the electron tail distribution in the experiment may differ from the Maxwellian assumed in the code. Diagnostics of the electron tail, where ionization occurs, are necessary. Actinometry using emission from highly excited states of tracer elements is one possibility.

### **Operational windows for transport systems**

In addition to gas breakdown calculations, our theory effort is directed toward other transport issues, such as instabilities (filamentation and two-stream) and transport efficiency (including the effects of beam energy loss, focus sweep from voltage variations, and module packing constraints). Using system design parameters such as time-of-flight bunching, background gas species/pressure, etc., operational windows for stable and efficient transport can be determined. For example, preliminary results for the BTSF scheme using baseline ICF design parameters indicate that it may be difficult to avoid filamentation growth in the transport region between the diode and the solenoidal lens. These results may be different for other parameter sets, and this complete system modeling is continuing.

### **Summary**

In conclusion, the applied-B diode, active anode source, and theoretical tools are ready for self-pinch transport experiments that will begin soon. Future work will center on refining both the diagnostics - the very sensitive Zeeman diagnostic, emission studies of the electron distribution, and measurement of the electron density using a highly sensitive ( $10^{-4}$  fringe) interferometer [9] - and our code and analytic treatment. All of this will eventually permit full system studies of light-ion ICF transport schemes.

It is a pleasure to acknowledge many helpful discussions with Mike Cuneo at Sandia and Peter Hoppe at FZK.

This work is supported by the US Department of Energy through Sandia National Laboratories.

### **References**

- [1] J. P. Quintenz et al, these proceedings.
- [2] C. L. Olson, et al, Laser Interaction and Related Phenomena, 557 (1994).
- [3] M. P. Desjarlais, Phys. Fluids **B1**, 1709 (1989).
- [4] J. P. Quintenz, Sandia National Laboratories, private communication.
- [5] see for example H. Laqua, H. Bluhm, L. Buth, and P. Hoppe, Jour. Appl. Phys. **77**, 5545 (1995), and references therein.
- [6] W. A. Noonan, T. G. Jones, and P. F. Ottinger, Rev. Sci. Inst., accepted for publication.
- [7] B. V. Oliver, P. F. Ottinger, and D. V. Rose, Phys. Plasmas, accepted for publication.
- [8] D. R. Welch, M. E. Cuneo, C. L. Olson, and T. A. Melhorn, Phys. Plasmas **3**, 2113 (1996)
- [9] B. V. Oliver and R. N. Sudan, BEAMS 92 conf. proceedings (1992), p.921.
- [10] B. V. Weber and S. F. Fulghum, Rev. Sci. Inst., accepted for publication.

## THE DECADE PERFORMANCE ASSESSMENT PROGRAM

**B. V. Weber, P. F. Ottinger, R. J. Commisso,**

*Naval Research Laboratory, Washington DC USA*

**J. R. Goyer, D. Kortbawi,** *Physics International Company, San Leandro, CA USA*

**J. Thompson,** *Maxwell Laboratories, Inc., San Diego, CA USA*

**J. E. Rowley, P. Filios,** *Defense Nuclear Agency, Alexandria, VA USA*

**M. A. Babineau,** *Sverdrup Technology, Tullahoma, TN USA*

### Abstract

Previous analyses of DECADE Module 1 experiments indicated significant current loss between the plasma opening switch (POS) and an electron-beam load. A program was initiated to diagnose and improve the power flow to assess the performance of a multi-module DECADE system. Power flow measurements between the POS and load indicate high vacuum flow, distributed current loss and azimuthal asymmetries. A decreased load impedance reduces the fraction of the load current flowing in vacuum. Improved plasma source symmetry reduces losses near the load for long conduction times. Increased POS impedance is required to significantly improve the power coupling to the load.

### INTRODUCTION

DECADE is a high power generator designed and built for the Defense Nuclear Agency (DNA) by Physics International Company. The system consists of 4-16 modular generators that drive independent electron-beam diodes. Each generator consists of a Marx bank, a water capacitor, six triggered output switches, a water line to sharpen the current rise time, a  $\sim 4$ -m-long vacuum line, a plasma opening switch (POS) and a short vacuum line to the load. Previously, experiments [1] were performed on a single generator, DECADE Module 1 (DM1), to predict the characteristics of a multi-module system. The performance of the pulsed power components upstream of the POS are described in Refs. [1] and [2]. With a short circuit at the POS location, the current rises to 1.8 MA in 300 ns. Optimum system performance, as determined by bremsstrahlung output, was found at a POS conduction time of 220 ns, when the generator current was 1.4 MA. The load voltage was about 1.8 MV when the POS opened.

An analysis[3] of the results, using available data, circuit code modeling and radiation modeling indicated that a  $700 \pm 100$  kA,  $58 \pm 8$  kJ electron beam was producing the measured bremsstrahlung, and that about 80% of the load current consisted of vacuum flowing electrons. The difference between the load current and the generator current at the time of maximum x-ray emission, 550 kA, represents loss between the POS and the load. The POS was modeled in the circuit simulation using a flow impedance[4] rising to  $1.4 \Omega$  in 28 ns after the 220 ns conduction time, then decaying with a  $1/e$  time of 55 ns. This flow impedance corresponds to a  $\sim 2$  mm vacuum gap in the plasma at the cathode radius.

Based on these results, a research effort was initiated to understand and improve the power coupling from the POS to the load for the DECADE system. The power coupling problem consists of two related parts: decreasing the current losses between the POS and

load, and increasing the POS impedance. Two POS techniques are being investigated in this program, the "standard" POS[5] that has been used on DM1 in the past, and the Magnetically Controlled POS (MCPOS) [6] developed at Sandia. The MCPOS will be tested on a second DECADE module, DM2, in the near future. This paper will describe measurements of the power flow between the POS and load for the standard POS on DM1.

## POWER FLOW BETWEEN THE POS AND LOAD

A sketch of the POS-load region on DM1 is shown in Fig. 1. This is an instrumented version of the configuration used for the experiments cited above. Plasma is injected between the inner and outer conductors a few  $\mu\text{s}$  prior to firing the generator using 12 plasma guns. Two gun configurations have been used: direct injection as shown in Fig. 1 and "manifold" injection, where the plasma flows through a  $90^\circ$  bend. The electron density is about  $10^{15} \text{ cm}^{-3}$  in the electrode gap. The plasma is generated by a surface flashover on Teflon, producing ions of F, C, and possibly H and O impurities. The center conductor radius in the POS region is 4.4 cm, increasing to 6.3 cm downstream. The plasma is injected through a 2-cm long aperture. The distance between the plasma guns and the load anode is 40 cm. The electron-beam diode in Fig. 1 has an anode-cathode (AK) gap of 2.5 cm, resulting in a relatively high load impedance ( $30 D/r = 12 \Omega$ ).

The power flow between the manifold-gun POS and load was diagnosed using  $\text{dB}/\text{dt}$  current monitors at various locations along the anode and cathode as shown in Fig. 1. At most axial locations, three monitors were positioned  $120^\circ$  apart. At the location closest to the POS on the anode, 6 monitors were positioned  $60^\circ$  apart. The monitors were recorded individually to analyze the symmetry of the current flow. Radiation diagnostics were used to supplement the electrical measurements: A filtered pin diode array[7] was used to determine the time-dependent load voltage, a calibrated pin diode was used to determine the electron current and

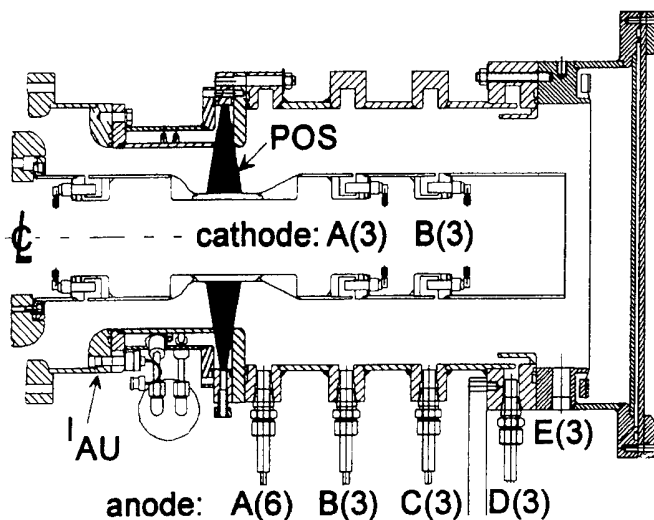


Figure 1. DM1 POS-load region instrumented with current probes.

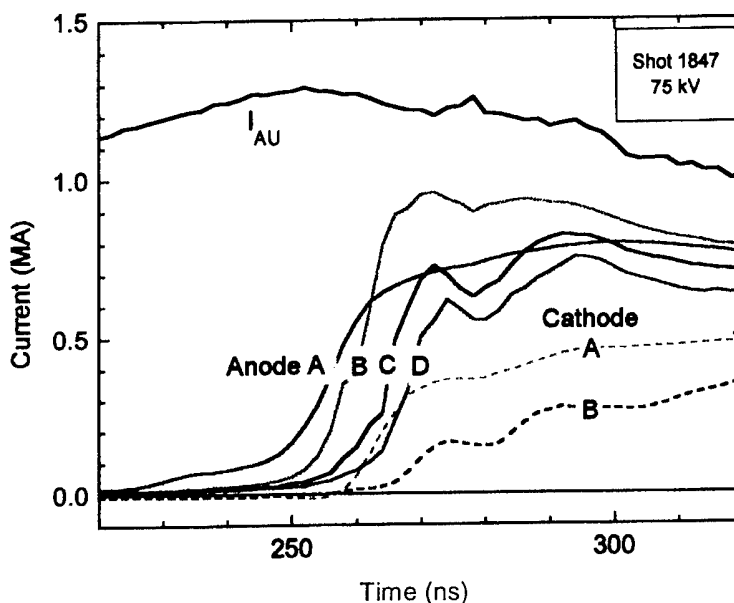


Figure 2. Current waveforms for a typical shot with a high impedance load ( $30 D/r = 12 \Omega$ ).

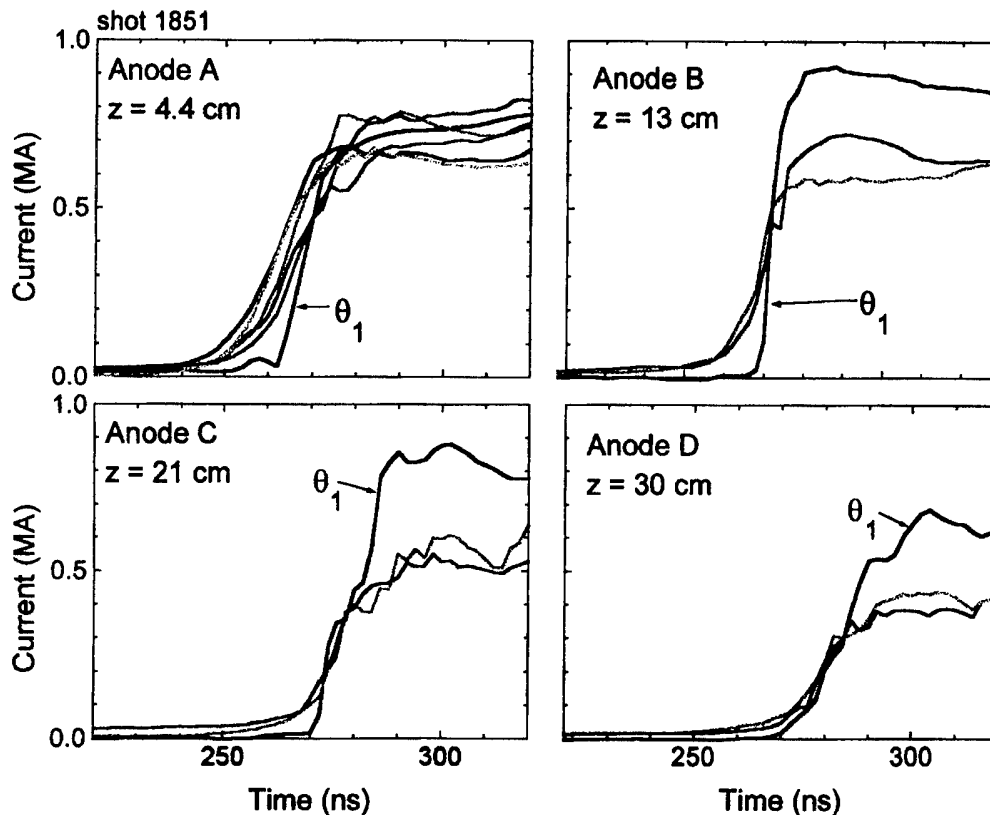


Figure 3. Azimuthal asymmetry of current propagation between POS and load (shot 1851).

radiated energy, and to calculate the load power, energy, and impedance. The measurements could be combined to estimate the POS flow impedance. A time-integrated pinhole camera recorded the end-on x-ray image.

Current waveforms for a typical shot with a high impedance load are shown in Fig. 2. Each waveform is identified by a letter corresponding to those in Fig. 1. Anode currents are indicated by the solid lines and cathode currents by dashed lines. Note that cathode monitor A is at the same axial location as anode monitor B. The POS voltage (not shown in Fig. 2) has a maximum value of 1.8 MV at  $t = 290$  ns. At this time, the generator current is 1.2 MA, the anode monitor closest to the load (D) indicates 700 kA, and 250 kA is indicated by the cathode monitor closest to the load (B). The decreasing trend of current with distance from the POS indicates that these values are probably upper limits to the actual load currents. These measured values agree with the conclusions cited above based on circuit simulations and radiation modeling[3]. About 500 kA is "lost" in the POS-load region, and of the 700 kA total current reaching the load anode, about 450 kA (or more) is flowing in vacuum. The high vacuum current is not unexpected considering the high load impedance.

The anode current waveforms in Fig. 2 show that the current propagates from the POS to the load with a velocity of about 2 cm/ns, ten times slower than vacuum flow in a MITL. If this current propagation corresponds to a current-carrying plasma, the speed is approximately the Alfvén speed, implying a plasma density of  $10^{12} - 10^{13} \text{ cm}^{-3}$ , small compared with the injected plasma density but high enough to have dramatic effects on the power flow. The current propagates slower along the cathode, indicating slanted current streamlines. At the time of peak voltage ( $t = 290$  ns) the current loss is distributed along the length of both the anode and cathode. The POS flow impedance for this shot at peak POS voltage is  $1.5 \Omega$ .



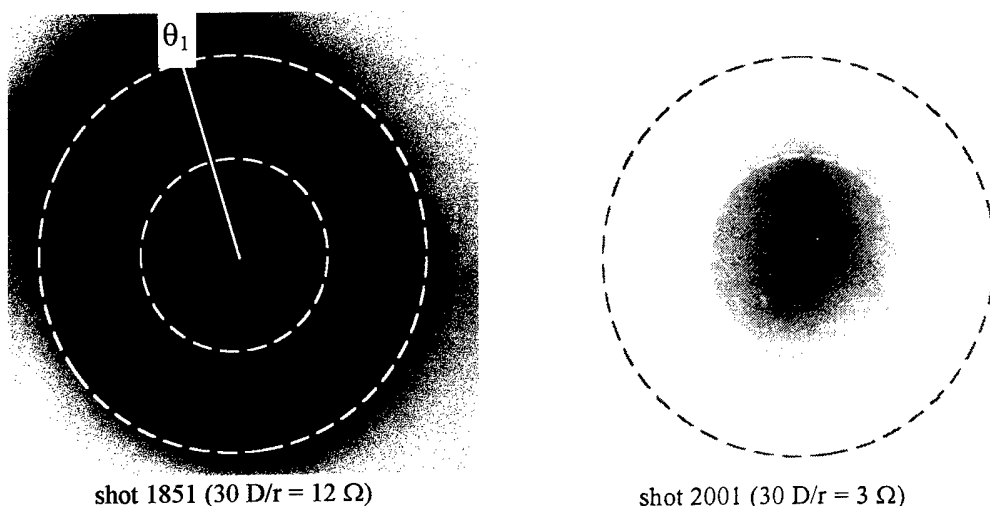


Figure 4. End-on x-ray pinhole images for a shot with a high impedance diode and asymmetric current flow (1851) and one with a low impedance diode and symmetric current flow (2001). The broken circles indicate the center conductor and outer conductors. The solid line indicates the angle  $\theta_1$ .

Variations between the individual current monitors at a given axial location indicate the azimuthal symmetry of the current. An illustrative example of a shot with asymmetric current flow is shown in Fig. 3. The current asymmetry is localized at one azimuth, (denoted  $\theta_1$  in Fig 3) where at location A on the anode, one probe out of six rises later than the others indicative of late opening at that location which corresponds to a local high density in the POS. The asymmetry propagates downstream past the B, C, and D probes and has the appearance of a localized current channel, indicating a higher current after the channel passes the probe location because of field lines looping around the localized current channel.

The end-on pinhole camera shows asymmetric radiation patterns when the current is asymmetric, with intense emission from the walls at the same azimuth as the propagating current channel, as shown on the left in Fig. 4. The azimuthal asymmetry is fairly random, but occurs more frequently at longer conduction times. The asymmetry is important for load coupling because it can be related to losses near the load.

The vacuum flow current can be reduced dramatically by using a lower impedance diode load. Current waveforms from a shot using a 6.4 mm AK gap (30 D/r = 3 Ω) are shown in Fig. 5, and the corresponding radiation pattern is shown on the right in Fig. 4. After a ~ 20 ns propagation time, the anode and cathode currents all agree, indicating negligible vacuum flow. There

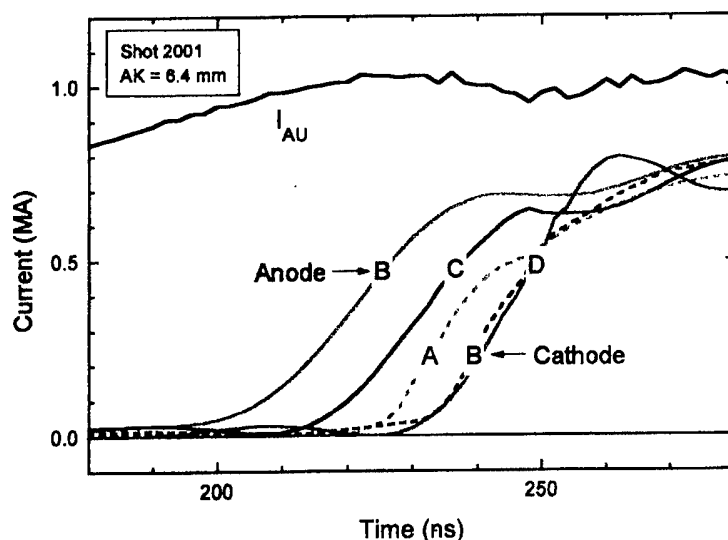


Figure 5. Current waveforms with a low impedance load (30 D/r = 3 Ω) showing negligible vacuum electron flow.

still is substantial current loss, about 300 kA for this shot, but it is now localized near the POS instead of being distributed throughout the entire POS-load region.

In general, low impedance diodes result in increased load energy (80-90 kJ) but longer pulse widths (50-100 ns). Ion currents are inferred in these diodes that constitute 10-30% of the diode energy. This unwanted ion current can be reduced with appropriate diode design. Centered, symmetric radiation patterns are possible with these diodes which is desired for a multi-module system, however, at long conduction times

(> 250 ns) the load coupling often deteriorates as the result of asymmetries described above.

The downstream plasma effects responsible for the slow current propagation can be ameliorated by changing the plasma sources. For example, using direct-injection plasma guns, doubling the number of guns to 24 and doubling the current and  $dI/dt$  in each gun results in the current waveforms shown in Fig. 6. The anode monitors at locations A, B, C, D, and E indicate very rapid current propagation after the C location. The individual monitors at different azimuths indicate very good symmetry. The particular shot in Fig 6 has a 290 ns conduction time, close to optimum for storing the available energy in the vacuum inductance. This plasma gun configuration results in reduced current loss near the load at the longest conduction times on DM1. Current losses are still observed, with 400 kA loss localized upstream of the C location. Improving the power coupling to the load requires increasing the POS flow impedance (increasing the ratio of gap size to radius).

## SUMMARY

Previous experiments on DM1 and analyses indicated significant (>40%) current loss between the POS and load. These losses have been diagnosed using current monitors and x-ray diagnostics. With a high impedance diode load, the current losses are distributed between the POS and load, and much of the load current consists of vacuum flowing electrons. The current propagates from the POS to the load with a  $\sim$  cm/ns velocity (faster along the anode than along the cathode), indicating a low density current-carrying plasma. At increased conduction times, the current tends to become azimuthally asymmetric, forming a localized current channel that propagates to the load. X-ray images indicate asymmetries that correspond to the asymmetry in the current flow.

The power flow can be changed using a lower impedance load to virtually eliminate the vacuum flow. If this is the only change, however, the current propagation, total current loss and current flow symmetry are unchanged. Changing the plasma sources to direct injection,

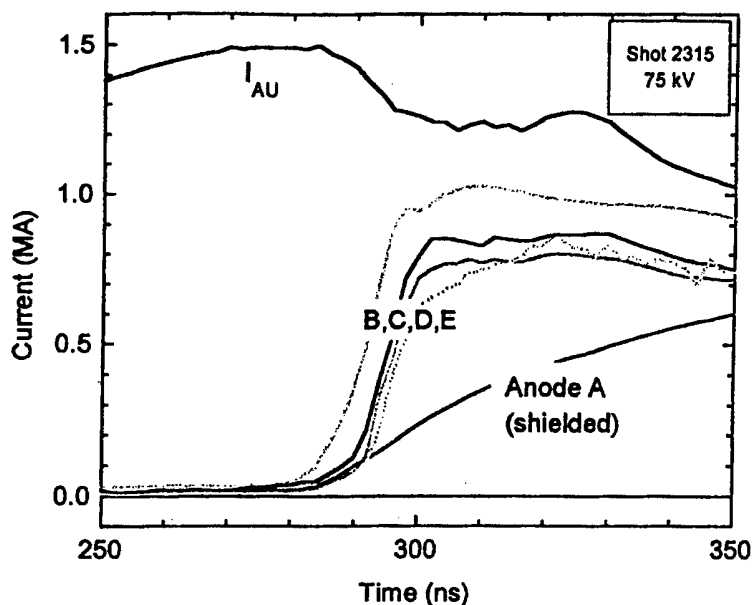


Figure 6. Current waveforms showing reduced downstream plasma effects by improving the POS plasma symmetry.

doubling the number of guns from 12 to 24 and doubling the gun current results in reduced losses near the load at long conduction times, probably because of improved symmetry in the POS plasma. Current losses still persist in this configuration, but they are now localized close to the POS. Improved power coupling to the load requires increasing the effective flow impedance of the POS.

DM1 experiments are planned to investigate methods to increase the POS flow impedance at long conduction times by varying the POS geometry and the plasma sources. POS experiments on DPM1 [8] with similar  $I \times t$  (conduction current times conduction time) products have demonstrated that anode geometry affects performance. Experiments on Hawk [9] and DPM1 [8] have demonstrated improved POS impedance depending on cathode shape and radius. These experiments have achieved POS flow impedances higher than those yet achieved on DM1, indicating the possibility for improvement. Other variations include increasing the plasma length and using "transparent" conductors consisting of wire arrays to reduce secondary plasmas from electrode surfaces. Plasma source variations have included increasing the number of sources and their driving current (as described above), and varying the radial location of the guns. These changes have already indicated improved power coupling.

The best combination of the above POS variations will be compared with the results of the MCPOS tests. This information will allow an assessment of the DECADE performance.

## ACKNOWLEDGMENTS

The authors are pleased to acknowledge J. Rauch and N. Qi for their contributions on diagnostics for DM1 experiments. We are also grateful for the expert technical assistance of the DM1 crew: P. Grunow, S. Hogue, G. Maciolek, and C. Schuppenhauer, and for the creative design work of S. Drury.

- [1] P. Sincerny, S. Ashby, K. Childers, J. Goyer, D. Kortbawi, I. Roth, C. Stallings, J. Dempsey, *Proc. 10<sup>th</sup> IEEE International Pulsed Power Conf.* (Albuquerque, 1995).
- [2] P. Sincerny, C. Stallings, K. Childers, J. Goyer, D. Kortbawi, I. Roth, J. Dempsey, L. Schlitt, these proceedings.
- [3] R. J. Commisso, J. R. Boller, D. V. Rose, S. B. Swanekamp, J. M. Grossmann, P. F. Ottinger, B. V. Weber, F. C. Young, and G. Cooperstein, *Proc. 10<sup>th</sup> IEEE International Pulsed Power Conf.* (Albuquerque, 1995).
- [4] C. W. Mendel, Jr., M. E. Savage, D. M. Zagar, W. W. Simpson, T. W. Grasser, and J. P. Quintenz, *J. Appl. Phys.* **71**, 3731 (1992).
- [5] J. R. Goyer, D. Kortbawi, F. K. Childers, J. A. Dempsey, I. S. Roth, and P. S. Sincerny, *Proc. 10<sup>th</sup> International Conf. High Power Particle Beams*, (San Diego, 1994), p. 1.
- [6] M. E. Savage, E. R. Hong, W. W. Simpson, M. A. Usher, *Proc. 10<sup>th</sup> International Conf. High Power Particle Beams*, (San Diego, 1994), p. 41.
- [7] J. C. Riordan, J. E. Faulkner, D. Kortbawi, J. S. Meachum, R. S. Mendenhall, I. S. Roth, and B. A. Whitton, *Proc. 8<sup>th</sup> IEEE International Pulsed Power Conf.*, (San Diego, 1991), p. 390.
- [8] J. R. Goyer, D. Kortbawi, P. S. Sincerny, D. Parks and E. Waisman, *J. Appl. Phys.* **77**, 2309 (1995).
- [9] P. J. Goodrich, R. J. Commisso, J. M. Grossmann, D. D. Hinshelwood, R. A. Riley, S. B. Swanekamp, and B. V. Weber, *Proc. 10<sup>th</sup> International Conf. High Power Particle Beams*, (San Diego, 1994), p. 299.

## MICROSECOND PLASMA OPENING SWITCH EXPERIMENTS ON GIT-4

V.M.Bystritskii, A.A.Kim<sup>1</sup>, V.A.Kokshenev<sup>1</sup>, B.M.Koval'chuk<sup>1</sup>, I.V.Lisitsyn,  
A.A.Sinebryukhov, V.A.Sinebryukhov

*Institute of Electrophysics RAS, Academy ave.4, Tomsk 634055, RUSSIA*

<sup>1</sup>*High Current Electronics Institute RAS, Academy ave.4, Tomsk 634055, RUSSIA*

### INTRODUCTION

The pulsed power generator design requires low inductance, low vacuum impedance magnetically insulated transmission lines (MITL) for efficient energy transfer to plasma opening switch (POS) and then to load. The problem becomes to be the most important for megaampere generators, where the inductive voltage drop in any circuit element reduces sufficiently the overall generator efficiency. In the generators utilizing a POS, the existence of a plasma filled region limits a minimum A-K gap spacing to the level of several centimeters. Therefore, this also limits minimum electrode diameters can be used in the POS region keeping low line vacuum impedance for effective energy coupling.

By the other hand, switch operation regimes depend strongly on self magnetic field magnitude in a coax, where POS is located. The recent POS study on GIT-4 generator at the current level up to 2 MA is aimed to better understanding of these limitations. The electrode diameters variation and applying of external magnetic field allowed to obtain criteria for effective switch operation in low impedance vacuum transmission line. The data of many recent experiments made elsewhere is also included into the analysis.

Another important problem considered is design of a plasma source as a key element of POS. The requirements for a low impedance POS based generators determine the requirements for a plasma fill system.

### PLASMA SOURCE

Plasma source in a high power microsecond POS must satisfy the following requirements. It should produce the plasma flow with high density, high plasma velocity and high ionization degree; and also location and number of plasma sources should provide high degree of azimuthal uniformity of plasma flow in a line with large electrode diameters. The following three types of plasma sources were applied to the POS experiments of terawatt power GIT-4 generator: cable guns (CG), flashboards (FB) and gas puff plasma guns (GPPG).

The usage of GPPG indicates some improvement of MPOS parameters compared to other plasma sources when light gases ( $H_2$ ,  $He$ ) are injected to discharge gap of plasma guns. This effect was seen both in the low scale proof-of-principle experiment ( $I_g = 200kA$ ,  $t = 1\mu s$ ) and in the full scale GIT-4 experiment. The measurements of plasma flow purity indicates that GPPG can not produce pure ions plasma flow. The reasons for such an improvement are not clear completely. The GPPG consist of many elements which must be tuned very finely. This limits the number of plasma guns in the POS, that makes difficult to achieve high azimuthal plasma uniformity. If even one gun firing is delayed, this deteriorates the POS parameters.

The flashboards are used successfully in most of MPOS experiments providing high plasma uniformity due to large number of elementary plasma sources on each FB. Our

experience in application of FB to many POS experiments showed their reliability and high efficiency. Nevertheless on megaampere GIT-4 their lifetime was limited within 10-20 shots, after that they must be replaced. Open FB surface was exposed by electron beam resulting in epoxy substrate destruction and copper electrode exfoliation.

As an important advantage of FB application the following could be mentioned. The usage of flashboards allows to decrease energy stored in feed capacitor bank compared to one required for other plasma sources keeping plasma parameters the same. In our experiments we used capacitor bank with stored energy of ten times lower driving FB instead of CG in order to provide the same switch current.

The most simple and reliable plasma source for high power MPOS is set of CG. The measurements showed that CG produces plasma flow in the angle of  $60^\circ$  at FWHM with plasma front velocity of  $10^7$  sm/s. The difference in plasma current between guns does not exceed usually 20%. The dielectric discharge surface of the CG is protected against direct electron flow and CG degradation is much slower compared to FB. Several hundreds of shots do not change sufficiently plasma flow characteristics.

Large divergence angle of CG plasma flow provides high plasma uniformity choosing sufficient distance between CG and POS cathode in absence of applied magnetic field in switch region. If plasma flows along field lines, angle of plasma flow is less than  $10^\circ$ . In order to realize uniform plasma flow in the MPOS with applied magnetic field we designed the CG providing the flow angle as high as in zero field. The angle weakly depends on field magnitude in the injection point. This design allows to improve the uniformity of the plasma flow and does not change plasma density and flow velocity. For the experiments with high current and corresponding high electrode diameters, lower number of plasma guns allows to simplify hardware design keeping high plasma flow uniformity.

## THE INFLUENCE OF ELECTRODE GEOMETRY ONTO MPOS OPERATION REGIMES

Numerous experiments with microsecond plasma opening switches (MPOS) showed that MPOS impedance and voltage are functions of the linear current density at the switch cathode [1, 2]. The most impressive amplitudes of voltage and shunt impedance were achieved in experiments with low electrode diameters. By the other hand, if the cathode diameter exceeds some value depending on generator current amplitude, switch regime characteristics become sufficiently worse. Such results correspond to the generally accepted concept of POS operation, where switch opening is forced by magnetic insulation of the electron flow in vacuum gap appearing due to electric and/or magnetic fields in plasma. Evidently, that the higher linear current density takes place at switch electrode, the higher voltage corresponds to the condition of magnetic insulation in a gap.

$$d \simeq 8500\beta\gamma r/I$$

The gap spacing derived from this formula depends on experimental conditions and weakly depends on load current if switch operates in the switch - limited regime.

Let us observe the set of experiments with MCPOS ( $t_{cond} \geq 500$  ns). The minimum linear current density providing at least two-fold voltage gain appeared to be of order of  $\sigma \simeq 20$  kA/cm. Noteworthy, that MPOS shunt impedance in many experiments can be expressed by the empiric formula:  $R \simeq 4U_{gen}/I_{POS}$  for different generator voltages and POS currents at  $\sigma \simeq 20$  kA/cm.

Generally speaking, if we analyze also the experiments at extremely low MPOS currents ( $\leq 100$  kA), we will obtain growing  $\sigma_{min}$  vs  $I_{MPOS}$  dependence. In the high wave

impedance MITL with high  $R_a/R_c$  ratio, that is acceptable for high impedance generator, the process of magnetic field penetration into plasma can sufficiently differ. So, the value of  $\sigma \simeq 20 \text{ kA/cm}$  is critical for MPOS in a low impedance ( $\rho \leq 30 \text{ Ohm}$ ) MITL. Lower value of linear current density realized in a MPOS results in strong deterioration of MPOS parameters.

The maximum cathode radius for a MPOS placed in a low impedance MITL can be found as:

$$R_c \simeq I_{POS}/2\pi\sigma_{min}$$

where  $\sigma_{min} \simeq 20 \text{ kA/cm}$ .

Nevertheless, we would like to mention the following exclusions.

1. In the experiments on GIT-4 we used MITL with cathode diameter much higher than given by above formula substituting generator parameters (480 mm). In this case both MITL electrodes were made as arrays of rods. Nevertheless, estimating the linear current density at the rod surface one can obtain the same value:  $\sigma \simeq 20 \text{ kA/cm}$  for uniform current distribution around each rod.
2. The experiments made in positive polarity of inner MPOS electrode [3] showed, that cathode current density can be lower than one in negative polarity experiments. The values of  $\sigma$  of  $7 \text{ kA/cm}$  on Double generator, and  $8 \text{ kA/cm}$  on Tesla (SNL) were realized. In the latter case, the limitation could be overcome using another type of POS - magnetically controlled POS.

The MITL anode diameter in the MPOS region can be estimated basing on condition of no interelectrode breakdown. The velocity of dense plasma expansion from the electrode surface is about  $10^6 \text{ cm/s}$  that gives for two side plasma expansion the following minimum interelectrode gap spacing for one microsecond conduction phase duration:  $d_{ie} \geq 2 \text{ cm}$ . The vacuum gap spacing sufficient for magnetic insulation is several millimeters and should be also added, but two centimeters gap is only rough estimate, because plasma expansion velocity depends on many conditions, which gives large error bar for this value.

In order to achieve maximum energy transfer efficiency and high load current, all inductances in the scheme high power generator - MPOS - load must be minimized. This is evidently, that the minimum MITL inductance takes place if line cathode is of maximum available diameter if A-K gap is fixed and limited by given above value. The expression for minimum inductance per unit length is:

$$L = 60 \ln[(R_c + d_{ie})/R_c]$$

where:  $R_c = I_{POS}/2\pi\sigma_{min}$ ,  $\sigma_{min} \simeq 20 \text{ kA/cm}$ ,  $d_{ie} \geq 2 \text{ cm}$ .

We carried out three experimental runs with different electrode diameters in the MPOS region in MITL with  $\rho < 20 \text{ Ohm}$ .

N exp. exp.	$D_{an}$ , mm	$D_{cat}$ , mm	$Z_{wave}$ , Ohm	$\sigma(1.8 \text{ MA})$ , $\text{kA/cm}$	Gap, mm
1	140	102	19	56	19
2	360	280	15.1	20.5	40
3	540	440	12.3	13	50

The optimum one was found the geometry shown in row 2 of the table that corresponds to given above model. Low POS voltage observed in the run for row 1 can be explained by very small interelectrode gap which can result in electron losses at high conduction times.

Noteworthy, that load - limited switch operation can decrease the limitations for  $\sigma_{min}$  in a MPOS. Really, if the switch voltage is limited by a load and becomes lower than one

realized in the switch - limited regime, the lower current value is required for magnetic insulation in vacuum gap.

$$d \simeq 8500 \beta \gamma r / I_l = \text{const}$$

$$d U^2 / I_l$$

This effect is realized in experiments with low impedance electron diode for a POS load. MITL parameters for this experiment can be found in the row 3 of the table, where  $\sigma_{min} \leq 15 \text{ kA/cm}$ . High electron current and diode power can be achieved despite of low POS voltage in switch - limited regime.

## MPOS OPERATION IN AN EXTERNAL MAGNETIC FIELD

The parameters of a pulse generated by MPOS are limited by the necessity to use high density plasma (up to  $10^{16} \text{ cm}^{-3}$ ). For such a plasma much time is required to produce a vacuum gap either by electric or magnetic force, that results finally in lower voltage and lower load current rise rate. MCPOS opening time makes up in most experiments 50—100 ns.

As it was shown in [4], applying of external magnetic field results in enlarging of the POS conduction time keeping plasma density low. We performed similar experiments in traditional POS scheme. Plasma was injected across applied magnetic field having axial and radial components in MITL gap. This is evident that current increases from some value of magnetic field strength despite of plasma flow suppressing.

Such experiments were carried out in not optimal geometry of MPOS electrodes ( $\sigma/20$ ), but nevertheless the POS voltage was 20 % higher for high B-field case compared to zero field case. The magnetic field strength was limited within 6 kGs by capacitor bank parameters, but nevertheless the parameters obtained seems to be useful for future work.

## CONCLUSION

The experiments performed allowed us to compare different kinds of plasma sources for high power MPOS applications. High electrode diameters and high switch energy deposition determine types of plasma source which can be used successfully. The analysis of many sets of experiments shows that high voltage/impedance switch operation can be achieved in linear current density at the POS cathode does not exceed the value of  $20 \text{ kA/cm}$ . This value limits a maximum cathode diameter of a MITL. Anode diameter is limited by condition of no gap closure with a dense electrode plasma. Application of external magnetic field decreases plasma density necessary for long POS conduction time operation.

## REFERENCES

- [1] Anan'in P.S., Karpov V.B., Krasik Ya.E. et.al. *Pribory i tekhnika Experimenta* ( Rus), 5, 149, (1989).
- [2] Weber B.V., Boller J.R., Comisso R.J. et. al. Microsecond-conduction-time POS experiments. *Proc. 9 Int. Conf. on high power particle beams*, Washington, 1992, pp. 375-384.
- [3] Bystritskii V.M., Lisitsyn I.V. and Krasik Ya.E. Experimental studies of a microsecond plasma opening switch in the positive polarity regime. *Proc. 9 Int. Conf. on high power particle beams*, Washington, 1992, pp. 529-534.
- [4] Mendel C.W., Savage M.E., Zagar D.M. et.al. *J. Appl. Phys.* 71, 3731, (1992)

# A 3-MA COMPACT-TOROID-PLASMA-FLOW-SWITCHED PLASMA FOCUS DEMONSTRATION EXPERIMENT ON SHIVA STAR

G.F. Kiuttu, J.D. Graham<sup>\*</sup>, J.H. Degnan, J.S. Brzosko<sup>\*\*</sup>, S.K. Coffey<sup>\*\*\*</sup>, D.G. Gale<sup>\*</sup>,  
C.D. Holmberg, B.B. Kreh, J.W. Meyers, C.A. Outten, E.L. Ruden, and K.D. Ware<sup>\*\*\*\*</sup>

*High Energy Sources Division, Phillips Laboratory, PL/WSQP  
Kirtland AFB, New Mexico, USA 87117-5776*

<sup>\*</sup>*Maxwell Laboratories, Inc., Albuquerque, New Mexico, USA*

<sup>\*\*</sup>*Avogadro Energy Systems, Inc., Staten Island, New York, USA*

<sup>\*\*\*</sup>*Physical Sciences, Inc., Alexandria, Virginia, USA*

<sup>\*\*\*\*</sup>*Defense Nuclear Agency, Alexandria, Virginia, USA*

## Abstract

We describe a novel dense plasma focus experiment using the Shiva Star capacitor bank, which uses a compact toroid (CT) magnetized plasma flow switch (PFS) to initiate the focus implosion. The CT armature stably and reproducibly translates up to 3 MA from the vacuum feed region through coaxial electrodes to the gas puff central load. The inertia of the 1 mg CT and the work that must be done in compressing the internal magnetic fields during the translation provide a delay in current delivery to the pinch of 5 - 10  $\mu$ s, which matches the bank quarter cycle time relatively well. Effectiveness of the current delivery was monitored primarily by inductive probes in the PFS region, fast photography of the focus, and x-ray and neutron measurements of the pinch. K shell X-ray yields using neon gas were as high as 1 kJ, and  $10^8$  neutrons were produced in a deuterium gas focus.

## Introduction

For the last several years we have studied experimentally and computationally the formation, acceleration, and compression of compact

toroid plasmas.[1,2] These toroidally shaped, low- $\beta$  plasmas are formed between concentric electrodes in a magnetized coaxial plasma gun geometry, and are enmeshed in closed toroidal and poloidal magnetic fields which are sustained by internal currents. They are particularly interesting since they spontaneously relax toward a minimum-energy (internally force-free) state characterized by parallel current density and magnetic field vectors. Thus, they are remarkably stable and robust entities.

There are many applications for CTs besides acceleration to high velocities and kinetic energies. For example, they were envisioned to be effective plasma flow switch armatures.[3] In this application, they conduct driver current while moving from an initiation location to a downstream load while the current builds toward maximum value. Computationally, they were shown to be superior to unmagnetized plasma armatures for driving hollow z-pinches because of their stability, higher speeds, and reduction of material accumulation in the implosion electrode gap.[4]

In our experimental investigations of translating CTs formed from moderate-Z gases, we noticed that they indeed



appeared to have characteristics suitable for use as PFS armatures. That is, they were long-lived (of order 100 microseconds), stable (over 10- $\mu$ s time and 1-m distance scales), azimuthally symmetric, and reproducible in their trajectories.[5] We, therefore, decided to investigate the possibility of using them to initiate plasma-focus-like discharges in a puffed gas load, as shown in Fig. 1.

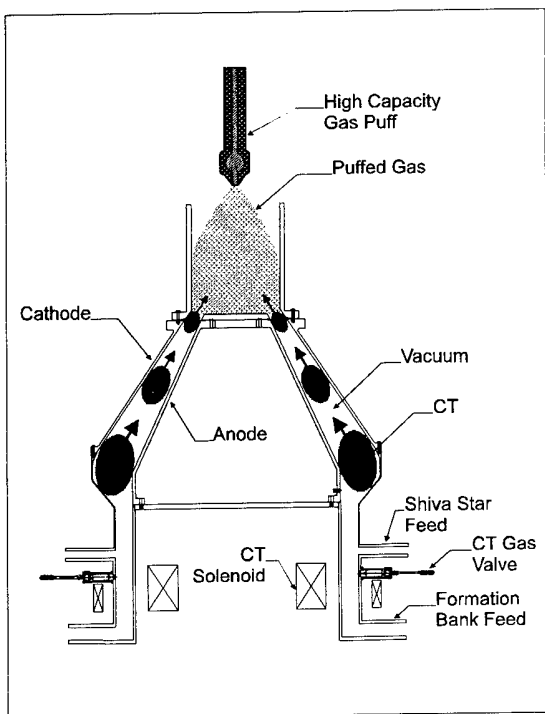


Figure 1 CT-switched puffed gas DPF concept.

In this scheme, the CT PFS essentially replaces the axial run-down phase in a conventional Mather-type dense plasma focus (DPF).[6] Of course, depending on the length-to-diameter ratio, a Filippov-type device can also be emulated.[7] The advantage in such a scheme is that insulator initiation is avoided. Furthermore, operation should be more resistant to electrical breakdown failure because the insulator is well shielded from the plasma, which radiates in the ultraviolet. Thus, it might be possible to operate at higher energies and currents than previously achievable with these devices.

## Experiment Description

We chose to use a modified three times radially converging electrode CT acceleration geometry which was successfully operated at 1 MJ stored energy (2.5 MA current) on the Shiva Star capacitor bank (110 - 1320  $\mu$ F, 30 - 120 kV).[8] The modifications consisted of raising the outer electrode to slightly increase the gap, removing the downstream straight coaxial section, adding a tungsten center electrode cap, and adding outer electrode return current conductor bars and steel screen electrode, as shown in Fig. 2. We also fabricated a set of copper extension electrodes to further converge the major radius another factor of two. This gave us the option of working with an 11-cm-diameter anode, as compared to 24 cm for the 3x geometry.

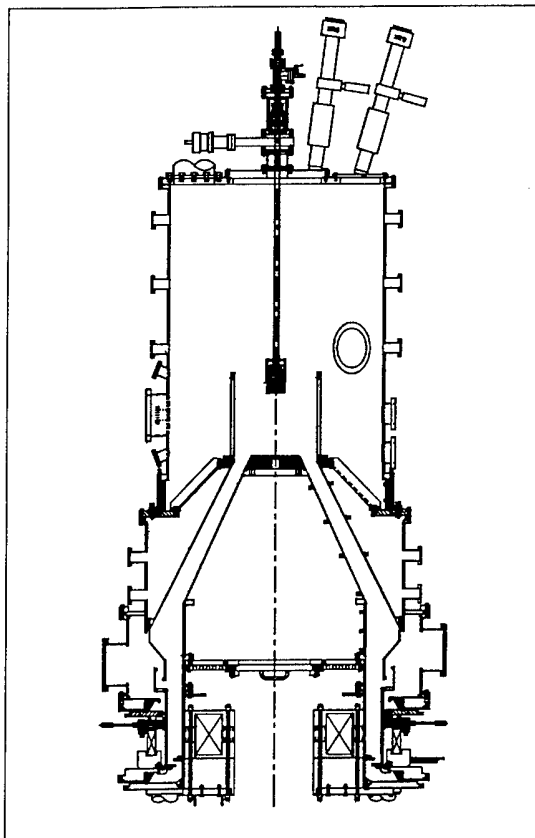


Figure 2 "3x" CT DPF configuration.

Also shown in Fig. 2 are numerous radial ports along the electrodes for inductive probes and through the vacuum vessel in the load region for various

photographic and radiation diagnostics for the pinch.

Operation with the 3x geometry was simulated using our 2-D MHD code MACH2.[9] The simulations showed effective PFS operation at 2 MJ stored capacitor bank energy, and greater than 3 MA delivered current. The effective risetime of the current pulse to the load was approximately 350  $\mu$ s. The simulations also showed a subsequent plasma-focus-like radial implosion of injected gas. However, approximately 50% of the current shifted back into the electrode gap during the implosion. Since there was an appreciable inductance change associated with this shunting, the driver current exhibited a sharp rise in value at the time of shunting.

### Results and Discussion

Experiments were performed with the 3x electrodes at 0.6 MJ and 1.0 MJ stored energies, and with the 6x electrodes at 0.6, 1.0, 1.5, and 2.0 MJ stored energies (2.2, 2.6, 3.0, and 3.1 MA peak currents, respectively).[10] CTs were usually formed from approximately 1.5 mg of argon gas, and had approximately 10 kJ of initial internal magnetic field energy.

No indication of current shunting (by the driver current jump) was observed for operation at any energy. A typical set of driver current and voltage monitor waveforms is shown in Fig. 3 for a 1 MJ shot with 3x electrodes. Note that the main discharge begins at 21  $\mu$ s. The current was measured by summing Rogowski coil signals from each of the six Shiva Star arms. The voltage was measured in the transmission line just outside the vacuum insulator, and therefore has a static inductive component. Additional parameters for this shot include 30 psia neon gas puff valve plenum pressure and 4.0 ms valve-to-formation-discharge delay.

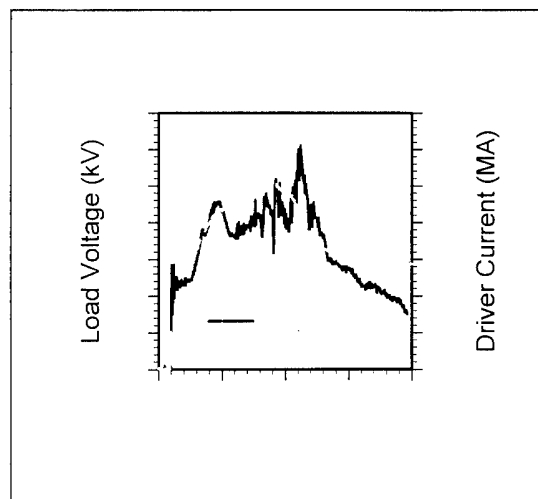


Figure 3 Voltage and current for a 1 MJ shot.

A set of turbine-mirror camera photos of the DPF taken in visible light for this shot is shown in Fig. 4. There is good

correlation between implosion radius from the photographs and from inductance derived from current/voltage analysis. For this particular shot, the load mass was too high for effective neon K shell x-ray production (implosion speed was only a few cm/ $\mu$ s, resulting in approximately 30 J). Other shots with lower load masses and/or higher driver currents produced up to 1 kJ of neon K shell radiation, primarily in the helium-like resonance and  $1s3p-1s^2$  lines, as measured by filtered vacuum x-ray diodes and curved crystal spectrographs.

A few shots were operated at up to 1.5 MJ with a deuterium gas load, and neutron yields up to  $10^8$  were measured with silver activation counters and shielded scintillator/photomultiplier detectors.

In both x-ray and neutron operation, yields were considerably below the largest reported DPF yields at comparable, or lower, peak currents. However, our experiments were far from optimized. We could not operate at sufficiently low gas injection masses for three reasons. First, the high-capacity puff valve would not seal at plenum pressures below 6 psia. Second, the valve opening time jitter was comparable to the optimum

gas injection time. Third, the valve suffered considerable damage from the high current densities in the late stages of the discharges, which compounded the previous problems.

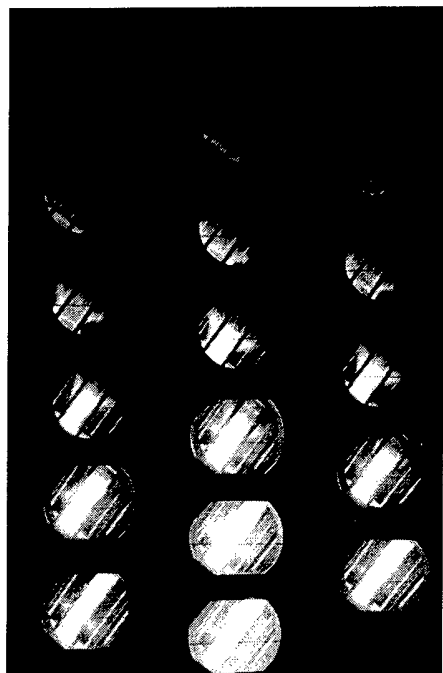


Figure 4 Framing photos (tilted approximately  $40^\circ$  with respect to vertical) of the pinch region. Interframe time is approximately 200 ns. Sequence is upper left to lower right.

There is also some uncertainty in the actual focus drive current. Although inductive probes in the vacuum electrode section indicated full current delivery, we could not place such probes close to the load region because of the high energy densities there. Future design iterations will incorporate shielded Rogowski loops in the center electrode at the end of the

conical electrodes and on the upper implosion surface.

Finally, there is a possibility that the CT armature itself introduces additional load mass. However, we formed the CTs from a different material (argon) than the load, and did not observe significant characteristic x-rays from argon. Still, more spectroscopy is warranted to resolve this issue.

### Conclusion

We have experimentally demonstrated plasma-focus-like discharges, initiated by magnetized plasma flow switches and using puffed gas loads without insulator initiation, at stored capacitor bank energies up to 2 MJ and peak currents in excess of 3 MA. In these experiments relatively symmetric initiation, implosion, and pinching were observed in neon and deuterium gas loads. It may be possible, through optimization of this technique, to increase deuterium neutron and neon K shell x-ray yields to much higher levels than obtained to date.

### Acknowledgements

The authors wish to thank D. Lileikis of Phillips Laboratory for computational support, and I. Vitkovitsky, J. Thompson, N. Filippov, and B. Freeman for technical input. This work was sponsored by the US Air Force and the Defense Nuclear Agency.

- [1] Degnan, J.H., *et al*: Phys. Fluids B 5 (1993) 2938
- [2] Kiuttu, G.F., *et al*: BEAMS 94 - Proc. of the 10th Intl. Conf. on High Power Particle Beams (1995) 150
- [3] Hartman, C.W. and Hammer, J.H.: Phys. Rev. Lett. 48 (1982) 929
- [4] Peterkin, R.E., *et al*: Proc. of the 8th IEEE Intl. Pulsed Power Conf. (1991) 277
- [5] Kiuttu, G.F., Degnan, J.H., Lileikis, D.E., and Ware, K.D.: Proc. of the 10th IEEE Intl. Pulsed Power Conf. (to be published)
- [6] Mather, J.W.: Phys. Fluids 8 (1965) 336
- [7] Filippov, N.V., Filippova, T.I., and Vinogradov, V.P.: Nucl. Fusion Suppl. (1962), Pt. 2, 577
- [8] Kiuttu, G.F. *et al*: Conf. Rec.—Abstracts, 9th IEEE Intl. Pulsed Power Conf. (1993)
- [9] Lileikis, D.E.: IEEE Conf. Rec.—Abstracts, 1995 IEEE Intl. Conf. on Plasma Sci. (1995) 172
- [10] Kiuttu, G.F., : Bull. Am. Phys. Soc. 1800 (1995) 4700

# NEW SOLID STATE OPENING SWITCHES FOR REPETITIVE PULSED POWER TECHNOLOGY

S.K.Lyubutin, G.A.Mesyats, S.N.Rukin, B.G.Slovikovskii, A.M.Turov

*Institute of Electrophysics  
Russian Academy of Sciences, Ural Division  
34, Komsomolskaya Str., Ekaterinburg, 620219, Russia*

## Abstract

In 1991 we discovered a semiconductor opening switch (SOS) effect that occurs in  $p^+-p-n-n^+$  silicon structures at a current density of up to  $60 \text{ kA/cm}^2$ . This effect was used to develop high-power semiconductor opening switches in intermediate inductive storage circuits. The breaking power of opening switches was as high as 5 GW with the interrupted current up to 45 kA, reverse voltage up to 1 MV and the current interruption time between 10 and 60 ns [1,2]. The opening switches were assembled from quantity-produced Russian-made rectifying diodes type SDL with hard recovery characteristic. On the basis of experimental and theoretical investigations of the SOS effect new SOS diodes were designed and manufactured by the Electrophysics Institute. The paper gives basic parameters of the SOS diodes. New diodes offer a greater value of the interrupted current and shorter time of current interruption accompanied by a considerable increase in the energy switching efficiency. The new SOS diodes were used to develop repetitive all-solid-state pulsed generators with an output voltage up to 250 kV, pulse repetition rate up to 5 kHz, and pulse duration between 10 and 30 ns.

## SOS effect among other methods of current switching in semiconductors

The basic principles of current switching by semiconductor devices stem from the processes that take place in the low-doped base of the structure: either filling of the base with the electron-hole plasma (current switches) or removal of the electron-hole plasma from the base (current opening switches). For example, the process of current switching by a fast thyristor or a reverse switched diistor (RSD) represents a slow ( $\sim 10^{-6} \text{ s}$ ) diffusion filling of the base with excess plasma. Therewith a high density of the switched current vs a low switching speed  $dj/dt$  is realized (see Table 1). When current is interrupted, a maximum speed of carriers is achieved in the base of drift step recovery diodes (DSRD). The switching time is as short as  $\sim 10^{-9} \text{ s}$ . However the density of the interrupted current is small, because there is no residual plasma in the base at the stage of current interruption. Still shorter switching time of  $\sim 10^{-10} \text{ s}$  can be achieved at low current densities in silicon avalanche shapers (SAS) [3].

Table 1. Comparison of semiconductor switching technologies.

	$j, \text{ kA/cm}^2$	$dj/dt, \text{ A/cm}^2 \cdot \text{s}$	$t_c, \text{ s}$	$U, \text{ V}$	$P, \text{ GW}$	Ref
RSD	1 — 20	$\sim 10^{10}$	$10^{-6} — 10^{-5}$	$2 \cdot 10^4$	$\sim 5$	[3]
DSRD	0.1 — 0.2	$\sim 10^{11}$	$\sim 10^{-9}$	$2 \cdot 10^4$	$\sim 10^{-3}$	[3]
SAS	0.6	$6 \cdot 10^{12}$	$\sim 10^{-10}$	$5 \cdot 10^3$	$\sim 10^{-3}$	[3]
SOS	1 — 60	$4 \cdot 10^{12}$	$\sim 10^{-8}$	$\sim 10^6$	$\sim 10$	[1,2]

The aforementioned methods of switching provide either a high density of current and slow switching (RSD) or fast switching and a low density of current (DSRD, SAS). A common drawback of the methods is a low working voltage, which in real devices does not exceed  $10^4$  V. The SOS-effect differs qualitatively from these switching methods in that current interruption is independent of the processes taking place in the base of the structure [4]. By the beginning of current interruption the base still has an electron-hole plasma whose concentration is approximately two orders of magnitude higher than the doping level of the base. The process of current interruption develops in a narrow high-doped region of the structure. The region of the structure covered by the electric field increases during current interruption to 15-25  $\mu\text{m}$  in  $\sim 10^{-8}$  s and the field is as high as 300-400 kV/cm. For these reasons the SOS-effect combines a high density of interrupted current and nanosecond interruption time.

One more distinctive feature of the SOS-effect is the mechanism of a uniform distribution of voltage in series-connected structures at the stage of current interruption. The mechanism is due to enhancement of the semiconductor ionization, which leads to additional generation of the electron-hole plasma and lowering of the field in the structures where it is higher than the average field. Then a large number of structures can be connected in series to obtain the working voltage at the megavolt level. There is no need for forced equalization of voltage across the structures. The parameters of the above-considered methods of switching are compared in Table 1 which lists both characteristic and maximum attainable parameters of developed devices.

#### Development of new SOS diodes

Experimental studies of the SOS-effect revealed that characteristics of the opening switches depend not only on the pumping regime (current density and time) but also on the initial doping profile of the  $p^+p-n-n^+$  structure. We have produced and tested more than 20 alternative structures with different combinations of the resistivity of the initial silicon, hole lifetime, base thickness, and doping profile of  $p^+$ ,  $p$  and  $n^+$  regions. Every version of the opening switch comprised 80 series-connected structures of the same type and its working voltage was up to 100 kV. The test parameters of the new SOS diodes proved to be much better than characteristics of the current interrupters employing standard high-voltage diodes. Fig. 1 shows the superposition of voltage pulses produced under the same conditions using an NTE 541 rectifier diode (soft recovery diode, USA), an SDL-0.4-800 diode (hard recovery diode, Russia), and the novel SOS diode.

Photographs of the novel SOS diodes are given in Fig. 2. By design a SOS diode is a stack of series-connected plates compressed with the help of insulation rods. Each plate is a copper heat-sink  $30 \times 30 \times 2$  mm or  $20 \times 20 \times 2$  mm in size with 4 structures soldered in series. The structures have a protective coating on the side and ground end contacts. The diode stack is provided with a device compensating for thermal linear expansion. The main technical characteristics of the SOS diodes are as follows:

Maximum peak reverse voltage -	120 kV
Interrupted current -	1 kA ( $S=0.25 \text{ cm}^2$ ), 4 kA ( $S=1 \text{ cm}^2$ ), 8 kA ( $S=2.2 \text{ cm}^2$ )
Current interruption time -	6 - 8 ns
Maximum overvoltage (idle regime) -	7
Recovery time -	< 1 $\mu\text{s}$
Maximum dissipation power	
(in transformer oil/in air with force cooling) -	
continuously	50-100 W/25-50 W
burst mode	500-1000 W/250-500 W
Dimensions -	(80-120) x (50-70) x (30-45) mm
Mass -	0.2 - 0.3 kg.

The pulse repetition frequency of the SOS diodes is fully and solely determined by particular conditions of heat removal from the structures, because their self-recovery time does not exceed 1  $\mu$ s. During the tests the devices operated at the pulse repetition frequency of 100 to 1000 Hz under the continuous mode and 1000 to 5000 Hz under the burst mode, the burst duration being 0.5 to 2 minutes.

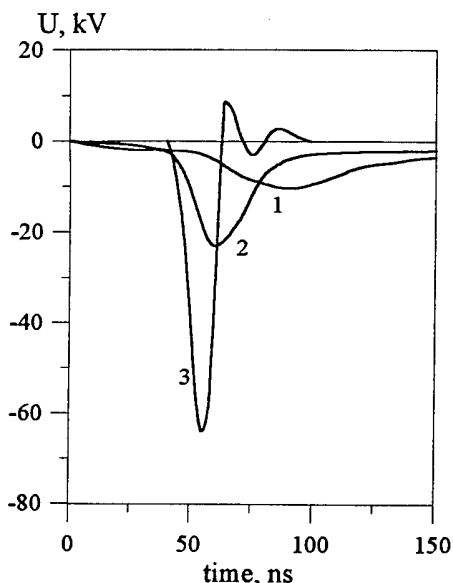


Fig.1. Oscillograms of voltage pulses at the interrupter when the voltage across the pumping capacitor is 9.5 kV: (1) NTE541; (2) SDL-0.4-800 diode; (3) new SOS diode.

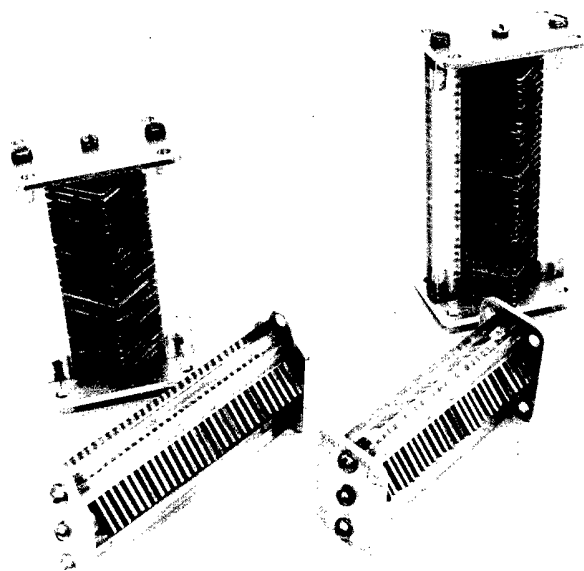


Fig.2. External appearance of new SOS diodes.

#### Application of new SOS diodes for repetitive pulsed power technology

The newly developed SOS-diodes can be used as the base of pulsed power technology with an all-solid-state switching system rated at the following output parameters:

voltage	10-1000 kV;
current	0.5-50 kA;
pulse duration	10-100 ns;
pulse repetition frequency	0.01-10 kHz;
pulse energy	0.1 J - 10 kJ;
average power	10 - 500 kW.

The required level of the output voltage is provided by simple series connection of the SOS-diodes, with voltage dividers being unnecessary. The required current is preset either by a proper selection of the surface area of the semiconductor structure or through parallel connection of smaller-area diodes. The pulse repetition frequency and the average power of the machine are fully determined by the heat removal conditions. Running-water cooling (also of SOS-diodes) provides an average power of hundreds of kW at the pulse repetition frequency from hundreds of herz to unities of kilohertz. In the pulse burst generation regime, where the machine runs under adiabatic thermal conditions, the pulse repetition frequency is limited only by the time of recovery of the thyristor switches in the charging device and can be as high as 10-20 kHz.

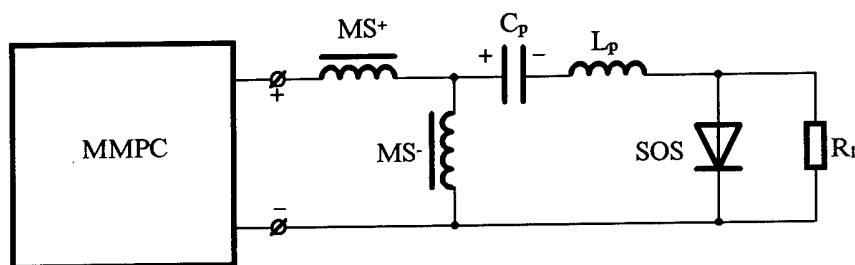


Fig.3. Matching diagram of the magnetic switches and the SOS.

The matching diagram of the magnetic switches and the SOS is shown in Fig. 3. In this approach, the SOS performs simultaneously the functions of a nanosecond pulse compressor and a voltage multiplier. For this reason, all other things being equal, SOS-based devices are simpler, more reliable and cheaper than traditional nanoseconds machines, imploring magnetic switches alone. Moreover, small specific thermal loads on the magnetic switches, which operate in the microsecond time range only, allow development of megavolt installations with the pulse repetition frequency of the kHz range. The microsecond compressor has cores made of cheap permalloy and capacitive storages are made up of standard commercial capacitors.

We have designed two all-solid-state nanosecond generators employing the new SOS diodes. Table 2 gives main parameters of the generators.

Table 2

Specifications	SM-1N	SM-2N
Voltage	250 kV	140 kV
Current	1.4 kA	0.4 kA
Pulse width	28 ns	25 ns
Pulse shape instability	<1%	<1%
Pulse repetition rate		
burst mode (30 s)	1000 Hz	5000 Hz
continuously	100 Hz	1000 Hz
Mass	~85 kg	~50 kg

## References

- [1] Kotov Yu.A., Mesyats G.A., Rukin S.N. et al. "A novel nanosecond semiconductor opening switch for megavolt repetitive pulsed power technology: experiment and applications". Proc. 9th IEEE Int. Pulsed Power Conf., Albuquerque, NM, 1993, p.134.
- [2] Mesyats G.A., Rukin S.N., Lyubutin S.K. et al. "Semiconductor opening switch research at IEP". Proc. 10th IEEE Int. Pulsed Power Conf., Albuquerque, NM, 1995.
- [3] Tuchkevich V.M., Grekhov I.V. "New principles of switching high power by semiconductor devices", Leningrad: Nauka, 1988 (in Russian).
- [4] Darznek S.A., Mesyats G.A., Rukin S.N., Tsiranov S.N. "Theoretical model of the SOS effect". Proc. 11<sup>th</sup> Int. Conf. on High Power Particle Beams, Prague, Czech Republic, June 10-14, 1996.

## BEAM-DRIVEN TRANSMUTATION TECHNOLOGY

Charles D. Bowman

*Chief Scientist, Accelerator-Driven Transmutation Technology Project  
Los Alamos National Laboratory, Los Alamos, 87545 NM, USA*

### **Abstract**

As concerns grow about the ultimate disposition of the large amount of waste produced by the nuclear weapons program in the U. S. and Russia and world-wide commercial nuclear power, the primary approach of permanent geologic storage is making little headway. Attention to means for destruction of these wastes by neutron transmutation is therefore growing. While reactors offer some potential for dealing with this problem, there are problems with both safety and completeness of this approach.

Accelerator-driven systems appear to offer improved safety in terms of subcriticality, capability for complete destruction of long lived higher actinide and fission product, and a more proliferation-resistant fuel cycle. The fundamental advantages of accelerator-driven systems over reactors in terms of neutron economy will be described. The salient features of the technology will be presented such as the basis for the choice of liquid fuel, the approach to front- and back-end separations, and a comparison of linac and cyclotron accelerator effectiveness.

The present status of this technology in the U. S. and world-wide is described. A plan for development and deployment of the technology is presented.

*(The full text has not been supplied.)*



# ANGARA-5-1 PROGRAM

## DEVELOPMENT OF SUPERFAST LINER IMPLOSION FOR ICF PHYSICS STUDY AND BASIC RESEARCH

A.V. Branitskii, E.V. Grabovskii, M.V. Fedulov, I.N. Frolov, D.V. Kuznetsov, V.O. Mishensky, S.L. Nedoseev,  
G.M. Oleinik, A.A. Otochin, V.E. Pichugin, V.P. Smirnov, G.S. Volkov, V.I. Zaitsev, V.V. Zajivikhin,  
S.V. Zakharov, M. V. Zurin.

*Troitsk Institute for Innovation and Thermonuclear Investigation, Troitsk, Moscow reg., Russia*

E.P. Velikhov - *Russian Scientific Center "Kurchatov Institute, Moscow, Russia*

K.E. Dyabilin, V.E. Fortov, M.E. Lebedev - *High Energy Density Research Center, Moscow, Russia*

K.V. Danilenko, A.V. Zakharov - *Research Institute of Pulse Technic, Moscow, Russia*

A.V. Gerusov, T.I. Razinkova, P.V. Sasorov - *Institute for Theoretical and Exp. Physics, Moscow, Russia*

A.F. Nikiforov, V.G. Nikiforov - *Applied Mathematics Institute, Moscow, Russia*

A.Yu. Krukovskii - *Institute for Mathematical Modeling, Moscow, Russia*

### ABSTRACT

Double Liner (DL) concept to utilize Pulsed Power for investigations on Inertial Confinement Fusion (ICF) and High Energy Density Physics is proposed. In this scheme external cylindrical plasma shell (liner) magnetically imploded in the generator diode collides with the internal one. Thermal X-ray radiation brought about by a high-velocity shock wave penetrates into the internal liner cavity and irradiates a spherical target. Investigations with ANGARA-5 generator were concentrated on a comprehensive study of physical processes and possibility of short radiation pulse generation. Soft X-ray radiation intensity up to  $3 \text{ TW/cm}^2$  with 3 ns rise time was obtained. As theoretical model predicts for the generator current higher than 15MA the radiation intensity would be close to an ignition threshold and magnetized plasma instabilities be suppressed. This paper reports on the concept, theoretical and experimental results.

### 1. INTRODUCTION

In general the efforts undertaken in ICF have met two major challenges: pellet with gain of several tens and a driver suitable for reactor of power plant. Up to now both of them are important but the need to demonstrate a capability of pellet ignition has a first priority. It is difficult to use for pellet design the knowledge from weapon experience due to a large differences in the parameters. As a result the wide physics pellet study has to be done to provide the successful microimplosion. We have to choose the most effective way to reach this goal. It would be very expensive to try to solve the problems of a pellet and reactor driver on the same facility.

The getting of microexplosion has to open also the wide possibilities for numerous research in basic and applied sciences due to the reaching of extreme matter parameters and radiation fluxes.

One of the most promising trends of physical research in the field of Inertial Confinement Fusion and High Energy Density Physics is utilization of Pulsed Power. This approach differs by most advanced technology, high efficiency and relatively low cost of a driver. Generators of the SNL (US), KALIF (KFK) (Germany) and ANGARA-5 (Russia) are applied for ICF driver experiments by means of light ion acceleration (PBFA-II) or plasma implosion (ANGARA-5, SATURN).

As it is known for indirect driven ignition experiment the target exposure about  $1 \text{ MJ/cm}^2$  with pulse duration of 2-5 ns is required. Requirements may be satisfied, for example, for Lithium ions focused beam with 30 MeV,  $10\text{-}15 \text{ MA/cm}^2$  (or, by other words, plasma flux with velocity of  $3 \cdot 10^9 \text{ cm/s}$ , and density  $0.1 \text{ } \mu\text{g/cm}^3$ ). Another approach is the magnetic implosion of plasma with lower velocity of  $5 \cdot 10^7 \text{ cm/s}$  but much higher density of  $10 \text{ mg/cm}^3$ .

Since 1988 the main purpose of investigations on ANGARA-5 (pulsed power facility consisting of 8 modules with maximum power of 9 TW, pulse rise time of 90 ns and a load current - 4 MA) by development of approaches for power sharpening of soft x-ray radiation through a conversion of kinetic energy of the cylindrical

shell (liner) imploded in generator diode to radiation and the application of intensive soft x-ray pulse for target studies.

We are discussing the cylindrical shells though the most effective way for energy concentration could be the scheme with 3-D plasma shell magnetic implosion (spherical like shells with conical electrodes). However there are problems with production of light mass distributed on shaped shells and its enhanced instability during 3-D compression under azimuthal (2-D) magnetic field pressure.

Double Liner (DL) concept was proposed in Ref. 1. It permits to convert liner kinetic energy to radiation pulse with a duration being significantly less than a generator pulse duration. Theoretical and experimental studies of DL with ANGARA-5 were carried out and first results were reported in Ref. 2, 3.

## 2. DOUBLE LINER CONCEPT

Double Liner is a cascade system of two coaxial liners doped by high charge ( $Z \gg 1$ ) substances (Ref. 1). The external liner accelerated by a magnetic field pressure collides with the internal one. A thermal X-ray radiation generated by a high-velocity shock wave ( $V = 4 \cdot 5 \cdot 10^7$  cm/s), penetrates into the internal liner cavity and irradiates a target like in hohlraum. The external liner realizes an energy confinement at the same time hindering radiation escape outside, thereby increasing the radiation intensity in the hot cavity. The inner liner serves both to stagnate the imploding outer plasma, converting plasma kinetic energy into radiation, and hydrodynamically isolate the target from the imploding plasma before its ignition.

To convert effectively the liner kinetic energy into radiation and to realize the energy confinement the liners should be produced of substances with high charge  $Z \gg 1$ . As it was shown in Ref. 4, a thermal pressure of liner multicharged plasma is much less than magnetic one ( $P \ll B^2/8\pi$ ) because of high radiation losses. Therefore, during the liner implosion its thickness is compressed up to skin-layer scale ( $\delta = \sqrt{c^2 t / 2\pi\sigma}$ ). The liner kinetic energy is determined mainly by the current amplitude ( $I$ ) and converging ratio ( $R/r$ , where  $R$  - initial radius and  $r$  - final one) and may be estimated as:

$$mV^2/2 \propto \alpha I^2 h \cdot \ln(R/r) \quad (1)$$

where  $m$ ,  $V$  - outer liner mass and velocity,  $h$  - its length,  $\alpha$  - coefficient depending on particular current pulse shape.

The external liner acceleration is accompanied by radiation of energy dissipated in the liner plasma. As a result, the internal liner is sublimated under irradiation and scattered with sound velocity. During strike the external liner deceleration and its kinetic energy conversion into radiation take place in the internal liner plasma with the characteristic time  $\tau = \delta/V$ .

The effective liner kinetic energy conversion into radiation realizes when a strongly radiative shock wave is excited during the collision process in the internal liner plasma, and the external liner is decelerated without shock. As followed from the model of MHD of strongly radiative plasma (Ref. 1, 4) such regime takes place when Alfvén velocity in the external liner plasma is comparable with the liner velocity.

A strongly radiative shock wave generated in the plasma of the second liner propagates with a time-variable velocity (Ref. 1):

$$D = \frac{V}{\left(1 + (2V/\mu) \cdot \int_{t_1}^t \rho dt\right)^{1/2}} \quad (2)$$

where  $\mu = m/(2\pi rh)$  is the external liner mass, per unit area;  $\rho$  is the internal liner plasma density in front of the shock wave; integration by time from the moment of collision start  $t_1$  is performed along the shock wave trajectory. The kinetic energy conversion into radiation in the shock wave propagating over a multi charged

plasma is a result of a chain on sequential events. Due to the ion viscosity mechanism the kinetic energy of adirected motion transfers into a thermal energy of ions. Plasma electrons heated in ion-electron collisions lose their energy mainly by means of multi charged ions excitation.

A high efficiency of the kinetic energy conversion to radiation and target irradiation may be achieved under appropriate choice of substances and parameters of liners (Ref. 1, 3). If the effective conversion conditions are met the following expression can be obtained for the thermal x-ray radiation intensity on the target (Ref. 1):

$$W = 1.33 \cdot (1 + 3\mu\kappa / 4) \rho D^3 \quad (3)$$

where  $\kappa$  is the mean mass radiation absorbtion coefficient in the external liner plasma. The coefficient ( $\mu\kappa$ ) in (3) describes the energy partial confinement in the cavity by the external cylindrical shell. The most important consequence results from (3). Due to increasing of the external liner optimum mass value with current  $\mu \propto I^2$  and the kinetic energy flux as  $I^2$  the thermal radiation intensity at  $\mu\kappa \gg 1$  rises as

$$W \propto I^4 \quad (4)$$

It means a target irradiation efficiency growth with current amplitude increase. The internal hohlraum temperature has to be higher than one on the outer (visible) surface of liners. To realize an outcome to the regime (4) along with a current amplitude and liner mass magnification it is nessesary to select materials of the outer liner for the energy confinement in the cavity. It has been demonstrated by spectral calculation in temperature range of 300 eV the use of neodim, xenon and some others elements give the best results.

The liner kinetic energy grows with convergence ratio increasing. But MHD instabilities restrict the convergence ratio at 10 - fold level ( $R/r < 10$ ); hence, the kinetic energy flux is limited. The external liner instability in the process of acceleration affects on the radiation pulse duration due to a width of the first cascade liner, as well as on the energy confinement efficiency in the cavity due to discontinuety of the external liner optical thickness.

Among various types of plasma instabilities for a multicharged current driven plasma of liners there are:

- an ionization instability in the early discharge stage (Ref. 7),
- a thermal instability at the initial stage of plasma current heating (Ref. 5),
- a thermal-radiating instability as a prolongation of the previous one on the stage of a radiation-heating equilibrium (Ref. 6),
- a non-isothermal instability after the first shock wave (Ref. 6, 8),
- MHD instabilities (like Raleigh-Taylor mode) with distinctions for the multicharged plasma,
- anomalous resistance of liner plasma due to different types of micro instabilities.

Influence of instabilities and anomalous resistance reduces with current growth under fixed convergence ratio because the plasma becomes unmagnetized and electron drift velocity decreases for higher liner densities.

Numerical simulations predict that for the generator parameters with current amplitude  $I = 15$  MA and voltage pulse rise time of 100 ns the liner with mass of 2.8 mg and radius  $R = 1.65$  cm is accelerated up to the velocity  $V = 5 \cdot 10^7$  cm/s. As a result of collision with the internal liner with mass of 4.5 mg and radius  $r = 0.2$  cm, the cavity of inner liner is filled by thermal radiation with an intensity on the target  $W = 500$  TW/cm<sup>2</sup> and pulse duration at a half-height  $\tau = 3.7$  ns. As calculations show this is enough for a target ignition.

### 3. DOUBLE LINER COLLISION EXPERIMENT

In experiments on ANGARA-5 the outer liner hollow gas puff with Mach number 6 was produced by a supersonic ring nozzle with diameter of 34mm and ring gap of 2 mm. Xenon, neon were used as working gases. A jet specific mass was 0.1-0.2 mg/cm, its height between cathode and anode grid - 1 cm. The internal liner with 4 mm diameter, wall thickness of 0.2 mm and specific mass of 0.2-0.3 mg/cm was prepared from a foam with average density of 10 mg/cm<sup>3</sup>, doped by Mo metallic powder with a grain diameter less than 1  $\mu$ m.

A radiation intensity was measured by time resolving spectroscopic methods, i.e. by polychromator in spectral lines of 130, 183, 277, 395, 430, 525 eV; by X ray diodes with different filters providing a sensitivity in

a range of 150-2500 eV. The intensity inside of liner cavity was defined through a radiation yield reradiated in the axial direction by a Bi coat on the liner bottom.

Typical liner velocity to the strike moment, being measured by optical and X ray streak cameras, is  $(4-6) \cdot 10^7$  cm/s. At the moment of collision of shells the radiation intensity from the outer surface grows up to  $1.5 \text{ TW/cm}^2$  with rise time of 3 ns. During the following 5 ns the outer surface temperature drops. The sharp elevation of the outer liner temperature seems to indicate the radiative (non-hydrodynamical) cooling of plasma. A radiation yield during liners strike reached 7-10 kJ. The cavity internal surface radiation intensity reaches  $3 \text{ TW/cm}^2$  with a rise time of 3-5 ns. The radiation intensity in the internal cavity remains on the same level or drops slightly as long as it decreases outside.

This difference of intensities inside and outside means the radiation screening effect by the outer liner. Radiation spectral characteristics at the strike moment differs from Planckian one corresponding to the intensity level measured. The color temperature of outside radiation is close to reported earlier (Ref. 2, 3) of 100-130 eV. Comparisons of simulations with experimental results permit to explain this difference by local character of the strike of the liners because of initial axial and azimuthal non-uniformities of the gas puff and instabilities. In fact, the radiation intensity rise time measured locally is 2 ns. Laser shadow and streak camera pictures show the presence of zipper- effect and instabilities mentioned above theoretically.

After strike liners implode further together due to inertia and magnetic field pressure, Z-pinch forms from stagnated plasma and high power radiation pulse occurs again with rise time of first compression about 5-10 ns, total radiation yield about 50 kJ and power of 3 TW.

Magnetically driven Double Liner implosion experiments have been performed also by international team on ANGARA-5 at current of 3-4 MA at TRINITI and on SATURN at 7-9 MA at the Sandia Laboratory. The international team involved groups from TRINITI, SNL, LANL and LLNL from the USA and UK. Experiments have been heavily diagnosed for better understanding of liner dynamics as well as for measurement resulting radiation characteristics. The results on hohlraum temperature shows that comparable values have been achieved using ion beams and magnetic implosion.

#### 4. LOAD DEVELOPMENT AND COLD START PROBLEM

Last experiments on Angara-5-1 have been directed onto achieving the more efficient convolution and so called integrated load development.

Instead the disk shape output vacuum feed 8 conical MITL connected with a small size final collector on the vicinity of a liner load were produced. As a result convolute inductance decreased from 23 nH to nH. Total size of null magnetic zones decreased also by factor of 10. Load current increased from 4.5 MA to 5.5 MA. Due to improvement of load - MITL set coupling stability of a current against the time spread of Angara units increased significantly.

New design of a load for DL scheme was based on the using a foam selfsustained liner for outer shell. Advantage of such design include the more controllable density distribution and the opportunity to suppress of zippering and Hall instability. Outer liner with specific mass of  $200 \mu\text{g/cm}^2$  22 mm diam were produced from 2-5 mg/ccm doped foam. Experiments without foam preionization have shown a pronounced filamentation arouse at initial stage of current sheath formation. To avoid it a rare  $10 \mu\text{g/cm}^2$  Xe gas corona with outer diam of 50 mm has been produced by supersonic nozzle. Due to ionization of Xe gas and plasma implosion onto a foam liner the uniformity of produced current sheath improved significantly.

However the fine laser shadow and streak pictures revealed the existence of numerous small size filaments. Then we have analyzed our previous experimental data, referring to gas-puff liners, and concluded, that as foam, so gas liners, driving by current, could be fractured before implosion due to effects of "cold start". This experimental basis forces us to, suppose, that the nonlinear phase of the current filamentation is the reason of early liner fracturing, which is the first cause of subsequent liner non-compact implosion; instabilities of, magnetically accelerating plasma could be the posterior factor,

As the matter of fact, all Z-pinch or fast liners implosion experiments, using (multi)terawatt pulsed power generators, begin the plasma implosion after "cold start" - electric breakdown of plasma producing substance - gas, solid or foam, positioned, in anode - cathode gap. The current filamentation due to thermal, instabilities of plasma conductivity is the specific feature of, this breakdown, being independent on initial homogeneity of plasma producing matter. No kind of preionisation, being realized in these experiments, could

prevent the filamentation. Really, currentless preionisation (flash - board radiation, etc.) has very small power in comparison with the power of liner plasma Joule heating just before beginning of implosion. The fast current switching method, being used in our experiments with foam liners, don't change the situation in principle. So, the "cold start" and the current filamentation in Z-pinch or liner initial plasma take place always. Because of breakdown random nature, filaments are introduced into liner bulk and the azimuthal magnetic field structure is non-regular and it can force azimuthal inhomogeneities of initial liner plasma in spite of homogeneous plasma producing matter. From energetic standpoint the magnetic energy of filamentary current is great in comparison with the homogeneous one. So, a perturbation of filamentary current magnetic structure to more rough axial and azimuthal structure could happen. Consequently, the "cold start" current filamentation can fracture the liner matter before the instabilities of magnetically accelerating plasma appear. It seems that most effective way to overcome "cold start" effects is to apply powerful currentless preionisation of  $\sim 0.1$  TW level. For example, ion beam could be treated for the purpose. But it takes rather complicate techniques.

Another possibility to overcome this "cold start" effect is to use liners with azimuthally structured plasma producing matter, like multiwire - array. There is no plasma producing matter between wires, consequently, no random filaments and no early liner fracturing during initial period of current rise for ideal wire-array. Of course, it is supposed that wire evaporation is finished before their acceleration and wire plasma doesn't fill the interval between wires. Being surrounded by its own magnetic field, the every wire plasma of that array is being accelerated by itself and its own instability doesn't spread to other ones. May be the recent excellent results of wire-array implosion on "Saturn" are the corroboration of this proposal.

## 5. STRONG SHOCK WAVE EXCITATION BY Z-PINCH GENERATED SOFT X-RAY ON „ANGARA-5-1“.

A fundamental problem in the use of concentrated fluxes of focused charged particles and laser light in the dynamic physics of high energy densities is the substantial spatial nonuniformity of the power which is released. This nonuniformity disrupts the symmetry of the spherical compression of the fusion fuel and hinders the excitation of plane shock waves in the experiments on the behavior of matter under extreme conditions. One of the most effective ways to solve this problem is use of x-ray emission from a plasma with an approximately thermal spectrum which arises when directed energy fluxes are applied to a target or during the electrodynamics compression of cylindrical shells in a Z-pinch geometry. Planar shock waves excited by this radiation, which are an extremely simple type of self-similar hydrodynamic flow may be a more natural and rich source of experimental information on both the matter-intensive x-ray radiation interaction and of the thermophysical properties of matter under influence of this radiation with condensed targets.

Z-pinch plasmas produced in powerful installations by electrodynamic compression of cylindrical liners seem to be one of the most favorable candidates for the source of such x-radiation.

On ANGARA-5-1 study of shocks with double liner scheme as a radiation source was started in a collaboration with Prof. V. E. Fortov teams. First measurements were carried out with Al, Sn, Fe, and Pb targets.

The soft x-rays radiation was incidental on a planar target positioned above the inner liner (at a distance of 1 mm). The experimental set-up was adjusted with top of double liner. The targets were made as step 16-32  $\mu\text{m}$  Al and 80-200  $\mu\text{m}$  Pb, or pure 180  $\mu\text{m}$  Pb, or stepped 16  $\mu\text{m}$  Sn and 180  $\mu\text{m}$  Pb plates being connected together. Such large thickness allowed to eliminate the preheating of the target by thermal wave. The diameter of target was about 5 mm. The velocity of the shock wave was defined by the optical base method as the difference between the moments in the flashes of light emitted as the shock waves break out at the rear surface of a sample.

The averaged (over the target volume) shock wave velocity for Al plus Pb stepped target is  $(7.3 \pm 0.6) \cdot 10^3$  m/s for 80 mm Pb thickness, and  $(4.6 \pm 0.3) \cdot 10^3$  m/s for 200 mm. In accordance with the lead Hugoniot, this means that the shock compression pressures were 3 Mbar and 0.9 Mbar correspondingly. In stepped Sn plus Pb target, a shock compression of lead (thickness 180 mm) about 1.20 Mbar was measured.

## 6. SUMMARY

As a result of investigations on ANGARA-5 the general features of implosion and strike of liners are studied. The effect of energy confinement by the outer liner is observed. High radiation power sharpening inside the cylindrical cavity with pulse rise time duration of 3-5 ns and kinetic energy conversion efficiency of 30-50%

was obtained in DL scheme. These values are comparable with code calculations, if the initial gas puff density distribution and liner instabilities are taken into account.

Detailed data on spectral and temporal behavior of radiation in DL scheme were obtained in joint experiments of TRINITY with SNL, LANL and LLNL on ANGARA-5 .

The development of technologies for foam liners production allows the use of liners with appropriate parameters. Experiments carried out on ANGARA-5 and calculations permit to consider the Double Liner as a high intensity soft X-ray source for ICF target ignition.

The results from shock wave experiments show that uniform intense shock waves can be generated by double liner scheme soft x-ray radiation. The uniformity of shock wave is very high. At a flux power about some  $\text{TW}/\text{cm}^2$ , a shock pressure of some hundreds GPa was achieved

It is of interest to get scaling for radiation intensity increasing at the expense of radiation trapping, kinetic energy growth and instabilities influence restriction at currents more than 10.MA.

The results discussed above have demonstrated a promising perspective of liner implosion to study indirect drive pellet physics as well as a pellet ignition.

Using of 3-D liner implosion scheme could relax the energy demands on a pellet ignition.

## 7. REFERENCES

- [1] Zakharov S.V., Smirnov V.P. et.al. Collision of Current Driven Cylindrical Liners. Kurchatov Institute of Atomic Energy. Moscow. Preprint 4587/6, 1988.
- [2] Smirnov V.P., Grabovskii E.V., Zaitsev V.I., Zakharov S.V. et.al. Progress in Investigations on a Dense Plasma Compression on ANGARA-5-1. Proc. of BEAMS'90. World Scientific, 1991. V.1, p.61 (I.07).
- [3] Zakharov S.V., Smirnov V.P., Tsarfin V.Ya. ANGARA-5 High Intensity Soft X Ray Source with Imploding Liner Cascade for Inertial Confinement Fusion. Proc. of 14<sup>th</sup> Int. Conf. on Pl.Phys. and Cont. Nuc. Fus. Res. Wurzburg, 1992. IAEA. Vienna, 1993. V.3, p.481 (IAEA-CN-56/G-3-9).
- [4] Grigoriev S.F., Zakharov S.V. Magnetohydrodynamics of Strongly Radiative Plasma of Liners. Sov. J. Tech. Phys. Lett. 13,254 (1987).
- [5] Vikharev V.D., Zakharov S.V., Smirnov V.P. et. al. Influence of Preionization Effect on the Acceleration Dynamics of Radiative Plasma Flux in High Current Discharges. Sov. J. Pl. Phys. 16, 388(1990).
- [6] Branitskii A.V., Vikharev V.D., Zakharov S.V. et. al. Investigations of the Liner Compression Initial Stage on ANGARA-5-1 Device. Sov. J. Pl. Phys. 17, 311 (1991).
- [7] Velikhov E.P., Pis'menny V. D., Rakhimov A. T. Dependent Gas Discharge Exiting Continuous CO2 Lasers. UFN (Russian), 122, 3, 419.
- [8] Gasilov V. A., Zakharov S. V., Panin V.M. Influence of Azimuthal Instabilities on the Acceleration Dynamics of Radiating Liners. Preprint IAE 5464/6, 1992.\_

## X-RAY POWER INCREASE FROM SYMMETRIZED WIRE-ARRAY Z-PINCH IMPLOSIONS\*

**T. W. L. Sanford**, G. O. Allshouse, B. M. Marder, T. J. Nash, R. C. Mock,  
M. R. Douglas, R. B. Spielman, J. F. Seamen, J. S. McGurn, D. Jobe,  
T. L. Gilliland, M. Vargas, K. W. Struve, and W. A. Stygar  
*Sandia National Laboratories, P. O. Box 5800, Albuquerque, NM 87185 USA*

J. H. Hammer, J. S. De Groot, and J. L. Eddleman  
*Lawrence Livermore National Laboratory, P. O. Box 808, Livermore, CA 94550 USA*

K. G. Whitney, J. W. Thornhill, P. E. Pulsifer, and J. P. Apruzese  
*Naval Research Laboratory, Radiation Hydrodynamics Branch, Washington, DC 20375 USA*

D. Mosher  
*Naval Research Laboratory, Pulsed Power Physics Branch, Washington, DC 20375 USA*

D. L. Peterson  
*Los Alamos National Laboratory, Los Alamos, NM 87854-0010 USA*

Y. Maron  
*Department of Nuclear Physics, Weizmann Institute, Rehovot 76100, Israel*

A systematic experimental study of annular aluminum-wire z-pinches on the Saturn accelerator shows that, for the first time, the measured spatial characteristics and x-ray powers can approach those of two-dimensional, radiation-magneto-hydrodynamic simulations when large numbers of wires are used. Calculations show that the implosion begins to transition from that of individual plasma wires to that of a continuous plasma shell, when the circumferential gap between wires in the array is reduced below  $1.4 \pm 1.3/-0.7$  mm. This calculated gap coincides with the measured transition of  $1.4 \pm 0.4$  mm between the observed regimes of slow and rapid improvement in power output with decreasing gap. In the plasma-shell regime, x-ray powers in excess of a factor of three over that generated in the plasma-wire region are measured.

Maintaining cylindrical symmetry in z-pinch implosions is an important element of plasma-radiation-source (PRS) load design. Ideal implosions require an annulus with perfect axial and azimuthal uniformity. The additional requirement of low mass, typically less than 500  $\mu\text{g/cm}$  for fast drivers such as Sandia's Saturn accelerator [1], makes fabricating the ideal cylinder challenging. The high-symmetry, low-mass tradeoff has historically led to the choice of gas jets, low-density foams, or thin foils over cylindrical-wire arrays for z-pinch loads. Thin foils have demonstrated similar peak power performance to that reported on here [2]. However, these thin foils were expensive and difficult to fabricate, which has precluded their routine use on Saturn.

Data [3,4] and analyses [5] suggest that reducing azimuthal asymmetries, such as the granularity introduced by discrete wires, leads to improvements in implosion quality. Here, implosion quality refers to high radial compression in the PRS required to (1) generate high thermal x-ray power for achieving high temperature in hohlraums, (2) achieve excitation of high-atomic-number K-shell x rays for nuclear-radiation-effects studies, and (3) provide a testbed for phenomenological studies of such sources with one- and two-dimensional computer codes.

Because of the potentially significant benefits derivable from the improved symmetry using wire arrays, we systematically studied experimentally and theoretically the dynamics of aluminum wire implosions as a function of the gap between wires while keeping the array mass fixed for two load geometries on Saturn. Aluminum was chosen for the large existing database

\*Work supported by U.S. DOE Contract No. DE-AC04-94AL85000

and because array mass, radius, and implosion-time constraints for maximum radiation output could be easily maintained over a large range of gap spacing.

The experimental arrangement was that of Ref. 6 and, in general, was similar to Ref. 7, except for the number of wires used in the array and the diagnostics employed. One load geometry consisted of a 615- to 656- $\mu\text{g}$  array of wires positioned at a radius of 8.6 mm whose wire number was varied from 10 to 136, and the other geometry consisted of an 820- $\mu\text{g}$  array positioned at a radius of 12 mm whose wire number was varied from 13 to 192. Eight current return posts were positioned at 17- and 27-mm radii for the small and large radius loads, respectively. For both load configurations, 20-mm wire lengths were used. About 7 MA with a  $\sim 35$ -ns 10-to-90% rise time flowed through the load. Radiation detectors included a bolometer, arrays of filtered x-ray diodes (XRDs) and photoconducting detectors (PCDs) covering x-ray energies from 200 to 7000 eV, a time- and radius-resolved KAP crystal spectrometer covering 150 to 3500 eV, and two time-resolved x-ray pinhole cameras having x-ray sensitivities above 200 and 1000 eV.

The detailed measurements made with these detectors are summarized in this paper and correlated with numerical simulations in the xy plane using a particle-in-cell magnetohydrodynamic code (MHC) [8] and in the r-z plane using a two-dimensional (2D) multi-photon-group Lagrangian radiation magnetohydrodynamic code (RMHC) [9], a 2D three-temperature Eulerian RMHC [10], and the 2D MACH2 RMHC [11]. The Lagrangian RMHC calculations for a 1-mm axial length permitted detailed comparisons with the measured radiation. The Eulerian calculations modeled the entire axial length prior to compression. The Eulerian RMHC permitted the simulations to be reliably extended beyond peak compression. Measurements of our large-wire-number implosions were highly reproducible and correlate well with the simulations. These correlations permit, for the first time [9], detailed studies of PRS phenomenology to be made without the complications of gross instabilities and significant asymmetries.

As the number of wires in either radius load is increased, the quality of the pinch is monotonically improved as determined by (1) the inductive current notch at the time of implosion (0 ns in Fig. 1), (2) the radial compression ratio, and (3) the radiation rise time, pulse width, and peak power [6]. As an example, Fig. 2 illustrates the significant reduction in rise time (from 48 to 2.3 ns) and in pulse width (from 60 to 3.2 ns), and the associated increase in power (from 0.7 to 5 TW) that occurs for one of the K-shell x-ray detectors when the number of wires is increased from 10 to 90 for the small radius load. Moreover, when the data from the various radiation detectors is plotted as a function of the circumferential gap between the wires, as illustrated in Fig. 3 for the total power, the data from the two radial scans appear to fit a single curve dependent on gap alone. This figure shows that not only does the total x-ray power increase with decreasing gap, but that below a gap of about 1.4 mm, the increase in power with decreasing gap becomes rapid—almost as if a transition between two different states of implosion is occurring. This transition from slow to rapid power increase at  $1.4 \pm 0.4$  mm is observed in all x-ray channels. Over the 6- to 0.4-mm range in gap explored, the associated total energy measured increases by about 60%. This increase is somewhat more than the increase in the calculated kinetic energy imparted to the implosion at stagnation due to the factor of two increase in the measured compression ratio.

Using the measured current and a 1D-Lagrangian RMHC, the dynamics of a single-wire plasma, starting from the solid state, was calculated and used as input to the xy code simulation. This simulation allows the merging and compression of the wire plasma to be tracked as illustrated in Fig. 4A and 4B, for a 10- and 40-wire load configuration, respectively. These simulations show that the plasma of each wire will remain localized and will *never* merge with its neighbor until stagnation is reached provided that (1) the plasma from the adjacent wire does not merge before the system begins to implode (Fig. 4A), and (2) the current in a single wire is high enough to generate self-pinching. Thus, the shot-to-shot time-dependent radiation output and low-power characteristics of the historically large-gap wire implosions are likely due to the random nature and shearing [4] of self-pinched wires and the straggling of the wire plasmas as they approach stagnation.



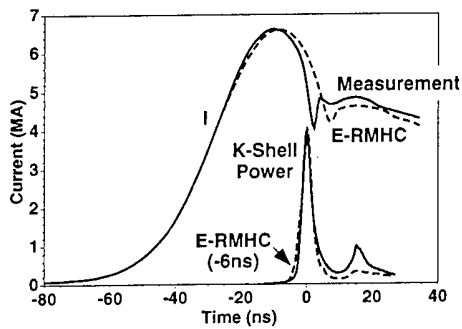


Fig. 1. Comparison of measured( solid) current with Eulerian RMHC simulation (dashed) showing associated experimental K-shell and the RMHC total relative powers.

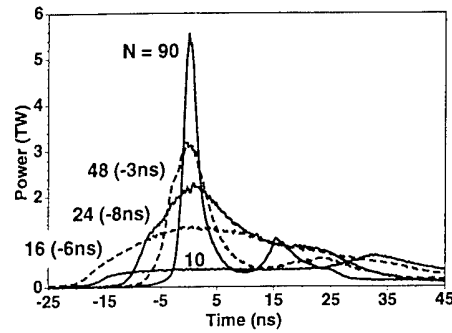


Fig. 2. K-shell power versus wire number. Times in parenthesis show shift required to align time of peak power.

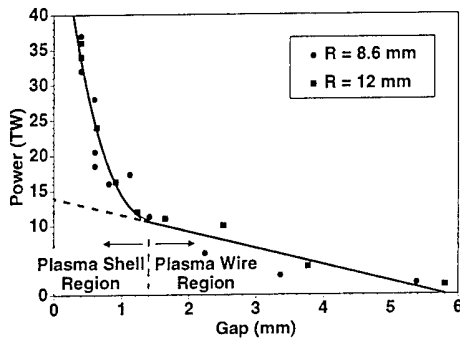


Fig. 3. Total x-ray power versus wire gap

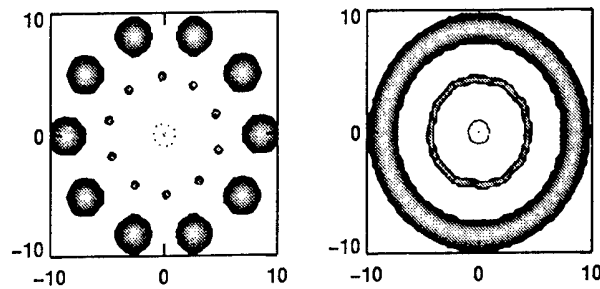


Fig. 4 x,y simulation in mm units of (A) 10 and (B) 40 wire implosions at 86, 11, 3, and 0 ns before stagnation for small radius load.

Importantly, these simulations show that only when the gap is reduced below  $1.4 \pm 1.3/-0.7$  mm do the wires begin to merge to form an annular shell that remains a shell throughout the implosion process (Fig. 4B). This calculated merge point of  $\sim 1.4$  mm coincides well with the measured transition between the regimes of slow and rapid increase in power with decreasing gap. It is also consistent with the measurements made with the fast-framing x-ray pinhole camera, which showed that even for gaps as small as 1.4 mm, the individual wires were seen to implode as separate entities until just before peak compression, whereas the high-power small gap shots showed the formation of a well-defined plasma shell. Moreover, the calculations also show an improvement in the merger with decreasing gap that helps explain the continued improvement in implosion quality with decreasing gaps below 1.4 mm (Fig. 3).

Figures 1 and 5A compare the current and total x-ray power measured for a 90-wire, 0.6-mm gap load with that simulated in the r-z plane by the Eulerian (E) and the Lagrangian (L) RMHCs, respectively, when small initial random density perturbations are assumed. The comparisons show that the behavior of such nearly azimuthally symmetric 90-wire loads can almost coincide with that calculated in the r-z plane using small ( $\sim 5\%$ ) values for an axial perturbation. However, the connection between the azimuthal symmetry and the seeding of axial perturbations has not yet been determined.

Such azimuthally-symmetric implosions exhibit a clear first compression followed by a second weaker-compression/expansion phase (measurements in Figs. 5A and 5B). Additionally, prior to the first compression, Rayleigh-Taylor bubble/spike structure are observed with short  $1.1 \pm 0.1$ -mm wavelengths in agreement with all the 2D RMHC simulations, which merge into longer  $3.4 \pm 0.4$ -mm wavelengths. The longer wavelengths appear to seed a  $2.9 \pm 0.6$ -mm sausage instability after the first compression. These instabilities are seen along with a second implosion in the Eulerian RMHC model (Fig. 1) that simulates the entire 20-mm length. This model used an adjustment to the electron-radiation energy coupling to generate the

Fig. 1 results. A second implosion is not observed in the Lagrangian RMHC result in Fig. 5A. There, the short axial length of the simulation prevented growth of longer-wave length instabilities that limit radial compression in the Eulerian result. High radial compressions lead to excessive radiation cooling that inhibited radial expansion following stagnation.

Analysis of the free-bound and K-shell line spectra shows that the pinch has a gradient structure composed of a hot core surrounded by a cooler plasma [12], in qualitative agreement with the 1D and 2D models. The electron temperature in the core reached temperatures of  $1.4 \pm 0.2$  keV and  $1.0 \pm 0.2$  keV at the first and second compression (Fig. 5C), respectively, with temperatures of 0.4 keV being measured in the surrounding plasma at peak compression. Although higher spectral resolution is needed than was available in order to draw more definitive conclusions, an analysis of the emission spectra in these experiments suggests that the K-series lines are Doppler broadened. The ion temperatures that are inferred from the widths of these lines, after a correction for line opacity is made, are in excess of  $\sim 20$  keV. Such inferences are consistent with the 1D and 2D simulations of the experiments.

We have shown that reducing azimuthal asymmetry by reducing the circumferential wire gap has provided significant gains in the radiated x-ray power with its limit not yet reached. However, other asymmetries like those generated by the predicted and observed Rayleigh-Taylor and sausage instabilities may ultimately limit what can be achieved for single-shell wire array loads. Meanwhile, the higher power performance already demonstrated using this small-gap technique with high-wire-number tungsten loads [13, 14] on Saturn may well be adequate to achieve 125-eV vacuum-hohlraum temperatures on PBFA-Z [13,15] and ignition-relevant ICF physics on the proposed X-1 accelerator [16].

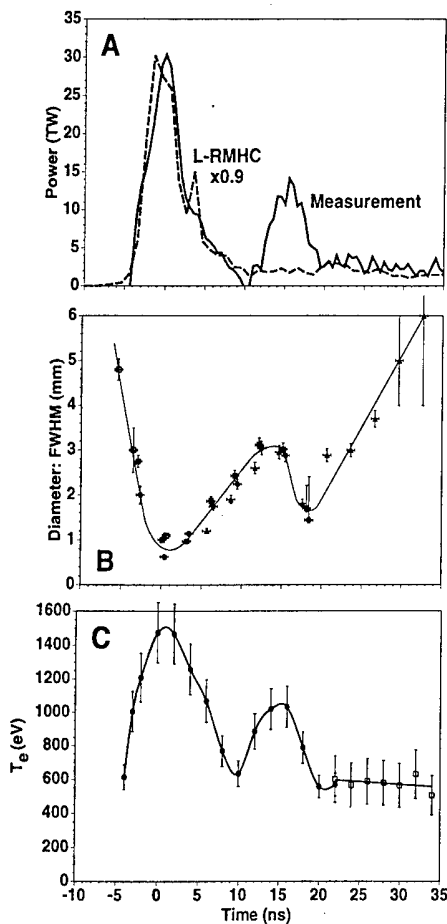


Fig. 5A Comparison of measured total power with Lagrangian RMHC simulation; 5B. Measured radial diameter; 5C. Measured core electron temperature

#### References

- [1] D. D. Bloomquist, et al., *Proc. 6th IEEE Pulsed Power Conf.*, 310 (1987).
- [2] D. H. McDaniel, Sandia National Laboratories, private communication (1995).
- [3] N. R. Pereira and J. Davis, *J. Appl. Phys.* **64**, R1 (1988).
- [4] K. G. Whitney, et al., *Phys. Rev. E* **50**, 2166 (1994).
- [5] D. Mosher, *Proc. 10th Intl. Conf. High Power Particle Beams*, 159 (1994).
- [6] T. W. L. Sanford, et al., *Bull. Am. Phys. Soc.* **4**, 1846 (1995) and to be submitted to *Phys. Rev. Lett.* (1996).
- [7] R. B. Spielman, et al., *Proc. 3rd Intl. Conf. Dense z-Pinches*, 404 (1994).
- [8] B. M. Marder, *Math Comp.* **29**, 434 (1975).
- [9] J. H. Hammer, et al., *Phys. Plasmas* **3**, 2063 (1996).
- [10] D. L. Peterson, et al., *Phys. Plasmas* **3**, 368 (1996).
- [11] M. H. Frese, Internal Report, NumerEx Corp. Albuquerque, NM (1986).
- [12] T. W. L. Sanford, K. G. Whitney, et al., *Rev. Sci. Instrum.* (submitted May 1996).
- [13] R. B. Spielman, et al., these proceedings.
- [14] C. Deeney, et al., to be submitted to *Phys. Rev. E* (1996).
- [15] D. L. Peterson, et al., Los Alamos National Laboratory, private communication (1996).
- [16] J. P. Quintenz, et al., these proceedings.

## PBFA Z: A 20-MA Z-PINCH DRIVER FOR PLASMA RADIATION SOURCES\*

R. B. Spielman, S. F. Breeze, C. Deeney, M. R. Douglas, F. Long, T. H. Martin, M. K. Matzen, D. H. McDaniel, J. S. McGurn, T. J. Nash, J. L. Porter, L. E. Ruggles, T. W. L. Sanford, J. F. Seamen, W. A. Stygar, J. A. Torres, D. M. Zagar, D. O. Jobe, D. L. Peterson,<sup>a)</sup> R. W. Shoup,<sup>b)</sup> K. W. Struve,<sup>c)</sup> M. Mostrom,<sup>c)</sup> P. Corcoran,<sup>d)</sup> and I. Smith<sup>d)</sup>

*Sandia National Laboratories, Albuquerque, NM 87185 USA*

### Abstract

Sandia National Laboratories is completing a major modification to the PBFA-II facility. PBFA Z will be capable of delivering up to 20 MA to a z-pinch load. It optimizes the electrical coupling to the implosion energy of z pinches at implosion velocities of  $\sim 40$  cm/ $\mu$ s. Design constraints resulted in an accelerator with a 0.12- $\Omega$  impedance, a 10.25-nH inductance, and a 120-ns pulse width. The design required new water transmission lines, insulator stack, and vacuum power feeds. Current is delivered to the z-pinch load through four, self-magnetically-insulated vacuum transmission lines and a double post-hole convolute. A variety of design codes are used to model the power flow. These predict a peak current of 20 MA to a z-pinch load having a 2-cm length, a 2-cm radius, and a 15-mg mass, coupling 1.5 MJ into kinetic energy. We present calculations showing MJ x-ray outputs from tungsten wire-array z pinches.

### Introduction

The PBFA-II accelerator<sup>1</sup> at Sandia National Laboratories, used by the light-ion-beam ICF Program, has been modified to allow its use as a z-pinch driver. Renamed PBFA Z, its electrical design optimizes the coupling of the generator to magnetically-imploded loads, typically z pinches. This paper describes the performance goals, the electrical design constraints, the modeling, and the predicted z-pinch x-ray performance.

### Performance Requirements and Basic Design Elements

We established the following performance goals: 20 MA delivered to a z-pinch load with a current rise time of  $\sim 100$  ns,  $> 1$  MJ of x-ray yield, and one shot a day capability. These goals drove the detailed design of PBFA Z. The 20-MA design goal was chosen as an intermediate pulsed power step to a desired 40-MA accelerator. The 100-ns driving pulse is a tradeoff between the desired, but expensive, short high-voltage pulses driving fast implosions and the Rayleigh-Taylor instabilities generated by cheaper, longer-pulse lower-voltage options. The requirement for shot rate is based on the perceived shots needed to get an acceptable learning rate in an R&D environment.

The basic mechanical and pulsed power design of PBFA Z, described in Ref. 2, was intended to minimize the cost of the modifications while meeting the performance goals. This resulted in modifying all of the components inside the coaxial pulse-forming lines (PFLs). (See Fig. 1.)

We used Screamer<sup>3</sup> and TLCODE<sup>4</sup>, transmission-line circuit codes, to model possible PBFA-Z designs over a wide range of electrical parameters such as driving impedance, load inductance, pulse width, and z-pinch mass. The optimum driving impedance to couple electrical energy to a z-pinch load is roughly set by the time constant of the system,  $Z \sim L/t$ . With a 100-ns driving pulse and a 10-nH inductance we found that the simple optimum of 0.1  $\Omega$  matched the more detailed Screamer prediction of 0.12  $\Omega$  quite well. Fig. 2 shows a series of Screamer calculations in which the driving impedance is varied while the input energy, inductance, and load mass are held fixed.

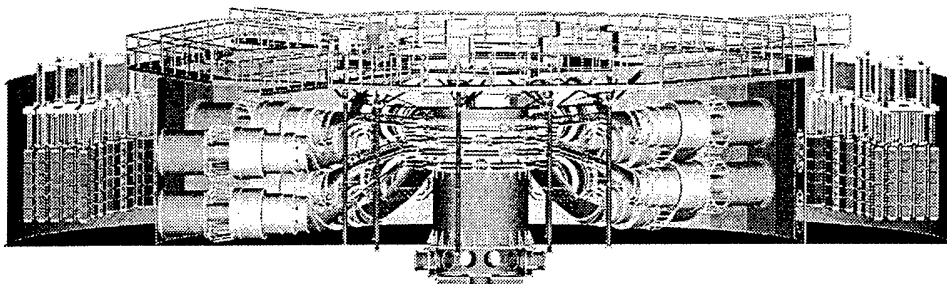


Fig. 1 A schematic of the proposed PBFA-Z accelerator showing the modifications planned inside the coaxial PFL section.

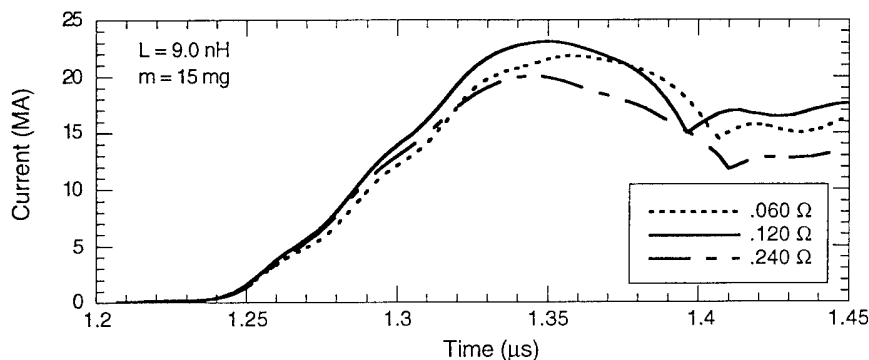


Fig. 2 A plot showing the effect of impedance on the current delivered to a z-pinch load with the input energy, total inductance, and pinch mass held constant.

The final PBFA-Z design uses a 0.12- $\Omega$  waterline, has a 120-ns pulse, and has a total inductance of  $\sim 10.25$  nH. The baseline z-pinch load is 2-cm long, 2-cm radius, and 15-mg mass. The peak kinetic energy is 1.5 MJ assuming a 10:1 convergence ratio. Experience on Sandia's Saturn accelerator shows that we can extract the entire kinetic energy of the z pinch together with additional 50% from ohmic heating as x rays for high-Z loads, yielding an expected total x-ray output of  $> 2$  MJ for PBFA Z.

### Electrical Design

The PBFA-Z electrical design consists of constant impedance water transmission lines, a water-vacuum insulator stack, four levels of disk magnetically-insulated transmission lines (MITLs), a vacuum post-host convolute, an inner disk MITL, and the z-pinch load.

The PBFA-Z water lines consist of a transition from the existing co-axial section through bi-plate lines to the insulator stack. The key design issues are to operate in a regime where the lines do not electrically breakdown and to have a constant impedance line. We tested the existing PBFA-II water lines to determine the water break down characteristics. These tests used two PBFA-II modules delivering 2.5-MV voltage pulses with a 100-ns rise time to simulated PBFA-Z water transmission lines. In this case we used a 4.5- $\Omega$  water line with an 11.4-cm spacing. The water lines carried the voltage pulse without failure. We established a baseline water line electrical design of 36, 4.5- $\Omega$  water lines having a 14-cm line spacing.

We built a new insulator stack to minimize inductance in order to meet the 20-MA milestone as well as the desired z-pinch kinetic energy. We based our initial PBFA-Z design on the four-stack Saturn design.<sup>5</sup> This was the lowest inductance design for a MITL system based on a post hole convolute. The height of each insulator stack was based on its self-consistent voltage

(generated from Screamer) and the insulator flashover criterion.<sup>6</sup> This resulted in the stack design shown in Fig. 3. We found that the optimal design had five insulators on A and B levels (the levels nearest the load) and six insulators on C and D levels. The insulator rings used were identical to PBFA II except that they are fabricated from cross-linked polystyrene.<sup>7</sup> The electric field grading across individual insulator stacks had a design criterion of  $\pm 5\%$  and was achieved by using flux excluders in the water just outside the insulators on C and D levels and by shaping the conductors near the insulators. The insulator stack will contain voltage and current monitors on each level.

The MITLs were designed using iterative applications of TLCODE,<sup>4</sup> SCREAMER,<sup>3</sup> TRIFL,<sup>8</sup> TWOQUICK,<sup>9</sup> and IVORY.<sup>10</sup> TRIFL is a new 1-D MITL simulation code. TWOQUICK and IVORY are 2-D E&M particle-in-cell codes. The design of the PBFA-Z vacuum MITLs is shown in Figure 3. The four axisymmetric MITLs shown are joined in parallel at a 7.6-cm radius by a double post-hole convolute.<sup>11</sup> Downstream of the convolute a single 5-cm-long MITL feeds power to the load. TWOQUICK simulations were used minimize the fraction of the total current carried by the electron-sheath. For the baseline load, the initial inductance inside the stack-vacuum interface is 10 nH. The double-post-hole convolute, an inherently three-dimensional configuration with magnetic nulls at current bifurcations, was modeled with QUICKSILVER,<sup>12</sup> a 3-D E&M particle-in-cell code. Current monitors will be located at three radial locations: in all four outer disk MITLs at an 80-cm radius, in all four outer disk MITLs just upstream of the convolute, and in the inner disk MITL.

### Z-Pinch Performance

The predicted performance of tungsten z-pinch loads, generating mostly sub-keV radiation, on PBFA Z was obtained using a 2-D Eulerian Rad-Hydro code<sup>13</sup> benchmarked against Saturn tungsten z-pinch data. The code uses a simplified circuit model, based on Screamer calculations, to drive the tungsten z pinch. For these calculations we have fixed typical code variables such as resistivity, thermal conductivity, and artificial viscosity at their classical values. The only variable that was used to match to the Saturn data was a stochastic density perturbation, intended to mock up the effect of Rayleigh-Taylor instabilities and unavoidable, three dimensional, azimuthal perturbations in the actual wire array load. A calculation modeling a 120-wire, 17.5-mm diameter, 2-cm long tungsten array is compared with Saturn data where we applied a 5% density perturbation.<sup>14</sup> (See Fig. 4.) The code input is then changed to reflect the pulsed power and load details expected on PBFA Z. Fig. 5 shows the results for such a calculated implosion on PBFA Z. The code predicts a total x-ray yield of 2 MJ and a peak x-ray power of 180 TW. Based on the earlier agreement with Saturn data, we believe that these results are reasonable estimates for PBFA-Z x-ray performance. Future work will be performed to benchmark the calculations in detail against the Saturn data.

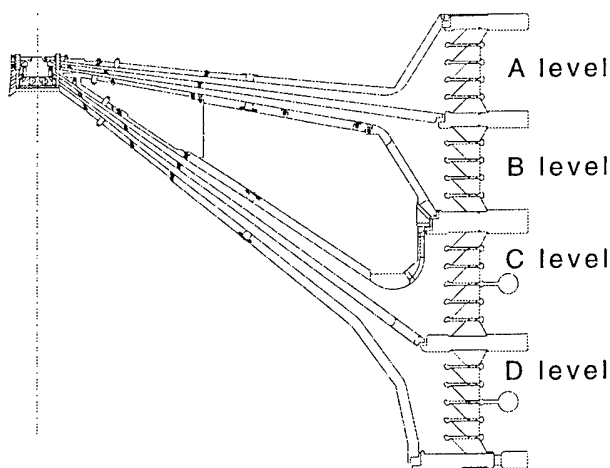


Fig. 3 A picture of the proposed MITLs for PBFA Z showing the transition from the insulator stack to the post-hole convolute.

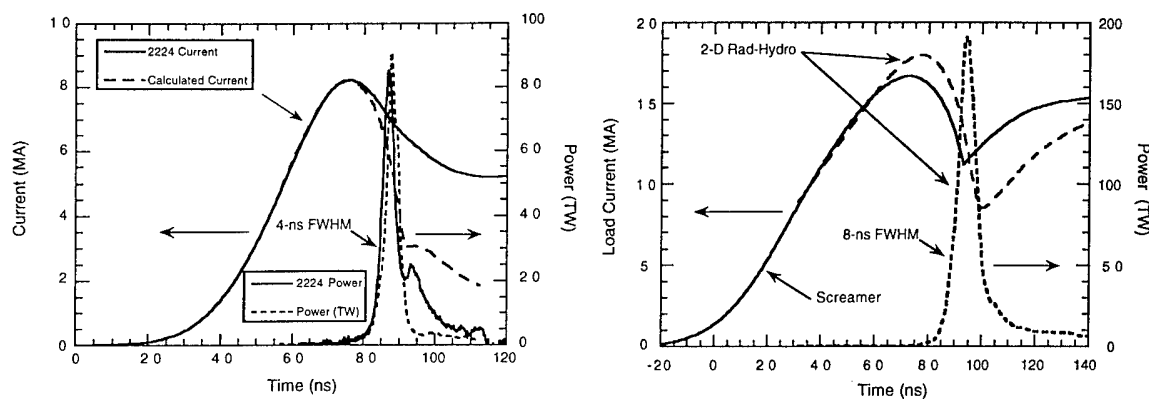


Fig. 4 The left plot shows a comparison of Saturn shot 2224 and Rad-Hydro calculations using a 5% perturbation. The right plot shows the same calculation done for PBFA-Z parameters.

## Conclusion

PBFA Z is a modification of the PBFA II accelerator for z-pinch implosion experiments. PBFA Z is expected to deliver 20 MA to a z-pinch load. We expect that PBFA Z will deliver 2 MJ of x rays based on the results of detailed electromagnetic design code and Rad-Hydro calculations and comparisons with Saturn data. Experiments to confirm the pulsed power performance and to measure the x-ray outputs will be completed by the end of 1996.

We acknowledge the support of the Sandia design team and the PBFA II operations team in preparing for PBFA Z and the Saturn crew for their support of the Saturn experiments.

\* This work was supported by the U.S. Department of Energy under Contract #DE-AC04-94AL85000.

<sup>a)</sup> Los Alamos National Laboratory, Los Alamos, NM 87854 USA.

<sup>b)</sup> Field Command Defense Nuclear Agency, 1680 Texas Street SE, Kirtland Air Force Base, NM 87117 USA.

<sup>c)</sup> Mission Research Corporation, Albuquerque, NM 87106 USA.

<sup>d)</sup> Pulse Sciences, Inc., 600 McCormick Avenue, San Leandro, CA 94577 USA.

[1] B. N. Turman, et al., *Proc. of the Fifth IEEE Pulsed Power Conf.*, Arlington, VA 1985, pp. 155.

[2] R. B. Spielman, et al., *Proc. of the Ninth IEEE Pulsed Power Conf.*, Albuquerque, NM 1995.

[3] M. L. Kiefer, et al., SCREAMER, A Pulsed Power Design Tool, 25 August 1995 (Sandia Internal Document).

[4] W. N. Weseloh, *Proc. of the Seventh IEEE Pulsed Power Conf.*, Monterey, CA 1989, pp. 989.

[5] D. D. Bloomquist, et al., *Proc. of the Sixth IEEE Pulsed Power Conf.*, Arlington, VA edited by P. J. Turchi and B. H. Bernstein (IEEE, New York, 1987), p. 310.

[6] J. C. Martin, Fast Pulse Vacuum Flashover, SSWA/JCM/713/157 and AFWL High Voltage Notes, Note 2, 16 March 1971.

[7] O. Milton, *IEEE Transactions on Electrical Insulation* Ei-7, #1 March 1972, pp. 9.

[8] C. W. Mendel (private communication).

[9] T. D. Pointon, *J. Comput. Phys.* **96**, 143 (1991).

[10] M. M. Campbell, B. B. Godfrey, and D. J. Sullivan, Mission Research Corporation Report AMRC-R-454, 1988 revised.

[11] R. B. Spielman, et al., in *Proc. of the 7th IEEE International Pulsed Power Conference* (1989), p. 445.

[12] D. B. Seidel, et al., 1991 *Proc. of the CP90 Europhysics Conf. On Computational Physics*, A. Tenner, ed., (World Scientific, Singapore), pp. 475-482 and J. P. Quintenz, et al., *Laser and Particle Beams* **12**, 283 (1994).

[13] D. L. Peterson, et al., *Phys. Plasmas* **3**, 368 (1996).

[14] C. Deeney, et al., to be submitted to *Phys. Rev. E*.

# S-300, NEW PULSED POWER INSTALLATION IN KURCHATOV INSTITUTE, INVESTIGATION OF STABLE LINER IMPLOSION

A.S.Chernenko, Yu.M.Gorbulin, Yu.G.Kalinin, A.S.Kingsep, Yu.V.Koba,  
V.D.Korolev, V.I.Mizhiritskii, L.I.Rudakov

*Russian Research Center "Kurchatov Institute"*  
*123182, Moscow, Russia*

**Introduction.** Starting from the beginning of 1996, experiments are being carried out in the Kurchatov Institute, based on the new S-300 machine, to study the stability of magnetic implosion. This installation has been constructed under the support of the Russian Ministry of Science and Technology and also of the French Atomic Energy Commission. The principal scheme is traditional one: Marx generator, intermediate, pulse forming and transporting water lines. By the optimal load and optimized charging voltage, this machine has to provide the total current of 8 modules as high as 6 MA. Heretofore, we operated in a reduced regime, so that the current was up to 4 MA on the load  $\sim$ several nH. Some typical oscillograms of the current are shown in Fig.1. The current was measured by the loops established on the input to the concentrator ( $I_{in}$ ) and close to the load ( $I_{out}$ ). Detailed description of the S-300 construction and features have been done in [1,2].

As a first point of our research, the instability of magnetic implosion has been chosen, earlier observed in many laboratories. Just the instability restricts the upper limit of the concentration efficiency. E.g., the Rayleigh-Taylor instability of the imploding shell is the inevitable feature of the inertial confinement. There exist the numerical codes, reliable enough, which can predict both parameters of saturation and consequences of this instability conditioned by the initial state of the shell. Magnetic implosion as a mechanism providing a powerful pulse of the X-rays demands higher velocities and, hence, the total number of particles involved into the dynamics should be respectively small. The current flow velocity of the electrons may, in principle, exceed both mass and thermal velocities of the ions. Conventional MHD theory describes, generally speaking, just the opposite limit. One can expect some new phenomena caused by the current instabilities which can modify the transport coefficients [3] and also some essential modification of the current flow itself due to the magnetic field freezing in the current-carrying electrons [4]. During the last decade, some codes have been created including two-component properties of a plasma. To wit, Hall terms have to be included into the Ohm's law. Some simulations of the fast Z-pinch dynamics and liner implosion have been brought about, perfectly confirming theoretical predictions on the new fast instabilities typical of these, essentially two-component

plasmas. Meanwhile, simulations shouldn't be used as a basis of planning future experiments without experimental verification. In particular, in most numerical 2-d models, up to now, the consequences of the small-scale turbulence aren't considered properly, moreover, 3-d effects are neglected in principle, in spite of their being very typical just of the Hall dynamics. Thus, our goal in the first series of the experiments on S-300 was to study this physics in details.

**Subject of study — imploding plasma.** The most typical shell is the hole cylindrical gas jet. As simulations show, in the case of  $A \geq 14-16$  ( $N_2, O_2$ ), the radiation losses support the temperature in the skin layer as low as some dozen eV, as a result, efficient ion charge number  $Z_{eff} \sim 4-5$  and hardly varies while acceleration. The typical skin space scale is of the order of several tenth of mm. The magnetic pressure creates the strong shock going away from the current layer and heating the plasma filling. This purely HD shock acceleration is stable. An instability may start after this phase when all the substance becomes concentrated in the thin shell which starts its acceleration caused by the magnetic pressure. Just this moment is that of the start of the Rayleigh-Taylor instability. However, even at the first stage current-carrying instabilities may develop in the skin layer. Due to the radiation cooling behind the shock front, plasma flows towards the current layer, as a result, its mass becomes growing and the density redistribution occurs following the balance of the inertia and magnetic pressure. According to the simulations, the gaseous pressure in the skin layer is much less than magnetic one. Such a layer turns out to be unstable. As a result, 2-d structure of both current and magnetic field arises [4], the acceleration efficiency and maximal aspect ratio of the compression decrease. It is rather difficult to differ Rayleigh-Taylor and Hall instabilities, nevertheless, it is important since the growth of the increment several times may ruin the program of the plasma implosion. If the Hall instability is "slower", it is reasonable to deal with jet which thickness at the first stage is comparable to its radius. Then Rayleigh-Taylor instability will develop only in the last stage of the thin shell. If, on the contrary, Hall instability is predominating one thus providing the fast mixing of the magnetic field and plasma, the thin solid shell may be better solution, as they do in some laboratories. Then Rayleigh-Taylor instability would start from very beginning of the implosion process. The applicability of conventional MHD may be presented in form of the displacement of the current-carrying electrons small compared to the current layer thickness  $\delta$ ,  $It/(Z_{eff}Ne) < \delta$ ;  $N = M/AM_p$ ;  $Z_{eff}, A$  are the efficient charge and mass number of the ion, respectively. Energetic balance ties both kinetic energy acquired by the shell,  $Mv^2/2$ , and magnetic energy,  $\Delta L \cdot I^2/2$ . Therefore, MHD may be used to describe the dynamics of a well-radiating shell:  $\delta \simeq \delta_s$ ;  $\delta_s \equiv c^2 t / 4\pi\sigma$ , if the current value exceeds some  $I_{cr}$  that (in megaamps) may be presented in form:

$$I_{cr} = 5 \cdot 10^{-2} A \cdot \left( \frac{v, \text{ cm/s}}{10^7} \right)^2 (t, 10^{-7} \text{ s})^{1/2} (\text{MA}). \quad (1)$$



**Experimental results.** This is typical of our experiments, that at the first stage outer boundary of the shell is looking in the visible light to move with a constant velocity. This stage may be identified as the compact shell formation in the process of the plasma heating by the shock wave going away and its cooling behind the shock front resulting in the accumulation of the cool plasma in the current layer. As it has been noticed above, no Rayleigh–Taylor instability may develop at this stage. Its duration is determined by the shell displacement to  $\sim 1/2$  of the initial radius. In some experiments, we observed an instability of the outer surface of the shell without any acceleration. Such an instability should be identified as that of the Hall origin. They are typical rather of the regimes of the fast implosion, i.e., of the small shell masses or of the higher  $Z$  materials ( $Xe$  in our case).  $N_2$  or  $SF_6$  shells are (statistically) more stable at this stage. Optical frames are shown in Fig.2 a) demonstrating the instability of a  $N_2$  jet, at the first stage. The same regime has been presented in Fig.2 b) for the  $Xe$  jet. The formation of the compact shell shown in Fig.2 c) occurs without instabilities. This is the case of the  $SF_6$  jet of the great mass. It turns out to be in agreement with the (1) criterion.

In another series, we used the shells with a linear mass in the range of  $10^{-4} - 10^{-3}$  g/cm, with the radius 12 mm and 6 mm, made of a plastic. To stimulate the transition of this plastic into the plasma phase, we used an additional  $Xe$  jet injected in the outer vicinity of the plastic shell. Dynamics of this experiment has been presented in Fig.3 a). Without this gaseous jet, compact implosion used to start with some delay, see Fig.3 b). This is a manifestation of the so-called magnetically-pushed-out discharge at the early stage of the implosion. That means that the shell thickness turns out to be less than  $\delta_s$ . As a result, plasma coating the inner surface of the shell becomes involved into the flow towards the axis. Only after some delay, the rest part of the shell started with implosion. In this regime, we observed the start of the instability just at the moment of starting acceleration ( $g$ ) of the outer layer of the shell. It was being realized in the form of distinct strati, normal to the axis. Their number is of the order of 5–7 per cm, i.e.  $k_z = 2\pi/\lambda \simeq 36\text{cm}^{-1}$ . They appear after the shell displacement along the radius  $\sim 1$  mm. If one supposes this instability to be of the Rayleigh–Taylor origin, with a growth rate  $\gamma \sim (k_z g)^{1/2}$ , then  $\int \gamma dt$  may be readily calculated on the base of the data presented in Fig.3:  $\int (k_z g)^{1/2} dt \simeq (k_z \Delta R)^{1/2} \simeq 2$ . That means, the initial inhomogeneity of the shell should be  $\sim 10\%$ . That is looking rather incredible, however, not forbidden. As for the Hall instability, its non-linear theory is presented in [4]. There exist rather good coincidence with experimental data. This fast instability develops with a typical time scale of the order of the skinning time. Unfortunately, experimental results do not allow us to identify one-to-one the unstable mode. Our study of the physics of the unstable imploding shells will be go on. We are going to establish the dependence of the non-linear growth rate on the liner composition and on the method to create it. It is necessary to learn, how to effect on the degree of the

unstable development varying the depth of the shell. In a future, we will optimize the matching of a load to the generator, increase the charging voltage and the net current. That will allow us to increase the velocity of implosion, thus providing better ability to study implosion physics and to test new original schemes of the magnetic energy conversion into radiation.

## References

- [1] Mizhiritskii, V.I. et. al., A High Current Pulsed Power Generator, to be published
- [2] Korolev, V.D. et. al., Energy Transportation on Vacuum 3-D Concentrator of the S-300 Machine, this Proceedings, paper P-3-72
- [3] Kingsep, A.S., Rudakov, L.I., On the Necessary Modifications of Z-Pinch Models, ibid. paper P-2-74
- [4] Rudakov, L.I., Sevastyanov, A.A., Current Instability of 'Snow-Plough', ibid, paper P-2-88

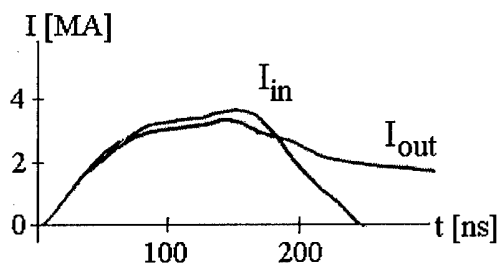


Fig. 1

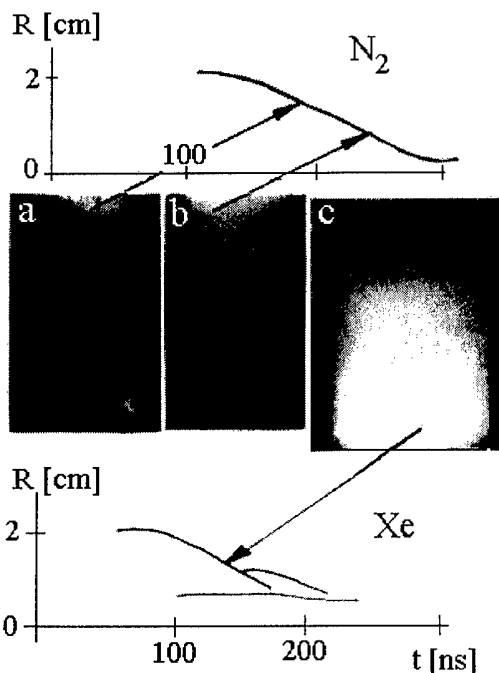


Fig. 2

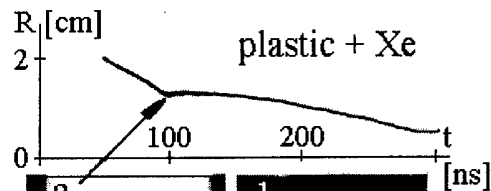


Fig. 3

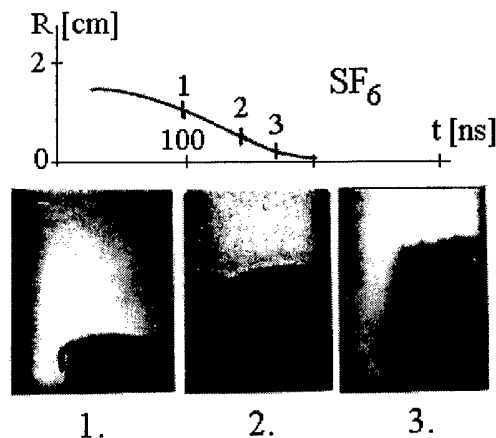


Fig. 4

## TEST OF EMG-720 EXPLOSIVE MAGNETO-CUMULATIVE GENERATOR

N.F. Popkov, A.S. Pikar, E.A. Ryaslov, V.I. Kargin, P.V. Mironychev,  
S.T. Nazarenko, V.S. Pavlov, G.F. Mackartsev, V.E. Gurin, P.V. Korolev,  
V.N. Kataev, V.N. Nudicov, A.S. Russkov, S.I. Semyonov,  
V.V. Chernyshev, V.I. Vorontzov, A.F. Saratov, G.I. Logunov.

*All-Russian Research Institute of Experimental Physics (VNIIEF), 607190, Sarov,  
Nizhniy Novgorod Region, Russia.*

J.H. Degnan, G.F. Kiuttu, S.K. Coffey.

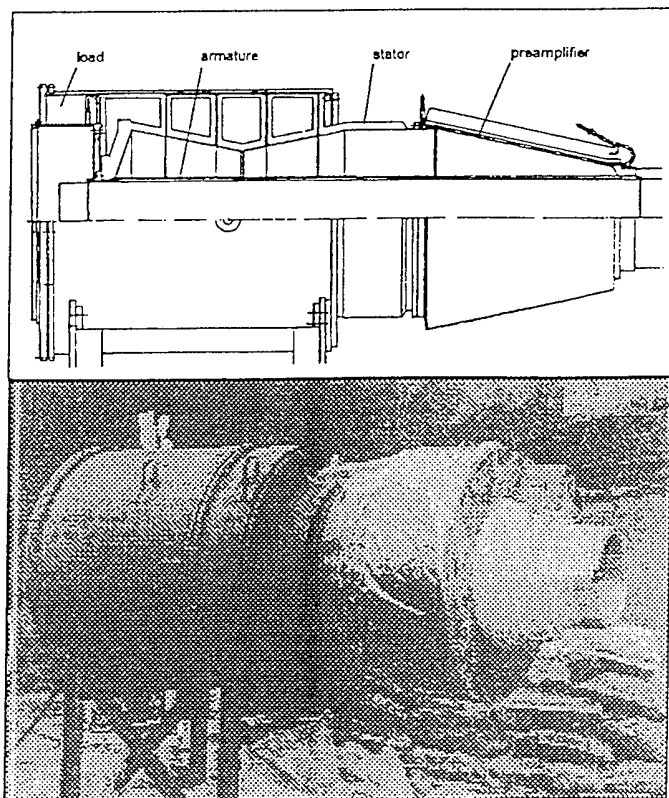
*High Energy Sources Division, Phillips Laboratory, Kirtland AFB, New Mexico, USA*

W. J. Summa and K.D. Ware

*Defence Nuclear Agency Alexandria, VA, USA*

The test results of 30 megajoule EMG-720 explosive magneto-cumulative generator are given here. The generator was powered from the capacitor bank.

Our purpose was to develop a comparatively simple and not expensive generator having the energy storage of several dozens of megajoules, which could be used as the energy source energizing the stationary electro-physical facility placed in a special explosion-protected bunker. Helical magneto-cumulative generators, C-320 [1] and MARK-IX [2], have a long operational period (100 ms), as to fast-operating coaxial [3] and disk [4] generators, they employ very low loads (1 nH) and, moreover, require quite a powerful powering source to get the initial energy. So, neither of the generators known could meet our requirements.



### Generator's dimensions:

length	2500 mm
diameter	1000 mm
HE weight	186 kg

### Electric parameters:

powering current	95 kA
powering energy	250 kJ
operation time	25 $\mu$ s
final inductance	22 nH
load current	48 MA
generated energy	25-30 MJ

Fig. 1. EMG-720 lay-out and generator's view.

To implement the project, the authors proposed the design including a slow-operating helical-cone preamplifier and fast-operating cone generator as well (Fig.1). Such a lay-out provides that the generator preserves the best properties of both helical and cone generators, high current amplification coefficient (500) and small characteristic current rise time (25 ms) and storage of up to 25 MJ of the electro-magnetic energy at a relatively high inductance of 22 nH.

EMG-720 magneto-cumulative generator is comprised by the following: input cable collector with the explosive closing switch and explosive opening switch of the powering circuit; multi-turn helical-cone preamplifier; cone generator; high-voltage multi-slot disk collector; coaxial energy transmission line with film insulation; oil-filled high-voltage cable collector; aluminium liner with HE charge and two-sided initiation system and regulated delay lines.

The distinctive feature of EMG-720 is that it is intended to operation with high magnetic fluxes. As is known, the magnetic energy is directly proportional to the magnetic flux square number and reversly proportional to the load inductance. The most simple way to increase the energy output is to reduce the load inductance. This is the way the most of developers go. Though, if you want not only to obtain the energy of dozens of megajoules, but also feed this energy into a real load, it is necessary to employ a higher magnetic flux. So, some complicated problems are to be solved in connection with the magnetic flux increase proportionally to that of the electric voltages. Besides, to provide for a little current rise time, the starter surface should precisely repeat the liner's shape at the end of the generator operation. In its turn, that required to run several experiments on the liner gas-dynamics working-through. To reduce the requirements to the shape of the surface, the starter's current conductor was divided into three cone sections. The use of the said sections ensures the magnetic flux outlet through four disk gaps and highly reliable insulation, avoiding formation of "traps" where the magnetic flux could be cut off.

In Fig.2. there are shown the views of the liner's surface obtained, using the fast-operating photo registrator. The time interval between the photo is 4,75 ms. The grid size is 48 mm.

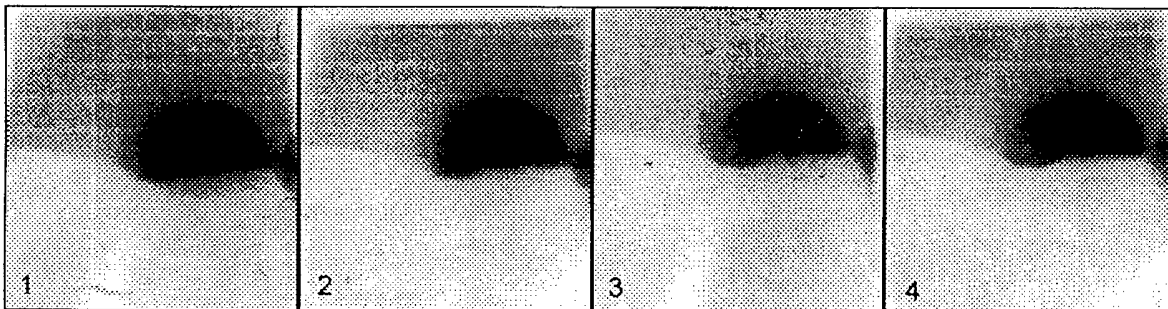


Fig.2. Liner's surface photographs.

EMG-720 testing was conducted at the explosive field of a special bunker. The generator was mounted 4 meters away from the bunker's armor shielding. At the 3d  $\mu$ s the starting pulse is fed to the explosive device initiating the detonators of the capacitor bank closing switch, generator powering cable line opening switch and those of the two lines of the generator's delayed operation. The explosive closing switch commutates the capacitor bank to the generator at the 39th  $\mu$ s. The 1st delayed operation line ensures the firing of the main generator's HE charge at the 260th  $\mu$ s; the 2nd one - at the 380th  $\mu$ s. Correspondingly, the generator powering begins at the 39th  $\mu$ s and finishes (the moment of the liner's connections to

the turns) at the 310th  $\mu\text{s}$ . The full current rise time in the load from zero to the maximum makes 225  $\mu\text{s}$ .

The equivalent experimental electric circuit is shown in Fig.3.

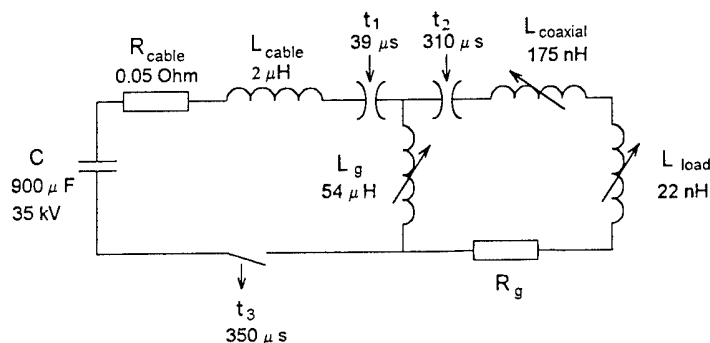


Fig.3. The equivalent experimental electric circuit.

Here:  $t_1=39 \mu\text{s}$  is the moment of the explosive closing switch operation and capacitor bank discharge starting;

$t_2=310 \mu\text{s}$  is the moment of the liner's connection to the helix;

$t_3=350 \mu\text{s}$  is the moment of the operation of the powering circuit explosive opening switch;  $R_g$  is the ohmic resistance of the generator circuit;

$L_{\text{load}}$  is the variable residual inductance of the generator depending on the liner's flight geometry, starter displacement and current conductors' manufacturing technology capabilities.

The currents measured in the powering circuit and load are represented in Fig.4.

The generator powering starts at the 39th  $\mu\text{s}$ . While the liner is moving, the flux is pushed from the generator to the powering circuit. The current in the bank's circuit begins to differ from that of the generator powering circuit by the moment of explosive opening switch operation, cutting off powering cable line at the 350th  $\mu\text{s}$ . The helical preamplifier starts to operate on to two parallel circuits after the magnetic flux capture between the liner and the turns at the 315th  $\mu\text{s}$ , namely: the powering circuit and that of the load.

By this moment the powering circuit current reaches 180 kA, which is higher than the computed number. That may be explained for, on the one hand, by the radial divergence of the helix turns caused by the self-produced magnetic field effect and, on the other hand, by the lower velocity of the liner flight at the edge leading to a later magnetic flux capture. This phenomenon leads to the partial pushing away of the flux from the generator to the bank circuit by the moment of the capture.

The current derivative of the helical preamplifier is rising comparatively rapidly for 50-60  $\mu\text{s}$ , then its rise is slowed down. The presence of high voltages inside the generator compels to take special measures to protect it from breakdowns, resulting in a more complicated generator design. Though, this is compensated by reaching a higher coefficient of the current increase in the helical preamplifier, i. e.  $\sim 200$ , at the helix length of 0,65 m. The generator powering current makes approximately 95 kA by the moment of the liner's movement beginning. The initial powering energy is respectively 250 kJ.

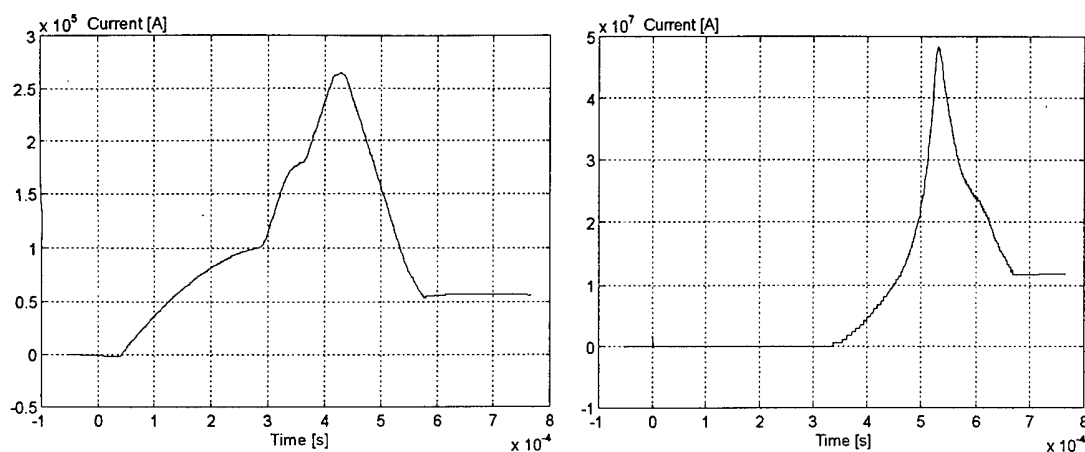


Fig.4. The current in the powering circuit and the current in the load .

By the end of the helical preamplifier operation at the  $490 \mu\text{s}$  the remaining computed circuit inductance makes  $100 \text{ nH}$  at the current of  $16 \text{ MA}$ . This corresponds to  $13 \text{ MJ}$  of magnetic energy.

The cone generator increases the helical generator operation current from  $16 \text{ MA}$  to  $48 \text{ MA}$  for a full time of  $40 \mu\text{s}$ .

The complete load inductance including the torroidal collector, line and oil collector makes  $20\text{-}22 \text{ nH}$  by the end of the generator operation. The magnetic energy storage is  $25\text{-}30 \text{ MJ}$  and magnetic flux is respectively is  $1.1 \text{ Wb}$ .

In some cases we purposefully enhanced the generator reliability, preventing reaching its ultimate parameters. Basically, it is reduced to the greater thickness of the helix conductors' electric insulation which leads to some degradation of the galvanic contact with the liner. Though, it prevents from the breakdowns inside of the generator and space between the helix turns.

The generator developed has the current increase coefficient of nearly 500 and the energy increase factor of 120. The full time of the generator operation is  $225 \mu\text{s}$ . The generator works at the inner voltages higher than  $100 \text{ kV}$ .

- [1]. Pavlovskii A.I, Lyudaev R.Z. et al "A multiwire helical magnetic cumulation generator", pp.585-593. in Megagauss Physics and Technology, ed. by P.J.Turchi. NY; L. Plenum Press, 1980.
- [2]. R.E.Reinovsky, I.R.Lindemuth, J.H.Goforth, R.S.Caird and C.M.Fowler "High-performance, high-current fuses for flux compression generator driven inductive store power conditioning applications", pp. in Megagauss Fields and Pulsed Power Systems. MG-V. ed. by V.M.Titov and G.A.Shvetsov Nova Science Publishers, New York, 1990.
- [3]. А.И.Павловский, Р.З.Людаев, Б.А.Бойко, и др. "Дисковые магнитокумулятивные генераторы" in Proceedings of the Third International Conference on Megagauss Field Generation and Related Topics, V.M.Titov, G.A.Shvetsov, eds., (Nauka, Moscow, 1984), pp. 347-351.
- [4]. Shearer J.W. et al. -J. Appl. Phys., 1968, vol.39,N4,p.2102

## Mechanism of Hot Spots Formation in Magnetic Z- pinch

P. Kubeš<sup>2</sup>, K. Koláček<sup>1</sup>, A. Krejčí<sup>1</sup>, J. Kravárik<sup>2</sup>, M. Paduch<sup>3</sup>, K. Tomaszewski<sup>3</sup>

<sup>1</sup>*Institute of Plasma Physics, Academy of Sciences CR, Za Slovankou 3, 180 00 Prague 8, Czech Republic*

<sup>2</sup>*Faculty of Electrotechnical Engineering, Czech Techn. Univ., Technická 2, 166 27 Prague 6, Czech Republic*

<sup>3</sup>*Institute of Plasma Physics and Laser Microfusion, P.O.Box 49, 00-908 Warsaw 49, Poland*

### Abstract

The evolution of neon implosion of low energy discharge (4 kJ, 40 kV, 150 kA, 1.1  $\mu$ s) was studied using X-ray, schlieren and high speed electrooptical visible gated Quadro camera diagnostics. The geometry, the helical structure of pinched column, two steps of pinching and X-ray emission have been studied. The diameters, electron density and temperature of the hot spots are determined. The hypothesis of axial component of magnetic field generation, of helical shape of magnetic and electric field lines, of the possibility of the release of magnetic energy and of the acceleration of the keV electrons and ions due to voltage induction during the second pinching of the column are discussed.

### 1. Introduction

The explanation of X-ray pulses and hot-spots generation, the investigation and minimisation of the development of instabilities and the mechanism of generation of fast electron and ion beams are the principal tasks of this Z-pinch discharge study. These phenomena are of interest not only for the X-ray generation, but also for controlled fusion research. A detailed study of the gas-puff Z-pinch and the dense plasma focus by schlieren and X-ray diagnostics has already been published in [1] - [3].

Some interesting phenomena have been observed in the comparable small experimental device [1]. The plasma column could be divided into several sections and each of them collapses by turns from the anode (zipper effect). A narrower necks of the column are formed more rapidly than wider nodes. The centres of some nodes correspond spatially to the hot-spots in which the energetic X-rays originate. The local part of the column grows up into helical structure during the column expansion.

The schlieren pictures of the dense plasma focus [2] show, that the further compression of a local neck region results in a tiny pinch column, with a physical feature reminding a miniature version of the original radial compression of the plasma, but this time with both radial and axial motions. Next, a significant increase in size of the flare structure on both axial sides of necking supports the idea of the continuous ejection of mass at the compression process. Plasma at the end of compression has much higher density and in its centre very small hot-spots are formed.

In paper [3] the perturbations with ring-like shape or helical shape around the plasma column are observed. These perturbations remain more or less frozen in until pinch time - not

tending to destroy the integrity of the collapsing column. But at the further development of the column these perturbations can lead to  $m = 0$  instability and disintegrate the column. Pinch column tends to develop into several necking along the column, each pushing plasma material away from the central point of the neck. The occurrence of two such necks would produce a jet-like transport of plasma into the region between them. Their positions are well correlated with regions of intense X-ray emission on pictures taken by time integrating filtered X-ray pinhole camera.

The authors of this paper confirmed experimentally the existence of helical structure, two phases of pinching, axial ejection of plasma to the centre of the nodes during necking in the second phase of pinching and a complex structure of pinched column. They measured parameters of hot spots and they described the temporal and spatial correlation between X-ray emission and secondary pinching of the necks. Further a hypothesis of acceleration of keV electrons and ions due to voltage induction during the neck pinching for hot spots radiation is given.

## 2. Experiments

A series of laser assisted measurements of gas-puff Z-pinch dynamics has been performed in IPP Prague. An annular gas column, injected to the vacuum chamber by valve and nozzle of diameter 21 mm, was driven by capacitor bank (40 kV, 4.3 kJ) to reach a pinch current 150 kA in quarter-period 1.1  $\mu$ s. Schlieren photography and Wollaston prism interferometry was utilised for visualisation of the plasma formations in the inter-electrode gap (distance 24 mm). A 15 ns pulse of Nd:YAG laser (energy 1 mJ in the second harmonic on the wavelength 532 nm) was synchronised with the discharge current. The pictures of pinch plasma were registered on film and/or by CCD camera for further image processing.

A disadvantage of this diagnostic system is that the laser can generate and the detection system can register only one shot per the pinch shot. Thus, in order to have a comparable sequence of pictures during implosion, pinch and decay phases of the discharge, we performed a series of shots in the same, rather reproducible working regime with Neon (plenum pressure 5 atmospheres, delay between gas valve and main spark-gap switching 350  $\mu$ s). This Z-pinch regime in the electrode configuration mentioned above is dominated by the only one powerful XUV peak with circa 100-300 ns FWHM (full width at the half magnitude), emitted from the bulk plasma at the end of implosion phase, when the plasma sheath strikes on itself on the discharge axis.

The XUV signal was detected by bare vacuum photodiode (XRD) with aluminium cathode. Soft X-ray region was covered by fast silicon p-i-n diode SPPD 11-04 (Russian product) filtered by sub-micrometer metal filters. The detectors were placed 70 and 140 cm apart pinch axis in the x-y plane. Moreover, two X-ray pinhole cameras were installed in some shots to take time-integrated images of the pinched plasma. The radiate characteristics of hot spots were studied by using of the absolutely-calibrated flat-crystal spectrometer with limited spatial resolution[5].

For detailed study of pinch evolution also a special advanced diagnostic was implemented. The diagnostic system, developed by IPPLM Warsaw and IMAL Ltd. Łódź [2], consists of two main parts: the QUADRO four frame high speed electrooptical camera and the automatic image capturing and processing system. The QUADRO camera imaged the whole electrode gap through the 596 nm (visible continuum) interference filter and three beam



splitters on the photocathodes of four image converters IC (type XX1050). These were gated from the common sparkgap by a 15 kV/1 ns pulse. The lengths of four "transmission lines" determined precise gate timing of image converters - in our case the gatings of individual ICs were in equal time intervals, which were taken to be either 10 or 20 ns. The images on screens of the ICs were registered by four CCD cameras. Their signals were digitised and recorded by IM 1024TDV frame grabber enabling simultaneous processing of up to four black & white camera signals.

### 3. Diagnostics results

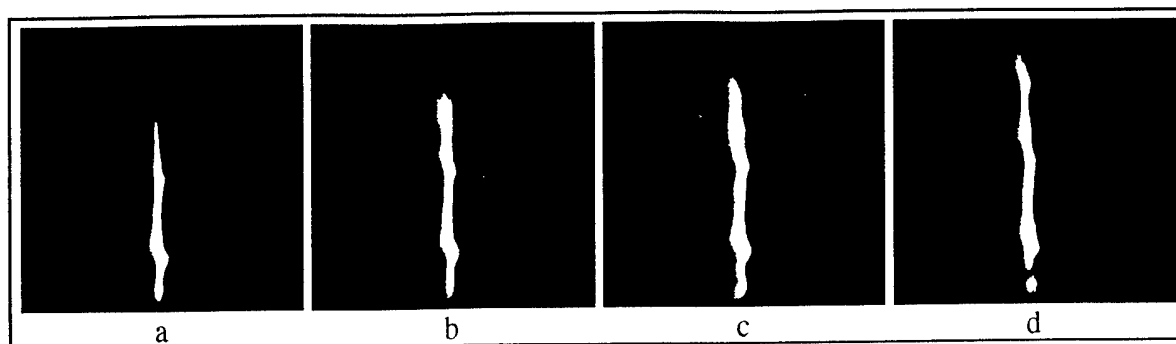
On the oscillograms of current (Rogowski coil signal) we can notice remarkable oscillations in the range of 10-30% of value of current during 100-300 ns. The beginning of these oscillations coincides with the onset of XUV signal, and the end corresponds by half to a time close after XUV maximum and by half to the end of XUV emission. The oscillations are probably caused by fast impedance variations of the discharge.

The time curve of XUV radiation has in 80% one main peak of FWHM of 160-240 ns, in 16% the sharp spike of FWHM of 200-320 ns and in 4% 2 peaks, the FWHM each of which is 100-140 ns. Time 0 - the first maximum of XUV emission.

On the sequence of images in Fig.1 the evolution of helical structure is visible. One term in the lower part of the column was created earlier (before the exposition of Fig. 1a) and the development of the second and the third turns in upper part of the column can be seen in Fig. 1a to 1d. The velocity of  $1-2 \times 10^4$  m/s of compression of helical current sheath in final implosion phases (at the diameters 1.5-3.0 mm) was evaluated.

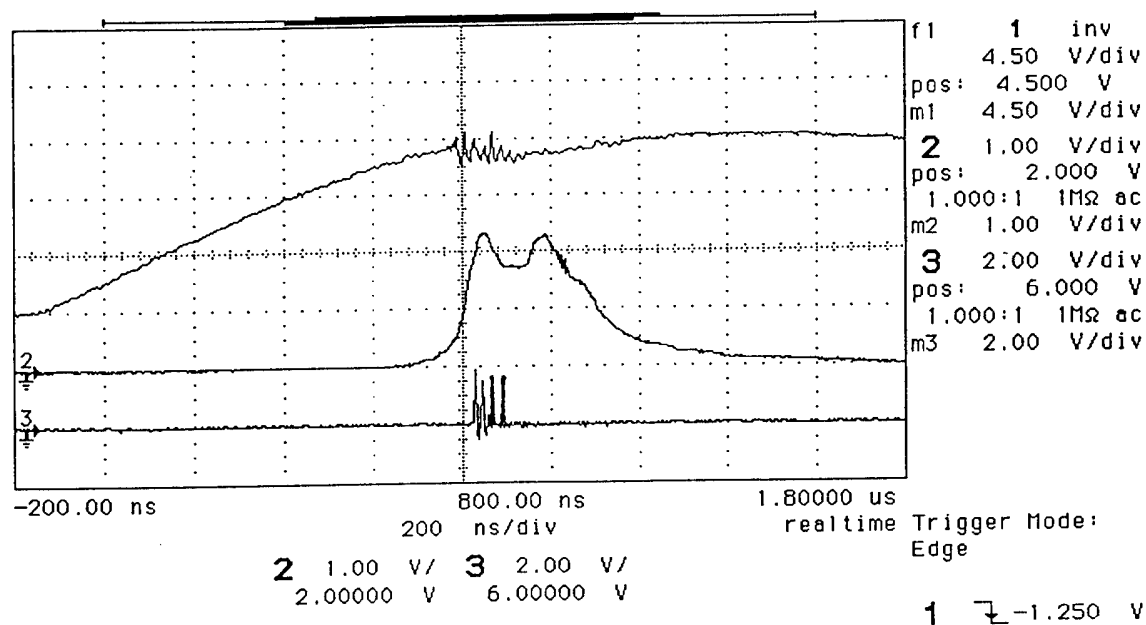
In Fig. 2 we can see the disintegration of the plasma column with some typical phenomena. Fig. 2a was exposed at the same moment as the pulse of the soft X-ray was registered, so this emission is in time correlation with the collapse of two neighbouring necks. The second X-ray pulse was emitted in the moment between expositions of Fig. 2b and 2c, when the collapse and disintegration of the next lower neck takes place. In Fig. 2a-2c an increase of diameter of the spheres located between necks can be observed as a consequence of the axial ejection of plasma from both necks. The existence of axial plasma ejection confirms the rotation of the "spoke" at the bottom of the Fig. 2a-2d. This rotation can be caused by different directions of both neighbouring necks. During this shot the X-ray pinhole camera was installed in the Z-pinch camera and 3 hot spots are observed in the space correlation with centres of 3 nodes.

X-pulses are emitted after the maximum of XUV radiation. The FWHM of pulses is 4-6 ns. The emission is observed ~10 ns after development of the instability of the neck in the moment, when the diameter of the neck decreases to ~100  $\mu$ m and ~10 ns before neck's interruption. During the emission a decrease of electric current ~10 kA is observed. The length of pinching necks is ~1-2 mm. The highest plasma density is formed first near the axis of the neck before X-ray pulse, second in the centre of the nodes after X-ray pulse. ~10 ns after the pulse the compact spherical structure with the diameter ~1 mm and the life-time ~20 ns can be generated in the centre of the nodes. The X-spectra of radiation obtained by imaging flat-crystal spectrometer are well correlated with positions of hot spots taken by pinhole camera.



pinch 25 6.6.1995

hp running-awaiting trigger



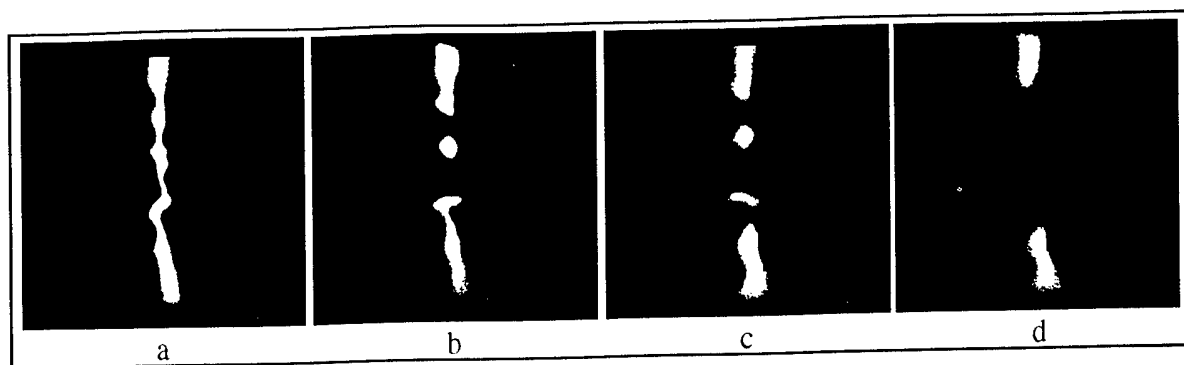
e

Fig 1 Shot No. 25 - formation of helical structure; a)-20, b) 0, c) 20, d)40 ns

e) trace 1 - current

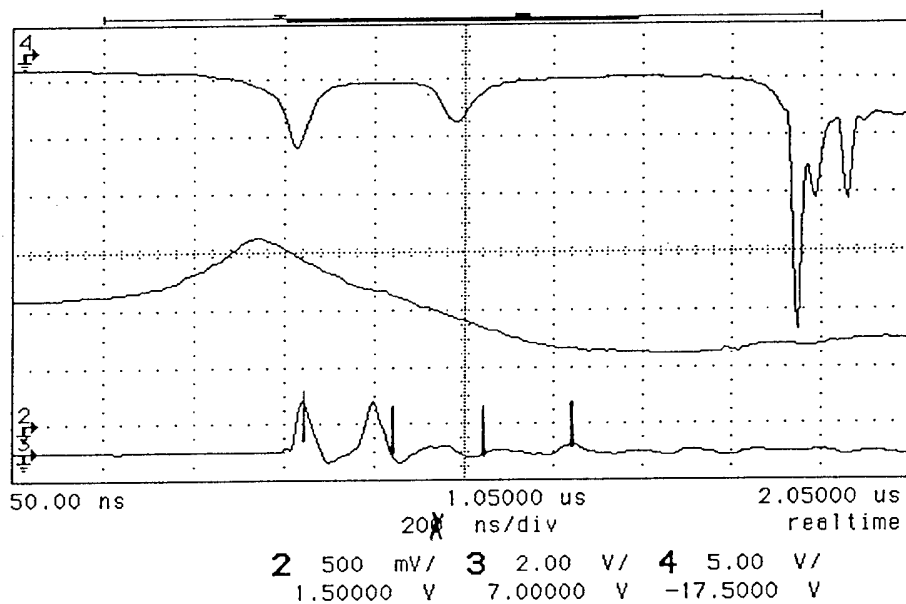
trace 2 - XUV signal

trace 3 - Quadro camera switch



pinch 55 magnif. - 12.6.1995

hp running-awaiting trigger



e

Fig 2 Shot No. 55 - decay of plasma column; a)100, b)120, c)140, d)160 ns

e) Upper trace - X-ray PIN signal.

middle trace - current

lower trace - switch of Quadro camera

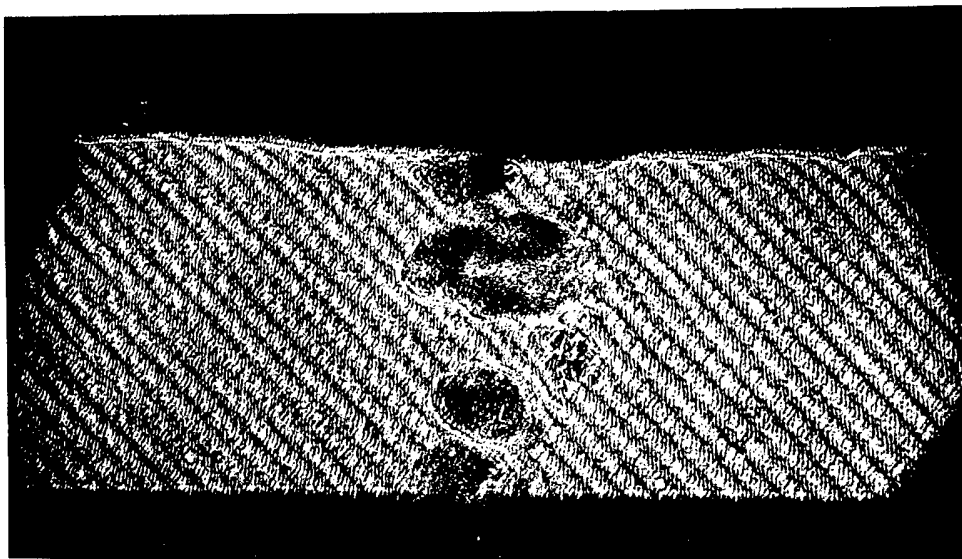
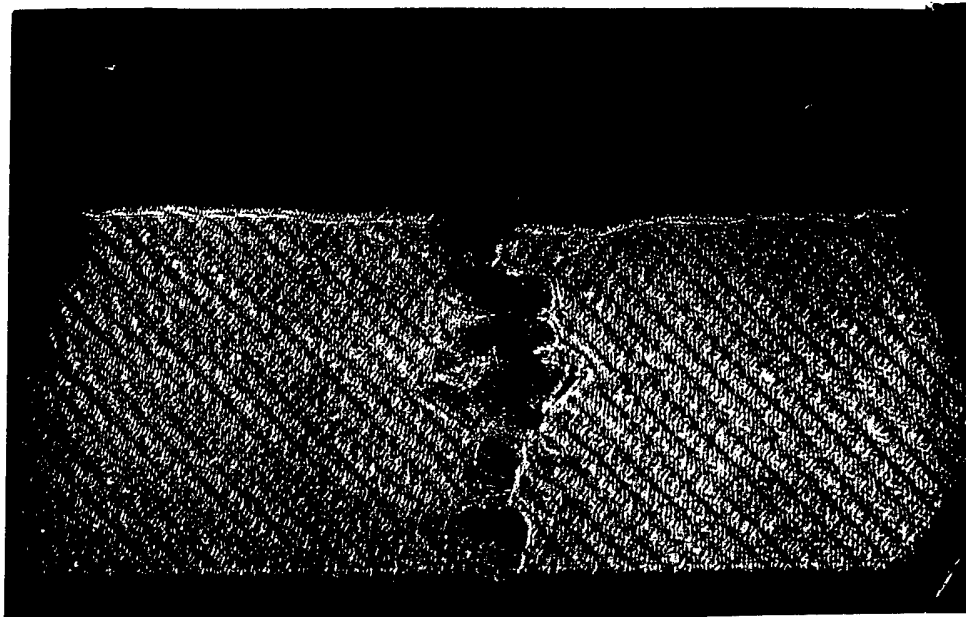


Fig 3 Shots No. 89, 87, Wollaston prism interferometry; up helical structure 100 ns, down spheres 150 ns

The absolute energy emitted from the hot spots was measured by the X-ray spectrometer:  $2.3 \times 10^{-3}$  J for Ne-like  $\text{He}_{\alpha}$ ,  $3.4 \times 10^{-3}$  J for Ne-like  $\text{Ly}_{\alpha}$ , and  $3.5 \times 10^{-3}$  J for Ne-like  $\text{He}_{\beta}$ . From the contours of the observed intensity ratios of these lines the 150 eV electron temperature and the  $10^{27} \text{ m}^{-3}$  electron density were estimated by using of the steady state collisional-radiative model [5].

In Fig.3 two phases of evolution of the plasma column are visualised by Wollaston prism interferometry. In the upper part of the figure the helical tube (with diameter 2 mm turning around an inner imaginary column with radii of 3-4 mm) and in the lower part of the figure the spheres (diameter 2-3 mm) formed during disintegration of the column are shown.

#### 4. Discussion

On the base of the complex and simultaneous X-ray and visible light diagnostics it is possible to formulate following conclusions.

The pinched plasma column creates gradually, first near the anode and next due to zipper effect in the parts closer to the cathode. Beginning of this pinching correlates with onset of the XUV emission and then both the emission and the length of pinched plasma column increase during 100-150 ns till the pinched plasma column is as long as the electrode gap; at this time the XUV emission reaches its maximum. On the surface of the column 2-3 nodes appear in distances 5-10 mm. Their contours are either symmetric (indicating spherical structure) or more complicated (in most cases resembling a helical-like current tube twisted on an imaginary column). The pinching of this part is slower than the pinching of the necks. A tendency of conversion of helical tubes into toroidal and spherical structures is also observed.

The plasma column has probably more complex form. The observed contour is influenced by the visualisation method. The innermost parts of plasma column of the radii of 0.3-0.7 mm have very high plasma density (greater then  $5 \times 10^{25} \text{ m}^{-3}$ ) and 2-3 nodes in distances of 5-10 mm. Contour of the nodes is often helical-like turn of the pitch of 2 mm. These shapes of column were registered with low sensitivity of the Quadro camera. In the pictures taken with higher camera sensitivity the radii of 0.7-1.5 mm of the plasma column (plasma density higher then  $10^{25} \text{ m}^{-3}$ ) were observed with typical axially symmetrical necks and nodes ( $m=0$ ). The Schlieren methods imagine the boundary of the column with electron density  $\sim 10^{25} \text{ m}^{-3}$ .

During subsequent evolution of the pinched column (10-150 ns after XUV maximum) it starts strangling (the second pinching) of one or more necks leading to disintegration (interruption) of the plasma column. This is followed by radial explosion of neighbouring nodes and by increase of plasma density in the centre of this node. This confirms the idea about axial acceleration of plasma from necks to nodes. During  $\sim 10$  ns before column interruption the short 4-6 ns soft X-ray pulses are registered. Further the spatial correlation between centre of nodes and hot-spots was confirmed.

From the electron temperature and density and the intensity of radiation of hot spots the diameter  $\sim 100 \mu\text{m}$  and plasma pressure  $2.5 \times 10^{10} \text{ Pa}$  was calculated. This values are in agreement with magnetic pressure in the fibre (current  $\sim 100 \text{ kA}$  in diameter  $100 \mu\text{m}$  produces magnetic field 200 T) and kinetic pressure (for the  $4 \times 10^4 \text{ m/s}$  velocity) during the second pinching of the necks.

During  $\sim 10$  ns of the second phase of pinching of the neck the current decreases from  $\sim 100 \text{ kA}$  to  $\sim 90 \text{ kA}$ , the inductivity increases from  $\sim 1.1 \times 10^{-9} \text{ H}$  to  $1.4 \times 10^{-9} \text{ H}$  and a few kV voltage can be induced. This electric field could accelerate the electrons and generate the X-ray pulse.

There is a lot of questions about origin of helical forms, secondary pinching and radial ejection of plasma. One possible explanation is given in this paper following a hypothesis of generation of axial magnetic field during plasma implosion, when the plasma column is formed (in analogy to  $\alpha$  effect and magnetic dynamo [4]). The resulting magnetic field lines in plasma column have not azimuthal but helical form. The helicity in the necks is lower than helicity in the nodes. A higher axial magnetic field in the nodes can result in slower compression and later formation of equilibrium in this part of the column. During the plasma implosion a part of

kinetic energy transforms into energy of frozen and pressed axial magnetic field. The second pinching can be connected with release and transformation of axial magnetic field lines into azimuthal (also  $\alpha$  effect). The relative equilibrium in column is broken and the instability begins to develop. The column is pinched, plasma is ejected in axial direction to the ends of the neck and the interruption of plasma column is observed. In the centre of nodes the plasma density increases.

## 5. Conclusion

- 1) During the development of the pinched column a helical structures were observed. The helicity in the inner part of the column is lower than the helicity in the outer layers.
- 2) In the development of the plasma column two phases of pinching can be distinguished. During the first phase a relatively stable thin column is formed. In places, where the helicity decreases with time, the column is locally further compressed creating thinner „necks“, contrary in places, where the column helicity increases, wider nodes are formed. This phase is connected with approximately linear increase of the XUV emission.
- 3) The second phase of pinching was observed during the plasma column disintegration. This phenomenon is accompanied by decrease of the XUV emission. It starts with straggling of the necks and the plasma transport from necks to nodes and short pulses of X-ray emission are imagined. In the centre of the nodes the compact dense structure is formed. X-pulse is emitted from the centre of the nodes. The energy density in hot spots is the same as the kinetic energy density of the second pinching and the magnetic energy density in the pinched neck's fibbers.
- 4) The hypothesis of generation of axial magnetic field during plasma implosion would give a possible exploration of the origin of helical form and double pinching. The resulting magnetic lines after first pinching have not azimuthal but helical form and part of kinetic energy is converted in compressed axial magnetic field. This energy is released during the second pinch phase.
- 5) During the second phase of pinching the inductivity of the column increases and the voltage of a few kV is induced. The energy density increases during the second pinch phase can produce hot spots and their X-ray emission.

## References

- [1] K. Takasugi et al, 3rd Int.Conf.on Dense Z-Pinches, AIP Conf. Proc. 299, London 1993, p.251.
- [2] P. Choi et al, 3rd Int.Conf.on Dense Z-Pinches, AIP Conf. Proc. 299, London 1993, p. 288.
- [3] P. Choi et al, 3rd Int.Conf.on Dense Z-Pinches, AIP Conf. Proc. 299, London 1993, p.299.
- [4] F. Krause, K.H. Radler: Mean-Field Magnetohydrodynamics Dynamo Theory, Akademie-Verlag, Berlin 1980.
- [5] O. Renner, E. Krouský et al, Beams'96, this Conf.

*This research has been supported by grant GACR No. 202-95-0178 „Stable Structures in Magnetic Pinches“*

## ION BEAMS FROM HIGH-CURRENT PF FACILITIES

M. Sadowski

*Soltan Institute for Nuclear Studies, 05-400 Otwock-Świerk n. Warsaw, Poland*

**Abstract:** The paper concerns pulsed beams of fast deuterons and impurity- or admixture-ions emitted from high-current PF-type facilities operated in different laboratories. A short comparative analysis of time-integrated and time-resolved studies is presented. Particular attention is paid to the microstructure of such ion beams, and to the verification of some theoretical models.

## 1. Introduction

Ion beams generated in PF facilities have been investigated in many laboratories, using different diagnostic techniques, e.g., nuclear-activation methods [1-3], magnetic ion spectrometers [4], Thomson-type analyzers [5-6], and time-of-flight measuring systems [7-8]. General characteristics of high-energy (>100 keV) deuterons beams, e.g., their angular distribution and energy spectra, have been studied by several authors [5-10]. Energy distributions of impurity (as nitrogen, oxygen) and admixture (as argon) ions in various ionization states have also been investigated [6]. Some attention has been devoted to temporal characteristics of ion pulses [8, 10] and their correlations with other PF phenomena [10-13].

The main aim of this paper has been to compare the ion emission characteristics of several PF facilities, to bring attention to the microstructure of such ion beams, and to comment on different physical models of the ion acceleration.

## 2. Analysis of experimental results

As regards a total amount of fast primary deuterons, accelerated and emitted from PF discharges performed with a deuterium filling, it has been shown that at a stored energy of about 70 kJ more than  $10^{15}$  deuterons are accelerated to energy above 300 keV, and more than  $10^{12}$  deuterons reach energy of several MeV [3, 6]. It has also been measured that within a 56-kJ PF-device the deuteron energy distribution decreases exponentially from about 300 keV to about 3 MeV [6], and within a larger 280-kJ PF-facility this exponential decrease is steeper and extends to 2 MeV only [14], while the total number of deuterons above 70 keV is about the same (up to  $10^{12}$  sr<sup>-1</sup> end-on and up to  $10^{11}$  sr<sup>-1</sup> side-on). In general, deuteron energy distributions depend strongly on the initial operational pressure. At lower initial pressures an increase in the X-ray and primary-ion emission is usually observed, and sometimes two different types of ion energy spectra are detected, as shown in Fig.1. It should also be noted that an exponential decay of the deuteron energy distribution was observed in many PF-devices, e.g. [4, 6, 12], while very energetic deuterons (up to about 10 MeV) were registered in a few experiments only [12].

As regards impurity- and admixture-ions, they have been analyzed with Thomson-

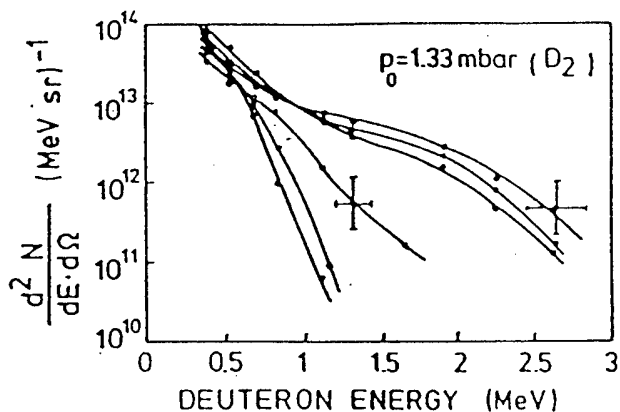


*Fig.1. Deuteron energy distributions obtained from several discharges within a 56-kJ PF device [6] operated at low initial pressure.*

type mass-spectrometers [6, 12, 16], as shown in Fig.2. Their energy distributions can be described by an exponential rise and an exponential decay with the maximum ranging from  $E/Z = 0.8$  MeV to 1.3 MeV. The spectra of the highly ionized species (with  $Z > 4$ ) extend to the value of  $E/Z = 1.8$ -1.9 MeV, while the lower ionized impurities (with  $Z < 4$ ) reach somewhat higher value  $E/Z = 2$ -2.8 MeV. It can be concluded that the similarity of energy distributions for different ion species, and proportionality of their maximum energy to electrical charge, indicate that impurity (admixture) ions are accelerated by similar processes involving strong electric fields.

Taking into account that ion emitting regions (sources) are of the submillimeter range, as deduced from the ion pinhole pictures [5], local electric field intensity can reach above 50 MV/cm. This value is much higher than that induced by rapid changes in inductance of the electrical circuit. Let us consider  $E_{ind} = I dL/dt$ , where  $L = \mu/2\pi \ln R/r(t)$ ,  $R$  - the maximum radius,  $r(t)$  - the radius of a current sheath. Hence  $E_{ind} = B_\phi dr/dt$ , where the magnetic field  $B_\phi = I \mu/2\pi r$ . Substituting  $I = 10^5$  A,  $R = 2.5$  cm,  $r_{min} = 5 \times 10^{-3}$  cm,  $(dr/dt)_{max} = 3.5 \times 10^7$  cm/s, one gets  $E_{ind} = 1.4$  MV/cm only. Therefore, the direct acceleration of charged particles to energy within a MeV region by the pinch-induced electrical fields is impossible, and other mechanisms have to be considered.

In order to shed some light on dynamics of the ion emission time-resolved measurements have been performed with different PF facilities [8, 11, 12]. Using an ion pinhole camera and miniature scintillation detectors placed in different points of a space-resolved ion image [10], it has been shown that the ion pulses reveal a coarse ( $\sim 30$  ns) and a fine ( $\sim 2$  ns) structure. Also mass- and energy-resolved measurements, as performed by means of a Thomson-type analyzer equipped with scintillation detectors, have demonstrated the multi-spike structure of ion pulses, e.g., for quasi-monoenergetic deuterons there were registered 3 separate pulses coming within 30-40 ns time intervals. It can be explained on the basis of a model assuming that fast deuterons (ions) are emitted from different microsources [9], in a form of numerous beams of various energy, at different instants after the current peculiarity.

The hypothesis about ion microbeams has been confirmed by detailed studies performed with ion pinhole cameras equipped with nuclear track detectors covered with different absorption filters. Typical ion pinhole pictures, demonstrating quasi-concentric structures composed of

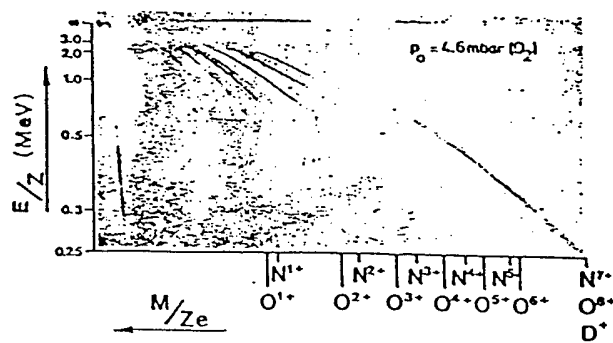


Fig.2. Typical ion spectra, as registered with a Thomson-type analyzer and nuclear track detector for a single shot within a 56-kJ PF device [16] operated at higher initial pressure.

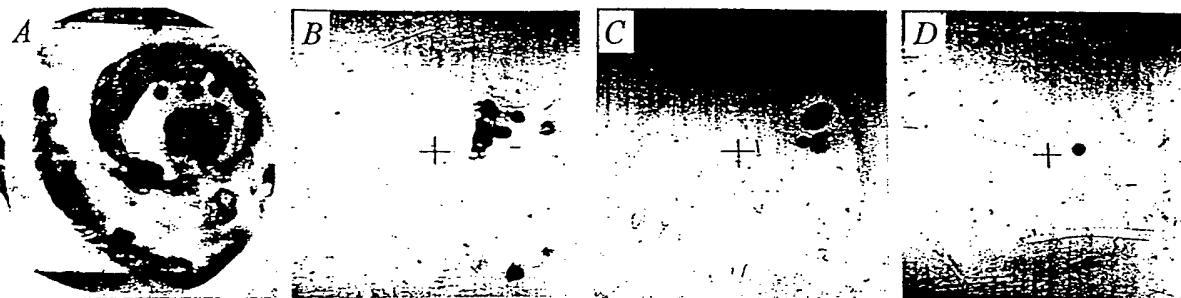


Fig.3. Ion pinhole pictures, as taken end-on by means of CN-films covered with different Al-filters: A - 1.5- $\mu$ m Al-filter,  $E_d > 220$  keV; B - 6.0- $\mu$ m Al-filter,  $E_d > 700$  keV; C - 20.0- $\mu$ m Al-filter,  $E_d > 1.7$  MeV; and D - 30- $\mu$ m Al-filter,  $E_d > 2.1$  MeV.



numerous microbeam spots [5], have been obtained only with thin ( $<3 \mu\text{m}$ ) Al-filters. With thicker filters the ion pinhole pictures demonstrated the deuteron microbeams, as shown in Fig.3. It is worthy to mention that an angular divergence of such ion microbeams, as measured by direct methods (2 ion pinhole cameras situated one behind the other), was found to be rather small ( $<8^\circ$ ).

In order to explain the ion emission different acceleration mechanisms have been considered by many authors, e.g. in [16-17] and numerous Refs. *ibid*. Some researchers apply a simple plasma-diode model, while other prefer more complicated models which involve various instabilities, e.g., electron cyclotron drift instability etc. Considering angular distributions of ions emitted from PF discharges, it should be noted that in several experiments of different energetics (ranging from 3.6 kJ to above 200 kJ) there were observed: assymetry in relation to the z-axis, a considerable decrease in the ion emission at  $\Theta$ -angles higher than  $20$ - $40^\circ$ , and characteristic emission dip at given angle (at  $\Theta=0^\circ$  in PGN device, and at  $\Theta=20^\circ$  in PF-360 facility) [18]. These features have also been observed in the PF-1000 device [19], as shown in Fig.4.

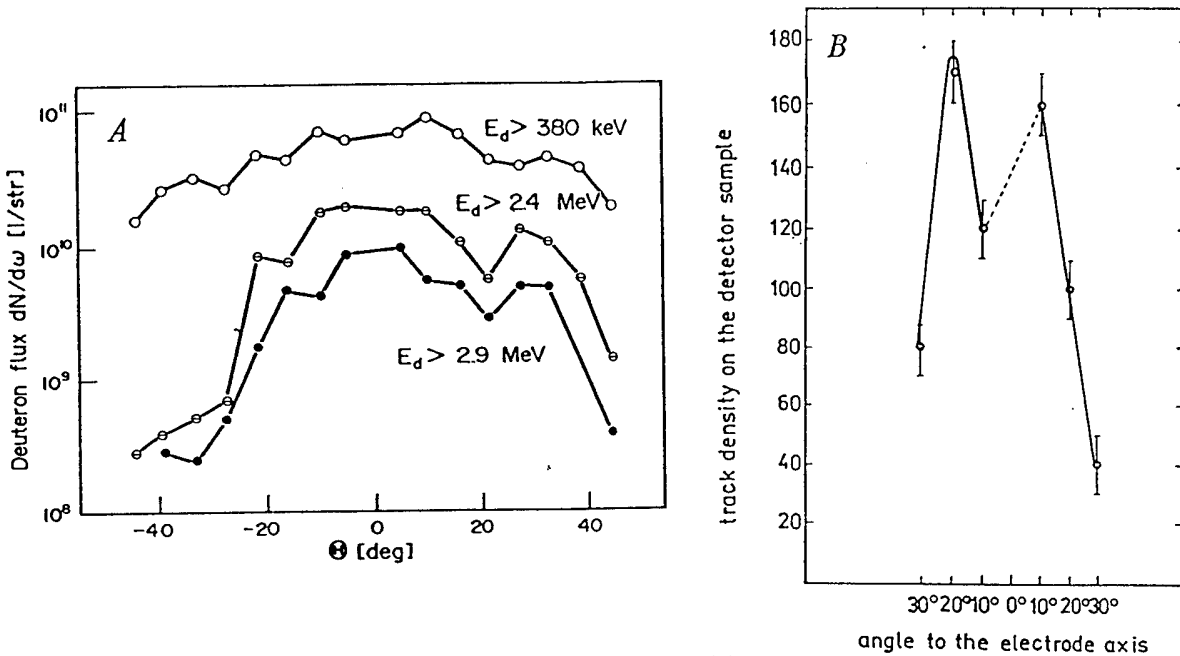


Fig.4. Angular distributions of high-energy deuterons, as obtained (A) for 126-kJ shots within the PF-360 device, and (B) for 240-kJ discharges within the PF-1000 facility.

With a pinch column surrounded by an azimuthal magnetic field, 2D calculations of ion trajectories (even without taking into account filamentation effects) show that an angular anisotropy is an inherent feature of all the PF discharges. Also deviations from axial symmetry can easily be explained by the stochastic formation of the ion microsources and by heterogeneity of local electromagnetic fields. The ion-emission minima (dips) observed at given angles might be connected with the lack of accelerated particles within a hole of an ion larmor diameter. Considering the minimum pinch radius and pinch current intensity one can estimate the magnetic field at the pinch surface, e.g., for  $r_{\min} = 2 \text{ mm}$ ,  $I_p = 800 \text{ kA}$ ,  $B_{\max} = 800 \text{ kG}$ . Under such conditions even 500-keV deuterons (with  $r_L = 1.3 \text{ mm}$ ) can be confined (trapped) by the current sheath, and along the pinch axis one can observe an ion emission dip. The pinch axis does not necessarily correspond to the z-axis of the PF facility.

Considering ion beams emitted from a focus region, one must take into account the attenuation of those in the focus region, and after that the slowing-down of deuterons by a neutral gas layer in front of a detector plate. These effects can be computed for different deuteron energies, as shown in Fig.5.

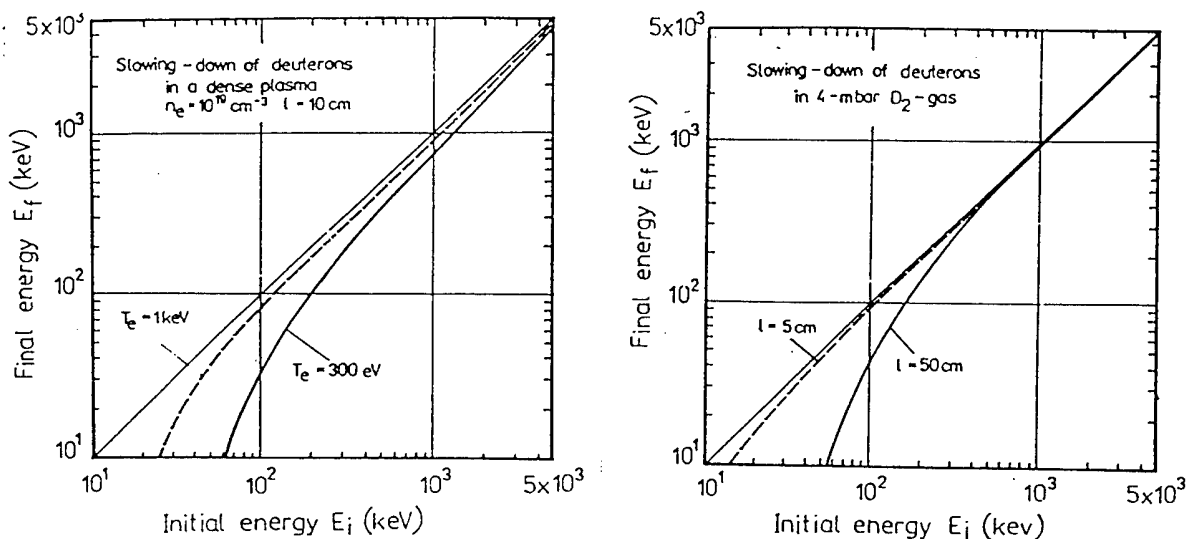


Fig. 5. Diagrams presenting the attenuation of deuterons by a dense plasma within a focus region (on the left), and by neutral  $D_2$  gas between the focus and a detector plane (on the right).

### 3. Summary and conclusions

The most important conclusions from this analysis can be formulated as follows:

1. Anisotropy in the ion emission from PF discharges can be explained by the fact that ion microsources (depending on local plasma parameters and fields) are formed stochastically and with a large symmetry jitter in relation to the  $z$ -axis.
2. The first mechanism of the ion acceleration can be attributed to ion reflections inside the collapsing current sheath (funnel) and to electrical fields generated inductively. Mechanisms of the generation of subsequent fast ion pulses are more complicated, and they are connected possibly with microturbulences and electric fields induced by decaying plasma microstructures.
3. Particular attention should be paid to studies of time correlations. Experimental data collected so far are insufficient to identify all the physical processes involved in the formation of the pinch column and the ion microsources.

### References

- [1] Ch.Maisonnier, J.P.Rager; Proc. 3rd Int. Conf. High-Power Electron and Ion Beams (Novosibirsk 1979), Inv. Paper.
- [2] N.V.Filippov, T.I.Filippova; JETP Lett. **25** (1977) 241.
- [3] R.L.Gullickson, H.L.Sahlin; J. Appl. Phys. **49** (1978) 1099.
- [4] H.Krompholz, L.Michel, K.H.Schonbach, N.Fisher; Appl. Phys. **13** (1977) 29.
- [5] L.Bertalot, H.Herold, U.Jager, et al.; Phys. Lett. **79A** (1980) 389.
- [6] A.Mozer, M.Sadowski, H.Herold, H.Schmidt; J. Appl. Phys. **53** (1982) 2959.
- [7] R.L.Gullickson, J.W.McClure, W.L.Pickles, et al.; Proc. Int. Conf. Plasma Sci. (Madison 1980), p.75.
- [8] G.Gerdin, W.Stygar, F.Venneri; J. Appl. Phys. **52** (1981) 3269.
- [9] L.Bertalot, R.Deutsch, H.Herold, et al.; Proc. 10th Europ. Conf. CFPP (Moscow 1981), p.D-1.
- [10] M.Sadowski, J.Zebrowski, E.Rydygier, et al.; Phys. Lett. **113A** (1985) 25.
- [11] K.Hirano, T.Yamamoto, K.Shimoda, H.Nakajima; J. Phys. Soc. Jap. **58** (1989) 3591.
- [12] W.H.Bostick, H.Kilic, V.Nardi, C.W.Powell; Nucl. Fusion **33** (1993) 413.
- [13] M.Sadowski, J.Baranowski, L.Jakubowski, et al.; Proc. 21st EPS Conf. CFPP (Montpellier 1994), p.1320.
- [14] H.Herold, L.Bertalot, U.Jager, et al.; Proc. 14th EPS Conf. CFPP (Aachen 1983), p.477.
- [15] H.Herold, A.Mozer, M.Sadowski, H.Schmidt; Rev. Sci. Instrum. **52** (1981) 24.
- [16] S.P.Gary, F.Hohl; Report LA UR78-518 (1978).
- [17] K.G.Gureev; Sov. Phys. Tech. Phys. **25** (1980) 192.
- [18] M.Sadowski, J.Zebrowski, E.Rydygier, J.Kucinski; Plasma Phys. Contr. fusion **30** (1988) 763.
- [19] M.Scholz and PF-1000 Team; Proc. 2nd Nat. Symp. PLASMA'95 (Warsaw 1995), Vol.II, p.15.

## Pinches and Micropinches in the SPEED 2 Plasma Focus

P. Röwekamp, G. Decker, W. Kies, B. Lucas, F. Schmitz, G. Ziethen

*Institut für Experimentalphysik, Heinrich-Heine-Universität, Universitätsstraße 1/25.42,  
40225 Düsseldorf, Germany*

D.M. Simanovskii, S.V. Bobashev

*A.-F.-Ioffe-Physico-Technical-Institute, Politechnicheskaya ulica 26, Russian Academy of  
Sciences, 194021 St. Petersburg, Russia*

### Introduction and Apparatus

Pinch plasmas are potential sources of soft x-radiation for applications such as x-ray microscopy or lithography. [1] Especially micropinches emitting a few Joules of soft x-rays ( $\lambda < 2$  nm) within less than 1 ns have been intensively studied. [2, 3] Unfortunately, micropinches appear very erratic in space and time so that their optimization and application are difficult. Micropinches are actuated in necked regions of the pinch column by local radiative collapse [4] if heavy gases (e.g. argon) are used for the discharge or injected into a deuterium discharge.

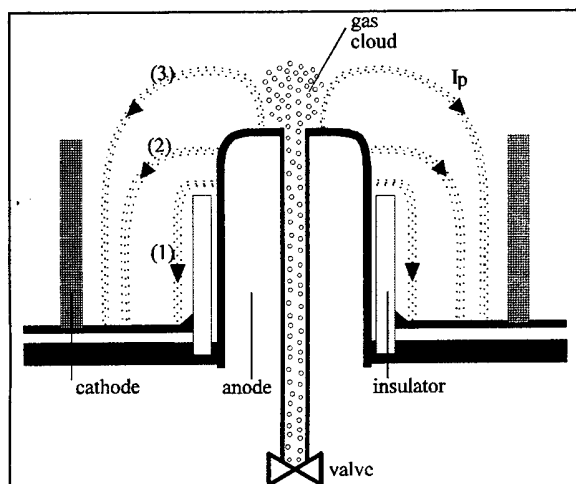


Fig.1: Plasma focus SPEED 2 with gas injection

The discharges in our SPEED 2 plasma focus (180 kV, 70 kJ, 1.5 MA) [5] are always initiated in pure deuterium along a cylindrical glass insulator with a plasma sprayed alumina surface. The deuterium plasma sheath then runs into a cloud of the doping gas that is formed above the anode by gas injection through a hole in the copper anode via a fast electric valve which is triggered a few ms before discharge initiation. Too short delay times result in pure deuterium pinches producing intensive neutron pulses but only weak soft x-radiation. Too long delay times with heavy doping gases prevent plasma sheath formation because these gases as well as impurities on the insulator surface lead to sheath break-up and decay and no pinch is formed.

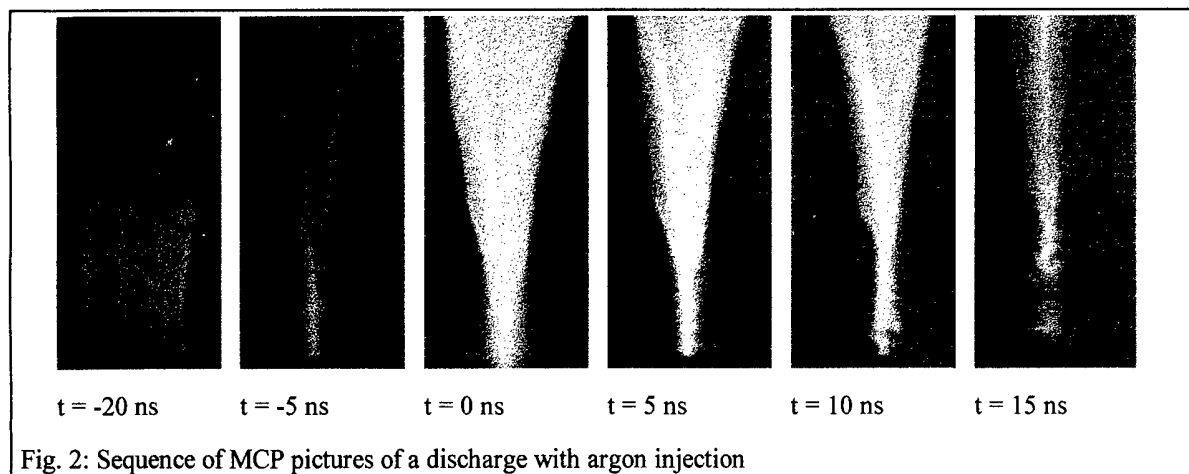
These cases are most easily realized from the neutron yield that almost vanishes if no proper sheath is formed. [1] This sensitivity against impurity, well known from high performance dynamical pinches [6], makes discharge initiation with premixed fillings impossible.

### Micropinch and Column Mode

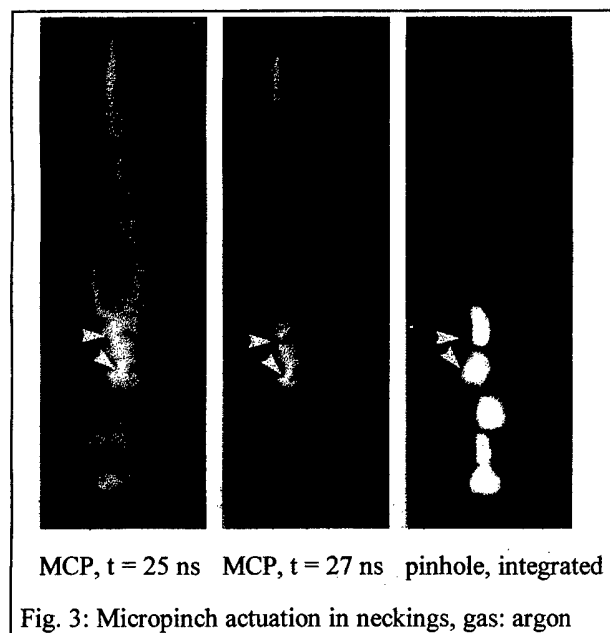
Different heavy gases (argon, krypton and xenon) were injected into a deuterium discharge in order to study the final compression and micropinch actuation by means of various imaging and spectrally resolving diagnostics in three different wavelength ranges. We found that using these noble gases several micropinches appeared along the axis of symmetry emitting soft x-rays with strong line radiation and especially helium- and hydrogen-like lines around 0.4 nm in argon. Framing pictures provide informations on the pinch dynamics. While the image sequen-

ces taken in the visible show only contours but no internal structures of the pinch column, the XUV-series (fig. 2) using a gated 4-frame-MCP-camera (3 ns) enables improved investigations.

The plasma cylinder is to be seen for about 100 ns starting 50 ns before the maximum compression, when the faintly radiating sheath runs into the cloud of heavy gas. Shortly before

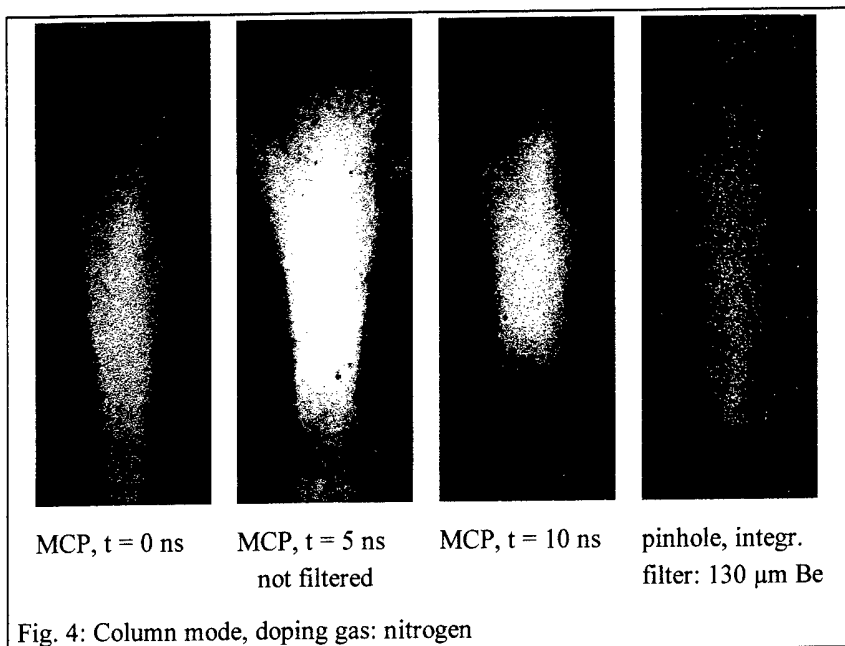


the maximum compression bright, filament-like structures occur, probably showing the current distribution in the sheath. A few nanoseconds after the strongest compression necked structures like  $m=0$ -instabilities are observed. The process starts close to the anode and happens later at higher  $z$ -positions, while the first neckings are already decayed and the intensity in the bottom part of the pinch column is already decreasing. After about 100 ns all structures have disappeared. Comparing these pictures with filtered time integrated pinhole pictures ( $\lambda < 2$  nm) it was found that the micropinches are actuated where the necked column decays, that is shortly before the neck decays. (fig. 3) It seems that the micropinch disrupts the neckings. [4] While for the early pinch phase a definite identification of necking and micropinching is only possible for stronger filtered pictures, from many examples of later times it can be safely



concluded that necking is a necessary condition for micropinches to be actuated, but not a sufficient one for them to occur. From the radiative collapse model [7] it seems plausible that in necked  $z$  positions of higher line density the starting conditions for micropinch formation are better than in neckings where the line density is lower and hence, the temperature is higher and (with comparable radial dimensions) the density lower. This is supported by estimations of the temperature and density evaluated from spatially resolved spectra of the helium-like emission of argon: The decreasing ratio of the intensity of the dielectronic satellites and the resonance line for micropinches close to the anode and at the top of the pinch indicates an increasing electron temperature.

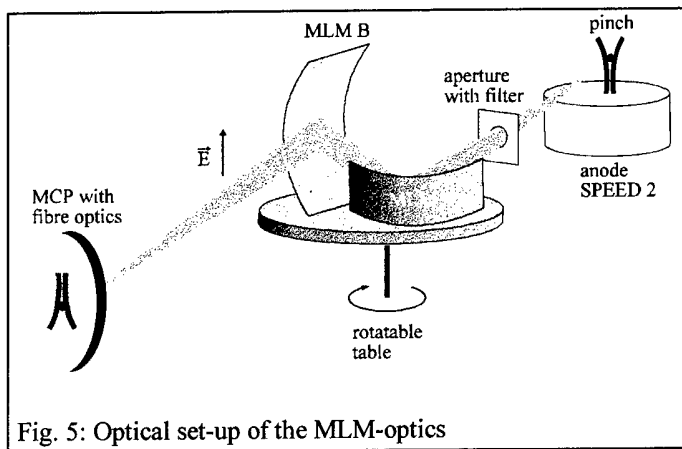
Injecting neon or lighter gases no micropinches appeared, instead within a straight pinch column of a few mm in diameter and about 10 mm in length a narrow ( $< 1$  mm) bright core plasma could be sometimes seen on time integrated pinhole pictures (column mode). Figure 4 shows a sequence of MCP pictures in combination with the corresponding time integrated pinhole picture of the pinch with the doping gas nitrogen. The pinch column at all times and in both wavelength ranges is rather uniform without substructures or neckings.



By contrast operation with the gas TMS (tetramethylsilane), containing the element of silicon ( $Z = 14$ ), exhibits both modes: it distinctly shows necked columns from which micropinches develop and a stable column. This behaviour is also observed in small plasma focus devices [8]. In case of efficient discharges (valued from voltage and current traces and from the neutron yield) the column mode is mostly favoured whereas less

efficient discharges tend to neckings and subsequent micropinch-like spots even in TMS. There is a tendency to the column mode for high energy density pinches with light gases ( $Z < 18$ ). This is astonishing since recent measurements showed, that also in the column mode line radiation is predominant. Further investigations on the SPEED 2 experiment (presently running) will show whether a global radiative collapse can be actuated even from the column mode where the radiation loss is reduced.

### Wavelength Selective Imaging



For applications aspects especially interesting are (besides the energy output [2]) the size and structure of the source in the water window (2.33 nm - 4.36 nm). To record spectral selective images an x-ray microscope based on cylindrically bent multilayer mirrors (MLM) mounted in a parallel configuration was developed (fig. 5). In a first series of experiments time integrated plasma images - using argon as doping gas - were taken at different wavelengths in the interval from 2.4 to

4.5 nm with a spectral resolution of  $\lambda/\Delta\lambda \cong 100$  and a spatial resolution of approximately  $80 \mu\text{m}$  within a 30 mm diameter field of view. A strong wavelength dependence of the shape

and the size in the emitting regions of the plasma was found. The images of the bright spots at  $\lambda = 2.5$  nm with a size of about 0.5 mm are identified with early stages of micropinches were obtained. [9]

The system was improved by gating the MCP detector, achieving an exposure time of about 3 ns. In a series of experiments (doping argon as before), in which the optics was tuned to 2.4 nm, pictures at different times during the discharge were recorded (fig 6). In an early phase (a)

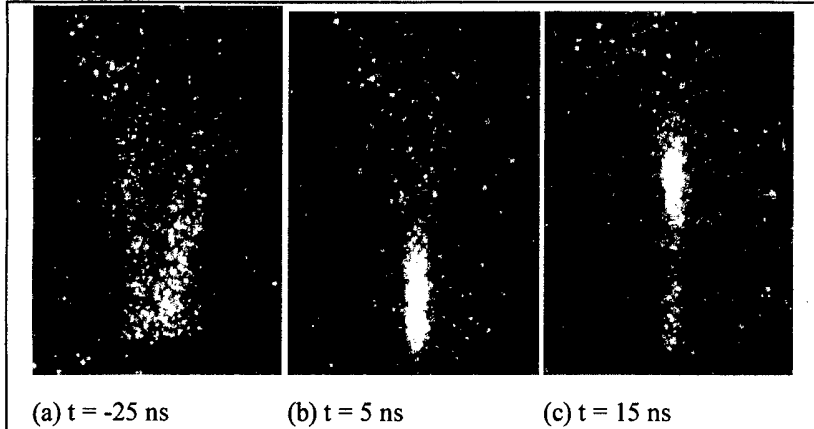


Fig. 6: Sequence of pictures taken with the MLM-optics, gated operation, doping gas: argon

the intensity emitted in this wavelength range is comparatively low but it stems from a large volume. During later phases of the discharges (b and c) enhanced intensity is emitted from the core of the plasma column with a diameter of only 1 - 2 mm. Since the emission corresponds to a certain ionization stage it can be concluded, that the same ionization stage is reached firstly close to the anode

(b) and later at higher z-positions (c).

## Summary

Pinch plasmas generated in a plasma focus configuration exhibit two different modes. The micropinch mode is experimentally investigated in detail and theoretically modelled. Therefore its characteristics e.g. temperature, density, life time and energy output are well known.

In contrast to this the column mode, which seems to be also suitable for investigations, is not equally well understood. Its remarkable features are the unexpectedly high stability (also if the critical current for a radiative collapse is exceeded) and its reproducibility, which are not yet fully exploited.

## References

- [1] J.M. Bayley, G. Decker, W. Kies, M. Mälzig, F. Müller, P. Röwekamp, J. Westheide, Yu.V. Sidelnikov, J. Appl. Phys. **69**(2), p.613, 1991
- [2] P. Röwekamp, G. Decker, W. Kies, F. Schmitz, G. Ziethen, J.M. Bayley, K.N. Koshelev, Yu.V. Sidelnikov, F.B. Rosmej, A. Schulz, D.M. Simanovskii, Third Int. Conf. on Dense z-Pinches, AIP Conf. Proceedings **299**, p.332, London UK, 1993
- [3] H. Schmidt, D. Schulz, P. Antsiferov, Third Int. Conf. on Dense z-Pinches, AIP Conf. Proceedings **299**, p.348, London UK, 1993
- [4] G. Decker, W. Kies, R. Nadolny, P. Röwekamp, F. Schmitz, G. Ziethen, K.N. Koshelev, Yu.V. Sidelnikov, Yu.V. Sopkin, Plasma Sources, Science & Technology, **5** (1), p.112, 1996
- [5] G. Decker, W. Kies, M. Mälzig, C. van Calster, G. Ziethen, Nucl. Instr. Meth. **A249**, p.477, 1986
- [6] W. Kies, Plasma Physics **28** (11), p.1645, 1986
- [7] V.V. Vikhrev, V.V. Ivanov, K.N. Koshelev, Sov. J. Plasma Phys. **8** (6), p.688, 1982
- [8] R. Lebert, A. Engel, K. Gäbel, D. Rothweiler, E. Förster, W. Neff, Third Int. Conf. on Dense z-Pinches, AIP Conf. Proceedings **299**, p. 324, London UK, 1993
- [9] S.V. Bobashev, D.M. Simanovskii, P. Röwekamp, G. Decker, W. Kies, Yu.Ya. Platonov, accepted for publication in Plasma Sources, Science & Technology; 1996

# GENERATION OF ROTATION AND SHEAR FLOW IN AN IMPLoding LINER

J.H. Hammer, D.D. Ryutov<sup>1</sup>

*Lawrence Livermore National Laboratory, Livermore, CA 94550, USA*

## 1. Introduction

As is well known, development of the Rayleigh-Taylor instability of the liner may cause a strong detrimental effect on the overall liner performance. A criterion for the onset of instability consists, roughly speaking, in that the effective gravity acceleration (in the rest-frame of the fluid) has the sign opposite to the density gradient. Accordingly, the instability can develop during the run-in phase (where it is predominantly localized near the outer surface of the liner) and near the turn-around point (where the inner surface becomes unstable).

For the recently re-assessed scheme of a compact pulsed fusion reactor with imploding liner [1], just this latter phase of instability is of most importance: it determines the behavior of the interface between a hot magnetized adiabatically compressed plasma and a relatively cold and dense liner. We will focus our present study on the processes near the turn-around point (though some effects occurring during the earlier phase of the implosion will also be briefly discussed in the final section of this paper). For a survey of phenomena occurring during the run-in phase (for non-rotating liners) we refer the reader to a recent paper [2].

It has been noted many years ago that liner rotation has a stabilizing effect on the Rayleigh-Taylor instability near stagnation point (see, e.g., [3,4]). Stabilizing contribution comes from the centrifugal force which is directed oppositely to the effective gravity force. To reach a strong stabilizing effect, one has to spend approximately half of the implosion energy on the liner rotation. This is a considerable energy penalty. The pay-off consists in that the inter-penetration (mix) of the liner and the fuel gets considerably slowed down, so that the overall energy performance may still be better than for the non-rotating liner.

The concept of the centrifugal stabilization has been recently revisited in paper [5], where the authors suggested using a cusp magnetic field to create an azimuthal torque which would appear because of the interaction of the z-component of the current and the r-component of the magnetic field.

In the present study, we study a very different technique which allows the spin up of the liner in the course of its implosion and the creation of azimuthal and axial shear flows at any desired depth of the liner (this technique has been recently suggested in conjunction with ablative implosion of the ICF pellets [6]). We emphasize that, if necessary, this technique allows one to excite not a uniform liner rotation but shear flow embedded in the liner structure. Preliminary analysis presented in paper [6] shows that the shear flow can partially stabilize the Rayleigh-Taylor instability and decrease the rate of mixing. In this latter case we assume that conditions are such that the liner behaves like a fluid and elastic forces are insignificant.

We have in mind metal liners with initial radius of order of 1 cm and initial thickness between 0.1 and 0.5 mm, suitable for adiabatic compression of closed-field-line plasma configurations (see Ref. [1] for details; the near-term applications of this system include pulsed X-ray and neutron sources, [1]).

Our present paper is not intended to present a comprehensive analysis of extremely rich physics related to the generation and evolution of liner rotation and shear flows. We are simply going to identify some key issues and describe an overall "morphology" of possible experiments.

## 2. Generation of rotation and shear flow

**2.1 Surface ablation.** This technique is based on generating an ablative torque on the liner surface. The torque can be produced by using a liner whose surface contains some fine east-west asymmetric structures (Fig.1). Ablation of these structures caused either by the thermal skin explosion or by intense laser illumination of the liner surface will produce the desired torque. As the use of the auxiliary laser is probably too demanding from the technical viewpoint (though more straightforward with regard to the physics involved), we discuss only the evaporation of the liner material caused by the Joule heating of the skin layer.

If the height of the surface structures is less than the skin-depth, then the initial motion of the evaporated material will not be affected by magnetic forces. The ablated material will create a halo and will impart the azimuthal momentum to the underlying structures of the liner. At the

<sup>1</sup> On leave from Budker Institute of Nuclear Physics, Novosibirsk 630090, Russia

early phase of the discharge, when the liner material still maintains some structural strength, the rotational motion will be transferred to the deeper layers of the liner with a sound speed of shear acoustic waves, 3-4 km/s for most of the materials. For the liner thickness of 0.1 mm, this corresponds to the propagation time of order of 30 ns. If the liner gets liquefied earlier than that, then the azimuthal momentum transport through the liner thickness can occur only via viscous forces. To achieve the best possible efficiency of the spin-up, one should use the coatings with a relatively low sublimation energy.

The evaporated material, obviously, has an angular momentum opposite to that of the liner and much higher initial azimuthal velocity (because of a lower mass). There are some reasons to believe that the halo will expand across the magnetic field because of the development of various microinstabilities [7]. In some scenarios, a low conductivity of the ablated material can be caused by its low ionization degree. For these reasons we will simply assume that, after having set the liner into the initial rotation, the halo does not play any active role in the further implosion.

In the course of implosion, rotation gets accelerated because of the angular momentum conservation. For the radial convergence  $C$ , the rotational energy gets increased by a factor of  $C^2$ . Therefore, if one is interested in the situation when the final rotation energy is comparable with the total mechanical energy, the initial rotational energy can be quite modest,  $\sim C^{-2}$  of the total mechanical energy ( $\sim 1\%$  in a hypothetical case of  $C=10$ ).

2.2 Interaction of the compression wave with embedded structures. The second technique is applicable in case of faster rise-time of the compressing magnetic field, when a non-linear compression wave or a shock-wave propagating through the liner material is formed. By using a liner with a structure of small tilted tiles [6] situated at some depth of the liner material, one can then expect that shear flow will be excited by the interaction of the compression wave with the structure. The tiles should have density somewhat different from that of the surrounding material. Fig.2 qualitatively illustrates the physics involved. Here we assume that the substance is already in a liquid state so that elastic forces do not play any role.

To get a somewhat more quantitative understanding of the phenomena involved, we considered a simple model of the interaction of a small-amplitude acoustic wave with a substance with small density variations of the type shown in Fig.2. The smallness of both amplitudes allows one to use the perturbation technique to find scattered acoustic wave. Equation describing generation of this wave can be presented as:

$$\frac{\partial^2 \tilde{\rho}}{\partial t^2} - s^2 \nabla^2 \tilde{\rho} = s^2 \nabla^2 \left( \int_{-\infty}^t dt' \nabla \cdot (\mathbf{v}_a \delta \rho) \right) \quad (1)$$

where  $\mathbf{v}_a$  is velocity perturbation in the incident acoustic wave,  $s$  is sound speed in a uniform gas,  $\delta \rho$  is the pre-existing left-right asymmetric density perturbation (which corresponds to the "tiles" shown in Fig.2) and  $\tilde{\rho}$  is a density perturbation in the "scattered" acoustic wave. When deriving Eq.(1) we assumed that density non-uniformities are initially (before arrival of the incident wave) in a pressure equilibrium with the surrounding medium and that the adiabatic index does not vary. What makes density vary, is the variation of the molecular weight (or, in some cases, temperature).

Detailed analysis of Eq.(1) as well as its generalization to the nonlinear incident wave will be presented elsewhere. Here we restrict ourselves to a few qualitative comments. First, the structures should not be too fine: the amplitude of the scattered wave decreases significantly if the scale-length of the structure becomes smaller than the spatial scale-length of the incident wave. This observation stems from the fact that, for a monochromatic incident wave, there cannot be scattered waves with the tangential wave-number exceeding the normal wave-number of the incident wave. Second, the amplitude of the scattered wave scales linearly with the amplitude of density non-uniformities. This means that the energy density in the scattered wave is quadratic in the amplitude of the density perturbations. The momentum density in the acoustic wave is proportional to the energy density [8] and, whence, also quadratic in density non-uniformities. Accordingly, we conclude that the average velocity which will be acquired by the layer where embedded structure is situated, scales as  $v_a (\delta \rho / \rho_0)^2$ . For strong enough incident wave, with  $v_a \sim s$ , the average flow velocity is  $s (\delta \rho / \rho_0)^2$ .

Angular momentum conservation arguments are applicable to this "submerged jet" (unless viscosity is very high). Therefore, implosion will cause an enhancement of the shear flow in very much the same way as it causes acceleration of the overall rotation.

Superimposed on this average flow, will be fine vortices appearing in the place of initial non-uniformities. These vortices will be stretched by the average shear flow and dissipated by viscosity (molecular or turbulent).



2.3 Generation of shear flow at the interface of two colliding liners. The third technique relies on the use of a two-shell liner, with the shells initially separated in the radial direction and with appropriate structures created at the inner surface of the outer shell and/or on the outer surface of the inner shell (Fig.3). When shells collide, a shear flow should be generated at an interface.

### 3. Effect of shear flow on Rayleigh-Taylor stability

The presence of shear flow at the interface between fluids of different density should have a stabilizing effect on the Rayleigh-Taylor perturbations: at high enough velocity shear, stretching of the perturbations in the parallel direction occurs so fast that the characteristic "spike" can never appear. A simple illustration of the interplay of shear flow and Rayleigh-Taylor instability is presented in Fig.4 that depicts a linear growth rate in the following system: a slab of the incompressible fluid with a uniform density and a linear velocity profile (zero at the bottom and  $v$  at the top of the slab), supported from below by a fluid with a very small density. In the example shown, a broad range of the wave numbers becomes stable at large enough velocity shear. Other interesting examples related to the effect of shear flow on gravitational instability can be found in book [9].

Of course, shear flow may serve as a source of its own, Kelvin-Helmholtz, instability and Fig.4 clearly shows this instability at small wave-numbers. However, according to a so called "Rayleigh theorem" [8], there exist stable velocity profiles, the ones that do not contain inflection point in the velocity distribution. "Rayleigh theorem" in its standard form pertains to the flow between two rigid walls but one can show that flow with one free surface can also be stable [10]. Whether the flow with two free surfaces can be ever stable, is an open question. However, even if Kelvin-Helmholtz instability is ubiquitous, it is quite possible that the mix caused by its development will occur slower than that caused by the Rayleigh-Taylor instability of the comparable growth-rate. This conjecture is based on the observation that Kelvin-Helmholtz instability does not produce fast growing "spikes" which are of prime concern in the mix caused by the Rayleigh-Taylor instability.

It has recently been shown that shear in *axial* velocity can have a favorable influence on the stability of an equilibrium diffuse pinch [11].

### 4. Summary

We have shown that there exist several techniques that can set the liner into rotation and/or excite an embedded shear flow ( $d\omega/dr \neq 0$ ) at any desired depth of the liner material. A common element of all these techniques is the use of properly chosen East-West asymmetric structures, situated either on the liner surface or embedded in the shell. Both rotation and shear flow get enhanced in the course of the liner implosion because of the angular momentum conservation. Initial azimuthally asymmetric structures get very quickly smeared out by the shear flow they have produced (or get blown-off from the surface); this decreases their unfavorable effect as seeds of possible instabilities.

As was shown in previous works (see, e.g. [3]), fast enough rotation should stabilize Rayleigh-Taylor instability near the turn-around point. We speculate (partly following the arguments of paper [6]) that the shear flow can also have a stabilizing effect on the stability of the interface. Indeed, specific model presented in our paper shows that the presence of a strong enough shear causes stabilization of a broad class of Rayleigh-Taylor perturbations.

Potentially interesting effects can occur if a modest shear in the  $z$ -direction is created ( $d\omega/dz \neq 0$ ). This type of shear should stabilize filamentation-type instabilities which sometimes appear at the early phase of the implosion.

Surface structures can be manufactured in a straightforward way, on the basis of thin-film technology [12]. Manufacturing of fine structures in the bulk of the liners 0.1-0.5 mm thick is a challenging problem but it does not seem to be beyond the limits of the modern technology. All in all, the use of the left-right asymmetric structure for generation of rotation and shear flow is an interesting new option for improvement of the quality of the liner implosions.

### Acknowledgments

One of the authors (D.R.) is grateful to Dr. R. Schock for his support. This work was performed under the auspices of the U.S. Department of Energy by the Lawrence Livermore National Laboratory under the contract No W-7405-ENG-48.

## References

- [1] R.P. Drake, J.H. Hammer, C. W. Hartman, L.J. Perkins, D.D. Ryutov. LLNL report UCRL-JC-120088, 1995; to be published in "Fusion Technology" (1996)
- [2] J.H. Hammer, J.L. Eddleman, P.T. Springler, M. Tabak, A. Toor, K.L. Wong, G.B. Zimmerman. Phys. Plasmas, **3**, 2063 (1996)
- [3] A. Barcion, D.L. Book, A.L. Cooper. Phys. Fluids, **17**, 1707 (1974)
- [4] P.J. Turchi, A.L. Cooper, R. Ford, D.J. Jenkins. Phys. Rev. Lett., **36**, 1546 (1976)
- [5] N. Rostoker, G.G. Peterson, H. Tashiri. Comments on Plasma Physics and Controlled Fusion. **16**, 129 (1995)
- [6] D.E. Baldwin, D.D. Ryutov. Comments on Plasma Phys. and Contr. Fusion, **17**, 1 (1995)
- [7] P.V. Sasorov. Sov. J. Plasma Phys., **17**, 874 (1991)
- [8] L.D. Landau, E.M. Lifshits. "Fluid Mechanics". Pergamon Press, 1987.
- [9] S. Chandrasekhar. "Hydrodynamic and Hydromagnetic Stability". Clarendon Press (1961)
- [10] D.D. Ryutov, in preparation.
- [11] U. Shumlak, C.W. Hartman. Phys. Rev. Lett., **75**, 3285 (1995).
- [12] "Handbook of Thin Film Technology", NY, McGraw Hill (1970)



Fig.1 Shown is a part of the outer surface of the liner; O is the liner axis. The grooves on the liner surface are parallel to the liner axis. It is assumed that the "East" and "West" sides of the grooves are coated with materials with a different density so that the ablation pressure is different on two sides and the azimuthal torque appears. The height of the structures is grossly exaggerated.

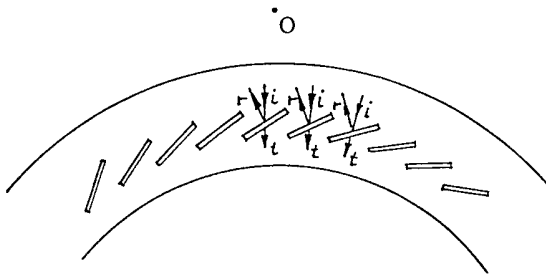


Fig.2 Interaction of a compression wave with an embedded structure. Shown is a part of the equatorial cross-section of the liner. The embedded structures are stretched along the axis. When an incident compression wave ("i" wave the Figure) interacts with the tiles, it gets reflected predominantly in one azimuthal direction, thereby imparting an azimuthal momentum to the region containing the tiles. The rest of the shell acquires an azimuthal momentum in the opposite direction and shear flow sets up. The presence of the shear flow causes a quick mixing-up of the embedded structures and the surrounded substance, eliminating any appreciable azimuthal density non-uniformities.

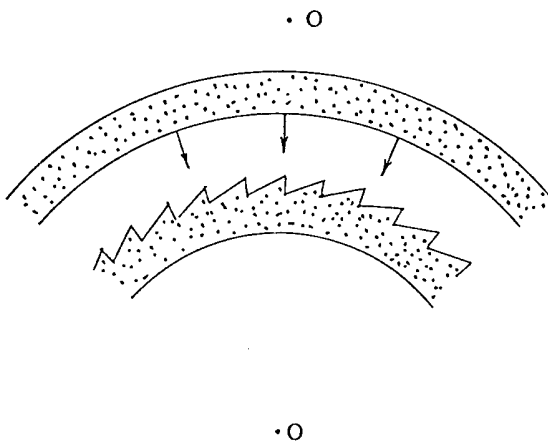


Fig.3 Generation of the shear flow at the interface of two colliding shells. This figure depicts the situation when the left-right asymmetric structure is present only at the surface of the inner liner which is initially at rest.

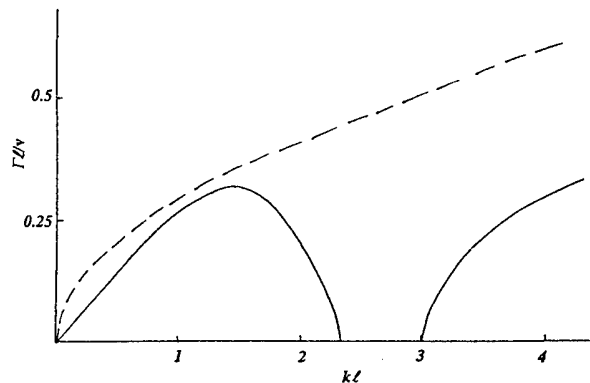


Fig.4 Growth-rate  $\Gamma$  in the units  $v/\ell$ . The slab thickness is  $\ell$ , the gravity acceleration  $g$  is such that  $v^2=12g\ell$ . At small wave-numbers  $k$ , the instability is of Kelvin-Helmholtz type. When the flow is absent, the growth-rate is  $(kg)^{1/2}$  for all  $k$ 's (dashed line, for  $g=v^2/12\ell$ ).

## FIRST RESULTS ON THE GOL-3-II FACILITY

M.A.Agafonov, A.V.Arzhannikov, V.T.Astrelin, V.B.Bobylev, A.V.Burdakov,  
 M.N.Chagin, P.V.Denisenko, Yu.I.Deulin, A.D.Khilchenko, V.S.Koidan,  
 V.V.Konyukhov, A.N.Kvashnin, O.A.Lee, A.G.Makarov, K.I.Mekler, P.I.Melnikov,  
 V.S.Nikolaev, S.S.Perin, V.V.Postupaev, R.V.Razilov, A.F.Rovenskih, E.P.Semenov,  
 S.L.Sinitsky, A.V.Tarasov, S.V.Vdovin, R.P.Zotkin

*SSC RF Budker Institute of Nuclear Physics, 630090, Novosibirsk, Russia*

## ABSTRACT

First results of the GOL-3-II facility are presented. Transport of the high-power microsecond electron beam through the 12 m turbulent plasma column, beam relaxation in the plasma and plasma heating are investigated.

## 1. INTRODUCTION

The GOL-3 facility is intended for a study of interaction of a high-power microsecond relativistic electron beam with a plasma mainly applied to the problem of the fast heating and confinement of a dense plasma ( $10^{15}$  -  $10^{17}$  cm<sup>-3</sup>) in a long open trap. The first stage of this device (see [1]) with a 7 m long plasma has been operated about six years at a beam energy content of up to 100 kJ. Main experimental results obtained for this period on GOL-3-I are the following:

- High level (up to 25-30%) of the collisionless energy losses of the microsecond electron beam in a plasma with a  $\sim 10^{15}$  cm<sup>-3</sup> density was obtained and an electron temperature of  $\sim 1$  keV was achieved [2,3].
- At an intense interaction of an electron beam with a plasma, its longitudinal electron thermal conductivity was found to be in 2-3 orders of magnitude lower than classic one [3,4].
- Feasibility of heating a dense ( $10^{16}$  -  $10^{17}$  cm<sup>-3</sup>) plasma with an electron beam by the "two-stage" scheme was demonstrated [5].
- Experiments on the interaction of an electron-hot plasma with various solid targets were carried out. This is important for the choice of ITER divertor material. The "target" plasma and the surface erosion which strongly dependent on the incident energy density were studied [6].
- First experiments on generation of a high-power ultraviolet "flash" from the dense plasma bunch at its various elemental compositions have been done [7].

In September, 1995 all experiments on the GOL-3-I device have been completed. The magnetic and plasma systems were disconnected from the beam generator U-3 (used up to this time) and disassembled. In a few months new magnetic, plasma and vacuum systems of the device have been assembled. Pair of new capacitor storage units for feeding the solenoid have been put into operation. A more capable beam generator U-2 was matched to the upgraded device. Thus, the second stage of the GOL-3 device has been assembled and got the name GOL-3-II. The first shots have been done in the end of 1995. This device is the next step in the study of the interaction of high-power electron beams with a plasma being carried out at the Budker Institute, Novosibirsk [8].

## 2. GOL-3-II FACILITY

Schematic of the device is given in Fig.1. The device consists of the beam generator U-2, plasma chamber, fore-plasma creating unit combined with an exit beam receiver, solenoid supplied by a 15 MJ capacitor storage.

One of the key improvements of the facility is a substantial increase in the energy content of the electron beam injected into the plasma. The beam generator U-2 enables one to obtain the beam with an energy content of up to 0.3 MJ. One-megavolt ten-microsecond pulse is produced by LC-generator and applied to the ribbon magnetically insulated diode [9]. The relativistic electron beam ( $\gamma \sim 3$ ) with the cross section of  $3.5 \times 140$  cm and current of up to 50 kA is produced by the fibrous graphite cathode and goes out through the anode slit into the vacuum slit channel of 1 m length with a guiding magnetic field of  $\sim 0.3$  T. Next to this channel is the beam shape transformer where the beam changes its transverse cross section from the ribbon to the round one according to the magnetic force lines. Then the beam is compressed in a rising up to 4.5 T magnetic field and injected into the plasma through the graphite limiter with 5.5 cm aperture and thin foil. The waveforms of diode voltage and beam current after the limiter are given in Fig.2.

Another essential change in the new device is an extension of a plasma column of the GOL-3-II up to 12 m compared with 7 m of the first stage of the device. New foil replacement system enables up to 5 sequential shots to be done. The plasma chamber is a metal pipe made of stainless steel with the inside built-in limiters and in-chamber diagnostics - diamagnetic loops and Rogowsky coils. The chamber is placed inside the solenoid with mirrors spaced by 12.2 m. The solenoid is powered by the capacitor storage whose energy content was increased from 10 to 15 MJ. This provides the magnetic field in the uniform part of solenoid of up to 5 T, and in mirrors of up to 10 T (these values were 4.5 T and 9 T for the first experiments). Behind the exit mirror there is the fore-plasma production unit and beam receiver. With the use of this system a fore-plasma column of a  $\sim 10^{15}$  cm $^{-3}$  density was obtained in a metal chamber.

In the experiments both the beam and plasma parameters are registered. The beam characteristics are measured with electrotechnical methods (voltages and currents at different points). The plasma pressure  $nT$  is measured by diamagnetic loops. The

### GOL-3-II

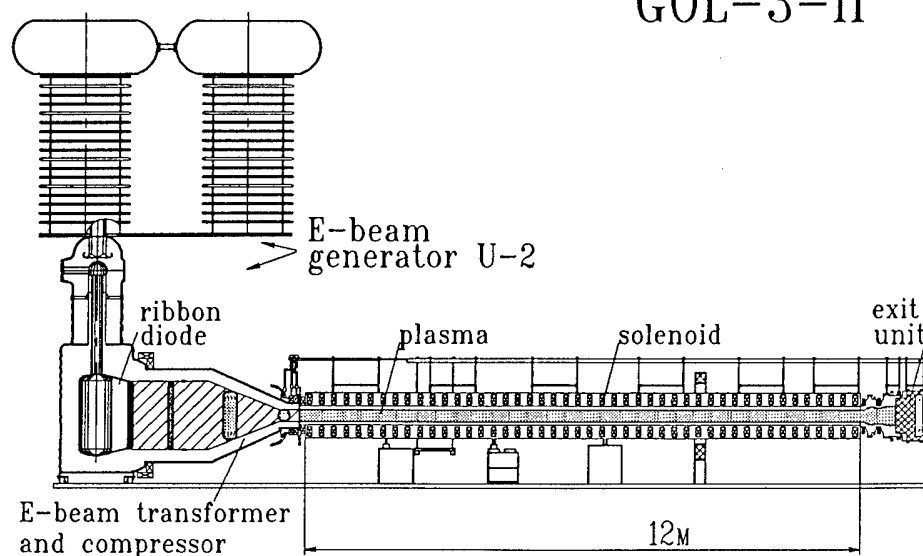


Fig.1 Schematic of the GOL-3-II device

density and temperature at 1.8 m distance from the input mirror is determined with a 90°-scattering of a ruby laser beam. At a 4 m distance from the input a 8° and 90° Thomson scattering with 2ω-Nd laser is placed. The spectral system based on the polychromator and framed photodiode array enables the registration of the plasma spectrum with high spectral (0.03 nm) and temporal (<100 ns) resolution. By the H<sub>α</sub> line profile and its shift it is possible to determine an electron density, ion temperature and velocity of plasma motion. An electrostatic analyzer of charge exchange particles is used for finding out characteristics of the plasma ion component. The analyzers of beam energy spectrum and plasma fast electrons are placed behind the output unit.

### 3. BEAM TRANSPORT THROUGH A 12 METER PLASMA COLUMN

During the injection of a high-power electron beam into a plasma of  $\sim 10^{15} \text{ cm}^{-3}$  density the beam-plasma collective interaction is observed. As a result, there is a high level of plasma turbulence in a plasma. This circumstance leads to the specificity of beam transport in such a system. The presence of oscillations causes the change of plasma properties compared to the classic ones. As is shown in the GOL-3-I experiments [3,4], an effective collision frequency of electrons changes substantially. In particular, this leads to a decrease in a plasma conductivity by a factor of 100-1000. Therefore, even at quite high plasma temperature (0.2-1 keV) its conductivity is still insufficient for the beam current compensation. In addition, increase in the effective frequency of collisions can lead to an abnormally high transverse diffusion of beam electrons.

At the first stage of the GOL-3 device (7 m long) the net beam current achieved 10-20 kA at the injection current of 30-40 kA. With an increase in the system length up to 12 m on the GOL-3-II device one could expect the Kruskal-Shafranov macroscopic

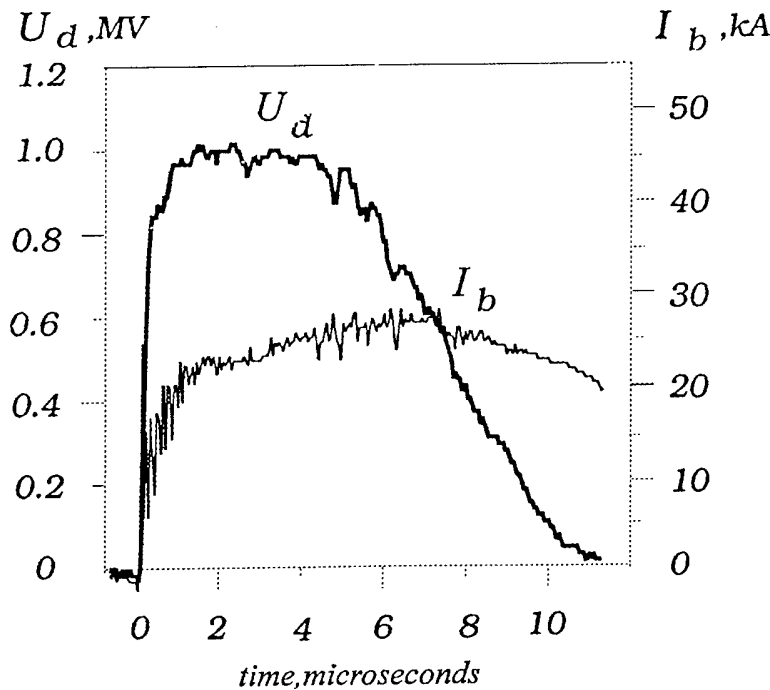


Fig.2 Electron beam parameters.  $U_d$  - diode voltage,  $I_b$  - input beam current. The energy content is 180 kJ.

instability of the beam-plasma system caused by such currents. Actually, according to [10] the critical current is determined by:

$$J_{crit} = \frac{cB\pi a^2 b^2}{L(b^2 - a^2)},$$

where  $a$  is the beam radius,  $b$  is a radius of a conducting wall,  $B$  is the axial magnetic field,  $L$  is the system length.

As is seen, with a 10-20 kA current in the 12 m system the Kruskal-Safranov instability can develop and the beam can be thrown to the wall of chamber or limiters as a result. In order to avoid this quite undesirable case practically complete beam current compensation is required.

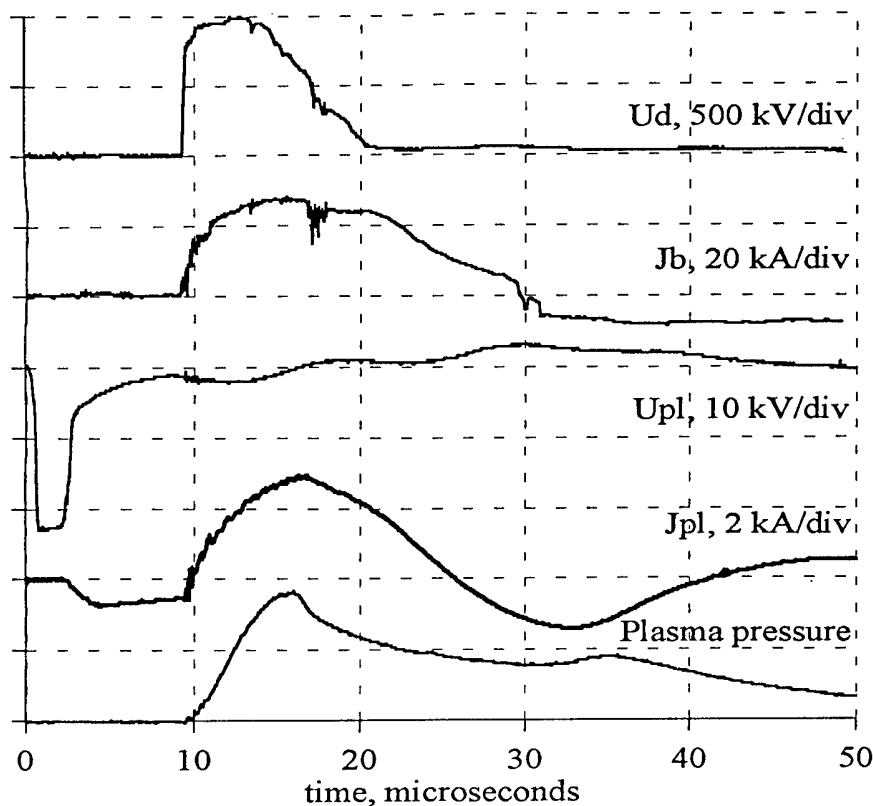


Fig.3 Typical waveforms:  $U_{pl}$  - voltage on the linear discharge,  $J_{pl}$  - total current in plasma. Plasma pressure - waveform of diamagnetic signal at 4.74 m from the input mirror.

better compensation of the beam current. Some typical waveforms for the case of good compensation are shown in Fig.3. Prior to the beam injection the voltage  $U_{pl}$  is applied to the system for producing the foreplasma. In 3  $\mu$ s after applying the voltage the breakdown of the gas occurs through the whole system length and the current  $J_{pl}$  starts to flow along the plasma. Few microseconds later the electron beam injection begins. It is seen that the input beam current  $J_b$  reaches the amplitude of 30 kA. The net current in the plasma decreases first, reaches zero, and finally changes its direction following the initial beam current. In the case described, net current does not exceed 3 kA, and the substantial macroscopic beam motion across the magnetic field is not observed. It should be mentioned that during the beam injection into a gas net current exceeds substantially this value and the beam displacements are observed at the device output.

Another important factor for the beam transport is the electron transverse diffusion occurred in a plasma with a high level of turbulence. This process is not yet studied in detail but it is probably manifested in the experiment by an increase in the transverse cross section of the electron beam at its propagation in a plasma.

#### 4. PLASMA HEATING

In the first GOL-3-II experiments the beam was injected into the plasma with the density ranging from  $5 \cdot 10^{14}$  to  $2 \cdot 10^{15}$  cm<sup>-3</sup> for different shots. According to scalings established at GOL-3-I, an energy content in a plasma column grows linearly with an increase in the energy content of a beam [3]. The main mechanism of an energy loss of the heated plasma bulk (the Maxwellian fraction) is the longitudinal electron thermal conductivity. In this case, the cooling characteristic time can be estimated as follows:

$$\tau = L^2 / \chi,$$

where  $L$  is the plasma column length,  $\chi$  is a temperature conductivity coefficient.

Following this one can expect that on the new GOL-3-II device the total energy content in the plasma will 2-3 times increase according to an increase in the beam energy content. Energetic lifetime of the plasma will grow approximately 3-fold.

The first experiments have shown that the given scalings are met. Fig.4 shows the comparison of the plasma energy content profiles for the experiments on the first stage of the GOL-3 device and that for the first experiments on the GOL-3-II device. It is seen that with an increase of the beam energy content the energy store increases too, and the character of the plasma energy content distribution over the length is conserved.

Preliminary estimates of a plasma electron temperature from Thomson scattering data have shown that the temperature of a plasma with density  $(0.3-1) \cdot 10^{15} \text{ cm}^{-3}$  exceeds 0.5-1 keV. The correct comparison of the laser and diamagnetic measurements is not yet performed but up to an accuracy of factor 2 one can say that similarly to the first stage of the device, the diamagnetic signals are mainly determined by the Maxwellian fraction of heated plasma electrons.

The heated electrons have enough time to transmit a fraction of their energy to plasma ions. For our typical parameters the ions should be heated by binary collisions up to 30-50 eV. This temperature was measured by the Doppler broadening of the  $H_\alpha$  line.

## 5. PROSPECTS OF THE GOL-3-II FACILITY

The first experimental results obtained on the GOL-3-II device are the good base for the successful development of the GOL-3 program. By present, the capability of the beam generator U-2 is not yet fully applied. An increase in the energy content of the beam injected into the plasma in a factor of 1.5-2 is possible. This should lead to the corresponding growth of the energy content of the plasma. Nevertheless with already available parameters of the injected beam the following experiments can be conducted.

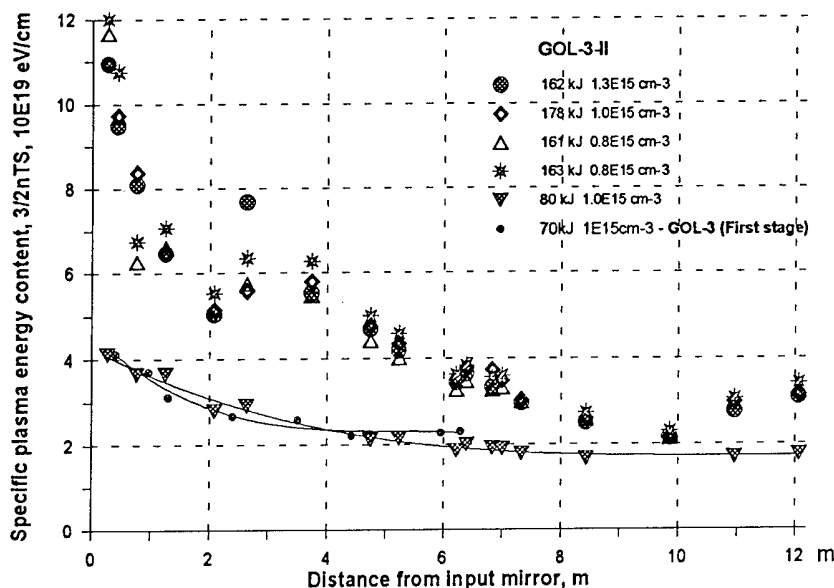


Fig.4 Distribution of specific plasma energy content over the device length at first stage of GOL-3 and at GOL-3-II.

First of all, these are experiments on a "two-stage" heating of a dense plasma bunches (see [5]). In this case, the bunch of a dense plasma ( $\sim 10^{16}-10^{17} \text{ cm}^{-3}$ ) is produced in the plasma chamber and the electrons heated in the region with a  $\sim 10^{15} \text{ cm}^{-3}$  density should transfer their energy to the bunch. Such experiments have been started on the first stage of the device. It was shown that the energy content of the dense bunch is  $\sim 10\%$  of the beam

energy content. These experiments are planned to be continued at a new energy level on the GOL-3-II device.

Further, of special interest are the experiments with two bunches being heated and then collided. At the place of collision, the ion temperature could reach sub-keV range. Then, the obtained hot plasma bunch could be confined in a local "magnetic pit", i.e. in the short part of solenoid with weakened magnetic field. In this case it is possible to obtain a plasma with local  $\beta > 1$  and to study a "wall" confinement of such a plasma.

Finally, existing magnetic system enables us to do inexpensive reconstruction of the GOL-3-II into a multimirror trap. The multimirror trap enables one to obtain a plasma with the density of  $\sim 10^{16}$ - $10^{17}$  cm<sup>-3</sup>, temperature  $\sim 1$  keV, lifetime  $\sim 0.1$  ms. The experiments with the multimirror confinement of hot plasma is one of the most important goals of the GOL-3 program.

## 6. CONCLUSION

The first GOL-3-II experiments on injection of 8  $\mu$ s, 200 kJ electron beam into a plasma of 12 m length were carried out. The possibility of macroscopically stable beam transport through the 12 m long plasma column has shown under the conditions of the developed plasma microturbulence. As a result of collective interaction of the beam with the plasma the effective heating of the plasma with density  $\sim 10^{15}$  cm<sup>-3</sup> is observed. Putting the facility into operation opens up a prospect to carry out the experiments with dense ( $\sim 10^{16}$ - $10^{17}$  cm<sup>-3</sup>) and hot ( $\sim 1$  keV) plasma in the multimirror trap.

This work was carried out under financial support of Ministry of Science of Russia at the GOL-3 facility.

## REFERENCES

- [1] Arzhannikov A.V., Burdakov A.V., Kapitonov V.A. et al. Plasma Physics and Contr. Fusion (Proc. 15<sup>th</sup> Europ. Conf., Dubrovnik, 1988), 30, p.1571.
- [2] Arzhannikov A.V., Burdakov A.V., Chikunov V.V. et al. Proc. 8<sup>th</sup> Intern. Conf. on High-Power Particle Beams, Novosibirsk, 1990, vol.1, p.14.
- [3] Burdakov A.V., Voropaev S.G., Koidan V.S. et al. ZhETP, 1996, vol. 109, N6, p.1 - in Russian.
- [4] Burdakov A.V., Postupaev V.V. Preprint INP 92-9, Novosibirsk, 1992 - in Russian.
- [5] Burdakov A.V., Chikunov V.V., Huber A.F. et al. Proc. 9<sup>th</sup> Intern. Conf. on High-Power Particle Beams, Washington, 1992, vol.2, p.1049.
- [6] Burdakov A.V., Filippov V.V., Koidan V.S. et al. J. Nucl. Mater., 1994, vol.212-215, p.1345.
- [7] Astrelin V.T., Burdakov A.V., Denisenko P.V. et al. Optika Atmosfery i Okeana, 1996, 9, No.2, p. 217 - in Russian.
- [8] Koidan V.S. Proc. XXII Intern. Conf. on Phenomena in Ionized Gases, Hoboken NJ, 1995, p.192.
- [9] Arzhannikov A.V., Bobylev V.B., Nikolaev V.S. et al. Proc. 10<sup>th</sup> Intern. Conf. on High-Power Particle Beams, San Diego, 1994, vol.1, p.136.
- [10] Lansky I.M., Shchetnikov A.I. Preprint INP 89-85, Novosibirsk, 1989 - in Russian.



## Multi-Kiloampere, Electron-Beam Generation using Metal Photo-Cathodes Driven by ArF and KrF Lasers\*

Randolph L. Carlson, Steven A. Moya, Rae N. Ridlon, Gerald J. Seitz, and Roger P. Shurter

*Los Alamos National Laboratory, Los Alamos, New Mexico, 87545, USA*

### Abstract

An electron-beam-pumped laser operating at ArF (193 nm) or KrF (248 nm) producing 35 MW (3.5 J in 100 ns) has been used to illuminate a micro-machined aluminum cathode. The cathode was pulsed to 2.75 MV at fields of 185 kV/cm (15-cm AK gap) using REX [1,2] (a 4-MV, 5-kA, 85-ns) pulsed-diode machine. The extracted current versus incident laser power (the quantum efficiency) was measured for KrF at  $5 \times 10^{-5}$  and for ArF which was significantly higher at  $1 \times 10^{-3}$ . Current densities of 100 A/cm<sup>2</sup> and total currents of 2 kA have been achieved, the latter by increasing the cathode area in proportion to the laser power.

### Introduction

A laser-driven photo-injector was first demonstrated [3] in 1985; afterwards, others [4-9] used available high power ArF and KrF lasers to pursue higher currents from the irradiation of simple metals via the photoelectric effect. These technologies presently provide the only known methods to reduce significantly the cathode source temperature and therefore, the emittance of present and future multi-kA injectors. Our present work is significant in that the cathode exists in the presence of outgassing materials with a background vacuum pressure in the mid  $10^{-6}$  torr region and 100-ns-long electron beams of several kA have been produced.

The quantum efficiency, QE, is defined in this paper as:  $QE = (I/P)(\text{eV/photon})$  where I is the emitted beam current, P is the laser power incident on the cathode, and the energy/photon is 5- and 6.4-eV for KrF and ArF, respectively. A companion paper [10] reports the results of small-scale, short-pulse ArF studies to further address the relative quantum efficiencies of other candidate metals, their preparation, and the effects of vacuum and mono-layer contaminants.

Table 1 lists typical properties of four materials suitable for a cathode [11,12]; micro-machined Aluminum alloy 6061-T6 was chosen for this work based upon our previous results [6-9]. The potential for laser damage to these materials was assessed by a calculation; the surface temperature rise is shown in Fig. 1 for an absorbed laser intensity, F, of 1 MW/cm<sup>2</sup>. The experimental laser pulse is shown overlaid with a trapezoidal fit (45-ns rise, 75-ns flattop, 125-ns fall) used to determine the temperature rise. The calculation of the surface temperature, T(z,t), follows the methods of Ready [13] using the parametric integral:

$$T(z,t) = k^{1/2}/(K\pi^{1/2}) \int_0^t \tau^{-1/2} F(t-\tau) \exp(-z^2/4k\tau) d\tau, \text{ which has an analytic solution for a ramp of slope}$$

$F/tp$  at  $z = 0$  given by  $T(0,t) = (4/3K)(F/tp)(k/\pi)^{1/2} t^{3/2}$ . The surface temperature profiles in the plot were obtained by using the ramp solution to make a piecewise trapezoid. Since  $T(0,t)$  is proportional to  $k^{1/2}/K = 1/(\rho C_p K)^{1/2}$  this parameter is also listed in Table 1. Magnesium reaches the highest temperature (220°C); diamond is a factor of four lower at (55°C). Considering the first phase change of diamond, its laser damage threshold could be ~20 times that of magnesium.

\*Work performed under the auspices of the U.S. Department of Energy.

Table 1. Properties of Some Cathode Materials.

	Mg	Al	Cu	Diamond
K (W/cm°C)	1.59	2.37	3.98	23.1
k (cm <sup>2</sup> /sec)	0.90	1.06	1.17	12.7
Cp (J/gm°C)	1.02	0.83	0.38	0.52
$\rho$ (gm/cm <sup>3</sup> )	1.74	2.70	8.96	3.52
$\rho \cdot Cp \cdot K$	2.81	5.31	13.55	42.0
Tmp(°C)	649	660	1083	~3550
WF (eV)	3.68	4.08	4.52	5.50

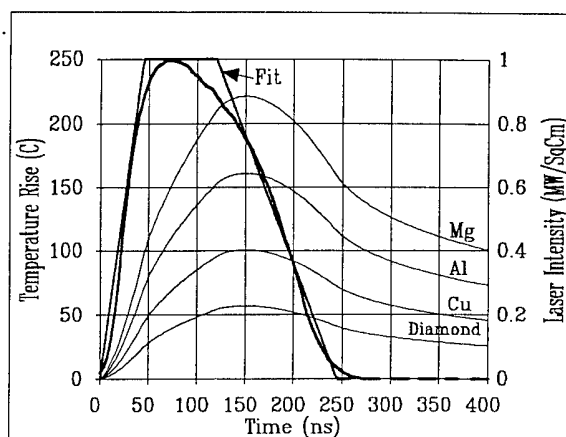


Figure 1. Material Temperature Rise.

### Experimental Test Setup

Figure 2 shows the layout of the REX Facility, E-beam diode head region, excimer laser diode with beam paths, and diagnostics. For QE measurements at normal incidence, the laser beam was directed by a turning mirror to a 20-cm-diam lens ( $f = 415$  cm) and focused through a window and onto the REX cathode. Nitrogen purged beam pipes were used to reduce the appreciable attenuation of ArF due to oxygen. The laser light was monitored by vacuum photodiodes at the source (SAM PD) and cathode (REX PD); a gated photo-multiplier was used to record visible light emission from the cathode. The energy and spatial profile of the beam were recorded at the cathode conjugates by an Energy Monitor (Pyrex based, Scientech Inc., 10-cm absorbing calorimeter) and a Profile Monitor (Star Tech Instruments Inc., BIP-3100/Z6/F100, 10-cm, UV to CCD converter). Beam current was monitored at the anode and at the test section entrance (205 cm from the cathode) with beam size and position adjusted at this location by the anode extraction magnet and x-y steering coils, respectively. The AK gap voltage was monitored by an array of four, integrated E-Dots flush-mounted on the anode face; these were cross-calibrated by an energy spectrometer. Initial beam temperature and QE measurements at 60 degrees incidence used the alternate laser beam path as shown. Beam temperature diagnostics included a Beam and Scintillator Mask as in [1,9] with an optical path to a shielded screen room.

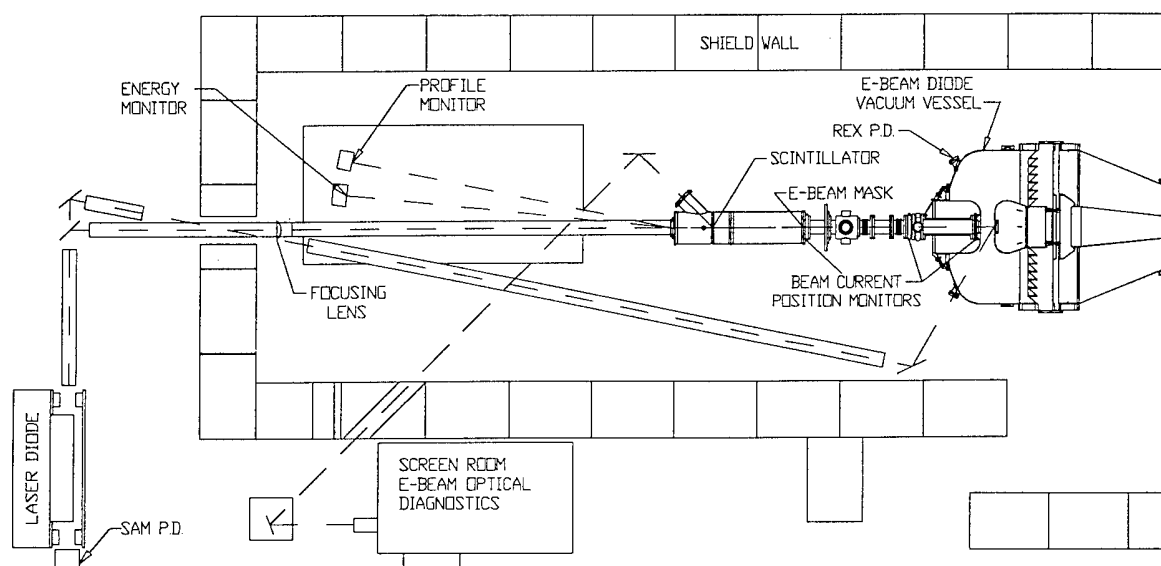


Figure 2. Layout of REX Electron-Beam Facility with Excimer Laser Diode.

## Results

Figure 3 shows the voltage/current (VI) characteristics of a 6.35-cm-diam velvet cathode with the calculated [14] space-charge-limited (SCL) current plotted in Fig. 4. REX produces both a primary and lower secondary pulse, the latter proved useful to study any late time emission from the cathode. As in Ref. 1, a coefficient following the energy scaling of Jory-Trivelpiece was fit to the points in Fig. 4. The current for cathode radius,  $R_c$ , and AK gap,  $d$ , is given by  $C(\gamma^{1/2} - 0.8471)^2(R_c/d)^2$  kA where the fit is  $C = 46.7 - 11.8(R_c) + 1.15(R_c)^2$ . At 2.6 MV this expression over predicts by 10% the current to be 2.45 kA versus the 2.18 kA measured.

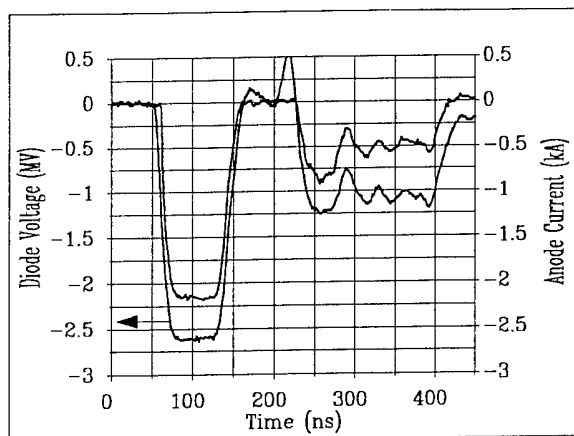


Figure 3. VI Characteristics of 6.35-cm-diam Velvet Cathode at 2.6 MV; AK Gap is 15 cm.

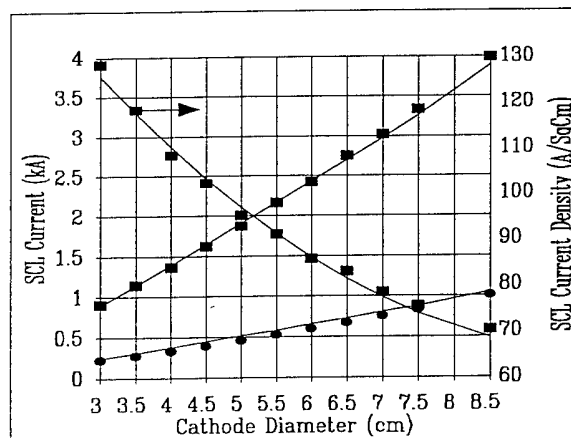


Figure 4. Calculated SCL Current at 2.75 MV (■) and 1.0 MV (●); AK Gap is 15 cm.

Figure 5 shows the anode current, diode voltage, and REX PD for a laser power of 8.3 MW under emission limited (current follows REX PD) conditions. As the laser power was increased to 11.6 MW, the current approached the SCL region (current follows voltage) as in Fig. 6. The laser beam had a  $1/e^2$  diameter of 6.5 cm; however, the effective beam area was smaller due to the 'parabolic' profile of Fig. 7(b). The fit of Fig. 4 gives a 90% SCL current of 1.95 kA for a 5.5-cm-diam cathode in good agreement with the effective beam diameter of 5.3 cm. Figure 7(a) shows the near 'top-hat' beam used for the lower power ( $< 8$  MW) 5.5-cm-diam tests.

The anode current versus laser power for three different Al samples and two beam sizes are plotted in Fig. 8 with QE fits for ArF and KrF. Although the cathodes were diamond turned

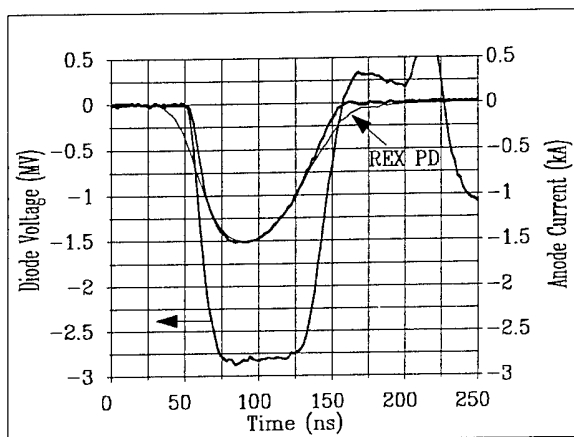


Figure 5. VI of Photo-Cathode at 8.3 MW.

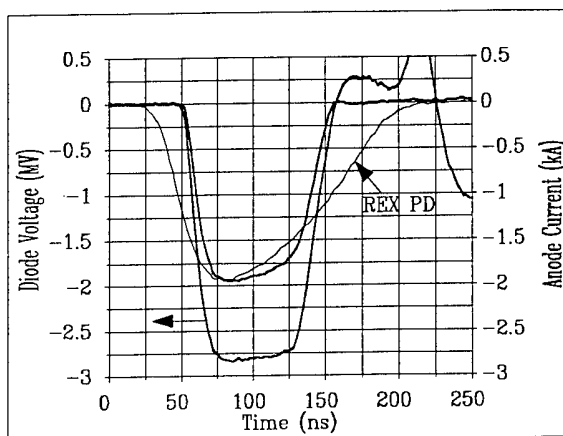


Figure 6. VI of Photo-Cathode at 11.6 MW.

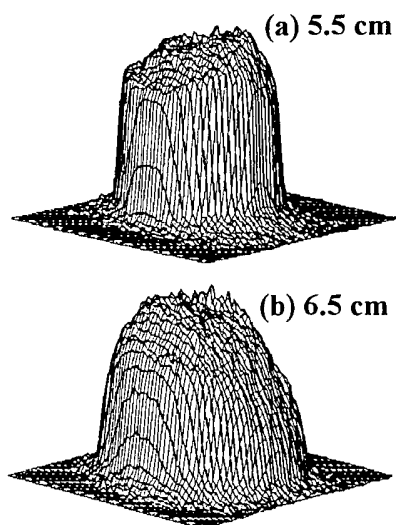


Figure 7. ArF Beam Profiles.

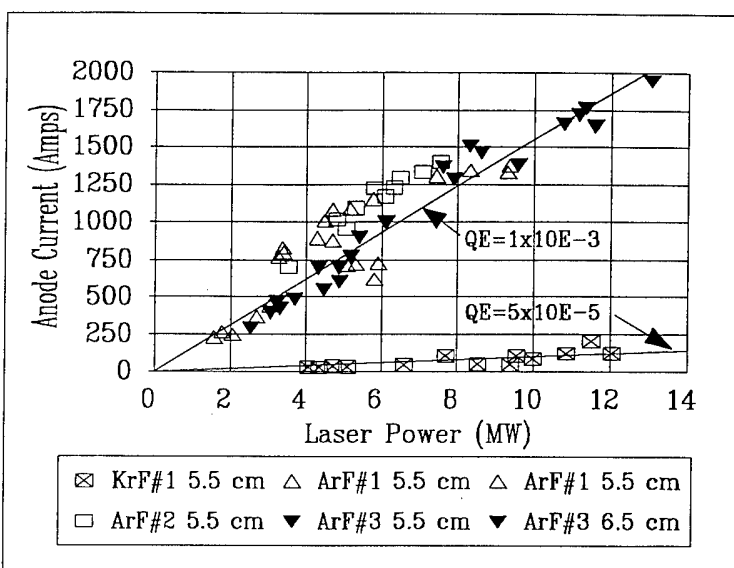


Figure 8. Anode Current vs Laser Power for Al 6061-T6.

mirror surfaces, small ( $\sim 0.1$  to  $1$  mm) damage sites developed (over  $< 1\%$  of the area) after tens of shots. This was not expected at even the highest peak laser intensities ( $\sim 0.85$  MW/cm<sup>2</sup>) since low temperature rises were predicted [Fig. 1]. These damage sites may be at inclusions of magnesium and silicon in the alloy. Initially, post-laser field emission occurred during the second pulse of REX [Fig. 3] but this gradually went away after apparent conditioning of the sample [Figs. 5,6]. Visible light emission tracked the ArF light on the cathode. A limited set of KrF data was taken since QE's  $\sim 5 \times 10^{-5}$  agreed with previous work [7-9] and higher ArF QE's  $\sim 1 \times 10^{-3}$  are of more interest. Figure 8 may suggest higher QE's due to sample conditioning and weak multi-photon processes at higher intensities when near-SCL data points are ignored. Initial results at 60 degrees normal incidence gave  $\sim 35\%$  lower ArF QE's probably due to increased sample reflectivity; the QE might be increased by micro-grooving the cathode surface [12].

In summary, current densities of  $100$  A/cm<sup>2</sup> and total currents of  $2$  kA have been achieved for  $100$ -ns-long ArF laser pulses on aluminum. By increasing the laser power per unit area, space charge limited operation has been demonstrated at  $1.25$  kA. Higher quantum efficiencies might be attained by using  $1:1:1$  diamond films [11] and a diamond-based cathode should also be more robust against laser damage. Beam temperature measurements are underway.

- [1] T.P. Hughes, R.L. Carlson, and D.C. Moir: *J.Appl.Phys.* **68** (6), (1990), pp. 2562-2571.
- [2] R.L. Carlson, et al: *Proc. of the 1991 IEEE Pulsed Power Conference*, pp. 82-85.
- [3] J. Fraser and R. Sheffield: *Nucl.Instr.&Meth.* **A250**, (1986), pp. 71-76.
- [4] S.W. Downey, et al: *Appl.Phys.Lett.* **49** (15), (1986), pp. 911-913.
- [5] J.D. Saunders, T.J. Ringler, et al: *Proc. of the 1987 IEEE Particle Accelerator Conference*, pp. 337-339.
- [6] Thomas J. Ringler: *THESIS*, Naval Postgraduate School, Monterey, CA, September, 1987.
- [7] T.J. Kauppila, et al: *Proc. of the 1987 IEEE Particle Accelerator Conference*, pp. 273-275.
- [8] T.J. Kauppila, et al: *Proc. of the 1989 IEEE Particle Accelerator Conference*, pp. 322-324.
- [9] T.J. Kauppila, R.L. Carlson, et al: *Proc. of the 1991 IEEE Particle Accelerator Conference*, pp. 2107-2109.
- [10] R.P. Shurter, et al: paper at this conference.
- [11] J. Fischer, T. Srinivasan-Rao, T. Tsang, and G. Brandes: *Nucl.Instr.&Meth.* **A340**, (1994), pp. 190-194.
- [12] T. Tanabe, Y. Kawamura, D. Li, and K. Toyoda: *Rev.Sci.Instrum.* **66** (2), (1995), pp. 1010-1014.
- [13] J.F. Ready: "Effects of High Power Laser Radiation," Academic Press, New York, (1971), p. 73, (eqs. 3.8, 3.9).
- [14] PBGUNS Code run by T.P. Hughes of Mission Research Corp., developed by J. Boers: *Proc. of the 1993 IEEE Particle Accelerator Conference*, (1993), pp. 327-332.

## NUMERICAL SIMULATION OF EXPLOSIVE MAGNETIC CUMULATIVE GENERATOR EMG-720

Yu.N. Deryugin, D.I. Zelenskii, I.F. Kazakova, V.I. Kargin, P.V. Mironytchev,  
A.S. Pikar', N.F. Popkov, E.A. Ryaslov, and E.G. Ryzhackova

*Russian Federal Nuclear Center All-Russia Research Institute of Experimental Physics,  
Sarov, Nizhni Novgorod Region, 607190, Russia*

### Abstract

In the present paper there are discussed the methods and results of the numerical simulations used in the development of a helical-coaxial explosive magnetic cumulative generator (EMG) with the stator diameter of up to 720 mm. In the process of designing separate units were numerically modeled, as well as the generator operation with a constant inductive-ohmic load. The 2-D processes of the armature acceleration by the explosion products were modeled as well as those of the formation of the sliding high-current contact between the armature and stator's insulated turns. The problem of the armature integrity in the region of the detonation waves collision was numerically analyzed.

### Introduction

There is a demand on EMG with high current rise velocity, current and energy amplification coefficients and amplitudes. Such EMG's have several advantages: the simplification of further formation of a submicrosecond meraampere pulse, no necessity to connect several generators into a cascade using transformers and cables, reduced requirements to the stored initial energy, which is more expensive as compared to the generator produced energy. Development of the new helical-coaxial generator EMG-720 was aimed at the above mentioned. Partially EMG-720 is described in the present paper. The task of obtaining 100 MA current pulse in 20 nH load with doubling time at the final stage of 20-30  $\mu$ s resulted in the generator design represented schematically in Fig. 1.

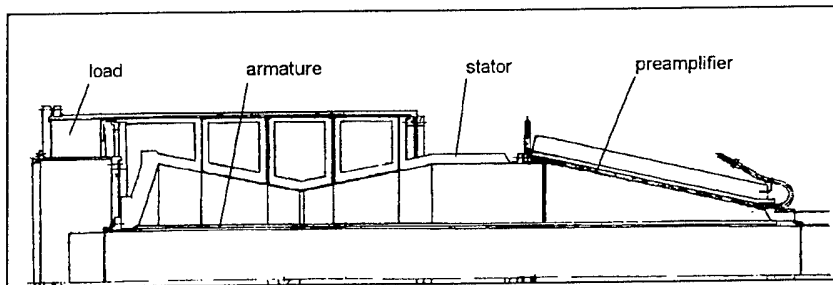


Fig. 1. Schematic of the EMG-720 generator.

The generator stator coaxial part is collected of two cones. The detonation waves propagation in the direction of collision allows to increase the armature active length by a factor of 2 and increase the value of  $dL/dt$  and the load voltage. The armature cones' length is limited by the ultimate tension degree of 2 prior to the formation of cracks in the armature metal tube. It is worth noting that such a method of the armature active length extension is simpler and more cost-effective in comparison with that of the simultaneous axial initiation.

The generator aluminum armature tube was 35 mm thick, 390 mm external diameter and 2.1 m length. To define the dimensions there were solved the problems of (1) the effective getting the HE energy due to a considerable tube weight, and (2) reaching a comparatively

high velocity to reduce the diffusion losses of the magnetic flux, and (3) providing for the required current duplication time at the final stage.

The HE charge is collected from ring-shaped sections. The hole in the charge was filled with the uniform aluminum blocks reducing the explosion products relaxation into the inside. The armature design ensured the shell velocity of 1.8 km/s.

The stator helical part is comprised by the turns of the coated 10 mm (14 mm) copper wires, using the maylar film. The helix is sectioned. The number of wires changes in the range of 1-64 and is duplicated from section to section. The initial inductance of the helix is nearly 54  $\mu\text{H}$ , the length is 65 cm. The helix diameters at the sides are 720 mm and 420 mm.

The cone shape of the helix provides some advantages. It makes it possible to join the helix with the coaxial part of the stator of a large diameter and have the highly inductive single-wire long section. The said shape also allows to lessen the peak electric voltages between the coil and armature in the generator working volume, as well as the losses caused by the magnetic flux cut-off's due to non-coaxialities and inaccurate assembling [2]. A high initial inductance of the generator leads to the considerable experimental current and energy amplification coefficients, 500 and 120 respectively.

#### Numerical simulation of the generator.

To define the armature extension shape, the 2D MHD modeling and experimental research were employed. To know the armature shape is necessary to choose the stator cone sizes and provide the simultaneous shot. The data agreement is quite good in this case. The computed flying shell shape is shown in Fig.2.

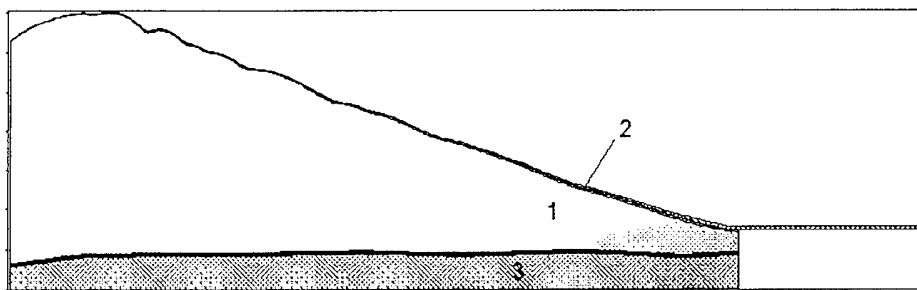


Fig.2. Schematic of the flying armature.  
1 - HE, 2 - armature, 3 - aluminum blocks.

The shell surface disturbances at very high tension correspond to more than double one and so are negligible.

Gas dynamics in the area of the detonation waves collision was researched because of the risk of the radial cutting of the tube with the cumulative jets. Various designs of this unit were numerically investigated, namely: incorporation of the air gap between the charges; that of the foam-filled or aluminum-filled one. In Fig.3 the gas dynamic image of the armature deformation is given, when the gap between the rings is filled with the foam as dense as 0.5 g/ccm. The lowest detonation nonuniformity in this place was reached in case of a partial filling of the volume with aluminum and the remainder with the foam. In the experiment the cracks were not found.

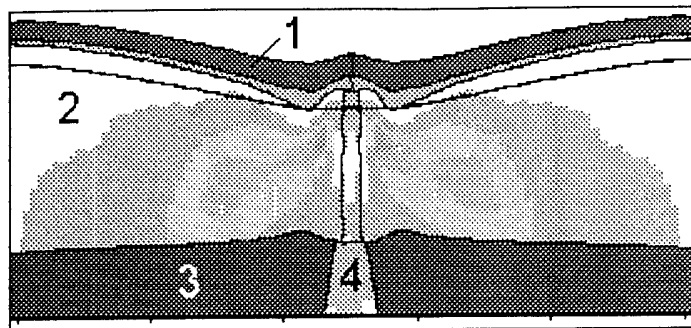


Fig. 3. Schematic of the armature deformation.  
1 - aluminum shell, 2 - HE, 3 - aluminum blocks, 4 - gap.

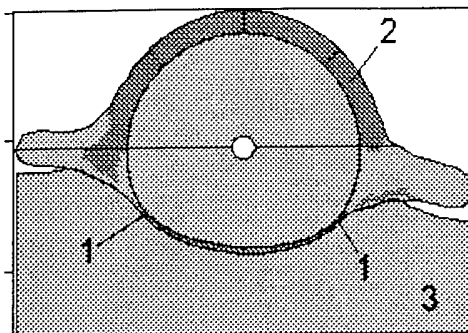


Fig. 4. Schematic of the wire insulation damage.  
1 - contact, 2 - insulation, 3 - cone armature.

There was paid a great attention to the area of the sliding contact between the helix and armature. A great thickness of the high-voltage insulation impedes the formation of the low ohmic contact and may become the main source of the magnetic flux losses. In Fig. 4 there is given the picture of damaging the 2 mm thick maylar insulation of the separated copper wire by the aluminum liner.

The contact is formed in  $2.23 \mu\text{s}$  after touching the insulation. The research revealed that the contact formation in case of a copper armature is faster and most probably more reliable.

In the generator current calculations the armature dynamics accounting for the magnetic field pressure was modeled using a simpler and more fast operating 3/2 D MHD code based on the method of independent cross sections [1]. In this case all the calculation methods and experiment as well proved to be in good agreement. In Fig.5 there is given the calculated EMG-720 inductance plot. In the final stage  $dL/dt = -1.3 \cdot 10^{-3} \text{ Ohm}$ .

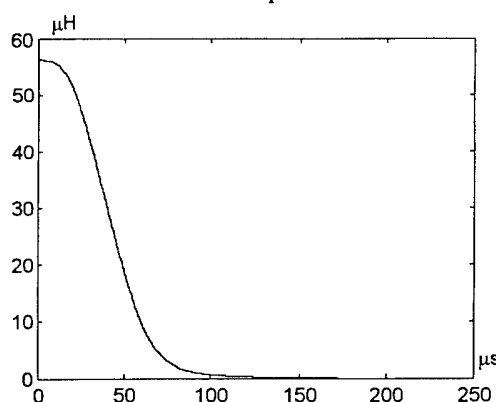


Fig. 5. Calculated generator inductance.

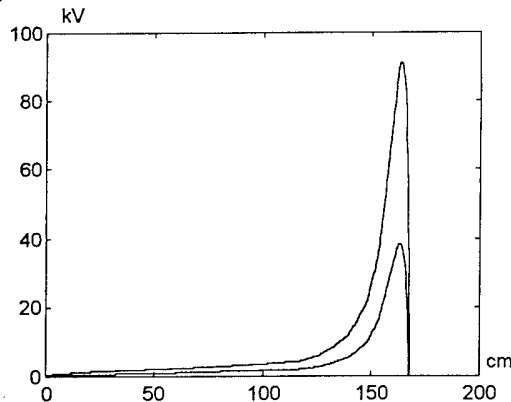


Fig. 6. Calculated helix-armature voltage distribution.

By the known generator inductance distribution along the length,  $L(z,t)$ , it is possible to derive the voltage distribution between the armature and helix:  $V(z,t) = d(L(z,t) \cdot J(t))/dt$  (with no account to the ohmic resistance).

In Fig.6 the calculated electric voltage plot is shown at the moment of the absolute voltage maximum in case of 37 kA and 75 kA powering. Choosing the wire insulation, we were oriented to peak value of the voltage at the maximum possible powering.

The considerable generator size and design peculiarities made us to consider the possibility to manufacture at least the stator coaxial part of ordinary quality steel to decrease the material cost and simplify the technology. Stator's massive units manufacturing of copper

or only coating with copper are unnecessary. Due to not widely spread steel application for such purposes in the high current equipment there was calculated the nonlinear diffusion of the pulsed magnetic field of megagauss amplitude into the steel having the initial magnetic permeability of  $\mu(H_0) \approx 3000$  and conductivity reducing in the process of heating. The calculation proved that similarly to the case of linearity as to a diamagnetic metal the magnetic field diffusion depth is  $\sim \sigma^{-1/2}$ ; and the generator performance degradation is not expected when replacing copper with steel in the coaxial part. In Fig. 7 there is represented the calculated magnetic induction distribution in copper, steel and aluminum at the exponential growth of the boundary field up to 0.5 MGs with the effective time of 30  $\mu$ s.

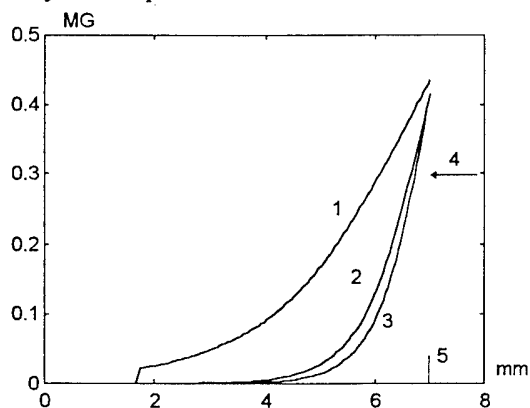


Fig. 7. Calculated magnetic induction distribution.  
1 - steel, 2 - aluminum, 3 - copper,  
4 - diffusion direction, 5 - metal boundary.

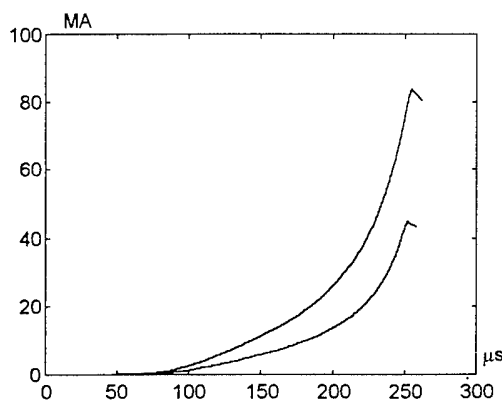


Fig. 8. Calculated generator currents with 20 nH load and 37 kA and 75 kA powering.

The calculated generator currents in case of the operation with 20 nH load and 37 kA and 75 kA powering are shown in Fig. 8.

### Conclusion

As was expected, the initial experimental results proved to be some lower than the numerical prognosis predicted which leaves great opportunities for the further development. First and foremost, we are planning to research the quality of the sliding contact because the critical flux losses were revealed in the helix. It would be useful to replace the aluminum armature with the copper one. This will somehow increase the generator inductance and upgrade the contact quality. We believe that the design potential in terms of the current is nearly 100 MA.

- [1]. Pavlovskii A.I., Lyudaev R.Z., Boyko B.A. et al. Numerical model for Helical Magnetic Cumulation Generators. In: Megagauss Fields and Pulsed Power Systems. Ed. by V.M. Titov and G.A. Shvetsov. Nova Science Publishers, NY, 1990, p. 233.
- [2]. Mironychev P.V. High Temperature, V. 33, N. 4, 1995, pp. 635-640.



## STUDIES OF COLLECTIVE PROCESSES IN REB-PLASMA SYSTEMS

Masaru Masuzaki

*Department of Physics, Faculty of Science, Kanazawa University, Kanazawa 920-11  
Japan*

### Abstract

This paper reviews the following papers presented at this Conference: "Experimental study of collective processes in REB" by L. U. Bogdanov and G. G. Sominski [1], "Spectrum of plasma electrons observed in strong Langmuir turbulence driven by REB" by L. N. Vyacheslavov, V. F. Gurko, I. V. Kandaurov, E. P. Kruglyakov, O. I. Meshkov and A. L. Sanin [2], "Energy and angular spreads of beam electrons and microwave radiation" by H. Koguchi, M. Masuzaki, M. Yoshikawa, S. Takahata, K. Toda, R. Ando and K. Kamada [3], "Macroscopic symptoms of collapse in REB-plasma interaction experiments in strong magnetic field" by V. S. Burmasov, I. V. Kandaurov, E. P. Kruglyakov, O. I. Meshkov, A. L. Sanin and L. N. Vyacheslavov [4], "Broadband mm radiation from beam driven strong turbulence" by M. Masuzaki, H. Yoshida, R. Ando, K. Kamada, A. Ikeda, C. Y. Lee and M. Kawada [5], and "Spectroscopic measurements of turbulent Langmuir fields at the Prague relativistic electron beam experiment" by J. Ullschmied, M. Šimek, K. Koláček and M. Řípa [6].

### INTRODUCTION

Recently the beam-driven strong Langmuir turbulence has attracted much attention theoretically, computationally and experimentally. At this Conference presented are five papers on the experimental study of the beam-driven strong Langmuir turbulence, which includes two papers from the Kanazawa University group, two papers from a group at Budker Institute of Nuclear Physics and one paper from a group at Institute of Plasma Physics, Czech Academy of Science. This paper reviews these papers as well as one paper on collective processes in REB.

### WORKS AT KANAZAWA UNIVERSITY

#### Summary of Previous Results

#### 1. Spectroscopic measurements of turbulent electric fields [7]

An intense relativistic electron beam (IREB) of 1.2 - 1.4 MeV, about 10 kA and 30 ns was injected into an unmagnetized plasma produced by a pair of rail-type plasma guns. The drift chamber, made of stainless-steel, 60 cm long and 16 cm in diameter, was filled with helium gas of 20 mTorr. The plasma density was varied with the delay time from the firing time of the guns. The ratio of the beam density to the plasma density was from 0.002 to 0.4. High frequency strong electric fields originating from interaction of the beam with the plasma were observed using two optical diagnostic techniques; the Stark shift measurement and the plasma satellite method. From the Stark shift measurement it was found that high frequency strong electric fields with Gaussian distribution existed in the plasma, and that the dimensionless electrostatic energy density  $W \sim 1.1$ . From this result it was concluded that the plasma was in a strong Langmuir turbulence state in which formation, collapse and burnout of cavitons are repeated. Here cavitons are spatially localized volumes with density depletion in which large amplitude electrostatic waves are trapped. From the plasma satellite method mean electric fields in the plasma was obtained. The strong field re-

gions were found, from electric fields obtained by both measurements, to occupy a few percent of the beam volume. After a tentative analysis using simulation results [8] the final scale of caviton was estimated to be about  $20 I_d$ .

## 2. Microwave measurements [9]

In the same experimental device strong microwave radiation into a observation window of 18 - 40 GHz was observed. The radiation was broadband above the plasma frequency. The radiation was found to be from beam electrons. There was optimal ratio of the beam density to the plasma density and it was about 0.01.

## 3. Correlation between microwave and strong Langmuir turbulence [10]

It was found that the strong Langmuir turbulence state was a necessary condition for the microwave radiation, but not sufficient one.

## Energy and Angular Spreads of Beam Electrons and Microwave Radiation [3]

For deeper understanding of the strong Langmuir turbulence state investigation of the beam properties after passing the plasma is also important as well as the spectroscopic measurements. The energy distribution and the angular spread (perpendicular velocity scattering) of the beam electrons after passing the plasma were measured by means of a magnetic energy analyzer and an angle analyzer, respectively. The measured energy distribution and the angular spread

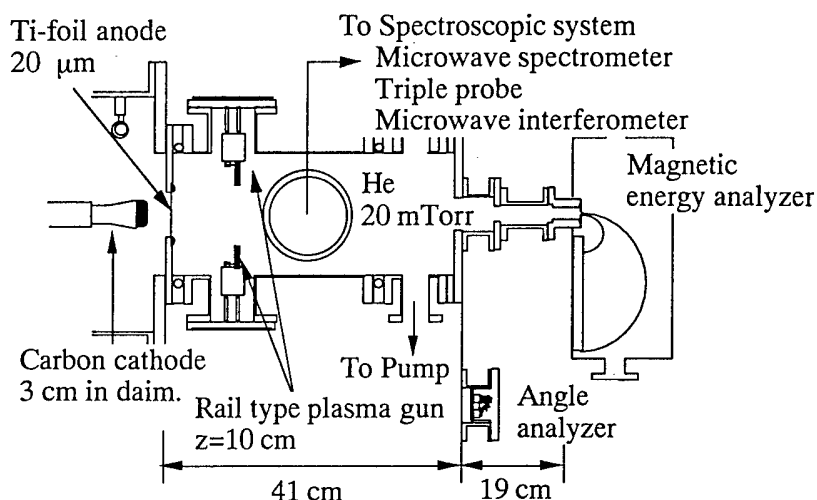


Fig. 1. The experimental setup

were analyzed using the theory of transit-time interactions [11].

Figure 1 shows the experimental setup which was the same as described above. Figure 2 shows the plasma density as a function of the delay time  $\tau$  after the firing time of the guns. The electron temperature without the IREB injection was 6 - 9 eV.

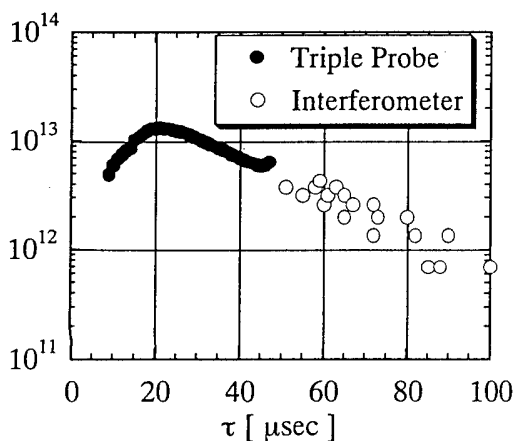


Fig. 2. The plasma density

The observable energy range of the magnetic energy analyzer in this experiment was 90 keV - 1.54 MeV. The energy resolution was 40 keV, and the time resolution was a few ns. During 15 - 30 ns into the beam pulse, the energy distribution showed Gaussian spectra. Fig. 3 a) shows the averaged standard deviation of the energy distribution as a function of  $\tau$ , where the initial spread of 58 keV is taken into account.

The angle spread (perpendicular scattering) was measured by an angle analyzer. It consisted of a Faraday cup of 0.6 cm in outer diameter and three brass disks of 0.2 cm thick which were set coaxially. The center Faraday cup covered the sinusoidal

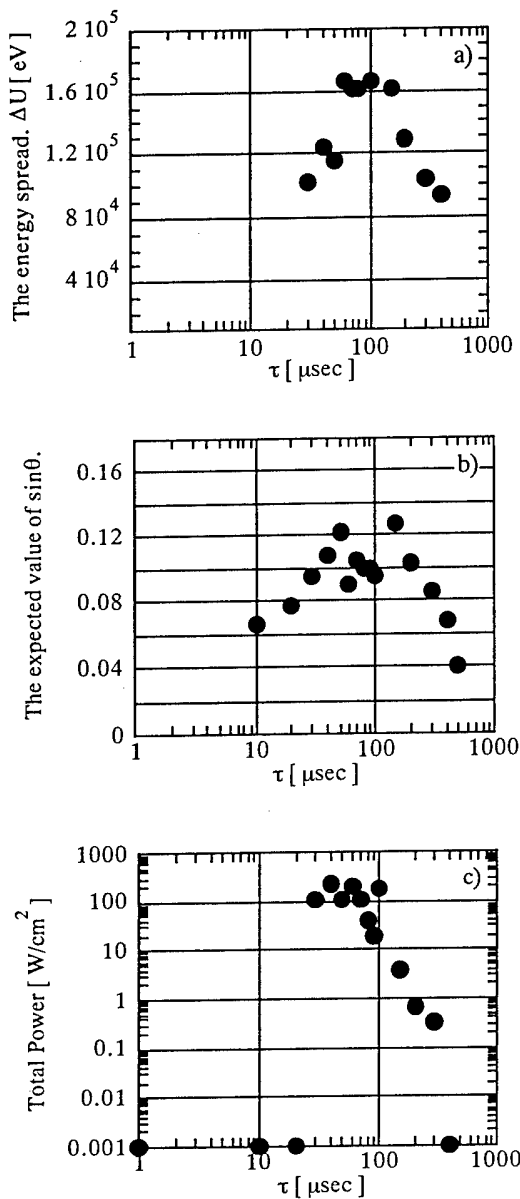


Fig. 3. The energy spread, the expected value of  $\sin\theta$  and the total power of the microwave radiation vs.  $\tau$ .

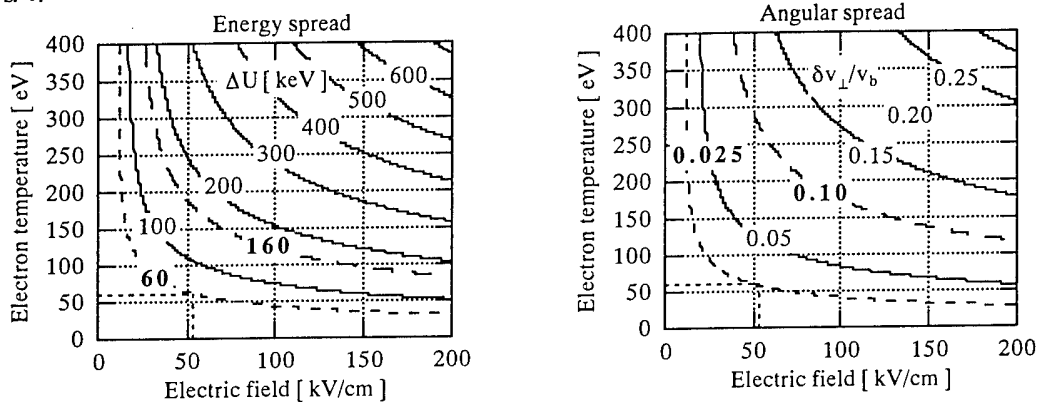


Fig. 4. The energy and angular spreads. The dipole moments of all cavitons are parallel to the beam direction.

range of the scattering angle of 0 - 0.1 and three disks covered 0.1 - 0.2, 0.2 - 0.3 and 0.3 - 0.4, respectively. The angle analyzer was set in the axis at the end of the chamber. The time-evolved expected values of the sine of the scattering angles were calculated from these output signals. Figure 3 b) shows the averaged expected values of the scattering angles as a function of  $\tau$ . The initial spread is taken into account.

The high power broadband microwave radiation was measured at 17.5 cm downstream from the anode by a 5-channel microwave spectrometer of filter-bank type. The frequency range covered was 18 - 40 GHz. The total power of microwave radiation in this frequency range is shown in Fig. 3 c) as also a function of  $\tau$ .

The electron temperature  $T_e$  after the IREB injection was estimated from the spectroscopic measurement of the intensity ratio of HeI 492.19 nm line to HeI 471.31 nm line by comparing the experimental results with the newly developed collisional radiative model [12]. The intensity of the high frequency turbulent electric field  $E_s$  was obtained measuring the Stark shift of HeI 501.57 nm line.

The energy and angular spreads of beam electrons are caused by scattering of beam electrons in energy and in perpendicular velocity during interaction with cavitons. The theory of multidimensional transit-time interactions was applied to analyze these spreads. The scatterings due to single interaction with a caviton was calculated, and then total energy spread  $\Delta U$  and angular spread (perpendicular scattering)  $\Delta v_{\perp}/v_b$  were estimated. Figure 4 shows  $\Delta U$  and  $\Delta v_{\perp}/v_b$  for the plasma density  $n_p = 1.6 \times 10^{12} \text{ cm}^{-3}$ . The dipole moments of all

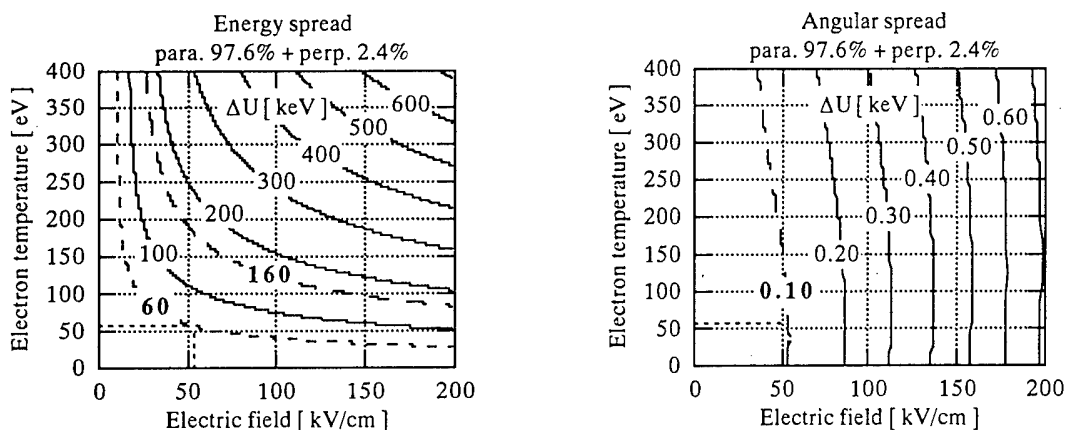


Fig. 5. The energy and angular spreads. Cavities with perpendicular dipole moment are assumed to be 2.4 %.

cavities are assumed to be parallel to the direction of the beam propagation. In this case  $T_e$  and  $E_s$  were 57 eV and 54 kV/cm, respectively. From the energy analyzer measurement  $\Delta U = 160$  keV and from the angle analyzer measurement  $\Delta v_{\perp}/v_b = 0.10$ , while the measured values of  $T_e$  and  $E_s$  give  $\Delta U = 60$  keV and  $\Delta v_{\perp}/v_b = 0.025$ . If it is assumed that dipole moments of some cavities are perpendicular to the direction of beam propagation, the angular spread obtained from the measured values of  $T_e$  and  $E_s$  can be made to coincide with that obtained from the angle analyzer measurement. Figure 5 shows  $\Delta U$  and  $\Delta v_{\perp}/v_b$  for the case in which cavities with dipole moment perpendicular to the direction of the beam propagation is assumed to be 2.4 %. Both values of  $\Delta v_{\perp}/v_b$  agree well and almost independent of  $T_e$ . However, difference between both values of  $\Delta U$  remains almost the same. One reason of this disagreement may be inaccuracy of  $T_e$  measurement. The electron temperature in the IREB pulse duration could not be obtained because of limitation of the measuring system. If  $T_e$  is higher than 100 eV,  $\Delta U$  determined from  $T_e$  and  $E_s$  will become close to that obtained from energy analyzer measurement.

From Fig. 3 it can be seen that the dependence of the microwave radiation on  $\tau$  is almost the same as dependences of the energy and the angular spreads on  $\tau$ . The wider the energy and angular spreads, the higher the total power of the radiation.

Followings are summaries.

1. The energy spread  $\Delta U$  and the angular spread  $\Delta v_{\perp}/v_b$  of IREB electrons after passing the plasma were measured using a magnetic energy analyzer and an angle analyzer, respectively.
2. Theory of multidimensional transit-time interactions was applied to analyze the experimental data.
3. The energy and angular spreads were also estimated using the spectroscopically measured intensity of high frequency electric fields and the electron temperature.
4. The energy spread obtained using the energy analyzer was higher than that obtained using the spectroscopic data.
5. One reason of this discrepancy may be inaccuracy of the electron temperature measurement. The electron temperature in the IREB pulse duration could not be obtained because of limitation of the measuring system.
6. The angular spread obtained using the angle analyzer and that obtained using the spectroscopic data agreed when the percentage of the dipole moments perpendicular to the direction of the beam propagation was taken to be 2.4 %.
7. The above result seems to show that not all of the dipole moments were parallel to the direction of the beam propagation.
8. In connection with the microwave radiation, the wider the energy and angular spreads, the higher the total power of the microwave radiation.

## Broadband MM Radiation from Beam Driven Strong Turbulence [5]

As there was evidence of emission of radiation higher than 40 GHz, the observation window was widened up to F band using a heterodyne spectrometer covering E band (60 - 90 GHz) and a full band detector covering F band (90 - 140 GHz) in addition to the filter-bank type spectrometer covering K, Ka and U bands (18 - 60 GHz) used previously. The radiation was measured radially at 17.5 cm from the anode. Figure 6 shows a schematic diagram of the heterodyne spectrometer and its setup for the radial measurement. It consisted of a downconverter unit, an IF unit and a power unit. The downconverter consisted of a bandpass filter, a variable attenuator, a mixer and a local oscillator with frequency of 50 GHz. The IF unit consisted of bandpass filters, Schottky diodes and pulse amplifiers. It covered 10 - 40 GHz in 5 channels. Filters and detectors used were diverted ones from the filter-bank type spectrometer. Calibration was made at 60 GHz. In this setup full band K, Ka and U band detectors were prepared, and simultaneous measurements were carried out. Figure 7 shows a schematic diagram of the F band detector and its setup for the radial measurements. It consisted of a bandpass filter, an attenuator, a Schottky diode and a pulse amplifier. In this setup full band Ka, U and E band detectors were also prepared and simultaneous measurements were done.

Figure 8 shows a typical radiation spectrum observed when the plasma frequency was about 13 GHz at the measuring position. In this case helium gas was not introduced. Results from two experimental runs are compiled into one. In one of them the setup shown in Fig. 6 was used, and in the other the setup shown in Fig. 7 was used. It was ascertained that radiation was emitted to at least about 140 GHz.

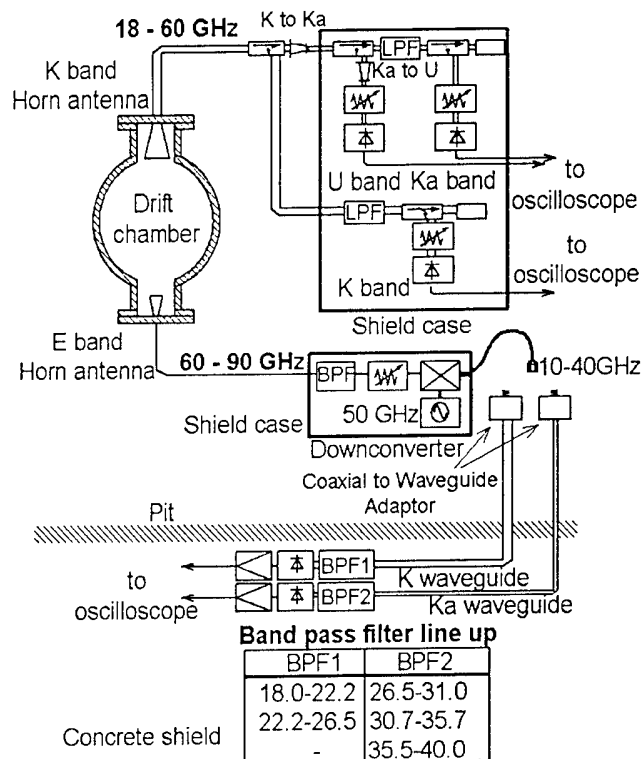


Fig. 6. The setup of the E band heterodyne spectrometer.

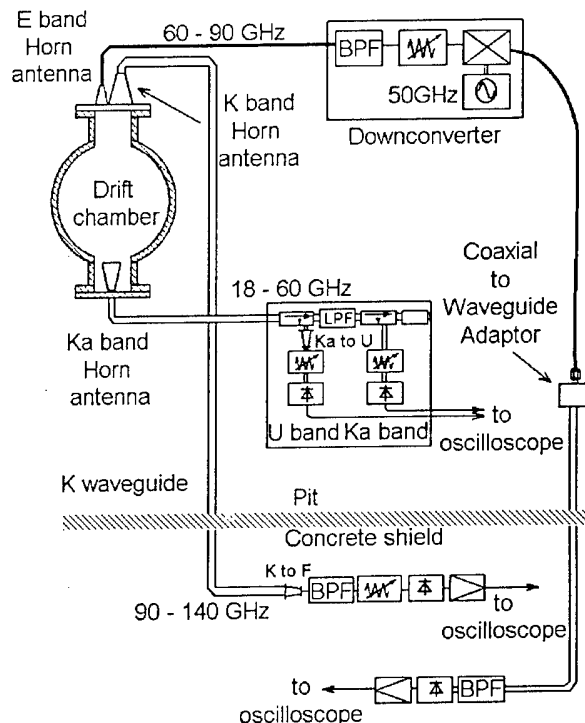


Fig. 7. The setup of the F band detector.

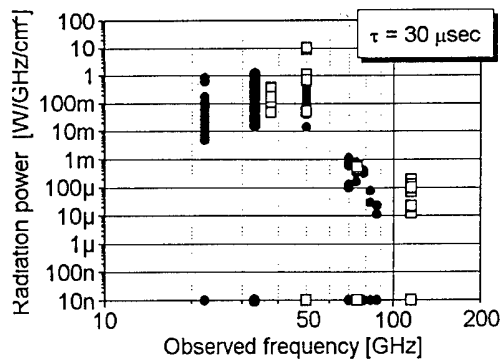


Fig. 8. An experimentally obtained spectrum.

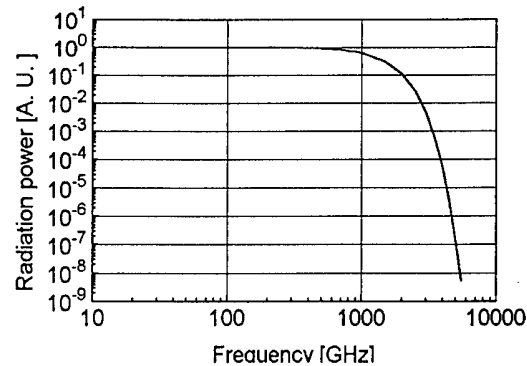


Fig. 9. An example of calculated spectrum.

The power level was high in K to U bands, but it decreased steeply in E and F bands.

Calculation of the radiation spectra was done according to the collective Compton boosting model. In this model the broadband intense radiation is due to the interaction of the density modulated beam electrons with intense high frequency electric fields in cavitons, their characteristic charge density oscillation being assumed to be dipolar. Several spectral density functions for the beam density modulation are assumed. Our calculation were done for each spectral density function and for each direction of the dipole moment. Figure 9 is an example for which Gaussian spectral density function and dipole moment perpendicular to the direction of the beam propagation are assumed. The experimental and calculated spectra resemble each other in shape qualitatively, although quantitatively they are very different.

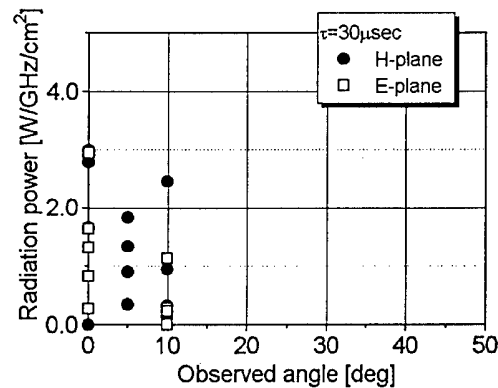


Fig. 10. Angular distribution of the radiation.

Angular distribution of the radiation in Ka band was measured at the end of the chamber varying the horn position. When the dipole moments of the cavitons are parallel to the beam direction, intensity in the axis will be null. On the other hand, when the dipole moments are perpendicular to the beam direction, the intensity in the axis will be maximum. It may be natural to think that the directions of all dipole moments are parallel to the direction of the beam direction, since the electrostatic fields are produced by the beam-plasma instability. Figure 10 shows the measured radiation power as a function of angle. The radiation power observed was almost the same when the horn was rotated 90° around its axis. The results suggests that not all of the dipole moments were aligned to the beam direction on the contrary to the expectation.

Followings are summaries.

1. Radiation was emitted to at least about 140 GHz.
2. The power level was high in K to U bands, but it decreased steeply in E and F bands.
3. At present the Compton boosting model seems to be not able to explain the experimentally obtained spectrum.

4. It is still thought that the radiation is due to beam electrons interacting with caviton fields. The reasons are: (1) The strong turbulence state was found to be a necessary condition for the radiation, and (2) it was found that the wider the energy and angular spreads of the beam electrons due to the interaction with the caviton

fields, the higher the total power of the radiation.

5. Angular distribution of the radiation was measured in Ka band, and the result suggests that not all of the dipole moments of the cavitons were aligned to the direction of the beam propagation.

Future plan includes (1) completion of the F band spectrometer which is a 3-channel Fabry-Perot interferometer type, (2) spectrum measurements in the axial direction and (3) measurement of the beam modulation.

## WORKS AT BUDKER INSTITUTE OF NUCLEAR PHYSICS

### Macroscopic Symptoms of Collapse in REB-Plasma Interaction Experiments in Strong Magnetic Field [4]

Up to now, as to the case of REB injection into a plasma in a strong magnetic field there is no experiment on the Langmuir waves collapse. This paper presents the first macroscopic manifestations of the Langmuir waves collapse for the case of strong REB-plasma interaction in a strong magnetic field.

The experiments were carried out on the GOL-M device. The parameters of target plasma were as follows: The plasma density was  $1.5 \times 10^{15} \text{ cm}^{-3}$ , the initial electron temperature was 1 eV, the diameter was 6 cm and the length was 250 cm. A strong mirror magnetic field was applied. The field strengths were 2.5 T in the uniform section and 4.5 T at the mirrors. The injected beam parameters were as follows: The energy was 700 keV, the maximum current was 2 - 3 kA, the diameter was 2 cm and the duration was 200 ns. After 40 ns from the starting time of the beam the plasma temperature increased up to 30 - 50 eV, so the plasma became a nonisothermal state (the electron temperature much higher than the ion temperature).

Two macroscopic indications of the existence of collapsing cavitons in the plasma were found.

1. Appearance of energetic tails on the electron distribution function.

At the final stages of collapsing cavitons, the energy of Langmuir waves trapped in the cavitons are transferred to a small portion of electrons crossing the cavitons during the time less than the period of electric field oscillations in the cavitons, and energetic tails appear on the electron distribution function. Such tails have been observed in the experiments carried out by this group. Some detail is described in the other paper [2].

2. Existence of intense ion-sound turbulence.

At the final stage of caviton collapse the Langmuir waves inside the caviton decay due to the electron damping. Since the plasma densities inside cavitons are low, ion-sound waves are excited. When the electron temperature is much higher than the ion temperature, the damping of the ion-sound waves is weak. So the collapse process should create an intense ion-sound turbulence.

The spectra of low frequency fluctuation were studied by the collective laser scattering method using a pulsed  $\text{CO}_2$  laser. The scattered radiation was detected at three angles,  $6^\circ$ ,  $11^\circ$  and  $16^\circ$  to the direction of the laser beam propagation. The frequency and the space spectra of low frequency fluctuations were studied. The spectrum of the scattered radiation was studied with the aid of a grating monochromator with a 30 GHz resolution. To identify the exact value of the frequency of oscillations an absorption cell with ammonia was installed between the grating and detector. The frequency of the low frequency fluctuations was found to be 2 GHz, which agreed well with the frequency of the ion-sound oscillations for the experimental conditions. It was ascertained that the ion-sound fluctuation was not excited by the return current, but appeared as a consequence of the strong Langmuir turbulence. The level of the strong Langmuir turbulence, observed using an additional channel at small angle ( $0.5^\circ$ ) to the laser beam direction, correlated well with the level of the ion-sound fluctuation. In Fig. 11 curve 1 is their first result of the measurements of the k-spectrum of the ion-sound turbulence in a strong magnetic field. From the space spectrum of the

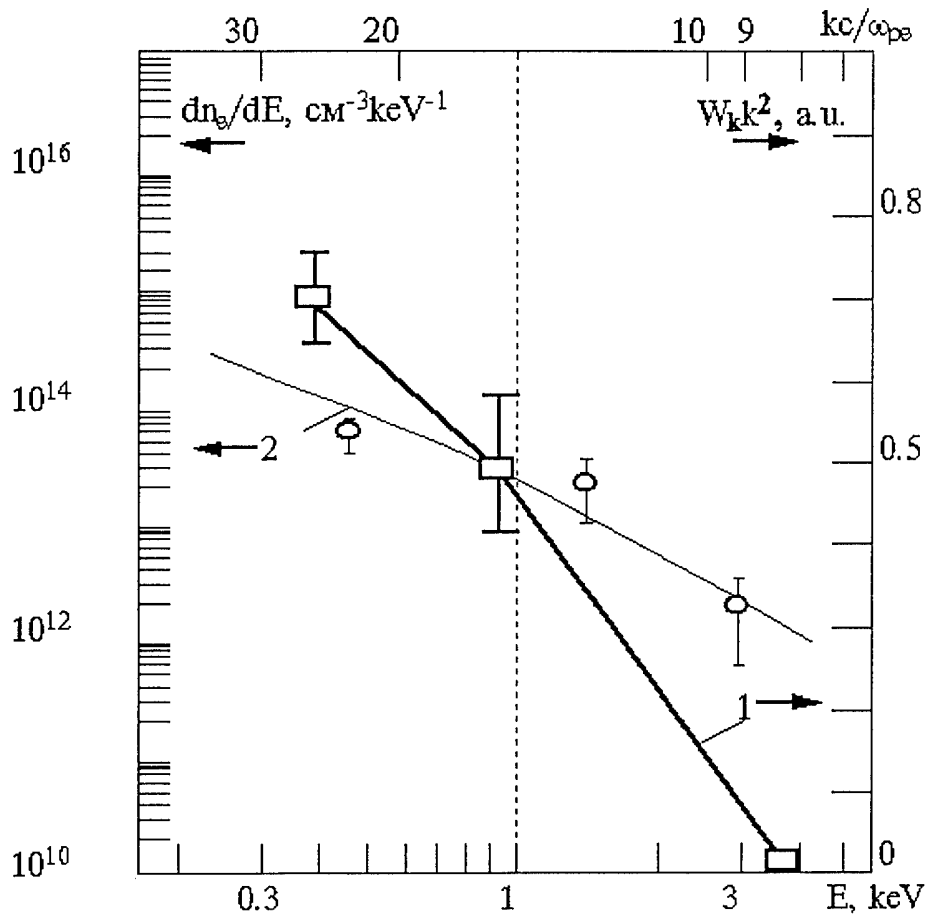


Fig. 11.  $k$ -spectrum of ion-sound turbulence (curve 1) and non-Maxwellian part of the electron distribution function of plasma electrons (curve 2) vs. electron energy  $E$  or vs. normalized wave number  $k$ . The scale of  $E$  and  $k$  correspond to each other through the ratio  $k = \omega_{pe}/v_e$ .

ion-sound turbulence the characteristic size of the cavitons at their final stage was estimated to be less than  $30 \lambda_d$ . This Figure also shows the non-Maxwellian tail of the distribution function of the plasma electrons after heating (curve 2).

#### Spectrum of Plasma Electrons Observed in Strong Langmuir Turbulence Driven by REB [2]

This paper presents the experimental observation of the non-Maxwellian electron distribution of a plasma due to strong REB-plasma interaction and a discussion of the possible mechanism of plasma heating.

The experimental device was the same as described above. The Thomson scattering technique was used for studying of a non-Maxwellian electron distribution function. Two simultaneously operating systems were employed for observation of light scattered at the angles of  $90^\circ$  and  $8^\circ$ , respectively. The former system was used to measure the temperature and the density of the bulk of plasma electrons, and the latter system was used for studying of the superthermal tails of the electron distribution function. A Nd-glass laser was used as the light source. In the latter system the scattered light was received by a 6-channel polychromator.

The laser pulse was delayed by 50 - 100 ns from the beginning of the REB pulse.



Signals were obtained in four channels in the latter system. It was assumed that the distribution function has the power law:  $f(E) \propto E_e^{-\alpha}$  for the energies above 300 eV (approximately 10 times the electron temperature), and  $\alpha = 2.5$  was the best fit to the experimental signals.

It is claimed to be evident that the heating of non-Maxwellian part of the electron distribution function is connected with the Landau damping of slow Langmuir waves. A discussion is given on the main mechanism of transferring of the energy of turbulent oscillations towards the short wavelength side of the spectrum.

## WORKS AT INSTITUTE OF PLASMA PHYSICS, CZECH ACADEMY OF SCIENCE

### Spectroscopic Measurements of Turbulent Langmuir Fields at the Prague Relativistic Electron Beam Experiment [6]

In the Prague REB-plasma experiment REBEX a REB (500 kV, 80 kA, 100 ns) is injected into a hydrogen plasma column 1 m long and 7 cm in diameter bounded in longitudinal direction by thin Al foils. A magnetic field of 0.6 T is applied. The plasma density is  $5 \times 10^{14} - 10^{16} \text{ cm}^{-3}$ . In order to estimate the intensity of turbulent Langmuir fields from the Stark component of Balmer emission lines three different spectroscopic apparatuses have been used. In this paper these three spectroscopic apparatuses are compared from the point of view of their suitability for measurements of emission line profiles in REB-plasma experiments.

The first apparatus was a 6-channel polychromator with a photomultiplier detection system. Its spectral and time resolution was 0.08 nm/channel and 20 ns, respectively. The time resolution of this system was sufficient for time-resolved measurements of the intensity and width of plasma emission lines, while its sensitivity and spectral resolution proved to be too low for performing any detailed studies of the line shape, and of the line wings in particular.

It should be noted that this group found the LF Stark effects of the intense ion-sound waves, remnants of the burned out Langmuir cavitons, using this spectrometer [13].

The second one was of the intracavity laser absorption spectrometer type, with a 256-pixel CCD camera detection system which made it possible to increase the spectral resolution up to 0.004 nm/pixel. The time resolution was 40 ns. The spectral resolution of this spectrometer was excellent, but the time dependences of the line shape could be constructed on the shot-to-shot basis only. A sufficient number of identical shots was to be collected.

Recently, a new spectroscopic system consisting of the 2-m spectrometer PGS2 Carl Zeiss Jena and of a 512-pixel detecting head (Jovin Yvon) with a computer controlling system has been introduced by this group. Preliminary test measurements suggest that both the sensitivity and the spectral and time resolutions of the system might be sufficient for studies of profiles of the most intense emission lines at the REBEX experiment, but we should wait for its full operation for a little while with expectation of excellent results.

## OTHER WORK

### Experimental Study of Collective Processes in REB [1]

This paper is not on the beam-plasma interaction, but on the space charge oscillation on a REB. A special low-disturbing technique was used for time and space resolved measurements of the space charge oscillation.

The experiments were done at the SER-1 setup at Saint-Petersburg Technical University. The beam voltage was 220 kV, the beam current was 0.7 - 1.1 kA and the pulse duration was 1 - 3  $\mu\text{s}$ . A magnetic field of 1 T was applied. Two local magnetic field bumps were applied. Using two HF probes temporal and spatial variations of the

oscillations were obtained. At the saturation level discrete peaks were discernible in spectra in the frequency range of 100 - 1500 GHz with the strongest in the 700 - 1200 GHz. The amplitude of the oscillations increased with distance from the cathode which indicates their convective nature. Application of the magnetic field bumps revealed the existence of electrons with relatively large transverse and small axial velocity components. It is thought that the space charge oscillations were mainly due to the double-stream instability caused by interaction of an electron flow emitted from the front surface of cathode plasma with maximum axial velocities with an electron flow from the outer generatrix of the plasma with maximum transverse velocity and so with minimum axial velocity. Other mechanisms are also discussed.

### CONCLUDING REMARK

Strong Langmuir turbulence state due to the REB-plasma interaction is an interesting research field not only in itself as one theme of fundamental plasma physics, but also in connection with plasma heating, high power microwave devices using REB-plasma systems and space physics. I hope further development of researches in theory, simulation and experiment in this field.

### References

- [1] L. Yu. Bogdanov and G. G. Sominski, paper P-1-2 in this Conf.
- [2] L. N. Vyacheslavov, V. F. Gurko, I. V. Kandaurov, E. P. Kruglyakov, O. I. Meshkov and A. L. Sanin, paper P-1-6 in this Conf.
- [3] H. Koguchi, M. Masuzaki, M. Yoshikawa, S. Takahata, K. Toda, R. Ando and K. Kamada, paper P-1-9.
- [4] V. S. Burmasov, I. V. Kandaurov, E. P. Kruglyakov, O. I. Meshkov, A. L. Sanin and L. N. Vyacheslavov, paper P-1-10 in this Conf.
- [5] M. Masuzaki, H. Yoshida, R. Ando, K. Kamada, A. Ikeda, C. Y. Lee and M. Kawada, paper P-1-12 in this Conf.
- [6] J. Ullschmied, M. Šimek, K. Koláček and M. Řípa, paper P-1-16 in this Conf.
- [7] M. Yoshikawa, M. Masuzaki and R. Ando, J. Phys. Soc. Jpn **63**, 3303 (1994).
- [8] P. A. Robinson and D. L. Newman, Phys. Fluids **B1**, 2319 (1989).
- [9] R. Ando, M. Masuzaki, H. Morita, K. Kobayashi, M. Yoshikawa, H. Koguchi and K. Kamada, to be published in J. Phys. Soc. Jpn **65** (1996).
- [10] M. Yoshikawa, M. Masuzaki, R. Ando and K. Kamada, to be published in J. Phys. Soc. Jpn **65** (1996).
- [11] P. A. Robinson, Phys. Fluids **B1**, 490 (1989).
- [12] S. Sasaki, Research Report NIFS-346 (1995).
- [13] K. Koláček, M. Řípa, J. Ullschmied, K. Jungwirth and P. Šunka, in Proc. of the 9th Intern. Conf. on High-Power Particle Beams (NTIS PB92-206168), Vol. II, p. 1337.

## NEW DEVELOPMENTS IN RELATIVISTIC KLYSTRON AMPLIFIERS

M. Friedman, D. Colombant, R. Fernsler, R. Hubbard, M. Lampe, V. Serlin, and S. Slinker

*Plasma Physics Division, Naval Research Laboratory, Washington, D.C. 20375*

**Abstract**

A relativistic klystron amplifier that employed cavities with inductively loaded wide gaps and a novel converter has achieved 50% energy efficiency, a significant advance over the previous state of the art of 20%. The new device was immersed in a 3 kG magnetic field and contained two innovations: (1) Wide gaps which include an inductively loaded return current structure that was opaque to the unmodulated beam space charge but transparent to the RF field. (2) A novel converter that was made of a "leaky" cavity with a radially-converging inductively-loaded structure that was inserted in the output wide-gap. This structure reduced the potential energy residing in the electron beam and maximized RF output energy.

**Introduction**

A high current "conventional" klystron amplifier has been considered as a candidate for a high power microwave (HPM) source<sup>(1)</sup>. However, klystrons that operate with high current are inefficient due to space charge effects and the large spread in the electron energy at the output gap. To reduce these effects a high beam voltage is required. But high voltage leads to beam stiffness that can only be overcome by injecting a high RF input power and/or by lengthening the drift region in klystrons.

Relativistic klystron amplifiers (RKAs) use the self field of annular intense relativistic electron beams (IREBs) to considerably reduce effects associated with beam stiffness<sup>(2,3)</sup>. These sources, while generating microwaves at frequency 1.3 GHz with peak power >10 GW for 100 ns duration, had efficiency that was limited by beam loading, RF breakdown, and the spread in the electron kinetic energies at the gaps.

We are presently developing a new generation of RKA sources based on two major innovations: (1) An annular "triaxial"<sup>(4)</sup> structure which can handle high power over a broad frequency bandwidth with improved compactness. (2) Inductively-loaded wide gaps to efficiently modulate the beam and extract microwaves at high power, while avoiding breakdown and DC space charge limits. In this paper we report substantial improvement in RKA operation when the narrow gaps used in previous RKAs are replaced with inductively loaded wide gaps. We have (1) increased the bunched beam peak current by more than 50%, while avoiding nonlinear effects that degrade the RF output pulse and (2) converted ~50% of the electron injected energy into RF.

**Electron Beam Modulation by Inductively Loaded Wide Gaps**

In previous implementations of the RKA, as in most klystron-like devices, the electron beam has been modulated by an unidirectional RF voltage applied to a gap whose length is less than a quarter wavelength<sup>(2-4)</sup> (Fig. 1 top). The precise length of the gaps was chosen by trial and error as a compromise between competing factors: short gaps reduce the beam potential energy while long gaps improve electrostatic insulation<sup>(5)</sup> and reduce beam loading<sup>(6)</sup>. For the high power

L-band RKA, with wavelength 23 cm, we found the optimum length to be 1.7 cm to 2.0 cm. Even with optimization of these narrow gaps, problems occurred when the beam was highly modulated: The effective gap length and the electron transit time across the gap depended on the amplitude and frequency of the modulated current<sup>(4)</sup>. Also, nonlinear effects associated with beam loading changed the RF characteristics of the gap-cavity system<sup>(6,7)</sup>. These effects reduced the efficiency of the RKA, degraded the rise time of the output RF pulse and introduced high-amplitude low-frequency fluctuations on the envelope of the RF pulse<sup>(4)</sup>. Moreover, at high power levels the electrostatic insulation<sup>(5)</sup> proved insufficient to prevent electron emission and breakdown at the gaps.

We reported earlier<sup>(8)</sup> that efficient modulation of an intense relativistic electron beam can be accomplished using a completely different gap geometry in which problems associated with narrow gaps were eliminated. In this geometry the gap length was about a half wavelength<sup>(8)</sup>, lowering the DC gap impedance and reducing the nonlinear beam loading. To keep the electrons in synchronism with the RF field while crossing such a long gap we imposed a bidirectional electric field, i.e., a field that at any given time changes its sign at the mid point of the gap. However the potential energy of an electron beam increased when it propagated through a wide gap. This constituted a significant drain on the kinetic energy, and could even lead to a virtual cathode formation. We prevent this increase in potential energy by stacking the wide gap with thin metallic washers (Fig. 1 bottom) that were connected inductively to ground. The washer structure effectively neutralized the beam space charge and provided a return path for the unmodulated current. However, the inductance of the washer-loaded structure was sufficient to prevent any substantial effects on the cavity mode.

### Efficient Relativistic Klystron Amplifiers<sup>(9)</sup>

#### Experiment

Even with the large improvement in IREB modulation in the RKA, the RF extraction was inefficient due to the wide energy distribution of the electrons at the output gap. The spread in kinetic energy results from the spatial distribution of the potential energy residing in the IREB and from the bunching mechanism. The particle code MASK<sup>(10)</sup> which successfully simulated the global operation of RKAs<sup>(8)</sup>, was used to obtain microscopic details of the modulated IREB such as density and energy distributions of the electrons (Figs. 2A-2D).

To achieve efficient operation of an RKA (or any klystron-like devices), the RF voltage across the output gap has to fulfill two conditions that are impossible to satisfy at the same time,

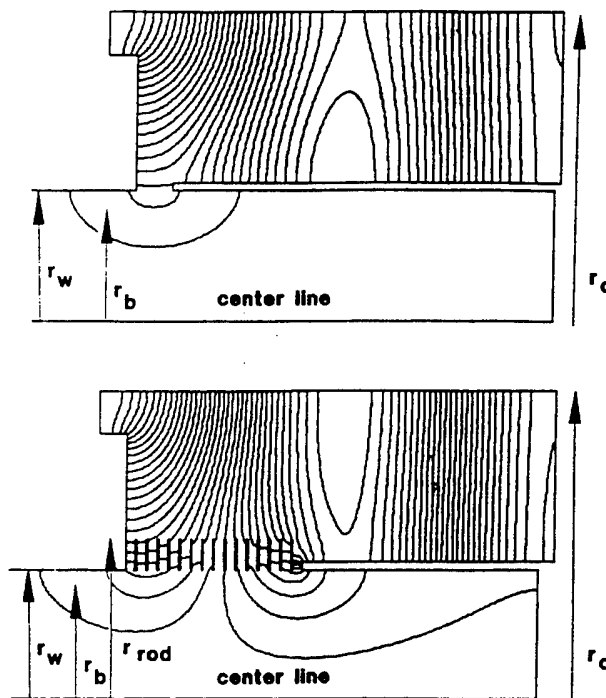


Figure 1. SUPERFISH calculation of electric field lines distribution in a narrow (top) and a wide (bottom) gap geometries.

especially for a modulated beam with a large energy spread: (1) It has to be low enough to avoid electron reflection that can cause a virtual cathode formation. (2) It has to be high to drain most of the electrons' energy so as to maximize the RF energy output. An energy efficiency of 20% and a power efficiency of 35% were obtained for RKA's at the Naval Research Laboratory<sup>(3)</sup>. Similar efficiencies were obtained at Los-Alamos National Laboratory<sup>(11)</sup> and at Physics International<sup>(12)</sup>. In this paper we will describe a mechanism that substantially increases the energy efficiency of RKAs to 50%.

The experimental apparatus is shown in Fig. 3. Three gaps each 10 cm long were inserted in a smooth wall drift tube of radius  $r_w=6.7$  cm. An electron beam propagating through an empty gap of such a length would have acquired a large potential energy. A reduction of the potential energy was achieved<sup>(8)</sup> by inserting structures inside the empty gaps. These structures consisted of a stack of 23 metallic washers of thickness 0.075 cm and outer radius  $r_{w2}=9.2$  cm. The inner radius of the washers inserted in the first two gaps was  $r_{w1}=6.7$  cm ( $=r_w$ ). The inner radii of the washers in the third gap changed sequentially from 6.7 cm to 6.2 cm. The IREB was stopped after crossing the third gap and next to the last washer. The washers were supported by four thin metallic rods mounted at radius  $r_{rod}=8.9$  cm connected across each gap. The first two gaps were connected to coaxial cavities tuned to 1281 MHz. The third gap was connected to a "leaky" cavity consisting of a coaxial transmission line with one end of the inner electrode serving as the electron dump. The inner electrode was supported downstream, at a null point of the standing wave, by six radial rods. The other end of the inner electrode was connected to a metallic disc. The resonant frequency,  $\omega$ , the quality factor,  $Q$ , and the shunt impedance,  $\mathcal{R}$ , of this cavity were tuned by changing the position and radius of the disc. The outer electrode was connected to a radiating cylindrical horn with a 1 meter diameter window. This third cavity is the RF converter. The apparatus was immersed in a quasi-DC magnetic field,  $B_z$ , and was evacuated to a base pressure  $<10^{-5}$  Torr. A diode injected an annular IREB of radius  $r_b=6.1$  cm, thickness 0.3 cm, and current  $I_0=11$  kA into the system. The maximum voltage pulse applied to the diode was 450 kV. The pulse duration was 130 ns at maximum voltage, with a voltage rise time of 30 ns and a fall time of 50 ns.

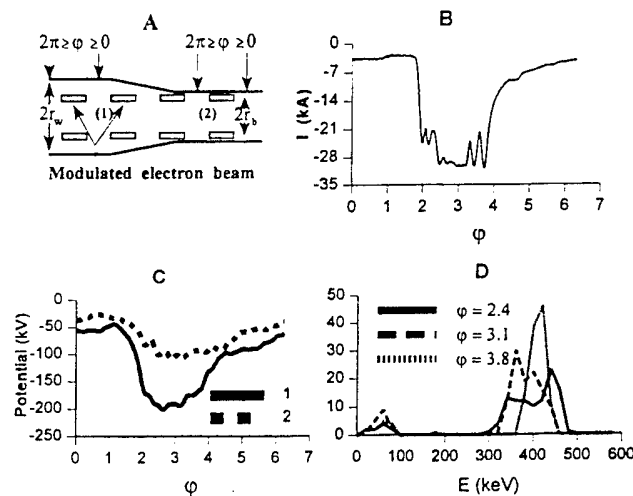


Figure 2.

(A) A section of the simulation geometry displaying a modulated electron beam propagating in an axisymmetric tube. (B) A current profile of a single bunch located at an axial position where the RF current amplitude reached its maximum.

(C) Potential energy residing in the bunch of Fig. 2B calculated for the inner most electrons and at an axial position where  $r_w=6.7$  cm (position 1) and  $r_w=6.4$  cm (position 2). (D) Electron kinetic energy distribution of the bunch displayed in Fig. 2B: at  $\phi=2.4$ ,  $\phi=3.1$ , and  $\phi=3.8$ .

RF waves at the resonant frequency penetrated easily into (and out of) the cavities through the inductive structures, establishing a bidirectional electric field mode inside the wide gaps. This mode ensured a synchronized interaction between the RF and the electrons<sup>(8)</sup>. A high

level of current modulation downstream of the first gap was observed when a RF pulse of power  $P_{in}=4$  MW was externally injected into the first cavity. The second gap was inserted at the axial position where the RF current reached a maximum. The beam was fully modulated downstream of the second gap. Radiated power was maximized by choosing the site of the third gap at an axial position where the 1<sup>st</sup> harmonic of the beam modulated current reached its peak ( $\sim 14$  kA), and by adjusting the geometry of the converter. The output RF pulse emitted from the conical antenna was sampled by a small horn. The electric field established in the receiving horn was displayed on a Tektronix oscilloscope model SCD 5000.

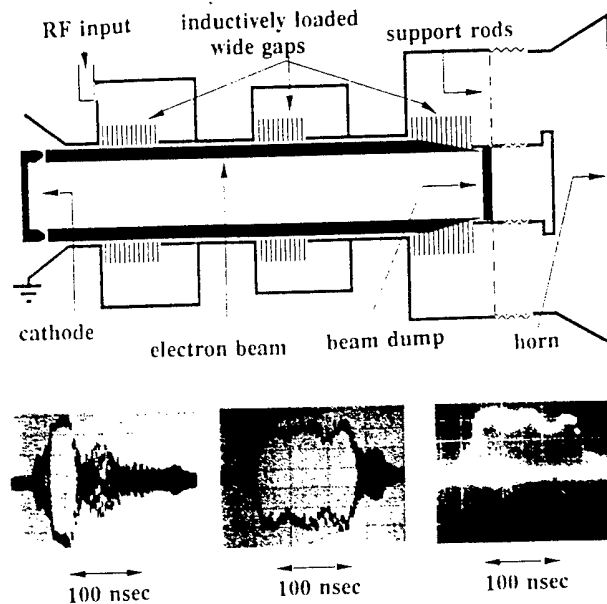


**Figure 3.** (Top) Schematics of the experiment. (Bottom- left) The RF output electric field signal for  $B_z=8$  kG. (Bottom- middle) The output RF electric field signal,  $B_z=3$  kG. (Bottom-right) RF output power sampled by a crystal detector,  $B_z=3$  kG.

The principal result of the experiment was that the peak output power was

$P_{out}=(2.85 \pm 0.15)$  GW, or about 60% power efficiency independent of the magnetic field intensity. When an 8 kG magnetic field intensity was used, the output RF pulse duration (Fig.3, bottom left ) was (50 ns) shorter than the input electrical pulse. At lower magnetic field intensities the output pulse duration lengthened, and it reached the full input electrical pulse duration at  $B_z \approx 3$  kG (Figs.3, bottom: middle and right). At this level of magnetic field intensity the energy efficiency of the device was 50%. Changing the frequency of the external input RF by  $\pm 5$  MHz reduced the output power by 3 dB.

### Theory

The high efficiency and the low solenoidal field needed to focus the IREB have never been observed before in narrow gap RKAs.

It had previously been shown<sup>(13)</sup> that, at a critical magnetic field intensity, the propagation of a magnetically focused annular IREB inside a smooth drift tube could be disrupted by inserting a single small wall perturbation. The energy of any electron inside the drift region  $(\gamma_{inj}-1)m_0c^2$  is shared between kinetic energy  $(\gamma_0-1)m_0c^2$  and potential energy  $\Phi=(m_0c^2)I_s/(I_0\beta_{||})$  where  $I_0$  is the beam current  $I_s=(2\pi\epsilon_0m_0c^3)(e \ln(r_w/r_b))$ ,  $\beta_{||}=v_{||}/c$  and  $v_{||}$  is the beam velocity parallel to the magnetic field. The kinetic energy can be divided into parallel kinetic energy,  $E_{||}$ , and perpendicular kinetic energy,  $E_{\perp}$ . At the vicinity of a wall perturbation the potential energy residing in the IREB increases, thus slowing down the electrons and reducing their kinetic energy. While propagating through the potential hill, electrons gain rotational velocity under the combined influence of an increased radial (self) electric field and the axial (external) magnetic field. The gain in perpendicular energy is balanced by a drain from the parallel energy. The rotational energy increases with a decrease in  $B_z$ . At a critical magnetic field the drain on the parallel energy is so large that electrons stop and a virtual cathode is formed.

In narrow gap RKAs, wall perturbations (i.e., gaps) were inserted in the drift tube walls. A strong axial magnetic field (10 kG) was needed for RKAs to perform stably. At low magnetic field intensity a virtual cathode was formed and the RKA mechanism was disrupted. When the narrow gaps were replaced by the inductively loaded wide gaps, the potential hill was almost eliminated. Here, a lower magnetic field intensity (3 kG) was sufficient for the RKA to operate.

The large improvement in the energy efficiency of the wide gap RKA at a 3-kG magnetic field can be explained by examining the radial motion of test electrons. These electrons are located on the beam envelop and are under the influence of the self and applied electric and magnetic fields. The electrons' position (r,z) inside the gap can be evaluated from the radial force equation applicable for an immersed cathode and azimuthal symmetry:

$$\frac{d}{dt}[\gamma_p m_0 \frac{dr}{dt}] = \frac{\mu_0 e I c}{2 \pi r} \frac{[1 - \beta_p \beta_b]}{\beta_b} - 0.25 \gamma_p m_0 \omega_{ce}^2 [1 - (\frac{r_0}{r})^4] r$$

$$z = z_0 + \int \beta_p c dt \quad (1)$$

where  $z_0$  is the position of the gap entrance,  $r_0$  is the initial radial position of the test electron,  $\omega_{ce} = eB/(\gamma_p m_0)$ ,  $\beta_J = v_J/c$ , the subscript J stands for b (= beam) or p (=test particle) and  $v_b$ ,  $v_p$  are the beam and the test electron velocity. By neglecting rotational and radial energies one obtains  $\beta_J = (1 - \gamma_J^{-2})^{1/2}$ . The kinetic energy  $(\gamma_J - 1)m_0 c^2$  was calculated from the injected energies  $(\gamma_{J, inj} - 1)m_0 c^2$ , from the height of the potential hill and from the axial voltage across the gap:

$$\gamma_{J, inj} = \gamma_J + \frac{I}{I_s \beta_b} + \frac{e}{m_0 c^2} \int \mathcal{E}_z dz \quad (2)$$

The instantaneous beam current can be expressed as  $I = I_0 [1 + \sum (A_n \sin(n\omega t) + B_n \cos(n\omega t))]$  where  $A_n$  and  $B_n$  are time independent coefficients. The electric field along the gap,  $\mathcal{E}_z$ , consisted of two components: (1) An inductive electric field that originated from the transit-like interaction of a bunch with the inductive structure<sup>(4)</sup>. (2) A resistive bipolar field,  $\mathcal{E}_R \cos(\pi z/D)$  where  $\mathcal{E}_R = \Re I_0 A_1 \sin(\omega t + \varphi)$ ,  $\Re$  is the shunt impedance,  $D$  is the gap length,  $z = v_p t$ , and  $\varphi$  is the phase (see fig. 2(A)) of the test electron. Note that when  $\beta_b = \beta_p$ , eq.1 is the envelope equation for a modulated IREB propagating through a wide gap. Equation 1 was solved numerically for test electrons with initial energies greater, smaller and equal to the beam electron energy. The following results were general in nature:

(1) The radial position of the test electrons,  $r$ , was an oscillatory function of the axial distance,  $z$  (Fig.4). The amplitude and wavelength of the oscillations grew with  $1/B_z$  and with the instantaneous beam current,  $I$ . The largest amplitude occurred at the third gap where the peak modulated current is maximum.

(2) There were three classes of test electrons:

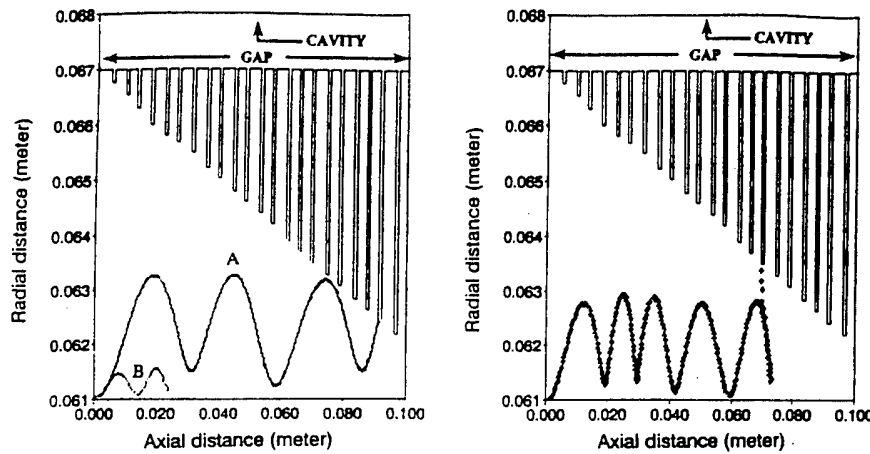


**Figure 4.** (Left) Trajectories of 500 keV test electrons,  $\varphi = \pi$ , traversing the output gap. (A)  $B_z = 3.6$  kG and (B)  $B_z = 8$  kG. (Right) Trajectory of a 375 keV test electron traversing the output gap,  $\varphi = 0.8 \pi$ ,  $B_z = 3.6$  kG. At  $B_z = 3.6$  kG the test electrons lost >65% of their total energy crossing the gap.

(a) Electrons that crossed the whole length of the gap, losing or gaining energy depending on the injection phase.

(b) Electrons that moved axially forward but intersected the radially converging structure located in the gap. (A in Fig. 4, left)

(c) Electrons that lost all their *kinetic* energy before reaching the end of the gap and reflected backward ( $\beta_b > 0$ ,  $\beta_p < 0$ ). At low magnetic field, these test electrons drifted radially and were removed from the beam by the inductive structure before regaining energy back from the RF field (Fig. 4, right). At high magnetic field these electrons moved back almost collinearly, missing the walls or structure and gaining energy from the RF field (B in Fig. 4, left).

(3) The radially converging axisymmetric grounded structure, used in the converter, transformed the beam potential energy to electron kinetic energy as the beam propagated along the wide gap. The simulation code confirmed the reduction in the potential energy residing in the IREB and the increase in electron kinetic energy as the modulated beam propagated in the radially converging drift region (Fig. 2C). Note that only kinetic energy can be converted into RF.

(4) By optimizing the experimental parameters (e.g., electric and magnetic field intensities) test electrons with  $\gamma_{p,inj}$ , that satisfy  $\gamma_{b,inj} + 0.4 > \gamma_{p,inj} > \gamma_{b,inj} - 0.4$ , lost >60% of their energy to the RF field.

To estimate the system efficiency, we assumed that the beam and the test electrons have the same energy (500 keV). The current profile was taken from Fig. 2B. We approximated the modulated current as a train of  $\cos^2$  pulses. Each pulse had a base to base width of 0.45 of the period and peak current of around  $I = 29$  kA. A DC current of 1 kA was superimposed on the modulated current. The efficiency was set equal to the sum of all the energies lost by test



electrons (which were injected with phases between 0 and  $2\pi$ ) divided by the sum of their initial energies. The efficiency was optimized by varying the amplitude of the gap axial electric fields. Cases were rejected when any test electron was reflected and not absorbed by the structure. Under these conditions we obtained a maximum of  $\approx 65\%$  efficiency with a magnetic field intensity of 3.6 kG.

### Conclusion

In conclusion we have shown that wide gap RKAs can be efficient sources for RF. We believe that the same mechanisms can also be employed in high power classical (non-relativistic) klystrons provided an annular beam is used. With such a system, klystron efficiency can be increased without resorting to depressed collector techniques.

### Acknowledgment

This work was supported by Office of Naval Research.

- [1] For example see Wilson, P. B. in Physics of High Energy Accelerators, edited by Carrigan, R. A. *et al.*, AIP Conference Proceedings No. 87 (American Institute of Physics, New York, 1982) pp. 450-563.
- [2] Friedman, M and Serlin, V., *Phys. Rev. Lett.*, **55**, (1985), pp. 2860-2863.
- [3] Serlin, V. and Friedman, M., *IEEE Plasma Trans.*, **22**, (1994), pp. 692-700 and references within.
- [4] Friedman, M., *et al.*, *Rev. Sci. Instrum.*, **61**, (1990), pp. 171-181.
- [5] Friedman, M., and Serlin, M., *IEEE Trans. On Electrical Insulation*, **23**, (1998), pp. 51-56.
- [6] Colombant, D. G., *et al.*, *SPIE*, **1407**, (1991), pp. 13-31.
- [7] Colombant, D. G. and Lau, Y. Y., *Phys. Rev. Lett.*, **64**, (1990) pp.2320-2323.
- [8] Friedman, M., *et al.*, *Phys. Rev. Lett.*, **74**, (1994), pp. 322-325.
- [9] Friedman, M., *et al.*, *Phys. Rev. Lett.*, **75**, (1995), pp. 1214-1217.
- [10] A. Palevsky, A. and Drobot, A., Proceedings of the Ninth Conference on Numerical Simulation of Plasmas, Northwestern University, Evanston, IL, July 1980 (unpublished).
- [11] Fazio, M. V. *et al.*, *IEEE Plasma Trans.*, **22**, (1994), pp. 740-749.
- [12] Levine, J. S. and Harteneck, B. D., *APL. Phys. Let.*, **65**, (1994) , pp. 2133-2135.
- [13] Friedman, M., *APL. Phys. Let.*, **24**, (1974), pp. 303-305.

## POWERFUL FEM-GENERATOR DRIVEN BY MICROSECOND SHEET BEAM.

M.A. Agafonov\*, A.V. Arzhannikov\*, N.S. Ginzburg\*\*,  
N.Yu. Peskov\*\*, S.L. Sinitsky\*, and A.V. Tarasov\*.

\* Institute of Nuclear Physics, Novosibirsk,

\*\*Institute of Applied Physics, N-Novgorod, Russia.

**Abstract.** Results of experimental and theoretical investigations on creation of powerful mm-band generator driven by a sheet beam, are presented. Microsecond pulse of mm-radiation with 200J energy content has been obtained in the experiments. Possibility to increase this energy content up to tens kJ, has been shown.

**Introduction.** Creation of pulse powerful (1-10 GW) sources of millimeter and submillimeter radiation gives new opportunities for scientific research and industrial applications. Taking into account of the possibility of energy recuperation for the used electron beam and a repetitive regime of the generator operation these sources can be used for solving the following problems: to clean top layers of the atmosphere from pollution as well as to restore the Earth's ozone layer, to transmit an energy in cosmic space and to create a plasma with the fusion parameters in a magnetic confinement reactor, to produce micrograin ceramics and etc. In order to achieve the mentioned level of the wave power one needs to pass an electron beam with a few tens of GW power through an electrodynamic system of the generator. For reaching such level of the power the beam current should be a few tens of kA at the electron energy about 1 MeV. The most promising way to realise the passing of such high current beam, is to use one with a strongly elongated cross section, so called ribbon or sheet electron beams. The millimeter wave generator driven by this beam, have to be constructed on outline of Free Electron Maser (FEM) or of Cyclotron Auto Resonance Maser (CARM). Starting from the end of the 80-s we investigate the possibility to create the FEM-generator on the base of the sheet beam [1,2]. Three main problems are solved: to generate the ribbon or sheet electron beam with a high current density ( $\cong 1 \text{ kA/cm}^2$ ) and a small angular spread ( $\Theta \cong 10^{-2}$ ), to transport the beams through a slit vacuum channel with an undulator magnetic field, to achieve the highest efficiency of an energy transfer from the E-beam to a spatial coherence electromagnetic waves. The given report is devoted to description of the solving of these problems.

**Generation of sheet beam and it's passing through a plane undulator.** For generation of the beams with the mentioned current density and the appropriate ( $\sim 10\mu\text{s}$ ) pulse duration a vacuum diode with a magnetic insulation of a cathode - anode gap has been chosen for the U-2 accelerator [1]. Experiments with this diode were carried out on the schematic like one presented in Fig.1. The thickness of the beam was varied in the interval from 20 mm up to 6 mm and we called one the ribbon beam. It has been shown that in case of cathode made of a graphite fibrous material, at 1MV voltage the diode with the magnetic field 5-10 kG generates the electron beam with the current per unit of the beam width (linear current) about 1 kA /cm and the pulse duration more than 5 $\mu\text{s}$ . The current density of such beam is reasonable enough for using in the FEM generators. As to an angular spread of the electrons the main factor for it's increasing is that the movement of the relativistic electrons in such diode is occurred on the boundary of preservation of the first adiabatic invariant. Numerical simulation and analytical consideration of the electron motion in

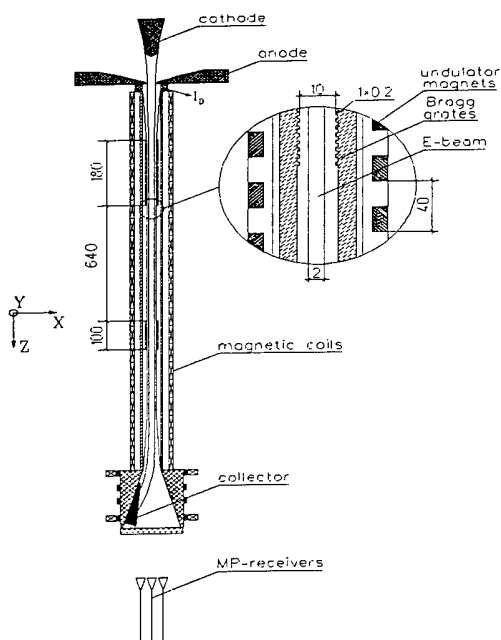


Fig. 1. Schematic of the experiment with the ribbon beam in a plane magnetic undulator.

experiments a charge neutralisation of the beam become in the time  $1 \mu\text{s}$  (see [1]) at the beam duration more than  $5 \mu\text{s}$ . So, the large part of the beam duration the electron flow was neutralised and these conditions the generation of electromagnetic radiation should be realised at a small spread of the electron velocities. It gives the opportunity to achieve the high electron efficiency in this generator. The first series of our experiments on passing of the beam through a slit vacuum channel with an undulating magnetic field, was performed at the U-2 device in a bounder of 80's and of 90's [2,3]. The schematic of the experiments is shown in Fig.1. The longitudinal magnetic field in the slit vacuum channel is created by coils. The transverse undulating component of the field is produced by a set of rods made of ferromagnetic material. These rods are stacked in the vacuum channel along the beam width, i.e. along the Y axis. Produced by such way the transverse component of the magnetic field remains approximately on the same level (about 1 kG) at a variation of the longitudinal magnetic field from 3 up to 13 kG. In the first experiments the gap between copper walls of the vacuum channel where the beam was passing, was 20 mm. The thickness of the beam was 4 mm. At this thickness and at a smaller one we call it the sheet beam. After passing through the channel the sheet beam is shifted from the middle plate of the chamber and absorbed by a graphite collector (See Fig. 1). The millimeter radiation is propagated in the channel and then go out from the vacuum chamber through a window. We measured beam parameters and time behaviour of the wave power in the band from 2 mm up to 15 mm wavelength. The total energy in the pulse of the mm-radiation was also measured by a calorimeter. It was shown in the experiments that in the ubitron regime of generation it was managed to pass the beam with linear current  $\sim 1\text{kA/cm}$  through the slit channel with one meter length. In these experiments we did not use any methods for selection of frequencies and modes of oscillations and a spontaneous generation was observed in wide range of wavelengths: 2 - 15 mm [2,3]. The power of the mm-radiation was achieved 300MW.

**Wavelength selection by 1-D Bragg grating resonator.** In the papers [3-5] we have pointed out the way of producing a monochromatic coherent radiation. This way is based on using of Bragg gratings as a selective element in such generator. One-dimensional Bragg

the diode for geometry realised in the experiments, give the decreasing of the angular spread of the particles from  $10^{-1}$  to the level  $5 \cdot 10^{-3}$  when the magnetic field strength increases from 2 kG up to 10 kG. This value of the angular spread is quite acceptable for using such beam in FEM. It should be pointed out that the angular spread of the electrons which trajectories are located near the plane of symmetry of the diode, is in order of magnitude less than the mentioned level. For the angular spread  $\Theta \approx 5 \cdot 10^{-3}$  the corresponding spread of the longitudinal velocities of the electrons is estimated on the level of  $\Delta\beta_1 \approx \beta_0 \cdot \Theta^2 = 3 \cdot 10^{-5}$ . In case of the electron beams with the high current the considerably greater contribution to the changing of the longitudinal electron velocity may be produced by the electrostatic potential induced by space charge of the electrons, but in our ex-

gratings with 2 mm spatial period of corrugation and 0.2 mm corrugation depth were used for the wavelength selection in our experiments [5, 6]. A resonator of the microwave generator was formed by a pair of the entrance copper gratings with the length of corrugated surface of 180 mm and by the second pair of the exit gratings with length of 100 mm (see Fig.1). The gap between the gratings was 10 mm and the distance between the entrance and exit pairs could be varied. This distance determined the length of resonator in which the radiation interacting with the electron beam, was accumulated. The calculated coefficient of reflection for TEM-mode of 4 millimeter radiation had a value of 95% for the entrance pair and 75 % for the exit one and, as a result, this resonator should select the radiation with a wavelength close to 4 mm. At the optimal value of the longitudinal magnetic field  $B_{opt} = 9.5$  kG the electron efficiency of this generator should be about 7% according to the computer simulations (see Fig.2). Measurements of selective properties of such resonator at the distance 340 mm have shown good selection properties for the wavelength 4 mm (see [5]). Oscillogramms for the typical short with

Fig. 2. Efficiency of generation as a function of time.

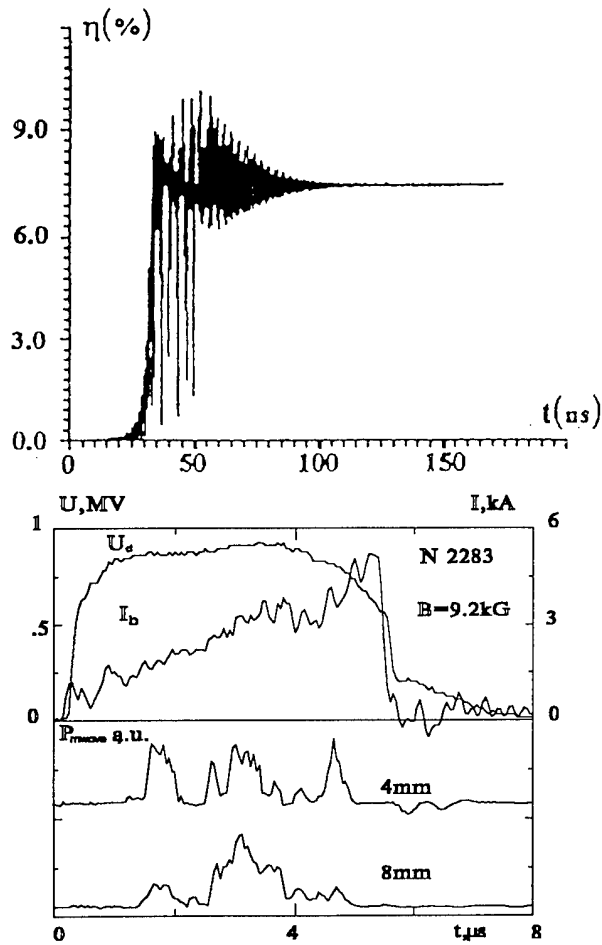


Fig. 3. Oscillogramms characterizing the generation of 4 and 8 mm wavelength.  $U_d$  is the diode voltage,  $I_d$  is the beam current at the entrance of resonator.

this resonator are represented in Fig. 3. The cross section of the beam in this experiment was  $4 \times 120$  mm. The generation of the millimeter radiation started in  $1 \mu s$  later than the beginning of the beam and the duration of the mm-radiation was  $3 \mu s$  at  $5 \mu s$  beam pulse duration. The total energy of the millimeter radiation in the pulse measured by the calorimeter in these optimal conditions, was on the level 100J. The main fraction of this energy was contained in the radiation with the wavelength  $\lambda \approx 4$  mm. According to this value of the energy content the power of the radiation was on the level of some tens of MW in these experiments. The level of power in these experiments was considerably lower than the result performed earlier without any resonator [2,3]. In the next series of the experiments we increased the distance between the entrance gratings and the exit ones up to 640 mm and decreased the thickness of the sheet beam from 4 mm down to 2 mm at the same current. These changing allowed us to increase the energy content in the microsecond pulse of the mm-radiation up to 200J. Taking into account that the energy content of the beam  $Q_b = 5$  kJ, we estimate the electron efficiency of the generator on the level 4% for these experiments. This value is in two times smaller than one predicted by the theory for the case of vanishing small longitudinally velocity spread.

**Prospect to increase power. 2-D distributed positive feedback.** In order to increase the radiation power on extremely high level ( $\sim 10\text{GW}$ ) it is necessary to generate the electron beam with the appropriate energy content. At the U-2 accelerator the electron beam has been already obtained with the cross section  $3.5 \times 130\text{ cm}$  and the energy content about of  $0.4\text{MJ}$ . The angular spread of the beam is less than 2 degrees (see [8]). So, the beam is sufficient for powerful FEM-generator operation, it exists. But the problem is that the one-dimensional gratings resonator can not provide the allocation of single mode of the oscillations on all width of the beam because the width is too large. For exchanging of energy between waves propagating along the beam in various points on the width we have to create resonator on the base of two-dimensional Bragg gratings [4-5,7]. It means that the surface of the plates is corrugated in two directions simultaneously. The solution of stationary problem for considered case gives the spectrum of eigen frequencies of the resonator, formed by two corrugated plates. TM-waves ( $E \parallel Y$  in Fig.1), including the lowest wave - TEM, have sufficiently large coupling parameters for this resonator. This polarisation of radiation can be used in such variants of FEL, as CARM and ubitron with guiding magnetic field. The consideration of interaction of the sheet REB with partial waves of the 2-D Bragg resonator in non-stationary approximation was made in [7]. The analysis shows that this scheme of the positive feedback permits to increase the width of the beam interacting with radiation at a keeping of the single mode of oscillations by decreasing of a coupling parameter of the waves (it can be reached, for example, by decreasing of corrugation depth). It should be taken into account, that the time of establishment of stationary regime is increased with the growth of the width of system. On the base of the performed theoretical consideration we estimate parameters of the FEM-generator with the ribbon beam obtained at the U-2 device. At the wavelength  $4\text{ mm}$  this generator needs  $\sim 150\text{ ns}$  for transition on stationary level of radiation power. The electron efficiency of the device in the stationary regime is evaluated on the level  $\sim 15\%$ . The power of the radiation should be about  $20\text{ GW}$  and the energy content -  $50\text{kJ}$ .

**Conclusion.** The microsecond pulse of mm-radiation with the energy content  $100 - 200\text{J}$  has been generated by the FEM with a sheet electron beam. The microsecond ribbon beam suitable for FEM has been obtained at the energy content  $0.4\text{MJ}$ . It is shown by the theoretical analysis that FEM-generator on the base of ribbon beam can be operated in a single mode regime at a few tens of  $\text{GW}$ .

1. A.V.Arzhannikov, V.T.Astrelin, V.A.Kapitonov et. al. Proc. of 9-th Intern. Conf. on High-Power Particle Beams, Novosibirsk, 1990, Vol.1, p. 256-263.
2. A.V.Arzhannikov, S.L.Sinitsky, M.V.Yushkov. Twelfth Intern. Free Electron Laser Conf., Paris, France, 1990. Program and Abstract, p. 105.
3. A.V.Arzhannikov, S.L.Sinitsky, M.V.Yushkov. Preprint of Institute of Nuclear Physics SB AS USSR 91-85, Novosibirsk, 1991.
4. N.S.Ginzburg, N.Yu.Peskov, A.S.Sergeev. Piz'ma v ZhTF, 18 (9), 1992, p. 23-28.
5. A.V.Arzhannikov, N.S.Ginzburg, V.S.Nikolaev et. al. 14-th Intern. Free Electron Laser Conf., Kobe, Japan, 1992, Technical Digest, p.214.
6. A.V.Arzhannikov, V.B.Bobylev, S.L.Sinitsky, A.V.Tarasov, N.S.Ginzburg, N.Yu.Peskov. Nucl. Instrum. Methods in Phys. Research, A358 (1995), p. 112-113.
7. A.V.Arzhannikov, N.S.Ginzburg, N.Yu.Peskov, A.S.Sergeev, S.L.Sinitsky. Nucl. Instrum. Methods in Phys. Research, A358 (1995), p. 189-192.
8. A.V.Arzhannikov, V.B.Bobylev, V.S.Nikolaev, S.L.Sinitsky and A.V.Tarasov. 10-th Intern. Conf. On High-Power Particle Beams, San Diego, 1994, p. 136-139.

# PULSE SHORTENING IN HIGH POWER MICROWAVE SOURCES

James Benford and David Price\*,  
 HPM Division, Physics International  
 2700 Merced St., San Leandro, CA 94577  
 and

Gregory Benford  
 Physics Dept., UC Irvine, Irvine CA 92717

Observations show that the ubiquitous pulse shortening problem is due to the formation of plasma, electron streaming, RF breakdown and beam disruption in the devices. We review recent experiments in terms of these mechanisms. Linear beam devices exhibit all these mechanisms; in relativistic magnetrons the dominant mechanism is resonance destruction by cathode plasma, probably from water contamination of the surface. We call for the introduction of improved surface conditioning, cathodes which do not produce plasmas and increased effort on measurements of the RF and plasma properties of HPM sources.

## INTRODUCTION

Higher power reduces pulse duration, limiting present-day sources to a few hundred joules. Is this limitation fundamental, or can we avoid it entirely? Pulse shortening is usually described as "gap closure" and "RF breakdown", but these mechanisms do not describe the breadth of phenomena observed. There are several kinds of effects layered so that they must be addressed separately.

We have inherited from the microwave tube community a *plasmaless* view of sources as only electron beams, conducting structures, bunching and radiation. Yet pulse shortening is largely due to plasma effects. The high energy densities of these beams produces plasma anywhere the beams terminate. Many other causes, such as x-rays, allow plasma generation throughout the device. Therefore we need to rethink how HPM sources really work, taking into account the plasma in them.

An extended review article<sup>1</sup> is in preparation; here we present key recent results which go some distance toward determining the principal causes of pulse shortening.

## MECHANISMS

We categorize the physical means by which pulse shortening occurs as:

Plasma Generation. Anywhere plasma appears, shorting of the pulsed power or the RF field can result. Examples: *Gap Closure.* Both cathode and anode plasmas can move axially and radially, resulting in diode impedance change, which then reduces beam/wave coupling in the Slow Wave Structure (SWS) *Electron Beam Expansion.* Electron beams generated from plasma-based sources can expand dramatically in radius because the collisional plasma from which they are extracted can diffuse across transverse magnetic fields, again affecting the beam/wave coupling processes. *Beam Interception.* Expanding beams intercept surfaces, for example, on the cathode side of the diaphragm surface or on the SWS. This generates moving plasma that disrupts the coupling between the beam and electromagnetic modes. *Electron Beam Collection.* When the electron beam dumps onto a collector surface the plasma may stream back along magnetic field lines into the microwave generation region.

Electron Streaming. Beam electrons generated from the cathode plasma can move upstream, away from the accelerating gap, and cause deterioration of the diode impedance characteristics. Secondary electrons from the collector may overcome

---

\*Work supported by the AFOSR HPM MURI Program

the beams' potential barrier and stream into the SWS.

**RF Breakdown.** High microwave electric fields within cavity structures can produce surface breakdown which disrupts the generation of microwaves. This is highly sensitive to surface treatment in cavity structures, vacuum conditions and any plastic components (or other hydrocarbon sources) in vacuum systems. Breakdown may occur on the output window due to surface flashover phenomena. Closely related is *Multipactoring*; microwave fields accelerate particles (field and photoemitted electrons, ionized residual gas molecules, plasma, etc.) toward surfaces, which deteriorate under the bombardment.

**Beam Disruption. Instabilities.** Since beam expansion can destroy the geometry needed for emission, resonant scattering of beam electrons may be critical. This occurs most easily when the beam itself produces waves in the background plasma which are very nearly resonant with the beam velocity; i.e., those which correspond to space-charge oscillations on the beam. Instabilities previously dismissed for short pulse experiments can develop in long pulses and decrease beam/electromagnetic structure coupling. Cross-B diffusion can do this from a variety of excited electric modes. Magnetic filamentation can destroy cylindrical symmetry, but requires a background plasma for instability. These seem the most probable interruption instabilities. Computer simulations have assumed azimuthal symmetry and ideal vacuum conditions. Complications of three dimensions and plasma may allow instabilities to develop over  $\sim 100$  ns.

**Beam Drift and Diffusion** It's clear experimentally (see below) that high microwave fields can cause transverse beam drift, beam diffusion across field lines and eventual beam breakup. This could arise simply by perturbing the beam electron orbits so much that they oscillate, reverse, etc. In the diode, electromagnetic fields evanescent upstream from the cutoff neck may nevertheless interact with the electron beam and beam-generated plasma in that region, causing diffusion.

## LINEAR BEAM DEVICES

The most extensive series of experiments on the cause of pulse shortening in linear beam devices has been done by the group at the General Physics Institute (GPI), Russian Academy of Sciences in Moscow. The principals are O. T. Loza, P. S. Strelkov, and S. N. Voronkov. In an extensive series of experiments they have shown in detail that pulse shortening accompanies sudden appearance of undesirable plasmas<sup>2</sup>. They use an electron beam produced in a magnetically-insulated diode emerging through a graphite anode diaphragm and propagating through a slow wave structure ending in a horn with a vacuum dielectric window.

When a linear source geometry was used, so that the electron beam directly struck the collector, electrons scattered back from the collector, overcame the 100 kV beam potential and traveled back along the axis outside the beam, hitting the slow wave structure. Later, arrival of collector plasma provoked a microwave breakdown and terminated the microwaves. To prevent this the electron beam was diverted from the accelerator transversally and a magnetic trap was placed at the collector. The curvature drift in the trap prevented plasma and electrons from entering the SWS. This doubled the microwave pulse duration from 200 ns to 400 ns. In fact, anything that produces electrons in the slow wave structure will terminate the microwaves because electrons moving in such a high field region create a plasma load which absorbs microwave energy. Even very high RF fields themselves can initiate the discharge.

Plasma formed on the cathode expands both axially and radially. Axial motion can short the electron generator to the anode diaphragm if accompanied by radial motion. Transverse expansion of the cathode plasma at velocity about 0.1 - 0.5 cm/ $\mu$ s causes the electron beam to approach the slow wave structure. Microwave generation in the system cuts off when beam electrons strike the diaphragms. Another mechanism for short circuiting of the SWS by plasma is arrival of plasma from the collector at axial velocity about 10 cm/ $\mu$ s.

Another effect suggested by Bugaev is that the RF field in the slow wave structure causes motion of the electron beam across field lines. The drift velocity  $V_d$  is due to the  $E_z$  and  $B_\theta$  of the TM mode fields. For typical fields at 200 MW of 100 kV/cm and 1 kG, radial drift is 0.6 cm/ $\mu$ s. Traversing a 30 cm slow wave structure displaces the beam several millimeters, consistent with measurements of beam growth by 2 mm obtained by the GPI group. They show that when the SWS is hidden by inserting a metallic sleeve, cross-field drift is much smaller.

As evidence for the microwave discharge in the SWS, Benford et. al.<sup>3</sup> reported emerging wall plasma in BWOs, measured by spectral lines of H and C (earliest, probably from anode-cathode and wall) and Cu (later, from the wall). Neutral atom radiation appeared about 100 ns after microwave cessation, with copper from the wall 200 ns afterward. Oscillating electric fields were as high as 34 kV/cm accompanied 75 MW microwaves throughout the 60 ns power pulse, with lower frequency fields of 10 kV/cm persisting until beam shutoff, presumably from Gould-Trivelpiece modes.

Beam expansion can destroy the geometry needed for emission. With typical E-fields 35 kV/cm, and persistence of 10 kV/cm fields after microwaves cease, the average correlation length  $d$  of resonant fields determines scattering:

$$X = 0.5 \text{ cm} \left( \frac{E}{10 \text{ kV/cm}} \right) \left( \frac{B}{10 \text{ kG}} \right)^{-1} \sqrt{\left( \frac{d}{\text{cm}} \right) \left( \frac{L}{10 \text{ cm}} \right)}$$

It is difficult to guess  $d$ , but  $X$  scales only as  $d^{1/2}$ , together with the system length,  $L$ . Even 10 kV/cm electric fields may cause high beam spreading if  $d \sim \text{mm}$ . Such significant expansions suggest that beam scattering alone may cause microwave cutoff. If so, only increasing  $B$  or lowering  $d$  through more precise geometry seem practical cures, and both are expensive. Finally, if plasma invades the resonant region, or is already there (as in the plasma BWO), the beam can split into magnetic filaments.

## RELATIVISTIC MAGNETRONS

Recent experiments at Physics International (PI) show that the time variation of the microwave frequency is the signature of the mechanism that shortens the microwave pulse. The mechanism appears to be motion of cathode plasma. A sequence of modes are excited sequentially until either 1) the phase velocity distribution associated with the newly excited magnetron mode changes so that it comes to have no overlap with the circulating electron azimuthal velocity distribution, ending the pulse or 2) the frequency of the next newly excited mode is below the cut-off of the magnetron output circuit, so microwaves are generated but cannot be extracted.

Explosive emission generates a cool, collisional plasma near the cathode surface. Optical measurements at both MIT and Varian have observed plasmas. Correlation of the plasma motion with the microwave pulse shortening is difficult because the dense plasma radiating in the optical is not necessarily the plasma that determines the RF boundary condition.

With constant applied DC voltage and magnetic field the effect of plasma expansion across the anode-cathode gap at velocity  $v_p$  is to shift  $\omega$ , the electron bunch angular frequency:

$$\frac{1}{\omega} \frac{d\omega}{dt} = \frac{2v_p}{(r_a - r_c)}$$

The observed magnitude of the frequency change can allow one to infer the dominant plasma generation site (either the cathode or the anode surface) within the magnetron diode.

For the two magnetrons under consideration, operating near 1.2 GHz over 100 ns, this effect should shift the resonant layer frequency upward by 60 MHz to 250 MHz. We observe upward shifts of  $\sim 50$  MHz, consistent with this model with  $v_p \sim 2$  cm/ $\mu$ s. Many researchers have observed  $1 < v_p < 3$  cm/ $\mu$ s, which can be consistent with the cool ( $T_i \sim 1-10$  eV) plasma we expect only if the plasma ion mass is low.



This implies that the main plasma constituent is hydrogen. The source of the hydrogen plasma is likely water vapor condensed on the interior surfaces.

In the PI magnetrons the slow wave frequency shift due to the expanding plasma is of opposite sign to that of the electron bunch angular frequency shift. Instead of being steady, the Bunemann-Hartree resonances are time varying as described above. The higher the magnetic field the longer the time required for the resonance to "rotate over" the operating point. To confirm this model, we fixed the driver voltage at 250 kV and parametrically mapped the magnetic field and found the  $\pi$ -mode microwave power maximum at 1.58 kG. As we increased the field above this value the output power *should* decrease as the operating point passes to the high field side of the Bunemann-Hartree resonance, where oscillations will not grow. But it does not. Instead the microwaves continue to occur but their onset time was continuously delayed as we increased the applied magnetic field strength above 1.58 kG. Clearly the resonance condition is changing with time. The data is consistent with a cathode plasma motion model with  $v_p \sim 1$  cm/ $\mu$ s.

The above plasma-driven effects can be reduced by ridding the system, especially the cathode, of water. Elevating cathode temperature drives away water molecules and prevents their subsequent reabsorption. This should increase the effective plasma ion mass by a factor of about ten, in turn reducing the plasma expansion rate and increasing the microwave pulse length by about three.

## CONCLUSIONS

These observations show that most pulse shortening is due to mechanisms dependent on the plasma formation. The GPI group showed pulse extension by controlling the electron flow to reduce plasma formation and backward injection of beam and secondary electrons. In virtually all contemporary HPM sources wall cleanliness is not sufficient to prevent plasma formation from surface layers of water. Improved surface conditioning is

essential to pulse lengthening. The cathode plasma formed in the explosive emission process leads to pulse shortening, so we must investigate non-plasma beam production, such as the new field emission and ferroelectric cathodes.

There is evidence in linear beam devices for beam cross-field diffusion enhanced by high microwave fields. Interaction of microwaves with the electron beam deteriorates beam quality so that it becomes unable to produce microwaves and moves radially to intercept the slow wave structure. It sometimes causes severe break-up of the beam. Means of reducing these microturbulent effects must be found, preferably by avoiding instability onset altogether.

The HPM community must better measure the RF and plasma properties of HPM sources to better understand pulse shortening. More detailed diagnostics are needed, particularly of microwave field distributions in-situ, plasma distribution and velocity distribution of both electrons and ions.

## REFERENCES

- [1] J. Benford and G. Benford, "Pulse Shortening in High Power Microwave Sources - A Review," in preparation.
- [2] O.T. Loza, P.S. Strelkov and S.N. Voronkov, Plasma Phys. Rpts., **20**, 418 (1994).
- [3] X. Zhai, E. Garate, R. Prohaska, A. Fisher and G. Benford, Phys. Lett. A., **186**, 330 (1994).

## GENERATION EFFICIENCY AND RADIATION STABILITY OF MULTIWAVE CERENKOV GENERATORS

M.P.Deichuly, V.I.Koshelev, A.A.Petkun

*High Current Electronics Institute, Siberian Division of Russian Academy of Sciences,  
Tomsk, 634055, Russia*

### Abstract

Relativistic electron beams - electromagnetic field interaction regimes in a 3-cm wavelength range multiwave Cerenkov generators (MWCG) have been investigated both theoretically and experimentally. The influence of the drift tube length, magnetic field value and hollow electron beam diameter on the efficiency, stability, wavelength, spatial-temporal structure and temporal dynamics of radiation spectrum in MWCG with a two-sectional slow-wave structure (SWS) has been studied. The stable generation regimes with generation efficiency up to 10% have been found. Optimization of a beam-field interaction in MWCG with a three-sectional SWS allowed to increase the radiation efficiency up to 25%.

### Introduction

The MWCG investigations can be conditionally divided into two stages. The main task of the first stage was to obtain experimental evidences of a possibility to realize effective one-frequency generation regimes as well as to obtain high-power ( $\leq 10^{10}$  W) radiation with satisfactory spatial and temporal coherence. The results of experimental and theoretical studies obtained at the first stage are presented in [1, 2].

The task of the second stage are detailed theoretical and experimental investigations of relativistic electron beams (REB) - electromagnetic field interaction in overmoded slow-wave structures near the  $\pi$ -type oscillations of  $TM_{01}$ -mode in order to realize high-efficient and stable regimes of radiation generation in MWCG. Theoretical (using a linear theory [3]) and experimental investigations [4-6] carried out recently revealed a determining influence of electron wave longitudinal resonances SCSW +  $TM_{01}$  (SCSW is the space charge slow wave) and a drift tube between a periodic waveguide sections on the main characteristics of MWCG and radiation.

### Experimental Investigation Results

The experimental investigations were carried out at a SINUS-7M accelerator. A  $2r_b = 10$  - 11.8-cm-diameter, 2-3-mm-wide hollow electron beam with the current  $I_b = 10$  kA was formed in a coaxial diode with magnetic insulation, the diode voltage  $U_d = 1$  MV. Pulse duration  $\tau_p = 40$  ns. A magnetic field changed in SWS region  $B = 5$ -15 kG. Radiation power was determined by the patterns in two ( $\theta$ - and  $\varphi$ -) polarizations measured in atmosphere. Radiation losses in a transmitting antenna were not controlled. To measure radiation spectral characteristics, bandpass filters with the band width of 0,5% were used.

The studies were carried out in two phases. At the first phase, MWCG with a two-sectional uniform (nonuniformity periods in the sections are equal) SWS were studied. In all the experiments, SWSs with the same internal diameter  $2R = 13$  cm were used.

A two-sectional SWS has the following geometry: the first section length  $L_1 = 13l$

( $l = 1,45$  cm,  $\lambda_\pi = 3,18$  cm); the second section length  $L_2 = 10l$ ; the drift tube length varied  $L_{dr} = 0 - 13.4$  cm. Dependence of the output radiation power  $P_\theta$  with indication of its instability from pulse to pulse on  $L_{dr}$  is presented in Fig. 1. Here and then the results obtained at the beam power instability no more than 20% and optimum values of a magnetic field and a gap between the beam and SWS are presented. As is evident from Fig. 1,  $P_\theta$  dependence on  $L_{dr}$  is a periodic one. The period is 1.6 - 1.7 cm that is close to the radiation half-wavelength.  $P_\theta$  instability from pulse to pulse varies from 8 - 10% to 100% for different  $L_{dr}$  and doesn't correlate with radiation power value. The following peculiar features of stable generation regimes can be noted: i) radiation

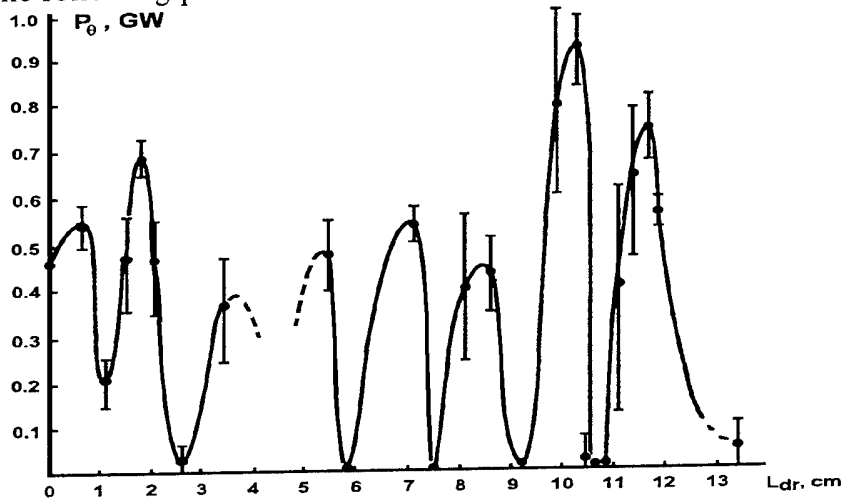


Fig. 1

power maxima with  $\phi$ -polarization correspond in time to maximum increase or decay of power with  $\theta$ -polarization that can point out the  $E_\phi$ -field influence in synchronization of the beam - field interaction in overmoded SWS; ii) radiation power part with  $\phi$ -polarization decreases to 10% of the full power (in

unstable regimes, this part reaches 50%); iii) disalignment of the beam in SWS in some limits doesn't result in the marked change of power though the pattern symmetry is distorted; iv) beam power instability increase doesn't result in proportional increase of radiation power instability (saturation of instability generation); v) temporal dynamics of the radiation pattern corresponds to the successive power decrease in its centre and its approximation in form to the pattern of  $TM_{01}$ -mode or, to be more precise, to the pattern of the sum of axially symmetric modes propagating in the overmoded SWS.

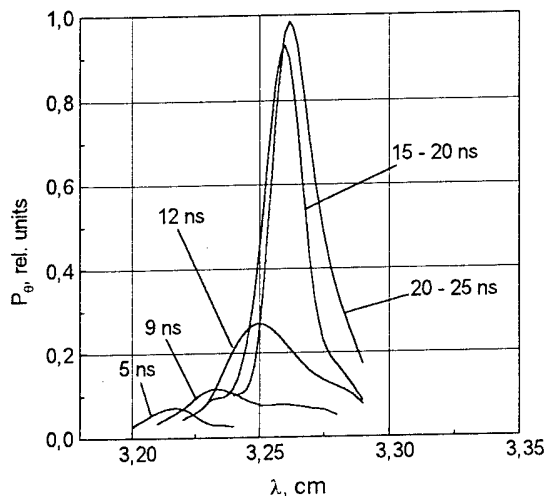


Fig. 2

Temporal dynamics of radiation spectrum depends on generation regime. Fig. 2 presents spectrum change in time for a stable regime. The short-wave spectrum part is seen to be ahead of the central spectrum one in time but it saturates faster and

even has some decay.

Radiation power dependence on the magnetic field has optimum at  $B_{opt} = 7 - 12$  kG shifting to the high magnetic fields when the gap between the beam and SWS  $b = R - r_b$  is decreased. Fig. 3 presents  $B_{opt}$  versus  $b$ . Such dependence is typical of stable generation regimes. Shaded region on the plane ( $B_{opt}$ ,  $b$ ) corresponds to  $< 20\%$

instability of radiation power. Decrease of  $B$  when is unchangeable or decrease of  $b$  at constant  $B$  result in the shifting of radiation spectrum maximum to a short-wave region and possible spectrum stratification when the spectrum maximum is shifted to the value larger than the half of the spectrum FWHM. When  $B$  is decreased and  $b$  is increased according to the dependence  $B_{\text{opt}}(b)$  (Fig.3), maximum in the spectral power distribution remains practically constant, generation is stable, and radiation pulse form is smooth. At the essential decrease of  $B$  relative to the curve  $B_{\text{opt}}(b)$ , radiation spectrum power, and radiation pulse form become irregular, unstable, and cutted-up, respectively. So, magnetic field influences the efficiency, stability, as well as dynamics of spectrum and radiation power.

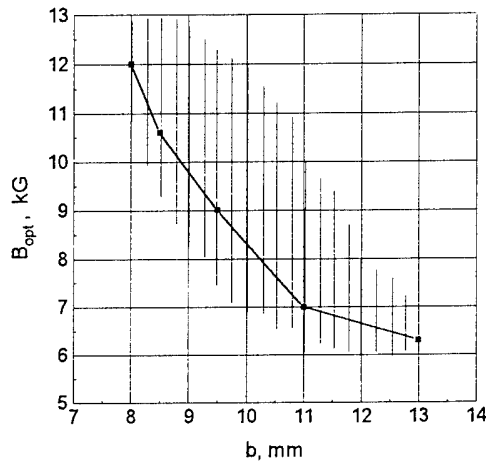


Fig.3

$\approx 1.5$  cm,  $\langle l_3 \rangle \approx 1.4$  cm) radiation pulses with the power  $P_0 = 2.3$  GW,  $P_\phi = 0.2$  GW, duration of 30 ns and spectrum width of  $< 1\%$  were obtained on the wavelength  $\lambda = 3.35$  cm. Symbol  $\langle \rangle$  means averaging of a period along the section length. The efficiency of generation radiation with  $\theta$ -polarization in the second case reaches 25% that is approximately two times higher than the efficiency of MWCG with a uniform two-sectional SWS.

### Nonlinear model and results of numerical simulation

The code created is an electrostatic particle- in- cell model in a cylindrical geometry. To determine proper waves of a finite SWS, the following procedure was used. Comparison of a power transmission coefficient  $T$  computed numerically in multiwave approach [ 5 ] with a transmission coefficient  $T_{01} = \tau_{01} \cdot \tau_{01}^*$  for  $TM_{01}$  mode allowed to obtain in analytical view a corrected complex field transmission coefficient for  $\tau_{01}^c = \tau_{01} + \tilde{\tau}$  so that  $\tau_{01}^c \cdot \tau_{01}^{c*} = T_{01}^c \approx T$  in a wide interval of wavelengths and SWSs. Analysis of cross-sectional integral distribution of the amplitude and phase of forward and backward waves along the structure allowed to present electromagnetic field near the SWS surface as a corrected  $TM_{01}$  - wave with the amplitude and group velocity variable in  $z$ . Wave correction algorithm is applicable at high ( $>100$ )  $Q$  factors of SWS. The field excited by electron beam is presented according to [7] as

$$E = C_s^+ E_s^+ + C_s^- E_s^- - E_q, \quad \text{where} \quad C_s^+(z) = \frac{1}{N_s} \int_{(z_1, z)} j_b E_s^- dV,$$

$C_s^-(z) = \frac{1}{N_s} \int_{(z, z_2)} j_b E_s^+ dV$ , are the coefficients depending on the longitudinal

coordinate  $z$ ;  $j_b$  is the beam current density;  $E_s^+ = E_s + R_s E_{-s}$  and  $E_s^- = E_{-s} + R_{-s} E_s$  are forward and backward corrected waves of SWS without beam;  $R$  is the reflection coefficient,  $N_s$  is the corrected norm. Coulomb field  $E_q$  is determined from solution of Poisson equation. Initially, in the model a resonance electromagnetic field structure is given. Self-consistence at the given frequency is provided by solving of one-dimensional equation of motion in the obtained summary fields. A visual interactive simulation regime is used.

At a numerical simulation, the main attention was given to the investigation of the beam bunching as well as to finding the conditions for obtaining compact stable electron bunches. As it follows from comparison of theoretical and experimental results, periodic dependence of  $P_0$  on  $L_{dr}$  in a two-sectional MWCG is due, in the first place, to the corresponding dependence of the structure  $Q$  factor on  $L_{dr}$ . Comparison of dependences of the beam instability increments  $G = \frac{1}{W} \int \langle j_b E \rangle dV$  obtained for different  $L_{dr}$  ( $W$  is the electromagnetic field energy) on the synchronous field strength  $E_{sz}$  with the experimental data has shown that decaying dependence  $G$  on  $E_{sz}$  corresponds to the stable regime of generation.

### Conclusion

1. Periodic dependence of the output power of a two-sectional MWCG on the drift tube length is due to the dependence of the  $Q$  factor of a SWS at resonance frequencies on  $L_{dr}$ .

2. Stable generation regimes are realized at the drift tube lengths to which the decrease of the electron beam instability increment with the increase of a synchronous electromagnetic field strength corresponds.

3. In stable generation regimes, the optimum magnetic field and the distance between the electron beam and SWS are connected by the relation  $B_{opt} \cdot b \approx \text{const}$ .

4. In MWCG with a nonuniform three-sectional SWS, realization of high-efficient and stable generation regimes with a narrow band of radiation frequency is possible.

\*The research described in this publication was made possible in part by Grant № NY6000 from the International Science Foundation and Grant № NY6300 from the International Science Foundation and Russian Government.

- [1] Bugaev, S.P., Cherepenin, V.A., Kanavets, V.I., Klimov, A.I., Kopenkin, A.D., Koshelev, V.I., Popov, V.A., Slepkov, A.I.,: IEEE Trans. Plasma Science, 18 (1990) 525.
- [2] Bugaev, S.P., Kanavets, V.I., Koshelev, V.I., Cherepenin, V.A.,: Relativistic Multiwave Microwave Generators, Nauka, Novosibirsk, 1991.
- [3] Pikunov, V.M., Chernyavsky, I.A.,: SPIE Proc. Series, 1872 (1993) 358.
- [4] Chernyavsky, I.A., Deichuly, M.P., Koshelev, V.I., Pikunov, V.M.,: SPIE Proc. Series, 2259 (1994) 542.
- [5] Deichuly, M.P., Koshelev, V.I., Pikunov, V.M., Chernyavsky, I.A.,: Radiotech. Electron., 40 (1995) 1440.
- [6] Deichuly, M.P., Koshelev, V.I., Pikunov, V.M., Chernyavsky, I.A.,: Radiotech. Electron., 41 (1996) 228.
- [7] Vainstein, L.A.,: Electromagnetic Waves, Radio Sviaz, Moscow, 1988.

# HIGH-POWER BROAD-BAND TUNABLE MICROWAVE OSCILLATOR, DRIVEN BY REB IN PLASMA

M.V.Kuzelev, O.T.Loza, A.V.Ponomarev, A.A.Rukhadze, P.S.Strelkov,  
A.G.Shkvarunets, D.K.Ulyanov

*General Physics Institute of Russian Academy of Sciences,  
Vavilova str. 38, Moscow, Russia.*

## Abstract

Radiation spectra of plasma relativistic broad-band microwave oscillator were measured in experiments. Hollow relativistic electron beam (REB) was injected into plasma waveguide, consisting of annular plasma in a circular metal waveguide. Radiation spectra were measured by means of a calorimeter-spectrometer with large cross section in the band of 3-39 GHz. Mean frequency is tunable in the band of 20-27 GHz, spectrum width is 5-25 GHz with power level of 40-85 MW. Calculations were carried out on the base of non-linear theory, considering electromagnetic noise amplification due to REB injection into plasma waveguide. The theory predicts, that radiation regime changes from single-particle regime to collective one, if plasma density and the gap between annular plasma and REB are increased. The comparison of measurement results with non-linear theory explains some peculiarities of the measured spectrum.

## Experimental setup.

The main part of the setup is the accelerator "Terek-2". Parameters of REB were invariable: electron energy 540 keV, beam current 2.4 kA, pulse duration 30 ns. The scheme of experiments is presented in Fig. 1.

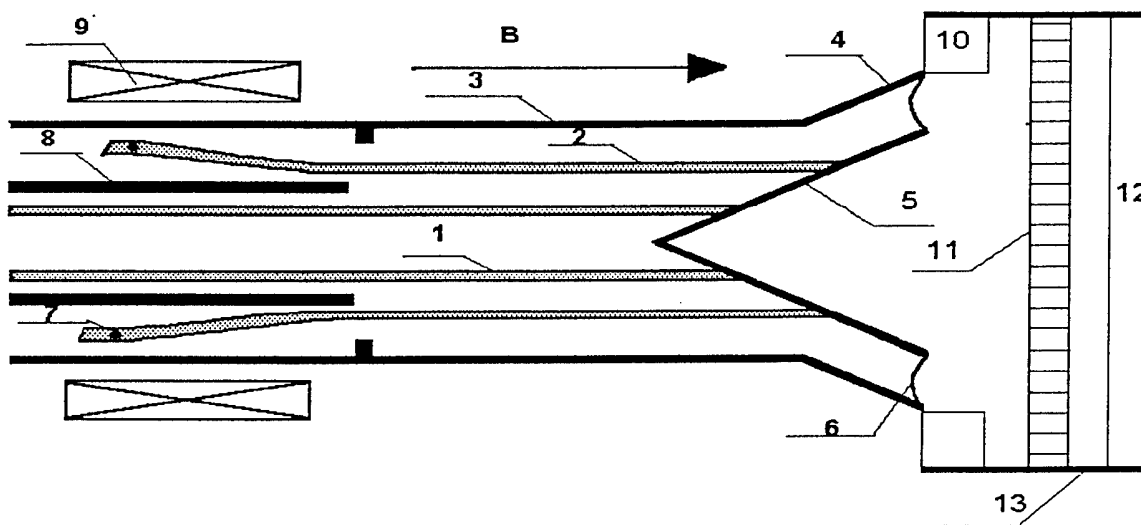


Fig.1.

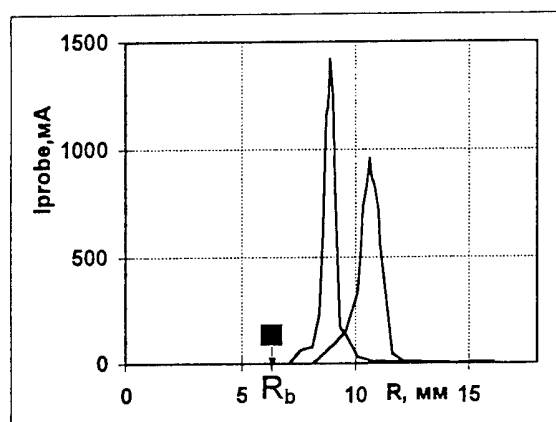
Annular electron beam 1 with the thickness of 1 mm propagates inside annular plasma 2 with the thickness of 1 mm. Coaxial plasma waveguide consists of annular plasma and metal waveguide 3. Plasma waveguide is transformed into conical coaxial horn with metal outer 4

and inner 5 walls. Microwaves are generated in plasma waveguide, then they propagate in the horn and are emitted outside through outlet dielectric window 6. Plasma is prepared as before [1] in a discharge with thermoionic ring-shaped cathode 7. Parameters of plasma source are: cathode voltage – 600 V, discharge current rose in time up to 80 A during 30  $\mu$ s, gas – Xenon, pressure –  $5 \cdot 10^{-4}$  Torr.

Plasma and REB propagate in guiding quasi-steady-state magnetic field 17 kG with half-period of  $T/2 = 5.4$  ms. Plasma radius was tuned by means of the coil 9, creating "fast" magnetic field ( $T/2 = 70$   $\mu$ s) in the area of plasma cathode, and copper screen 8, opaque for this magnetic field, but transparent for the guiding one.

#### Diagnostics.

In every shot we registered discharge current of plasma source, accelerator cathode voltage, magnitudes of guiding and "fast" magnetic fields, gas pressure and parameters of microwaves.



Preliminary experiments revealed definite correspondence between plasma density and discharge current of plasma source. Radial profiles of plasma density are shown in Fig.2. Typical thickness of annular plasma is 1 mm, that corresponds to the tungsten wire diameter 0.8 mm of the thermoionic cathode. It is shown also that the magnetic field of "fast" coil being switched on, plasma diameter diminishes from 21 mm to 17 mm, and the thickness  $\Delta_p$  – from 1 mm to 0.7 mm.

Fig.2.

The most important results were obtained with the calorimeter-spectrometer (see Fig.1). High-frequency part of radiation from the horn 4 propagates through cut-off filter 11 to the calorimeter 12. Residual (low-frequency) part of radiation reflects from the filter and is absorbed by the calorimeter 10. Hence, all the radiation, confined by the metal box 13, is registered.

There were 6 filters with cut-off frequencies  $f_i = 5,1; 9,3; 15,3; 24,1; 32,5$  and 39 GHz correspondingly. For  $f < f_i$  the filters were completely opaque, and for  $f > f_i$  their transparencies were from 76% to 83% and did not depend on the radiation polarization. The filters were installed in turn, and the difference of results in two consequent measurements presented radiation energy in a certain band.

This method has not temporal resolution, but its great advantage is due to high reliability in measurements of absolute values of total radiation energy in a definite frequency band.

#### Measurements of microwave spectra.

Main experimental results are presented in Fig.3 a,b,c. It is worth noting that the signals of microwave power, obtained with semiconductor detector, had the same form as being transmitted through any cut-off filter, as without them. It means that all the spectrum is radiated concurrently. The signal has a bell-shaped form with the half-width of 18 ns. Every picture in Fig.3 a,b,c is an average of 30 shots, so they present an average power. The topmost pulse energy was about 1.5 J, that corresponds to the power of 85 MW with the efficiency of 7%.

As it was before [1], radiation power was the topmost when plasma density is a little more than some threshold value. With the further increase of plasma density up to 8 times, microwave power drops twice.

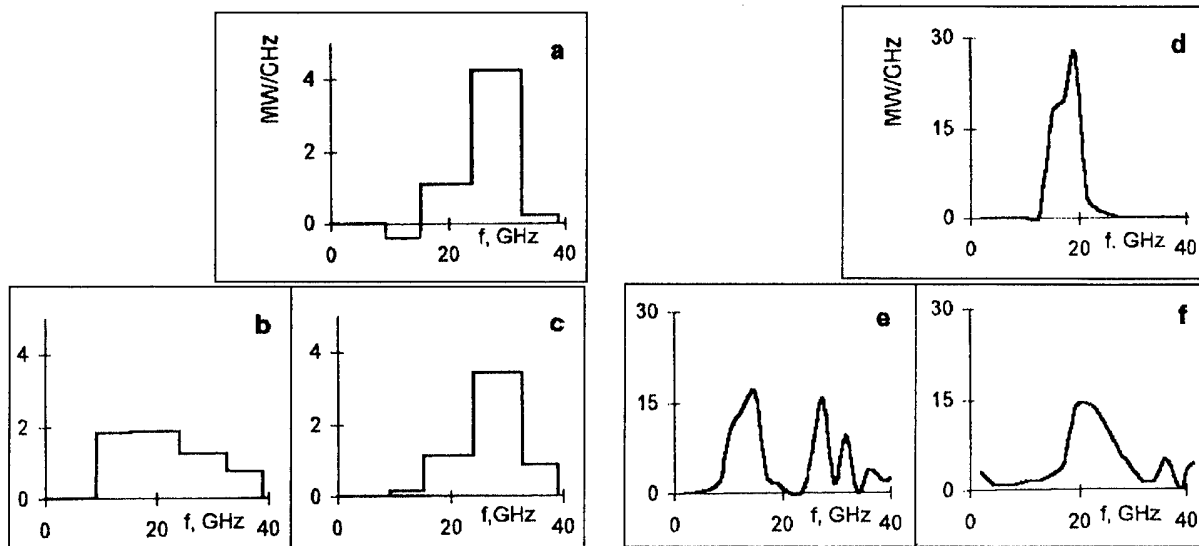


Fig.3.

In the low row in Fig.3b,c spectra are shown for plasma radius  $R_p=8$  mm,  $\Delta_p=0.7$  mm and two values of plasma density: b -  $n_p=3 \cdot 10^{13}$  cm $^{-3}$ , c -  $n_p=7 \cdot 10^{13}$  cm $^{-3}$ . With low plasma density -  $3 \cdot 10^{13}$  cm $^{-3}$  the spectrum is broad: from 10 GHz to 39 GHz. Plasma density being increased to  $7 \cdot 10^{13}$  cm $^{-3}$ , the spectrum narrows down, and the mean frequency rises from 21 GHz to 27 GHz. In Fig.3a  $R_p=10.5$  mm,  $\Delta_p=1$  mm, plasma density  $n_p=5 \cdot 10^{13}$  cm $^{-3}$ . Comparing Fig.3a with Fig.3c note that the gap between REB and plasma increased, but the parameter  $n_p \cdot \Delta_p$ , that mainly determines the spectrum form, is invariable. It follows from Fig.3a,c that the increase of the gap between REB and plasma causes a minor narrowing of the spectrum.

#### Theory and comparison with experiments.

##### *Linear theory, regarding finite value of beam current.*

Dispersion equation of plasma-beam system was solved for thin annular beam and plasma as a task of amplification. Frequency band was searched in which amplification coefficient  $\delta k = \text{Im } k_z(\omega) > 0$ , e.g. microwave amplification takes place. In case of single-particle regime the amplification coefficient is big, and the amplification takes place in a broad frequency band. Dispersion curves  $\omega(k_z)$  for the case of equal beam and plasma radii and real parameters of the system, written above, are shown in Fig.4. ( $R_b = R_p = 0.65$  cm,  $\Delta_b = \Delta_p = 0.1$  cm,  $n_p = 4 \cdot 10^{13}$  cm $^{-3}$ ,  $I_b = 2$  kA,  $\gamma = 2$ ). In this case pure single-particle regime of amplification takes place in the band of 0 — 34 GHz. It is also shown in Fig.4b, where frequency dependence of the amplification coefficient  $\delta k$  is presented. Vertical lines 1 and 2 in this figure correspond: 1 — to the resonance frequency of plasma wave and beam wave  $\omega = k_z u$  (resonance “particle-wave”), and 2 — to the resonance frequency of plasma wave and slow beam wave (resonance “wave-wave”). Amplification is observed at both resonances and in remote frequency areas.

Another situation takes place when beam and plasma radii are not equal: it leads to diminishing of amplification coefficient and to realization of collective regime of amplification. In this case narrow frequency band is amplified. In Fig.5 dispersion curves and amplification coefficient are presented for the same parameters of REB, as in Fig.4, but the mean radius of plasma is more than that of REB:  $R_p=11$  mm,  $R_b=6.5$  mm. This, at first sight minor removal of plasma from the beam (the gap between them is only 3.5 mm), diminishes severely the coupling between them and substantially changes the amplification regime. Amplification frequency band becomes narrow, about 17 — 25 GHz, the most amplification coefficient being at the “wave-wave” resonance frequency. Moreover, at the frequency of “wave-particle” resonance the amplification is absent at all.



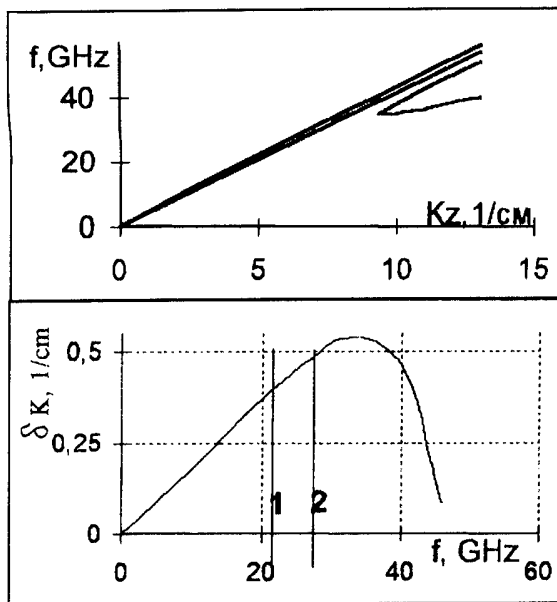


Fig.4.

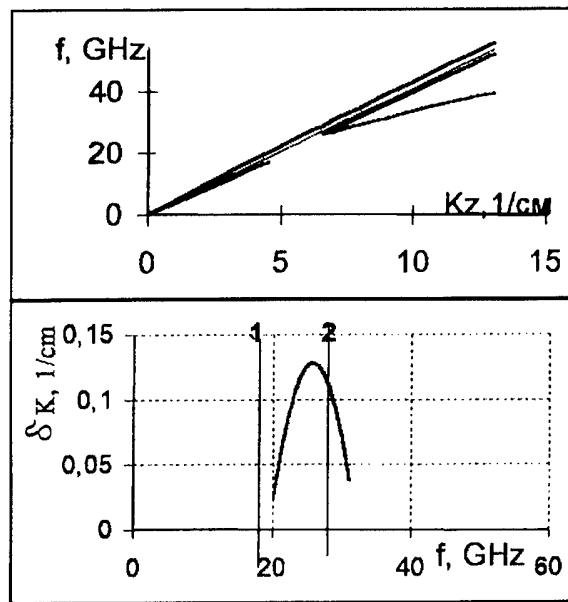


Fig5.

*Comparison of experimental spectra with calculated ones.*

In Fig.3d,e,f radiation spectra, calculated accordingly to non-linear theory, are presented. Main ideas of this theory of plasma microwave amplifier are described in [2]. Calculation were carried out as follows. The system input was fed with white noise, and numerical solution of non-linear equations determined established radiation spectrum. The established output spectrum occurred to depend weakly on the amplitude and spectrum of the input signal.

In Fig.3d,e,f the calculated spectra correspond to the spatial point, where the power reaches its saturation level (Fig.3d —  $R_p = 11$  mm,  $\Delta_p = 1$  mm  $n_p = 2,8 \cdot 10^{13} \text{ cm}^{-3}$ ; Fig.3e —  $R_p = 8$  mm,  $\Delta_p = 1$  mm  $n_p = 1,4 \cdot 10^{13} \text{ cm}^{-3}$ ; Fig.3f —  $R_p = 8$  mm,  $\Delta_p = 1$  mm  $n_p = 2,8 \cdot 10^{13} \text{ cm}^{-3}$ . Calculated spectra properly represent frequency band, observed in experiments. Narrowing of the spectra and increase of the mean frequency (Fig.3b,c) are confirmed by calculations (Fig.3e,f). Narrowing of the spectra with increase of the gap between REB and plasma, predicted by the calculations — Fig.3f,d — does not contradict to the experiments: compare Fig.3a and Fig.3c. Nevertheless, this effect has not been definitely detected in experiments.

Comparing the results of calculations with that of experiments, note the difference of plasma density values (parameter  $n_p \Delta_p$  differs 1.6 times). Perhaps, the difference in plasma densities is due to both the errors of its absolute measurements and the difference of plasma density profile in experiments and calculations. It was admitted in calculations that  $n_p = \text{const}$  inside the plasma tube. Note also the big difference of absolute values of microwave radiation power in experiments and calculations.

This work was carried out with partial support of Russian Ministry of Sciences on setup "Plasma relativistic microwave oscillator" (N 01-04), Russian Foundation of Fundamental Investigations (N 94-02-03437) and International Science Foundation (# MO 3000 and # MO 3300).

[1] M.V.Kuzelev, F.H.Mukhametzianov, M.S.Rabinovich, etc. JETP, 83, N4(10), p.1358 - 1367 (1982); Reports of USSR Academy of Sciences 267, N4, p.829-832 (1982).

[2] M.V.Kuzelev, V.A.Panin, A.P.Plotnikov, A.A.Rukhadze. JETP, 101, p.460-478 (1992).

# BEAM - PLASMA GENERATORS OF STOCHASTIC MICROWAVE OSCILLATIONS USING FOR PLASMA HEATING IN FUSION AND PLASMA - CHEMISTRY DEVICES AND IONOSPHERIC INVESTIGATIONS

L.A. Mitin, V.I. Perevodchikov, A.L. Shapiro, M.A. Zavjalov

*State Science Center "All-Russian Electrotechnical Institute"*  
Krasnokazarmennaja 12111250, Moscow, Russia

Yu.P. Bliokh, Ya.B. Fainberg

*National Science Center "Kharkov Institute of Physics and Technology"*  
Academicheskaya 1, 310108, Kharkov, Ukraine

## ABSTRACT

The results of theoretical and experimental investigations of generator of stochastic microwave power based on beam-plasma inertial feedback amplifier is discussed to use stochastic oscillations for heating of plasma.

The efficiency of heating of plasma in the region of low-frequency resonance in the geometry of "Tokomak" is considered theoretically. It is shown, that the temp of heating is proportional the power multiplied by spectra width of noiselike signal.

The creation and heating of plasma by stochastic microwave power in oversized waveguide without external magnetic field is discussed to plasma-chemistry applications. It is shown, that efficiency of heating have been defined by the time of phase instability of stochastic power.

## 1. STOCHASTIC MICROWAVE OSCILLATORS BASED ON HYBRID BEAM-PLASMA SYSTEMS

The high-power beam-plasma generators of stochastic microwave signals are considerable interest for both pure and applied research. On the one hand, they can contribute to the study of fundamental problems of the stochastic dynamics of nonlinear dynamic systems with distributed parameters. On the other hand, they have wide applications in controlled nuclear fusion (as a radiation source for stochastic plasma heating), in nonequilibrium plasma chemistry (stochastic microwave discharge techniques), in charged particle stochastic acceleration, etc.

The nonlocality of the electron beam interaction in travelling wave systems in conjunction with the nonequilibrium and broad-band character of this interaction leads to an unstable system behaviour in the presence of a delayed feedback circuit. At certain nonequilibrium parameter values, the system instability regarding automodulation processes at the nonlinear interaction stage can result in a stochastization of the microwave oscillations accompanied by the formation of broad noise-type spectra. Numerous papers were devoted to the purely physical and applied aspects of this problem [1-6]. The generator of stochastic

microwave oscillations based on a hybrid beam-plasma amplifier with an external delayed feedback circuit belongs to such systems.

In [3], the evolutionary partial differential equations pertaining to the nonstationary model of the electron beam-wave interaction were reduced to an integral equation of the form

$$F(\tau + \theta) = \Psi\{|G_o(F(\tau)|, \nu(\tau)\} \cdot \exp\{\arg(G_o F(\tau))\} \quad (1)$$

Here,  $F$  represents the dimensionless complex signal amplitude;  $\tau$  denotes the dimensionless time;  $\theta$  is the delay time;  $G_o$  is a difference kernel operator:

$$G_o F(\tau) = \int_{-\infty}^{\tau} G(\tau - \tau') F(\tau') d\tau'$$

which defines the interaction linear stage; and  $\Psi\{|GF(\tau)|, \nu\}$  is a nonlinear function describing the nonlinear stage and depending on the instantaneous values of signal level  $x = |GF(\tau)|$  and frequency  $\nu(\tau)$  at the end of the linear interaction stage. Equation (1) explicitly defines the generator signal current value according to the totality of past signal values, i.e., it transforms the solution process into a certain functional mapping iteration. This equation, in contrast to the partial differential equations, can be analytically analysed for stability rather easily. The disruption of monochromatic regimes [1-6] followed by automodulation and signal stochastization occurs (for example, at some point of beam current growth) if either of these conditions is satisfied:

$$|a(\nu)| \left| \frac{\partial}{\partial x} |\Psi| \right| > 1 \quad (2)$$

$$\frac{d^2}{d\nu^2} |a(\nu)| - |a| \cdot |\Psi| \cdot \frac{d^2}{d\nu^2} \arg(a) \cdot \frac{d}{dx} \arg(\Psi) > 0 \quad (3)$$

Here,  $a(\nu)$  represents the device frequency response in a linear amplification regime and is equivalent to the Fourier transform of function  $G(\nu)$ . The first condition connects the disruption of monochromatic generation regimes with a steepening of the dropping part of the amplifier amplitude characteristic. The second condition is related to the amplifier frequency response. Therefore, the first mechanism of stability loss is called the amplitude mechanism, and the second, the phase mechanism.

The identification of the mechanism responsible for the oscillation stochastization is very important, because it determines the signal spectral characteristics and the scenario of the transition from a regular to a stochastic generation mode. Here are the characteristic features of the amplitude mechanism: transition via a chain of period doubling bifurcations; and low probability of large signal amplitudes, and, consequently, a rather small electron efficiency. The phase mechanism involves an intermittent turbulence and a high electron efficiency when the amplitude nonlinearity is weak.

As shown above, the deep amplitude nonlinearity mode involves a significant current deposition onto the slow-wave structure, which is undesirable in high-power CW devices.

The noted advantages of the phase stochastization mechanism were decisive in our choice of our stochastic oscillator scheme.

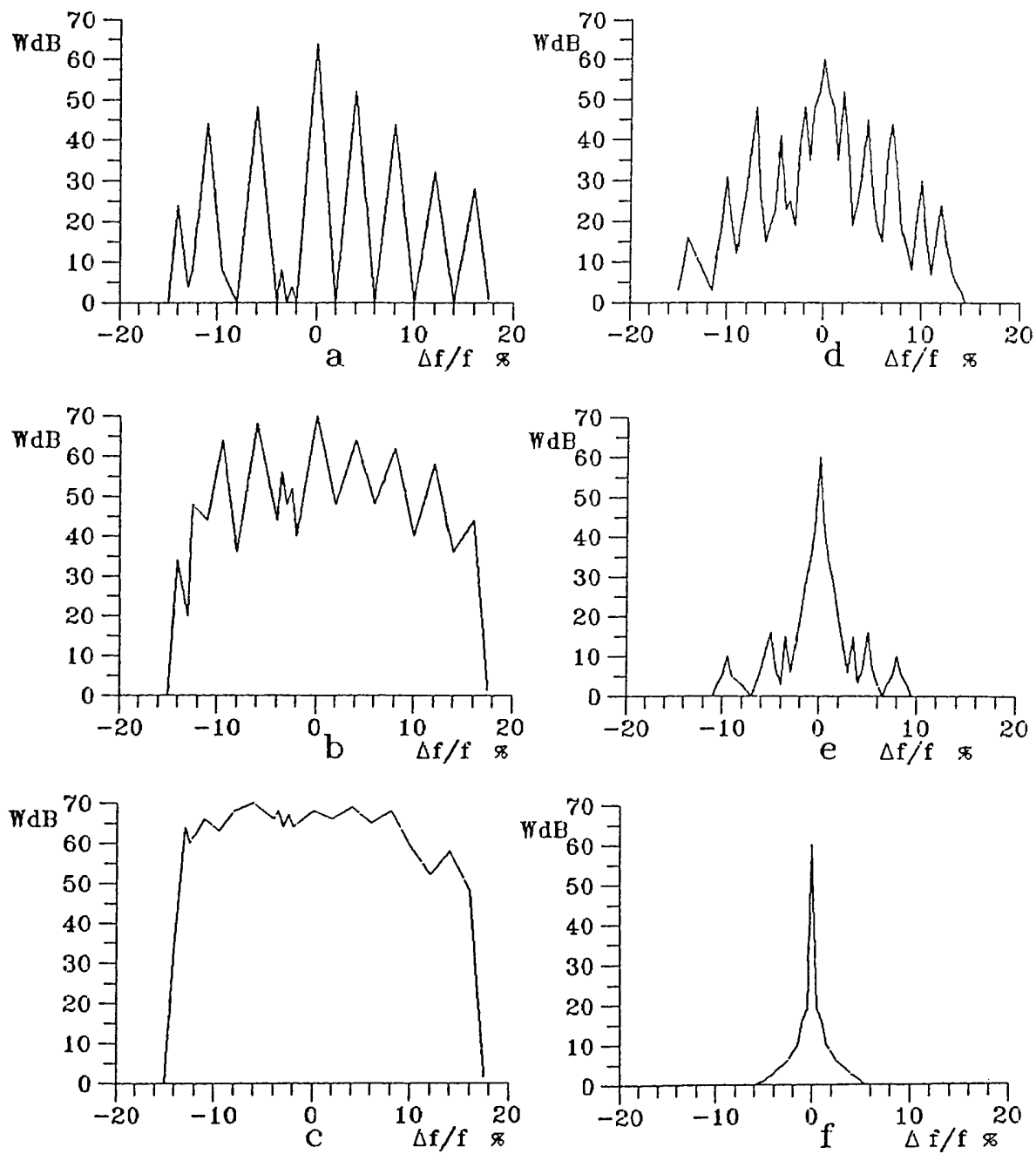


Fig.1.  
Oscillation spectra for different power levels of feedback circuit signal:  
(a) 0.5, (b) 0.8, and (c), 1.2 mW; (d), (e), and (f), in the presence of control  
signal of 0.2, 0.8, and 1.2 mW, respectively.

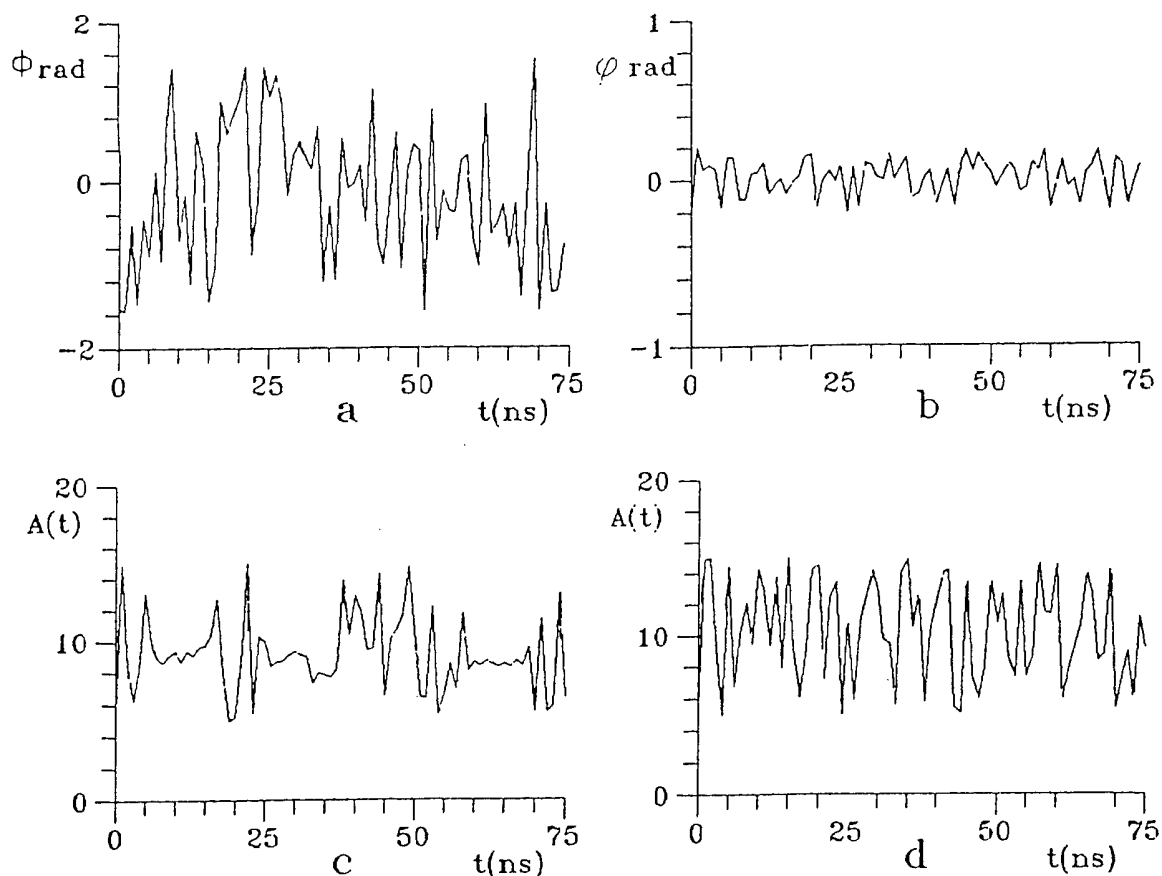


Fig.2.

Time dependence of (a) phase of stochastic signal with a wide frequency bandwidth, (b) phase of output signal in the spectrum compression regime, (c) output signal amplitude at 1.8 A electron beam current, (d) output signal amplitude at 3 A electron beam current.

The experiments were carried out for the same electron beam parameter set, as before, in the amplification regime. Figures 1a-1c present the generated oscillation spectra at various power levels of the feedback signal. As the feedback signal increased, the system passed through a multifrequency generation regime toward stochastic oscillation spectra covering the whole bandwidth defined by the dispersion characteristic. The maximal output power obtained in this regime was 20 kW. In a 30 % relative frequency bandwidth, the spectrum of oscillations was flat within 3 dB. Figures 2a, 2d show the signal phase and amplitude (signal envelope) as functions of time. One sees that in the wide-band generation regime the signal is random character both in oscillation amplitude and phase. The phase mechanism of transition to a stochastic behaviour is confirmed by the signal realisations recorded at different beam currents (Figs. 2c and 2d). One clearly discerns quasi-monochromatic zones peculiar to the intermittent turbulence regime. They disappeared when the electron beam current was increased.

The wide-band generation mode is hard to control. In addition, it is energetically unprofitable. Therefore, it is not desirable in many applications, unless one needs wide microwave oscillation spectra. In this connection, we realized and studied the regime of frequency spectrum compression by means of an external control signal. The control signal was fed to the input of the travelling wave tube, being a part of the feedback circuit. Figures 1d-1f present the dependence of the generated spectra on the control signal power. For a 1 mW

signal power at the travelling wave tube input (100 W at the beam-plasma amplifier input), the spectrum bandwidth was reduced by two orders of magnitude. At the same time, the integral output microwave power remained unchanged at the level of 20 kW. Figure 2b presents the time dependence of the signal phase in the spectrum compression mode. Note that the signal is still a noiselike one, although the phase dispersion is small. It was possible to retune the generated frequency over a bandwidth of about 25 %, where the spectrum nonuniformity was within 3 dB.

## 2. THE PLASMA HEATING AND THE ARTIFICIAL IONIZED LAYER (AIL) CREATION BY STOCHASTIC ELECTROMAGNETIC RADIATION

By way of example, consider the Earth's ionosphere plasma heating by stochastic electromagnetic radiation. The interaction of the powerful electromagnetic radiation with the Earth ionosphere is one of few accessible methods of active influence on the space plasma. Among different effects connected with powerful electromagnetic radiation the local thermal instability is one of the essential because it leads to the most marked changing of ionospheric parameters. The efficiency of plasma heating by monochromatic electromagnetic radiation is determined by electron collision frequency, which in the ionosphere is rather small ( $\nu \leq 10^3 \text{ s}^{-1}$  on the height about 300 km).

In the case of stochastic signal, as it was shown in [7,8], the efficiency of energy transference to plasma electron component is determined by the reciprocal correlation time  $\tau^{-1}$ . Its value may be much larger than collision frequency ( $\tau^{-1} \gg \nu$ ). It allows to reduce the radiation source power and to increase the frequency. The latter makes accessible on influence all ionosphere, including the region above F-layer.

In [9,10] was shown that the growth rate of particle average kinetic energy is determined by following expression:

$$\frac{d}{dt} \left( \frac{m|V|^2}{2} \right) = \frac{e^2}{m} \frac{(|E|^2)}{(w^2 + \tau^{-2})\tau} \quad (4)$$

where  $w$  is the carrier frequency of a electromagnetic radiation.

As follows from comparison (4) with the analogous formula for plasma heating by monochromatic radiation [11], the role of collision frequency in (4) plays the value  $\tau^{-1}$ . It means, that the efficiency of the plasma heating by stochastic radiation is greater than heating by monochromatic radiation in ratio of  $1/\nu\tau$ . In ionosphere the value  $1/\nu\tau$  may be very large and it allows to use signals with  $w \gg w_{pm}$  ( $w_{pm}$  is the maximal value of plasma frequency in the region of F-layer), which can warm thoroughly the whole width of the ionosphere. For this case the dependence of heating rate and the electron steady temperature as functions of height will be discussed further.

Taking into account the angular diverging and the loss of energy it is possible to obtain the following expression for dependence of steady electron temperature  $T_\infty$ , on height:

$$\frac{\Delta T}{T_o} \equiv \frac{T_\infty - T_o}{T_o} \sim \frac{e^2 P_{eff} \Delta f}{mcw^2 h^2 \nu(h) \delta T_o(h)} \cdot \exp \left( -\frac{3}{4} \frac{\Delta f}{c} \int_0^h dh' \frac{w_p^2(h')}{w^2} \right) \quad (5)$$

Here  $T_0$  is ionospheric heavy component temperature,  $\delta \sim m/M \sim 10^{-3}-10^{-4}$  is the part of energy losses due to collisions of electrons with ions or neutrals,  $P_{\text{eff}}$  is an effective power of the radiation source,  $\Delta f$  is radiation spectrum width:  $\Delta f \sim \tau^{-1}$ .

Let us consider as an example the ionospheric plasma heating by stochastic electromagnetic radiation with following parameters:  $f \sim 10 f_p \sim 50$  MHz,  $\Delta f \sim 5$  MHz,  $P_{\text{eff}} \sim 10$  MW

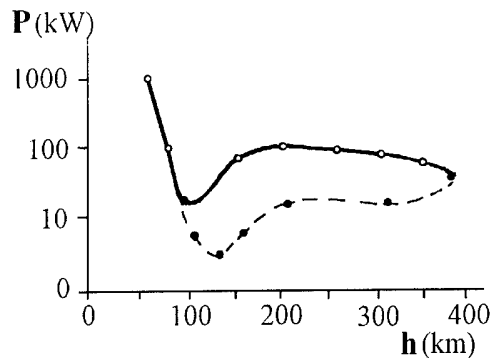


Fig.3. The dependence  $P(h)$  of ground-based radiation source power that is necessary for AIL creation on the height  $h$ . The carrier frequency is chosen about 1 GHz, the spectrum width is 10% and the antenna growth coefficient is  $10^3$ . Solid and dotted lines correspond to day and night ionosphere.

To height about 1000 km the loss of power may be neglected and dependence  $T_e(h)/T_0$  is determined by function  $\varphi(h)=h^2 \nu(h)$  which has a sharp maximum on the height of F-layer. It means that the largest value of the relative temperature growth is to be expected on the heights more and less than F-layer height. This fact illustrated the essential difference between heating by monochromatic and stochastic signals.

The value  $\Delta T/T_0$  for above mentioned parameters is about 1 on the height 200 km and higher. The transition time to a steady state is about 10 s.

Formula (5) allows to assess radiation power  $P_{\text{eff}}(i)$ , which is necessary for neutral component ionization. Dependence  $P_{\text{eff}}(i)$  is determined by function  $\varphi(h)$ . The minimal power  $P_{\text{eff}}(i)$  is essential for an AIL creation on the height 150-250 km. The dependence of assess for AIL creation power  $P(h)$  of ground-based source of electromagnetic radiation, that was obtained using standard Earth's ionosphere parameters, is shown on Fig. 3. If the radiation power is not very large than changed in a random manner wave amplitude exceed threshold of gas discharge only during short time intervals. In this case the discharge has pulse character that is favourable for ozone production. The point is that in the stationary air discharge the ozone formation is intensive only during initial stage. After that the ozone formation is decreased and some unhealthy nitrogen compounds appear [12]. High efficiency of ionosphere heating and pulse character of discharge make possible to use stochastic electromagnetic radiation for ozone reproduction, for example, in the regions of ozone "holes" that appear during space missiles launching.

The stochastic radiation can be used for long-distance transporting of electromagnetic radiation in the ionosphere. High efficiency of plasma heating make possible to use sources with relatively small power for wave-guide channel creation, where plasma density drop prevent the wave beam divergence. As an example, for the stochastic radiation with carrier frequency  $\sim 1$  GHz and spectrum width  $\sim 100$  MHz the power that is necessary for wave-guide channel creation in the F-layer region is about some kW. Corresponding power of monochromatic radiation with frequency  $\sim 1$  GHz is about 105 kW. Such high difference between powers is connected with very low collision frequency  $\nu$  in the ionosphere ( $\nu \sim 10^3 \text{ s}^{-1}$ ) that make non-effective heating by monochromatic radiation.

### 3. THE HEATING IN THE FIELD OF STOCHASTIC POTENTIAL WAVE IN MAGNETIZED PLASMA

In the homogeneous waves fields the heating rate is determined only by their correlation time  $\tau_c$ . But in the case of non-homogeneous wave created, for example, by localized source (antenna), the heating of plasma electrons is defined not only by temporary but by space correlation characteristics as well. In the dispersive media which plasma is, this characteristics change according to removal from radiation source. The plasma heating efficiency changes according to this one. Below the magnetized plasma heating by localized source of stochastic potential waves is considered. The interest to this wave type is connected with investigation of possibility of stochastic radiation sources using for plasma additional heating in Tokomaks. In the presence the regular low and high hybrids waves are applied particularly. The results about stochastic signal propagation, which are described in this report, can represent also a special interest for Earth's ionosphere physics and removal sensing.

The dispersion of potential magnetized plasma waves connects frequency with direction of wave propagation only. In [13] was shown that on large distance from localized source (antenna) of such waves the correlation time  $\tau$  determines only a wave beam width, but not the correlation parameters in it. The correlation length in transversal direction and correlation time in a wave beam do not depend on  $\tau$ .

The constancy of transverse to wave beam direction correlation length  $l_{\perp}$  when mean beam radius increases is a consequence of specific property of considered wave in anisotropic media: their frequency determines only direction of the wave vector but not its modulus. Therefore each spectral harmonic, which propagates at corresponding angle with respect to anisotropy direction (magnetic field), "carries" the source image as a whole. Because in the stationary stochastic processes the spectral components are statistically independent, the space correlation vanishes when two points of observation are separated one from another at distance greater than source size  $a$ . So, on the great distance from antenna the transverse correlation length is determined by source dimension only:  $l_{\perp} \sim a$ .

The independence of correlation time  $\tau_*$  in the wave beam on  $\tau$  may be explained by following. The signal harmonics from source with a size  $a$  may come to the removal observation point only if they are contained in frequency interval  $\Delta\omega \sim a/z$  ( $z$  is the distance between observation point and antenna). If  $\Delta\omega \ll \tau^{-1}$  then signal spectrum in the observation point is much smaller than initial spectrum width  $\sim \tau^{-1}$ . The media at issue acts as a frequency filter, which bandwidth decreases as  $z^{-1}$  when  $z$  increases. The correlation time  $\tau_*$  of stochastic signal which passes through narrow-band filter is determined not by initial correlation time  $\tau$ , but by frequency band width  $\Delta\omega$ :  $\tau_* \sim \Delta\omega$ .

Now we shall estimate the electron heating rate. The field that acts on a moving electron has a correlation time  $\tau_e$  which is determined by expression:

$$\tau_e^{-2} \sim \frac{v_o^2}{l_{\perp}^2} + \tau_*^{-2} \quad (6)$$

First term in the right part of (6) connects with transversal stochastic space structure of wave beam, and the second one - with stochastic time variations of the field. According to (3) the temperature  $T$  grow rate is described by the following expression:

$$\frac{dT}{dt} \sim \frac{e^2}{m} \frac{(E^2)}{w^2 \tau_*} \sim \frac{e^2}{m} \frac{E^2}{w^2} \sqrt{v_o^2 / l_{\perp}^2 + \tau_o^{-2}}.$$



A particle crosses the region with dimension  $R$  during the time interval  $\Delta t \sim R/v_0$ , so the total particle energy charge<sup>1</sup> during one pass through whole wave beam is

$$\Delta T \sim \frac{e^2}{m} \frac{(E^2)}{w^2} \sqrt{v_0^2 / l_z^2 + \tau_0^{-2}} \cdot \frac{R}{v_0} \quad (7)$$

As it following from (7), the slow particles acquire greater energy during one crossing of a wave beam than fast ones. This circumstance may be very important, because such "priority" of slow particles prevent the formation of high-energy "tails" in the electron distribution function and it leads to more uniform energy distribution in the plasma electron component.

Let us compare now the expression for  $\Delta T$  with similar ones for monochromatic signal<sup>2</sup>. In this case the particle energy changing occurs only at the moment when particle crosses a beam boundary<sup>3</sup>, and the value  $\Delta T$  is determined by the squared oscillation velocity in the wave field:

$$\Delta T \sim \frac{e^2}{m \cdot w^2} \quad (8)$$

Note, that the expression (5) is the upper boundary for  $\Delta T$  value and is satisfied for beams with sharp boundaries and uniform intensity distribution across the beam. If the intensity smoothly decreases toward boundary then the particle energy increasing may be much smaller.

In the considered media the radiation of antenna represents the conic shell with axis that is parallel to anisotropy direction. Let us define  $D$  as a diameter of cone and  $R$  as a shell width in the observation point (for regular radiation  $R \cong a$  in the considered approximation). The formulas (7) and (8) expressed in terms of radiation source power  $P$  may be rewritten in the form:

$$\Delta T_s \sim \frac{e^2}{mc} \frac{P}{D w^2 a} \sqrt{1 + a^2 / (v_0^2 \cdot \tau_*^2)}, \quad (9)$$

$$\Delta T_r \sim \frac{e^2}{mc} \frac{P}{D w^2 a}, \quad (10)$$

where  $\Delta T_{s,r}$  are the particle energy changing for stochastic and regular radiations, respectively.

As it follows from comparison (9) and (10), the heating efficiency for "slow" electron in the stochastic wave beam's field exceeds the heating efficiency by regular wave with the same power and created by the same source, and for "fast" particles these efficiencies are equal.

<sup>1</sup> It is assumed here that energy change is small:  $\Delta T \ll T$ .

<sup>2</sup> Here only stochastic mechanism of energy exchange between regular wave and particles is considered. Resonance interaction may be more effective but it affects only small group of particles.

<sup>3</sup> It is assumed that the electron collision frequency  $\nu$  in a media is small enough:  $\nu \ll v_0/R$ .

#### 4. CONCLUSION

As it was shown mentioned above examples, the stochastic radiation interaction with plasma may be in some conditions more strong as for regular one. It is possible to say that in the general case the stochastic heating is more effective than heating in the regular fields if the collision frequency is smaller compare to reciprocal correlation time  $\tau_e$ . Such condition may be fulfilled in the plasma with low density (Earth's ionosphere) or in the high temperature plasma (thermonuclear plasma).

This work is supported partially by Ukrainian State Committee of Science & Technology (grant N 2.3/552).

#### 5. REFERENCES

- [1] V.Ya.Kislov, *Lektsii po Elektronike SVCh i Radiofizike* (Lectures on Microwave Electronics and Radiophysics), Saratov: Saratov. Gos. Univ., 1980, vol.5, p.78.
- [2] N.S.Ginzburg and S.P.Kuznetsov, *Relyativistskaya Vysokochastotnaya Elektronika* (Relativistic High-Frequency Electronics), Gor'kii: Inst. Prikl. Fiz., Akad. Nauk SSSR, 1981, p.104.
- [3] S.P.Kuznetsov, *Izv. Vyssh. Uchebn. Zaved., Radiofizika*, 1982, vol.25, p.101.
- [4] V.S.Anishchenko, *Slozhnye Kolebaniya v Prostykh Sistemakh* (Complex Oscillations in Simple Systems), Moscow: Nauka, 1990.
- [5] A.S.Dmitriev and V.Ya.Kislov, *Stokhasticheskie Kolebaniya v Radiofizike i Elektronike* (Stochastic Oscillations in Radiophysics and Electronics), Moscow: Nauka, 1989.
- [6] Yu.P.Bliokh, A.V.Borodkin, M.G.Lyubarskii, et al., *Izv. Vyssh. Uchebn. Zaved., Prikladnaya Nelineinaya Dinamika*, 1992, vol.1, p.34.
- [7] F.G.Bass, Ya.B.Fainberg, V.D.Shapiro, *Sov. Phys. "JETP"*, v.49, p.329, 1965.
- [8] Yu.P.Bliokh, Ya.B.Fainberg, M.G.Lyubarskii, V.O.Podobinskii, *Sov. J. "Plasma Phys."*, v.19, N 3, 1993.
- [9] Yu.P.Bliokh, Ya.B.Fainberg, E.A.Kornilov, L.A.Mitin, *Plas. Phys. Rep.*, v.20, N 9, 1994.
- [10] Ya.B.Fainberg, Yu.P.Bliokh, M.G.Lyubarskii, P.I.Markov, I.N.Onistchenko, G.V.Sotnikov, *Plasma Phys. Rep.*, v.20, N 9, p.681-689, 1994.
- [11] *The Thermal Nonlinear Phenomenon in Plasma*, Gorky: Inst. App. Phys., 1979.
- [12] A.L.Vikharev, A.M.Gorbachev, O.A.Ivanov, A.L.Kolisko, A.G.Litvak, *Phys. Letters A*, 179, p.122-126, 1993.
- [13] Yu.P.Bliokh, *Plasma Phys. Rep.*, v.21, N 8, 1995.

## DESIGN AND COLD-TESTING OF TWO 100 MW GYROKLYSTRON AMPLIFIERS FOR COLLIDER APPLICATIONS

W. Lawson, J. Cheng, M. Castle, G. Saraph, J. Anderson, B. Hogan, V. L. Granatstein, and M. Reiser

*Institute for Plasma Research, University of Maryland, College Park, MD 20742 USA*

### Abstract

In this paper we present the design details of both a first harmonic two-cavity coaxial gyro-klystron and a second harmonic three-cavity amplifier tube, each of which is designed to produce over 100 MW of output power. Both tubes utilize a fundamental mode  $TE_{011}$  input cavity which is driven by a 150 kW magnetron at 8.56 GHz. The former tube also has an 8.56 GHz  $TE_{011}$  output cavity while the latter system has a buncher cavity and an output cavity that resonate at twice the drive frequency in the  $TE_{021}$  mode. We present details of all system aspects, including the test bed modifications required to produce the enhanced beam characteristics, simulated beam properties, and simulated circuit interactions. HFSS modeling of the drive cavities is also reported and cold test results of both tubes are detailed. Results to date indicate that both systems should be at least 40% efficient.

### Introduction

At the University of Maryland, we have been running a comprehensive program to study the suitability of gyrotron amplifiers for linear collider applications. All previously reported experimental results have stemmed from our test bed which produced a small-orbit beam with a nominal voltage and current of 450 kV and 200 A, respectively. Published accounts of our effort include an amplified power level of 27 MW at 32% efficiency in a three-cavity first harmonic gyro-klystron [1]; 32 MW at 28% efficiency in a two-cavity second harmonic gyro-klystron [2]; 28 MW in a second harmonic coaxial gyro-klystron [3]; and 22 MW at 22% efficiency in a fundamental gyrotwyston [4]. Large signal gains have been in the 25 - 40 dB range.

We are nearing the completion of an upgrade to our facility which should enable us to produce amplified microwave powers in excess of 100 MW. Our modulator voltage and current have been augmented to 500 kV and 800 A, respectively. We have designed a single-anode Magnetron Injection Gun (MIG) which is capable of producing a 480 - 720 A rotating electron beam at the nominal beam voltage with an axial velocity spread less than 7%. This gun has been constructed and installed. Finally, we have modified the magnet system, vacuum hardware, and microwave diagnostics to accommodate the new MIG. In the following section we present the results of our simulations. The cold-test results are described in the third section and the project status is summarized in the final section.

### Theoretical design results

A detailed design analysis has been carried out with coaxial, two- and three-cavity gyro-klystron systems. The input cavity is in resonance with the signal frequency at 8.568 GHz and the output cavity is resonant with either the first (8.568 GHz) or the second harmonic (17.136 GHz) frequency. In a three-cavity system, an additional buncher cavity is introduced which is resonant at either the first or second harmonic frequency.

The two-cavity first harmonic tube is shown in Fig. 1 and consists of an input cavity and an output cavity separated by a drift section. Both cavities are resonant at 8.568 GHz in the  $TE_{011}$  mode. The drift section has inner and outer radii of 1.825 cm and 3.325 cm, respectively and is cutoff to the operating mode. The input cavity Q-value is brought down to 50-65 by loading the cavity with lossy dielectric materials. Power is injected through two radial coupling ports which are separated by  $180^\circ$  and excited in phase. The start-oscillation code predicts that the input cavity is completely stable up to a current of 800 A. This code also predicts the output cavity to be stable at the nominal current, which is given in Table I along with the other operating parameters. The efficiency is nearly 40% and the output power is about 95 MW. The dependence of tube efficiency on velocity spread is plotted in Fig. 2 with the solid line.

The simulated velocity spread of the electron gun is 6.4 % at the nominal current.

The second harmonic design is a three-cavity system. The buncher cavity operates at the second harmonic and is formed with non-adiabatic radial wall transitions. Mode conversion from the  $TE_{02}$  mode to the  $TE_{01}$  is estimated to be about -40 dB. Dielectric loading of the cavity is used in order to obtain a Q of 389 and is achieved by reducing the thickness of the copper sections that separate the cavity from the drift tube dielectrics. The linear start oscillation code indicates that the buncher cavity is stable to beam currents below about 1000 A at the design value of the magnetic field ( $B_0 = 4.81$  kG). The output cavity is also designed with non-adiabatic radial wall transitions. The scattering matrix code estimates the purity of the  $TE_{02}$  operation in the output cavity to be 97%. The ratio of the power flowing into the drift tube to the power flowing into the output waveguide is better than -24 dB. Furthermore, the lossy dielectric loading in the drift tube, which will have a minimum effect on the Q-value of the operating mode, will suppress the excitation of the spurious modes and reduce the cross-talk.

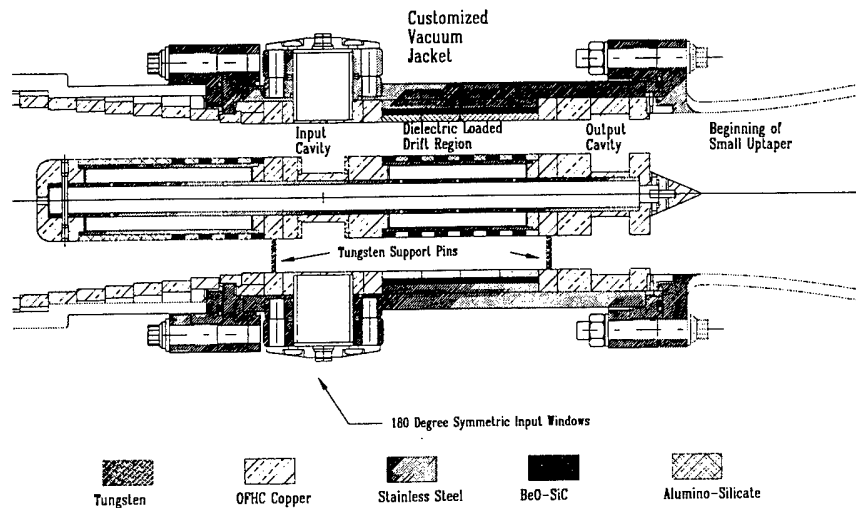


Fig. 1. The first harmonic two-cavity tube.

Table I. Comparison of the 1<sup>st</sup> and 2<sup>nd</sup> harmonic designs.

Parameters	1 <sup>st</sup> harmonic	2 <sup>nd</sup> harmonic
Voltage	500 kV	500 kV
Current	480 A	770 A
Velocity ratio	1.508	1.508
Input Cavity Q	50	50
Buncher Cavity Q	-	389
Output Cavity Q	122	320
Gain	21 dB	49 dB
Efficiency	39.4%	41.1 %
Output Power	94.6 MW	158.2 MW

The output cavity is highly overmoded and is linearly stable only up to a current of 400-450 A for the operating regime from 4.8 kG to 5.0 kG. The beam can excite various other modes at higher current levels. In the actual system the signal injected in the input cavity modulates the beam. The length of the drift section is chosen such that the beam is tightly bunched (in gyro-phase) when it enters the output cavity. The well-bunched beam at 8.568 GHz leads to forced excitation of the operating mode ( $TE_{021}$ ). The operating mode grows in amplitude first. Then, in the presence of the large amplitude operating mode, the gain of the other modes is suppressed. Nonlinear gain calculations show that the cavity is stable under the operating conditions given in Table I.

The simulated results at the nominal operating point are indicated in the final column of Table I. The optimal current according to the simulations is 770 A and the estimated peak output power is over 150 MW. The corresponding gain and efficiency are 49 dB and 41%, respectively. The dependence of efficiency on velocity spread is shown as the dashed line in Fig. 2. Note that the efficiency begins to drop off fairly rapidly for spreads above 7%. However, these simulations are not re-optimized with respect to magnetic field profile, etc., at each point, and additional investigations indicate that higher efficiencies can be achieved if the velocity spread is higher than expected.

We continue to work on improving our simulation capabilities. We have recently started using the commercial High-Frequency Structure Simulator software package (HFSS). The HFSS code uses the Finite Element Method to find a solution to Maxwell's equations for a given geometry and set of boundary conditions and can handle lossy dielectrics. We have been using it to model the second harmonic buncher cavity and preliminary results indicate agreement with experiment. We hope to soon begin modeling the drive cavity in order to optimize the design of the coupling apertures. In conjunction with the Naval Research Laboratory, we are working to add time-dependent capability to our codes so that we can study mode competition in greater detail.

### Cold-test results

Considerable progress has been made on the construction and cold testing of the first experimental tube. Preliminary cold-testing yielded the approximate dimensions of the input cavity required to achieve the frequency of 8.568 GHz and a quality factor of 55. The cavity's length is 2.286 cm with inner and outer radii of 1.100 cm and 3.325 cm, respectively. Two lossy ceramic rings will be used (as shown in Fig. 1) to obtain the required quality factor. The drive cavity has reached the final stages of its construction. The actual injection slots have yet to be cut, but their final size will be determined soon from a final cold test.

All of the metal hardware for the inner and outer drift tubes has been fabricated. All lossy ceramics have been constructed or procured.

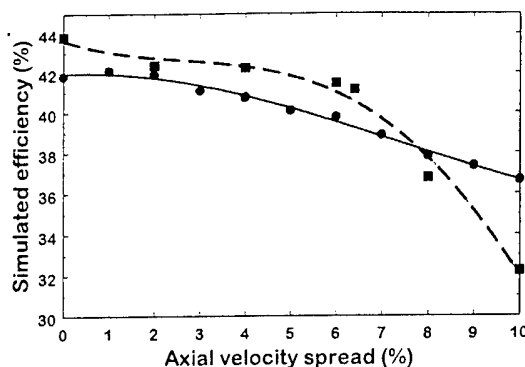


Fig. 2. Efficiency of the first (solid line) and second harmonic (dashed line) tubes vs. velocity spread.

The output cavity has twelve separate metal pieces and has been completely fabricated and cold-tested. The output cavity has a length of 1.70 cm with a 0.90 cm long diffractive lip. The cavity's outer radial wall extends to 3.59 cm while the inner radial wall dips to 1.007 cm. As indicated in Fig. 1, a fairly short taper of the inner conductor radius follows immediately after the diffractive lip to convert the coaxial waveguide to a circular waveguide. Cold testing of the output cavity (and adjacent drift tube region) was performed with a symmetric injection scheme and the resonant frequency and quality factor of the operating  $TE_{011}$  mode were found to be 8.565 GHz and 134, respectively.

The construction of the vacuum jacket is well under way. The stainless steel housing for the microwave circuit has been machined. Custom flanges are required in order to fit the tube into the bore of our existing magnetic field coils. These flanges have all been roughed out and are awaiting the final machining of the gasket grooves and brazing tabs. The final step will be to braze the flanges onto the stainless steel housing.

Since the second harmonic tube utilizes the same input cavity as the first harmonic system, no additional effort is required. An aluminum mock-up of the buncher cavity has been constructed and is in the process of being cold-tested. Preliminary results have indicated that the required quality factor and frequency can be achieved for this design. Furthermore, measurements of the  $TE_{011}$  mode indicated a resonant frequency of 8.395 GHz and a quality factor of 55. The cavity has a length of 1.748 cm and inner and outer radii of 1.62 cm and 3.52 cm, respectively. According to the simulations described earlier, this quality factor is low enough to guarantee that the cavity will be stable to the  $TE_{011}$  mode at the design operating point. We are now in the process of verifying these results with symmetric injection. Because this cavity configuration is quite novel, we are performing a fairly complete sensitivity study of parametric variations. When this is completed, we will begin fabrication of the vacuum-compatible version of the cavity.

A mock-up of the second harmonic output cavity is currently under construction. Two mode converters are required for a symmetric injection scheme; one has been procured and the other is under development. The main section of the abrupt transition output cavity has an outer diameter of 3.501 cm and an inner diameter of 1.610 cm, at a length of 1.696 cm. The diffractive lip has a length of 0.7 cm and inner and outer radii of 1.75 cm and 3.35 cm, respectively.

The output waveguide of the second harmonic tube will have to be modified slightly to reduce radial mode conversion of the amplified  $TE_{021}$  signal. The designs of the new components are complete and fabrication is expected to begin shortly.

### Summary

The upgrade of our facility is essentially complete. We have designs of first and second harmonic tubes that promise to produce peak powers of 100 MW or more with efficiencies of at least 40%. The cold-testing of the initial microwave tube is at an advanced stage and all the results are encouraging. This summer we expect to complete the fabrication and assembly of all components necessary for the two-cavity first harmonic system. The first hot test results are expected this fall. The second harmonic tube test is scheduled for early next year.

- [1] S. Tantawi, et al. *IEEE Trans. Plasma Sci.*, **20**, (1992) 205.
- [2] H. W. Matthews et al., *IEEE Trans. Plasma Sci.*, **22**, (1994) 825.
- [3] M. K. E. Flaherty, et al., *J. Appl. Phys.*, **76**, (1994) 4393.
- [4] W. Lawson, et al., *J. Appl. Phys.*, **78**, (1995) 550.

## FIRST EXPERIMENTAL OBSERVATION OF CYCLOTRON SUPERRADIANCE

N.S. Ginzburg, I.V. Zotova, A.S. Sergeev, and I.V. Konoplev,  
*Institute of Applied Physics, Russian Academy of Science*  
603600, Nizhny Novgorod, Russia

V.G. Shpak, M.I. Yalandin, C.A. Shunailov, and M.P. Ulmaskulov  
*Institute of Electrophysics, Russian Academy of Science*  
620219 Ekaterinburg, Russia

### Abstract

The first experimental observation of cyclotron superradiance from subnanosecond high-current electron bunches moving through waveguide systems is reported. Ultrashort microwave  $K_a$  band pulses with power amounted 200 kW and duration less than 0.5 ns was observed in the regime of group synchronism when electron bunches drift velocity coincide with group velocity of electromagnetic waves.

Superradiance (SR) in ensembles of classical electron-oscillators has recently attracted considerable attention [1-9]. By superradiance we understand coherent stimulated emission from electron bunches under specific conditions when the bunch sizes exceed the wavelength but nevertheless smaller than the interaction distance. This report is devoted to the first experimental observation of cyclotron SR. This phenomena involves the process of azimuthal self-bunching and consequent coherent emission in ensembles of electrons rotating in a uniform magnetic field. Cyclotron SR can be utilized to generate intense, ultrashort pulses of millimeter and submillimeter wave range radiation.

It was shown theoretically [8-9] that conditions of group synchronism when the electron-bunch drift velocity coincides with the e.m. wave group velocity is the most favorable regime for cyclotron type of SR. In fact, this regime includes some the advantages of gyrotrons [10], as far as in moving reference frame electron like in gyrotrons radiated at quasi-cutoff frequencies.

A RADAN 303 accelerator with a subnanosecond slicer was used to inject typically a 0.3-0.5 ns, 1 kA, 200 keV electron pulses [11-13]. These electron pulses were generated from a magnetically insulated coaxial diode which utilized a cold explosive emission cathode. Typical oscillograms of the electron current and diode voltage are presented in Fig. 1a,b. High current electron pulses were transported through the interaction space of total length up to 30 cm in a longitudinal guide magnetic field of up to 2 T. For measurement of the radiation a hot-carrier germanium detector which had a transient detector characteristic of 200 ps was used. The electron beam current and accelerating voltage probes possessed a similar transient characteristic. To change the electron current in the rang 50-1000 A special collimators have been used. Transverse momentum with pitch factors  $g$  about one was imparted to the electrons by the kicker installed right after the collimator.

By variation of the strength of the magnetic field microwave pulses were observed in two separated regions corresponding to grazing with the dispersion curves of the mode  $TE_{21}$  and  $TE_{01}$ . For the first mode generation occurred in the range of magnetic field between 0.11 - 0.14 T. The oscillograms presented in Fig. 1c,d confirms the behavior described theoretically in [9]. The radiation is a monopulse with duration less than 0.5 ns when the magnetic field less

than the value corresponding to grazing condition  $H < 0.12T$  and is converted to a double pulse when the magnetic field exceeds this value.

To prove that for the double pulse regime frequency in the first pulse exceeded the frequency in the second pulse set of cut-off waveguides has been used. The dashed line in oscillogram Fig.1c illustrates the essential suppression of the second low frequency pulse for waveguide with cut-off frequency 38GHz. In general, measurements showed that full spectrum of microwave pulse occupied the interval 34-40 GHz and, therefore, the relative spectrum width amounted to 20%.

Important confirmation of the stimulated nature of the observed emission can be found from the dependencies of peak power on the emission distance (in fact, on the interaction time). The graphs plotted in Fig.2 have been obtained by variation of the length of the homogeneous magnetic field for two different values of the electron current. In the initial stages the peak power grows according to an exponential law. The corresponding gain was approximately two times less than the predictions a computer simulation for as an ideal bunch. Such a discrepancy can be easily explained by the electron velocity and energy spread. Note that if the emission was caused only by the initial modulation electrons over azimuthal phases (without subsequent selfbunching) near cut-off regime the power should grow as the square root of the emission distance. In the case of a current 290 A saturation was observed of the growth of peak power. Under a smaller current of 180 A saturation for the given maximum length was not achieved.

Absolute radiation power was estimated by integrating detector signal over radiation pattern. For mode  $TE_{21}$  this power exceeded 200 kW which corresponded to an efficiency of energy transformation more than one percent.

Thus, in this work new mechanism of stimulated emission - cyclotron superradiance have been observed and powerful microwave pulses with recordly small duration have been registered.

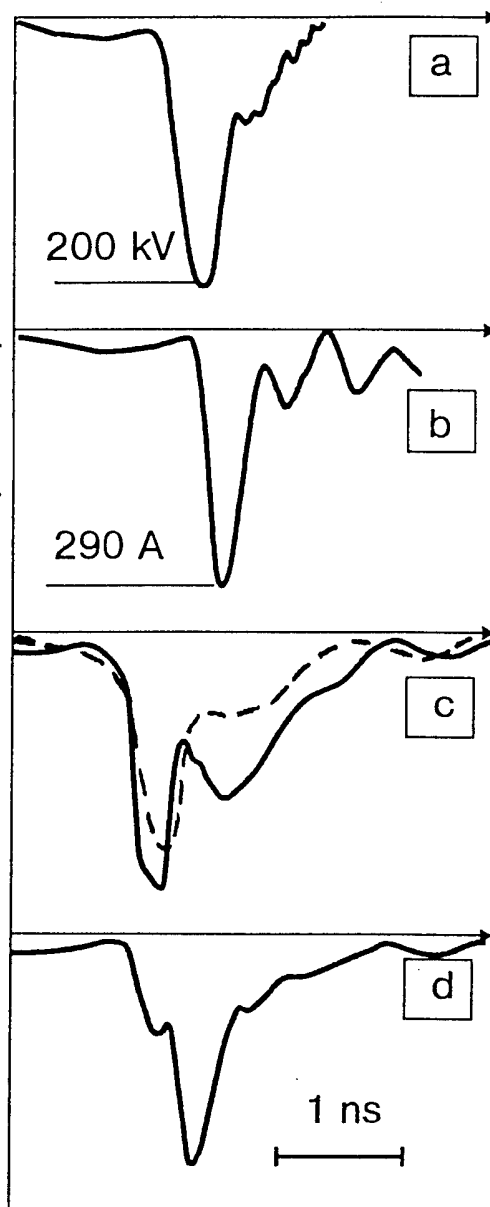


Fig.1 Oscillograms:

a - accelerating pulse on the cathode,  
b - current pulse on the entrance of the drift chamber,  
c,d - microwave signals from a detector with a 1.25 and 1.15 T, respectively .  
(Dash line on Fig.1c corresponds to the signal, passing through the filter with cutoff frequency 38GHz)



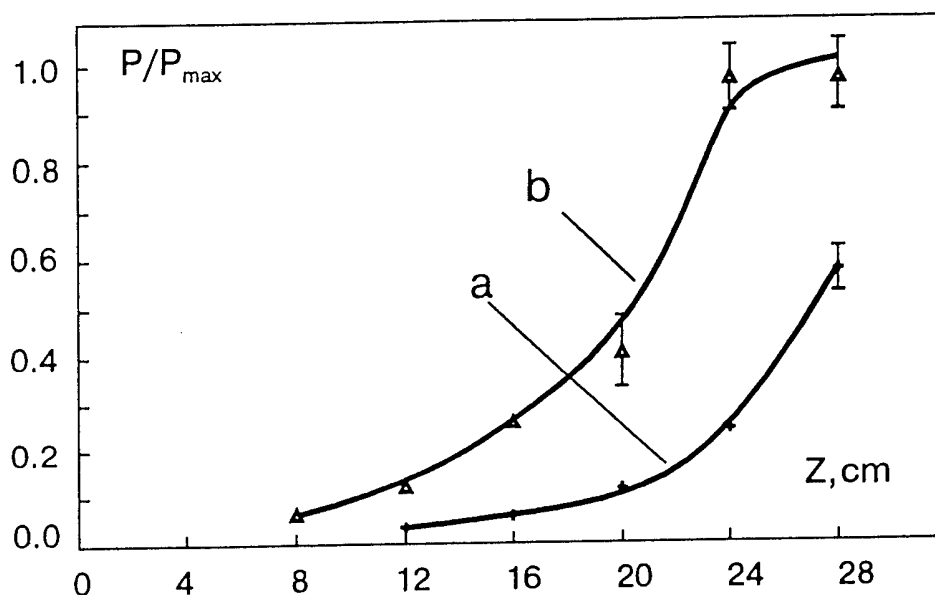


Fig.2 Peak power of a subnanosecond cyclotron superradiance pulse as a function of the travel distance of an electron swarm in a longitudinal magnetic field of 1.2 T :  
a - beam current is 180 A, b - beam current is 290 A.

### References

1. R.H.Bonifacio, C.Maroli, N.Piovella, Opt.Comm. 68 (1988) 369.
2. R.H.Bonifacio, N.Piovella, B.W.J.McNeil, Phys. Rev. A44 (1991) 3441
3. V.V.Zheleznyakov, V.V.Kocharovsky, V.I.V.Kocharovsky, Usp.Fiz. Nauk 159 (1989) 194.
4. N.S.Ginzburg, Pis'ma v ZhTF 14 (1988) 440.
5. N.S.Ginzburg, A.S.Sergeev, Opt.Comm. 91 (1992) 140.
6. N.S.Ginzburg, A.S.Sergeev, ZhETF, 99 (1991) 171.
7. N.S.Ginzburg, Yu.V.Novozhilova, A.S.Sergeev Nucl.Inst and Meth.Phys.Res.A Vol.341 P.230 (1993)
8. N.S.Ginzburg, I.V.Zotova, A.S.Sergeev, Sov. JETP Lett. 15 (1994) 83.
9. N.S.Ginzburg, I.V.Zotova, A.S.Sergeev, these proceedings
10. V.A.Flyagin, A.V.Gaponov, M.I.Petelin, V.K.Yulpatov, IEEE Trans. on Microwave Theory and Techniques, 1977, v.MTT-25, N6, p.514
11. G.A.Mesyats, V.G.Shpak, M.I.Yalandin, S.A.Shunailov. Compact High- Current Repetitive Pulse Accelerators, in Proc.8th Int.Pulsed Power Conf., 1991, San-Diego, USA, p.73
12. B.M.Kovalchuk, G.A.Mesyats, V.G.Shpak. Generation of Powerful Subnanosecond Pulses, in Proc. Pulsed Power Conf., 1976, Lubbock, USA, 1D5.
13. V.G.Shpak, S.A.Shunailov, N.R.Ul'maskulov, M.I.Yalandin, I.V.Pegel, V.P.Tarakanov, these proceedings

# HIGH EFFICIENCY FEL WITH BRAGG RESONATOR DRIVEN BY LINEAR INDUCTION ACCELERATOR

N.S. Ginzburg, A.A. Kaminsky, A.K. Kaminsky, N.Yu. Peskov,  
S.N. Sedykh, A.P. Sergeev, A.S. Sergeev

*\*Institute of Applied Physics RAS, 46 Ulyanov Str., 603600 Nizhny Novgorod, Russia*

*\*\*Joint Institute for Nuclear Research, Dubna 141980, Moscow region, Russia*

A narrow-band high-efficiency FEL-oscillator with a Bragg resonator was constructed based on a linear induction accelerator which formed a 1MeV, 200A, 200ns electron beam. At the frequency 31GHz radiation with power 31MW and efficiency 25% was measured. High efficiency and narrow spectrum width of spectrum was achieved by the selective properties of the Bragg resonator in combination with the high quality of the helical electron beam formed in the reversed guide field regime.

## Introduction.

The aim of this work was to design, build and construct a high efficiency, narrow-band spectrum FEL-oscillator which operated in the millimeter wavelength range. To achieve this the high selective property of a Bragg resonators [1] was combined with the advantages of operating the FEL in the, so-called, reversed guide magnetic field regime. When operating in this regime previous investigations [2, 3] demonstrated the possibility of forming a helical electron beam with a low spread of parameters and, thus, the possibility of achieving high efficiency.

## Numerical simulation of excitation of a FEL with Bragg resonator.

Preliminary, dynamics of FEL operation with a two-mirror Bragg resonator was studied theoretically. Time domain analysis taking into consideration the dispersion properties of the Bragg reflectors was used. The numerical simulation of excitation of a FEL by a relativistic electron beam and oscillation build-up was performed. Analysis of the frequency spectrum and the dependence of the output power on time indicates a two stage transient process. The first stage of the transient process is accompanied by large oscillations of efficiency and output power (Fig. 1a). Such oscillations are caused by excitation of all longitudinal modes disposed at the zone of Bragg reflections. Firstly all longitudinal modes disposed at the zone of the Bragg mirrors are excited by the electron beam (Fig. 1b). Later at the second stage one of the longitudinal modes grows and suppresses other modes due to a nonlinear mode competition mechanism. This results in a single mode being established (Fig. 1c) and consequently stationary single frequency operation.

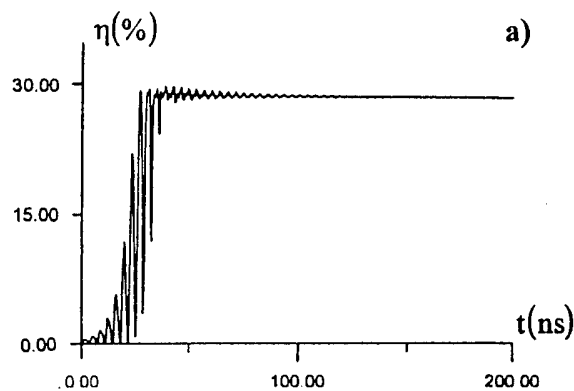


Fig.1 Computer simulation of excitation of the FEL-oscillator with two-mirror Bragg resonator and oscillations build-up under optimal experimental conditions  
( $E_{\text{beam}} = 0.8\text{MeV}$ ,  $I_{\text{beam}} = 150\text{A}$ ,  $f = 31\text{GHz}$   
 $B_0 = -2\text{kG}$ ,  $B_w = 1\text{kG}$ ,  $Q = 450$ )

a) time dependence of efficiency

### Microwave system of the FEL.

The calculations discussed above were used to design and construct a two-mirror Bragg resonator for the FEL experiment. The cavity consisted of two Bragg reflectors separated by a central 22mm inner diameter uniform cylindrical waveguide. The Bragg reflectors were constructed by machining 0.3mm deep and 5.4mm period corrugations on the inner wall of the waveguide. A 16.2cm long Bragg reflector was positioned at the cathode side of the cavity with Bragg reflectors of different lengths positioned at the collector side of the FEL. In agreement with calculations, three effective reflections of the operating  $TE_{1,1}$  wave of the circular waveguide into backward waves were observed in "cold" microwave measurements of the Bragg reflectors. For a launched  $TE_{1,1}$  wave at a frequency of 29GHz, the backward  $TM_{1,1}$  and  $TM_{1,2}$  waves at a frequency of 31GHz and 38GHz respectively were measured. Dependence of the reflectivity of the Bragg mirrors as a function of frequency is shown in Fig.2a. The number of high-Q-factor longitudinal modes for every reflection zone was 3-7 (Fig.2b) when a regular 30cm to 70cm long cavity section was used. The Q-factors of these modes for different lengths of regular cavity sections and reflectors are given in Table 1.

### Experimental results.

An experimental study of the FEL was performed on the LINAC-3000 (JINR, Dubna) which generated electron energies up to 1MeV and a 200A beam current pulse of duration 200ns at a repetition rate of 2Hz. The helical wiggler with period of 6cm and amplitude of transverse magnetic field on the axis up to 3.5kG was used to pump the oscillation velocity to the electrons. The wiggler field was slowly up-tapered over the initial six periods, providing an adiabatic entrance for the electron beam. The wiggler was immersed in a uniform axial magnetic field generated by a solenoid. The strength of this field could be varied up to 10kG. Also, it was possible to vary the direction of the guide field.

Free Electron Laser operation in the reversed guide magnetic field regime (marked by "-" sign) was studied. In such a regime the direction of rotation of the electrons in the uniform axial guide field is opposite to its rotation in wiggler field. An advantage of operating the FEL in the reverse guide magnetic field regime, far from the cyclotron resonance regime is the ability to form a high-quality helical electron beam with low spread of parameters.

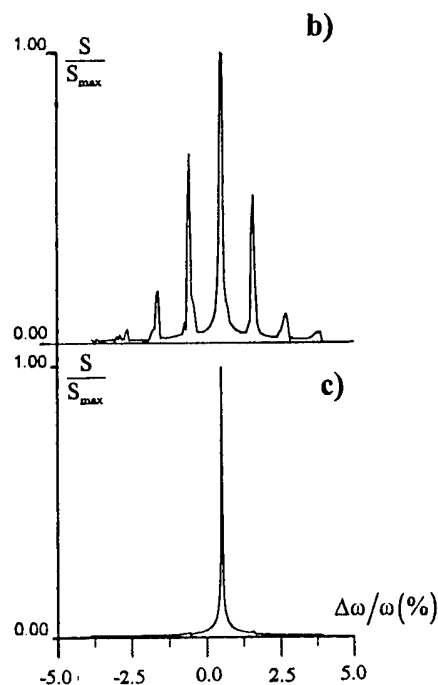


Fig.1 (continuation)

b) the spectrum of radiation in the transient stage ( $t < 500$  ns)

c) the spectrum of radiation in the stationary regime ( $t > 50$  ns)

Radiation at the designed circularly polarized  $TE_{1,1}$  wave and separate frequencies corresponding to all the feedback waves mentioned above was detected. Selection of the feedback regime was achieved by changing both the wiggler and guide fields.

The duration of RF pulse measured was approximately 100ns (Fig.3). The radiation frequencies detected were in good agreement with the measured reflection bands of Bragg mirrors (Tabl.1). The highest radiation power (measured by means of a calorimeter and calibrated semiconductor detectors) as well as the narrowest bandwidths were measured at a frequency of 31GHz. Reflection coefficients of the Bragg mirrors and, consequently, the Q-factors of the longitudinal modes corresponded to the optimal value calculated from the computer simulation. Initially a 10cm long output Bragg reflector was used which was later decreased in length to 3cm. Calculations indicated that FEL efficiency should increase by reducing the length of the output Bragg reflector. At the same time the length of the central regular waveguide section was increased from 30cm to 70cm. By measuring the radiation spectrum width and power for the different Bragg cavity configurations mentioned above it was discovered that both remained relatively constant. These experiments demonstrate that this type of FEL is a flexible system which maintains high efficiency and high selectivity over a large range of cavity configurations.

The spectrum of the radiation was determined by means of a set of waveguide cut-off filters which were used to measure the wavelength in the band 0.7 - 1.2 cm to an accuracy of 1%. The measured spectrum width of the output radiation in all cases did not exceed the reflection band width of the Bragg mirrors. Comparison of the measured spectrum of radiation (Fig.2c) with that measured in "cold" microwave experiments (Fig.2b) shows that only one eigenmode of the cavity lies inside the measured frequency region of the radiation. Computer simulations predict that the electron beam does not shift the frequency of the radiation from the eigen-frequency of the cavity. Thus measurement of a single longitudinal cavity mode in the experiment does not contradict the theoretical prediction of realization of single-mode single-frequency operation of the FEL

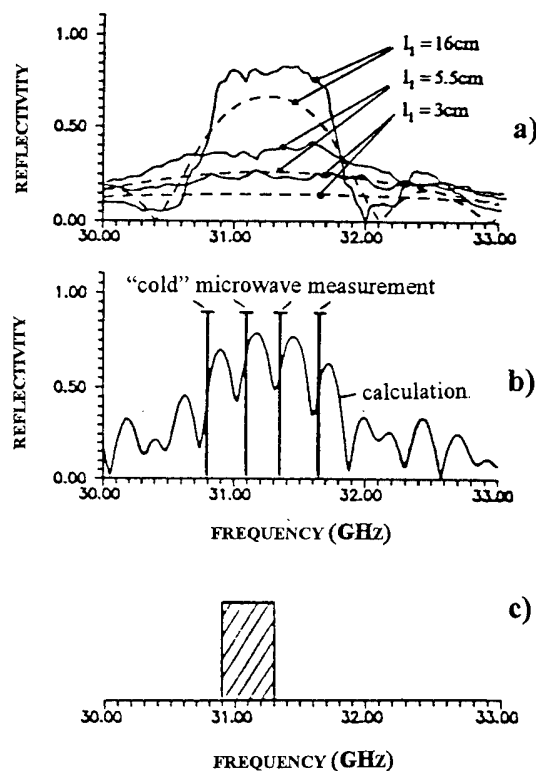


Fig.2

- a) Reflection coefficient of separate Bragg mirrors having different lengths versus frequency (for feedback circle  $TE_{1,1} \leftrightarrow TM_{1,1}$ ): solid line corresponds to "cold" microwave measurements, dotted line corresponds to the calculations.
- b) Reflection coefficient of two-mirror Bragg resonator ( $l_1 = 16\text{cm}$ ,  $l_0 = 40\text{cm}$ ,  $l_2 = 3\text{cm}$ ) versus frequency. Minimum of the reflection coefficient correspond to eigenmodes of the Bragg resonator "Cold" microwave measurements of the eigen-frequencies are shown.
- c) "Upper estimation" of radiation spectrum measured in "hot" experiments using a set of cut-off waveguide filters.

## Conclusion.

A narrow band FEL-oscillator with a reversed guide magnetic field which generated microwave radiation at different feedback regimes of the Bragg resonator was realized. The FEL parameters under which microwave generation was observed were in good agreement with numerical simulation. Measured radiation frequencies coincided with the results of "cold" microwave experiments. At the frequency 31GHz the output power was 31MW which corresponded to a FEL efficiency of ~25%. The efficiency achieved outstrips the efficiency of previous FEL-oscillator experiments which used a guide magnetic field. It is important to note, that high efficiency was realized at the full current produced by the accelerator (without the need to reduce the current in the beam).

The observed frequency band width was less than 1%. The radiation spectrum most probably consisted of one resonator mode or, perhaps two such modes. This rather narrow spectrum width was possible because of the high quality of the helical electron beam formed in the reversed guide field regime as well as the excellent selective properties of the Bragg resonator. We believe presented here is only an upper estimation of real frequency bandwidth. In later experiments more precise measurement of the spectrum will be attempted.

This work was supported by the grant N:R8B300 from International Science Foundation and grants N:94-02-04481 and N:95-02-05697 from Russian Foundation for Fundamental Research.

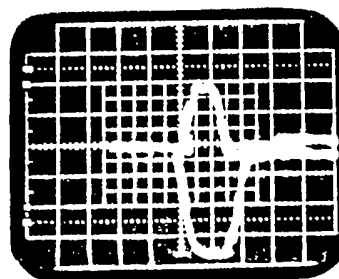


**Fig.3** The typical oscilloscope traces of the beam current (lower signal, 50A/div) and RF power (upper signal, 15MW/div); horizontal scale 100ns/div

**Table 1.** Summary of experimental results ( $I_{beam} = 150A$   $E_{beam} = 0.8MeV$ )

Interaction region length (cm)	40	70	40	30	40
Output reflector length (cm)	10.8	5.4	3.0	5.4	10.8
Undulator field (G)	1100		900		610
Solenoid field (G)	-2200		-1800		-1440
Radiation frequency (GHz)	29.3±0.3		31.1±0.2		38.2±0.9
(corresponding backward wave)	TE <sub>1,1</sub>		TM <sub>1,1</sub>		TM <sub>1,2</sub>
Output power (MW)	6	20	31	23	3
Efficiency (%)	5±1	16±3	25±5	19±4	2.5±0.5

## References

1. V.L.Bratman, G.G.Denisov, N.S.Ginzburg and M.I.Petelin, IEEE J. of Quant. Electr. QE-19 (1983) 282.
2. A.A.Kaminsky, A.K.Kaminsky, S.B.Rubin et al., Particle Accelerators 33 (1990) 189.
3. M.E.Conde and G.Bekefi, Phys. Rev. Lett. 67 (1991) 3082.

## Plasma Technology for Treatment of Waste\*

Daniel R. Cohn\*\*

*Plasma Fusion Center*

*Massachusetts Institute of Technology*

*167 Albany Street*

*Cambridge, MA 02139, USA*

### ABSTRACT

Meeting goals for waste cleanup will require new technology with improved environmental attractiveness and reduced cost. Plasma technology appears promising because of the high degree of controllability; capability to process waste without the adverse effects of combustion; and a very wide temperature range of operation. At the Plasma Fusion Center at the Massachusetts Institute of Technology, we are investigating a range of plasma technologies. "Hot" thermal plasmas produced by DC arc technology are being investigated for treatment of solid waste. In conjunction with this activity, new diagnostics are being developed for monitoring arc furnace operating parameters and gaseous emissions. Electron-beam generated plasma technology is being investigated as a means of producing non-thermal "cold" plasmas for selective processing of dilute concentrations of gaseous waste.

### INTRODUCTION

Plasma technology is showing promise for a variety of waste processing applications. Conventional approaches for high throughput waste processing have significant drawbacks. Landfilling raises concerns about release of hazardous materials to water, the ground, and air. There is also a shortage of acceptable space for landfilling in many areas of the world. Incineration raises concerns about undesirable air emissions and toxic ash. Plasma technology has the potential to remove these concerns and to reduce cost. The attractiveness of plasmas results from the capability to provide high temperatures, a high degree of controllability, and the use of electricity for heating rather than heat from combustion.

The temperature range of interest for plasma applications extends from approximately 10,000° C to room temperature. At MIT we are studying the use of high temperature (10,000° C range) arc plasmas for "hot plasma" treatment of solid waste and room-temperature range "cold" plasmas for treatment of gaseous waste.

### HOT PLASMA VITRIFICATION OF WASTE

We have been investigating vitrification of solid waste using heating provided by a graphite electrode dc arc plasma furnace. The high temperature heating can melt almost any type of material and facilitate transformation into glass. The objective of the program, which is a joint effort with Battelle Pacific Northwest Laboratories, is to develop an improved means to treat mixed waste (radioactive and chemical) for U. S. Department of Energy needs.

The goal is to develop a process for a high throughput system to turn solid waste into stable non-leachable products which can be safely stored and to greatly reduce air pollution relative to incineration. Because the heating is electrical rather than combustion-powered, there is less off-gas, and there can be a significant reduction in entrained particulates. Moreover, because the atmosphere of the plasma furnace can be non-oxidizing, production of hazardous compounds such as dioxin can be greatly reduced or eliminated.

For radioactive waste, with treatment costs of over \$1,000 per ton, the electricity cost for plasma processing (for example, \$50 per ton assuming 1000 kWhr per ton and \$.05 per kW hr) is not an important cost factor.

\*Work sponsored by Office of Technology Development, Environmental Restoration and Waste Management, DOE.

\*\*In collaboration with L. Bromberg, K. Hadidi, D. Y. Rhee, J. E. Surma, P. Thomas, C. H. Titus, and P. P. Woskov.

Plasma vitrification could also be used for treatment of hazardous waste, medical waste, and incinerator ash. Costs for incineration and landfilling are typically in the \$200-\$1000 per ton range. In addition plasma vitrification has potential for economically competitive treatment of municipal waste. Generation of electricity using combustible gas produced by plasma processing would be used to reduce cost. The present relatively low cost for treatment of municipal waste (\$30-\$100/ton plus transportation cost) imposes demanding requirements on plasma vitrification costs.

The plasma in our furnace is created between a cylindrical electrode and waste material which is in a graphite crucible. The plasma is in thermal equilibrium with approximately equal electron, ion, and neutral temperatures. Typical central plasma temperatures are around 10,000° C. The material is typically heated to temperature in the 1500° C range. The plasmas are produced in atmospheric-pressure range nitrogen gas.

Graphite electrodes are used because of their ruggedness and capability for carrying high current. An important mode of operation that is facilitated by use of a graphite electrode is submerged operation where the plasma is formed in a cavity underneath the surface of the material to be processed. This mode of operation greatly reduces particulate emission. The material on top of the plasma acts as a "cold top" to prevent emissions.

A small graphite electrode dc arc plasma furnace, the Mark 1, has been used to melt a variety of simulated wastes of interest to the Department of Energy Cleanup Program. These wastes have consisted of mixtures of soils, metals, and combustibles. The furnace produced a black glass which is very stable and passed standard leaching tests[1]. The Mark 1 was batch-fed and typically operated at power levels of 30 kW.

A pilot-scale research furnace with continuous feed capability, the Mark 2 furnace, has undergone initial tests at the MIT Plasma Fusion Center. Figure 1 shows a schematic diagram of the Mark 2 pilot-scale research furnace. The furnace has been operated at power levels in the 250 kW range. It has processed waste material at a rate of about 200 pounds per hour.

A key future direction is to study the effect of various furnace conditions upon particulate and hazardous metals emission from the graphite electrode arc plasma furnace.

New monitoring technology is being developed to optimize furnace performance and to ensure that environmental quality goals are met. One diagnostic uses a microwave-generated plasma to make continuous sensitive measurements of off-gas metals emission[2]. The plasma is formed in a special robust waveguide inserted into the off-gas system. Material that passes through the plasma is vaporized, ionized, and electrically excited. Light emitted from the plasma is conducted by fiber optics to a spectrometer for analysis.

Figure 2 shows metals that have been measured in an initial test on simulated waste processed in the Mark 2 furnace. A determination of sensitivity for furnace use has not yet been made. Laboratory tests have indicated a sensitivity in the one to ten parts per billion range for a number of metals and this type of sensitivity should be possible in furnace operation.

The microwave plasma continuous emissions monitoring has also been used to make sensitive laboratory measurements of plutonium at Battelle Pacific Northwest Laboratories.

Another diagnostic is a millimeter wave pyrometer which determines the temperature of the material to be processed and the temperature of the walls of the furnace by measurement of millimeter wave radiation which is emitted from these hot bodies. An important advantage of this approach relative to conventional infrared pyrometers is that millimeter radiation can be seen through the hostile smoky environment of the plasma furnace, and the system is very rugged [3].

The millimeter wave pyrometer, microwave plasma metals sensor, and other diagnostics will be used to study a wide range of dependences of particulates, metals, and organic gas emissions on various furnace operating parameters. Over the long term, this information may be used for feedback control of the waste treatment units.

### COLD PLASMA WASTE TREATMENT

Cold plasmas with gas temperatures in the room temperature range are useful for treating hazardous gases with dilute concentrations of contaminants. The plasma is in a non-equilibrium condition where the electron temperature is much greater than the ion and neutral temperatures. The plasma electrons and radicals selectively attack the contaminant molecules. As a result, the process is highly efficient because, in contrast to thermal processes where every

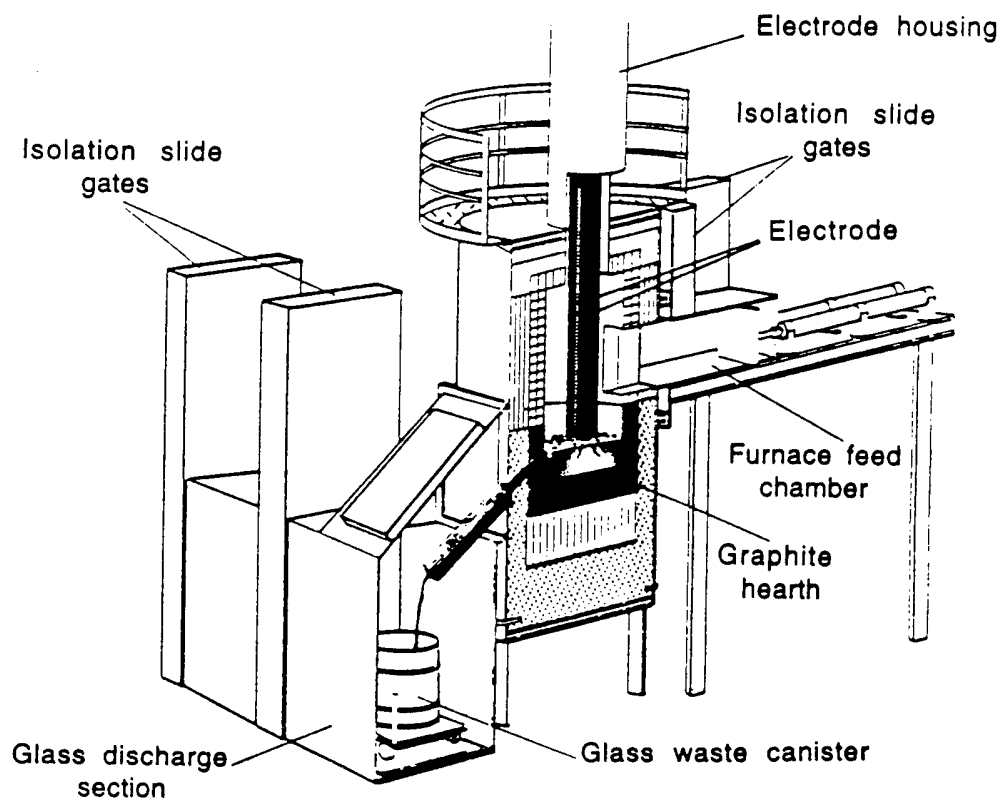


Figure 1 Mark 2 graphite electrode dc arc furnace.

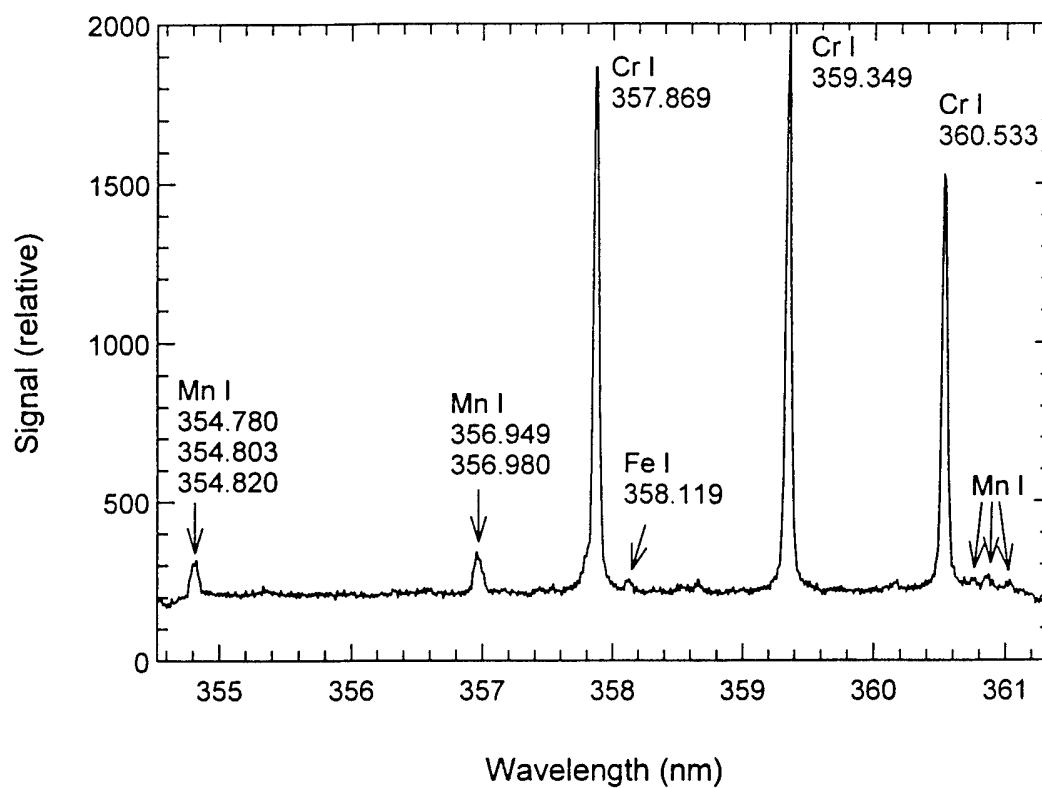


Figure 2 Mark 2 exhaust spectrum with high-resolution spectrometer just prior to start of soil loading. Waste material temperature 1410° C.



molecule in the gas stream must be heated up to temperatures needed for decomposition, the energy in the plasma is highly directed into the molecules that it is the goal to destroy.

In order to develop a practical high throughput system, it is desirable to operate at atmospheric pressures. The attainment of non-equilibrium conditions at atmospheric pressures requires special conditions because of the high collision rate among electrons, ions, and neutrals which tends to equilibrate their temperatures. At MIT, an electron beam is being used to generate the cold plasma. Electron beams are a very efficient way to generate low-energy electrons in a cold plasma. In contrast to standard plasma discharges, less energy is lost in the production of excited atomic and molecular states.

The electron-beam vacuum is separated from the gas to be processed by a thin foil. The electron beam energy is in the 150-300 keV range. Special external shielding is not needed for this range of energies, and highly reliable commercial systems are available.

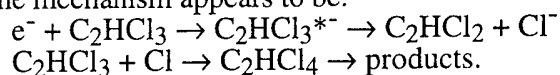
We have used the electron-beam generated plasmas to decompose various chlorinated compounds in air streams. This work is motivated by the need for a system to provide low cost, environmentally attractive decomposition of solvents that are vacuum-extracted from the ground. The work has been supported by the Department of Energy.

For chlorinated compounds like carbon tetrachloride and trichloroethylene, the decomposition process appears to be electron-attachment-induced decomposition:

$e^- + CCl_4 \rightarrow CCl_4^{*-} \rightarrow CCl_3 + Cl^-$  where \* indicates an activated unstable species. The decomposition initially breaks off a chlorine ion. The resulting product chlorine radical  $CCl_3$  undergoes further decomposition. The final products are simple molecules such as chlorine which can be readily converted into benign products such as salt.

As shown in Figure 3, laboratory studies of carbon tetrachloride indicate that around 60 eV of energy is needed per molecule decomposed for 75 percent decomposition of  $CCl_4$  in air streams with concentrations in the 300-600 ppm range. Decomposition measurements were made with a gas chromatograph and a mass spectrometer. The 60 eV requirement is consistent with a requirement of approximately 30 eV for electron-beam generation of an electron. Approximately 100 eV is needed for 95 percent decomposition due to competition for electrons from the decomposition products. Competition for electrons also leads to higher energy requirements for lower initial concentrations.

For trichloroethylene, which is perhaps the most widely encountered solvent in remediation activities, about 10 times less energy is required per decomposition relative to the amount required for the decomposition of  $CCl_4$ . The energy expense is typically 10 eV per molecule decomposed. It appears that the reason for this decrease in energy expense is due to the presence of a chain reaction where chlorine ions released in the decomposition in turn create more decompositions. The mechanism appears to be:



TCE which has a double carbon bond is vulnerable to chlorine ion attack, whereas carbon tetrachloride is not vulnerable[4], [5].

The 10-eV energy requirement for decomposition of trichloroethylene is orders of magnitude less than the energy that would be required if a thermal process were used for 100-ppm range initial concentrations. Assuming approximately 0.2 eV required per molecule for thermal decomposition, the energy required per contaminant molecule is  $0.2 \text{ eV}/10^{-4} = 2000 \text{ eV}$ . This amount of energy is 200 times that required for non-thermal decomposition. This increase in efficiency can more than compensate for the increased cost of an electron-beam generated plasma system relative to thermal treatment systems.

Laboratory studies have been made of the decomposition of a variety of other volatile organic compounds[5]. These compounds include toluene in addition to various chlorinated compounds.

Following a wide range of laboratory tests, an electron-beam generated cold plasma field unit was assembled in a trailer. Figure 4 shows the field test unit as assembled in a 43-foot trailer. The unit included a commercial electron beam and a conventional scrubber which converted the decomposition products, such as chlorine, into benign final products such as salt. The unit used infrared detectors to monitor inlet and outlet concentration levels. It was designed for automatic control without the presence of an operator. The unit was employed in

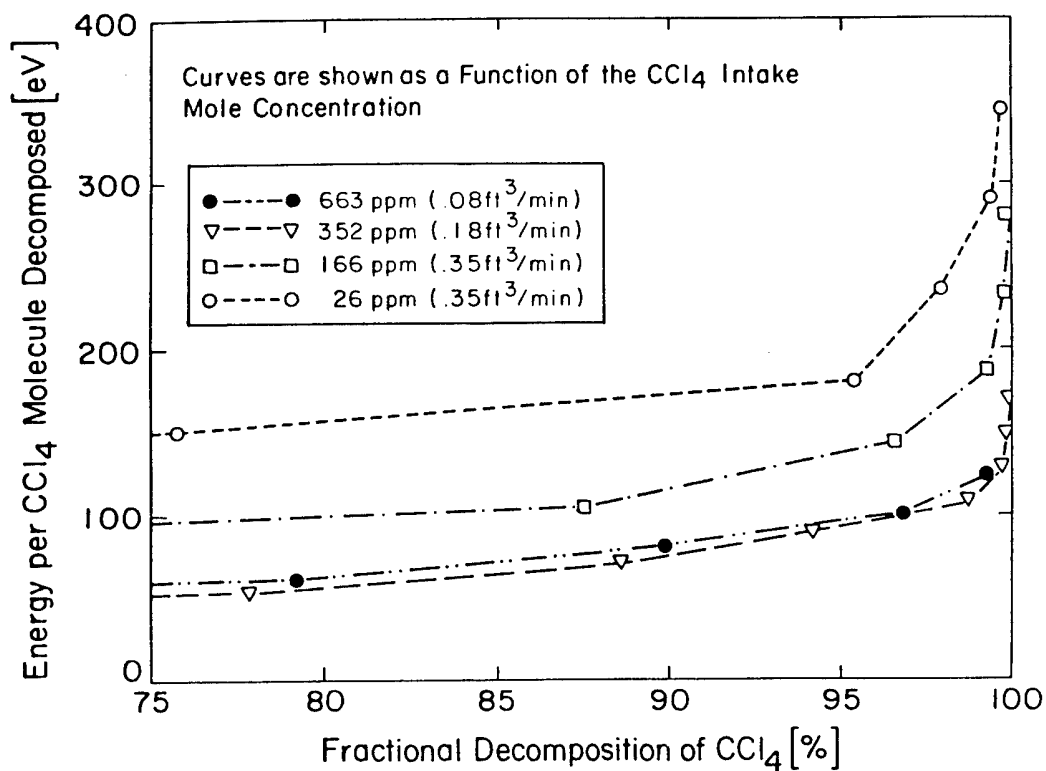


Figure 3 Energy requirement per  $\text{CCl}_4$  molecule decomposed as a function of fractional decomposition.

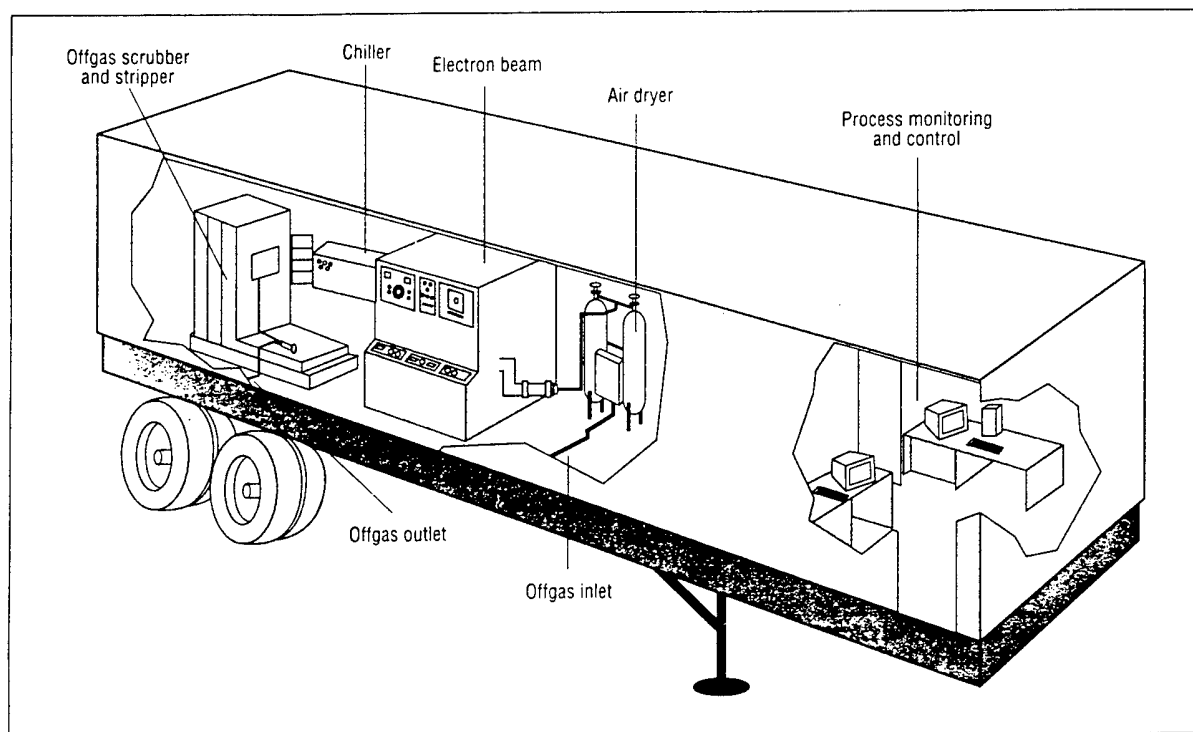


Figure 4 Field test unit as assembled in a 43-foot trailer.

initial field tests at the DOE Hanford site and operated successfully for 300 hours. It was used to decompose  $\text{CCl}_4$  in the 300-ppm concentration range in vacuum-extracted air streams.

In addition to use for treating vacuum-extracted solvents, the cold plasma technology could also be used for treatment of contaminants which are air-stripped from contaminated water. Another potential area of research is the treatment of industrial process emissions.

### SUMMARY

To date combustion heating has been virtually the only means used to create changes in states of matter for environmental applications. The wide temperature capability and controllability of plasma technology may add important new capability in applications to waste treatment. Significant practical applications are likely within this decade.

### ACKNOWLEDGEMENTS

The author would also like to acknowledge the collaboration of Dr. Richard M. Patrick (deceased) and Dr. Mathias Koch.

### REFERENCES

- [1] Surma, J. E., W. E. Lawrence, C. H. Titus, J. K. Wittle, R. A. Hamilton, D. R. Cohn, D. Rhee, P. Thomas, and P. P. Woskov, Treatment of Simulated INEL Buried Wastes Using a Graphite Electrode dc Arc Furnace, Proceedings of International Topical Meeting on Nuclear and Hazardous Waste Management Spectrum '94, Atlanta, GA, Aug. 14-18, 1994 (published by the American Nuclear Society, Inc., La Grange Park, IL 60525).
- [2] Woskov, P. P., D. R. Cohn, D. Y. Rhee, C. H. Titus, J. K. Wittle, and J. E. Surma, MIT Plasma Fusion Center Report No. JA-93-28, Proceedings of 6th International Symposium on Laser-Aided Plasma Diagnostics, Bar Harbor, Maine, Oct. 24-28, 1993.
- [3] Woskov, P. P., D. R. Cohn, D. Y. Rhee, P. Thomas, C. H. Titus, and J. E. Surma, Active Millimeter-Wave Pyrometer, Rev. Scientific Instruments 66(8), 4241, 1995.
- [4] Koch, M., D. R. Cohn, R. M. Patrick, M. P. Schuetze, L. Bromberg, D. Reilly, K. Hadidi, P. Thomas, and P. Falkos, Electron Beam Atmospheric Pressure Cold Plasma Decomposition of Carbon Tetrachloride and Trichloroethylene, Environmental Science & Technology 29(12), 2946, 1995.
- [5] Vitale, S. A., K. Hadidi, D. R. Cohn, L. Bromberg, and P. Falkos, Decomposing VOCs with an Electron-Beam Plasma Reactor, CHEMTECH 26(4), 58, 1996.

# PULSED POWER SYSTEMS FOR COMMERCIAL TREATMENT OF MATERIALS USING SHORT PULSE, INTENSE ION BEAMS

Eugene L. Neau, QM Technologies, Inc.,  
Larry X. Schneider and Kim W. Reed, Sandia National Laboratories

*QM Technologies, Inc.  
3701 Hawkins St. NE  
Albuquerque, NM, 87109*

## Abstract

The high peak power, single-pulse technology developed for government programs during the mid-60's through the mid-80's is being adapted for use in continuously operating, high average power commercial materials processing applications. A new thermal surface treatment technology, called Ion BEam Surface Treatment (IBEST), uses repetitive high energy (kJ's per pulse), pulsed ( $\leq 500$  ns) ion beams to directly deposit energy in the top 1-20 micrometers of the surface of any material <sup>(1)</sup>. A high average power IBEST processing system is made up of a magnetic pulse compressor (MPC), a Magnetically confined Anode Plasma (MAP) ion beam source, an ion beam transport system, a materials handling system and various cooling and reset systems. System issues such as cost, reliability, size, maintainability, and design-for-manufacturability that were of secondary importance behind specific performance requirements for the earlier government applications are now the primary issues in proposed industrial systems. Research systems are now obtaining lifetime, reliability, and design-rules information for high average power short-pulse components. Beam sources are being developed that are suitable for industrial systems operating at 5-100 kW, 0.1-2.0 MeV, and  $\leq 500$  ns pulse widths. Capital equipment costs, operating and financing costs, and sizing issues are being weighed against specific economic benefits obtained in short-pulse ion beam treatment of selected products. Dependable equipment designers and suppliers, facility integrators, and servicing organizations are being combined with development teams from end-user companies for final technology integration into major manufacturing facilities. An IBEST prototype commercial system is being designed and fabricated by QM Technologies for initial operation in mid-1997.

## Introduction

Recent advances in high average power, pulsed ion beam systems are enabling a new technology to achieve rapid melt and resolidification of surfaces. Researchers at Quantum Manufacturing (QM) Technologies, Sandia National Laboratories, Applied Pulsed Power, and Cornell University are developing the capability to produce 1-100 kW average power, pulsed ion beams at 0.1-2 MeV energies. These repetitive (up to 120 Hz) systems use component design concepts with expected long lifetimes. This new capability is enabling us to develop a commercial-scale thermal surface treatment technology called Ion Beam Surface Treatment (IBEST). This new technique uses high energy, pulsed (typically  $\leq 500$  ns) ion beams to directly deposit energy in the top 1-20 micrometers of the surface of any material as shown in the tool steel example (Figure 1). The depth of treatment is controllable by varying the ion energy and species. Deposition of the energy in a thin surface layer allows melting or vaporization of the layer with relatively small energies (1-10 J/cm<sup>2</sup> for metal surfaces). The thin heated region allows rapid cooling of the melted layer by thermal diffusion into the

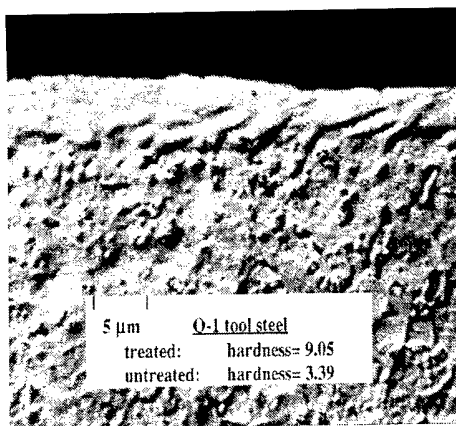


Fig. 1 - IBEST treated O-1 tool steel showing IBEST homogenized 5 micron surface layer with 3x increased hardness.

underlying substrate. Solidification of metals at cooling rates of up to  $10^9$  °K/sec results in the production of non-equilibrium microstructures (nano-crystalline and metastable phases) in the surface layer. These surface layers have significantly improved corrosion, wear, and hardness properties. The IBEST process also allows the for surface mixing of materials that are immiscible during normal quenching <sup>(2)</sup>.

### System Requirements

**Specific IBEST driver requirements** - The IBEST system requirements are set by evaluating energy requirements, per pulse, on the target material for the required application and type of material modification.

For most metals, the energy required is about 5 to 8 J/cm<sup>2</sup> to cause melt and/or ablation leading to homogenization of the top 1-10 micrometers. The total area treated with the ion beam, per pulse, with the initial system is on the order of a few hundred's cm<sup>2</sup> to minimize heat effected zones and edge effects. These considerations imply a total required ion beam energy of about 1500 J per pulse. The MPC system delivers  $\leq 500$  ns pulses, at  $\leq 200$  kV, to a 2 or 3 stage induction voltage adder to give the desired beam acceleration potential. Based on evaluations of expected product throughput requirements, the maximum repetition rate is being set at 10 pulses per second (PPS). The MPC technology, however, has the capability of being extended to greater than 100 PPS for operation in high speed linear processing applications.

**General system design considerations** - Thyatron or SCR technology combined with magnetic switching and induction voltage adders forms a robust and reliable technology base suitable for commercial IBEST systems. The industrial scale capabilities of this short-pulse high average power technology has been demonstrated at Sandia National Laboratories RHEPP-II accelerator<sup>(3)</sup>, a 300 kW, 2 MeV system. Power levels from kilowatts to 100's of kilowatts are possible with this modular, all solid-state technology base. While RHEPP-II has demonstrated the performance and operational characteristics needed for commercial applications such as IBEST or high-throughput electron-beam processes, the design of this research system did not emphasize lifecycle cost, or manufacturability issues to the extent needed for commercial systems. A concurrent engineering process focusing on reducing lifecycle costs and design for manufacturability issues is underway to address system cost

reductions, reliability, operating costs, and production and assembly costs. An additional focus on establishing the integrated logistics needed to provide a long-term support network of Original Equipment Suppliers (OEM's), service providers, and training capabilities for future customers is also in progress at QM Technologies. Technical challenges in commercialization of this technology base also exists in areas such as component reliability, industrial packaging, diagnostics, and beam uniformity. Assuring consistent surface treatment, for example, without an array of complex and expensive digitizers represents a major design challenge. Packaging for minimum

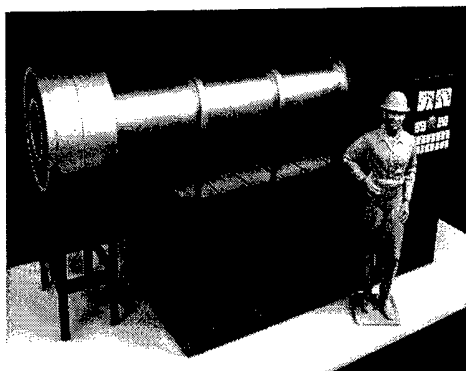


Fig 2 - Conceptual design of a compact QM1 processor.

volume and footprint along with accessibility and maintainability results in a conceptual design of the compact IBEST system shown in Figure 2. Cooling of the MPC switches and MAP ion diode magnetic field coils and components is being provided by flowing liquid cooling through external heat exchangers. The amount of heat to be removed can be minimized by using energy recovery circuits in both the MPC and MAP systems to recover unused or reflected energy. Specific material handling equipment custom designed for each application will be supplied by a vendor specializing in robotic systems.

**System and Component Reliability** - Reliability will be a key issue in the lifecycle cost of commercial IBEST systems. Replacement of major components will need to be limited to intervals of thousands of hours of operation. For a 10 pps processing system with a 60% usage factor, a system Mean-Time-To-Failure (MTTF) will need to reach an approximate  $10^9$  pulse characteristic lifetime figure to realize a 5 year operating period without major incurred service expenses. For a system with 50 critical components, this requires individual lifetimes of greater than  $3 \times 10^9$  pulses, assuming a normal failure mode distribution. Initial component designs may have multiple failure modes, induced by manufacturing processes, which will create infant mortality or broader distribution failures. Manufacturing, assembly, and maintenance processes will need to be refined until the failure modes are dominated by electric field design levels, average and peak current levels, and intrinsic material characteristics, not production related variables.

Development of a component reliability database and design guidelines for long-life component performance is a high priority. Magnetic compression circuits, at energies of 5-6 Joules/pulse, have demonstrated MTTF of over 2500 hours at a pulse rate of 4.5kHz in the

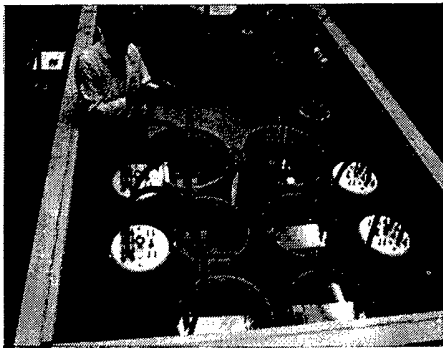


Fig. 3 - Dual pulser test bed is designed to address magnetic compressor reliability and synchronization issues.

copper laser program<sup>(4)</sup>, however, the individual component operating parameters are different enough to warrant a continued examination of reliability issues. Sandia National Laboratories has constructed a 100 PPS test bed to generate component lifetime data with well characterized operating electric fields, temperatures, etc. (Figure 3). This system uses semiconductor primary power conditioning stages and modular magnetic switch and linear induction voltage adder configurations combined with electrical and thermal diagnostics required for repetitive operation. This system design explores the possibility of packaging pulse compression switches and energy stores, running at up to 150 kV and

120 J/pulse, in sealed containers. The switching and transformer components are oil impregnated under vacuum and the use of sealed, modular packaging may contribute to simpler servicing at the added cost of interconnection devices. The importance of having highly reliable auxiliary cooling and reset systems also plays a key role in system availability which is easily overlooked during the design process. QM Technologies plans to construct at least one complete IBEST electrical driver module, which can be run around the clock (perhaps at an increased repetition rate), to gain early system and component MTTF information.

**Operational issues** - Computer control and monitoring a high average power IBEST system can be done using a commercial Programmable Logic Controller, such as the Allen Bradley model SLC-500 (Figure 4), which is used to fully automate the RHEPP-II accelerator. Special



Fig 4 - A PLC, with touch panel input, monitors and controls the RHEPP-II, 300 kW, 2 MeV facility.

purpose input/output modules provide the closed-loop interface to the various high voltage sub-systems. In this facility, a single touch panel is employed to set the pulse repetition rate and the total number of pulses. When used in a batch processing application, the PLC will interface and synchronize the accelerator with the robotic material handling equipment according to preset surface treatment parameters. It will be desirable to have all operating parameters internally monitored and to have this information available for remote dial-in diagnostics in event of system operations problems.

**Safety considerations** - A 450 kV electrical pulse generating system with associated vacuum and oil containment systems will require early and careful attention to local and federal regulations concerning operator and environmental safety issues. The possibility of generating small amounts of low energy x-rays (from the 25% leakage electron current in the MAP source) requires the careful design of a self shielding enclosure for the ion beam source. The oil-filled linear induction voltage adder<sup>(5)</sup>, used to transform the initial pulse up to the final ion accelerating potential, can provide shielding around the MAP source, while metallic end plates can be used to provide on-axis shielding. Since the efficiency of x-ray production is proportional to the electron accelerating potential and target atomic number and density, all components that can experience electron strikes will be constructed of low atomic number materials.

**Conclusion:** - Demonstrated high energy per pulse repetitive systems form the basis for a commercially viable technology using high intensity, short-pulse ion beams to improve the surfaces of materials. The high efficiency pulse compression and voltage adder systems combined with broad area repetitive ion beam sources help to reduce treatment costs to levels well below those of other competitive technologies. A prototype IBEST system for industrial applications is being designed for operation in mid-1997.

#### References:

- 1) R. W. Stinnett, D. C. McIntyre, et al. "Ion Beam Surface Treatment: A New Capability for Surface Enhancement," Tenth International Conference on High Power Beams, June 1994.
- 2) S. A. Chistjakov, A. M. Gagarin, et al. "Ion Mixing of Near Surface Layers in Au-Cu, Cu-Mo Systems Irradiated by HPIB," Physics Letters, Vol. 131, No. 1, 8/1, 1988
- 3) E. L. Neau, "High Average Power, High Current Pulsed Accelerator Technology," Proceedings of the 1995 Particle Accelerator Conference and International Conference on High-Energy Accelerators, May 1995.
- 4) E. G. Cook, D. G. Ball, et al. "High Average Power Magnetic Modulator for Copper Lasers," Eighth IEEE International Pulsed Power Conference, June 1991.
- 5) H. C. Harjes, K. J. Penn, et al. "Status of the Repetitive High Energy Pulsed Power Project," Eighth IEEE International Pulsed Power Conference, June 1991.

# APPLICATION OF LOW-ENERGY, HIGH-CURRENT ELECTRON BEAMS FOR SURFACE MODIFICATION OF MATERIALS

D.I. Proskurovsky, V.P. Rotshtein, and G.E. Ozur

*Institute of High Current Electronics,  
Russian Academy of Sciences, 634055 Tomsk, Russia*

## Abstract

The paper describes the characteristics of original sources of low-energy (10–45 keV), high-current (up to 50 kA) electron beams of microsecond duration, designed for surface thermal treatment of materials.

Under the action of this type of beam, graded structures are formed that may impart improved physicochemical properties and strength to the surface layers. This permits the use of these beams for improving the strength and electrochemical properties of pieces and tools and for increasing the electric strength of vacuum insulation. Some technological operations, such as deposition and removal of coatings and surface alloying can be realized in the intense evaporation mode.

## Introduction

Under the action of concentrated energy flows (intense pulsed laser, electron, and ion beams and pulsed plasma flows) on a material, there occur superfast heating, melting, evaporation, and superfast solidification of the material and dynamic temperature and stress fields are formed. These processes produce new structure-phase states in the surface layers that are able to provide improved physicochemical and strength properties of the material, unattainable with ordinary surface treatment techniques.

In recent years, low-energy high-current electron beams (LEHCEBs) have extensively be used as concentrated energy flows. Below we give the characteristics of the LEHCEB sources, the main regularities of the formation of the beam-affected zone, and some examples of using these beams for surface treatment of metallic materials and articles.

## LEHCEB sources

Conventionally, LEHCEBs, like high-energy beams, have been produced using direct-action vacuum diodes with explosive-emission cathodes. The beam duration in these diodes is generally  $\sim 10^{-7}$  s. The electron beams generated in these diodes are characterized by the presence of substantial local nonuniformities in the current density distribution. LEHCEBs of duration  $\sim 10^{-6}$  s allow one to improve substantially the uniformity of the beam-cross-section energy density distribution and reduce abruptly the mechanical stresses generated in the material on irradiation. The beam duration can be increased and the beam homogeneity can be improved by using plasma-filled diodes [1,2].

Table gives the characteristics of the electron sources we have developed. The comparatively low accelerating voltage ensure the X-ray safety of the technology and the simplicity, reliability, and economy of the electron source. The sources have been in use from two to six years.

Source parameters	Type 1	Type 2	Type 3
Electron energy, keV	10–30	10–30	20–45
Beam current, kA	up to 2	up to 15	up to 50
Pulse duration $\tau$ , $\mu$ s	0.5–1.2	1–5	2–4
Beam energy density $E_s$ , J/cm <sup>2</sup>	0.5–6	1–10	2–40
Beam cross-section area, cm <sup>2</sup>	up to 3	up to 30	up to 50
Pulse repetition rate, Hz	up to 0.2	up to 0.2	up to 0.2

## Formation of the beam-affected zone

The principal factors that determine the state and properties of the beam-affected zone are the nonstationary temperature fields that appear in the surface layers as a result of



the absorption of the beam energy and the stress fields caused by the nonuniform heating of the material.

Figures 1 and 2 present the results of calculations for iron irradiated in the characteristic melting and evaporation modes. From the calculations it follows that the velocity of the crystallization front sharply increases near the very surface reaching 8 m/s in the melting mode. The cooling rate reaches its maximum ( $\sim 3 \times 10^9$  K/s) at the surface im-

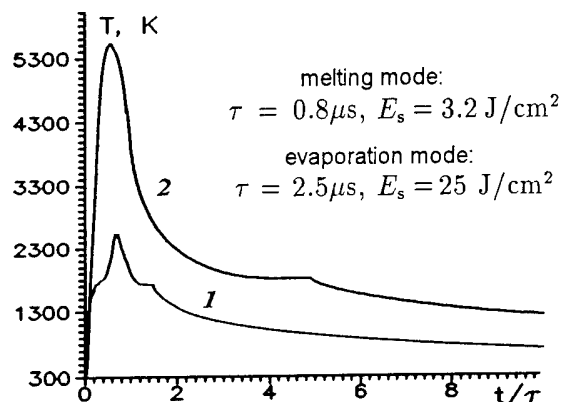


Figure 1. Time dependence of the surface temperature for iron irradiated in the mode of melting (1) and evaporation (2).

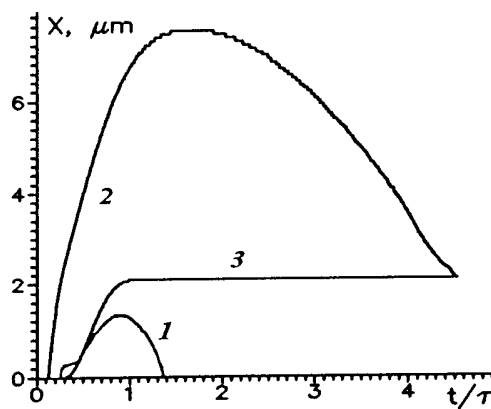


Figure 2. Variation of the position of the melt-solid boundary for iron irradiated in the melting mode (1); the same (2) and the variation of the surface coordinate (3) for iron irradiated in the evaporation mode.

mediately after the passage of the crystallization front. The thickness of the heat-affected zone (HAZ) where the maximum temperature exceeds the recrystallization temperature increases from  $\sim 7$  to  $\sim 20$   $\mu\text{m}$ , in going from the melting to evaporation mode.

An analysis of the data available in the literature [3] suggests that in iron irradiated by an LEHCEB in the initial melting mode a bipolar stress wave is formed whose amplitude is far below the dynamic yield limit of the material,  $\sigma_{0.2}^{\text{dyn}}$ . In addition, quasi-static compressive stresses act in the HAZ, whose magnitude, according to estimates [4], may be over  $\sigma_{0.2}^{\text{dyn}}$ . In the intense evaporation mode, the stress wave amplitude, according to estimates [3], is close to the yield limit of the material and it should be taken into account in analyzing the conditions under which the HAZ is formed.

Investigations of the structure and properties of metals and alloys irradiated by LEHCEBs have made it possible to reveal the regularities as follows:

1. The action of an LEHCEB results in the formation of an extended ( $\sim 10^{-2}$  cm) graded structure showing a nonmonotonic depth variation of the stress-strain state and the degree of hardening [5]. This effect is related to the fragmentation of martensite and the formation of the particles of cementite under the action of low-amplitude bipolar stress waves.

2. The melt-quenched layers ( $\leq 10^{-3}$  cm) show reduced etchability in acids which is related to the fact that the structure formed is more homogeneous than the initial one. The most pronounced structure-phase changes occur in the near-surface layers [5], which correlates with the fact that the cooling rate and the velocity of motion of the crystallization front reach their maxima at the surface. In these layers secondary phases (carbides and intermetallides) are partially or completely dissolved.

#### Use of LEHCEBs for surface treatment

The graded structures formed on LEHCEB irradiation may impart improved physico-chemical and strength properties to the surface layers. In the intense evaporation modes, some important technological operations can also be realized. The principal results obtained on this lines are presented below.

Improvement of tribotechnical characteristics. Tests with a friction pair consisting of a rotor (steel, HRC 55) and a plate (ball bearing steel, HRC 60) in the presence of lubricant

have shown that on irradiation the wear rate of the plates decreased by a factor of 1.5 and the friction moment decreased by a factor of 1.7 [3]. Under the conditions of dry friction, the wear rate of irradiated plates almost halved. With that, the depth of the friction trace was  $\sim 25 \mu\text{m}$ , which corresponds to the position of the first maximum of microhardness. This points to the fact that there is a correlation between wear resistance and microhardness.

Increasing the life of steel tools. For optimal modes of hardening of tool steels the thickness of the molten layer is not over  $\sim 1 \mu\text{m}$ . Therefore, the irradiation might be the finishing technological operation. Tests have demonstrated that the irradiation allows a 2-3-fold increase in the life of drills, cutters, punches, mandrels, and other tools.

Treatment of hard-alloy cutting tools. It has been established that the irradiation of cutting plates made of hard alloys of type BK8 (WC-8%Co) and type T5K10 (WC-5%TiC-10%Co) increases the tool life by a factor of two to five (Fig. 3). The increase in tool life correlates with the increase (by 15-20%) in microhardness at the surface, which is related to the additional dissolution of the carbides in the cobalt binder.

Treatment of titanium alloys. The irradiation of titanium alloys in the initial melting mode not only makes the surface much smoother but also cleans it from oxygen and carbon impurities and improves the uniformity of the element distribution in thickness in the surface layer. Subsequent annealing recovers the phase composition, increases the microhardness, and raises the fatigue strength of the parts by about an order of magnitude. The latter, as is evidenced by fractography, is due to the fact that the surface destruction mechanism changes to the subsurface one [6].

Smoothing of heat-resistant protective coatings. Heat-resistant protective coatings based on Ni (e.g., Ni-Cr-Al-Y) have a rather rough surface. Experiments have shown [7] that melting of a thin surface layer of such a coating allows an increase in heat resistance (by 25% at  $1050^\circ\text{C}$ ) due to the sharp reduction of the surface roughness.

Removal of heat-resistant protective coatings. The existing technology for removing worked-out coatings is characterized by a high laboriousness and harmful working conditions. To eliminate these disadvantages, LEHCEBs can be used. Experiments have shown that a beam of energy density  $\geq 20 \text{ J/cm}^2$  can efficiently ( $1-2 \mu\text{m}$  per pulse) remove this type of coating, changing the substrate structure only slightly [7].

Production of highly concentrated surface alloys. With beam energy densities of over  $10 \text{ J/cm}^2$ , there is an opportunity of the production of surface alloys by pulsed deposition of coatings and remelting of the surface layer. The results of this "micrometallurgical" process are presented in Fig. 4.

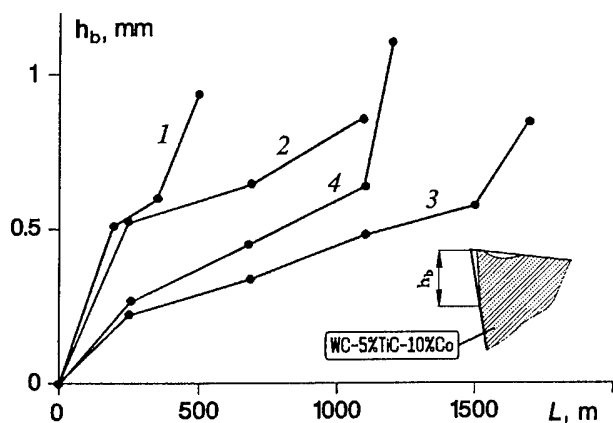


Figure 3. Wear of a cutter as a function of cutting length before (1) and after (2-4) irradiation with different values of  $E_s$ .

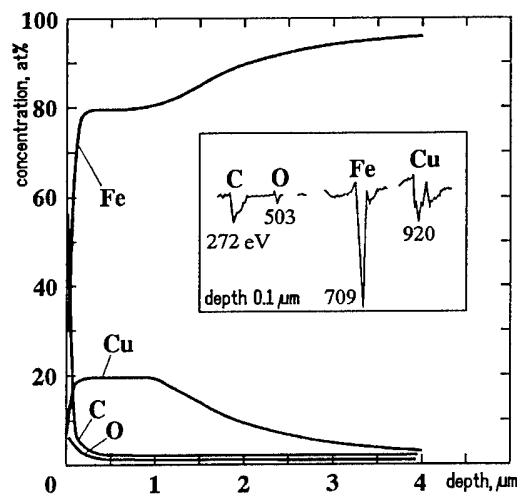
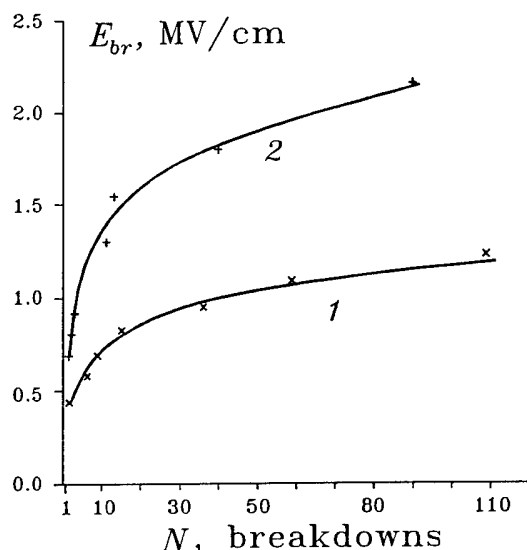


Figure 4. Concentration profiles of the elements in the surface Cu-Fe alloy formed with the use of an LEHCEB on a Fe substrate.

Similar results have been obtained for the systems Al-Fe, Ti-Fe, W-Fe, Ti-Cu, Al-Ti, and the like. The thickness of the layers produced is an order of magnitude greater than that attained by ion implantation.

Enhancement of the corrosion resistance of stainless steel. Cyclic treatment of type 12X18H10T steel (steel 302 being US analog) in the mode of weak evaporation of the surface layer efficiently cleans the surface from undesirable impurities and results in the formation of a fast-quenched structure with a smoothed microrelief. The increased degree of chemical homogeneity of the surface leads to a shift of the stationary potential to the positive region and to a significant decrease in dissolving current [8].



Enhancement of the electric strength of vacuum insulation. It has been established [9] that the irradiation of electrodes efficiently smoothes the working surface due to its melting and cleans the near-surface layers from impurities and dissolved gases. This treatment followed by conditioning of the vacuum gap with low-current pulsed discharges reduces substantially the prebreakdown currents and enhances the electric strength of the vacuum insulation (Fig. 5). The best effect has been achieved for stainless-steel electrodes.

Figure 5. Conditioning curves (250 kV, 40 ns) for vacuum gaps with stainless-steel unirradiated (1) and preliminary LEHCEB-irradiated (2) electrodes.

### Summary

The characteristics of the sources of wide LEHCEBs based on an electron gun with an explosive-emission cathode and a plasma anode are described. It has been shown that the use of these sources makes it possible to develop new efficient techniques for surface treatment of materials.

### Acknowledgments

This work was partially performed under Contracts AM-7681, AM-2868, and AL-1102 with Sandia National Laboratories, USA.

- [1] Ozur G.E. and Proskurovsky D.I., :XIVth Intern. Symp. on Discharges and Electrical Insulation in Vacuum, (1990) 665.
- [2] Ozur G.E., Proskurovsky D.I., and Nazarov D.S., :(these proceedings).
- [3] Rotshtein V.P., :D. Sc. thesis, Tomsk, (1995).
- [4] Dudarev E.F., Pochivalova G.P., Proskurovsky D.I., et al., :Izv. Vyssh. Uchebn. Zaved. Fizika, No. 3 (1996) 126.
- [5] Ivanov Yu.F., Itin V.I., Lykov S.V., et al., :Metally, No. 3 (1993) 130.
- [6] Nochovnaya N.A., Shulov V.A., Proskurovsky D.I., et al., :(these proceedings).
- [7] Yagodka Yu.D., Pastukhov K.M., Kuznetsov S.I., et al., :Fizika i Himiya Obrabotki Materialov, No. 5 (1995) 111.
- [8] Goncharenko I.M., Itin V.I., Isichenko S.V., et al., :Zashchita Metallov, **29** (1993) 932.
- [9] Batrakov A.V., Markov A.B., Ozur G.E., et al., :IEEE Trans. on Dielectrics and Electr. Insul., **2** (1995) 237.

## Progress Toward a Microsecond Duration, Repetitively Pulsed, Intense-Ion Beam

H.A. Davis, J.C. Olson, W.A. Reass  
Los Alamos National Laboratory,  
Los Alamos New Mexico 87545 USA

D. M. Coates, J. W. Hunt, H. M. Schleinitz  
DuPont Central Research and Development  
Wilmington, Delaware 19880 USA

R. H. Lovberg  
University of California  
San Diego, California 92093 USA

J. B. Greenly  
Cornell University, Laboratory of Plasma Studies  
Ithaca, New York 14853 USA

### Abstract

*A number of intense ion beams applications are emerging requiring repetitive high-average-power beams. These applications include ablative deposition of thin films, rapid melt and resolidification for surface property enhancement, advanced diagnostic neutral beams for the next generation of Tokamaks, and intense pulsed-neutron sources. We are developing a 200-250 keV, 15 kA, 1  $\mu$ s duration, 1-30 Hz intense ion beam accelerator to address these applications.*

### I. Introduction

Several promising applications of intense ion beams have emerged in the past few years requiring repetitive beams. These include: (1) Processing of materials including surface modification through rapid melt and resolidification, ablative deposition for producing high-quality coatings and nanophase powder synthesis;<sup>1</sup> (2) Production of intense neutral beams for charge-exchange recombination spectroscopy<sup>2</sup> (CXRS) for ITER (International Tokamak Experimental Reactor) which is the primary diagnostic of ion temperature, rotational velocity, and helium ash concentration in tokamaks;<sup>3</sup> and (3) Intense pulsed neutron sources for non-metallic mine detection, neutron radiography and spent nuclear fuel assay. We are developing an new accelerator called CHAMP (Continuous High Average-

Power Microsecond Pulser) to investigate these applications. Below we describe the design of a 200 - 250 keV, 15 kA, 1  $\mu$ s duration pulser initially operated at 1 Hz, but with provision for extension to 30 Hz.

Traditional single-shot diodes normally using a surface-flashover anode are unacceptable for repetitive operation because of limited anode lifetime, excessive heat loading, and high gas production. Also polymer anodes produce debris, have poor uniformity and reproducibility, and do not allow the selection of the ion species. To circumvent these problems, our system will use a MAP (Magnetically confined Anode Plasma) diode having a pre-formed plasma as the ion emitter.<sup>4,5</sup> Rather than the traditional Marx generator and high-voltage pulse lines, used in single shot operation we will use a

modulator architecture akin to a high-power radar modulator to accelerate ions. The energy will be stored in a set of lumped element Blumlein lines and switched with high-voltage thyratrons. The voltage will be stepped up to the 200-250 kV level with a transformer.

## II. Diode Design

The CHAMP diode will use a magnetically insulated extraction diode in ballistically focused geometry ( $45^\circ$  full focusing angle with 30-cm focal length). Extension to a straight unfocused beam or longer focal length beams for is straight forward. The diode shown in Fig. 1 operates as follows. The anode consists of a flat pulsed induction coil<sup>6</sup> in an aluminum housing. The high-voltage coil is formed from four parallel sets of two turn spiral

voice-coil mechanism. When the gas puff is properly distributed, a fast rising current pulse ( $10 - 20 \text{ kA}$ ,  $\tau_{\text{rise}} = 1-2 \mu\text{s}$ ) delivered to the induction coil breaks the gas down and induces azimuthal current in the plasma at the coil surface. The  $\mathbf{j}_\theta \times \mathbf{B}_r$  force on the plasma accelerates the plasma to the radial opening in the aluminum anode housing where it is stagnated against the applied radial magnetic field. Ions are accelerated from this location. The cathode consists of the tips of two thin concentric metal conical sections. The gap between the cathode tips and the plasma anode is 2 cm. Before application of the induction coil and accelerating voltages, a  $200 \mu\text{s}$  risetime magnetic field of about  $1.5 \text{ kG}$  ( $B \approx 2 B_{\text{crit}}$ ) is applied transverse to the anode-cathode gap by two magnetic field coils -- one located inside the inner cone and one located outside the outer cone. At peak field and when the plasma is in position at the anode housing aperture, a positive accelerating voltage supplied from a high-voltage modulator is applied to the anode. The expected beam parameters are  $E = 200-250 \text{ keV}$ ,  $I = 15 \text{ kA}$ , and  $\tau = 1 \mu\text{s}$ .

We have modeled the dynamics of the plasma layer in planar geometry using a snowplow type model which assumes the plasma is entrained by a thin, conducting current sheet driven away from the coil surface by currents in the inductive coil. The model solves the coupled circuit equation and the equation of motion of the plasma with a model for the plasma resistivity derived from previous experimental data.<sup>7</sup> The circuit inductance as a function of current sheet position from the coil surface required for these calculations is determined from calculations of the magnetic field for various current sheet positions (Fig. 2) to be given by the expression:  $L(z) = 993 (1 - e^{-z/1.35}) \text{ nH}$ , where  $z$  = the current sheet position above the coil surface in cm.

The procedure used was to vary the capacitor charge voltage so that the plasma is brought to rest against the applied magnetic

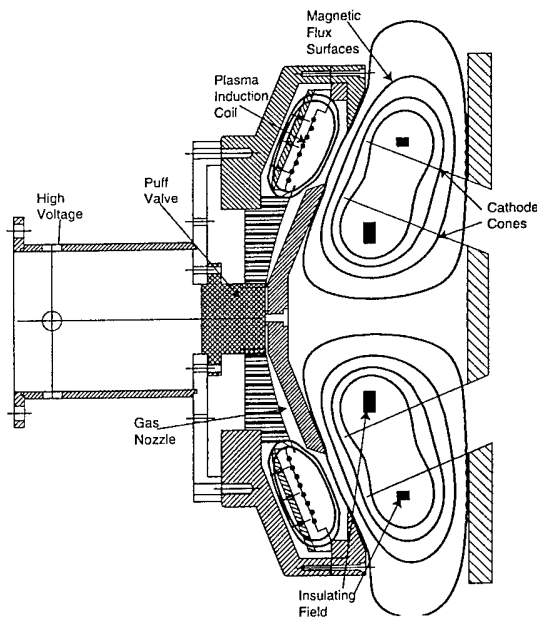


Fig. 1 Diode layout.

windings coaxial with the system axis. The coil in focusing geometry is in the form of a cone having a normal to the surface of  $22.5^\circ$  with respect to the system axis. The plasma anode is formed by first radially ducting a puff of gas with a fast acting valve (risetime  $\sim 100 \mu\text{s}$ ), located on axis, over the coil surface. The valve will be actuated by a metallic diaphragm driven either by eddy currents or a

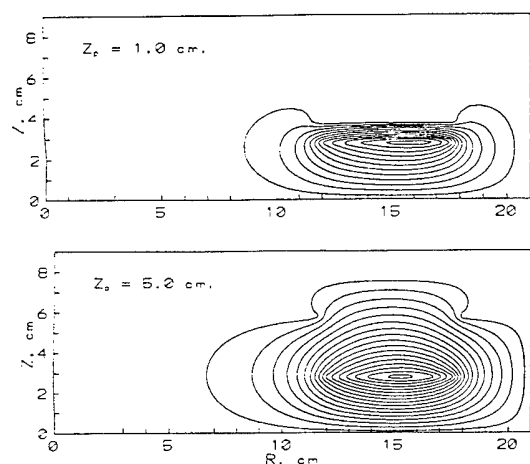


Fig. 2 Magnetic flux surfaces for the inductive coil with the plasma current sheet located at 1.0 cm (top) and 5.0 cm (bottom) from the coil surface.

field at the diode gap entrance. For a gas fill of  $2.5 \times 10^{15}$  molecules/cm<sup>3</sup> corresponding to 80 mTorr of D<sub>2</sub> at the coil surface before acceleration, a capacitor charge voltage of 14 kV is required. The density was chosen to insure good gas breakdown. The stored electrical energy is 50 J. It takes 1.5  $\mu$ s for the plasma to be driven into position at the anode housing aperture with a peak current sheet velocity of just over 20 km/s (Fig. 3).

Finite element thermal modeling of the coil has been performed. It was found that without a supplemental means to transfer heat dissipated in the coil, at 30 Hz unacceptably high temperatures on the order of 600° C develop in the coil. Three solutions to this problem were investigated: (1) increase the thermal conductivity of the epoxy insulator by filling it with high-thermal-conductivity material such as diamond dust; (2) transfer the heat from the windings to the aluminum coil housing with heat pipes; and (3) remove the heat by flowing a cooling medium such as air, water or oil through hollow windings. The model results indicated that all three methods would reduce the maximum temperature of the coil, but that the flowing coolant was the most effective and gave acceptable temperatures.

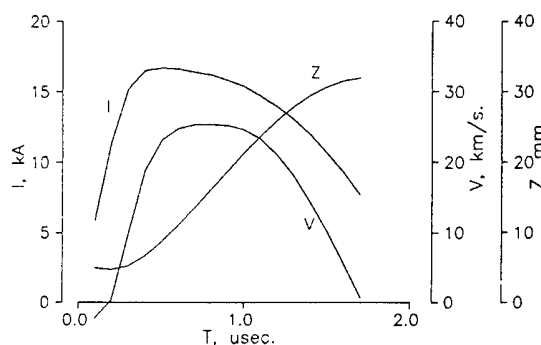


Fig. 3 Current (I), and position (z) and velocity (v) versus time of the plasma layer for a D<sub>2</sub> fill density of  $2.5 \times 10^{15}$  cm<sup>-3</sup> and capacitor charge voltage of 14 kV.

### III. Electrical Design

A key system parameter, the pulse duration, was chosen from a study of overall system electrical efficiency including plasma formation and magnetic-field energy requirements, scaling of diode performance from the Los Alamos Anaconda accelerator operated with 1  $\mu$ s pulses, tokamak diagnostic signal-to-noise optimization, thermal transport modeling of beam energy deposition in targets (for materials applications), and electrical engineering considerations. The beam electrical system requires many modulator sub-systems synchronized with each other and the ion acceleration pulse (Fig. 4). A gas puff modulator and the induction coil modulator sub-system will be housed in a "hotdeck" chassis at common potential with the pulsed anode. For electrical isolation, fiber optic cables will carry fast control and diagnostic signals. Solid-state switches will be used to deliver current from storage capacitors to the magnetic field coils at ground potential. Energy recovery techniques will be used in the final design, although in initial tests energy recovery will be omitted for simplicity. A dedicated fast sequence and monitor system will confirm the proper sub-system parameters before the main acceleration pulse is initiated to minimize damage to components in case of off-normal operation.

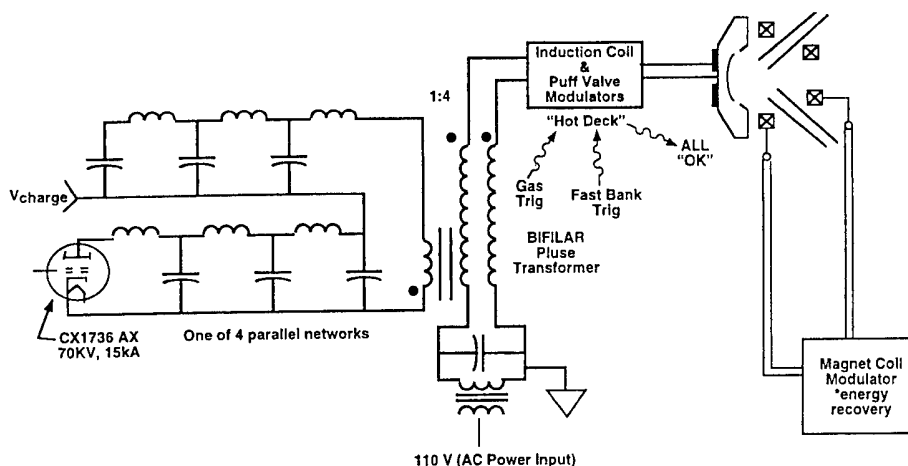


Fig. 4 Diagram of the electrical circuits.

The accelerating power system will utilize 4 parallel type "E" Blumlein lines each switched with an English Electric Valve CX1736AX thyatron. This tube is a 11.4-cm diam., 70 kV, two gap, hollow anode device. The hollow anode design was selected because it permits reverse voltage and current (up to 50% of the maximum rating) in the event of diode mismatch. We selected Blumlein lines rather than conventional pulse lines because they provide an output pulse voltage into a matched load equal to the charge voltage rather than half the charge voltage. This reduces by two the transformer turns ratio and the number of parallel thyratrons required. The lower turns ratio decreases the transformer leakage inductance enabling pulse rise and fall times to be decreased by a factor of four. Another benefit of the Blumlein line choice is the end inductors nearest the transformer and thyratrons can be trimmed to offset the transformer leakage and thyatron inductances. The number of networks comprising each Blumlein line will depend on optimum beam energy spread required by each application. For materials applications, square voltage and current waveforms are not desired since a spread in ion energy leads to a more uniform deposition profile in targets (this eliminates the Bragg peak near the end of the ion range produced by a monoenergetic beam). For spectroscopic applications, monoenergetic beams are preferred to optimize the charge exchange signal and to

simplify the data interpretation. Blumlein lines can be tuned to produce very low ripple square waveforms.

The accelerator will be housed in a metal tank approximately 2 m x 2m x 2 m. The overall system length including the vacuum system, but not the neutralizer, is about 3 m. The initial system will use recycled capacitors for the Blumlein lines to minimize development cost. With higher energy-density state-of-the-art capacitors the modulator footprint could be reduced further. The modulator tank will be filled with high-voltage transformer oil. An estimate of the electrical efficiency is  $30 \pm 10\%$  including power to make the plasma and the pulsed magnetic field.

### Acknowledgment

Work sponsored by Los Alamos, Laboratory Directed Research and Development under US DOE contract W-7405-ENG-36).

<sup>1</sup> H. A. Davis, et. al., Bulletin of Mater. Res. Soc., Aug. 1996 (in Press).

<sup>2</sup> R. J. Fonck, D. S. Darrow and K. P. Jaehnig, Phys. Rev. A **29** 3288 (1984).

<sup>3</sup> H. A. Davis, et. al., Rev. Sci. Instrum., accepted for publication.

<sup>4</sup> W.A. Noonan, S.C. Glidden, J.B. Greenly, and D.A. Hammer, Rev. Sci. Instrum. **66** (1995) p.3448.

<sup>5</sup> J. B. Greenly, M. Ueda, G. D. Rondeau, and D. A. Hammer, J. Appl. Phys., **63** 1872 (1989).

<sup>6</sup> C. L. Dailey and R. H. Lovberg, AIAA paper 79-2093, Oct. 1979.

<sup>7</sup> R. H. Lovberg and C. L. Dailey, NASA Contract Report No. 191155, 1994.

# PULSED ELECTRON BEAM FACILITY GESA FOR SURFACE TREATMENT OF MATERIALS

G.Mueller<sup>1</sup>, G.Schumacher<sup>1</sup>, D. Strauss<sup>1</sup>,

V.Engelko<sup>2</sup>, A.Andreev<sup>2</sup>, O.Komarov<sup>2</sup>, N.Schegolichin<sup>2</sup>

<sup>1</sup>Forschungszentrum Karlsruhe GmbH, INR, D-76021 Karlsruhe, Germany

<sup>2</sup>Efremov Institute of Electrophysical Apparatus, 189631 St.Petersburg, Russia

## Abstract

The paper describes the new pulsed electron beam facility GESA developed for investigations in the field of pulsed heat treatment of materials and optimization of electron beam parameters. At present the electron beam has the following parameters: electron kinetic energy 50-150 keV; power density up to 2 MW/cm<sup>2</sup> and energy density up to 50 J/cm<sup>2</sup> at the target. The pulse duration is controllable with time increments of 1  $\mu$ s in the range from 5 to 40  $\mu$ s. The beam diameter at the target is 6÷10 cm.

## 1 INTRODUCTION

Pulsed heat treatment by intense electron beams is a modern and ecologically sound technique applicable in the field of material surface modification [1, 2]. For realization of the treatment procedure, electron beams capable of melting the surface layer of any material into depths of tens of  $\mu$ m at a rate of 10<sup>9</sup> K/s are required. It is preferable to heat the treated layer without marked evaporation and boiling of the melted phase and also without significant energy loss due to thermal conductivity inside the bulk material. The conditions mentioned above can be satisfied by using a controlled volumetric heat source such as an intense electron beam of kinetic energy  $\geq 100$  keV. Calculations show that for an electron kinetic energy of 150 keV, the beam energy density and maximum pulse duration ensuring the heating of the treated layer without significant energy loss due to thermal conductivity lie in the range 20÷50 J/cm<sup>2</sup> and from microseconds to

tens of microseconds correspondingly. The microsecond range of the pulse duration is not only convenient for beam parameter control, but also essential to achieve sufficient energy deposition when the treatment chamber is separated from the electron injector by a drift channel which limits the max. achievable current [3]. On the base of these considerations the electron beam facility GESA for investigation of material surface modification was developed.

## 2 DESIGN OF THE FACILITY

The principle layout of the facility is shown in Fig.1. The main parts are the following: electron injector (EI); high voltage generator (HVG) with a pulse duration control unit; focusing magnetic coils (MC); drift channel (DC); chamber for samples treatment (SC); radiation protection (RP); controlling unit (CU).

The electron injector consists of a high voltage insulator, a multipoint explosive emission cathode, a controlling grid, and an anode, forming a triode arrange-



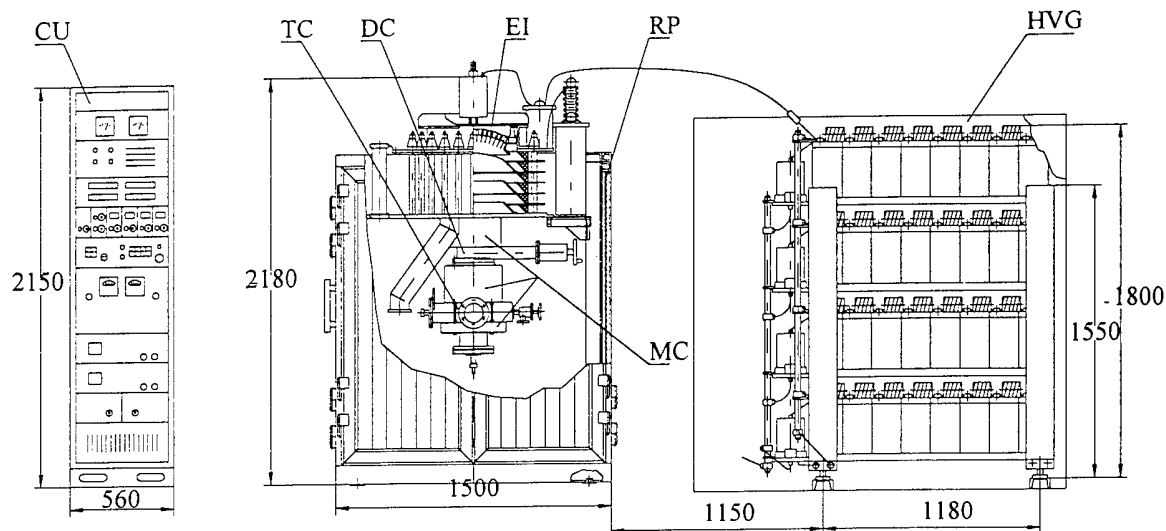


Fig. 1. Scheme of the GESA facility

ment. The controlling grid is connected with the grounded anode through the resistor  $R_g$ . This allows :

- 1) to control the current magnitude of the electron beam in a certain range without changing the kinetic energy of electrons at the outlet of the injector;
- 2) to create a sufficiently high electric field strength near the cathode surface at the beginning of the pulse, necessary for homogeneity of electron emission.

As a source of electrons a multipoint explosive emission cathode (MPC) with stabilised cathode plasma [4] is used. Such a cathode does not require heating, it operates under moderate vacuum conditions, and it is not poisoned by atmospheric gases or vapours from samples being treated. The area of the GESA cathode emissive surface is  $700 \text{ cm}^2$ .

The high voltage generator (HVG) corresponds to the Marx scheme. It consists of four stages, which are artificial pulse forming lines, containing 8 cells with correcting RC networks. The duration of the flat part of the pulse is around  $40 \mu\text{s}$ , the amplitude on a matched load reaches 150 kV. The duration of the high-voltage pulse  $\tau$  can be controlled by the pulse duration control unit with time increments of  $1 \mu\text{s}$ .

At the beginning of the pulse, the total voltage produced by HVG is applied to the cathode-grid gap, because the grid is grounded through the resistor. This ensures homogeneous excitation of the electron emission. After appearance of the electron current the total voltage is distributed among the cathode-grid and grid-anode gaps:  $U_{cg}=U_0-U_{ga}$ ,  $U_{ga}=IR_g(1-\alpha)$ , where  $U_0$  is the total voltage,  $I$  the electron current,  $R_g$  the grid resistors and  $\alpha=0,8$  the grid transparency. In the grid-anode gap, electrons are accelerated to an energy corresponding to the total voltage applied to the injector. The electron beam is also magnetically compressed in this region.

The magnetic focusing system consisting of six coils provides formation, transport and variation of the beam diameter in the range of  $6 \div 10 \text{ cm}$ .

The volume of the treatment chamber is separated from the volume of the injector by means of a gate valve. This allows to replace samples without distortion of the vacuum conditions in the injector and to use different treatment chambers. For transportation of the beam from the injector to the treatment chamber a drift channel is used, which is a stainless-steel tube with the diameter of 15 cm and a length of 50 cm. The residual gas pressure in the working volume is  $10^{-5} \div 10^{-4} \text{ mbar}$ .

### 3 BEAM PARAMETERS

Calculation of the electron beam parameters showed that the average value of the electron transverse energy  $E_{\perp}$  represents around 8% of the total kinetic energy  $E$ . Pulsations of the beam boundary in the drift channel are characterised by a wavelength of 4.0 cm and a magnitude of 2.5 mm for a beam radius of 5.0 cm. Nonuniformity of the current density distribution along the beam radius in the treatment chamber is about 20%. The angle distribution of the electrons is of Gaussian type with a mean angel of 16 degree.

The knowledge of the angle distribution of electrons  $f(\theta)$  is necessary because of pulsed treatment conditions the temperature distribution inside the sample is sensitive to the beam energy deposition profile  $E(z)$  affected by  $f(\theta)$ . This is illustrated by Fig.2 in which calculated results of  $E(z)$  are shown with (curve B) and without (curve A) taking into account a homogeneous angle distribution of electrons.

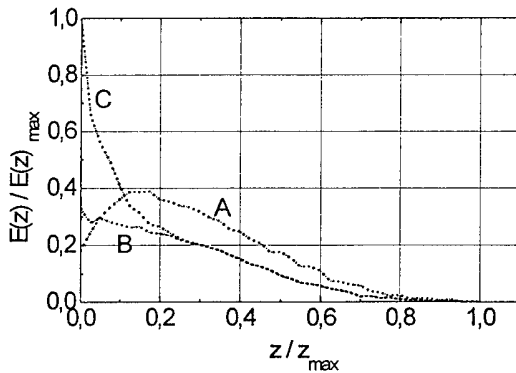


Fig. 2: Energy deposition vs. Depth

When calculating  $E(z)$  it is necessary to take into account the part of electrons reflected by the treated specimen. In the presence of a magnetic field these electrons will reenter the specimen after reflection from the injector region. Since reflected electrons have a wide energy and angle spectrums, they increase significantly the energy deposition near the surface (curve C).

There are two sections limiting the beam current magnitude: the cathode-grid

gap, and the drift channel. The limiting value of the cathode-grid current  $I_{cg}$  can be determined from the following equation

$$I_{cg} = k\alpha \frac{[U_0 - I_{cg}R_g(1-\alpha)]^{3/2}}{a^2(r_c/r_g)} \sin^2(\varphi/2) \quad (1)$$

where:  $k=2.934 \cdot 10^{-5} \text{ A} \cdot \text{V}^{-3/2}$ ;  $\alpha$  is the grid transparency;  $r_c$  and  $r_g$  are the cathode and grid curvature radii, respectively;  $a^2$  is the Langmuir function for a spherical diode;  $\varphi=\arctg(R_c/r_c)$ , where  $R_c$  is the cathode radius. The limiting drift tube current  $I_{dc}$  can be estimated by the expression [3]

$$I_{dc} = 17 \cdot \frac{\gamma}{\gamma_{||}} \cdot \frac{(\gamma_{||}^{2/3} - 1)^{3/2}}{1 + 2 \ln(R_{chan}/R_{beam})} \quad (3)$$

where:  $\gamma=(1-v^2/c^2)^{-1/2}$ ,  $\gamma_{||}=(1-v_{||}^2/c^2)^{-1/2}$ ;  $R_{chan}$  and  $R_{beam}$  are the respective radii of the drift tube and the electron beam.

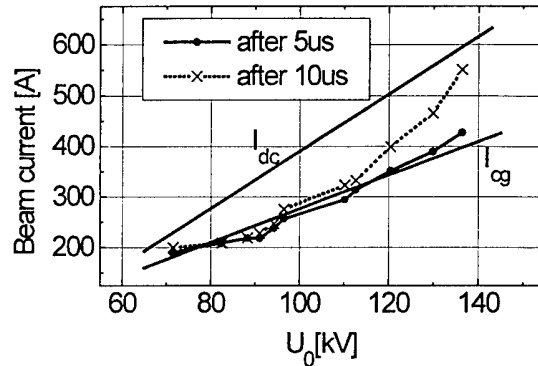


Fig. 3: Beam current vs. voltage for  $R_g=575\Omega$

In Fig.3 the dependencies of  $I_{cg}$ , and  $I_{dc}$  on  $U_0$  for the facility conditions realised presently are shown. Note that  $I_{cg}$  can be increased by means of changing of the corresponding gaps geometry. To increase the limiting current of the drift tube, neutralisation of the beam space charge is required.

Fig. 4 shows an example of the dependencies of the electron beam current on  $R_g$ . One can see that variation of  $R_g$  allows to change the electron beam current by a factor of two.

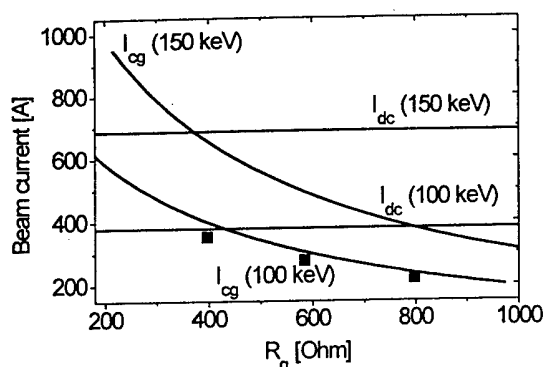


Fig. 4: Beam current vs.  $R_g$

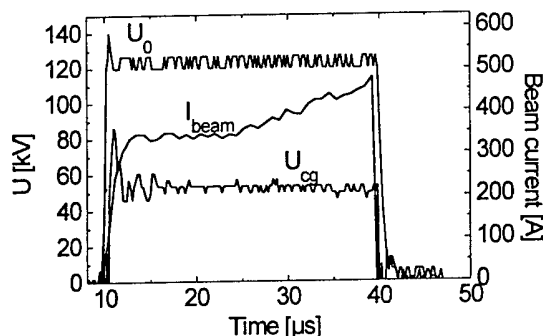


Fig. 5. Typical oscillogrammes of the GESA facility operation

In Fig. 5 typical oscillogrammes of the accelerating voltage  $U_0$ , grid current  $U_{cg}$  and collector current  $I_{beam}$  are shown. One can see that the beam current magnitude reaches its quasi steady-state value 1-2  $\mu s$  after the beginning of the pulse. During that time the formation of the cathode plasma emissive surface takes place. The increase of the beam current after 10 microseconds is caused by the influence of the gas desorbed from the controlling grid on cathode operation.

In Fig. 2 the example of the measured electron beam current in the treatment chamber dependence on the total accelerating voltage  $U_0$  is shown.

Some results of the measurement of the beam current dependence on the grid

resistance are shown in Fig. 3. One can see that under present conditions the possibility to change the beam current by means of  $R_g$  variation exist only in the range of  $R_g > 400$  Ohm. At smaller  $R_g$  values the beam current is restricted by the limiting drift tube current.

The magnitudes of the current density, power density and energy density in the treatment chamber can be controlled in the range  $1 \div 12$  A/cm<sup>2</sup>, up to 2 MW/cm<sup>2</sup> and up to 50 J/cm<sup>2</sup> correspondingly. The radial current density distribution has a symmetrical shape. Its inhomogeneity is higher than calculated one (30% instead of 20%). The origin of the current density oscillations and its elevated inhomogeneity are so far not clear.

Some results of application of the GESA facility for heat treatment of materials is given in an accompanying paper [5].

## 4 CONCLUSION

The electron beam facility GESA was developed for investigations of material surface modification under pulsed intense electron beam treatment. The design of the facility allows to control all vital parameters of the electron beam (kinetic energy of electrons, beam current, pulse duration).

Presently the electron beam has the following parameters: electron kinetic energy 50÷150 keV, power density on the sample up to 2 MW/cm<sup>2</sup>, energy density up to 50 J/cm<sup>2</sup>. The pulse duration is controllable in the range of 5÷40  $\mu s$  in steps of 1  $\mu s$ .

Application of the GESA facility for pulsed heat treatment of materials is in progress.

## 5 REFERENCES

- [1] A.D.Pogrebnyak and D.I.Proskurovskii, Phys. Stat. Sol. (a), 145, 9 (1994).
- [2] V.I.Engelko, A.V.Lazarenko, O.P.Pechersky, *Proc. Int. Conf. on High-Power Particle Beams*, edited by D. Mosher and G. Cooperstein (NTIS, Springfield, VA, 1992).
- [3] A.A.Ruchadze, L.S.Bogdankevich, S.E.Posin-sky, V.G.Ruchlin, *Physics of high-current relativistic electron beams* (Atomizdat, Moscow, 1990) (in Russian).
- [4] M.A.Vasilevskii, I.M.Roife, V.I.Engelko, Sov. Phys.-Tech. Phys., 26, 671 (1981).
- [5] G. Müller, G. Schumacher, D. Strauß, V. Engelko, A. Andreev and V. Kavaljov, BEAMS 96, in press

## LASER SOURCES OF MULTIPLY CHARGED HEAVY IONS

K. Rohlena, B. Králiková, J. Krása, L. Láška, K. Mašek, T. Mocek, M. Pfeifer, J. Skála,  
P. Straka,

*Institute of Physics, Academy of Sciences of the Czech Republic, Prague,  
180 40, Czech Republic*

J. Farny\*, P. Parys, J. Wołowski, E. Woryna,  
*Institute of Plasma Physics and Laser Microfusion, P.O.Box 49, Warsaw, 00 908, Poland*  
\*Meranierring 28/7, Bayereuth, 95 445, Germany

W. Mróz,  
*Institute of Optoelectronics, MUT, Warsaw, 01 489, Poland*

A. Golubev, B. Sharkov, A. Shumshurov,  
*Institute of Theoretical and Experimental Physics, Moscow, 117 259, Russia*

J. Collier, H. Haseroth, K. Langbein,  
*PS-Division, CERN, Geneva 23, 1211, Switzerland*

Intense studies of laser ion sources (LIS) at present are motivated mainly by the growing demand for high current beams of multiply charged heavy ions for large accelerators [1,2]. It was demonstrated [3,4], confirmed [5,6] and generally accepted that LIS can produce by 1-2 orders of magnitude higher current densities and also higher ion charges than the electron cyclotron resonance (ECR) sources, which are presently favored as heavy ion injectors. However, LIS can also be utilized for various technological purposes, like for a material modification, VLSI circuit fabrication, ion implantation, laser mass spectrometry etc. Depending on parameters of the laser used LIS can deliver ions of different atomic mass from  $A = 1$  to  $A \sim 200$  amu (any materials can be evaporated and ionized) with charge states from  $z = 1$  up to  $z \sim 50$  and with energies from hundreds eV up to even about 10 MeV [6-8]. Experiments performed so far with Nd:glass and iodine lasers proved that the short wavelengths ( $\sim 1 \mu\text{m}$ ) and short pulse lengths ( $\sim 1$  ns) lasers are more suitable for production of highly charged ions than the  $\text{CO}_2$  lasers [9].

The photodissociation iodine laser system PERUN [10] operating with  $\lambda = 1.315 \mu\text{m}$  is available for this kind of experiments at the Institute of Physics AS CR in Prague. It has maximum output energy of 50 J at 350 -700 ps pulse duration. The efficiency of the available conversion to the second ( $0.657 \mu\text{m}$ ) and third ( $0.438 \mu\text{m}$ ) harmonics is about 50%. The laser beam is focused onto the target either with an aspherical  $f/2$  optics (L) or with a parabolic

mirror (M) with  $f = 300$  mm; the diameter of the focal spot is about  $100\text{ }\mu\text{m}$  in both the cases (the highest power density delivered on the target is  $\sim 10^{15}\text{ W/cm}^2$ ). The use of parabolic mirror with a hole in the center instead of focusing lens allows for ion measurements along the laser beam axis. This arrangement (see Fig. 1) results in an two fold increase in the ion extraction.

The principal diagnostic techniques for the laser-produced ions in a far expansion zone are based on the time-of-flight method [11]; ion collectors (IC), a cylindrical electrostatic ion energy analyzer (IEA) and a Thomson parabola spectrometer (TS) were constructed at IPPLM, Warsaw. The path of flight for the IEA was higher than 2 m and for the IC varied between 1 - 2 m. Two ion collectors of different constructions were used: a standard circular collector (IC2, IC3) and a ring collector (IC1), which makes the measurement close to the axis of the IEA or the TS possible. The IC measures a time-resolved ion current signal, from which the energy-charge product and the total charge carried by ions, as well as the ion velocity (energy) can be derived. The IEA gives the possibility to identify the ion species produced, i.e. to determine the mass-to-charge ratios, energies and abundance. If realistic values of the secondary ion-electron emission coefficients of the detector material are available, the ion current density and the corresponding number of ions can be calculated from the IEA and IC signals. The determination of energy distribution of ion species by an IEA requires a large number of laser shots; for the evaluation of the IEA experimental spectra and for further data processing, a computer program was developed [12]. The Thomson parabola spectrograph can register the velocity distribution of all the ion species in a single laser shot. Although the TS has a low energetic dynamic range and a low mass resolution for energetic highly charged heavy ions, it can provide a useful and quick information on ion species and the underlying physical processes in the plasma. It is an excellent device for the analysis of contaminants and low-Z plasma studies.

Examples of the signal from the IEA and IC1 for Au plasma are presented in Fig. 2, and a parabola image from the TS is shown in Fig. 3. The experimental results for different target materials are summarized in Tab. 1.

Element	Al	Co	Ni	Cu	Ta	Ta*	W	Pt	Au	Pb	Bi
$z_{\text{max}}$	13	25	26	25	55	48	49	50	49	51	51
$E_{i,\text{max}}$ MeV	0.35	2.6	2.5		8.8	7.7	4.9	8.5	4.8	5.1	5.1
$\langle z_{\text{fast}} \rangle$		22	20			42	45	40	38	40	40
$\langle E_{i,\text{fast}} \rangle$ , MeV		1.9	0.92			2.3	2.0	3.1	3.1	3.3	2.7
$j$ , mA/cm <sup>2</sup>		14.2	18.5		12.8	22.8	22.8	12.8	7.0	8.5	10.0
illum. system	L	M	M	L	L	M	M	M	M	M	M

\*  $L_{\text{IC1}} = 94\text{ cm}$ ; \*\*  $L_{\text{IC1}} = 174\text{ cm}$

Table 1

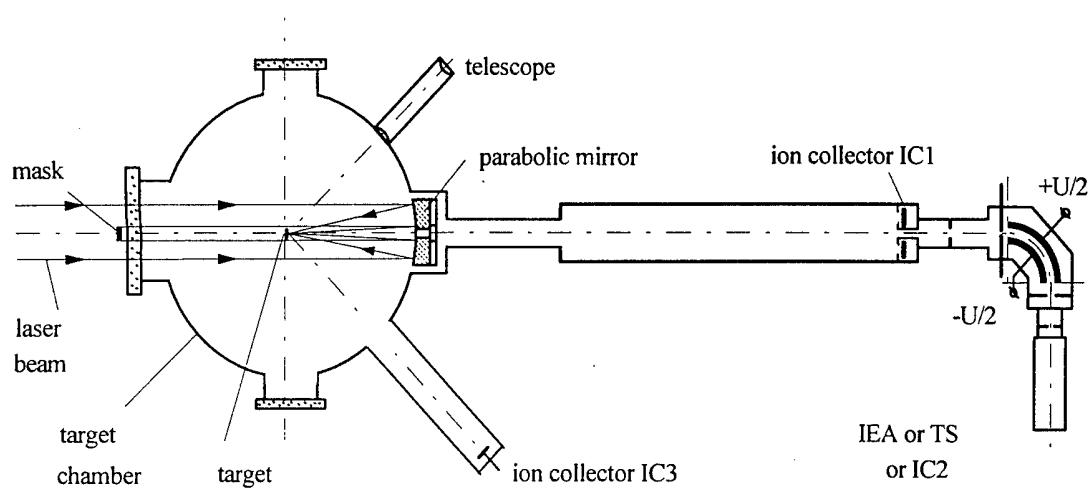


Fig. 1 Experimental arrangement with a parabolic mirror.

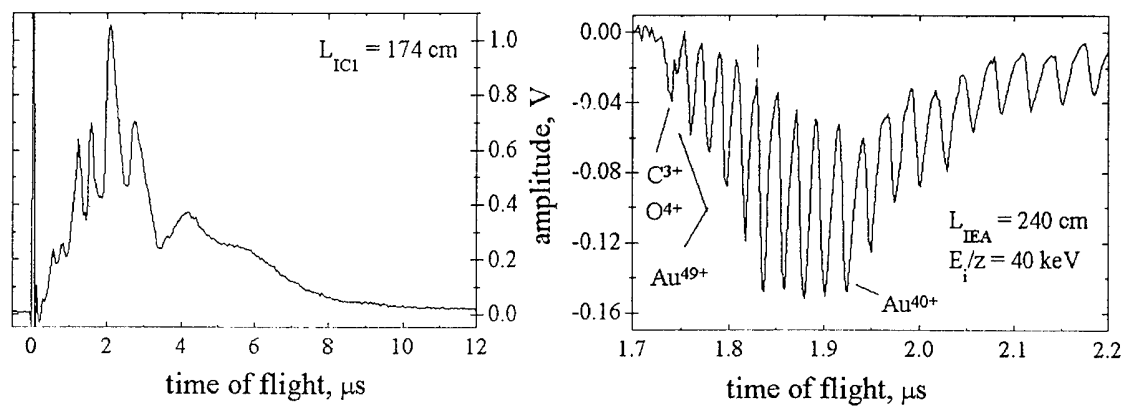


Fig. 2 IC1 signal (left) and IEA spectrum (right) of Au plasma.

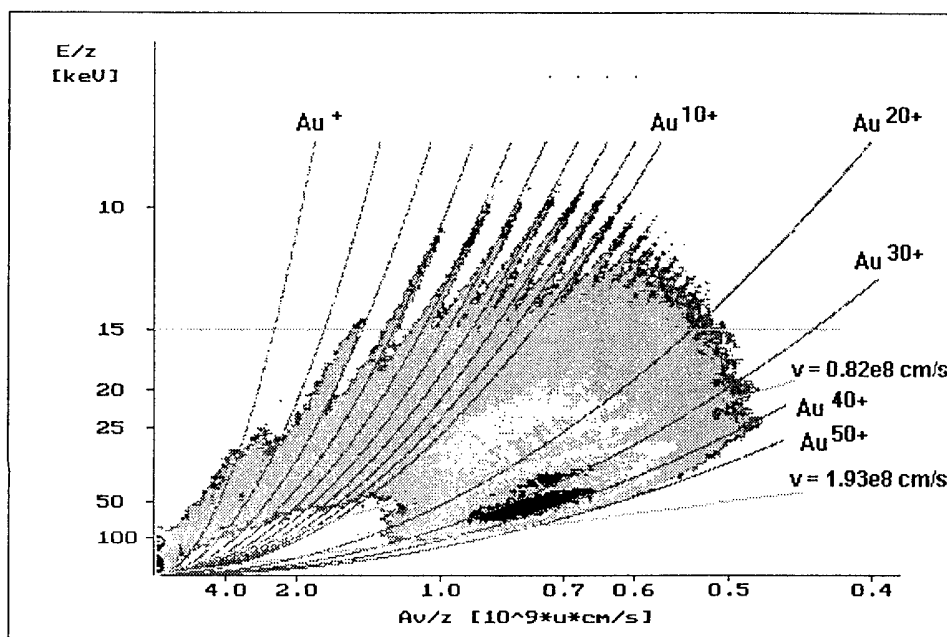


Fig. 3 Thomson parabola picture of Au plasma.

Explanation of occurrence of the highly charged ions in the far expansion zone is based on the mechanism of two temperature plasma expansion. The expansion of the fast ion group is lead by the fast electrons with and the ions follow accelerated by the effect of double layer. With the two groups of electrons present the expansion is two fold. The high charge states are guided through the dangerous recombination zone by the fast electrons. This enhances the phenomenon of charge state "freezing" and the ions originally present in the corona survive. The thermal group of electrons, which expands due to the hydrodynamic pressure, does not accelerate the ions sufficiently for an efficient survival.

The present results proved the existence of highly charged ions with  $z > 40$  in a far expansion zone and their survival during the recombination processes occurring in an early stage of expansion. The higher laser power density is applied, the higher ion charge states are generated (measured  $z_{\max} = 55$  for Ta). The highest ion energy up to 8.8 MeV as well as maximum ion current density  $j \sim 20 \text{ mA/cm}^2$  (in the distance of 94 cm) was measured also for Ta. Construction of laser ion source with ions of  $z \sim 40$  or  $E_i \sim 1 \text{ MeV}$  and with ion current density  $j \sim 10 \text{ mA/cm}^2$  in the distance of  $\sim 100 \text{ cm}$  seems thus not to be a pricipal, but rather a technological problem.

The work was performed in a partial fulfillment of the research grant project No. A1010525 sponsored by the Academy of Sciences of the Czech Republic and the grant project No. 202/95/0039 sponsored by the Grant Agency of the Czech Republic.

#### References

- [1] Billinge R. et al., CERN Report 90-91, Geneva 1990
- [2] Haseroth H. and Hora H., in Advances of Accelerator Physics and Technologies (Ed. H. Schopper), World Scientific, Singapore, 1993, p. 446
- [3] Korschinek G. and Sellmair J., Nucl. Instr. Meth A 268 (1988) 473
- [4] Golubev A.A. et al., ITEP Report 134-88, Moskaw, 1988
- [5] Kozochkin S.M. et al., Kurchatov Institute Report IAE-5635/7, Moscow, 1993
- [6] Haseroth H. et al., Proc. 23rd ECLIM'94, Oxford, 1994, p. 293
- [7] Láska L. et al., Rev. Sci. Instrum. 67 (1996) 950
- [8] Woryna E. et al., Appl. Phys. Lett. - submitted
- [9] Mróz W. et al., 1995 Int. Symp. on Heavy Ion Inertial Fusion, Princeton, 1995
- [10] Chvojka M. et al., Czech. J. Phys. 42 (1992) 899
- [11] Denus S. et al., J. Tech. Phys. 18 (1977) 25
- [12] Pfeifer M. et al., Proc. 2nd Symp. Plasma'95, Warsaw, 1995, Vol. 1, p. 77

## LARGE-SCALE PLASMA SOURCE ION IMPLANTATION AND DEPOSITION EXPERIMENTS\*

D.J. Rej, R.J. Faehl, I. Henins, C.P. Munson, M. Nastasi, J.T. Scheuer, K.C. Walter,  
and B.P. Wood

*Los Alamos National Laboratory, Los Alamos, NM 87545, USA*

### Abstract

Plasma source ion implantation [1] (PSII) is a technique which enables implanting a high dose of ions in a simple, fast, efficient, and cost-effective manner. In PSII a negative high-voltage pulse is applied to a workpiece which is immersed in a plasma. Plasma ions are accelerated by the electrical potential and are implanted into the surface of the workpiece. PSII offers several improvements over conventional beamline techniques in that it is a non-line-of-sight process enabling conformal implantation simultaneously into all exposed surfaces of the workpiece. System efficiencies are improved since the perpendicular ion trajectories into the workpiece eliminate the need for masking. Implant times are short when compared to beamline techniques since high-current, pulsed-power supplies compatible with this process can provide up to two orders of magnitude higher average currents than conventional accelerators.

In this paper we report recent results obtained on the large-scale PSII facility (1.5-m diam, 5-m long) at Los Alamos [2]. Pulsed power is supplied by a hard-tube modulator capable of providing 125-kV, 60-A, 0.02 ms-long pulses at 2 kHz [3]. Most of our research has been focused on metallurgic wear and corrosion applications. Improved tribological properties (increased hardness, lower friction, and significantly reduced wear) are observed with nitrogen and carbon implantation into several steel alloys and chromium. Metallic ion generation and implantation have been accomplished with a cathodic arc ion source. By combining PSII with plasma enhanced chemical vapor deposition, adherent diamond-like carbon films have been deposited onto relatively large batches of aluminum automotive components. Films are hard ( $> 20$  GPa) with a low coefficient of friction. The PSII process is found to create a graded interface between coatings and substrates, significantly improving film adhesive properties.

[1] J.R. Conrad et al, J. Applied Physics 62, pp. 4591-4596 (1987)

[2] B. P. Wood et al., J. Vac. Sci. Techn. B12, pp. 870-874 (1994)

[3] W. A. Reass, J. Vac. Sci. Techn. B12, pp. 854-860 (1994)

\* Research support by the U.S. Dept. of Energy.



## SYRINX - A RESEARCH PROGRAM FOR THE PULSED POWER RADIATION FACILITY

B.Etlicher, A.Chuvatin, P.Choi, L.Frescaline, L.Aranchuk, B.Cassany, G.Avrillaud, V.Frolov, C.Rouillé, P.Auvray, S.Semushin, C.Dumitrescu-Zoita, J.F.Léon\*, F.Kovack\*, P.Monjaux\*, F.Lassalle\*, F.Bayol\*, A.Johan\*, B.Kovalchuk†, and A.Kim†

*Laboratoire de Physique des Milieux Ionisés, Laboratoire du CNRS,  
Ecole Polytechnique, 91128 Palaiseau, France*

*\* Centre d'Etudes de Gramat, 45600 Gramat, France*

*† High Current Electronics Institute, 631055 Tomsk, Russia*

### ABSTRACT

Syrinx is a targeted research program with the objective to study, through practical examples, the fundamentals necessary to define the details of all parts which will be required for a new powerful plasma radiation source. The current level of activities of Syrinx is in the design and construction of a multi-megajoule class IES based pulsed power driver which will use long conduction Plasma Opening Switch technology. The present paper reviews mainly the basic experimental research of the POS and Z-pinch accomplished in the framework of Syrinx project. This work has a unique international level of participation, from conceptual designs to particular investigations.

### INTRODUCTION

To provide for the radiation output expected to be of relevance in many applications, a pulsed power facility with a primary energy storage in the tens to hundred megajoule regime is anticipated. Apart from the simple consideration of costs, the problem of delivering electrical energy of this magnitude, from the storage region to the load region efficiently, is a formidable issue to be tackled. Among the issues of pulsed power science that one must address, one could group them under a number of headings; primary energy storage, energy transfer, secondary energy storage, closing and opening switches, power delivery, power concentration, energy to radiation conversion.

The Syrinx project was initiated in 1991 with joint participation from CEG and LPMI. As a research program, it can combine an open-minded approach to new technologies and novel concepts, while guided by well established methodologies and expertises. A number of existing technologies are possible candidates for scaling up to the very high energy system foreseen. Primarily, the selection criteria is constrained by cost and efficiency. Inductive Energy Storage (IES) approach based on the Plasma Opening Switches (POS) technology seems to be rather attractive from the point of view of cost, while additional POS physical investigation should be done and aimed to optimize a POS at high power levels.

On the other hand, physical study and optimization of the Plasma Radiation Source (PRS) also represents a scientific challenge of the project. Existing Z-pinch facilities like Saturn is already producing radiation in the 70-90 TW region in the keV band with radiative energy in excess of 0.5 MJ [1]. New facilities coming on line could bring this figure to the 1 to 2 MJ regime. While a Plankian radiation spectrum may be desirable for some applications, it is sometimes not the most efficient way of utilizing the available energy resources in certain test environment, where the effect in a particular spectral band is to be studied. This has led in the past to extensive development of K-shell plasma radiation sources for emission in the 1-5 keV region. Above 100 keV, traditional beam-target bremsstrahlung sources have been successful in fulfilling the requirement. In between, the issue and the solution is not so clear. Particularly in the 10 - 40 keV region, where the efficiency of routine plasma radiation sources is low, efforts have still to be made to find an optimal solution. The Composite Pinch (CP) scheme being currently studied for Syrinx represents here one of the candidates for such PRS load.

## LONG-CONDUCTION-TIME POS INVESTIGATION

The POS problem has been under investigation in the *Laboratoire de Physique des Milieux Ionisés, Ecole Polytechnique* (PMI) during the last five years [2]. We studied POS operation in coaxial and strip-line geometries on MAG-1 generator for the 0.5-1  $\mu$ s conduction times and 200-400 kA conduction current level. Investigation of a 2 MA conduction current, 1  $\mu$ s conduction time POS was carried out in collaboration with *High Current Electronics Institute* on GIT-8 IES facility.

### A 200-400 kA conduction current POS in cylindrical geometry

In this series of experiments the POS operated with electrodes in cylindrical geometry on the MAG-1 inductive storage generator [3]. A low-inductance capacitor bank provided at full charging voltage a 500 kA upstream current with a quarter-period of 900 ns into the switch. POS opening switched a 400 kA current with a 100 ns rise-time into a 25 nH inductive load.

In the series when plasma density diagnostic was applied the installation was charged at a lower voltage with the aim to decrease the level of electromagnetic noise. We used the laser interferometry as a diagnostics [4], and the time history of the line density integrated in the cordial direction was investigated. This approach allowed us to determine the geometry of the density evolution, to measure some temporal characteristics of this process and to compare them with the characteristic velocities of magnetic field penetration [5]. A typical time history of the line integrated density during the POS operation is shown in Fig. 1. This picture was obtained when the probe beam was located at the load side of the plasma, in the middle of the interelectrode gap. At this radial position along different axial locations of the probe beam the density time behavior was similar: after a certain increase it decreased till the absolute limit which could be resolved by our technique.

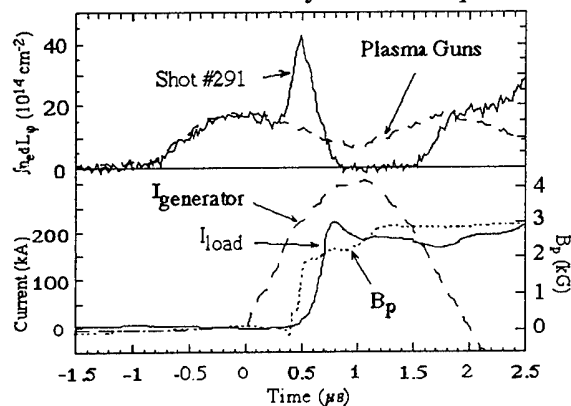


Fig. 1

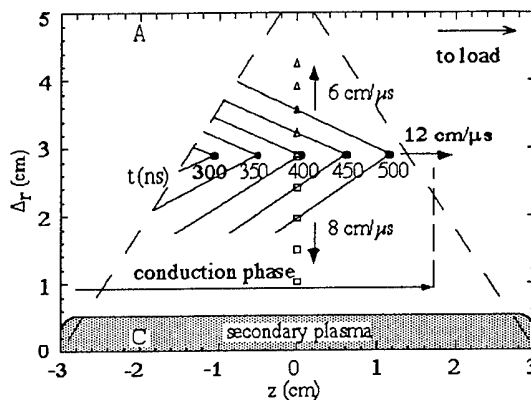


Fig. 2

Fig. 1. Measured time integrated density for the position of 2.9 cm from the cathode and 1.4 cm from the gun axis towards the load for the gun shot only (dashed line) and with MAG1 (solid line). There are also shown: upstream ( $I_g$ ) and downstream ( $I_{load}$ ) currents, magnetic field near the downstream plasma border ( $B_p$ ).

Fig. 2. Reconstruction of the density maximum propagation through the plasma. Dashed lines indicate the initial plasma boundary. Moments of the peak maximum arrival are referred to the start of the upstream current.

The time sequence of the density maximum appearance with respect to the opening is shown in Fig. 2. The shock process had a wedge-like profile. The thickness of the shock front was estimated from the experiment with use of typical rise-time of the density peak  $\sim 100$  ns and typical velocity in axial direction  $u_f \sim 10^7$  cm/s, that gave  $\delta \sim 1$  cm.

In case of magnetic field penetration into the bulk of plasma the ions can be considered to be motionless when the velocity of this penetration is higher than the Alfvén velocity,  $u_f \gg v_A$ . Such theoretical solution does exist in frames of Electron Magnetohydrodynamics (EMH) [6, 7] where the magnetic field and electron current flow is governed by the Hall effect on the background of fixed ions. At the same time, such a "pure" EMH penetration (KMC-type [8]) cannot be accompanied by density perturbations. Another limit case (MHD shock-wave) corresponds to the density jump running away from the magnetic field piston. Most probably, our situation corresponded to the frontier case, when EMH criterion is satisfied at the magnetic

field front,  $\delta < \delta_i = c/\omega_{pi}$ , and ions acquire velocities behind this front ( $u_p(R) = v_A^2/2u_f$ ) (so-called Hall shock-wave [5, 9, 10]). We note, that the maximum piston velocity is reached when  $u_p = u_f$  and corresponds to the snow-plow approximation with  $u_p^{\max} = v_A/\sqrt{2}$ . With this consideration, a satisfactory explanation of the experimentally observed shock profile is obtained.

### A 200 kA conduction current POS in planar geometry

On a new high-power inductive storage POS facility the plasma switch should be coupled to a magnetically-insulated transmission line (MITL) and a load. Planar geometry of the POS/MITL assembly would allow, in principle, more compact and less inductive design of a multimodule system. Plane geometry of the plasma switch was tested at 200 kA level of the conduction current on the two-module version of MAG-1 installation [11], Fig. 3.

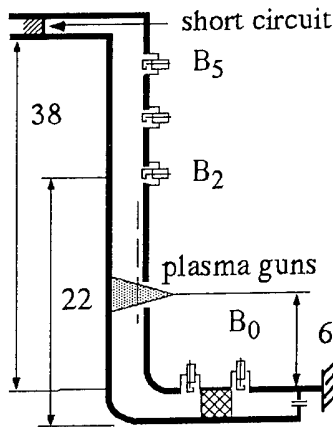


Fig. 3

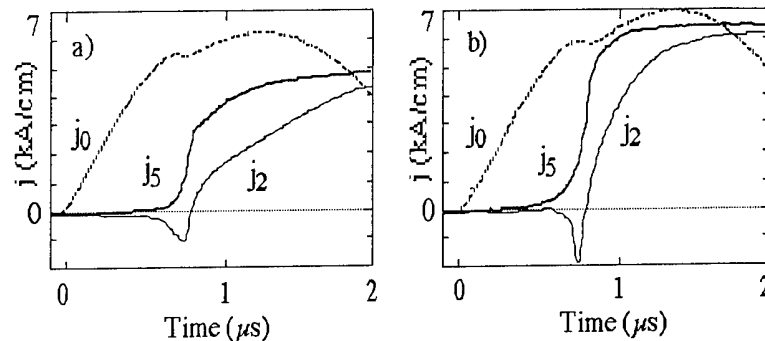


Fig. 4

Fig. 3. General design of one MAG-1 strip-line module (side view).

Fig. 4. Upstream and downstream current densities measured in the center of the anode for two cases: (a) initial configuration without the anode "wings", 16 guns, and (b) with the "wings", 10 guns.

In the initial strip-line configuration, the generator charging voltage of 30 kV yielded the maximum conduction current  $I_{0\max} = 200$  kA in one module, conduction time  $t_c = 700$ -800 ns and the opening time not less than  $t_s = 150$ -200 ns (Fig. 4a). Plasma current losses after the opening were as high as 10-20% of  $I_{0\max}$ . In this configuration, in spite of initially homogeneous plasma injection, the plasma motion had different velocities in the center and at the borders of the strip-line. Therefore, relatively long opening time could be a result of asymmetry of our plasma system. To suppress this effect, we installed two additional anode "wings" in the plasma injection region. These electrode "wings" partially closed the opened strip-line borders and prevented the plasma to exit from the interelectrode gap. The opening became faster (Fig. 4b) and the plasma current losses became smaller. From our point of view, this fact confirms the influence of the initial plasma density homogeneity on the "quality" of the opening at least in the planar configuration of electrodes.

Synchronization of two modules with the help of a low-inductive upstream connection between them [12] was also verified experimentally. First, the synchronization was tested for the conduction time difference changing from 200 to 500 ns. In this case the rise-time for the sum of both load currents was shorter than in absence of the connection between the modules. Second series was performed when the initial plasma density and  $t_c$  were approximately the same for both modules. The result of this series was opposite to that of the first series. If  $\Delta t_c < t_s$ , the external upstream connection often made  $\Delta t_c$  even bigger. Therefore, one can conclude that the procedure of synchronization proposed in [12] was efficient only in the case when the difference of the conduction times of two plasma switches was bigger than the opening time of one POS.

## A 2 MA conduction current POS on GIT-8 generator

High-current Plasma Opening Switch was experimentally studied on GIT-8 inductive generator in collaboration with *High-Current Electronics Institute*. The GIT-8 POS was operating at 2 MA current with the conduction and opening times of 1  $\mu$ s and 100-150 ns accordingly. Interesting peculiarity of the GIT-8 POS was an axial plasma injection, towards the generator [13].

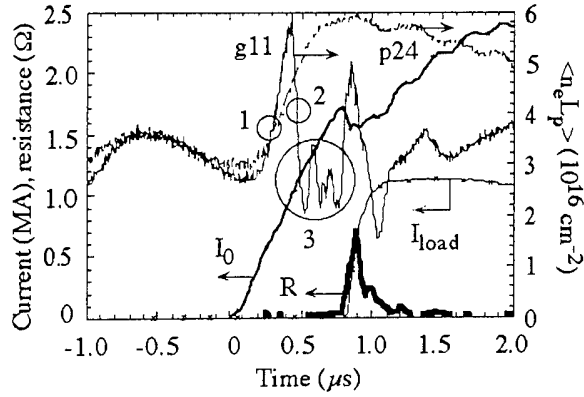


Fig. 5

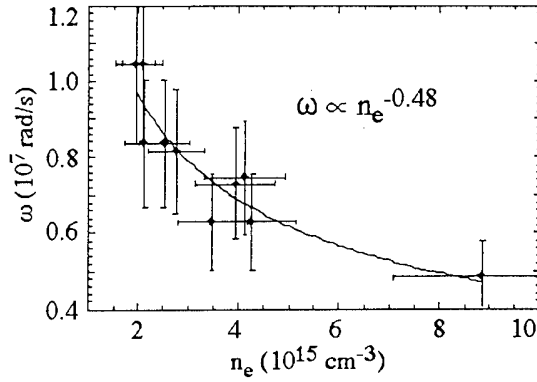


Fig. 6

Fig. 5. Typical plasma density behavior at  $\Delta = 21.5$  mm with the GIT-8 current (g11) and during the plasma guns firing only (p24). R denotes the POS resistance estimated as  $V/(I_0 - I_{load})$ ;

Fig. 6. Variation of the measured plasma density oscillation frequency with the averaged plasma density,  $n_e = \langle n_e L_p \rangle / L_p$ .

Plasma density was measured again with the help of interferometer described in [4]. The scene beam crossed from shot to shot the GIT-8 POS plasma along different chords at 28 mm from the plasma injection plane and at different radial positions of the gap,  $\Delta = r - r_c$ .

Typical time history of the line integrated density during the POS operation is shown in Fig. 5. Until the current starts to flow through the plasma channel and during 300-500 ns after the beginning of the upstream current, the line-integrated plasma density,  $\langle n_e L_p \rangle$ , follows the one measured during the gun firing only. Then, the density increases over the guns-only density (region 1 in Fig. 5) and drops abruptly (region 2). This fact can be an indication of the passage of a shock-wave through the point of measurements [5, 10]. Then, the linear plasma density rests almost at the same level as when the upstream current starts. The most interesting peculiarity of the plasma density behavior was an appearance of fast density oscillations with the characteristic frequency  $\omega \sim 5 \times 10^7 - 10^8$  rad/s, prior and during the opening (region 3). Separate series with pulsed-power allowed identification and consecutive suppression of different sources of noise. The refraction effect could interfere only during and after the opening. Therefore, the earlier fast oscillations were produced by a real plasma process.

We applied also hard X-ray diodes to register Bremsstrahlung radiation produced by fast electron leakages along the plasma injection region. This electron leakage is the most intensive at the downstream plasma edge and allows its location to be determined [14]. The timing of X-ray radiation showed that the final POS opening process occurred in the region of plasma density measurements and the registered fast oscillation reflected some feature characterizing the opening process.

Fig. 6 demonstrates that the registered plasma oscillations strongly depend on the mean density. The function which fits the experimental data with the minimum absolute dispersion is approximately  $\omega \sim n_e^{-0.5}$ . Most probably, the measured oscillations were a result of hydrodynamic plasma instability having characteristic frequency equal to  $v_A/\lambda$ , where  $v_A$  is the Alfvén velocity, and the instability wavelength  $\lambda \sim 0.5$  cm yields already an absolute value of frequency close to the experimentally measured. One of important consequences of this conclusion is that the well-known Hall plasma resistance may increase N times with respect to

the value  $30u/c$  [15], where  $N = \Delta_{ak}/\lambda$  is the number of the plasma necks in the interelectrode gap  $\Delta_{ak}$ .

### POS optimization

For effective inductive energy storage the POS conduction time,  $t_c$ , should be close to the time of discharge of a given primary energy source. On the other hand, successful POS/load coupling on a new inductive storage facility is possible only with a preliminary information about maximum POS resistance and its rise-time,  $t_s$ . A number of empirical scalings for  $t_c$  value already exists and gives a satisfactory correspondence with the  $\mu s$  POS experiments (see, e.g., Refs. in [10]). However, existing relations for the conduction time often contain a free parameter which is chosen only after comparison with already realized plasma switch design. In addition, no theoretical estimate for the opening time of a  $\mu s$  POS exists for the moment.

Our point of view is based on the POS physics understanding represented in Refs. [5, 9, 10, 16]. In the long-conduction-time POS ( $L_p > \delta_i$ ,  $L_p$  is the plasma length) the conduction phase is limited by the value  $t_c = L_p/u_i \approx \sqrt{2}L_p/\langle v_A \rangle$ , where  $\langle v_A \rangle$  is the mean Alfvén velocity averaged over the conduction time. This value is determined by the maximum piston velocity which is realized in the interelectrode gap by the Hall shock-wave. In terms of the charge density passing through the cathode surface during the conduction phase,  $q/S_0$  ( $S_0 = 2\pi r L_p$  denotes the surface occupied by the injected plasma), the conduction phase is terminated when

$$\frac{q}{S_0} \approx 1.8 \times 10^{-11} \sqrt{n_p} \left( \frac{C}{\text{cm}^2} \right), \quad q = \int_0^{t_c} I dt \quad (1)$$

where  $n_p$  denotes the ion density in  $\text{cm}^{-3}$  and the most widely used carbon plasma is supposed.

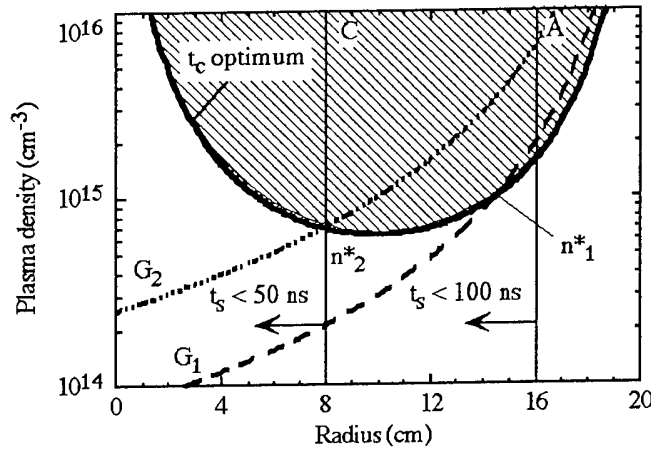


Fig. 7. Optimization of the POS configuration on the new inductive storage generator for  $h_g = 20$  cm (see text).

At the end of the conduction time, when the plasma length which remains ahead the shock leading edge is small,  $\Delta z < \delta_i$ , the magnetic field starts to penetrate rapidly in front of the plasma piston and arrives to the load. The characteristic time of this process can be estimated for  $C^{2+}$  as follows [10]:

$$t_s = \frac{c}{\omega_{pi} u_f} \approx 3.2 \times 10^{-11} \frac{\sqrt{n_p}}{B} \delta_r \text{ (s)} \quad (2)$$

where  $u_f$  is the KMC velocity [8],  $B$  is the maximum magnetic field in Gauss and  $\delta_r$  expresses a strong interelectrode plasma density inhomogeneity ( $\partial n_p / \partial r \sim n_p / \delta_r$ ), or the measure of curvature of the magnetic field lines in cylindrical geometry ( $\delta_r \sim r/2$ ). If one substitutes roughly

$\delta_r \sim \delta_i$ , a universal estimate can be obtained:  $t_s \sim 1.25 \times 10^{-3}/B$ . This signifies that for sufficiently fast opening ( $t_s < 100$  ns) the magnetic field must exceed a certain value,  $B > 10$  kG. To be more rigorous, this equation is an estimate of the plasma resistance rise-time, which can differ from the experimentally measured load current rise-time in case if the latter is "load-limited",  $t_{\text{Lexp}} \sim L_2/R \geq t_s$  ( $L_2$  is the load inductance and  $R$  is the resistance of the load circuit).

Comparison of Eqns. (1) and (2) with recent POS experiments requires additional information about the initial plasma density. Such comparison is presented in [10] and confirms Eqns. (1, 2) to be valid for rather large range of plasma switch characteristics.

An example of the diagram used to design the POS configuration in the project of a new six-module inductive storage generator is shown in Fig. 7 ( $t_c = 0.7$   $\mu$ s,  $I_0 = 0.8$  MA for one module). Initial density profile in the gap ( $n_g(r)$ , or  $G_1$  and  $G_2$ ) is assumed to be known [4]. Therefore,  $n_g(r)$  curves can be easily represented together with  $n^*(r)$  curves defined by Eqn. (1) ( $n^*$  is the density corresponding to the optimum conduction time). Anode and cathode radii are chosen to have the opening time in the range 50-100 ns. The distributions  $G_1$  and  $G_2$  must satisfy inequality  $n \geq n^*$  inside the interelectrode gap.

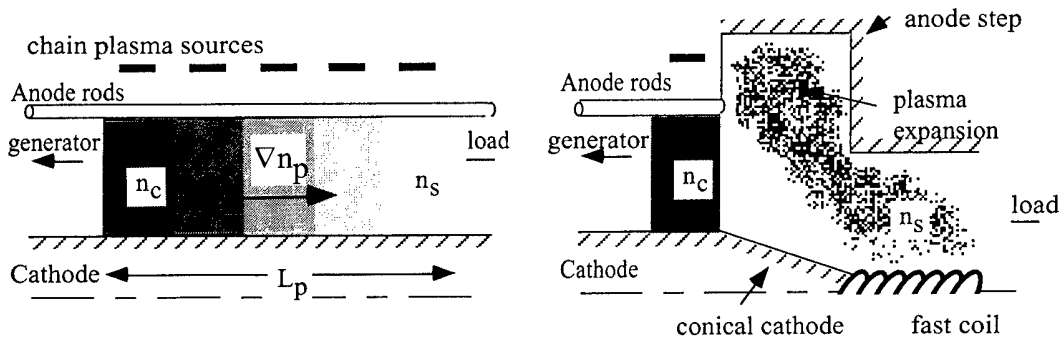


Fig. 8

Fig. 8. (a) Examples of the POS with extended length and axial plasma density gradient. (b) example of the plasma switch in PF and PFS configurations.

Fundamentally, the scalings (1), (2) allow better pre-definition of the POS geometry on an IES system in a project. Besides, these relations suggest several modifications of a POS in order to improve its performance (i.e. shorter  $t_s$  and higher POS resistance). First, a plasma switch with extended axial length,  $L_p$ , should be investigated. Then, a spatial decoupling of the plasma densities,  $n_c$  and  $n_s$ , "responsible" for the duration of the conduction and opening phases should be incorporated accordingly. Such decoupling might be done through an axial plasma density gradient, directed from a generator to a load (Fig. 8a), or by using the axial plasma motion and plasma expansion during the conduction phase (Fig. 8b). In the last case, the POS geometry resembles somewhat the Plasma Focus (PF), or Plasma Flow Switch (PFS) configurations.

#### INVESTIGATION OF THE COMPOSITE Z-PINCH

The simplest CP consists of two parts [16], an external hollow cylindrical plasma of fairly low density and an axial high-density plasma core. During the shell compression, RT or  $m = 0$  MHD instability is supposed to form rarefied regions in the local plasma density. When the plasma thickness in front of the instability leading edge becomes smaller than  $c/\omega_{pi}$  one should describe this plasma in the frames of Electron MHD [7]. Electrical resistance of these plasma "necks" can be estimated as the so-called Hall resistance [15]. This resistance provides a current,  $I_z$ , on the axial core with the following characteristic rate of rise

$$\frac{dI_z}{dt} = \frac{c/\omega_{pi}}{\lambda} \frac{I_0}{t_c} \frac{1}{2\ln(r/r_c)} \quad (3)$$

where  $\lambda$  is the macro-instability wavelength,  $I_0$  is the generator current,  $r$  is the shell radius at which the disruption occurs,  $r_c$  is the CP axial core radius and  $t_c = r/v_s \sim r/v_A$  is the additional compression time of the external shell after its disruption ( $v_A$  is the Alfvén velocity). In addition to the Hall potential there is also a reactive resistance  $|dL/dt|$  ( $L$  is the inductance between the inner core and external shell) which can increase  $I_z$ . This term can be important in case of vanishing of the described disruption.

Therefore, if the disruption occurs at small residual distance between the external shell and the inner CP core and at sufficiently high value of the generator current  $I_0$ ,  $dI_z/dt$  can reach much higher values than  $dI_0/dt$ , as given by Eqn. (3). This CP property promises already higher homogeneity of the axial core if compared with EW regimes and harder X-ray radiation than in the liners. Indeed, the experimental results demonstrated higher hard X-ray power to be produced by a high-temperature/density uniform plasma [17].

### Composite Pinch experiments on GIT-4 generator

Experiments were carried out on GIT-4 inductive storage generator [17]. The technical purpose of this series of experiments was to obtain a powerful homogeneous PRS radiation in the near- 10 keV region. The Plasma Opening Switch (POS) provided a 1.5 MA current with the rise-time of 150 ns into a CP load. External plasma was formed by a hollow preionized double-shell Ar liner with varying linear masses of both shells. Inner axial core consisted of metal Al, Ti, Ni and W wires with linear masses in the range of 30-90  $\mu\text{g}/\text{cm}$ .

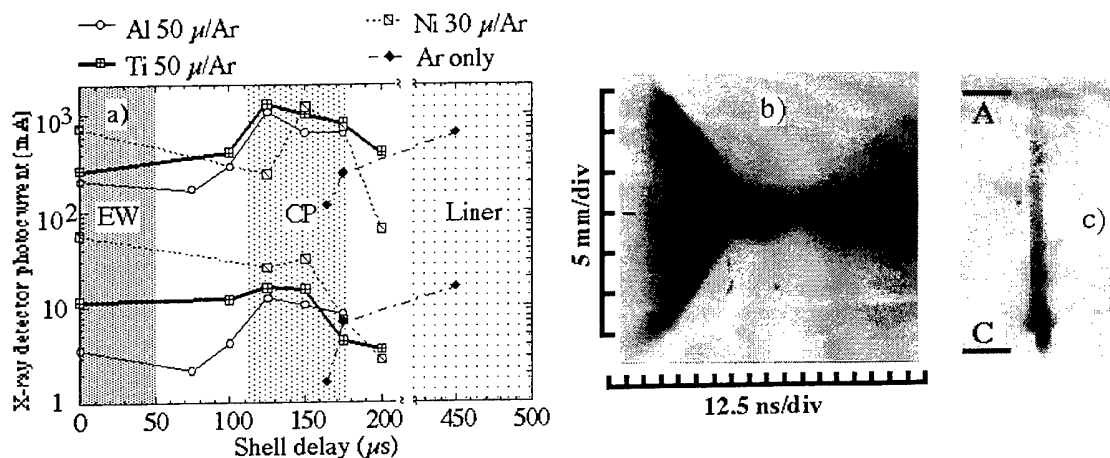


Fig. 9

Fig. 9. (a) Maximum responses of two X-ray channels sensitive to the radiation in 2-5 keV (upper curve) and 5-20 keV (lower curve) photon energy regions. Best shots for C-pinch, exploding wire and liner configurations for different time delays of the gas injection ( $\tau = 0$  corresponds to the wire only shots).

(b) Typical streak picture of the C-pinch. (c) Typical time-integrated image on HP-5 film behind a 200  $\mu$ -diameter pin-hole and 20  $\mu$  Al filter.

The internal plasma shell and the axial core were considered as a C-pinch. Initial plasma density was controlled by varying the delay,  $\tau$ , of the generator current start with respect to the internal shell injection. The optimum  $\tau$  were expected to be in the range  $\tau = 50$ -250  $\mu\text{s}$ ., which corresponded to the shell mass  $m_L = 2$ -40  $\mu\text{g}/\text{cm}$ .

Optimized C-pinch regimes were characterized by a narrow single-peak above-1 keV X-ray pulse, axial core preradiation on the streak photos (Fig. 9b), and tight homogeneous image of the PRS on time-integrated X-ray pictures (Fig. 9c). Besides, for all the axial core materials used a higher X-ray power was achieved in this scheme, when compared with "pure" or near-liner regimes as well as the EW regime. Optimum delays,  $\tau = 100$ -200  $\mu\text{s}$  (mean initial density in the range  $5 \times 10^{15}$ - $5 \times 10^{16} \text{ cm}^{-3}$ ), correlated well with the model predictions. Shots from the central region on the diagram of Fig. 9a correspond in the experiment to the clearly apparent C-pinch effect (better spatial and temporal homogeneity of the source, etc).

Time-resolved X-ray spectrum in the optimized Ar/Ni C-pinch indicated also successful heating of the Ni plasma. Intense radiating Ni K-shell lines and practical absence of the Ar K-shell radiation in the spectrum indicate efficient energy transfer from the external plasma layers towards the axial core.

## CONCLUSIONS

In conclusion, this paper overviews several aspects of the POS and Z-pinch physics which would have a considerable impact to the Syrinx project. These two elements are considered to be the most critical in the project and require further detail scientific examination. In particular, reliable scalings of the conduction and opening time, as well as of the POS resistance are required to scale the POS operation to higher power levels. Analysis of MAG-1 data proposes already some scaling relations for the conduction and opening phases. Plasma density measurements on GIT-8 reveal some new features of the POS resistance formation in high-density regime of the switch operation. Our Z-pinch study allowed us to introduce a concept of the Composite Pinch. First attempts on the modeling of this scheme were based on the assumption of disruptions of the current in the C-pinch plasma. Controlled plasma instabilities are shown to lead to a staged efficient current transfer from the external plasma layers towards the internal radiating core. Proper choice of initial parameters allowed higher radiated power, easier X-radiation spectrum control, spatial and temporal homogeneity of the final collapse. Finally, our POS and Z-pinch research programs are closely connected; both of them are oriented to better understanding of the current transfer mechanisms in complex IES plasma systems.

## ACKNOWLEDGMENTS

We would like to acknowledge all the scientists and institutions participating in the collaborative part of the Syrinx project. In particular, the work presented here could not be accomplished without contribution of the experimental teams of GIT-4 and GIT-8 (*HCEI*, Tomsk), as well as without theoretical support from the Applied Physics Department in *I.V.Kurchatov*, Moscow. This work is partially supported by DRET under the contract #92.134 and by ETCA/CEG under the contract #420/115/01.

- [1] R.B.Spielman, in *Proceedings of the Ninth International Conference on High-Power Particle Beams*, edited by D.Mosher and G.Cooperstein (NTIS, Washington, 1992), Vol. 3, p. 2002.
- [2] L.Véron, B.Etlicher, A.S.Chuvatin, C.Rouillé, J.P.Stephan, *IEEE Trans. Plasma Sci.* **21**, 529 (1993).
- [3] A.S.Chuvatin, L.Véron, N.S.Edison, B.Etlicher, C.Rouillé, J.P.Stephan, H.Lamain, and P.Avray, *PMI* 2621, Nov. 1992; see also *Bull. Amer. Phys. Soc.* **37**, 1565 (1992).
- [4] A.S.Chuvatin, B.Etlicher, N.S.Edison, and C.Rouillé, *Rev. Sci. Instrum.* **64**, 2267 (1993).
- [5] A.S.Chuvatin and B.Etlicher, *Phys. Rev. Lett.* **74**, 2965 (1995).
- [6] A.S.Kingsep, K.V.Chukbar, and V.V.Yan'kov, in *Reviews of Plasma Physics*, edited by B.Kadomtsev (Consultants Bureau, NY, 1990), Vol. 16, p. 243.
- [7] A.V.Gordeev, A.S.Kingsep, and L.I.Rudakov, *Physics Reports* **243**, 215 (1994).
- [8] A.S.Kingsep, Yu.V.Mokhov, and K.V.Chukbar, *Sov. J. Plasma Phys.* **10**, 495 (1984).
- [9] A.S.Chuvatin, *Ph.D.thesis*, PMI-2874, Ecole Polytechnique, 1993.
- [10] A.S.Chuvatin, L.I.Rudakov, and B.Etlicher, this conference proceedings, paper P-4-63.
- [11] V.Frolov, A.Chuvatin, S.Semushin, and B.Etlicher, this conference proceedings, paper P-4-67.
- [12] G.I. Dolgachev et al., *Sov. J. Plasma Phys.* **17** (10), 1171 (1991).
- [13] A.Chuvatin, C.Rouillé, B.Etlicher, F.Bayol, A.Morell, A.Kim, S.Loginov, V.Kokshenev, and B.Kovalchuk, this conference proceedings, paper P-4-64.
- [14] L.E.Aranchuk, A.S.Chuvatin, A.V.Gordeev, "Model for calculation of output characteristics of nanosecond REB generator with Plasma Opening Switch", *Eighth Int. Conf. on High-Power Particle Beams*, Novosibirsk, USSR, July 2-5, 1990.
- [15] K.V.Chukbar and V.V.Yan'kov, *Sov. Phys. Tech. Phys.* **33**, 1293 (1988).
- [16] A.S.Chuvatin, P.Choi, and B.Etlicher, *Phys. Rev. Lett.* **76**, 2282 (1996).
- [17] A.Chuvatin, P.Choi, B.Etlicher, S.Semushin, C.Dumitrescu, M.Vié, F.Bayol, A.Morell, A.Shishlov, A.Fedyunin, R.Baksht, I.Datsko, A.Russkikh, B.Kovalchuk, A.Kim, V.Kokshenev, S.Loginov, and A.Bastrikov, in *Proceedings of the 10<sup>th</sup> International Pulsed Power Conference*, Albuquerque, NM, USA, July 10-13, 1995.



## INDUCTIVE-ENERGY POWER FLOW FOR X-RAY SOURCES

K. D. Ware, P. G. Filios, R. L. Gullickson, M. P. Hebert, J. E. Rowley,  
R. F. Schneider, W. J. Summa and I. M. Vitkovitsky\*

*Defense Nuclear Agency, 6801 Telegraph Road, Alexandria, Virginia, 22310, USA*

*\*Logicon RDA, 2100 Washington Blvd., Arlington, VA 22204, USA*

## ABSTRACT

The Defense Nuclear Agency (DNA) has been developing inductive energy storage (IES) technology for generating intense x-rays from electron beam-target interactions and from plasma radiating sources (PRS).<sup>1</sup> Because of the complex interaction between the commutation of the current from the plasma and the stable dissipation of the energy in the load, DNA has supported several variations of power flow technology. Major variations include: (1) current interruption using a plasma opening switch (POS); (2) continuous current commutation through current-plasma motion against neutral, ionized, or magnetized medium [i.e., dense plasma focus-like (DPF) and plasma flow switch (PFS) technologies]; and, in addition, possible benefits of (3) directly driven complex PRS loads are being investigated. DNA programs include experimental and theoretical modeling and analysis with investigations (1) on Hawk and a Decade module in conjunction with the development of the bremsstrahlung sources (BRS), and (2) on Hawk, ACE-4 and Shiva-Star, as well as cooperative research on GIT-4 and GIT-8, in conjunction with PRS.

## INTRODUCTION

Before 1985, the high-powered, 0.1  $\mu$ s x-ray simulators built by DNA were based on high-voltage capacitor banks, power conditioned through a series of one or more water-line capacitors and low inductance switches.<sup>2</sup> This resulted in the 10 TW-class of simulators for DNA, such as Python, Blackjack-5, Double-Eagle (DE), and Phoenix, and for Sandia National Laboratories (SNL) simulators such as Proto II and Saturn. Looking for more compact and affordable technology for scaling to higher energy systems, DNA and others have been developing IES technology and extending the stability of radial implosions<sup>3,4,5</sup> to permit use of simpler capacitor banks. IES offers the potential advantages of smaller size and lower cost in comparison to conventional water-line technology. This advantage in cost and compactness increases with the amount of energy delivered to the diode. It also provides a means for concentrating the energy more effectively for high fluence requirements. The critical technology is the transfer of the relatively long-time IES energy into a short-duration pulse megavolt electron beam for BRS or into a high-current z-pinch for PRS. The z-pinches require the high currents for radial compression and, therefore, can utilize slower (and lower voltage) power sources, provided the stability can be maintained during the compression period. These technologies have been the subject of research supported by DNA during the past decade.

The IES sources being developed utilize conducting plasmas to commutate current from an inductor to the electron beam diode or to a z-pinch to produce hot or cold radiation, respectively. In the current DNA IES program, the POS<sup>6</sup> is the primary opening switch being used. The complex interaction between the commutating plasma and load affects the stability of the load dynamics, causing poor conversion of energy to radiation. Therefore, DNA is supporting several power flow technology investigations. Major efforts include: (1) current interruption using a plasma opening

switch (POS); (2) continuous current commutation through current-plasma motion against neutral, ionized, or magnetized medium [i.e. dense plasma focus-like (DPF) and plasma flow switch (PFS) technologies]; and (3) directly driven complex radial PRS loads. These approaches have been studied as part of the IES technology to develop effective methods for coupling the energy to radiation sources. Controlling this interaction leads to an improved energy transfer to the load enhancing the x-ray production and providing other desirable characteristics, such as decreased x-ray pulse rise time and improved energy spectrum. In the case of PRS, the interaction studies also include investigations of the resistive or compressional heating observed in some implosions<sup>7,8</sup> in order to increase the efficiency of converting the electrical energy into radiation.

IES approaches can be categorized by the conduction time scale of the opening switch. In DNA's initial work on IES at the Naval Research Laboratory (NRL), plasma opening switches with a conduction time of around 100 ns were used to sharpen the pulse of the Aurora gamma ray simulator<sup>9</sup> at the Harry Diamond Laboratories in Adelphi, Maryland. The present DNA effort is focused on understanding 300 to 1300 ns power flow at high power density to provide optimum transfer of energy from pulsed power sources to BRS or PRS loads. This effort utilizes several large pulsers. The Decade<sup>1</sup> simulator, to be located at the Arnold Engineering Development Center (AEDC), Tullahoma, Tennessee, is based on the IES concept. Upon completion, the full simulator will consist of 16 modules storing approximately 9 MJ and will deliver over 2 MJ to a radiation source load. The first two modules of Decade, DM-1 and DM-2, have been constructed at Physics International in San Leandro, California, to optimize opening switch performance. A four-module Quad is also planned for assembly at AEDC to drive PRS and BRS loads. DM-1 uses a plasma gun POS, conducting a current provided by a Marx capacitor bank, a water transfer capacitor, and output line. The POS conduction time is approximately 300 ns. A transfer capacitor is used to match the discharge time of the Marx generator to the conduction time of the POS. The DM-2 module is being fitted with the magnetically controlled plasma opening switch (MCPOS)<sup>10</sup> developed at SNL, in Albuquerque, New Mexico, and will be operated in the fall of 1996. The ACE-4 facility at Maxwell Laboratories, Inc., in San Diego, California, is an R&D test bed using a single coaxial POS to conduct up to 6 MA for 1.3  $\mu$ s before opening to a PRS load. It is also used to drive a continuous plasma-current commutation, Tandem Puff/DPF and to directly drive the PRS load. The DNA program also includes experimental and theoretical modeling and analysis and investigations on Hawk at the NRL in Washington, DC, and Shiva-Star at the Phillips Laboratory (PL) in Albuquerque, New Mexico, as well as cooperative research on GIT-4 and GIT-8 at the High Current Electronics Institute (HCEI) at Tomsk, Russia. Reference 1 describes these IES facilities in more detail.

Figure 1, showing a four-module Quad configuration, represents an intermediate step to the full Decade simulator, combining the DM-1 modules in parallel and operating with a POS or MCPOS for BRS and with or without opening switches for the PRS output. It will provide 5 - 7 MA to the load in about 150 and 300 ns with or without the POS, respectively,

### ISSUES

In contrast to pulse-forming line (PFL)-driven radiation loads, where typically the closing switches are isolated from the loads, the IES systems contain the opening switches in the proximity of the load. This becomes a dominant factor at terawatt levels, with several phenomena affecting the efficiency of the power flow and the ability to concentrate the energy in the load. As power to the load increases, there appear more potential bottlenecks to efficient energy flow and concentration. The most important of these are listed in Table 1 for BRS, PRS loads and for complex loads with direct drive. The X's in Table 1 indicate the existence of a bottleneck to the efficient power flow to the load. These will now be discussed along with examples of recent results.

Table 1. Power Flow and Energy Convergence Phenomena at High Power Levels

	Current Interruption ( BRS /PRS )	Current Commutation ( PRS )	Direct Drive ( PRS )
A. Plasma Current/Load Interaction	X	X	---
B. Vacuum Electron Current Losses	X	---	---
C. Inductive Transfer Losses	X	X	---
D. Enhanced Ionization of Neutrals (POS)	X	---	---
E. Load Stability	---	---	X
F. Voltage Limitations	X	---	---
G. Capacitor Discharge Time	---	X	X
H. Pulse Duration	X	X	X

Dispersion of the switching or commutating plasma into the POS/Load region (item A in Table 1) is an important effect that influences the power flow to the load. The pulser circuit requires that the inductance between POS and the load be minimum to optimize the current transfer to the diode, and, on the other hand, the POS plasma can interfere with the x-ray diode, requiring a minimum distance between the two. Factors determining the critical distance were investigated on DM-1. The POS/Load region of DM-1, shown in Fig. 2, has been instrumented to measure the effects of the dispersed plasma. Figure 3 shows the distribution of currents measured by B-dot probes in DM-1. These measurements show that the current propagates more than an order of magnitude more slowly than it would in a plasma-free vacuum. These probes further show that the vacuum electron current is a small fraction of the total current and that when current losses occur, most of the loss is near the POS<sup>11</sup> (Table 1, Item B). Both the probe measurements and x-ray pin-hole photographs illustrate the growth of azimuthal asymmetries in the current flow to the diode<sup>11</sup>, as the diode gap increased. It was also noted that asymmetry of the current increases with the POS plasma delay time, which is also associated with longer conduction time. Such asymmetries lead to partial losses of electrons to the wall and to poor reproducibility of the radiation pulses.

The presence of plasma in the POS/load region and the vacuum component of the current commutated by the switch appear to contribute to an effective lowering of the inductance in that region. With reference to Table 1, Item D, the typical DM-1 vacuum inductance of the POS/diode section is 60 nH; however, the initial analysis of the effective inductance, in the presence of the POS plasma, shows it to be 20 - 40 nH, providing a significant gain in current transfer to the BRS load. The diode, operating stably without impedance collapse under these conditions, delivers 90 kJ to the load.

In systems such as DM-1, electron losses can occur in the POS/load region, but also in the magnetically insulated transmission line (MITL), upstream of the switch. The losses in the POS/load region are described in detail in Ref. 11. Figure 4 demonstrates that such losses are possible in the MITL (5 ohms) when POS is not activated. However, no losses are observed when the MITL output is loaded by the POS, which lowers the MITL voltage during the charging of the inductor. As the MITL impedance is lowered to 3 ohms, a small MITL loss appears even when POS is operating and may influence the opening switch behavior.<sup>12</sup>

The study of power flow to implosion loads has been performed using Hawk<sup>9</sup> and ACE-4 pulsters for moderate and large current levels, respectively, as well as using GIT-4/8 in collaboration with HCEI. Reference 13 describes an HCEI optimization of the POS/load region, with axially injected switch plasma, by minimizing the separation, as well as gap dimensions, of this region for 2 - 3 MA operation. Figure 5 shows the current transfer in the Hawk pulser from the inductor to the imploding load, utilizing POS for commutation in an unoptimized POS/load region. At Hawk 0.5 MA levels, POS/load separation of 55 cm is sufficient to prevent the load from being affected by the POS plasma. These results in Fig. 5 also show that, characteristically for inductive systems, the pinch occurs considerably after the current has reached the maximum value. Hawk POS/PRS results were scaled for the ACE-4 facility (shown in Fig. 6) operating at 5 the MA level, generating nearly 1 MV output across a 94 nH load, as shown in Fig. 7.

Rapid changes in the plasma distribution in the critical regions can also occur during the opening phase. The effect of these changes on switch opening (e.g., final resistance) must also be understood for optimizing the Hawk and ACE-4 results and for scaling them to the Quad operation (Table 1, Item B). One source for these changes is the POS plasma which contains some fraction of neutrals from the flashboards, injected behind the conduction front, or from the cathode, released by plasma ion bombardment on the cathode. Experiments on Hawk (Fig. 8) and on ACE-4 show that a late time electron density increase progresses outward from the cathode. The increase occurs during the opening phase and current transfer. The typical time scale for the increase is 100 ns. It is postulated that the increase is due to the dense cathode plasma moving toward the anode and/or due to ionization of neutrals during the voltage pulse. The ionization of neutrals has been also investigated at the ACE-4 (at 3 MA level), since this could lead to significantly reduced POS impedance at the full level of 6 MA.<sup>14</sup>

The efficiency of IES energy and power delivery to the load depends on the nature of the load, i. e., on the importance of the resistive and inductive components of the load. As the inductive component increases, the transfer losses in high-power systems become significant (Table 1, Item D). Flux and energy conservation arguments provide an expression for the transfer efficiency to imploding loads. Applying this, for example, to the ACE-4 circuit, its relatively low efficiency of energy transfer suggests that it is worthwhile to consider approaches which utilize more of the magnetic energy than just that stored in the initial puff volume and that higher compression ratios, requiring increased stabilization of implosions, should be exploited. Figure 9 is a notional illustration of the direction being taken in exploring the potential for improving the performance of the cold x-ray sources. Exploiting the dense plasma concepts, a Tandem Puff experiment<sup>14</sup> on ACE-4 (shown in Fig. 10) tested energy coupling and stability of large diameter implosions. The initial results indicate good implosions (Fig. 10) with 40 ns FWHM (Fig. 11), 6 - 8 kJ Ar K-shell yield.

The efficiency of radiation production depends strongly on the quality of the implosion: implosion velocity, compression, and axial synchronism. These parameters are determined by the degree of radial flow stability that can be achieved for a given driver condition. Both modeling and experiments on Hawk, ACE-4 and on GIT-4 and -8 have shown that the stability regime can be considerably extended, in relation to that demonstrated to be stable for short implosion times and small initial radius, to radii > 10 cm and implosion times of at least 300 to 1000 ns.<sup>3,5,15</sup> Figure 10 illustrates the results of modeling the implosions with structured density distributions (hollow shell with exponentially outward fall-off) of the type reported in Ref. 15. These initial experiments add confidence that the bottleneck indicated in Table 1 (Item E) can be overcome and that direct drive is a feasible approach for reducing pulsed power source complexity and cost. ACE -4 (charged to 600 kV) is presently conducting direct drive experiments to extend this approach to the 5 - 6 MA range.

To explore the regime allowing even longer driving times (allowing the use of capacitor banks with lower charging voltages -- Table 1, Item F and G), large initial radius, implosions under the stabilizing conditions of the DPF configurations, a compact toroid (CT) -- acting as a magnetized plasma flow switch -- was used to commutate the current of up to 3 MA from the Shiva-Star capacitor bank (charged to  $< 60$  kV) to a Ne gas puff. The CT armature performed stably and reproducibly.<sup>16,17</sup> A 1 mg Ar CT provided sufficient inertia to conduct the current for 5 - 10  $\mu$ s, matching the rise time of the capacitor bank relatively well. Current commutation to an unoptimized load exhibited no current losses and resulted in stable 1  $\mu$ s implosions of neon gas puffs.<sup>17</sup>

Finally, because a narrow range of values of x-ray pulse duration is required, the options available for improving the system efficiency are limited. As indicated in Table 1, Item H, this continues to remain an issue, because, for example, the BRS pulse duration is determined by  $L/Z_{\text{diode}}$ , which effectively constrains the design parameters. On the other hand, the PRS pulse duration is solely determined by the quality of the implosion and does not appear to depend directly on the pulser parameters, limiting the options to some extent.

### CONCLUSIONS

We have made substantial progress in understanding the coupling between plasma opening switches and power flow as the impact load performance. In the Decade development program, this understanding has already resulted in the ability to increase the energy delivery to the diode by more than 50%. Additional understanding and improvements in opening switches are needed before the IES lives up to its promise in driving short-pulse, high-voltage loads such as the bremsstrahlung diode. Current opening switch performance may be adequate for driving plasma radiation loads. If the stability problems associated with the implosion of such loads can be solved, then simpler power sources with risetimes of several hundred nanoseconds to microseconds can be used to drive loads directly without switches. Progress in the design of such loads has been made at NRL and HCEI.

The broad effort to understand and enhance the transfer of energy from pulsed power sources to a variety of radiation loads at high power levels has provided the information necessary to select the candidates for further optimizing the performance of radiation sources. Regarding the BRS sources, it is now possible to combine modules at a level of almost 3 GW/cm<sup>2</sup>, as is planned for Decade. The multiprong approach to developing PRS sources has resulted in cold x-ray outputs from single-stage capacitor banks like ACE-4 and Hawk with efficiencies (1.1 % for Ne and 0.3 % for Ar, using ACE-4 Tandem Puff/DPF) approaching that of the PFL systems (0.6 % and 1.0 % on Saturn, respectively and 1.7 % and 4.5 % on DE, respectively) and DNA is now poised to apply optimized designs to establish the ultimate capability of the new approaches.

### REFERENCES

1. W. J. Summa, et al., "Advances in X-Ray Simulator Technology," 10th IEEE Pulsed Power Conference Proceedings, 1995, to be published
2. K. D. Ware, "Pulsed Power Technology for X-ray Simulators (a primer)," Simulation Fidelity Workshop III, MLR-3460 (September 1989)
3. A. L. Velikhovich, F. L. Cochran, J. Davis, Naval research Laboratory, submitted for publication, (April, 1996)
4. Radiation Hydrodynamics Branch, "Advanced Radiation Theory Support Annual Report", NRL/MR/6722-95-7656 (July, 1995)
5. R. Baksht, "GIT-4 Plasma Radiation Source", DNA Contract Report, HCEI, Tomsk (August, 1994)
6. B. V. Weber, et al., "Plasma Opening switch Conduction Scaling", Phys. of Plasma, 2,

3893 - 3901 (1995)

7. K. Whitney et al., "Optimization of K-shell Emission in Al Z-pinch Implosions; Theory and Experiment", *Phys. Rev. E*, **50**, 2166 (1994)
8. R. Baksht, "GIT-4 Aluminum Load", DNA Contract Report, HCEI, Tomsk (July 1995)
9. B. Bernstein, I. Smith, *IEEE Trans. Nuc. Sci.*, **20**, 294 (1973)
10. M. E. Savage, "Plasma Opening Switch Experiments at SNL", *Beams 94 Proceedings*, 42 (1995)
11. B. V. Weber, et al., "The DECADE Performance Assessment Program", *Beams 96* (June 1996)
12. J. Goyer, Private communication (April 1996)
13. B. Kovalchuk, R. Baksht, "GIT-8 AL Load", DNA Contract Report, HCEI, Tomsk (October 1995)
14. P. Coleman et al., 23-rd IEEE Int. Conf. on Plasma Sci., Boston (June, 1996)
15. J. Davis, F. L. Cochran, A. L. Velikhovich, "Stable Implosions of Structured Gas Puff Loads from Large Radii", *Beams 96* (June, 1996)
16. G. F. Kiuttu, J. D. Graham, J. H. Degnan, J. S. Brzosko, S. K. Coffey, D. G. Gale, C. D. Holmberg, B. B. Kreh, J. W. Meyers, C. A. Outten, E. L. Ruden, K. D. Ware, "A Compact-Toroid-Plasma-Flow-Switched plasma Focus Demonstration Experiment on Shiva Star", *Beams 96*, Paper O -3 - 4 (June, 1996)
17. G. F. Kiuttu, J. D. Graham, J. H. Degnan, J. S. Brzosko, S. K. Coffey, D. G. Gale, C. D. Holmberg, B. B. Kreh, J. W. Meyers, C. A. Outten, E. L. Ruden, K. D. Ware, "New Method of Initiating Multi-megampere, Multi-megajoule Plasma Focus Discharges using Magnetized Plasma Flow Switches", *ICOPS 96*

#### FIGURES

- Figure 1. The Decade Quad designed to provide 20 krad(Si) over  $2500 \text{ cm}^2$ ; the system consists of a Marx generator driving four pulse IES sections, using a POS to transfer power to the load.
- Figure 2. Front-end section of DM-1 module, showing POS, connecting region and BRS load, with typical diagnostic instrumentation.
- Figure 3. Current probe signals showing the propagation of current from POS to BRS load.
- Figure 4. Signals from current probes located upstream of the POS demonstrating loss of the electron current in the MITL for initially open circuit load.
- Figure 5. Power flow characteristics of the HAWK-driven POS/PRS system; Ne K-shell radiation indicates high (X15) radial compression of the pinch.
- Figure 6. ACE-4 Facility, consisting of the four Marx banks with outputs connected to a central load.
- Figure 7. ACE-4 charging and load current traces, with POS operating at 1 MV.
- Figure 8. Current-density relationship for HAWK-driven POS at a distance of 3 mm from the cathode surface, showing POS density increase during switching.
- Figure 9. Evolution of the understanding of the vacuum power flow and energy transfer to imploding loads, with a rather mature state of understanding of waterline PFL systems.
- Figure 10. ACE-4 Tandem Puff configuration used in studies of Ar plasma implosions and typical pinch.
- Figure 11. X-ray pulse associated the pinch in Fig. 10.
- Figure 12. Kinetic energy, per wavelength, of the radial and axial components of the imploding plasma driven by nearly linearly rising current to 5 MA at 200 ns.

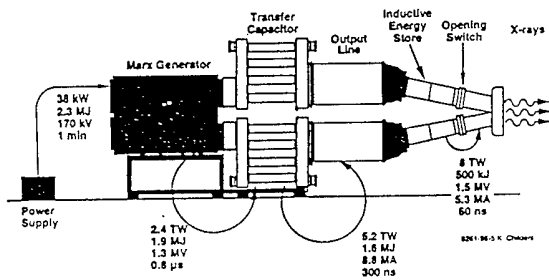


Figure 1

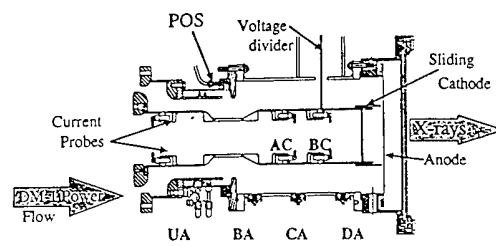


Figure 2

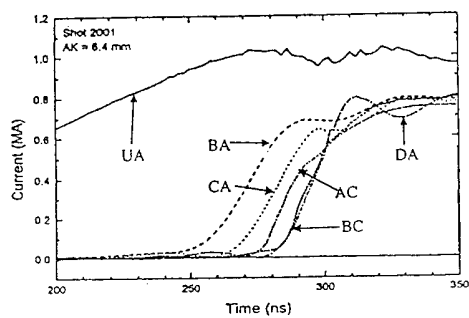


Figure 3

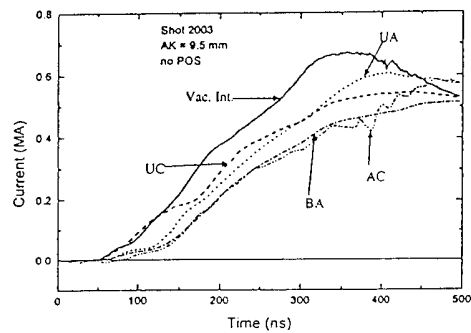


Figure 4

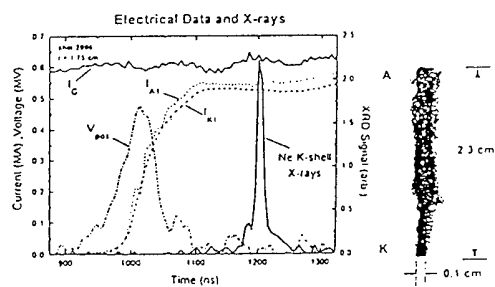


Figure 5

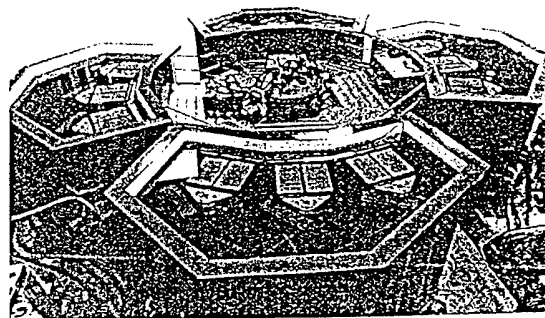


Figure 6

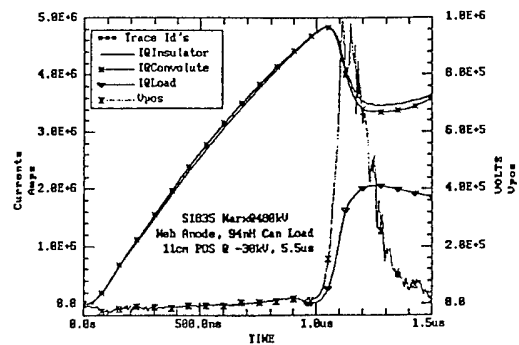


Figure 7

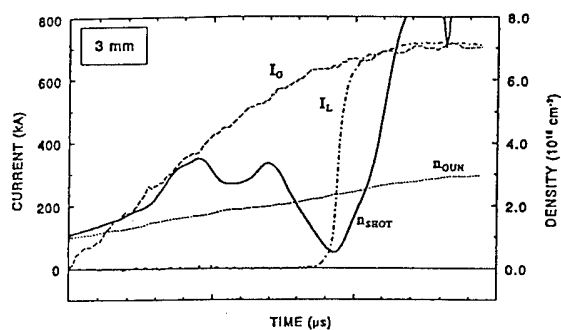


Figure 8

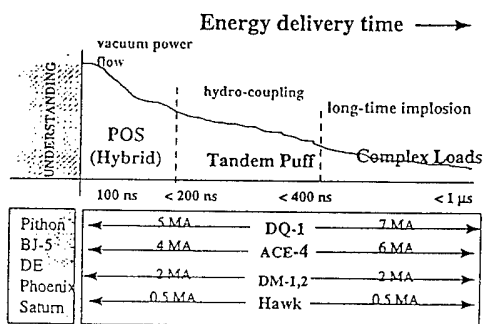


Figure 9

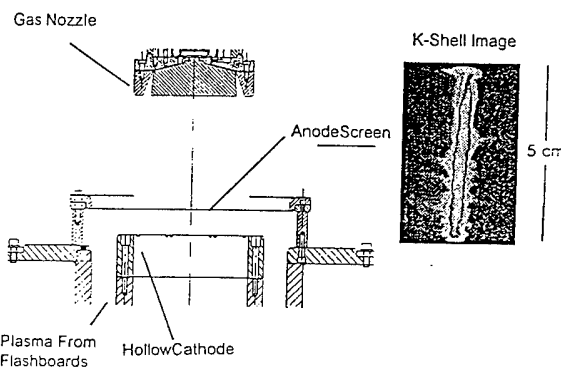


Figure 10

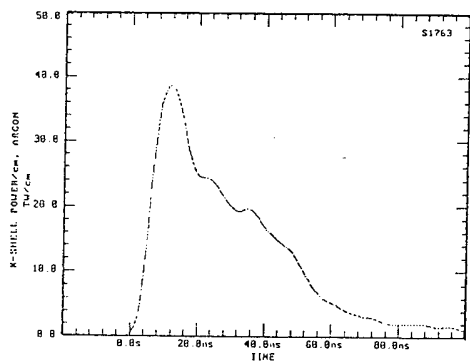


Figure 11

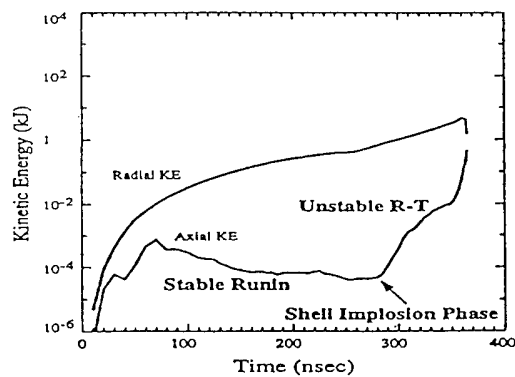


Figure 12



## EXCITATION OF INTENSE SHOCK WAVES BY SOFT X - RADIATION.

A. V. Branitskij, V. E. Fortov, K. N. Danilenko, K. S. Dyabilin,  
E. V. Grabovskij, O. Yu. Vorobiev, M. E. Lebedev, V. P. Smirnov,  
A. E. Zakharov, I.V. Persiansev

*Troitsk Institute of Innovative and Fusion Research, Troitsk,  
142092, Russia*  
*High Energy Density Research Center, Izhorskaya 13/19, Moscow  
127412, Russia*

### Introduction

A fundamental problem in the use of concentrated fluxes of charged particles and laser light in the dynamic physics of high energy densities [1] is the substantial spatial nonuniformity of the power which is released. This nonuniformity disrupts the symmetry of the spherical compression of the fusion fuel [2] and hinders the excitation of plane shock waves in the experiments on the behavior of matter under extreme conditions. One of the most effective ways to solve this problem is to use x-ray emission from a plasma with an approximately thermal spectrum which arises when directed energy fluxes are applied to a target [3] or during the electrodynamic compression of cylindrical shells in a Z-pinch geometry [4]. Planar shock waves excited by this radiation, which are an extremely simple type of self-similar hydrodynamic flow [5], may be a more natural and rich source of experimental information on both the intensity of the incident x-radiation and of the thermophysical properties of matter under influence of this radiation with condensed targets.

Z-pinch plasmas produced in big installations by electrodynamic compression of cylindrical liners seem to be one of the most favorable candidates for the source of the such x-radiation. In a case when Z-pinch plasma is used as a radiative source it is preferable to use the so called double liner scheme. In this scheme the external annular plasma liner is compressed in the magnetic field with the velocity about  $5 \cdot 10^5$  cm/s coincides with the internal liner. Liners are prepared of the substances with the large atomic numbers. At the supersonic strike and strong shock wave generation in the internal liner plasma the intensive thermal X-ray radiation appears. The external liner provides the confinement of the thermal energy inside the plasma and the intensity of the soft x-ray radiation in the liner hole increases substantially.

This paper presents the measurements of the shock waves intensities generated by soft x-radiation in Al, Sn, Fe and Pb targets. The scheme with the conversion of the laser to soft x-radiation, described in [6,7], is different from that used here: the soft x-radiation was induced by the dynamic compression and heating of the plasma in the cylindrical Z-pinch geometry in the ANGARA-5-1 installation [8,9]. As a result, the radiation pulse duration was about an order of magnitude more, with the power level being nearly the same as in [6,7].

### Experiment and theory

The Z-pinch plasma radiates soft x-rays with a temperature on the order of 60-120 eV. The x-ray pulse duration was 30 ns FWHM [9]. This radiation was incident on a planar target positioned above the inner liner (at a distance 1 mm) [10]. The experimental set-up is shown in Fig. 1. The targets were made as step 16-32  $\mu\text{m}$  Al and 80-200  $\mu\text{m}$  Pb, or pure 180  $\mu\text{m}$  Pb,

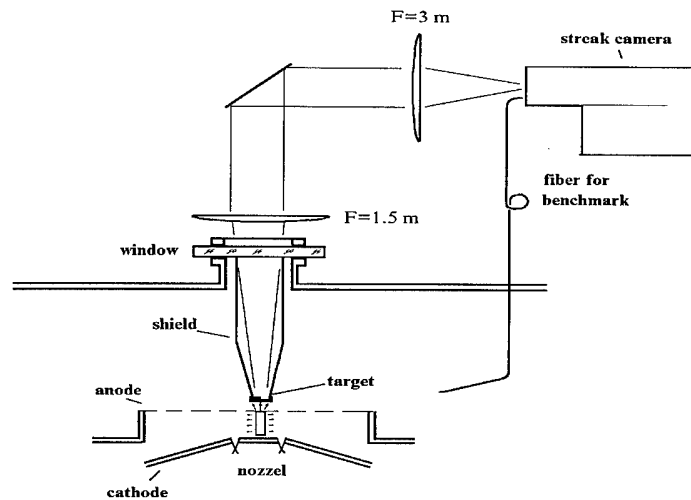


Fig.1 Experimental set-up

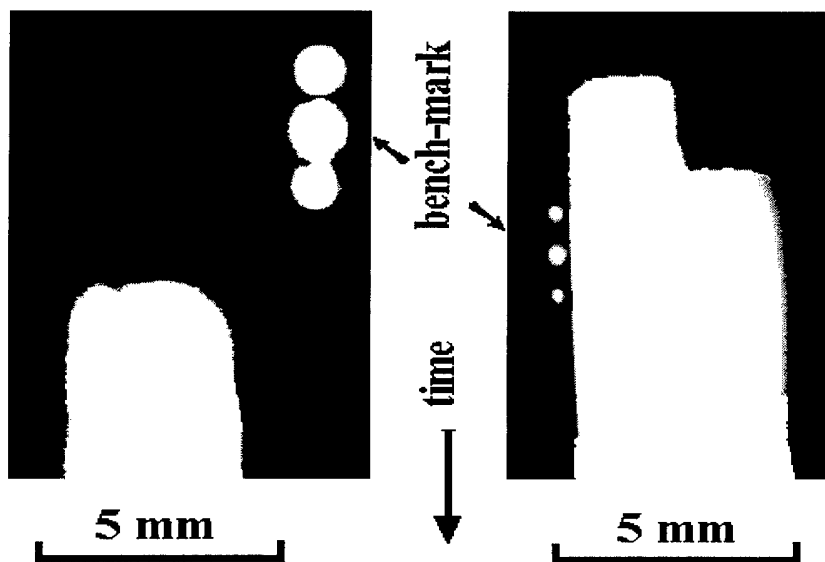


Fig.2 Streak camera records (positive) of shock break out from sample obtained in ANGARA-5-1 experiments: left - plane target: lead-180  $\mu\text{m}$ ; right - stepped target: tin-16  $\mu\text{m}$ , lead-180  $\mu\text{m}$ . Between bench-marks - 13 ns

or stepped 16  $\mu\text{m}$  Sn and 180  $\mu\text{m}$  Pb plates being connected together. Such large thickness allowed the elimination of the thermal preheating of the target. The diameter of target was about 5 mm. The velocity of the shock wave was defined by the optical base method as the difference between the moments in the flashes of light emitted as the shock waves break out at

the rear surface of a sample. The sample was imaged with the help of a f/10 ( $f=1.5$  m) objective and a f=3 m objective with 2 - fold magnification onto the photocathode of a SNFT-2 streak camera. Spatial resolution corresponds to 20 lp/mm in sample plane; temporal resolution less than 0.3 ns was provided. Optical fibers (quartz-polymer, length 80 m, 0.4 Db dumping, bandwidth 2 GGz) were also used, providing the high enough noise shielding from the experiment apparatus. The ends of a fibers (400  $\mu$ m in diameter) were butted directly against the free surfaces of the stepped sample. To eliminate the influence of the hard x-ray, which can induce the light inside the fibers, they were positioned inside the steel tube. Optical radiation from the fibers was detected by silicon photodiodes with a time resolution less than 1 ns. The time difference between the signal fronts was used, so temporal resolution of less than 1 ns in this fiber method was provided.

Typical streak camera records are shown in Fig. 2.

To describe the dynamics of the target under x-ray action Euler equation closed by wide range semiempirical EOS [11] were used, taking into account melting, vaporization and ionization of matter. Energy transfer by x-ray radiation was treated in multigroup diffusive approximation, which allow one to replace quasi-stationary transfer equations by equations of radiation diffusion. Spectral opacities were used calculated in the frame of modified Hartri-Fock-Sletter model in wide range of temperatures and densities. To validate opacity model Rosseland mean opacities coefficients were compared with other semiempirical formulas. Euler equation were integrated by Godunov method. For calculation of energy transfer an implicit numerical scheme was employed.

The result of calculations are shown in Fig. 3.

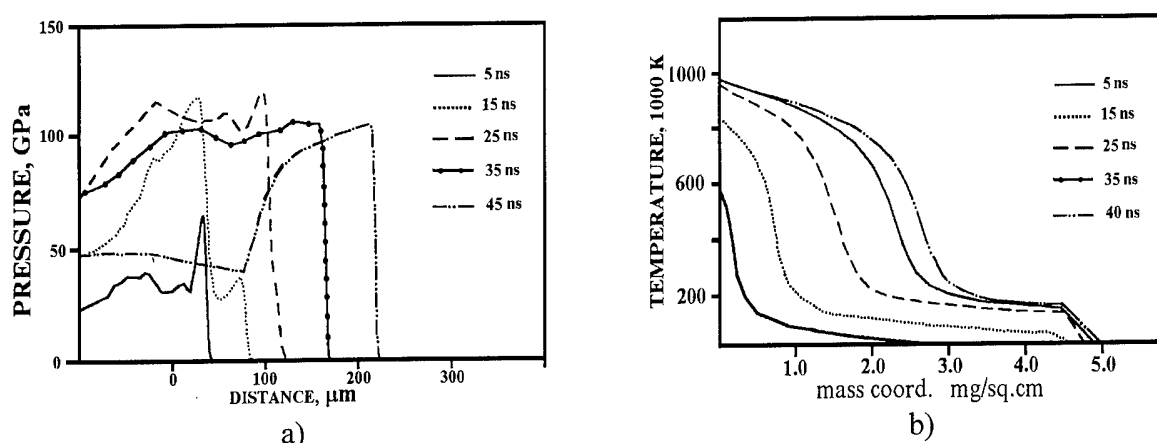
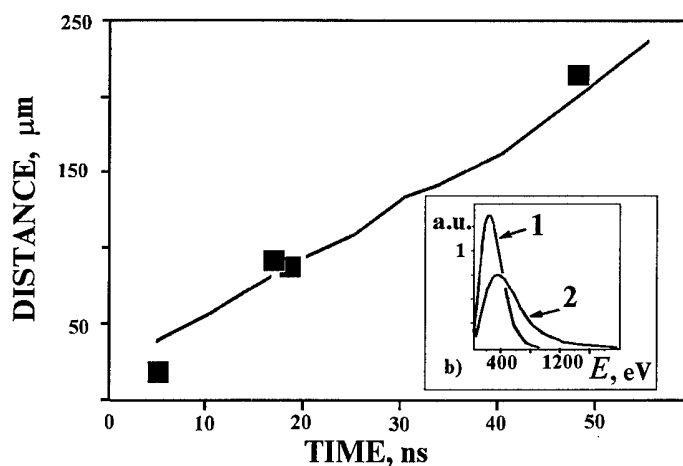


Fig.3. Numerical simulation of soft x-ray interaction with condensed Al target: a) Pressure evaluation; b) temperature evaluation. Power level  $2 \cdot 10^6$  W/m<sup>2</sup>

The results of the experiments and calculations are shown in Fig. 3. The averaged (over the target volume) shock wave velocity for Al plus Pb stepped target is  $(7.3 \pm 0.6) \cdot 10^3$  m/s for 80  $\mu$ m Pb thickness, and  $(4.6 \pm 0.3) \cdot 10^3$  m/s for 200  $\mu$ m. In accordance with the Huguenot lead adiabat this means that the shock compression pressures are 300 GPa and 90 GPa correspondingly [10]. In stepped tin plus lead target shock compression of lead (thickness 180  $\mu$ m) about 120 GPa was measured.



a)

Fig. 3 a) Shock front vs. time position for stepped "sandwich" (Al 30  $\mu\text{m}$  + Pb 200  $\mu\text{m}$ ) target, power level  $1.2 \cdot 10^6 \text{ W/m}^2$ , squares - experiment, solid line - calculation b) soft x-ray spectra used in calculations: 1 - Color temperature - 80 eV, 2 - Color temperature - superposition of 120 eV and 300 eV

## Conclusion

The results presented above show that uniform intense shock waves can be generated by Z-pinch soft x-ray plasma radiation. The uniformity of shock wave is very high. At a flux power about some  $\text{TW/cm}^2$ , a shock pressure of some hundreds GPa was achieved.

## References

1. S. Anisimov, V. Fortov and A. Prohorov *Sov. Phys. Usp.* **27** (1984) 181.
2. J. J. Duderstadt, *Inertial Confinement Fusion* (New York, 1982).
3. D. L. Matthews et al., *J. Appl. Phys.* **54** (1983) 4260.
4. P. J. Turchi and W. L. Baker, *J. Appl. Phys.* **44** (1973) 4936.
5. Ya. B. Zel'dovich and Yu. P. Raizer, *Physics of Shock Waves and High Temperature Hydrodynamic Phenomena*, (Academic Press, New York, 1966).
6. T. Endo et al., *Phys. Rev. Lett.* **60** (1988) 1022.
7. Th. Lower and R. Sigel, in *Proc. 7th Int. Workshop of the Physics on Nonideal Plasma*, (Markgrafenheide, 1993).
8. V. Smirnov et al., in *Proc. 8th Int. Conf. BEAMS-90*, (Novosibirsk, 1990).
9. V. Gasilov, S. Zakharov and V. Smirnov, *JETP Lett.* **53** (1991) 83.
10. E. Grabovskij et al., *JETP Lett.* **60** (1994) 3.
11. A. Bushman, V. Fortov. *Sov. Tech. Rev. B Term. Phys.*, **1**: 219, (1987).

## PLASMA X-RAY SOURCES POWERED BY MEGAJOULE MAGNETOCUMULATIVE GENERATORS.

N.F. Popkov, V.Ya. Averchenkov, A.S. Pikar', E.A. Ryaslov, V.I. Kargin, S.A. Lazarev,  
V.V. Borovkov, S.T. Nazarenko, and G.F. Mackartsev.

*Russian Federal Nuclear Center All-Russian Research Institute of Experimental Physics  
(VNIIEF), Sarov, Nizhni Novgorod Region, 607190, Russia.*

We have performed experiments using magnetocumulative generators (MCGs) to power three different types of high-energy-density plasma discharges suitable for intense x-ray generation. They include the  $H$ -pressed discharge, the capillary  $z$ -pinch, and the  $\theta$ -pinch. The MCGs were operated with, and without, plasma opening switches. The characteristic currents were approximately 10 MA and characteristic time scales approximately 1  $\mu$ s. In this paper we describe the characteristics of these experiments.

### Introduction

The use of magnetocumulative generators (MCGs) with exploding plasma switches as energy sources for mega-ampere, microsecond pulses opens wide opportunities for dense, high-temperature plasma physics investigations at high current densities and with high internal and external magnetic fields [1, 2]. In this paper, we present descriptions of three different high-current-density, x-ray-producing plasma discharge experiments powered by MCGs: an  $H$ -pressed discharge, a capillary  $z$ -pinch, and a  $\theta$ -pinch.

### $H$ -pressed Discharge

The  $H$ -pressed discharge is a variety of  $z$ -pinch in which plasma is pressed against a dielectric barrier by its internal azimuthal magnetic field. These discharges are intense sources of visible and ultraviolet radiation. The experimental configuration is shown schematically in Fig. 1. The system basically consists of a single-turn MCG and a plasma load chamber. Inside the chamber there is a dielectric cylinder with a thin metal coating across the anode-cathode electrode gap (labeled 8 in Fig. 1). Current from the capacitor bank loads flux into the MCG and also explodes the metallic film, filling the load chamber with plasma. Under operation of the MCG, megampere currents are driven through the plasma.

The interaction between the plasma, magnetic field, and dielectric surface leads to strong plasma turbulence. This turbulence is confirmed by high anomalous resistance of the plasma and by structure shown on the magnetic field probe oscillograms. Soft x-rays are generated at the time of compression of the plasma/field mix. A typical discharge current oscillogram is shown in Fig. 2a. Characteristic features associated with the increase of plasma resistance can be seen along the leading and trailing pulse edges. Time-correlated singularities are also observable on oscillograms of the voltage (labeled 2) and current derivative (labeled 1), and recorded in the plasma chamber (Fig. 2b).

The most typical oscillograms are current derivatives recorded in the plasma chamber at various locations near the anode (Fig. 2c). One can see fluctuations with characteristic time scales of 0.1-1.0  $\mu$ s. Peak current in the  $H$ -pressed discharge plasma channel reaches  $10^7$  MA, the current density in plasma near the dielectric obstacle makes 3.2 MA/cm.

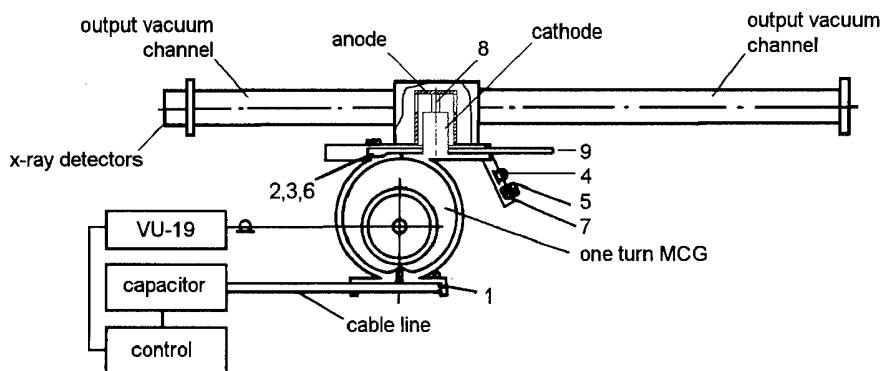


FIG. 1. The *H*-pressed discharge experimental scheme: (1) capacitor bank current (*I*) and current derivative (*dI/dt*) probes; (2, 3, 6) MCG and load current and current derivative probes; (4) inductive divider; (5) discharge current derivative probe; (7) discharge voltage probe; and (8) polyethylene insulator.

Provided the x-ray quantum energy was greater than 1 keV, the x-ray yield was 100 kJ, with a 10  $\mu$ s pulse width. The average photon energy in the spectrum was approximately 5 keV. The energy produced in the plasma channel for the said time was 10 MJ.

The evolution of the discharge was studied with the help of a fast camera; plasma density evolution was investigated with an interferometer (Fig. 3). During the initial stage of the discharge, splitting of interference bands is seen. This effect is due to small-scale electron density inhomogeneities in the plasma for the time interval of 1  $\mu$ s, determined by the filamentary structure of the channel. During the further discharge phase, the electron density is approximately  $2 \cdot 10^{18}$  cm<sup>-3</sup>. Later in the pulse, the interference strips disappear, which may be attributed to a high plasma excitation.

### Capillary Z-pinch

The high-density wall-confined z-pinch (capillary discharge) is high-intensity x-ray source. Capillary discharge experiments were carried out using MCGs with explosive plasma opening switches for pulse shaping [3].

The experimental apparatus for capillary discharge investigations consists of the following main elements: the cable line for energy transport, the megampere storage inductor, and the plasma load (Fig. 4). The MCG in this case was four single-turn generators connected in series. The initial power supply inductance was  $10^{-6}$  H, the cable line inductance  $10^{-8}$  H, and the storage  $10^{-7}$  H. The exploding plasma opening switch opened at the inner radius of the coaxial storage inductor to form short, megampere pulses.

During MCG operation, current reaches a value of  $10^7$  A. At peak current, the switch opens, transferring current to the load. The current derivative associated with switching is  $10^{13}$  A/s, with a switching time of 0.5  $\mu$ s. The peak switched current is  $5 \cdot 10^6$  A (Fig. 5). Charged particle flux measurements were made outside the plasma chamber, indicating approximately 2 MA of electron current and 100 kA of ion current.

### $\Theta$ -pinch

MCG-powered  $\theta$ -pinches were investigated to study high energy plasmas produced by ultrahigh magnetic fields. The  $\theta$ -pinch under investigation is related to staged pinches, in which both implosion plasma heating and subsequent pinch compression are important. In this case, pinch initiation and implosion take place under initial MCG operation, and the ultrahigh magnetic fields produced compress the plasma channel.

The  $\theta$ -pinch plasma chamber looks like a cylindrical ampule, made of quartz optical glass, inside a copper solenoid that serves as the MCG load. A thin metallic film is deposited on the inside surface of the ampule, and the volume is evacuated to approximately  $10^{-5}$  mm Hg before being sealed at the ends. Sectioned copper rings are installed at the solenoid ends to confine plasma to the region of relatively uniform magnetic field (Fig.6).

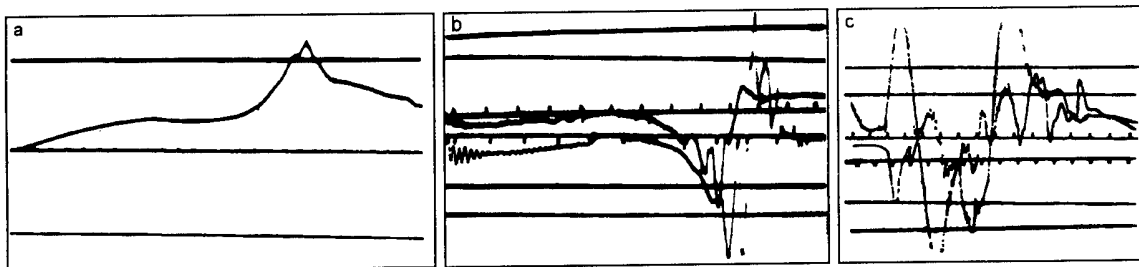


FIG. 2. (a) Typical current oscillogram in the discharge circuit ( $5 \mu\text{s}/\text{div}$ ), (b) voltage (labeled 1) and current derivative (labeled 2) for the plasma channel ( $10 \mu\text{s}/\text{div}$ ), and (c) current derivative oscillograms recorded near the plasma channel on the anode side.

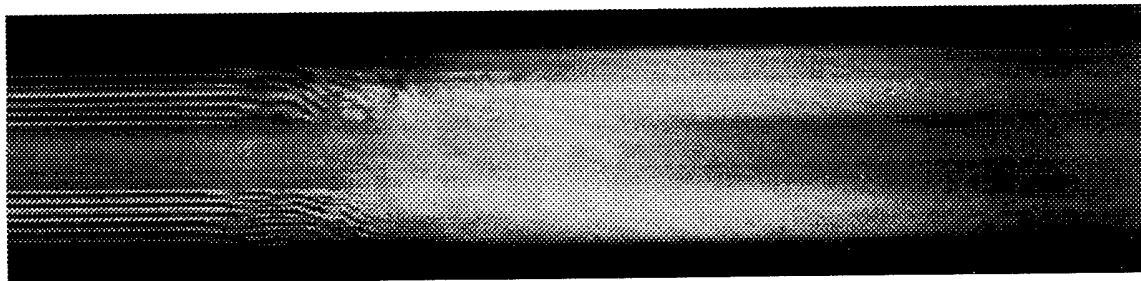


FIG. 3. Discharge interferogram in streak mode ( $6 \text{ mm}/\mu\text{s}$ ).

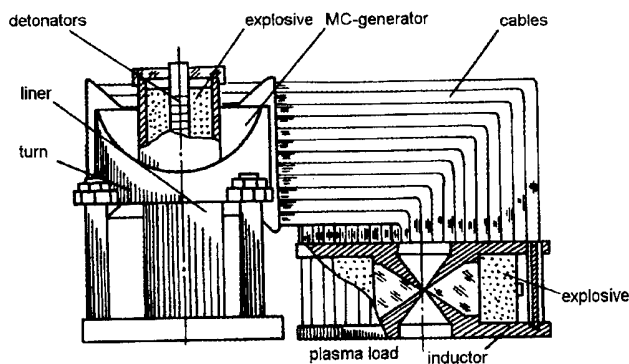


FIG. 4. Z-pinch in a capillary.

When the field in the solenoid reaches approximately  $10^4$  Oe from flux generation, the metal layer explodes electrically, forming an ionized  $\theta$ -pinch plasma shell. As the solenoid current rises to the value of  $10^7$  A, the plasma shell current reaches approximately 2 MA. The x-ray pulse has a width of  $20 \mu\text{s}$  and appears when the magnetic field in the solenoid reaches 400 kOe. The x-ray yield above 30 keV is 10 kJ.

### EMG/PIRIT: High-Power X-ray Flux Modeling Technology

In the course of the research and development of x-ray plasma sources powered by MCGs (magnetocumulative generators) two complicated problems were posed, the successful solution of which defines the prospect of the MCG use in electro-physical experiments. The 1st one is connected with obtaining of the necessary electric pulse volt-ampere and time characteristics. The 2nd one is a result of the required plasma chamber and diagnostics protection from the shock wave and debris occurred in case of the explosive generator operation.

There are known the short high-voltage pulse shaping techniques and the variations of the latter are described in several papers.

The explosive experiment conduct practice reveals that to meet the protection requirements the effective distance/obstacle combination is to be employed.

The authors proposed and implemented the experimental lay-out represented in Fig. 7. The facility is designed so that only the MCGs and energy transport line are destroyed in the experiment, while the remaining facility part, all technological and diagnostic systems paced in the protective bunker are preserved.

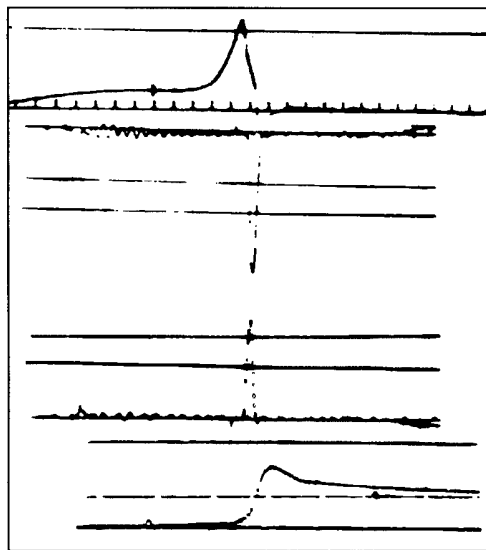


FIG. 5. Voltage and ampere characteristics of the capillary z-pinch discharge: (1) Inductive store current ( $10 \mu\text{s/div}$ ), (2) opening switch voltage ( $10^6 \text{ V peak}$ ,  $2 \mu\text{s/div}$ ), (3) storage inductor  $dI/dt$   $10^{13} \text{ A/s}$ ,  $2 \mu\text{s/div}$ , and (4) z-pinch current ( $5 \text{ MA peak}$ ,  $2 \mu\text{s/div}$ ).

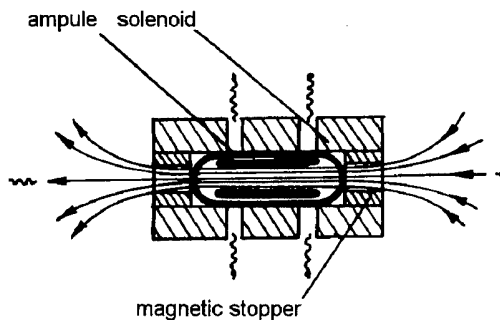


FIG. 6. The  $\theta$ -pinch scheme.

MCG number and performance employed in each experiment depend on the goal to be attained. So, each MCG energizes the 1st-stage pulse shaping inductor through the cable line. To break the said inductor circuit, it is used the explosive plasma beaker operating for nearly  $1 \mu\text{s}$  at the break voltage of  $10 \text{ V}$ . In the experimental version shown in Fig. 7, 4 inductive storages are connected in series in the single circuit, so that the voltage at the 2nd-stage vacuum magneto-insulated inductor output is summated and reaches  $4 \text{ MV}$ .

The above mentioned inductor contour is broken with the plasma erosion breaker for approximately  $100 \text{ ns}$ . In this case, the 2nd pulse shaping stage voltage may reach  $10 \text{ MV}$ .

The high-temperature plasma obtaining technique is rather significant in terms of getting a considerable x-radiation flux energy density. As the x-ray sources there are used the organic plasma discharges ( $H$ -pressed capillary, z-pinch); imploding plasma liners, high-velocity plasma torroids. The x-ray sources of the above types are researched by the authors, using "PIRIT-2" laboratory facility having the primary energy storage of  $2 \text{ MJ}$ , provided the current is up to  $5 \text{ MA}$  and its rising time is less than  $100 \text{ ns}$ .

The facility under research (Fig. 7) is one of the EMG-PIRIT power equipment set modules. The project of the equipment-to-be envisions creation of 8 similar modules synchronously operating for a single plasma radiator.

To experimentally implement the EMG-PIRIT project, it is reasonable to apply one module to study both many related physical processes and all the power equipment set functional systems.

### Conclusion

The results of investigations involving various high-power plasma discharges ( $H$ -pressed discharge, capillary z-pinch, and  $\theta$ -pinch) have been described.

The  $H$ -pressed discharge is a variety of z-pinch wherein the plasma is held against a cylindrical dielectric surface by the magnetic field. the current in such experiments was as high



as 10 MA. One megajoule of energy was dissipated in the discharge in 10  $\mu$ s, and the x-ray yield in the photon energy range 1-20 keV was 100 kJ.

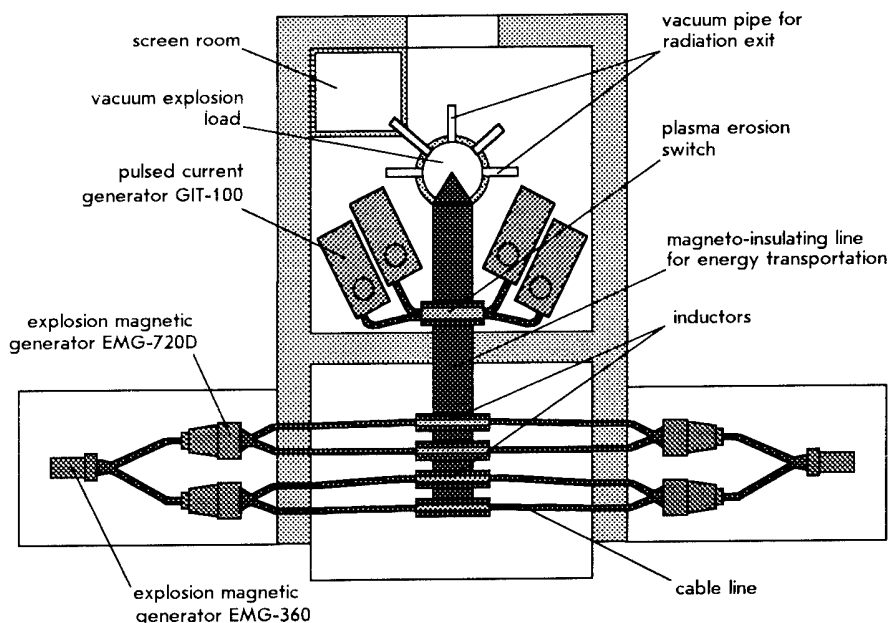


FIG. 7. EMG-PIRIT.

Experiments with a z-pinch discharge in a capillary were carried out with an MCG with a plasma erosion switch (PES), producing a 5 MA load current with a 0.5 s characteristic time. The x-ray yield was as high as 600 kJ, for a stored energy of 3.2 MJ.

Investigations of radiating plasmas produced by high-field (1 MOe)  $\theta$ -pinches were conducted. High-photon-energy ( $>30$ keV) x-ray yields of 10 kJ were obtained.

These experiments demonstrate the possibility of studying different types of high-energy-density discharges with high internal and external magnetic fields at current levels of 100 MA and time scales of 1  $\mu$ s using relatively simple inexpensive magnetocumulative generators.

The EMG/PIRIT multi-module quasi-stationary power equipment set lay-out is proposed and experimentally realized as to one such module. In further experiments the EMG current pulse is supposed to be used to power the x-ray plasma source. In this case, the primary energy source (MCG) and the 1st pulse shaping stage are destroyed by the explosion. The 2nd pulse shaping stage, plasma chamber, technological and diagnostic equipment remain intact because they are protected from the explosion in a special bunker.

- [1]. A.I. Pavlovskii, R.Z. Lyudaev, ET AL., in "Megagauss Physics and Technology" (P.J. Turchi, Ed.), p. 585, Nova, New York, 1980.
- [2]. A.I. Pavlovskii, N.F. Popkov, ET AL., in "Megagauss Fields and Pulsed Power Systems" (V.M. Titov and G.A. Shvetsov, Eds.), p. 679, Nova, New York, 1989.
- [3]. A.I. Pavlovskii, N.F. Popkov, et al., in "Megagauss Fields and Pulsed Power Systems" (V.M. Titov and G.A. Shvetsov, Eds.), p. 503, Nova, New York, 1989.

## RS-20 TYPE REPETITIVE GENERATOR WITH PLANAR CONFIGURATION OF PLASMA OPENING SWITCH

V.P. Agalakov, N.U. Barinov, G.S. Belenki, G.I. Dolgachev, L.P. Zakatov  
Russian Research Center "Kurchatov Institute", Moscow, 123182, Russia

Qiu A.C., Shen Zh.K., Sun F.J., Wang X.H., Xu R., Zeng J.T.  
"Northwest Institute of Nuclear Technology" P.O. Box 69, Xian 710024 PR of China

*Existing experience in production of rep. rate accelerators with a high peak power (over than  $10^{10}$  W) and average power above 50 kW enables to resolve a row of physics and technology tasks which are connected with reliability and life of the accelerator. This paper considers the design and results on optimization of simple plasma opening switch (POS).*

*Final design of the POS provided voltage up to 2 MV and had their life at more than  $10^5$  pulses including 4 hours of continuous operation under 4 Hz rep. rate and wall plug power 65 kW.*

*This unit had been tested at RS-20 type accelerator both in the Kurchatov Institute and in Northwest Institute of Nuclear Technology (NINT) in China.*

### INTRODUCTION

While creating rep. rate beam accelerators we are being faced with the problem of high peak power loads on elements of the machine. This problem becomes more important when using plasma opening switch technology power intensifying elements. Heat removal from high-voltage elements using cooling liquids results in a sufficient complication of the machine and finally is ineffective due to surface destruction under high peak power flow which is becoming faster other than heat transport mechanisms take place. The most effective is a radiate cooling from the surface; this fact determines its material and area. Increasing of the radiated surface is limited and followed by the increasing of POS volume resulted in less power multiplication factor.

Thus in design the power sharpening machine one could solve the following problems: correct choice of geometry and materials for POS; increasing of the efficiency, which permit to reduce heat allotment without reducing final parameters. The design also should be simple, reliable and cheap.

The paper present one of the solutions of such problems used in the creation POS for repetitive X-ray RS-20 type generator, which was delivered to NINT in Xian, China in 1995.

### RS-20 TYPE GENERATOR

The RS-20 generator [1] contains (FIG.1,2):

- 1) Four Marx (2) with 20 stages in each; triggering disperse not exceed 30 ns. Marx discharge voltage 800-850 kV and capacity  $C_g = 4 \cdot 10^{-8}$  F; its inductance  $L_g = 1,8 \cdot 10^{-6}$  H.
- 2) High-voltage drive and vacuum line have inductance  $L_l = 2,5 \cdot 10^{-6}$  H. The parameters of the Marx-POS circuit are follows:  $T = 2,4 \mu s$ ,  $\rho = 10 \Omega$
- 3) The vacuum chamber contains POS and load.

## POS DESIGN AND OPTIMIZATION

POS represents quasi-planar two-electrode system (4,5). The anode (5) is the carbon plate inclined to the flat wall of the vacuum chamber (3), which is the POS cathode. Plasma guns are placed at the cathode in one row. It was found that current channel during current rise is pushed down along the anode and compressed in the diametrical direction. This is followed from the electron bombardment track of the anode (FIG.3) and from POS image in X-rays (FIG.4). The first effect leads to the increasing of POS impedance; the second - to the electron flow focusing at the stage of sharpening. This is followed by the strong erosion and to destruction of electrodes (particularly anode). Thus one should find such POS geometry that the first effect is sufficient (plasma accelerates up to sufficient velocity; the latter determines the impedance rise time) and diametrical compressing could not decrease the effective anode surface below the critical value corresponding to anode destruction. With given arrangement of plasma guns, anode-cathode angle, distance between the electrodes one can empirically obtain the anode dimensions using larger anode which is destroyed during operation. The tracks of destruction in dependence of operation time is shown at FIG.3.

During the destruction the time of conductivity phase (and the current amplitude correspondingly) decreases. One can optimize this time by changing the anode-cathode angle, the distance between the electrodes and the number of plasma guns.

Performed investigations results in following POS geometry: anode 45 cm  $\times$  35 cm is inclined at 30° to the flat wall of the vacuum chamber. The distance between the bottom edge of anode and the wall is 11 cm. 10 plasma guns is placed at the cathode 12 cm above the bottom edge of anode. The distance between the guns is 2.5 cm. The load is a system of vacuum diodes which anodes are the X-ray converters.

Analysis of the data shown at FIG.5 gives the following accelerator parameters: 15 kA, 2 MV electron beam, pulse width - 150 ns, repetition rate - 1- 4 Hz, peak dose rate - 0.6 MGy/s, average dose rate - 0.15 kGy/hour.

## CONCLUSION

Described planar POS design has lesser (in compare with coaxial [1]) gain in voltage. Nevertheless it has advantages in simplicity of manufacture, high reliability and recurrence of X-ray pulses. At present the X-ray generator where the analogous POS represents X-ray source is elaborated. One expected the increasing of its efficiency because one can avoid the leakage's accompanied the energy transfer to the load. The direction of X-ray pulse from the POS anode as in ordinary diode is anticipated.

## REFERENCES

- [1] N.U.Barinov, G.S.Belenki, G.I.Dolgachev et al. "Plasma-Opening-Switch-Based Repetitive Generator" // IEEE Trans. on Plasma Science, 1995, v. 23, N.6, p. 945.

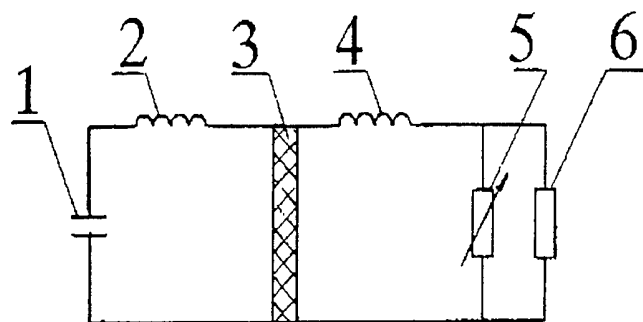


FIG.1 A scheme of the generator with the POS.

1. Marx generator - charged to  $U_c$  voltage.
2. Inductance of the Marx-  $L_c$ .
3. Inductance of the vacuum line -  $L_{line}$ , ( $L=L_c+L_{line}$ ).
4. Vacuum-air high-voltage insulator.
5. POS ( $R_{POS}$ ).
6. Load ( electron diode)(  $R_d$ ).

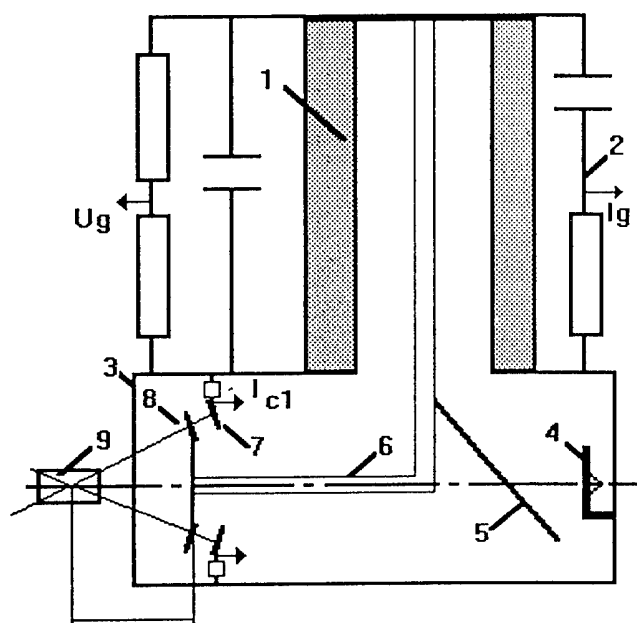
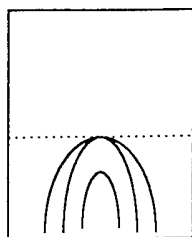


FIG.2 Planar repetitive POS setup.

Figure captions.

- 1 - High-voltage insulator.
- 2 - Marx generator.
- 3 - Vacuum chamber.
- 4 - POS cathode with plasma guns.
- 5 - POS anode plate.
- 6 - Current drive.
- 7 - Diode multi-cathodes.
- 8 - Diode anode.
- 9 - Irradiated target.



$t_3 > t_2 > t_1$

FIG.3 The tracks of anode destruction in dependence of operation time.

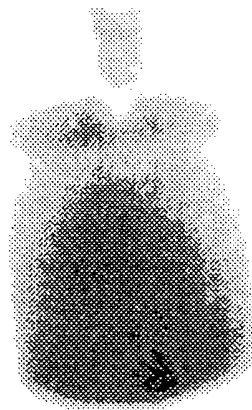


FIG.4 POS image in X-rays

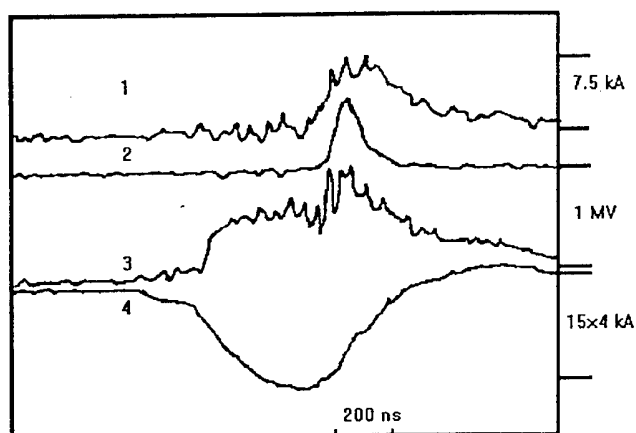


FIG. 5. Oscilloscopes from RS-20 with rep. rate planar POS.

- 1 - Beam current measured at the cathode.
- 2 - X-ray signal measured by sharp scintillation detector (relative units).
- 3 - Voltage at the Marx generator. Measured amplitude is 1 MV. Recalculated value of the voltage taking in account inductance ratio is ~2 MV.
- 4. Drive current in 4 Marx modules measured by ohmic monitors. Horizontal axis labels - 200 ns.

## STUDIES ON PULSED HOLLOW CATHODE CAPILLARY DISCHARGES

P. Choi, C. Dumitrescu-Zoita, J. Larour, and J. Rous

*Laboratoire de Physique des Milieux Ionisés, Ecole Polytechnique  
Palaiseau 91128, France*

M. Favre, M. Zambra\*, J. Moreno, H. Chuaqui, and E. Wyndham

*Facultad de Física, Pontificia Universidad Católica de Chile  
Casilla 306, Santiago 22, Chile*

*\*Comisión Chilena de Energía Nuclear, Casilla 188-D, Santiago, Chile*

C.S. Wong

*Plasma Research Laboratory, University of Malaya  
59100 Kuala Lumpur, Malaysia*

### ABSTRACT

We present preliminary results on radiation characteristics of pulsed hollow cathode capillary discharges. The device combines the on axis electron beam assisted ionization capabilities of the transient hollow cathode discharge with a novel high voltage low inductance geometrical design, which integrates the local energy storage into the electrode system. A nanosecond regime high temperature plasma is produced in a long, high aspect ratio capillary, with light emission in the UV to XUV region. The discharge is operated from near vacuum to pressure in the 1000 mTorr range.

### INTRODUCTION

Capillary discharge with large length to diameter ratio has been proved useful as a very high brightness emission source in the VUV and soft X-ray region [1]. It has also recently been demonstrated to be a suitable medium for discharge based X-ray laser studies [2]. The successful operation of a capillary discharge as a high temperature plasma radiation source depends partly on the initial formation of a conducting plasma column away from the wall and partly in the ability to provide a high rate of current rise into a high impedance load. The rapid formation of the ionization path is a necessary condition for the preparation of the current channel while the rate of current rise determines if and when the plasma column will expand or contract when it is heated by the input current. In this paper we report on preliminary results on a fast capillary discharge which operates in the nanosecond regime with current in the kA region into a sub-millimetre diameter capillary. The device combines the physics of ionization growth in a transient hollow cathode discharge [4] and a very low inductance discharge geometry, obtained by integrating the energy storage medium directly onto the discharge electrodes of the capillary system, to obtain UV radiation with ns rise time. A collaboration effort by three teams has been initiated to study this pulsed hollow cathode capillary discharge using devices with identical design to permit direct comparison and correlation of the results. In the following, we will present the design realized and some preliminary results on the radiation characteristics in the VUV and soft X-ray region under different operating conditions of the device.

### PRINCIPLE OF DESIGN

The critical issue concerns the delivery of energy into a plasma column and heating it to a high temperature, rather than to the confining dielectric surface of the capillary tube and hence to

the resulting high density low temperature wall plasma. The rate of current rise required is dictated by the impedance of the plasma channel. At the initial stage of discharge formation this is dominated by the resistive part. To prevent the channel from expanding so as to heat the plasma under pressure equilibrium during energy delivery, a rate of current rise of order  $dI/dt \geq 10^{15} \text{ A.s}^{-1}$  is required for an initial plasma temperature of  $< 1 \text{ eV}$ . [3] This is hardly achievable in practice. At a low rate of rise of current, significant amount of the input energy is delivered to the confining dielectric surface of the capillary tube and this results in a high density low temperature wall plasma. To achieve a high rate of energy delivery to the plasma, some form of additional mechanism to perform and to preheat the plasma channel is therefore necessary. In the present design, to achieve the rapid formation of the discharge column, the initial ionization path is prepared through the transient hollow cathode effect [4]. This discharge is characterized by a rapid voltage collapse accompanied by the growth of an intense electron beam leading to a very high current density channel on axis event at near vacuum operating conditions [5]. The electron beam facilitates the formation of an on-axis ionization channel, which develops throughout a moving virtual anode [6]. As a result of this, the capillary discharge could be accurately synchronized to an external triggering event by increasing the ionization growth processes within the hollow cathode region [7]. To produce the high rate of current rise required, it is necessary to operate at high voltage, with low circuit inductance. A novel high voltage discharge geometry with very low inductance is used, which integrates the energy storage medium directly onto the discharge electrodes of the capillary system. The discharge chamber is arranged on the axis of a pair of parallel plate electrodes, separated by a thin dielectric to form a local energy storage capacitor. No additional switches are included, in order to maintain the inductance at a minimum. The local energy storage capacitor is pulse charged throughout a primary capacitor using a triggered switch. The long formative time in low pressure discharge enables a high over-voltage to be established across the electrodes and for the discharge to be triggered externally. By minimizing the circuit inductance, a very fast rising current of  $> 10^{12} \text{ A.s}^{-1}$  can be obtained at voltage below 30 kV.

#### EXPERIMENTAL APPARATUS

In the device developed, a pair of 90 mm diameter brass electrodes form the anode and cathode of the discharge, as well as the parallel plate capacitor. The capillary is located on axis between the two electrodes. On the cathode side, an additional plate is used to provide the optimum geometry of the aperture for the operation of the transient hollow cathode assisted ionization. The insulation that separates and isolate the two electrodes is also the dielectric medium for the capacitor, and so there is a trade off between the requirement for a material with high breakdown strength and high dielectric constant. Materials like PET, with high breakdown strength, and PVDF, with high dielectric constant, have been tested, resulting in capacitances from 1 to 5 nF. Alumina capillaries of 0.8 to 8 mm diameter, 10 to 30 mm long, and Teflon capillaries 1mm diameter, 10 mm long, have been used in different experimental configurations. A primary DC charged capacitor of 5 nF is used to pulse charge the storage capacitor within 100 ns. A novel set of current and voltage monitor has been integrated into the ground side of the electrode which forms part of the energy storage capacitor, in order to measure the voltage and current local to the discharge. At a charging voltage of 30 kV, current above 10 kA is produced through the capillary, with a 10-90% current rise time of below 5 ns. The discharge is triggered by means of an auxiliary discharge from a small cable plasma gun, located a few mm behind the cathode aperture, with a delay of 80 to 100 ns. This triggering method allows the capillary discharge to operate successfully at

pressures below 1 mTorr in Argon. Best results have been obtained by pumping the cathode region through the capillary, thus allowing a higher pressure in the hollow cathode region, while maintaining a lower pressure in the capillary to produce a lower line density plasma. These are second generation designs and the capillary discharge system will be referred to as Mark-II devices. Three identical devices are operational, at LPMI, at PUCCh and at UM. A wide pressure range of 1-1000 mTorr has been investigated, using different working gases (Argon, Nitrogen and Hydrogen). A variation of an earlier design was also studied at UM. This device, UMCDIII, uses a 1 mm diameter, 10 mm long capillary in a PTFE block and is energized by a ceramic capacitors array of 22 nF at 40 kV maximum. This device is operated mainly near vacuum or at a few mTorr range. The discharge is triggered by an auxiliary spark discharge inside the hollow cathode region. In the experiment, charging voltages between 10 to 30 kV has been used to study energy coupling. Apart from the voltage and current measurements, the plasma emission is studied in the visible with PIN diodes, in the VUV region with time resolved spectroscopy and in the soft X-ray region with filtered PIN diodes and scintillator-photomultiplier assembly.

### EXPERIMENTAL RESULTS

Figure 1 shows characteristic electric and X-ray signals obtained with the Mark-II device, operating at 30 kV, with a 0.8 mm diameter, 10 mm long alumina capillary, in Argon. The soft X-ray pulse is detected with a scintillator-photomultiplier filtered by 2  $\mu$ m Mylar with 80 nm of aluminium. The X-ray intensity scale in the 15 mTorr graph is 1/4 of that in the 80 mTorr graph. Other vertical scales are the same. Experiments using the Mark-II device, operating at 25 kV, with a 0.8 mm diameter, 30 mm long alumina capillary in argon, show that the discharge can be successfully triggered by the auxiliary discharge in the 10-150 mTorr pressure range when pumped through the capillary. A short, 10 ns light pulse is emitted at breakdown. The visible output signal is in general very different from the soft X-ray signal. At low pressure, a double humped signal with duration of 30 ns or more is obtained. The pulse width decreases with increasing pressure and a single peak signal of < 15 ns is measured at pressure above 100 mTorr. Figure 2 shows time resolved VUV spectra obtained in the UMCDIII device operating at 27.5 kV, with the 1 mm diameter, 10 mm long PTFE capillary, in air. Pressure is 0.8 mTorr. The spectra were recorded on a grazing incidence spectrograph using a 1200 ln/mm grating with a three frame gated intensified microchannel plate detector. Exposure time is 5 ns and the three frames correspond to  $t = 0$ , 7 and 20 ns. The dominant lines in the spectra are those of FVI, FVII and FVIII, and OVI and OVII, in the 10 to 40 nm region.

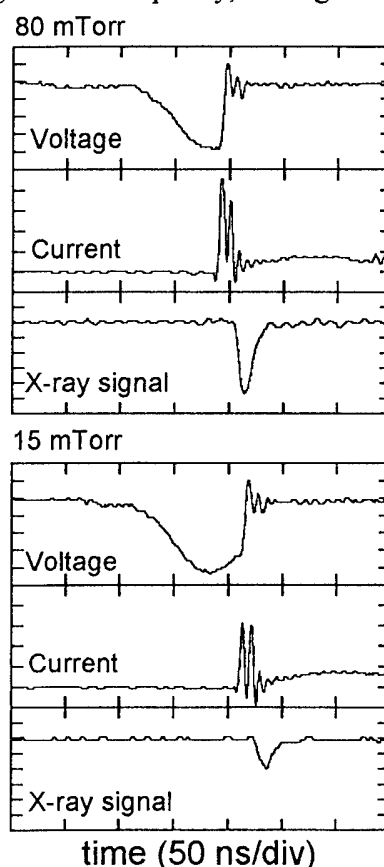


Figure 1: characteristic electric and X-ray signals from the Mark-II device.



## DISCUSSION

The electric signals presented in Fig. 1 show successful triggering of the discharge. A less than 5 ns rise time, 10 ns current pulse is applied to the capillary plasma. A 10 ns soft X-ray pulse is emitted. The intensity of the soft X-ray pulse increases by an order of magnitude when the pressure is increased from 15 to 80 mTorr. At pressures above 150 mTorr, however, this X-ray signal is significantly reduced, indicating that efficient energy coupling into the capillary plasma is attained only on a narrow pressure range. The spectroscopic data shows clearly the fast evolution of the capillary plasma. At very low pressure, below 1 mTorr, VUV emission falls rapidly in a 20 ns time scale. An even faster decay is observed when the pressure is increased up to the 1 mTorr level. These results clearly demonstrate the operational principles of the pulsed hollow cathode discharge. The plasma channel is heated up very rapidly, in the sub-10 ns time scale, within a few ns after current rise. This can be attributed to the transient hollow cathode effect, with the electron beam assisted ionization producing an on axis initial current path and a fast current pulse being delivered by the local energy storage. The short duration of the current pulse allows the capillary plasma to expand and cool by radial transport to the wall. As a result of this, VUV to XUV light is emitted only in a very short pulse associated with the duration of the current.

## ACKNOWLEDGMENTS

This work has been partially funded by FONDECYT grant No. 1950798 in Chile, a CNRS-CONICYT collaboration programme and an ICTP Visiting Scholar programme on joint work.

## REFERENCES

- [1] R.A. McCorkle, *Appl. Physics A*, **A26**, p. 261, 1981.
- [2] J.J. Rocca et al., *Phys. Rev. Lett.* **73**, p. 2192, 1994.
- [3] S.I. Braginskii & V.D. Shafranov, *Plasma Physics and the Problem of Controlled Thermonuclear Reactions*, Ed. by M.A. Leontovich (Pergamon, New York), Vol. II, p. 39, 1959.
- [4] P. Choi et al., *IEEE Trans. Plasma Sci.* **15**, p. 428, 1987.
- [5] P. Choi et al., *IEEE Trans. Plasma Sci.* **17**, p. 770, 1989.
- [6] P. Choi et al., *Appl. Phys. Lett.* **63**, p. 2750, 1993.
- [7] H. Chuaqui et al., *Appl. Phys. Lett.* **55**, p. 1065, 1989.

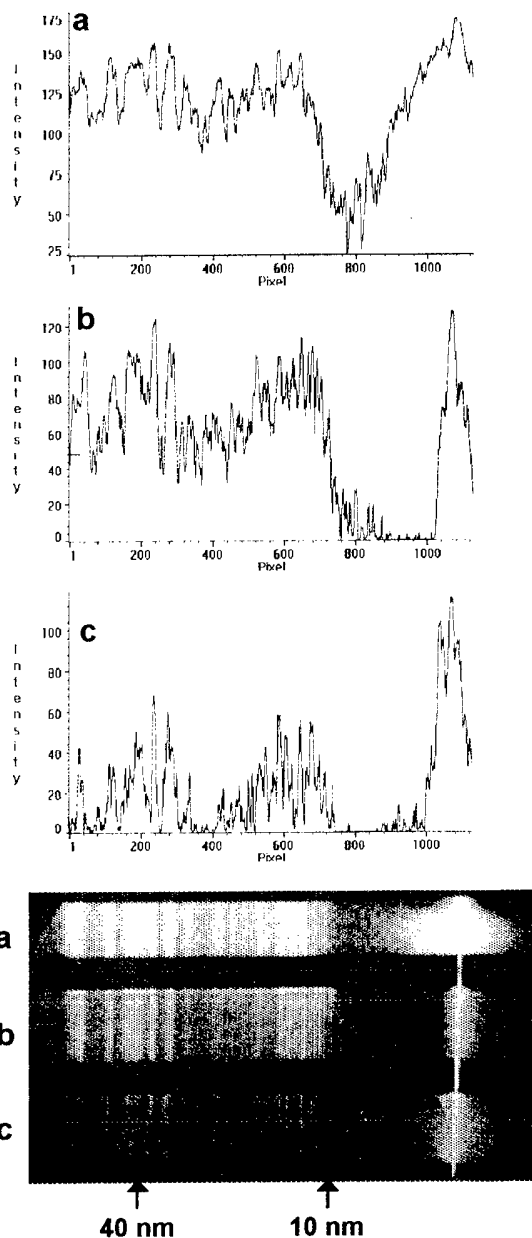


**Figure 2:** single shot, 5 ns exposure time resolved spectra obtained in the UMCDIII device. a) 0 ns, b) 7 ns, and c) 20 ns.

# POWERFUL ACCELERATORS FOR BREMSSTRAHLUNG AND ELECTRON BEAMS GENERATION ON THE BASIS OF INDUCTIVE ENERGY-STORAGE ELEMENTS\*.

V.S.Diyankov, V.P.Kovalev, A.I.Kormilitsin, B.N.Lavrentiev.

*RFNC - VNIITF, P.O.Box 245, Snezhinsk, 456770, Russia.*

## Summary

The report summarizes RFNC - VNIITF activities from 1963 till 1995 devoted to the development of pulsed electron accelerators on the basis of inductive energy storage with electroexplosive wires. The name of these accelerators is IGUR. These activities resulted in the development of a series of generators of powerful radiation being cheap and easy in manufacturing and servicing. Accelerators enabled following maximum parameters:

- the diode voltage	up to 6 MV;
- the diode current	up to 80 kA;
- current of the extracted electron beam	30 kA;
- density of the extracted electron beam energy	500 J/cm <sup>2</sup> ;
- bremsstrahlung dose	250 000 Rads;
- bremsstrahlung dose rate	10 <sup>13</sup> Rads/sec.

## Introduction

In the beginning of the 60s there was a necessity in determining resistance of electronic equipment and components to ionizing radiation. That's why the problem of developing equipment for investigating and testing of resistance to gamma-radiation appeared.

A team of VNIITF physicists addressed to this problem. They proposed an original circuit of high voltage source to supply energy to the diode where it was planned to have high voltage due to overvoltage arising on the inductor in the case of break in the current circuit. Electric explosive wires were proposed as a switch.

A special testing equipment was created for investigation of wire electroexplosion process. The first stage was devoted to experimental development of the switch. Wires of various materials, such as copper and aluminium were investigated. Wires were exploded in different media (air, oil, sand). This effort resulted in the development of the switch consists from copper wires. Best results were obtained when copper wires were exploded in the air.

Released power in the load in the modes of capacitive and inductive storages were subjected to comparative analysis. It demonstrated the mode of inductive storages to ensure significant gain in the amount of released energy.

## Facility of IGUR type

The high-voltage source consists from Marx generator, point inductance and electrical explosive wires was created by the beginning of 1967. The diode was

---

\* The work was supported by ISTC project #271

designed and manufactured by the end of 1968. The electron accelerator was put

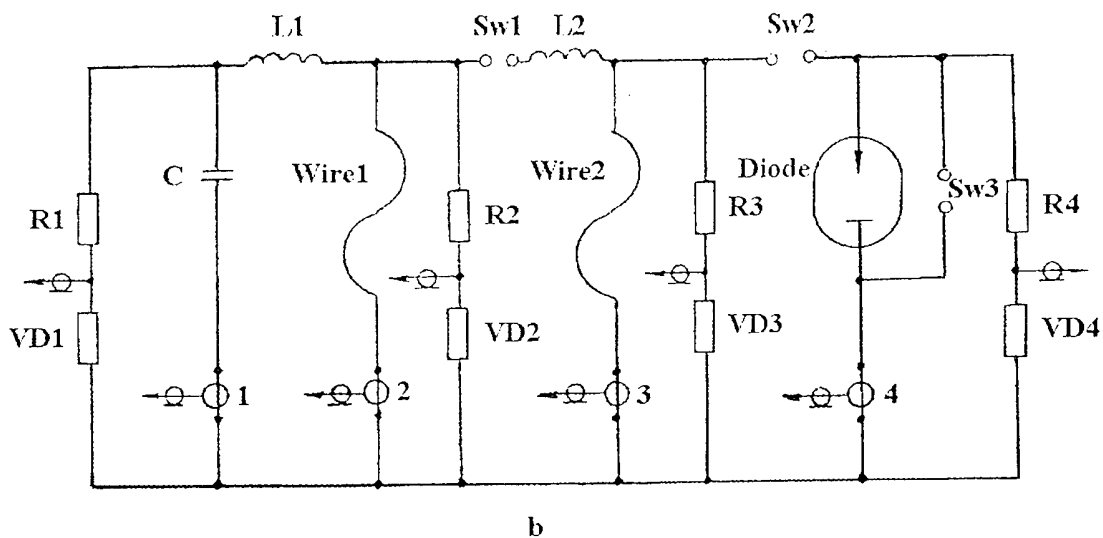
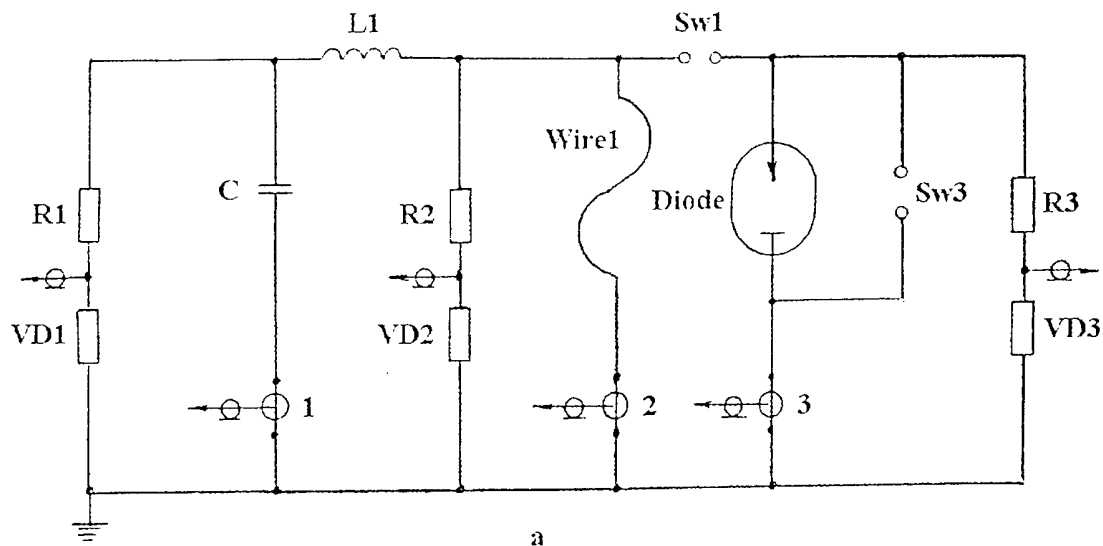


Fig 1. Curcuit diagramm of accelerators

a) IGUR-1; b) IGUR-2

C - capacitance

L1, L2 - inductance of the 1st and 2nd cascades

Wire1, Wire2 - electric explosive wires of the 1st and 2nd cascades

Diode - acceleration tube

R1-VD1, R2-VD2, R3-VD3, R4-VD4 - voltage dividers

Sw1, Sw2, Sw3 - commutators in accelerator

1, 2, 3, 4 - "Rogovsky belt" to measure current in accelerator circuit

into operation and was named IGUR-1 (Radiation pulse gamma-ray facility) [1]. This facility development and manufacture costed 60,000 USD.

Fig.1a gives the simplified electric circuit of the accelerator. This accelerator has been used during 15 years.

Operation of the inductive storage with electric explosive wires (EEW) was studied on the "Sigma" test bench. It was used to investigate cascade switching on of inductive storages [2]. Voltage multiplication coefficient of 15 was obtained in the case with two cascades of electric explosive wires. Voltage of 600 kV was obtained at the output of the second cascade with the 40 kV input voltage. The dependence between the multiplication coefficient and energy loaded rate into EEW has been shown.

When results on "Sigma" test bench have been obtained it was decided to develop IGUR-2 electron accelerator. IGUR-2 high - voltage power source consisted from Marx generator and two cascades of the inductive storage with electric explosive wires. Fig. 1b gives the picture of the IGUR-2 simplified electric circuit.

IGUR-2 accelerator was the largest facility where the air insulation of high-voltage units was used. It also used the diode with a sectioned insulator.

The diode was operated in three modes:

- bremsstrahlung generation mode;
- mode of operation with the electron beam, extracted into atmosphere;
- mode of operation with the electron beam propagation in the diode

Main parameters for IGUR-1 and IGUR-2 accelerators are given in Table 1.

Table 1. Main parameters of IGUR-1 and IGUR-2 Facilities.

Main characteristics	IGUR-1	IGUR-2
Stored energy, kJ	135	300
Marx generator output capacitance, $\mu\text{F}$	0.29	0.15
Marx generator output voltage, MV	0.96	2
Inductance of the first cascade, $\mu\text{Gn}$	36	28
Inductance of the second cascade, $\mu\text{Gn}$	-	3
The first cascade voltage, MV	3.1/5*	3.7/7*
The second cascade voltage, MV	-	4.5/12*
Diode inductance, $\mu\text{H}$	2	3.7
Diode voltage, MV	2.8	3.7
Diode current, kA	44	70
Bremsstrahlung pulse duration, $\mu\text{sec}$	0.1 - 0.5	0.1 - 0.5
Bremsstrahlung pulse rate on 1 m, Rads/sec	$5 \cdot 10^8$	$2 \cdot 10^9$
Density of electron beam energy, $\text{J}/\text{cm}^2$	300	300/2500**

\* Data refer to the loadfree (open circuit) operation mode.

\*\* Measurements in vacuum at the anode plane.

Using of air insulation in order to reach voltages of megavolt range results in the increasing volume of the facility and therefore to the increasing of inductance of the circuit units. As a result the maximum of output power of accelerator is limited. A new generator IGUR-3 with units deposition in transformer oil has been developed in order to avoid this limitation.

### IGUR-3 facility

For the designing of IGUR-3 accelerator the following developments and investigations were necessary:

- selection of the low-inductance design of the accelerator; [4]
- development of the low-inductivity diode;
- study of electric energy commutation in transformer oil;
- study of electric explosion of wires in various media; this enabled the development of a simple and easily servicing electrical explosive wire unit;
- development of a gas switch for 100 kV and 250 kA to switch Marx generator.

This work was done on specially designed test bench. Theoretical studying and numerical simulation of EEW behaviour under different application conditions were performed at the same time with experiments.

A.V.Luchinsky and Yu.D.Bakulin have developed MHD code for one-and two cascade electric explosion of wires on the basis of equations of state for copper and aluminium obtained at VNIITF [5].

Simple similarity relations, which enabled quick and rather accurate practical determination of EEW main parameters in the maximum power mode were developed for engineering designing.

Experimental research and numerical simulation efforts resulted in the development of IGUR-3 electron accelerator which was manufactured and put into operation in the end of 1978. The accelerator design is given in Fig.5.

High-voltage pulse is formed by inductive storage with the switch based on electroexplosive wires. The primary storage consists of 1.4 MV two Marx generators. Total stored energy is 300 kJ. Marx generator is located in a tank with 1.2 m in height and 7.5 m in diameter. Its axis coincides with the axis of a container with 8.5 m in height and 2 m in diameter. This container incorporates an inductive storage, a wire explosion unit, an oil discharge shaping switch to decrease the pulse front and diode. The wire explosion unit consists of 15 tubes with 110 mm in diameter. The diode insulator has a sectioned design. It has 1.3 m in height and 0.9 m in diameter. Insulation rings are manufactured from kaprolon and the "gradient" rings are made from aluminum AMG alloy. All accelerator components are situated in the transformer oil.

Up to 7MV voltage pulse is formed when IGUR-3 accelerator inductive storage current is switched. Varying steepness of voltage increasing of  $10^{11}$  V/s up to  $10^{14}$  V/s is the particularity of this pulse. It enables the current (voltage) pulse front to be formed in 15...200 ns range on the diode due to the breakdown of the two-

electrode shaping switch at different  $\frac{du}{dt}$  [6]. Voltage pulse decay is formed due to the voltage pulse cut-off on EEW in EEW circuit and is controlled within 25...200

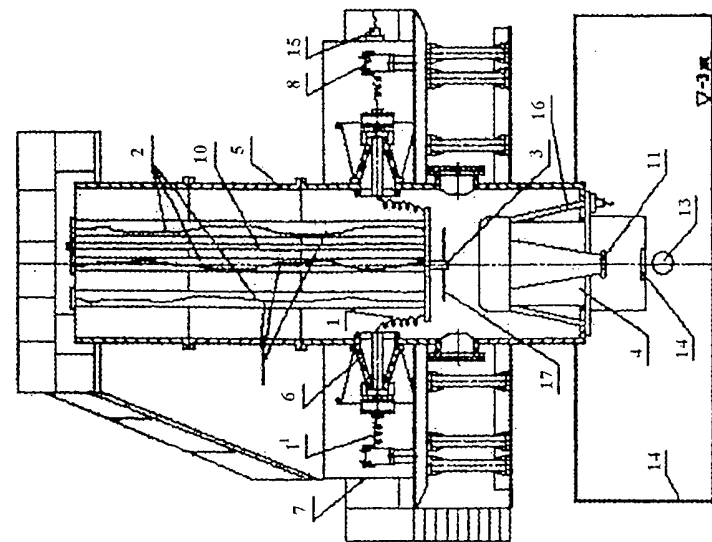


Fig 2. Accelerator IGUR-3 schematic design

1. Inductive storage; 2. Electrically exploding wires;
3. Sharpening discharged switch; 4. Accelerator tube (AT);
5. Pulse forming system tank; 6. Parfision insulator;
7. Matrix generator tank; 8. Matrix generator module;
9. Polyethylene tubes; 10. Electrically exploding wire voltage divider; 11. AT cathode; 12. AT anode; 13. Tested object; 14. Shielded box; 15. Grounding blocking;
16. AT capacitive - resistive voltage divider; 17. Shield.

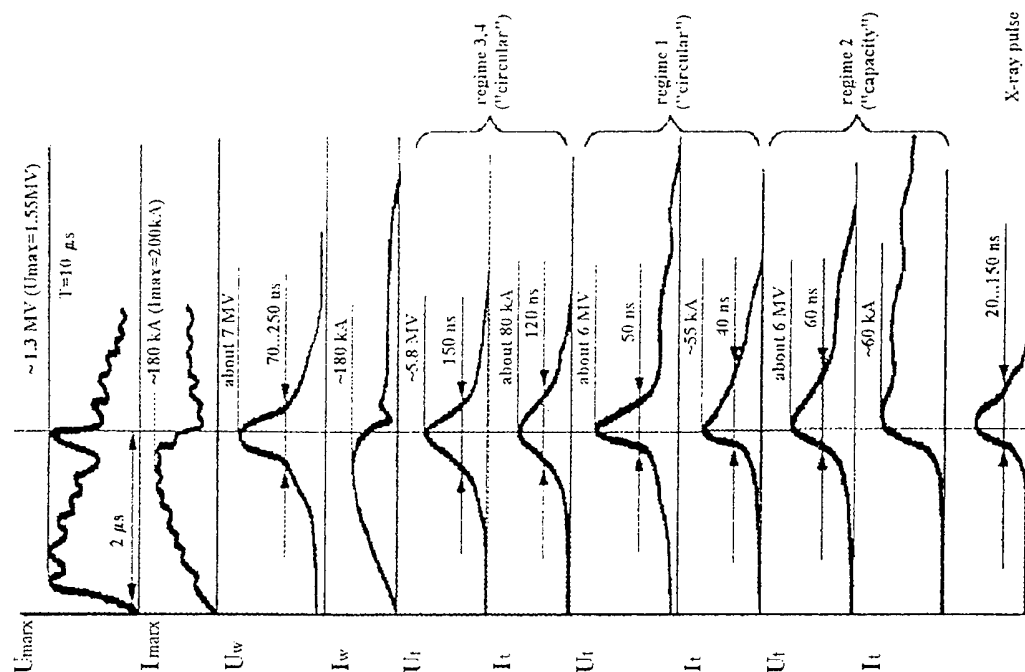


Fig 3. Typical wavefronts for the IGUR-3 accelerator electric circuit

ns range [7]. Processes of current (voltage) decay and rise shaping on the acceleration tube are interconnected. This ultimately enables shaping of bremsstrahlung pulses in  $\tau/2 \sim 15...150$  ns duration range and electron beam pulses in  $\tau/2 \sim 20...400$  ns duration range on the diode due to the gap change in the shaping switch. Main parameters for modes of bremsstrahlung pulse and electron beam pulse shaping selected for operation are given in Table 2. The Table gives seven bremsstrahlung producing modes and one electron beam producing mode.

Modes used to generate bremsstrahlung pulses of complicated shape and two series of pulses are possible due to the accelerator circuit reconstruction. One day is required to perform this reconstruction.

The mode for generating bremsstrahlung pulses of microsecond duration at  $\tau/2 \leq 4$  mcsec was developed for the case when the diode is connected to Marx generator outlets. Fig.3 shows typical oscillograms for the first four operation modes (see Table 2).

Table 2. Main characteristics of the IGUR-3 accelerator exploitation regimes

Regime	Marx Storage Energy kJ	X - ray Pulse Duration	Accelerator Tube Voltage	Accelerator Tube Current	Radiation Dose Power, Anode R/s	Radiation Dose Power, R=1 m R/s
		ns	MV	kA		
1	300	25	5,8	55	$4 \cdot 10^{11}$ ( $S=300 \text{ cm}^2$ )	$10^{10}$ -maximum $7 \cdot 10^9$ - work regime
2	300	25	6	60	$10^{13}$ -maximum $7 \cdot 10^{12}$ -work regime ( $S=1,5 \text{ cm}^2$ )	$2 \cdot 10^9$
3	300	80	5,8	80	$2,5 \cdot 10^{12}$ ( $S=6 \text{ cm}^2$ )	$3 \cdot 10^9$
4	300	80	5,8	70	$4 \cdot 10^{11}$ ( $S=300 \text{ cm}^2$ )	$7 \cdot 10^9$
5	300	about 4 $\mu\text{s}$	1	30	$10^{10}$	$10^7$
6		Regime of the "complex-form- pulse" generation 20-50->300-1000				
7		Regime of the "successive- pulse" generation 150-220 + 15- two-60			about $3 \cdot 10^{10} + 3 \cdot 10^{10}$	about $10^8 + 10^8$

Electron beams:	pulse duration	- 20...400 ns
	beam current	- about 30 kA
	maximum energy density profile of the beam	- about 500 J/cm <sup>2</sup>
	total beam energy	- about 10 <sup>4</sup> J
	mean electrons energy	- 2,5 MeV

### EMIR - M facility

EMIR - M facility is a combination of two pulse high-voltage devices. The first one is the electron accelerator consists from Marx generator, the inductive storage, the current switch on EEW, the commutator unit and the diode. The second one- is the pulse high-voltage generator and the field-generating system (FGS) designed to generate the electromagnetic field. The devices are combined in the way, that the

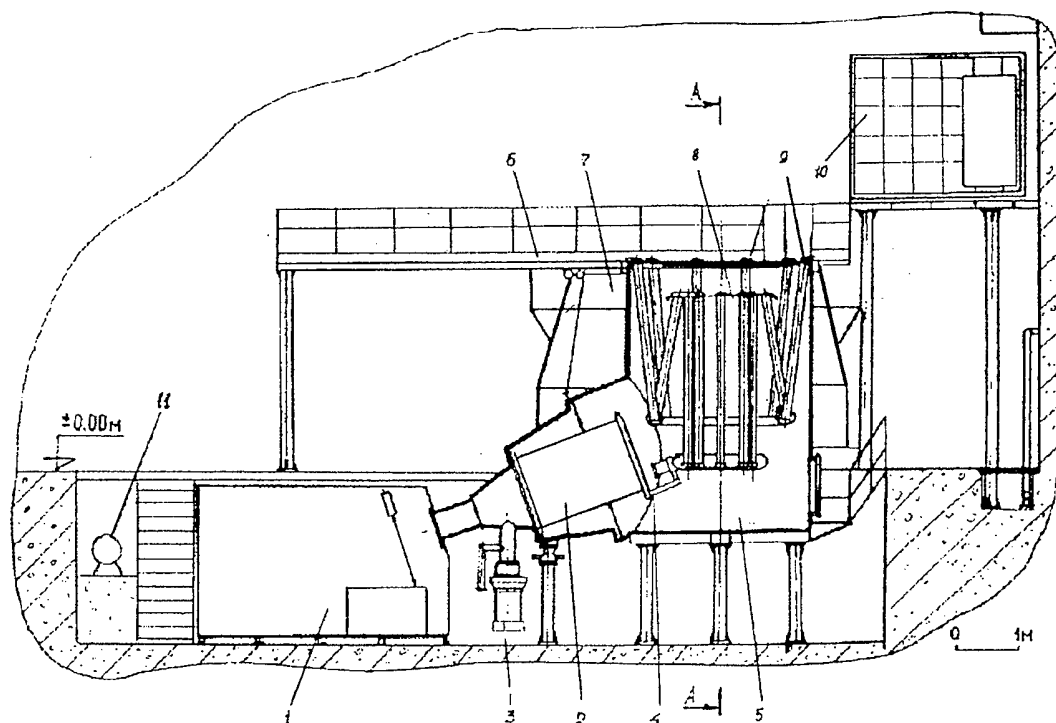


Fig 4. EMIR-M facility.

1. Testing box; 2. Acceleration tube; 3. Vacuum pump; 4. Acceleration tube commutator; 5. Container of wire explosion unit; 6. Technological platform; 7. Container of modulis unit; 8. Wire explosion unit; 9. Polyethylene tubes to place explosive wires; 10. Screened box with recording and measuring instruments; 11. Motor - generator of independent power supply.

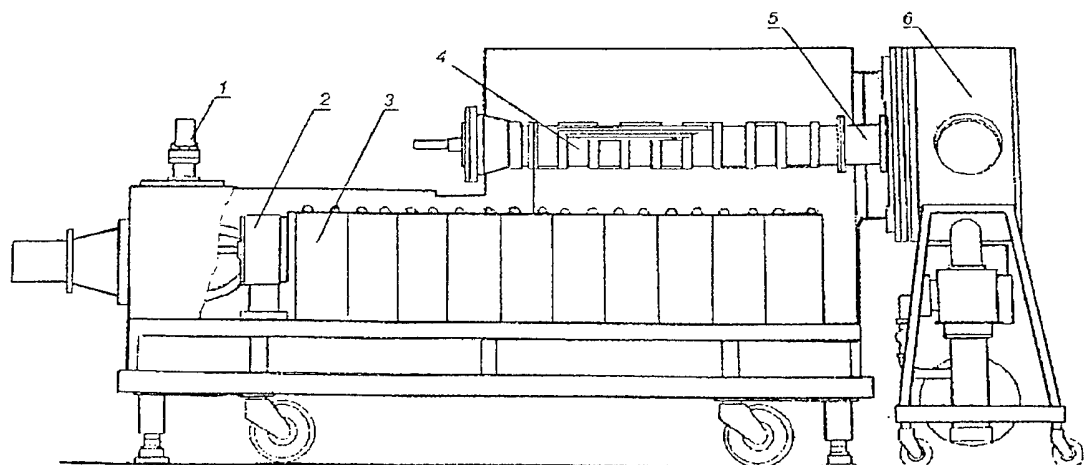


Fig 5. "Signal-20" accelerator.

1. Interlock; 2. Commutating discharger; 3. Capasitor bank; 4. Pulse generator system; 5. Discharger reducing a pulse front; 6. Laser vessel.



pulsed gamma-ray yield or electrons flow and the electromagnetic field can be generated in the testing zone simultaneously or independently.

In addition, Marx generator design and its configuration in the form of independent units enable the generation of two pulses with controlled time interval using one diode. Fig.4 gives the common view of EMIR-M facility.

Accelerator output characteristics were experimentally investigated depending on the following parameters:

- EEW (length, diameter, number);
- diode commutator;
- cathode-anode design.

When joint radiation and electromagnetic actions are performed on the tested objects, the time interval between these actions may be controlled in wide range.

Main characteristics of operation modes for EMIR-M facility are given in Table3.

Table 3. Main characteristics of operation modes for EMIR-M facility.

1. Bremsstrahlung pulse generation mode:	
Marx generator-stored energy	580 kJ
dose rate near the target	$2 \cdot 10^{12}$ rad/s
dose rate at 1 m distance from the target	$3 \cdot 10^9$ rad/s
radiation pulse duration	60 ns
average energy of $\gamma$ -ray	$\approx 1$ MeV
2. Extracted electron beam mode:	
Marx generator-stored energy	290 kJ
energy density of extracted beam	$300 \text{ J/cm}^2$
duration of beam current pulse	$\leq 100$ ns
beam current	up to 20 kA
3. Electromagnetic field-generation mode:	
the electromagnetic radiation generator stored energy	up to 1.5 kJ
electric field strength	$\leq 400 \text{ kV/m}$
magnetic field strength	$\leq 1.2 \text{ kA/m}$
pulse front duration	$\approx 40$ ns
pulse duration	$\approx 1$ mcs
4. Joint action of $\gamma$ -ray pulse and electromagnetic radiation pulse mode has parameters mentioned for modes 1 and 3.	

### SIGNAL facility

The technology developed for IGUR type accelerators was used as the basis for the development of low-impedance accelerators with low-inductive energy storages and electric explosive wires.

The first low-impedance generator SIGNAL-20 (High-Current Pulse Laser Pumping Generator for 20 kJ) was developed in the beginning of 80 s. It was specially developed to pump eximer laser by the electron beam. The common view of the facility is given in Fig.5. The primary energy storage consists from capacitor bank of  $4 \mu\text{F}$  capacity and  $0.25 \mu\text{H}$  inductance which is switched by the gas switch.

The capacitor bank is discharged into the stored capacitor through the coaxial system of electric explosive wires. The pulse shaped on the inductor is applied to the coaxial diode with the blade-like cathode and the cylindrical anode of 50 mm thickness titanium foil through the shaping gas switch. The anode is used as a one wall of the laser vessel. Energy release density of  $0.2 \text{ J/cm}^2$  for the electron beam having  $\pm 20\%$  ununiformity at the edges was obtained in the laser vessel with 31 cm length and 4 cm diameter. The diode with the plane anode was used in the modes for producing the extracted electron beam and the bremsstrahlung. In this case, electron current pulses up to 80 kA with electron energy 400 keV and up to 100 ns pulse duration were generated. The accelerator is  $3.3 \times 0.7 \times 1.6 \text{ m}^3$  in size and has a movable design.

The same technological scheme was used for the creation of SIGNAL-24 accelerator which is designed for radiation investigation of electronic components and materials.

At present time SIGNAL-24 accelerator has been upgraded. Plasma opening switch is used as the interruptor instead of electric explosive wires. The accelerator is used to investigate Z-pinch on wire. Current higher than 200 kA with rate up to  $10^{13} \text{ A/s}$  is loaded into Z-pinch. Those facilities are easily available physical laboratories due to their small size and relatively low cost. A small-scale accelerator with megaamps current in a load is being currently developed on the basis of principles and technical solutions used in SIGNAL-type facilities.

### Conclusion

The idea is conceived in VNITF in early 60 th years, on the generation of the powerful pulses of electron beams by the accelerators with an inductive storage of energy and commutation by the electroexplosive wires, was developed into a new direction of pulse high-current high-voltage electronics. Fruitful work on accelerators development for many years made by Institute staff permitted to create, on this basis, the generators for radiation investigations, having wide range of output parameters.

Main advantages of developed accelerators are the following:

- high density of energy and therefore the small dimension;
- higher power output compare to capacity storage;
- large range of output parameters, obtained at one accelerator;
- possibility of variation of output pulse duration in large time range /20ns-400 ns/ without changing accelerator design;
- simple manufacture technology and relatively low cost.

At present time the experience of work with inductive storage and electric-explosive wires is of a great importance and it can be used in investigations of plasma switches.

It should be noted a major contribution of Zysin, Yu.A., Luchinsky, A.V. and Martynov, V.I. to the formation of this direction in accelerating technology.

## REFERENCES

1. Baculin YU.D., Diyankov V.S., Kovalyev V.P., Kormilitsyn A.I.  
" Direct action accelerators with inductive storage of energy and explosive conductors" . PTE Journal, N2 p.34-37(1979) (in Russian)
2. Kovalyev V.P., Luchinsky A.V., Martynov V.I.  
Certificate of authorship N                with priority.
3. Kovalyev V.P., Kormilitsyn A.I., Luchinsky A.V etc.  
" IGUR-1 - electron accelerator with inductive storage of energy and explosive conductors". Journal of Technical Physics, v.51 (9), 1865 (1981) (in Russian)
4. Diyankov V.S., Kovalyev V.P., Luchinsky A.V., Martynov V.I.  
Certificate of authorship N
5. Baculin YU.D., Kuropatenko V.F., Luchinsky A.V.  
ZhTPh Journal v.XLVI, issue 9, (1963).
6. Kormilitsyn A.I., Diyankov V.S., Martynov V.I.  
"Device to form generate the pulse of powerful electron beam".  
Certificate of authorship N92144 (1981).
7. Bratchikov V.B., Diyankov V.S. " Multichannel triggering spark gap".  
Certificate of authorship N1101133 (1984).

# CONTRIBUTED PAPERS P-1

Beam-Plasma Interaction

Electron Beam Physics

Electron Beam Physics - Theory

Free Electron Lasers

High Power Microwaves

## EXPERIMENTAL STUDY OF COLLECTIVE PROCESSES IN REB.

L.Yu. Bogdanov, G.G.Sominski

*Saint-Petersburg Technical University.  
29, Polytekhnicheskaja, St.-Petersburg, 195251, Russia  
(E-mail: sominski@phtf.hop.stu.neva.ru)*

Possibilities of application of relativistic electron beams (REBs) to ultra-high-power microwave generation determine considerable interest in studies of their properties. Unfortunately, the data obtained by now on REB space charge oscillations and structure dynamics are rather scarce and fragmentary because of difficulties arising during complicated experimental measurements in high-voltage and high-current electron flows.

A special low-disturbing techniques [1,2] for experimental investigation of "instant" parameters of REB space charge oscillations in different parts of drift channel and of the beam structure in collector region was developed by our group in St.-Petersburg State Technical University (Physical Electronics Department). In this paper we present the data obtained recently with this techniques on collective processes and their influence upon REB formation and transportation.

Experiments were done at the SER-1 setup, which is described in detail in [1,2]. The scheme of experimental layout is shown in Fig.1. Electrons emitted by an explosive edge cathode (1) were accelerated by a voltage 220 kV formed by a Marx generator and applied to the gap between the cathode and a drift tube (2). The REB (3) was confined in the drift tube ( $L=1.2$  m long and  $D=32$  mm in diameter) by axial magnetic field  $B_0$  of solenoids (4). Thus the most part of the drift channel, with the exception of the collector region, was immersed in uniform, with less than 10% inhomogeneity, magnetic field 1T in magnitude (fig.1). For elaboration of the REB collective

processes model we studied influence of introduction of local rises of magnetic field upon the beam space charge oscillations. These local rises were created with additional coils (5) and (6) situated at distances 20 and 60 cm from the cathode and were up to 60% in magnitude (compared with the uniform field) and about 10 cm FWHM along the beam axis. Measurements were made with stainless steel and graphite cathodes with outer diameter  $D_c$  20 or 12 mm. The gap between the cathode edge and a drift tube rim

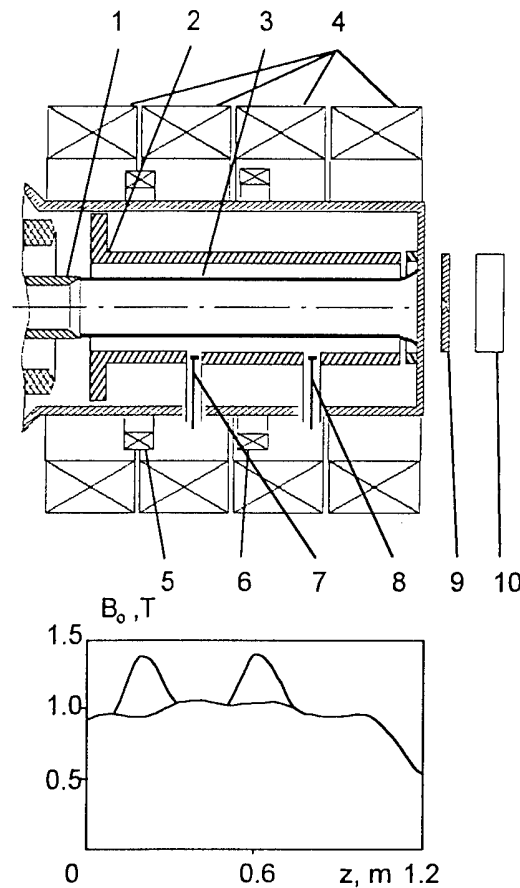


Fig.1 Experimental layout.

$L_{ac}$  was also varied between 12 and 27 mm. The REB current to the collector varied in the range of 0.7...1.1 kA and current pulse duration was 1...3  $\mu$ s.

Parameters of space charge oscillation were obtained from the signals of HF probes (7) and (8) registered in 6...15 ns time series ("realizations") with different delays from the REB current pulse front. Two probes were situated at 40 and 80 cm from the cathode. Fourier analysis of these realizations gave us information on "instant" oscillation spectra. To obtain integrated over broad frequency band oscillations amplitude and study its dynamics during the beam current pulse the signals of the probes were detected and registered in all-over-the-pulse view. The probes were "coupled" predominantly to HF fields in the nearest to them zone and thus to moving past them space charge formations [1]. Bremsstrahlung distribution over collector surface was registered with pinhole camera (9) and a specially designed X-ray electron-optical image converter (10) [2] and yielded REB transverse structure with time resolution no worse than 100 ns.

We found that characteristics of the space charge oscillations varied in time and along the beam axis. The rate of the temporal variation depended on the cathode material and the beam formation region geometry (i.e. cathode diameter, distance between the cathode and drift tube edge). All the other parameters of the oscillations were similar for all investigated systems. So hereinafter we are taking as an example a system with 20-mm diam. stainless steel cathode and 27-mm cathode-drift tube gap.

At the moments with comparatively small, less than 0.5...0.6  $\mu$ s delay (relative to the front of the current pulse) oscillations had a small amplitude and rather low frequencies - in the band of 100...300 MHz. Then the amplitude grew and was limited, to all appearance, by non-linear processes in the beam at the level of about 1 MV/m. At this stage of the development of the oscillations discrete peaks were discernible in spectra in the frequency  $f$  range of 100...1500 MHz with the strongest of them in the 700...1200 MHz interval.

Temporal and spatial variations of the oscillations were obtained from the detected probe signals (fig.2). For a nearest to the cathode probe (7) the signal increased considerably for  $t$  exceeding 1.2  $\mu$ s (fig.2a), which we attribute to the effect of dense cathode plasma reaching the first probe position

by the time. The second probe (8) was not sensitive to the cathode plasma oscillations during the current pulse. In this paper we will discuss characteristics of collective

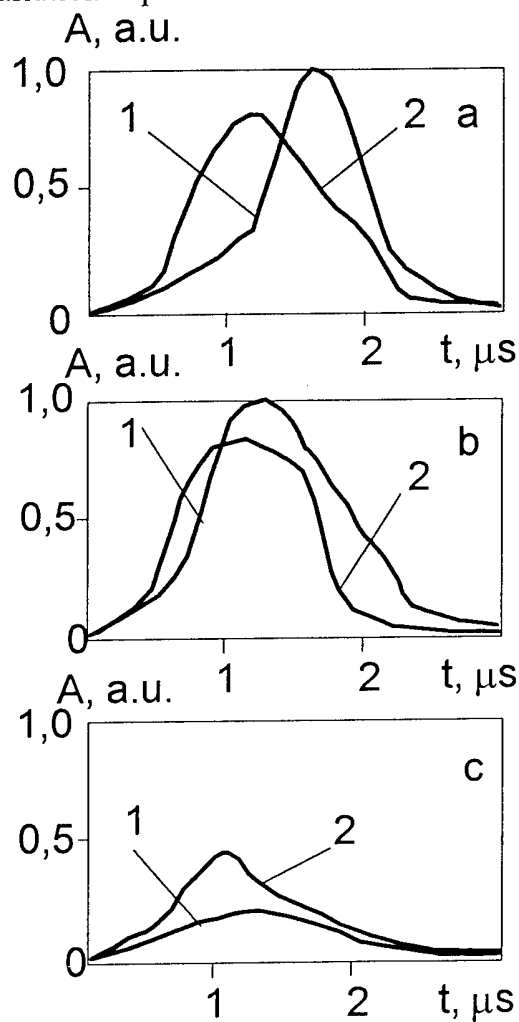


Fig.2 Probe signals amplitude evolution.  
1-probe 7 (fig.1), 2-probe 8

processes developing only in electron space charge of the REB. The amplitude of the REB oscillations increased with distance from the cathode (fig.2a) which indicates their convective nature. Local magnetic field rise introduced with the furthest from the cathode additional coil (6) increased the rate of development of oscillations in regions near both HF probes (fig.2b). The similar rise introduced with the other coil (5) decreased the amplitude of the oscillations (fig.2c).

The influence of mirror-type magnetic field rises we attribute to reflection of electrons, having relatively large transverse  $V_{\perp}$  and small axial  $V_{\parallel}$  components of velocity, into the cathode direction. 30...60% in magnitude magnetic mirror can cause reflection of electrons with about 100 keV transverse energy. Upon our estimates, such an energy can be acquired by electrons emitted from the outer generatrix surface of the cathode plasma when the plasma in its axial extension enters the region with strong, about  $10^8$  V/m in magnitude, radial electric field  $E_r$ . And electric field intensity can reach this order of values near protuberances on the surface of plasma emitter approaching the drift tube edge. Thus, on our opinion, inertia in large-transverse-velocity electron flow formation in the REB halo results in delay of the space charge oscillations amplitude rapid growth. The delay ( $t_d$ ) was clearly noticeable in the detected signal of the furthest from the cathode probe and depended on the cathode diameter  $D_c$  and material and cathode-drift tube gap width  $L_{ac}$ . Measured values of the delay  $t_d$  were in good agreement with the ones ( $t_{dc}$ ) given by calculations taking into account device geometry and characteristic velocities of cathode plasma axial propagation and radial expansion [3]. Some of these data are summarized in table:

Cathode material	stainless steel	graphite			
$D_c$ , mm	20	12		20	
$L_{ac}$ , mm	27	12	27	12	27
$t_d$ , $\mu s$	0.5-0.6	0.2	0.4-0.5	0-0.1	0.3-0.4
$t_{dc}$ , $\mu s$	0.6	0.15	0.4	0.1	0.35

On the base of this discussed above influence of electrons with large transverse velocity components a hypothesis on possible mechanism of space charge oscillations development can be proposed. We think that these oscillations can have an origin in the double-stream instability [4] caused by interaction of discrete electron flows with different axial velocities: a flow emitted by the "front" surface of cathode plasma with maximum axial velocity  $V_{\parallel max}$  and  $\omega_{p1}$  plasma frequency; and a flow of electrons from the outer generatrix of the plasma with maximum transverse and so with minimum axial velocity ( $V_{\parallel min}$ ,  $\omega_{p2}$ ). In this case:

$$f = (V_{\parallel max} \omega_{p2} + V_{\parallel min} \omega_{p1}) / 2\pi(V_{\parallel max} - V_{\parallel min}),$$

Estimation of frequency for the instability developing due to coupling of a slow space-charge wave in the first of the beams with a fast space-charge wave in the second one gave us a value  $f$  of about 500 MHz which agrees with experimental data. For these calculations the data on electron density distribution are necessary to determine reduced plasma frequencies of the flows, and we used our experimental data on the REB transverse structure.

Double-stream model of development of the oscillations can, in principle, explain not only registered in experiments waveband but also the difference in influence of

magnetic mirrors placed at different positions along the drift tube on amplitude parameters of oscillations. Increase of the oscillations that was observed when the furthest from the cathode magnetic field rise was introduced can be attributed, for example, to the effect of interaction of primary and reflected electron flows. Certainly, interaction of this type had to occur as well in the case of introduction of the nearest to the cathode additional coil (5). But in this case because of small distance between the cathode and the mirror the time of the interaction could be insufficient for perceptible growth of oscillations.

Registered in our work space charge oscillations can partially be caused not only by the double-stream interaction. Of all possible alternative mechanisms we should like to note especially the one involving azimuthal space charge waves in the flow of electrons emitted by the outer surface of plasma emitter. Diocotron instability in this flow can cause development of revolving formations in the REB halo. Characteristic frequency of this process depends on the drift velocity  $V_d = E_r / B$  and an azimuthal mode number  $n=1,2,3,\dots$  and for SER-1 geometry, 220 kV voltage and first mode  $n=1$  would be also about 500 MHz. Instability of the same type can occur in the space charge of electrons confined in a specific trap between the cathode and the magnetic mirror. If the REB electrostatic potential relative to the drift tube is about 50 kV, then frequencies of azimuthal space charge oscillations in the trap for mode number  $n$  would be about  $n \cdot 150$  MHz.

Thus a number of oscillatory mechanisms can be proposed for explanation of the experimental data obtained in the work but the data are not sufficient to esteem contributions of different mechanisms in the observed oscillations.

Thus the main results of the work are the follows:

- amplitude-frequency characteristics of the REB space charge oscillations in the drift channel were determined;
- influence of local rises of magnetic field upon these oscillations was studied;
- influence of collective processes in the REB on the beam structure was also observed;
- possible mechanisms of development of the oscillations were proposed.

The work was partially supported by the Russian Fund for Fundamental Research.

[1] L.Yu.Bogdanov, G.G.Sominski, Tech. Phys., v.40 (1995), p.1245-1248.

[2] A.V.Arhipov, L.Yu.Bogdanov et al.- In: Lectures on microwave electronics and radiophysics. 10th Winter Seminar School for Engineers, Pt.2, Saratov, "College", 1996, p.3-34 [in Russian].

[3] S.P.Bougaev, V.I.Kanavets, V.I.Koshelev, V.A.Cherepenin. Relativistic Multiwave Microwave Oscillators, Novosibirsk, "Nauka", 1991 [in Russian].

[4] M.I.Rabinovich, D.I.Trubetskov. Introduction in Theory of Oscillations and Waves. Moscow, "Nauka", 1984 [in Russian].

□



# THEORETICAL ASPECTS OF THE ELECTRONICAL DEVICES OPERATING DUE TO INTERACTION BETWEEN ANNULAR ELECTRON BEAMS AND THE AZIMUTHAL SURFACE WAVES

Girka V.O., Girka I.O.

*Kharkiv State University, Svobody sq., 4, Kharkiv, 310077, Ukraine. Fax: (0572)353-977.*

## Abstract

The paper considers physical basis of the electronical devices operating due to the beam or dissipative instability of the azimuthal surface waves (ASW). The ASW are the electromagnetic surface waves with extraordinary polarization (with field components  $E_r, E_\phi, H_z$ ), they propagate across the axial external steady magnetic field  $\vec{B}_0 || \vec{z}$  in the metal cylindrical waveguide with cold plasma filling. The ASW fields are described by Maxwell equations. To solve the problem we use the Fourier method and numerical simulation of the obtained equations. The ASW excitation under the conditions of the beam and dissipative instabilities due to the electron beam motion is examined. We also study the correction to the ASW eigenfrequencies caused by the waveguide chamber noncircularity. The ASW delaing leads to the negative frequency correction. The ASW energy can be emitted from the narrow slot in the metallic chamber of the waveguide. We found the optimum wavenumber range where increments values are much greater than those of the ASW decrement caused by their energy radiation.

## Introduction

Theory of vacuum electronical devices has been developed completely enough till now: their working parameters are rather close to those theoretically predicted. Utilization of plasma insertions in waveguiding elements of electronical devices allows to achieve much better characteristics than those of vacuum devices. First, frequency range of the generating waves becomes more wide. Second, the top value of the current caused by the beam which is transporting in the device increases. Third, the possibility to control fluently the frequency of the generating waves arises, etc. At the last time annual beams of charged particles become to

be used for increasing the efficiency of such electronical devices as gyrotron and laser on free electrons [1]. Increments of beam instabilities and efficiency of transformation of beam particles kinetic energy into the energy of radiating waves increase due to utilization of annual beams as compared with the case of longitudinal propagation of charged particles beams.

Interaction of annual electron beam, rotating between the cylindrical metallic chamber of the device and coaxial plasma insertion, with eigen modes of the waveguide is studied here. These modes propagate across external steady magnetic field with azimuthal wave number  $m$  and are called therefore as azimuthal surface waves. Let us consider cylindrical metallic waveguide of the radius  $R_2$  with coaxial plasma insertion of the radius  $R_1 < R_2$ . Plasma can be gaseous or semiconductor one. Concentration  $n_p$  of plasma particles is much greater than that  $n_b$  of electrons in beam,  $\xi = n_b/n_p \ll 1$ . Electrons of the beam rotate either in steady magnetic field or in crossed  $\vec{E}_0 \perp \vec{B}_0$  fields. In the latter case radial electric field  $\vec{E}_0$  is produced in the region  $R_1 < r < R_2$  with the help of special additional electrodes. The space is supposed to be uniform in  $z$  direction ( $\partial / \partial z = 0$ ).

### Delaying of the surface waves in the noncircular chamber

If metal wall of the waveguide is not ring,  $R_2 = R_0 \cdot (1 + h \cdot \sin(n \cdot \varphi))$ , then delaying of the ASW occurs as compared with the case of the ring,  $h = 0$ , waveguide. Here  $R_0$  is mean value of  $R_2$ , the value  $h$  is small,  $h \ll \Lambda = (R_0 - R_1) \cdot R_1^{-1}$ ,  $n$  is integer. Such approach allows to model any shape of the metal waveguide cross-section, for example, a magnetron-like one. Frequency correction  $\Delta\omega(n)$ , caused by the noncircularity of the metallic chamber, appears to be the small value of the second order,

$$\frac{\Delta\omega(n)}{\omega} \sim \frac{-h^2 \cdot \Lambda \cdot m^2 \cdot (m+n) \cdot (m+n)!}{16 \cdot \pi \cdot m! \cdot (\omega \cdot R_1 \cdot c^{-1})^{2+n}} \quad (1)$$

### Dispersion relation

Distribution of electromagnetic field of the ASW inside the chamber was determined from Maxwell equation. It was found that the main part of the ASW energy is located in the

region  $R_1 < r < R_2$ , where  $|H_z|, |E_r| > |E_\phi|$ . Dispersion relation, which describes excitation of the ASW by electron beam, is obtained due to applying linear boundary conditions. It has the following form [2],

$$\frac{I'_m(z)}{\psi \cdot I_m(z)} + \frac{m \cdot \epsilon_2}{z \cdot \psi \cdot \epsilon_1} + \frac{\Lambda}{k \cdot R_l} \left( k^2 \cdot R_l^2 - \frac{m^2}{\epsilon_b} \right) = 0, \quad (2)$$

here  $z = k \cdot R_l \cdot \psi$ ,  $\psi = \sqrt{\epsilon_1 - \epsilon_2^2 \cdot \epsilon_l^{-1}}$ ,  $k = \omega/c$ ,  $b = \gamma \cdot \omega/\omega_c$ ,  $\alpha = \frac{m \cdot v_0 \cdot \gamma}{\omega_c \cdot R_l}$ ,

$\gamma = (1 - v_0^2/c^2)^{-1/2}$ ,  $I_n(z)$  is modified Bessel function, index means a derivative,

$$\epsilon_b = 1 + \frac{2 \cdot \xi \cdot \Omega^2}{\omega_c^2} \sum_{n=0}^{\infty} \left[ \frac{n^2 \cdot \gamma \cdot J_n^2(\alpha)}{(n^2 - b^2) \cdot \alpha} + \frac{n^2 \cdot \gamma \cdot J_n^2(\alpha) \cdot v_0^2}{(n^2 - b^2) \cdot \alpha^2 \cdot c^2} \cdot (n^2 + b^2) \right]$$

$v_0$  is beam velocity,  $c$  is light velocity,  $\Omega$  and  $\omega_c$  are Langmuir and cyclotron electron frequencies respectively,  $\epsilon_l$  and  $\epsilon_2$  are components of the plasma dielectrical permeability tensor in hydrodynamical approach,  $J_n(z)$  is the Bessel function. The ASW energy can be emitted through the narrow slot [3] in the metal wall of the waveguide. We found the optimum wave number range,  $0,1 < |m| \cdot \delta / R_l < 0,5$ , in which increments of the beam and dissipative instabilities are greater than damping rates of the ASW caused by their energy radiation, here  $\delta = \Omega / c$  is skin depth. The results of the numerical investigation of the considered problem are presented on fig.1.2 for the ASW with azimuthal wave numbers  $m = -2$  and  $m = -3$ . Dependences of the ASW frequency and of the increments of beam  $\Gamma_b$  and dissipative  $\Gamma_d$  instabilities upon the effective wave number  $k_0 = |m| \cdot \delta / R_l$  are drawn by lines marked by figures 1,2 and 3 respectively on the upper part of coordinate plane. Dependence of the ASW damping rate caused by their radiation through a slot in the metal screen with the following angular dimensions,  $\Delta\phi = 0,02 \cdot \pi$ , is drawn on its lower part and is marked by figure 4. Here we represent the results of the numerical calculation which are concerned the case when  $\Omega = 10 \cdot \omega_c$ ,  $\xi = 0,01$ ,  $\nu = 0,007 \cdot \Omega$ ,  $\nu$  is effective value of the collisional frequency for plasma electrons. In the case of the dissipative instability the value of  $\nu$  is much greater than the beam instability growth rate  $\Gamma_b$ . For reader's comfort we drawn the increments values  $\Gamma_b$

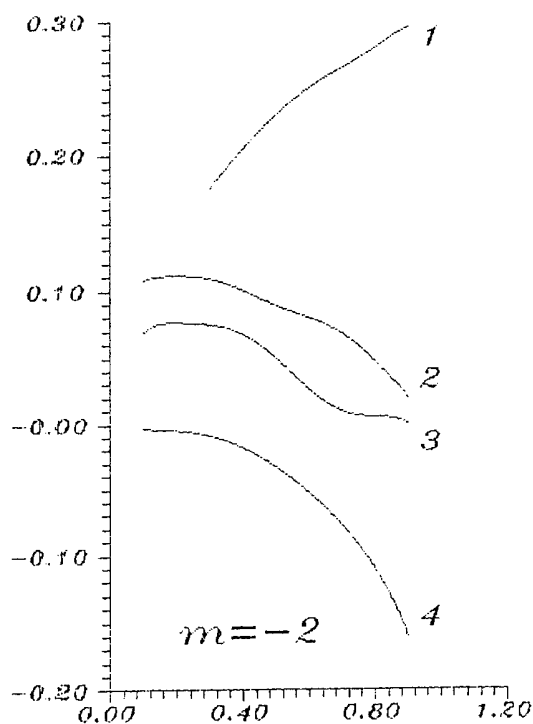


Fig.1

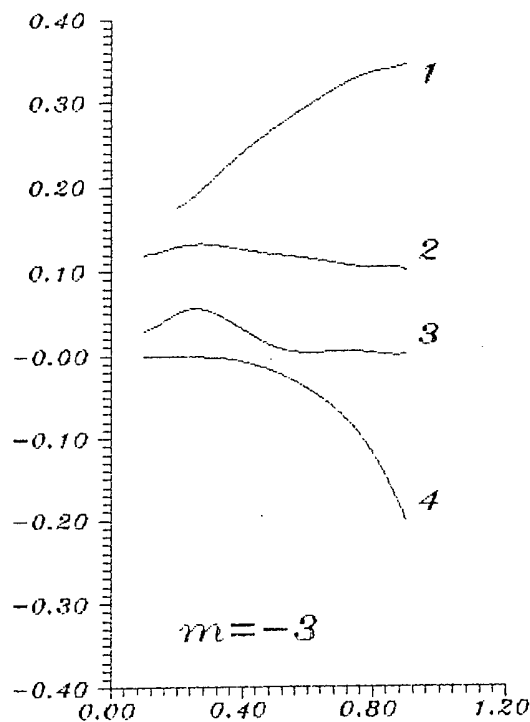


Fig.2

and  $\Gamma_d$  multiplied by 100 and divided by  $\Omega$ . Curves marked by 1 and 4 show us respectively the dependences of the ASW frequency and damping rate both divided by  $\Omega$  on  $k_0$  value.

### Conclusion

In our opinion the construction of electronical devices proposed has such advantages and qualities: achievement of the short wavelength energy radiation, opportunity to change the radiation frequency in wide range, small longitudinal dimensions. Utilization of surface waves allows to hope that wave-beam interaction becomes more efficient as compared with the case of volume waves. ASW energy is located mainly in that region where the beam rotates, amplitudes of ASW fields monotonously decrease when going from plasma boundary  $R_l$  to its axis. The utilization of annular electron beam has some advantages as compared with longitudinal beams, so our studies can be interesting for the plasma electronics.

[1] Gisler, G.R.:Phys.Fluids, **30** (1987) 2199, Saito, H., Wurtele, J.S.:ibid,2209.

[2] Girka, V.O., Girka, I.O., Olefir, V.P., Tkachenko, V.I.:Sov.Tech.Phys. Lett., **17** (1991) 35.

[3] Girka, V.O., Girka, I.O.:Sov.Journ. of Commun. Technol. and Electronics, **37** (1992) 32.

# SPECTRUM OF PLASMA ELECTRONS OBSERVED IN STRONG LANGMUIR TURBULENCE DRIVEN BY REB

L.N. Vyacheslavov, V.F. Gurko, I.V. Kandaurov, E.P. Kruglyakov,  
O.I. Meshkov, A.L. Sanin and V.F. Zharov

*Budker Institute of Nuclear Physics, Novosibirsk, 630090, Russia*

**Abstract** In the presented experiments the Thomson scattering technique, based on the second harmonic of Nd-glass laser was used for studying of a non-Maxwellian electron distribution function of the plasma, heated by REB. Two simultaneously operating systems were employed for observation of light scattered at the angles of 90 and 8 degrees, respectively. The first obtained results and the mechanisms of plasma heating are discussed.

## Introduction

It is known that the collision damping of resonantly excited fast Langmuir waves can not provide the energy balance with the pumping by the powerful relativistic electron beam (REB) under the regime of strong REB-plasma interaction. The nonlinear collisionless damping rate of these waves is still lower. In an isothermal non-magnetized plasma, the collapse [1] is a sole mechanism to shift the waves into the short wavelength region, where they could transfer their energy to the plasma electrons. In the case of non-isothermal ( $T_e \gg T_i$ ) plasmas, the collapse leads to production of a high level of short wavelength ion-acoustic oscillations, which are able to switch on two other processes of the energy transfer through the turbulence. First, it is the conversion on the ion-acoustic oscillations [2,3] — the nonlinear transfer of the Langmuir waves from the pumping region directly to the damping region. Second, in a magnetoactive plasma (when the magnetic addition in dispersion of the Langmuir waves greatly exceeds the thermal addition) the resonant scattering of the waves, excited by REB, along the lines of constant frequency in a momentum space. Both these processes as well as the collapse lead to a "tail" formation, i. e. to the heating of a small fraction of plasma electrons. This work presents the experimental observation of the electron distribution function of a plasma, heated by a powerful REB, and an analysis of the possible mechanisms of this phenomenon.

## Experimental setup

In the presented experiments for studying of a non-Maxwellian electron distribution function the Thomson scattering technique was used. Two simultaneously operating systems were employed for observation of light scattered at the angles of 90° and 8°, respectively. The plasma and the electron beam parameters were as follows:

### Plasma:

Density:  $n_e = (1 - 1.5) \cdot 10^{15} \text{ cm}^{-3}$

Initial temperature:  $T_e = 1 \text{ eV}$

Final temperature:  $T_e = 20 - 60 \text{ eV}$

Magnetic field:  $B_0 = 2.5 \text{ T}$ ;

### Electron Beam:

Density:  $n_b = (3 - 5) \cdot 10^{11} \text{ cm}^{-3}$

Energy:  $E_e = 700 \text{ keV}$

Duration:  $\tau_b = 200 \text{ ns}$

Diameter:  $d_b = 1.8 \text{ cm}$

Detailed description of the experimental installation and the REB source can be found in [4].

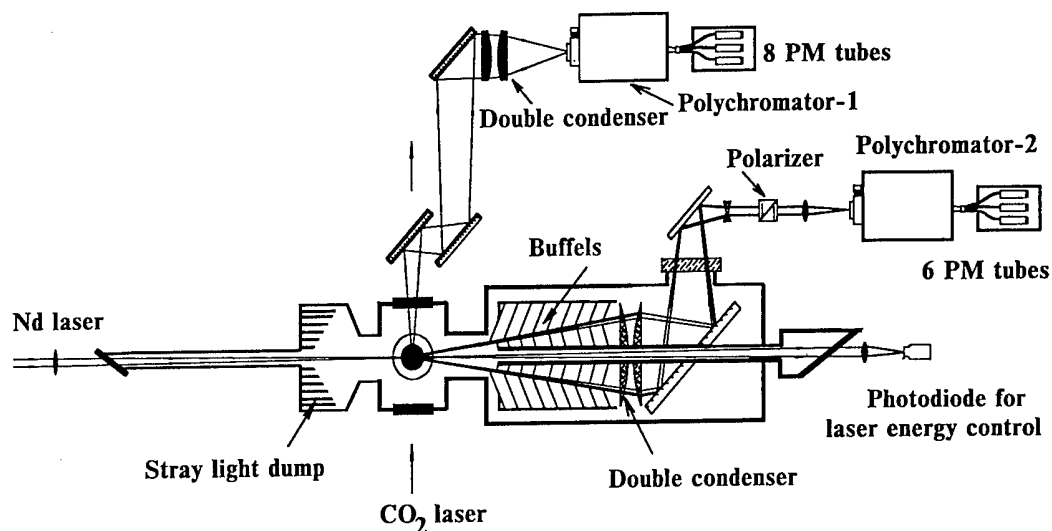


Figure 1. Scattered light collection system for 90 and 8 degrees

The small-angle geometry of non-collective Thomson scattering enables one to increase the spectral density of the scattered radiation and to observe angular dependence of non-Maxwellian electrons relative to REB running direction. Thus, the registration of scattered light at the angle of  $8^\circ$  was adopted for studying of the superthermal "tails" of the electron distribution function. The temperature and the density of the bulk of plasma electrons were measured simultaneously by the  $90^\circ$  system. This system allows to measure electron temperature at the range of 5–150 eV, where the upper value is limited by the plasma background light during the REB injection.

The Nd-glass laser was used as the source of the probe beam with the parameters that are given below:

Energy of the pulse: up to 40 J / 15 J (at wavelength 1060 nm / 530 nm)

Pulse duration: 8 – 10 ns

Beam divergence:  $2 \cdot 10^{-4}$  rad

The stray scattered light that occurred due to a scattering of the laser radiation on the elements of construction and, predominantly, on the low-temperature bulk of plasma electrons, was suppressed in  $8^\circ$  system by the high-contrast interference filters\* with a transmission adjusted to the positions of corresponding registering channel of the polychromator-2. The instrumental functions of the channels versus wavelength are shown in Figure 2a. In Figure 2b one can see the relative sensitivity of the channels as function of the energy of plasma electrons. The latter dependency starts abruptly from the side of lower energies and has a long slope from the side of higher energies.

\* The filters were manufactured by *Barr Associates, Inc.*

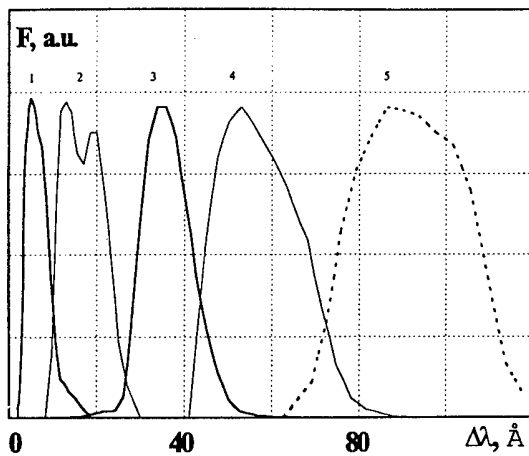


**Figure 2a.** Instrumental functions of the channels of  $8^\circ$  system

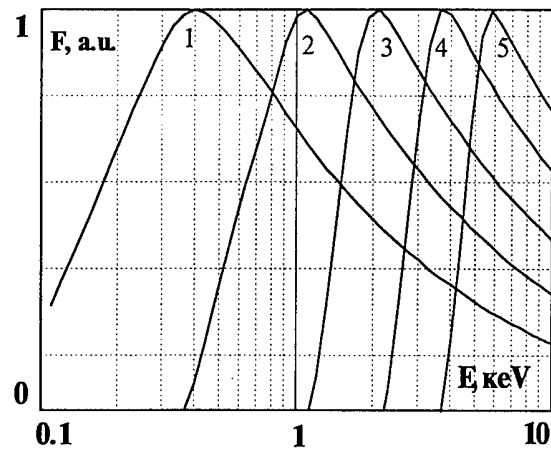


**Figure 2b.** Fraction of scattered light in the channels depending on the electron energy

The laser pulse is delayed by 50 — 100 ns relative to the beginning of the REB pulse. During the first series of the experiments the clear signals were obtained in four channels. It was assumed for the signal processing that the distribution function has the power law:  $f(E_e) \propto E_e^{-\alpha}$  for the energies  $E_e > 300$  eV (approximately  $10 T_e$ ). The scattering signals were calculated numerically for the given index of a power  $\alpha$ , by its convolution with the instrumental functions of the channels. The value of  $\alpha=2.5$  provides the best fitting of the calculated signals to the experimental ones. The shape of the distribution function is illustrated in Figure 3.

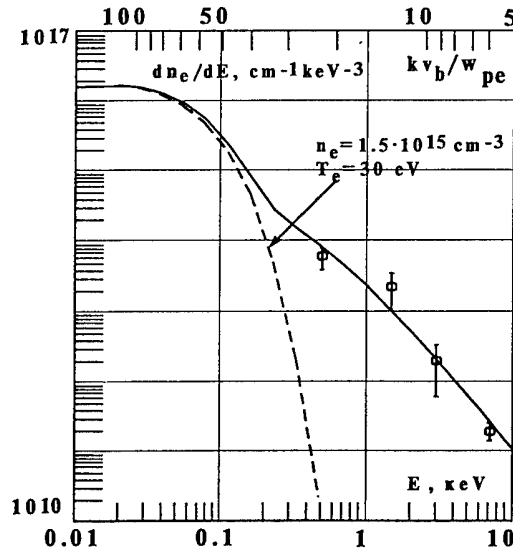


**Figure 3.** Distribution function of plasma electrons during the REB injection: the density of superthermal electrons is  $2.5 \cdot 10^{14} \text{ cm}^{-3}$ , the average energy is about 0.5 keV.

### Discussion and conclusion

As it was shown earlier [5], the collision damping of Langmuir oscillations is responsible for increasing of the temperature of the bulk of plasma electrons. It is

evident, that the heating of non-Maxwellian part of the electron distribution function is connected with the Landau damping of slow Langmuir waves (real or virtual, as it is in the case of the conversion). The question is how to determine the main mechanism of transferring of the energy of turbulent oscillations towards the short wavelength side of the spectrum. It is unlikely that the fastest mechanism among those mentioned in the introduction part of this paper, the resonant scattering of Langmuir waves on the ion-acoustic oscillations, provides the required energy flow. As it was proved earlier [6], the energy is pumped through the oscillations, propagating at not too oblique angles according to the REB direction ( $\theta < 30^\circ$ ). The dispersion law permits interaction of these waves only with the ion-acoustic waves with  $k < 8\omega_{pe}/c$ , whose intensity is low [7,8]. The dispersion law limits also the deceleration of Langmuir waves by the rather high phase velocity, which corresponds to the energy of associated resonant electrons of about 10 keV. The conversion rate can be estimated after the work [3], without regard to magnetic field, because for  $k > 8\omega_{pe}/c$  the thermal addition in the dispersion exceeds the magnetic one. At the same time, the results of this work should be considered with a care referring to our experimental conditions, where the ion-acoustic turbulence is not weak. The estimation of the conversion rate shows, that it could provide the energy balance with the pumping. The final corroboration of the theoretical conclusions about the guiding role of the conversion in the mechanism of the energy flow, where the collapse acts only as the catalyst, is still requires the additional experiments.

- [1] V. E. Zakharov, Sov. Phys. JETP 35 (1972) 908.
- [2] P. K. Kaw, A. T. Lin, and J. M. Dawson, The Phys. of Fluids 16 (1973) 1967
- [3] A. A. Galeev, R. Z. Sagdeev, V. D. Shapiro, V. I. Shevchenko, Sov. Phys. JETP 46 (1977) 711.
- [4] V. S. Burmasov, I. V. Kandaurov, E. P. Krurglyakov, and O. I. Meshkov, IEEE Trans. on Plasma Sci., 23 (1995) 952
- [5] I. V. Kandaurov, E. P. Krurglyakov, O. I. Meshkov, in Proc. IX Int. Conf. on High Power Particle Beams, (Washington, D.C., USA, May 1992) vol.2 (1992) 1027.
- [6] L. N. Vyacheslavov, V. S. Burmasov, I. V. Kandaurov, E. P. Krurglyakov, O. I. Meshkov, and A. L. Sanin, Phys. Plasmas 2 (1995) 2224.
- [7] V. S. Burmasov, I. V. Kandaurov, E. P. Krurglyakov, O. I. Meshkov, A. L. Sanin, and L.N.Vyacheslavov, presented at XI Int. Conf. on High Power Particle Beams, (Prague, Czech Republic, June 1996).
- [8] V. S. Burmasov, I. V. Kandaurov, E. P. Krurglyakov, O. I. Meshkov, A. L. Sanin, and L.N.Vyacheslavov, in Proc XXII Europ. Conf. on Controlled Fusion and Plasma Phys. (Bournemouth, England, June 1995) vol.1 (1995) 445



## Energy and Angular Spreads of Beam Electrons and Microwave Radiation due to Strong Beam-Plasma Turbulence

H. Koguchi, M. Masuzaki, M. Yoshikawa,\*

S. Takahata, K. Toda, R. Ando and K. Kamada

*Department of Physics, Faculty of Science, Kanazawa University,  
Kanazawa 920-11, Japan*

*\* Plasma Research Center, University of Tsukuba,  
Ibaraki 305, Japan*

### Abstract

A plasma becomes a strong Langmuir turbulence state when an intense relativistic electron beam (IREB) is injected into it. Investigation of the beam properties after passing the plasma is important. The energy and angular spreads of the IREB were measured by a magnetic energy analyzer and an angle analyzer, respectively. The theory of transit-time interactions was applied to analyze the observed energy and angular spreads and to estimate the turbulent field strengths. These results were in good agreement with the spectroscopic measurements. The broadband microwave radiation was also observed simultaneously with the angular spread measurement. We found correlation between the radiation and the angular spread of the IREB. The wider the angular spread, the stronger the microwave radiation.

Recently, the beam-driven strong Langmuir turbulence has attracted much attention theoretically, computationally<sup>1,2)</sup> and experimentally.<sup>3-15)</sup> In the strong Langmuir turbulence state, generation, collapse and burnout of cavitons are repeated by the nucleation process.<sup>16-19)</sup> Here a caviton is a density cavity in which high intensity oscillating electrostatic fields are trapped. In our recent experiments, spectroscopic measurements of high intensity oscillating electrostatic fields in cavitons and measurements of high power broadband microwave radiation were carried out in the same experimental setup.<sup>11-14)</sup> For understanding the strong Langmuir turbulence state, investigation of the beam properties after passing the plasma is also important. So the energy distribution and the angular spread of the IREB were measured by means of a magnetic energy analyzer and an angle analyzer, respectively. The measured energy distribution and angular spread of the IREB were analyzed using the theory of transit-time interactions.<sup>20)</sup>

The results of the analysis shows the presence of localized intense electric fields, and this fact is in good agreement with the spectroscopic measurements.

High power broadband microwave radiation was measured simultaneously with the angular spread measurement. The radiation was observed only during the IREB pulse as had been observed in the previous experiment. This fact shows that the radiation source was the beam electrons. There was correlation between the angular spread of the IREB and the microwave radiation. This result was consistent with a previously obtained result that the strong Langmuir turbulence state was a necessary condition for the radiation.<sup>21)</sup>

Figure 1 shows the experimental setup. Pulserad 110A produced by Physics International was used to produce an IREB. The diode consisted of a carbon cathode of 3.6 cm in diameter and a titanium foil anode of 20  $\mu\text{m}$  thick. The IREB (3 cm in diameter, 1.4 MeV, 10 kA, and 30 nsec) was injected into a carbon

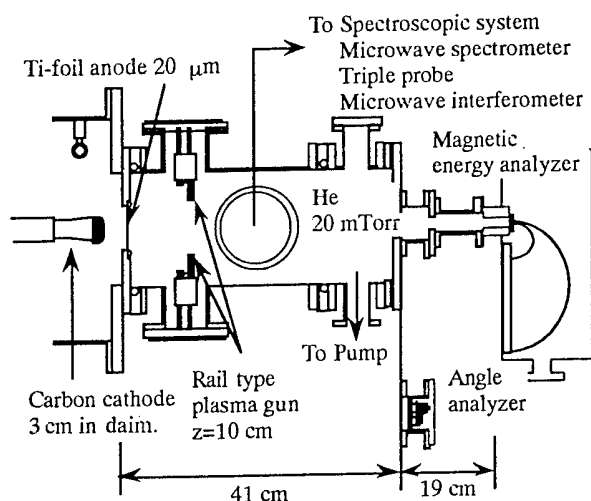


Fig. 1. The experimental set up

plasma. The drift chamber, made of stainless-steel, 60 cm long and 16 cm in diameter, was filled with 20 mTorr He gas for the spectroscopic measurement. The background pressure was around  $5 \times 10^{-5}$  Torr. The carbon plasma was generated by a pair of rail type plasma guns set opposite to each other at 10 cm downstream from the anode foil. Figure 2 shows the plasma density as a function of the delay time  $\tau$  of the IREB injection after the firing time of the guns. The plasma density was varied from the order of  $10^{11}$  to the order of  $10^{13} \text{ cc}^{-1}$  by changing  $\tau$ . The electron temperature without the IREB injection was measured by the triple probe, and it was 6 - 9 eV. When the IREB was injected into the plasma, the electron temperature,  $T_e$ , was estimated from the spectroscopic measurement of the intensity ratio of HeI 492.19 nm line (singlet) to HeI 471.31 nm line (triplet) by comparing the experimental results with the newly developed

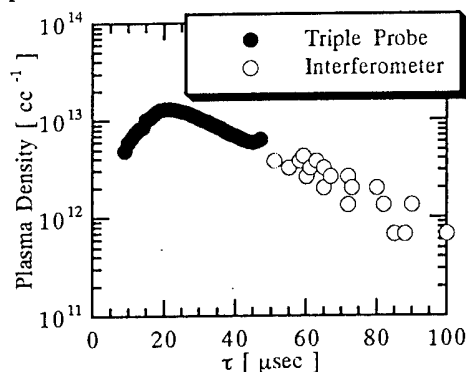


Fig. 2. The plasma density.

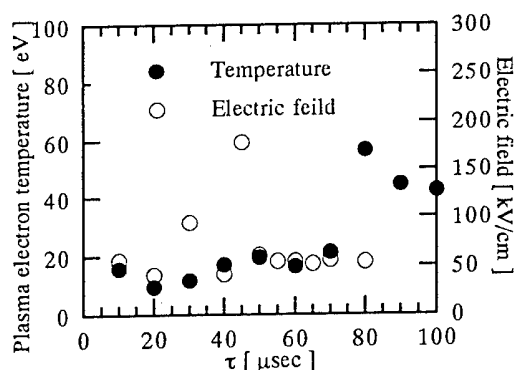


Fig. 3. The plasma electron temperature and the electric fields.

collisional radiative model.<sup>22)</sup> Figure 3 shows  $T_e$  as a function of  $\tau$ . The intensity of the high frequency turbulent electric fields was obtained using the Stark shift measurement. The HeI 501.57 nm line ( $3^1P_1-2^1S_0$ ) shifts to the blue side by high frequency electric fields. Figure 3 also shows the electric field strength  $E_s$  measured by the Stark shift.

The energy distribution of the IREB was measured by a magnetic energy analyzer at the end of the drift chamber. The magnetic field of 0.053 T was applied, and the observable energy ranges was 90 keV - 1.54 MeV. The energy resolution was 40 keV. Usually 6 - 10 channels out of 22 channels were used. The time resolution of the analyzer was a few nsec.

The angular distribution was measured by an angle analyzer. Figure 4 shows the angle analyzer. It consisted of a Faraday cup of 0.6 cm in outer diameter (a) and three disks (b) of 0.2 cm thick which were made of brass and set coaxially. The center Faraday cup covered the sinusoidal range of the scattering angle 0 - 0.1,

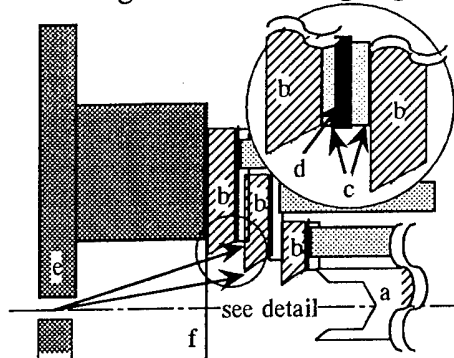


Fig. 4. The angle analyzer.

and three disks covered 0.1 - 0.2, 0.2 - 0.3, and 0.3 - 0.4, respectively. The angle analyzer was placed in the axis at the end of the chamber. The time-evolved expected value of the sine of the scattering angle was calculated from these output signals.

The high power broadband microwave radiation was measured at 17.5 cm downstream of the anode by a 5-channel microwave spectrometer of filter-bank type. The received microwaves were distributed into 5 channels (18.0 - 22.2 GHz, 22.2 - 26.5 GHz, 26.5 - 31.5 GHz, 30.7 - 35.7 GHz, and 35.5 - 40.0 GHz) by directional-couplers, and passed through the band-pass filters. The signal of each channel was detected by a crystal

detector.

In Fig. 5 a) the averaged standard deviation of the energy distribution is shown as a function of  $\tau$ , where the initial spread 58 keV is taken into account. The averaged expected value of the sine of the scattering angles taking the initial spread 0.09 into account is also shown as a function of  $\tau$  in Fig. 5 b). The total power of microwave radiation is calculated from signals of 5 channels microwave spectrometer, and shown in Fig. 5 c) as also a function of  $\tau$ .

The energy and angular spread are caused by scattering of beam electrons in energy and in angle during interaction with cavitons. We applied the theory of multidimensional transit-time interactions<sup>20)</sup> to calculate the scattering. We calculated the single interaction with a caviton, and then estimated total energy spread  $\Delta U$  and angular spread  $\Delta v_{\perp}/v_b$ . Figure 6 shows  $\Delta U$  and  $\Delta v_{\perp}/v_b$  for the plasma density  $n_p = 1.6 \times 10^{12} \text{ cc}^{-1}$ . In this case, the experimental values of  $T_e$  and  $E_s$  are 57 eV and

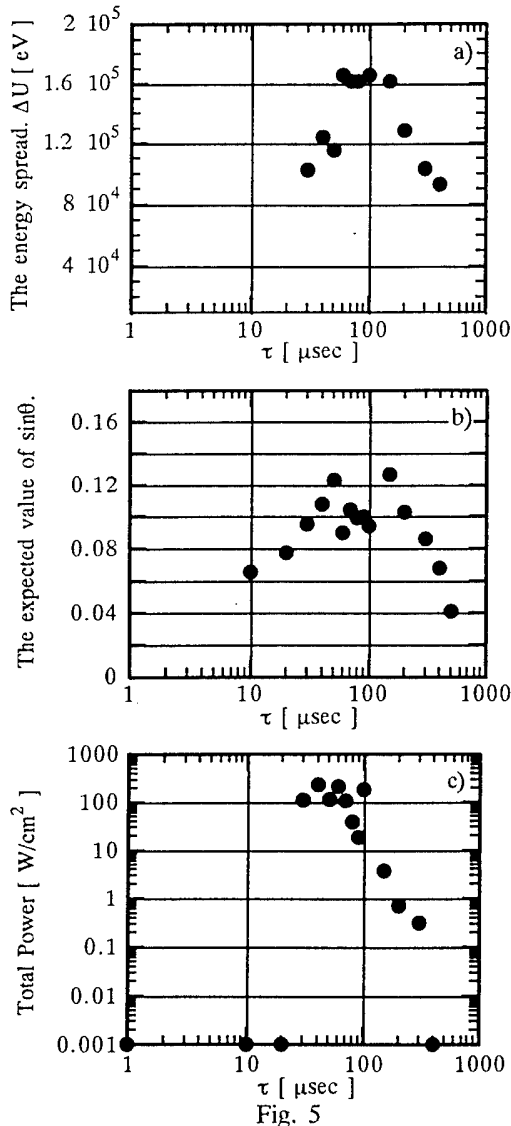


Fig. 5

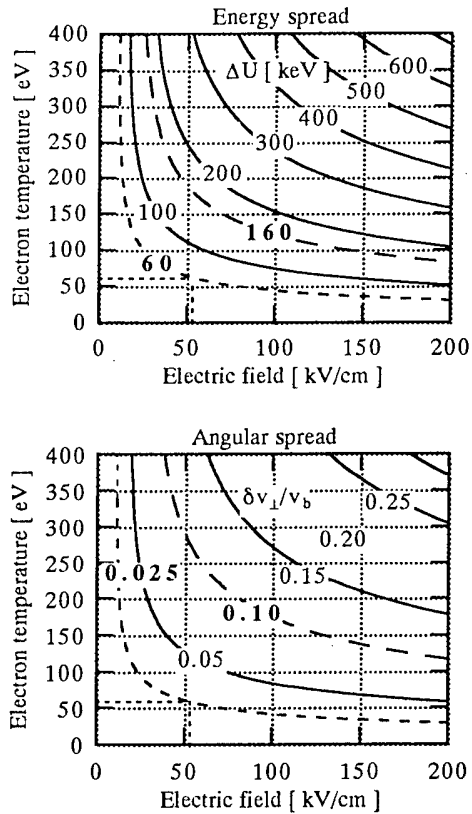


Fig. 6. Energy and angular spreads

54 kV/cm, respectively. These parameters give the  $\Delta U = 60$  keV and  $\Delta v_{\perp}/v_b = 0.025$ . The experimental results are  $\Delta U = 160$  keV and  $\Delta v_{\perp}/v_b = 0.10$ . The experimental values of  $\Delta U$  and  $\Delta v_{\perp}/v_b$  are wider than the calculation. These differences may be caused by the assumption that the dipole axes of all cavitons are aligned on the IREB direction. Besides, we neglect the beam energy loss associated with the generation of the cavitons. However, in our calculation range, the minimum electric field is 26 kV/cm for  $\Delta U = 160$  keV at  $T_e = 400$  eV. This result suggests the existence of strong turbulent fields. We also calculate  $\Delta U$  and  $\Delta v_{\perp}/v_b$  for the case that the dipole axes of all cavitons are perpendicular to the IREB direction. In this case,  $\Delta v_{\perp}/v_b$  is much larger than in the parallel case, but  $\Delta U$  is same order. We estimate the percentage of perpendicular component in order that the calculated  $\Delta v_{\perp}/v_b$  may agree with the experimental value, and obtain that it is 2.4%.

From Fig. 5 we can see that the dependence on  $\tau$  of the microwave radiation is almost the same as these of the energy and angular spreads. The wider the energy and angular spreads, the stronger the total power of the microwave radiation.

We measure the energy distribution and angular spread of the beam electrons in order to investigate the beam-driven strong Langmuir turbulence state. The theory of transit-time interactions was applied to analyze the measured energy and angular spreads. The high frequency electric fields obtained were compared with those obtained from the spectroscopic measurements. The results of analysis suggested the existence of strong turbulent field.

The microwave radiation is observed simultaneously with the angular spread measurement. We found correlation between the radiation and the angular spread of the IREB. The wider the energy and angular spreads, the stronger the total power of the microwave ra-

diation.

Part of this work was supported by Grant-in-Aid for Scientific Research from the Ministry of Education, Science and Culture.

### References

- [1] P. A. Robinson and D. L. Newman: Phys. Fluids **B1** (1989) 2319.
- [2] P. A. Robinson and D. L. Newman: Phys. Fluids **B2** (1990) 3120.
- [3] G. C. A. M. Janssen, J. H. M. Bonnie, E. H. A. Granneman, V. I. Kremmentsov, and H. J. Hopman: Phys. Fluids **27** (1984) 726.
- [4] G. C. A. M. Janssen, E. H. A. Granneman, V. I. Kremmentsov, and H. J. Hopman: Phys. Fluids **27** (1984) 726.
- [5] H. J. Hopman and G. C. A. M. Janssen: Phys. Rev. Lett. **52** (1984) 1613.
- [6] D. Levron, G. Benford and D. Tzach: Phys. Rev. Lett. **58** (1987) 1336.
- [7] G. Benford, X. Zhai and D. Levron: Phys. Fluids **B3** (1991) 560.
- [8] D. Levron, G. Benford, A. Ben-Amar Baranga and J. Means: Phys. Fluids **31** (1988) 2026.
- [9] A. Dovrat and G. Benford: Phys. Fluids **B1** (1989) 2488.
- [10] K. G. Kato, G. Benford and D. Tzach: Phys. Fluids **26** (1983) 3636.
- [11] M. Masuzaki, R. Ando, A. Yoshimoto, M. Ishikawa, M. Yoshikawa, K. Kitawada, H. Morita and K. Kamada: *Proceedings of 8<sup>th</sup> International Conference on High-Power Particle Beams*, eds. B. N. Breizman and B. A. Knyazev (World Scientific, Singapore, 1991) Vol. 2, p.683.
- [12] M. Masuzaki, R. Ando, M. Yoshikawa, H. Morita, J. Yasuoka and K. Kamada: *Proceedings of 9<sup>th</sup> International Conference on High-Power Particle Beams*, eds. D. Mosher and G. Cooperstein (Washington, DC., 1992) Vol. 2, p.1227.
- [13] M. Yoshikawa, R. Ando and M. Masuzaki: Jpn. J. Appl. Phys. **32** (1993) 969.
- [14] M. Yoshikawa, M. Masuzaki and R. Ando: J. Phys. Soc. Jpn **63** (1994) 3303.
- [15] G. Benford and J. C. Weatherall: Phys. Fluids **B4** (1992) 4111.
- [16] G. D. Doolen, D. F. DuBois and H. A. Rose: Phys. Rev. Lett. **54** (1985) 804.
- [17] D. Russel, D. F. DuBois and H. A. Rose: Phys. Rev. Lett. **56** (1986) 838.
- [18] D. Russel, D. F. DuBois and H. A. Rose: Phys. Rev. Lett. **60** (1988) 581.
- [19] D. F. DuBois, H. A. Rose and D. Russel: Phys. Rev. Lett. **61** (1988) 2209.
- [20] P. A. Robinson: Phys. Fluids **B1** (1989) 490.
- [21] M. Yoshikawa, M. Masuzaki, R. Ando and K. Kamada: To be published.
- [22] S. Sasaki, Research Report NIFS-346 (1995).

# MACROSCOPIC SYMPTOMS OF COLLAPSE IN REB-PLASMA INTERACTION EXPERIMENTS IN STRONG MAGNETIC FIELD

V. S. Burmasov, I. V. Kandaurov, E. P. Kruglyakov, O. I. Meshkov,  
A. L. Sanin, and L. N. Vyacheslavov

*Budker Institute of Nuclear Physics, Novosibirsk, 630090, Russia*

At present, it is well recognized that strong Langmuir turbulence is excited during the process of intense REB-plasma interaction. According to theoretical predictions the energy of Langmuir oscillations can be transferred to plasma electrons by a collapse mechanism. Experimental evidence of the collapse phenomenon has been already observed in a rare nonmagnetized plasma with an electron beam of low energy. As to the case of strong turbulence of broad spectrum of Langmuir oscillations in the presence of a magnetic field, up to now there is no theoretical grounds of the Langmuir waves collapse as a nonlinear stage of modulational instability. Besides, at present, there is no any experiment on the collapse phenomenon observation in a strong magnetic field. In this paper the first macroscopic manifestations of the collapse are presented. The minimum size of the collapsing cavitons is estimated as  $\ell_{\min} < 30r_D$ .

Since the moment of the prediction by Zakharov [1] of the collapse of Langmuir waves, a lot of experimental data have been obtained corroborating an existence of this phenomenon in a strong Langmuir turbulence regime. However, up to now, modern capabilities of mathematical modelling do not permit to perform the kinetic description of a strong developed Langmuir turbulence even in the absence of a magnetic field (under strong developed turbulence one assumed a large number of caverns existing at different stages of collapse). As to the case of a plasma in the magnetic field, \*) at present, there is no direct evidence of the collapse as a nonlinear stage of the modulational instability.

In this paper, some experimental signatures of the collapse existence are presented for the case of powerful REB-plasma interaction in a strong magnetic field. In principle, there are two macroscopic indications of the existence of collapsing caverns in a plasma.

1. The energy of Langmuir waves, trapped in the collapsing caverns is dissipated by plasma electrons. At the final stages of the collapse, this energy is transferred to a small portion of the electrons crossing the caverns during the time less than the period of electric field oscillations inside the caverns. Due to this effect, energetic "tales" on the electron distribution function appear. Such tales have been observed (see Refs. [2, 3, 4]) in the experiments on interaction of powerful REB with a plasma in a strong magnetic field as a result of the Langmuir turbulence excitation.

2. At the final collapse stages, when the electron damping is switched on and HF pressure decreases, the ion-sound waves excitation occurs due to a plasma

---

\*) The case is assumed when the magnetic addition in the dispersion law for Langmuir waves is larger than the thermal one, that is  $3(kr_D)^2 < (\omega_{Be}/\omega_{pe})^2$ .

density (and gas-kinetic pressure) drop inside caverns. As a result of the interaction with the resonant ions, these short wavelength ion-sound oscillations damp quickly. But in nonisothermal plasma ( $T_e \gg T_i$ ), the sound wave damping becomes weak. In this case, the collapse process should create an intense ion-sound turbulence.

The experiments were carried out on the GOL-M device. The preliminary hydrogen plasma ( $n_e = 1.5 \cdot 10^{15} \text{ cm}^{-3}$ ,  $T_{e0} = 1 \text{ eV}$ ,  $D = 6 \text{ cm}$ ,  $L = 250 \text{ cm}$ , magnetic field in homogeneous part is  $B_0 = 2.5 \text{ T}$ , in the mirrors  $B_m = 4.5 \text{ T}$ ) was created by a discharge. The beam with the energy of electrons  $E = 700 \text{ keV}$  was injected into the plasma through one of the mirrors. The beam parameters were: the maximum current  $I_b = 2 \div 3 \text{ kA}$ , the diameter  $d_b = 2 \text{ cm}$ , the duration of the beam  $\tau_b = 200 \text{ ns}$ . Due to collisional damping of Langmuir oscillations, 40 ns later of the injection start the plasma electron temperature has increased up to  $30 \div 50 \text{ eV}$ . Thus, the condition of nonisothermality ( $T_e \gg T_i$ ) was fulfilled practically during all the time of REB injection into the plasma.

For the beam and plasma parameters mentioned above the Thomson scattering method allows to determine the parameters of the non-Maxwellian distribution function as follows.

1. The portion of a density of electron with an energy  $E > 10 T_e$  is high enough (more than 15%). Thus, the energy, contained in the tail is significantly larger than that in the bulk of plasma.

2. The distribution function of these electrons is described as  $f(E) \sim E^\alpha$ , here  $\alpha = -2.5$ . The parameters presented here are obtained for the time moment  $\tau = 100 \text{ ns}$  after the beginning of the REB injection. More detailed information one can find in Ref.[4].

The spectra of low frequency fluctuations \*) were studied at the same experiments by the collective laser scattering method with a pulse  $\text{CO}_2$  laser as a source of light ( $Q = 10 \text{ J}$ ,  $\tau = 10^{-6} \text{ s}$ ). The scattered radiation was detected at the angles  $\theta = 6^\circ$ ,  $11^\circ$  and  $16^\circ$  to the direction of the laser beam propagation. The frequency and the space spectra of low frequency fluctuations were studied. The spectrum of the scattered radiation was studied in the range of  $\omega_l \pm 1.5\omega_{pe}$  (here  $\omega_l$  is the laser frequency,  $\omega_{pe}$  is Langmuir one) with the aid of a grating monochromator with a 30 GHz resolution. The scattered radiation has been observed only in a channel in the vicinity of the laser frequency. To identify the exact value of the frequency of oscillations an absorption cell with ammonia was installed in the monochromator between the grating and detector (Si:B cooled by liquid helium). The ammonia has a single line asR(1,1) which practically coincides with R14 line of  $\text{CO}_2$  laser ( $\lambda = 10.288 \mu$ ). The shift between the absorption line and the laser one equals to  $\Delta\nu = 1.45 \text{ GHz}$ . Due to the effect of a line broadening by the pressure (see Ref.[5]) one can observe an increase in the scattered line absorption with an increase in the ammonia pressure in the cell. Typically scattered signal drops significantly at the ammonia pressure of 30 Tor in the cell of 15 cm length. Using the effect of the absorption growing with the pressure and measuring the value of the scattered signal at different pressures we have found that the frequency of the low frequency

---

\*) Under "low frequency" fluctuations are assumed those whose frequencies are significantly less in comparison with the Langmuir frequency.

fluctuations is to be  $\Delta\nu=2$  GHz. This value is in a good agreement with the frequency of the ion-sound oscillations for the conditions of our experiment. It is necessary to note that in some cases, the ion-sound instability can be excited by the return current.

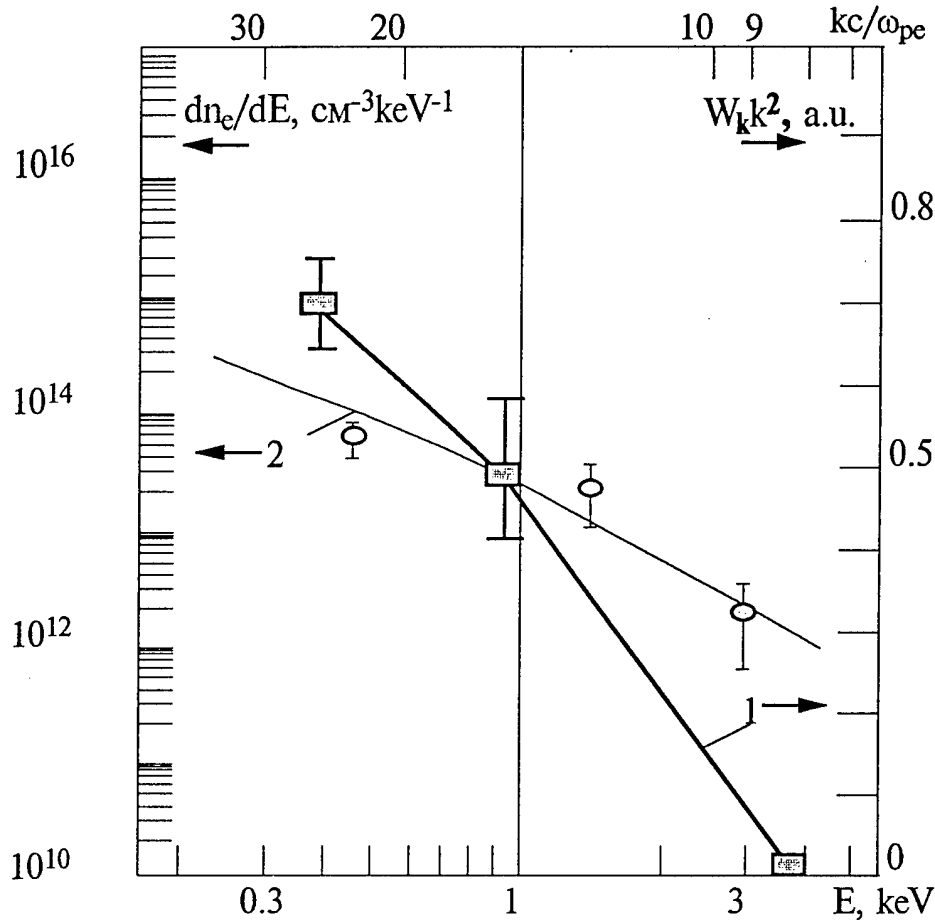


**Fig. 1** k-spectrum of ion-sound turbulence (curve 1) and non-Maxwellian part of the electron distribution function of plasma electrons (curve 2) vs. electron energy  $E$  or vs. normalized wave number  $k$ . The scales of  $E$  and  $k$  correspond to each other through the ratio  $k = \omega_{pe}/v_e$ .

To check the nature of the ion sound observed in our case, some special experiments were carried out. It was shown that when electron beam was injected into a plasma through the thick foil, both Langmuir and ion-sound turbulences were not excited even for increased current density of REB. The beam angular spread grows with the foil thickness increase. It leads to a dramatic decrease in the growth rate of a two stream instability ( $\Gamma \sim 1/\Delta\theta_b^2$ ) and to low effectiveness of REB-plasma interaction. On the other side, special experiments have indicated that the ion-sound fluctuations appear as a consequence of excitation of strong Langmuir turbulence. The level of this turbulence correlates well with the level of the ion-sound instability. To demonstrate this effect, an additional channel at small angle ( $\theta = 0.5^\circ$ ) to the laser beam direction was used to observe Langmuir turbulence.

Thus, one can conclude that ion-sound turbulence observed in our experiments

is not excited by the return current and is the consequence of strong Langmuir turbulence. In Fig.1, the first results are presented on the measurements of a  $k$ -spectrum of the ion-sound turbulence in a strong magnetic field (curve 1). The value of errors is determined by a statistic spread of signals for different shots. The maximum spectral density of the energy of oscillations exceeds significantly the level of thermal fluctuations ( $W_k/W_k^T \approx 10^5$ ). The non-Maxwellian tail of the distribution function of plasma electrons after the heating is also presented in the Figure (curve 2). One can see that both spectra (of nonisothermal plasma electrons and ion-sound turbulence) cover at the same range of the  $k$ -space. It looks natural, because the collapse should stop by the effect of the energy absorption of plasma waves trapped in the caverns by the fast electrons passing through the caverns. The space spectrum of the ion-sound oscillations allows to estimate the characteristic size of the caverns at the stop point:  $\ell_{\min} < 30r_D$ .

Thus, the obtained results demonstrate the macroscopic evidence of the collapse of Langmuir waves in the plasma in a strong magnetic field.

### References

- [1] V.E. Zakharov, Zh. Eksp. Teor. Fiz., 62, 1745 (1972) [ Sov. Phys.-JETP 35, 908 (1972)].
- [2] Burmasov V.S., Khilchenko A.D., Kruglyakov E.P., Lukuyanov V.N., Podyminogin A.A., Tsidulko Yu.A., Vyacheslavov L.N., In: Proc. 10th Europ. Conf. on Controlled Fusion and Plasma Physics, 1, C2, Moscow, 1981.
- [3] Arzhannikov A.V., Burdakov A.V., Vyacheslavov L.N., Koidan V.S., Postupaev V.V., Sinitskij S.L., Proc. of the Intern. Conf. On Plasma Physics, Lausanne, 1984, Inv. Paper, 1, p.285-309.
- [4] L.N. Vyacheslavov, V.F. Gurko, I.V. Kandaurov, E.P. Kruglyakov, O.I. Meshkov, A.L. Sanin and V.F. Zharov, Spectrum of plasma electrons observed in strong Langmuir turbulence driven by REB, in Proc. of 11th int. Conf. On High Power Particle Beams, Prague 1996, (to be published).
- [5] L.N.Vyacheslavov, E.P.Kruglyakov, M.V.Losev, and A.L.Sanin, Rev. Sci. Instrum. 64(6), 1398 (1993).



# BROADBAND MM RADIATION FROM BEAM DRIVEN STRONG TURBULENCE

M. Masuzaki, H. Yoshida, R. Ando, K. Kamada, A. Ikeda, C. Y. Lee and M. Kawada

*Department of Physics, Faculty of Science, Kanazawa University, Kanazawa 920-11, Japan*

## ABSTRACT

In order to measure broadband mm radiation emitted from relativistic beam electrons interacting with localized high frequency electrostatic fields in a strong Langmuir turbulent plasma, three types of spectrometer were prepared, a 6-channel filter-bank type covering K, Ka and U bands (18 - 60 GHz), a heterodyne type covering E band (60 - 90 GHz) and a full band detector covering F band (90 - 140 GHz). The spectrum of the mm radiation was measured radially, and also its angular distribution was measured at the end of the chamber. When the plasma frequency at the measuring position was about 13 GHz, the power level was high in K, Ka and U band range, but it decreased steeply in E and F band range. The angular distribution showed the radiation was intense in the axis. This implies the dipole moment of the caviton electric fields were not aligned to the beam direction.

## INTRODUCTION

When an intense relativistic electron beam (IREB) is injected into an unmagnetized or weakly magnetized plasma and the beam density is near the plasma density, high-power broadband electromagnetic radiation above plasma frequency is emitted [1 - 5]. On the other hand, in a similar situation several experiments show that localized strong oscillating electrostatic fields distribute in the plasma [6 - 8]. This phenomenon is interpreted as that the plasma becomes strong Langmuir turbulence state in which creation, collapse and burnout of cavitons are repeated [9]. Here a caviton is a density cavity in which large amplitude electrostatic waves are trapped. It has been shown experimentally that when the radiation is emitted the plasma is in a strong Langmuir turbulence state [10]. G. Benford and J. C. Weatherall proposed the collective Compton boosting model for the radiation [11]. Measurement of detail of the spectrum shape is necessary to compare the experimental results with the model. Our old observation window for the radiation was only K and Ka bands (18 - 40 GHz). However, as there was evidence of emission of radiation with higher frequencies, we widened the observation window up to F band, using a heterodyne spectrometer for E band (60 - 90 GHz) and a full band detector for F band (90 - 140 GHz).

## EXPERIMENTAL APPARATUS

The experimental conditions were the same as those in our previous experiments [2 - 4, 8, 10]. Figure 1 shows a schematic diagram of the experimental apparatus. A modified 110A produced by Physics International, which can generate accelerating voltage up to 1.5 MeV and diode current up to 27 kA with a pulse duration of 30 ns, was used to generate an IREB. The diode consisted of a carbon cathode of 3.6 cm in diameter and a titanium foil anode of 20  $\mu$ m thick. The anode-cathode distance was 3 cm. The drift chamber of stainless-steel was 16 cm in inner diameter and 16 cm long. It had two observation port at 17.5 cm downstream from the anode. The base pressure was kept below  $4 \times 10^{-5}$  Torr. A plasma was produced using a pair of rail-type plasma guns set up

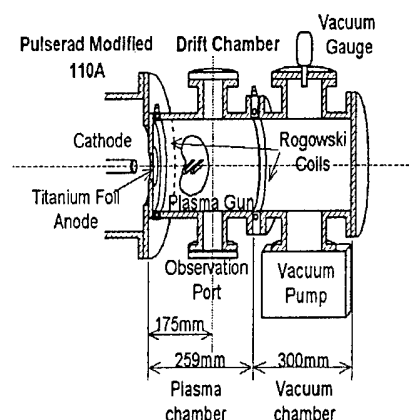


Fig. 1. The experimental setup.

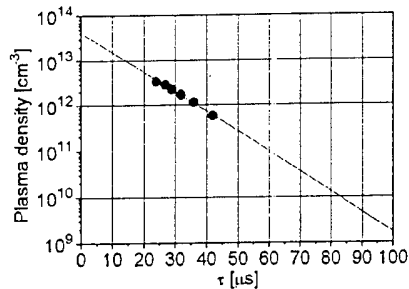


Fig. 2. The electron density vs.  $\tau$ .

posite to each other, which were installed at 10 cm downstream from the anode foil. The discharge current reached its peak about 8  $\mu$ s after the gun firing and decayed with the time constant of about 20  $\mu$ s. The plasma density,  $n_p$ , at 17.5 cm downstream from the anode was measured by a Langmuir probe and a microwave interferometer. Figure 2 shows the relation between  $n_p$  and the delay time,  $\tau$ , after the gun firing. An IREB of about 1.4 MeV and about 10 kA was injected into the plasma at a preset  $\tau$ , which was taken as a parameter during the experiment.

The mm radiation was measured radially and at the end of the chamber. Spectrometers used were; a filter-bank type one for K, Ka and U bands (18 - 60 GHz), a heterodyne type one for E band (60 - 90 GHz) and a full band detector for F band (90 - 140 GHz). The filter-bank type used was an improved one of the previously used 5-channel spectrometer. The heterodyne type spectrometer and the full band detector were newly constructed. Figure 3 shows a schematic diagram of the heterodyne type spectrometer and its setup for the radial measurement. It consisted of a downconverter unit, an IF unit and a power unit. The downconverter consisted of a bandpass filter, a variable attenuator, a mixer and a local oscillator with frequency of 50 GHz. The IF unit consisted of bandpass filters, Schottky diodes and pulse amplifiers. It covered 10 - 40 GHz in 5 channels. Filters and detectors used were diverted ones from the filter-bank type spectrometer. Calibration was made at 60 GHz. In this setup full band K, Ka and U band detectors were

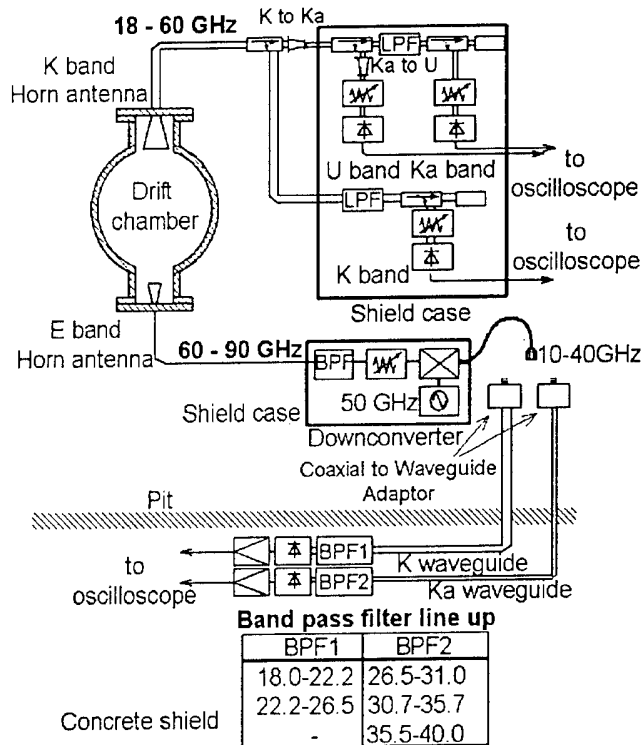


Fig. 3. The setup of the E band heterodyne spectrometer

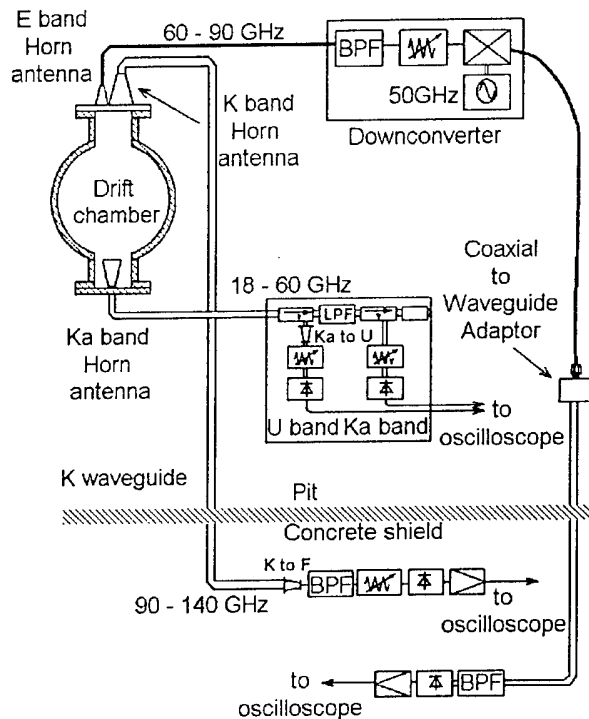


Fig. 4. The setup of the F band detector

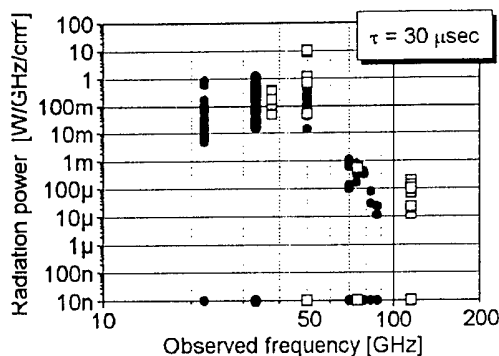


Fig. 5. An experimentally obtained spectrum

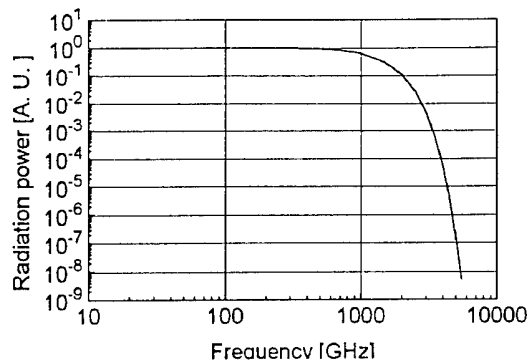


Fig. 6. An example of calculated spectrum

prepared, and simultaneous measurements were carried out. Figure 4 shows a schematic diagram of the F band detector and its setup for the radial measurements. It consisted of a bandpass filter, an attenuator, a Schottky diode, and a pulse amplifier. In this setup full band Ka, U and E band detectors were also prepared and simultaneous measurements were done.

### EXPERIMENTAL RESULTS AND DISCUSSIONS

Figure 5 shows a typical radiation spectrum observed at  $\tau = 30 \mu s$ , at which the plasma frequency was about 13 GHz at the measuring position. Results from two experimental runs are compiled into one. In one of them the setup shown in Fig. 3 was used, and in the other the setup shown in Fig. 4 was used. It was ascertained that radiation was emitted to at least about 140 GHz. The power level was high in K to U bands, but it decreased steeply in E and F bands.

We calculated radiation spectra according to the collective Compton boosting model [11]. In this model the broadband intense radiation is due to the interaction of the density modulated beam electrons with intense high frequency electric fields in cavitons, their characteristic charge density oscillation being assumed to be dipolar. Several spectral density function for the beam density modulation are assumed. Our calculations were done for each spectral density function and for each direction of the dipole moment. Figure 6 is an example for which Gaussian spectral density function and dipole moment perpendicular to the direction of the beam propagation are assumed. The experimental and calculated spectra resemble each other in shape qualitatively, although quantitatively they are very different. We could not find the calculated spectra which coincided with the experimental spectrum yet.

It is interesting to measure the angular distribution of the radiation. When the dipole moment of the caviton is parallel to the beam direction, intensity in

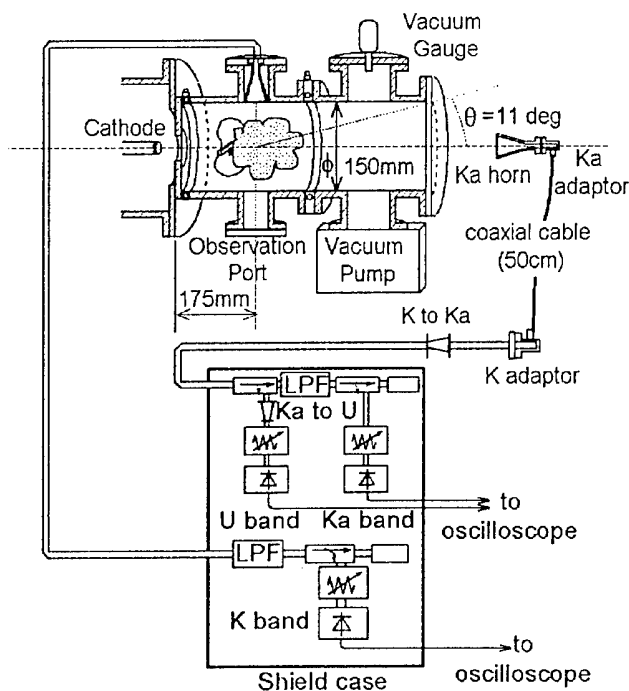


Fig. 7. The set up for measurement at the end of the chamber

the axis will be null. On the other hand, when the dipole moment is perpendicular to the beam direction, the intensity in the axis will be maximum. We measured the radiation in Ka band at the end of the chamber varying the horn position. Figure 7 shows the experimental arrangement. Figure 8 shows the measured radiation power as a function of angle. The radiation power observed was almost the same when the horn was rotated 90° around its axis. Now let all the dipole moment be aligned to the beam direction, since the electrostatic fields are produced by the beam-plasma instability and it may be natural to think that their direction is parallel to the direction of the beam propagation. In this case the radiation intensity in the axis would be very low level. However the observed power level was rather high in the axis. This result suggests that not all of the dipole moment were aligned to the beam direction.

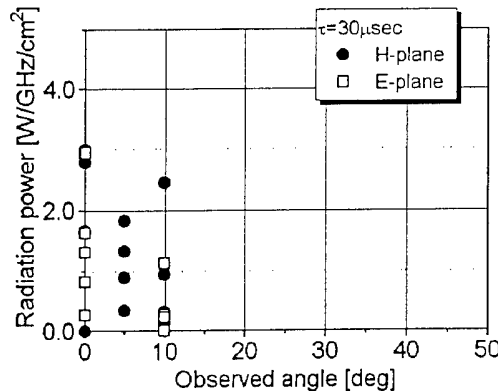


Fig. 8. Angular distribution of the radiation

## SUMMARY AND CONCLUDING REMARKS

In order to widen the observation window for measurement of radiation emitted when an IREB is injected into an unmagnetized plasma, we prepared a heterodyne receiver covering E band in 5 channels and a full band detector covering F band in addition to the 6-channel spectrometer covering K, Ka and U band. In the observed spectra, power level was high in the frequency region of K, Ka and U bands, but in the E and F band region it reduced to much lower level contrary to our expectation. We calculated radiation spectra according to the collective Compton boosting model, but could not find the spectrum which coincided with the experimental spectrum yet. However we still think that the radiation is due to beam electrons interacting caviton fields because of the following reasons. (1) The strong Langmuir turbulence state was found to be a necessary condition for the radiation [10], and (2) it was found that the wider the energy and angular spreads of the beam electrons due to the interaction with the caviton fields, the stronger the total power of the radiation [12]. Measurements of the angular distribution of the radiation suggest that not all of the dipole moments of the cavitons were aligned to the direction of the beam propagation.

We are now preparing spectrum measurement in the axial direction. Also we are forming a plan of measurements of the beam modulation to clarify the collective effect on the radiation.

The authors would like to thank S. Oyama and H. Tsukuda for their assistance in the experiments.

## References

- [1] K. G. Kato, G. Benford and D. Tzach, *Phys. Fluids*, **26**, 3636 (1983)
- [2] M. Masuzaki, A. Yoshimoto, M. Ishikawa, M. Yoshikawa, K. Kitawada, H. Morita and K. Kamada, *Proc. of the 8th Intern. Conf. on High-Power Particle Beams* (World Scientific, Singapore 1991) Vol. 2, p. 683.
- [3] M. Masuzaki, R. Ando, M. Yoshikawa, H. Morita, J. Yasuoka and K. Kamada, *Proc. of the 9th Intern. Conf. on High-Power Particle Beams* (NTIS PB92-206168, 1992) Vol. 2, p. 1227.
- [4] R. Ando, M. Masuzaki, K. Kobayashi, M. Yoshikawa, H. Morita, H. Koguchi, D. Yamada and K. Kamada, *Proc. of the 10th Intern. Conf. on High-Power Particle Beams* (NTIS PB 95-144317, 1995) Vol. 2, p. 933.
- [5] M. S. DiCapua, J. F. Camacho, E. S. Fulkerson and D. Meeker, *IEEE Trans. Plasma Sci.* PS-16, 217 (1988).
- [6] G. C. M. Janssen, E. H. A. Granneman and H. J. Hopman, *Phys. Fluids*, **27**, 736 (1984).
- [7] D. Levron, G. Benford and D. Tzach, *Phys. Rev. Lett.*, **58**, 1336 (1987).
- [8] M. Yoshikawa, M. Masuzaki and R. Ando, *J. Phys. Soc. Jpn.*, **64**, 3303 (1994).
- [9] P. A. Robinson and D. L. Newman, *Phys. Fluids*, **B2**, 3120 (1990).
- [10] M. Yoshikawa, M. Masuzaki, R. Ando and K. Kamada, to be published in *J. Phys. Soc. Jpn.*
- [11] G. Benford and J. C. Weatherall, *Phys. Fluids*, **B4**, 4111 (1992).
- [12] H. Koguchi, M. Masuzaki, M. Yoshikawa, S. Takahata, K. Toda, R. Ando and K. Kamada, paper P-1-9, in this Conference.

# SPECTROSCOPIC MEASUREMENTS OF TURBULENT LANGMUIR FIELDS AT THE RELATIVISTIC ELECTRON BEAM EXPERIMENT REBEX

Jiří Ullschmied, Milan Šimek, Karel Koláček, M. Řípa

*Institute of Plasma Physics, Czech Academy of Sciences  
P.O. Box 17, 182 00 Prague 8, Czech Republic*

## Introduction

The relativistic electron beam experimental facility REBEX operated in IPP Prague for already many years (cf. e.g. [1]) makes it possible to study the beam-plasma interaction in a large variety of beam and plasma parameters. The facility (Fig.1) consists of an electron beam accelerator and of a vacuum interaction chamber with plasma sources and external magnetic field system. Numerous beam and plasma diagnostics, and a sophisticated data acquisition system represent an integral part of the experiment.

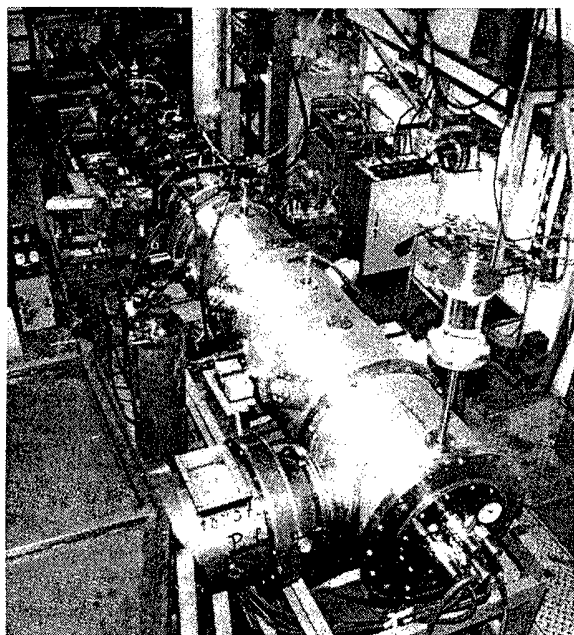


Fig. 1

The REBEX experiment

Primary source	8-stage Marx gen.
Erected voltage	640 kV
Erected capacity	1.7 nF
Pulse forming line	coaxial Blumlein type, water-insulated
High voltage diode	metallic plane cathode 5-20 $\mu\text{m}$ Al foil anode
Beam energy	400-500 kV
Beam current	50-70 kA
Pulse duration	100 ns
Beam diameter	40-50 mm
Magnetic field	0.4-1.0 T
Plasma source	coaxial gun
Plasma density	$5 \cdot 10^{14} - 5 \cdot 10^{15} \text{ cm}^{-3}$
Plasma radius	70 mm
Plasma col. length	1 - 1.5 m
Gas inlet	electromagnetic valve
Working gas	hydrogen
Chamber diameter	150 mm

Table 1

The most original feature of the REBEX facility it offers is perhaps the possibility to study the beam plasma interaction in two different beam regimes:

In the reflex regime, the electron beam is injected into a short plasma column and reflected back into the plasma by a virtual cathode arising spontaneously at the vacuum end of the plasma column.

In the single-pass regime, the electron beam impinges upon a grounded collector plate, which prevents it from being reflected back into the plasma.

The beam reflection increases effectively the interaction length and results in increasing the efficiency of the beam energy deposition in a plasma. Moreover, our experiments show that in both the reflex and single-pass regimes the mechanisms of beam energy transfer differ.

## REB-plasma interaction

In the investigated range of the electron beam and plasma parameters (see Table 1) the overall picture of REB-plasma interaction in REBEX corresponds well with the generally accepted two-stream instability concept [2,3]. A substantial increase of the plasma energy content during the beam injection (up to  $2 \cdot 10^{19}$  eV/cm) is witnessed e.g. by the observed diamagnetic signals [4], the example of which is shown in Fig.2. The heating of the plasma electron component was studied by soft X-ray diagnostics [5]. The oscillations seen on both the diamagnetic and the X-ray signals (cf. Fig.2 and 3) are caused by magnetoacoustic configurational oscillations of a dense magnetized plasma in a relatively weak REBEX magnetic field. These oscillations were successfully simulated by using an original model of the REB-heated plasma dynamics [6,7].

As the interaction results in a strongly non-equilibrium electron distribution and the tail electron escape freely along magnetic fields lines, the resulting

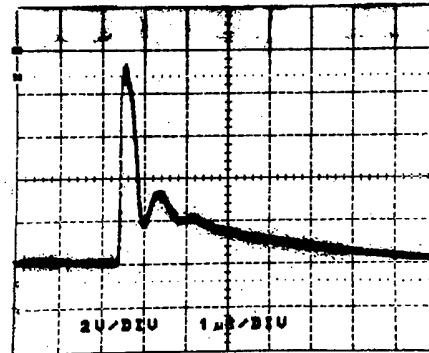


Fig. 2  
Typical REBEX diamagnetic signal

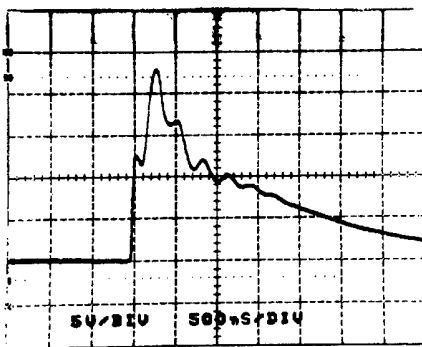


Fig. 3  
Example of the REBEX soft X-ray signal

electron temperature of plasma bulk remains relatively low (max 50-60 eV). The soft X-ray measurements did not show any substantial increase of the electron temperature even in the reflected beam regimes, even though the plasma energy content was found there to be by a factor of 3 higher than in the single-pass beam regimes.

Recently, also a fast (with a characteristic time  $\approx$  beam injection time, e.g. much less than that of the collisional energy transfer from electrons) ion heating in REBEX has been proved by using a 'double' time-of-flight analysis of charge-exchange neutrals [8]. and Fig. 4 There are basically two competing turbulent mechanisms which might be responsible for

the observed ion heating. The first one is the strong high-frequency Langmuir turbulence, the threshold of which is highly exceeded in REBEX conditions. Ions might be directly heated in collapsing Langmuir cavitons and due to non-linear decay processes of Langmuir waves. The second, somewhat less probable mechanism, is the ion acoustic turbulence induced directly by the beam current. The latter process may occur at beam currents exceeding the Alfvén limit, which is the case in most REBEX shots. Another proof of the heating of the ion plasma component was given by the spectroscopic measurements described below.

## Langmuir turbulence at REBEX

In the REBEX conditions, the high-frequency Langmuir fields can easily reach the extremely high amplitudes corresponding to a strongly turbulent state. Theoretical and experimental parameters characterizing the turbulent processes in REBEX (turbulence level  $\eta$ , wave or plasma energy density  $W$ , wave field strength  $E$ , and electron temperature of the plasma bulk  $T_e$ ) are summarized in Table 2. The value of  $W$  in the Rows 1,2,4,5,7 is the wave energy density, in the Rows 3 and 6 it is the energy deposited in a plasma per unit beam volume, and in the Row 8 the density of the kinetic energy of the beam.

Table 2

	parameter	$\eta$	W [J/m <sup>3</sup> ]	E [kV/cm]	T <sub>e</sub> [eV]
1.	Turbulence threshold for B=0	0.000097	0.47	3.2	-
2.	Turbulence threshold for B=0.6 T	0.0014	6.7	12.3	1.73
3.	Ohmic heating only	-	60.2	-	7.3
4.	Calculated from the temperature excess	0.057	273	78.5	22.7
5.	Calculated from Stark broadening (0.2 nm)	0.036	175	62.8	
6.	Calculated from the bulk temperature	-	247	-	30
7.	Calculated from quasi-hydrodynamic model	(0.194)	933	145	78,0 $\pm$ 20°
8.	Available in the beam	-	24300	-	-

The turbulence level in the *Row 4* is calculated from the observed growth of the plasma bulk temperature [9]; in the *Row 5* it is calculated from the observed broadening of the hydrogen H $\alpha$  line, interpreted according to [10] as the Stark broadening. It should be stressed that our interpretation is different: we assign most of this broadening to the thermal Doppler effect caused by hot ions.

The plasma bulk temperatures in *Rows 2* and *8* are calculated from the collisional energy transfer of waves at a given turbulence level, in *Row 3* from the collisional dissipation of the return current; the values of T<sub>e</sub> in *Row 4* and *6* are derived from the experiment.

Clearly, the Langmuir turbulence threshold is highly overcome in the REBEX experiment, nevertheless the turbulence level can hardly reach the maximum value calculated according to [11] (*Row 8*). In any case, most of the wave energy must be transferred to the tail plasma electrons (up to 700 J/m<sup>3</sup>). The turbulence level calculated from the temperature growth (*Row 4*) does not say much, as the turbulence can change substantially the effective collisional frequency. For the same reason the contribution of the return current may be underestimated. The situation is even more complicated in the typical for the REBEX experiment reflected beam regimes, in which the drifting reflected beam electrons may substantially increase the level of the ion acoustic turbulence.

The amplitude of the turbulent Langmuir fields is extremely difficult in the REBEX conditions. First, due to an unpleasant frequency range (submillimeters) and, second, due to the extreme space and time localization of the Langmuir packets. In such a situation the only way out seemed to be to estimate the Langmuir field strength from the measured Stark component of the plasma emission lines.

#### Spectroscopic measurements at REBEX

Three different spectroscopic apparatuses have been used for detailed measurements of profiles of Balmer series emission lines [12]:

The first one was a six-channel polychromator with a photomultiplier detection system, the scheme of which is shown in Fig. 4. Its spectral and time resolution amounted to

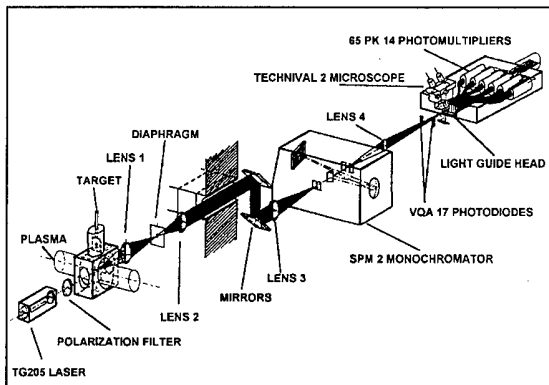


Fig.4  
The 6-channel polychromator system

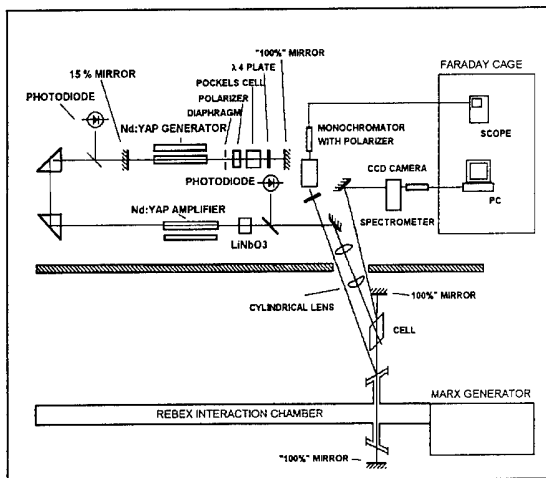


Fig. 5

The dye laser absorption spectrometer

resolved measurements of the intensity and width of the  $H_\alpha$  and  $H_\beta$  emission lines, while its sensitivity and spectral resolution proved to be too low for performing any detailed studies of the line shape, and of the line wings in particular.

Contrary, the intracavity laser absorption spectrometer with a CCD camera has an excellent spectral resolution, nevertheless the time dependencies of the line shape can be constructed on the shot-to-shot basis only. Moreover, the spectral resolution of the spectrometer was substantially deteriorated by a persistent stochastic modulation of the dye laser spectra. Thus, the behaviour of the line shapes might be studied just on a statistical basis, providing that a sufficient number of identical shots is collected.

Thus, the line profile measurements performed up to now were too rough for the Stark component of the lines to be distinguished and gave just an upper estimate for the amplitude of h.f. Langmuir fields:  $E \leq 30$  kV/cm. As for the line widths, both methods gave almost identical results: the hydrogen emission lines broaden fast during the beam injection up to 0.4 nm [cf. 8,13]. Most of this broadening seems to be due to the thermal Doppler effect.

The new spectroscopic system with a gated computer-controlled Jobin-Yvon detection head combines the advantages of the two systems used before. Preliminary test measurements suggest that both the sensitivity and the spectral and time resolutions of the system might be sufficient for studies of profiles of the most intense emission lines at the REBEX experiment, nevertheless the final results are expected to be obtained only in the second half of the year.

This work has been supported in part by the Grant Agency of the Czech Academy of Sciences under contracts No 14358 and A1043504

## References:

- [1] V. Babický et al.: Proc. BEAMS'90, July 2-5 1990 Novosibirsk, Vol. I, p. 225
- [2] Thode L.E., Sudan R.N: Phys.Fluids **18** (1975) 1564
- [3] Cheung P.Y., Wong A.Y.: Phys.Fluids **28** (5) 1985
- [4] V. Piřil et al.: Proc BEAMS'92, May 25-29 Washington, Vol. II, p. 1221
- [5] J. Rauš, V. Babický: Czech. Jour. Phys., **42** (1992), No. 4, p. 395
- [6] J. Ullschmied, M. Člupek: Proc. 16th Symp. on Plasma Phys. and Tech., Prague 1993, p. 27 (inv. paper)
- [7] J. Ullschmied: Proc. 17th Symp. on Plasma Phys. and Tech., Prague 1995, p. 147
- [8] J. Ullschmied et. al.: Proc BEAMS'94, June 20-24 San Diego, Vol. II, p. 735
- [9] I.V. Kandaurov et al.: Proc. BEAMS'90, July 2-5 1990 Novosibirsk, Vol. I, p. 233
- [10] V.S.Burmasov et al.: Proc BEAMS'94, June 20-24 San Diego, Vol. II, p. 590
- [11] Thode L.E.: Phys.Fluids **19** (1976) 305
- [12] K. Koláček et. al.: Proc BEAMS'92, May 25-29 Washington, Vol. II, p. 1337
- [13] K. Koláček et. al, Proc. BEAMS'90, July 2-5 1990 Novosibirsk, Vol. II, p. 835

0.08 nm/channel and 20 ns, respectively [13].

The second one was of the intracavity laser absorption spectrometer type, with a 256-pixel CCD camera detection system that made it possible to increase the spectral resolution up to 0.004 nm/pixel. The time resolution of this spectrometer - 40 ns - was given by the pulse duration of the dye laser used [8].

Recently, a new spectroscopic system consisting of the 2-m spectrometer PGS2 Carl Zeiss Jena and of a 512-pixel detecting head (Jobin Yvon) with a computer control system (SPECTRALINK Jobin Yvon) has been introduced.

The time resolution of the first spectroscopic system was quite sufficient for time-



## HIGH POWER MICROWAVE EMISSION AND DIAGNOSTICS OF MICROSECOND ELECTRON BEAMS

R.M. Gilgenbach, J.M. Hochman, R. Jaynes, J.I. Rintamaki,  
Y.Y. Lau, J. Luginsland, and J.S. Lash  
*Intense Energy Beam Interaction Laboratory*  
*Nuclear Engineering and Radiological Sciences Dept.*  
*University of Michigan*  
*Ann Arbor, MI 48109-2104*

T.A. Spencer  
*Air Force Phillips Lab*  
*Kirtland AFB, NM*

### Abstract

Experiments have been performed to generate high power, long-pulse microwaves by the gyrotron mechanism in rectangular cross-section interaction cavities. Long-pulse electron beams are generated by MELBA (Michigan Electron Long Beam Accelerator), which operates with parameters: -0.8 MV, 1-10 kA, and 0.5-1 microsecond pulselength. Microwave power levels are in the megawatt range. Polarization control is being studied by adjustment of the solenoidal magnetic field. Initial results show polarization power ratios up to a factor of 15. Electron beam dynamics ( $V_{\text{perp}}/V_{\text{par}}$ ) are being measured by radiation darkening on glass plates. Computer modeling utilizes the MAGIC Code for electromagnetic waves and a single electron orbit code that includes a distribution of angles.

### Introduction

High power/ energy microwaves have important applications to radar systems, plasma heating, and industrial processing. A challenge in utilizing high power microwaves for applications is to control the polarization for launching in an appropriate antenna. One approach to polarization control is the rectangular-cross-section (RCS) gyrotron [1]. A related concept is the active-circulator-gyrotron, which operates in tapered rectangular waveguide and has been studied theoretically [2]. Initial UM experiments have concentrated on a RCS gyrotron oscillator to study issues including microwave polarization control, mode competition, and pulse shortening [3].

Electron beam diagnostics are also a crucial part of high power microwave experiments. In the gyrotron, the alpha ( $V_{\text{perp}}/V_{\text{par}}$ ) determines the maximum efficiency. In this paper, we extend the interpretation of an e-beam diagnostic which exploits radiation darkening on glass plates [4].

### Experimental Configuration

Figure 1 depicts the experimental configuration of the rectangular-cross-section gyrotron. The electron beam is generated by the Michigan Electron Long Beam Accelerator (MELBA) which operates at parameters: Voltage = -0.8 MV, Current = 1-10 kA, and pulselength = 0.5-1  $\mu\text{s}$  (adjustable by crowbar switch delay). An annular electron beam is generated by explosive emission from a  $(2.25 \pm 0.25 \text{ cm})$  radius bare aluminum strip on a Glyptal-coated cathode. The graphite anode has a 4.55 cm radius aperture. The diode region is surrounded by large magnetic field coils which generate about 1 kG. The electron

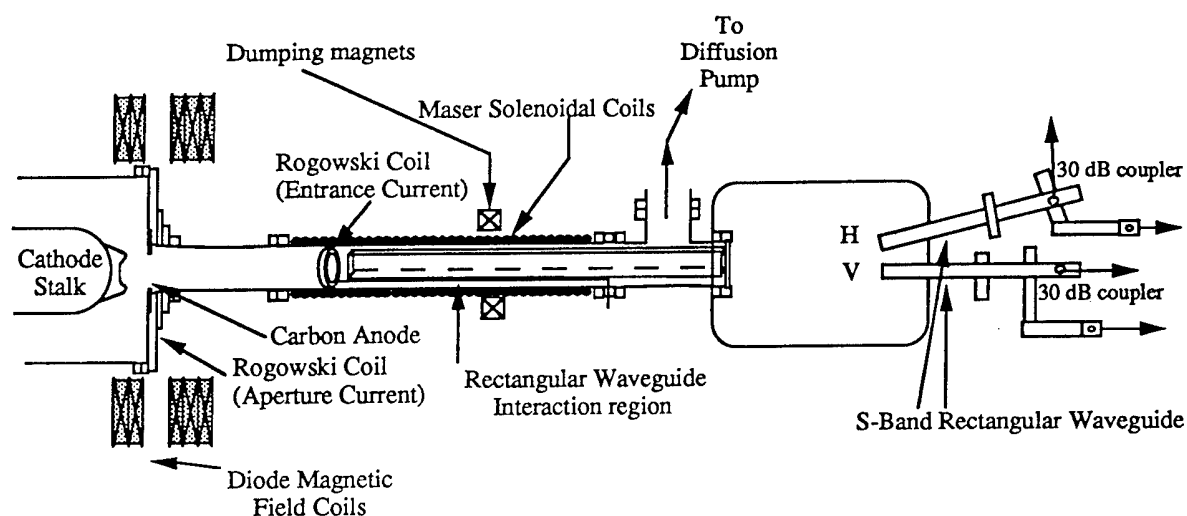


Fig. 1. Experimental configuration of rectangular-cross-section gyrotron. The upper receiving waveguide detects horizontally polarized radiation; the lower waveguide detects vertical polarization.

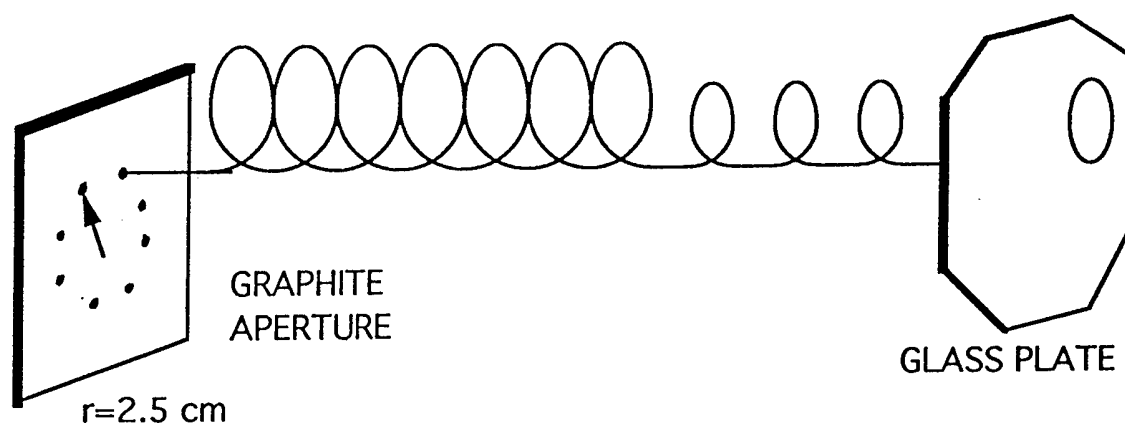


Fig. 2. Schematic illustration of apertured graphite anode and glass plate for radiation darkening diagnostic of electron beam dynamics.

beam is adiabatically compressed by an increasing magnetic field (adjustable 2-4 kG) of the solenoidal interaction region. The 21-cm-long, rectangular interaction cavity is fabricated of two sections of S-band waveguide modified by removing the broadwalls and soldering together to give dimensions of 5.4 cm by 7.2 cm. An aperture (2.6 cm radius) is located at the entrance end of the interaction cavity. The exit end of the cavity has removable copper strips which are used to vary the cavity Q. The microwave output is directed through a rectangular waveguide section with the same cross section as the cavity.

The high power microwave emission is radiated into a large chamber lined with microwave absorber. In this chamber are located two open ended S-band waveguides rotated 90 degrees with respect to one another. The entrances of the waveguides have thin copper wires laced, so as to prevent cross polarized electric field components from entering at higher frequencies. Directional couplers and attenuators lower the microwave power to the level which can be transmitted by coaxial cable to the Faraday cage. Inside the Faraday cage, the frequency is diagnosed by a four-channel (2-2.5, 2.5-3, 3-3.5, 3.5-4 GHz) filter system fabricated by microstrip circuits.

Electron beam diagnostic experiments (Figure 2) utilize a 3 mm-thick, graphite anode with eight apertures of diameter 1 mm drilled on a circle of radius 2.5 cm. The electron beamlets are spun up by the adiabatically increasing magnetic field. A glass witness plate is located in the uniform magnetic field region. The radiation darkened patterns (typically after 10-15 shots) are dark enough to analyze visually.

For comparison, a computer code has been written to model the trajectories of single electrons. An angular distribution of electrons is input to the code and the x-y position of each electron is plotted at the axial (z) position which corresponds to the glass plate. These patterns are then compared to experimental data.

### Experimental Results

Figure 3 shows typical waveforms for a high power microwave pulse. The MELBA voltage is very flat for over 0.5  $\mu$ s. Electron beam current shows only slight fluctuations. The microwave power is shown for both horizontal (H) and vertical (V) polarizations in Figure 3. The H polarization has a peak power of about 2 MW, while the V polarized emission is about 0.5 MW. Both polarizations exhibit microwave pulse shortening, an area for future study.

Figure 4 shows a comparison between experimental radiation darkened pattern of a single beamlet (outlined and cross-hatched) and the computed electron trajectories. These data were for a case where the cathode radius (3.5 cm) was mismatched to the radius of the aperture pattern (2.5 cm). This results in a half-spiral pattern, which agrees well between experiment and code for an average alpha ( $V_{\text{perp}}/V_{\text{par}}$ ) of 0.3.

### Acknowledgments

\* Research supported by the AFOSR MURI program through a subcontract from Texas Tech Univ. and by Northrop Grumman Corp.

### References

- [1] D.J. Radack, K. Ramaswamy, W.W. Destler, and J. Rodgers, J. Appl. Phys. 73, 8139 (1993)
- [2] Y.Y. Lau, L.R. Barnett, J.M. Baird, IEEE Trans. Elect. Dev. ED-31, 337 (1984)
- [3] R.M. Gilgenbach, J.M. Hochman, R. Jaynes, M.T. Walter, J.I. Rintamaki, J.S. Lash, Y.Y. Lau, J. Luginsland, and T.A. Spencer, Proc. of Twentieth International Conference on Infrared and Millimeter Waves, Dec. 1995, Orlando, FL
- [4] J.J. Choi, R.M. Gilgenbach, T.A. Spencer, P.R. Menge, and C.H. Ching, Rev. Sci. Inst. 63 1671 (1992)

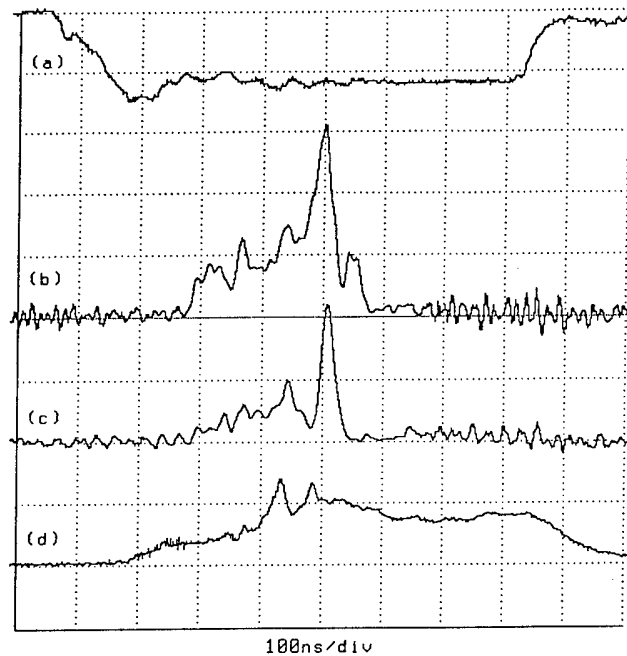


Fig. 3. Experimental signals (cavity oriented with longer dimension horizontal):  
 a) Electron beam voltage (620 kV/div)  
 b) Microwave signal (horizontally polarized); peak power  $\sim 2$  MW,  
 c) Microwave signal (vertically polarized); peak power  $\sim 0.5$  MW,  
 d) Electron beam current before entrance to cavity (1.7 kA/div).

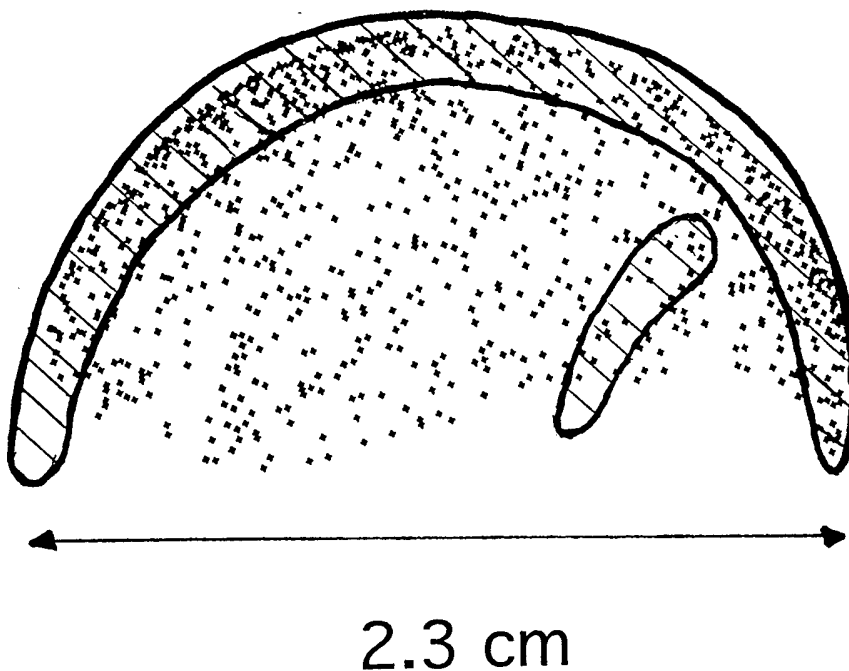


Fig. 4. Comparison of experimental radiation darkened region (outline and cross hatching) versus electron trajectory code with skewed angular distribution to account for mismatch between cathode radius (3.5 cm) and aperture pattern radius (2.5 cm).

## MULTI-STAGE AUTOACCELERATION OF AN INTENSE RELATIVISTIC ELECTRON BEAM

K. Kamada, D. Hasegawa, H. Igarashi, T. Kusunoki,  
C.Y. Lee, H. Koguchi, R. Ando and M. Masuzaki

*Department of Physics, Faculty of Science, Kanazawa University,  
Kanazawa, 920-11, Japan*

### Abstract

Two-stage autoacceleration is accomplished by using different length cavities. Two cavities are located with the distance longer than the beam duration. The electron kinetic energy increases from 500 to 700 keV at the first stage and from 700 to 900 keV at the second, while the beam duration decreases 10 to 5 ns at the first stage and 5 to 2.5 ns at the second.

An intense relativistic electron beam (IREB) generation with particle energies exceeding 10 MeV and/or with sub-nanosecond pulse width involve physics, engineering and financial problems.<sup>1)</sup> Autoacceleration is an energy transfer process for an IREB from the first half of the beam pulse to the second half by only using a passive coaxial cavity structure. The beam energy increases at the expense of pulse length. The autoacceleration process is potentially simple approach to a sub-ns electron beam with high particle energies. One stage autoacceleration experiments with various energies of IREB were reported extensively in the 1970s.<sup>2-5)</sup> Multicavity au-

toacceleration experiments with the same length cavities had also already been reported.<sup>6,7)</sup> In reference 6, the concept of a collective autoaccelerator was realized. An electron beam of 200 keV, 800 ns was accelerated to 3 MeV, 6 ns with a two cavity system. The energy of the beam electrons was transferred to a small part of the beam.

In our scheme of the multi-stage autoacceleration, the length of the  $n+1$  th cavity is the half of that of the  $n$  th cavity. An IREB is expected to decrease its pulse width to half at each stage with increase of its particle energy to double ( in other words, IREB compression ) as shown in Fig.1.

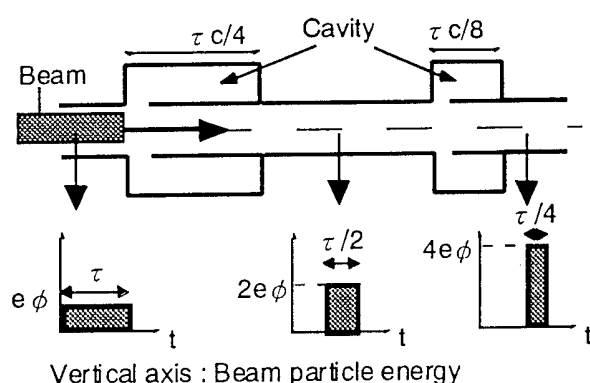


Fig. 1. Schematic of 2-stage autoacceleration.

The beam energy increases from  $e\phi$  to  $4e\phi$  at the expense of pulse length ( $\tau$  to  $\tau/4$ ).

A Pulserad 105A ( Physics International ) which utilized a conventional Blumlein line is used as a beam source. A 650 kV, 16 kA, 10 ns pulse is available to a matched load. Schematic of the experiment is shown in Fig. 2. An annular electron beam with a diameter of 2.4 cm and a thickness of 1 mm is injected into a 3 cm i.d., 3 m long conducting drift tube. Long pulse (10 ms) axial magnetic field of 1 T is applied by solenoid coils with total length of 3 m. The first coaxial cavity connecting to the drift tube through an accelerating gap is located 1 cm downstream side

of the anode ( $z=1\text{cm}$ ). The cavity length and impedance are 75 cm ( a quarter of the 10 ns beam length ) and 50 ohm, respectively. The second cavity length is 37.5 cm ( a half of the first cavity ) with the same impedance. To avoid the interference between cavities through the beam, the second cavity is located 2 m ( longer than the length of the 5 ns beam compressed by the first cavity ) apart from the first cavity. The beam current is measured by a Faraday cup. The base pressure in the system is maintained below  $1 \times 10^{-5}$  Torr.

Typical waveforms of the diode voltage ( $V_d$ ), the diode current ( $I_d$ ) and the beam current ( $I_b$ ) are shown in Fig. 3. The peak voltage of the diode is  $\sim 500$  kV. The beam current is typically 3.5 kA with the half width of  $\sim 10$  ns. The beam particle energy is estimated by placing aluminum foils in front of the Faraday cup and measuring the transmitted current. The Faraday cup waveforms with different

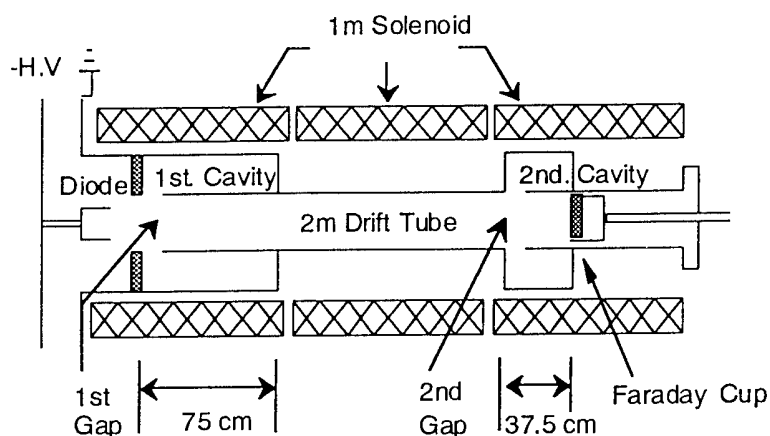


Fig. 2. Schematic of the experiment.

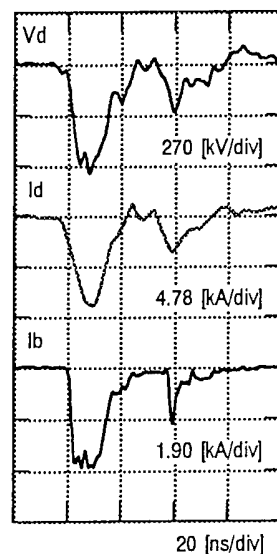


Fig.3. Typical waveforms.

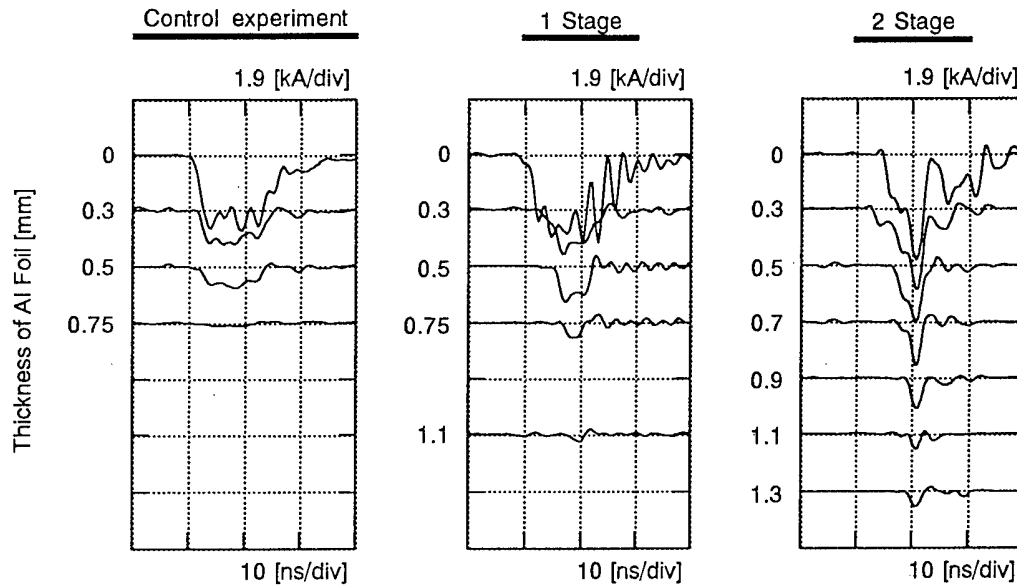


Fig.4 Faraday cup waveforms with different thickness of aluminum foils.

foils are shown in Fig. 4. The beam current in the control experiment without foil appears smaller than the current shown in Fig.3 because of the attachment device of the foil. In the control experiment, the cavities are not mounted. The beam propagating through the drift tube without the accelerating gap is detected at  $z = 42$  cm. In the one-stage ex-

periment, the Faraday cup is located at  $z = 42$  cm between the first and the second gaps. In the two-stage experiment, the beam current passing through the first and the second gaps is monitored at  $z = 250$  cm. The trailing part of the beam waveforms is seen to increase its energy at the expense of the pulse width with increase of the number of stages.

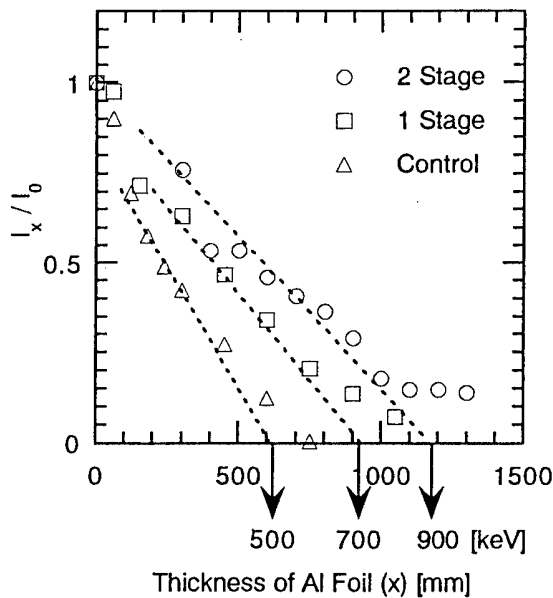


Fig. 5. Relative beam current through different thickness of aluminum foils.

The ratio of the transmitted current,  $I_x$ , through different thickness of aluminum foils to the current,  $I_0$ , detected without foil is plotted against the thickness of aluminum foils,  $x$ , in Fig. 5. The particle energies of control, one-stage and two-stage experiments are estimated to be 500, 700 and 900 keV, respectively, by the range-energy relations for relativistic electrons. The estimated values of the acceleration voltage at each gap (200 kV) are roughly equal to the product of the beam current (3.5 kA) and the cavity impedance (50 ohm).<sup>4)</sup>

According to the simple model of autoacceleration<sup>5)</sup>, the electrons in the first half of

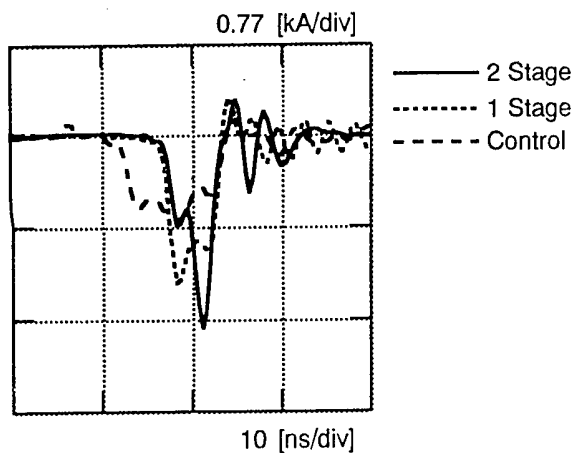


Fig. 7. Faraday cup waveforms passing through 0.5 mm aluminum foil.

the beam duration lose their kinetic energy, and those in the second half gain the same amount of energy. The Faraday cup waveforms passing through 0.5 mm aluminum foil are shown in Fig. 7. The first half of the beam waveform of the one- and two- stage experiments clearly disappeared. The rough estimation of the lost energy of the electron in the first half agrees with the gain energy of the second half.

The waveforms of the two-stage experiment show the effect of two cavities in accordance with the model mentioned above. The characteristic times of the first and the second cavity to influence the beam are 5 and 2.5 ns, respectively. The beam electrons of the two-stage experiment in 0-2.5 ns of the beam duration lose their energy twice by the 2 cavities. Those in 2.5-5 ns are decelerated by the first cavity and accelerated by the second cavity. Those in 5-7.5 ns are accelerated by the first cavity and decelerated by the second cavity. Those in 7.5-10 ns are accelerated by both cavities. In Fig.7, the beam with the energy of 900 keV ( gain the energy

twice) appears in 7.5-10 ns from the current rise of the control waveform, and the beam with the lower energy is observed in 5-7.5 ns.

The long distance between the first and second cavities makes the experimental result of the two-stage autoacceleration clear. When the second cavity is set just behind the first cavity, the Faraday cup waveform detected downstream side of the second gap shows surplus peaks that indicate the interaction between two cavities. The arrival time analysis of the peaks infers that the surplus peaks originate in the reflection at the gaps. This result also suggests that the impedances of the cavity and the accelerating gap play an important role in this experiment.

The multi-stage autoacceleration using cavities with decreasing lengths is demonstrated experimentally. The limitation of this scheme lies how short the cavity length can be. Now we are trying to obtain the beam with an energy of  $> 2$  MeV and width of 1.25 ns.

The authors gratefully acknowledge Mr. M. Miyamoto and Mr. H. Tsukuda for their helpful assistance.

#### REFERENCES

- [1] M. Friedman, Phys. Rev. Lett. 31, 1107 (1973).
- [2] L. N. Kazanski, A. Kiisletsov and A. N. Lebedev, At. Energ. 30, 27 (1971).
- [3] M. Friedman, Phys. Rev. Lett. 32, 92 (1974).
- [4] I. A. Grishaev, A. N. Debik, V. V. Zakutin, I. I. Magda, Yu. V. Tkach and A. M. Shenderovich, Sov. Phys. Tech. Phys. 19, 1087 (1975).
- [5] M. Friedman, Appl. Phys. Lett, 41, 419 (1982).
- [6] T. R. Lockner and M. Friedman, J. Appl. Phys. 51, 6068 (1980).
- [7] M. Friedman, V. Serlin, Y. Y. Lau and J. Krall, Phys. Rev. Lett, 63, 2468 (1989).



# TRANSPORT CONTROL OF INTENSE ELECTRON BEAM USING INSULATOR GUIDE

M. Mori, S. Nishiyama, S. Kawata, S. Hanamori,  
K. Naito<sup>1</sup>, S. Kato<sup>1</sup>, Y. Kawakita<sup>1</sup>, M. Hakoda<sup>1</sup>

*Department of Electrical Engineering, Nagaoka University of Technology,  
Nagaoka 940-21, Japan*

<sup>1</sup>*Nissin Electric Co., Ltd., Kyoto 615, Japan  
e-mail: kawata@voscc.nagaokaut.ac.jp*

## Abstract

We present a new interesting feature in an intense-electron-beam transportation system using an insulator guide: the ion extraction from a plasma generated at the insulator surface is self-regulated by the net space charge of the electron beam in order for the effective charge neutralization. This paper also presents a numerical study on a plasma generation effect at the insulator guide surface on an intense-electron-beam transportation through the insulator beam guide. The plasma at the insulator surface is generated by the local electric field which is created by beam electrons. The ion extraction from the plasma is delayed by the plasma-generation time. The simulation results present that 1) the head of the electron beam pulse is used to generate the plasma, and 2) the electron beam transport efficiency is not fatally but slightly degraded.

## Introduction

In order to utilize pulsed power technologies and particle beams effectively,[1-5] we proposed a new system[4,5] for an intense-electron-beam transportation by using an insulator guide: a fraction of beam electrons hits the insulator surface, and generates a local electric field, which induces local discharges. The local discharges produce a plasma at the insulator surface. By the electron beam net charge, ions extracted from the plasma at the insulator surface expand over the transport guide region which is covered by the insulator beam guide. Then the ions are extracted from the guide region by the electron beam charge into the outer region which is not covered by the insulator. After the ion expansion into the outer region, the beam charge is neutralized effectively by the ions in the whole transport region. Consequently, the electron beam propagates through the short insulator beam guide.

## Intense-Electron-Beam Transport

In this paper we present numerical simulation results for the intense-electron-beam transport using the insulator guide.

The simulation results show that the following interesting feature of self-regulated effective charge neutralization: the ion extraction from the plasma generated at the insulator surface is controlled by the beam net charge.[5] Consequently advantages of our system are 1) the self-regulated charge neutralization, and 2) the simplicity of the system.

This paper also presents a numerical study on a plasma generation effect at the insulator guide surface on an intense-electron-beam transportation through the insulator beam

guide. The ion extraction from the plasma is delayed by the plasma-generation time. Consequently the electron beam charge neutralization is also delayed by it. However the simulation results present that only the head of the electron beam pulse is used to generate the plasma, and the electron beam transport efficiency is not fatally but slightly degraded.

Figure 1 shows a model for electron beam transportation in a vacuum through the insulator beam guide. The self-regulated charge neutralization is a unique feature in the transportation system. However, the current is not neutralized. Therefore the beam is pinched by the self-magnetic field. In order to prevent the pinching, an external parallel static magnetic field is required.[4] We study the plasma generation effect on the intense-electron-beam transportation by a computer simulation.

Our simulation model employed is as follows: we assume that the phenomenon concerned is cylindrically symmetric. In this work, we employ the following plasma generation model: a magnitude of electric field is monitored, and a local plasma is generated at each mesh at the insulator beam guide surface, when the magnitude of electric field at the guide surface is beyond the threshold[2] for a local discharge which generates the plasma. We also assume that the plasma consists of protons and electrons, and that the thickness of the plasma layer is infinitesimal; a sufficient amount of plasma is generated at the insulator surface so that the charged particles emitted from the insulator inner surface are limited by the space charge.[1] The beam outer radius coincides with the inner radius of the insulator. We assume that the outermost boundaries of the computational area are conductors. In this study, we carry out a particle-in-cell (PIC) simulation.[6] The PIC code used is a 2.5-dimensional one. The field components  $(E_r, E_z, B_\theta)$ , and the particle position and velocity  $(r, z, v_r, v_\theta, v_z)$  are solved by using the Maxwell equations and the relativistic equation of motion. In the system an external parallel static magnetic field  $B_{z0}$  is applied. At the time  $t = 0$ , the transport area is in a vacuum. The beam-parameter values employed in this paper are as follows: for the input electron beam wave form the maximum current is 25 kA, the maximum particle energy 150 keV, the pulse width 200 ns, and the rise and fall times are 20 ns. The beam radius  $r_b$  is 3.0 cm. The average longitudinal speed  $v_{z0}$  of the beam electrons injected is determined by the input wave form, and the beam temperature is 10 eV. The average  $v_{z0}$  is  $0.63c$  at  $z = 0$ . Here  $c$  is the speed of light. At the beam entrance, that is,  $z = 0$ , the beam electrons pass through cylindrically symmetric ring slits with an aperture ratio of 70 %; the aperture ratio is defined as (the total slit aperture area)/(the total area of  $\pi r_b^2$ ). The transport computation area is  $0 \leq z \leq Z_l (= 10.0 \text{ cm})$  and  $0 \leq r \leq R_l (= 5.0 \text{ cm})$  (see Fig. 1). The relative permittivity of the insulator beam guide is 5.[5] The external parallel static magnetic field  $B_{z0}$  is 0.20 T. By using the parameter values, the peak magnetic field at the beam outer radius is estimated to be 0.17 T, which is comparable to  $B_{z0}$ . The threshold for a local discharge which generates the plasma is assumed to be  $1 \times 10^7 \text{ V/m}$ . [2] The peak electric field generated by the electron beam is  $7.93 \times 10^7 \text{ V/m}$  at the insulator inner surface.

The particle maps for the beam electrons and the particles emitted from the insulator inner surface are shown in Fig. 2. The plasma is generated until 11.5 ns in this case. After that, the ions extracted from the insulator inner surface expand over the transport area. The beam electrons are transported through the volume in which the extracted ions exist. The ion cyclotron radius is sufficiently large compared with the beam radius[4]. Therefore the ions expand over the transport area. Figure 3 presents histories of total space charges of the beam electrons and the ions in the transport region. During the first 120 ns, the

ions emitted are expand over the whole transport region. After that, the beam electrons are transported well. Figure 3 also shows the self-regulated feature of the system. The electron beam current wave forms are shown in Fig. 4. Figures 4(a) and 4(b) show the current wave forms at  $z = 4$  cm and  $z = 8$  cm, respectively. The transport efficiency, which means a ratio of the electron beam total charge to the total input charge injected at  $z = 0$ , is 47.8 % at  $z = 4$  cm and 44.1 % at  $z = 8$  cm. The transport efficiency is slightly degraded compared with the previous results [5] in which the plasma generation effect is not included: in the case without the plasma generation effect, the transport efficiency was 63.3 % at  $z = 4$  cm and 58.1 % at  $z = 8$  cm. When we change the threshold of the local discharge to  $0.5 \times 10^7$  V/m, the plasma is generated at the insulator surface before 6 ns, and the transport efficiency is 52.2 % at  $z = 4$  cm and 49.3 % at  $z = 8$  cm.

## Conclusions

In this paper, we studied the plasma generation effect on the electron beam transportation through the insulator beam guide. The time lag of the plasma formation is numerically included in the present study. The simulation results present that 1) the self-regulated charge neutralization, 2) the head of the electron beam pulse is used to generate the plasma, 3) the electron beam transport efficiency is not fatally but slightly degraded, and 4) the simplicity of the system. Consequently, the electron beam propagated efficiently through the insulator beam guide.

- [1] R. B. Miller: *An Introduction to the Physics of Intense Charged Particle Beams* (Plenum, New York, 1982).
- [2] H. C. Miller: IEEE Trans. Electr. Insul. **24** (1989)765.
- [3] T. Vijayan, P. Roychowdhury and S. K. Iyyengar: IEEE Trans. Plasma Sci. **22** (1994)199.
- [4] S. Nishiyama, S. Kawata, K. Naito, S. Kato and M. Hakoda: Jpn. J. Appl. Phys., **34** (1995)L520.
- [5] S. Kawata, S. Nishiyama, M. Mori, K. Naito, S. Kato and M. Hakoda: Jpn. J. Appl. Phys., **35** (1996)L120.
- [6] A. B. Langdon and B. F. Lasinski: Meth. Comp. Phys. **16** (1976)327.

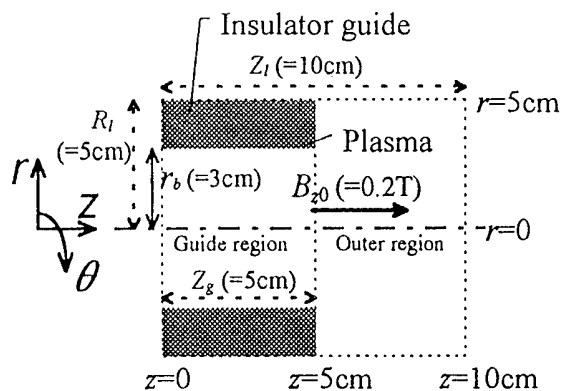


Fig.1 Electron beam transport through an insulator beam guide. The beam radius  $r_b$  is 3.0cm. The insulator guide length  $Z_g$  is 5cm. The external parallel static magnetic field is applied. A fraction of beam electrons hits the insulator surface, and generates a local electric field, which induces local discharges. The local discharges produce a plasma at the insulator surface. By the electron beam net charge, ions extracted from the plasma at the insulator surface expand over the transport guide, and neutralize the electron beam space charge in a self-regulated manner.

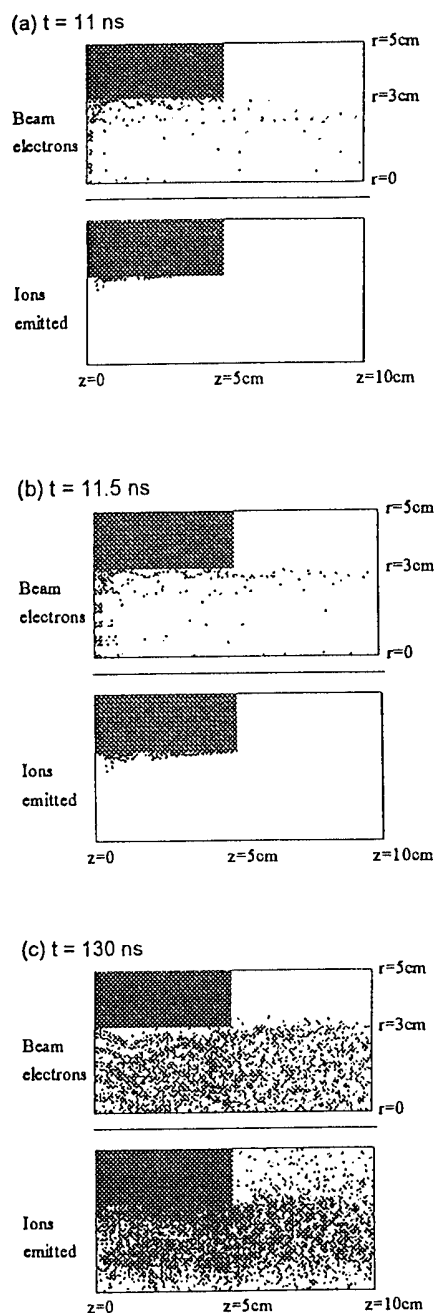


Fig2 Particle maps: (a) at  $t=11$  ns, (b) at  $t=11.5$  ns and (c)  $t=130$  ns. The upper map shows the beam electrons and the lower shows the ions emitted from the insulator inner surface. During the first 11.5 ns, the plasma generated covers the whole insulator surface. In this case the threshold for the local discharge which generates the plasma is assumed to be  $1 \times 10^7$  V/m.

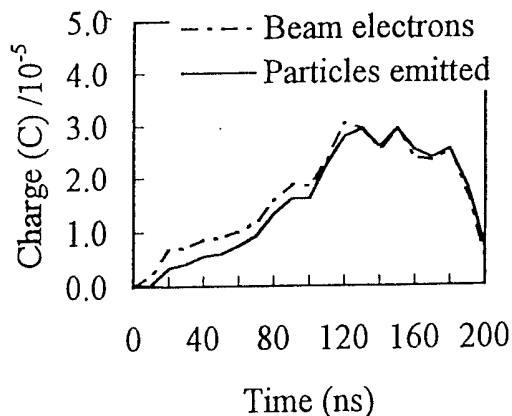


Fig3 Histories of the total space charges of the electrons and the ions in the transport region. The ions emitted neutralize the electron beam space charge in a self-regulated manner.

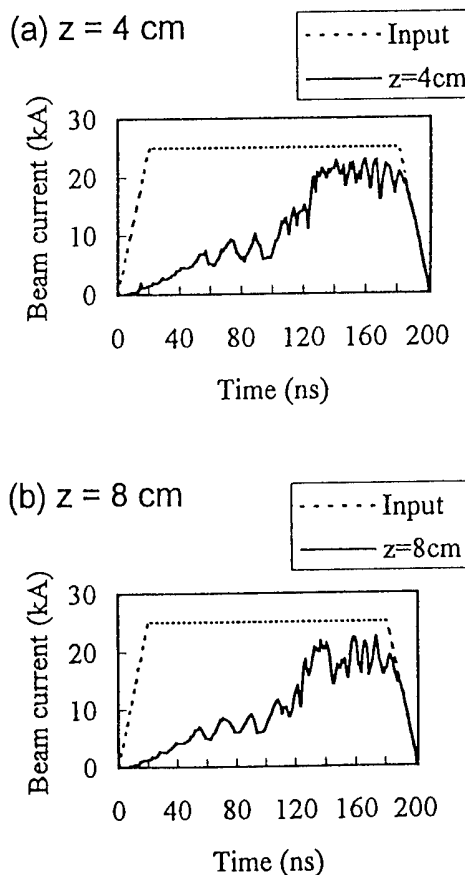


Fig4 Electron beam current wave forms: (a) at  $z=4$  cm and (b) at  $z=8$  cm. The transport efficiency is 47.8% at 4 cm and 44.1% at 8 cm.

# GENERATION AND TRANSPORTATION OF LOW-ENERGY, HIGH-CURRENT ELECTRON BEAMS

G.E. Ozur, D.I. Proskurovsky, and D.S. Nazarov

*Institute of High Current Electronics, Russian Academy of Sciences, Tomsk, 634055, Russia*

## Abstract

Experimental data on the production of low-energy, high-current electron beams in a plasma-filled diode are presented. The highest beam energy density achieved is  $\approx 40 \text{ J/cm}^2$ , which makes it possible to treat materials in the mode of intense evaporation of the surface layer. It has been shown that the use of a hollow cathode permits of improved beam homogeneity. The feasibility of the production of low-energy high-current electron beams in a gun with plasma anode based on the use of reflective discharge has been demonstrated.

## Introduction

The low-energy (10–40 keV), high-current electron beams (LEHCEBs) of microsecond duration are of great interest of surface modification studies and applications [1, 2]. For the production of the LEHCEBs explosive-emission-cathode plasma-filled diodes hold much promise. The plasma-filled systems are distinguished, compared to vacuum systems, by the high perveance of the electron flow, by the feasibility of microsecond pulses of the electron beam, and by some technological advantages [3–5]. However, the techniques for the production of LEHCEBs of high current density ( $10^2 - 10^3 \text{ A/cm}^2$ ) especially for their generation and transportation, have not been adequately investigated, first of all, from the viewpoint of providing the electron beam homogeneity acceptable for technological use. The present study is an extension of our previous investigations in this area.

## The experimental setup and results

We explain the principle of the LECHEB generation in a plasma-filled system by the example of an electron gun developed by us a few years ago [3–5].

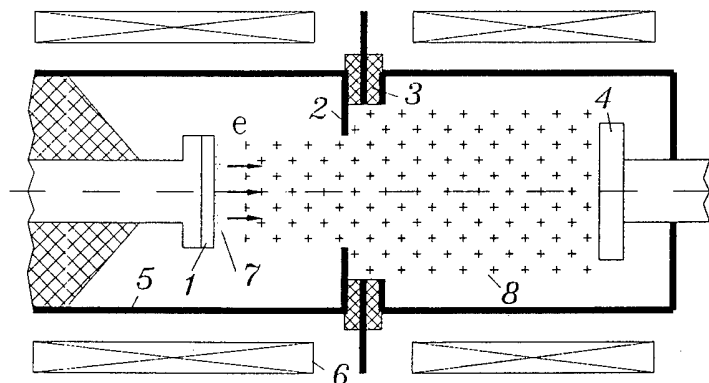
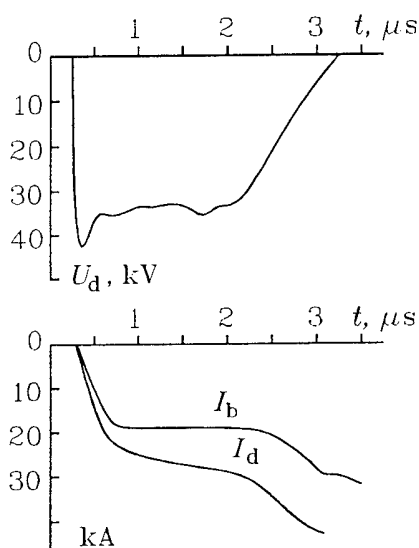


Fig. 1. Block diagram of the electron gun. 1 – cathode; 2 – anode; 3 – arc plasma sources; 4 – collector; 5 – vacuum chamber; 6 – solenoid; 7 – cathode plasma; 8 – anode plasma.

The block diagram of the electron gun is given in Fig. 1. The anode plasma generated by 12 arc sources arranged in a circle around the hole in the anode electrode preliminarily fills the acceleration gap and the beam drift space. The plasma density  $n_p$ , and the electron temperature are typically  $10^{11} - 10^{12} \text{ cm}^{-3}$  and 1 – 3 eV, respectively [5]. After a time  $t_d \approx 2 - 5 \mu\text{s}$ , an accelerating voltage pulse is applied to the cathode. Owing to its good conductivity, the anode plasma acquires the potential of the anode, and the effective gap in the diode shortens. Thus the electric field is localized in near-cathode layer of the

ion space charge whose thickness ( $\sim 1 - 2$  mm) is much smaller than the cathode and anode separation ( $2 - 5$  cm). The explosive electron emission initiated at the cathode results in the formation of dense plasma blobs that coalesce (in  $10^{-7}$  s) into a continuous emitting surface. The electron beam is generated in the double layer between the cathode and the anode plasmas across which the voltage applied to the diode is localized. Having passed through the hole in the anode electrode, the beam is transported in the plasma to the collector on which the specimen or workpiece to be irradiated can be placed. To prevent the beam from pinching, a guide magnetic field of strength up to 5 kOe is applied.

**Increasing the beam energy content and improvement of the electron flow uniformity.** Our former LEHCEBs [3-5] were capable of producing electron beams with an energy density  $W$  below  $10$  J/cm<sup>2</sup>, which permitted treating materials in the mode of melting or initial evaporation of the surface layer. For the evaporation to be intense, it is necessary to increase  $W$  to  $15 - 30$  J/cm<sup>2</sup> or even to higher values. To realize this mode, we have developed and built a higher-power voltage generator with a substantially lower impedance of the discharge circuit and a  $1.5 - 2$  times higher density of the anode plasma. These and some other measures have enabled us to produce LEHCEBs with an energy density of up to  $40$  J/cm<sup>2</sup>, a pulse duration of  $2 - 4$   $\mu$ s, and a beam current of up to  $50$  kA.



**Fig 2.** Typical waveforms of the diode voltage  $U_d$ , the diode current  $I_d$ , and the beam current  $I_b$ . Charge voltage of the pulse generator  $U_c = 40$  kV;  $H_z = 3$  kOe; cathode diameter -  $6$  cm.

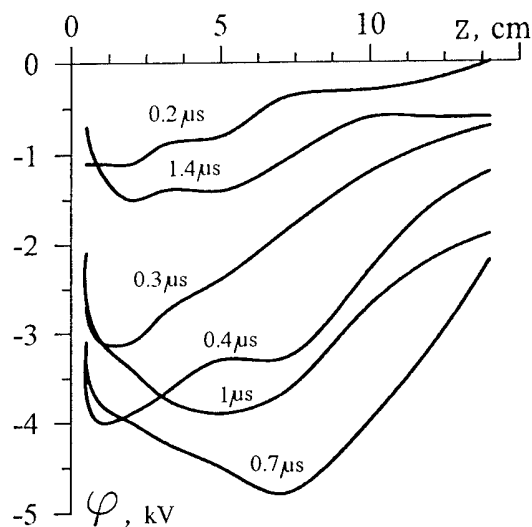


**Fig. 3.** Dynamics of potential "well" in the drift space.  $z$  - distance from the collector,  $U_c = 20$  kV.

Figure 2 presents typical waveforms of the voltage across the diode, the diode current, and the beam current onto the collector. As can be seen from the waveforms, the density of the electrons injected into the anode plasma,  $n_b$ , increases in fact throughout the pulse. Starting from a certain point in time,  $n_b$  becomes higher than  $n_p$ , and in the drift space an unneutralized space charge of electrons appears that creates both an axial and a radial electric fields. We directly observed the presence of a potential "well" in the beam with the use of a floating probe introduced into the beam along its radius. The typical time behavior of the potential "well" is illustrated by Fig. 3. It should be noted that the reduction of the potential sag, starting from a certain point in time ( $t > 0.7$   $\mu$ s), promotes penetration of the collector plasma ions into the diode since for an ion decelerating electric

field appears to be lower than the accelerating electric field. The ions of the anode plasma as well as of the collector plasma that appears after a time are accumulated within the pulse, under the action of the radial electric field in the near-axis region of the beam. With that, the collector plasma ions may penetrate into the diode thereby increasing the current density in the double layer. In the end, the energy (current) density in the near-axis region of the beam becomes higher than in the peripheral regions, even if the energy density distribution over the beam cross section was uniform energy early in the pulse.

The undesirable effect of the accumulation of ions in the center of the beam can be

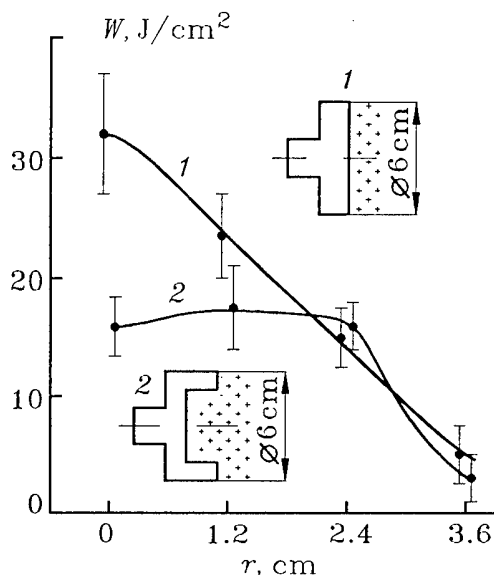


Fig. 4. Cross-sectional energy density distribution of the beam for two types of the cathode: 1 - plane cathode; 2 - hollow cathode.

whose results are illustrated by Fig. 4 a decrease in  $n_p$  in the beam center only by 10–15 % compared to that in the peripheral regions results in a decrease in energy by a factor of 1.5 – 1.7.

**Use of a reflective discharge to create a plasma anode.** To produce a plasma anode in the electron guns developed up to now, the erosion plasma of a vacuum arc was used. Obviously, this plasma used for the above purpose has some disadvantages. The erosion products may pollute the surface layer of the material under treatment. The parameters of erosion plasmas are not so reproducible as those of gas-discharge plasmas because of the non-steady-state nature of the electrode erosion in arc. When there is a need to produce a long plasma channel, it is necessary to place additional arc plasma sources in the drift space, which reduces the reliability of operation and complicates the design of the electron gun. Furthermore, the energy required to generate the anode plasma is rather high since the total current the arc plasma sources is generally comparable to the diode current [4, 5], although only the ion component of the anode plasma is used in the beam generation. It is also important that for a plasma column produced in a reflective discharge the plasma density distribution in radius can be made highly uniform [6].

We pioneered in developing an electron gun with the anode plasma generated by a pulse reflective (Penning) discharge (Fig. 5). The cathodes of the Penning discharge are the beam collector and the explosive-emission cathode of the gun. The gas (argon) pressure was  $(4 - 10) \times 10^{-4}$  Torr. The discharge was powered from a  $0.5 \mu\text{F}$  capacitor charged to 4 – 5 kV. The discharge current was 40 – 80 A.

compensated by reducing artificially the electron current density in this region of the beam during its generation in the double layer. This can be done, for instance, by properly choosing the cathode shape. Figure 4 gives typical energy density distributions,  $W(r)$ , for a plane cathode and for a hollow cathode. It can clearly be seen that the  $W(r)$  distribution for the hollow cathode is substantially more uniform than that for the plane cathode, although the pulse-integrated beam energy is somewhat lower. This difference in the form of the  $W(r)$  curves is related, in our opinion, to the fact that the density of the anode plasma that preliminarily fills the diode falls with distance from the plane where the spark sources are placed [5]. Hence initially the current density will be lower in the near-axis region of the beam formed in the cathode cavity than in its peripheral regions and this in the end will reduce the density of the ion accumulated in the center of the beam. Curiously, in the experiment

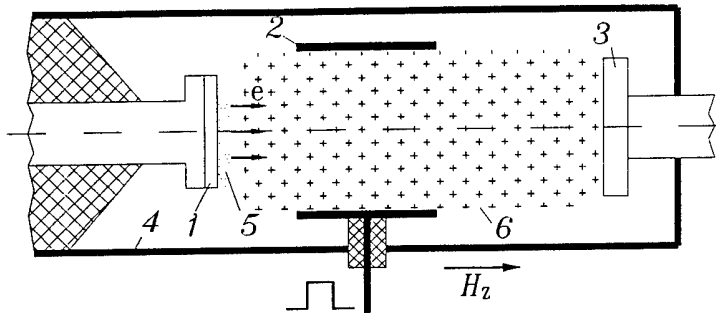


**Fig. 5.** Block diagram of the electron gun. 1 – cathode; 2 – Penning anode; 3 – collector; 4 – vacuum chamber; 5 – cathode plasma; 6 – anode plasma.

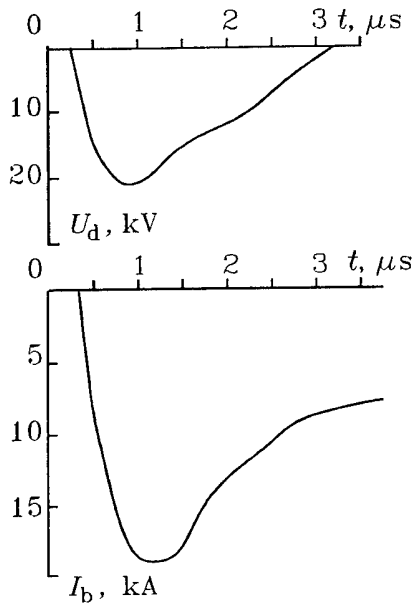


**Fig. 6.** Typical waveforms of the diode voltage  $U_d$  and the beam current  $I_b$  ( $U_c = 30$  kV,  $H_z = 2.4$  kOe).

From the waveforms of the discharge current and the discharge gap voltage we found the time delay to the initiation of the discharge as a function of gas pressure. The values of this time were then used to bring the instant of application of the acceleration voltage to the cathode into step with the discharge operation. Figure 6 gives typical waveforms of the diode voltage and the beam current onto collector. It can be seen that the current onto collector reached 19 kA. The total beam energy was about 200 J for a beam diameter of 8 cm.

### Summary

1. The LEHCEB parameters achieved ( $\sim 40$  J/cm<sup>2</sup>) make it possible to treat materials not only in the surface melting mode but also in the mode of intense evaporation of the surface layer.
2. The unneutralized negative space charge appearing in the drift space gives rise to accumulation of ions in the near-axis region of the beam. This in turn causes an increase in beam energy density in this region. Using a hollow cathode improves the uniformity of the beam energy density cross-sectional distribution.
3. It has been demonstrated that the generation of an LEHCEB in a plasma-anode system whose operation is based on a reflective discharge is quite feasible.

- [1] Pogrebnyak A.D. and Proskurovsky D.I. :Phys. Stat. Sol., **145** (1994) 9.
- [2] Proskurovsky D.I., Rotshtein V.P., and Ozur G.E. :(these proceedings).
- [3] Ozur G.E. and Proskurovsky D.I. :Pis'ma Zh. Tekh. Fiz., **14** (1988) 413.
- [4] Ozur G.E. and Proskurovsky D.I. :Proc. XIV Int. Symp. on Discharges and Electr. Insulation in Vacuum, Santa Fe, USA (1990) 665.
- [5] Nazarov D.S., Ozur G.E. and Proskurovsky D.I. :Izv. Vyssh. Uchebn. Zaved. :Fizika, **3** (1994) 100.
- [6] Arzhannikov A.V., Burmasov V.S., Vyacheslavov L.N., Koidan V.S. :Fizika Plazmy, **10** (1984) 175.



# **FOCUSING AND GUIDING INTENSE ELECTRON BEAMS BY A SUPERCONDUCTOR TUBE**

Peter Roth

*Gerstenstrasse 1, D-85276 Pfaffenhofen, Germany*

## **Abstract**

An intense electron beam travelling axially through the opening of a superconductor tube is studied. Our model calculations show that the beam is focused by the superconductor tube when the space-charge effect of the beam electrons is compensated. The tube functions as a lens for electrons injected parallel to the tube axis and also for electrons having a small initial radial velocity component. The electron trajectories are computed, and the focal length of the superconductor tube is estimated.

## **Introduction**

Recently, a superconductor lens [1-4] has been proposed which comprises a superconductor tube through which electrons or any other charged particles can travel axially. Perfect superconductors show an infinite electrical conductivity and a diamagnetic behavior in response to an externally applied magnetic field. Thus, the principle of the focusing by a superconductor tube is assumed to be as follows: When an electron beam is injected into a type-I superconductor tube, for example, the self-magnetic field of the beam cannot penetrate into the inner wall of the tube. The amount of the self-magnetic field must be smaller than the critical field strength of the superconducting material. The magnetic pressure generated due to the Meissner effect of the superconductor causes the self-magnetic field to be confined between the electron beam and the inner tube wall. Accordingly, the compressed magnetic self-field acts back on the beam and tends to focus it. Experiments carried out by Matsuzawa et al. [1, 2] using intense pulsed electron beams indicate the focusing ability of high- $T_c$  oxide superconductor lenses. Cooling down such a lens, a reduced diameter of the focused electron beam has been observed at temperatures below the superconducting transition temperature  $T_c$ . This temperature-dependent focusing supports the idea that a superconductor model can be applied to explain the focusing effect.

In the present paper we suggest a superconductor-tube model considering a complete expulsion of the flux of the self-magnetic field from the superconductor due to the Meissner effect. For simplification, a non-pulsed continuous electron beam is considered.

### Superconductor-tube model, electron trajectories, and focal length

As a model of the superconductor tube we suppose a circular channel of radius  $R$  through a space filled with a perfect superconductor. To determine the magnetic field generated by a continuous electron beam carrying a current  $I$  through the tube (channel), a current image method is used [4]. Further, inside of the tube are positive ions of a number density per axial length  $n_+$ . The space charge of the electrons having a number density  $n_-$  is thus partly neutralized. The space-charge effect is supposed to be compensated so that the relation  $n_+/n_- = 1 - \beta^2$  is satisfied, where  $\beta = v_y/c$  is the ratio between the axial electron velocity along the tube axis  $v_y$  and the speed of light in free space  $c$ . The force acting on electrons travelling nearly parallel to the tube axis tends to drive the electrons toward the tube axis because it is created by a repulsive interaction between the electron beam and induced superconducting screening currents flowing within the superconducting tube material. If the amount of the radial distance  $x$  of the electrons from the tube axis is small as compared to the inner tube radius  $R$ , the equation of electron motion is written as

$$\ddot{x} + \omega^2 x = 0, \quad (1)$$

where

$$\omega^2 = \mu_0 e I v_y (1 - \beta^2)^{1/2} (2\pi m_0)^{-1} R^{-2}. \quad (2)$$

In Eq. (2),  $\mu_0$  denotes the permeability of free space,  $e$  the electron charge,  $I$  the electron current, and  $m_0$  the electron rest mass. The solution of Eq. (2) is a harmonic oscillation around the tube axis :

$$x(t) = x_0 \cos(\omega t) + (v_{x0}/\omega) \sin(\omega t), \quad (3)$$

where  $x_0$  is the initial radial distance of the electrons,  $v_{x0}$  the initial radial velocity of the electrons at the tube inlet ( $v_{x0} \ll v_y$ ), and  $\omega$  the electron oscillation frequency (multiplied by  $2\pi$ ).

When the electrons are injected parallel to and near the tube axis ( $v_{x0} = 0$ ,  $x_0 \ll R$ ), their frequency  $\omega$  is related to a focal length  $f$ ,

$$f = (\pi^3 m_0 c / 2 e \mu_0)^{1/2} R^{-1/2} \{ [(eU/m_0 c^2) + 1]^2 - 1 \}^{1/4}, \quad (4)$$

where  $U$  denotes the electron acceleration voltage corresponding to  $v_y$ . The ratio between the focal length  $f$  and the inner tube radius  $R$  as a function of the electron current  $I$  is plotted for typical values of the acceleration voltage  $U$  in Fig. 1.

Figure 2 shows a set of exemplary electron trajectories computed without the ap-

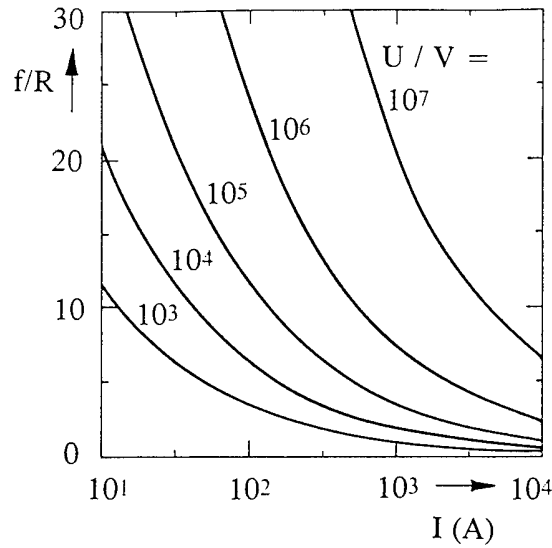


Fig. 1: Ratio between the focal length  $f$  according to Eq. (4) and the inner radius  $R$  of the superconductor tube as a function of the electron current  $I$ . The parameter of the curves is the electron acceleration voltage  $U$  corresponding to the axial electron velocity  $v_y$ .

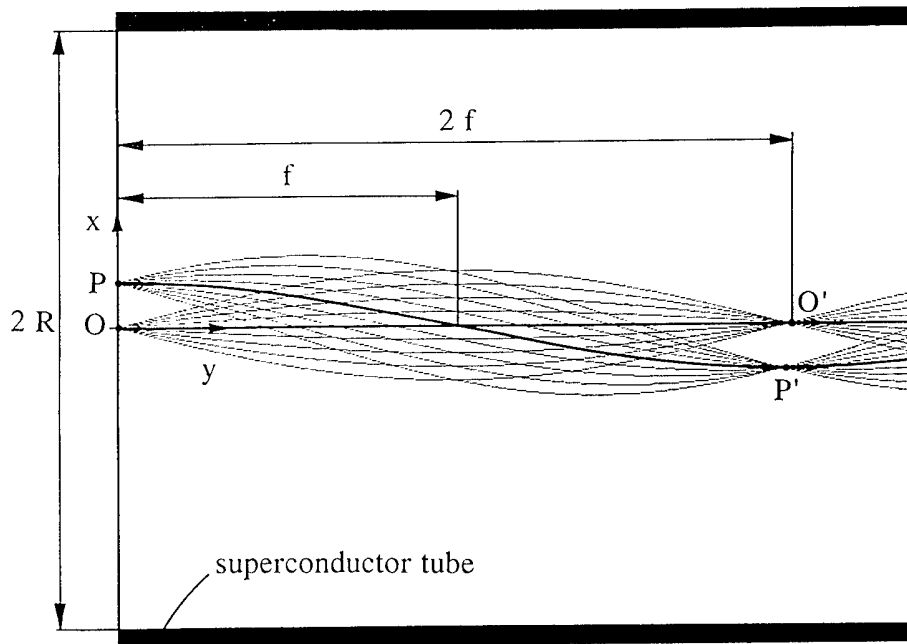


Fig. 2: Trajectories of electrons travelling through a superconductor tube having the inner radius  $R$ . The parameters of the trajectories are  $R = 1$  cm,  $U = 270$  kV and  $I = 800$  A. The space-charge effect is compensated ( $n_+/n_- = 0.42$ ). The focal length is about  $f = 5.5$  cm. The electrons start from the center  $O$  of the tube inlet and from the point  $P$  at a radial distance of  $x_0 = 0.15 R$ . The initial radial velocities are set to be  $v_{x0} = n (\pm 3 \cdot 10^6 \text{ m/s})$ ,  $n = 0, 1, 2, 3, 4$ , respectively.

proximation used to get Eq. (1). In a first case, the electrons start on the tube axis ( $x_0 = 0$ ). The corresponding trajectories ( $O \rightarrow O'$ ) shown in Fig. 2 intersect each other on the tube axis if the injection angle of the electrons is small ( $\arctan(v_{x0}/v_y) \ll 1$ ). The focal length is  $2f$ . In a second case, the electrons are emitted from a point P located at a radial distance  $x_0$  from the tube axis. The electrons emitted from point P cross the tube axis at various points, however, they are focused to the common point P'. The focal length remains nearly unchanged when the radial distance  $x_0$  of the point P is increased, provided that the value of  $x_0$  is kept small compared to the tube radius R. When  $x_0$  is further increased, however, the focal length is reduced because the focusing force increases when the beam approaches the inner wall of the tube. The distance of the focus point P' from the tube axis is  $x_0$ . The superconductor tube functions as a conventional lens; however, in contrast to a well-known magnetic electron lens the image (P') is not rotated with respect to the object (P).

### Conclusion

We have computed the trajectories of electrons which travel through a superconductor tube and the space-charge effect of which is compensated. The electrons oscillate around the tube axis. If they move in the vicinity of the tube axis, their harmonic oscillation frequency is given by Eq. (2). Therefore, the superconductor tube may function not only as an electron lens or guide but also as a wiggler for free-electron lasers [5]. To verify our model, the focal length of superconductor tubes should be investigated experimentally. For example, we evaluate with  $I = 800$  A,  $U = 270$  kV, and  $R = 1$  cm a focal length of about  $f = 5.5$  cm according to Eq. (4). Similar parameters  $I$ ,  $U$ , and  $R$  has been used in the experiments [1] in which the total length of the superconductor tube was in the range of about (3 ... 14.5) cm. The value of  $f = 5.5$  cm estimated employing our focal length equation (4) is found to be within this range. Obviously, the electron motion will be affected by damping effects which are, however, beyond the scope of our simple model. Further, in contrast to the above experiments using pulsed electron beams, we have considered here non-pulsed ones. An electron pulsation added to our superconductor-lens model is under investigation [6].

- [1] H. Matsuzawa, O. Ohmori, H. Yamazaki, J. Ueno, A. Furumizu, A. Saito, T. Takahashi, and T. Akitsu : J. Appl. Phys., **65** (1989) 2596
- [2] H. Matsuzawa : J. Appl. Phys., **74** (1993) R111
- [3] P. Roth and E. Hegenbarth : Exp. Tech. Phys., **38** (1990) 119
- [4] P. Roth : J. Appl. Phys., **77** (1995) 4914
- [5] P. Roth : J. Appl. Phys., **78** (1995) 2874
- [6] P. Roth : unpublished.

# REDUCTION OF ANGULAR SPREAD AT NONADIABATIC ELECTRON MOTION IN MAGNETICALLY INSULATED DIODE

A.V.Arzhannikov, S.L.Sinitsky

Institute of Nuclear Physics, Novosibirsk, 630090, Russia

Behaviour of the electron pitch-angle is investigated by analytical and numerical methods for the case of a magnetically insulated diode with a ribbon geometry. It has been shown that at the boundary of the adiabaticity of the electron motion the angle can be reduced in many times by a choice of a special nonhomogeneity of the magnetic field. Analytic expressions for the final pitch-angle of the beam electrons are given.

**1. Introduction.** High-power electron beams with a high current density and a small angular spread are a base for various scientific researches and practical applications. However a generation of such beams is not a problem solved now. Using of relativistic diodes with a magnetic insulation is investigated by us as one of the promising ways to generate them. The main goal of the investigations is to obtain a long duration of the beam pulse (up to tens of microseconds) at appropriate values of the density and angular spread. Theoretical estimation made according to [1] for the influence of a nonzero angle between the electric and magnetic fields near the emitting cathode for the typical diode parameters, has given the electron pitch-angle on the level of 0.01. But experimental measurements under similar conditions [2] and our numerical simulations [3] have shown that the pitch-angle of the electrons exceeds this level more than in ten times. In order to describe the influence of various factors on the electron pitch-angle we have created a theoretical model considering the motion of the beam electrons in

the diode with a ribbon geometry for the case of nonhomogeneous electric and magnetic fields.

**2. Analytical model.** The schematic of the ribbon magnetically insulated diode that is homogeneous along the y-axis, is shown in the Fig. 1. An electron flow (1) emitted by the cathode (2), is accelerated along the guiding magnetic field. Then it passes through the anode slit (3) and propagates in the slit vacuum channel (4). To simplify equations describing the electron motion in this system, let us suppose a few assumptions. Firstly, self magnetic field of the beam  $\bar{H}_b$  is small enough in comparison with external magnetic field  $\bar{H} = (H_x, 0, H_z)$ . Secondly, the values of the electron pitch-angles are much less than 1. Thirdly, the shortest spatial scale  $L$  of the magnetic and electric field variations in the diode and in the channel is larger than Larmour radius of the electron  $\rho_L$  calculated on its total velocity in this region. Let's consider that a beginning of a local frame is placed in the centre of the electron Larmour

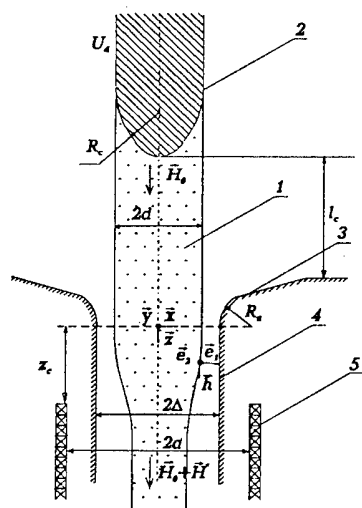


Fig. 1. The schematic of the diode geometry

circle,  $\bar{h}$  is an unit vector tangent to the magnetic field line,  $\bar{e}_2$  is an unit vector parallel to the y-axis, and the unit vector  $\bar{e}_1 = [\bar{e}_2 \times \bar{h}]$  is perpendicular to both of them. A system of equations for the electron motion in approximation of a small value of the parameter  $\rho_L / L$  can be easily transformed to the equation of classic oscillator with a time dependent frequency and a driving force  $\dot{p}_{dr}$ . This equation is :

$$\ddot{\mathbf{r}} + \omega_H^2(t)\mathbf{r} = -\dot{p}_{dr}, \quad (1)$$

where  $r = p_1 / \omega_H(t)$ ,  $\dot{r} = p_2 - p_{dr}$ ;  $p_1$ ,  $p_2$ ,  $p_{||}$  are the components of the momentum vector along the unit vectors  $\bar{e}_1$ ,  $\bar{e}_2$  and  $\bar{h}$  respectively,  $\omega_H(t)$  is a cyclotron frequency of the electron, and  $p_{dr} = p_{||} v_{||} (\bar{e}_1 (\bar{h} \nabla) \bar{h}) / \omega_H(t) - \gamma m c E_{\perp} / H - \gamma m v_{||} H_b / H$  is a momentum of the electron drift motion. The first part of this expression for the drift momentum is an inertial drift, the second one is a  $\bar{E} \times \bar{B}$  drift and the last one is a result of the addition of the beam magnetic field to the external one. In quasiclassic approximation a full solution of the equation (1) is the following:

$$p_{\perp}(t) = ip_1(t) + p_2(t) = p_{dr} - e^{i\varphi(t)} \cdot \int_{t_0}^t \frac{\omega_H(t')}{\omega_H(t)} \dot{p}_{dr} e^{-i\varphi(t')} dt + i \sqrt{\frac{\omega_H(t)}{\omega_0}} p_0 e^{i\varphi(t)}, \quad (2)$$

where  $\varphi(t) = \int_{t_0}^t \omega_H(t') dt' + \varphi_0$  is a phase of rotation,  $p_0 = 4\pi m c j_c \sin(\epsilon) / (e H_c^2)$  is a

transverse momentum of the electron due to the angle between  $\bar{E}$  and  $\bar{H}$  fields near the cathode surface (see [1]). The electron has this momentum  $p_0$  in that moment of time  $t_0$  when its motion becomes magnetised. Since at the electron motion the variation of the vector  $\bar{h}$  is directed perpendicularly to  $\bar{h}$ , one can modify the expression for

$p_{dr}$  by using  $(\bar{e}_1 (\bar{h} \nabla) \bar{h}) \approx h_x \nabla_{||}$  that is correct with accuracy of the first order on the parameter  $\rho_L / L$ . Here it is assumed that  $h_z \approx 1$  because the angle between the magnetic field line and z-axis is small enough. To transform the part of  $p_{dr}$  that is connected with the  $\bar{E} \times \bar{B}$  drift, one can split up the transverse electric field in two parts:  $E_{\perp} = E_v + E_b$ . The first one  $E_v$  is created by the charges induced on the surface of the anode slit and the walls of the channel. This component of the electric field is sharply changing near the anode slit. The second one  $E_b$  is provided by the self space charge of the beam far from the cathode where the electron velocity becomes close to the speed of light  $c$  and as a result, it is almost invariable. It should be pointed that the strengths of the fields  $E_b$  and  $H_b$  are determined by the linear charge and the linear current of the ribbon beam respectively, so they are practically invaried along the trajectory of the electron. After transformations of the integral in the expression (2) we have obtained the final transverse momentum of the electron in that part of the channel which is far from the anode slit, and on this reason the electric and magnetic fields are invariable there. The expression for this momentum is the following:

$$p_{\perp}(t) = -\frac{e(E_b - \beta_{||} H_b)}{\omega_H(t)} + e^{i\varphi(t)} \int_{t_0}^{\infty} \frac{\omega_H(t')}{\omega_H(t)} e^{-i\varphi(t')} \times \\ \times \left\{ i e E_v + \frac{e H_x(t')}{\gamma m c} p_{||} - \frac{e(E_b - \beta_{||} H_b)}{\omega_H^2(t)} \cdot \dot{\omega}_H(t) \right\} \cdot dt' + i \sqrt{\frac{\omega_H(t)}{\omega_0}} p_0 e^{i\varphi(t)} \quad (3)$$

Obtaining this expression we have considered that  $p_{||}$  and  $\gamma$  are invariable in regions of nonhomogeneities of the electric and magnetic fields near the anode slit.

Analysis of the expression (3) shows that the main addition to the transverse momentum of the electron is collected on these parts of the electron trajectory where the electric field  $E_v$  or the magnetic field  $H_x$  as well as the cyclotron frequency  $\omega_H$  are changing sharply. This effect is substantially increased on that part of the trajectory where the guiding magnetic field has a small value. The another significant conclusion from expression (3) will be obtained in the following part of the paper.

Let us assume that the magnetic field in the diode gap is homogeneous and equal to  $H_0$ . Then the field rises along the  $z$ -axis at the entrance of the channel to the value  $H_0 + H^* = H_0(1 + \alpha)$  due to the placement of the additional semi-infinite plane coil (5) outside the channel. The components of the field are given for this case by following expressions:

$$H_x(x, z) = \frac{\alpha H_0}{4\pi} \ln \frac{(z - z_c)^2 + (a + x)^2}{(z - z_c)^2 + (a - x)^2}, \quad H_z(x, z) = H_0 + \frac{\alpha H_0}{2\pi} \left[ \pi + \operatorname{arctg} \left( \frac{z - z_c}{a - x} \right) + \operatorname{arctg} \left( \frac{z - z_c}{a + x} \right) \right] \quad (4)$$

where  $z_c$  is the coordinate of the beginning of the winding and  $2a$  is the gap between plates of the coil.

In the described case the electron beam should be like a plane layer with a linear current  $I'$ . The highest value of the charge density of the beam is near the cathode surface due to a small velocity of the electrons there. For the case of  $\gamma \gg 1$  the electron velocity becomes close to the speed of light  $c$  when it goes from the cathode surface on a small distance. On this reason the charge density is practically independent on  $z$  coordinate in the main part of the diode gap. Taking into account the pointed peculiarity we replace the space charge of the beam by a homogeneously charged cylinder with a radius equalled to the cathode one  $R_c$  and by a homogeneously charged layer with the density  $\rho = I'/(2dv_{||})$ . As a result of these approximations we have obtained the following expressions for the varied part of the electric field:  $E_v = E_{v1} + E_{v2}$ ,

$$E_{v1} = \begin{cases} E_0(x) \left[ \frac{R_a + \Delta + x}{z^2 + (R_a + \Delta + x)^2} - \frac{R_a + \Delta - x}{(R_a + \Delta - x)^2 + z^2} - \frac{2x}{(R_c + l_c - z)^2} \right], & \text{at } z < 0 \\ E_0(x) / \operatorname{ch} \left( \frac{z\pi}{2\Delta} \right), & \text{at } z \geq 0 \end{cases} \quad (5)$$

$$E_{v2} = \frac{\pi I' R_a z}{v_{||}} \left[ \frac{1}{(R_a + \Delta - x)^2 + z^2} - \frac{1}{(R_a + \Delta + x)^2 + z^2} \right],$$

$$\text{where } E_0(x) = \frac{U_d}{2 \ln \left( \frac{l_c}{R_c} + 1 \right) + \ln \left( \frac{l_c}{R_a} + 1 \right) + \ln \left( \frac{l_c + R_a}{(R_a + \Delta)} \right)} \cdot \frac{2x}{(R_a + \Delta)^2 - x^2}$$

Then we have obtained the final result for the transverse momentum by putting the expressions (4) and (5) in the expression (3):

$$p_{\perp}(t) = p_{dr} + (p_C + p_E e^{-i\varphi_a} + p_H e^{-i\varphi_c}) \cdot e^{i\varphi(t)}, \quad \text{where } p_C = p_0 \sqrt{1 + \alpha},$$

$$p_E = \sqrt{1 + \alpha} \{ e E_0(x_a) A_1(x_a) + 2\pi I' e A_2(x_a) \} \quad \text{and} \quad p_H = \sqrt{\frac{1 + \alpha}{1 + \alpha/2}} \cdot A_3(x_c) \quad (6)$$

Variables  $A_1$ ,  $A_2$  and  $A_3$  are given in Appendix.  $\varphi_a$  and  $\varphi_c$  are the phases of the electron rotation at which it passes through the regions with the maximal value of  $E_v$  and  $H_x$ . Position of these regions are corresponded to the position of the anode slit and the beginning of the additional coil (5) (see Fig.1).  $x_a$  and  $x_c$  are the coordinates of the center of the electron Larmour circle at its passing through the mentioned regions respectively. Expression (6) shows that the resulting transverse momentum of the electron is equal to a sum of a constant vector and three vectors shifted on the angle and rotating with the same velocity. The component  $p_C$  is connected with the angle

between  $\vec{E}$  and  $\vec{H}$  fields near the cathode, the second component  $p_E$  is determined by the nonhomogeneity of the electric field and the third component  $p_H$  is due to the magnetic one. Further we show that the transverse momentum can be essentially decreased by appropriate shift of phase  $\varphi_c$  in respect to  $\varphi_a$ .

**3. Calculations.** The obtained formula for the transverse momentum has been checked up by comparison of its results with ones of the numerical simulation of self-consistent problem. For example, we have taken the geometry of the diode used in the experiments on the U-2 accelerator [3] with following parameters:  $R_a=2.5\text{cm}$ ,  $R_c=3\text{cm}$ ,  $l_c=10\text{cm}$ ,  $H_0=2\text{kOe}$ ,  $H^*=6\text{kOe}$ ,  $a=4.3\text{cm}$ ,  $\Delta=2.5\text{cm}$ ,  $d=1.1\text{cm}$ ,  $U_d=1\text{MV}$ ,  $I'=0.3\text{kA/cm}$ . Using this data we have obtained the values of the three mentioned vectors  $p_E=0.06p_{\parallel}$ ,

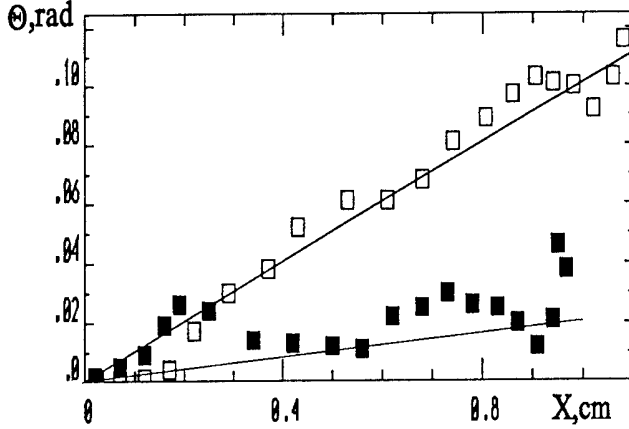


Fig.2. The electron pitch-angles in the beam cross section, derived from analytical and numerical calculations.

$p_H=0.04p_{\parallel}$  and  $p_C=0.01p_{\parallel}$  for the beam boundary. The dependencies of the electron angle  $\Theta$  on  $x$  coordinate both for analytical model (lines) and numerical simulation (squares) are represented in the Fig. 2 for two cases. The upper line and unfilled squares show the case when the components  $p_E$  and  $p_H$  are added at the phase difference  $\varphi_a - \varphi_c \approx 2\pi$  ( $z_c=12\text{cm}$ ). The electron angle increases with an increase of  $X$  and becomes close to 0.1 at the beam boundary. From another hand, by appropriate choosing of the coil location we can obtain this phase

difference close to  $\pi$ . For this case (lower line and filled squares) the resulting angle becomes in many times smaller and has value not more than 0.02. The oscillations of squares near the lines can be explained by the behaviour of the momentum component  $p_C$ , which has varied phase across the beam in respect to components  $p_E$  and  $p_H$ .

So, both the analytical model and numerical simulations have shown that the angular spread of the electron beam generated by the magnetically insulated diode can be reduced in many times by a choice of the special nonhomogeneity of the guiding magnetic field.

[1] Ryutov D.D. Proc. of 9-th Intern. Conf. on High-Power Particle Beams, Washington, 1992, p.1009-1014.

[2] Sloan M.L., Davis H.A. Phys. Fluids, 1982, v.25, N 12, p. 2337-2343.

[3] Arzhannikov A.V., Astrelin V.T., Kapitonov V.A. et al. Proc. of 8-th Intern. Conf. on High-Power Particle Beams, Novosibirsk, 1990, p.256-263.

#### Appendix

$$A_1 = i\pi \frac{(R_a + \Delta)^2 - x^2}{2xv_{\parallel}} e^{-\frac{R_a + \Delta}{\rho_L}} \text{sh}\left(\frac{x}{\rho_L}\right) + \frac{i\Delta}{v_{\parallel} \text{ch}\left(\frac{\Delta}{\rho_L}\right)}, \quad A_2 = \frac{\pi R_a}{v_{\parallel}^2} e^{-\frac{R_a + \Delta}{\rho_L}} \text{sh}\left(\frac{x}{\rho_L}\right), \quad \rho_L = \frac{cp}{eH_0},$$

$$A_3 = \left[ p_{\parallel} \text{sh}\left(\frac{x}{\rho_L^*}\right) - \gamma mc \left( \frac{E_b - \beta_{\parallel} H_b}{H_0 + H^*/2} \right) \text{ch}\left(\frac{x}{\rho_L^*}\right) \right] e^{-\frac{a}{\rho_L^*}}, \quad \rho_L^* = \frac{cp}{e(H_0 + H^*/2)}, \quad E_b = \frac{2\pi I' x}{v_{\parallel} d}, \quad H_b = \frac{2\pi I' x}{d}$$



## EXPERIMENTAL STUDY OF A HIGH-POWER TWT ELECTRON BEAM

A.V.Arhipov, G.G.Sominski

*St.Petersburg Technical University,  
29. Polytekhnicheskaja ul., St.Petersburg. 195251, Russia*

An electron beam of a high-power travelling-wave tube (TWT) amplifier designed for continuous operation had been experimentally investigated in collector region. Optimal tube operation parameters were: 13kV, 700 mA, 5.8 GHz, 1.6 kW, 33 dB amplification, periodical magnetic system with field magnitude 0.2 T. But in our studies we varied beam current and acceleration voltage in rather broad ranges:  $I=0.1...0.85$  A,  $U=10...15$  kV.

For the measurements a special analyzer was attached to the tube instead of its collector section (Fig.1). In the analyzer a current of a partial beam cut by a pin-hole diaphragm was measured, as well as an electron energy distribution in this partial beam. Registration of HF partial beam current modulation (that accompanied usually spurious microwave generation) was also possible. Scanning with the analyzer in two transverse directions we obtained distributions of beam parameters in some cross-section of collector area. Moving the analyzer along the axis of the tube we changed the cross-section. Remote from the TWT transportation channel (TC) cross-sections gave us beam angular distribution (in the collector region electron trajectories are not significantly disturbed by space charge forces), and thus the whole beam distribution function in collector area was available. The measurements were made in rather long (up to  $\sim 1$  ms) single pulses to explore specific continuous mode processes but avoid analyzer destruction.

In regimes with beam current exceeding 500 mA and voltage in 11.5...13.5 kV band (i.e. when amplification of input microwave signal was the highest) various modes of spurious generation were observed. The nature of these oscillations had not yet been investigated in detail but we found that they considerably affect the beam spatial and energetic distributions. In this paper we will discuss data obtained only in comparatively uncomplicated regimes without spurious generation.

Current density distribution was bell-shaped near the TC opening and acquired more complicated and evolving in time form at greater distances. Fig.2 shows current density distributions  $j(r)$  obtained in static regime (i.e. when input HF signal  $P_{in}=0$ ) at different distances  $z$  from TC and in moments with different delays  $t$  relative to the current

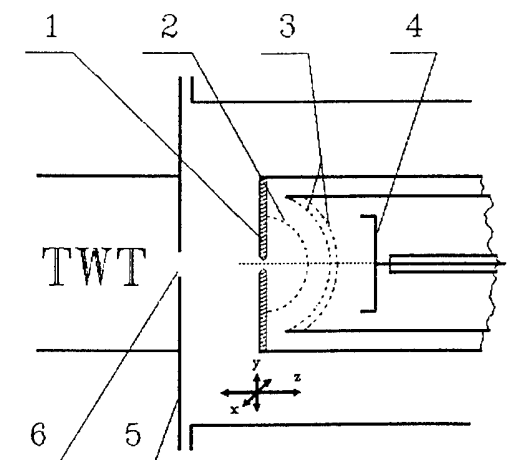


Fig.1 Scheme of the analyzer of the beam parameters.  
1-pinhole diaphragm; 2-grounded spherical grid;  
3 - analyzing grids; 4- collector; 5-TWT flange;  
6 - transportation channel opening.

pulse front. We attribute these temporal alterations to ion focusing and accumulation of ions in the beam volume. Considerable evolution of the current distribution far from TC opening when near it the beam structure is almost constant signifies that the neutralization affects angular distribution of electrons much more than their radial distribution in TC.

In our experiments spatial distribution of current was not strongly affected when the device was fed with input microwave power. But forms of energy spectra became quite different (Fig.3). In static regime (curve 1) almost all electrons have primary energy  $eU$ . But when the microwave output power is significant two principal groups of electrons form. In the spectrum of outer layers of the beam (curve 4) electrons with energy about  $0.6eU$  are most numerous while in the central part (curve 2) because of lower efficiency of interaction with TWT HF circuits electrons are not slowed down. In the intermediate layers of the beam these groups are both present in some proportion (curve 3).

For more reliable definition of origin of ions responsible for evolution of the beam spatial distribution in collector region we investigated this process more closely in different regimes of the tube operation. We found that with increase of the TC residual gas pressure the rate of the evolution considerably grew which indicated that at list one of the sources of ion generation is residual gas ionization in the device volume. On the other hand, the evolution rate grew with the beam current, so bombarded by the beam electrodes are also somehow involved in the neutralization process.

Another prove of this fact we found in dependence of this process development on comparatively small voltages applied to electrodes in collector region. Fig. 4 illustrates this dependence. Current density in the center of spatial distribution  $j_c$  in furthest from TC opening cross-sections we found to be a measure of angular divergence of the beam in our experiments: the more focused the beam was, the more was its density in the center. Each curve in Fig.4 corresponds to zero or negative voltage  $U_d$  applied to the diaphragm of the analyzer (electrode 1 at Fig.1) relative to the grounded transportation

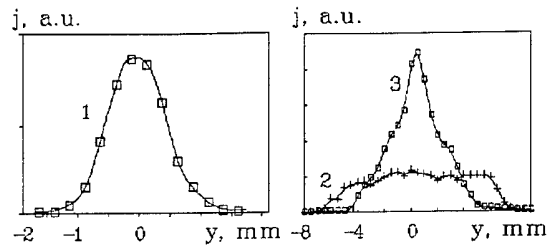


Fig.2. The beam spatial distributions along a transverse axis. Beam parameters are:  $U=13$  kV,  $I=0.5$  A. 1-cross-section  $z=15$  mm (from TC opening),  $t=40$   $\mu$ s; 2-  $z=55$  mm,  $t=20$   $\mu$ s; 3-  $z=55$  mm,  $t=80$   $\mu$ s.

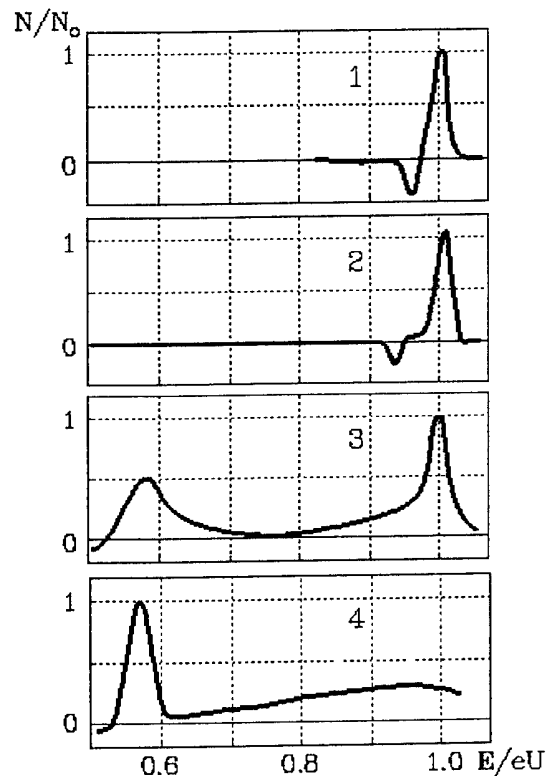


Fig.3. Electron energy spectra in static (1) and dynamic (with maximum output 6 GHz power) (2 - 4) in different radial layers. 13 kV, 0.5 A, 30  $\mu$ s,  $z=35$  mm. 1, 2 -  $r=0$ ; 3 -  $r=3$  mm; 4 -  $r=5$  mm.

channel. If no voltage was applied the current density (and a degree of beam ion focusing) increased, then reached maximum and fell a little and stabilized at the intermediate (between initial and maximum) value. If applied voltage was negative with magnitude less than 50 V or positive with any magnitude up to 250 V, the curve  $j_c(t)$  coincided with that for  $U_d=0$ . For greater  $U_d$  voltages the  $j(t)$  curves coincided with zero-voltage curve only before the latter reached its maximum. At the rest of the current

pulse the current density was the greater, the more voltage (in magnitude) was occurred and decreasing the fall after the maximum, until at  $U_d \leq -200V$  no perceptible fall was registered. At this level ( $U_d \leq -200V$ ) the effect saturated and further increase of the voltage magnitude caused no alteration in the characteristic.

On our opinion, this effect can be explained only by influence of a flow of secondary particles from a collector region onto ion processes in the transportation channel. A considerable value of the delay of the effect relative to the pulse front (about 100  $\mu s$ ) and dependence of this delay on the beam current indicate the thermal nature of this delay. Thus a presumption can be made that on some bombarded electrode a plasma formation is generated after a certain dose of heat energy is accumulated. In relativistic electronics the threshold of "collector plasma" generation is determined as 1...10 J/cm<sup>2</sup>[1], which agrees with delays registered in our experiments. This plasma formation, directly during its extension or acting as an emitter of intensive ion flows, can affect the process of neutralization of the beam with ions from other, "milder" sources and thus put a limit to the ion focusing of the beam. In this model a voltage applied to electrodes will redistribute ion flows and thus shield, to some extent, the TC from these flows. The thresholds observed in the effect of the diaphragm 1 (Fig.1) potential on the focusing processes can be explained by superposition of its electrostatic field with the space-charge field of the beam.

Microwave electromagnetic fields also affect accumulation of ions and the beam focusing. Their influence is illustrated by Fig.5. Curve 1 here is similar to curve  $U_d=0$  in Fig.4 and represents the temporal evolution of current density in the center of its distribution and thus the degree of beam focusing for the case with no HF input signal. Curve 2 was acquired when the input signal ensured maximum continual output power. The rate of focusing here was lower than in the first case and the maximum occurred earlier. Most interesting results were obtained when the tube was fed with rather short (0.5...20  $\mu s$ ) input microwave signal with

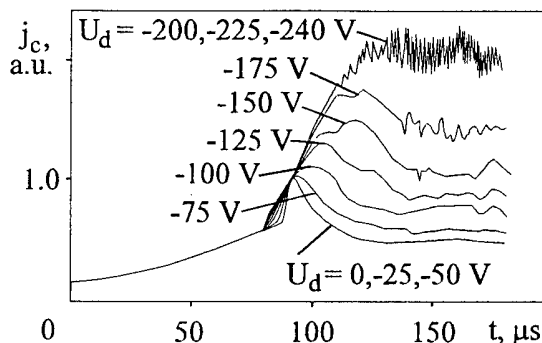


Fig.4. Dependence of evolution of current density in the centre of cross-section on the potential of pinhole diaphragm  $U_d$ . 11 kV, 640 mA.

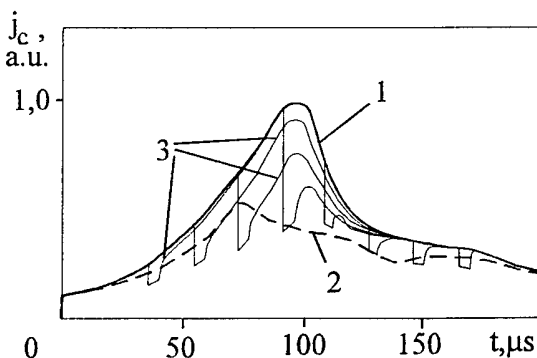


Fig.5. Evolution of current density in the centre of  $z = 55$  mm cross-section regimes with different microwave input signals. 12 kV, 500 mA. 1-static regime ( $P_{in}=0$ ); 2- maximum output power; 3- a set of curves obtained with single 5  $\mu s$  input power pulses with different delays.

varied delay from the current pulse front (curves 3). If the microwave pulse was turned in before the beam focusing reached its maximum it caused a considerable, even below the curve 2, fall of the current density. And after the end of the microwave pulse the density didn't return onto the curve 1 but resumed the rise with the unaltered rate from an intermediate (between curve 1 and minimum) value. The moment when this rise brought the curve to the maximum coincided with maximum with curve 1. But if the input signal was turned in after the moment of maximum focusing its effect on this characteristic was hardly perceptibly and no long-lasting influence was registered. So microwave power considerably affected the focusing only if it was not already affected by plasma or secondary processes.

To the moment we can not present the detailed model of the phenomena described above. But, on our opinion, this model have to involve accumulation of ions in electrostatic traps in the TC originating in inhomogeneity of potential of the beam confined by periodical magnetostatic system. These ions cause, at least on certain stages of their accumulation, the decrease of angular divergence of the beam. But the focusing can be affected by HF fields and flows of secondary particles.

We believe that results of the work can be used for elaboration of the model of processes not only in long-pulsed or continuous high-power TWT amplifiers but in a broad class of similar devices.

The work was partially supported by the Russian Fund for Fundamental Research.

[1] S.P.Bougaev, V.I.Kanavets, V.I.Koshelev, V.A.Cherepenin. Relativistic Micromave Multiwave Oscillators, Novosibirsk, "Nauka", 1991 [in Russian].

## MODELLING OF ELECTRON STREAM DISCHARGE

P.Vrba

*Institute of Plasma Physics, Acad. Sci.,  
Za Slovankou 3, 180 69 Prague 8, Czech Republic*

## Abstract

Planar many-particle model [1-4] is used to simulate the gas discharge initiated by high current, middle energy, hot electron stream ( $I_e \approx 10\text{kA}$ ,  $\varepsilon_e \approx 10\text{keV}$ ,  $\delta_e \approx 1\text{keV}$ ) in atomic and molecular gases (H, Ar,  $\text{N}_2$ ,  $p \leq 133\text{Pa}$ ). Such electron stream has been observed during the relativistic electron beam-plasma interaction at the experimental REBEX facility [5-7]. The stream electrons are injected through the entrance foil into the drift tube fulfilled by neutral gas and leaves the target body via exit foil which serves as the reference zero potential for the system. Current is closed via external RC circuit without any external voltage/current source.

## The gaseous target

The gaseous target is limited by the entrance and exit foils. The distance between the foils may be changed,  $l \geq 0.4\text{ cm}$  and the tube cross section area  $= 25\text{ cm}^2$ . The drift tube is filled by atomic (H, Ar) or molecular ( $\text{N}_2$ ) gases. The gas pressure varies in the range  $p = 13.3 - 133\text{ Pa}$  and the gas temperature remains constant  $T_g = 300^\circ\text{ K}$ .

Electron stream propagates along the axis from the left to the right with the mean energy  $\varepsilon_e = 10\text{ keV}$  and the energy spread  $\delta_e = 1\text{ keV}$ . The initial value of electron stream current is  $I_e = 10\text{ kA}$ .

Both, elementary and collective, processes are running inside gaseous target. The former is connected with electron- and ion-neutral collisions, the later with the negative charge cumulation in creating virtual cathode (VC). During the initial stage the electric field of arising VC decelerates stream electrons. Owing to ionizing events substantially increase and VC is filled by creating ions. The VC disappears when the quasineutrality of ionized gas is achieved. Since the time the number of negatively and positively charge carries increase exponentially, the discharge is ignited [8]. The simulation was finished after many computational cycles, when the quasi-steady state was achieved.

## The formation of virtual cathode

When the electron stream is injected into the neutral gas, the body of target charges negatively and the deep potential well of Virtual Cathode (VC) is formed (see Fig. 1). The period of VC creation corresponds to the several transits of stream electrons through the gaseous target ( $t_{vc} \simeq 5 \times l/v_{01} \approx 3 \times 10^{-10}\text{s}$ , where  $v_{01} = \sqrt{2\varepsilon_e/m_e} \approx 5.94 \times 10^7\text{m/s}$ ). The bottom of VC lies approximately in  $\frac{1}{2}$  of target length and depth of the potential well ( $|\varphi_{\min}| \leq m_e v_{cl}^2/2e$ , where  $v \leq v_{cl} = 9 \times 10^7\text{m/s}$ ) corresponds to maximum energy value of injected electrons. The electric field of the front part of VC slows down the electrons while the back part speeds up them. The energy of reflected electrons near the entrance foil surface differs slightly from the origin one  $\varepsilon_{rff} \simeq \varepsilon_e$ .

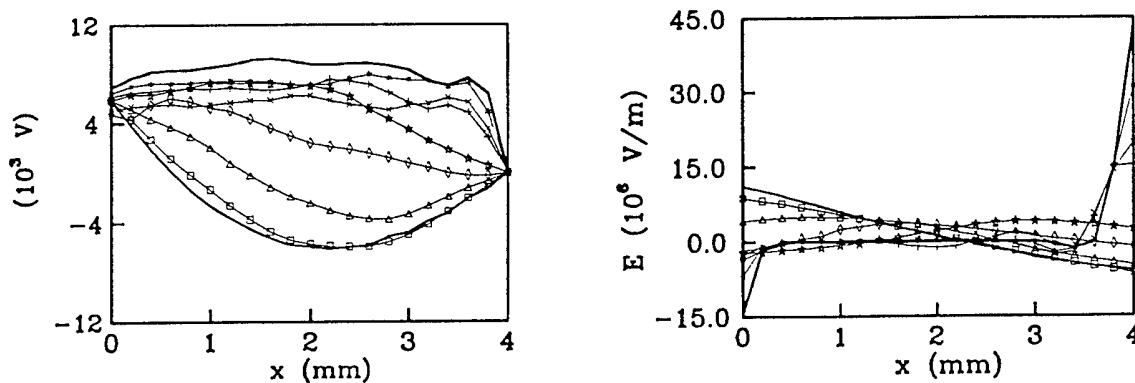


Figure 1: The potential and electric field of stream discharge ( $N_2$ ,  $p = 133\text{Pa}$ )

—... $4.2 \times 10^{-11}\text{s}$ ,  $\square$ ... $8 \times 10^{-11}\text{s}$ ,  $\triangle$ ... $1 \times 10^{-10}\text{s}$ ,  $\diamond$ ... $1.32 \times 10^{-10}\text{s}$ ,  $\star$ ... $1.62 \times 10^{-10}\text{s}$ ,  $+$ ... $2.55 \times 10^{-10}\text{s}$ ,  $\times$ ... $3 \times 10^{-10}\text{s}$ ,  $\ast$ ... $5 \times 10^{-10}\text{s}$ , —... $7.65 \times 10^{-10}\text{s}$ .

The stream electrons propagating through the gas collides with neutral atoms. The elastic and inelastic (e.g. excitation, ionization) collisions with atoms are taken into account. The charge exchange between the ion and neutral atom is also considered.

The deceleration of stream electrons by the electric field of VC is highly desired phenomenon. The number of ionizing events substantially increases with the decreasing electron energy. The ionization of neutral atoms prevails in the vicinity of VC bottom, where the electrons are highly decelerated. The potential well is gradually filled by slow ions. The secondary electrons according to the position with respect to the bottom escape through the entrance  $x \leq x_{\text{bottom}}$  or exit  $x_{\text{bottom}} \leq x$  foil. The shape of VC is changed and the depth of potential well decreases. The VC begins to move in the direction of electron stream (see Fig. 1). At a certain time the shallow bottom of VC arrives the surface of exit foil. The corresponding velocity of the bottom of potential well depends on gas composition and pressure. The electrons pushed by the VC are absorbed by exit foil.

### The Ignition Phase of Gaseous Discharge

During the initial phase of VC creation the total number of negatively charged macroparticles grows up linearly. After that, the increment is decreasing and the local maximum value of negatively charged macroparticles is achieved. The number of macroparticles and the shape of VC potential well doesn't change for a certain time which depends on gas composition and pressure. The decreasing pressure of gas supports the creation of VC and the stable period of VC is longer. For the increasing gas pressure the collisions processes become dominant. The negative charge of VC is balanced more quickly by positive charge of creating ions and the stable stage of VC is shortened (see Fig. 2).

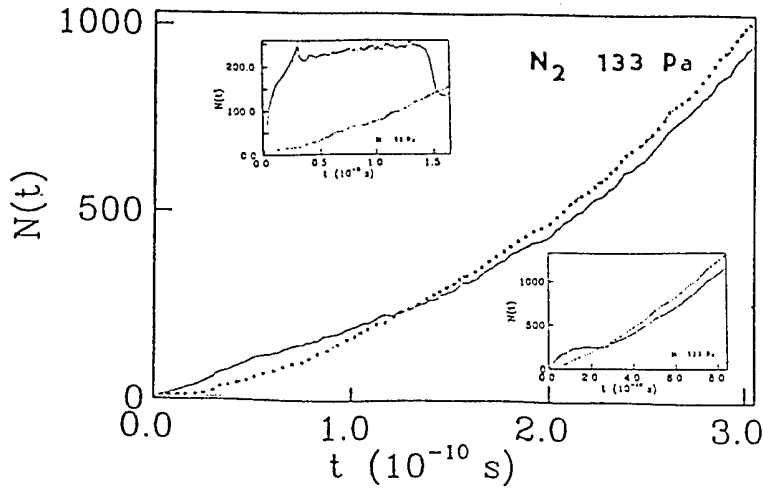


Figure 2: Time dependence of the number of macroparticles, e - full line, i - dotted line

When the bottom of VC arrives the exit foil, the total negative and positive charge is balanced ( $N_e \approx N_i$ ). Since that time, the number of negatively and positively charge carriers increases exponentially, the discharge is burned by electron stream in gaseous target. We stopped our simulation when the allocated computer memory was exhausted.

### The Diagnostics confirming discharge mechanism

The various diagnostics were performed during the calculation to confirm the discharge mechanism. The dependence of electric field intensity  $E(x)$  on the distance  $x$  was calculated (see Fig. 1). The position of zero-point of electric field intensity coincides with the bottom of moving VC. At the final stage, the value of the electric field intensity is  $E(x) \approx 0$  and remains unchanged in the broad internal region of discharge (more than 85 % of discharge length). The quasineutrality is disturbed near the foils, the electric field at the surface of exit foil equals  $E(x) \approx 4.4 \times 10^7 \text{ Vm}^{-1}$ .

The variation of scalar potential  $\varphi_{1/2}(t)$  in the middle of ionized column is a good indicator of discharge behaviour, see Fig. 3. During the formation of VC  $0 \leq t \leq t_{vc}$  the potential decreases rapidly to the value  $\varphi_{1/2} \approx -6.5 \text{ kV}$ . During the short period of stable stage of VC remains practically constant. The middle potential changes its sign at  $t = 1.2 \times 10^{-10} \text{ s}$ . When the VC removes from gaseous target the value of middle potential increases to value  $\varphi_{1/2} \approx \epsilon_e/e \approx 9.0 \text{ kV}$ . Some oscillations of middle potential are detected at final stage of gaseous discharge.

The foil charge diagnostic displays the time history of the wall charge convected to the entrance foil surface by the all species, see Fig. 3. The slope  $dQ_{\text{wall}}/dt$  is real particle current (no displacement current) flowing into left wall. It is approximately equal to stream current  $dQ_{\text{wall}}/dt \approx 9.7 \text{ kA} \approx I_e$  in the period of formation of VC. At the end of this period falls to the value  $dQ_{\text{wall}}/dt \approx 1.89 \text{ kA}$  because the charge is cumulated by the potential well of VC. Then the current grows up to the value  $dQ_{\text{wall}}/dt \approx 6 \text{ kA}$  at  $t_d = 3.0 \times 10^{-10} \text{ s}$  when the gaseous discharge is burned. At the end of our simulation the value of real particle current is practically the same as the external current flowing in RLC circuit.

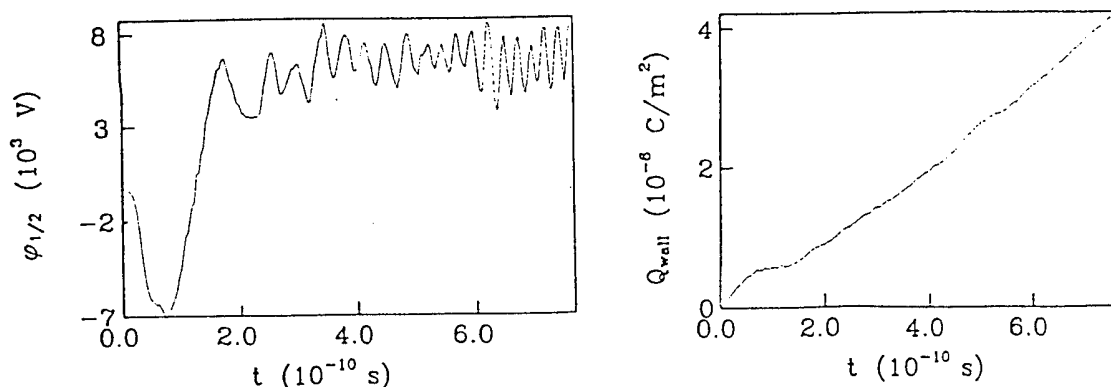


Figure 3: The time dependence of middle potential and wall charge.

The different stages of gaseous discharge (molecular nitrogen at  $p_{N_2} = 133$  Pa) can be deduced from the diagnostic performed in the phase  $v_x - x$  plain. The VC is filled very quickly by creating ions and secondary electrons, owing to the depth of potential well is shallow. The movement of secondary electrons and creating ions has the opposite sign and depends on their positions with respect to the moving bottom of VC. The virtual cathode is removed from the system at the time  $t_{vc} = 1.62 \times 10^{-10}$  s. For the latest time the electron and ion components are redistributed similar to DC discharge.

The history of stream and secondary electrons and ions is seen on Figs. 4 and 5. In final stage of the stream discharge the quasineutrality of ionized gas is achieved practically in the whole gas target ( $> 85\%$ ) instead of narrow cathode or anode boundary sheets. The electric field of cathode boundary sheet accelerates the ions up to the energy  $E_i \approx 75$  eV. The electrons are practically removed from the sheet. The electron energy distribution function near the vicinity of entrance foil confirms that the energy of secondary electrons is ten times less than the energy of stream electrons.

### References

- [1] Birdsall C.K., Langdon A.B., : Plasma Physics via Computer Simulation, New York, 1991.
- [2] Birdsall C.K., : IEEE Transac. on Plasma Sci. **19** (1991) 65
- [3] Verboncoeur J.P., Alves M.V., Vahedi V., : Memorandum No. UCB/ERL M90/67 Berkeley, 1990.
- [4] Verboncoeur J.P., Vahedi V., Alves M.V., Birdsall C.K., : Reference Manual XPDP1, Univ. of California, Berkeley, 1993
- [5] Astrelin V.T., Vrba P., Ullschmied J., lupek M., : Laser and Particles Beams, **6**(3) (1993) 587
- [6] Vrba P., Piffi V., : Czech. Journal of Physics, **43** (1993) 1117
- [7] Piffi V., Vrba P., : Conf.Proc. BEAMS 94 Book of abstracts, P3-3
- [8] Vrba P., : Czech. Journal of Physics, **45** (1995) 1083



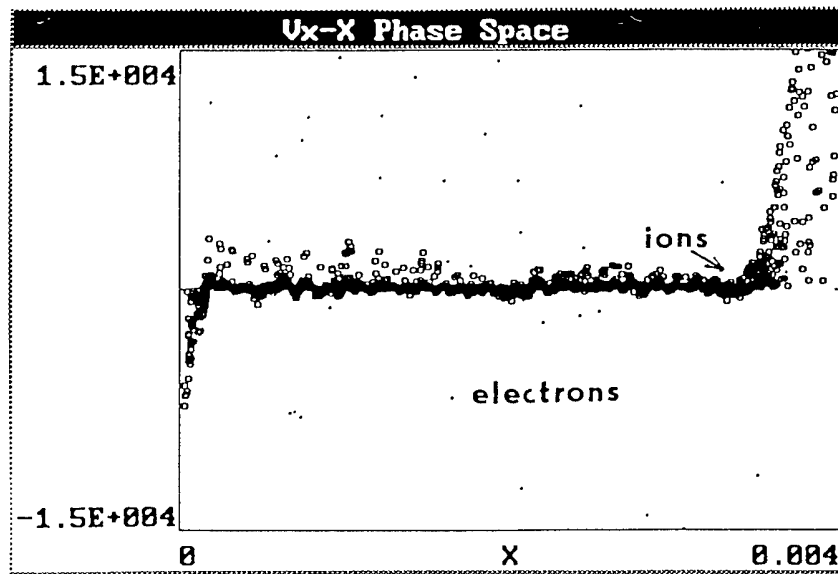
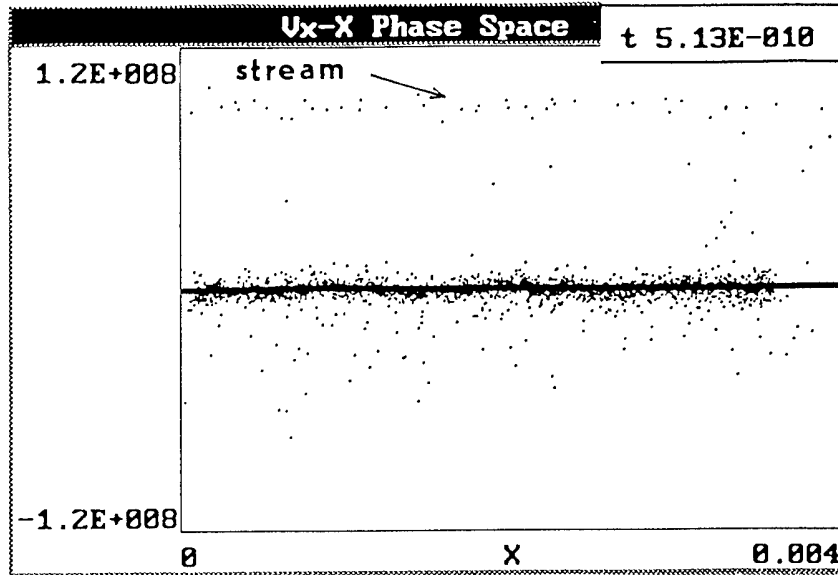


Figure 4: The history of stream and secondary electron velocities and ions velocities in  $v_x - x$  phase space ( $N_2$ ,  $p = 133\text{Pa}$ )

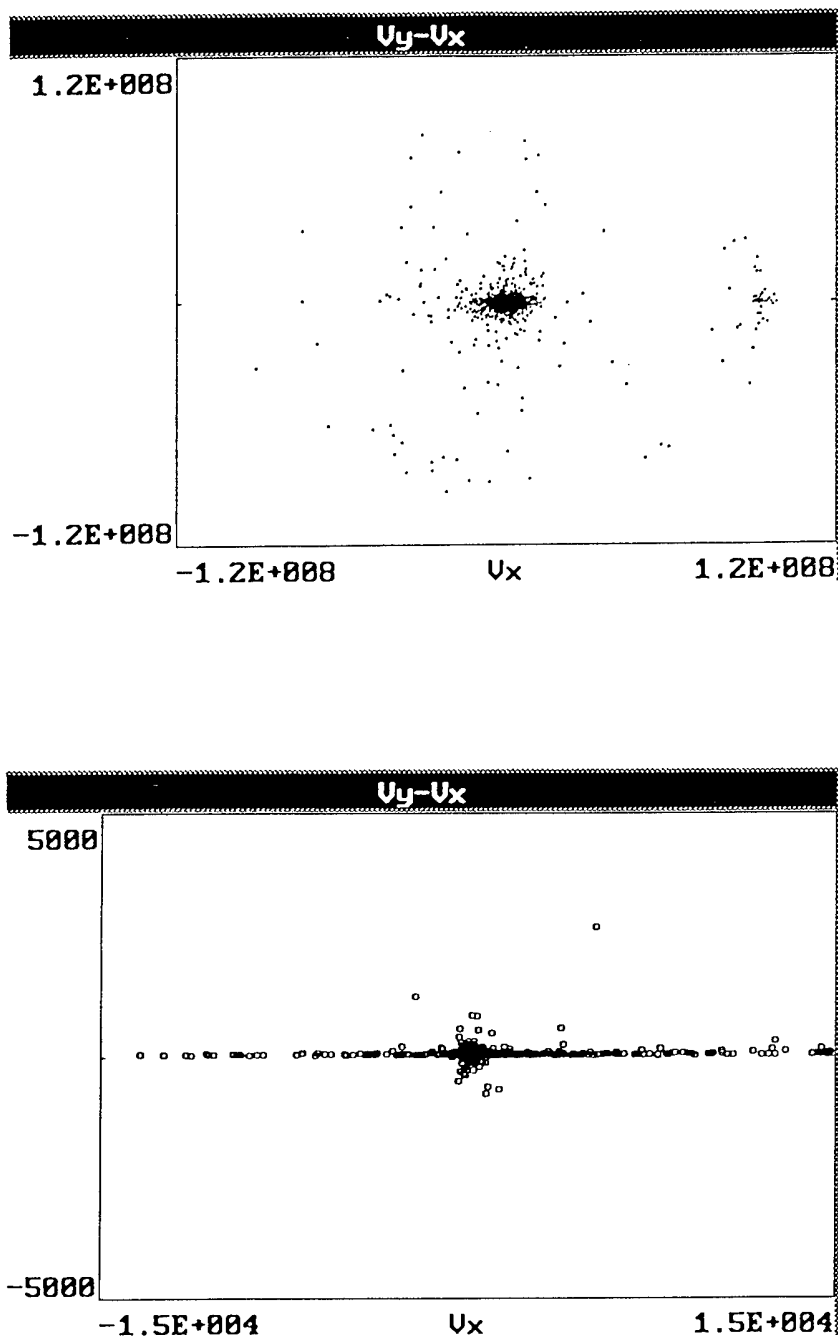


Figure 5: The history of stream and secondary electron velocities and ions velocities in  $v_x - v_y$  phase space ( $N_2$ ,  $p = 133\text{Pa}$ )

# CHAOTIC DYNAMICS OF ELECTRON BEAM WITH VIRTUAL CATHODE IN THE BOUNDED SYSTEM

V.G.Anfinogentov

*College of Applied Science, 83 Astrakhanskaya str., Saratov 410026, RUSSIA*

## Abstract

The electron beam with virtual cathode in the bounded system with feedback is studied with the help of PIC simulation. Different types of nonlinear behaviour are shown. The typical structures are recognized and influence of feedback on the structure formation are investigated. Relations between nonlinear oscillations and structure formation and interaction are discussed.

## Introduction

The microwave electron devices with supercritical current recieved a widespread attention in the last decade [1]. Dynamics of such devices determined by the formation of the region with space charge potential close to the accelerating voltage. This region is usually called a virtual cathode (VC). The practical significance of the devices with the VC is connected with problems of inertial confinement fusion and superhigh power radiation [2].

Experimental data and theoretical models reveales a strong nonlinearity of the regimes with the VC in the electron beam, including an appearance of deterministic chaos [1]. Thus the problem of governing the characteristics of chaotic oscillations is very important for application to such devices.

One of the most common methods of controlling an active system is to incorporate a feedback. The aim of our work is to investigate the feedback influence on the processes in the electron beam with the VC, especially in the chaotic regimes. Simple triode which consists of two diode regions with a common grid was investigated. In each of the diodes the beam propagates between two infinitely wide grounded grids [3]. The space between the grids is filled by a background of immobile positive ions. Electron velocity and charge density are kept constant at the input of the system. The only bifurcation parameter of this system is

$$\alpha = \omega_p L / v_0. \quad (1)$$

Here  $\omega_p$  is the plasma frequency corresponding to the charge density on the input grid,  $L$  is the distance between the grids and  $v_0$  is the initial velocity of the beam.

In the case of external feedback a microwave signal from the second diode is fed into the first one through a transmission line with a delay time  $d$ . This model may be treated as a simplest model of a virtod [4]. In the second case (internal feedback) the electrons transmitted through the VC in the second diode are reflected by the output grid and they interact with the nonreflected ones. The bifurcation parameter is the potential of the output grid  $f_2$ . Such a system may be treated as a simplest model of the reflecting triod [1].

## Nonlinear dynamics

The influence of the feedback on the dynamics of the electron beam with the VC was investigated with help of PIC-simulation [5]. The bifurcation diagrams are presented on

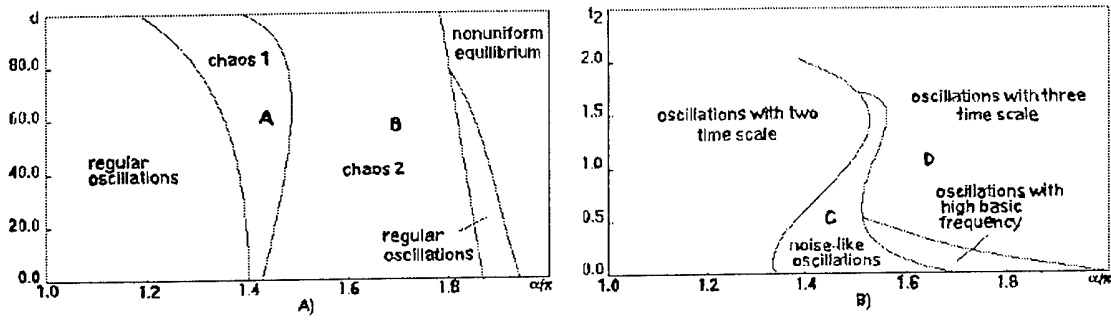


Figure 1: Bifurcation diagrams for external (a) and internal (b) feedback.

plane  $(\alpha, d)$  for the external feedback (Fig.1a) and on the plane  $(\alpha, f_2)$  for the internal one (Fig.1b).

The external feedback leads to the regular oscillations of the VC for small values of  $\alpha$  as well as for  $\alpha$  near  $2\pi$ . The oscillations of the VC becomes chaotic when  $\alpha$  increases. The strange attractor may appear either on the base of one unstable cycle which coincides with the limit cycle for  $\alpha < 1.4\pi$  (Fig.2a), or on the base of set of unstable periodical orbits (Fig.2b). Transition from regular oscillations to chaotic ones take place through a sudden destruction of the cycle in the phase space whereas the transitions between different chaotic regimes occur through intermittency.

The internal feedback leads to the strongly irregular behaviour for any values of  $\alpha$ . For small values of  $f_2$  (which means weak reflection) there are two different time scales of the VC oscillations. Two sharp peaks which correspond to these scales can be easily recognized on the power spectrum for small values of  $\alpha$ . The increasing of  $\alpha$  leads to the noise-like oscillations with the basic frequency growing with the growth of  $\alpha$ . The uniform structure of the attractor (Fig.2c) means that a large number of degrees of freedom is exited. For large values of  $f_2$  high-dimensional irregular oscillations are observed again, and a third sharp peak appears in the power spectra when  $\alpha$  increases (Fig.2d).

## Structures

The internal structure of the electron beam is investigated with the help of the time histories of space charge density. The method of proper ortogonal decomposition is applied [6]. The typical kinds of spatial space charge distribution (further named as modes) are obtained, and time histories of their amplitudes as well as relative energies were calculated (Fig.3).

In the regular regime with the external feedback three modes appear, and the first one

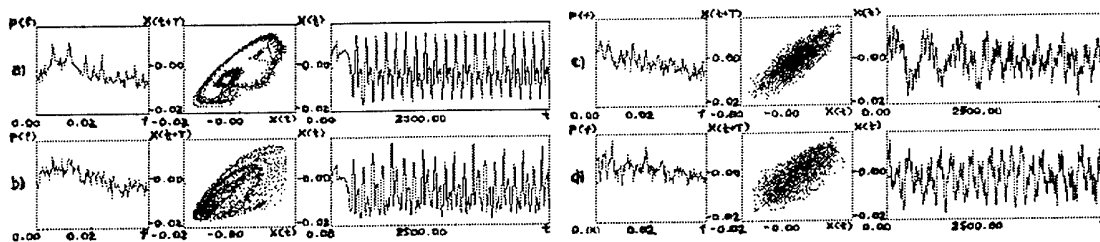


Figure 2: Phase portraits, power spectrum and time histories for different types of chaotic oscillations at external (a,b) and internal (c,d) feedback.

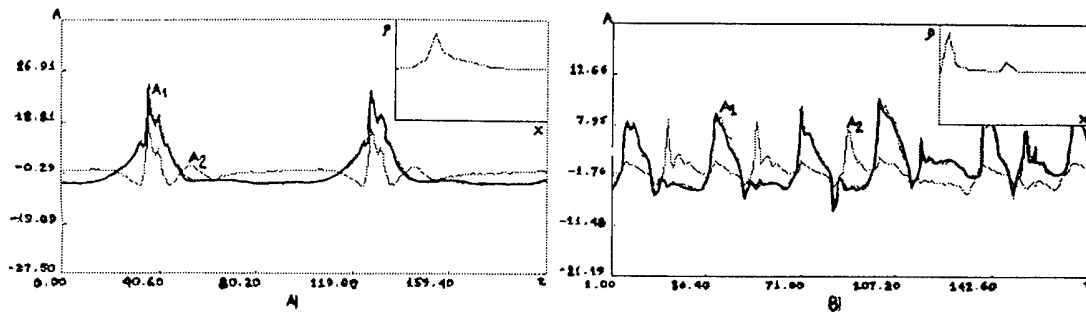


Figure 3: Time histories of mode amplitudes for external (a) and internal (b) feedback.

contains a main part of the energy. The space charge distribution in this mode coincides with that one at the VC appearance (the inner picture on Fig.3a), and the dynamics of its amplitude governs the behaviour of the system (see Fig.3a).

Transition to the chaotic oscillations is accompanied by the excitation of new modes and more smooth energy distribution among them. The basic mode again corresponds to the appearance of the VC, but the following ones have more complicated distributions corresponding to simultaneous existence of more than one bunches in the interaction space. The amplitudes of different modes are almost equal and they are excited simultaneously.

In the case of external feedback the typical distribution of the charge density is demonstrated in the inner picture in Fig.3b. Not only the first sharp peak which corresponds to the VC but also the second one is clearly visible. This peak corresponds to the second structure in the interaction space. The energy of oscillations is distributed smoothly among the modes (the highest mode contains less than 45 % of energy in all regimes). When there exist two time scales, two modes are excited and they exchange the energy during the oscillations, as it is shown on the Fig.3b. Transition to the noise-like oscillations is accompanied by the excitation of a large number of the modes with almost equal amplitudes.

Incorporation of the feedback can lead to changing of the number of the excited modes (external feedback) as well as to changing of its origin (internal feedback). On the other hand chaotic oscillations are accompanied by excitation of a large number of modes with close amplitudes. As well as in the Pierce diode without feedback [7], this excitation occurs simultaneously.

### Physical processes

The typical modes may be interpreted as a set of electron bunches (patterns) in the interaction space. This description is based on the strongly nonuniform character of the space charge distribution. There are the following kinds of the structures with different types of instability. The VC (Fig.5a) appears as a result of electrostatic instability, and

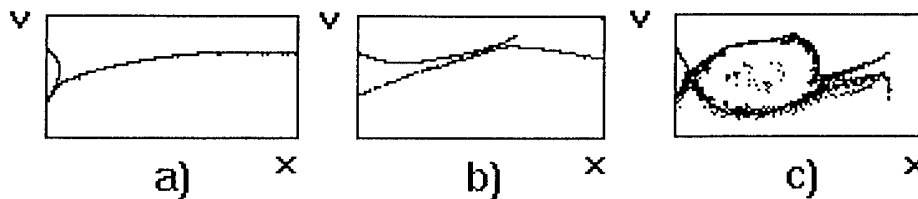


Figure 4: Phase space for different types of structures: (a) – virtual cathode, (b) – bunch, (c) – vortex.

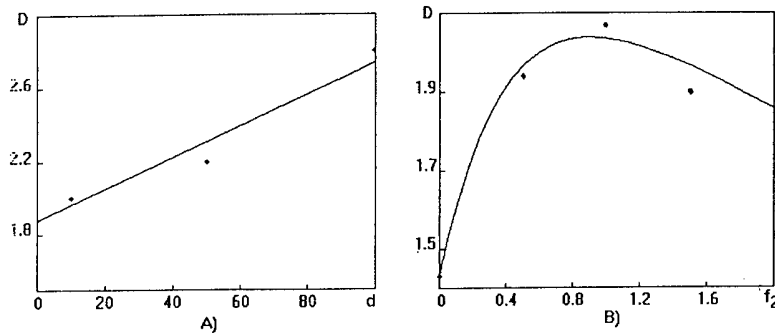


Figure 5: Dependences of attractor dimensions on the parameter of (a) external and (b) internal feedbacks.

it determines the behaviour of the system and the main time scale. The bunches (Fig.5b) in the flow which transmits through the VC are formed on the base of kinematic instability for the external feedback. The vortex in the phase space (Fig.5c) is formed after growing of the two-stream instability for the internal feedback.

There are three different types of the electron trajectories corresponding to these structures: reflection from the VC, deceleration in the VC region followed by drifting to the output, and repeated rotation in the vortex. Each motion provides its own time scale.

Transition to the chaotic regimes is caused by increasing of the number of structures and by strengthening of interaction between them. Increasing of  $d$  leads to the increasing of the number of bunches for the external feedback. The complication in this case is confirmed by the enhancement of the attractor dimension (Fig.5a).

In the case of the internal feedback when the potential  $f_2$  is sufficiently large, and, hence, there is a considerable reflected current, a rather uniform vortex emerges in the phase space. Interaction between the structures strengthens and the oscillations become more chaotic. Maximal value of attractor dimension corresponds to just this values of  $f_2$  (Fig.5b). The further increasing of  $f_2$  makes the vortex to close upon itself and thus leads to breaking of the interaction and to decreasing of attractor dimension.

## Conclusion

Incorporating of the external or the internal feedback leads to the significant transformation of nonlinear behavior of the electron beam. This process, determined by the structures formation and interaction, may cause simplification as well as complication of oscillations in comparison with the beam without a feedback.

This work is supported by the Committee of Higher Education and Science of Russian Federation (Programme "Fundamental Researchs in Radio Engineering and Electronics" Grant No.2-33).

- [1] Selemir V.D. et al., Plasma physics, **20** (1994) 682.
- [2] Thode L.E., in High Power Microwave Sources, Artech House, Boston, 1987.
- [3] Pierce J., J.Appl.Phys, **15** (1944) 721.
- [4] Gadetsky N.P. et al., Plasma physics, **19** (1993) 530.
- [5] Birdsall C.K., Langdon A.B., Plasma physics via computer simulation, McGraw-Hill, NY, 1985.
- [6] Lumley J.U., in Atmospheric Turbulence and Radio Wave Propagation, Nauka, Moscow, 1967.
- [7] Anfinogentov V.G., in Proc. of International School on Nonlinear Science, N.Novgorod, (1995) 6.

# EFFECTIVE CODE FOR NUMERICAL SIMULATION OF THE HELICAL RELATIVISTIC ELECTRON BEAMS

V.K.Lygin, V.N.Manuilov, Sh.E.Tsimring

*Institute of Applied Physics of Russian Academy of Sciences,  
46 Uljanov Street, 603600, Nizhny Novgorod, Russia*

## Abstract

The method to calculate the beam space charge electric field, based on the integral equations method and introduction of three additional meshes is developed. Method diminishes the calculation time essentially. The new approach to the space charge limited current regime simulation is presented. The current density distribution  $j(R)$  is calculated directly from the zero condition for the normal component of the electric field on the emitter. It leads as well to the reducing of the  $j(R)$  as beam properties calculation errors.

## Introduction

The main problem arising in the numerical simulation and optimization of the intense electron beams is diminishing of the calculation time (CT) for condition of keeping the accuracy of calculations. The characteristic features of the beams for most of the high power electronic tubes are a large length and small ratio of the beam thickness to the transverse dimensions of the electron-optic system (EOS). The importance of these factors especially increases for the simulation of the helical relativistic electron beams (HREBs).

The main part of the simulation time deals with the solving of the Poisson equation. In wide known codes, such as EGUN [1], BFCPIC [2], DAPHNE [3], CIELAS [4] etc., the finite element (finite differences) method is used to solve the Poisson equation and so it is necessary to cover all EOS region by the potential mesh (PM). As the result, it takes a big number of cells and the CT to obtain the solution.

## The method of theoretical analysis.

Below the new approach based on the integral equations method for solving the Poisson equation is used. Calculation of potential  $U$  in any point  $R$  is carried out according to the formula of a simple layer

$$U(R) = \frac{1}{4\pi\epsilon_0} \int \frac{\rho dv}{R_0} + \frac{1}{4\pi\epsilon_0} \int \frac{\sigma ds}{R_i} \quad (1)$$

where the first integral is calculated on over beam volume, the second one on over electrode surface. Charge density distribution  $\rho(R)$  is calculated by discretisation of charge in the current pipes and the further distribution of the discrete charges  $Q_m$  on points of the special mesh (space charge mesh - SCM, steps are  $h_{rq}, h_{zq}$ ).  $\sigma$  is approximated by the circular charges  $Q_i$ , which placed on small distance behind electrodes. As a result, potential in some point with coordinates  $r_A, z_A$  is (below axisymmetric systems are considered) :

$$2\pi^2 \varepsilon_0 U(r_A, z_A) = \sum_{i=1}^N Q_i \Psi_i + \sum_{m=1}^M Q_m \Psi_m \quad (2)$$

Here  $\Psi_j = \frac{K(t)}{\sqrt{(r_A+r_j)^2+(z_A-z_j)^2}}$ ,  $t^2 = \frac{4r_j r_A}{\sqrt{(r_A+r_j)^2+(z_A-z_j)^2}}$ ,  $j=i, m$

$K(t)$  - the full elliptic integral of the first kind. It allows to introduce the potential mesh (PM) and SCM which cover the beam region only. Electric field components  $E_r$ ,  $E_z$  then are calculated using potential values in 9 nodes nearest to the point of observation on the electron trajectory (9-point mould) according to quadratic interpolation. This is the first step to reduce the calculation time. However, the CT is still remain the quadratic function of the beam length.

The further reducing of the CT is reached by introducing the additional space charge mesh (ASCM) with big steps  $h_{rqb} \gg h_{rq}$ ,  $h_{zqb} \gg h_{zq}$ . It is clear, that the accuracy of space charge potential, providing by distant from the point of view part of the beam, may be decreased without lossing the total accuracy of potential calculation. So equation (2) may be represented as

$$2\pi^2 \varepsilon_0 U(r_A, z_A) = \sum_{i=1}^N Q_i \Psi_i + \sum_{m=1}^M Q_m \Psi_m + \sum_{p=1}^P Q_p \Psi_p \quad (3)$$

Here the first sum includes an auxiliary charges behind the electrodes. The charges  $Q_m$  contained in the second sum, are placed in the region with length  $L$  in nodes of the SCM near the point of view. Finally, the third sum defines potential of the distant charges  $Q_p$ , which are placed in the ASCM nodes. Each of such charge is the sum of those charges  $Q_m$ , which are placed in one cell of the ASCM outside the region with length  $L$ .

In this case CT of the long extent beam trajectories becomes practically the linear function of the beam length considerably and decreases essentially in comparison with algorithms, which don't use separate calculation of the nearest and distant charge potentials.

Note, that for given boundary conditions on the electrodes, and known values of  $Q_m$ , the relation (2) becomes the system of  $N$  linear equations with respect to  $Q_i$ . After finding  $Q_i$  equation (2) allows to calculate the potential in any point of PM.

The complicated beam geometry (for example, systems with the curvilinear electron trajectories, electron optic systems of TWT and klystrons with the high compression and multy flow systems also) makes the difficult conformation of the potential mesh with the beam form. Therefore, it is necessary to use the mesh region with essentially larger size than space of the beam region. But the geometry of trajectories is not known on the stage of mesh building. It leads to very approximate definition of the mesh surplus degree. As a result, a lot of "blank" nodes appears. They contain potential values obtained from formula (3) but aren't used during electric field calculations. However, the calculation of potentials in the auxiliary mesh nodes is the main part of full time of numerical analysis.

The special algorithm permits to cut all "blank" nodes of PM. Before starting each trajectory iteration all potential array elements in corresponding nodes are to be set to zero. After that the trajectory calculation is began. The potential values on each step of integration of the motion equations are calculated only in those mesh nodes, which is included in 9-point



mould, relating to the given observation point. If in some mould nodes potential is not equal to zero, i.e. this node was already included in some other moulds, potential is not recalculated. So "blank" nodes are absent in considering algorithm. Mesh region surplus leads to increase of requirement memory only.

The developed algorithm is effective not only for static regimes, but also may be used for the investigations of time-dependent processes in HREBs (PIC method).

The most of electron-optic systems work in space-charge limiting current regime. Up to now in most codes the Child law for planar diode is used to obtain the current density distribution along the cathode. But this approach may lead not only to the essential errors in calculation of  $j(R)$  for cathodes with small curvature radius or placed in the magnetic field. The errors in  $j(R)$  cause the variations in the space charge distribution in the beam and so lead to deviation in calculated beam properties especially in the curvilinear beams.

The more universal approach to this problem is to calculate current density distribution directly from the condition  $E_n=0$  for normal component of the emitter electric field. It leads to the following system of nonlinear equations about the currents  $I_k$  in  $K$  current pipes:

$$F(E_k) = f_k(I_1, I_2, \dots, I_k) = 0, \quad k=1, 2, 3, \dots, K \quad (4)$$

Here  $E_k$  is the normal component of the electric field in the  $k$ -th electron start point,  $F(E_k)$  is the specially choosed function of the electric field, which equals to zero at  $E=0$ . Below  $F(E)=E^2$ . To solve the system (4) the iteration scheme based on Broyden method [5,6] is used. In this method one solution of the self-consistent beam equations on each iteration is used only. The current on  $(j+1)$  iteration is calculated on formula

$$I_{j+1} = I_j + S_j, \quad (5)$$

where  $S_j$  are received from solution of the linear equations system

$$A_j S_j = -F(E_j) \quad (6)$$

Matrix  $A_j$  is analogous to matrix Jacoby and is obtained from recurrent formula:

$$A_{j+1} = A_j + \frac{Y_j - A_j}{S_j^T S_j}, \quad Y_j = F_{j+1} - F_j \quad (7)$$

$F_j$  is caculated from the self-consistent beam equations on each iteration.  $T$  is the transperence symbol. The iteration process is finished when the condition

$$\max_k \left| \frac{I_k^{(j+1)} - I_k^{(j)}}{I_k^{(j)}} \right| < \varepsilon \quad (8)$$

is valid. Here  $\varepsilon$  is the given relative error.

To start the iteration procedure it is necessary to have two sets of currents  $I_k$  and corresponding values of electric fields  $E_k$ . Initial vectors of currents are choosed as

$$I_k^{(j)} = \alpha_j I_{Lk}, \quad j=1,2, \quad k=1,2,\dots,K. \quad (9)$$

where  $I_L$  - current, calculated from the Child law, coefficients  $\alpha_j$  are satisfied to relations

$$0 < \alpha_j < 0.5, \quad |\alpha_1 - \alpha_2| < 1, \quad \alpha_1 < \alpha_2$$

Electric field  $E_k$  is obtained from the self-consistent beam equations with mentioned above currents  $I_k$ . Then initial approximation of matrix  $A^0$  is obtained from the formula

$$A_{mn}^0 = \begin{cases} \frac{f(E_m^{(2)}) - f(E_n^{(1)})}{I_m^{(2)} - I_n^{(1)}}, & m = n \\ 0, & n \neq m \end{cases} \quad n, m = 1, 2, \dots, k \quad (10)$$

The developed procedure has some importance advantages on compare with conventional approach based on the using Child law only:

- a) The analysis of multy flows beam is possible;
- b) The method is applicabled for the magnetically confined beams;
- c) The method permits to analyze systems with the arbitrary emitter curvature radius.
- d) The computer time and the calculating errors reduce essentially.

### Conclusion

The separate calculation of the nearest and distant charge potentials and special algorithm to cut all "blank" nodes of potential mesh allow to diminish the CT by an order or more especially for a long crew electron beams. Calculation the current density distribution from the nonlinear equations for the beamlet currents on the base of Broyden method increases the accuracy of  $j(R)$  definition and diminish the obtained beam properties errors.

The developed above algorithms are realized in computer code EPOS.

- [1] Hermannsfeld W.B. Electron Trajectory Program SLAC-226, Stanford University, Stanford, CA, 1979.
- [2] Borie E., Gruber C., Westermann T. Calculation of MIG Guns for Gyrotrons using BFCPIC code. Int. J. Electronics, **78**, 1995.
- [3] Tran T.M., Whaley D.R., Merazzi S., Gruber R. DAPHNE, a 2D Axisymmetric Electron Gun Simulation Code. 6-th EPS-APS International Conference on Physics computing, Lugano, Switzerland, August 1994.
- [4] Edgecombe C.J. Sources of velocity spread in electron beams from magnetron injection guns. Int. J. Infrared and Millimeter Waves, **16** (1995), 83-98.
- [5] Dennis J.E., Schnabel R.B. Numerical Methods for Unconstraining optimization and Nonlinear Equations, Prentice-hall Inc., 1983.
- [6] Raisky B.V., Tsimring Sh.E. About the calculation of systems forming the intense electron beams in space charge limiting current regime. Izvestiya VUZ'ov. Radiophysika, **36** (1993), 955-958.

# ELECTRON, ION AND ATOMIC BEAMS INTERACTION WITH SOLID HIGH-MOLECULAR DIELECTRICS

V.V. Milyavskii, V.A. Skvortsov

*High Energy Density Research Center Russian Academy of Science  
IVTAN, Izhorskaya 13/19, Moscow, 127412, Russia*

## Abstract

A mathematical model is constructed and numerical investigation performed of interaction between intense electron, ion and atomic beams and solid high-molecular dielectrics under various boundary conditions. The model is based on the equations of mechanics of continuum, electrodynamics and kinetics, describing the accumulation and relaxation of space charge and shock-wave processes, as well as the evolution of electric field in the sample. A semi-empirical procedure is proposed for the calculation of energy deposition by electron beam in a target in the presence of non-uniform electric field.

## Introduction

The mathematical model of interaction between an intense particle beam and a solid high-molecular dielectric [1,2], earlier constructed by authors and applied in this paper, is based on the equations of mechanics of continuum, electrodynamics and kinetics, describing the accumulation and relaxation of space charge and shock-wave processes, as well as the evolution of electric field in the sample. The processes of the volume charge accumulation and relaxation and the electric field evolution in the sample was described with the aid of Rose-Fowler system of equations and the equations for calculation of high-energy carriers of charge kinetic. For description of hydrodynamic processes the system of equations of continuum mechanics in elastic-plastic approximation and the wide-range equation of state were used. A semi-empirical procedure was proposed for the calculation of energy deposition by electron beam in a target in the presence of non-uniform electric field. The above-described mathematical model was used to perform numerical experiments on the interaction of monoenergetic and energy-distributed particle beams with parameters, characteristic for modern small-size accelerators, with plates of polystyrene of various thickness. The primary objective of our investigation was to find out what is the place of processes of the accumulation and relaxation of volume charge in total picture of interaction between a particle beams and a solid dielectrics. Some of the calculation results is presented below.

## Results and discussion

On Fig.1 you can see some calculation results of the effect of a monoenergetic electron beam with the sinusoidal time dependence of current density, pulse duration 50 ns, kinetic energy of electrons in the beam 0.5 MeV, time-average current density 0.5 kA/cm<sup>2</sup>, on a grounded plate of polystyrene (thickness 2.5 mm). The calculations were performed twice: once including (case *A*) and once ignoring (case *B*) the processes of volume charge accumulation and relaxation. Fig.1 illustrates the distribution of specific internal energy over the target thickness for cases *A* and *B*. One can see that the electric field emerging in the sample and the conduction current induced under the effect of this field cause a significant variation of the space distribution of energy contribution: the region of energy release narrows down (the space charge electric field has a slowing-down effect on the beam electrons), ohmic heating causes a variation in the profile of

the energy release curve (owing to this heating, an increase in the density of energy contribution is observed in the regions adjoining the front surface of the sample). These two factors cause an increase of the absolute magnitude of specific internal energy in the sample. The narrowing down of the region of energy contribution considerably affects the behavior of hydrodynamic motion of the medium, in particular, it leads to an appreciable delay in the compression wave arrival to the free surface (Fig.1). More carefully the interaction between an electron beams and a dielectrics was discussed in [1,2].

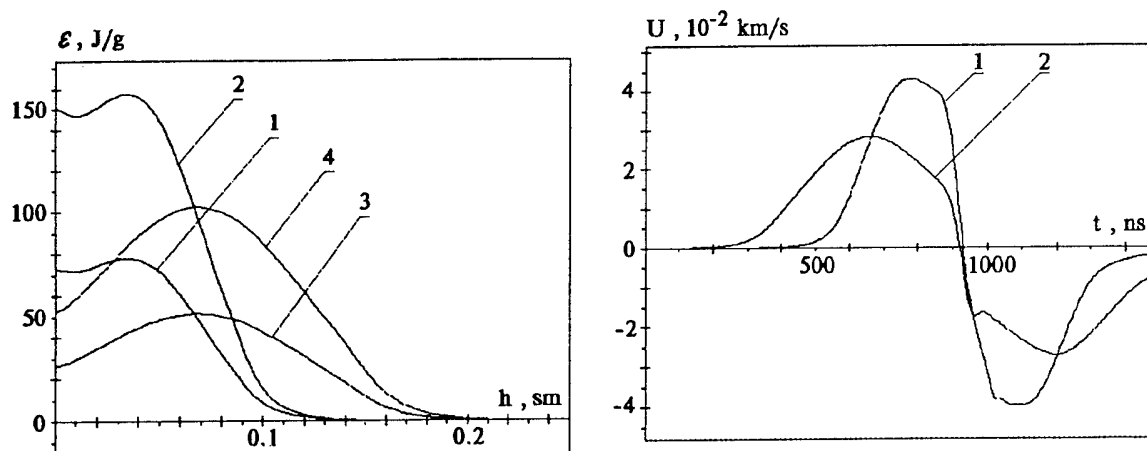


Fig.1. Distribution of specific internal energy over the sample thickness by the moment of time  $t=25$  ns (1,3) and  $t=50$  ns (2,4): 1,2 - case A, 3,4 - case B (on the left) and time dependences of the velocity of free surface of samples: 1 - case A, 2 - case B (on the right).

On Fig.2 and Fig.3 you can see some calculation results of the effect of an atomic (hydrogenous) beam on a plate of polystyrene (thickness 3 mm) with free surfaces. The dependence of current density from time and energy was described as

$$J_b(T, t) = \frac{\pi \cdot \bar{J}}{2e} \cdot \sin(\pi t / \tau) \times \frac{1}{\sqrt{2\pi} \cdot \sigma} \cdot \exp\left(\frac{-(T - \bar{T})^2}{2\sigma^2}\right) \quad (1)$$

with following parameters:

$$\bar{J} = 20 \text{ A / cm}^2; \bar{T} = 10 \text{ MeV}; \tau = 50 \text{ ns}; \sigma = 1 \text{ MeV}.$$

The volume charge accumulation and relaxation in this case is characterized by following peculiarities: first electrons subside in neighborhood of the front surface of the plate and define the negative charge accumulation in this region, but protons penetrate to the depth of the sample, where a positive charge is accumulated (Fig.2). As a consequence of this, a two-layers charge structure, like condenser, forms and an internal electric field arises (Fig.2). Under action of radiation, conductivity of the dielectric strongly increases (Fig.3) and the charge structure becomes unstable: the counter motion of a charge carrier begins and lead to redistribution and compensation of the charge in the sample. Under this condition, formation of the additional charged layers is observed. After the termination of irradiation, the value of conduction slowing down dramatically, and the layers remain "frozen" in the sample during long time. As for hydrodynamic processes, note that when we say about hard particles, the effect of beams deceleration by the electric field is not essential, and any peculiarities in this case, in contradiction to the case of electron beams, is not observed (see Fig.3, for example).

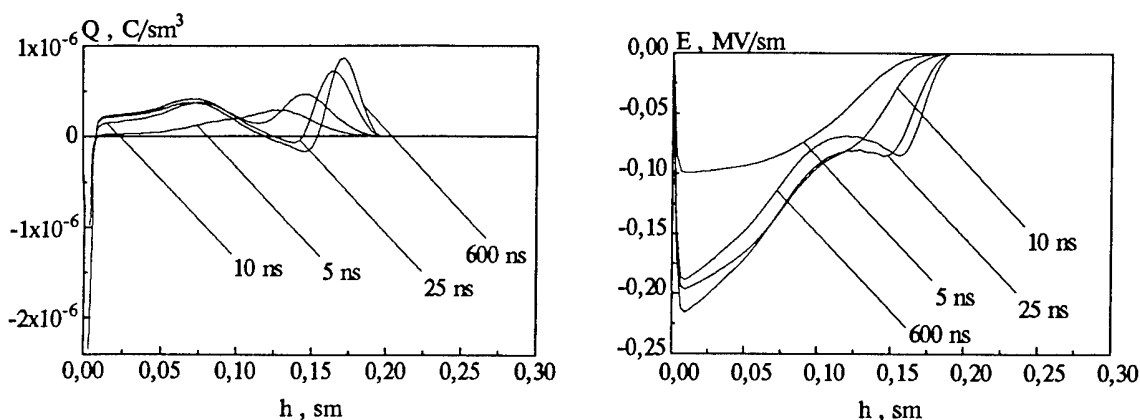


Fig.2. Distribution of the density of electric charge (on the left) and electric field (on the right) over the sample thickness at the different moments of time.

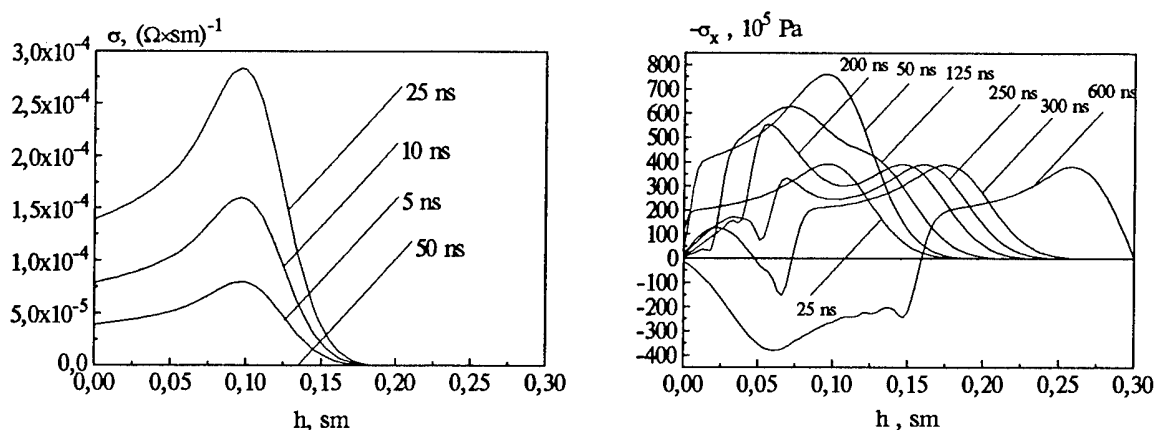
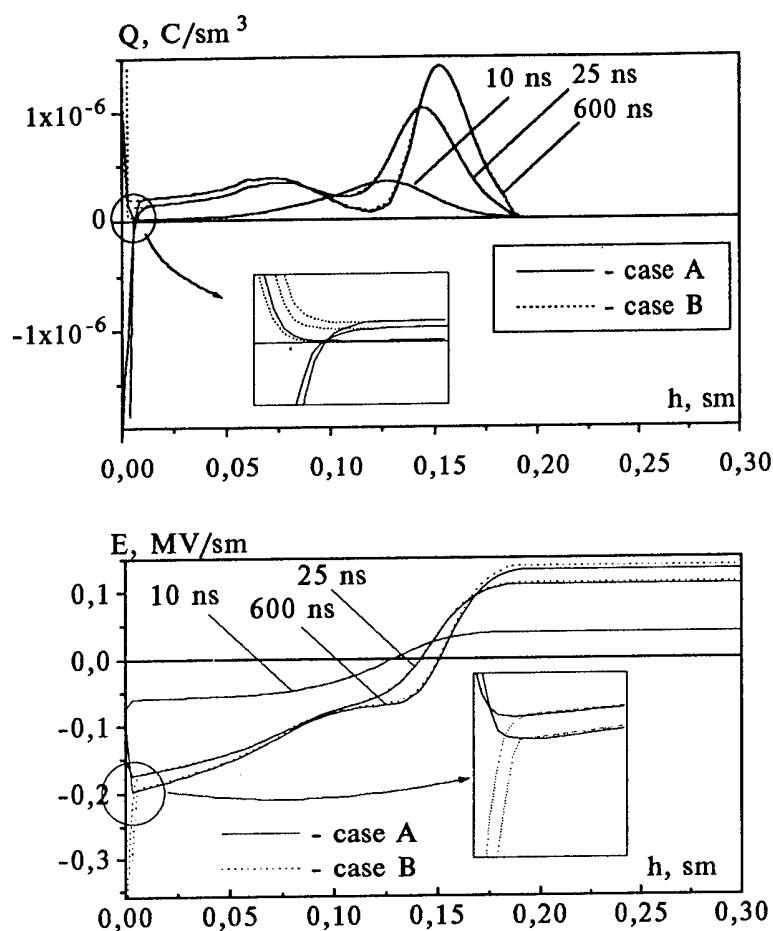


Fig.3. Distribution of radiation conduction (on the left) and total stresses (on the right) over the sample thickness at the different moments of time.

The influence of boundary conditions on the processes of the accumulation and relaxation of the volume charge is discussed on the base of numerical simulation of the interaction between an ion (hydrogenous) beam and a plate of polystyrene (thickness 3 mm), placed into grounded metal foil. The dependence of current density from time and energy was described by equation (1) with following parameters:

$$\bar{J} = 5 \text{ A / cm}^2; \bar{T} = 10 \text{ MэВ}; \tau = 50 \text{ нс}; \sigma = 1 \text{ MэВ}$$

We proposed, that the charge carriers exchange between the dielectric and the metal foil is realized by autoelectron emission from the foil to the sample. The calculations were performed twice: for metal-dielectric pair with the height of potential barrier 0.1 eV (case *A*) and 2 eV (case *B*). In the case *B*, as a consequence of the big height of the potential barrier, the injection of electrons into the dielectric practically is absent. Otherwise in case *A* positive charge, initially accumulated nearby the front surface of the sample, is neutralized during irradiation, and then change a sign (Fig.4). Under this the constriction of the electric field growth in neighborhood of the front surface of the sample is observed (Fig.4).



**Fig.4.** Distribution of the density of electric charge (up) and electric field (down) over the sample thickness at the different moments of time for cases *A* and *B*.

### Conclusion

The calculations demonstrate that under the beams interaction with the samples, the volume charge is accumulated and the internal electric field of high intensity, up to breakdown intensity, is arisen. As it was obtained for electron beams, in case when breakdown does not take place, the region of energy deposition considerable decreases as a result of electrons deceleration by the electric field. Under this conditions the temperature, the pressure and the internal energy in the sample are increased, and a part (10-20%) of full energy absorbed in the sample, is released as a result of ohmic heating by the electric currents. Besides this, the delay of coming of compression waves to back face of the target is observed. In case when electric breakdown takes place, the sample quickly discharges, and the effect of electron beams deceleration by the electric field is not essential (as well as in the case of ion and atomic beams). For ion and atomic beams was observed the formation of multi-layer (sandwich) structures of volume charge (the sign of charge is changed several times lengthwise the sample thickness). Besides this, the influence of boundary conditions on the processes of the volume charge accumulation and relaxation was investigated.

- [1] Milyavskii V.V., Skvortsov V.A. : Chemical Physics Reports, **14** (1995) 113.  
 [2] Milyavskii V.V., Skvortsov V.A. : High Temperature, **33** (1995) 789.

## AN EXPERIMENTAL STUDY ON CYCLOTRON-CHERENKOV RADIATION

C. Y. Lee, M. Masuzaki, H. Yoshida, N. Toyosugi, K. Kamada and R. Ando

*Department of Physics, Faculty of Science, Kanazawa University,  
Kanazawa 920-11, Japan*

### Abstract

We searched numerically dielectric-loaded cylindrical waveguide configurations with an injected electron beam in which the growth rate of the cyclotron-Cherenkov instability surpassed that of the Cherenkov instability, and found such a configuration. This configuration consists of a metallic core and an outer metallic cylinder with a dielectric liner on the inner surface. In order to investigate experimentally radiation due to the cyclotron-Cherenkov instability, we designed and assembled an experimental device using the computational results. We studied beam propagation in the dielectric-loaded coaxial waveguide and microwave radiation due to the cyclotron-Cherenkov instability and the Cherenkov instability.

### I. Introduction

When a linear electron beam is injected into a dielectric-loaded slow-wave structure immersed in an axial magnetic field and the phase velocity of the electromagnetic wave is less than the beam velocity, the Cherenkov and cyclotron-Cherenkov instabilities occur.<sup>1-3)</sup> The former instability arises from the coupling of the slow electromagnetic wave to the slow space charge mode and the latter arises from the coupling of the slow electromagnetic wave to the slow cyclotron mode. An oscillator or amplifier based on the Cherenkov instability is known as the Cherenkov free electron laser and several works have already been carried out.<sup>4-7)</sup>

Recently an oscillator or amplifier based on the cyclotron-Cherenkov instability, i.e. the cyclotron-Cherenkov free electron laser, has attracted much attention.<sup>8-9)</sup> This free electron laser has several advantages.<sup>3)</sup> First, a purely axial electron beam can be used. Secondly, there is no need of a periodic structure. And finally, it has the potential for large frequency tuning by varying the magnetic field and/or the beam energy.

We have searched coaxial waveguide

configurations with an injected linear electron beam in which the growth rate of the cyclotron-Cherenkov instability surpass that of the Cherenkov instability, and found such a configuration as shown in Fig.1.<sup>10)</sup> This configuration consists of a metallic core and an outer metallic cylinder with a dielectric liner on the inner surface. We designed and assembled an experimental device. We studied beam propagation and microwave radiation due to the cyclotron-Cherenkov instability and the Cherenkov instability in this device.

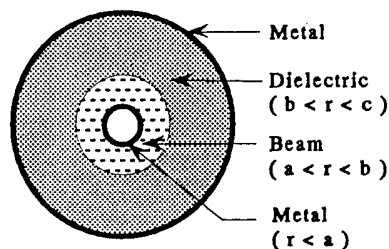


Fig.1. The configuration of coaxial dielectric-loaded waveguide.

### II. Theory

The dispersion relations for the dielectric-loaded coaxial waveguides are derived using Maxwell's equations, the relativis-

tic equation of motion, and the continuity equation. An axial magnetic field is assumed to be applied. Also, it is assumed that there is no gap between the electron beam and the dielectric, and between the beam and the conductor, and that the system is azimuthally symmetric. We consider in the analysis azimuthally symmetric  $TM_{0n}$  modes.

In the beam region and the dielectric region, the axial electric field is obtained from the following differential equation.

$$\frac{1}{r} \frac{\partial}{\partial r} \left( r \frac{\partial}{\partial r} \right) E_z(r) + \left( \omega'^2 - \omega_p^2 / \gamma^3 \right) \times \frac{\left[ \left( \epsilon \omega^2 / c^2 - k^2 \right) \omega'^2 - \omega'^2 \omega_p^2 / c^2 \gamma^3 \right]}{\omega'^2 \left( \omega'^2 - \omega_p^2 / \gamma^3 \right)} E_z(r) = 0,$$

where  $\omega' = \omega - k v_0$  and  $\omega'^2 = \omega^2 - \Omega^2 / \gamma^2$ ,  $\epsilon$  is the dielectric constant,  $\omega_p$  is the beam plasma frequency, and  $\Omega$  is the electron cyclotron frequency. In the beam region  $\epsilon = 1$ , and in the dielectric region  $\omega_p = 0$ ,  $\Omega = 0$ .

The solution for  $E_z(r)$  in the beam region is

$$E_z(r) = C J_0(pr) + D N_0(pr)$$

for  $p^2 > 0$ , and

$$E_z(r) = C I_0(pr) + D K_0(pr)$$

for  $p^2 < 0$ , where

$$p^2 = \left( \omega'^2 - \omega_p^2 / \gamma^3 \right) \frac{\left( g^2 \omega'^2 - \omega'^2 \omega_p^2 / c^2 \gamma^3 \right)}{\omega'^2 \left( \omega'^2 - \omega_p^2 / \gamma^3 \right)}$$

and

$$g^2 = \omega^2 / c^2 - k^2.$$

The solution for  $E_z(r)$  in the dielectric region is

$$E_z(r) = A J_0(qr) + B N_0(qr)$$

where

$$q^2 = \epsilon \omega^2 / c^2 - k^2.$$

The boundary conditions are that the

axial electric field is continuous on the boundaries and that surface current density equals charge density times beam velocity. The dispersion relation is obtained from components of the electromagnetic fields in the both regions and the boundary conditions. The dispersion relation is obtained as follows; for  $p^2 < 0$ ,

$$\frac{\epsilon}{q} \frac{\left[ J_0(qc) N_1(qb) - N_0(qc) J_1(qb) \right]}{\left[ N_0(qc) J_0(qb) - J_0(qc) N_0(qb) \right]} = \chi \frac{\left[ K_0(p'a) I_1(p'b) + I_0(p'a) K_1(p'b) \right]}{\left[ K_0(p'a) I_0(p'b) - I_0(p'a) K_0(p'b) \right]},$$

where  $\chi = \left( \omega'^2 - \omega_p^2 / \gamma^3 \right) / \omega'^2 p'$  and  $p'^2 = -p^2$ .

Figure 2 shows an example of typical growth rates of both instabilities.

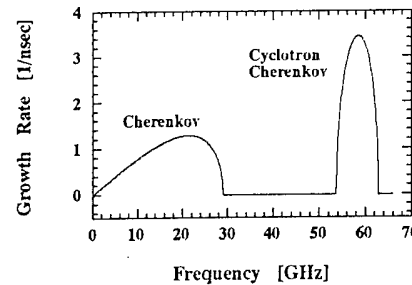


Fig.2. The growth rates of both instabilities for a dielectric-loaded coaxial waveguide.  $a = 1.05$ ,  $b = 1.25$ ,  $c = 1.35$ cm,  $E = 1.0$  MV,  $I = 2$  [kA],  $B_g = 0.5$  T,  $\epsilon = 2.01$

### III. Experimental setup, results and discussions

We designed and assembled an experimental device using the computational results, and studied beam propagation and microwave radiation. A Physics International Pulserad 220G is used as the beam source. This system can supply a beam pulse of  $\sim 1$  MV, 30 kA and 200 ns. The diode consisted of a hollow cathode of diameter 2.5 cm and a carbon anode with an aperture 2.7 cm in diameter. The cath-



To PI-220G

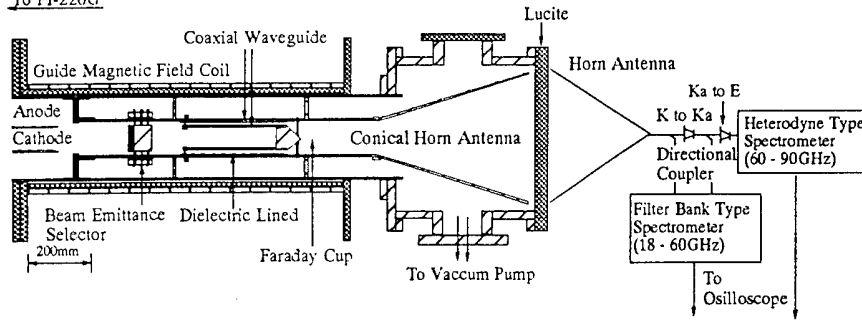


Fig.2. A schematic of the experimental setup

ode-anode gap was 15mm. The thickness of the hollow beam determined by damage pattern on brass plates was  $\sim 2$ mm. A guide magnetic field of up to 1.5T was applied using a solenoid coil of 100cm long. As a dielectric teflon ( $\epsilon = 2.01$ ) was used. The base pressure was  $2 \times 10^{-5}$  Torr. Experimental parameters are shown in Table I.

Table I. Experimental parameters

r [cm]	a = 1.05, b = 1.25, c = 1.35
E [kV]	770, 810
$B_g$ [T]	0.6, 0.9, 1.2

A schematic of the experimental setup is shown in Fig.2. The beam current through the interaction region was measured by a Faraday cup. The microwave radiation produced was guided from the interaction region into free space through a vacuum window and conical horn antenna of 30cm long. A horn was attached to the free space side of the lucite vacuum window. The RF signal was measured using filter-bank type spectrometer (K band; 18 - 26.5 GHz, Ka band; 26.5 - 40 GHz, and U band; 40 - 60 GHz) and Heterodyne type spectrometer (E-1 band; 68 - 72.2 GHz, E-2 band; 72.2 - 76.5 GHz, E-3 band; 76.5 - 81 GHz, E-4 band; 81 - 85.5 GHz, and E-5 band; 85.5 - 90 GHz). Typical pulse waveforms are shown in Fig.3.

Figure 4 shows beam current through interaction region vs. the guide magnetic field. When the guide magnetic field was varied from 0.6T to 1.2T, the beam current through interaction region varied from 100A to 1.7kA.

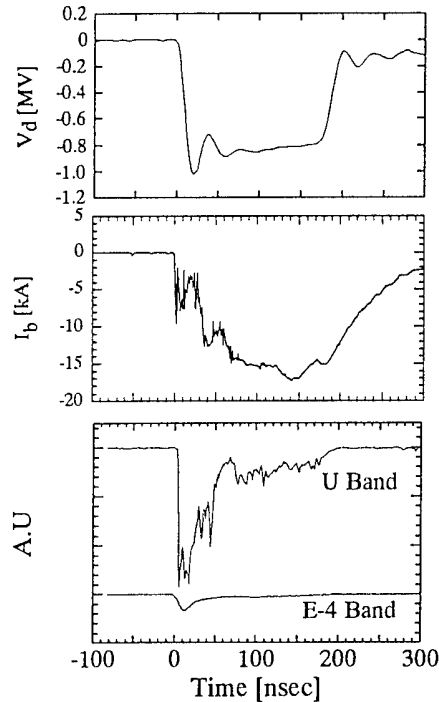


Fig.3. Typical pulse waveforms; the diode voltage(top), the beam current(middle) when through the dielectric-loaded coaxial waveguide, and RF signal of U and E-4 bands.

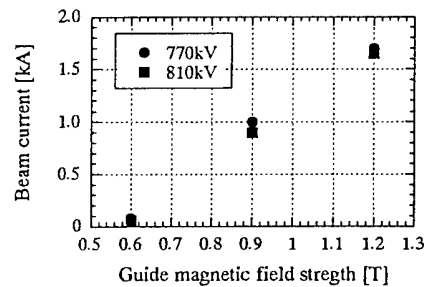


Fig.4. The beam current through interaction region vs. the guide magnetic field. E = 770 and 810kV,  $B_g = 0.6, 0.9$  and 1.2T

Figure 5 shows experimental results of microwave radiation. Here, peak value of the

RF signal of each band is plotted.

From Fig.5 it is clear that there are two types of radiation. The frequency range of one of them is 18 - 60 GHz, and that of the other is 70 - 90 GHz. The former radiation is independent and the latter radiation is dependent on the guide magnetic field, respectively. The computational results of the growth rates of both instabilities vs. oscillation frequency are shown in Fig.6. Comparing the experimental results with the computational results, we can say that the former radiation is due to the Cherenkov instability and the latter is due to the cyclotron-Cherenkov instability.

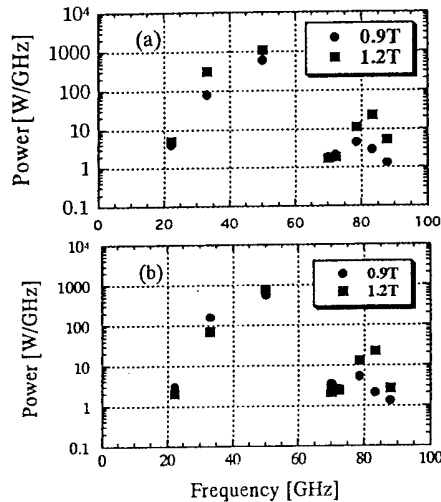


Fig.5. The microwave power vs. oscillation frequency; (a) the beam energy 770kV, (b) the beam energy 810kV. The guide magnetic field; 0.9 and 1.2T

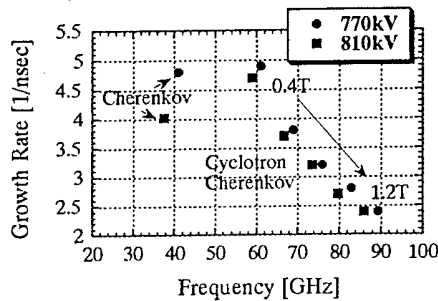


Fig.6. The growth rates of both instabilities verse oscillation frequency.  $E = 770$  and  $810\text{kV}$ ,  $B_g = 0.4, 0.6, 0.8, 1.0$  and  $1.2\text{T}$

The microwave power increased by increasing the guide magnetic field strength. We think that this is because the beam current through the interaction region increased with the guide magnetic field. The power of the

radiated microwave increased as the beam current increased from 100A to 1.7kA.

#### IV. Summary

Beam propagation and the microwave radiation was investigated experimentally varying the beam energy and the guide magnetic field. The beam current through the interaction region was from 100A to 1.7kA. The results of the microwave measurements showed that both the Cherenkov radiation and the cyclotron-Cherenkov radiation were emitted. This result agrees well with the computational results.

We are now preparing power measurements of the radiation.

The authors would like to thank H. Tsukuda and T. kusunoki for their helpful assistance and discussions.

#### Reference

- [1] W. B. Case *et al.*, "Space-charge-Cerenkov and Cyclotron-Cerenkov instabilities in an electron-beam dielectric system," J. Appl. Phys., Vol. 55, pp. 2651, 1984.
- [2] T. H. Kho and A. T. Lin, "Slow-wave electron cyclotron maser," Phys. Rev. A., pp. 2883, No. 6, 1988.
- [3] T. H. Kho and A. T. Lin, "Cyclotron-Cherenkov and Cherenkov Instabilities," IEEE Trans. Plasma Sci., Vol. 18, pp. 513, 1990.
- [4] Victor. L. Granatstein and Igor Alexeff., High-Power Microwave Sources, pp. 397 - 421.
- [5] E. Garate, R. Cook, P. Heim, R. Layman and J. Walsh, "Cerenkov maser operations at lower-mm wavelengths" J. Appl. Phys., 58(2), 15, 1985.
- [6] W. Main, R. Cherry and E. Garate, "High-Power Dielectric Cherenkov Maser Osillator Ezperiments," IEEE Trans. Plasma Sci., Vol, 18, No. 3, 1990.
- [7] W. Peter, E. Garate, W. Main, and A. Fisher, "High-Gain X-Band Dielectric Cherenkov Maser" Phys. Rev. Lett., Vol. 65, No. 24, 1990.
- [8] A. N. Didenko, A. R. Borisov, G. P. Fomenko, A. S. Shlapakovskii, Yu. G. Shtein, "Cyclotron maser using the anomalous Doppler effect," Sov. Tech. Phys. Lett., 9, 572, 1983.
- [9] A. N. Didenko, A. R. Borisov, G. P. Fomenko, A. S. Shlapakovskii, Y. G. Stein, "Generation of short wavelength radiation with intense REB in dielectric-loaded waveguides," Proc. Beams' 86.
- [10] M. Masuzaki, C. Y. Lee, R. Yamashita, "Cyclotron-Cherenkov instability in dielectric-loaded circular waveguides," Proc. Beams' 94.

# HARMONIC MILLIMETER RADIATION FROM A MICROWAVE FEL AMPLIFIER

Y-H. Liu and T. C. Marshall

*Department of Applied Physics, Columbia University, New York, NY, 10027, USA*

## Abstract

The objective is to generate a strong millimeter-wave FEL signal in a single pass, using a coherent microwave source (24GHz) to prebunch the electron beam for harmonically-related wave growth; the millimeter wave output is thus phase-referenced to the coherent microwave source. We use the Columbia FEL facility, operating the electron beam at 600kV, 100A; undulator period = 1.85cm and 200G ( $K = 0.2$ ); electron beam diameter = 3 mm inside a 8.7 mm ID drift tube; guiding field of 8800G. Both the microwave signal (5kW input) and the harmonic millimeter signal show travelling-wave gain in the TE11 FEL waveguide modes. Obtaining power gain of ~20 for the 24GHz input wave, we have observed appreciable radiation at the second and third harmonics and a coherent relationship of the third harmonic and fundamental. Also presented are numerical solutions of the growth of the two waves using the FEL equations with slippage. Also, a strong seventh harmonic is produced, owing to the fact that the wave speeds of the TE11 (24GHz) and TE72 (168GHz) waves are the same, and providing that the electron beam is displaced off-axis.

## Introduction

If an electron beam undergoing FEL interaction is prebunched by a coherent source, then the radiation at the harmonics can be coherent with the source; the prebunching causes the harmonics to grow from an initial condition which is very much above noise input. The radiation at the harmonics will be related in phase and frequency to the source which bunches the electron beam. Recently, Piovela et al [1] have studied a waveguide FEL where the beam is prebunched by a growing wave at the low-frequency intersection, prompting growth at a harmonically-related high frequency upper intersection (or FEL mode); a similar idea was described by Sternbach [2]. Thus one might generate frequency and phase stable millimeter power using a microwave source for prebunching. We have reported on an experiment which studies harmonic radiation from a FEL - configured as a travelling wave amplifier - using a magnetron source to drive the low-frequency FEL mode [3]. In this paper, we give further information regarding the experimental properties of this source as well as a numerical study of the physics. We also report the recent observation of appreciable seventh harmonic power.

## Experiment

Figure 1 shows a schematic of the experimental layout, and column 2 of Table I summarizes the parameters. In this waveguide FEL, there are two unstable roots of the dispersion relation which represent growing TE11 waves at 24 and ~72GHz (third harmonic); the frequencies are given by an approximate formula, neglecting the Raman effect:

$$\omega_{1,2} = \frac{\omega_s}{1 + \beta} [1 \pm \beta \sqrt{1 - X}] \quad (1)$$

where  $\omega_s = \frac{c\beta k_w}{1 - \beta}$  and  $k_w = 2\pi/l_w$ .  $X$  involves the cutoff frequency of the waveguide,

$$X = \left( \frac{1.84}{2\pi R_g} \frac{l_w}{\beta \gamma_{||}} \right)^2 \quad \text{Table I, column 1 shows corresponding parameters appropriate to}$$

this "Compton" theory. A 24GHz 5kW signal is launched along a cylindrical waveguide, enclosed by a helical undulator. A relatively small value of undulator field (~250G) is chosen so that the

system behaves like a travelling-wave amplifier with a gain  $<50$ , in which case oscillation is avoided; also, a low undulator field will give stable well-behaved electron orbits in the combined undulator and guide fields. According to Table I, column 2, the apparatus is constructed so that the 24GHz wave and its third harmonic are resonant according to eq. (1).

We have found 24GHz power gain in the range of 10-20, and the spectrum of the first three harmonics (a few kW) was reported[3]. No harmonic power is obtained[3] unless there is appreciable gain for the 24GHz wave. The kW level third harmonic power output was found to be greater than the second, and both are much greater than the fourth (Figure 2). If the interaction were non-resonant, then the power of the harmonics should fall off very rapidly[4]. Figure 3 shows the result (lower trace) of mixing the 72GHz FEL third harmonic signal with the frequency tripled magnetron signal, demonstrating a fixed frequency relationship of the FEL harmonic power pulse with the lower frequency FEL wave driven by the magnetron.

We have also observed the emission of appreciable seventh harmonic power (168GHz), obtained again only when we have appreciable gain for the 24GHz FEL wave (spectrum, Figure 2). The seventh harmonic signal level is of the order of 17 kW or more, whereas the 24GHz signal is amplified to  $\sim 80$  kW level. The seventh harmonic is not a "resonant FEL interaction" and its appearance depends on two special factors. The first is that the temporal and spatial spectrum of the seventh harmonic electromagnetic wave must move at the same wave velocity as the temporal and spatial spectrum of its electron current source (the "beam wave"), the latter being set up by the seventh temporal harmonic of the bunching caused by the amplified TE11 24GHz wave. The EM wave in question that satisfies this constraint turns out to be the TE72 mode of the cylindrical waveguide[5]. The second factor is that the electron beam must be moved off-axis to overlap one of the electric field maxima of the TE72 wave-- this is done by a deliberate misalignment of our system in which the electron beam was moved about 2mm off the waveguide axis.

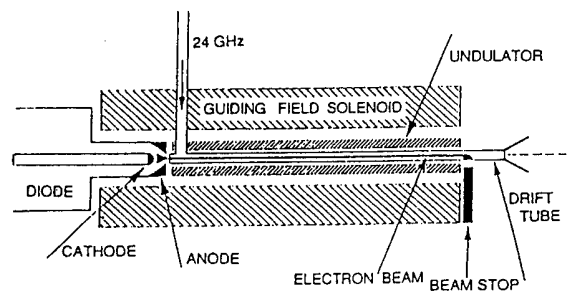


Fig. 1

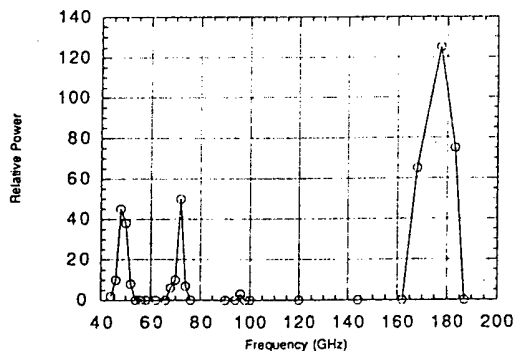


Fig. 2

Figure 1: Schematic-: a pulseline source provides a negative 150nsec pulse to a graphite diode.

Figure 2: Power spectrum scan, covering harmonics 2 - 8; beam is off-axis for 7th harmonic.

Figure 3: From below: beat signal envelope of FEL third harmonic mixed with magnetron tripled frequency; 24 GHz gain signal; diode voltage of accelerator; 72GHz detector signal

Table I

	Col. 1	Col. 2
electron energy	600kV	>600kV
low frequency FEL mode	24GHz	24GHz
high frequency FEL mode	72GHz	72GHz
undulator period	2.5cm	1.85cm
aw, effective undulator		
parameter	0.2	0.2
guide field	0G	8800G
TE11 cutoff frequency	18.4GHz	20.7GHz
electron beam current	$\sim 100$ A	$\sim 100$ A
electron beam dia.	3mm	3mm

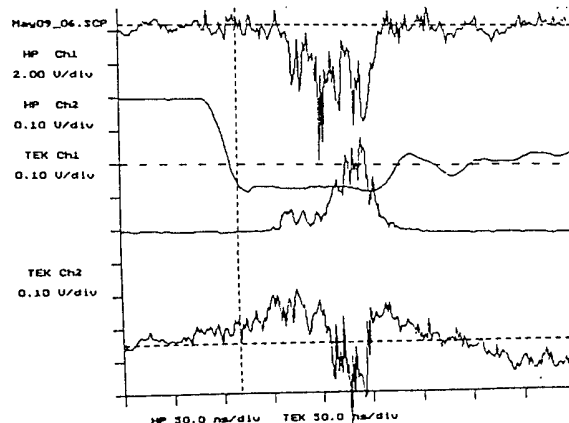


Fig. 3

## Theory

To study the coupling between the harmonically related waves, we solve numerically the set of FEL equations with slippage for the electron dynamics and two interacting waves [3]. For simplicity, we disregard the space-charge (Raman effect), which will decrease the gain and require a shorter undulator period to provide the same frequencies as this calculation. The parameters of the calculation are given in Table I, column 1. The low frequency (24GHz) TE11 FEL mode has group velocity  $\sim c/2$ , as does the seventh harmonic TE72 wave; the second and third harmonic TE11 FEL wave group velocities are higher than the electron speed ( $\sim 0.88c$ ).

We first define the variables  $x$  and  $y$  as

$$x = A \left[ t - \frac{z}{v_{g2}} \right], \quad y = A \left[ \frac{z}{v_{\parallel}} - t \right]$$

where  $A = \left[ l_w \left( \frac{1}{v_{\parallel}} - \frac{1}{v_{g2}} \right) \right]^{-1}$  and  $v_{g1}, v_{g2}$  are the group velocities of  $\omega_1$  and  $\omega_2$ ,  $v_{\parallel}$  is the electron axial speed, and  $z, t$  are the axis and time variables. Defining  $a_1$  and  $a_2$  ( $a_1 = a_{s1} e^{-i\phi_1}$ ) as the normalized vector potentials of waves 1 and 2 which have respectively axial wavenumbers  $k_1$  and  $k_2$  in the waveguide, and  $a_w$  the undulator potential  $\frac{eB_w l_w}{2\pi m c^2}$  where  $B_w$  is the undulator field, the electron and wave equations for the  $j^{\text{th}}$  electron are:

$$\frac{\partial \theta_{2j}}{\partial x} = l_w \bar{k}_{w2} \left( 1 - \frac{\gamma_{r2}^2}{\gamma_j^2} \right) \quad (2)$$

$$\frac{\partial \gamma_j}{\partial x} = -l_w \frac{a_w}{\gamma_j v_{\parallel j}} \left[ \omega_1 a_{s1} \sin(\alpha \theta_{2j} + \phi_{1j}) + \omega_2 a_{s2} \sin(\theta_{2j} + \phi_{2j}) \right] \quad (3)$$

$$\left\{ \frac{\partial}{\partial y} + \left( \frac{1}{v_{g1}} - \frac{1}{v_{g2}} \right) \frac{\partial}{\partial x} \right\} a_1 = \frac{i}{A \left( \frac{1}{v_{\parallel}} - \frac{1}{v_{g1}} \right)} \frac{\omega_p^2 a_w}{2c^2 k_1} \left\langle \frac{e^{-i\alpha \theta_2}}{\gamma} \right\rangle \quad (4)$$

$$\frac{\partial a_2}{\partial y} = i l_w \frac{\omega_p^2 a_w}{2c^2 k_2} \left\langle \frac{e^{-i\theta_2}}{\gamma} \right\rangle \quad (5)$$

These equations also involve the following quantities:  $\omega_p$ , the beam plasma frequency;  $\alpha$ , the harmonic number;  $\theta_2 = k_w z + k_2 z - \omega_2 t$ ;  $\phi_{1,2}$ , the optical phase; also:

$$\bar{k}_{w2} \equiv k_w + k_2 - \omega_2/c, \quad \gamma_{r2}^2 \equiv k_2 (1 + a_w^2)/2\bar{k}_{w2} \quad \text{and} \quad a_s = cE_s/k_s m c^2.$$

In the simulation, the FEL works as a travelling-wave amplifier. The spatial distribution of simulation electrons has a rectangular profile, the electrons are taken to be monoenergetic, and at the undulator entrance  $z = 0$  they are uniformly distributed inside the beam length with 100 simulation electrons per undulator period. For each wavelength-size strip of particles, the relative phase location of the electrons with respect to the radiation field is uniformly distributed between  $-\pi$  and  $\pi$ . For the output format of the computational results, the electron beam pulse and the radiation

pulse (each taken to be flat-topped) are plotted as a function of the variables  $x$  and  $y$ , which imply two moving "windows," the former at  $v_{g2}$  and the latter at  $v_{||}$  respectively; both are scaled in units of the undulator period. The electron motion is parallel to the  $x$ -axis while the  $\omega_2$  wave moves parallel to the  $y$ -axis; the  $\omega_1$  wave moves along the characteristic

$$x - \left( \frac{1}{v_{g1}} - \frac{1}{v_{g2}} \right) \left( \frac{1}{v_{g1}} - \frac{1}{v_{g2}} \right)^{-1} y = \text{constant}$$

The finite radial size of the electron beam is accounted for in the code using a multiplicative "filling factor" of .07 for the radiation current term on the right-hand sides of eqs. (4,5). While this can be estimated from the geometry, it is also a convenient parameter to adjust the gain of the 24GHz power so that it corresponds to our observations.

Figure 5 is an example we calculated that is relevant to this experiment. It shows the peak power growth along the undulator of the 24 and 168GHz waves starting from an initial signal of five kW at 24GHz in the right circular "rotating" mode; the two waves travel at the same speed in this case and the computed power levels are similar to those in the experiment.

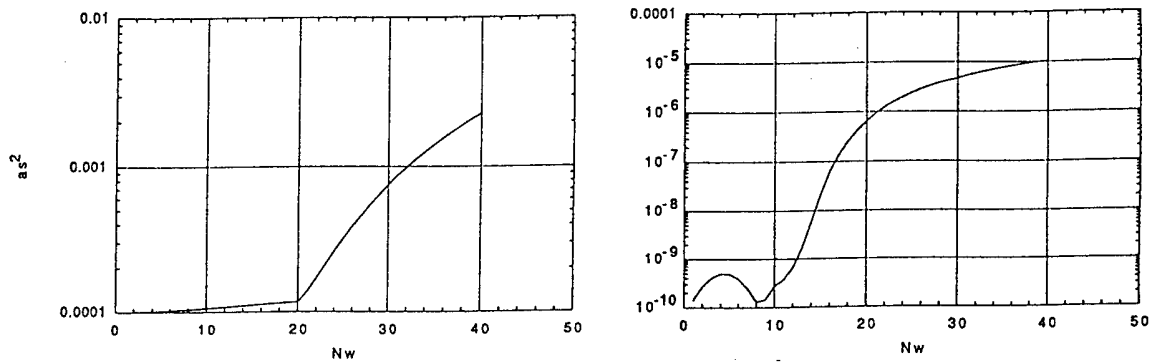


Figure 5: 24 GHz power gain (left) and 168GHz power growth from noise level.

### Conclusions

We believe the harmonic power we have observed can be of use to create coherent, phase-referenced power in the millimeter spectrum for applications such as radar and accelerator physics. The third harmonic need not compete with the seventh for the free energy of the bunching, because the seventh harmonic can be suppressed by moving the beam onto the axis. On the other hand, one can suppress the lower harmonics by making the FEL interaction resonant at one microwave frequency only (by arranging that the second term in the square brackets of eq. (1) vanishes), and then move the electron beam off-axis to enhance the seventh harmonic. The latter approach may represent a very convenient way to generate appreciable 2mm wavelength power, using a FEL operating at comparatively low beam energy driven by a microwave source with kW level power output. We foresee applications of such a high power millimeter source in accelerator physics and for the purpose of plasma heating by electron cyclotron resonance.

Acknowledgement: This research was supported by the Office of Naval Research.

- [1] N. Piovella et al., Phys. Rev. Lett. **72** (1994) 88
- [2] E. Sternbach and H. Ghalila, Nucl. Instrum. Meth. in Phys. Res. **A304** (1991), 691
- [3] Y. -H. Liu and T. C. Marshall, Nucl. Instrum. Meth. in Phys. Res. (to be publ.) (1996)
- [4] Y. -P. Chou and T. C. Marshall, Nucl. Instrum. Meth. in Phys. Res. **A318** (1992) 528
- [5] C. Wang, J.L. Hirshfield, and A.K. Ganguly: Phys. Rev. Lett. (to be publ.)

## HIGH-HARMONIC RELATIVISTIC GYROTRON AS AN ALTERNATIVE TO FEL

V.L. Bratman, Yu.K. Kalynov, N.G. Kolganov, V.N. Manuilov, M.M. Ofitserov,  
S.V. Samsonov, and A.B. Volkov

*Institute of Applied Physics, Russian Academy of Science, 46 Ulyanov St.,  
Nizhny Novgorod, 603600, Russia*

### 1. Introduction

In spite of a number of brilliant experimental results on the FELs their necessity for millimeter and submillimeter wavelength ranges is far from that which is convincingly proved. Moreover, it is obvious, that in some cases more "traditional" devices with a voltage significantly lower than that for the FEL are much simpler to be realized. Among such devices, no doubt, the gyrotron is one of the most attractive. Already at subrelativistic electron energies the gyrotron provides a giant radiation power up to 1 MW with a pulse duration of a few seconds at the short-millimeter waves [1], as well as about 100 kW of power with tens of microsecond pulse duration at the wavelengths shorter than 0.5 mm [2]. The subrelativistic gyrotron operating at the higher cyclotron harmonics is proved to be able to produce the radiation at the wavelengths as short as 0.4 mm [3] which makes it promising for many applications. Based on these results and the theory [4,5] we are trying to develop a gyrotron for submillimeter waves spectroscopy, operating at moderately relativistic electron energies 200-300 keV instead of 3-6 MeV for the FELs. Already at the mentioned comparatively low particle energies coupling of the electron beam, having a large pitch-factor, with cavity modes at higher harmonics is as strong as at the fundamental. Using high pulsed magnetic fields up to 20-30 T and providing selective excitation of the separate modes for the resonances up to the 5-7th harmonics it would be possible to obtain from a single device coherent radiation with broadband frequency step-tuning for all the submillimeter wavelength range.

The creation of a submillimeter relativistic gyrotron providing the stable generation at the higher cyclotron harmonics is obviously a complicated problem requiring significant improvement of methods for electron beam formation and parasitic modes discrimination. As a first modeling step to solve the mentioned problems, we have started our experiments at millimeter waves with well-known [5] Large Orbit Gyrotrons (LOGs). Due to a certain symmetry of the system where a thin electron beam encircles the axis of an axisymmetric cylindrical cavity a significant mode separation takes place, namely, in a LOG only the modes having the azimuthal index equal to the number of a resonant harmonic can be excited. If the electron beam has a small velocity spread then it makes possible a selective excitation of a single cyclotron harmonic or at least simultaneous generation of a number of higher harmonics at high frequencies.

Starting from the LOG we are realizing a known method of parasitic mode discrimination. At the same time we paid the main attention to the helix electron beam formation trying to provide less spread in particle velocity than that obtained in traditional magnetron injection guns. The necessary electron beam is produced in several stages. First, a thin rectilinear beam with as small as possible transverse particle velocity is formed in a guiding magnetic field. Then

a transverse velocity is imparted to all the particles in a short non-adiabatic magnetic system (kicker) which is low-sensitive to positional spread of electrons as well as to the value of the guiding field. The last is very important for the frequency step-tuning at changing the operating cyclotron harmonic number in the interaction region. We use such a method for electron-optical systems based on the explosive as well as on the thermionic electron emission. In the first case we need to select only the small central part of the whole high-current beam [6]. In the second case we have designed a system providing high quality for the whole electron beam. For both cases we expect to obtain an electron beam with a power of 1-10 MW. Even for relatively low efficiency of the generation at the higher cyclotron harmonic (the efficiency amounted to not less than a few percent according to calculations) we hope to provide radiation power of order of 100 kW at the frequency step-tuning in all the millimeter wavelength range. The devices having such parameters at nanosecond and, especially, microsecond pulse durations can be useful for a number of applications.

## 2. Elements of the theory and calculations

A general theory of the electron-wave interaction in the relativistic gyrotron at the cyclotron harmonics was developed in Ref.[4] as a direct generalization of the well-known theory of the subrelativistic gyrotron. According to the theory, for a uniform magnetostatic field a maximum electron efficiency for the resonance at the  $s$ -th harmonic is determined by the following estimation

$$\eta \sim 1 \, sN(1 - \gamma_0^{-1}),$$

where  $N$  is the number of electron gyrooscillations inside the cavity,  $\gamma_0$  their initial Lorentz factor. At comparatively large beam current for which a cavity length and correspondingly the number  $N$  can be chosen to be not very large:  $N \sim 5-10$ , the efficiency at the higher harmonic ( $s \sim 5-10$ ) amounts to a few percent which is sufficient for a number of applications.

In order to obtain the mentioned efficiency it is necessary to have an electron beam with small energy spread  $\Delta\gamma_0 / \gamma_0 \leq 1/sN$  and comparatively large transverse velocity (from the quantum point of view, to place the particles to the high Landau level). In addition, to provide a single mode generation at the higher harmonic the parasitic modes should be effectively suppressed. In principle, it can be achieved using only electrodynamics methods but it is more effective to use them in combination with electron methods controlling a coupling coefficient between the electron beam and the mode. The last method is used in the LOG [5] where a thin electron beam encircling the axis of an axisymmetric cylindrical cavity excites only the modes having the azimuthal index equal to the number of a resonant harmonic, namely, rotating transverse-electric modes  $TE_{s,p,q}$ . The field structure of these modes near the cavity axis coincides with a structure of the corresponding rotating multipoles ( $2s$ -poles). The coupling of the electrons with such a multipole is determined by the value  $J_s^2(s\beta_\perp)$ , which strongly depends on the electron transverse velocity  $\beta_\perp c$ .

When one uses a traditional gyrotron cavity in the form of a cylindrical waveguide, bounded by a conical cut-off narrowing at the cathode side and conical tapering for the diffraction radiation output at the collector side, then the highest diffraction Q-factor,  $Q_d$ , have the modes with the minimal longitudinal index  $q=1$ , and  $Q_d \propto (L/\lambda)^2$ , where  $L$  is the cavity length and  $\lambda$  is the wavelength generated at the  $s$ -th harmonic.



As for the radial mode index  $p$ , it determines a separation between the modes and the value of the Ohmic Q-factor,  $Q_{ohm} \sim r/\delta$ , where  $r$  is the characteristic transverse scale of the mode field and  $\delta$  is the skin depth. For the  $TE_{s,1,1}$  modes  $r$  is the transverse distance between successive reflections of the wave from the cavity walls. Both values  $r$  and  $\delta$  decrease approximately in the same manner when the azimuthal index increases. Correspondingly, the Ohmic Q for the first ten harmonics differ from each other by not larger than 5%. In order to avoid too high Ohmic losses we limit the cavity length by the value for which  $Q_{ohm}$  of the highest operating harmonics are at least not less than their  $Q_d$ . For such a case the total cavity Q increases with the harmonic number.

Increasing of the electron-wave coupling for large transverse electron velocities and the increasing of the Q of the fixed gyrotron cavity with increase of the harmonic number lead to a significantly smaller difference in the operating currents of the different harmonics as compared to a subrelativistic situation. Moreover, the minimal starting current in a LOG corresponds to a higher harmonic rather than to the fundamental. For example, already for a moderate electron energy 250 keV, a pitch-factor  $\beta_{\perp}/\beta_{\parallel} = 2$ , and the cavity length corresponding to  $N=8$  of electron gyrorotations inside the cavity, the 3-rd harmonic has the minimal starting current, and the starting current for the 6-th harmonic is equal to that for the fundamental. It is important to emphasize that according to calculations the frequency non-equidistance of the first  $TE_{s,1,1}$  modes is sufficiently large, thus having the electron beam with a small velocity spread one can expect the selective excitation of the cavity modes from  $s=1$  to  $s=7$ .

### 3. Preliminary experiments

In order to check the theory predictions we designed two gyrotrons of millimeter wavelength range, LOG-1 and LOG-2, with the thermionic and the explosive emission cathodes, correspondingly.

The LOG-1 was designed for its operation at the new high-voltage installation "CARM" described in [7] and intended for the study of two types of relativistic devices, namely, gyrotrons and Cyclotron Autoresonance Masers (CARMs). The operating electron voltage and current are 250 kV and 10 A at pulse duration 10  $\mu$ s. The diode quasi-Pierce electron gun with a spherical thermionic cathode, and tapering guiding magnetic field permits the electron beam to be compressed from diameter 20 mm at the cathode, where the magnetic induction is equal to only 1.4 mT, to diameter 1.2 mm in 0.4 T magnetic field with sufficiently low amplitude of radial pulsations when predicted transverse velocity in the beam does not exceed 0.05 c. In the magnetic field of 0.4 T the beam is pumped to the operating transverse velocity by a kicker in the form of a current frame sloped to the axis of the guiding field. Then this transverse velocity is increased to 0.6 c by adiabatic tapering of magnetic field to 1.6 T. A traditional gyrotron cavity with the operating  $TE_{5,1,1}$  mode with the wavelength of 2 mm excited at the 5th cyclotron harmonic is used as a microwave system. The designed power at 2 mm wavelength with a microsecond pulse duration is more than 100 kW. Now fabrication of the LOG-1 components is finishing.

The LOG-2 was designed for its operation at the high-current "Sinus-6" accelerator. The operating electron voltage and current are 300-350 kV and 25-35 A at pulse duration of about 20 ns. In the LOG-2 we use our experience of high quality helix beam production obtained with CARMs [6]. In order to produce a thin rectilinear electron beam with a small velocity spread from an explosive emission cathode we select only a small central part with diameter 1.5 mm from a high current beam. The above mentioned values of current were obtained for

uniform magnetic fields 0.7-1.2 T. After pumping in the kicker which is similar to the kicker of the LOG-1 electrons enter a traditional gyrotron cavity with diameter of 8.2 mm and length of cylindrical part of 42 mm bounded by the input and output conical tapering 1.6° and 3.4°, correspondingly. In the experiment, changing the operating magnetic field, we clearly observed successive selective excitation of the modes  $TE_{s,1}$  at the fundamental and the cyclotron harmonics from  $s=1$  to  $s=5$ , which was confirmed with measurements of the radiation frequency by means of set of cut-off waveguide filters. The measured values of the operating magnetic fields and of the frequencies corresponded to the calculations very well. We observed also maximums of the receiving signal at the magnetic fields, corresponding to the 6-th and 7-th harmonics, but the wavelengths of radiation for those fields have not yet been measured. Up to now we received the radiation using the only horn and semiconductor detector calibrated at the wavelengths of about 8 mm. The maximum signal was registered at the 3-rd cyclotron harmonic when the wavelength of the radiation was equal to 6.1 mm and the output power was not less than 100 kW. The radiation power at the second harmonic, when  $\lambda=8.4$  mm, was more than 50 kW. The most important point is that the signal at the 5-th harmonic, when  $\lambda=4$  mm, was not weaker. Taking into account the decrease in the detector sensitivity at higher frequencies the power radiated at the 5-th cyclotron harmonic was not less than 100 kW.

- [1] M.V. Agapova et al., Digest of 20th Int. Conf. IR&MM Waves, Orlando, USA, 1995, p.205.
- [2] V.A. Flyagin, A.G. Luchinin, and G.S. Nusinovich, Int. J. IR & MM Waves, 4, 629 (1983).
- [3] T. Idehara and G.F. Brandt, Submillimeter Wave Gyrotron Development & Applications, Fukui Univ., 1995.
- [4] V.L. Bratman, N.S. Ginzburg and G.S. Nusinovich, Pis'ma v Zh. Tekh. Fiz., 3, 961 (1977) (in Russian).
- [5] D.B. McDermott, N.C. Luhmann, A. Kupiszewski, and H.R. Jory, Phys. Fluids, 26, 1936 (1983).
- [6] V.L. Bratman, G.G. Denisov, B.D. Kolchugin, S.V. Samsonov, A.B. Volkov, Phys. Rev. Lett. 75, 3102 (1995).
- [7] V.L. Bratman, I.E. Botvinnik., Yu.D. Grom, Yu.K. Kalynov, M.M. Ofitserov, Proc. SPIE of 16th Int. Symp. on Discharges and Electrical Insulation in Vacuum, Moscow-St. Petersburg, Russia, 1994, p.538.

**ELECTROMAGNETIC PROPERTIES OF CORRUGATED AND  
SMOOTH WAVEGUIDES  
FILLED WITH RADIALY INHOMOGENEOUS PLASMA**

A. Shkvarunets, S. Kobayashi, J. Weaver, Y. Carmel, J. Rodgers, V.L. Granatstein  
and W.W. Destler

*University of Maryland, College Park, MD 20742, USA*

**Abstract**

The creation and diagnosis of plasmas in high power microwave devices remains one of the primary challenges of plasma microwave electronics. In the present work we deal with

- (a) diagnostics techniques for characterization of radially nonuniform plasma columns suitable for use in high power microwave sources and
- (b) the effects of such plasmas on the electromagnetic properties of finite length, spatially periodic slow wave structures.

Experimental studies were performed both for a strong and a weak guiding magnetic field. Using a combination of a microwave resonator (X-band) and a Langmuir probe, both the plasma peak density and its transverse profile were measured in situ. The frequency shifts of the  $TM_{01n}$  modes in an open corrugated cavity were measured as a function of the background plasma density. The dispersion diagrams were reconstructed, for the first time, up to peak plasma density of  $10^{12} \text{ cm}^{-3}$ . Frequency upshifts and "flattening" of the dispersion curves were observed for both strong and weak guiding magnetic fields.

(The full text has not been supplied)

## A 2-GIGAWATT, 1-MICROSECOND, MICROWAVE SOURCE

G. Caryotakis, E. Jongewaard, R. Phillips, G. Scheitrum, S. Tantawi  
*Stanford Linear Accelerator Center, Stanford University, Stanford, CA 94309, USA*

N.C. Luhmann, Jr.  
*University of California, Davis*

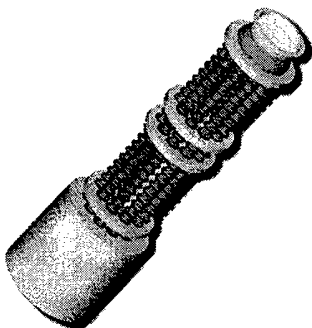
### ABSTRACT

For the last decade or more, researchers in a number of US government laboratories have been attempting to develop L-band microwave sources capable of generating one or more gigawatts, with one-microsecond pulses. In order to produce the required high beam currents, the common approach has been to employ field emission cathodes. For this and other reasons the devices which have been built (MILOs, RKAs, relativistic magnetrons) have operated with a poor vacuum, a condition not consistent with the necessity to hold off the very high rf and dc gradients encountered at these power levels. As a result, the microsecond goal has never been attained. Although in some cases several gigawatts have been generated, pulse duration is limited to about 100 ns. This condition is referred to as "pulse shortening".

The proposed source is based on periodic magnetic (PPM) focusing and is an outgrowth of work performed at SLAC on very high peak power X-band klystrons for a future electron-positron linear collider. These tubes must be focused with permanent magnets, for economic reasons. The new device (GMBK, for Gigawatt Multiple Beam Klystron) is entirely within the state-of-the-art and need only depend on good vacuum tube practice to perform to its specification. It employs thermionic cathodes, loaded to about 40 A/cm<sup>2</sup>, a current density which is within the state-of-the-art for microsecond pulses.

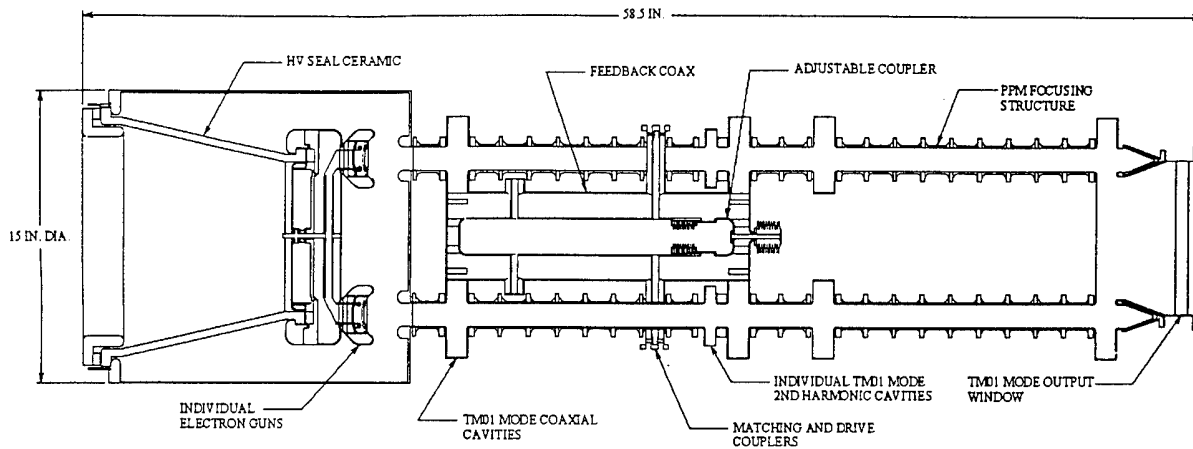
### PROPOSED GMBK

The GMBK pictured below consists of ten beams, each with microperveance 1.4, traversing four common cavities and ten individual second harmonic cavities which enhance efficiency. Each beam is focused in a periodic magnet stack, with magnetically compensated openings to accommodate the cavities. Neodymium iron boron magnets are used. Unlike ordinary multi-beam klystrons, where a single solenoid is used to focus several beams, each GMBK beam occupies the axis of symmetry of the field focusing it. The first three cavities are toroidal and operate in the TM<sub>01</sub> mode. The last cavity is full and supports the TM<sub>02</sub> mode. It couples to a circular waveguide in the TM<sub>01</sub> mode, which terminates in a quarter-wave ceramic window.



### GMBK PARAMETERS

Output Power:	2GW
Pulse duration:	1 $\mu$ s
Frequency:	1.5 GHz
Voltage:	600 kV
Current:	6,700 A
Repetition rate:	10 Hz
Gain:	30 db (tube is self-oscillated)
Efficiency:	50 % (heaters not included)
Heater power:	2.3 kW (oxide cathodes)
Focusing:	PPM
Size:	15 inch diameter, 5 ft long cylinder
Weight:	180 lbs
Cooling:	Inertial

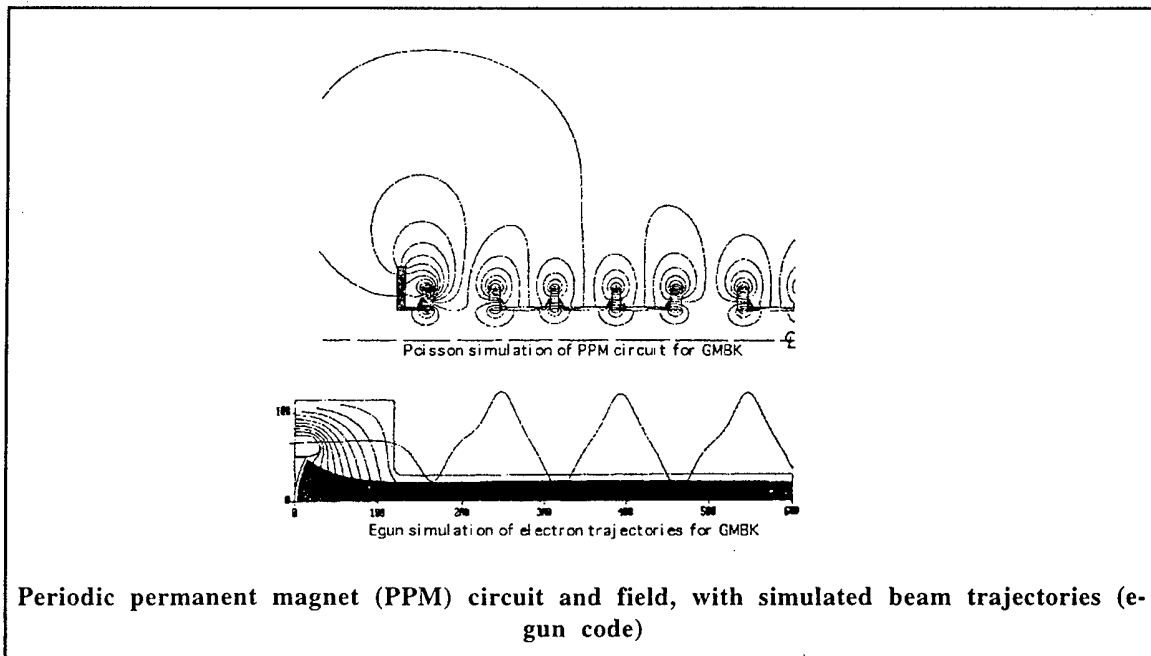


Since the device will operate at a fixed frequency, there is no need for a separate source to drive it. Instead, power from the third cavity is used to excite the first and the tube is made to oscillate. Power is fed to the first cavity completely symmetrically by a coaxial arrangement and through slots in the internal wall of cavities 1 and 3. Provisions are made to vary the amplitude and phase of the feedback signal.

The GMBK should produce 2 gigawatts with an efficiency of 50 %. At this power output, the maximum dc gradient at the gun of the tube is approximately 300 kV/cm and the maximum rf gradient at the output cavity 200 kV/cm. Both are lower than equivalent gradients in experimental tubes operated at SLAC. Naturally, a good tube vacuum is necessary (10<sup>-8</sup> Torr, or better).

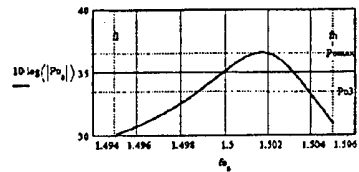
The computer evaluation of the GMBK is nearly complete, with most aspects of its operation simulated in two dimensions. SLAC is collaborating with LANL in this development, which is funded by the Air Force Office of Scientific Research. The design of the tube will be finalized when a 3-D ISIS simulation of its rf performance is completed at Los Alamos.

The concept of a multiple-beam klystron with individually focused PPM beams is also applicable to lower power (and lower voltage) klystrons. The advantages are the same: low voltage, light weight and, in the case of CW tubes, the possibility of an inexpensive depressed collector.



Data Inputs

V0=600000.	Beam Voltage (V)	Number of Data Points	npoints=128
I0=666	Beam Current (A)	Calculation Bandwidth (GHz)	BW=.01
f0=1.5	Center Frequency (GHz)	$\Delta f = 1.495 \text{ (}\Delta f - \Delta\text{)} = 1000 = 10$	$\Delta f = 1.505$ RESBW=.020
a=.015	Tunnel Radius (m)	J0max=40	Average Cathode Loading (A/cm <sup>2</sup> )
b=.01	Beam Radius (m)		
P0=2.10 <sup>8</sup>	Desired Output Power (W)		



S=1  
P0max=36.554  
(compares to 37 db in the Japandisk simulation)

The 2nd cavity is a 2nd harmonic individual cavity between the 1st and 2nd in this calculation and is not taken into account.

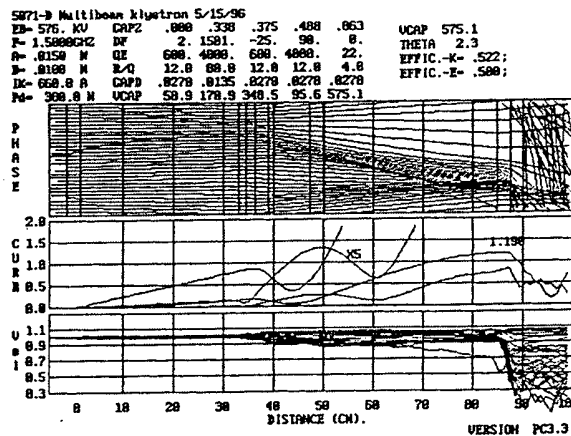
N=4 Number of Cavities

Cavity Rn/Q (Ohms)	External Q and Q0	Cavity Frequency (GHz)	Gap-Gap L (m)	Gap Length (m)
RQ <sub>1</sub> =12	Qc <sub>1</sub> =600 Qo <sub>1</sub> =4000	f <sub>1</sub> =1.502	l <sub>1</sub> =0.0	d <sub>1</sub> =.027
RQ <sub>2</sub> =12	Qc <sub>2</sub> =600 Qo <sub>2</sub> =4000	f <sub>2</sub> =1.476	l <sub>2</sub> =0.375	d <sub>2</sub> =.027
RQ <sub>3</sub> =12	Qc <sub>3</sub> =∞ Qo <sub>3</sub> =4000	f <sub>3</sub> =1.595	l <sub>3</sub> =0.11250	d <sub>3</sub> =.027
RQ <sub>4</sub> =4	Qc <sub>4</sub> =25 Qo <sub>4</sub> =4000	f <sub>4</sub> =1.5	l <sub>4</sub> =0.375	d <sub>4</sub> =.027

Beam Loading Conductance and Q		Gap Distance (m)	Coupling Coefficient (induced current)	Drift Length (degrees)	Gap transit angle (radians)
Gb <sub>1</sub> =1.056·10 <sup>-3</sup>	Qb <sub>1</sub> =788.804	Zb <sub>1</sub> =0	M <sub>1</sub> =0.932	β <sub>01</sub> =0	βc-d <sub>1</sub> =0.962
Gb <sub>2</sub> =1.056·10 <sup>-3</sup>	Qb <sub>2</sub> =788.804	Zb <sub>2</sub> =0.375	M <sub>2</sub> =0.932	β <sub>02</sub> =32.32	βc-d <sub>2</sub> =0.962
Gb <sub>3</sub> =1.056·10 <sup>-3</sup>	Qb <sub>3</sub> =788.804	Zb <sub>3</sub> =0.487	M <sub>3</sub> =0.932	β <sub>03</sub> =9.696	βc-d <sub>3</sub> =0.962
Gb <sub>4</sub> =1.056·10 <sup>-3</sup>	Qb <sub>4</sub> =2.366·10 <sup>3</sup>	Zb <sub>4</sub> =0.863	M <sub>4</sub> =0.932	β <sub>04</sub> =32.32	βc-d <sub>4</sub> =0.962

K=1.433	Gun Microperveance (uA/V <sup>1.5</sup> )	Gun Area of Convergence	Osc=5.3
Vod=576333	Beam Energy with Depression (V)	Cathode Diameter (in)	Dc=1.813
Pb=3.996·10 <sup>8</sup>	Supply Power (W)	Beam Power (W)	Pbd=3.838·10 <sup>8</sup>
Eff=50.05	Klystron Efficiency - Pout/Pb - (%)	γb=0.167	γs=0.251
βbr=695.508	Brillouin Field (Gauss)	Plasma Frequency (rad/s)	ωp=4.064·10 <sup>9</sup>
R=0.098	Plasma Red. Factor (dimensionless)	Red. Plasma Frequency (rad/s)	ωq=3.981·10 <sup>8</sup>
βc=35.615	Electron Prop. Constant (rad/m)	Plasma Prop. Constant (rad/m)	βq=1.504

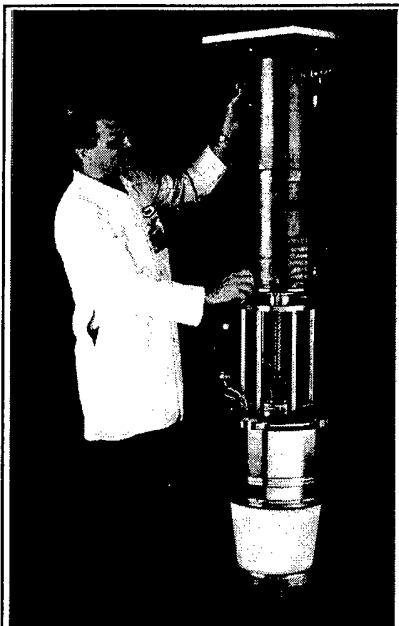
## GMBK Parameters and small-signal gain calculations



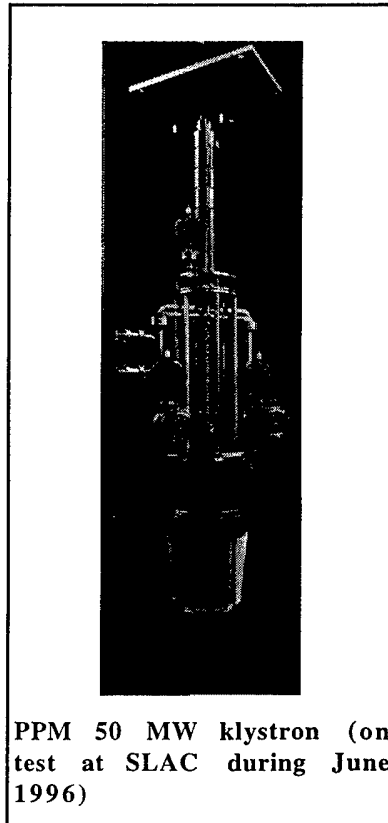
## GMBK one-dimensional large -signal simulation (J-disk code)

## RELATED MICROWAVE SOURCE DEVELOPMENT AT SLAC

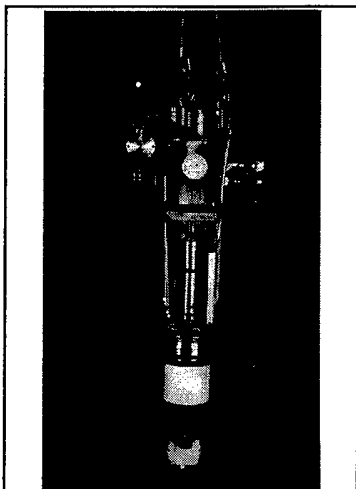
The XL4 is the solenoid focused prototype for the 50 MW PPM focused klystron. The PPM beam tester was operated to 490 KV without measurable beam interception.



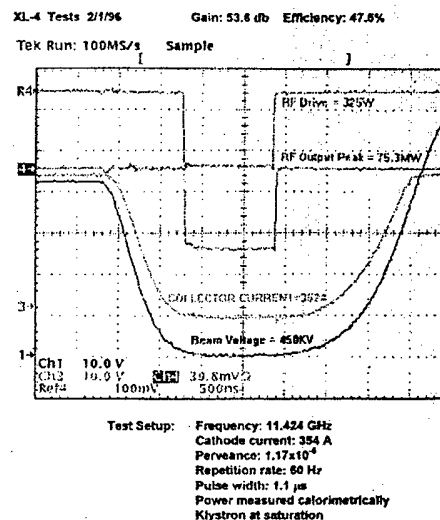
PPM beam tester built to evaluate beam optics for a 50 MW 11 GHz PPM klystron for a future e+/e- collider



PPM 50 MW klystron (on test at SLAC during June 1996)



Solenoid-focused 50 MW klystron (XL4) used in experimental X-band Accelerator at SLAC



Performance of XL-4 Klystron

# HIGH-SELECTIVITY RESONATOR FOR POWERFUL MICROWAVE SOURCES

E.B. Abubakirov, M.I. Fuchs, N.F. Kovalev

*Institute of Applied Physics, Russian Academy of Sciences  
Nizhny Novgorod, Russia*

## Abstract

A simple and effective method for providing of single-mode operation regime of relativistic microwave generators with oversized electrodynamic system is suggested. Required solitary structure of microwave field is achieved by additional channels of selective feedback. Such method is realized in resonant traveling wave tube (TWT) in which a stable operation with output radiation in the form of Gaussian wave beam is obtained with combination of Bragg type reflectors with different azimuth symmetry of their wall corrugation.

## High-power oscillators with Bragg reflectors

Due to limitations set by electric reliability, the increase of output power in sources of coherent microwave radiation requires larger cross-sections of their electrodynamic systems. An efficient way to provide spatial coherence of the output radiation of such sources is to use the selective feedback by means of Bragg reflectors placed at the ends of an over-sized electrodynamic system. As a rule, powerful microwave generators use reflectors made as sections of a cylindrical waveguide with periodic helical  $n$ -start or axially symmetric ( $n = 0$ ) corrugation. In such a system all the pairs of modes, the azimuth indexes of which are connected by the expression

$$m_{i1} \pm n = m_{i2}, \quad (1)$$

and the sum of longitudinal propagation constants of which equal to the constant  $\bar{h} = 2\pi/d$  of periodic systems of reflectors ( $d$  is period of corrugation)

$$h_{i1} + h_{i2} = \bar{h}, \quad (2)$$

acquire the resonance coupling ( $i$  is a number of the mode pair). As the transverse cross-section grows, the spectrum of resonance modes

$$k_i = [(\bar{h}^2 + k_{i1}^2 + k_{i2}^2)^2 - 4 k_{i1}^2 k_{i2}^2]^{1/2} / 2 \bar{h} \quad (3)$$

( $k_i = 2\pi/\lambda_i$ ,  $\lambda_i$  is wavelength,  $k_{i1}$  and  $k_{i2}$  are transverse wave numbers) condenses fast, in reverse proportion to the squared radius  $R$  for reflectors based on cylindrical waveguides, whereas the band of mode transformation in the reflector

$$\Delta k/k \approx 2h_{i1}h_{i2}\delta/\bar{h}k^2, \quad (4)$$

taking into consideration that the coefficient  $\delta$  of a couple between rotating H-modes is equal to [1]

$$\delta_{HH} = (l/2R)\{m_{i1}m_{i2}(k^2 + h_{i1}h_{i2})/[h_{i1}h_{i2}(\nu_{i1}^2 - m_{i1}^2)(\nu_{i2}^2 - m_{i2}^2)]^{1/2}\}, \quad (5)$$

between E-modes

$$\delta_{EE} = (l/2R)[(k^2 + h_{i1}h_{i2})/(h_{i1}h_{i2})^{1/2}], \quad (6)$$

between E and H modes



$$\delta_{EH} = (l/2R) \{m_H k \bar{h} / [h_E h_H (\nu_H^2 - m_H^2)]^{1/2}\} \quad (7)$$

(here  $l$  is the amplitude of sinusoidal corrugation,  $\nu$  is a root of derivative from Bessel function corresponding to transforming H mode) is close to the ratio  $l/R$  if neglect by individual mode characteristics. It is supposed that the reflector length is sufficient for only one longitudinal mode to stay in the band.

However, even in the case of isolated resonances (which are not overlapped) a frequent situation is when an electron beam interacts with several modes at about the same conditions. in the microwave generator with oversize electrodynamic system. The results of experimental investigation of a relativistic resonant traveling wave tube (TWT) described below (some results see [2]) illustrates the statement.

In experiments it is used a section of TWT-amplifier in which the fundamental harmonic of the operating mode is synchronous to the electron beam. The slow wave structure has the following parameters: the average radius is  $R = 2.792$  cm, the period of axis-symmetric corrugation of sinusoidal profile is  $d = 0.671$  cm, its amplitude is  $l = 0.342$  cm and length  $L$  of homogeneous part of corrugation changes may vary from  $25d$  to  $46d$ . Dispersion characteristics for some low modes which calculated by method [3] of integral equations are shown in Fig.1. At ends of the slow wave structure the corrugation amplitude decreases gradually for matching with a regular cylindrical waveguide. The use of a decelerated wave makes it possible to realize the maximum high spatial increment  $\kappa$  of microwave field limited by the condition of the single-mode regime, in which the increment should not exceed the difference between longitudinal wave numbers,  $h$ , for the operating mode and the closest parasitic mode,  $h_{par}$ :

$$\kappa \sim \kappa_{max} \leq |h - h_{par}|. \quad (8)$$

The high increment makes it also possible to achieve a wide amplification band

$$\Delta\lambda/\lambda \sim \kappa\lambda \quad (9)$$

(here  $\lambda$  is the wave length). that provides adaptivity of the TWT to various perturbation in the electron beam.

It is supposed that the resonant TWT should operate on mode  $EH_{11}$  with the selective feedback on mode  $H_{41}$  producing by Bragg reflectors with 3-start helical corrugation of sinusoidal profile. Average radii of reflectors are  $R = 2.5$  cm and periods are  $d = 2.22$  cm. In the input reflector amplitude and length of corrugation are  $l = 0.18$  cm and  $L = 12$  cm accordingly, reflection coefficient of microwave power is  $k_p = 0.8$ . Three output reflectors with  $k_p = 0.2, 0.05$  and  $0.02$  differing by the product  $lL$  are used in experiments for determination of amplification coefficient. It is found that linear amplification is achieved 1 dB per period of TWT wave structure. Resonant wavelength is  $\lambda = 2.8$  cm.

In experiments at voltage  $V$  about 1 MV and electron beam current  $I \approx 8$  kA the output power achieves  $P \approx 1.5$  GW. Matched parts on ends of TWT slow-wave structure serve also as mode converters which transform the operating mode  $EH_{11}$  of TWT into mode  $H_{11}$  when these parts are interface with cylindrical waveguide adiabatically smooth. The horn antenna forms the radiation with pattern which is close to the form of Gaussian beam (Fig.2a).

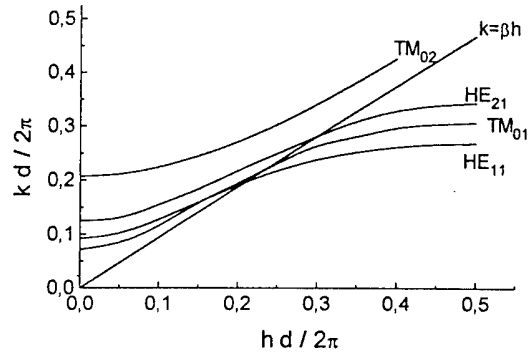


Fig.1. Dispersion curves for modes in a TWT slow wave structure.

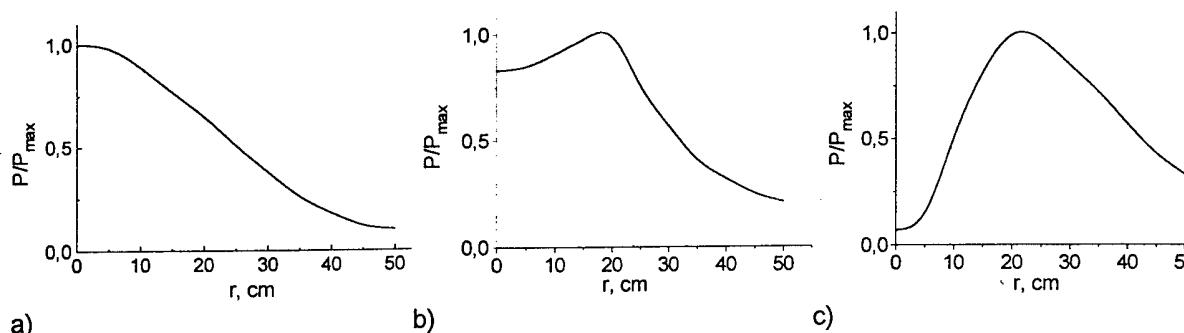


Fig.2 Radiation patterns for different position of reflectors

However it is observed only at the definite relative azimuth position of reflectors. If one reflector is turned then the pattern becomes to distort (Fig.2b) and then the pattern corresponding to the  $E_{01}$  mode appears (Fig.2c). In this case radiation wavelength is  $\lambda = 3.3$  cm. This is due to existence of the resonant mode combination  $E_{01} - H_{31}$  with reflection coefficients  $k_p = 0.7$  for input reflector and  $k_p = 0.2$  for output one. If the slow wave structure with a wide frequency band is used and coupling impedances for both observed modes are closed, a mode competition has place. A change of interaction conditions owing to drift of resonant frequencies on different position of reflectors, lead to the advantage of that or the other mode combination.

### Selection

Mode selection in Bragg resonators can be significantly improved by additional channels of the feedback forming of resonant combinations of more than 2 rotating modes. For example, the resonant combination of 4 rotating modes can be realized by placing a pair of reflectors (consequent or combined) with helical corrugations at each end of the electrodynamic system. It is easily seen that in the case of different periods there is only one resonant combination of four modes. For any other set mode transformations at one frequency is impossible. Along with that, even at the same periods the spectrum of resonance 4-wave oscillations is rather sparse, if the order of reflector azimuth symmetry at one end of the resonator differs from one at the other end [4]. In this case the closest parasitic resonant mode combination is the operating combination in which one of modes is differed by  $E$  or  $H$  - polarization. In consequence of it solitary mode combinations (without overlapped frequency band) are kept when cross size of such resonator is twice as much a cross size of a resonator with identical azimuth symmetry reflectors in which the closest mode combination has azimuth indexes differed on unit.

In aforesaid resonant TWT the 3-start helical reflectors were replaced with two combined reflectors having  $R = 2.8$  cm,  $d = 1.85$  cm,  $l = 0.3$  cm: 5-start corrugations (right-hand helix and left-hand helix) with  $L = 10$  cm and  $k_p = 0.8$  on the input end of slow wave structure and 3-start corrugations with  $L = 6$  cm and  $k_p = 0.2$  at the output end. of the TWT. The generator preserving of its output parameters operated only with a combination of four rotating modes forming a pair of linearly polarized  $EH_{11} - H_{41}$  modes. Two synchronous waves  $EH_{11}$  rotating in opposite directions interact with tubular electron beam, and two rotating modes  $H_{41}$  realize a feedback. The wave beam polarization vector at the generator output depends on relative azimuth position of the reflectors.

### **Conclusion**

This method to produce high-selectivity resonance systems to be used in powerful high-frequency electronics may be realized in many different ways, e.g. by using additional mode converters, similar to the way used in multi-mirror laser resonators.

### **Acknowledgment**

The report is supported by Russian Foundation of Basic Researches, Grant No. 95-02-04281.

1. Katsenelenbaum B.Z., Theory of irregular waveguides with smooth changed parameters: Moscow, Academy of Sciences of USSR (1961) p.135.
2. Abubakirov E.B., Fuchs M.I., Gintsburg V.A. et al., Cherenkov relativistic oscillators of coherent electromagnetic radiation with multimode sections electrodynamic systems: Proc.Conf. "Beams'90" (1990) pp. 1105-1110
3. Kovalev N.F., Fil'chenkov S.E., Yunakovski A.D., Electrodynamic systems of relativistic carcinotrons: Preprint 268, IAP AS USSR (1990) P.32.
4. Fuchs M.I., Kovalev N.F., System for amplification of electromagnetic oscillations: Copyright 1828325 with priority from 1990. Bulletin of copyrights (Russian) 32 (1996)

## EXPERIMENTAL INVESTIGATIONS OF BEAM POTENTIAL DEPRESSION EFFECT IN GYROTRONS

A.N.Kuftin, V.E.Zapevalov

*Institute of Applied Physics, Russian Academy of Sciences, 46 Ulyanov Street, 603600 Nizhny  
Novgorod, Russia*

### Abstract

The factor of the helical electron beam (HEB) potential depression in the gyrotron cavity caused by the eigen beam space charge and its influence on the gyrotron parameters is discussed. The procedure of the experiment of defining the depression effect on HEB parameters is given and the experimental set-up is described. The experimental results are compared with the calculated data.

### Introduction

Gyrotrons of mm wavelength band are used for ECR heating and active plasma diagnostics and recently its have been used also in technological application. Gyrotron designing and optimization requires the presence of reliable information on the parameters of active medium - helical electron beams (HEB) and also the factors and processes affecting these parameters. One of such factors is HEB potential depression in the gyrotron cavity caused by the eigen beam space charge. This factor exerts a considerable influence in superpowerful gyrotrons when intense HEB and space-developed operating modes of oversized open cavities are used. The peculiarities of the effect of the potential depression for HEB are studied theoretically in number of papers [1,2]. The calculated models of different complexity show that the effect of depression on HEB parameters is stronger than in the case of straight electron beams. However the conclusions of the theory have not been verified experimentally and even the procedure of such verification has not been proposed. The present paper is the attempt to fill this gap to some extent

The study of the problem performed before is reviewed. On the basis of analysis of the existing data it is shown theoretically that the potential depression is a significant factor limiting the power and efficiency of gyrotrons with cavity in the form of weakly irregular sections of cylindrical waveguides. The analogous calculation performed for the case of coaxial cavities have shown that the depression effect in them is essentially weak.

### Procedure of the experiment

Below the procedure of the experiment of defining the depression effect on HEB parameters is given and the experimental set-up is described.

Usually for experimental determination of HEB parameters a method of a retarding field [3-6] is used, the set-up of which is represented on fig. 1. Directly measured value here is a component of velocity longitudinal to the magnetic field, which is determined on a cut off curve of a current of a collector 4, installed together with a retarding grid 5 and diaphragm 6 in the region of a uniform magnetic field (the magnetic field distribution is also shown on fig. 1). The oscillatory velocity is calculated on longitudinal velocity from integral of energy. The diaphragm 6 with narrow sector gap serves for removal electron, reflected from a retarding grid. In this case reflected electron after azimuth drift (in crossed fields near cathode region) appear

already over other part of the emitter and do not influence on formation of an investigated beam. In the region of cathode electron are reflected again in the direction of a collector and after one more turn in crossed fields caught by diaphragm 6. The diaphragm 6 at the same time, being in working space under potential of the gyrotron case, practically liquidates influence of the space charge of the beam, and, hence, potential depression. Thus, in the given variant of the set-up parameters of a beam are measured in absence of potential depression. That, as a rule, takes place in operating regime of long pulse and CW gyrotrons (due to ion compensating [7]).

The experiment is based on the modified retarding field method with the measurement of HEB parameters in two different cross-sections and the subsequent recalculation of beam parameters using the adiabatic invariant. At first, parameters of a beam are measured by the usual means - at the analyzer placed in a uniform field (beam without voltage depression). Using measured parameters of a beam without voltage depression and the result of [2] it is possible to estimate parameters of a beam with voltage depression.

After this analyzer have to be displaced in a falling down magnetic field (in a direction of an axis  $Z$ ), measurement of a cut off curve made and value of relative transversal energy in the location of the analyzer  $t_{\perp}$  determined. Then, using circumstance, that the transverse velocity is connected with adiabatic invariant ( $\beta_{\perp}^2 B = \text{const}$ ) [7], we recalculate  $t_{\perp 0}$  in operating space  $t_{\perp 0} = t_{\perp} B / B_0$ , where  $B_0$  and  $B$  the values of a magnetic induction in the uniform part of a magnetic field and in the location of the analyzer. If  $B/B_0 \sim 1$ , it is possible to neglect the amendment connected with an inclination of the B-field force line on the analyzer. The received parameters of a beam can be compared with specified earlier estimations.

### Results of experiments

Below some results of experiments, directed on finding - out of character of influence voltage depression of a beam on parameters of HEB (average relative oscillatory energy, relative velocity spread), are resulted. For experiments the shortpuls prototype of the longpuls 140 GHz gyrotron [8] with an operating voltage 80 kV was used. The measurements were carried out in a scale down regime, at which electron trajectories are kept (factor of scale  $k=0.1$  is chosen) [6,9]. The shift of the analyzer got out 100mm and thus correspond  $B/B_0=0,73$ . For measurements automated experimental installation [9] was used. Note, that the spent experiment is rather labor-consuming and requires, at least, double vacuum outpumping and conditioning of installation on a working regime.

Ordering and analysis of experimental results is spent, and comparison to settlement data is carried out. On fig. 2 dependencies of relative oscillatory energy  $t_{\perp}$  and velocity spread  $\delta v_{\perp}$  for a beam without voltage depression (curve 1) and received from measurements in a falling down field and recalculated with the adiabatic invariant (curves 2) are presented.

The experimental results are systematized and analyzed; they are compared with the calculated data. The experimental and the calculated data are found to have not a quite good agreement, especially for velocity spread, when simple theoretical models are used.

### Conclusion

The spent experiments have shown essential influence of effects of voltage depression on parameters of HEB and necessity of essential development of the theory and technique of experiments both. On the basis of received results possible directions further theoretical and experimental researches of a voltage depression problem, in particular influences of effects of beam potential depression on function of distribution electron on transverse and longitudinal velocities are planned

# References:

- [1] Drobot A. T. , Kim K.. Int. J. Electronics, v. **.51**, n.4, (1981), P. 351.
- [2] Tsimring Sh. E. " Radiotekhnika and elektronika ", **35**, n. 6, (1990) P. 1284, .
- [3] Goldenberg A. L., et al., book "Gyrottron." Gorky. (1981), P. 86.
- [4] Avdoshin E.G., Goldenberg A.L. Izv. Vish.Uch. Zav, Radiofizika, v.16, n.10, (1973), P. 1605.
- [5] Avdoshin E.G. et al., Izv. Vish.Uch. Zav, Radiofizika, v 16, n.4, (1973), P. 605.
- [6] Kuftin A.N. et al. Int. J. Electronics, v.72, nos.5 and 6,n. (1992), P.1145.
- [7] Varentsov V. A., Tsimring Sh. E. Journal of technical physics, v. **53**, n.2., ( 1983), P. 264
- [8] Zapevalov V.E. et al.. Electronic industry, n.6, (1991), P.71.
- [9]. Andronov A.N et. al. Conf. Proc. 20 Int. Conf. on IR & MM waves. 1995. Orlando, USA. P.141

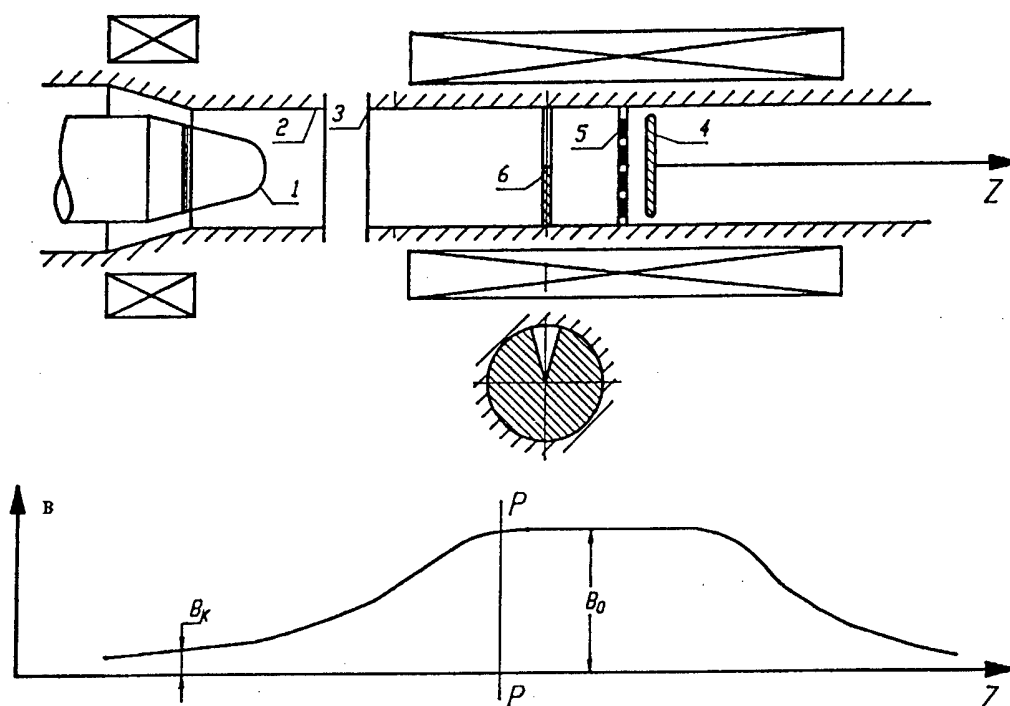


Fig.1. General scheme of experimental installation and distribution of a magnetic field (1-cathode, 2-anode, 3- gyrottron case, 4-collector, 5-grid, 6-diaphragm).

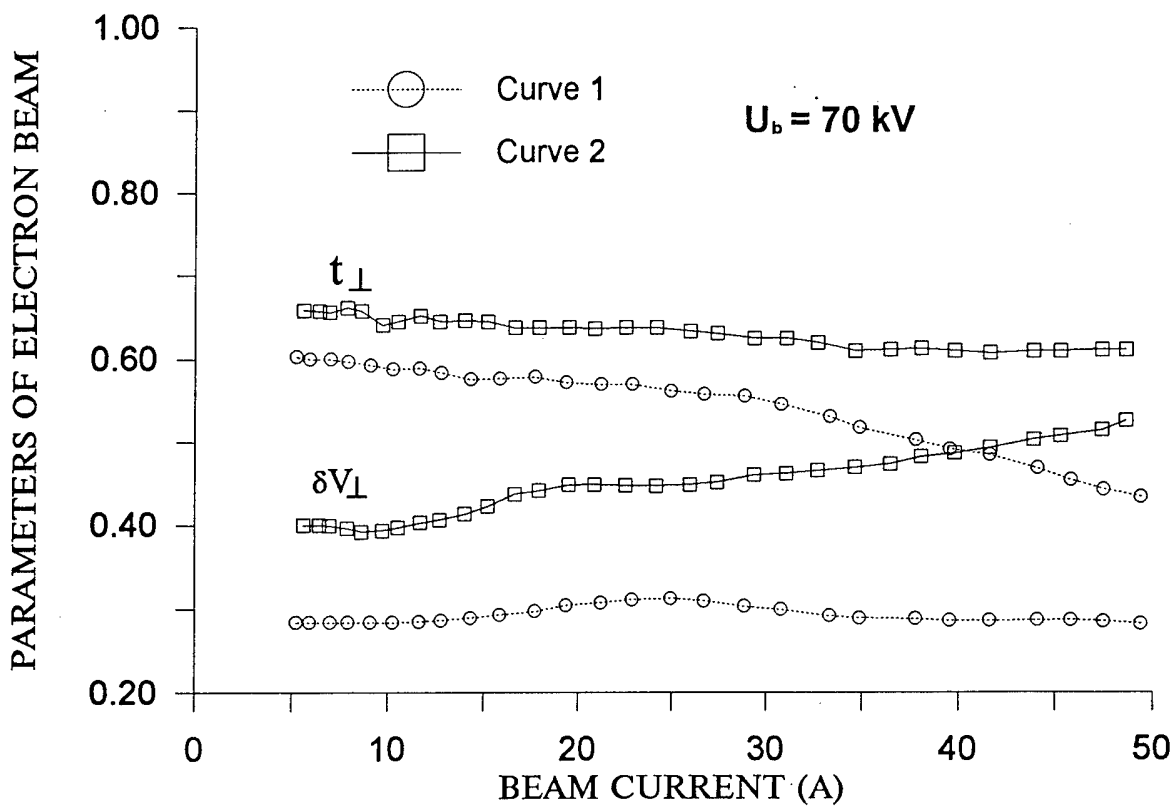
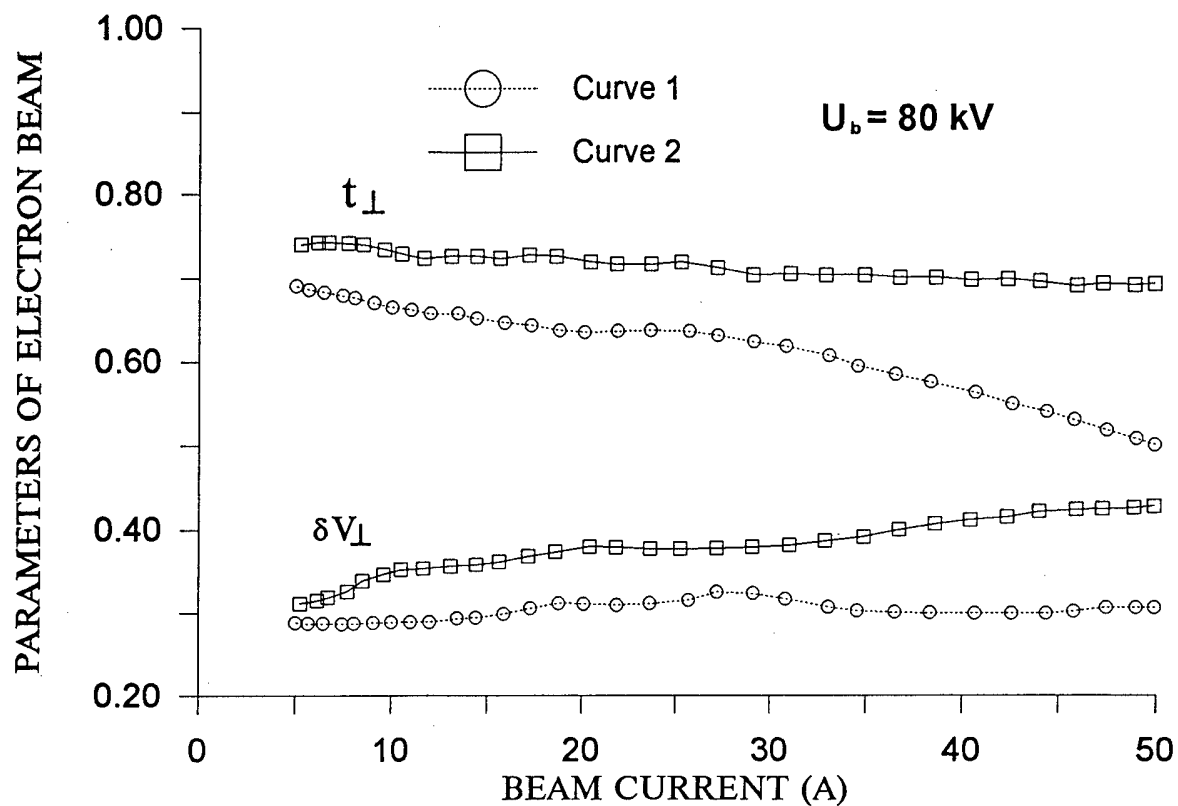


Fig.2. Dependence of velocity spread and relative oscillatory energy on a beam current (1-measured in a homogeneous magnetic field, 2- measured in a falling down field and recalculated).

# STUDY OF SPACE CHARGE OSCILLATIONS IN GYROTRON

O.I.Louksha, G.G.Sominski

*Saint-Petersburg Technical University,  
29, Polytechnicheskaja, St.-Petersburg, 195251, Russia*

## Abstract

The results of experimental measurements and numerical simulations of the space charge oscillations in gyrotron electron-optical system are presented.

## Introduction

Collective processes in the space charge of helical electron beams (HEB) play an important role in the operation of powerful gyrotrons. They determine the HEB quality, gyrotron efficiency and spectral characteristics. There is interest in investigation of the space charge oscillations at frequencies much lower than cyclotron frequency. These spurious oscillations occur in gyrotron electron-optical system even in the absence of high-Q cavity. In present paper the results of experimental study and numerical simulation of gyrotron space charge oscillations are summarized.

## Experimental set-up

The measurements were made in gyrotron-type experimental device described in [1,2]. The device configuration was comprised of magnetron-injection gun, increasing magnetic field region for creation the beam with high rotating energy, HEB drift region at magnetic field plateau and collector. Impregnated metallic-porous cathodes operating in temperature-limited regime were used. The configuration and beam parameters are given in Table 1.

The oscillations characteristics were measured with broadband probes registering the induced signals from the HEB near-zone. Probes P1 and P2 were located, respectively, at the end of the magnetic field compression region and in the collector section where magnetic field decreased. Probe P3 was located in uniform magnetic field region and could be moved along the z-axis.

The probes signals were carried by coaxial cables to spectrum analyzer or broadband oscilloscope. In the first case the oscillations spectra averaged over the a long series of

Parameter	
Cathode diameter	83 mm
Distance cathode - anode	7 mm
Distance cathode - magnetic field plateau	22-26 cm
Drift tube diameter in plateau region	22 mm
Beam voltage	5-15 kV
Plateau magnetic field	2.0-3.5 T
Magnetic compression (ratio of plateau magnetic field to cathode magnetic field)	20-25
Beam current	0.1-15 A
Beam pulse duration	5 - 100 ms
Pitch-factor (ratio of transverse velocity to longitudinal velocity) in plateau region	0.8-1.7

Table 1. Main experimental parameters



pulses with repetition frequency of 50 Hz were measured. In the second case Fourier analysis of single 10-1000 ns oscillograms of the probes signals gave information about the "instantaneous" oscillations spectra.

The azimuthal distributions of the cathode emission current density  $j_e(\theta)$  and the current density to the collector  $j_{col}(\theta)$  were determined by the methods described in [1-3]. Information about the effect of the azimuthal HEB structure non-uniformities on the oscillations characteristics was obtained by comparing the probes signals for cathodes with different azimuthal distribution of the emission current.

The sources of magnetic field were superconducting solenoid (periodic and single beam current pulses regimes) or pulse solenoid (single beam current pulses regime).

### Experimental results

All the probes registered the oscillations in broad range of frequencies. Typical spectra from the probe P3 registered with spectrum analyzer is shown in Fig. 1. The low-frequency (LF) oscillations (10- 150 MHz) occurred when values of pitch-factor at magnetic field plateau  $g$  and beam current  $I$  were above the threshold ones ( $g_{tr,LF} \sim 1.0$ ,  $I_{tr,LF} \sim 0.5$  A). In the region  $f < 50$  MHz discrete peaks at approximately multiple frequencies were caused by electron reflection from magnetic mirror and oscillatory motion in the trap between the gun cathode and magnetic field plateau. The detailed investigation of the "trap" oscillations in various experimental configurations was made in [3]. We found that amplitude of these oscillations varied strongly along the system axis. The changes registered with the probe P3 as it moved along the z-axis were most revealing. Oscillations amplitude decreased monotonously as the probe P3 receded from the trap in the uniform magnetic field region (curve 1 in Fig. 2).

In the case of  $I > I_{tr,HF} = 2-$

5 A the measured spectra of oscillations included higher frequency (HF) modes between 800 and 1400 MHz (see Fig. 1). Oscillations amplitude increased with beam current growth. At a fixed current HF oscillations intensity increased with decreasing electron longitudinal velocity, which varied by varying plateau magnetic field, beam voltage and magnetic compression coefficient. These data indicate that the HF oscillations amplitude growth can be caused by increase of the electron beam density in the drift region at magnetic field plateau. In contrast to the LF oscillation, amplitude of the HF modes increased rapidly as the probe moved in the collector direction (curve 2 in Fig. 2 corresponds to 900 MHz peak).

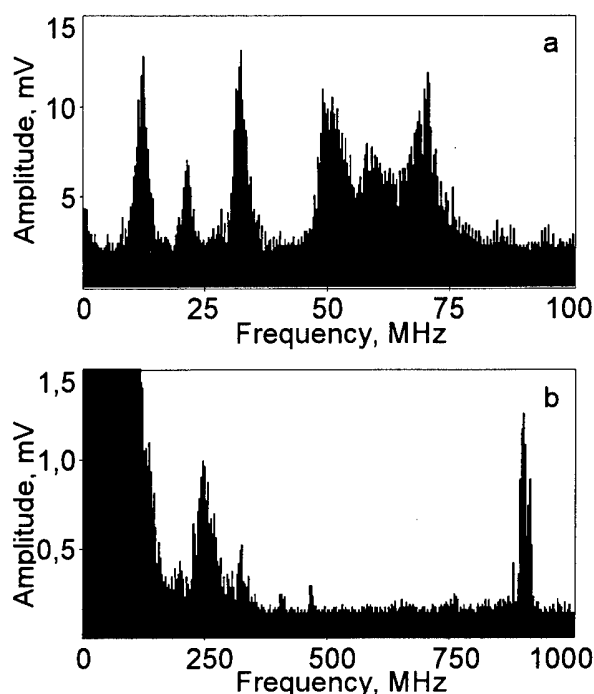


Fig. 1. Spectra of signal from the probe P3 in the frequency ranges 0-100 MHz (a) and 0-1000 MHz (b). Beam voltage  $U_0 = 8$  kV, plateau magnetic field  $B_0 = 2.3$  T, beam current  $I = 8$  A.

Our results show that the HF oscillations have a convective nature. The characteristics of these oscillations can be explained by invoking the mechanism of "double-stream instability" of space charge waves. In the investigated HEB discrete streams with different longitudinal velocities  $v_{\parallel}$  occurred due to non-uniformity of emission over the cathode surface. For used cathodes the non-uniformities of emission were 10-100 % of average values. Comparison of the dependencies  $j_e(\theta)$  and  $j_{col}(\theta)$  showed that the main features of emission current azimuthal distribution remained in the HEB transverse structure down to collector. According to [4] the difference in the values of  $v_{\parallel}$  for electron streams emitted from different cathode areas can amount to ~ 5-10 %.

The changes in the distribution  $j_e(\theta)$  had effect on the threshold and amplitude of the oscillations.

Analysis of the probes signals oscillograms and instantaneous spectra showed that during a few first microseconds of beam current pulse LF oscillations amplitude decreased and HF oscillations amplitude increased. Fig. 3 shows the oscillograms with duration of ~ 13 ns and the corresponding spectra obtained for two different delay times  $\Delta\tau$  relative to the current pulse front: 0.5  $\mu$ s (Fig. 3,a,b) and 6  $\mu$ s (Fig. 3,c,d). The rapid decay of the LF signals could indicate that the changes of the electric field and current on the voltage pulse front could strongly affect the "trap" oscillations development.

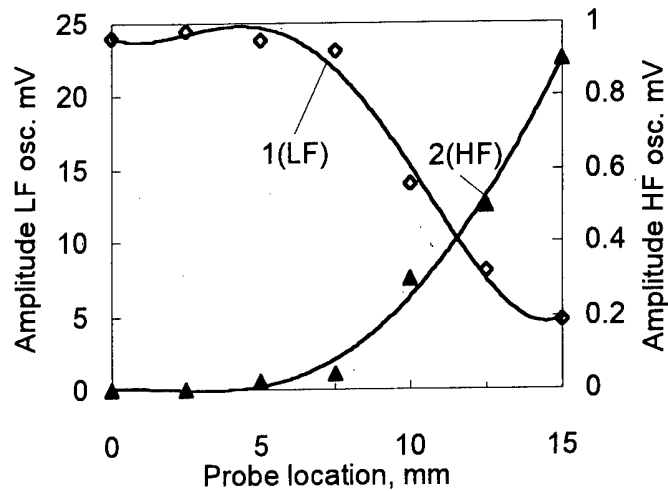


Fig. 2. Amplitudes of low- and high-frequency oscillations as a function of the axial location of the probe P3.  $U_0 = 8$  kV,  $B_0 = 2.05$  T,  $I = 7$  A.

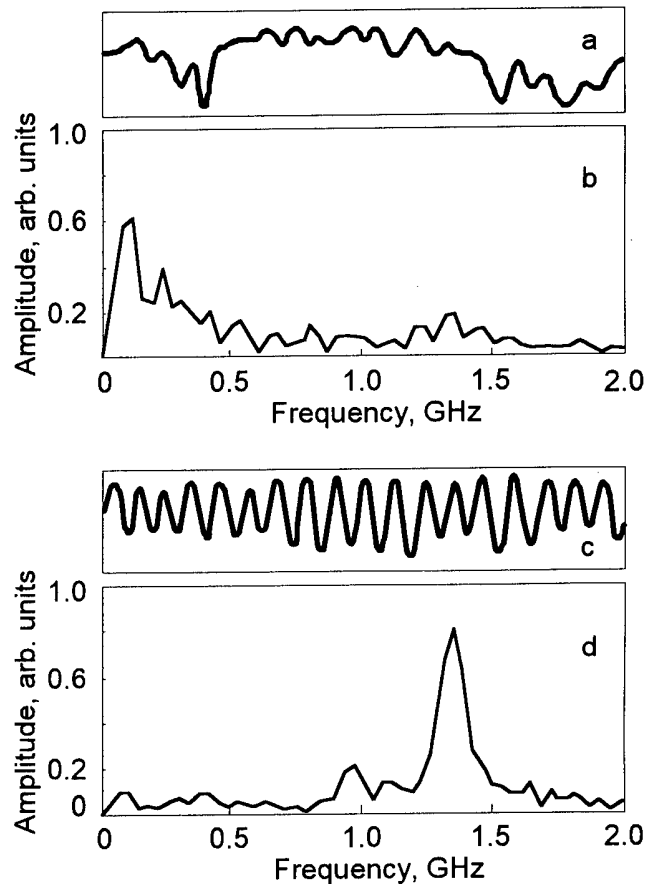


Fig. 3. Oscillograms of signal from the probe P3 with 13 ns duration (a,c) and corresponding spectra (b,d) with delay relative to the current pulse front of 0.5  $\mu$ s (a,b) and 6  $\mu$ s (c,d).  $U_0 = 8$  kV,  $B_0 = 2.3$  T,  $I = 8$  A.

### Results of numerical simulation

The processes of space charge accumulation and bunching in the trap were modeled in the calculations based on a particle-in-cell method and drift adiabatic paraxial approximation. One-dimensional axial motion of the electron orbit centers was considered taking into account transverse velocity spread  $\delta v_{\perp}$ . The self-consistent equations of motion were solved with a time step of 0.2 ns. The trap region between cathode and magnetic field plateau was divided into 100 cells.

The simulation geometry was closed to experimental one in which the LF oscillations were investigated earlier [3]. Fig. 4 shows the temporal evolution of beam potential  $-U$  in 70-th cell 16.8 cm downstream from cathode for  $I = 0.2$  A,  $\delta v_{\perp} = 25\%$ ,  $g = 1.2$ . During the first  $\sim 600$  ns potential  $-U$  and number of the particles locked in the trap increase. For  $t \geq 600$  ns the locked particles charge reaches about half of the total charge in the simulation region ( $\sim 9500$  particles form this total charge). Afterwards we see the growth and saturation of the HEB potential modulation. The modulation period is about 10 ns. The obtained simulation results confirm the experimental data on LF oscillations as the axial oscillations of the space charge bunches in the trap.

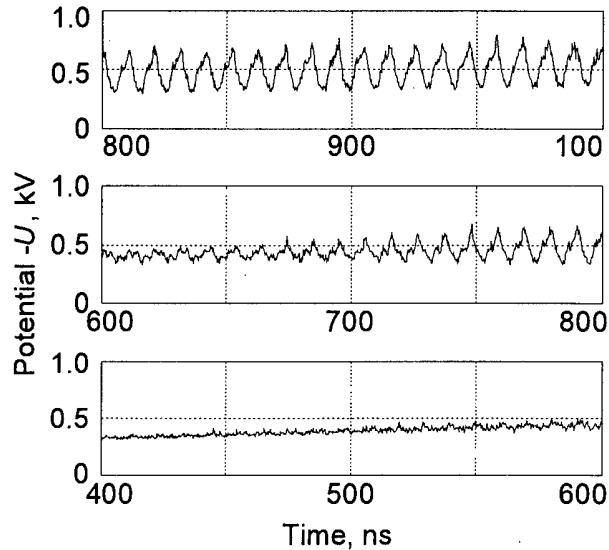


Fig. 4. Calculated beam potential as a function of time.  $I = 0.2$  A,  $\delta v_{\perp} = 25\%$ ,  $g = 1.2$ .

### Conclusions

Methods have been developed for experimental investigation and numerical simulation of the collective processes occurring in the HEB of gyrotron electron-optical system.

Characteristics of the space charge oscillation in the frequency range 10-1500 MHz were determined.

It was found that the low-frequency oscillations resulting from the axial motion of the electron bunches in the trap between cathode and magnetic field plateau decay rapidly in time and down the HEB drift space in uniform magnetic field. In such conditions the high-frequency oscillations, which are related with the convective development of space charge waves, increase.

The authors would like to thank D. Borzenkov for assistance in the calculations.

- [1] Louksha O.I., Sominski G.G. : Zh. Tech. Fiz., **64** (1994), 160.
- [2] Louksha O.I., Sominski G.G. : Zh. Tech. Fiz., **65** (1995), 198.
- [3] Louksha O.I., Tsybin O.Yu : in Lectures on Microwave Electronics and Radio Physics [in Russian], 9-th Winter School-Seminar, Saratov (1993), 20.
- [4] Gol'denberg A.L., Lygin V.K., Manuilov V.N., Petelin M.I., Tsimring Sh. E., : in The Gyrotron [in Russian], Gorky (1981), 86.

## CO-OPERATIVE HIGH-POWER RADIATION OF TWO BEAMS AT THE DUAL VIRCATOR COMPLEX

I.I. Magda, Yu.V. Prokopenko

*National Science Center  
"Kharkov Institute of Physics and Technology"  
Akademicheskaya, 1, Kharkov, 310108, Ukraine*

### Abstract

The possibility of creating a high-power microwave radiation source (HPM) of ultra-short pulse duration (USP) on base of the phased-antenna arrays (PAA) was considered. The virtode-type oscillators are used as basic elements of such a source. The design and technical features of phased arrays of HPM-sources on the base of high-current relativistic electron beams (REB) are presented.

### Introduction

One of the major directions of HP electronics is the creation of high-power microwave radiation sources with ultra-short pulse duration for applications in the high-energy physics (HEP), heavy particles accelerators, systems of ultra-long-distance radiocommunications and radars. In recent years, owing to the possibility of generation and focusing of electromagnetic fields with critical strength values, such devices are considered as perspective sources for creating artificial ionization regions in the upper atmosphere in order to destroy the freon populations and protect the ozone layer. They also find applications in the plasma heating for nuclear fusion, pumping of HP gas lasers and directional electromagnetic energy transportation.

An attractive feature of the oscillators employing a super-critical REB current in order to convert its energy into microwave radiation energy is a possibility to increase, practically, without limit the beam injection current with an appropriate increase in HPM-radiation which, in this case, is determined by the electric strength of the RF-duct, only. Microwave devices of the vircator type (VCO) have a rather simple structural and some of them can be readily tuned in frequency and amplitude of output signal in a wide range of frequencies. The capability to control a relatively low power external signal and a process of forming the output microwave radiation in VCO's is the especially important pre-condition for their applications as basic elements of a very high-power radiation source on the base of the PAA [1,2].

This paper considers the possibility of creating the HPM USP sources on the base of PAA (PAA-based HPM USP sources) where a special attention is given to the conditions of their coupling with energy sources and related interactions.

The virtode experimental studies demonstrated that stabilization of the oscillation phase in the system with supercritical REB current was ensured by injection of the external RF-signal (external feedback signal) into the region of electron acceleration with the power  $P_y = 0.15P_{puls}$  where  $P_{puls}$  is the microwave radiation pulsed power. Variation of the driving electromagnetic wave phase relative to the oscillation phase permitted to adjust the amplitude of the output microwave radiation within 8 dB. The mode selection of charge density oscillations allowed to perform tuning of the virtode generation frequency within 30% with the invariable efficiency of



The diagram illustrates a four-channel microfluidic device. A central vertical channel (1) is intersected by two horizontal channels (2). Four inlet/outlet channels (3) are connected to the horizontal channels. Two sets of valves (4) are located on these channels. The device is flanked by two vertical channels (7) with cross-sections (8). A dashed line indicates the PAA (polyacrylamide) region.

The diagram illustrates the architecture of the proposed HVPFC and PAA. The HVPFC block consists of a sequence of nodes 1 through 7. Node 1 is connected to node 2, which is connected to node 4. Nodes 3, 4, 5, 6, and 7 are connected in a linear sequence. The PAA block consists of a sequence of nodes 8 through 10. Node 8 is connected to node 9, which is connected to node 10. There is a bidirectional connection between the two node 9s. The HVPFC block is connected to the PAA block via a connection from node 7 to the first node 8.

Experimental studies indicate that in such microwave radiation sources the condition of impedance matching between all its constituents is of a paramount importance. In the case of an impedance mismatch between the high-voltage pulse forming circuit and the vacuum diode a difference was observed between the microwave radiation pulse and REB current. The impedance mismatch of vacuum diode channels caused the REB current exchange redistribution, and consequently, the difference in the microwave power levels by each channel individually. Besides, the parametric dependence of vacuum diode channel impedances on the REB currents ensured lowering of the excitation threshold and a preferential operation of one of the channels due to the different duration of the instability buildup in virtode type oscillators.

### **Conclusion**

The above experimental studies indicated that for creation of a high-power microwave radiation source USP based on PAA an effective way is the creation of a parallel circuit of feeding its low- $Q$  driving elements of a virtode type. A special attention in such microwave devices should be paid to impedance matching between its components.

### **References**

- [1] Woo W., Benford J., Fittinghoff D., Harteneck B., Price D., Smith R., and Sze H. : *J. Appl. Phys.*, V.65 (1989) P.861-866.
- [2] Gadetsky N.P., Magda I.I., Niceteter S.I., Prokopenko Yu.V. et al : *Plasma Physics* (in Russian), V.19 (1993) P.530-537.

## COAXIAL PLASMA-FILLED STRUCTURES

I.N.Onishchenko, V.A.Balakirev, A.M.Korostelev,  
 P.I.Markov, D.Yu.Sidorenko, G.V.Sotnikov  
 NSC "Kharkov Institute of Physics and Technology"  
 310108 Kharkov, Ukraine

## Abstract

*The high-power generators and amplifiers provide efficiency enhancement and spectrum complexity due to plasma filling. For widening frequency band of radiation and tuning diapason the hybrid slow-wave plasma filled structures should be of coaxial type. Three kinds of coaxial structures have been investigated: inversed chain of inductively coupled cavities, magnetically insulated slow-wave coaxial wavguide, plasma-filled corrugated coaxial line. Numerical calculations are carried out for the set of parameters characterizing the structure geometry, plasma and electron beam. The formation of electron flow and generation process take place in the same device. It was shown that the generation frequency slightly changes over the voltage, that ensures its stability in operating regime.*

## Introduction

In our previous report [1] the theoretical investigation, simulation and experimental studies of some new slow wave structures has been represented. It was traditional slow wave structures, partially filled with plasma. Several advantages were revealed comparatively to those of the traditional vacuum structures. The main merits of these hybrid structures are the efficiency enhancement and spectrum variety. For the widening of frequency band the coaxial slow wave structure with dispersiveless cable mode should be taken for hybrid plasma filled structure considered. On the other hand, coaxial type of slow wave structure is naturally conjoined with tubular electron beam for excitation of the RF-radiation. It allons to enlarge e-beam cross-

section and to increase the power of the beam and the total RF-power.

In inversed chain of cavities (ICC), proposed in [2], the tubular electron beam blows round the chain of cavities, placed on the axis of the structure. The dispersion equation is obtained. In the linear approximation the interaction of the electron beam with eigen modes of the plasma filled ICC structure is studied. Calculation are carried out for the net of parameters characterizing the structure geometry, plasma and electron beam. It was found that at operation on dispersiveless quasi-coaxial mode coupling coefficient are increasing with plasma filling.

The formation of electron flow and RF generation process can be realized in the same device — magnetically insulated slow wave



coaxial line. The preliminary investigations were carried out for a flat magnetically insulated transmission line with a comb anode [3]. The generation of power RF-oscillations is obtained due to electron flow interaction with slow eigen modes during its drift motion in crossed electric and magnetic fields.

For relativistic e-beam the plasma filled corrugated waveguide is used. For widening of the frequency band we proposed plasma filled corrugated coaxial line [4]. The properties of the eigen mode are investigated at various plasma density. The REB interaction with such structure are investigated in dependence on plasma density energy and current of the beam.

## Inversed Chain of Cavities

Geometry of investigated slow wave structure is depicted in Fig. 1.

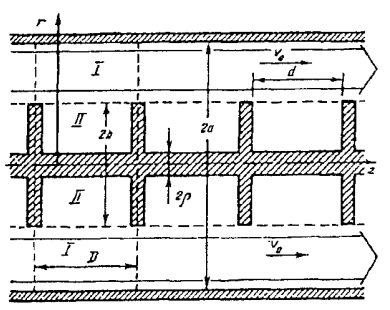


Figure 1:

Let us suppose that magnetized plasma occupies the flight region I in which electron beam moves. Considering the wave of E-type with components are  $E_z$ ,  $E_r$ ,  $H_\varphi$ , we solve this problem by the method of partial regions. The set of Maxwell equations were solved for each region and by their matching at the boundary  $r = b$  we obtain dispersion

equation:

$$\frac{J_1(kb)N_0(k\rho) - N_1(kb)J_0(k\rho)}{J_0(kb)N_0(k\rho) - N_0(kb)J_0(k\rho)} = k\varepsilon_3 \sum_{m=-\infty}^{\infty} \frac{\sin(k_m \frac{d}{2})}{k_m \frac{d}{2}} \frac{J_0(k_m \frac{d}{2})}{\tau_m} \times \frac{J_1(\tau_m b)N_0(\tau_m a) - N_1(\tau_m b)J_0(\tau_m a)}{J_0(\tau_m b)N_0(\tau_m a) - N_0(\tau_m b)J_0(\tau_m a)} \quad (1)$$

Note that for method improvement the non-regularity of the electric field on the disc edges at  $r = b$  can be taken into account using Meixner condition. Due to structure periodicity the eigen mode satisfy the Floquet theorem, so  $z$ -dependence takes from  $\exp(ik_m z)$ ,  $k_m = k_0 + m \frac{2\pi}{D}$ ,  $k_0$  is longitudinal wave vector. For the investigation of the excitation of the RF-oscillations in plasma filled ICC structure by an electron beam we use by the conjugated theorem that allows to obtain the expression

$$\frac{(k_z^2 - k_0^2)(k_z^2 - k_0^2)}{k_0^2} = \frac{\omega_b^2 k_c (k_z^2 - k_z^2)}{\omega_b^2 - (\omega - v_0 k)^2 \varepsilon_3} \quad (2)$$

where  $\omega_b = (4\pi e^2 n_b / m_e)^{1/2}$  is plasma beam frequency,  $n_b$ ,  $v_0$  are density and the velocity of the beam,  $k_0$ ,  $k_z$  are propagation constants without and with beam,  $k_c = \frac{k}{2k_0 P} \int_S |E_{0z}|^2 ds$  is coupling coefficient

of the electron beam with electromagnetic wave,  $P = \frac{c}{8\pi} \text{Re} \int_S [EH^*] a_z ds$  is averaged

over oscillation period power flow through cross-section of transmit region I.

Writing  $k$  in the form  $k = k_0(1 - i\delta)$  we obtain the equation of 4-th power of  $\delta$ . In general case it can be solved numerically.

The interaction efficiency  $\eta = \frac{P_{\max}}{n_b W_b v_0 S_0}$  can be estimated proceed from condition of electrons trapping by the wave

$$eE_z^{\max} = W_b k_0 (\text{Im} \delta)^2. \quad (3)$$

Here  $W_b$  is electron energy,  $S_0$  — cross section of the beam,  $P_{\max} = \frac{c}{8\pi} \int_S E_r^{\max} H_\varphi^{\max} ds$  is maximum power flow of the exited wave. For the structure with parameters  $a/D = 3.0$ ,  $b/D = 6.0$ ,  $\rho/D = 1.0$ ,  $d/D = 0.8$  the numerical calculations give the following results.

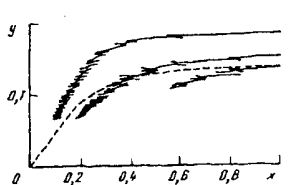


Figure 2:

In Fig. 2 the dispersion curves are represented for vacuum case (dotted curve) and for plasma filling  $\omega_p = 0.2\pi c/D$  (continuous curves). For vacuum case there exists coaxial mode with slow phase velocity. Besides the main coaxial mode in plasma filled ICC structure there are a lot of plasma modes corresponding to various Floquet (spatial) and radial modes of the tubular plasma column.

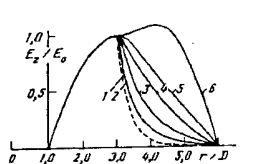


Figure 3:

For plasma case the fields topography of the excited waves changes essentially. In Fig. 3 the radial dependence of the longitudinal electric field on the plasma density is represented at cross-section  $z = 0$ . It can be seen that vacuum surface mode becomes volumetric one at plasma filling.

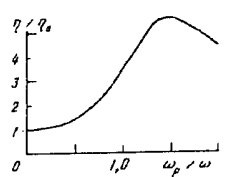


Figure 4:

The efficiency enhancement is shown in Fig. 4 where the dependence  $\eta$  upon plasma density at  $k_0 = 0.375\pi/D$  is represented. It is seen that at  $\omega_p \cong 1.5\omega$  the efficiency is maximum. At larger plasma density the longitudinal component of electric field is prevailed, that leads to decreasing of RF-power flux.

## Magnetically Insulated Line

The system of this type can be used as powerful microwave amplifiers and oscillators. In the Magnetically Insulated Line Oscillator (MILO) the Brillouin flow formation and generation of radiation are combined.

The dispersion equation for TM waves can be obtained by matching the field impedance in vacuum gap [3]. It was solved numerically for minimal current and different slow-wave structure geometries and applied voltage values. As calculations show for small wave number the Brillouin flow is stable and two waves propagate in it. Oscillations grow in the frequency range  $\omega/\omega_c > 1$ . The gain in the growth rate is due to wave being in resonance with the slow-wave structure. As the voltage increase, the growth rate peak shifts to the low frequency range and the increment values of the maximum decreases. For higher voltage the resonance instability growth rate is essentially less than the one of magnetron instability.

The frequency of the wave excited by resonance instability practically does not de-

pend on voltage  $V$ . The anode efficiency of the oscillator can be determined as  $\eta = K_i(\gamma - \gamma_*)/(\gamma - 1)$ .  $K_i$  is the ratio of the flow current in the line to the total current,  $\gamma = 1 + \varepsilon U/mc^2$ ,  $\gamma_*$  is the electron relativistic factor on the flow boundary. So far  $U = 0.5 \text{ MV}$   $\eta = 17\%$ .

## Corrugated Coaxial Waveguide

We consider the coaxial waveguide with straight inner cylinder of radius  $R_0$ , and sine-shaped outer cylinder:  $R_g(z) = R_{0g}[1 + \delta \sin(k_0 z)]$ , where  $k_0 = 2\pi/D$ , and  $D$  is the ripple period. The waveguide is filled with a spatially-uniform plasma; the system is immersed in a strong axial magnetic field; an axially symmetric monoenergetic hollow electron beam with density  $n_b(r) = [J/(2\pi e V_b R_b)]$ , propagates along the system axis, where  $J$ ,  $V_b$  and  $R_b$  are the current, electron velocity, and radius of the beam, respectively.

To derive the dispersion equation we divide the interaction region of the considered system into two partial regions, viz.,  $r < R_b$  and  $r > R_b$ . The electromagnetic field components can be expanded in space harmonics:

$$F(\vec{r}_\perp, z) = \sum_{n=-\infty}^{\infty} A_n f(\vec{r}_\perp) e^{ik_n z}, \quad (4)$$

The transverse components of the electromagnetic field is sought as the expansion in the Bessel and Neumann functions. Solving Maxwell equations in each part of the interaction region with the boundary conditions and taking (4) into account, one obtains the dispersion equation.

Solving numerically, we choose the following parameters of the rippled waveguide:  $\delta = 0.1$ ,  $D = 10 \text{ cm}$ ,  $R_0 = 2 \text{ cm}$ ,  $R_{0g} = 4 \text{ cm}$ .

Dispersion curves on the plane  $(\omega, k)$  show that in the range  $\omega > \omega_p$  eigenfrequencies of the electromagnetic modes are shifted above.

In the range  $\omega < \omega_p$  the frequency of the cable mode changed insignificantly, but the mode becomes strongly split due to its interaction with the radial and Floquet modes of the plasma wave. It is this case, when the eigen mode of the slowing down vacuum structure (SWS) is over-lapped by the plasma modes, that is of interest for case in hybrid SWS.

Now, let us consider the interaction of the electron beam with hybrid SWS eigenmodes. Here after we assume  $R_b = 3 \text{ cm}$ ,  $J = 200 \text{ A}$ .

At low  $\gamma$  and in the presence of plasma, the growth rate is much greater than that in the vacuum SWS; in this case, the higher the plasma density, the higher the growth rate.

The obtained dependence of maximum growth rate versus beam current for  $\gamma = 1.4$  shows that, in the current range  $10 \text{ A} < J < 1000 \text{ A}$ , the maximum growth rates in the plasma-filled SWS are much higher than those in the vacuum SWS.

## References

- [1] A.N.Antonov, A.K.Berezin, Yu.P.Bliokh et al, Beams'94, Proc. of the 10 Int Conf. on High-Power Particle Beams, San-Diego, USA, June 20-24, 1994, v.1, p.260.
- [2] E.A.Kornilov, A.N.Korostylev, A.V.Lodygin et al, Ukrainian Journal of Physics, 1995, v.40, p.312.
- [3] V.A.Balakirev, D.Yu.Sidorenko, G.V.Sotnikov et al, Beams'94, Proc. of the 10 Int Conf. on High-Power Particle Beams, San-Diego, USA, June 20-24, 1994, v.2, p.892.
- [4] I.N.Onishchenko, D.Yu.Sidorenko, G.V.Sotnikov Plasma Physics Reports, 1995, v.21, p.670.

**BEAM-PLASMA PROCESSES RELEVANT TO HIGH-POWER  
WIDE BAND PLASMA-FILLED MICROWAVE SOURCES**

M.A. Zavyalov, L. A. Mitin, V.I. Perevodchikov, A.L. Shapiro,

*State Science Center "All Russian Electrotechnical Institute"  
Krasnokazarmennaya 12, Moscow 111250, Russia*

**Abstract**

Main features of non-relativistic Cherenkov-type beam-plasma microwave amplifier with hybrid plasma-cavity slow-wave structures are described. The estimations of fundamental parameters of beam-plasma microwave device based on analysis of cylindrical beam-plasma system in external magnetic field are presented:

Plasma density (up to  $10^{12} \text{ cm}^{-3}$ ), electron beam (3 A, 20 kV,  $3 \cdot 10^9 \text{ cm}^{-3}$ ), magnetic field (0.25 T), working gas pressure ( $1 \cdot 10^{-3}$  Torr) and also current threshold for electron-electron instability as a stage of beam-plasma discharge.

Results of experimental investigation of beam-plasma in propagation channel of electrodynamic structure carried out in the presence of microwave generation are given. Beam-plasma amplifier has been created to operate at output microwave power over 20 kW, electron efficiency up to 35 % and pass-band width 30 %.

(Full text not available)

## DEPENDENCE OF MICROWAVE GENERATION ON BEAM PLASMA SYSTEM LENGTH

M.A. Krasilnikov, M.V. Kuzelev, A.A. Rukhadze

*General Physics Institute, Moscow, 117942, Russia*

It is known from experiments [1, 2] that microwave oscillators on beam-plasma (BP) instabilities have the highest efficiency when exceeding of interaction space length or beam current over the threshold of BP systems takes place. The present work deals with numerical simulation research of the radiation dynamics dependence on interaction space length in the case of the Compton BP instabilities mechanism. The Compton instability is stabilized by capture of beam electrons by plasma wave [3].

Let us start with the case of short lengths, when the capture does not occur in the BP system without reflection of plasma wave from radiating cone. If the reflection of plasma wave is taken into consideration the stationary level of output plasma wave is obtained. The value of the output plasma wave amplitude has the order of the capture wave amplitude, that is higher than in the system without reflection when the ordinary plasma wave space amplification takes place.

This case is illustrated by Fig.1. The curve 1 corresponds to the system without reflection, whereas the curve 2 corresponds to the system with reflection when the output amplitude becomes higher. (This figure and the following one show the dependence of radiation efficiency on time.)

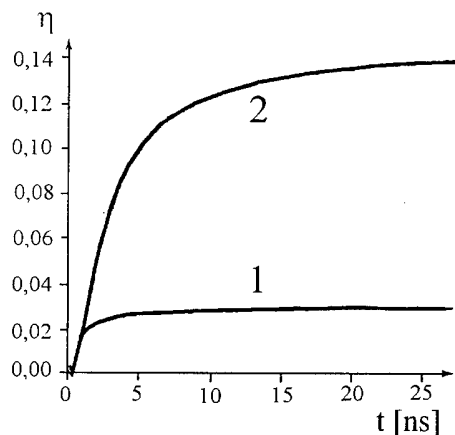


Fig. 1

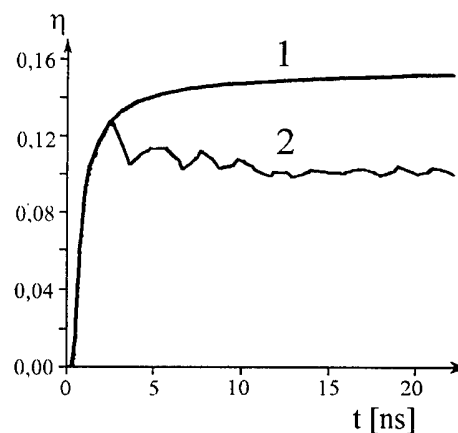


Fig. 2

The different situation is obtained for long systems. Here the presence of feedback by means of reflection causes efficiency decreasing and stationary disruption. (Fig.2, curve 1 - system without reflection, curve 2 - reflection present.)

The similar dependence can be observed when beam current increases and the system length is fixed.

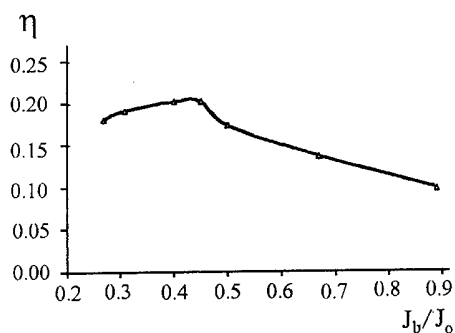


Fig. 3

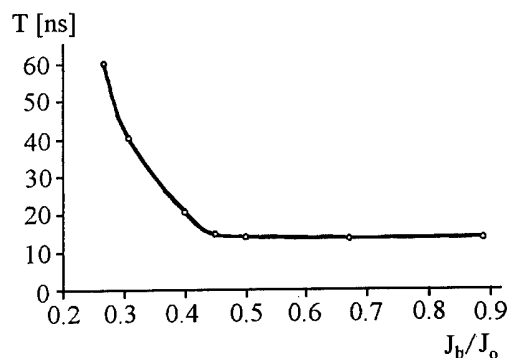


Fig. 4

The efficiency dependence on the beam current ( $J_0$  - is the corresponding limiting current) in this case is presented on the Fig.3. The curve on the Fig.4 shows the time for establishment of stationary level of output radiation when the beam current increases. It occurs much longer than the beam flight time across the system. The optimal value of the beam current  $J_b/J_0 \cong 0,45$  corresponds to the maximal efficiency  $\eta \sim 22\%$ .

## References

- [1] I.A. Selivanov, P.S. Strelkov, A.V.Fedotov, A.G. Shkvarunets, Plasma Physics Reports, 1989, v.15, p.1283;
- [2] A.G. Shkvarunets, A.A. Rukhadze, P.S. Strelkov, Plasma Physics Reports, 1994, v.20, p.686.
- [3] A.N. Kondratenko, V.M. Kuklin, Osnovi plasmennoi elektroniki, Energoatomizdat, Moscow, 1978.

# APPROACHES TO ACHIEVING HIGH EFFICIENCY, LONG PULSE, VACUUM BACKWARD WAVE OSCILLATOR OPERATION

E. Schamiloglu, J. Gahl, C. Grabowski, and C. Abdallah

*Department of Electrical and Computer Engineering  
University of New Mexico  
Albuquerque, NM 87131, USA  
edl@eece.unm.edu*

## Abstract

This paper describes recent achievements in the study of short pulse (10s of nanoseconds) high power backward wave oscillators (BWOs) and the difficulties associated with applying these results to long pulse (100s of nanoseconds) microwave generation. Finite length effects observed in the short pulse studies were reproduced in electromagnetic particle-in-cell simulations. These results motivated the incorporation of concepts from control theory to design a frequency agile BWO. High temporal and spatial resolution plasma diagnostics will be installed on the long pulse experiment to assess the effects of plasma on pulse shortening.

## Introduction

Considerable progress has been made recently in the understanding of the efficient operation of high power backward wave oscillators (BWOs) in the short pulse (10s of nanoseconds) regime [1-3]. Experiments using a Sinus-6 electron beam accelerator, coupled with electromagnetic particle-in-cell (PIC) simulations, have provided detailed understanding of finite length effects on both microwave generation frequency and efficiency. These results motivated the use of concept from control theory to design a frequency agile BWO [3,4]. These achievements, unfortunately, do not readily scale to long pulses (100s of nanoseconds). In an effort to better understand the interaction environment within the slow wave structure (SWS) during long pulse experiments a laser diagnostic has been designed and will be used to characterize the evolution of plasma in the proximity of the SWS walls. This paper summarizes the achievements of the short pulse studies and describes experiments performed on the long pulse experiment with the goal of mitigating the so-called pulse shortening phenomenon.

## Short Pulse BWO Studies

The importance of finite length effects on relativistic BWOs was studied using the Sinus-6 repetitively pulsed relativistic electron beam accelerator. Beam energies ranging from 450-700 keV and corresponding beam currents ranging from 3.5-6.0 kA were used in these experiments. (Detailed information on the experimental system can be found in [1,3].) Figure 1 schematically shows the experimental setup for studying finite length effects. An 8 ripple period SWS was used with each ripple having a period of 15 mm and corrugation amplitude of 2.25 mm. A long uniform magnetic field with magnitude 2.7 T was used for beam transport. The radiated power was measured using a crystal detector and the frequency was obtained on each shot by heterodyning this signal with a known frequency source. The RF efficiency was obtained by dividing the measured peak RF envelope power by the input beam power.

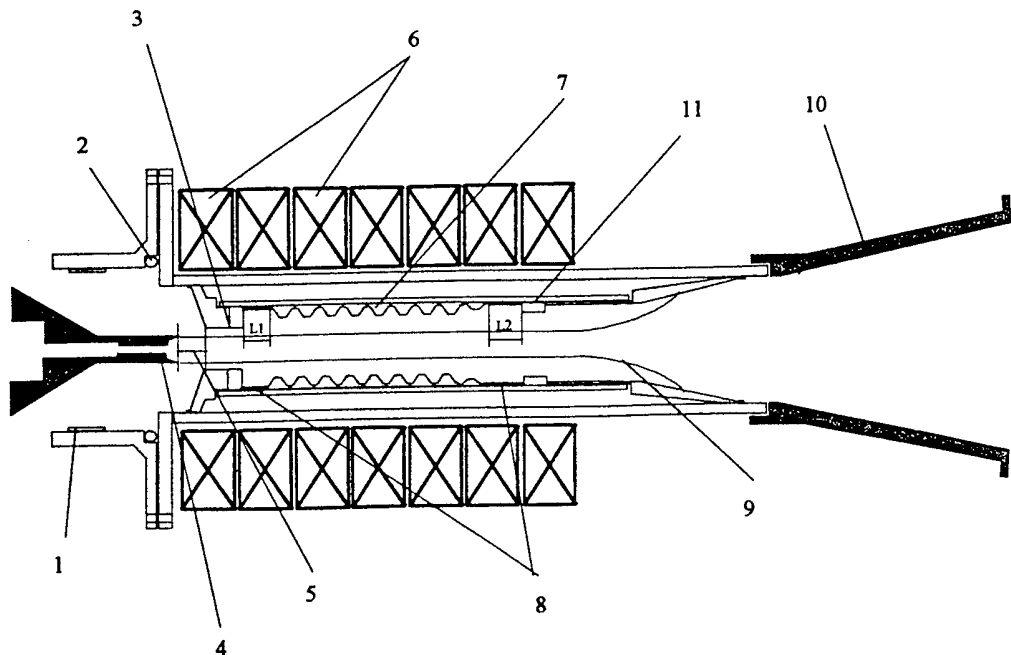


Figure 1. Experimental setup for studying finite length effects in a relativistic BWO. Shown are (1) voltage monitor, (2) current monitor, (3) cutoff neck, (4) cathode, (5) A-K gap, (6) magnetic field coils, (7) SWS, (8) smooth circular waveguide and shifting lengths  $L_1$  and  $L_2$ , (9) electron beam, (10) output horn antenna, and (11) reflection ring.

Finite length effects were studied by introducing sections of smooth-walled waveguide between the cutoff neck and the SWS ( $L_1$  in Fig. 1). We refer to this as “forward shifting.” These sections of waveguide change the phase between the forward and backward traveling waves in the BWO, as well as the volume of stored electromagnetic energy in the SWS (see [3] for additional detail). The results of experiments and PIC simulations of the dependence of microwave generation efficiency and radiated frequency are shown in Figs. 2 and 3. Note that

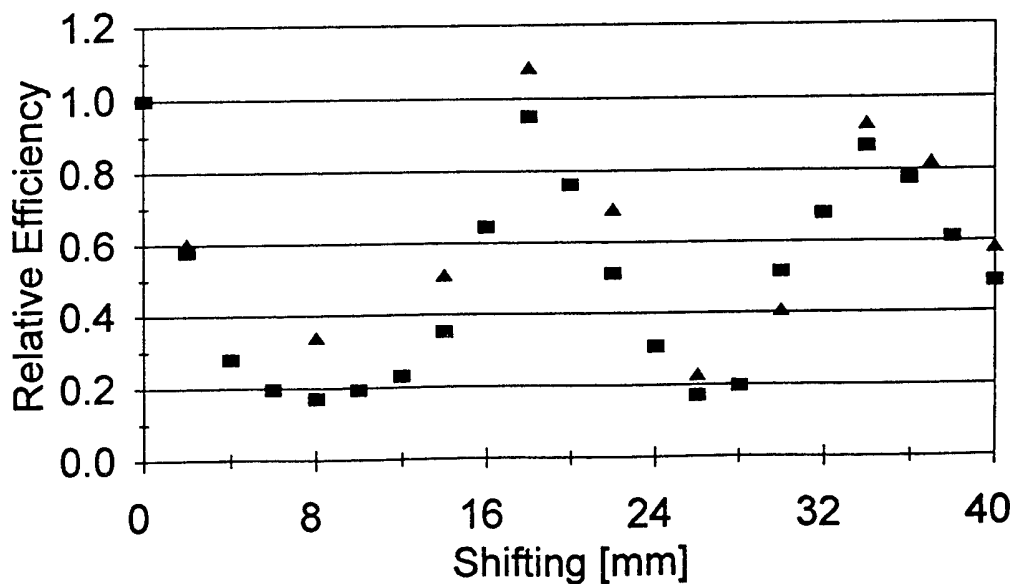


Figure 2. Efficiency (normalized to the unshifted case) as a function of varying  $L_1$  as observed in experiment (squares) and PIC simulation (triangles) (for 505 kV  $\pm$  2.5%, 3.1 kA  $\pm$  2.5%).



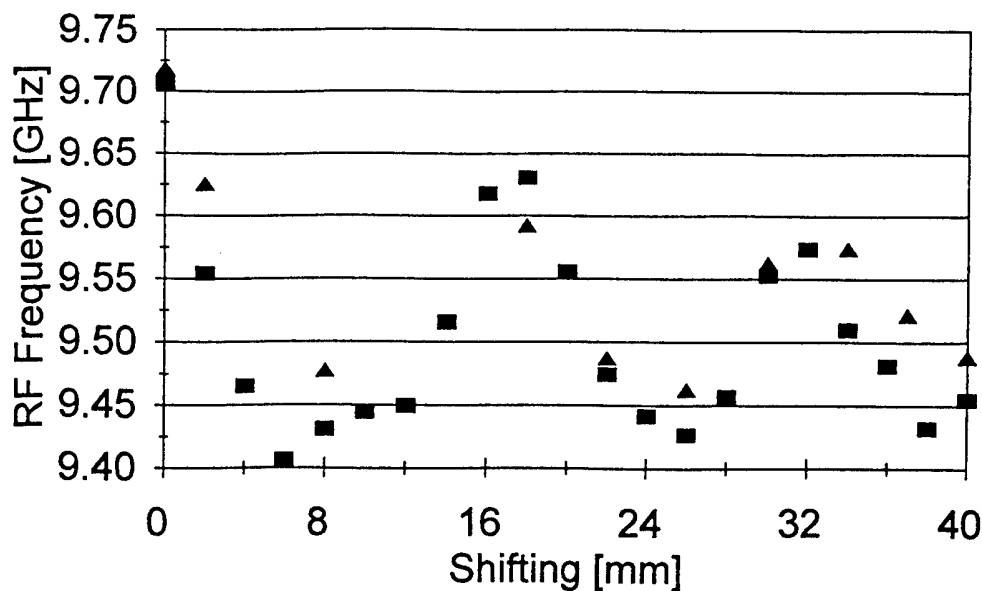


Figure 3. Radiated frequency as a function of varying  $L_1$  as observed in experiment (squares) and PIC simulation (triangles) (for  $505 \text{ kV} \pm 2.5\%$ ,  $3.1 \text{ kA} \pm 2.5\%$ ).

there is excellent agreement between experiment and simulation. These results suggest an intriguing possibility of maintaining a constant output power of a couple 100 MW at a center frequency of 9.5 GHz and bandwidth of about 500 MHz. A block diagram of a control scheme to accomplish this is shown in Fig. 4 [3,4].

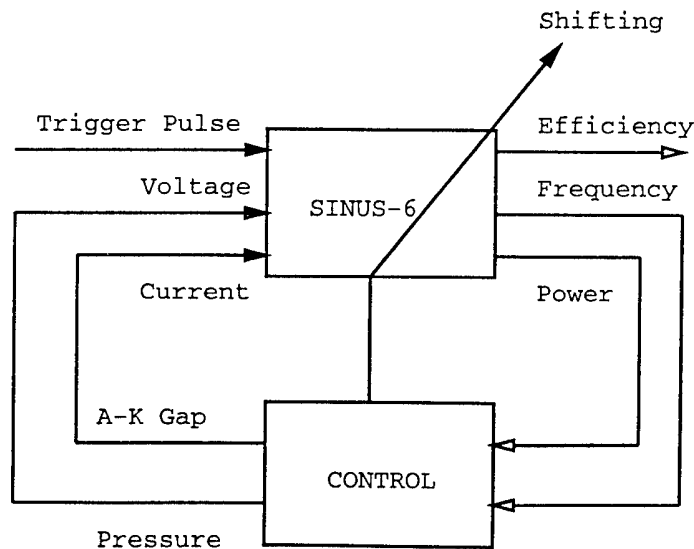


Figure 4. Block diagram of computer controlled, frequency agile BWO.

### Long Pulse BWO Studies

The University of New Mexico long pulse BWO experiment is similar to the setup shown in Fig. 1 (the SWS system being identical to the one described as the "Long Tube" in [1]) except that it is driven using a modified PI-110A accelerator with beam and current parameters

comparable to the Sinus-6 except with a FWHM current pulselength of about 450 ns. Recent experiments have concentrated on establishing hypotheses and remedies for pulse shortening (microwaves at 100s MW power levels are generated for less than 100 ns) [5]. Pulse shortening is ubiquitous among pulsed high power microwave sources and has been observed in BWOs for two decades [6,7]. The termination of microwaves in this experiment is closely correlated with a non-optimum radial distribution of beam electrons in the downstream portion of the SWS [5]. Furthermore, plasma and/or energetic secondary electrons are measured near the SWS wall when microwaves are abruptly terminated [5]. A Nd:YAG laser system (1064 nm) will be used to attempt to correlate the evolution of axially line-averaged plasma density between the electron beam and SWS ripple boundary during the course of microwave generation. (Infrared lasers have been used in the past to measure plasma densities in ion diodes and plasma opening switches [8]. In addition, this laser can be used to measure the spread in axial beam momentum, as in [9].) This will be important in assessing the role plasma plays in pulse shortening in this class of sources. (A residual gas analyzer has recently been installed in the experiment to monitor background gas constituents following a microwave pulse.) In an attempt to improve long pulse BWO performance experiments have begun using SWSs whose inner surfaces were coated with 200-500 nm layers of  $\text{TiO}_2$ . Once conditioned, these coatings were shown in earlier quasi-DC experiments to increase the breakdown electric field strengths of bare stainless steel by as high as a factor of two [10].

### Acknowledgments

The authors wish to thank Dr. R.W. Lemke (Sandia National Laboratories) for performing the PIC simulations. The authors also wish to thank Drs. S.D. Korovin and A.M. Roitman (Institute of High Current Electronics, Tomsk, Russia) for useful discussions. This work was supported through a High Energy Microwave Devices Consortium funded by an AFOSR/DOD MURI grant and administered through Texas Tech University.

### References

- [1] L.D. Moreland, E. Schamiloglu, R.W. Lemke, S.D. Korovin, V.V. Rostov, A.M. Roitman, K.J. Hendricks, and T.A. Spencer, "Efficiency enhancement of high power vacuum BWO's using nonuniform slow wave structures," *IEEE Trans. Plasma Sci.*, vol. 22, pp. 554-565, 1994.
- [2] A.M. Roitman, S.D. Korovin, S.D. Polevin, V.V. Rostov, L.D. Moreland, and E. Schamiloglu, "A high power microwave generator based on a relativistic BWO," *SPIE*, vol. 2557, pp. 422-433, 1995.
- [3] L.D. Moreland, E. Schamiloglu, R.W. Lemke, A.M. Roitman, S.D. Korovin, and V.V. Rostov, "Enhanced frequency agility of high power relativistic backward wave oscillators," to appear in *IEEE Trans. Plasma Sci.*, June, 1996.
- [4] C. Abdallah, W. Yang, E. Schamiloglu, and L. Moreland, "A neural network model of the input/output characteristics of a high power backward wave oscillator," to appear in *IEEE Trans. Plasma Sci.*, June, 1996.
- [5] J.M. Gahl, C. Grabowski, D. Young, and O. Ishihara, "Pulse shortening in a high power backward wave oscillator," Invited presentation at the IEEE Int'l Conf. on Plasma Sci. (Boston, MA, USA, 1996).
- [6] A.S. El'chaninov, F. Ya. Zagulov, S.D. Korovin, G.A. Mesyats, and V.V. Rostov, "Limitation on the length of high-power microwave pulses in a relativistic carcinotron," *Sov. Tech. Phys. Lett.*, vol. 7, pp. 499-500, 1981.
- [7] S.N. Voronkov, O.T. Loza, and P.S. Strelkov, "Limits on the length of radiation pulses generated by microwave oscillators using microsecond relativistic electron beams," *Sov. J. Plasma Phys.*, vol. 17, pp. 439-442, 1991.
- [8] M. Tuszewski, W.J. Wagenaar, and M.P. Desjarlais, "Electron density measurements in a magnetically insulated ion diode," *J. Appl. Phys.*, vol. 77, pp. 6188-6193, 1995, and references therein.
- [9] S.C. Chen and T.C. Marshall, "Thomson backscattering from a relativistic electron beam as a diagnostic for parallel velocity spread," *Phys. Rev. Lett.*, vol. 52, pp. 425-428, 1984.
- [10] C.S. Mayberry, B. Wroblewski, E. Schamiloglu, and C.B. Fleddermann, "Suppression of vacuum breakdown using thin-film coatings," *J. Appl. Phys.*, vol. 76, pp. 4448-4450, 1994.

# OBSERVATIONS OF ELECTRON BUNCHING IN THE MICRO-PULSE ELECTRON GUN\*

J. Shiloh, F. Mako, and W. Peter

*FM Technologies, 10529-B Braddock Rd  
Fairfax, VA 22032 USA*

## ***Abstract***

We report on the first observations of electron bunching in the Micro-Pulse Gun (MPG). The MPG is an electron gun based on the resonant amplification of an electron current by secondary electron emission in an *rf* cavity. Electron emission is enhanced by a secondary emission material coated on the cavity walls and the resonant amplification creates electron bunches much shorter than the *rf* period. The beam is extracted through a grid and can be used as a source for *rf* accelerators and microwave devices. Analytic theory and Particle-in-Cell (PIC) simulation of the beam show that the natural bunching process creates one bunch for each *rf* period. A proof of principle experiment was designed and operated at 1.3 GHz and direct measurements of the beam confirm the existence of short bunches.

## ***Introduction***

*RF* accelerators and various microwave devices accelerate short bunches of electrons. Present day accelerators and high current accelerators under development require injection of electron bunches with high currents, short pulses and low beam emittance. The MPG is a novel concept for a new type of electron gun for short bunches, based on the process of secondary emission from the walls of an *rf* cavity in the presence of *rf* fields [1]. The resonant amplification of the electron current is based on a "multipacting" process that creates short bunches of electrons inside the cavity. Extraction of a portion of these bunches generates a pulsed electron bunch with parameters that fit the requirement of *rf* accelerators.

Figure 1 shows the principle of the MPG. A small area at the center of both cavity walls is coated with material of a relatively high Secondary Emission (SE) coefficient. The multipacting process starts from a small number of electrons in the gap that are accelerated by the *rf* field and hit the wall of the cavity. High SE material at the wall will generate more electrons than in the incident beam at very low energies (few eV). If the acceleration of the electrons in the gap is in synchronization with the *rf* field, the beam current will increase. This current grows, but is eventually brought to saturation due to the space charge of the beam. Only electrons in a small phase range can actually be in synchronization with the *rf* field and therefore bunched beams are generated and amplified inside the gap. The beam can be extracted through one of the walls with the use of a grid that lets a portion of the beam out of the cavity on each cycle of the *rf* field.

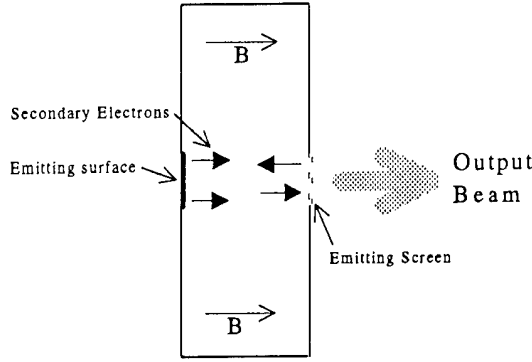


Figure 1: MPG concept for generation of bunched beams.

For SE emission coefficient  $\delta$  and grid transmission  $T$ , the requirement for current amplification is:

$$\delta^2(1 - T) > 1 \quad (1)$$

Therefore, in order to have high current beams extracted from the MPG it is necessary to have a high SE emission coefficient. The current density  $J$  will grow in the gap and after  $n$   $rf$  periods, excluding space charge effects, it is given by:

$$J_n = J_0[\delta^2(1 - T)]^n \quad (2)$$

The beam parameters were studied analytically and with a 2 1/2 D Particle-In-Cell (PIC) code [1]. The PIC code was especially developed for this study and is fully electromagnetic and relativistic, and includes a special surface physics package to treat secondary electron emission. An example of the predicted beam current is shown in Figure 2 for a frequency of 6.4 GHz, gap spacing of 0.5 cm, and a gap voltage in the cavity  $V=105$  kV. The current is "measured" near one of the walls. The sharp negative spikes correspond to the high energy electrons being accelerated towards the wall, and about to leave the cavity. The positive spikes that occur soon after the negative ones are the new secondary electrons emitted from the wall just starting to be accelerated in the opposite direction. Figure 2 shows that the current reaches saturation due to space charge in less than 10 cycles and the saturated current for a frequency of 6.4 GHz reaches  $2.8 \text{ kA/cm}^2$ . The saturated current as a function of the frequency  $f$  increases as  $f^3$ . For frequencies in the range of 1-10 GHz, the current density range is  $10\text{-}1000 \text{ A/cm}^2$ . The created bunches can have current density as high as  $10 \text{ kA/cm}^2$  and a pulse length of 1.5-10% of the  $rf$  period. The total charge of the bunch is in the range of  $1\text{-}1000 \text{ nC}$  and the emittance is as low as  $3 \text{ mm mrad/nC}$ .

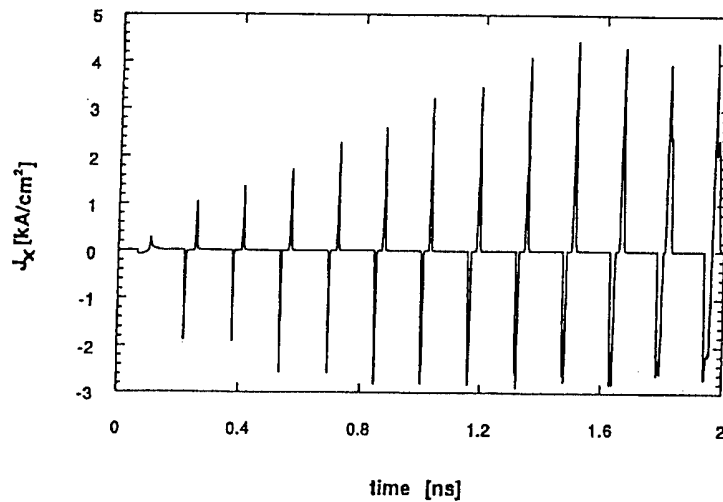


Figure 2: Current density as a function time for  $f=6.4$  GHz

### Experimental Results

The experimental set-up of the MPG experiment is shown in Figure 3. The MPG cavity is made of stainless-steel with dimensions of  $16 \times 16 \times 1$  cm, designed to support a  $TE_{101}$  mode at 1.3 GHz. An area of  $1 \text{ cm}^2$  at the center of each of the cavity walls is coated with material of high secondary emission coefficient and on one wall we introduced small holes to allow for beam extraction. Measurements of the beam current are done through a port at the center of the cavity wall. The cavity is fed from the side through an iris. The  $rf$  source is a magnetron tube with maximum power of 500 kW at  $4 \mu\text{s}$  and 150 Hz. The  $rf$  power is fed from the magnetron into a WR-650 waveguide and from the waveguide into the vacuum system. A tapered waveguide is employed between the WR-650 waveguide and the cavity to allow for smooth flow of the  $rf$  power. A vacuum window separates the vacuum system from the waveguide in air.

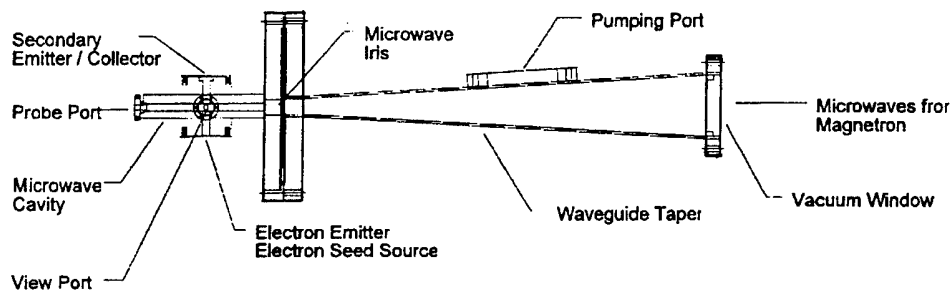


Figure 3: The MPG experimental set-up.

At normal operating conditions of the MPG experiment the gap voltage is about 7 kV and the expected beam energy under loaded conditions is somewhat lower. Conventional

techniques for bunch length measurements, such as transient radiation, are not applicable to the low-energy MPG and we therefore employed direct charge collection to determine the bunch length and intensity. For a frequency of 1.3 GHz the expected bunch length is 40-80 ps. To be able to resolve such pulses we used a beam collector and a vacuum feed-through with a high bandwidth and registered the signal generated by the charge collector on a 50 GHz sampling scope (HP54750A). The use of a sampling scope for such measurements requires that the bunch formation will be very reproducible from one macro pulse to the next and have low jitter within each macro pulse between the bunches. For triggering of the scope we used a signal from an *rf* probe inside the cavity. An example of the results from these measurements is shown in Figure 4. In this example 1024 consecutive macro pulses were used to generate the equivalent pulse shape. The *rf* period is 800 ps and we can clearly observe short bunches every *rf* period. More detailed measurements show bunch lengths of about 70 ps, in agreement with the theory.

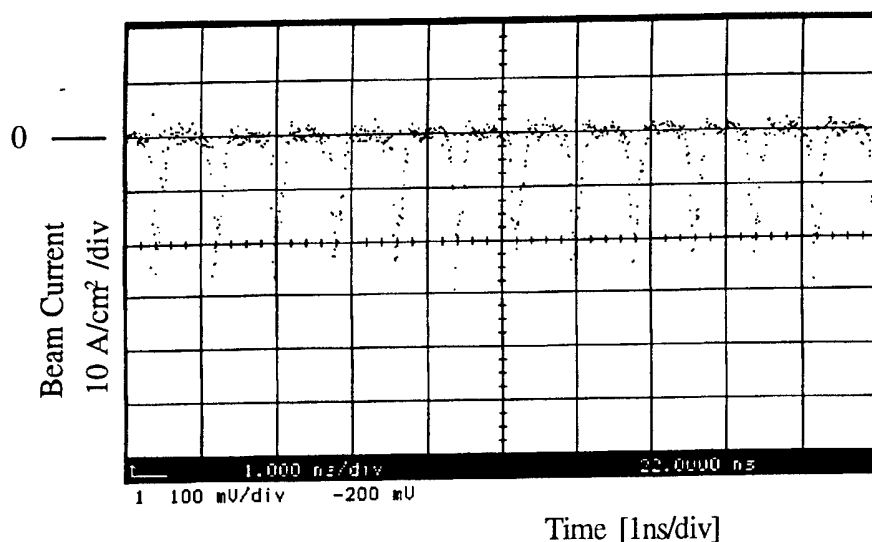


Figure 4: MPG bunch formation

### Summary

The Micro-Pulse Gun (MPG) was studied experimentally using *rf* power at 1.3 GHz. Multipacting in the cavity generated short bunches of electrons and beam extraction created one bunch for every *rf* period to be ejected from the cavity. The experiment was optimized to operate reproducibly so that a sampling scope could be used to measure the bunch length of the electron bunches. Electron bunches were observed with pulse lengths of ~70 ns. A higher frequency MPG will enable the use of shorter bunches at higher current densities.

\*Supported by the US DOE under the SBIR program.

Patent Pending.

[1] F.M. Mako and W. Peter, in *Proceedings of the 1993 IEEE Particle Accelerator Conference, Washington, DC, 1993* (IEEE, New York, 1993), p. 2702.

# WIDE-BANDWIDTH HIGH-POWER TRAVELING WAVE TUBE AMPLIFIERS: COMPARISON OF DIELECTRIC AND PERIODIC SLOW-WAVE STRUCTURES

A. S. Shlapakovskii

*Institute of Nuclear Physics of Tomsk Polytechnical University,  
P. O. Box 25, Tomsk, 634050 Russia*

At present, many various kinds of high-power microwave sources driven by relativistic high-current electron beams have already been developed and are under development and investigations. There is, however, a class of devices which remains practically unexplored. Those are wide-bandwidth amplifiers capable of hundreds MW power level and, at the same time, allowing frequency tuning over a range of up to an octave. Recently, it has been shown that rather wide (40-50%) -3 dB bandwidth can be achieved in the dielectric Cherenkov maser (DCM) amplifier [1]. As it is a smooth slow-wave structure, a dielectric-lined waveguide does not have stopbands, and a liner of a small to moderate dielectric constant may provide it with rather weak dispersion over a very wide frequency range at relativistic values of phase velocities. A DCM is a good candidate for a high-power wide-bandwidth amplifier, however, presence of a dielectric causes significant problems connected with charging a surface, RF breakdown along it, etc. This is a serious drawback of DCMs.

In the case of conducting periodic slow-wave structures (such as corrugated or ridged waveguides), there are no such problems. Relativistic Cherenkov oscillators with corrugated waveguides reliably operate in rep-rate regime and are already investigated as emitting units of radars [2]. Despite of the fact that periodic waveguide passband is always limited, it may be, nevertheless, rather wide; and weak dispersion at relativistic phase velocities is possible as well. For this, the period of the structure should be much less than the depth of corrugation or ridges and the depth, in its turn, should be much less than the operating wavelengths. The question arises: could the amplification band due to the beam-wave interaction in such waveguides be so wide as achievable in DCMs?

Let us consider the simplest model of a circular ridged waveguide of infinitely small period, i. e., not taking the space harmonics into account. Such a simplification will result in the wider amplification band than in reality as it results in wider waveguide passband. One can make certain conclusions concerning periodic structure potential to provide broad amplification band even from the analysis of no-beam system dispersion. For symmetric TM-modes, the dispersion relation is following [3]

$$\frac{I_1(qa)}{I_0(qa)} = \frac{q F_1(ka, kb)}{k F_0(ka, kb)}, \quad (1)$$

where  $F_0(x, y) \equiv J_0(x)Y_0(y) - J_0(y)Y_0(x)$ ,  $F_1(x, y) \equiv J_1(x)Y_0(y) - J_0(y)Y_1(x)$ ,  $k = \omega/c$ ,  $q^2 = h^2 - k^2$ ,  $\omega$  and  $h$  stand for frequency and longitudinal wavenumber,  $a$ ,  $b$  are inner and outer radii of ridges, respectively,  $c$  is the speed of light,  $J_{0,1}$ ,  $Y_{0,1}$ ,  $I_{0,1}$  are Bessel functions. In Fig.1, phase velocity vs frequency obtained from Eq.(1) is plotted for various geometries. For comparison, the curve is presented in Fig.1 illustrating

dispersion of circular dielectric-lined waveguide lowest  $TM_{01}$  mode at parameters providing an X-band DCM amplifier with wide bandwidth for 600 keV electron energy level [1].

One can see the very significant difference. There is rather weak dispersion for a dielectric-lined waveguide where the dielectric fills the substantial portion of the waveguide cross-section (inner to outer liner radius ratio  $a/b = 0.5$ ). For ridged waveguide with  $a/b = 0.5$ , dispersion is very strong (curve 1). It becomes weaker as the degree of waveguide filling reduces (at increased waveguide radius, in order to have phase velocities of 0.8-0.9c in the X-band), and becomes so weak as for dielectric-lined waveguide only at very small filling ( $a/b = 0.9$ , curve 3).

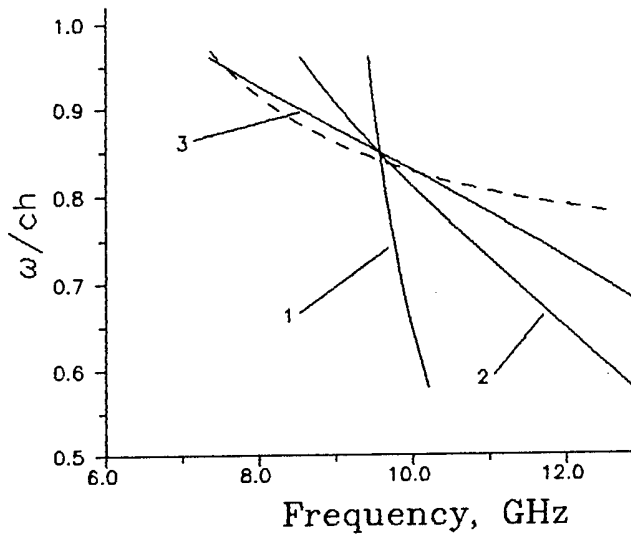


Fig. 1. Phase velocity vs frequency for various ridged waveguide geometries (solid curves).  
1 -  $a/b = 0.5$ ,  $b = 1.3$  cm;  
2 -  $a/b = 0.8$ ,  $b = 2$  cm;  
3 -  $a/b = 0.9$ ,  $b = 3.3$  cm.  
Also plotted (dashed curve) is dielectric-lined waveguide  $TM_{01}$  mode dispersion (dielectric constant  $\epsilon = 2$ ,  $a/b = 0.5$ ,  $b = 2$  cm).

Meantime, it was noted in [1] that substantial filling with a dielectric is the important condition for obtaining a wide bandwidth in a DCM amplifier. Otherwise, the wave field is strongly evanescent, and the beam-wave coupling exponentially decreases as the frequency increases restricting the amplification band. Fig.1 shows that for ridged waveguides, substantial filling the cross-section is not compatible with the requirement of weak dispersion, the main condition necessary for wide-bandwidth amplifier operation. Therefore, one can expect not so large bandwidth values in that case.

To determine actual quantitative values, let us derive the dispersion relation for the system with a hollow electron beam assuming it to be infinitely thin, monoenergetic, and fully magnetized. In linear consideration, the jump of the radial derivative of the longitudinal electric field component  $E_z$  at the beam surface can be written as

$$\left\{ \frac{dE_z}{dr} \right\}_{r=r_b} = -\frac{2I_b}{\beta\gamma^3 I_A} \frac{q^2}{(k - \beta h)^2} \frac{E_z(r_b)}{r_b}, \quad (2)$$

where  $r_b$  is the beam radius,  $\beta$  is the dimensionless beam velocity,  $\gamma = (1 - \beta^2)^{-1/2}$  is Lorentz factor,  $I_b$  denotes the beam current,  $I_A = mc^3/e = 17$  kA. Matching the solutions of the wave equation for electrical Hertz vector in various regions and taking Eq.(2) into account, one can finally obtain the following dispersion relation:



$$\left[ \frac{I_1(qa)}{I_0(qa)} - \frac{q F_1(ka, kb)}{k F_0(ka, kb)} \right] (k - \beta h)^2 =$$

$$\frac{2q^2 I_b}{\beta \gamma^3 I_A} \frac{I_0(qr_b)}{I_0(qa)} \left[ \mathcal{F}_1(qa, qr_b) - \frac{q F_1(ka, kb)}{k F_0(ka, kb)} \mathcal{F}_0(qa, qr_b) \right] \quad (3)$$

Here,  $\mathcal{F}_0(x, y) \equiv I_0(x)K_0(y) - I_0(y)K_0(x)$ ,  $\mathcal{F}_1(x, y) \equiv I_1(x)K_0(y) + I_0(y)K_1(x)$ ,  $K_{0,1}$  are Bessel functions. One can prove that Eq.(3) is the particular of more general equation derived in [4] where the space harmonics and also the finite ridge thickness and electron energy spread were taken into consideration.

In Fig.2, the results of the Eq.(3) numerical solution are presented for the same parameters as in Fig.1 at fixed values of beam current, electron energy and distance to the ridges. The solution of the DCM dispersion relation [1] is also presented here. One can see that for the case of dielectric-lined waveguide (dashed curve) the spatial growth rate dependence on frequency is much more slightly sloping than for ridged waveguides. At substantial filling and small radius of the ridged waveguide (curve 1), the beam-wave coupling is very strong, and the dependence maximum is quite sharp. At small filling and larger radius, the growth rate approach the maximum more gently from the low frequency side, however, at the high frequency side, it drops drastically as expected.

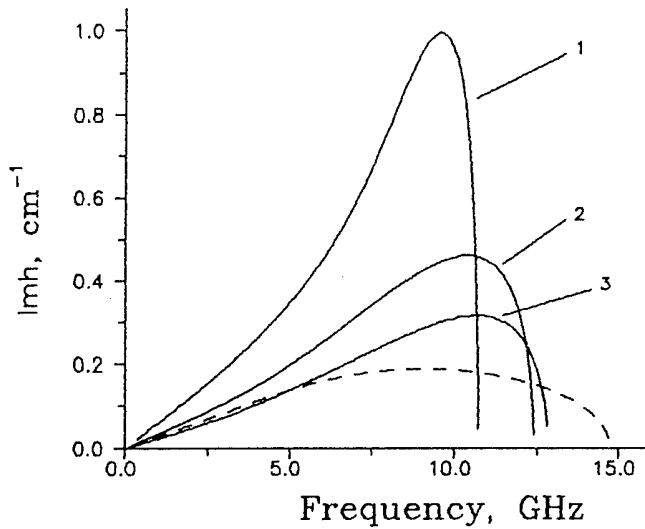


Fig. 2. Spatial growth rates vs frequency for various geometries of the system with a hollow beam. Ridge waveguide (solid curves) and dielectric-lined waveguide (dashed curve) parameters are the same as in the Fig. 1. For all curves, the beam parameters are:  $\gamma = 2.2$ ,  $I_b/I_A = 0.4$ ,  $r_b = a - 2\text{mm}$ .

The most direct comparison is the comparison of -3 dB bandwidth values which can be determined from growth rate vs bandwidth dependences for given peak gain  $G$ . If the gain is large, the traveling wave tube theory formulas [5] yield

$$\frac{\Delta(Im h)}{(Im h)_m} \approx \frac{3}{G[\text{dB}] + \alpha}, \quad (4)$$

where  $\Delta(Im h)$  is the difference between the maximum growth rate  $(Im h)_m$  and the growth rate corresponding to -3 dB power level, and  $\alpha$  equals to 9.5 dB for the single-particle (Compton) regime or 6.0 dB for the collective (Raman) regime. Using formula (4), the curves are obtained plotted in Fig.3 as -3 dB bandwidth vs beam current dependences for the same other parameters as in Fig.2 and  $G = 40$  dB. They demonstrate differences between amplifiers employing dielectric-lined and periodic

waveguides as slow-wave structures. Qualitatively, for ridged waveguides, there is a saturation in the bandwidth vs current dependence, in difference of a maximum in DCM case. It is naturally explained by the stopband existence resulting in the limited frequency upshift in the collective regime. For DCMs, the amplification band shifts to higher frequencies as the current increases without any limit so that the beam-wave coupling decreases somewhere enough for bandwidth narrowing. And the main difference is, of course, the quantitative difference. Maximum achievable bandwidth values for periodic structures (at weak dispersion) are only of the level of 20% whereas for dielectric-lined waveguides, they approach 50% at the same parameters of the electron beam.

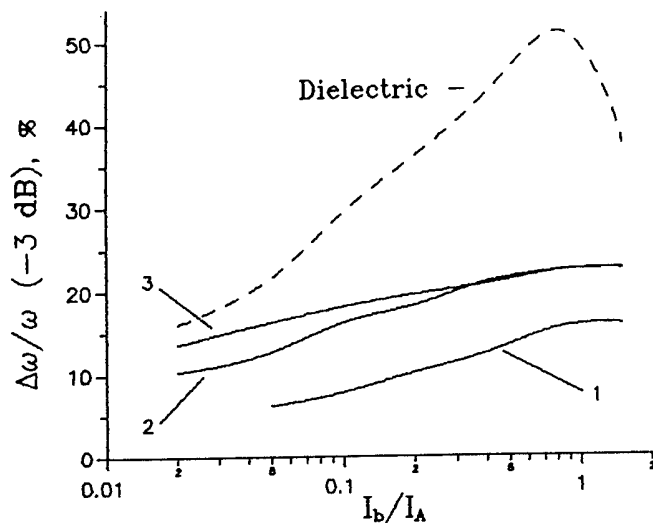


Fig. 3. -3 dB bandwidth vs beam current for periodic (solid curves) and dielectric (dashed curve) structures. For all curves, parameters are the same as in Fig.2. The peak gain  $G = 40$  dB.

In summary, periodic conducting slow-wave structures, even at weaker dispersion, can not compete with dielectric-lined waveguides for wide-bandwidth relativistic traveling wave tube operation. The reason is in the fact that the requirements of weak dispersion at relativistic phase velocities and substantial filling the waveguide cross-section are not compatible for periodic waveguides so that the synchronous wave field significantly reduces as the frequency increases. It means, therefore, that the demands of the development of high-power superwide-bandwidth amplifiers will motivate future researches on high-current DCMs aiming, in particular, to overcoming problems caused by dielectric presence in order to explore the long-pulse and repetition-rate modes of operation.

The author is grateful to Dr. S. D. Korovin for the stimulating discussion.

#### References

- [1] A.S.Shlapakovskii and K.A.Chirko. IEEE Trans. Plasma Sci., v.22, no.5, pp.544-546, 1994.
- [2] B.V.Bunkin, A.V.Gaponov-Grekhov, A.S.Eltchaninov *et al.* BEAMS 92. Proc. 9th Int. Conf. High-Power Particle Beams, 1992, Volume 1, pp.195-202.
- [3] L.A.Vainshtein. Electromagnetic waves (in Russian). M.: Radio i sviaz, 1988.
- [4] H.E.Brandt and H.S.Uhm. IEEE Trans. Plasma Sci., v.13, no.6, pp.553-558.
- [5] V.N.Shevchik and D.I.Trubetskov. Analytical methods in microwave electronics (in Russian). M.: Sov. radio, 1970.

## REFLEX TRIODE WITH RESONANT CAVITY AS A LOAD FOR INDUCTIVE STORAGE

Andrey N.Didenko, Kirill V.Gorbachev, Alexander E.Kogutnitskii,  
Victor M.Mikhailov, Eugeny V.Nesterov, Serge A.Roschupkin,  
Vladimir P.Shumilin, Vadim A.Stroganov

*High Energy Density Research Center, Russian Academy of Sciences,  
IVTAN, Izhorskaja St. 13/19, Moscow, 127412, Russia*

### Abstract

To increase the oscillation efficiency of vircator in external magnetic field, recently it has been suggested to use the resonant cavity. Numerical simulations showed [1,2] that this procedure brought about the suppressing of strong dependencies of the microwave oscillation on the electron energy spread and of frequency on the beam current.

We have found by PIC simulations (code KARAT) that the same effect takes place in vircator without external magnetic field also. This fact gives reasons to hope for increase of generation efficiency by using the resonant cavity in reflex triode too.

In our experiments we tried to check this suggestion by use of the resonant cavity with inner diameter 78 mm and length 14 mm. The radius of the coupling hole between the cavity and virtual cathode region was 10 mm. Experiments were conducted with following parameters : electron energy  $\sim 400$  keV, beam current  $\sim 15$  kA, microwave pulse duration  $\sim 100$  ns, frequency  $\sim 3$  GHz. Experimental results are presented.

### Introduction

Microwave generators based on the virtual cathode oscillations technique have rather simple design. As a rule, they are variations of cathode/anode systems, for instance: in vircator an electron beam with over limiting current is injected into anode drift tube; in reflex triode the drift tube boundary is under cathode potential.

In microwave electronics several wide-used methods exist for increasing of radiation efficiency and narrowing the band width. Unfortunately, their application in high-current devices such as virtual-cathode ones is rather difficult because of both low quality of the beam generated by use of explosive emission and instability of virtual cathode itself. The first successful attempts to overcome these difficulties were theoretical investigations of Japanese scientists: W.Jiang, K.Masugata, and K.Yatsui [1,2]. In both publications authors considered vircator (exactly, reditron) scheme. The resonator was placed between diode and virtual cathode region.

Numerical simulations were made in assumption of diode gun output as monochromatic electron beam with constant current. The beam passed through the thin cylindrical resonator and entered the cylindrical waveguide where formed the virtual cathode. It was assumed also, that the system was immersed into a strong axial magnetic field, so electrons were allowed to move only in axial direction. Separating wall between resonator and waveguide was considered to be absolutely transparent for electrons.

Numerical simulations pointed out deep modulation of electron beam passed through the resonator. This modulation corresponds to natural resonator frequency. In addition, electrons reflected from the virtual cathode make their contribution into

quick increase of oscillations in resonator cavity when having proper phases. Due to this fact, the authors mentioned the important role of coupling hole between resonator and waveguide, the proper size of which is determined by the reasons of both oscillations intensity in the resonator to be non-excessive and don't lead to reflection of primary beam electrons and electrical break-down of resonator. Authors [1] declared that equality of  $TM_{010}$  resonator mode frequency and that of virtual cathode oscillation increased generation efficiency of vircator.

In [2] numerical simulations were made with another parameters to investigate the amplitude and frequency of electrical field in waveguide as a function of both energy spread of beam electrons and beam current changes. Thus, 3 % energy spread of electrons leads to practically full suppression of electrical field oscillations in waveguide without anode resonator but in the presence of resonant cavity this effect was not found at all. Moreover, 25 % increase of beam current results in 50 % enhancement of virtual cathode oscillations frequency in case of resonant cavity absence, however, the same current change doesn't influence on frequency modulation of the beam injected into waveguide in the presence of resonant cavity.

### **Numerical simulations of vircator with anode resonant cavity**

The authors [1,2] supposed a strong external field to be used in their device. As mentioned above, the most attractive feature of virtual cathode devices is their ability to operate without external magnetic field. This is why a number of calculations investigating anode resonant cavity influence on the operation of the system without external magnetic field was made by use of KARAT-code [3]. Axisymmetric modification of vircator (Fig.1) was simulated with following parameters: electrons energy 500 keV (exactly, 500 kV amplitude TEM-wave was launched from the left hand into coaxial waveguide), beam current 17 kA, increment of current front 2 ns, outer and inner radii of cathode zone of emission were 3 and 1 cm respectively, cathode/anode gap 7 mm, radius of resonator  $R=3.8$  cm, resonator width 1 cm (natural frequency of  $TM_{010}$  resonator mode was  $\sim 3$  GHz). Calculations were carried out for 1 mm step in both coordinates which defined 7 mesh modes for anode/cathode gap. Meanwhile, such relatively rough mesh provides calculation of fields with adequate accuracy for PIC method.

Modulation of current in different cross-sections was investigated. These cross-sections are represented by points in Fig.1. They are situated: just behind the first grid, just behind the second grid and at 1 cm behind the virtual cathode. In current spectra it is easy to distinguish two frequency bands: one of them corresponds to virtual cathode oscillations, which varies within 4.5-6 GHz band width depending on the coupling hole area (determined by radius "r" of the hole), and another is natural resonator frequency 2.5-4.5 GHz.

Fig.2 shows Fourier-amplitudes of current oscillations corresponding to virtual cathode frequency (\*) and natural resonator frequency (0) as a function of  $r/R$  ratio for  $z=3.3; 4.3$  and  $6.2$  cm. One can see the absence of low-frequency oscillations ( $f \sim 2.5-4.5$  GHz) at the inlet of the resonant cavity ( $z=3.3$  cm) because the beam couldn't be effected by resonant fields yet. High-frequency oscillations ( $f \sim 4.5-6$  GHz) are stipulated by electrons reflecting from the virtual cathode. Just behind the resonant cavity ( $z=4.3$  cm) the natural frequency of resonator could be found in current oscillations, besides there exists an optimum ratio of coupling hole radius to radius of resonator  $r/R \sim 0.2-0.3$ . Behind the virtual cathode ( $z=6.2$  cm) the low-frequency oscillations are dominated.

This way, in the absence of external magnetic field for proper size of coupling hole the beam will be modulated at natural frequency of anode resonator cavity regardless of virtual cathode oscillation frequency (that is, dependless on beam current and anode/cathode gap). This fact gives reasons to hope for enhancement of reflex triode generation efficiency by use of anode resonator.

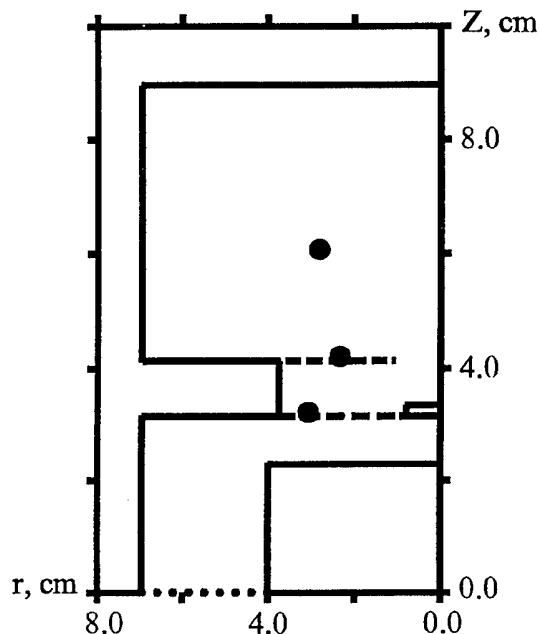


Fig.1. Numerical simulation geometry.

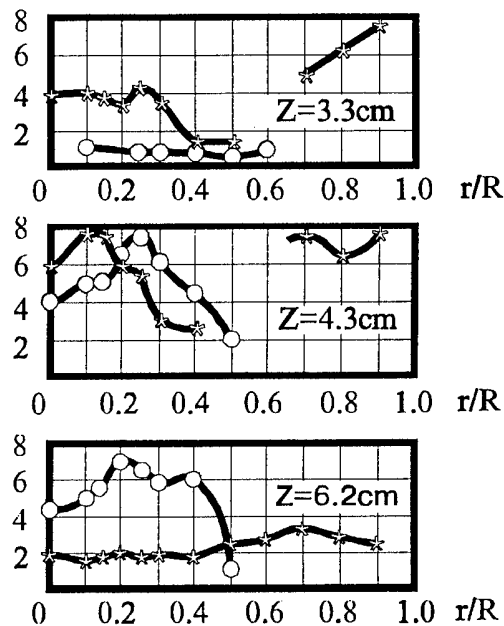


Fig.2. Fourier-amplitudes of current oscillations corresponding to virtual cathode frequency (\*) and natural resonator frequency (0) as a function of  $r/R$  ratio for  $z=3.3; 4.3$  and  $6.2$  cm.

#### Experimental researches of reflex triode with anode resonator

Numerical simulation of vircator with anode resonant cavity in absence of external magnetic field showed the possibility to increase the generation efficiency. As concern reflex triode, numerical simulation must be carried out by use of 3-D code which is possible, but requires a lot of time of calculations. Based on the numerical results obtained for vircator, the experimental researches of reflex triode with anode resonant cavity were fulfilled by use of installation described in [4]. The only part being changed was anode unit, which represents now a metal disk 200 mm in diameter with resonator built into the center of the disk.

Resonator was a copper circle with inner diameter 78 mm and height 14 mm (Fig.3). Both grids were formed by copper wire 0.25 mm in diameter applied radially. Central part of the grid faced to cathode forms a solid disk 26 mm in diameter, while the central part of the grid faced to virtual cathode forms the similar disk but with central hole 20 mm in diameter. Both grids consist of 48 sectors. Velvet cathode 70 mm in diameter was used.

Experiments were carried out for different cathode/resonator gaps ( $L$ ) and for various supply voltages ( $V$ ). Diode voltage was  $\sim 400$  kV, beam current  $\sim 15$  kA. The envelope of microwave pulse ( $\tau \sim 100$  ns) electrical field was checked. For  $L=9-11$  mm (when frequency of virtual cathode oscillations exceeded twice approximately the

natural frequency of resonator) the abrupt radiation power dependence on both anode/cathode gap and supply voltage was observed (see Fig.4, where y-coordinate is the maximum electrical component of wave at the distance 3 m from output window expressed in relative units). Experiments showed also that radiation power is practically independent of anode/cathode gap and supply voltage for  $L=20$  mm (when the frequency of virtual cathode oscillations was about the natural frequency of resonator). This way, results of preliminary experiments prove the initial assumption about positive effect of anode resonant cavity on the generation efficiency of reflex triode.

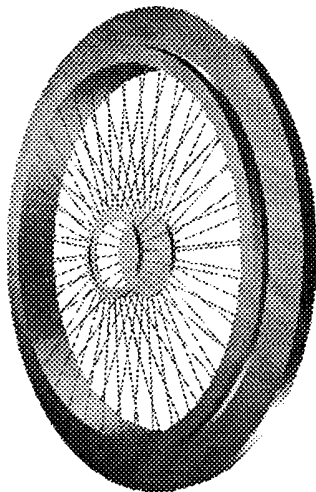


Fig.3. Appearance of anode resonator.

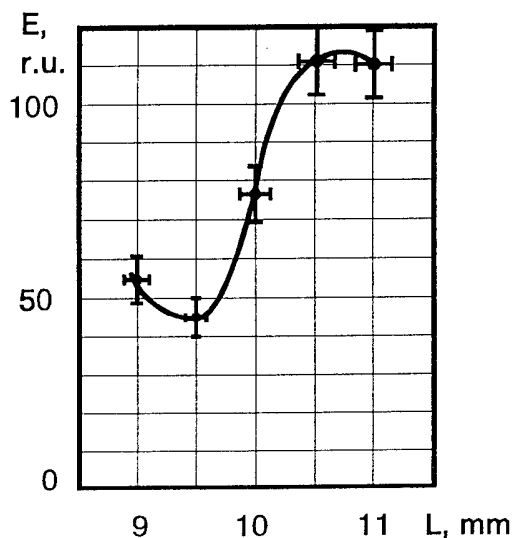


Fig.4. E-component of microwave (in relative units) versus anode/cathode gap.

### Conclusion

Recently, high power microwave generators on the base of virtual cathode devices without external magnetic field are of great interest for researches because of their design simplicity and ability to obtain high efficiency as regards total power consumption. The work presented in this paper shows one of the easy ways, for instance, the use of anode resonant cavity to improve the performances of such devices.

The work was supported by Russian Fund of Fundamental Researches.

- [1] W.Jiang, K.Masugata, and K.Yatsui: SPIE **2154** (1994) 13.
- [2] W.Jiang, K.Masugata, and K.Yatsui: Proc. of the 10th Int. Conf. on High-Power Particle Beams, June 20-24, 1994, San Diego, California. Ed. by W.Rix and R.White.Vol. II, (1994), 909.
- [3] V.P.Tarakanov: User's Manual for Code KARAT, BRA, Inc., V.A., USA, 1992.
- [4] E.V.Chernikh, A.N.Didenko et. al.: Proc. of the 10th Int. Conf. on High-Power Particle Beams, June 20-24, 1994. San Diego, California, Ed. by W.Rix and R.White, Vol.I, (1994),383.

## EXPERIMENTAL STUDIES OF A GENERATION DELAY TIME IN REFLEX TRIODE WITH INDUCTIVE STORAGE

Andrey N. Didenko, Vladimir E. Fortov, Kirill V. Gorbachev, Eugeny V. Nesterov,  
Sergey A. Roschupkin, Vladimir P. Shumilin, Vadim A. Stroganov

*High Energy Density Research Center, Russian Academy of Sciences,  
IVTAN, Izhorskaja St. 13/19, Moscow, 127412, Russia*

### Abstract

It has been found recently that the process of high power microwave oscillation in reflex triode with inductive storage distinguished considerably from that in conventional schedules, when as the source of a voltage, the high current accelerators with forming lines were used. This is because of the delay time between the beginnings of the oscillations and current pulse in diode. The generation was began, as a rule, in a phase when the current decreased, and the power efficiency in this case was rather low. The fact that the generation delay time was proportional to the current rise-time gave some hopes to increase the efficiency by shortening the current rise-time.

We have found experimentally that the decrease of the current pulse rise-time causes the shortening of the generation delay time, but the power efficiency was not increased. As a result of the increase of the beam maximum current the generation starts at the current pulse forward front.

### Introduction

Reflex triodes are highly promising microwave oscillators. The capability to operate without external magnetic field is the most advantageous distinguishing feature of such devices. If the problem is to design the compact pulse microwave generator, this feature is very important.

The generation process in reflex triodes was investigated in papers [1-7]. The energy supply system included forming lines. It was revealed, that the power efficiency (the ratio of the peak microwave power to the beam power) for some conditions may reach 40% [2]. The generation time duration was varied from tens nanoseconds to some microseconds.

This diode voltage pulse duration demands large-sized forming lines and bulky primary energy storages. For this reason it is convenient to use the inductive storage with some type of opening switch to design the compact microwave source [8-11]. One of such opening switches, which was well built up for itself in practice, is the electroexploding opening switch.

The first attempts to realize in practice the scheme with reflex triode and inductive storage met the following problems: it was appeared that the process of microwave oscillation in reflex triode differed considerably from that in conventional schedules, when as the sources of a voltage, the high current accelerators with forming lines were used [9,10]. This is conditioned by the time-delay between the beginnings of oscillations and current pulse in the diode. The generation begins, as a rule, in a phase when the current and voltage decreases. The power efficiency in this case is rather low.

The causes of this anomalous generation delay time has not been understood yet. The authors [10] believed that this effect was connected with big current pulses rise-times. In our experiments we tried to check this supposition. We produced the current pulses in reflex diode with the peak values and front-times being close to those,

received with the help of conventional forming lines. The results of our research clearly showed that the power efficiency did not depend on the generation delay time. In turn, the generation delay time value depended on the current rise-time and beam current.

### Generation delay time

The experimental investigations of the reflex triode generation regime with forming lines showed [1-7]: a) the generation started at forward diode current pulse front; b) there existed some definite diode current value (starting current  $I_s$ ), at which the generation took place. Depending on the experimental conditions it was about  $I_s \approx 5 \div 10$  kA; c) the power efficiency was  $\sim 10 \div 40$  %.

The existence of the starting current brings to some generation delay time ( $\tau_d$ )  $\tau_d = I_s < dI/dt >^{-1}$ , where  $< dI/dt >$  - is the average time derivative of the current at forward pulse front.

The first experiments with reflex triode and inductive storage [9,10] showed: a) depending on  $< dI/dt >$ , the generation started at both forward or rear diode current pulse fronts. So at  $< dI/dt >^{-1} > 10$  ns/kA the generation started at forward front, in other cases - at rear front; b) there existed rather big generation delay time. So at  $< dI/dt >^{-1} \sim 5$  ns/kA  $\tau_d \geq 80$  ns; c) the generation delay time grew along with  $< dI/dt >^{-1}$ ; d) the generation power efficiency was about 1%.

The low generation efficiency could be owned by the big generation delay time, which, in turn, is the consequence of the high  $< dI/dt >^{-1}$  value.

In our experiments we tried to check these suppositions. For this purpose we achieved the values of  $< dI/dt >^{-1}$  about  $1 \div 10$  ns/kA. So, by use of inductive storage with reflex triode we attained the rise-time characteristics of the pulse forward front nearly the same as for forming lines fronts [11]. The current forward front rise-time at the diode was varied by the tuning of the sharpening discharger and electroexploding opening switch (EOS). It was really observed that the generation may start at both forward and rear fronts. However, it was found that the fact of the generation at rear front was connected with low diode current. Figure 1 shows the dependence of the ratio  $\tau_d/t_m$ , where  $t_m$  - is the time corresponding to maximum diode current, versus  $I_m$  - the maximum diode current value. For fixed anode-cathode gap the spread of the current values can be due to 1) non-optimizing regime of the current switching to the diode and 2) space nonuniformity of the electron beam. Three data groups are presented: a) for the needle cathode of  $\sim 300$  sqcm area, anode-cathode gap 2 cm, primary voltage  $U_0 = 50 \div 60$  kV ( $\square$ ); b) for the edge cathode of  $\sim 60$  sqcm area, anode-cathode gap 2 cm,  $U_0 = 70$  kV ( $\otimes$ ); c) for velvet cathode of  $\sim 60$  sqcm area, anode-cathode gap 1.5 cm,  $U_0 = 50$  kV ( $\circ$ ).

For the needle cathode at high diode currents the generation starts always at the current pulse forward front ( $\tau_d/t_m < 1$ ). For cathodes with the lower areas this dependence is nearly the same, but not so pronounced. It should be noted that this effect is not connected with the cathode type or area: the experiments with the same needle cathode at the anode-cathode gap 1 cm showed that there is rather high spread of  $\tau_d/t_m$  at higher current values, which looks nearly like the situation with little area cathodes. Nevertheless one can notice that as a result of the increase of the beam current, the generation starts at the current pulse forward front.

Figure 2 shows the dependence of the  $< dI/dt >^{-1}$  versus generation delay time  $\tau_d$ . The results given in the paper [10] were included in data points. Dashed lines correspond to the relation  $\tau_d = I_s < dI/dt >^{-1}$  for  $I_s = 5$  kA and  $I_s = 10$  kA. Dark points correspond to the cases  $\tau_d/t_m \geq 1$ .



Thus the decrease of the current pulse rise-time really caused the decrease of the generation delay time, but the power efficiency did not increase.

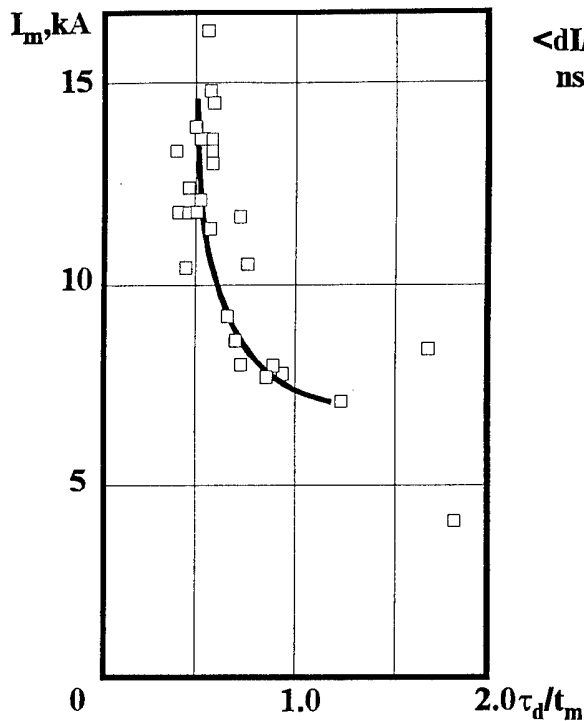


**Figure 1.** Dependence of the ratio  $\tau_d/t_m$  on the maximum diode current values ( $I_m$ ) for inductive storage with reflex triode.  $\tau_d$  - generation delay time;  $t_m$  - maximum diode current time.

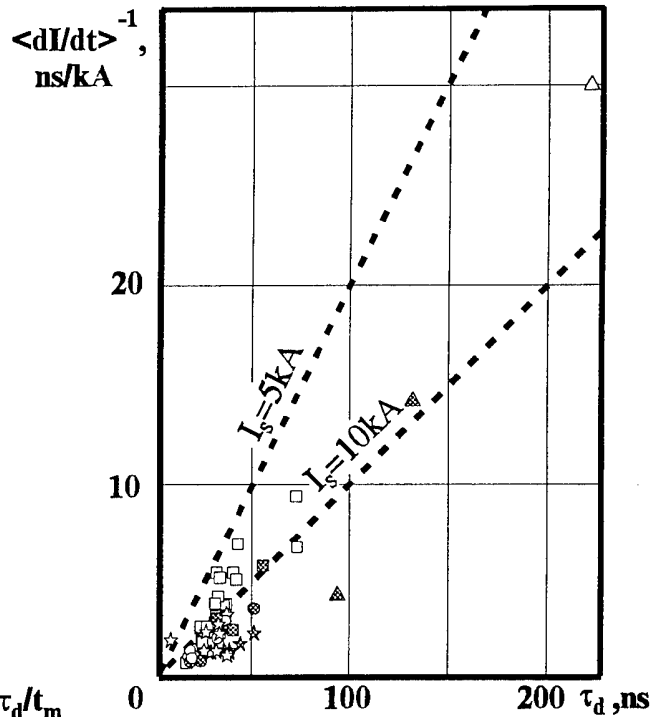


**Figure 2.** Dependence of the reciprocal of average time derivative of the diode current at forward pulse front ( $\langle dI/dt \rangle^{-1}$ ) on the generation delay time ( $\tau_d$ ) for inductive storage with reflex triode.

### Conclusion

We have investigated the generation delay time in reflex triode with inductive storage and obtained the following results:

- 1) as a result of the increase of the beam maximum current the generation started at the current pulse forward front;
- 2) the decrease of the current pulse rise-time caused the decrease of the generation delay time;

### Acknowledgments

The authors would like to thank to A.G. Zherlitsin, K.S. Dyabilin, and V.A. Kamensky for the help and fruitful discussions.

The work was supported by Russian Fund of Fundamental Researches.

- [1] Didenko A.N., Krasik Ya.E., Perelygin S.F., and Fomenko G.P.: Pis'ma v J. Tech. Phys. (Russian), **5** (1979) 321.
- [2] Didenko A.N., Zherlitsin A.G., Sulakshin A.S., Fomenko G.P., Zvetkov V.I., and Shteyn Yu.G.: Pis'ma v J. Tech. Phys. (Russian), **9** (1983) 1510.
- [3] Didenko A.N., Zherlitsin A.G., Kuznetsov S.I., Melnikov G.V., Filipenko N.M., and Fomenko G.P.: Radiotech. and Electronics (Russian), **32** (1987) 837.
- [4] Grigoryev V.P., Zherlitsin A.G., Kuznetsov S.I., and Melnikov G.V.: J. Tech. Phys. (Russian), **57** (1987) 1863.
- [5] Didenko A.N., Grigoryev V.P., Koval T.V., Kuznetsov S.I., Zherlitsin A.G., and Melnikov G.V.: Proc.of the 7th Int.Conf.on High-Power Particle Beams, Karlsruhe, Germany, July 4-8, 1988, Vol II, (1988) 1402.
- [6] Grigoryev V.P., Zherlitsin A.G., Kuznetsov S.I., and Melnikov G.V.: Plasma Phys. (Russian), **14** (1988) 210.
- [7] Zherlitsin A.G., Melnikov G.V., and Kuznetsov S.I.: Radiotech. and Electronics (Russian), **35** (1990) 1274.
- [8] Brodsky A.Ya., Vdovin V.A., Korzhenevsky A.V., Kravchenko A.S., Pavlovsky A.I., Selemir V.D., Sokolov S.A., Cherepenin V.A., and Chernov Z.S.: Dokl. Acad. Nauk USSR, **314** (1990) 846.
- [9] Azarkevich E.I., Didenko A.N., Dolgoplov P.V., Zherlitsin A.G., Isakov V.P., Leont'ev A.A., Lopatin M.V., Mintsev V.B., Ushnurtsev A.E., Fomenko G.P., Fortov V.E., Zvetkov V.I., Shneider V.B., and Yaselsky B.K.: Dokl. Acad. Nauk USSR, **319** (1991) 352.
- [10] Azarkevich E.I., Didenko A.N., Zherlitsin A.G., Karpushin Yu.V., Leont'ev A.A., Mintsev V.B., Ushnurtsev A.E., Fortov V.E., Zvetkov V.I., Shneider V.B., and Yaselsky B.K.: Microwave Pulses Generation from Chemical Energy of High Explosive, Preprint, Russian Academy of Sciences, Chernogolovka (1992).
- [11] Chernikh E.V., Didenko A.N., Gorbachev K.V., Fortov V.E., Ivanov A.B., Nesterov E.V., Roschupkin S.A., Shumilin V.P., Stroganov V.A., and Tarakanov V.P.: Proc.of Int.Symp.of Electromagnetic Environments and Consequences, EUROEM'94, Bordeaux, France, May 30-June 4, 1994, Vol I, (1995) 290.

# VIRTUAL CATHODE DRIVEN BY SHORT PULSE ELECTRON GUN

I. P. Spassovsky, Sung Oh Cho, Jongmin Lee, Byung-Cheol Lee, Young Uk Jeong,

G. Messina\*, I. G. Yovchev\*\*, N. A. Nikolov\*\*,

*Laboratory for Quantum Optics, Korea Atomic Energy Research Institute, P.O. Box 105,  
Yusong, Taejon, 305-600, Korea*

*\*ENEA, INN-FIS-LAC, P.O. Box 65, I-00044 Frascati (Roma), Italy*

*\*\* Sofia University, Faculty of Physics, J. Bourchier 5, Sofia 1126, Bulgaria*

## I. INTRODUCTION

In the past few years several laboratories and research centres concentrated their efforts in development and construction of new low cost, high repetition and flexible electron guns for applications in medicine, material treatment, spectroscopy, radars etc. Such machine has been already designed and constructed at ENEA (Italy) to power a free-electron laser (FEL) operating in the far infrared region. However, it can be used successfully to drive various microwave sources. In this paper numerical simulations, that have been performed for the future foil-diode vircator experiment, carried out at the ENEA gun are reported.

## II. ELECTRON GUN DESIGN

A schematic diagram of the machine is shown in Fig. 1. The compactness required for the accelerator has brought the constructors to develop a pulser operating at high repetition rate with very short pulse duration. As can be seen from the principal scheme the electron gun is simply composed of five main components. Firstly, a 20 kV power supply charges a capacitor bank  $C_0$  up to 20 kV, which plays a role of a primary energy storage reservoir. Next, discharge by the tyratron generates a  $1\mu\text{s}$  long pulse. the transformers. Afterward six stages magnetic pulse compressor (PCS) reduces the pulse down to 30 ns and rises the voltage up to 350 kV at the final condenser of the compressor (the double pulse forming line - PFL) with energy transfer efficiency of about 70%. The line is filled with distilled water in order to minimise the size of the system. Its length is calculated so that it forms a 3ns output pulse. Since the gun is designed to drive a FEL the pulse is transformed additionally using a transmission line transformer (TLT). It consists of three coaxial 80 Ohms cables charged in parallel from the Blumline side and discharged in series on the diode load. If the diode is mismatched the voltage pulse could raise up to 1.8 MV. In our simulations we used a reduced scheme without TLT, i.e. the selftriggering line powers directly the diode. This gives the possibility of getting higher beam current at lower voltages. The short pulse duration is interesting because it gives rights to decrease considerably anode-cathode gap avoiding eventual gap closure. Moreover, it has been experimentally demonstrated that for few nanosecond pulse a gradient of 900 MV/m can be held [1].

### III. SIMULATIONS WITH AN ANODE FOIL MODEL

It is the purpose of this paper to report a numerical investigation concerned with the optimal values of the solid cathode radius and pulse flat top duration with respect to the microwave radiation power and beam-to-microwave energy conversion efficiency for the future vircator experiment driven by short pulse machine.

An outline of the modelled axisymmetric system is shown in Fig. 2. The electron beam is formed in a foil diode with a 44-mm-radius anode tube. The electrons are generated by an explosive plasma emission from a solid cathode. A guiding magnetic field is not used. Beyond the anode foil positioned at a distance of  $d = 6$  mm from the cathode front surface, the electrons propagate in an output drift tube (output waveguide) with a radius of  $R_w = 40$  mm. Both the anode tube, and the output waveguide including the foil are grounded.

The program KARAT [2] was used in numerical simulations of the described system. The code is fully relativistic, electromagnetic, 2 1/2 dimensional - two spatial dependencies ( $r$ ,  $z$ ) and three velocity components in a cylindrical coordinate frame, based on the particle-in-cell method.

The simulation was performed for a cathode radius of  $R_c = 3.4$  cm. A 300 kV transverse electromagnetic (TEM) wave is input from the left-hand boundary of the modelled system, which drives the cathode negative. The rise and the duration time of the pulse are 0.8 ns and 6.2 ns, respectively. We suppose that a relatively low field (a field emission threshold of 20 kV/cm) causes space-charge limited emission from the front surface of the cold cathode towards the anode foil. On the other hand, the electron emission from the cathode side surface is neglected. These two suppositions are realistic enough if the front surface is covered with a velvet in a real experiment [3] and the side surface is well polished so that the field emission threshold would be increased above  $5 \cdot 10^5$  V/cm (considerably lower than the values of the gradient, which can be held by the metal surfaces at short pulses). The electron beam-to-microwave power conversion efficiency  $\epsilon$ , calculated for the pulse flat top with a duration  $\Delta t = 1.2$  ns is approximately the same (about 1.5 - 2.0 %) as well as for a long flat top ( $\Delta t = 4$  ns). The simulations show a 10-15 % increase of  $\epsilon$  at  $\Delta t$  shortening to 0.6 ns. However, this occurs when the anode mesh transparency is high (80-90%). Considerable enhancement of the efficiency (about four times) for  $\Delta t = 0.6$  ns has been calculated if the cathode side surface is brought near to the anode tube (from  $\approx 0.5$  % at cathode radius  $R_c = 1.6$  cm to  $\approx 2.0$  % at  $R_c = 3.8$  cm). For better understanding the mechanism of the microwave emission, we follow the method, reported in [4], where the azimuthal component of the RF magnetic field  $H_\phi$  is monitored at the right-hand boundary (here in the point, -  $r = 3.5$  cm,  $z = 22$  cm), and the axial current  $I_{ax}$  is monitored at the anode foil. In Fig. 3 and Fig. 4 the Fourier transforms of  $H_\phi$  and  $I_{ax}$ , respectively are presented. Evidently, the  $H_\phi$  peak coincides in frequency with the peak of  $I_{ax}$  ( $\approx 9$  GHz), which indicates that the main source of microwave radiation are the reflected electrons, oscillating between the real and the virtual cathodes.

The frequency  $f_\mu$ , corresponding to the maximum amplitude in the  $H_\phi$  Fourier transform ( $\approx 9$  GHz) is higher than the  $TM_{01}$  and  $TM_{02}$  cut-off frequencies for a 4-cm radius waveguide - 2.87 GHz and 6.59 GHz, respectively, but lower than the  $TM_{03}$  cut-off frequency - 10.34 GHz. Consequently, the dominant modes, excited in the waveguide are  $TM_{01}$  and  $TM_{02}$ .

waveguide cross-section near the end of the simulated region. The total power  $P_t$ , determined at  $z = 22$  cm and averaged in the time range (1.5 - 2.2) ns is  $\approx 130$  MW. From 2.2 ns to 2.9 ns,  $P_t$  is approximately 80MW (Fig. 5). The decrease of  $P_t$  is considerable and is closely connected with the process of electron bunching

## REFERENCES

- [1] V. Baglin et al., "High gradient experiments with nanosecond pulses", in *IEEE Proc.*, 1993.
- [2] V. Tarakanov, "User's Manual for Code KARAT", BRA, inc, V. A., USA, 1992.
- [3] L. E. Thode, "Virtual-cathode microwave device research: experiment and simulation", in *High- Power Microwave Sources*, V. L. Granatstein and I. Alexeff, Eds, Artech House, Norwood, pp. 507-562, 1987.
- [4] H. A. Davis, R. R. Bartch, L. E. Thode, E. G. Sherwood, and R. M. Stringfield, "High-power microwave generation from a virtual cathode device", *Phys. Rev. Lett.*, vol. 55, pp. 2293-2296, 1985.

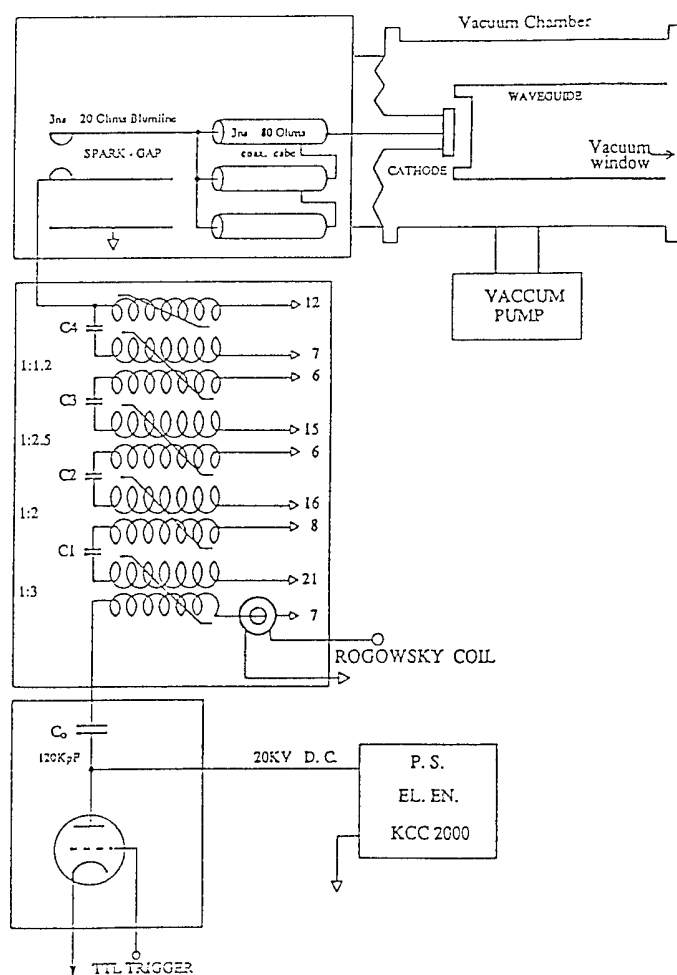


Fig.1 Schematic diagram of electron gun

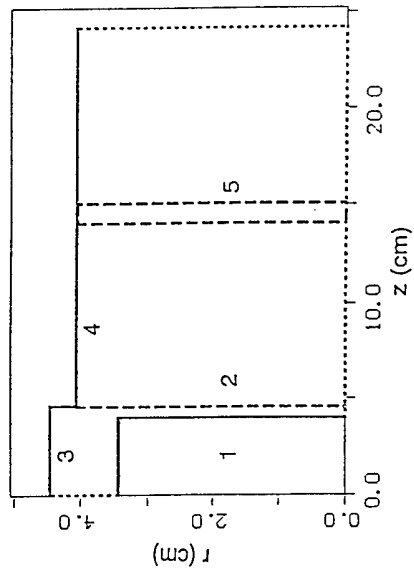


Fig. Outline of the modelled system: 1 cathode; 2 anode foil; 3 anode tube; 4 waveguide; 5 electron absorber;

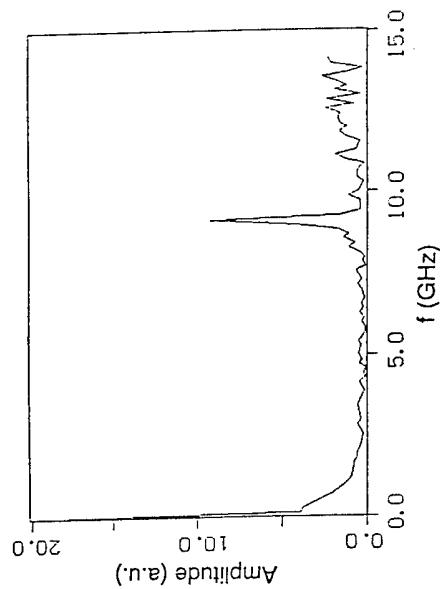


Fig.4 Fourier transform of the beam current through the anode foil.

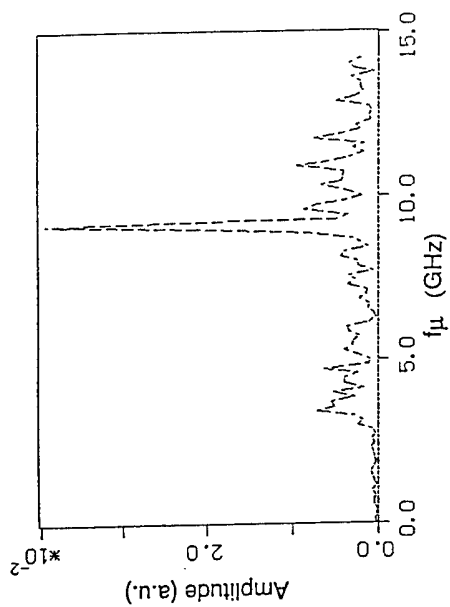


Fig.3. Fourier transform of the azimuthal magnetic field.

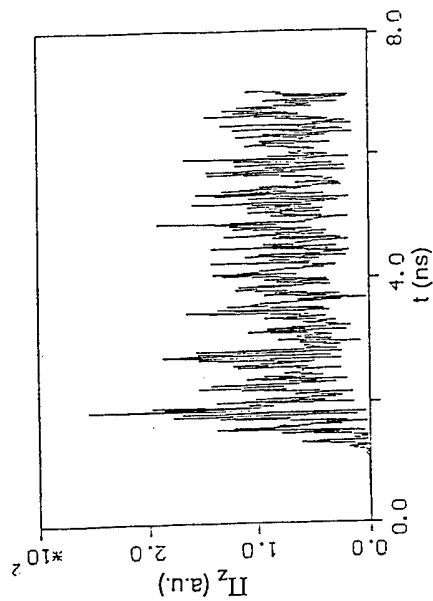


Fig.5 Time history of the poynting vector.

# ACCELERATOR FOR HIGH POWER MICROWAVE GENERATION

Eugeny V. Chernych, Vladimir E. Fortov, Kirill V. Gorbachev, Eugeny V. Nesterov,  
Vadim A. Stroganov, Vladimir P. Shumilin

*High Energy Density Research Centre, Russian Academy of Sciences,  
 IVTAN, Izhorskaja St. 13/19, Moscow, 127412, Russia*

## Abstract

The application of inductive storages for power supply of high power microwave oscillators leads to a significant decrease of installation volume and weight in total. Wide use of these systems is restricted by the low electron beam quality. We tried to solve this problem by use of the forming line instead of the inductive coil. The experimental testing of this modified inductive storage with reflex triode showed the increase of the power efficiency and microwave pulses reproducibility.

## Introduction

There is some interest in the inductive storages for HPM applications. By use of electrically exploded wires as an opening switch (EEOS), it's possible to generate efficiently the powerful electron beams with several GW power level.

Main disadvantage of the scheme is the low quality of generated electron beam because of both accelerating voltage instability and high output impedance of a generator. Influence of these factors on reflex triode operation was considered in

[5]. We tried to solve this problem by use of forming line (FL) instead of a coil.

The installation design and results of some HPM generation experiments are presented.

## Installation Design

The equivalent circuit for the installation is shown in Fig. 1. Process of charging of FL doesn't differ significantly from that of coil with inductance  $L = Z_0 t$  (where  $Z_0$  is the impedance of

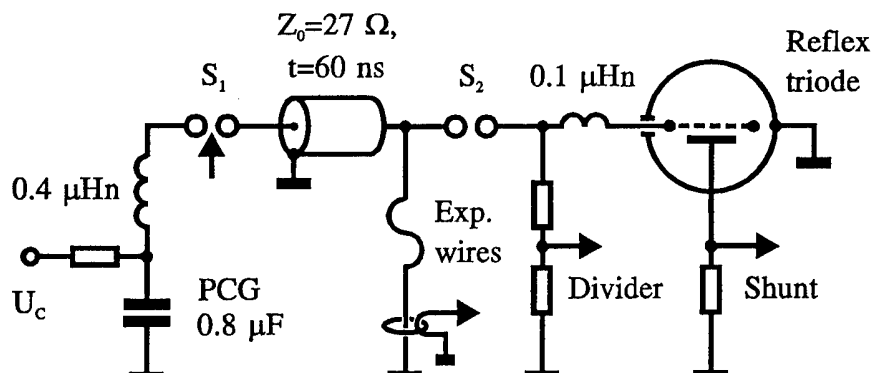


Fig. 1. The equivalent circuit for the experimental installation.

FL and  $t$  is its electrical length) before the wires explosion, since characteristic time of the process is much more then the double electrical length of FL. After the EEOS opening, accumulated current is switched to the load. If the EEOS opening time ( $\tau$ ) is less then double electrical length of the FL, the voltage pulse, delivered to the load, has a peak value  $U_L \approx I_0 Z_0 Z_L / (Z_0 + Z_L)$  and duration  $2t$  ( $I_0$  - current, stored in FL at the wires explosion moment,  $Z_L$  - load impedance).

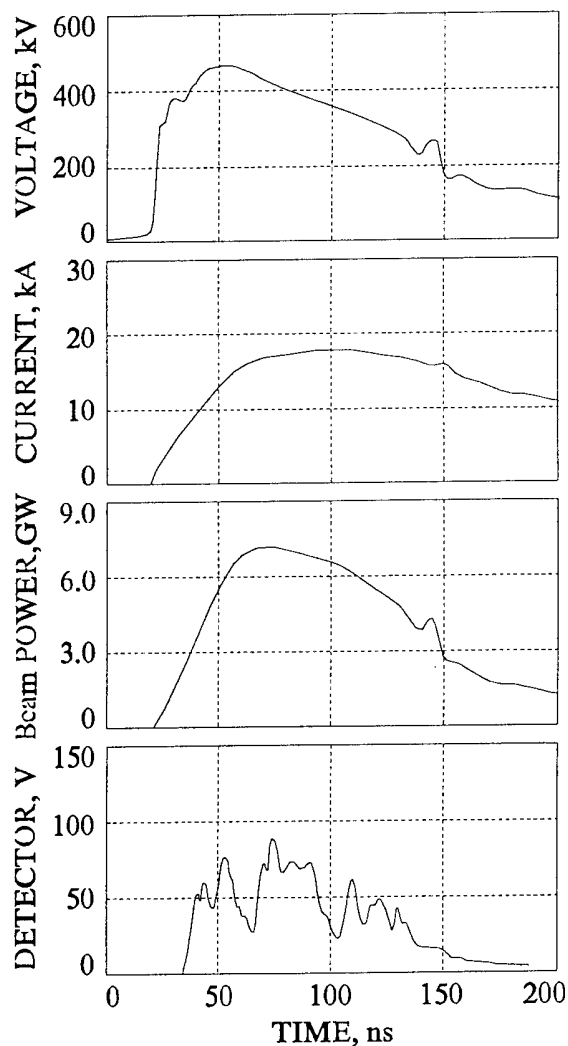


Fig. 2. Experimental data for a typical shot at 86-kV charging voltage.

27-Ohms FL was used in discussed installation. FL was current supplied by magnetic cumulative generator MCG or pulsed current generator (PCG) charged up to 70...90 kV. Reflex triode, described in details in [2], was used for accelerator tests. Graphite cathode was 83 mm in diameter. Anode was made of stainless steel grid with 0.7 transparency. Anode/cathode gap was varied from 7.5 up to 14.5 mm.

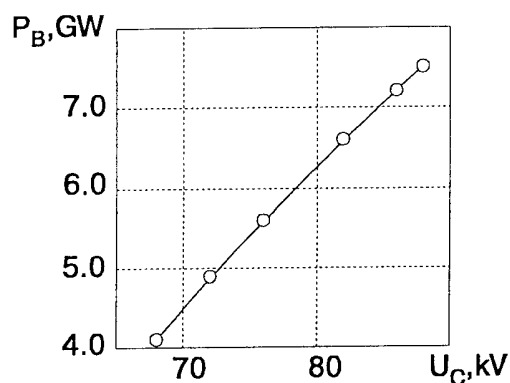
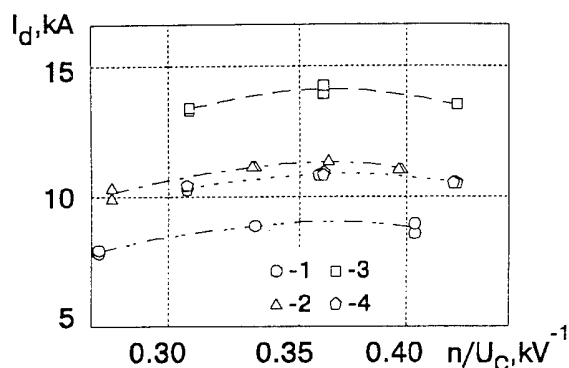


Fig. 3. Beam power versus charging voltage  $U_C$  (9.5 mm gap, 28 copper wires with 0.05 mm diameter and 400 mm length).

Diode voltage, current and microwave pulse waveforms at 86-kV charging voltage are shown in Fig. 2. The diode voltage was tuned by wires number and PCG charging voltage. The peak beam power dependence on charging voltage for 9.5-mm gap is shown in Fig. 3. The influence of wires number on generated pulse is more weak (Fig. 4). There is an optimum wires number for each charging voltage value  $n_{opt} / U_C = 0,36 \text{ kV}^{-1}$ , adjacent to which diode voltage and pulse waveform remains practically constant.





**Fig. 4.** Diode current as a function of relative wires number to charging voltage for different charging voltages: 1 -  $l = 400$  mm,  $U_c = 66$  kV; 2 -  $l = 400$  mm,  $U_c = 72$  kV; 3 -  $l = 400$  mm,  $U_c = 78$  kV; 4 -  $l = 500$  mm,  $U_c = 78$  kV.

Accelerator demonstrated a good operation stability. The beam power deviation at the same initial conditions was less than 3%, which corresponded to charging voltage measurement accuracy. Beam power,  $n_{\text{opt}}$  and FL storage time were in good correspondence with numerical simulation results.

### HPM generation experiments

Microwave radiation parameters were measured by wide-band detectors and pulsed power microwave calorimeter [4]. Microwave generation began at the forward current pulse front, when diode current achieved value of  $I_S = (7.5 \pm 0.7)$  kA. Start current  $I_S$  didn't depend on cathode/anode gap and current amplitude value (Fig. 5). When the diode current significantly exceeded  $I_S$ , we observed good oscillation reproducibility. In this case, both microwave pulse energy and detector signal waveform were stable.

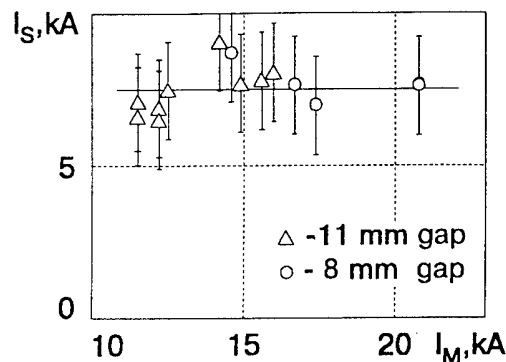


**Fig. 5.** The reflex triode start current versus diode current amplitude for 8-mm and 11-mm cathode/anode gap.

Microwave energy 5.6 J was obtained for 9.5-mm gap corresponding the best matching between reflex triode and pulsed power generator. The peak microwave power was about 200 MW at 7-cm wavelength. Experimental data representing microwave pulse energy and beam energy are given in Fig. 6.

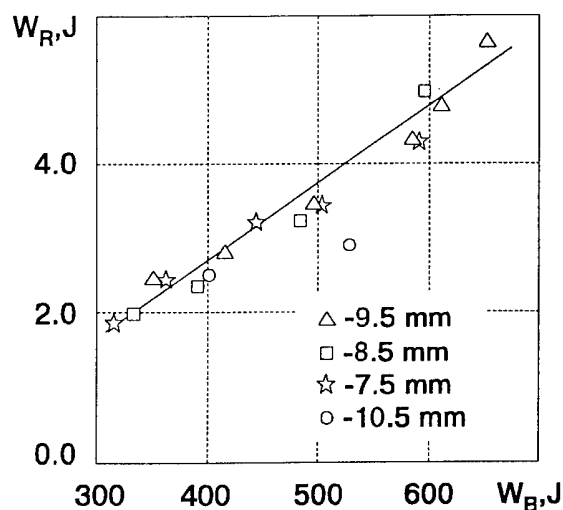


**Fig. 6.** Microwave pulse energy versus beam energy for different cathode/anode gaps.

The same efficiency was obtained in our experiments with 42-mm diameter

cathode at wavelength  $\lambda \approx 4$  cm. For high frequency range we encountered some difficulties: among them are the bad matching between the load and FL because of the influence of cathode plasma boundary motion on diode impedance and fast destroying of the grid.

60-mm magnetic cumulative generator (MCG) was also used for power supply of the accelerator. The MCG consisted of two cascades: preamplifier and high voltage cascade. 4.5 kJ energy was stored in FL in experiments without current switching to the vacuum diode. It was obtained 440 kV, 18 kA pulses in HPM generation experiments. Microwave pulses energy was about 5 J.

## Conclusion

For increasing of beam quality in inductive storage systems it was suggested to use FL instead of a coil. To check this suggestion the new accelerator was designed. Fulfilled experiments showed a positive influence of this modification on pulsed power generator operation stability and reflex triode efficiency. Moreover, some peculiarities of reflex triode behaviour were elucidated, among them is energy efficiency independence of cathode/anode gap.

Presented results demonstrate essential relationship between microwave generation in reflex triode and conditions of beam formation.

The work was supported by Russian Fund of Fundamental Researches.

- [1] Benford J., Swegle J., Application of high power microwaves: Proc. of the 9<sup>th</sup> Int. Conf. on High-Power Particle Beams, Washington, USA, May 25-29, 1992, David Mosher and Gerald Cooperstein ed., Naval Research Laboratory, vol. I (1992), p. 341.
- [2] Didenko A.N., Krasik Ya.E., Pereygin S.F. and Fomenko G.P., High-power microwave generation in triode system driven by relativistic electron beam: Pis'ma v J.Tech.Pys. (Russian), vol. 5(1979), p. 321.
- [3] Shvetsov G.A., Matrosov A.D., Vzryvnoy generator s vneshnim возбуждениem: Proc. of the 3<sup>th</sup> Int. Conf. on Megagauss Magnetic Field Generation and Related Topics, Novosibirsk, June 13-17, 1983, Titov V.M. and Shvetsov G.A. ed., Nauka, p. 263.
- [4] Lisichkin A.L., Nesterov E.V., Stroganov V.A.: Pribory i Tekhnika Eksperimenta, 1 (1996), p. 82.
- [5] Chernykh E.V., Didenko A.N., Gorbachev K.V., Fortov V.E., Ivanov A.B., Nesterov E.V., Roschupkin S.A., Shumilin V.P., Stroganov V.A. and Tarakanov V.P.: Proc. of Int. Symp. of Electromagnetic Environments and Consequences, EUROEM'94, Bordeaux, May 30 - June 4, 1994, vol. I (1995) p. 290.

## PULSED POWER MICROWAVE CALORIMETER

Alexander L. Lisichkin, Eugeny V. Nesterov, Vladimir P. Shumilin  
Vadim A. Stroganov

*High Energy Density Research Center, Russian Academy of Sciences,  
 IVTAN, Izhorskaja St. 13/19, Moscow, 127412, Russia*

### Abstract

The calorimeter for detection of pulsed power microwave radiation (from several ns to 1 s duration) is developed. The operation of the calorimeter is based on absorption of microwaves by polar fluid with its further expansion into capillary tube and measurement of fluid level in capillary by variable-capacitance transducer.

Absorbing surface area of the calorimeter is  $1300 \text{ cm}^2$  ( $36 \times 36 \text{ cm}$ ). The energy measurements are ranged from several mJ to  $\sim 100 \text{ J}$  (minimum registered energy density  $Q_s$  is  $\sim 3 \mu\text{J}/\text{cm}^2$ ). The calorimeter absorbs from 90 % to 99 % of falling microwave power with wavelengths 7.5 - 12 cm and 2.3 - 3.7 cm. The measurement error for absorbed energy is less than 5 % for energy  $Q > 20 \text{ mJ}$ .

### Introduction

Recently, the high power ( $\sim \text{GW}$ ) microwave oscillators are wide studied. As a rule, the electrical diagnostic facilities are used for power measurements of microwave. Meanwhile it's often necessary to check the measurements by independent method. Calorimeter technique could be used for this purpose, but there are a number of difficulties for developing of the proper calorimeter. Usually, the microwave pulse duration is not longer than  $10 \div 100 \text{ ns}$  and total energy is small - from 0.1 to 100 J. Moreover, high-power microwave generators have significant apertures (to eliminate the breakdown along the surface of output window) thus the energy density is small.

In this paper the results of design of high-sensitive, broadband (as regards the measured energy) calorimeter for frequency of microwaves about  $f = 3 \text{ GHz}$  and 10 GHz are given.

### General consideration

It is well known, that polar fluid well absorbs the energy of microwave radiation. This way, it is heated and is expanded, if possible. The fluid volume enhancement, which is a function of absorbed energy, could be measured by use of capillary tube. This principle was used for determination of electrical properties of fluids and for measurements of electromagnetic field components  $E$  and  $H$  by use of fluids with known dielectric properties [1]. The calorimeter described in [2] is based on the same principle.

The main problems concerning design of this calorimeter are: the proper choice of material for calorimeter body, as well as working (absorbing) fluid (w.f.) and configuration of absorbing layers. This parameters should provide from one hand, the maximum absorption coefficient for the wavelength band as wide as possible and from another hand the high sensitivity and wide range of measured energy.

The mentioned requirements are easily satisfied for short wave part of centimetric wave band and for millimetric wave band. For long wave band of microwave, to diminish the volume of w.f. it is necessary to use more complicated multi-layer designs, which were optimizing by use of proper computer codes.

Let's consider the thermal physics problems dealing with absorption of energy of short ( $\sim 100$  ns) microwave pulses by fluid. During the pulse, the pressure and temperature of fluid rises. After finishing of pulse, because of the variations of absorption, the temperature and pressure in different parts of w.f. are different; appearing waves of disturbances equalize pressure in all volume for the time  $\tau_c \sim L_c/a$  (where  $L_c$  - characteristic size of w.f.,  $a$  - speed of sound). After this, during the time interval  $\tau_p$  defined by viscosity of w.f., diameter of capillary tube and some other factors, the fluid is expanded and its level in capillary tube rises. For adiabatic process, the change of mean temperature  $\Delta t$ , pressure  $\Delta p$ , fluid volume  $\Delta V$  and level in capillary tube  $\Delta h$  are connected with energy supplied  $Q$  by relations:

$$\Delta t = Q / (c_p V); \quad \Delta p = \beta Q / (c_p \gamma V); \quad \Delta V = Q \beta / (c_p); \quad \Delta h = Q \beta / (S_c c_p),$$

$c$ ,  $\rho$ ,  $\beta$ ,  $\gamma$ ,  $V$  - are heat capacity, density, coefficient of volume expansion, compressibility and volume of w.f. accordingly,  $S_c$  - cross-section of capillary.

As dynamic and static pressure enhancement as capillary cross-section area effects on the measurement accuracy.

As was shown by estimate calculations and by experiments, the adiabatic condition is fulfilled for chosen design when the time of signal measurements is less then  $\sim 1$  s.

To eliminate the measurement errors connected with temperature dependence of w.f. properties it was decided to carry out all measurements at the same temperature. This temperature must be higher then possible environmental temperature and could be reached and held by use of electric heater immersed into w.f. In this case for vertical installation of capillary tube the filling in calorimeter is done once. During time intervals between working periods the level of fluid remains in special flash cavity.

This principles were used for developing of  $330 \text{ cm}^2$  absorbing surface area calorimeter [3]. Device described in this paper differs from mentioned above by enlarged absorbing surface area, enhanced absorption characteristics and has more stable showings relative to various disturbances (has better signal/noise ratio).

### Calorimeter design

On the basis of calculations and probe experiments ethanol was chosen as absorbent (working) fluid, acrylic plastic (Plexiglas) - for calorimeter body material, and configuration of absorbing and matching layers was defined.

Absorbent unit is made in shape of parallelepiped ( $400 \times 400 \times 63$  mm) with filling in channels. The channels are connected with each other and all together with glass capillary tube. Two electric heaters are placed into absorbing fluid, one of them serves for heating of w.f. up to operating temperature and maintaining its level in capillary, another serves for calorimeter calibration. In upper part of the body the flash box with capillary is placed. The total area of absorbing surface is  $1300 \text{ cm}^2$ . The body of calorimeter is placed into heat insulation.

The measurements of w.f. level were made as follows. Two metallic strips constituting capacitor were bond symmetrically to outer surface of capillary. Absorbing energy was registrated by measuring of capillary capacitance change. The signal was recorded by digital oscilloscope operating in continuous scanning mode.

### Testing of the calorimeter

The calorimeter test includes following procedures:

#### 1. Measurements of reflectance for wavelength from 2.3 to 12 cm.

The measurements showed (see Fig.) that the power absorption coefficient for  $\lambda = 7.5 - 12$  cm and  $\lambda = 2.3 - 3.7$  cm was  $k_a = 0.90 - 0.99$  both for E parallel to the axes of channels (curve a) and for E perpendicular to the axes of channels (curve b). Solid lines correspond to calculational results, separate points - to experimental data. For  $\lambda = 3.7 - 7.5$  cm  $k_a$  is greater then 75%.

#### 2. Determination of calibration curve (c.c.) $S = dU/dQ = f(h)$ .

Determination was done by rectangular voltage pulses (duration  $\tau = 1.12$  s) applying to calibration heater. The energy of pulses was 2.9 J. The calibration was done for every w.f. level in capillary inside the capacitor. The c.c. deviation from constant was less then 3%.

#### 3. Determination of accuracy of measurement of absorbed energy.

Determination of accuracy of absorbed energy measurement was made in the same way for energy range  $Q = 4$  mJ - 2 J for pulse duration  $\tau_p = 2 - 1000$  ms. Experiment showed, that the accuracy of the measurement of absorbed energy (which is double standard deviation - s.d.) was:

$\pm 30\%$  for  $Q = 4$  mJ,

$\pm 5\%$  for  $Q = 20$  mJ,

$\pm 1.5\%$  for  $0.2 - 2$  J.

The given data for  $Q \leq 20$  mJ are obtained with help of special capillary - capacitor arrangement.

It should be mentioned that s.d. of temperature and fluid height in the capillary was in the best case  $0.08$   $\mu$ deg and  $0.25$   $\mu$ m accordingly.

#### 4. Test at high energy.

Test of the calorimeter at high microwave energy was carried out by 200-kW, 280-ns pulsed magnetron at wavelength  $\lambda = 3$  cm. The measurements were made for series pulse operation at pulse repetition frequency  $f = 1000$  s<sup>-1</sup> and number of pulses in series  $n = 190-2200$ . Experiments showed, that the linear dependence of signal on microwave energy was conserved at least up to  $Q = 120$  J (s.d. = 1.24 J).

#### 5. Measurements of microwave pulses energy generated by reflex triode.

The measurements of microwave by the reflex triode driven by 450 kV, 18 kA, 100 ns pulsed power generator, when calorimeter was placed closely to output window, showed the absence of signal from ultraviolet or x-radiation and full absence of noise in measurable energy range from 10 J down to tens of mJ.

### Conclusion

We can resume the following:

1. The high sensitive to absorbed energy calorimeter is designed. The minimum energy density detected is  $Q_s \sim 3$   $\mu$ J/cm<sup>2</sup> while the absorbing surface area is 1300 cm<sup>2</sup>.

2. The calorimeter can be used for wide energy range: from several mJ up to 120J.

3. Calorimeter possesses high relative accuracy of measurements of absorbed energy (for example, for energy about several J the accuracy is about 1.5 %).

4. The workability of calorimeter is independent of microwave pulse power level and its duration over the range from ns to 1s.

5. The power absorption coefficient is from 90 % to 99 % over the wave bands  $\lambda = 7.5 - 12$  cm and  $\lambda = 2.3 - 3.7$  cm.

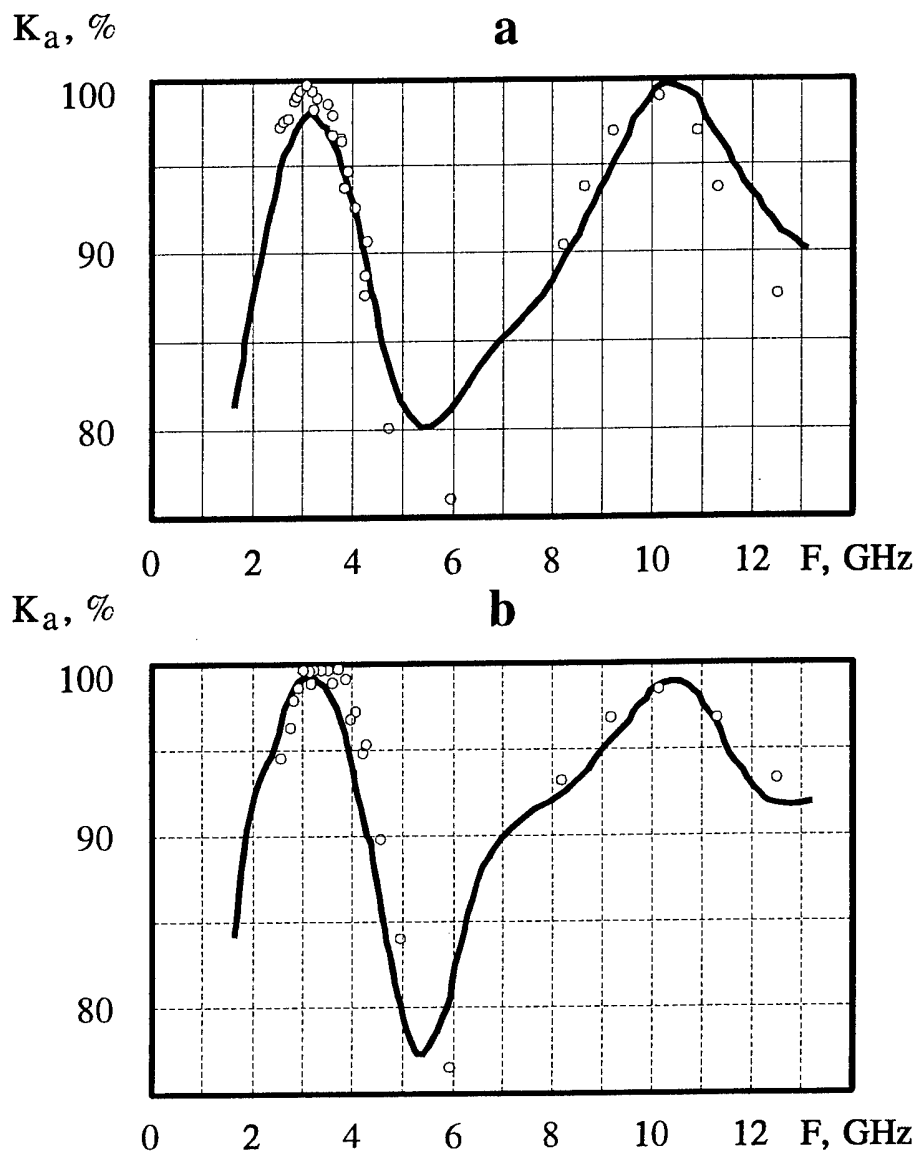


Fig. Absorption coefficient as a function of microwave frequency.

6. The calorimeter is easy to use and is ready for full automatic control of pre-starting procedures, measurements and data processing.

#### Acknowledgments

The authors want to express their gratitude to Antonov A.S. for the opportunity to make calculations by use of developed numerical code for microwaves propagation through the multilayer structures.

- [1] Brandt A.A., Issledovanie dielektrikov na sverkhvysokikh chastotakh, Moscow: Fizmatgiz, 1963 (in Russian).
- [2] Shkvarunets A.G., Rurhadze A.A. and Strelkov P.S., Fiz. Plazmy, 1994, vol.20, no. 7 and 8, pp.682-685.
- [3] Lisichkin A.L., Nesterov E.V., Stroganov V.A., Pribory i Tekhnika Eksperimenta, 1 (1996), pp. 82-84

## AIR BREAKDOWN INDUCED BY A HIGH-POWER SHORT-PULSE MICROWAVE

T. Wakisaka, M. Yatsuzuka and S. Nobuhara

*Department of Electrical Engineering, Himeji Institute of Technology,  
Himeji, Hyogo 671-22, Japan*

### Abstract

Air breakdown induced by a high-power short-pulse microwave in the pressure range from 100 to 760 Torr has studied experimentally. The high-power microwaves with the peak power of 20 MW, frequency of 12 GHz and pulse duration of 14 ns is irradiated to a pair of needle and plane electrodes biased at the potential less than the breakdown voltage. The gap separation between the needle and plane electrodes is 1.5 cm. Microwave-induced breakdowns occur at the pressure range from 150 to 760 Torr for negative potential and from 150 to 350 Torr for positive polarity at the presence of corona discharges. At the pressure range less than 150 Torr, the microwave-induced breakdown occurs without corona discharge at both polarities.

### Introduction

Recently, high power microwaves of its power levels in excess of 1 GW have been generated using intense relativistic electron beams with accelerating voltage of the order of a MV and current in excess of kA[1,2]. High power microwaves offer new applications in a variety of fields such as particle accelerations, impulse radar, laser pumping, power beaming and environmental cleanup. Research on laser-triggered lightning has received considerable attention in the recent years[3]. One problem in laser-triggered lightning experiments is strong attenuation of laser energy by rains, clouds, and laser-produced plasma. If microwave-triggered lightning is possible instead of laser, microwaves propagate with a small loss in thunderclouds compared with lasers and also are able to radiated much extensive region of targets. In this paper we report on the fundamental experiment of air breakdown induced by a high-power short-pulse microwave.

### High-Power Microwave Source

The high-power, short pulsed microwave is generated with a axially extracted vircator at Himeji Institute of Technology[4]. The vircator diode consists of an annular cathode of diameter of 3 cm and 1 mm in thickness and a stainless mesh anode (mesh wire diameter: 0.25 - 0.37 mm and transparency: 62.8 - 68.4 %). Figure 1 shows the typical time evolution of diode voltage, electron beam current and microwave emission from the top. As seen in Fig. 1, the peak power of microwave is 20 MW and the pulse duration (Full Width at the Half Maximum: FWHM) is 14 ns. Although not shown here, the radiation frequency was found to be 12 GHz.

## Apparatus and Procedures for Microwave-Induced Air Breakdown

A schematic of experimental set up for microwave-induced air breakdown is shown in Fig. 1. The conical horn with a dielectric lens mounted at the horn aperture is used as a transmitting antenna. High-power microwaves through the dielectric lens are focused on a discharge electrode gap in the center of a stainless steel vacuum chamber with a diameter of 31 cm and length of 32 cm. The discharge electrode consists of a pair of needle (a diameter of 7 mm and a tip angle of  $19.3^\circ$ ) and plane (diameter of 6 cm) electrodes. The gap spacing between the needle and plane electrodes is 1.5 cm which is less than the wavelength of microwave. Then, the microwave power density should be uniform in the gap spacing between the electrodes. The acrylic window and microwave absorber (Eccosorb CV) at the opposite side of the transmitting antenna allow incident microwaves to transmit in the vacuum chamber without reflection. Thunderclouds usually occur at the height of 3 - 10 km at which air pressure is estimated to be 200 - 500 Torr. Then, the experiment presented here was done under the air pressure range from 100 to 760 Torr. Lights of corona discharge and breakdown were observed with a polaroid camera at a side window of vacuum chamber.

At first, a DC voltage was applied to the discharge electrode without microwave irradiation. The DC voltage increased gradually till an onset of corona discharge to obtain the corona onset voltage. By further increasing DC voltage exceed the corona onset voltage, the gap-breakdown voltage was measured. Secondly, the microwave irradiated to the electrode gap space biased at the potential less than the breakdown voltage.

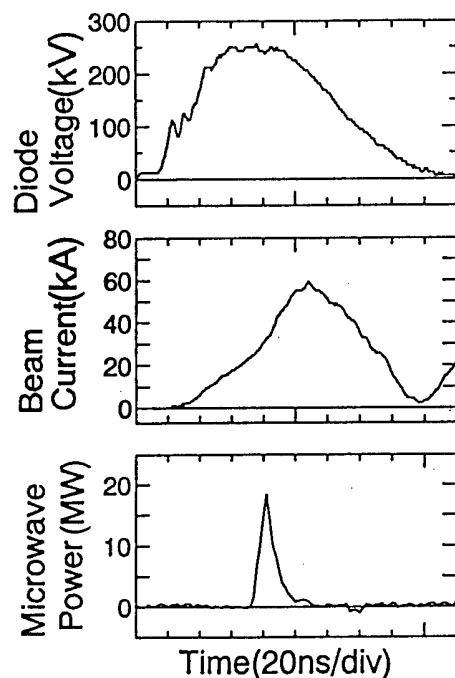


Fig. 1. The time evolution of diode voltage, electron beam current and microwave emission from the top.

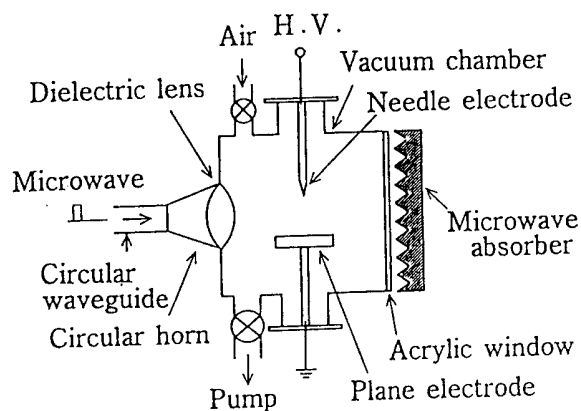


Fig. 2. The experimental setup for microwave-induced air breakdown.



## Results and Discussion

Figure 3 shows the DC voltage applied to the electrodes vs. air pressure for the negative polarity which means the needle electrode is negative voltage, where ■ stands for the corona onset voltage  $V_C$ , ● the DC breakdown voltage  $V_B$ , and ○ the minimum voltage of microwave-induced breakdown  $V_M$ . The hatched region indicates the biased voltage between the electrodes at which the microwave irradiation causes the breakdown between the electrodes. As seen in Fig. 3, the microwave-induced breakdown occurs at the pressure range from 100 to 760 Torr, and at the pressure range less than 150 Torr, the microwave induces the breakdown at the biased voltage less than the corona onset voltage. In the pressure range above 200 Torr, the presence of corona discharges is necessary for microwave-induced breakdown. Figure 4 shows the photographs of (a) the corona discharge before microwave irradiation and (b) the breakdown induced by microwave irradiation at the pressure of 200 Torr, where the black and white of photographs were inversed using a computer.

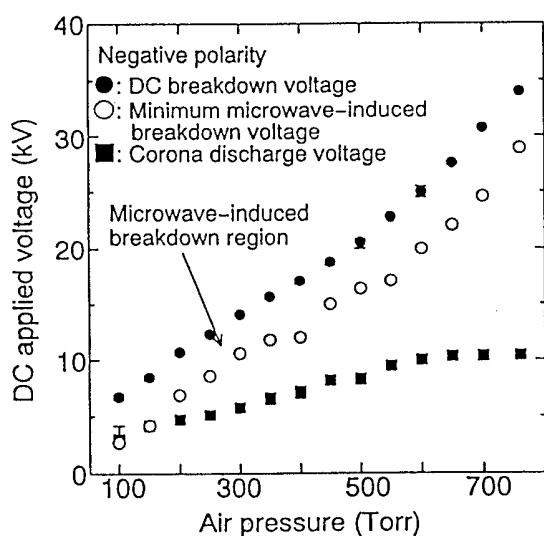


Fig. 3. Microwave-induced breakdown for the negative polarity.

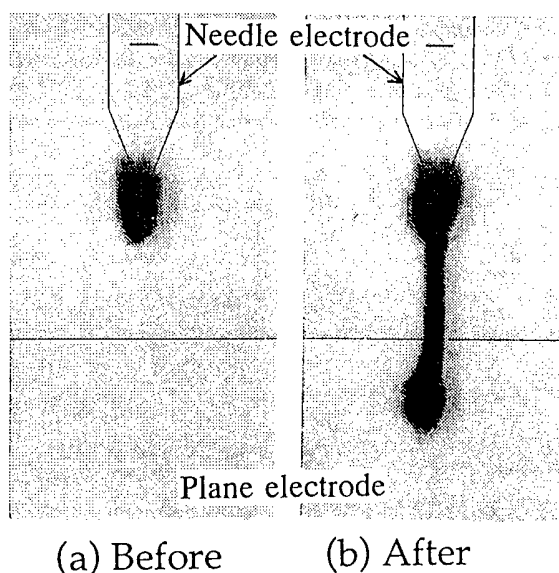


Fig. 4. Photographs of (a) the corona discharge before microwave irradiation and (b) the breakdown induced by microwave irradiation at the air pressure of 200 Torr.

The ratio of the minimum microwave-induced breakdown voltage  $V_M$  to the DC breakdown voltage  $V_B$  is plotted as a function of air pressure in Fig. 5, where ○ is for the negative polarity and ● is for the positive polarity. As seen in Fig. 5, the microwave-induced breakdowns occur at the air pressure range less than 300 Torr and  $V_M/V_B$  reduces with decreasing air pressure in both polarities. Figure 5 also shows that the high-power microwave can easily induce breakdown for the negative polarity than for the positive polarity. At the pressure larger than 300 Torr, no microwave-induced breakdown appears for the positive

polarity. These results are ascribed to the presence of many electrons, generated by corona discharges, in the gap space at the negative polarity. Because negative corona discharges release a large number of electrons in the gap space, but positive coronas drive little electrons.

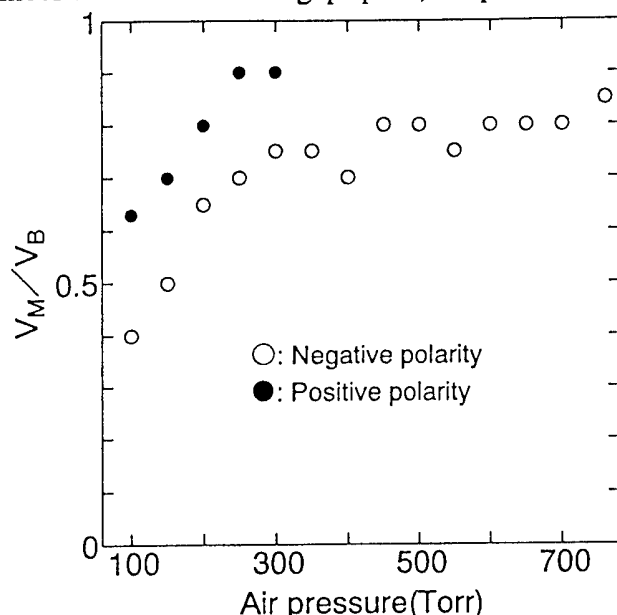


Fig. 5. The ratio of the minimum microwave-induced breakdown voltage  $V_M$  to the DC breakdown voltage  $V_B$  as a function of air pressure, where  $\circ$  is for the negative polarity and  $\bullet$  is for the positive polarity.

### Conclusion

Air breakdowns induced by a high-power, short-pulse microwave with the peak power of 20 MW, frequency of 12 GHz and pulse duration of 14 ns were studied experimentally with the needle-plane electrode system. The conclusions obtained are as follows:

- (1) At the pressure range less than 150 Torr, the microwave-induced breakdown occurs without corona discharge at both polarities.
- (2) For the negative polarity, the microwave irradiation causes gap breakdowns with the presence of corona discharges at the pressure range from 150 to 760 Torr.
- (3) Microwave-induced breakdowns at the negative polarity occur easily than at the positive polarity. At the pressure range larger than 300 Torr, no microwave-induced breakdown appears for the positive polarity.

From the studies mentioned above, triggered lightning by a high-power pulsed microwave might be possible, provide that there are a large number of initial electrons or with further higher-power microwave sources.

- [1] V. L. Granatstein and I. Alexeff: "High-Power Microwave Sources", (Artech House, Boston, 1987).
- [2] J. Benford and J. Swegle: "High-Power Microwaves", (Artech House, Boston, 1992).
- [3] T. Shindo and S. Sasaki: J. IEE Jpn. **111** (1991) 739.
- [4] M. Yatsuzuka, K. Nagakawa, Y. Hashimoto, O. Ishihara and S. Nobuhara: IEEE Trans. on Plasma Science, **22** (1994) 939.

## COAXIAL VIRCATOR SOURCE DEVELOPMENT

Kevin Woolverton, M. Kristiansen, L. L. Hatfield

Pulsed Power Laboratory  
Department of Electrical Engineering  
Texas Tech University  
Lubbock, TX 79409-3102

### Abstract

A study of efficiency improvement for a coaxial vircator cathode oscillator is presented. The coaxial geometry has many physical parameters that can be changed to alter the performance of the system. The parameters of interest include diode length, anode-cathode gap spacing, and an electron absorbing collection rod. The center rod also has two changeable variables, rod length and rod radius. The rod radius appears to be the critical parameter, making the radius too large results in too many electrons being collected, resulting in a decrease in produced microwaves; making the radius too small results in little effect. MAGIC, a 2- $\frac{1}{2}$  dimension particle-in-cell code, is used to simulate the different geometries. Conclusions on varying the parameters are given.

### Introduction

Vircators are high-power microwave sources based on the bremsstrahlung radiation of relativistic electrons oscillating in electrostatic fields and are important microwave sources due to their simplicity and the fact that no external magnetic field is required for their operation. They require no heavy external coils or high-current power supplies. Vircators have been shown to be tunable and able to be phase-locked. Yet, vircators are not very efficient, with typical efficiencies on the order of 1%, and in highly advanced vircators, efficiencies increase to typical values around 10%[1]. Hence, improvement in efficiency is an area that has been extensively studied and which little is known about. Many different geometries have been studied to increase efficiency, including the reflex triode, the reditron, and more recently the virtod [2].

The virtual cathode is formed by the space charge limiting current being exceeded, resulting in a depressed electrostatic field which overcomes the kinetic energy of incoming electrons. The electrons decelerate, giving up energy to the microwave field. Then the electrons are accelerated away from the virtual cathode back towards the anode and towards the real cathode in a process called reflexing. This reflexing continues and produces microwaves at a frequency which is proportional to the square-root of the applied potential and inversely proportional to the anode-cathode gap spacing. But this is not the only mechanism for microwave production. When the virtual cathode forms, it is highly unstable and it changes in magnitude and position which is another mechanism for microwave production. This frequency of oscillation, often differing and competing with the reflexing frequency, is the plasma frequency of the virtual cathode.

Efficiency can be improved by trying to match the two frequencies or by eliminating one source of microwave production to let the other dominate, thus eliminating competition, resulting in higher efficiency. The geometry under consideration is a coaxial vircator in which the microwaves are axially extracted perpendicular to the electron beam. Figure 1 shows the coaxial geometry. The anode is pulsed positive and a toroidal virtual cathode is formed.

MAGIC, a 2- $\frac{1}{2}$  dimension particle-in-cell code, is used to simulate several different geometries.

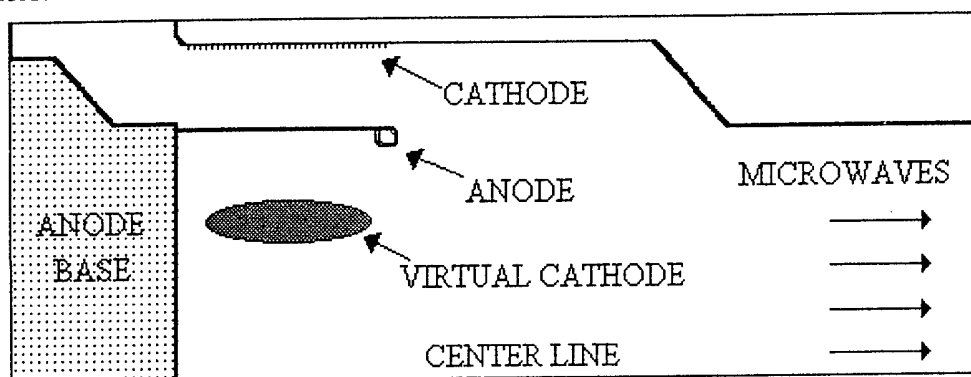


Figure 1: Coaxial Vircator Geometry

It has been put forward that the efficiency of the coaxial geometry is dependent upon a mechanism known as electron phase separation [3]. Phase separation is a mechanism that contains what are termed wrong-phased electrons and right-phased electrons. The wrong-phased electrons are the electrons that are accelerated at the expense of energy from the microwave field. The right-phased electrons are the electrons that are trapped in the potential well between the real and virtual cathodes. In the coaxial geometry, the right-phased electrons oscillate in the potential well and the wrong-phased electrons move towards the center axis where they are repelled by Coulombic forces. This process of electron movement has been observed in animated phase-space plots from MAGIC. Thus, the wrong-phased electrons are caught in the interaction space, stored there, and radiate their own microwaves out of phase with the right-phased electrons. To eliminate these wrong-phased electrons, it has been suggested to place a center conducting rod down the center [3], [4].

### Simulations

Simulations were run to determine the effect of placing a rod down the center of the system. In the determination of the rod's effectiveness, the input power, output power and efficiency is calculated at the dominant frequency. Most geometries studied here have the same dominant frequency and direct comparison is only meaningful if this is the case. If the dominant frequency is different, then total power is used for comparison. Generally, the spectrum desired is a highly coherent signal with few peaks at multiple frequencies. Yet, in certain circumstances it might be desirable to have a wide range of frequencies at high power. Figure 2 shows the efficiencies of the different geometries at the dominant frequency. The graph is normalized to the case where no rod is placed down the center to obtain a relative measure of the effect of the change in geometry at the dominant frequency. The rods have the following radii: 1 corresponds to a 4 millimeter radius, 2 corresponds to a 7.8 millimeter radius and 3 corresponds to a 11.5 millimeter radius. Also, a surprising result occurred when a hole was placed in the anode base instead of a rod, efficiency then increased significantly, both in the power at the main frequency and in the overall signal power.

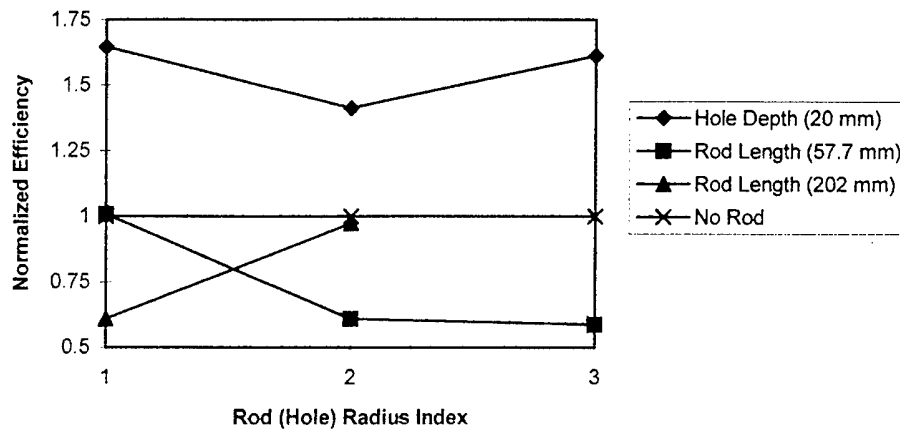


Figure 2: Efficiency at the Main Frequency Normalized to no Rod

The calculation of the efficiency was performed by taking a Fourier transform of the output signal to find the dominant frequency of the signal and the magnitude at the dominant frequency. Then, with an assumed mode, the power could be calculated. Similarly, the entire power in the signal was calculated where all frequencies were taken into account. Figure 3 shows the total output power, again normalized to the no-rod case.

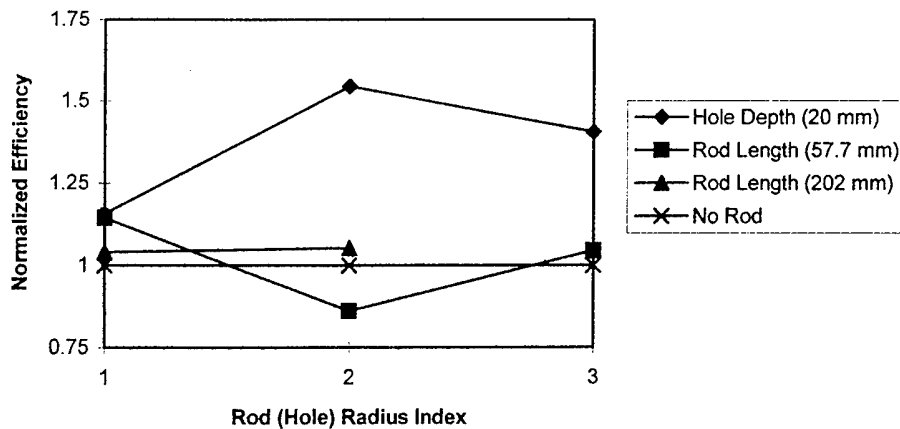


Figure 3: Efficiency Using Total Power Normalized to no Rod

What is most notable from these figures is that the placement of a hole in the anode base increased the efficiency considerably, both in the efficiencies obtained from a single dominant frequency and in the overall signal. While the greatest efficiency for the main frequency occurred for a hole with a radius of 4 millimeters, the greatest increase in total power efficiency occurred for a hole a radius 7.8 millimeters. The placement of a rod decreased the efficiency at the main frequency and did little in most cases in the overall power efficiency.

For a given anode-cathode gap spacing, a maximum in output power can be achieved by matching the diode impedance to the transmission line impedance [3]. This was considered but the change in impedance was negligible, differing by only a couple of hundredths of an ohm in the worst case, so a better match of the impedances was not considered to be the cause.

MAGIC was used to gain insight into the inner workings of the different geometries. Different cases were tried and of particular interest were the phase-space diagrams in the radial direction, the location of the particles and the radial electric field in the region where the virtual cathode forms. The radial electric field was observed at five positions beneath the anode foil and extending all the way to the cathode. What appeared to occur is that the hole in the anode created a radial electric field, all along the axis, that discouraged electrons from entering the region of wrong-phased electrons. More electrons remained in the reflexing area and fewer entered the region where the electrons get accelerated at the expense of the field. The radial electric field fluctuated positively and negatively, but mostly remained negative near the axis. The repelling field for the case with the hole was also greater in magnitude than for the case with a rod or with no hole or rod. For the case with the rod, more electrons were drawn towards the axis where more electrons get accelerated at the expense of the field. For the case with the rod, the radial electric field was generally more positive in magnitude and occurrence (in a statistical sense) than for the other cases. Phase-space plots also confirmed these results by showing more electrons with greater momentum outside the reflexing area for the geometry with a rod and fewer electrons with lower momentum outside the reflexing area for the geometry with a hole.

Figure 4 shows the electric field down the waveguide for the no rod, no hole case, on the left, and the hole case with hole radius of 7.8 millimeters on the right. A significant increase in calculated field strength is observed.

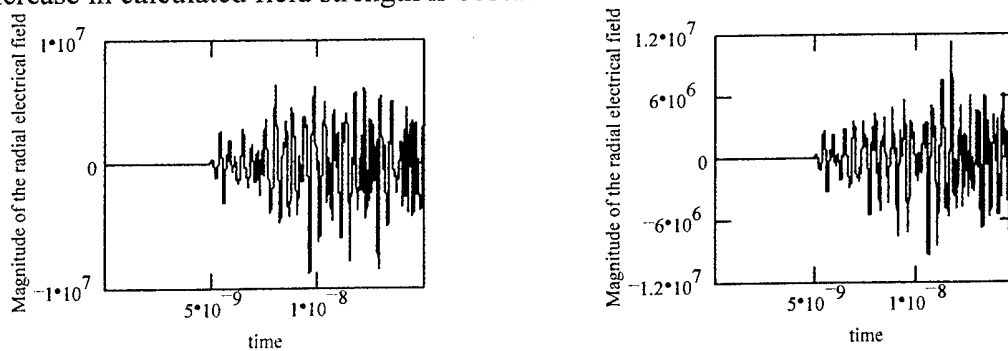


Figure 4: Field Strength in the waveguide

Further improvements might be made by further adjusting the hole size and depth. Also, a ring could be used instead of a hole, and this might better match the retarding field with the reflexing and increase efficiency further.

### Acknowledgements

This work is supported by AFOSR/DOD MURI.

- [1] Benford, J. Swegle, J., "High-Power Microwaves", Boston: Artech House, Inc. 1992.
- [2] S. B. Bludov, N. P. Gadetskii, K. A. Kravtsov, et. al., "Generation of High-Power Ultrashort Microwave Pulses and Their Effect on Electronic Devices", Plasma Physics Reports, vol. 20, no. 8, 1994, pp. 712-717.
- [3] Selemir, V. D., Alekhin, B. V., et. at., Plasma Physics Reports, 1994, vol.20, no.8, pp. 621-639.
- [4] Crawford, Mark, Ph.D. Dissertation, Texas Tech University 1994.

# A 70-GHz HIGH-POWER REPETITIVE BACKWARD WAVE OSCILATOR WITH A PERMANENT-MAGNET-BASED ELECTRON-OPTICAL SYSTEM

V.G. Shpak\*, S.A. Shunailov\*, M.R. Ulmaskulov\*, M.I. Yalandin\*  
A.E. Ermakov\*\*, S.V. Zhakov\*\*, V.G. Gass\*\*, and A.Yu. Korobeinikov\*\*

\* *Institute of Electrophysics, Ural Division of Russian Academy of Sciences  
34, Komsomolskaya Str., 620049, Ekaterinburg, Russia*

\*\* *Institute of Metal Physics, Ural Division of Russian Academy of Sciences  
18, S.Kovalevskaya Str., 620049, Ekaterinburg, Russia*

## Abstract

A focusing magnetic system based on NdFeB permanent magnets creating a field of quasi-solenoidal configuration with a strength of 14.5 kOe in a uniform-field region has been developed. The system has been tested as a unit of a nanosecond, 70 - GHz relativistic BWO with megawatt output power and PRF of 100 Hz. The limitations related to the formation of a shunting radial electron beam in a vacuum diode and to the collimation of the electrons by the anode unit are discussed.

In most cases, the use of high-current relativistic electron beams (REBs) involves their transportation over long vacuum channels. For high-current-density ( $10^3 - 10^4$  A/cm<sup>2</sup>) unneutralized REBs, the only applicable way to transport such a beam is to focus it in a strong longitudinal magnetic field. In experimental practice, magnetic fields of several tens of kiloersted are created by pulsed solenoids with a capacitive energy store or by superconducting coils. For the first case, the accelerator - magnetic field generator energy ratio is typically 1:10. A pulsed magnetic focusing system (MFS) generally fails to provide for long - term operation of a microwave device with a high pulse repetition rate. Superconducting systems do not meet the requirement for self - contained operation, moreover, they are rather complicated and costly. Earlier we investigated the operation of millimeter-band high-power small-sized relativistic backward-wave oscillators (BWOs) with a pulse duration of 3-4 ns [1]. The optimized pulsed MFSs of the 70-GHz devices had stepwise channels of small diameter (14-10 mm). The quasi-uniform region of the focusing field was not long,  $\sim 45$  mm (see Fig. 1a). With the pulse duration being a few nanoseconds and the peak accelerating voltage 250 - 300 kV, the diameter of the magnetically insulated coaxial diode (MICD), including the vacuum insulator, was as small as 50 mm. This is why the configurations of the MICD and of the slow-down system of the 70-GHz relativistic BWO were most convenient for the design of an experimental permanent

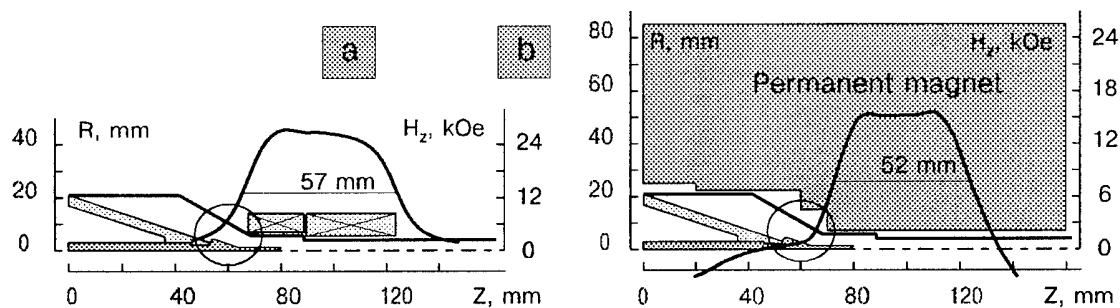
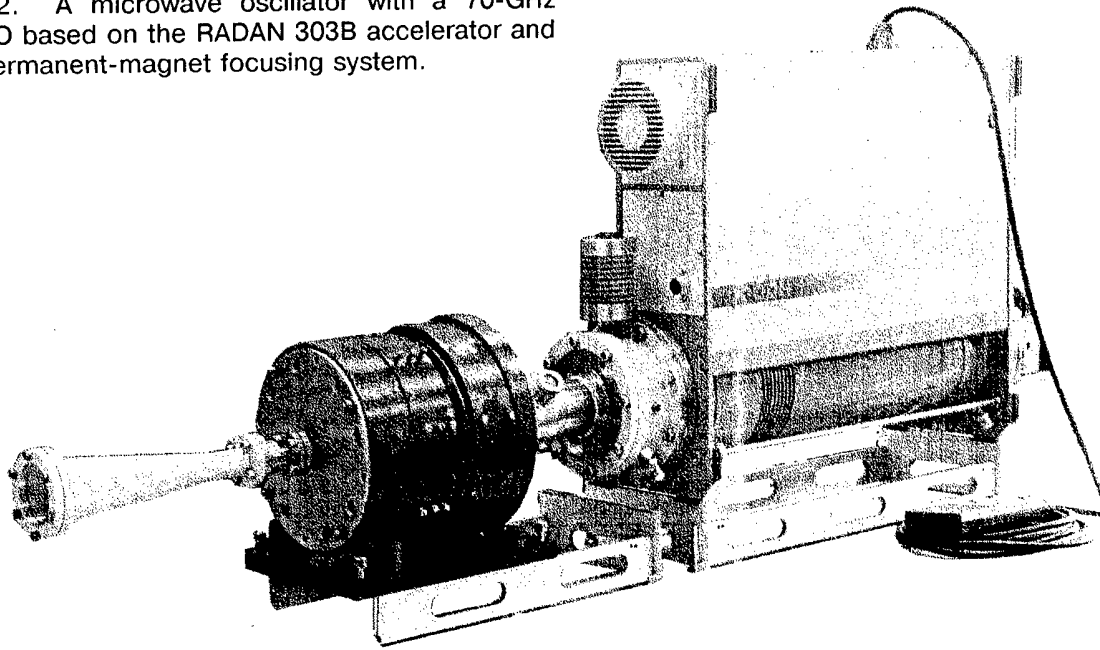


Fig.1. Configuration of a vacuum diode with a pulsed solenoid and the axial field distribution [1] (a) and a vacuum diode with a permanent-magnet focusing system and the axial field distribution (b).

Fig.2. A microwave oscillator with a 70-GHz BWO based on the RADAN 303B accelerator and a permanent-magnet focusing system.



magnet - based MFS (PMFS). Like in our earlier experiments [1], we used the RADAN 303B compact accelerator [2] as a high-current electron beam source.

To determine the required field strength of the permanent magnet, we took into consideration the effect of the magnetic field on the starting current of the device [3] and on the uniformity of the electron beam in the vacuum diode [4] as well as the problems associated with the efficiency of energy exchange between the beam electrons and the field of the synchronous microwave during the transportation of the beam in a finite magnetic field. The requirements that should be met are as follows:

(1) To produce accelerating voltage pulses of nanosecond duration, the emitting surface of a hollow explosive-emission cathode should be acceptably homogeneous which can be attained with a magnetic field over 10 kOe [4].

(2) The axial magnetic field should differ from that at which the effects of a cyclotron resonance between the electron beam and the main spatial harmonic of the wave generated are observed. To prevent an increase in the starting current of the device (and a corresponding decrease in output power), it should be tuned away from precise resonance by 10-15 % [3].

(3) For the energy exchange between electrons and a synchronous electromagnetic wave (in our case with the first backward spatial harmonic,  $E_{01}$ , of the wave) to be efficient, the magnetized annular beam should be thin. That is its "wall" thickness ( $\Delta r_b$ ) should be smaller than the characteristic scale for the fall of the synchronous harmonic field in the radial direction, which was  $\sim 0.3$  mm for the conditions of our earlier experiments [1]. The value of  $\Delta r_b$  can be estimated as twice the cyclotron radius of the trajectory of an electron rotating in an axial magnetic field. In doing this, the maximum transverse velocity of the electrons is found by analyzing their motion in the crossed electric and magnetic fields of the MICD with the supposition that the emission centers are located on the cylindrical surface of the tubular cathode.

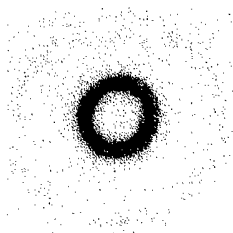


Fig.3. Autograph of an electron beam on dozimetric film. Average diameter = 2.2 mm.

These requirements and our earlier experimental data on the performance of a BWO with a pulsed MFS [1] require the minimum acceptable axial magnetic field of the PMFS to be at a level of 15 kOe. This field is achievable for permanent magnets based on advanced materials such as the Nd-Fe-B alloy. This alloy shows a residual induction of



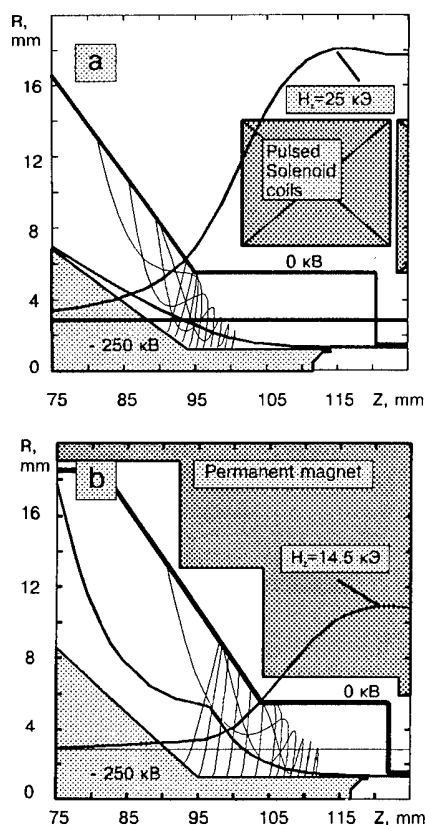


Fig.4. Single-body simulation of the paths of the shunting electron beam in the vacuum diode of a BWO with a pulsed magnetic system (Fig.1a) (a) and the same for a BWO with a permanent-magnet focusing system (Fig.1b) (b).

field reversal point into the region of comparatively low radial electric field at the potential (cathode) electrode. This enabled us to prevent the critical shunting of the vacuum diode by the stray radial electron beam emitted from the cathode electrode in the low magnetic field region.

The structure of the PMFS field was such that for the 70-GHz BWO of compact geometry the tubular cathode of diameter 2.5 mm was in a region where the magnetic field was no less than 10 kOe and the slow-down system in a region with  $H_z \sim 14.5 \text{ kOe}$ . Using a movable end collector beam autographs on dozimetric film were obtained at various points of the drift chamber. At the outlet of the anode unit the beam had a rather uniform annular structure (Fig.3). The average diameter of the autograph ( $\sim 2.2 \text{ mm}$ ) indicates that the densest electron beam fraction is emitted by the inner edge of the tubular cathode. This completely agrees, for instance, with the calculations reported in Ref.6. The electrons emitted from the outer cylindrical surface of the cathode have elevated transverse velocities and, correspondingly, an increased radius of the cyclotron orbit. As a result, the "inner" annular beam whose wall thickness is 0.3 mm and current density  $\sim 5 \times 10^4 \text{ A/cm}^2$  is surrounded by a lesser dense background. The presence of the external electron fraction is responsible for the electron beam losses in the anode unit (inner diameter of 3 mm) that cause an erosion of the latter. These circumstances are critical for the 70-GHz BWO where the parameter  $\delta r$  was  $\sim 0.3 \text{ mm}$  and the beam was transported along the slow-down system walls at a distance comparable with this value. The situation associated with the collimation of the beam by the anode hole can be simplified by increasing the cathode diameter and by using a 35-GHz slow-down system with the cross section two times as large.

$B_r = 1.0\text{--}1.2 \text{ T}$  and a nearly rectangular hysteresis loop. Adding the rare-earth elements Dy and Tb increases its coercitive force to  $H_c \sim 20 \text{ kOe}$ . The actual system was designed based on the general principles underlying the optimized designing of magnetic systems [5]. The system developed is certainly an approximation to a perfect system and its parameters have been determined based on a trade-off of complexity against achievable performance. A numerical simulation has shown that with  $B_r = 1 \text{ T}$  and  $H_c = 17\text{--}20 \text{ kOe}$ , an axial magnetic field of  $\sim 15 \text{ kOe}$  is quite realizable within a distance of 40 mm. Magnets with  $H_c = 19\text{--}20 \text{ kOe}$  and  $B_r = 1.15 \text{ T}$  had been made that produced an induction of 0.95–1.02 T at the working point. The magnetic system was fabricated from individual units whose dimensions were optimized to produce the highest possible axial field uniform to within 5% in the working region. The external appearance of the RADAN 303B accelerator and of the BWO with a permanent MFS is shown in Fig.2.

For comparison, Fig.1a and Fig.1b give the geometries of the pulsed solenoid winding [1] and the cross-sectional profile of a permanent magnet which provide an axial magnetic fields with nearly identical lengths of uniform regions. Herein, the axial field distribution in the focusing systems is also given. The  $H_z(z)$  dependence for the PMFS (see Fig.1b) is characterized by a sharper fall on both sides of the uniform region and by subsequent field reversal. This was not problem for the region at the beam collector (where the PMFS channel diameter is a minimum). It is more difficult to provide the required field profile in the vacuum diode region. In our case, however, the MICD envelope diameter was rather small and the input section of the magnet enclosed entirely the diode envelope. Thus, we were able here to shift the

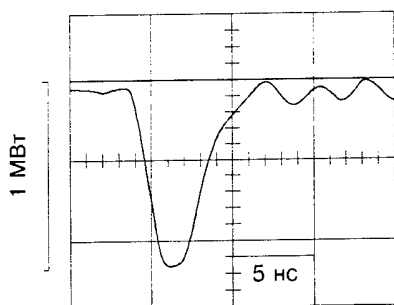


Fig.5. Waveform of a microwave pulse generated by a relativistic BWO with a permanent-magnet focusing system.

Measurements have shown that the beam operating current (0.7 - 0.8 kA) was insignificantly higher than the starting current of the BWO (0.5 kA). In addition to the mentioned collimation of the beam, emission centers were observed on the cathode holder that produced a shunting current. The position of the emission centers coincided in the main with the region where, according to a numerical simulation [7], electrons with the "shortest" paths to the anode electrode are emitted (Fig.4b). The presence of a shunting beam can be considered as another reason for the decrease in beam operating current in our experiment. When the beam current was a little higher than the starting current the microwave oscillation was unstable. This manifested itself in a strong dependence of the microwave power level on the spread in peak accelerating voltages, which is not typical of BWOs. Nevertheless, the microwave pulse duration (fig.5)

corresponded to the beam current duration and the output power of the device achieved 1 MW ( $E_{01}$  mode) at 100 pps.

Thus, a permanent magnet focusing system for a 70-GHz relativistic BWO has been realized experimentally. The field strength and configuration were quite suitable for the formation and transportation of a uniform annular REB of duration 4 ns with a current of  $\sim 1$  kA and an energy of  $\sim 250$  keV. The electron-optical system based on permanent magnets has reduced substantially (by an order of magnitude) energy consumption of the high-repetition-rate relativistic microwave oscillator. This lifts some restrictions for the practical use of high-power microwave devices with high-current REBs. Note that this evidently offers promise for compact short-wave systems but is questionable for long-wave, high-current devices, for systems with hyperdimensional resonators, and for long-pulse systems. For the last three types of devices, the restrictions will be related to the large transverse dimension of the magnetic system channel in the resonator region (typically  $\sim 4 - 5$  cm) and, especially, in the vacuum diode region. Here, to satisfy the requirements for electric strength, with large pulse durations one will have to increase substantially the vacuum insulator and screening electrode diameters. It seems questionable whether it is possible to cover by a permanent magnet the envelope of such a vacuum diode to provide the required magnetic field and the shift of the field reversal point into an acceptable region.

## References

- [1] M.I.Yalandin, G.T.Smirnov, V.G.Shpak, et al.. In: Proceedings of 9th IEEE International Pulsed Power Conference.- Albuquerque, NM, USA, 1993, pp.388-391.
- [2] V.G.Shpak, S.A.Shunailov, M.I.Yalandin, et al. IET, 1993, Vol. 36, Issue 1, pp.106-111.
- [3] N.M.Bykov, V.P.Gubanov, A.V.Gunin, et. al.. In: Relativistic High-Frequency Electronics, Issue 5, Gorky: IPF AN SSSR, 1988, pp.101-124, (in Russian).
- [4] A.S.Elchaninov, F.Ya.Zagulov, S.D.Korovin, et al.. In: Relativistic High-Frequency Electronics, Issue 2, Gorky: IPF AN SSSR, 1981, pp.5-21, (in Russian).
- [5] S.V.Zakov, Yu.G.Lebedev, V.G.Gass. In: Proceedings of Intern. Symp.: Investigations of problems connected with development of magnetic systems for new electrical machines... Suzdal, USSR, May 21-26,1990. Moscow: Interelectro,1991, pp.72-80.
- [6] S.D.Korovin, I.V.Pegel. JTE, 1992, Vol.62, Issue 4, pp.139-145 (in Russian).
- [7] M.A.Tiunov, B.M.Fomel, V.P.Yakovlev. SAM-Interactive Code for Electron Gun Evaluation, Preprint INP-87-35, Novosibirsk, 1985, (in Russian)

## High Power Microwave Oscillator: Vircator-Klystron

Weihoa Jiang, Katsumi Masugata, and Kiyoshi Yatsui  
*Laboratory of Beam Technology, Nagaoka University of Technology*  
*Nagaoka, Niigata 940-21, Japan*

A new method for obtaining current modulation of intense relativistic electron beam is proposed and demonstrated by numerical simulations. The mechanism of the modulation is based on the virtual cathode oscillation. Two-dimensional particle-in-cell simulation results have shown that, within a distance of 4 cm in the direction of beam propagation, the electron beam with the electron energy of 500 keV and the current of 3.3 kA is modulated with a current modulation amplitude up to  $\sim 57\%$ . This modulation mechanism is expected to be used in high power microwave oscillator "vircator-klystron".

### I. Introduction

Microwave emission by an electron beam is the result of the interaction between the electromagnetic wave and the modulation of the electron current. There are many bunching mechanisms that are associated with various high-power microwave sources.[1,2] Meanwhile, in most of these devices, the beam current is strictly limited by the space-charge effect of the electron beam. The limit in the beam current is one of the limitations in the microwave output power of many microwave generators.

The space-charge effect itself can become a bunching mechanism of the high-current electron beam. In virtual cathode oscillator, the electron currents of both reflected and transmitted electron beams are modulated due to the oscillation of the virtual cathode which is formed by the space-charge of the electron beam. The current modulation of the reflected electron beam interacts with the electromagnetic wave. In this beam-field interaction, net power flow from the beam to the wave may occur if a certain phase relation is satisfied. This is the mechanism of microwave generation by virtual cathode oscillator.[3]

The current modulation of the transmitted beam can be also used in microwave generation. For example, one can pass the transmitted electron beam through a resonator, which may be the same as the output cavity of the relativistic klystron amplifier [4,5], where part of the beam energy can be converted to microwave energy due to the interaction of the current modulation of the beam with the resonant mode of the electromagnetic field. However, in the virtual cathode oscillator, the modulation amplitude of the transmitted beam current is usually very small compared to the total injected electron current. This phenomenon is the result of the following facts. When the ratio of the injected current to the space-charge limited current ( $I_{in}/I_{sc1}$ ) is high, most of the electrons are reflected by the virtual cathode so that the transmitted beam current is only a small fraction of the total injected beam current. When  $I_{in}/I_{sc1}$  is close to unity, the reflected beam current is low so that the feedback of the beam to the field is weak resulting in small oscillation amplitude of the virtual cathode.

It is found in this paper that, if the electron energy of the injected beam is modulated,

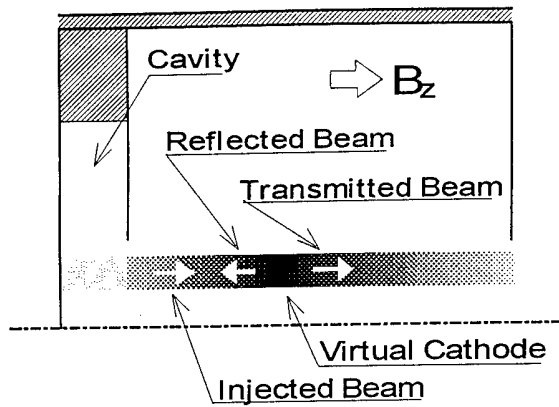


Fig. 1 Model for two-dimensional, electromagnetic, relativistic particle-in-cell simulation.

large amplitude of current oscillation of the transmitted beam can be obtained when the injected current is closed to, or even smaller than, the space-charge limited current.

This modulation mechanism is proposed for use in a new microwave oscillator "vircator-klystron". As in the klystron, the electron energy of the injected beam is modulated in the bunching cavity and the microwave energy is extracted in the output cavity from the current modulation of the electron beam. The difference from klystron is that, in the vircator-klystron, the energy modulation of the electron beam is converted to current modulation due to virtual cathode oscillation and that the bunching cavity is energized by the reflected electron beam rather than an external microwave source.

## II. Two-Dimensional Particle-in-Cell Simulation Results

Particle-in-cell simulations are carried out to explore the current modulation of an annular electron beam induced by the virtual cathode oscillation. The simulation code is 2.5-dimensional (two-dimensional in space and three-dimensional in momentum), electromagnetic, and relativistic. The simulation model is shown in Fig. 1, which consists of two areas, the cavity area and the virtual cathode area. An annular electron

beam is injected from the left-hand side boundary. When the injected current is higher than the space-charge limited current, a virtual cathode is formed in the virtual cathode area. It is expected that the reflected electron beam excites the cavity mode which modulates the energy of the injected electron beam. As a result, the virtual cathode oscillates in the frequency of the fundamental TM mode of the cavity so that the transmitted electron beam is modulated.

The parameters used in the simulations are: the electron energy 500 keV, the electron current 3.3 kA, the beam outer radius 8 mm, the beam thickness 2 mm, the cavity radius 4.5 cm, the cavity width 1 cm, the cavity center-opening radius 1 cm, the virtual cathode area radius 4 cm, the virtual cathode area width 3 cm, and the strength of the axial magnetic field 8 kG. The boundaries are all conducting surfaces except that at the central axis.

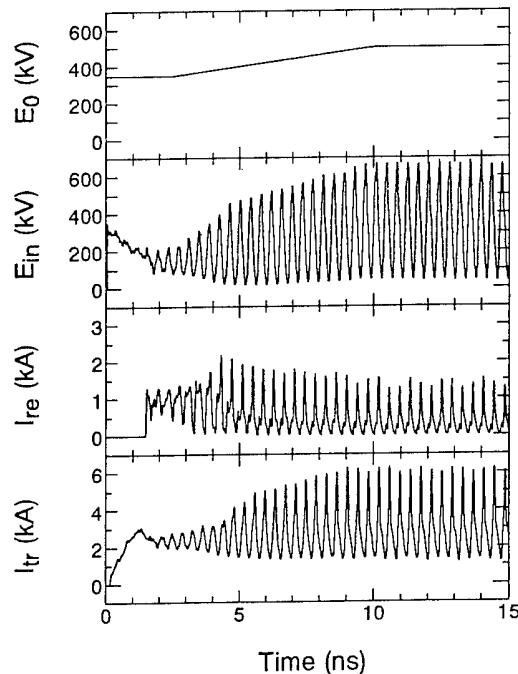


Fig. 2 Time histories of the initial electron energy ( $E_0$ ), the electron energy obtained at the boundary between the cavity and the virtual cathode area ( $E_{in}$ ), the reflected electron current ( $I_{re}$ ), and the transmitted electron current ( $I_{tr}$ ).

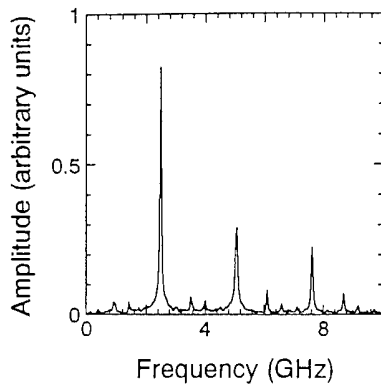


Fig. 3 Fourier transform of the transmitted electron current ( $I_{tr}$ ) shown in Fig. 2.

Figure 2 shows the initial electron energy ( $E_0$ ), the electron kinetic energy obtained at the boundary between the cavity and the virtual cathode area ( $E_{in}$ ), the reflected current ( $I_{re}$ ), and the transmitted current ( $I_{tr}$ ). The reflected and the transmitted currents are obtained at the left and the right boundaries, respectively. The injected current is lower than the space-charge limited current ( $\sim 4.8$  kA) in order to obtain higher transmitted-to-reflected current ratio. However, if the beam is injected with the electron energy of 500 keV and the current of 3.3 kA from the beginning, all electrons will be transmitted and there will be no oscillation and modulation, since the cavity oscillation does not occur before the electron reflection is initiated. In order to initiate the electron reflection, the electron injection energy is reduced to 350 keV at  $t = 0$ . The electron energy is increased to 500 keV in the following several nanoseconds during which the cavity oscillation grows and the electron energy is modulated so that the virtual cathode oscillation and the electron reflection continue even when the current is lower than the space-charge limited current. The average currents carried by the transmitted and the reflected beams are 2.87 kA and 0.43 kA, respectively, corresponding to  $\sim 87\%$  and  $\sim 13\%$  of the injected current.

Figure 3 shows the Fourier transform of the transmitted current ( $I_{tr}$ ) shown in Fig. 2.

The peak obtained at  $\sim 2.55$  GHz gives an amplitude of the current oscillation of  $\sim 1.9$  kA, about 57 % of the injected current.

It is noted that the energy modulation of the injected electron beam is induced by the cavity oscillation which is driven by the current modulation of the reflected beam. Consequently, for given electron beam parameters, the oscillation frequency is not a free parameter since the beam parameters determine the phase relation between the cavity oscillation and the virtual cathode oscillation.[6] Therefore, the frequency of the cavity fundamental mode has to be chosen so that the current modulation of the reflected beam is in an appropriate phase to energize the cavity oscillation.

### III. Vircator-Klystron

The simulation results presented in the above sections have shown that the intense relativistic electron beam can be modulated by the virtual cathode oscillation. One of the most important applications of the modulated electron beam is the generation of high-power microwave. By adopting part of the configuration of the relativistic klystron amplifier, we propose a new type of high-power microwave oscillator which is shown schematically in Fig. 4. The whole system is immersed in an axial magnetic field. An annular electron beam is generated by a foilless diode and is passed through a gap feeding the first cavity. A virtual cathode is formed in the virtual cathode area. The simulation results given in the last section show that most of the electron current can be transmitted to the output cavity with the current modulation induced by the virtual cathode oscillation. In the output cavity, electromagnetic energy is extracted from the current modulation of the electron beam, in the same way as the relativistic klystron amplifier. Using the results given in the last section, it is estimated that the maximum microwave power of  $\sim 470$  MW can be obtained from the electron beam with elec-

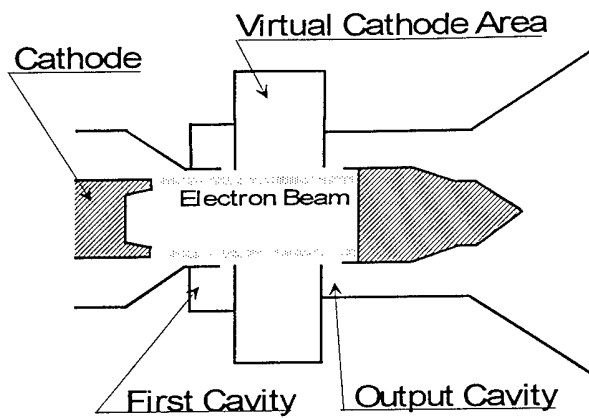


Fig. 4 Microwave oscillator "vircator-klystron".

tron energy of 500 keV and beam current of 3.3 kA, with the beam-to-microwave efficiency of  $\sim 28.5\%$ .

The vircator-klystron is compared with the klystron and vircator as follows.

In the relativistic klystron amplifier [4,5], the electron beam is modulated by exciting the space-charge waves with a cavity that is pumped by an external microwave source. The space-charge waves in the electron beam grow when the beam is propagated through a drift tube and interacts with another cavity. For a certain diameter of the drift tube, the electron beam current that can be propagated is limited. In order to increase the output microwave power, it is necessary to increase the beam current. Accordingly, the diameter of the drift tube is increased, resulting in lower frequency of the microwave. In the new configuration shown in Fig. 4, however, there is no drift tube on the way of electron beam propagation. Therefore, it is expected that higher current can be modulated by the virtual cathode oscillation than by the relativistic klystron. In addition, by eliminating the drift tube and the external microwave source, the vircator-klystron is expected to be more compact than the relativistic klystron.

In the virtual cathode oscillator (vircator)[3], the electron beam is modulated by the virtual cathode oscillation. However, most of the injected electron

current is reflected by the virtual cathode. In this case, the application of the modulated electron beam is very difficult. Insufficient interaction between the current modulation and the electromagnetic field is the major reason for the low efficiency of the vircator. In contrast, the modulation mechanism proposed in this paper offers a modulated electron beam that is propagated toward the downstream. By using the rf energy extraction technology developed for the relativistic klystron amplifier, high-efficiency microwave generation can be obtained from the electron beam modulation. Therefore, the vircator-klystron is expected to be more efficient than the vircator. In addition, since the frequency is determined by the cavity mode, a narrow microwave bandwidth can be expected, unlike the vircator where the oscillation frequency is determined by the electron beam parameters.

## References

- [1] *High Power Microwave Sources*, edited by V. Granstein and I. Alexeff (Artech House, Norwood, 1987), Chapters 4 - 14.
- [2] J. Benford and J. Swegle, *High-Power Microwaves* (Artech House, Boston and London, 1992), Chapters 5 - 10.
- [3] W. Jiang, K. Masugata, and K. Yatsui, *Phys. Plasmas* **2** (1995) 982.
- [4] M. Friedman, J. Krall, Y. Y. Lau, and V. Serlin, *Rev. Sci. Instrum.* **61**, 171 (1990).
- [5] M. V. Fazio, W. B. Haynes, B. E. Carlsten, and R. M. Stringfield, *IEEE Trans. Plasma Science* **22**, (1994) 740.
- [6] W. Jiang, K. Masugata, and K. Yatsui, "New Configuration of Virtual Cathode Oscillator for Microwave Generation", *Phys. Plasmas*. **2** (1995) 4635.

# EFFECT OF PLASMA FORMATION ON ELECTRON PINCHING AND MICROWAVE EMISSION IN A VIRTUAL CATHODE OSCILLATOR

M. Yatsuzuka, M. Nakayama, S. Nobuhara, D. Young\* and O. Ishihara\*

*Himeji Institute of Technology, Himeji, Hyogo 671-22, Japan*

*\* Texas Tech University, Lubbock, Texas 79409-3102, U.S.A.*

## Abstract

Time and spatial evolutions of anode and cathode plasmas in a vircator diode are observed with a streak camera. A cathode plasma appears immediately after the rise of a beam current and is followed by an anode plasma typically after about 30 ns. Both plasmas expand with almost the same speed of order of  $10^4$  m/s. The anode plasma was confirmed as a hydrogen plasma with an optical filter for  $H\beta$  line and study of anode-temperature rise. Electron beam pinching immediately followed by microwave emission is observed at the beam current less than the critical current for diode pinching in the experiment and the simulation. The electron beam current in the diode region is well characterized by the electron space-charge-limited current in bipolar flow with the expanding plasmas between the anode-cathode gap. As a result, electron bombardment produces the anode plasma which makes electron beam strongly pinched, resulting in virtual cathode formation and microwave emission.

## Introduction

Electron pinching immediately followed by microwave emission was observed in the virtual cathode oscillator (vircator) with a large aspect ratio, when a electron beam current exceeded a critical current for electron beam pinching[1,2]. On the contrary, the experiment in Himeji showed the strong microwave emission associated with electron pinching at the beam current below the critical current [3,4]. And the electron beam current in the diode region was found to be well characterized by the electron space-charge-limited current in bipolar flow, suggesting the presence of anode and cathode plasmas expanding between the anode-cathode gap. In this paper we report the experimental observation of plasma formation at the anode and cathode surfaces with a streak camera and the simulation results of strong electron pinching due to the presence of anode plasma.

## Experiment

The vircator diode consists of an annular cathode with its outer radius  $R_c$  of 1.5 cm and thickness of 1.0 mm and an aluminum foil anode of 15  $\mu$ m in thickness. The A-K gap length  $d$  was varied from 0.2 to 0.7 cm. Electron beam currents were measured using a ns-response Rogowskii coil at the upstream (1.1 cm from the anode) and downstream (0.1 cm from the anode). The diode voltage was measured by a resistive divider at the location close to the anode. The emitted microwave propagated along a circular waveguide (radius  $R = 2.25$  cm and 2 m in length) and emitted into a free space through a conical horn. The microwave signals were detected by an open-ended rectangular waveguide antenna (WRJ-10) located at the distance of 1 m from the conical horn. The total microwave power was calculated by numerically integrating the radiation pattern. The microwave frequency was determined with a

long waveguide dispersive delay line (WRJ-10, cutoff frequency  $f_c = 6.55$  GHz, and length  $L = 105.7$  m). The light from the anode and cathode plasmas was imaged onto the slit of the streak camera (HAMAMATSU C1587) through a quartz window of the wall at the diode region and a focusing lens. X-rays radiated from the anode due to electron beam bombardment were measured using a scintillator ( $\text{BaF}_2$ ) and a photomultiplier, where the spatial resolution for X-ray measurement was  $\pm 7$  mm which is less than the cathode radius.

### Results and Discussion

The typical time evolution of electron beam current, microwave emission and X-ray from the anode center for  $d = 5$  mm is shown in Fig. 1. As seen in Fig. 1, microwave emission appears at the same time of the strong radiation of X-ray from the anode center after about 70 ns of rise of beam current. The beam cross-section measured with an X-ray pinhole photograph was typically 8 mm in diameter. When the axial magnetic field of 0.14 T is applied, the beam cross section was an annular with almost the same diameter as the cathode and there was no microwave emission. These results indicated that strong beam pinching is essential for microwave radiation. The critical current for diode pinching is estimated to be 35 kA with the present experimental parameters (beam energy = 350 kV,  $R_c = 1.5$  cm and  $d = 5$  mm) which is larger than the observed diode current of 27 kA at the maximum of microwave emission in Fig. 1.

Figure 2 shows the typical time history of diode voltage, beam current, microwave emission, and plasma luminosity at both surfaces of anode and cathode for  $d = 5$  mm. As seen in Fig. 2, a cathode plasma appears on the cathode surface immediately after the rise of a beam current. After about 30 ns of the rise of beam current, an anode plasma on the anode surface is formed. The cathode and anode plasmas in the initial phase expand with approximately the speed of  $1.8 \times 10^4$  m/s and  $2.6 \times 10^4$  m/s, respectively. The A-K gap is

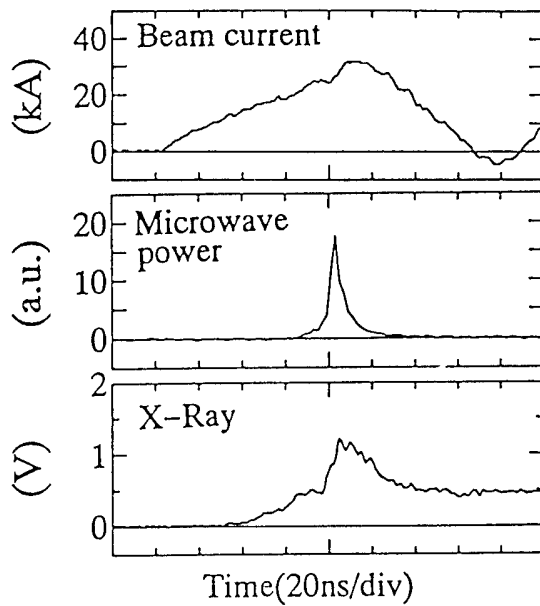


Fig. 1. Time history of beam current, microwave emission and X-ray radiated from the anode.

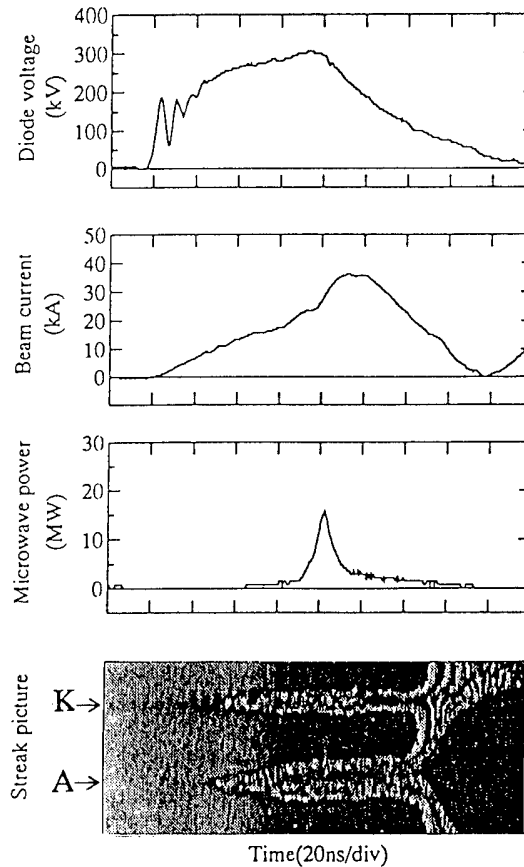


Fig. 2. Time history of diode voltage, beam current, microwave emission and luminosity of anode and cathode plasmas.



closed by both plasmas after about 140 ns from the onset of anode plasma. The maximum microwave emission occurs after 80 ns of the rise of beam current before the gap closure. The microwave peak power was 15 MW with the frequency of 11 GHz and pulse duration of 10ns.

To identify the source of anode and cathode plasmas, the plasma luminosity through an optical filter for  $H_{\beta}$  line (wavelength: 487 nm and band width:  $\pm 5\text{nm}$ ) was examined and is shown in Fig. 3. After passing through the optical filter, the luminosity of anode plasma remains, but that of the cathode plasma disappears. This suggests that the anode plasma source is the impurities such as water and oils adhered or absorbed on the anode surface, while the cathode plasma is the ionized metal of cathode material. To estimate the temperature rise caused by electron beam bombardment to the anode, we assume that electrons pass through the anode foil once before microwave emission, because the potential of virtual cathode is not enough to repel incoming electrons to the anode. As the electron range  $X$  in the aluminum is much larger than the anode thickness  $\delta$ , we also assume that  $\delta/X$  of the beam energy  $E$  deposits in the anode. Then, the temperature rise of the anode is written as

$$\Delta T = \frac{\delta}{X} \frac{E J_b t \times 10^{-9}}{\rho C_p X} \quad (^{\circ}\text{C}) \quad (1)$$

where  $J_b$  is the beam current density,  $t$  is time, and  $\rho$  and  $C_p$  are the mass density and the specific heat of the anode material, respectively. The electron range in the aluminum is given by [5]

$$X = \frac{0.407E^{1.38}}{\rho} \quad (\text{cm}) \quad (2)$$

Substituting the values of beam energy and beam current in Fig. 2 into eqs. (1) and (2), the anode temperature rise is estimated with  $\rho=2.69 \text{ g/cm}^3$  and  $C_p=0.81 \text{ J/g} \cdot ^{\circ}\text{C}$  for aluminum, the result of which is shown in Fig. 4. Here the annular beam cross section of the same dimension as the cathode was assumed to estimate the beam current density from the beam current in the diode region, since the electron beam should be annular before its pinching. As

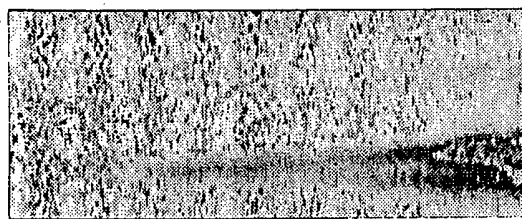


Fig. 3. Streak picture of plasma luminosity through an optical filter for  $H_{\beta}$  line.

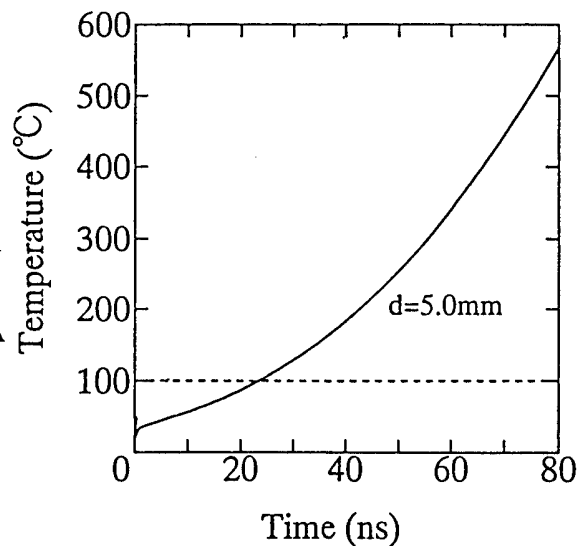


Fig. 4. The anode temperature rise due to electron bombardment.

seen in Fig. 4, at the onset of anode plasma ( $t=30\text{ns}$ ) the anode temperature is  $130^\circ\text{C}$  which is enough to vaporize the impurities such as water or oils adhered on the anode surface, but less than the melting point of aluminum ( $660.4^\circ\text{C}$ ). These temperature studies support our conclusion that the impurities on the anode surface form the anode plasma.

The trajectory plot of the cathode electrons by MAGIC simulation code is shown in Fig. 5 (a) for non-ion emission from the anode and (b) for ion emission from the anode, where the anode plasma is assumed to expand with the speed of  $0.85\text{cm}/\mu\text{s}$ . As seen in Fig. 5, the strong pinching of electrons is observed with the presence of anode plasma.

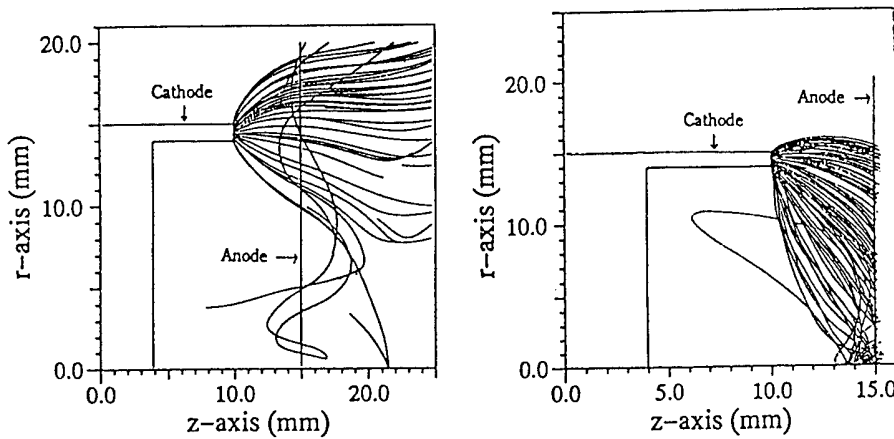


Fig. 5. The trajectory of electrons (a) for non-ion emission and (b) for ion emission.

### Conclusion

A cathode plasma appears on the cathode surface immediately after the rise of beam current. After about 30 ns of the rise of beam current, an anode plasma is formed. Both plasmas expand with approximately the same speed of  $2\text{ cm}/\mu\text{s}$ . After 30 ns, the anode temperature is estimated to be approximately  $130^\circ\text{C}$  which is enough temperature for releasing adsorbed gases such as  $\text{H}_2\text{O}$  from the anode, but is less than the melting point of aluminum. The anode plasma was confirmed as a hydrogen plasma with plasma observation through an optical filter for  $\text{H}\beta$  line as well as anode-temperature rise. The MAGIC simulation of electron trajectory shows the strong electron pinching with the presence of anode plasma.

In summary, electron bombardment to the anode produces the anode plasma which makes electron beam strongly pinched, resulting in virtual cathode formation and microwave emission.

- [1] Benford, J., Sze, H., Woo, W. and Harteneck, B.: Phys. Rev. Lett., 56 (1986) 344.
- [2] Sze, H., Benford, J., Woo, W. and Harteneck, B.: Phys. Fluids, 29 (1986) 3873.
- [3] Yatsuzuka, M., Nagakawa, K., Hashimoto, Y., Aoki, K., Nobuhara, S. and Ishihara, O.: Proc. of 10th Inter'l Conf. on High Power Particle Beams, (1994) 869.
- [4] Yatsuzuka, M., Nagakawa, K., Hashimoto, Y., Ishihara, O. and Nobuhara, S.: IEEE Trans. on Plasma Science, 22 (1994) 939.
- [5] Glendenin: Nucleonics, 2 (1948) 12.

## FORMATION AND DIAGNOSTIC OF HELICAL GYROTRON ELECTRON BEAMS

A.N.Andronov, V.N.Ilyin, V.A.Khmara, A.N.Kuftin, V.K.Lygin, O.I.Luksha,  
V.N. Manuilov, A.S.Postnikova, S.V.Robozerov, G.G.Sominsky, Sh.E.Tsimring,  
V.E.Zapevalov

*Institute of Applied Physics, GYCOM Ltd., Nizhny Novgorod, Russia*  
*St.Petersburg Technical University, St.Petersburg, Russia*

### Abstract

The improved method of calculating intense helical electron beams based on assigning the initial velocity spread and finding functions of electron distribution over oscillatory and longitudinal velocities is presented. The methods of ensuring and testing the cathode emission homogeneity are discussed. The data obtained in numerical simulation modeling and experimental measurements for beams with various topologies and emitter properties are compared. The evolution of the function of electron distribution over oscillatory velocities as the beam current grows is traced.

### Introduction.

In order to provide helical electron beams (HEB) of powerful gyrotrons, magnetron-injection guns (MIG) with effective thermocathodes operating in the regime of the emission current limitation are used. The HEB quality and gyrotron performances are defined both by the cathode emission processes and the processes occurring in the electron beam during its formation and transportation.

Therefore it is necessary:

- To develop the theory and practical methods of calculating gyrotron HEBs, which include the refinement of calculated models, the development of the corresponding procedures of calculation and software numerical simulation, and the optimization of magnetic and electron-optic systems ( with the optimization of the electrode form );
- To refine the technology of fabricating and control of the emitter quality to achieve a high homogeneity of the electron work function and the temperature on the cathode surface;
- To develop and refine the methods of the experimental study of HEB characteristics, static and dynamic effects in the process of the HEB formation and transformation as well as the development of the routine diagnostics of HEB quality.

### The method of the theoretical analysis of HEB.

The model with zero initial velocities  $v_0$  (EPOSR-code) used recently conforms rather well to the experimental data for the value  $t_{\perp}$  (the ratio of the oscillatory energy to the total one) and gives essential divergence of the velocity spread  $\delta v_{\perp}$  [1]. In this connection at the first stage the procedure of finding HEB parameters adequate to the experimental one was developed ( for the correct comparison of the calculated and experimental HEB parameters).

In the numerical simulation the initial velocity spread [2] is taken into account in the calculated model (EPOS-V); as the result the electron distribution function over oscillatory velocities  $f(v_{\perp})$ , longitudinal velocities (energies), the curve of the cut-off of the passing

beam current and the portion of electrons captured into the magnetic trap are found. Note that in this case  $\delta v_{\perp}$  may be calculated using any levels including those adopted for the experimental measurements 0.1, 0.5 and 0.9 levels of the curve of the collector current cut-off [2]. The given procedure permits to take into account more correctly the influence of the electrons, reflected from the magnetic trap, and the azimuthal inhomogeneity of the current density on HEB parameters.

### **Experimental set-ups.**

The experimental study of MIGs of powerful gyrotrons which form intense HEBs of various topologies and various types of emitters was performed in the automatic set-up in the scaling regimes using the retarding field method [3]. The refined automation experimental set-up permits to define the HEB characteristics ( $t_{\perp}, \delta v_{\perp}, f(v_{\perp})$  and etc). The application of this system allows to increase the accuracy and the quality of measurements, to obtain and process a large volume of the experimental data for a short period of time.

The other complex of the measuring apparatuses is meant for the study of the analysis of the cathode surface composition, the inhomogeneity of the electron work function, the temperature and the emission density, as well as the study of the oscillation of the space charge in the beam, HEB inhomogeneity and their connection with emission inhomogeneity.

### **The results of numerical simulation, technological developments and experimental study.**

The results of a new numerical simulation procedure and the experimental data for the basic beams with various topology are presented. For each beam type the calculated and experimental dependences of  $t_{\perp}$  and  $\delta v_{\perp}$  on the beam current are compared, including the results obtained in the model with  $v_o = 0$  (fig.1-4). Evolution of  $f(v_{\perp})$  for each beam type as the current grows is studied (fig.5-8). As it is seen, in some cases the function  $f(v_{\perp})$  stops being single-mode as the beam current grows.

Taking into account the electrons reflected by the magnetic trap, the dynamics of the time variation of the electric field on the cathode,  $t_{\perp}, \delta v_{\perp}, f(v_{\perp})$  and the share of trapped particles is studied for various beam current [4]. Some calculation of MIGs are performed taking into account the azimuthal inhomogeneity of the current density [5].

The technology of fabricating impregnated metallic-porous emitter of cathodes with low operating temperature 1050°C and the lifetime up to 10000 hours is developed. The modern technology allows to create the cathodes, the emission inhomogeneity from whose surfaces do not exceed 10% of the average value.

Both low-frequency (up to 100 - 150 MHz) in the trap between the cathode and the magnetic field mirror and high-frequency (500 - 1000 MHz) oscillations caused by the space charge waves in the regime of HEB drift are discovered. The appearance of high-frequency oscillations is of threshold character. The value of the threshold current depends on the magnetic field distribution, emission inhomogeneity and electron velocities. Those oscillations are of a convective character and their amplitude increases in the drift space with moving away from the cathode. The amplitude of low-frequency oscillations falls in this region.

### **Conclusion.**

- The procedure of the numerical simulation of the processes in intense HEB is modernized essentially and it permits now to obtain the electron distribution functions over transverse velocities which allows to compare correctly calculated and experimental data.

- the properties of HEBs are studied experimentally in various regimes using modified automation set-ups, including the obtaining of current-voltage characteristics and the electron distribution functions over longitudinal and transverse velocities.

- the technology of fabricating effective thermoemitters and control of their quality (homogeneity, contrast, stability of characteristics in time, etc.) are developed.

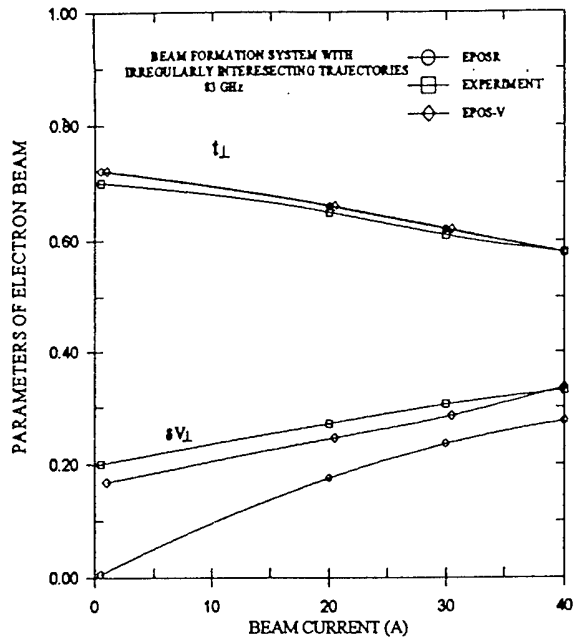


Figure 1

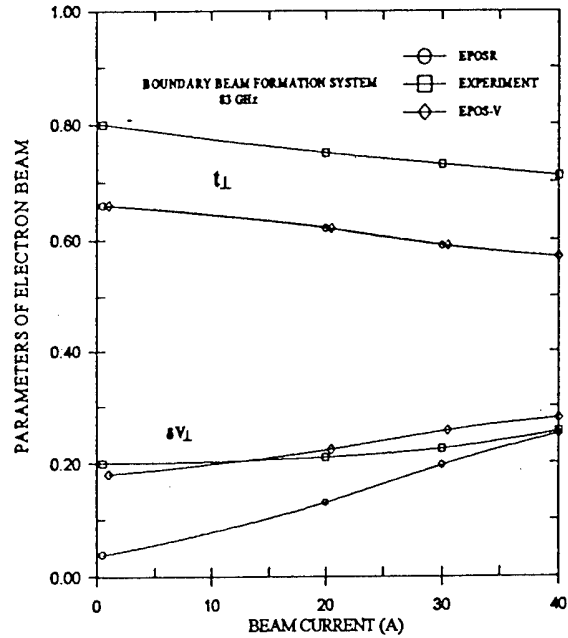


Figure 3

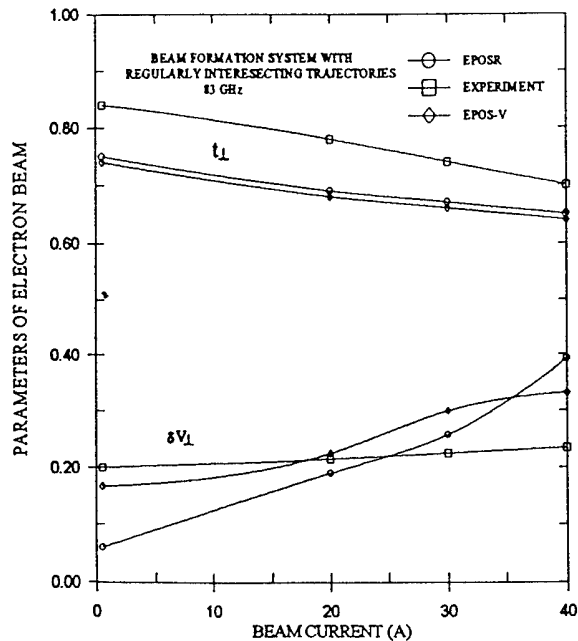


Figure 2

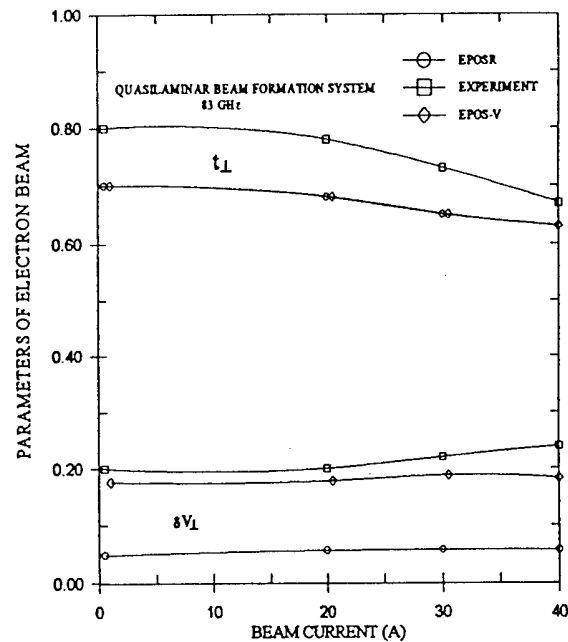


Figure 4

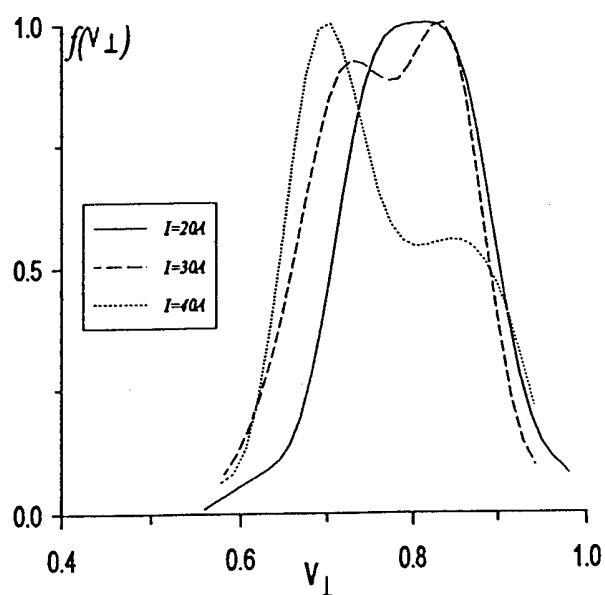


Figure 5: Oscillatory velocity distribution functions in a system with a mixed beam at various currents.

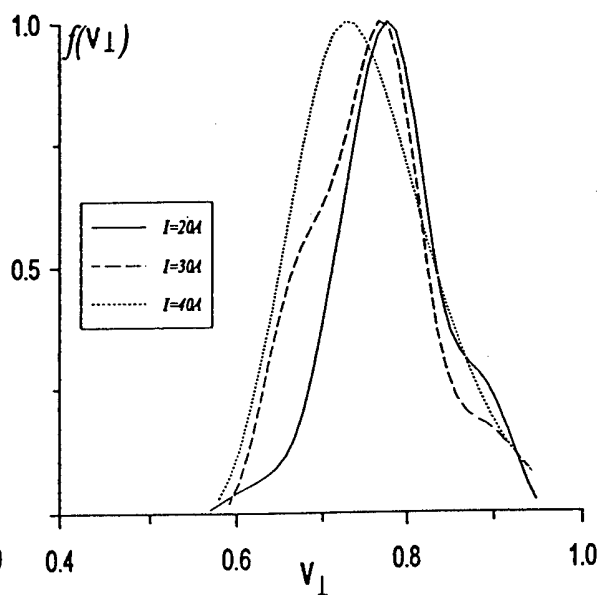


Figure 7: Oscillatory velocity distribution functions in a system with a boundary beam at various currents.

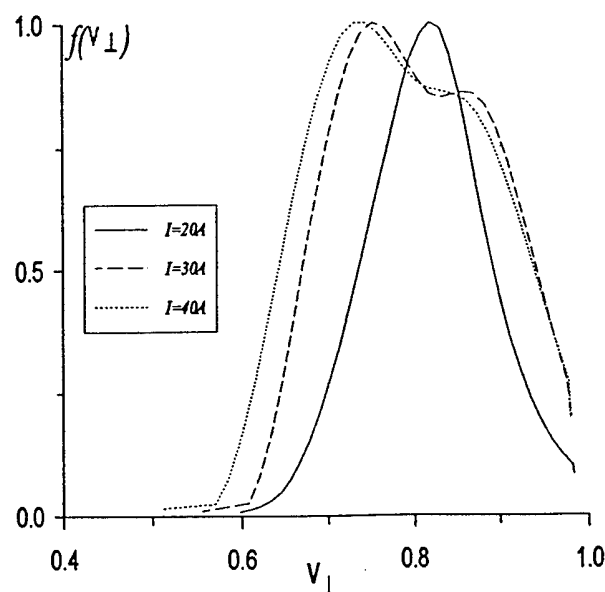


Figure 6: Oscillatory velocity distribution functions in a system with a regularly intersecting beam at various currents.

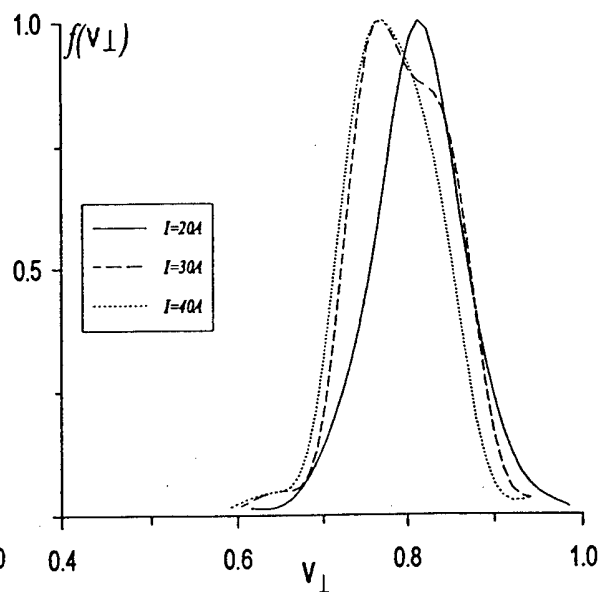


Figure 8: Oscillatory velocity distribution functions in a system with a quasilaminar beam at various currents.

- [1]. Kuftin A.N., Lygin V.K., Tsimring Sh.E., and Zapevalov V.E. Int. J. Electronics, 72(1992), pp.1145-1151.
- [2]. Lygin V.K. Int. J. of Infrared and Millimeter waves, 16(1995), pp.363-376.
- [3]. Avdoshin E.G. and Gol'denberg A.L. Izvestiya Vysshikh Uchebnykh Zavedenii, Radiofizika, 16(1973), pp.1605-1612.
- [4]. Lygin V.K. and Manuilov V.N ITG-Fachbericht, 132,(1995), pp.197-200.
- [5]. Lygin V.K. ITG-Fachbericht, 132,(1995), pp.201-205.

# MULTI-FREQUENCY MICROWAVE PULSE PRODUCTION IN A VIRCATOR

A.G.Zherlitsyn, A.N.Liakshev, G.V.Melnikov

*Nuclear Physics Institute, Lenin Str. 2a, Tomsk 634050, Russia*

## Abstract

The work presents results of the research on microwave pulse production in vircator with multi-frequency content. The vircator is shown to generate electromagnetic irradiation on several frequencies simultaneously, as well as with irradiation frequency re-turning for the generation process.

## Introduction

In present time, relativistic microwave devices generate gigawatt pulses in wide frequency band. This work presents results of researches on production of microwave pulses with multi-frequency content by vircator triode.

## Experimental and Discussion

The microwave irradiation frequency in triode can be changed by changing of cathode-anode gap [1]. The wave length of generated oscillations in triode is determined by conditions of electron beam formation and virtual cathode, and does not depend on external circuit parameters. It allows to use the external circuit with geometrical sizes much higher than irradiation wave length [2].

According to these features, cathode of such generator can be made of separate elements, and their emitting surface can be on different distances from anode. It allows to form separate oscillating electron beams, where oscillation frequency depends on size of cathode-anode gap. So, the microwave pulse with several carriers, i.e. with multi-frequency content, is formed.

But the lack of theoretical and experimental research on such generator operation does not allow to understand, how the oscillations with several carriers change the generation process.

To understand this process, the experiments on triode operation for microwave pulse with different carriers were carried out.

Fig. 1 presents the scheme of experiments. The cathode consisted of two emitters. The gap between 1 emitter and anode was  $d_1=2$  cm, between 2 emitter and anode -  $d_2=1.6$  cm. The triode cathode and anode were in vacuum chamber-resonator with 80 cm diameter and 80 cm length. This chamber was used as an external circuit of the generator.

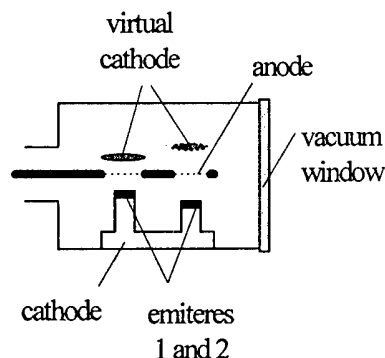


Fig.1. The experimental arrangement.

The voltage source provided the voltage pulse with 500 kV amplitude, 100 nsec duration and 15 kA current in triode. Microwave irradiation was extracted from the resonator through vacuum-tight window. The microwave irradiation power was evaluated by the irradiation directional pattern, the oscillation frequency was measured by tunable pass-band waveguide filters with 38MHz transmission band.

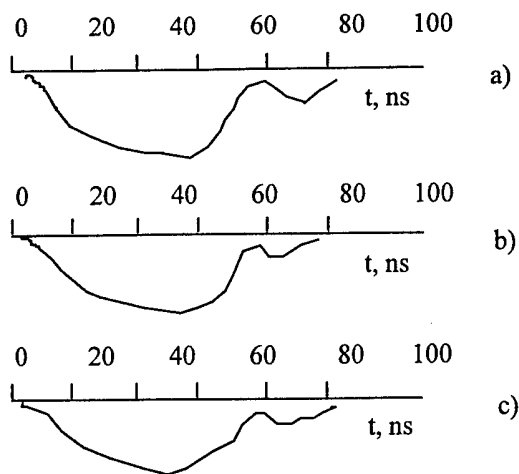


Fig.2. Microwave power output pulse: (a) - without waveguide frequency filter, (b) - after filter  $f = 2530$  MHz, (c) - after filter  $f = 2760$  MHz

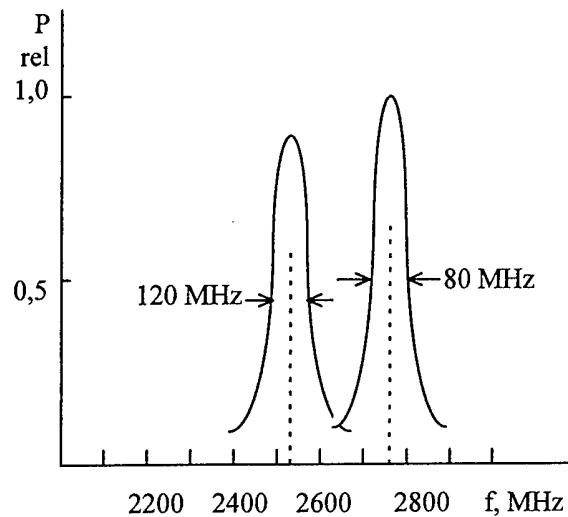


Fig. 3. Frequency spectrum of microwave output pulse.

Figs. 2 and 3 present results of the measurement of microwave pulse irradiation. The microwave pulse parameters show the stable generation in this kind of generators. The high power microwave pulse, containing two frequencies simultaneously, was fixed on the generator output (fig. 2); in  $d_1 = 2$  cm gap with  $f_1 = 2760$  MHz frequency and 300 MW power and in  $d_2 = 1.6$  cm gap with  $f_2 = 2760$  MHz frequency and 400 MW power. The oscillograms of microwave pulses after waveguide filters (fig. 2 b) and c) turned in carrier frequencies, show the appropriate microwave pulse content by these frequencies. On the both carriers, the spectrum width did not exceed 4-5 % (fig. 3). The triode with one emitter (2 emitter,  $d = 1.6$  cm), irradiates on  $f_0 = 2820$  MHz frequency with spectrum width on the half-level of power about 4%, with 1.1 GW power.

The other possibility to produce different irradiation frequency is an operation of vircator triode with microsecond duration voltage sources. In this case, the irradiation frequency is changed for the time of microwave pulse. Fig. 4 shows oscillograms of voltage pulse, current and microwave pulses without filter and after pass-band waveguide filters, turned on different frequencies. The figure shows, that irradiating frequency is changed smoothly for the time of generation.

The analysis of generation process of such irradiated pulses shows, that the voltage pulse amplitude should be constant, and cathode surface should be filled with cathode plasma homogeneously for the effective operation of the generation. The formation of voltage pulse of required shape can be reached by construction and scheme of voltage source. The homogeneous filling of the cathode surface by cathode plasma provided by using of specific multi-needle cathode.

The changing of irradiation frequency for the generation time in vircator is caused by changing of effective gap between anode and emitting surface. In this case, the emitting surface is a boundary of cathode plasma, which moves towards anode. The reduce of effective gap under constant voltage for the time of generation leads to the increase of irradiation frequency. Fig. 4 shows, that the changing of the irradiation frequency is smooth, with rate about 2.1-2.4 MHz/nsec.



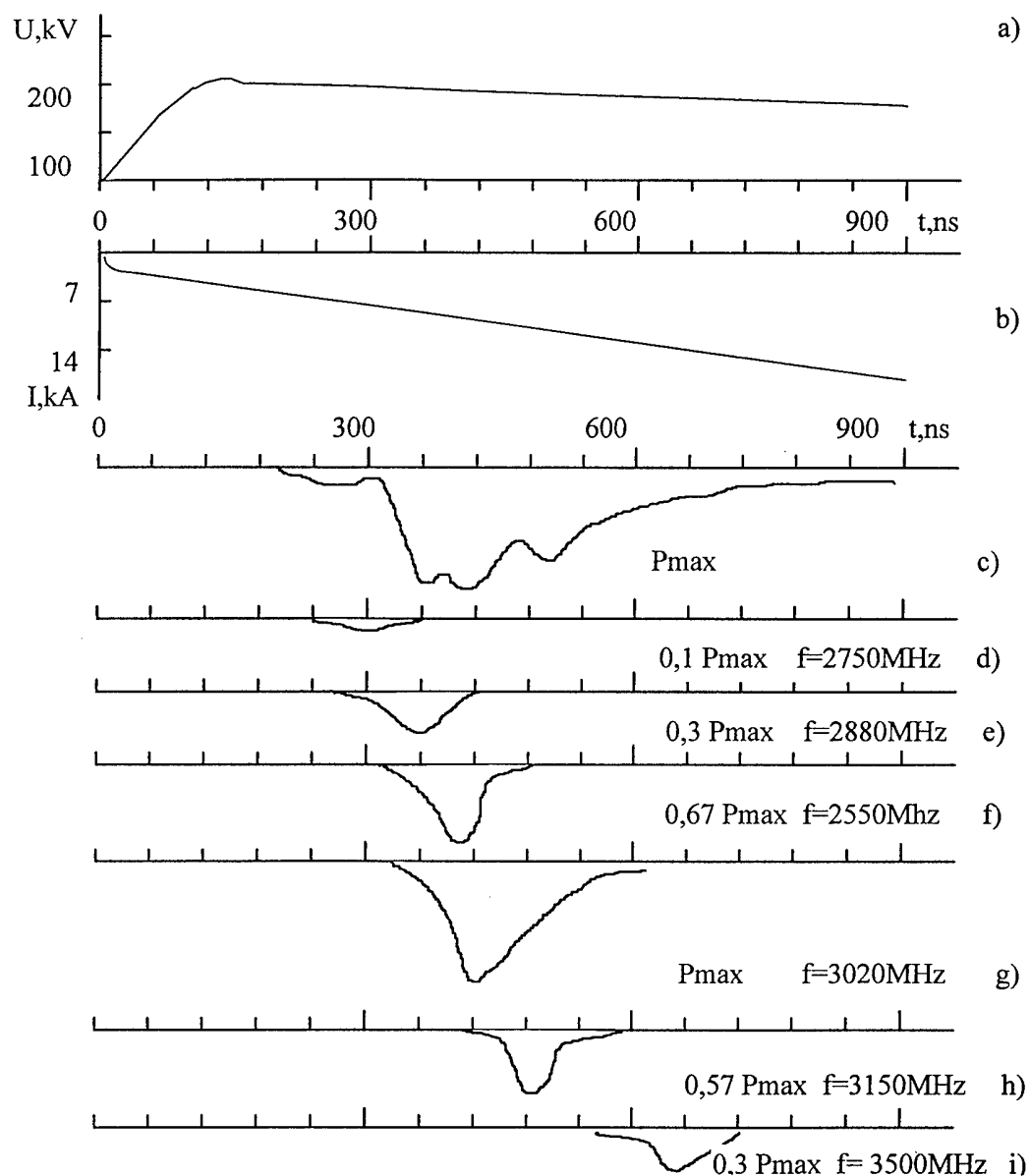


Fig.4. Typical traces for: (a)voltage and (b)current pulses of triode with VC,  
 (c)-microwave output pulse without filter and (d-i)- after filter,  $P_{max}=220$  MW.

### Conclusion

The experimental research shows the possibility to form microwave pulses with multi-frequency content in vircators. The electromagnetic irradiation can be generated simultaneously on several frequencies, as well as with changing of irradiation frequency for the generation process.

### References

1. A.N.Didenko, G.P.Fomenko, I.Z.Gleizer, Ya.E.Krasik, G.V.Melnikov, S.F.Perelygin, Yu.G.Stein, A.S.Sulakshin, V.I.Tsvetkov, A.G.Zherlitsyn. Proc. of 3-th Intern. Conf. on High Power Electron and Ion Beam. Novosibirsk, 1979, v.2, p.683.
2. A.G.Zherlitsyn, G.V.Melnikov, S.I.Kuznetsov. Radiotekhnika i elektronika, 1990, v.35, issue 6, p. 1274.

## RESEARCH OF THE GENERATION OF MICROSECOND MICROWAVE IRRADIATION IN VIRCATOR

A.G.Zherlitsyn, G.I.Kotlyarevski, A.N.Lyakshev, V.I.Tsvetkov

*Nuclear Physics Institute, Lenin Str. 2a, Tomsk 634050, Russia*

### Abstract

The work presents the results of experimental research on microwave microsecond pulse generation in vircator of triode with virtual cathode type. As a result of researches, microwave pulse was formed with the following parameters: 10 cm wave band, 1.1  $\mu$ sec pulse duration, 1.2 GW pulsed power, 600-700 J pulsed energy and 10-12% efficiency.

### Introduction

The increasing of microwave pulse energy in relativistic microwave devices by the increasing of pulse duration has a practical interest.

To form microwave pulses with high level of energy ( $10^2$ - $10^3$  J), a microsecond pulsed high voltage source ( $10^5$ - $10^6$  V) and a high current electron microwave source, which generate electromagnetic irradiation of microsecond duration with gigawatt power level, are used.

The research of the electromagnetic irradiation generation in relativistic microwave devices shows, that the irradiation pulse duration is limited by either plasma, generated by electron beam, or by microwave brakedown in electrodynamics system [1,2]. To eliminate microwave break-down in the device, space-developed systems with geometrical sizes, which exceed the generated wave length, are used. These systems were used in devices of multi-wave Cherenkov generator [3].

The other device, which has the big volume of electrodynamics system, is a vircator triode [4].

### Experimental and Discussion

The earlier researches show the possibility of formation of long microwave pulses in vircator triode [4]. But the power level did not exceed 150 MW. As measurements show, the microwave pulse duration in triode system is limited by time, which is need for plasma to cover cathode-anode distance, as well as by time, which is need for anode plasma to fill vircator triode region. The higher plasma concentration, the shorter the generation process in vircator triode. The low power level of irradiation is caused by small values of accelerated voltage and electron beam current with microsecond duration of pulses. It allows to form the electron beam with high quality (homogeneous on cross-section, small energy dispersion) and high efficiency.

The increasing of power level needs the increasing of accelerated voltage amplitude and electron beam current. The increasing of electron beam power can lead to the increase of cathode and anode plasma concentration, to the worsening of the beam quality and, hence, to the premature stopping of generation and to the reduce of the efficiency. That is why the further researches were directed to the solving of these problems.

The researches of microwave pulsed microsecond generation of high power level ( $>10^8$  W) in vircator triode show, that vircator triode generates when electron beam will reach a certain value of current. This "start current" value is 7-10 kA. It is obvious, that the shorter

voltage pulse front, the faster "start current" value will be reached and the triode microwave generation will start at the less plasma concentration.

With formation of high voltage pulse on the diode cathode-anode gap of vircator triode and extraction of electron flow, the gap is filled by plasma, and diode impedance is reduced. It can lead to the premature voltage reduce in gap and, hence, to the premature generation breakdown. Hence, to support the process of the most smooth voltage change in vircator triode, the voltage source has to have internal resistance much less than diode impedance.

So, for the effective generation in triode system, the voltage source is to form voltage pulses of microsecond duration with short front and "plate" top. These conditions for vircator triode can be satisfied only by energy capacitor of voltage generator type, such as Arkadyev-Marx generator. This generator has a low internal resistance; it forms microsecond pulse with "plate" top and short front. Moreover, it is simple and reliable. The use of sources with induction energy storage does not allow to form microsecond voltage pulse without additional expenses and complex decisions.

The development of microsecond voltage source for triode system has characteristics as a following: 24 kJ energy, 33 nF shock capacity, 6  $\mu$ Gn induction, 1.2 MV output voltage, 120 nsec front duration with 30 Ohm load, 1000x1000x2000 mm size.

The electron beam duration, the beam quality (beam homogeneity, electron energy dispersion) are depending on high current electron source. The triode system needs in electron source, which can form homogeneous microsecond flow of large cross-sections ( $\approx 100 \text{ cm}^2$ ) in vacuum conditions. Moreover, the electron source is to operate with the higher electric field strength. These conditions can be satisfied by high current diodes, where anode is a metal cell with a certain transparency, and cathode is a multi-needle field emission cathode (MNFEC) [5, 6].

To form the homogeneous flow, [6] proposed to input additional resistance to the needle circuit, and to form a changed potential field on the metal substrate; the needles are to pierce through the metal substrate. But it was found that application of such cathode in triode is not effective. The irradiated beam was not homogeneous on cross-section, the plasma covered the accelerated anode gap very fast. It was found, that input of the additional resistance to the needled circuit and application of the substrate for the formation of homogeneous beams are advisable, when the electron beams are formed under the electron field strength in accelerated gap of 10-20 kV/cm and current density of 1-10 A/cm<sup>2</sup>. At the same time, for the effective generation, the triode current density should be no less than 100 A/cm<sup>2</sup> and electric field strength should be much than 200 kV/cm.

The numerical and experimental investigations were carried out on the optimization of MNFEC for triode. As a result, the MNFEC, which allows to form electron beams with necessary for effective microwave microsecond pulse generation parameters, was found. The cathode consists of metal substrate and needles. The needle diameter, height and disposition on substrate depend on the form of voltage pulse. The emitting surface of the cathode has a shape, which provide the constant electric field strength. The needles are made of stainless steel. It is a most erosion resistant material. The cathode operation resource is about  $10^5$  pulses. The copper, tungsten and graphite needles are not erosion resistant, and it leads to the breach of the beam homogeneity.

Fig. 1 presents the pulse oscillograms of voltage, current and bremsstrahlung for the operation of diode with MNFEC. The bremsstrahlung show the time, which need for plasma to cover the diode accelerated gap. Fig. 1(a) presents the pulse oscillograms for MNFEC, made according to results of [6]. Fig. 1(b) presents the pulse oscillograms for MNFEC of new

construction. Compare the oscillograms, it is seen, that MNFEC of new construction allow to increase the time, which need for plasma to cover the diode accelerated gap, by factor of 1.5-2.

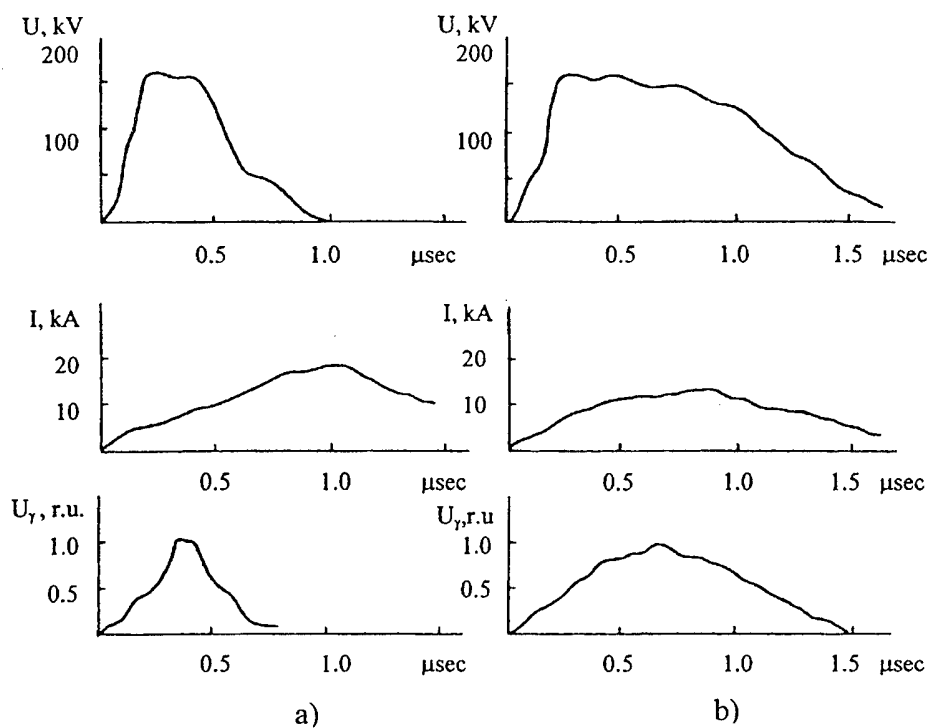


Fig. 1. Oscillograms of pulse voltage, current in diode, bremsstrahlung.

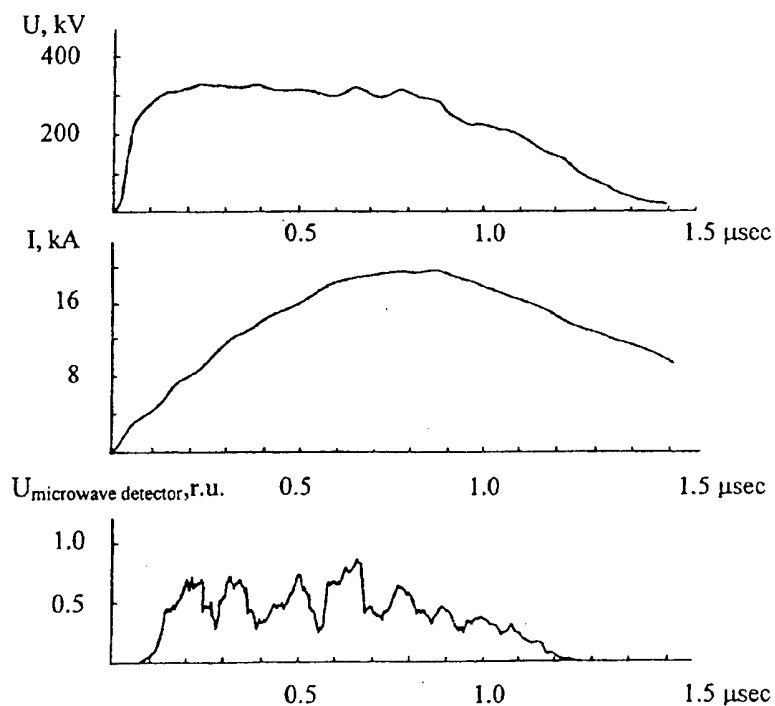


Fig. 2. Oscillograms of pulse voltage and current in vircator triode microwave irradiation envelope.

## Conclusion

The researches on the electron beam formation in triode system allow to develop the facility to investigate high power microwave pulses of long duration. Now this facility can form the microwave pulse with the following parameters: pulsed power - 1.2 GW, microwave pulse duration - 1.1  $\mu$ sec, pulse energy - 600-700 J, irradiation efficiency for the time of generation - 10-12%, irradiation in 10 cm band. Fig. 2 present the typical pulse oscillograms of voltage, current and microwave irradiation. The spectrum of the irradiation is investigated also. The change of irradiation frequency was found to caused by the change of effective gap between anode and emitting surface of MNFEC.

The work [7] presents the research of irradiation spectrum in triode system in details.

## References

1. M.M.Ofitserov, N.I.Zaitsev, N.F.Kovalyov, *etc.* J.T.Ph. Letters, 1981, v.7, issue 14, p.874.
2. I.Z.Gleizer, A.N.Didenko, A.S.Sulakshin, *etc.* J.T.Ph. Letters, 1980, v.6, issue 1, p.31.
3. S.P.Bugayev, V.I.Kanavets, V.I.Koshelev, V.A.Cherepenin "Relativistic Microwave Multi-wave Generators", "Nauka" Publ., Novosibirsk, 1991.
4. A.N.Didenko, A.G.Zherlitsyn, A.S.Sulakshin, *etc.* J.T.Ph. Letters, 1983, v.9, issue 24, p.1510.
5. S.P.Bugayev, G.M.Kassirov, B.M.Kovalchuk, G.A.Mesyats. J.E.T.Ph. Letters, 1973, v.18, p.82.
6. M.A.Vasilevsky, I.M.Roife, V.I.Engelko. Journal of Technical Physics, 1981, v.51, p.1183.
7. A.G.Zherlitsyn, A.N.Lyakshev, G.V.Melnikov. *to be published in* Proc. of 11-th International Conference on High Power Particle "BEAMS-96" (Prague, Czech Republic, 1996).

# GENERATION OF ULTRASHORT MICROWAVE PULSES BASED ON CYCLOTRON SUPERRADIANCE EFFECT

N.S. Ginzburg, I.V. Zotova, A.S. Sergeev

*Institute of Applied Physics Russian Academy of Science,  
603600, Nizhny Novgorod, Russia*

## Abstract

Specific features of superradiance in a waveguide under group synchronism conditions are studied theoretically. This process can be utilized to generate intense ultrashort electromagnetic pulses.

The report is devoted to theoretical study of cyclotron superradiance (SR) from short electron bunch under group synchronism conditions. Such emission was experimentally observed in [1,2]. Let us suggest that bunch of electrons rotating in homogeneous magnetic field moves through waveguide. The regime of group synchronism is realized when dispersion curves of the wave  $h = c^{-1} \sqrt{\omega^2 - \omega_c^2}$ , and of the electron flux  $\omega - hv_{\parallel} = \omega_H$ , are tangent (Fig.1a) and electron drift velocity is equal to e.m.wave group velocity.

It is reasonable to analyze SR under group synchronism condition in a reference frame  $K'$  moving with the electron bunch. Using Lorentz transformations, we easily find the longitudinal wave number  $h'$  and the transverse component of the magnetic field in the  $K'$  frame tends to zero. As a result this process reduces to the radiation of immovable ensembles of rotating electrons at a quasi-cutoff frequency (Fig.1b) i.e. the gyrotron-like operating regime [3].

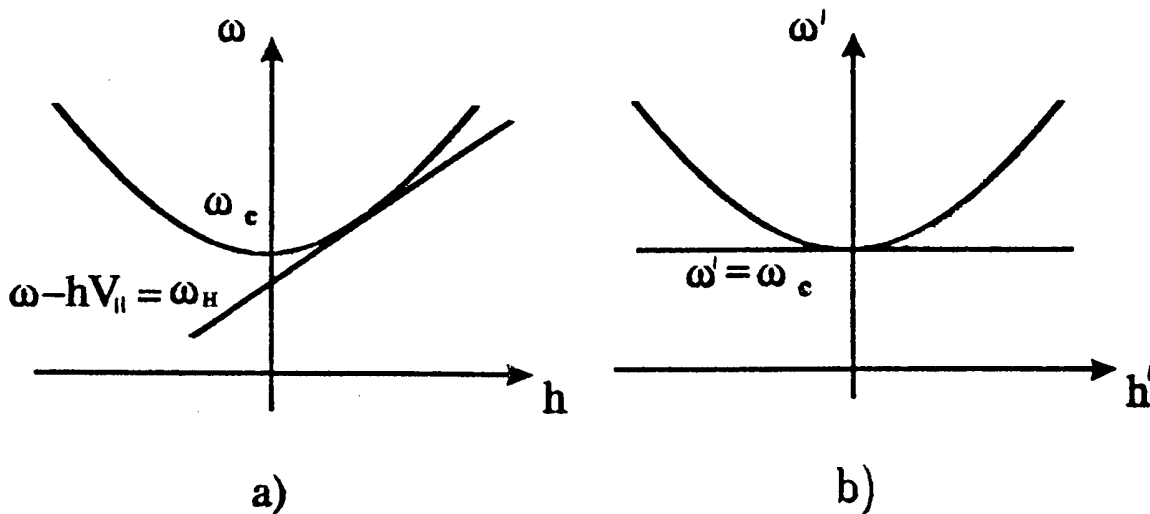


Fig.1 Dispersion diagram of the group synchronism regime in the lab frame of reference (a) and in the comoving frame (b)

Under the assumption that transverse structures of the radiation is the same as that of the waveguide mode, we present radiation field as  $\vec{E}' = \text{Re}[\vec{E}'_{\perp}(\vec{r}'_{\perp})A'(z', t') \exp(i\omega_c t')]$  where the function  $\vec{E}'_{\perp}(\vec{r}'_{\perp})$  is mode transverse structure and the evolution of the longitudinal field distribution is described by parabolic equation

$$i \frac{\partial^2 a}{\partial Z^2} + \frac{\partial a}{\partial \tau} = 2if(Z)G\langle\hat{\beta}_+\rangle_{\Theta_0} \quad (1)$$

The azimuthal self-bunching is caused by dependence of gyrofrequency on the electron energy and described by the equation of nonisochronous oscillators

$$\frac{\partial \hat{\beta}_+}{\partial \tau} + i\hat{\beta}_+ (|\hat{\beta}_+|^2 - \Delta - 1) = ia. \quad (2)$$

Under the assumption that in the initial state the electrons are distributed uniformly in cyclotron-rotation phases, aside from small fluctuations ( $r \ll 1$ ), we can write the initial condition on the system (1), (2) as follows

$$\hat{\beta}_+|_{\tau=0} = \exp i(\Theta_0 + r \cos \Theta_0); \quad \Theta_0 \in [0, 2\pi], \quad a|_{\tau=0} = 0 \quad (3)$$

Here we are using dimensionless variables:  $\hat{\beta}_+ = (\beta'_x + i\beta'_y)/\beta'_{\perp 0}$  is the normalized transverse electron velocity;

$$a = \frac{2eA'}{mc\omega_c\beta'^3_{\perp 0}} \cdot J_{m-1}(R_0\omega_c/c), \quad Z = z'\beta'_{\perp 0}\omega_c/c, \quad \tau = t'\beta'^2_{\perp 0}\omega_c/2,$$

$\Delta = 2(\omega'_H - \omega_c)/\omega_c\beta'^2_{\perp 0}$  is the detuning of the cyclotron frequency from the cut-off frequency;

$$G = \frac{1}{2\pi} \cdot \frac{eI_0}{mc^3} \cdot \frac{1}{\beta^4_{\perp 0}\beta_{\parallel 0}\gamma^3_{\parallel}} \cdot \frac{\lambda^2}{\pi R^2} \cdot \frac{J^2_{m-1}(R_0\omega_c/c)}{J^2_m(\nu_n)(1 - m^2/\nu_n^2)}$$

is a form-factor written under the assumption that the electron bunch is hollow with an injection radius  $R_0$ ;  $I_0$  is the total current in the lab frame;  $\lambda = 2\pi c/\omega_c = 2\pi R/\nu_n$ ;  $R$  - is radius of the waveguide,  $m$  - is the azimuthal index of the waveguide mode; and  $\nu_n$  is the  $n$ th root of the equation  $J'_m(\nu) = 0$ . The function  $f(Z)$  describes the distribution of the electron density.

Based on the Exs.(1),(2) we simulate cyclotron SR under the parameters close to the experimental value. Operating mode is  $TE_{21}$ . Waveguide radius is  $R = 10$  mm, beam injection radius -  $R = 2.5$  mm, electron transverse velocity -  $v_{\perp} = 0.5c$ , total current -  $I = 150$  A, pulse duration -  $\tau = 300$  ps, magnetic field -  $H_0 = 12.5$  KGs. In normalized variables we have  $G = 0.15$  and  $B = \tau v_{\parallel}\beta_{\perp 0}\omega_c/c = 10$ . Dependence of radiation power in moving frame  $K'$  on time for different value of detuning are plotted in Fig.2. Note that maximal growth rate and peak power correspond to the grazing condition  $\Delta = 0$ . However SR also occurs for both negative and positive  $\Delta$ . Possibility of radiation under negative  $\Delta$  are caused by electron frequency detuning: in spite that  $\omega_H$  less than  $\omega_c$  radiation frequency exceeds cutoff one. Meanwhile such detuning can support radiation

only in the limited range of  $\Delta$ , and under  $\Delta$  less than  $-1$  instability ceases. At the same time under positive  $\Delta$  for considered ideal bunch instability and the radiation persists at any  $\Delta$ . The growth rate only slightly fall with increasing  $\Delta$ .

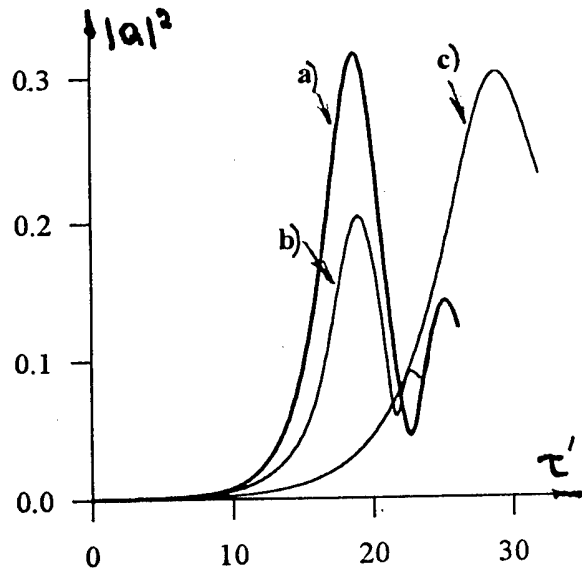


Fig.2 Dependence of radiation power in moving frame  $K'$  on time for different value of detuning  $\Delta$ :  
 (a) -  $\Delta = 0$ ,  
 (b) -  $\Delta = 1$ ,  
 (c) -  $\Delta = -0.5$

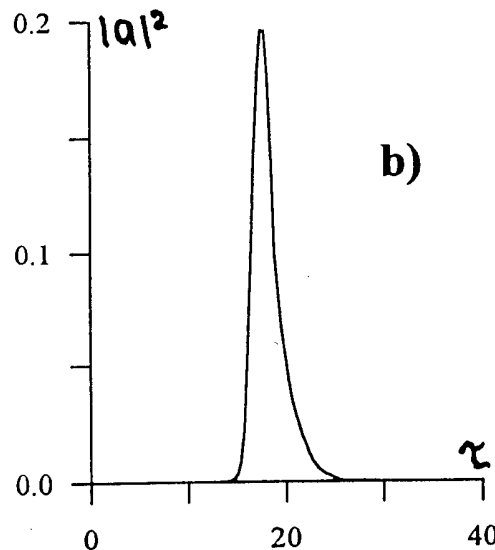
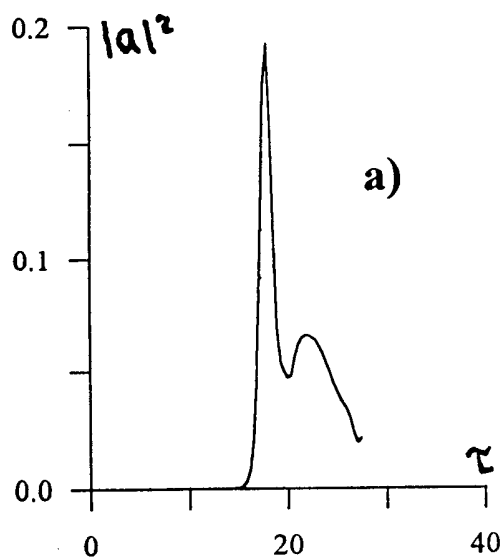


Fig.3. Dependencies of the radiation power on time in lab frame for the case (a)  $\Delta = 0$ , (b)  $\Delta = -0.5$

However it is reasonable to expect that this dependence will be much more sharp in the case of real bunches with finite spread of parameters, including different longitudinal velocities. In the moving frame for such a bunch different electrons can drift with respect to each other. The longitudinal mutual displacement will essentially influence the radiation if displacement exceeds the waveguide wavelength  $\lambda' = 2\pi/h'$ . In the exact group synchronism regime  $h'$  tends to zero (Fig.1.b),  $\lambda'$  - to infinity. As a result longitudinal



displacement of electrons isn't essential. But as we increase  $\Delta$  and go away from grazing regime -  $h'$  increases,  $\lambda'$  falls and displacement can strongly deteriorates radiation. Such behavior have been actually observed in the experiments [].

In  $K'$  frame the electron bunch radiate isotropically in the positive  $+z'$  and negative  $-z'$  directions along the waveguide axis. In the lab. frame at the observation point (detector) situated in the direction of bunch motion at the beginning radiation will arrive which was emitted in the  $+z'$  direction and then ( under the condition that the speed of the bunch exceed the group velocity) radiation emitted in the  $-z'$  direction. Dependencies of the radiation power on time in lab frame are presented in Fig.3a for the case  $\Delta = 0$ .

We see that the radiation appears as a set of two pulses. Naturally, the first pulse is created by photons emitted in  $K'$  frame in  $+z'$  direction while the second one by photons emitted in the opposite direction. It is evident that due to the Doppler effect the frequency in the first pulse exceeds the frequency of the second pulse. For the same reason the peak power of the first pulse is essentially greater than that of the trailing pulse and naturally the duration of the first pulse exceed the duration of second pulse.

However for negative  $\Delta$  the difference between group velocities for forward and backward propagating radiation becomes so small that for a given observation distance in the lab frame received signal on the detector will look like a monopulse (Fig.3b).

Note in the conclusion that results of experimental study of cyclotron SR under group synchronism condition confirms pattern described above. In particular both double and monopulses have been observed.

## References

1. N.S.Ginzburg, I.V.Zotova, I.V.Konoplev, A.S.Sergeev, V.G.Shpak, S.A.Shunailov, M.R.Ul'maskulov, M.I.Yalandin, JETP Lett, **63** (1996) 331.
2. N.S.Ginzburg, I.V.Zotova, A.S.Sergeev, I.V.Konoplev, V.G.Shpak, M.I.Yalandin, S.A.Shunailov, M.R.Ul'maskulov, these proceedings
3. V.A.Flyagin, A.V.Gaponov, M.I.Petelin, V.K.Yulpatov, IEEE Trans on Microwave Theory and Techniques, 1977, v.MTT-25, N6, p.514



## CONTRIBUTED PAPERS P-2

Capillary Discharges

Hollow Cathode Discharges

Laser Plasma

Imploding Liners

Plasma Foci

Pseudosparks

Radiation Sources

Z-Pinches

## Dynamics of Capillary Discharges Driven by Fast Pulse Power Generator

Tomonao HOSOKAI, Mitsuo NAKAJIMA, Takayuki AOKI,  
Kazuhiko HORIOKA and Masao OGAWA  
*Department of Energy Sciences, Tokyo Institute of Technology,  
Nagatuta 4259, Midori-ku Yokohama 226 Japan*

### Abstract

The plasma dynamics of capillary Z-discharges have been studied by filtered photo diodes and fast streak images. The capillary load filled with argon of 200-1kPa was directly driven by fast pulse power generator LIMAY-I ( $3\Omega$ -50ns). The lasing possibility in shorter wavelength region depends on whether we can avoid unstable implosion of the column to get denser and hotter plasma condition. In order to investigate the dynamics of capillary discharges, light emission from the column was measured. Obtained results suggest that the plasma column can implode stably without MHD instabilities up to 1kPa Ar. Probably because of well controlled preionization and fast rising current pulse, the experimental observation was consistent with the results of 1D-MHD simulation. These results indicate that the annular density profile can be produced in the gain region by fast capillary discharge in high pressure region. So it seems to be possible to produce the optimum gain profile by control of discharge parameters.

### 1. Introduction

For the lasing plasma in soft X-ray region, both high temperature more than 100eV and high electron density more than  $10^{19}\text{cm}^{-3}$  are generally needed. Furthermore, the plasma must be stable, uniform and liner to obtain good optical property. The production of such a plasma column is a challenging problem, because the column must be compressed dynamically without MHD instabilities. Recently, it was reported that fast Z-discharge through argon of about 100Pa in capillary of 4mm diameter and 120mm length could produce lasing condition in XUV region (Ne-like Ar 46.9nm), and achieved a gain-length product of 14 [1,2]. Enlargement of output energy and extending these techniques to the operational range of shorter wavelength are of major concern of our present study. Here we discuss the possibility of plasma dynamics control to produce optimum lasing profile in shorter wavelength range.

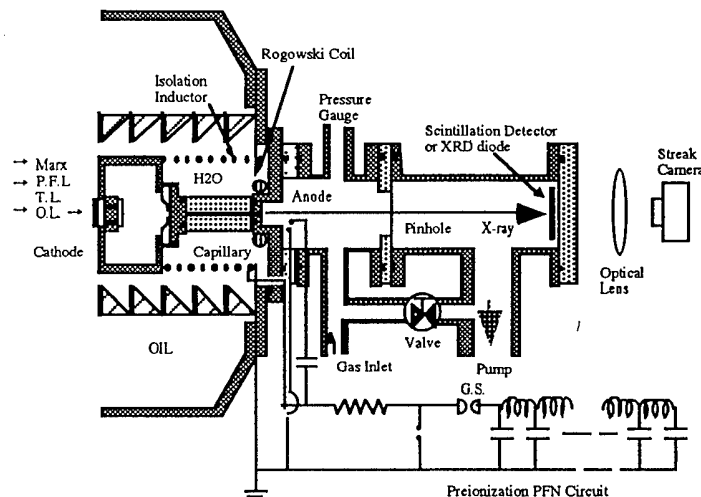


Fig.1 Typical setup of the experiment

### 2. Experimental Setup

The typical setup of the experiment is shown in figure 1. The capillary load is coaxially set inside a Z-stack insulator of pulse forming line (PFL), which is filled with pure water to prevent

from break-down along the capillary outer surface. This structure has only small stray inductance and helps fast current rise. The drive current above 200kA with the rise time less than a few tens nsec was easily available.

Experiments were conducted using polyacetal capillaries of 3mm diameter with length of 100mm which was filled with argon gas. The initial gas pressure was varied from 200Pa to 1k Pa using a differential pumping system. The background pressure of detector chamber was lower than  $4 \times 10^{-4}$  torr. The drive current is monitored by a Rogowski coil inside the Z-stack insulator of PFL.

In the experiments, the care was taken to make well-defined discharge condition. Then the plasma was directly driven by fast pulse power generator LIMAY-I. Undefined factors such as spark plasma column in the gap switch and the effect of wall ablation were eliminated from the discharge process. To suppress the effect of wall ablation, the inner surface of the capillary was laminated with an alumina tube. To make well controlled pre-ionized Ar gas, a rectangular current pulse of about 15-20A and duration of several tens  $\mu$ sec was generated by pulse forming network (PFN). It was applied just before the main power pulse through an isolation inductor.

### 3. Light Emission from Plasma Column

The light emission from the plasma column is observed through a pinhole from axial direction as shown in Fig.1. We can get spectral resolution by filtered scintillation detectors and XRD diodes[3]

The filtered scintillation detector consists of an absorption filter and an aluminum coated plastic scintillator (NE102A) with photo-multiplier. The coated aluminum ( $\sim 2000\text{\AA}$ ) cuts off almost all visible light components. A mylar sheet of 4  $\mu$ m thickness is set in front of the scintillator. The plastic scintillator is relatively insensitive for the photon energy below about 50eV. In case of mylar filter which has carbon-K edge, the detector is sensitive from about 100 to 300eV. Without mylar filter, the aluminum coated scintillator, has sensitivity below 100eV radiation.

The filtered XRDs are consist of a metal photo cathode of effective diameter of 20mm and wire mesh anode. Photo-electrons from the cathode surface are accelerated across the cathode-anode gap. The sensitivity of the detector is determined by cathode material which have different quantum efficiency. Au of  $1000\text{\AA}$  on Cu or C of  $1000\text{\AA}$  on Cu plate is chosen as the cathode metal from their quantum efficiency profiles [4]. Then the XRD with the Au on Cu cathode is sensitive below about 100eV and also over 300eV radiation, and with the C on Cu cathode is below about 40eV and over 300eV respectively.

The discharge dynamics was observed with a fast streak camera (HAMAMATSU C-2830) from Z axis direction. The visible light emission from the capillary images on the slit of the camera through a pinhole and an optical lens as shown in Fig.1.

### 4. 1D-MHD Simulation

We have carried out numerical simulations on the plasma dynamics of the capillary Z-discharge using 1D-MHD code MULTI-Z [5,6], which can simulate the dynamics of the current sheet and shock waves self-consistently including the effect of radiation process and the skin effect. The initial condition of the simulation is as follows; the argon gas has uniform temperature of 0.1eV and density of  $3.29 \times 10^{-6} - 1.65 \times 10^{-5} \text{g/cc}$  (corresponding to the argon gas pressure of 200 - 1k Pa). In this simulation, we gave the experimentally obtained discharge current as the input parameter.

### 5. Results

Figure 2 shows the typical wave forms of the end-view XRD signals and the drive current (initial pressure;  $P=400\text{Pa}$ ). The X-ray spectrum shows that the emission is drastically changed from soft region below 40eV to hard region of 150-300eV at about 60nsec. The point of inflection on the signals is gradually shifted to late time with initial pressure. Figure 3 shows the typical streak image ( $P=400\text{Pa}$ ). The column implodes stably for about 40nsec and expands to the wall at about 60 nsec. The radiation increases abruptly after the plasma column expands to the wall. The spectrums and streak images have good reproducibility in the first phase as long as using preionization. The experimental results show clearly that the preionization contribute to

the stable implosion. The motion of imploding boundary in the streak images have parabolic shape.

Figure 4 shows the typical flow diagram of the implosion process ( $P=400\text{Pa}$ ). The calculated results of imploding process can explain fairly well the experimental by observed plasma behavior. Figure 5 shows the typical time-space distribution of calculated electron density ( $P=400\text{Pa}$ ). These results predict that the annular profiles satisfied enough the lasing conditions of Ne-like Ar more than 10nsec in compression and expansion phases.

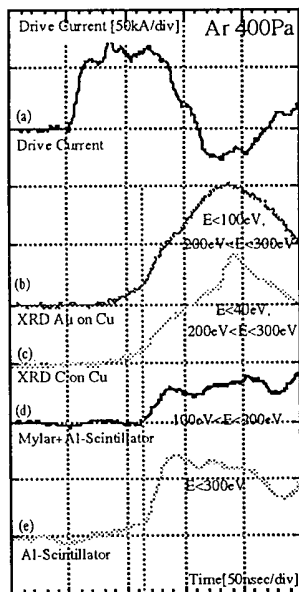


Fig.2 Typical waveforms of detectors and drive current

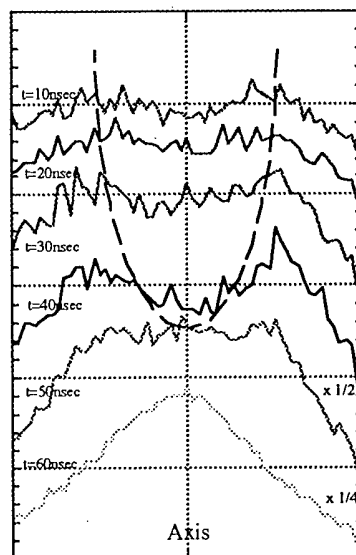


Fig.3 Typical streak image of the Plasma Column. (Initial Pressure; 400Pa )

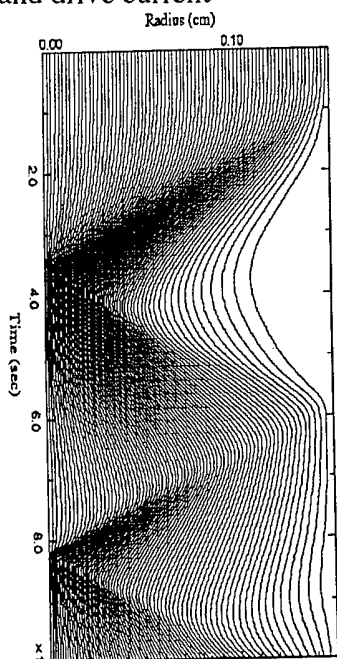


Fig.4 Flow Diagram of Capillary Discharge

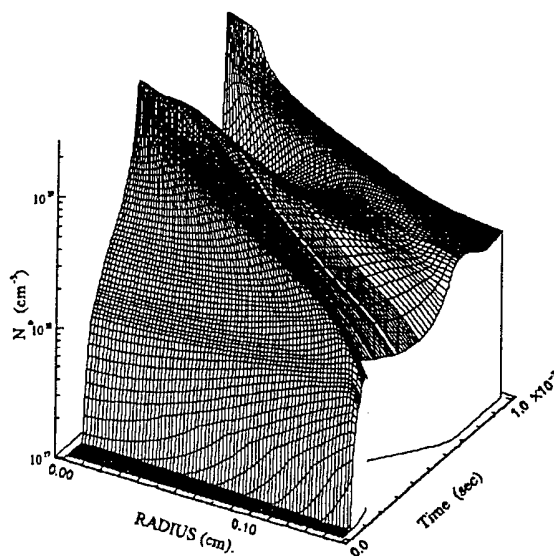


Fig.5 Time-Space Distribution of Electron Density

## 6. Discussion

For collisionally excited X-ray laser by the Z-discharges, the possibility depends on whether we can stably implode the column with sufficient uniformity to get the lasing condition. If we can stably implode, this means, we can make use of various implosion scheme. Controllability of the implosion process seems to be important for output energy enlargement and wavelength shortening.

While a dynamic compression produce hot and dense region only in narrow region on the axis, the slow implosion produce hot and dense region with broad annular shape around the axis. If the column can be imploded stably in wide pressure range, the tailoring of density and temperature profiles can be possible. So if the lasing profiles can be optimized, the optimum gain profiles may be produced by the Z discharges.

The annular profiles will also bring enlargement of volume of hot and dense region and of compression duration. Generally, extended high energy density region prevent from cooling of 3s level and reduce the laser gain. In the plasma column, ions have both kinetic and thermal velocities of about order of 100eV in the compression phase. In order to discuss the laser gain, we have to investigate Doppler shift and broadening of the spectrum. Although there are some unknown factors, the annular gain profile by slow compression has a possibility of increasing the output laser energy. Furthermore, they has an advantage for X-ray transport. The lasing soft X-ray is confined and transported through such a gain region like an optical fiber cable.

## 7. Conclusions

We have driven capillary Z-discharge in pressure of 200 - 1k Pa of Ar by fast pulse power generator LIMAY-I. In order to investigate dynamics of the fast capillary discharge, the light emission was observed by a XRD diodes and a fast streak camera. Numerical simulation was done using 1D MHD code. All of the experimental results were well explained by the 1D-calculation. These results indicate that we can control the dynamics by discharge parameters in wide range. It seems to be possible to produce optimum density profiles for lasing by the capillary discharge.

## 8. Reference

- [1].J.J.Rocca et al., Phys.Rev.Lett.**73**,2192 (1994)
- [2].J.J.Rocca et al., SPIE, Vol.**2520**,201 (1995)
- [3].J.Raus and V.Piffl, Czech.J.Phys.,**B38**,1222 (1988)
- [4].R.H.Day,P.Lee,E.B.Saloman,D.J.Nagel,J.Appl.Phys,**52**,6965 (1981)
- [5].R.Ramis,R.Schmalz and J.Meyer-Ter-Vehn, Comput.Phys.Commun.,**49**,475 (1988)
- [6].T.Aoki and J.Meyer-Ter-Vehn, Phys.Plasmas., **1**(6),1962 (1994)

# TIME RESOLVED OBSERVATIONS OF PLASMA EVOLUTION IN THE HOLLOW CATHODE REGION OF A TRANSIENT HOLLOW DISCHARGE

M. Favre, M. Zambra\*, J. Moreno, F. Chuaqui, E. Wyndham, and P. Choi\*\*

*Facultad de Fisica, Pontificia Universidad Catolica de Chile  
Casilla 306, Santiago 22, Chile*

*\*Comision Chilena de Energia Nuclear, Casilla 188-D, Santiago, Chile*

*\*\*LPMI, Ecole Polytechnique, Palaiseau 91128, France*

## ABSTRACT

It is known that in a transient hollow cathode discharge (THCD), the formation of a moving virtual anode in the A-K space is causally linked to the emission of high energy electron beams originated in the hollow cathode region (HCR). In this work we report on time and space resolved observations of the formation and evolution of plasma inside the HCR, which are time correlated with ionization processes inside the A-K gap. The experiments have been performed in Hydrogen, at pressures between 50 to 500 mTorr, at 30 kV applied voltage. Capacitive probes are used to monitor ionization growth in the A-K gap, in conjunction with time and space resolved spectroscopic observations in the HCR. High energy electron beams are also measured. Stark broadening observations of the  $H_\beta$  line indicate that the electron density inside the HCR increases up to a few times  $10^{15} \text{ cm}^{-3}$  some time before breakdown in the A-K gap. This time is also related with the electron beam activity.

## INTRODUCTION

Several investigations on THCD, both experimental and theoretical, have highlighted the intimate relationship existing between ionization processes in the A-K gap and plasma formation inside the HCR [1,2]. We have previously reported on the formation of a moving virtual anode in the A-K, which is causally linked to the emission of high energy electron beams originated in the HCR [1]. Ionization in the A-K gap has been found, at pressures in the tens to few hundreds mTorr range, to proceed throughout the extension of the anode potential towards the cathode by the virtual anode, under the assistance of the electron beams. Extension of the anode potential up to a point close to the cathode has been found to be a necessary, but not sufficient condition to achieve electric breakdown [3]. This is particularly noticeable when operating at low pressures and with narrow cathode apertures. In this work we report on time and space resolved observations of plasma formation and evolution inside the HCR, which are time correlated with ionization processes in the A-K gap. Plasma light emission from the HCR is observed to start before breakdown in the A-K gap. The emission is seen first along the axis of the discharge, close to the cathode aperture, and then to proceed along the axis, further inside the HCR. The expansion of the light emitting plasma appears to be related with different periods of electron beam activity. Stark broadening observations of the  $H_\beta$  line allow the time evolution of the electron density inside the HCR to be measured. Typical data indicates that the electron density inside the HCR increases up to a few times  $10^{15} \text{ cm}^{-3}$  some time before breakdown in the A-K gap.

## EXPERIMENTAL APPARATUS

A 30 kV voltage pulse, with less than 50 ns rise time, is used in the experiments [4]. Virtual anode formation and evolution is monitored with an array of six capacitive probes in the A-K [5] gap and a beam target detector is used for high energy ( $E > 2.5 \text{ keV}$ ) electron beam



measurements [4]. Light emission from the HCR is recorded with a 30 cm focal length, 2400 ln/mm spectrometer, coupled to a 1-D, 20 ns gated intensifier (Optical Multichannel Analyzer). The experiments have been performed in Hydrogen, at pressures between 50 and 500 mTorr, using a 5 mm diameter cathode aperture, with 10 cm A-K separation. The discharge was operated at 0.2 Hz. 20 ns exposure time spectra in the 300-750 nm wavelength region were recorded on a shot to shot basis.  $H_{\alpha}$  line emission in the HCR is space and time resolved by imaging onto a linear array of filtered optical fibres connected to PM detectors. Further details on the experimental set-up have been published elsewhere [4].

### EXPERIMENTAL OBSERVATIONS

Figure 1 shows characteristic electric signals which are time correlated with light emission from the HCR: from top to bottom, they correspond to the time derivative of the applied voltage, the high energy electron beam, a capacitive probe at 4.5 cm from the anode (A1), a capacitive probe at 2.5 cm from the cathode (A5), and  $H_{\alpha}$  line emission imaged from different

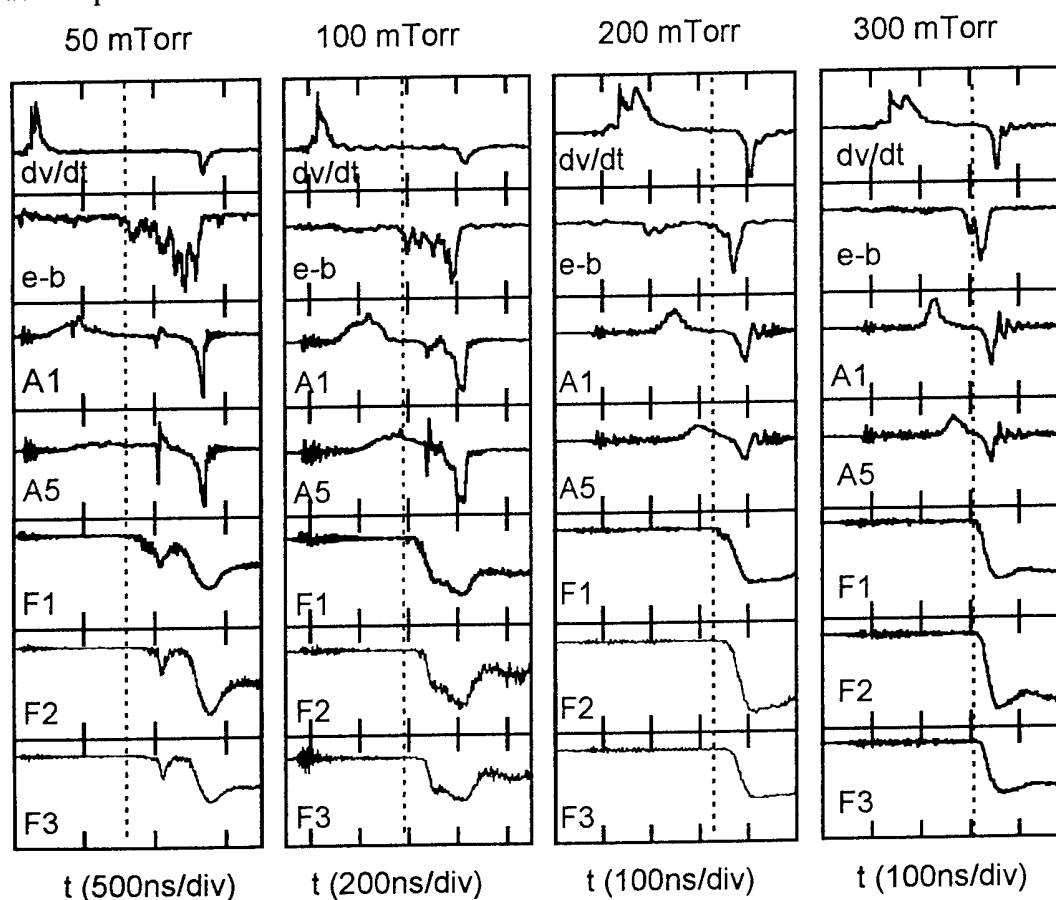


**Figure 1:** characteristic electric signals with simultaneous recording of light  $H_{\alpha}$  emission from the HCR.

positions along the axis, inside the HCR (F1, immediately behind the cathode aperture, F2 and F3, from points at 1.5 and 3.0 mm from the cathode aperture). The dotted line in each graph indicates the onset of light emission, as indicated by F1, which coincides in all cases with a marked increase in the electron beam activity, as shown by the e-b trace. Electric breakdown is indicated by the sharp negative excursion seen in the capacitive probe signals. It can be seen

that light emission starts before electric breakdown in the A-K gap, and propagates from the cathode aperture towards the inside of the HCR.

Figure 2 shows the time evolution of the electron density inside the HCR, as measured from the half width of the  $H_\beta$  line, at 100 and 400 mTorr. Each point represents a time average over a constant length time interval. A total of 1000 shots were recorded at different times relative to breakdown ( $t = 0$ ). Statistical dispersion is due to jitter in the triggered spark gap. Within the error bars, a clear trend is observed. The electron density is seen to reach maximum value before electric breakdown, and then to decay throughout the breakdown and conducting phases of the THCD. When compared with the electric signals in Figure 1, it is seen that the time of maximum electron density is more or less coincident with the onset of the high energy electron beam, which is followed by the expansion of the light emitting plasma inside the HCR.

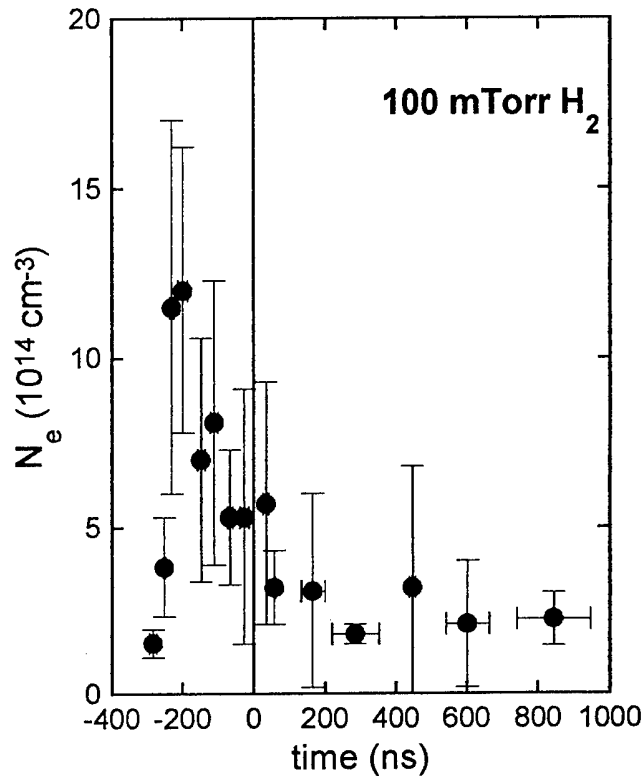


Figure 2: time evolution of the electron density inside the HCR.

## DISCUSSION

The identification of a causal link between ionization and breakdown processes in the A-K gap and the emission of energetic electron beams from the HCR highlights the importance of the plasma processes in the HCR in determining the particular features of THCD. It has been shown by computer simulations [6] that local field enhancement inside the HCR is required in order to sustain the ionization growth which is needed for electron beam extraction by the virtual anode close to the cathode aperture. Plasma formation inside the HCR prior to electric breakdown in the A-K gap has been previously identified in streak camera observations [7]. In these observations plasma is seen to form first at the cathode aperture and then to expand inside the HCR. At this time complex processes take place inside the HCR and A-K gap. Electron beams of low energy and high current, with a high energy low current precursor are injected from the HCR into the A-K gap. These beams are fundamental in creating in the A-K gap suitable ionization conditions for final electric breakdown. Our results show that at the time when the electron beams leading to breakdown are emitted, a light emitting plasma appears next to the cathode aperture and starts expanding inside the HCR. Light emission increases up to breakdown in the A-K, and then decreases, which appears to be an indication of decoupling between the HCR and main gap plasma. Particularly noticeable is the fact that at 50 mTorr, initial light pulses coincide with pulses of electron beams and charge movements

in the A-K gap, as shown by the capacitive probe signals, which do not lead to full electric breakdown. This situation has been discussed elsewhere [3]. The electron density measurements show that near the cathode aperture, inside the HCR, the electron density grows from a non detectable value up to a few times  $10^{15} \text{ cm}^{-3}$ , in a time scale shorter than 100 ns. According to computer simulations [6,8], the electron beams are emitted from the HCR when plasma formed in the A-K gap by the evolution of the virtual anode, enters the HCR. After entering the HCR, the plasma expands rapidly. Our observations appear to be in agreement with the computer simulations. The decay in the measured electron density can be ascribed to rapid expansion of the HCR plasma. Further analysis of the time evolution of the electron density inside the HCR requires more refined measurements, which should include time correlated measurements of ionization growth using the capacitive probe array inside the HCR, and better spatial resolution in the spectroscopical measurements. The role of energetic ions drifting from the A-K gap inside the HCR, in contributing to local ionization cannot be clarified with these observations. A series of experiments to identify fast ions by Doppler shift of  $H_{\alpha}$  line in fast neutrals that have undergone charge exchange collisions is presently under way.

#### ACKNOWLEDGEMENTS

This work has been funded by FONDECYT project 1950798 and a CNRS-CONICYT collaboration programme. J. Moreno has been awarded a scholarship by CONICYT.

#### REFERENCES

- [1] P. Choi et al., Appl. Phys. Lett. **63**, p. 2750, 1993.
- [2] M. Favre et al., Appl. Phys. Lett. **60**, p. 32, 1992.
- [3] M. Favre et al., IEEE Trans. Plasma Sci. **23**, p. 212, 1995.
- [4] M. Favre et al., IEEE Trans Plasma Sci. **20**, p. 53, 1992.
- [5] P. Choi and M. Favre, Rev. Sci. Instrum. **65**, p. 2281, 1994.
- [6] J.P.Boeuf and L. Pitchford, IEEE Trans. Plasma Sci. **19**, p. 286, 1991.
- [7] P. Choi et al., IEEE Trans. Plasma Sci., **17**, p. 770, 1989.
- [8] L.C. Pitchford, J. Appl. Phys. **75**, p. 7227, 1994.

**IMPROVEMENT ON THE PHYSICAL DESCRIPTION OF THE BOUNDARY CONDITIONS  
BETWEEN THE HOLLOW CATHODE REGION AND THE A-K GAP  
IN A TRANSIENT HOLLOW CATHODE DISCHARGE**

**Y. Kaufman**

*Physics Department, NRC-Negev, Beer-Sheva 84190, Israel*

**P. Choi**

*Laboratoire de Physique des Milieux Ionisés,  
Ecole Polytechnique, Palaiseau 91128, France*

**ABSTRACT**

An important connection between the main gap and the hollow cathode region (HCR) in a pulsed hollow cathode discharge is in the positive ions created in the main gap which subsequently enter the HCR through the cathode aperture. These energetic ions control the ionization growth rate inside the HCR through both secondary electron production and in the formation of a positive space charge immediately behind the cathode aperture. The result is the creation of a highly localized plasma on axis inside the HCR, from which the injection of a large electron flux leads to the final breakdown. A 2-D fluid code reported previously modelled the ionization growth within the HCR using swarm parameters based on a local field approximation and the growth of this on axis plasma source was predicted. The model adopted to treat the ion flux was based on continuity with the electron flux leaving the HCR. This assumption ignores the ionization events within the main gap. In this paper, we report on a new model which tackles the physics of collisions in the main gap using a 1-D description in order to return a proper ion flux for the 2-D calculation in the HCR. The methodology is computationally efficient and corrects the discrepancy observed in the relationship of breakdown delay and operating pressure.

**Introduction**

In a high voltage low pressure discharge, the collision mean free path of an electron under the applied field is large compared with the inter-electrode separation and Townsend ionization is not sufficient to lead to the charge multiplication necessary for the breakdown of the gas. Secondary events must take place in order to produce an electron population large enough for discharge formation. In a presence of a hollow cathode geometry, the situation can be completely different. Within the hollow cathode region (HCR) the ionization and collision parameters are drastically different as the electric field inside is smaller and the lower  $E/N$  value favours local ionization growth. The magnitude of this leakage electric field is determined by the cathode aperture and has a crucial importance. This small but finite field ensures the creation of events within the HCR which control the initiation of breakdown in the main gap region. Thus, the actual breakdown formation process in the main gap is coupled to events occurring within the HCR. An important connection between the main gap and the HCR is in the positive ions created in the main gap which subsequently enter the HCR through the cathode aperture. These energetic ions control the ionization growth rate inside the HCR through both secondary electron production and in the formation of a positive space charge immediately behind the cathode aperture. The result is the creation of a highly localized plasma point on axis within the HCR. It is the injection of a sufficiently large number of electrons from this plasma source into the main gap which leads to the formation of the breakdown channel in the main discharge region.

## Previous Work

In an earlier work, we described the simulation of the ionization growth phenomena in a transient hollow cathode discharge. The 2-D numerical code, SPARK 2, was developed to model the ionization growth phenomena within the HCR region.[1] It is based on a fluid model using swarm parameters in local field approximation. The model comprises the time-dependent continuity equations for ions and electrons with the equations of motion replaced by a drift parameter. Both primary and secondary ionization processes are included. In addition Poisson's equation is solved for the whole of the HCR taking into account of both the detailed geometry and the effect of space charge using a boundary-fitted coordinate technique. The coupling between the A-K gap and the HCR is treated by a continuity assumption. The model produces good agreement with the general features of the ionization growth process inside the hollow cathode region, including the formation of a point like plasma region immediately behind the hollow cathode hole. It identifies the importance of the divergence of the electron flux at this region and the resulting ion space charge in enhancing the local ionization growth, thus controlling the electron beam production and the breakdown formation in the main gap. Some of the key prediction of the code and the corresponding experimental observations are shown in Table I. As it is shown, the major short-coming in the simulation is in the dependence of ionization growth with pressure.

In the simulation, the role of primary and secondary coefficients in current density growth were examined. The flux of ions, returning through the hole from the main gap into the HCR, was found to be of great importance in controlling the ionization within the HCR and therefore the delay to breakdown. The treatment of this flux in the previous model was simplistic, using continuity argument to balance the ion flux with the flux of electrons leaving the HCR. The assumption of isolating the physics in the A-K gap, is not entirely satisfactory. It assumes that the amount of fast ions is related totally to the electron leaving the HCR which in turn means that the dependence is only on ionization phenomena within the HCR. This assumption is the underlying physics which leads to the code predicting that the breakdown delay would be increased as the operating pressure is increased, which is opposite to what is observed in experiments at pressure below 1 Torr. The prediction, however, is entirely physical for the condition within the HCR. The reason being that the ionization coefficient is increasing with increasing E/N at the regime of operation

**Table I**                      **SPARK 2**                      **Experimental**  
   **Predictions**                      **Observations**

*	point like plasma formation on axis inside HCR	☑
*	on axis high current density electron beam injection into A-K gap	☑
*	rate of ionization growth increases with voltage	☑
*	rate of ionization growth increases with size of cathode aperture	☑
*	rate of ionization growth decreases with thickness of cathode electrode	☑
*	rate of ionization growth decreases with A-K gap spacing	☑
*	rate of ionization growth increases with initial charge distribution (pre-ionization)	☑
*	rate of ionization growth decreases with pressure	☒

inside the HCR and for a constant operating voltage, when the operating pressure is increased, the  $E/N$  decreases and hence the ionization rate also decreases.

### **Present Model**

In a more realistic assessment, the presence of the coupling between the A-K gap and the HCR means that the ionization within the main gap will always be augmented by the injection of electrons from the HCR while the ionization within the HCR will be influenced by the fast ions, created in the main gap and returning into the HCR. For the treatment of the high  $E/N$  condition in the A-K gap, the use of a local field approximation is no longer valid. A Monte Carlo approach was used in the work of [2] in order to describe the collision parameters in the main gap in 2-D but the method is highly computational intensive even at moderately high  $E/N$  values. To resolve this problem, the new model tries to tackle the physics of collisions in the main gap in 1-D and hence return a proper ion flux into the HCR, which remains being modelled in 2-D. In this way, the overall ionization growth includes a suitable description of the ionization in the A-K gap.

In the present scheme, the treatment of the ion production rate is based on the injected electron beam from the HCR. The ionization is described in terms of collision mean free path and ionization cross-section in the main gap region. We take into account the flux of ions returning from the main gap to the HCR. This treatment of the collisions in the main gap is done by an additional subroutine coupled to the main calculation. The stages of this subroutine are as follows:

1. The main gap is divided into a fine mesh with cell dimensions which are of the same order of magnitude as the mean free path for elastic collisions, and smaller than the mean free path for ionization in the pressure range relevant to our conditions.
2. The potential in each mesh point is calculated by the Poisson solver and thus the electric field in each mesh point is known.
3. We enter the subroutine with the rms values of the velocity and flux of the electrons traversing from the HCR into the main gap.
4. In each cell five species are treated: (I) electrons having no collisions in the cell. (II) electrons having only ionizing collisions in the cell. (III) electrons having only elastic collisions in the cell. (IV) electrons newly born in the cell. (V) positive ions newly born in the cell.
5. The movement of these species is treated using Newton's laws of motion and the cross sections for ionization and momentum transfer.
  - The electrons are moved from cell to cell. In each cell new electrons and a same number of positive ions are created through ionization.
  - The new electrons join the total electron flux advanced to the next cell.
  - At the end of this stage, the flux and velocity of electrons accelerated towards the anode and of ions drifting towards the HCR and entering the hole, are known at each mesh point.
6. The positive ions are advected to the hole, taking into account their drift velocity and a "loss cone" of ions removed through transverse diffusion. The ion flux is accumulated at the HCR boundary.

7. The rms values of the ion flux and velocity at the HCR boundary is calculated and their density derived.
8. The value of the ion density on the HCR boundary is fed back into the main program and added to the ion density in the cells inside the HCR adjacent to the boundary.

## Results

As it was expected, the major change in the incorporation of the collisions in the main gap region is to resolve the discrepancy of the ionization growth rate with pressure. This is illustrated in Fig.1, which shows the on axis current density leaving the HCR and entering into the main gap region for 5 different pressures between 100 mTorr and 800 mTorr. Only the periods when this current density is above  $10 \text{ mA.cm}^{-2}$  are shown. The simulation is for an A-K gap of 10 cm at an applied voltage of 25 kV. The hollow cathode region is separated by an aperture of 5 mm diameter and 6 mm depth. Two minimum time step limit of 2 ps and 0.1 ps have been used in the runs in order to assess the possible errors introduced by high drift parameters in the transport of the fast ions at very high E/N values. In general, for a given pressure, the data for higher and lower voltages show similar trend. At low pressure, the delay to breakdown becomes a sensitive function to the exact value of the secondary coefficient for electron production by ion impact which takes place primarily at the wall opposite to the cathode aperture.

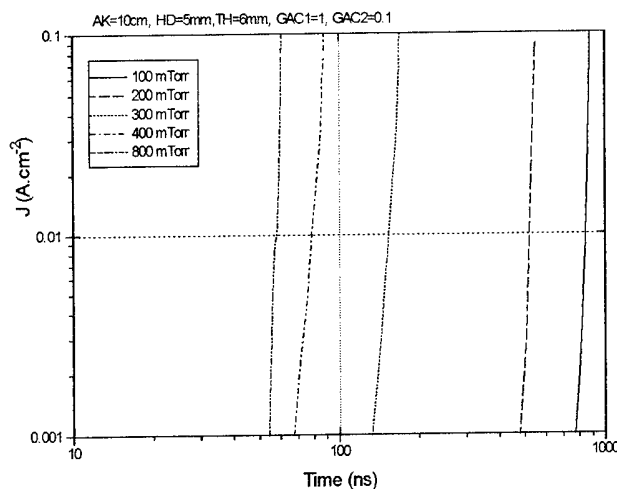


Fig.1 Growth of on-axis current density for different operating pressures

## Discussion

While the present treatment of the collision parameters in the main gap is relatively simple, the limitation of fluid code has been overcome by separate treatment of ionization growth in the main gap region where the fluid approximation is not valid. The overall simulation of ionization growth in a transient hollow cathode discharge now includes a coupled description of the ionization processes in both the main gap region and the HCR. Correct dependence of the rate of ionization growth with pressure is obtained when ion feedback is included. The methodology is computationally efficient and allows the treatment of discharge condition at very high E/N and very low pressure conditions. The 1-D description, while less precise, enables more extensive set of collision phenomena in the A-K gap region to be treated. It also allows different geometry of the hollow cathode and different coupling geometries to be explored with realistic computational resources.

## Reference

- [1] K. Mittag, P. Choi & Y. Kaufman. Nucl. Instrum. & Methods. A292(1990)p.465
- [2] J.P. Boeuf & L. Pitchford. IEEE Trans. Plasma Sci., 19(1991)p.286

# INVESTIGATION OF ECTONS DYNAMICS IN LASER - INDUCED BREAKDOWNS

V.A.Skvortsov , N.I.Vogel (\*)

High Energy Density Research Center, Russian Academy of Sciences,  
127412, Moscow, Izhorskaya, 13/19, IVTAN, Russia

(\*) University of Technology Chemnitz-Zwickau, Department of  
Physics, D-09107, Chemnitz, Germany

## Abstract

This paper deals with the computer simulation of plasma-emissive processes under nanosecond vacuum discharges induced by picosecond laser beams and applied voltages (with moderate values of 240 V). In particular, a new results of numerical investigation of electrohydrodynamics of so called "ectons" [1] - emissive centers, which are produced on the cathode surface by high density electric current with a preliminary elimination cathode by picosecond laser beams are represented. A principal new physical effects the current selffocusing (and defocusing) as well as the "shooting solitons"-generation were observed. Based on considered nonlinear phenomena a new mechanism of charge particle generation from nucleus of quasi stellar radio sources (QSS), radio Galaxies and stars is proposed.

## Introduction

Considerable attention to the electro-explosion processes on the cathode surface under high voltage vacuum discharges is associated with the development of intensive sources of charged particles, industrial accelerators, drives for magnetic and inertial confinement fusion devices etc. [1].

We used the two-dimensional mathematical model [2], which is based on the electrodynamic, hydrodynamic and heat-transfer equations, at which a semiempirical wide-range equation of state (EOS) was applied to determine the pressure and temperature as a functions of the specific internal energy and matter density [3] (EOS describes the high-temperature melting, evaporation, ionization, experimental data of shock-wave compression in megabar pressure range, including a high temperature plasma). It is very important that thermal and electrical conductivity were calculated including effects of strongly coupled plasma [4,5].

Recently [6], it had been shown, that this laser-induced intense electron emission had a similar features with the explosive electron emission processes [1] in temporal structure and total charge of intense bursts of electrons. An intense electron beam was most created after plasma formation in the vicinity of cathode surface.

Let us consider the nonlinear dynamics of dense plasma produced in result of influence of picosecond laser pulse on cathode surface (copper) with an applied voltage (240 V) and electrode gap distance on the order of 100  $\mu\text{m}$  for concrete experiment [6] when intensity was about of  $3 \cdot 10^{13} \text{ W/cm}^2$  in focal spot size of 40  $\mu\text{m}$  diameter, the length of wavelength -1.06  $\mu\text{m}$ . At such parameters of laser beam the initial temperature  $T_0$  may be reach up to 70 eV, as it was established in precisely estimation by using one-dimensional radiative hydrodynamical code HERA [7]. We consider namely this case of initial temperature and compare some new results with that which was obtained earlier for cases of  $T_0=10$  and 20 eV [6,8].

## Nonlinear plasma emissive dynamics of laser-induced vacuum breakdowns

The present computer simulation at  $T_0 = 70$  eV confirmed the main results of our investigation: the generation of pulsed solitons at the moving boundary of the microtorch



plasma, from which intense electron beams with current density on the order of  $10^6 - 10^8$  A/cm<sup>2</sup> are almost synchronously created. These solitons are able to increase their amplitude in several orders of magnitude and followed we can classify them as "shooting solitons" (SS). The solitons life time is very short, only 10 - 100 ps. After its generation the overheating instability can take place in result of the return back wave of thermal heating occurs. Such return thermal flux to the vicinity of cathode crater produce an additional energy input. Hence an intensification of hydrodynamical and electron emissive processes take place. The evolution of spatial distributions of plasma temperature (which can increase up to few hundred eV [6] on the outside of the cathode torch), density of current and electrical potential can be the result of nonlinear processes in "regime of aggravation" [9], when in some small regions the mentioned above values are increased for a limited time. The similar phenomena were examined in different physical system, for example; under the burning of matter [9]. Figure 1 shows a typical example for current density distribution within the laser induced plasma for the different times after ignition by IR-laser pulse. It was evident, that the amplitude of current density varies rapidly in few orders of magnitude during short interval of 3 ns. It is well seen how evaluated with time the emissive centers ("ectons") having ring-like form. Its radius increases due to propagation a strong shock wave, which is generated by high current densities (see Fig.1,a,b). The generation of SS can be owing the current selffocusing ("volumetric generation" see Fig.1,c) or due to the increasing of electric tension on some region of cathode torch boundary ("surface generation", see Fig.1,d) in contrary to the usual "ectons" [1], which are produced on the cathode (or anode) surface.

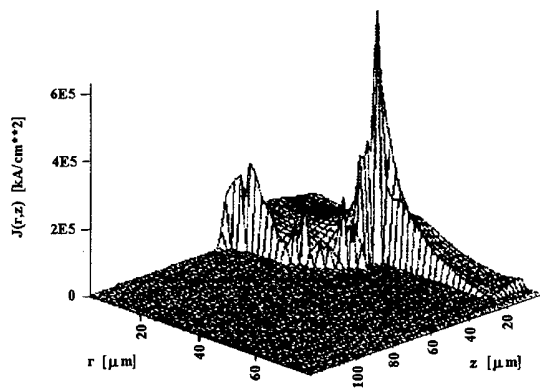
The main plasma parameters at time  $t=3$  ns are represented on Fig.2. These parameters are mostly the same as was in a case with another  $T_0$  [6,8]. By the way, the considered plasma-emissive dynamics at  $T_0=70$  eV in many features is analogous to that at the initial temperatures 10 and 20 eV. There are some differences in temporal behavior of plasma torch and in values of its external parameters, which may be obtained due to overheating instability [6,8].

It is interesting, that when plasma torch reaches the anode, in some its region the plasma temperature and conductivity can drastically decrease and in another - increase. Other words: the plasma-erosion break off take place (see Fig.1,d). During such processes the positive potential of plasma is strongly increased (in our case up to few kV).

The short life time of described above "shooting solitons" can be explained by intensive heat and particle flow transfer from the SS. Simultaneous with an electron emission an directed ion flux must be generated because of emitted electrons can effectively extract ions and accelerate its up to the same velocities. So we can estimate a generation of plasma jets too.

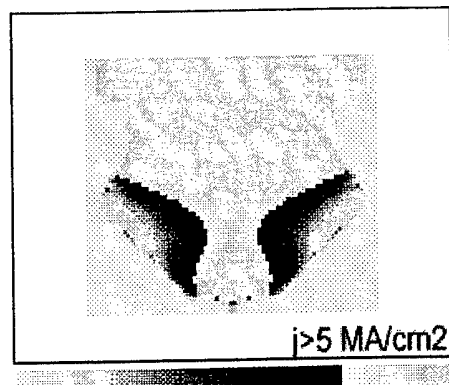
### **High-power particle beams generation by electrical discharges near the neutron stars**

The great interest to considered above "shooting solitons" is connected by its possible manifestation in Stellar atmosphere processes. Earlier [6] we proposed that the considered above effect can explain the generation of strong electron jets from neutron stars. Now we represent some results of direct computer simulation of such exotic electrical discharge (Fig.3,4). As it is known [10] at the surface of neutron stars there exist a thermoemission processes with plasma temperature on the order of 20 eV and more higher up to 200 eV. The tension of electric fields near the surface of neutron stars may be 100 MV/cm in accordance with estimations [10]. In this simulation we proposed that the distance between surface of neutron star crust (with density of iron about of  $10^5$  g/cc) and its magnetosphere equals to 100 as well as in [11]. As it is shown in central region of plasma torch, which is produced by electrical discharges near the neutron star, it is really the current selffocusing and volumetric generation of "shooting solitons" take place. So we may conclude that super high power

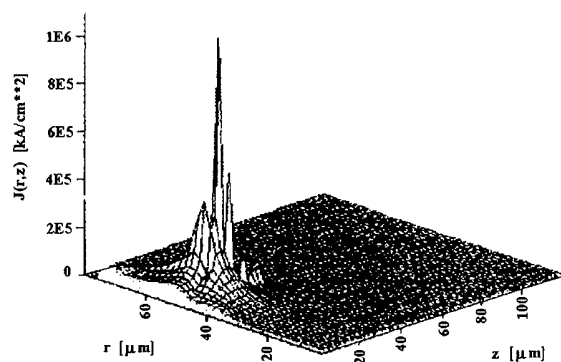


$t = 1.00 \text{ ns}$

a)

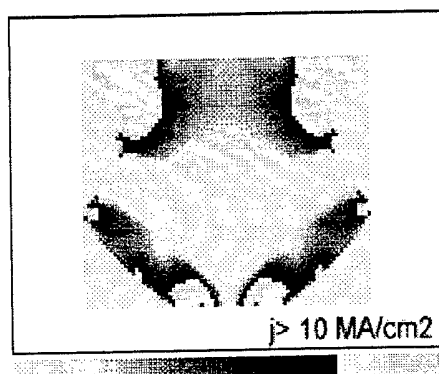


c)



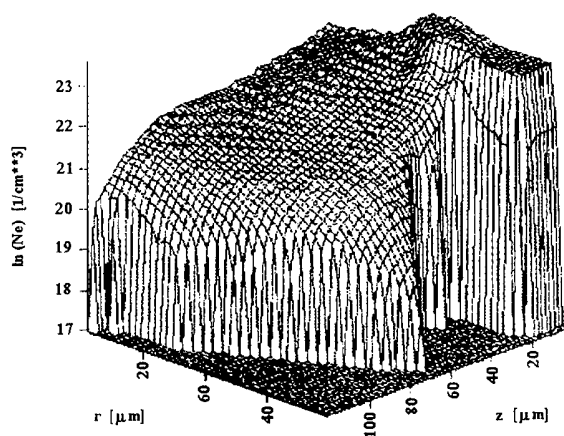
$t = 2.01 \text{ ns}$

b)



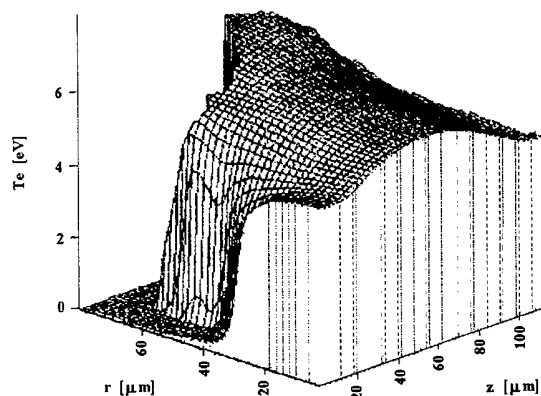
d)

**Fig.1** Current density distribution for  $t = 3.0 \text{ ns}$  (a) and  $t = 3.36 \text{ ns}$  (b) after ignition.



$t = 3.02 \text{ ns}$

a)



$t = 3.02 \text{ ns}$

b)

**Fig.2** Spatial distribution of plasma density (a) and temperature (b) at  $t = 3.0 \text{ ns}$ .

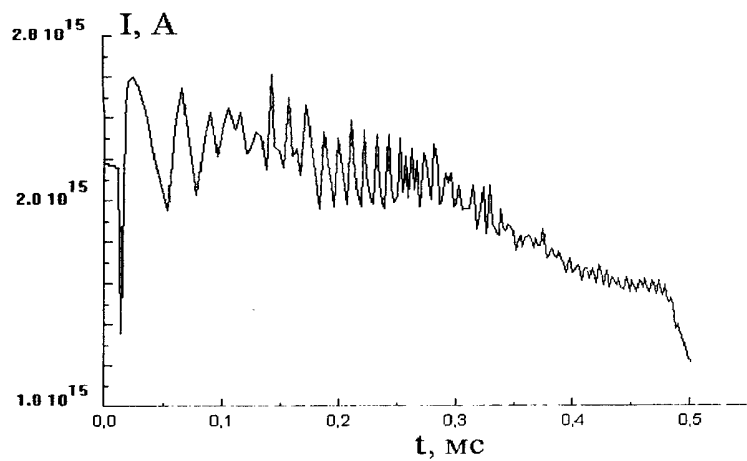
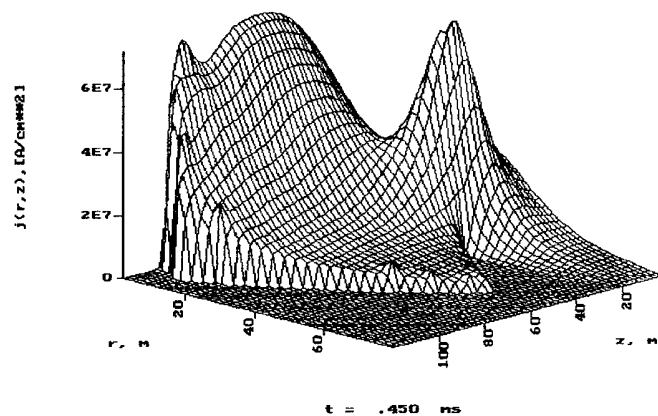
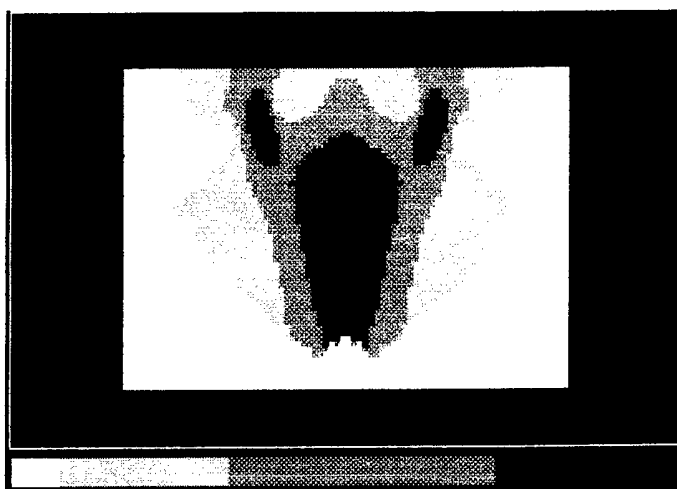


**Fig.3.** Temporal dependence of total current  $I(t)$ .



a)



a)

**Fig.4.** Spatial distribution of current density in plasma torch of neutron star at  $t=0.45 \text{ ms}$ .

electron beams are generated due to this nonlinear phenomena, which then can be accelerated in strong electric fields of stars up to relativistic energies. Note that mechanism of the generation such beams was a grate unsolved problem of modern astronomy. It is obvious that during such electrical discharges (which has character times 0.5-1 ms) the generation of high power electromagnetic radiation take place. Hence now we can explain of some nonunderstand features of electromagnetic bursts of pulsars and QSS by aperiodic processes of considered electrical discharges and so on (see in more detail [6,12]).

### Conclusions

It had been established:

- 1) a selffocusing and defocusing of current owing to the production of channels of high conductivity during the transition metal - dielectric takes place in strongly coupled plasma of cathode torch;
- 2) a surface and volumetric generation of "shooting solitons" (SS) can take place during vacuum breakdowns;
- 3) a new mechanism of selfcontinuation of cathode spots is represented, which is based on the generation of return thermal flux due to SS-generation and overheating instability;
- 4) a new mechanism of relativistic particle beams generation and plasma jets as well as the bursts of electromagnetic (including X-ray radiation [6]) radiation

### Acknowledgment

Authors would like thank to P.V.Milyutin for help in calculations on astrophysical part.

- [1]. Mesyats G.A.: The Ectons. Part.1.Ekateriburg. UIF. (Nauka.1993).
- [2]. Skvortsov V.A., : Proc. of the 40 IEEE Holm conference on electrical contacts. Chicago. (1994) 43.
- [3]. Bushman A.V., Kanel G.I., Nee A.L., Fortov V.E.: Thermophysics and Dynamics of Matter at High Energy Densities. (Hemisphere Publishing Corporation. N.Y.,1992)
- [4]. Gathers G.R. International J. of Thermophysics, 4 (1983) 209.
- [5]. Ebeling W., Fortov V.E., Gryaznov V.K., Forster A., Polishchuk A.Ya.: Thermophysical properties of hot dense matter (Leipzig : Teubner-Texte zur Physik. 1990).
- [6]. Skvortsov V.A., Vogel N.I. , : Proc. of the International Conf. on Physics of Strongly Coupled Plasmas, (1995) 343.
- [7]. Gasilov V.A., Krukovsky A.Yu., Otochin A.A. et al. Preprint Keldysh Institute of Applied Mathematics. Moscow (1990). No. 163.
- [8]. Vogel N.I., Skvortsov V.A. Proc. :Int. Symposium on Electrical Discharges and Insulations in Vacuum, Berkeley (1996).
- [9]. Samarsky A.A., Galaktionov V.A., Kurdyumov S.P., Mikhailov A.P., The regimes with aggregation in problems for quasilinear parabolic equations, (Moscow, Nauka, 1987).
- [10]. Tsygan A.I., : Priroda (1994) 82.
- [11]. Ruderman M.A., Sutherland P.G.: The Astrophysical Journal, 196 (1975) 51.
- [12]. Skvortsov V.A., Milyutin P.V., Zh. E. T. F. (to be published).

# THE GENERATION OF HIGH-POWER CHARGE PARTICLE MICRO BEAMS AND ITS INTERACTION WITH CONDENSED MATTER

Nadja Vogel<sup>1</sup>, Vladimir Skvortsov<sup>2</sup>

<sup>1</sup>University of Technology Chemnitz-Zwickau, Department of Physics, D-09107, Chemnitz, Germany

<sup>2</sup>High Energy Density Research Center, Russian Academy of Sciences  
127412, Moscow, Izhorskaya, 13/19, IVTAN, Russia

## Abstract

As it was observed in experiment [1], during influence picosecond laser beam on the Al-target in air a generation and acceleration of high-power micro electron and ion beams take place. The original theoretical model for describing of generation and particle acceleration of such micro beams in result of micro channeling effect are represented. It had been established, that the extreme states of matter with compression in Gbar pressure range can be produced by such micro beams.

## Introduction

As at first was established in [1] during interaction of high- intensity picosecond laser beam with aluminum target in air an effect of micro-channeling with the generation of an intense electron beam ( with the particle density of about  $6 \times 10^{20} \cdot \text{cm}^{-3}$  ) and following extracting and acceleration (up to few MeV) of an intense (with maximum current density  $j_0 = 4 \cdot 10^8 \text{ A/cm}^2$  ) ion beam appears. For explanation of this phenomena we took into account the possibilities of electron beam focusing and acceleration by pondermotive force of ultra short laser pulse [2]. In contrast to [3] we propose, that the mechanism of ion acceleration is connected with three phenomena, which take place simultaneously :

- the microchanneling of directed energy flows (electron, laser and ion beams);
  - the collective acceleration of heavy ions by the wave of space charge of electron beam, which initially generated by laser beam;
  - the ion acceleration by magnetic field of electron beam (due to Fermi acceleration), which at initial stage has a tubular form, so the during magnetic field compression the ions can have an additional acceleration like as in plasma layer system [4] or in plasma focus system [5,6].
- Perhaps the mechanism of charged particle beams in our case is also due to an azimuthal instability of tubular current carrying plasma [7].

Note that such micro beams of heavy ions may be used for generation of a short pulse of neutron flux and for initiation of controlled thermonuclear fusion in micro volume of gold target with D-T mixture [8]. This paper is a continuation of mentioned above work and deals with an experimental and theoretical investigation of high-power ion beams generation and its interaction with condensed matter (gold targets). The computer simulation of micro ion beams (with pulse duration  $\tau = 100 \text{ ps}$ , current density  $400 \text{ MA/cm}^2$ , diameter of beam  $5 \mu\text{m}$ ) interaction with a condensed matter was produced by using mathematical model [9,10], in result of which it is predicted that the extreme states of matter with compression in Gbar pressure range accur.

### The generation and acceleration of micro beams

In result of analysis of different possible mechanism of charged particle acceleration [2-7] we conclude that none of them has a single operation in our case. Probably some of them combination takes place. Especially great interest for our opinion has theoretical model [7], because of namely the tubular plasma jet generation takes place (see Fig.1) at initial stage as it was established in experiments with a good repetitions. Unfortunately, in [7] a simplest case of dynamic particle acceleration in tubular uncompressive plasma jet with fixed boundary was considered and hence we can not directly use this model.

We think that the observed acceleration of intense charged particle beams may be explained by the following scheme: 1) selffocusing laser beam and production channel of hot air with small diameter (about of 10  $\mu\text{m}$ ) for transportation of electrons, which are extracted from Al-plate; 2) the generation, acceleration (by pondermotive force of laser wave) and transportation a high intense electron beam in such channel; 3) the collective (by space charge of electrons) and Fermi like acceleration of Al-ions.

The measurement of magnetic field by using Faraday effect shows that the induction of magnetic field may reach the values up to 7.6 MG, and tension of electric field -  $10^8$  V/cm. So due to this fields the AL-ions (with mean charge  $Z=4$ ) can accelerates up to 8 MeV.

At the later stage the electron current can return back (see Fig.2, at which two electron flows moving in opposite directions are shown). In this experiments the laser probe pulse was with  $\lambda=532$  nm. For our estimation the ion acceleration take place during approximately 100 ps. So let us consider the dynamics namely ion micro beams with matter. For this purpose we produce the next computer simulation.

### The interaction of heavy ion micro beams with matter

We used the mathematical model, which is based on the system of two-dimensional hydrodynamic equations (in  $r$ - $z$  -geometry) and is complemented by wide-range equations of state (analogous as in [10]), corresponding correlations for the calculation of beam energy loss in the matter (with taking into account the dependence of stopping power on the temperature). The hydrodynamic equations were integrated on a rectangular region by the big particles method [11] of the first degree of approximation on time and space. The energy loss by radiation and energy input due to thermonuclear reaction (in a corresponding cases of D-T targets) were taken into account. Equations of energy and number of particles (D, T,  $^3\text{He}$ ,  $^4\text{He}$ , protons and neutrons) balance of thermonuclear reactions were solved with taking into account the present-day information about cross-section and rate coefficients of the resonance thermonuclear reactions [12]. In our calculations we varied parameters ( $E_0, j_0, \tau$ ) of heavy ion beam (Al-ions, at  $1.6 \cdot 10^{12}$ - $3 \cdot 10^{16}$  W/cm $^2$ ) and targets as well as material of target and percentage of D:T. But now we consider mainly the case when the maximum current density of ion beam was equal  $4 \cdot 10^5$  A/cm $^2$  (such current density may be easy obtained in experiment). In these examples ion beams are uniform cylindrical beams with the parabolic pulse time form:  $j(t)=j_0 (t/\tau)[1-(t/\tau)]$  for  $t<\tau$ , and  $j(t)=0$  for  $t>\tau=100$  ps. The total energy  $E_t$  of such beam is  $j_0 E_0 \pi d_s^2 / 24$  and equals 0.00002 J. Note, that the energy of laser pulse was about of 0.06 J. So in this a case may be realized if only 0.03 % of laser beam energy is transferred to ion beam.. Some spatial distribution of the main matter parameters for the time  $t=1$  ns are represented on Fig.3. These are not record parameters. At the end of pulse influence at time  $t=0.1$  ns the maximum value of pressure in the target reaches 8 Mbar, specific internal energy -23 kJ/g.

Note, that, as it was obtained in our computer simulation the possibility of extreme state generation with pressure of about few Gbar in Au-target by heavy (Al-) ion beam with more higher intensity may be achieved. For example in case when the current density of micro ion beam was 400 MA/cm<sup>2</sup> and energy of Al-ions was 8 MeV the corresponding maximum values were 0.77 Gbar and 23.7 MJ/g. In a case when  $j = 4$  GA/cm<sup>2</sup> the maximum pressures increased up to 3.3 Gbar and specific internal energy was about of 128 MJ/g. As it was shown in [8] at such ion beam parameters (when its total energy equals 0.001-0.01 J) the initiation of thermonuclear reaction is possible in D-T mixture, which is arranged between two thin gold plates.

### Conclusions

It had been shown, that during short pulse laser discharge the complex mechanism of heavy ion acceleration can take place in result of which the ions can accelerate up to 4-8 MeV on the distance of 100  $\mu$ m. In principal one can continue ion acceleration to more higher energies by using the second and so on laser beams.

- [1]. Vogel N.I., Heinzinger J.,: Proc. XXII - ICPIG (1995) 4, 11.
- [2]. Letokhov V.S.,: Pis'ma v Zh. E.T.F., 61 (1995) 787.
- [3]. Andreev N.E. et al.,: Zh. E.T.F., 90 (1990) 881.
- [4]. Men'shikov L.I. et al.,: Atom. Energy, 71 (1991) 511 (In Russ.).
- [5]. Filippov N.V., A.N.Filippov, Brzosko J.R.,: Proc. ICPIG (1995) 4, 9.
- [6]. Browne P.F.,: Laser and Particle Beams, 6 (1988) Part.3, 409.
- [7]. Kutvitskii V.A., Solov'ev L.S.,: Zh. Tech. Fiz., 65 (1995) No.11, 198.
- [8]. Skvortsov V.A., Vogel N.I., Lebedev A.N.,: Proc. Int. Symposium on Electrical Discharges and Insulations in Vacuum. (Berkeley, 1996).
- [9]. Skvortsov V.A., Fortov V.E.,: SPIE Proc. from Conference Vol.1629: "Intense Microwave and Particle Beams III". Los Angeles, CA USA, (1992) 379.
- [10]. Fortov V.E., Skvortsov V.A., Lomonosov I.V. et al.,: Proc.Int.Conf. on High Power Particles Beams. (Washington, 1992).
- [11]. Belotserkovskii O.M., Davydov Yu.M.: Method of Large Particles in Gas Dynamics, (M.: Nauka, 1982)
- [12]. Gus'kov S.Yu. et al.,: Atom. Energy, 63 (1987) 252.

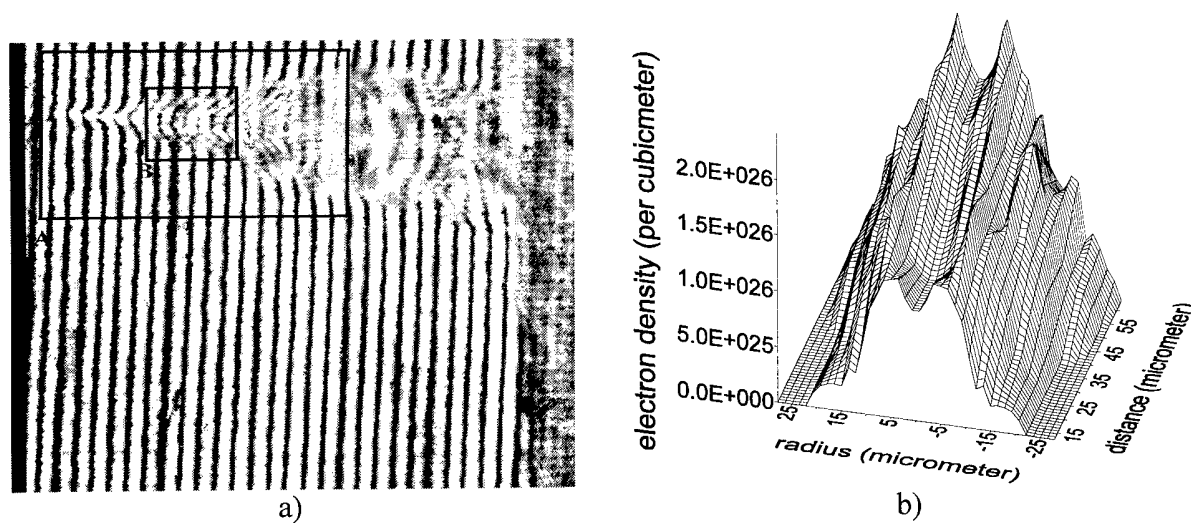
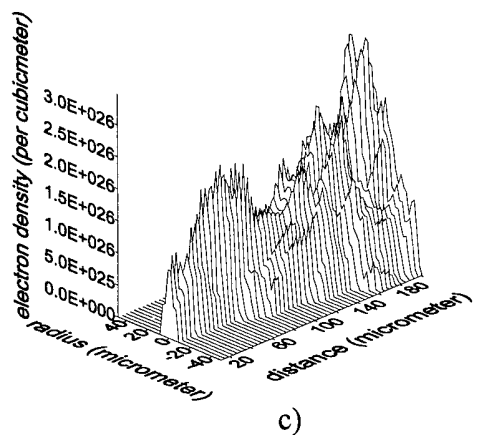


Fig. 1

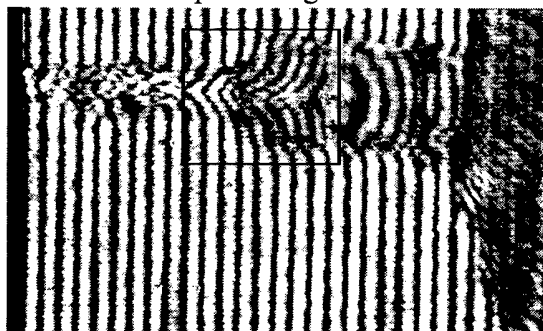


c)

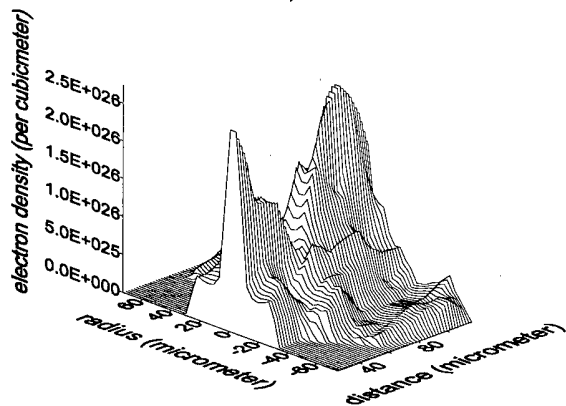


d)

Fig.1 The interferogram (b), electron density distribution (b,c) and Absorbion image (d), for time  $t=250$  ps after ignition.

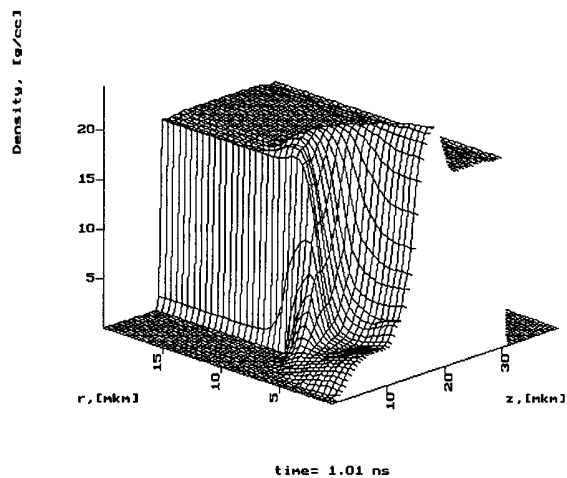


a)

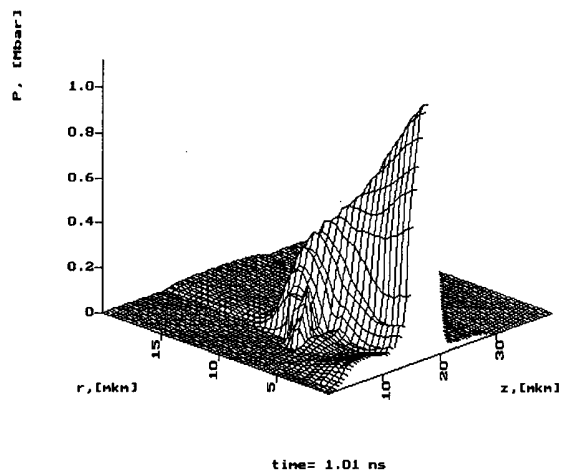


b)

Fig.2. The interferogram (a) and electron density distribution (b) for delay time  $t=1.16$  ns after ignition.



a)



b)

Fig.3: The distributions of density -(a) and pressure (c) of matter at  $t=1.0$  ns.



# THE RAYLEIGH-TAYLOR INSTABILITY AND K-SHELL RADIATION YIELD FOR IMPLODING LINERS

R.B.Baksht, I.M.Datsko, A.Yu.Labetsky, A.G.Rousskikh, A.V.Fedyunin

*High Current Electronics Institute, 4 Akademichesky Ave., Tomsk, 634055, RUSSIA*

## Abstract

The experiments on the GIT-4 1.5 MA inductive generator with the 1.2  $\mu$ s current delivery to the inductive store were carried out. A single gas puff with the initial diameter of  $\varnothing 28$  mm was used as a load. Three different kinds of gas Kr, Ar, Ne were used. Dependence of the X-ray yield on mass of the gas liner has been investigated. Experimental investigation of RT-instability has been carried out with the help of a streak camera. The comparison between the RT wave amplitude and X-ray yield was performed.

## Introduction

One of the parameters that determine the power of X-ray emission for liner compression is simultaneity of liner shell compression as a whole. Such simultaneous liner compression is possible only if in the plasma all instabilities causing breaks in the plasma shell are suppressed. RT-instability is the main reason of the low coefficient of compression in imploded radiation load [1-4]. Experimental study of RT-instabilities as a function of gas puff mass and the atomic number of gas is the main goal of the work.

## Experimental setup

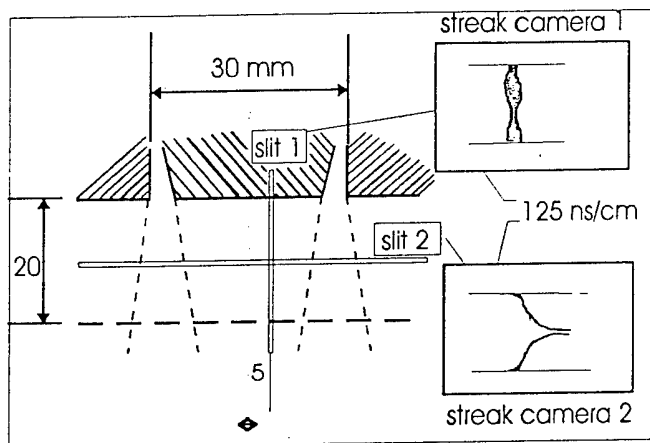


Fig.1. Experimental setup.

The experimental setup is shown in Fig.1. Using two different streak cameras with a 100  $\mu$ m slit (axial slit1 and radial slit2) to the liner we have a possibility of knowing the velocity  $v$ , the acceleration  $g$  and the shape of the liner shell at the moment when the liner's radius is equal to  $r = 5$  mm. The input of x-ray was measured by filtered XRD in the range below 1 keV and in the range more then 1 keV. The K-shell radiation was measured for Ne and Ar gas puff, and L-shell radiation for Kr. The

liner current has 120 ns rise time, 300 ns plateau; current amplitude was  $1.2 \pm 1.5$  MA.

## Results

Experimental results are shown in Fig.2-4 for Kr, Ar and Ne, respectively. The gas puff mass was varied from 7 to 230  $\mu$ g/cm. For all kinds of gas we observed the trend to suppress instabilities when the mass of the imploding liner was increased. For low liner mass the development of RT-instability leads to reduction of K-shell emission because of nonsimultaneity of liner shell compression. In the case of Ar and Kr liner, the predominant mode is  $m = 0$ , in the case of Ne liner the predominant mode is  $m = 1$ . The breaks in the gas shell that appear through the short-wave modes of the developing RT-oscillation are responsible for complete disappearance of the K-radiation of the low-mass liners.

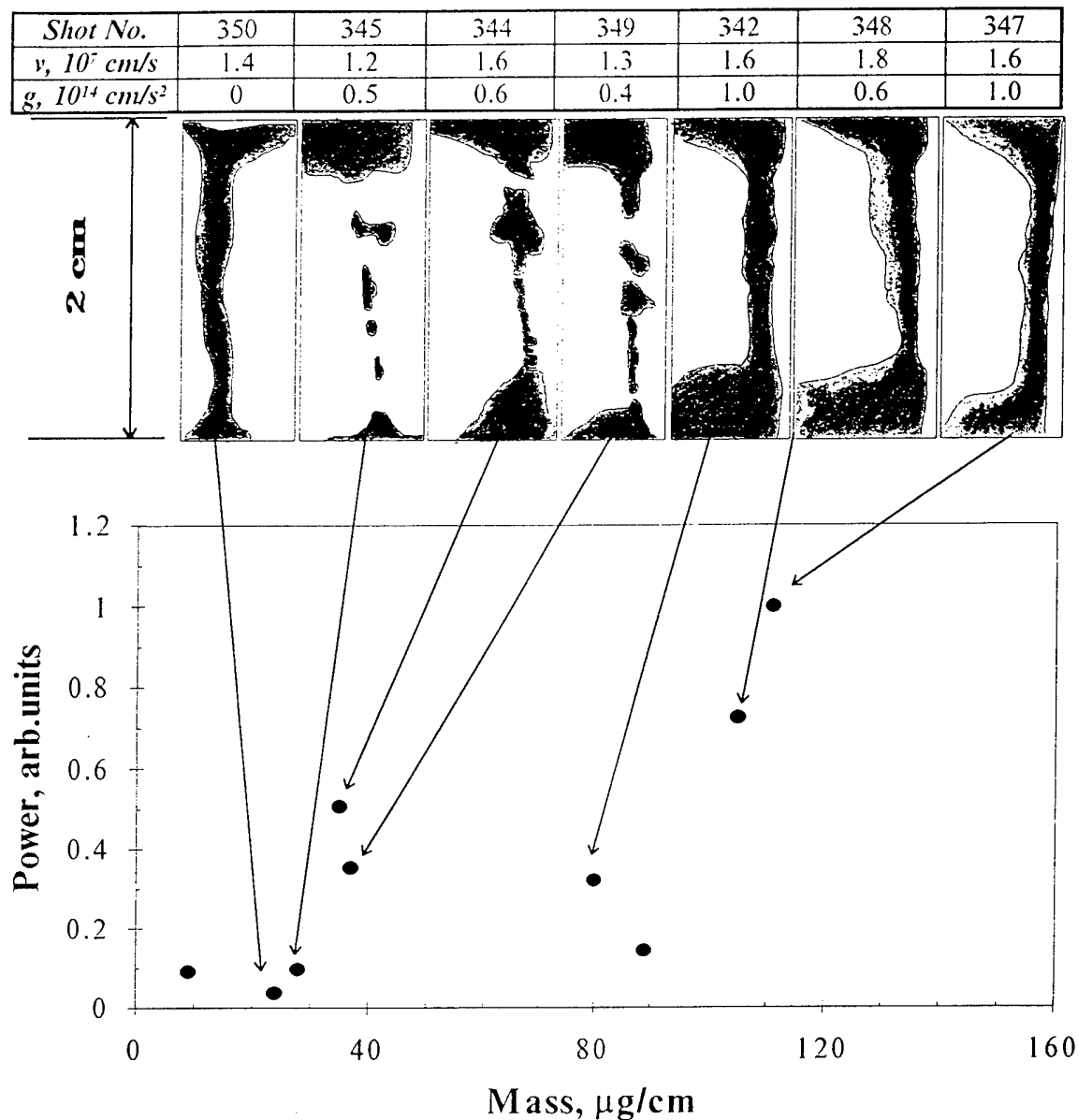


Fig.2. (top) Experimental velocity and acceleration at the moment when the plasma radius is 5 mm for some shots of Kr ( $A = 80$ ) gas puff with different mass. (middle) Axial streak camera pictures for the same shots. (bottom) L-shell radiation power versus on the gas puff mass. The instability wave amplitude is reduced with the mass increase. The Marx charge voltage is 45 kV.

It is necessary to say that the implosion is stable for the separate shots with low mass (for example, Sh.No.350 for Kr), but L-yield in this case is zero. In all shots of this kind the acceleration is zero and 40-50 ns before the moment of compression an intensive X-ray emission in range below 1 keV was observed. We are inclined to think that in the shots there is a breakdown and formation of a current sheet in gas with low concentration inside the shell. Also the embedded B-field results in the suppression of RT-instabilities and, on the other hand, reduces the X-ray yield harder 1 keV /5/.

#### Summary

The amplitude of RT-oscillations is reduced with liner mass for all examined gases. In linear approximation the oscillation amplitude  $\Delta r$  is given by:

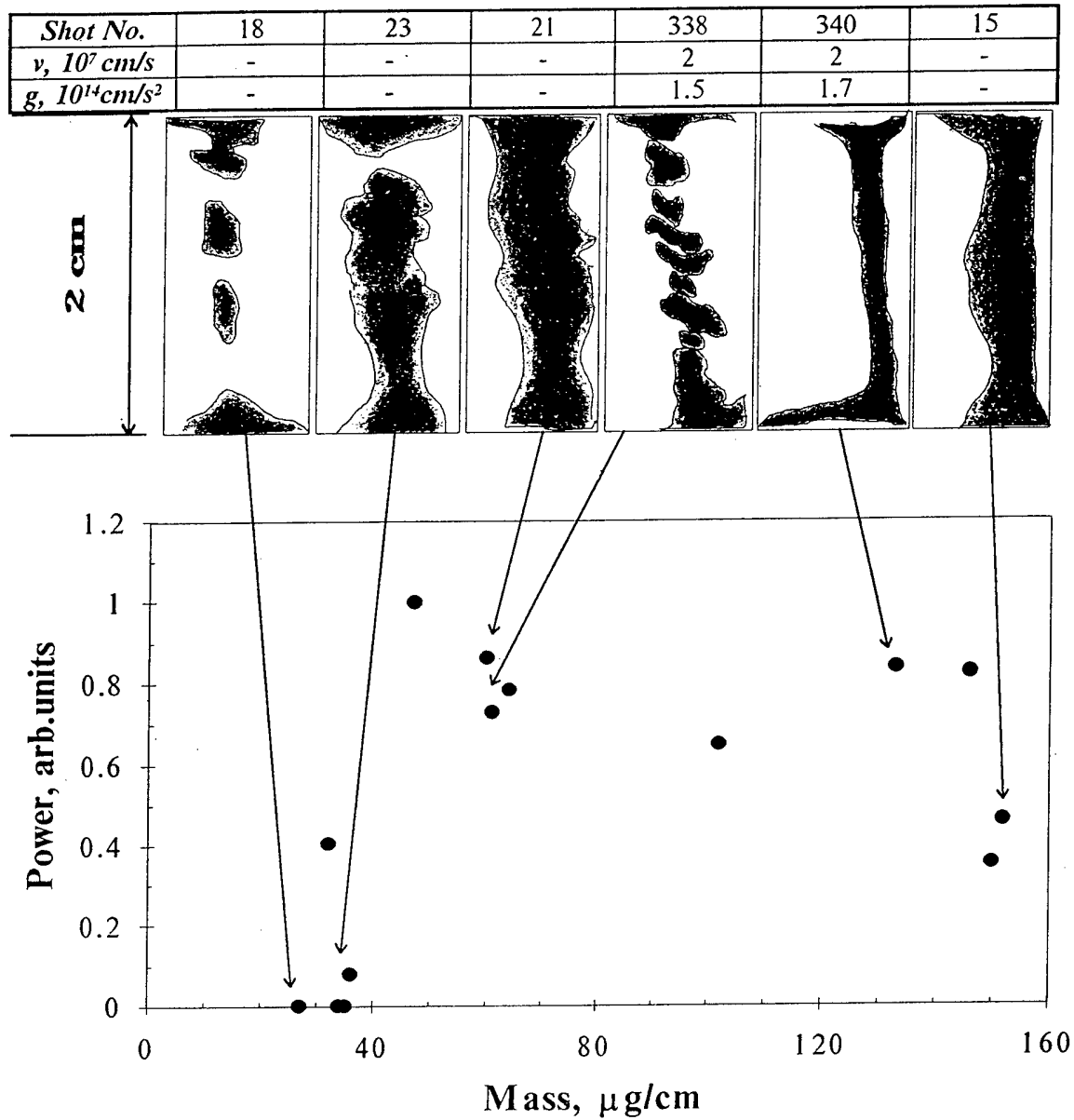


Fig.3. (top) Experimental velocity and acceleration at the moment when the plasma radius is 5 mm for some shots of Ar ( $A = 40$ ) gas puff with different mass. (middle) Axial streak camera pictures for the same shots. (bottom) K-shell radiation power versus on the gas puff mass. The instability wave amplitude is reduced with the mass increase. The Marx charge voltage is 50 kV.

$$\Delta r \approx \exp \left\{ \int (g \cdot k)^{1/2} dt \right\} \quad (1).$$

Using experimental data, we find that the integral value to be almost the same for light and hard liners. At the same time, if the instability increments are calculated using the magnitudes and the radial profiles of MHD functions (temperature, magnetic field, density) that are established in the liner after the propagation of the shock wave, the interpretation of the experimental results obtained becomes possible: the instabilities grow more intensely in light liners than in hard ones, which can be accounted for by the presence in light liners higher gradients of magnetic field and material density [3].

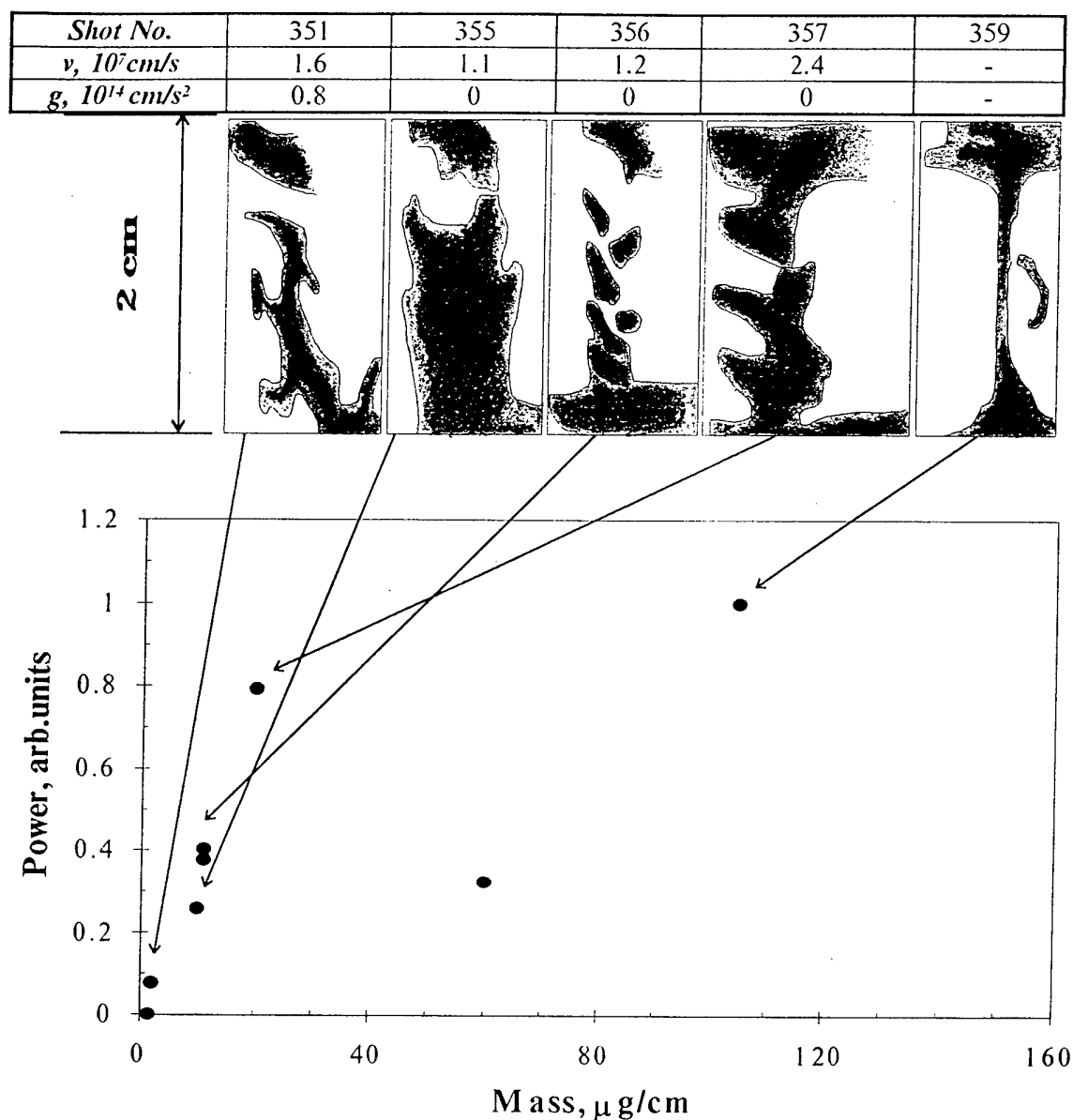


Fig.4. (top) Experimental velocity and acceleration at the moment when the plasma radius is 5 mm for some shots of Ne ( $A = 20$ ) gas puff with different mass. (middle) Axial streak camera pictures for the same shots. (bottom) K-shell radiation power versus on the gas puff mass. The instability wave amplitude and the visible light thickness of gas shell are reduced with the mass increase. The Marx charge voltage is 45 kV.

#### References

- [1] Roderik N.F., Hussey T.W. AIP Conf. Proc., Dense Z-pinchs, 195, (1989), p.157.
- [2] Branitskii A.V., Vikharev V.D., Zakharov S.V. *et al.* Fizika Plazmi, 17, (1991), p.531.
- [3] Baksht R.B., Datsko I.M., Kim A.A. *et al.* Plasma Phys. Rep., 21, (1995), p.959.
- [4] Peterson P.L., Bowers R.L., Brownell J.H. *et al.* AIP Conf. Proc., Dense Z-pinchs, 299, (1993), p.388.
- [5] Sorokin S.A., Khachatryan A.V., Chaikovsky S.A. Fizika Plazmi, 17, (1991), p.1453.

# INVESTIGATION OF ENERGY AND CURRENT CONCENTRATION IN COMPOSITE Z-PINCH THROUGH IT'S SOFT X-RAY EMISSION ON ANGARA-5-1

A.V. Branitsky, E.V.Grabovsky, S.V.Zakharov, M.V.Zurin, G.M.Oleinik,  
V.P.Smirnov, I.N.Frolov, V.V.Borisov\*, Yu.K.Slavnov\*, Yu.K.Usov\*.

*Troitsk Institute of Innovative and Fusion Research,  
Troitsk, 142092, Russia*

*\* Scientific Research Institute of Impulse Technique,  
Moscow, Russia*

## Abstract

Z-pinch of thin dense fiber with gas shell (Composite pinch) was investigated at level of current  $\sim 2-3$  MA on "Angara-5-1" generator. High efficiency of generator power transfer into the pinch of 0.6-1 mm diameter was achieved when masses of gas and wire was comparable ( $20-40 \mu\text{g/cm}$ ). At time of increase of a current  $\sim 90$  ns powerful ( $\sim 0.5-1$  TW) pulses of soft X-Ray radiation with front rise time up to 1 ns were obtained. Up to a maximum of a pulse of radiation the current from an external plasma shell penetrates mainly into plasma corona of the fiber. The corona consists of small part of fiber substance which is evaporated by radiation during compression of external shell.

## 1. Introduction

The high current Z-pinchs constantly attract attention of the researchers due to an opportunity of achievement of a super dense and high-temperature conditions of substance, applications for bright sources of radiation, ICF and fundamental researches. However instabilities destroy a pinch before the substance will be essentially compressed. From here it is clear aspiration to use as a starting basis solid-state fibers with rather small amount of substance [1-3], to ensure fulfillment of conditions of the Bennet at temperature of  $\sim 1-10$  keV and currents of a megaampere level. Thus source of a current should have short duration of a pulse to avoid premature explosion of a fiber and multimegavolt level due to high inductance if thin wire. As result, the installation becomes a rather complex and expensive structure.

In 1992 in [4] at a level of a current 200 kA other approach was practically realized. There is a wire surrounding by low dense plasma shell, sharply lowering initial inductance of system. In an ideal picture of the phenomenon magnetic compression of the shell on the wire results in partial transfer of a current on a fiber or its corona, which can arise because of preliminary energy input. However the instabilities should complicate processes.

1992-93 years under the initiative B.Etlicher (Ecole Polytechnique, Paris, France), P.Choi (Imperial College, London, England) and F.Vessel (California University, Irvine, USA) on installation "Angara-5-1" [5] (TRINITI, Troitsk, Russia) were spent two joint experiments on compression of a gas puff on a wire, directed on finding - out of efficiency of transfer of a current and energy on an axial loading. In comparison with [4] the current in experiments was on the order above ( $2-3$  MA). Output power of installation was up to 6 TW.

A wide set of diagnostics from different countries was used. This publication is based on only part of Russian diagnostics: X-Ray photo diodes (XRD) 0.15-2 keV, optical and X-Ray (0.15-2keV) streak cameras, 3 frame laser shadow pictures.

## 2. Experimental setup and diagnostics

The pinch was formed by discharge through the dense fiber ( $\varnothing 5-30 \mu\text{m}$ ) of Cu, Al,  $\text{CD}_2$

with high Z gas shell (Xe, Ar and its mixture, 10-70  $\mu\text{g}/\text{cm}$ ). Nozzle for gas puff was 20 mm wide. For energy penetration investigation wires were coated by  $\text{SiO}_2$ , Pd, Ti, agar-agar with NaCl or uncoated. The experiments were done on "Angara-5-1" facility on 2-3MA current level. The current rise time was about 90ns.

The soft X-Ray (SXR) radiation was tested by vacuum X-Ray photo diodes (XRD) and X-Ray streak-camera CXP-3 with time resolution 0.5-1 ns. Using of some filtered XRDs have allowed to deconvolute a flux and a rough spectral distribution of emission in the range 0.1-2keV, that falls the main part of power on. X-Ray streak camera allowed to obtain emitter space size in this  $h\nu$  range. In addition 3 frame (2ns) ruby laser shadowgraphy [6] and optic streak camera CΦЭP-2 [7] were used.

XRD filters [ $\mu\text{g}/\text{cm}^2$ ] in 1st experimental run were [8] :X1: mylar(340), X4: mylar(680), X3: mylar(1020), X2: mylar(2030)+Al(100). In 2nd run filters were changed to allow higher sensitivity: X1: mylar(340); X2: mylar(340)+Al(100); X3: Al(810); X4: mylar(340)+Sn(70) (shots 101-106), mylar(640) (##107-115), Cu(400) (##116-120).

Cathodes were aluminum [9]. X5 had carbon stable absolutely calibrated cathode with filter mylar(150). XRDs were placed at 2-3 m from radiation source. All diagnostics described have seen Z-pinch in radial direction. The collimator (2 mm slit along a radial direction) was placed at the distance  $\sim 25\text{cm}$  from the center to exclude zipper-effect.

Current was measured by dB/dt probes at radius 110 mm.

### 3. General scheme of pinch formation

The picture of pinch compression looks as follows. After breakdown gas shell implodes by it's own current. Skin layer thickness is 0.3-1 mm as it is seen from laser, optic streak pictures (fig.1). Due to bad profile of nozzle zipper-effect is rather large,  $\sim 10$  ns.

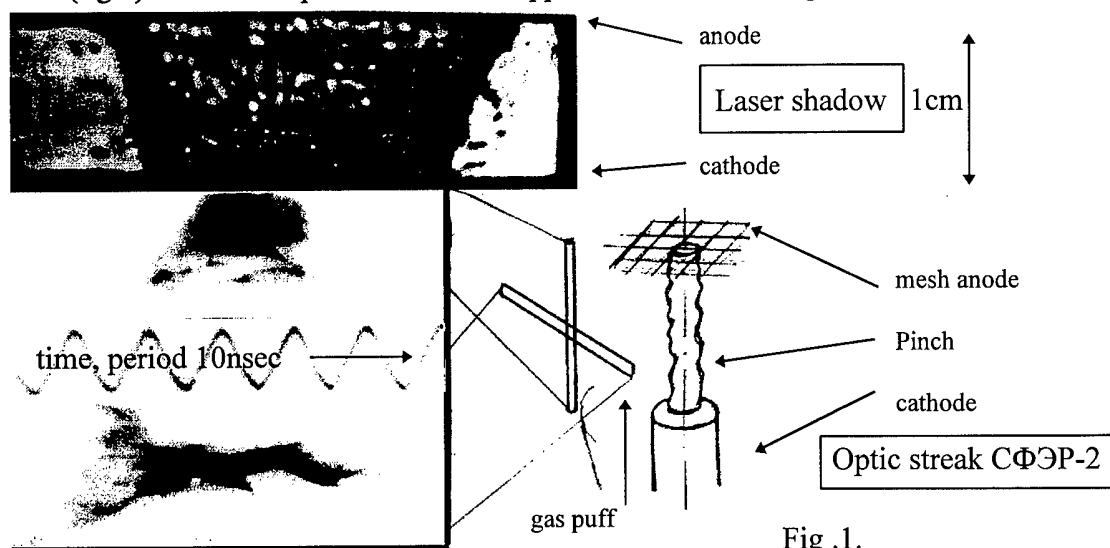


Fig.1.

Upper layer of fiber evaporates due to outer shell emission and, possibly, thermoconductivity, making fiber corona of  $\varnothing 4-10$  mm. Imploding current shell strikes fiber corona with velocity  $5-10 \cdot 10^7 \text{cm}/\text{sec}$  (fig.1). A part of magnetic energy of outer shell can be transferred into corona this moment. Strike is seen as first spike or short front on XRD signals (fig.2). After  $\sim 15\text{nsec}$  pinch collapses down to diameter 0.6-1.5 mm. This correspond to maximum emission. This spike was 2-5 nsec long for Xe and Xe+Ar gas. For pure Ar it was 8-12 nsec. Total emission duration is 20-30 nsec without and 7-10 nsec longer with zipper effect. In contrary to pinch from single fiber no or few necks are seeing in Composite pinch. The pinch is more uniform as it was shown by laser and streak pictures. Central part of fiber remains compact and weekly heated just before first pinch collapse. After collapse instabilities

$m=1$  develops on pinch and it explodes. Sometimes additional collapses follow the first one.

#### 4. Influence of an external plasma shell

In our case of strongly emitting plasma radiation losses  $W_{\text{rad}}$  is predominant. For example, even for  $T_e=1$  keV power of losses through electronic thermoconductivity [11] ( $L=1\text{cm}$ ,  $I=2\text{MA}$ )

$$W_{\text{end}} = 2.5(kT_e I)/(eL) \sim 10^9 - 10^{10} \text{ W} \ll W_{\text{rad}} \sim 10^{11} - 10^{12} \text{ W}$$

Therefore more emission correspond to more effective energy transfer to pinch. Most powerful radiation was registered for every substance in case of comparable masses of outer shell and wire, about  $20-40\mu\text{g/cm}$ . For Xe and Ar with Xe (1/20 on atomic density) power were maximum, up to  $0.7-0.9\text{TW}$ . For Ar emitted power was 2-3 times less ( $\sim 0.3\text{TW}$ ). For  $\text{D}_2$  radiation was  $\sim 0.1-0.15\text{TW}$ . Flux and spectral features were measured by XRD set.

	Xe 0.4 bar	Ar 1.4 bar	Xe 0.1bar + Ar 0.6bar
front rise time	1-2nsec	$\sim 5\text{nsec}$	like Xe
peak length	2-4nsec	$\sim 10\text{nsec}$	like Xe
max. power	$\sim 0.7\text{TW}$	$\sim 0.3\text{TW}$	$\sim 0.8\text{TW}$ , like Xe
position of spectral maximum	0.3-0.4keV	0.4-0.6keV and 1-2keV	0.4keV, like Xe
oscillations	yes	no	no, like Ar

From time integrated spectrographs measurements in band  $0.7-5$  keV [10] plasma electron temperature is  $T_e=600-800\text{eV}$ . Registered radiation power corresponds to much lower temperature of main part of pinch matter  $150-250$  eV. It should be noted that so high temperature characterizes rather small part of pinch substance (hot core).

For Xe outer shell oscillations of the pinch take place. And no oscillations with Ar and Ar+Xe. It possibly can be explained by long ion-electron energy exchange time  $\tau_{ei}$  for Xe.  $\tau_{ei} = 5 \cdot 10^4 \cdot (m_i/m_e) \cdot (T^{3/2}/Z^2 n_i m_e) \sim 80\text{nsec}$  for Xe and  $\sim 10\text{nsec}$  for Ar for the same mass per pinch length due to lower atomic mass and higher  $T$  for Ar. For Xe  $\tau_{ei} \sim$  time of implosion, ions can't loose they energy in first collapse and there are a set of spikes. For Ar+Xe  $\tau_{ei}$  is determined by Ar and emittance by more radiative Xe (see fig.2).

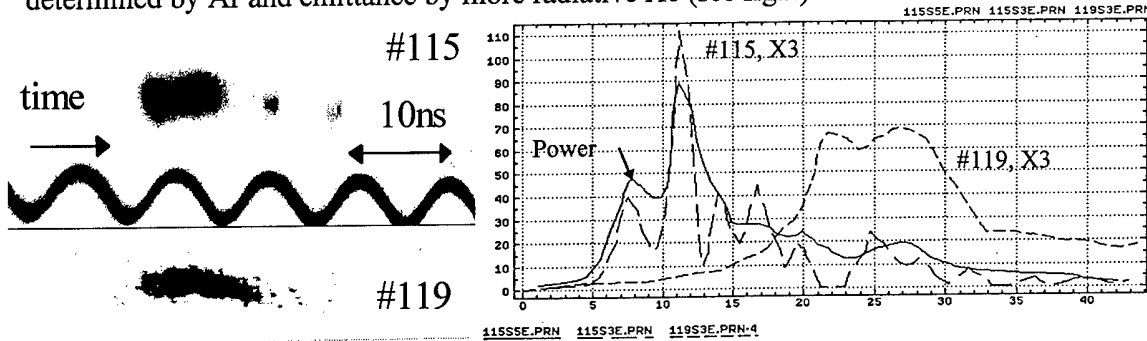
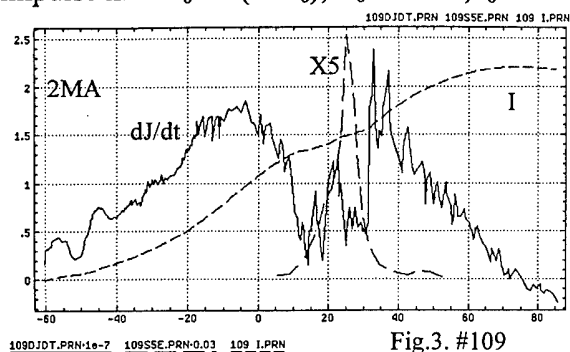


Fig. 2. #115 - Xe 0.4 bar, pinch diam. 1.5 mm. #119 - Ar 1.4 bar, pinch diam. 0.6 mm.

#### 5. Fiber corona formation, energy and current concentration.

Upper layer of fiber also influences radiation power, spectral features and XRD signals shape. Radiation flux for  $\text{CD}_2$  was 2-4 times less than for other fibers. It was more (4-8) additional small spikes on signals. Al and Cu with  $\sim 1\mu\text{m}$   $\text{SiO}_2$  coating fibers give almost the same emission in spite of twice more  $Z$  for Cu. But additional  $\sim 1\mu\text{m}$  Pd coating of Cu+  $\text{SiO}_2$  gives more soft and powerful radiation, especially in the moment of outer shell striking to the fiber corona. This allow us to conclude that only upper layer ( $\sim 1\mu\text{m}$ ) of wire material evaporates and explodes during current shell implosion and that current penetrates mainly into this part of fiber matter up to the first pinch collapse on axis.

"Angara-5-1" generator input to the load  $W_{AS} = (2E - rI)I - (L_c - L(t))dI/dt$ . Generator impulse  $E = E_0 \cos(\pi t/t_0)$ ,  $E_0 = 1.2$  MV,  $t_0 = 120$  nsec. Maximum  $E(t=0)$  usually occurs  $\sim 20$  nsec after



$dI/dt$  maximum. "Angara-5-1" wave resistance  $r = 0.25$  Ohm, inductance  $L_c = 18$  nH  $\gg L(t)$ . Even for pinch collapse (1 mm diameter) load inductance  $L(t) = 7$  nH. In the moment of first collapse on axis radiation is maximum,  $W_{rad} \sim 0.7-0.8$  TW,  $E = 1-1.2$  MV,  $dI/dt$  has minimum and low,  $I \sim 0.8-1.2$  MA. Therefore generator energy transfer into pinch of 0.5-1.5 mm diameter (measured by X-Ray streak, see fig. 2) is very effective,  $W_{rad}/W_{AS} \sim 50\%$ .

We can roughly estimate the current through such a pinch assuming that radiation losses equals to Joule heating  $W_{rad} = W_{joule} = \pi R^2 h J^2 / \sigma_E$ . Here  $R$  and  $h$  are pinch radius and height,  $J = I / \pi R^2$  - current density. This gives us  $I = (\pi R^2 \sigma_E W_{rad} / h)^{1/2}$ . Taking Spitzer conductivity for our conditions ( $T_e \sim 200$  eV,  $W_{rad} \sim 0.7$  TW,  $h = 1$  cm, skin  $\sim 0.2-0.4$  mm) we obtain about  $I = 0.3-0.6$  MA through 0.5-1.5 mm diameter. Current gauge gives 0.8-1.4 MA this moment.

## 6. Summary

So, in Z-pinch from a thin wire and light outer gas shell of comparable weights it is possible to compress significant part of a pinch current (on MA level) up to a diameter 0.6 mm.  $R_0/R_{fin} = 20-30$ . At time of increase of a current  $\sim 90$  ns we achieve powerful ( $\sim 0.5-1$  TW) pulses of soft X-Ray radiation with front rise time up to 1 nsec with high efficiency of generator power transfer into the load.

Down to a maximum of a pulse of radiation the current from an external plasma shell penetrates mainly into plasma corona of the fiber. This corona consists of small part of fiber substance which is evaporated by radiation during compression of external shell.

## 7. Acknowledgments

This work was done in frame of JEX'92-93 experiment. The authors would like to thank B. Etlicher, P. Choi and F. Wessel for fruitful coworking and financial support, M. V. Fedulov and S. L. Nedoseev for discussions. The work was also supported on "Angara-5-1" by Department of Science and Technology of Russia. Cont. 01-42.

- [1] Hammel J.E., Scudder P.W. Proc. of 14th Europ. Conf. On Contr. Fus. And Plasma Phys. Madrid, 1987. Ed. by F. Englman, J.L. Alvarez. Europ. Soc. Geneva, 1987, p.450.
- [2] Sethian J.D., Robson A.E., Gerber K.A., De Silva A.W. Phys. Rev. Lett. 1987, v.59, p.8992.  
M.G. Haines. Proc. of the workshop on Physics of Alternative Magnetic Confinement Schemes, 1990, Varenna, Italy, p.227-287.
- [3] Yankov V.V. Preprint N4218/7. M.: IAE., USSR. Sov. J. of Plasma Physics. 1991, v.17, p.521.
- [4] Wessel F.J., Etlicher B., Choi P. Phys. Rev. Lett., 1992, v.69, p.3181-3185.
- [5] Grabovsky E.V., Smirnov V.P., Yampolsky I.P., e.a. "Angara-5-1 facility". Atomic Energy, 1989, v.69(3), p.45.
- [6] Dorokhin L.A., Smirnov V.P., Tulupov M.V., Tsarfin V.Ya Preprint IAE-3814/7, M.: 1983.
- [7] Borisov V.V., Vikharev V.D., Tsarfin V.Ya, e.a. Pribory i Tekhnika Eksperimenta (Rus.), n.1, p.215-217, (1989).
- [8] Veigele Wm.J. Atomic Data Tables, 5, 51, p.51-111, (1973).
- [9] Day R.H., Lee P. S. Appl. Phys., v.52, n.11, p.6965-6973 (1981).
- [10] Rosmej F.B., Rosmej O.N., Komarov S.A., e.a. AIP conf. proc. 299. Dense Z-pinch. 3d intern. conf., p.552-559. London, UK, 1993.
- [11] Robson A.E. Physics of a Dense Z-Pinch Fusion Reactor. Proc. of the workshop on Physics of Alternative Magnetic Confinement Schemes, 1990, Varenna, Italy, p.595-609.



## MEASUREMENTS OF SOFT X-RAY POWER AND SPECTRAL FEATURES ON "ANGARA-5-1"

A.V.Branitsky, G.M.Oleinik

*Troitsk Institute of Innovative and Fusion Research,  
Troitsk, 142092, Russia*

### Abstract

In many tasks, related with high temperature plasmas and ICF, it is important to investigate power and spectrum features of radiation with nanosecond resolution. The methods of measurements and signal processing for finding them are presented. They were used in experiments on "Angara-5-1" facility in 0.1-2 keV band. Time resolution 0.5ns.

### 1. Introduction.

Eight-modules generator "Angara-5-1" (Russia) [1] was built for ICF and related research. In liner implosion [2] and Z-pinch experiments [3] on "Angara-5-1" the hot plasma radiates about 10ns in the range 0.1-2 keV. Soft X-ray yield reached 100kJ [4]. The knowledge of radiation power and spectrum features is very important in these experiments. Methods described below allowed us to measure them.

### 2. XRDs, cathodes, filters.

Using of several X-ray diodes (XRDs) with different filters has allowed to measure the power and, roughly, the spectral distribution of emission. Pickups (front rise time 0.5ns and 1 ns) had a massive Al, Ni or C photo cathode and were filtered by different filters. Three sets from last experiments are listed below for example (in brackets densities are in  $[mg/cm^2]$ ):

Set	channel 1	channel 2	channel 3	channel 4
1	mylar(340)+Sn(183)	mylar(475)+Al(135)	Cu(620)	mylar(680)
	Al cathode	Al cathode	Al cathode	Al cathode
2	mylar(340)+Sn(135)	mylar(340)+Sn(135)	Cu(620)	mylar(290)
	Ni cathode	Al cathode	Al cathode	C cathode
3	mylar(340)	cellulose(220)	Cu(664)	mylar(475)+Al(135)
	C cathode	C cathode	C cathode	C cathode

We used also wide band XRD for single channel power measurement. It was with polished carbon cathode and filter of cellulose  $\sim 200\mu g/cm^2$  or mylar  $\sim 0.7\mu m$  (fig.1).

Distances from XRDs to a source were from 1m to 3m. Between XRDs and a source was situated anti-noise greed with transparency 0.7-0.9. XRD signals were recorded in immediate proximity to pickups by fast oscilloscopes (frequency band  $>1.4$  GHz).

### 3. XRD signals processing.

Relation between current from XRD  $J$  [A] and spectral density of power flux  $F(h\nu)[W/(cm^2 \cdot eV \cdot sr)]$  does not depend on time and is presented below:

$$J_i = g_i \frac{S_i}{r_i^2} \int_0^\infty Cat_i(h\nu) \cdot e^{-\sum_j \mu_{j,i}(h\nu) \cdot d_{j,i}} \cdot F(h\nu) \cdot d(h\nu) \quad (1)$$

Here  $i$  is XRD number,  $h\nu$ [eV] - quantum energy,  $Cat(h\nu)$ [A/W] - XRD cathode response,  $j$ - index of filter layer,  $\mu$ [cm/g] - mass absorption coefficient,  $d$ [g/cm<sup>2</sup>] - density of filter,  $S$ [cm<sup>2</sup>] - XRD cathode area,  $g$  - anti noise greed transparency,  $r$  [cm] - distance from XRD to emitter. The data about Al photo-cathode quantum efficiency were taken from [5,6], about filter transmission from [7].

A finding of the function  $F(h\nu)$  from measured XRD signals is an incorrect task. For its solving we used and investigated several models of spectrum:

1. The spectrum was suggested **like black body** with temperature as a parameter.
2. Spectrum corresponds to the **Plank spectrum with color temperature** and grey coefficient (2-parameter model).
3. Spectrum corresponds to **one-hump function** for that it's important three parameters: left limit of hump, right limit of hump and amplitude.
4. The spectrum corresponds to **two-temperature** emission and is the sum (with different coefficients) of two spectrums from model 2.

Remarks about finding of parameters from XRD's signals for models 1-4.

\* All these models were fitted to obtained XRD signals on the method of the least squares. It should be mentioned, that the solution exist everywhere.

\* Really we are interested in interval of parameter values, which corresponds to measurement results and depends on the level of measurement errors. This error level was evaluated to be about 10%. Code for parameter interval finding was developed. We looked for the interval width and existence.

**5. Linear combination method.** All previous methods take some presumptions about emission spectrum. It will be better to calculate flux without any preliminary spectrum information, at least in some intervals. Portion of power inside  $h\nu$  interval may be easily calculated, if response (or spectrum) is constant inside this interval and is zero outside this interval. Really XRD responses are not rectangle, but one can approximate they as rectangles or believe the spectrum to be flat in the region of nonzero response. Often filters have more than one region of transparency. In this case linear combinations  $R(h\nu)$  (with coefficients  $K$ ) of XRD responses may be taken to produce different combined responses with one zone of transparency on interval:

$$R_k(h\nu) = \sum_i Cat_i(h\nu) \cdot \exp(-\sum_j \mu_{ij}(h\nu) \cdot d_{ij}) \cdot K_{ki}$$

The linear combinations have to be with small responses outside interesting interval of quantum energy and with responses as constant as possible inside them.

These intervals can be overlapping. In this case flux spectral density in region of overlapping was taken as average from all non zero linear combinations in this band. In regions where it was no nonzero response the flux spectral density was taken as average between neighborhood values. It was assumed that  $F(h\nu=0)=0$ .

**6. Wide band XRD.** It is a variant of previous method with only one channel with wide and relatively flat response (fig.1). Usually cathode quantum efficiency drastically changes

with  $h\nu$ . But if one take filter and cathode from close materials, filter will be transparent in band of low cathode sensitivity and vice versa it will be opaque in band of cathode high sensitive region. Therefore total response can be relatively flat for rather wide band of quantum energy (0.1-1 keV for our XRD). This method gives reliable single channel pickup of emitted power.

#### 4. Analysis of main models errors.

**4.1 Investigation of 2-parameter model.** Mathematical experiment was carried out to investigate the deconvolution code for model 2. Used spectrum shape had form: (Plank spectrum)<sup>q</sup>, where  $q=0.3-3$ . Theoretical signals for different  $q$  were calculated according equation (1), and then noise (10%) was added to this signals for modeling errors of measurement. After this power flux and mean quantum energy were calculated by deconvolution code.

The mathematical experiment shown that for Plank spectrum 10% level of measurement errors does not influence on result. Power flux and mean quantum energy can be obtained with the errors of about 15%. For wide spectrum ( $q=0.5$ ) ratio of initial power flux and one after deconvolution can be about 1.5. For narrow spectrum ( $q=2$ ) the situation is worse, this ratio can be about 2-3.

**4.2 Linear combinations model.** In this method errors of deconvolution are simply proportional to errors of signal measurements for enough smooth spectrum. If spectrum contains large part of power in lines, errors of deconvolution stay dependent on shape of responses of linear combinations. In real situation there are a set of lines. Therefore errors of deconvolution not exceed some dozens percents. One needs to avoid linear combinations with

subtraction of near equal signals. The best is simply one signal or one signal with small correction. We provide this in our sets of filters.

**4.3 Wide band XRD.** Voltage to power coefficient was calculated with different  $h\nu$  bands. It gave us interval 0.1-1 keV with power measurements errors less than 25% (see total response on fig.1). Even for single line errors should be less than 50%.

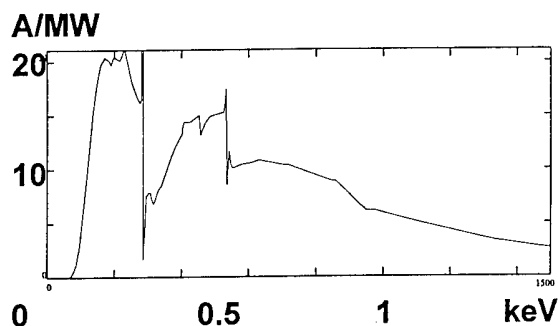


Fig.1 Wide band XRD spectral response.

#### 5. Experimental results.

The algorithms were used for radiated power and spectrum features calculations during a set of experiments. There were Double Liner experiments in 1993 on "Angara-5-1" [8] and in 1994 on "Saturn" (Sandia), and now they are standard for "Angara-5-1". Wide band XRD now is used as emitted power monitor in all shorts of installation. It was found that most accurate and reliable are linear combination method, wide band XRD and 2 parameter model (method 2). In spite of the difference between these models, a power flux divergence is less than 20-25% (see fig.2).

Model 1 is too rough, models 2 and 3 satisfy the measurements in general. Model 4 gives too wide interval of parameters, so it was too many parameters for 4 channel XRD set. For methodes 5, 6 exists always. Results of XRD signal processing with methodes 2, 5, 6 were compared with Sandia Ni bolometers. Also Sandia XRDs signals were processed with our algorithms. The divergence was in the same interval 20-25%.

The analysis of spectral features obtained in liner implosion experiment shows, that radiation spectrum is not blackbody one, because the mean quantum energy is higher, than it has to be in the case of Planck spectrum or, by another words, grey coefficient  $\ll 1$ .

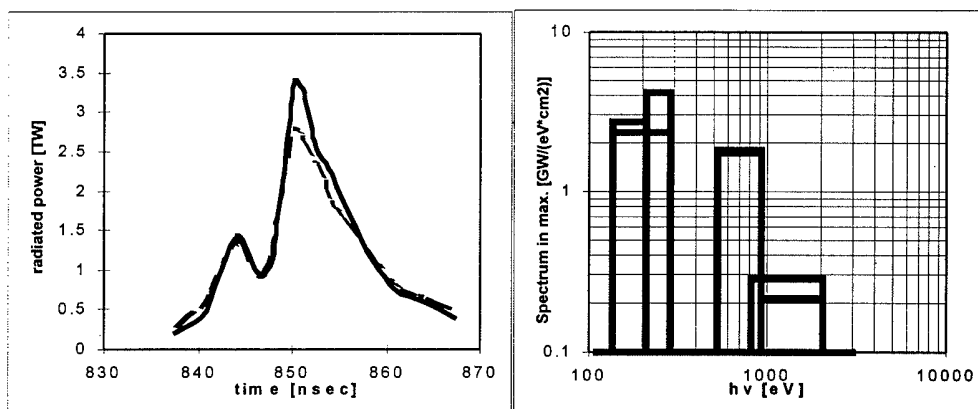


Fig. 2

Emitted power from methods 2 and 5 and spectrum form method 5 in pinch collapse.

## 6. Conclusions.

Using of several X-ray diodes with described above filters sets and deconvolution codes have allowed to measure the power and the spectral features of emission.

Wide band XRD with cathode and filter from close materials was tested. It is simple, reliable and convenient single channel pickup of soft X-ray radiation power with subnanosecond resolution.

XRD filter sets were chosen for energy range 0.1-2 keV. Most reliable algorithms are linear combinations, 2-parameter models and wide band XRD. They showed close values of power flux. Errors of power measurements were less than 25%.

## 7. Acknowledgements.

The authors would like to thank E.Grabovsky, R.Spielman, J. Seamen, .T.Porter, J.McGurn and all "Angara-S-1" and "Saturn" teams. The work was supported also on "Angara-S-1" by Department of Science and Technology of Russia, contract 01-42.

## References

- [1] Z.A.Al'bikov, E.P.Velikhov, A.I.Veretennikov, et all. Soviet atomic energy, vol.68, n.1, 1990, p.34-45.
- [2] A.V. Branitsky, V.D. Vikharev, E.V. Grabovsky, et all. Proceedings of the 8-th international conference on high-power particle beams (Beams'90). Novosibirsk, 1990, v.1, p.437-442.
- [3] A.V.Batunin, A.V.Branitsky, I.N.Frolov, et all. AIP Conf. Proc. p.299. Dense Z-pinchs 3d Inter. Conf. London 1993.
- [4] M.V.Bekhtev, V.D. Vikharev, S.V.Zakharov, et all. Soviet physics JETP, v.68, N.5, 1989, p.955-962.
- [5] Day R.H., Lee P.. J.Appl.Phys., v.52, n.11, p.6965-6973 (1981).
- [6] R.Spielman. Cathodes efficiencies. Private communication.
- [7] Veigele Wm.J. "Photon cross sections from 0.1 keV to 1 MeV for elements Z=1 to Z=94". Atomic Data Tables, 5, 51, p.51-111, (1973).
- [8] Final report on contract AF-0657 and AF-0658 between SNL, USA and TRINITI, IIAPT Russia (1994).

# INVESTIGATION OF LAYERED Z-PINCHES ON ANGARA-5-1

A.V.Branitski, E.V.Grabovski, S.V.Zakharov, M.V.Zurin, S.L.Nedoseev, G.M.Oleinik,  
V.P.Smirnov, I.N.Frolov

*Troitsk Institute of Innovative and Fusion Research, Troitsk, 142092, Russia*

## Abstract

Experimental results of layered Z-pinch investigations on Angara-5-1 are presented. Current level was 3-4 MA through load with 70-90ns rise time. Initial to final radius ratio increase from 10-15 for traditional single pinch up to 30-50 for double layered scheme. Power flux about 8-12 TW/cm<sup>2</sup> is achieved with front rise time about 3ns. Final pinch diameter was down to 0.5-1mm

## Introduction

The double - layer scheme was investigated at ANGARA-5-1 [1] to get maximal X-ray emission at moment of strike outer and inner liner. A Z-pinch started from homogeneous plasma cloud was also investigated to get maximal emission. The compression ratio of Z-pinch produced by unhomogeneous plasma clouds like to double - layer scheme (layered z-pinches) is more than it for homogeneous one.

## Experimental arrangement

Angara-5-1 is eight module 4 MA current generator with rise time of current 90ns. The experimental layout is presented on fig. 1.

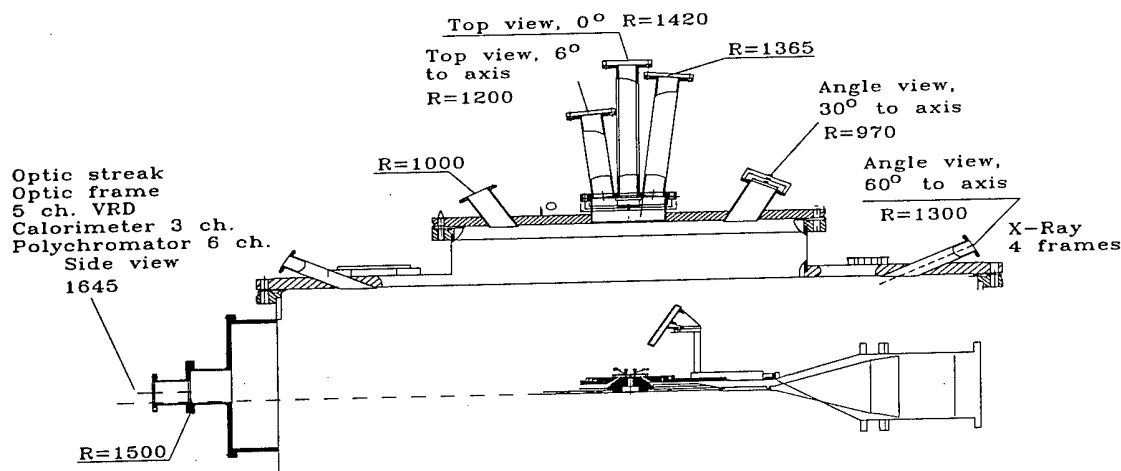


Fig. 1. Experimental layout.

Superfast Z-pinch researches are shifting now to complex configurations of mass and emittance space distributions of plasma generating substances. Experiments were done on

Angara-5-1 with double - layer cylindrical load configurations. There were two coaxial cylinders of gas (of diameter 20-35mm and mass 180 mkg) and low density agar foam ( diameter 4.5mm and mass 200 mkg). Fig. 2.

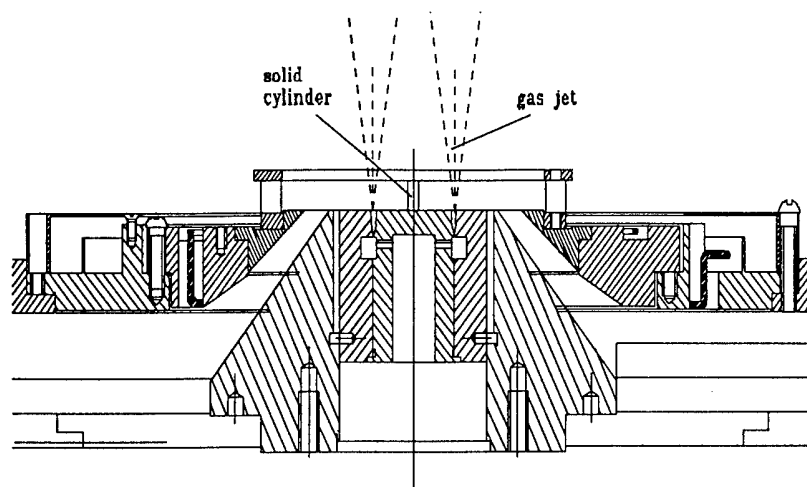


Fig. 2. Central unit with gas puff and agar-agar cylinder.

### Diagnostic arrangement.

The next time resolved diagnostics were used in the experiment:

a current-voltage probes, 3-channel calorimeter, 5 XRD channels, laser shadow 3 frame photos, 2D 4-frame (1- 2ns) soft X-Ray micro channel plate, optical streak-camera, ), optic frame EOP (~1ns, 3 frames). The placing of diagnostics are presented in Fig.1.

Using of some XRDs have allowed to estimate a power and a rough spectral distribution of emission in the range 0.1-2keV, that falls the main part of power on. For laser shadow 3 frame photos in this work an exposure to liner plasma by short (duration 3ns) laser pulses with obtaining of 3 frame of shade- or shlieren- photos was used. A laser with wave length 0.69mm and energy in pulse 0.1-0.2J was used. Optical streak camera use two slits for Z-pinch investigation. Slit images in time of visible light radiation of liner were obtained with help of optical streak-camera 'SFER-2'. The camera time resolution was no more than 30ps, spectral sensitivity was in the range from 400 to 650nm. The scanning of streak-camera was synchronized with XRDs and laser with accuracy no worse than 2ns. An optical scheme allowed to obtain the images in time of two object sections: horizontal section (perpendicular to liner axis) and vertical one (parallel to liner axis). The images of these sections are transferred to the entrance slit of the device and we can see both this images. The vertical slit was placed near internal liner axis with accuracy to 2mm, horizontal one - at the middle between anode and cathode.

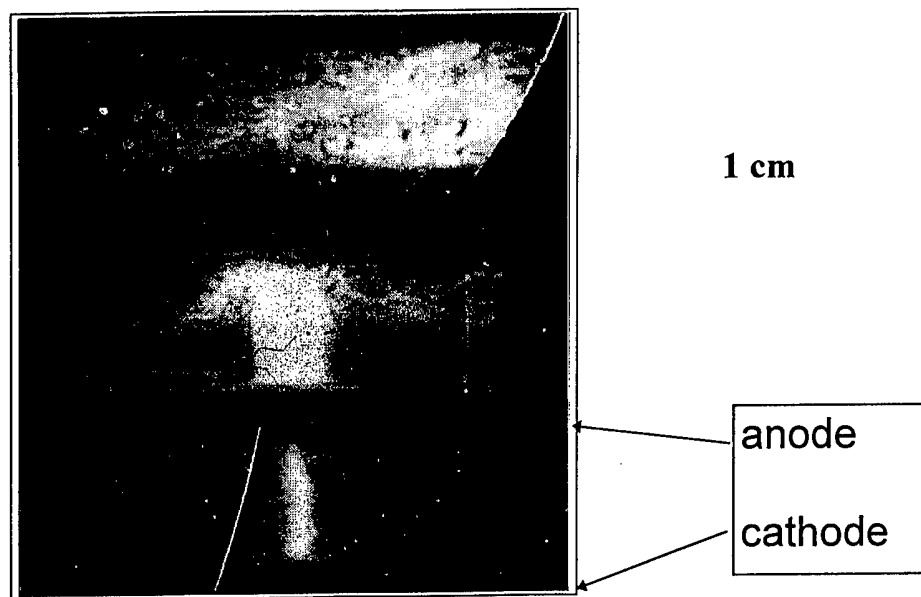


Fig . 3. Soft X-Ray micro channel plate for gas puff- foam load. Last frame show homogeneous pinch at final stagnation moment.

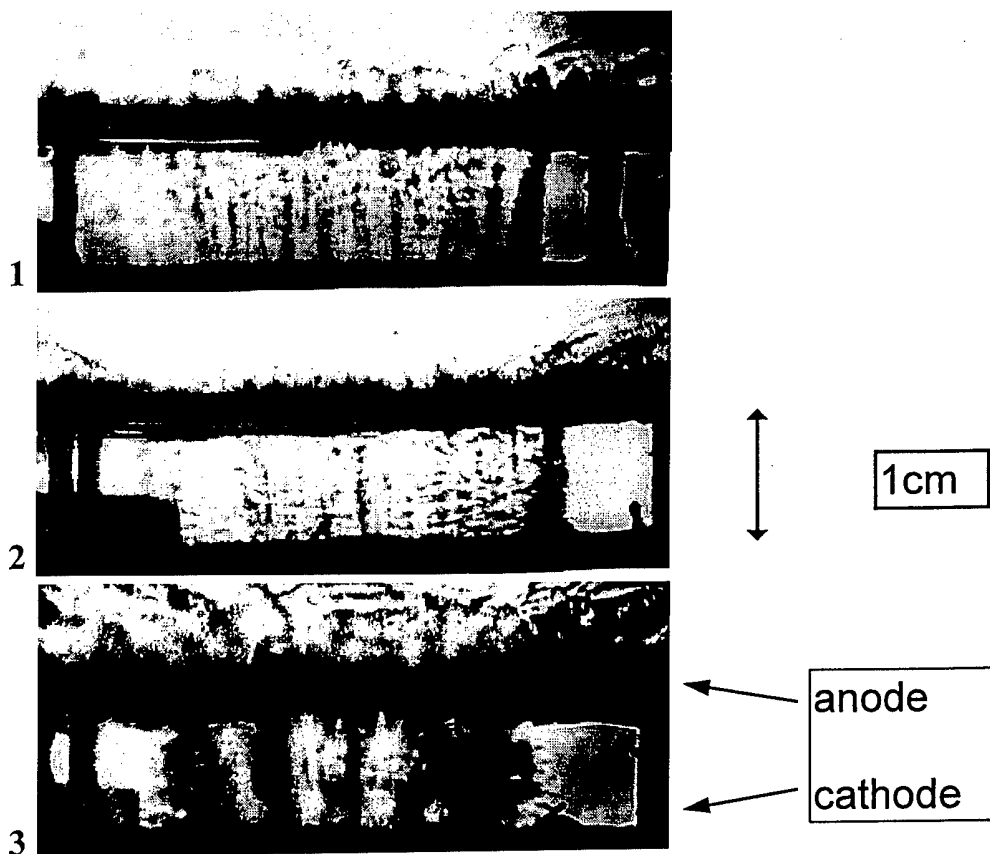


Fig .4. Laser shadow, schlieren, interferograms. 3 frame, 2 nsec,  $\lambda=640\text{nm}$  13 ns between frames.

Inhomogeneities of current shell dramatically decrease when it strike the inner cylinder if the masses of last one and of outer plasma are comparable. Current, close to maximum, penetrates on to inner cylinder in 1-2ns. In light mass outer shell current can be switched onto inner cylinder due to outer shell break by instabilities. Really after strike we have again start of implosion of fully ionized plasma with cylindrical shape of very good quality from small diameter (about 1-4mm) and with current, close to maximum. These schemes lead to more tight final pinching with higher plasma parameters than in traditional single Z-pinch on ANGARA-5-1.

Fig. 3. show us example of compression for gas puff and agar load. After collision of gas puff on agar cylinder the homogeneous plasma cylinder take place. The compression start again from good initial conditions.

Fig 4 (gas puff without agar) show us the gas shell destroyed at one half of initial radius by instabilities.

Initial to final radius ratio increase from 10-15 for traditional single pinch up to 30-50 for double layered scheme. Power flux about 8-12TW/cm<sup>2</sup> is achieved with front rise time about 1.5ns for current through load 3-3.5MA. Final pinch diameter was down to 0.5- 1mm. Rough spectral distribution in final pinching moment is presented. The most tight pinches, highest fluxes were obtained on Angara-5-1 in these schemes.

Multi-layered Z-pinch is prospective source of plasmas with enhanced parameters and X- Ray emission.

This work was supported on ANGARA-5-1 by Department of Science and Technology of Russia under contract 01-42.

#### References

1. Z.A.Albikov, et all. Impulse thermonuclear installation Angara-5- 1. Sov. J. Atomic Energy, 1990, v.68, n.1, p.26-35.



Some Features of Liners Convergence Accelerated with the  
Help of Powerful EMGs

B.E.Grinevich, V.K.Chernyshev, V.N.Buzin, A.A.Petruhin,  
E.I.Zarinov

Russian Federal Nuclear Center. All-Russian Science and  
Research Institute of Experimental Physics (VNIIEF)  
607200, Sarov, Nizni Novgorod Region, Russia, Mira, 37

Introduction

The experiments devoted to condensed, nonexploding during the flight liners convergence under the influence of current are described. To provide the liners with the energy of not less than 25 MJ, powerful explosive magnetic 1000 mm diameter generators were used. Interesting effects arising during the liners flight were found out.

Comparison of experimental results and calculation carried out according to SMOG program has shown that the calculated current value is 20% more than the experimental one. At the same time the experimental speed value excels the rated one, calculated to the known current curve.

Asymmetry of current distribution along the liners is defined depending on time. Some conclusions concerning current spread sumitivity are made.

Description of the Experimenta Arrangement.

Table 1.1 provide the results of thickness and diameter measurements of liners used in tests. The thickness of liners were mesared in six azimuth directions (after every 60°). There measurements were carried out in each direction: in the center of the liner and at a distance  $Z = 20$  mm to both sides from the center (to DEMG - sign "+" in Table 1.1 and from DEMG - sign "-").

Tests Results. Current in DEMG.

The value of disk EMG feeding current was in the first test 10.5 MA, in the second test 11.6 MA and in the third test 10.4 MA. We offer some data characterizing the work of EMG. Maximum value of current derivative in the first two tests were  $3.8 \cdot 10^{12}$  and  $4.2 \cdot 10^{12}$  A/sec respectively and were achieved for 45 .sec, in the third test for 43 .sec maximum value of current derivative was  $3.1 \cdot 10^{12}$  A/sec. Maximum value of current in the first test was 83 MA, in the second - 89 MA and in the third 75 MA. Some smaller current value in receiver in

the third test in comparison with the first two tests is connected to the fact that a lighter aluminum liner was run up in this test. Aluminum liner picked up speed faster than copper one; inductance of the PU for which DEMG worked increased and lead to reducing of current value.

Comparison of the experiment's results with calculation to "SMOG" program shows that rated current value is 20% more than that found out experimentally.

The value of resistance is defined, which should be put into calculation for calculation results to coincide with experimental ones Fig.1 provides the diagram of this resistance dependence on time in the first test. Maximum resistance of  $10E-3$  corresponds to the time moment of liner leaves the steps.

It can be supposed, that the experimental results disagreement with calculation is connected with contact resistance that appears during the liner's movement in the places of its contact with the walls.

#### Current Asymmetry.

Current asymmetry and magnet field asymmetry connected with it were defined by means of differential method in three directions at the angle of  $120^\circ$  to each other Diagrams of asymmetry dependence on time are provided at Fig.2 and Fig.3. It can be seen from the diagrams that in the first test maximum magnet field asymmetry was 8%. Before starting liner's movement (40 .sec) current spread asymmetry practically equals to zero.

Liner movement asymmetry calculations to the known current spread asymmetry show that in the first test azimuth asymmetry maximum value on the receiver installation radius is 2.2 mm.

It should be noted that current derivative changes its sign. As it can be seen from Fig1, Fig2 not only current derivative changes the sign, but also value  $\Delta I$ . This takes place during the liner's movement already after the current in the circuit achieves its maximum value. The most possible explanation of the current derivative sign changing is existence of mechanism allowing to the level the current. Thus current growth in some marked direction will cause local heating of liner contact surface. As a result local resistance increases that causes current decrease in given direction. Existence of the some levelling mechanism is also possible in PU with exploding liner.

The second reason that can lead to derivative sign changing is in the fact that asymmetric current spread can be caused by asymmetric liner flight because of its different

thickness and density etc. The fact that current asymmetry begins on 45 .sec when the liner starts its movement, testifies the connection between current spread symmetry and movement symmetry.

The largest current asymmetry was watched in the second test where liner manufacture precision was less than in the two other (see Table 1) and the liner was stucked to isolator.

#### Flight Speed of Liner

The results of liner speed detection to the time of base 10 mm fly-by showed that in the first test liner flight speed was 4.1 km/sec, in the second - 5 km/sec and in the third - 15 km/sec. Time from the beginning of DEMG work to the liner fly-up to the receiver were: 74.2 .sec in the first test, 65.7 .sec in the second test and 59.5 .sec in the third. These time values correspond to measured speed values. The understated result in the second and third tests gives speed definition to the value  $I(t)$ . In the first test liner speed calculation to dependence  $I(t)$  gives the value 4.2 km/sec practically coinciding to the measured one (4.1 km/sec). The reasons of speed growth in comparison to calculation is now being analyzed. Possibly they are related to liner mass decrease when it is speeded up to such speeds.

Liner movement characteristics can be considered according to liner acceleration. In Fig.4 it is provided the dependence of liner acceleration on the distance. The liner gains maximum acceleration at the distance of 2 cm from its original position.

#### Conclusion

Tests on speeding up of unexploding liners with the help of 1000 mm diameter disk EMGs are carried out.

Some interesting effects are detected related either to current leveling in the process of liner movement or to liner speed increase in experiments in comparison to the speed calculated to the known dependence of current on time, in supposition that the whole liner is effectively speeded up speed values corresponding to measured ones.

#### Literature

1. V.K.Chernychev, B.Ye.Grinevuch, V.V.Vakhruchev, V.I.Mamychev. Skaling Image of 90 MJ Explosive Magnetic Generators. Megagauss Field and Pulsed Power Systems, Nova Science Publishers, New-York, 1990.

Test No	z mm	Liner thickness, mm						Average liner thickness
		Azimuth $\varphi$ , deg						
		0	60	120	180	240	300	
1	+20	1.37	1.38	1.36	1.36	1.35	1.37	1.37±0.007
	0	1.37	1.36	1.37	1.36	1.36	1.37	
	-20	1.37	1.37	1.37	1.37	1.36	1.36	
2	+20	1.44	1.43	1.46	1.47	1.46	1.43	1.44±0.021
	0	1.44	1.43	1.43	1.47	1.44	1.43	
	-20	1.44	1.39	1.42	1.47	1.43	1.39	
3	+20	1.94	1.95	1.93	1.96	1.94	1.97	1.95±0.014
	0	1.95	1.96	1.94	1.96	1.94	1.97	
	-20	1.95	1.97	1.95	1.96	1.94	1.98	

Table 1.1

Results of liner thickness measurements

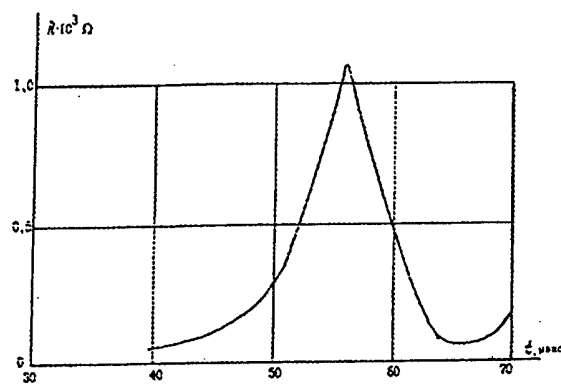


Fig. 1

Contact resistance dependence on time  
(Test No 1)

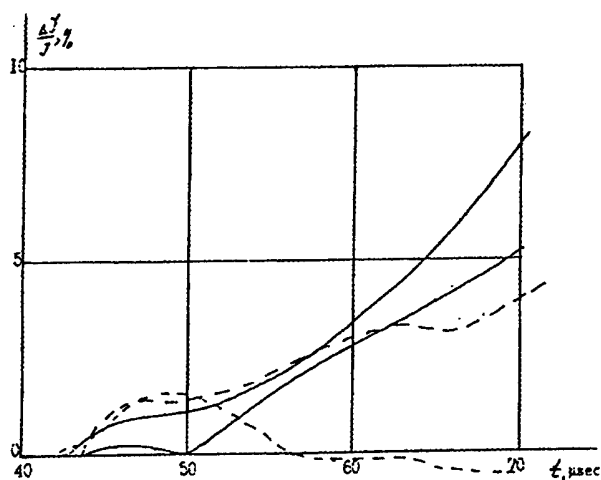


Fig. 2

Current spread asymmetry dependence on generator  
working time in the test No 1

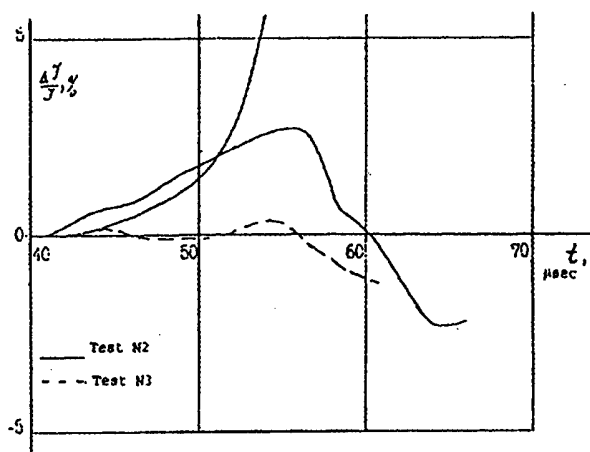


Fig. 3

Current spread asymmetry dependence on generator  
working time in the tests No 2 and No 3

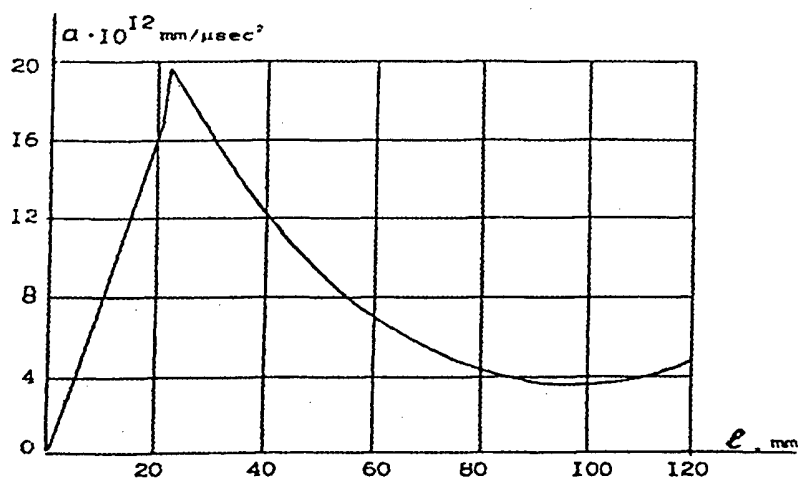


Fig. 4

Copper liner acceleration dependence on the way passed  
(Test No 1)

## INVESTIGATION OF SUPERFAST COMPOSITE PINCH WITH UNSTABLE EXTERNAL LINER ON "ANGARA-5-1"

A.V.Branitsky, E.V.Grabovsky, M.V.Fedulov, I.N.Frolov, D.V.Kuznetsov,  
S.F.Medovshikov, V.O.Mishensky, S.L.Nedoseev, G.M.Oleinik, V.E.Pichugin,  
P.V.Sasorov\*, V.P.Smirnov, V.I.Zaitsev, S.V.Zakharov, M.V.Zurin.

*Troitsk Institute of Innovative and Fusion Research,  
Troitsk, 142092, Russia*

*\*Institute for Theoretical and Experimental Physics, Moscow, Russia.*

### Abstract

Results of an experimental investigation on "Angara-5-1" multiterawatt installation of nonlinear stage of instability of composite pinch are presented. It is shown that the energy transfer from light outer shell to inner load takes place due to abnormal magnetic flux falling. Some part of plasma penetrates with current too. It takes place before maximum compression of outer shell. It is possible that mechanism of this process is new and unknown.

### Introduction

One of the main questions in Z-pinch and liner investigations is the development of the instabilities, which destroy outer shell and decrease the compression ratio [1-3]. From the other hand, this instabilities can be used for the fast current switching to the central load. It was proposed at first in [4]. High current rise, up to 1MA/ns, which is important for discharge in dense matter, can be achieved.

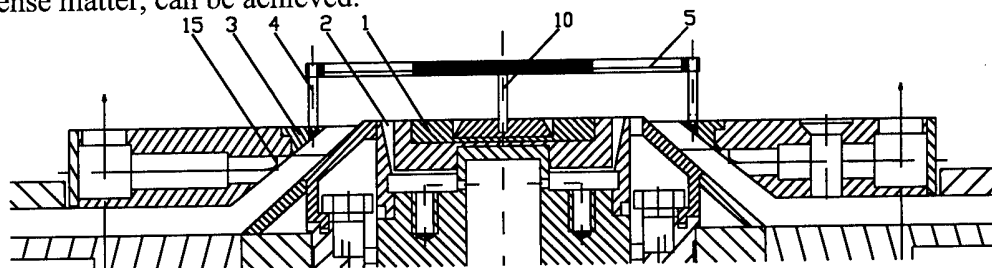


Fig.1. Target unit. Vertical gap 1cm. 1 - cathode, 2 - supersonic part of ring nozzle, 3 - anode, 4 - eight 3mm wires, 5 - anode grid, 10 - inner load, 15 - current prob.

Raleigh - Taylor (RTI), sausage MHD instabilities [1] and the instabilities of magnetized collisionless plasma [2,3] are treated as most dangerous ones for imploding liners. The (RTI) can destroy the plasma current shell as a whole. (RTI) is important during acceleration phase, but a lot of experimental data shows, that large liner stratification is seen on the initial phase, when acceleration is very small. The instabilities of magnetized plasma can provide an anomalous diffusion of azimuthal magnetic flux through the outer shell. The attempts of explanation of this process are done in [5]. This explanation predicts the appearance of large voltage on the internal surface of outer shell. We have checked this voltage and have find it much smaller than predicted.

### Experiment arrangement

Schematic of target unit is shown on Fig.1. Cathode -anode gap was 1cm. The external liner was provided by nozzles. Nozzles could produce extremely low outer liner mass (5-50 microg/cm) with diameter of 32mm or 55mm. Xe or  $C_3H_8$  were used as working gases.

The inner radiator with 50-250 microg/cm was low density solid microfoam of agar. It had diameter 1-4mm or 22mm and was doped with 30% KCl or 50% Mo or 50% CsJ. This foam was positioned at the axis and was an indicator of the energy flux, which penetrated through the unstable liner.

We have measured soft X-ray radiation power of the inner radiator with set of XRD. Instant (3ns) laser shadow pictures of imploding plasma gave the shape of unstable liner. Nevertheless composite pinch radiates in soft X-ray region and optical transitions of radiation may disappear at increasing of object temperature, it is possible to investigate the implosion process in visible light. We have used optic streak camera and time resolved registration of light intensity. An optical scheme allowed to obtain the images in time of two object sections: perpendicular to liner axis and parallel to liner axis. In some shots voltage divider was used for measuring of voltage inside the outer shell.

### Experimental results

Because of small mass and large impedance of fast imploding load the current reached 2-3MA.

On fig.2 typical form of current derivative ( $dJ/dt$ ) and soft X-ray radiation (SXR) are presented. Maximum of SXR power (0.7TWt) coincide with sharp decreasing of  $dJ/dt$ . It was in the instability moment, current generator active power being  $\sim 1.5TWt$  this moment. In this process about 50% of generator power is radiated in SXR. Rise time of SXR was 2-3ns.

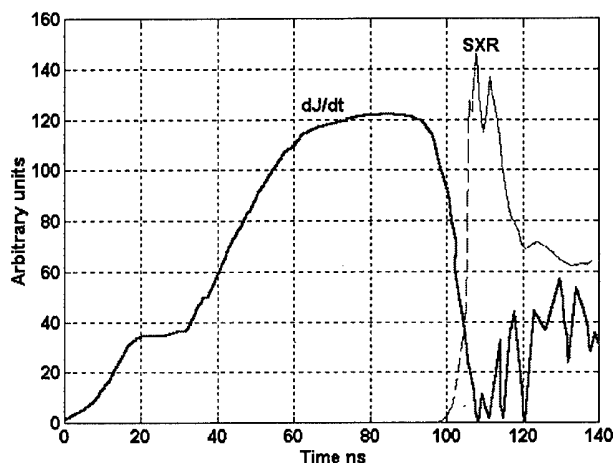


Fig.2. Typical form of current derivative ( $dJ/dt$ ) and soft X-ray radiation (SXR).

The following picture of development of composite Z-pinch is presented below. It is similar to [4].

The breakdown of discharge gap occurs at the radius greater then the ring nozzle radius. The external surfaces of liner consist of large number of filaments with

diameters of 0.5-0.6mm (see fig.3\_1). At this stage the external liner has form of cone - the radius of shell is a little greater near the anode. The petty-scale axial nonuniformities with wave length 0.5-0.8mm of small amplitude (0.2mm) are seen at external surface of Xe liner as well.

During implosion the amplitude and wave length of axial nonuniformities are increased, but azimuthal nonuniformities do not changed or decreased (see fig.3\_2). Wave length of axial nonuniformities is about 1.5mm.

When the shell radius became less then the ring nozzle radius and current achieved megaampere level, the amplitude of axial stratification of external surface is considerably

increase. Outer liner is practically cut on different rings, so that current begins to leave behind the considerable liner matter part (see fig.3\_3). We treat the effect as an anomalous penetration of the azimuthal magnetic flux through external liner due to its instability.

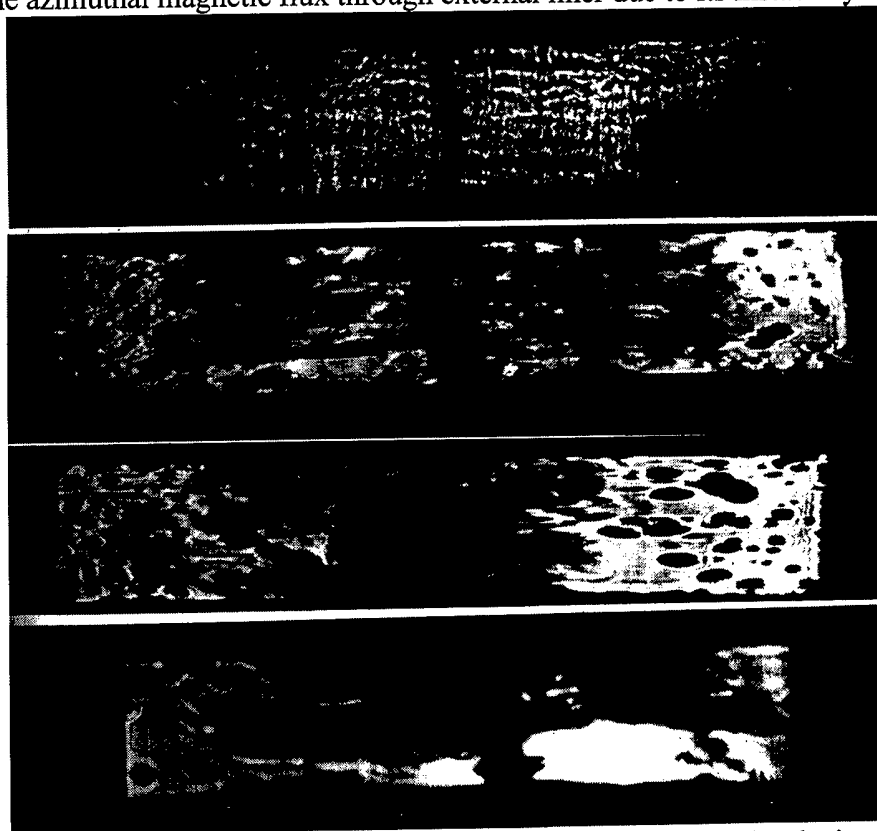


Fig.3. Laser shadow pictures of liners in different stages of implosion. Vertical gap 1cm.

Cathode plasma cutoff (see fig.3\_4) takes place before SXR maximum. It is important to mention that SXR takes place before maximum compression of all outer shell matter.

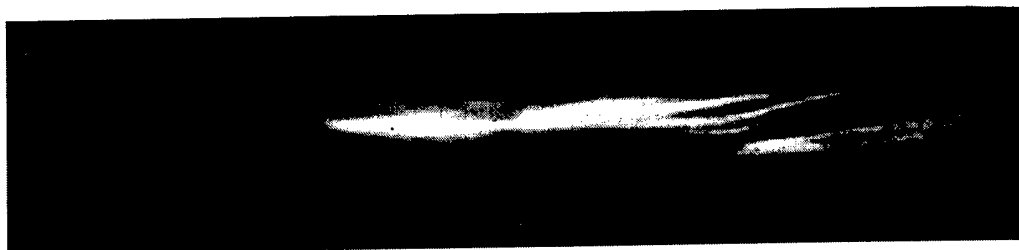


Fig.4. Optic-streak picture. Size: vertical - 30mm, horizontal - 130ns

On optic-streak picture(see fig.4) it is seen that inner load flashes out before filaments arrive. The flashing of dropped behind substance is seen too.

Some methods (optic streak-camera, X-ray streak-camera, laser, estimation of accelerated mass on imploding time) show that the moment of impact comes too early. The moving of inner layers of outer shell was sometimes with great velocities (up to 1mm/ns). This can mean that some part of current with some part of outer shell mass falls through external liner till inner load. A possibility of such process is theoretically considered in [6]. The reason of it - the development of axial inhomogeneities.

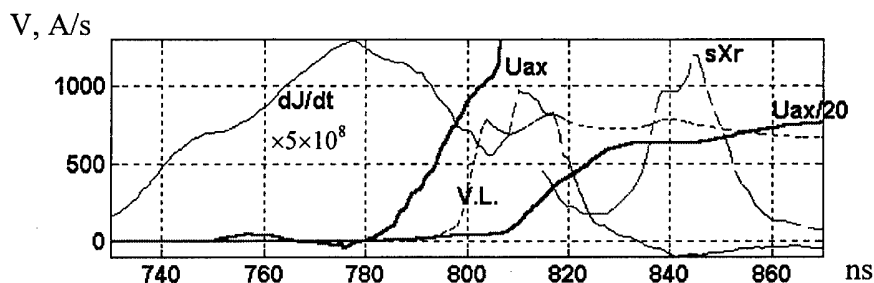
### Voltage on axis

$dJ/dt$  decreasing in instability moment can be in case of increasing of effective resistivity in electric circuit. Current falling through external liner could be treated as abnormal high resistivity of outer shell. Measuring of voltage on the liner axis could allow to evaluate the effective plasma conductivity and skin depth. Voltage divider on the axis of the system was connected to anode and cathode for measuring the voltage inside inner liner. In this case agar foam had 22mm diameter. It should underline that electric field on axis is potential and does not depend on  $dJ/dt$ .

Main result (see fig.5) obtained in this measurements is that voltage on axis ( $U_{ax}$ ) before switching process is very small. Time  $t=780\text{ns}$  is the beginning of switching process: -  $U_{ax}$  begins to increase. At  $t=800\text{ns}$  current switches to inner load and visible light intensity (V.L.) is hardly increased. During switching  $U_{ax}$  reached only 1kV, after 20ns - 14kV. It is smaller dramatically then predicted on [5].

Small voltage on axis during switching process shows that effective plasma conductivity is very large and skin depth is very small. That means that current falls through outer shell with plasma, having such large conductivity and could put some doubts on the efficiency of magnetized plasma instabilities as the reason of current downfall onto inner load.

Fig.5. Measurement of voltage on axis.  $U_{ax}$  - voltage on axis,  $dJ/dt$  - current



derivative, sXr - soft X-ray intensity, V.L. - visible light intensity.

### Conclusion

So, the instability of the external liner was used to generate high current rise (of 1MA/ns) in the inner radiator and to produce nanosecond terawatt X-ray pulse. Current instability and poor compression of low mass external liner were specific features of this composite Z-pinch. Current falls through outer shell with a large conductivity plasma.

This work was supported on Angara-5-1 by Department of Science and Technology of Russia. Cont. 01-42.

- [1] R.B.Baktsch, I.M.Datsco, A.A.Kim et all. Fizika plasmy, translated from Russian: Plasma physics, V.21, N11, p959-
- [2] A.V.Branitsky, C.A.Dan'ko, A.V.Gerusov, et all. Fizika plasmy, under publishing
- [3] L.I.Rudakov, A.A.Sevast'janov. Fizika plasmy, under publishing
- [4] A.N.Batunin, A.V.Branitsky, E.V.Grabovsky, et all. AIP Conf. Proceedings 299, Dense Z-pinchs, 3rd Intern. Conf. London, UK, 1993 . pp.580-586.
- [5] A.Chuvatin, P.Choi, B.Etlicher. Phical review letters, V.76, N13 p.2282-2285.
- [6] I.K.Aivazov, L.B.Nikandrov, V.P.Smirnov, et all. Pis'ma Zh.Eksp.Teor.Fiz. v.45, No.1, p.23-25 (1987).



## **NEW CONCENTRATOR OF 5 MA ON "ANGARA-5-1" FOR LINER IMPLOSION.**

Grabovsky E.V., Nedoseev S.L., Oleinik G.M., Pichugin V.E., Smirnov V.P.,  
Zajivikhin V.V.

*TRINITI, Troitsk, Moscow region, 145092 Russia.*

### **Abstract**

The new current concentrator on multimodule "Angara-5-1" was designed for low impedance loads (imploding liners). The optimization of concentrator scheme was based on the optimum between effects of inductance and electron losses in vacuum magnetically insulated transmission lines (MITL). The scheme with a small diameter magnetic separatrix was chosen for eight unit current addition in vacuum.

### **Introduction.**

The methods of power addition for multimodule generators is important for the projects of large facility creation. Especially it is important for installations with MITL that use parallel power addition on low impedance loads like liners.

On installation "ANGARA-5-1" [1] two types of concentrators - disc and conic with compact separatrix was investigated. The results of these measurements permits us to evaluate reliability of numerical simulation and to make some qualitative conclusions.

The main goals of a concentrator upgrade were:

1. To reduce total inductance of a concentrator by decreasing of a parts of magnetic field in the area outside of separatrix and increasing a parts of magnetic field inside separatrix. It permits us to reduce complete inductance without reduction the gap between MITL electrodes.
2. To reduce inductance inside separatrix for increase of stability of a concentrator to jitter of separate modules.

### **Angara-5 disc concentrator design**

"Angara-5-1" generator consist of eight separate modules. The output voltage of every module is equal to 1.1MV, module current - 0.6-0.8 MA, pulse duration ~90 ns. The disk concentrator design is shown at Fig 1. It was used for our investigation up to summer 1995. It consists of eight cylindrical vacuum MITLs with diameter 30 cm and gap 10 mm connected to two flat discs with diameter 60 cm.

The gap between anode (top) and cathode (bottom) disks decreases from 3 cm at 30 cm radius to 0.7 cm in central part of concentrator. The total inductance of disc concentrator is equal 10 nH for liner length 1 cm and liner diameter 30 mm. The total inductance of all vacuum arrangement between water-vacuum interface is equal 16.5 nH for the same load sizes. The total current through the load was measured by magnetic probe, consisted of 8 magnetic loops, placed uniformly on radius 14 cm and connected in parallel. The signal from probe was registered by oscilloscopes (1.5 GHz, 1 GHz including cable line).

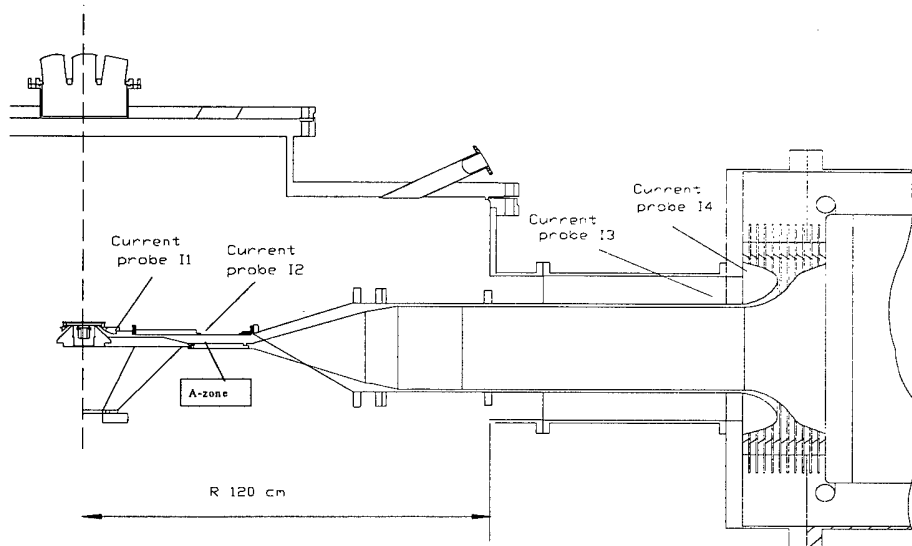


Fig 1. Disc concentrator design

### Angara-5 conic concentrator design

The layout of conic concentrator is presented on Fig. 2. In comparison of disc concentrator the MITL length is increased. The radius of all MITL connection is decreased from 30 cm to 13 cm. The current probe for conic concentrator consists of eight magnetic loops. This probe is like to the current probe of disk concentrator but the every loops are measured separately.

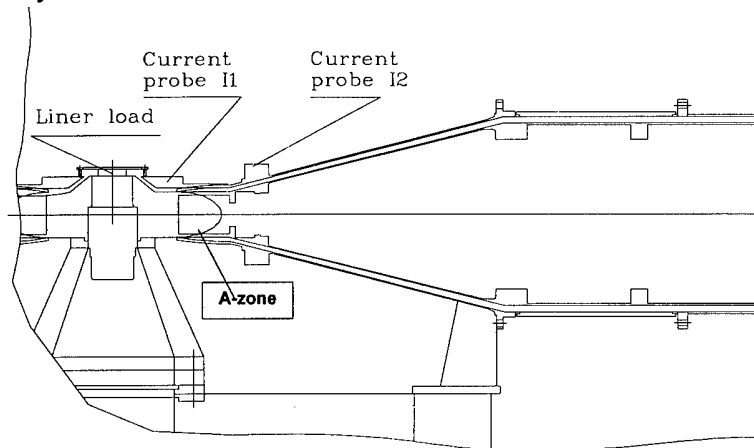


Fig 2. Conic concentrator design.

The total current is measured by numerical addition of all loops signals. This method allow us checking the uniformity of current distribution near the liner. The anode-cathode gap for cylindrical MITL is equal to 10 mm. The minimal gap between anode ad cathode take place in conic part near the liner and is equal to 6 mm.

### Experimental results

Two types measurements have made on both concentrators. We have measured the dependence of total current on load inductance for different foil cylinders. For such type load the signals of separate loops of a current probe I1 coincides one to another under the form and amplitude. For shots using loads containing gas flows the these signals can be different. We connect this fact with penetration of a small amount of gas density in a MITL gap near the probe I1.

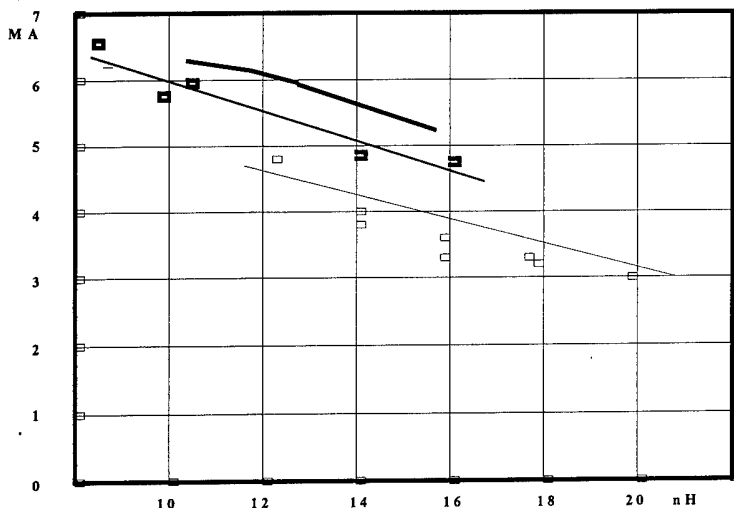


Fig.3. Dependence load current from concentrator inductance. Line - calculation for conic concentrator. Points-experiment for disk concentrator. Bold points-experiment for conic concentrator.

We have also measured the dependence of total current on a module jitter for Xe jet loads. All these measurements have made for amplitude of pulse formed by generator equal to 1.1 MV. The mass of Xe jet was equal to 180-200mkg/cm and height was equal to 10mm. To analyze current-jitter dependence, we have chosen shots with approximately uniform

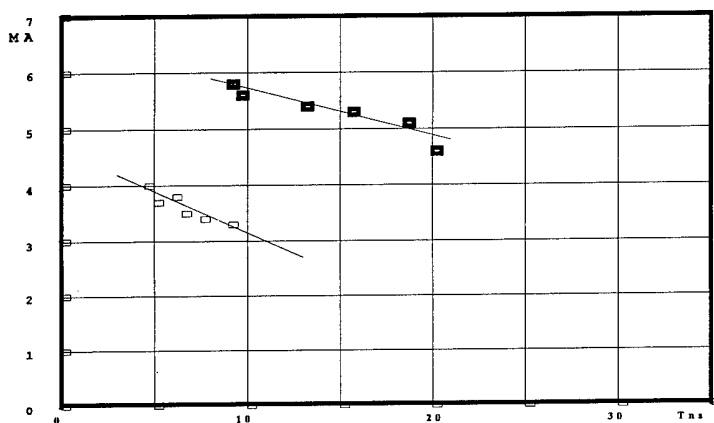


Fig.4. Dependence load current from jitter. points - disc concentrator. Bold points - conic concentrator. Xe jet 180mkg.

distribution of pulse time T1-T8 in a band less than 20 ns. Quantitatively jitter is a square mean of time delay of modules T1-T8, when voltage of every module gets 0.1 of its maximal value. These moments can be defined with  $\pm 2$  ns accuracy. The current-inductance

dependence is presented on Fig. 3. The current-jitter dependence is presented on Fig.4. For definition of the generator output parameters the numerical model suggested in [2,3] was used. In this model the main electromagnetic processes presence in MITL : electron leakage current, self-magnetic insulation, wave processes in the line were took into account. There were fulfilled two series of the calculation to simulate jitter of the installation influence. In the first one the ignition time of each modules have been taken from the experiment and in the second value of the current maximum have been obtained by means of averaging over a set of calculations with ignition time distributed in accordance with Gauss distribution.

### Discussions

The question on losses in MITL was investigated for axial lines. Connection several parallel lines one to another leads to 3-D problems for E and H fields. From topological reasons it is possible to show, that manifoldity of magnetic surfaces results to existence of points with a zero magnetic field on a surface MITL at any distribution of currents between MITLs. The dimension of these areas depends on the current distribution on MITL surface and can be determined from 3-d calculation. Our calculation according to code [1,2] can be use only for estimation of current losses in this zone. We mark this zone on MITL surface as A-zone in our drawing Fig. 1 and Fig.2. The total current losses we can separate into two parts - the first part is the losses in cylindrical MITL and the second part is the losses in A-zone. The coincidence of measured current and the current calculated by code [1,2] for conic concentrator show us that the current losses in A zone are less than losses in cylindrical MITL. For disc concentrator had the difference between calculated and measured current.[4]

Fig. 3 shows increase of a current through a load for a conic concentrator with comparison on disc one. This increase was predicted by a code [1,2]. The load current for conic concentrator is more than it for disc concentrator for the same value of total inductance. We believe this is because current losses decreasing in A zone. This decreasing is due to two reasons. The first is decreasing of dimension of A zone for conic concentrator in compare to disc one. The second is decreasing of voltage amplitude in A zone due to decreasing of inductance inside separatrix. Fig. 4 show us the decreasing of sensitivity of load current to the module jitter. We also explain it by losses in A area decreasing.

### Conclusions

Conic concentrator has the less than disc one inductance in area inside separatrix and has less current losses. We believe that concentrators with compact separatrix is good as a multimodule current adder for high power installation.

This work was supported on ANGARA-5-1 by Departament of Science and Technology of Russia under contract 01-42.

### References

1. Z.A.Albikov, et all. Impulse thermonuclear installation Angara-5- 1. Sov. J. Atomic Energy, 1990, v.68, n.1, p.26-35.
2. V.V. Bulan, V.V. Zajivikhin. Proc. 8 Int. Con. On High Power Particles Beams. V.2, p. 990-995, 1990, Novosibirsk, USSR.
3. V.V. Zajivikhin. Proc. 9 Int. Con. On High Power Particles Beams. V.1, p.592-597, 1992, Washington, US.
4. Grabovsky E.V., Nedoseev S.L., Oleinik G.M., Pichugin V.E., Smirnov V.P., Zajivikhin V.V. Current addition by MITL in vacuum. Proceed. XVI Int. Simp. on DEIV.,v2259, p.431, 1994, Moscow-St-Petersburg, Russia.

# LINER-CONVERTER EXPERIMENT ON AMBIORIX

A.M. GASQUE, P. GRUA, P. ROMARY, J.M. SAJER,<sup>†</sup>

D. FRIART, P. ZEHNTER,<sup>††</sup>

L. JACQUET, J. PORNET,<sup>†††</sup>

S. DAN'KO, Y. GORBULIN, Y. G. KALININ, A. KINGSEP <sup>‡</sup>

<sup>†</sup>CEA/CESTA, BP 4, 33114 Le Barp, France

<sup>††</sup>CEA/ Bruyères le Chatel, BP12, 91680 Bruyères Le Chatel, France

<sup>†††</sup>CEA/Limeil Valenton, BP 27, 94190 Villeneuve Saint Georges, France

<sup>‡</sup>Russian Research Center Kurchatov Institute, Kurchatov sq., 123182 Moscow, Russia

## Abstract

A new way to transform a quite large part of magnetic energy stored in a Z-pinch plasma into X-rays, was first proposed by L. Rudakov [1] : using an axial magnetic field  $B_z$ , a large part of the energy is expected to be transferred by axial electron conductivity to a converter which is placed perpendicularly to the axis of the plasma in order to produce a bright soft X-rays source. In this paper, experimental results obtained on the "AMBIORIX" generator are presented. A hollow cylindrical liner of Helium is driven by a current reaching 2 MA in 50 ns. The implosion is studied with and without axial magnetic field, a steady regime of implosion is observed using  $B_z = 0.3$  T. The plasma parameters and the heating of an aluminium converter are measured using various diagnostics. In the discussion part, the detailed analysis of experimental data and their comparison with numerical simulations are given.

## Introduction

A collaboration between french CEA parts and the Kurchatov Institute of Moscow has begun in 1993 on Z-pinch and HPP subjects. Within this collaboration, it seemed to be interesting to test the "Liner-convertor" concept on AMBIORIX generator, before the S300 Kurchatov generator can operate. The experimental goals are the following :

- the demonstration of the possibility to create the bright pulse source of soft x-rays as a result of thermal conductivity transport of the energy to the tip of the imploding liner,
- the experimental verification of the physical concept this idea is based on.

The optimal parameters of the experiment correlated with the AMBIORIX output parameters were calculated with the 1.5D "PLASMA" code in Kurchatov Institute.

## Experimental set-up

That present experiment [2] has been made on AMBIORIX [3], a pulsed power generator located at CESTA. Ambiorix is constituted with a 300 kJ Marx bank feeding water lines : two coaxial intermediate storage lines ( $t = 1 \mu s$  and  $t = 170$  ns), a triaxial pulsed forming line ( $t = 30$  ns) and a triaxial transmission line. The output parameters are : 1.2 MV, 2.4 MA with a 50 ns rise time on a  $0.5 \Omega$ , 10 nH vacuum diode.

For this experiment, the "optimized" liner parameters have been computed with the 1.5 D "PLASMA" code. The scheme of the experiment is given in figure 1. The helium liner is produced with a supersonic annular nozzle : the mean diameter of the nozzle is 40 mm with a shell thickness of 1.5 mm and a length of 10 mm. Two Helmholtz coils are located around the diode in order to produce a uniform axial  $B_z$  in the liner volume. The aluminium converter is placed generally perpendicularly to the plasma axis, on the anode side. On some experiments, it is placed tilted to  $45^\circ$  on the cathode side.

The experimental density profile of the liner has been measured with a Michelson interferometer and also computed with an aerodynamic code. Results are given in figure 2, the measured and computed profiles are in good agreement. It must be noted that the calculations performed with the "PLASMA" code in order to design the experiment used a step profile. The best results of these calculations had been obtained using a  $60 \mu\text{g}$  liner but, in fact, the experimental liner mass is rather  $80 \mu\text{g}$ .

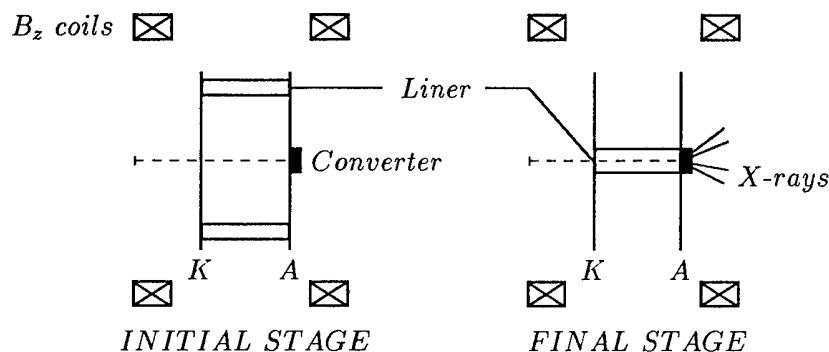


Figure 1: Scheme of the "liner-converter" experiment.

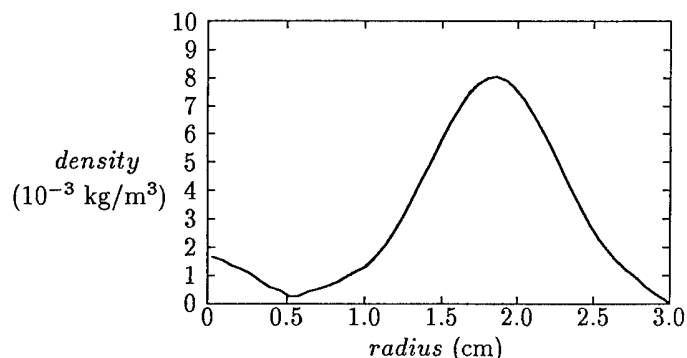


Figure 2: Experimental density profile of the liner at 5 mm from cathode.

Different diagnostics, located on radial or axial side, have been used to measure the plasma parameters and the heating of the converter :

- Time evolution of the pinch compression : visible streak cameras
- Temperature and density of the helium plasma at final stage of implosion : several XRD measuring the bremsstrahlung spectrum decay and spectrometers measuring the K-lines intensities of tracers mixed in 1% atomic addition on pure helium. Neon (for  $200 \text{ eV} < \text{Te} < 500 \text{ eV}$ ) and Argon (for  $\text{Te} > 1000 \text{ eV}$ ) have been used as tracers
- X-rays Helium plasma yield : various XRD's and PIN diodes,
- Stability and radius of the plasma : Pin-hole cameras and 8 stripline X-ray microchannel plate detectors
- Temperature and emission area of the rear side of the converter : an optical probe ( $\lambda = 830 \text{ nm}$ ) or 3 XRD's softly filtered compared with a computed signal obtained for a given temperature and emission area

## Experimental results and discussion

More than 40 shots have been performed during two runs. The weight of several parameters have been studied as : the initial  $B_z$  level, the use of pure He or He + tracers, location, diameter and thickness of the converter. The main experimental results obtained for the plasma parameters are given in table 1 and compared with pure helium numerical simulations. These results were obtained with  $B_z = 0.3$  T, that is the best value of  $B_z$  to stabilize plasma without  $T_e$  decrease.

	He with tracers	pure He	"PLASMA" code simulation [4]	Limeil code simulation	PZP code simulation
Liner mass ( $\mu\text{g}$ )	85	85	60 (step profile)	85	85 (exp. profile)
Implosion time (ns)	170 $\rightarrow$ 230	155 $\rightarrow$ 200	150	155	185
plasma core radius (cm)	0.05 - 0.1		0.08	0.08	0.05
$T_e$ (eV)	1100	2200	1600		2500
$n_e$ ( $\text{cm}^{-3}$ )	$8 \cdot 10^{19}$	$2.2 \cdot 10^{19}$	$1.2 \cdot 10^{20}$	$6.3 \cdot 10^{19}$	$2 \cdot 10^{19}$
plasma corona radius (cm)	0.16 - 0.28		0.11	0.25	0.3
thickness (cm)	0.11 - 0.18		0.04	0.18	0.2
$T_e$ (eV)	200	300	200	500	400
$n_e$ ( $\text{cm}^{-3}$ )	$5.4 \cdot 10^{20}$	$4.2 \cdot 10^{20}$	$1.2 \cdot 10^{21}$	$1.3 \cdot 10^{20}$	$1.3 \cdot 10^{20}$
Energy transferred to the converter (J)		$\approx 200$	220	200	
Radiated energy (J) by :					
- Helium	< 10			50	50
- Tracers	> 100				500
- Converter	< 10			150	

Table 1 : Experimental plasma parameters compared with simulations.

Experimental results and simulations are in rather good agreement. The discrepancies observed for the numerical simulation with the "PLASMA" code are mainly due to the liner mass and to the initial density profile. The compression ratio between the initial liner radius and final corona radius is in the order of 10. During the stagnation, the plasma has the following structure :

- a core with high  $T_e$  ( $>1000$  eV) and low density ( $<5 \cdot 10^{19}$  e/cm<sup>3</sup>)
- a corona with lower  $T_e$  ( $\approx 200$  eV) and higher density ( $\approx 5 \cdot 10^{20}$  e/cm<sup>3</sup>)

The plasma electron temperature without tracers is higher (2200 eV) than with tracers, but the plasma seems to be more instable according to pin-hole images. The results of the analysis of the output radiation from the converter are given in table 2. The converter was located on the anode side; two diameters and three thicknesses were used.

For a 6 mm diameter converter, color temperature is 30 eV - 40eV but the emissive area is smaller than the converter area ( = 28 mm<sup>2</sup> ). In this case, one possible explanation is that the magnetic field lines could be trapped in the converter and that could prevent the compression of the plasma and  $B_z$  field in the vicinity of the converter during the final implosion stage. The heating of converter could be conditioned by the energetic electron heat flux propagating along the Z axis. For a 3 mm diameter converter, color temperature is 15 eV and decreases when thickness of converter increases. The emissive area is equivalent to the converter area. These values are in good

agreement with numerical results obtained using a 2D hydrodynamic code, taking into account a 200 joules external electron heat flux into the converter [5].

Converter diameter (mm)	Converter thickness ( $\mu\text{m}$ )	temperature taken from ratio of $0.1 \mu\text{g}/\text{cm}^2$ filtered to open XRD (eV)	temperature taken from ratio of $0.06 \mu\text{g}/\text{cm}^2$ filtered to open XRD (eV)	Emissive area ( $\text{mm}^2$ )
6	2	38	41	0.06
6	2	40	31	0.08-0.14
3	2		15.5	2.9
3	2		14	2.4
3	5		10.5	5.2
3	5	10	8	4-7
3	10	5		7

Table 2 : Experimental results of the converter heating.

## Conclusions

The purpose of this studies conducted on Ambiorix facility is the experimental verification of the physical concept proposed by L. Rudakov. The experimental goal is the demonstration of the possibility to create a bright pulse source of soft Xrays as a result of the thermal conductivity transport of the helium plasma energy onto the aluminium converter. The measured temperature of the back side of the converter is about 15 eV. This result would allow us to estimate the front side temperature between 100 to 300 eV. As the theory predicts, the transfer of the thermal energy onto the converter occurs just in the end of the liner compression. At this stage, the electron temperature and density of the helium plasma are sufficiently high to transfer 200 joules approximately along the z-axis. We may consider the experimental data in quite good accordance with our calculated results, despite experimental uncertainties and the fact that some experimental data are not taken into account in the simulations. It will be interesting to carry out the same program of experiments on a more powerfull generator, as the S300 facility in Kurchatov Institute in Moscow, in order to confirm these conclusions.

## References

- [1] L.I. RUDAKOV, K.A. BAIGARIN, Yu.G. KALININ et al. , Phys.Fluids B, V.3 (8), p.2414 (1991).
- [2] A.M. GASQUE, Ph.ROMARY and al., CEA Internal Report (1996).
- [3] P.ROMARY, P.EYL and JM.ANGLES, 10<sup>th</sup> Pulsed Power Conference, Albuquerque(NM,USA), 1995.
- [4] Kurchatov Institute Team, Final Report on contract CEA/DAM (1994).
- [5] L. Jacquet, J. Pornet, CEA Internal Report (1995).



# GENERATION OF ROTATION AND SHEAR FLOW IN AN IMPLoding LINER

J.H. Hammer, D.D. Ryutov<sup>1</sup>

*Lawrence Livermore National Laboratory, Livermore, CA 94550, USA*

## 1. Introduction

As is well known, development of the Rayleigh-Taylor instability of the liner may cause a strong detrimental effect on the overall liner performance. A criterion for the onset of instability consists, roughly speaking, in that the effective gravity acceleration (in the rest-frame of the fluid) has the sign opposite to the density gradient. Accordingly, the instability can develop during the run-in phase (where it is predominantly localized near the outer surface of the liner) and near the turn-around point (where the inner surface becomes unstable).

For the recently re-assessed scheme of a compact pulsed fusion reactor with imploding liner [1], just this latter phase of instability is of most importance: it determines the behavior of the interface between a hot magnetized adiabatically compressed plasma and a relatively cold and dense liner. We will focus our present study on the processes near the turn-around point (though some effects occurring during the earlier phase of the implosion will also be briefly discussed in the final section of this paper). For a survey of phenomena occurring during the run-in phase (for non-rotating liners) we refer the reader to a recent paper [2].

It has been noted many years ago that liner rotation has a stabilizing effect on the Rayleigh-Taylor instability near stagnation point (see, e.g., [3,4]). Stabilizing contribution comes from the centrifugal force which is directed oppositely to the effective gravity force. To reach a strong stabilizing effect, one has to spend approximately half of the implosion energy on the liner rotation. This is a considerable energy penalty. The pay-off consists in that the inter-penetration (mix) of the liner and the fuel gets considerably slowed down, so that the overall energy performance may still be better than for the non-rotating liner.

The concept of the centrifugal stabilization has been recently revisited in paper [5], where the authors suggested using a cusp magnetic field to create an azimuthal torque which would appear because of the interaction of the z-component of the current and the r-component of the magnetic field.

In the present study, we study a very different technique which allows the spin up of the liner in the course of its implosion and the creation of azimuthal and axial shear flows at any desired depth of the liner (this technique has been recently suggested in conjunction with ablative implosion of the ICF pellets [6]). We emphasize that, if necessary, this technique allows one to excite not a uniform liner rotation but shear flows embedded into the liner structure. Preliminary analysis presented in paper [6] shows that the shear flow can partially stabilize the Rayleigh-Taylor instability and decrease the rate of mixing. In this latter case we assume that conditions are such that the liner behaves like a fluid and elastic forces are insignificant.

We have in mind metal liners with initial radius of order of 1cm and initial thickness between 0.1 and 0.5 mm, suitable for adiabatic compression of closed-field-line plasma configurations (see Ref. [1] for details; the near-term applications of this system include pulsed X-ray and neutron sources, [1]).

Our present paper is not intended to present a comprehensive analysis of extremely rich physics related to the generation and evolution of liner rotation and shear flows. We are simply going to identify some key issues and describe an overall "morphology" of possible experiments.

## 2. Generation of rotation and shear flow

**2.1 Surface ablation.** One technique consists of generating an ablative torque on the liner surface. This can be achieved by using a liner whose surface contains some fine East-West asymmetric structures (Fig.1). Ablation of these structures caused either by the thermal skin explosion or by intense laser illumination of the liner surface will produce the desired torque. As the use of the auxiliary laser is probably too demanding from the technical viewpoint (though more straightforward with regard to the physics involved), we discuss only the evaporation of the liner material caused by the Joule heating of the skin layer.

If the height of the surface structures is less than the skin-depth, then the initial motion of the evaporated material will not be affected by magnetic forces. The ablated material will create a halo and will impart the azimuthal momentum to the underlying structures of the liner. At the

<sup>1</sup> On leave from Budker Institute of Nuclear Physics, Novosibirsk 630090, Russia

early phase of the discharge, when the liner material still maintains some structural strength, the rotational motion will be transferred to the deeper layers of the liner with a sound speed of shear acoustic waves, 3-4 km/s for most of the materials. For the liner thickness of 0.1 mm, this corresponds to the propagation time of order of 30 ns. If the liner gets liquefied earlier than that, then the azimuthal momentum transport through the liner thickness can occur only via viscous forces. To achieve the best possible efficiency of the spin-up, one should use the coatings with a relatively low sublimation energy and avoid using too sharp fronts of the current pulse (shorter than 10-15 ns).

The evaporated material, obviously, has an angular momentum opposite to that of the liner and much higher initial azimuthal velocity (because of a lower mass). There are some reasons to believe that the halo will expand across the magnetic field because of the development of various microinstabilities [7]. In some scenarios, a low conductivity of the ablated material can be caused by its low ionization degree. For these reasons we will simply assume that, after having set the liner into the initial rotation, the halo does not play any active role in the further implosion.

In the course of implosion, rotation gets accelerated because of the angular momentum conservation. For the radial convergence  $C$ , the rotational energy gets increased by a factor of  $C^2$ . Therefore, if one is interested in the situation when the final rotation energy is comparable with the total mechanical energy, the initial rotational energy can be quite modest,  $\sim C^{-2}$  of the total mechanical energy ( $\sim 1\%$  in a hypothetical case of  $C=10$ ).

**2.2 Interaction of the compression wave with embedded structures.** The second technique is applicable in case of faster rise-time of the compressing magnetic field, when a non-linear compression wave or a shock-wave propagating through the liner material is formed. By using a liner with a structure of small tilted tiles [6] situated at some depth of the liner material, one can then expect that shear flow will be excited by the interaction of the compression wave with the structure. The tiles should have density somewhat different from that of the surrounding material. Fig.2 qualitatively illustrates the physics involved. Here we assume that the substance is already in a liquid state so that elastic forces do not play any role.

To get a somewhat more quantitative understanding of the phenomena involved, we considered a simple model of the interaction of a small-amplitude acoustic wave with a substance with small density variations of the type shown in Fig.2. The smallness of both amplitudes allows one to use the perturbation technique to find scattered acoustic wave. Equation describing generation of this wave can be presented as:

$$\frac{\partial^2 \tilde{\rho}}{\partial t^2} - s^2 \nabla^2 \tilde{\rho} = s^2 \nabla^2 \left( \int_{-\infty}^t \mathbf{v}_a \cdot \nabla \rho_m dt' \right) \quad (1)$$

where  $\mathbf{v}_a$  is velocity perturbation in the incident acoustic wave,  $s$  is sound speed in a uniform gas,  $\rho_m$  is the pre-existing left-right asymmetric density perturbation (which corresponds to the "tiles" shown in Fig.2, the subscript "m" means "mass") and  $\tilde{\rho}$  is a density perturbation in the "scattered" acoustic wave. When deriving Eq.(1) we assumed that density non-uniformities are initially (before arrival of the incident wave) are in a pressure equilibrium with the surrounding medium and that the adiabatic index does not vary. What makes density vary, is the variation of the average molecular weight.

Detailed analysis of Eq.(1) as well as of its generalization to the nonlinear incident wave will be presented elsewhere. Here we restrict ourselves to a few qualitative comments. First, the structures should not be too fine: the amplitude of the scattered wave decreases significantly if the scale-length of the structure becomes smaller than the spatial scale-length of the incident wave. This observation stems from the fact that, for a monochromatic incident wave, there cannot be scattered waves with the tangential wave-number exceeding the normal wave-number of the incident wave. Second, the amplitude of the scattered wave scales linearly with the amplitude of density non-uniformities. This means that the energy density in the scattered wave is quadratic in the amplitude of the density perturbations. The momentum density in the acoustic wave is proportional to the energy density [8] and, whence, also quadratic in density non-uniformities. Accordingly, we conclude that the average velocity which will be acquired by the layer where embedded structure is situated, scales as  $v_a(\rho_m / \rho_0)^{1/2}$ . For strong enough incident wave, with  $v_a \sim s$ , the average flow velocity is  $s(\rho_m / \rho_0)^{1/2}$ .

Angular momentum conservation arguments are applicable to this "submerged jet" (unless viscosity is very high). Therefore, implosion will cause an enhancement of the shear flow in very much the same way as it causes acceleration of the overall rotation.

Superimposed on this average flow, will be fine vortices appearing in the place of initial non-uniformities. These vortices will be stretched by the average shear flow and dissipated by viscosity (molecular or turbulent).

2.3 Generation of shear flow at the interface of two colliding liners. The third technique relies on the use of a two-shell liner, with the shells initially separated in the radial direction and with appropriate structures created at the inner surface of the outer shell and/or on the outer surface of the inner shell (Fig.3). When shells collide, a shear flow should be generated at an interface.

### 3. Effect of shear flow on Rayleigh-Taylor stability

The presence of shear flow at the interface between fluids of different density should have a stabilizing effect on the Rayleigh-Taylor perturbations: at high enough velocity shear, stretching of the perturbations in the parallel direction occurs so fast that the characteristic "spike" can never appear. A simple illustration of the interplay of shear flow and Rayleigh-Taylor instability is presented in Fig.4 that depicts a linear growth rate in the following system: a slab of the incompressible fluid with a uniform density and a linear velocity profile (zero at the bottom and  $v$  at the top of the slab), supported from below by a fluid with a very small density. In the example shown, a broad range of the wavenumbers becomes stable at large enough velocity shear. Other interesting examples regarding the effect of shear flows on gravitational instability can be found in book [9].

Of course, shear flow may serve as a source of its own, Kelvin-Helmholtz instability and Fig.4 clearly shows this instability at small wave-numbers. However, according to a so called "Rayleigh theorem" [8], there exist stable velocity profiles, the ones that do not contain inflection point in the velocity distribution. "Rayleigh theorem" in its standard form pertains to the flow between two rigid walls but one can show that flow with one free surface can also be stable [10]. Whether the flow with two free surfaces can be ever stable, is an open question. However, even if Kelvin-Helmholtz instability is ubiquitous, it is quite possible that the mix caused by its development will occur slower than that caused by the Rayleigh-Taylor instability of the comparable growth-rate. This conjecture is based on the observation that Kelvin-Helmholtz instability does not produce fast growing "spikes" which are of prime concern in the mix caused by the Rayleigh-Taylor instability.

It has recently been shown that shear in axial velocity can also have a stabilizing influence on pinch stability [11].

### 4. Summary

We have shown that there exist several techniques that can set the liner into rotation and/or excite an embedded shear flow ( $d\omega/dr \neq 0$ ) at any desired depth of the liner material. A common element of all these techniques is the use of properly chosen East-West asymmetric structures, situated either on the liner surface or embedded into the shell. Both rotation and shear flow get enhanced in the course of the liner implosion because of the angular momentum conservation. Initial azimuthally asymmetric structures get very quickly smeared out by the shear flow they have produced (or get blown-off from the surface); this decreases their unfavorable effect as seeds of possible instabilities.

As was shown in previous works (see, e.g. [3]), fast enough rotation should stabilize Rayleigh-Taylor instability near the turn-around point. We speculate (partly following the arguments of paper [6]) that the shear flow can also have a stabilizing effect on the stability of the interface. Indeed, specific model presented in our paper shows that the presence of a strong enough shear causes stabilization of a broad class of Rayleigh-Taylor perturbations.

Potentially interesting effects can occur if a modest shear in the  $z$ -direction is created ( $d\omega/dz \neq 0$ ). This type of shear should stabilize filamentation-type instabilities which sometimes appear at the early phase of the implosion.

Manufacturing of the fine structures in the liners 0.1-0.5 mm thick is a challenging problem but it does not seem to be beyond the limits of the modern technology. The surface structures can be manufactured in a straightforward way, on the basis of thin-film technology [12]. All in all, the use of the left-right asymmetric structure for generation of rotation and shear flow is an interesting new option for improvement of the quality of the liner implosions.

### Acknowledgments

One of the authors (D.R.) is grateful to Dr. R. Schock for his support. This work was performed under the auspices of the U.S. Department of Energy by the Lawrence Livermore National Laboratory under the contract No W-7405-ENG-48.

## References

- [1] R.P. Drake, J.H. Hammer, C. W. Hartman, L.J. Perkins, D.D. Ryutov. LLNL report UCRL-JC-120088, 1995; to be published in "Fusion Technology" (1996)
- [2] J.H. Hammer, J.L. Eddleman, P.T. Springler, M. Tabak, A. Toor, K.L. Wong, G.B. Zimmerman. Phys. Plasmas, **3**, 2063 (1996)
- [3] A. Barcion, D.L. Book, A.L. Cooper. Phys. Fluids, **17**, 1707 (1974)
- [4] P.J. Turchi, A.L. Cooper, R. Ford, D.J. Jenkins. Phys. Rev. Lett., **36**, 1546 (1976)
- [5] N. Rostoker, G.G. Peterson, H. Tashiri. Comments on Plasma Physics and Controlled Fusion. **16**, 129 (1995)
- [6] D.E. Baldwin, D.D. Ryutov. Comments on Plasma Phys. and Contr. Fusion, **17**, 1 (1995)
- [7] P.V. Sasorov. Sov. J. Plasma Phys., **17**, 874 (1991)
- [8] L.D. Landau, E.M. Lifshits. "Fluid Mechanics". Pergamon Press, 1987.
- [9] S. Chandrasekhar. "Hydrodynamic and Hydromagnetic Stability". Clarendon Press (1961)
- [10] D.D. Ryutov, in preparation.
- [11] U. Shumlak, C.W. Hartman. Phys. Rev. Lett., **75**, 3285 (1995).
- [12] "Handbook of Thin Film Technology", NY, McGraw Hill (1970)



Fig.1 Shown is a part of the outer surface of the liner; O is the liner axis. The grooves on the liner surface are parallel to the liner axis. It is assumed that the "East" and "West" sides of the grooves are coated with materials with a different density so that the ablation pressure is different on two sides and the azimuthal torque appears. The height of the structures is grossly exaggerated.

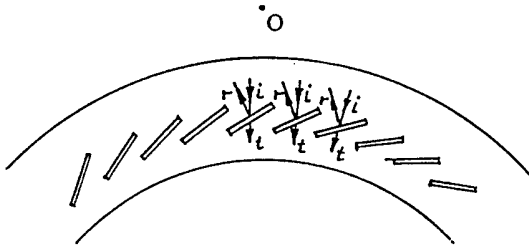


Fig.2 Interaction of a compression wave with an embedded structure. Shown is a part of the equatorial cross-section of the liner. The embedded structures are stretched along the axis. When an incident compression wave ("i" wave the Figure) interacts with the tiles, it gets reflected predominantly in one azimuthal direction, thereby imparting an azimuthal momentum to the region containing the tiles. The rest of the shell acquires an azimuthal momentum in the opposite direction and shear flow sets up. The presence of the shear flow causes a quick mixing-up of the embedded structures and the surrounded substance, eliminating any appreciable azimuthal density non-uniformities.

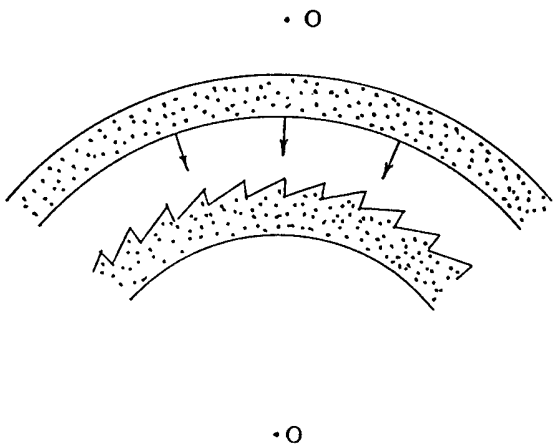


Fig.3 Generation of the shear flow at the interface of two colliding shells. This figure depicts the situation when the left-right asymmetric structure is present only at the surface of the inner liner which is initially at rest.

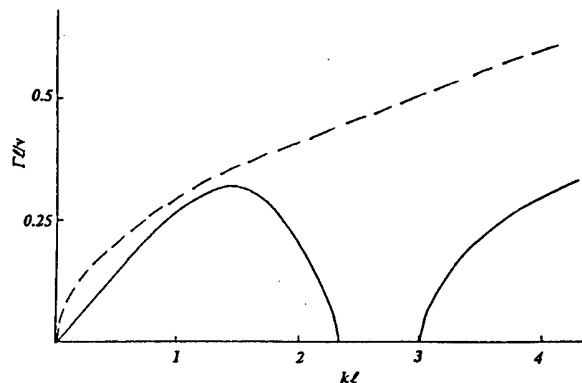


Fig.4 Growth-rate  $\Gamma$  in the units  $v/\ell$ . The slab thickness is  $\ell$ , the gravity acceleration  $g$  is such that  $v^2 = 12g\ell$ . At small wave-numbers  $k$ , the instability is of Kelvin-Helmholtz type. When the flow is absent, the growth-rate is  $(kg)^{1/2}$  for all  $k$ 's (dashed line, for  $g = v^2/12\ell$ ).

## **STUDY OF IMPLoding LINER-ELECTRODE WALL INTERACTION**

V.K. Chernyshev, Ye.I. Zharinov, V.N. Mokhov, S.F. Garanin, B.E. Grinevich,  
I.D. Kudelkin, V.M. Buzin, A.I. Ionov, O.V. Sokolova, S.D. Zimakov, B.T. Yegorychev,  
V.N. Yerichev, V.Sh. Shaidullin

*Russian Federal Nuclear Center, All-Russia Scientific Research Inst. of Experimental Physics  
607190, Sarov, Nizhni Novgorod region, Russian Federation*

J.H. Degnan, T.H. Hussey, G.F. Kiuttu

*Air Force Weapons Laboratory, Kirtland AFB, NM, USA*

### **INTRODUCTION**

Acceleration of solid liners, which do not explode during the flight, is widely used to obtain ultra-high magnetic fields, to compress plasma, to study the properties of various materials under high magnetic pressure and etc. [1-4].

When the liner interacts with electrode walls the following phenomena can appear: advance or lag of liner boundaries (azimuthal and axial asymmetry), melt and evaporation of liner material, local distortions of a shape, etc. These phenomena depend on magnetic field voltage, strength properties of liner and electrodes, angle of electrode walls slope and other reasons.

The main goal of the experiments was to define the picture of interaction between aluminum liners and electrode walls and choose the method to bring a liner into a contact with electrode walls, which provides continuous contact between the liner and electrode walls.

To get more data from the experiments we used a liner system consisting of two independent liners consequently connected in a discharge circuit. It enables us to record simultaneously different liner positions at the same discharge current.

We used a helical explosive magnetic generator (EMG) 100 mm in diameter and 0.7 m in length as an energy source.

The shape of liners at various stages of movement was recorded using an radiograph facility with charge voltage up to 700 kV and time of exposure was from 50 to 70 ns. The current action integrals, the radius of compression and liner flight velocity, were calculated for the experiments by 1-D MHD code with the given equation of state and aluminum conductivity [5]. The experiment and calculations were compared.

### **1. DESCRIPTION OF A LINER SYSTEM**

A liner system (LS) represents a coaxial facility (Fig. 1.1), consisting of two cylindrical liners (1) and (2), located between lateral electrodes (3) and (4) and central electrode (5), dividing LS into two independent portions: massive outer casing (6) and insulator (7). In some assemblies in order to achieve uniform current spreading we put a cylinder (8) made of aluminum foil above the liners. The foil thickness was 0.045 mm, its ends were lap-connected with electrode walls. The connection between liners themselves and electrodes was either "overlapping" or "joint". Position (9) denotes location of inductive probes.

The outer casing (6) with wall thickness of 10 mm was made of aluminum alloy, AMZ and insulator of 2-mm in thickness was made of mylar.

In the first set of three shots the liners from aluminum alloy AHZ 2.73 g/cm<sup>3</sup> density [6], were tested. Electrodes were made from the same alloy. The external radius of liners was 30 mm, wall thickness was 1 mm, length was 30 mm.

In the second set of two shots we tested liners of A 995 aluminum with 2.7 g/cm<sup>3</sup> density. Electrodes were made of steel (mark 30).

## 2. RESULTS OF EXPERIMENTS AND THEIR COMPARISON WITH CALCULATIONS

Two sets of explosive shots were conducted using liner systems. The goal of the first set of the experiments was to study a liner shape and its interactions with electrode walls. Based on these studies we tried to choose a method to connect a liner with walls with which the continuous contact could be provided.

The second set of experiments was carried out to eliminate instabilities occurring in the regions nearby the walls at the points of contact between the liner and electrodes.

As will be shown below, it was found from the results obtained in the first set of experiments that the most probable reason of the unstable picture in the interaction between the liners and walls is the presence of gaps and so the absence of good electrical contact between the ends of liners and electrodes. In the second set experiments another method of joint, namely, the hot fitting of liner to electrode shoulders was applied to avoid this phenomena. Such fitting provided intimate mating of liner ends and electrode surface and eliminated possible gaps along the perimeter between the liner and electrodes.

As it is known from work [7], while accelerating flat metallic plates by the magnetic field the plate velocity is proportional to the value integral of current action  $I = \int_0^t J^2(t) dt$ , the flight distance is proportional to the value of double integral current action  $II = \int_0^t \int_0^t J^2(t) dt dt$ .

When the double integral is taken as a criterion for cylindrical liners to define liner compression radius and the effect cumulation at the instant of focusing is negligible, the results of experiment performed with similar LS to compress the liner radius in terms of double integral may be presented as  $R = f(II)$ , where  $R$  is an outer liner radius.

### THE FIRST SET OF EXPERIMENTS

**Shot 1.** The design of a liner system with the main dimensions is shown schematically in Fig. 2.1.

The left liner was located between flat electrodes, the right one - between conical electrodes with slope angle of 3°. Both liners were mounted on electrode plateau 0,5 mm by their overlapping ends and had a loose fit over the diameter.

LS radiograph made with used radiograph facility is given in Fig. 2.2. EMG current derivatives according to probes of various sensitivity were averaged and  $I(t)$  current curve was plotted by integration the averaged dependence (Fig. 2.3).

Peak EMG current derivative was  $3 \cdot 10^{11}$  A/s, current - 4,9 MA, and to the moment of radiography  $t_r = 74,2 \mu s$  current action integral was  $I_r = 2,98 \cdot 10^8 A^2 s$ , double effect integral  $II_r = 2,5 \cdot 10^3 A^2 s^2$ .

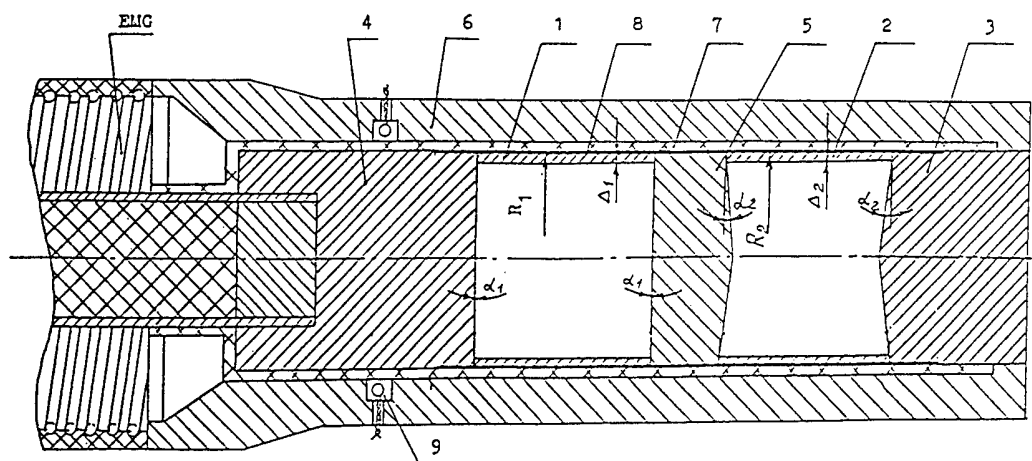


Fig. 1.1  
Liner system

### SHOT 1

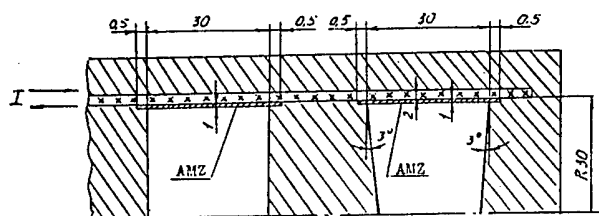


Fig. 2.1  
LS design

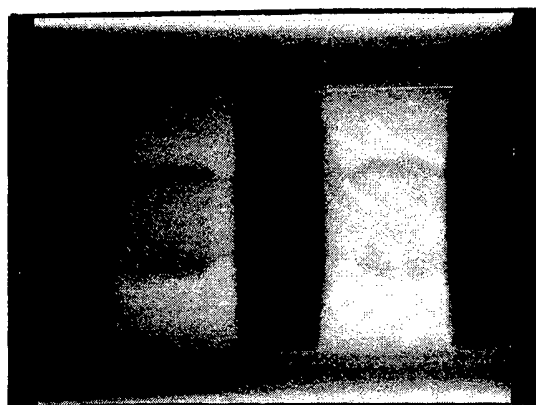


Fig. 2.2  
Radiograph ( $t_r = 74.2 \mu s$ ,  $\Pi_r = 2.5 \cdot 10^3 A^2 s^2$ )

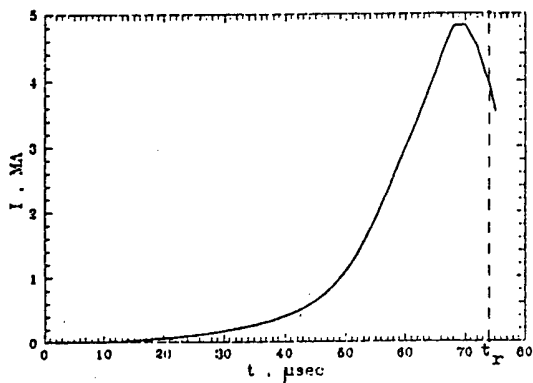


Fig. 2.3  
EMG current dependence on time

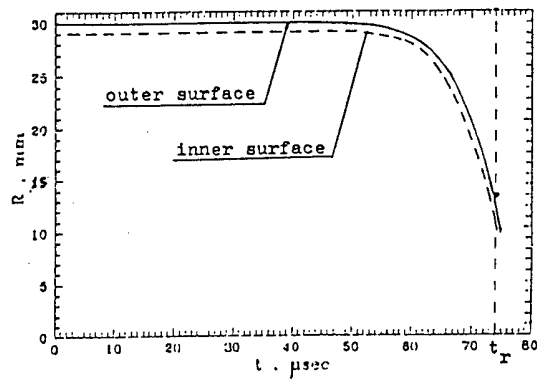


Fig. 2.4  
Dependence of liner radius on time

As it is seen from a radiograph central liner parts have been moving along the radius sufficiently symmetrically. No noticeable perturbances or non-uniformities were seen on the outer surfaces.

The perturbation of the ends in the wall areas in both liners is observed. The ends of the right liner, located between conical electrodes are ahead of the central part from both sides. From the left side one can observe the initial stage, when the liner end leaves the electrode wall. The right end of the left liner, located between the electrodes with straight walls, also is ahead of the central part. The liner practically completely leaves the electrode wall in the left wall area.

Calculated dependence of a liner radius on time, obtained by 1-D MHD code for experimental EMG current dependence in shot 1, is shown in Fig. 2.4. In the same figure one can see a point, which denotes the radius of the outer liner surface, obtained in the experiment, which practically matches the calculation data.

**Shot 2.** In this shot LS design (Fig. 2.5) distinguished from LS design in the shot 1 only by the fact that the liner ends, which are "joint", came across electrode walls, the cylinder of aluminum foil 0.045 mm thick was put above the liners. The foil came tightly across the liner surface, its ends were squeezed between the electrode and casing.

In this shot radiography LS was made at the moment  $t_r = 76.6 \mu s$  at the later stage of their movement (Fig. 2.6), than in shot 1.

As it is seen from a radiograph (Fig. 2.6) the picture of interaction between liners and walls comparatively with shot 1 has changed significantly. The ends of left liner, located between flat electrodes practically along the whole perimeter blew up and separated from the walls. The right liner located between conical electrodes flew close to the axis with a symmetry good enough. A good contact of liner ends with electrode walls has been retained.

EMG current dependence on time, is given in Fig. 2.7. From the experiment the following is obtained at the moment  $t_r = 76.6 \mu s$ :  $I_{max} = 4.7 \text{ MA}$ ,  $J_r = 2.9 \text{ MA}$ ,  $I_r = 2.9 \cdot 10^8 \text{ A}^2 s$ ,  $II_r = 2.8 \cdot 10^3 \text{ A}^2 s^2$ . Calculated dependences of radii and liner velocities on time are given in Fig. 2.8 and 2.9. The point in Fig. 2.8 shows the radius of outer liner surface obtained at the moment  $t_r$ .

**Shot 3.** From the point of view of the design shot 3 was the repetition of shot 2 (Fig 2.5). Its goal was to verify the results of shot 2, where the liner, located between conical electrodes, came up to the axis with the symmetry good enough.

Fig. 2.10 shows, that picture is changed. The right liner located between conical electrodes, has already separated from the left end. The ends of the left liner continue to be in continuous contact with the flat walls.

Fig. 2.11 shows the dependence of EMG current on time. There are:  $I_r = 2.8 \cdot 10^8 \text{ A}^2 s$ ,  $II_r = 2.2 \cdot 10^3 \text{ A}^2 s^2$ .

The analysis of results of the first set of experiments showed the unstable picture of interaction between liners and walls for the both methods of connection ("joint" and "overlapping").

The most probable reason of this instability is the presence of gaps between liner ends and electrodes.

## THE SECOND SET OF EXPERIMENTS

In this set of experiments we tested a liner system, where we took measures to provide more tight contact between liner ends and electrode walls. For this purpose overlapping liners



## SHOT 2

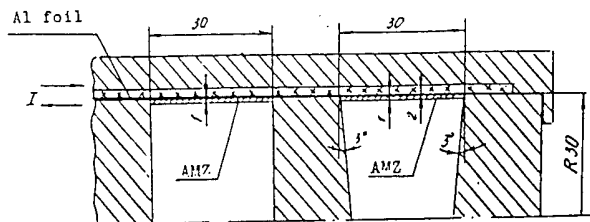


Fig. 2.5  
LS design

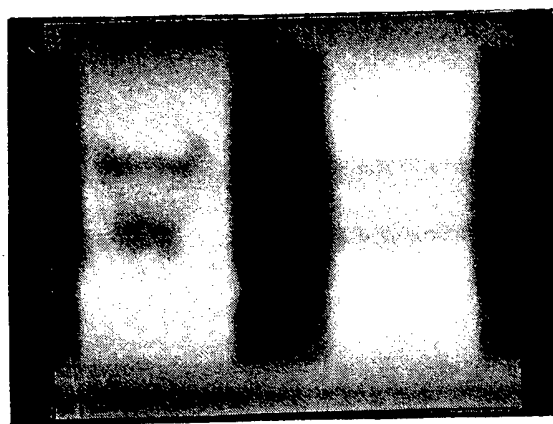


Fig. 2.6  
Radiograph ( $t_r = 76.6 \mu s$ ,  $\Pi_r = 2.8 \cdot 10^3 A^2 s^2$ )

## SHOT 3

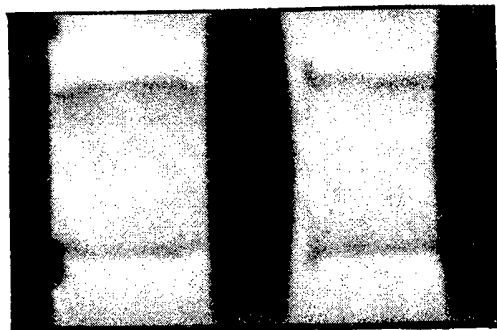


Fig. 2.10  
Radiograph ( $t_r = 77.0 \mu s$ ,  $\Pi_r = 2.2 \cdot 10^3 A^2 s^2$ )

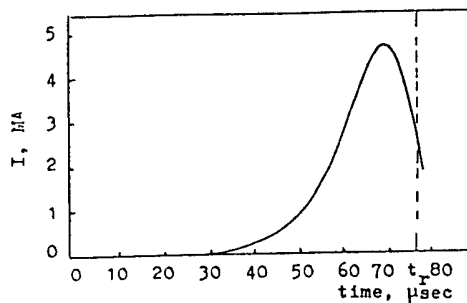


Fig. 2.7 EMG current dependence on time

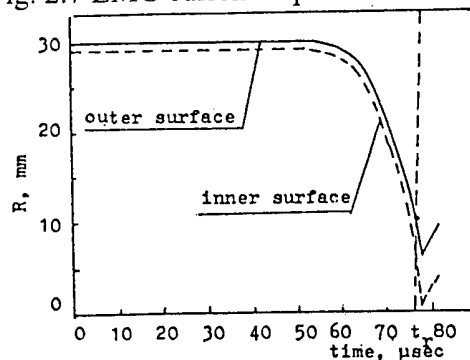


Fig. 2.8 Dependence of liner radius on time

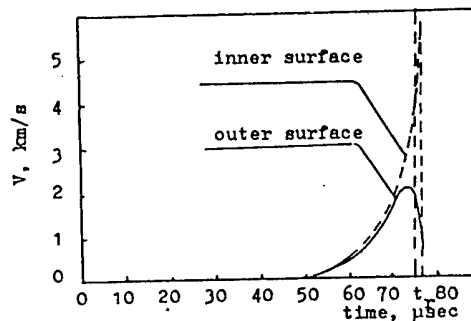


Fig. 2.9 Liner velocity versus time

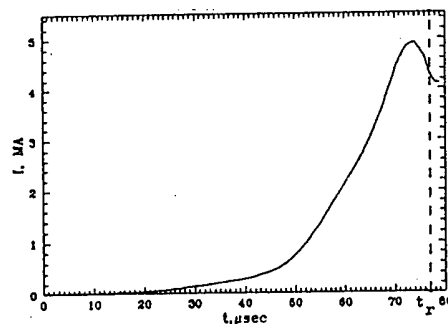


Fig. 2.11 EMG current dependence on time

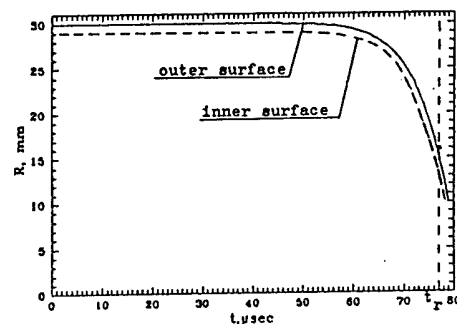


Fig. 2.12 Liner radius versus time

## SHOT 4

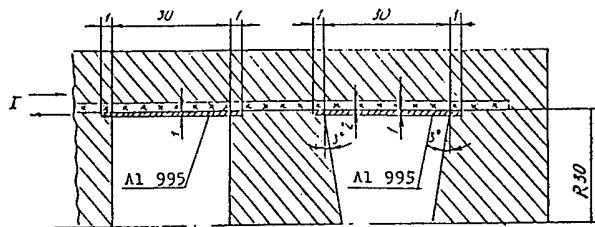


Fig. 2.13  
LS design

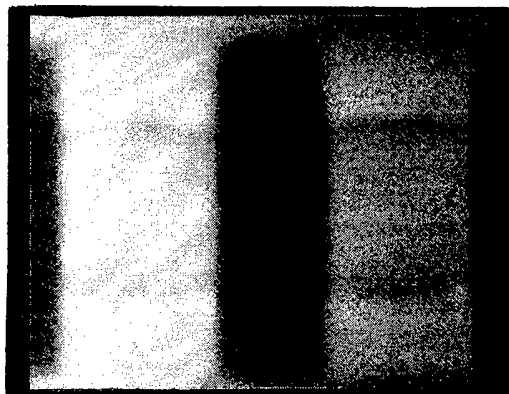


Fig. 2.14  
Radiograph ( $t_r = 73.0 \mu s$ ,  $I_{lr} = 1.93 \cdot 10^3 A^2 s^2$ )

## SHOT 5

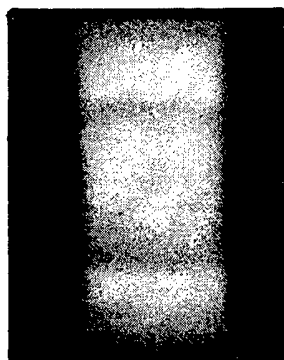


Fig. 2.17  
Radiograph ( $t_r = 72.7 \mu s$ ,  $I_{lr} = 1.78 \cdot 10^3 A^2 s^2$ )

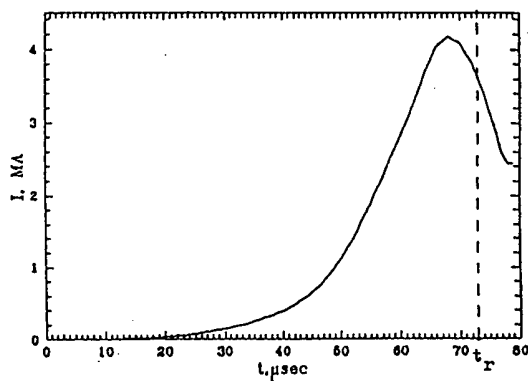


Fig. 2.15 EMG current dependence on time

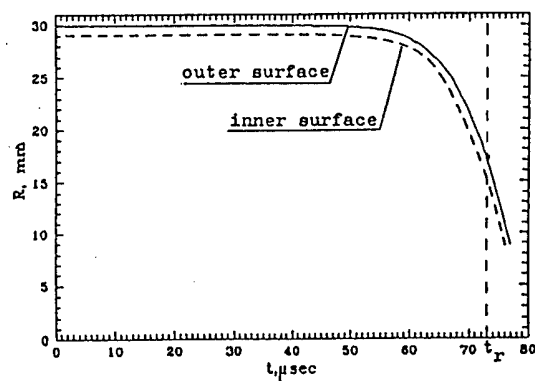


Fig. 2.16 Dependence of liner radius on time

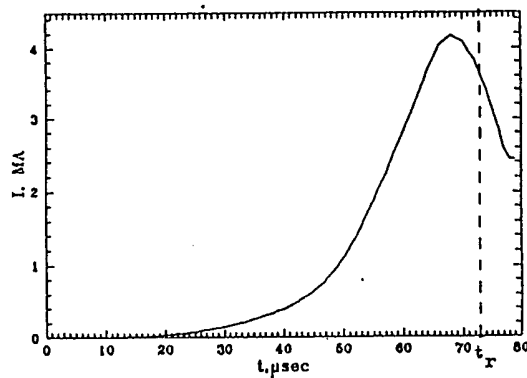


Fig. 2.18 EMG current dependence on time

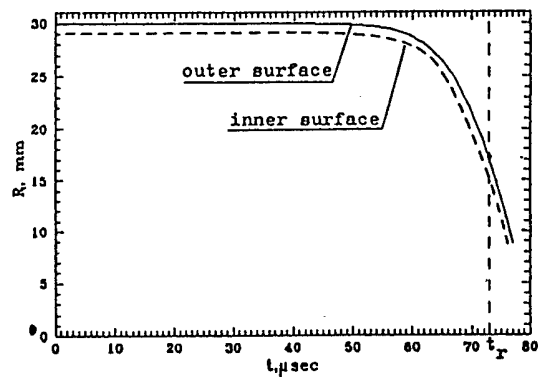


Fig. 2.19 Liner radius versus time

were mounted on the electrode plateau 1.0 mm thick and were fixed there by the method of hot fit. It provided reliable electrical contact along the whole perimeter of a liner inner side.

**Shot 4.** A design of a liner system with a new method of joint is given in Fig. 2.13 and LS radiograph is given in Fig. 2.14.

As it is seen from a radiograph, a constant contact between liner ends and electrode walls has been retained up to the moment of radiography using this method of fix. No local explosions on the surface of liners and walls were observed; liner edges were ahead of a central part which moved symmetrically.

Fig. 2.15 shows current dependence on time, where at the moment of radiography  $t_r = 73 \mu s$ ,  $I_r = 2.3 \cdot 10^8 A^2 s$ ,  $I_{lr} = 1.93 \cdot 10^3 A^2 s^2$ .

Fig. 2.16 shows the dependence of the liner radius on time. The point on the curve shows the external liner radius obtained in the experiment at the moment of radiography.

**Shot 5.** To confirm the result obtained above, conducted the second shot with the same LS (Fig. 2.13). A radiograph of the shot was shown in Fig. 2.17.

Unfortunately in this shot we managed to photograph only a liner between conical electrodes.

Fig. 2.18 shows EMG current dependence on time, where  $I_r = 2.1 \cdot 10^8 A^2 s$ ,  $I_{lr} = 1.78 \cdot 10^3 A^2 s^2$ , and Fig. 2.19 shows calculated radius dependence on time.

Now let us pass to the construction of  $R(I)$  curve and examine its specific features.

The calculated curve describing the compression radius of aluminium liner with the initial radius of 30 mm and wall thickness 1 mm is shown in Fig. 2.20 as a function of double integral of current action.

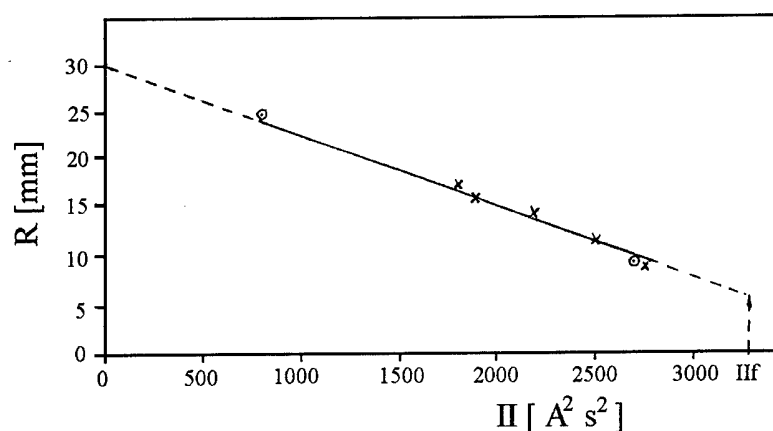


Fig. 2.20

The experimental data are marked by crosses and the data taken from the work [4] are indicated by circles. It is shown that  $R(II)$  curve decreases with increasing of  $II$  according to linear law.

The arrow normal to the abscissa axis shows the magnitude of current double integral at the instant of LS focusing.

## CONCLUSIONS

The analysis of results obtained in the first set of experiments has shown that the symmetry of liners flight and instability of their behaviour in the region nearby the wall considerably depended on the method of connecting the liner and electrodes. The instability has made itself evident in the fact that with the same liner geometry and experimental procedure there were or there were not the electrical explosion of liner ends and the liner detachment from the walls.

The main possible reason capable to explain such instability is in local joint gaps between the liner and electrodes walls in "joint" contact and bad contact between liner walls and electrodes in the case of "lapped" clearance fit.

In the second set of experiments the well-known technique to joint two pieces eliminating the gaps, that is the hot fit of liners on the electrodes shoulders, has been applied to provide reliable electrical contact. Using such fitting the close adjacement between the liners and electrodes surfaces has been achieved. The second set of experiments showed that such joint permitted to avoid electrical explosions and to provide continuous contact between the liner ends and walls.

It should be noted that with the discharge currents up to 6 MA the radial symmetry of liner central parts has been rather satisfactory, although the flight base has achieved 10-15 of initial thickness.

The calculations performed under HHD program, based on the experimental current curve have demonstrated that with EMG discharge current of about 5 MA the velocity of aluminium liner outer surface with the initial radius of 30 mm and the wall 1 mm thick has been about  $\sim 2$  km/s at of focusing instant; the velocity of the inner one has been  $\sim 5,4$  km/sec.

The double integral of current action has been taken as criterion to estimate the radius of liner compression.

## REFERENCES

- [1] Pavlovskii A.I. Ultrahigh Magnetic Fields Cumulation. Mtegagauss Fields and Pulsed Power Systems. MG-V, Edited by V.M. Titov and G.A. Shvetsov, Nova Science Publishers, New York, p.1-13.
- [2] Degnan J.H., Baker W.L., Beason J.D., Clouse C.J., Dietz D., Hall D.J., Holmes J.L., Price D.W., Sovinic C.R. et al. Multi-Megajoule Shaped Solid Liner Implosions: Ibid, p.623-630
- [3] Degnan J.H., Alme M.L., Baker W.L., Buff J.S. et al. Hulti-megajoule Solid Liner Implosions. Megagauss Technology and Pulsed Power Applications. MG-IV, Edited by C.M. Fowler, R.S. Caird and D.J. Erickson, Plenum Press. New York and London, 1987, p. 699-706.
- [4] Chernyshev V.K., Zharinov Ye.I., Kudelkin I.D., Huzin V.N., Ionov A.I., Grinevich B.Ye., Vlasova H.A., Yegorychev B.T., Yerichev V.N. et al., Cylindrical Liner: Implosion Dynamics Under EHG Magnetic Pressure. Book of Abstracts, HG-VI, 1992, Albuquerque, New Mexico (DSA), p.92.
- [5] Bujko A.H., Garanin S.F., Demidov V.A., Kostjukov V.N., Kuzjaev A., Kuldgin A.A., Mamyshev V.I., Mokhov V.N., Petrukhin A.A., Piskarev P.N., Protasov H.S., Chernyshev V.K., Yakubov V.H., Investigation of Dynamics of a Cylindrical Exploding Liner Accelerated by a Magnetic Field in the Megagauss Field Range. Megagauss Fields and Pulsed Power Systems. Edit. by V.H. Titov and G.A. Shvetsov. VG-V, Nova Science Publishers, p.743.
- [6] Kudryavtsev I.V., Luzhnikov L.P., Materialy v mashinostroenii (Part I), Moscow, Mashinostroenie 1967, p. 20 (in Russian)
- [7] Chernyshev V.K., Zharinov E.I., Grinevich B.E., Kudelkin I.D., Buzin V.N., Zimakov S.D., Ionov A.I., Egorychev B.T., Yerichev V.N., H.E., Uskorenie ploskikh metallicheskih i dielektricheskikh lainerov magnitnym polem. Zababakhinskie nauchnye chtenia 14-17 Jan 1992 (tezisy dokladov), Kyshtym, Dal'niaia Dacha (in Russian)

## ELECTRICAL CHARACTERISTICS OF A SMALL PLASMA FOCUS DEVICE

P. Choi\*, M. Favre, P. Silva, H. Chuaqui, and E. Wyndham

*Pontificia Universidad Católica de Chile, Facultad de Física  
Casilla 306, Santiago 22, Chile*

*\*LPMI, Ecole Polytechnique, Palaiseau 91128, France*

### ABSTRACT

Efficient plasma focus operation relies on uniform initial breakdown across the insulator surface. In this paper, we discuss basic plasma focus electric circuit, in order to highlight circuit modifications that produce high voltage oscillation at initial breakdown time. Superimposed on the main discharge voltage such oscillating voltage has been found in real systems to enhance the initial gas breakdown by localizing the initial current path across the insulator surface. PSpice circuit simulations are compared with electric signals from different operational plasma focus devices.

### INTRODUCTION

Plasma focus device is one of the experimental apparatus which is capable of producing transient dense magnetized plasmas of interesting parameters. Very high temperature and density plasmas can be produced in modest size machines at the kJ level. Apart from basic scientific interests, such plasmas are of fundamental importance in the production of X-rays and particle beams for a wide range of technological applications. A number of previous studies have outlined the design principles and the operating characteristics of the plasma focus [1,2]. However, the scaling of the plasma parameters do not fall into the general trend when the bank energy of the system is above a few hundred kJ or below a few kJ [3,4]. The importance of the initial breakdown formation processes and the power limit in very high energy system has been pointed out [5]. The operation at the lower energy regime is less well characterized. In general, the initial breakdown and the formation of the current carrying plasma sheath determine the formation of a snow-ploughing structure during the axial run down phase. The structure of this propagating sheath directly influences the behavior of the plasma in the final collapse phase. The initial breakdown occurs along the insulator under the effect of an applied voltage and subsequently develops into a current carrying sheath which lifts off from the insulator surface. An important point in the optimization of the sheath formation process would be by the control of the shape and amplitude of the initial applied voltage. The circuit for a typical plasma focus consists of a capacitive discharge system with the rate of application of voltage and current determined by circuit inductance and capacitance. The maximum voltage is limited to that of the charging voltage on the capacitor bank and could not be adjusted independent of the energy storage system. In this paper, we discuss basic plasma focus circuits and circuit modifications, which enable the creation of a high frequency, high voltage oscillating waveform superimposed on the main capacitive discharge waveform. Such oscillating voltage is found in real operating systems [6] to enhance the initial gas breakdown and localizes the development of the current path.

## CIRCUIT SIMULATION AND EXPERIMENTAL RESULTS

Circuit simulation using PSpice is used to model the voltage across the base plate of a typical small plasma focus device, at the time of initial breakdown. Figure 1 shows two different circuits used in the simulation. Fig. 1-a corresponds to a simple plasma focus, with an LC configuration. In Fig. 1-b, a coupling transmission line has been added after the spark-gap that switches the bank energy into the focus.  $C_B$  is the capacitor bank,  $L_B$  corresponds to the capacitor bank inductance, SG is the transfer spark-gap,  $R$  is a typical high impedance damping resistor,  $C_F$  represents either the base plate stray capacitance or any additional capacitance added in parallel,  $S_F$  represents the breakdown across the insulator, and  $L_L$  is the initial focus inductance, at breakdown time.  $T$  is a transmission line, of realistic impedance and transit time.

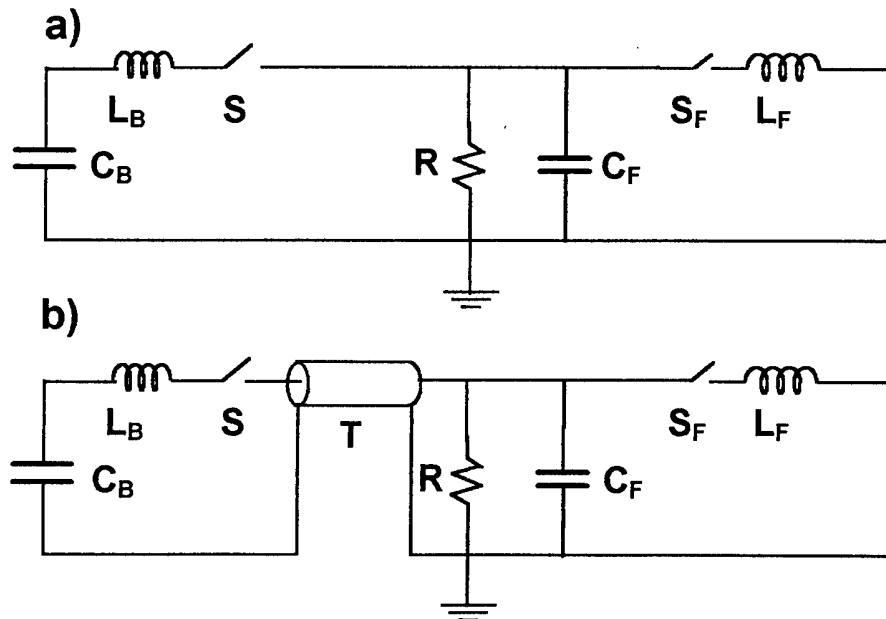
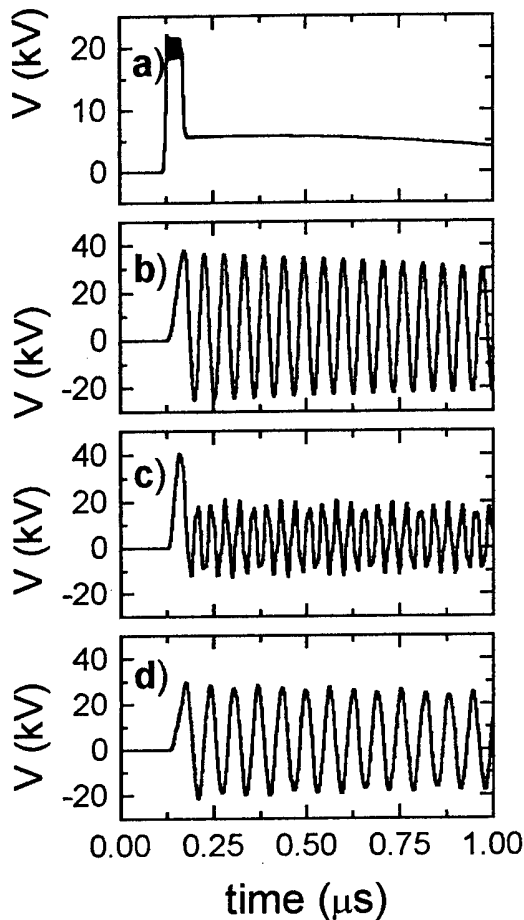


Figure 1: a) basic plasma focus LC circuit. b) basic plasma focus circuit with additional transmission line after the main spark-gap.

PSpice simulations of the above circuits are shown in figure 2. Realistic circuit component values have been used, similar to those corresponding to a small low energy plasma focus device. Fix values in the simulation are:  $C_B = 9 \mu\text{F}$ ,  $L_B = 50 \text{ nH}$ ,  $R = 3.4 \text{ k}\Omega$ ,  $L_F = 20 \text{ nH}$ . SG closes at  $t = 100 \text{ ns}$ , with a closing time of  $50 \text{ ns}$ .  $S_F$  closes at  $t = 150 \text{ ns}$ , with a transition time of  $40 \text{ ns}$ . Charging voltage of the capacitor bank is  $20 \text{ kV}$ . Figs. 2-a and 2-b correspond to the basic circuit in Fig. 1-a. In Fig. 2-a, a small realistic value of the base plate capacity,  $C_F = 20 \text{ pF}$ , is used. In Fig. 2-b, additional capacitance in parallel is added, and  $C_F = 5 \text{ nF}$  is used. Figs 2-c and 2-d correspond to the circuit with additional transmission line shown in Fig. 1-b. A transmission line of  $4.2 \Omega$  impedance,  $8 \text{ ns}$  single transit time is used. Values of  $C_F$  in Figs. 2-c and 2-d are the same than in Figs. 2-a and 2-b, respectively.

One immediately obvious feature obtained, when an additional capacitance is introduced next to the load is the almost doubling of the voltage delivered to the load chamber in the beginning. This voltage enhancement is the result of transferring charge from the relatively

large bank capacitance to a much lower capacitor across the load chamber. When a suitable transmission line is added, similar voltage doubling is obtained. In the case of the transmission line the doubling is due to the reflection off the practically open circuit at the load side, before breakdown occurs. Another feature is the enhanced high frequency ringing after breakdown is initiated. Here, a very simple model has been used to describe the sheath and no resistivity history of the plasma is included. the circuit simulation is simply providing a guide line to the oscillating component in the circuit. In reality, significant damping of the ringing would be expected as a result of the finite resistivity sheath plasma at the early time.



**Figure 2:** Pspice simulations of basic plasma focus electric circuits.

cable guns. The discharge is highly resistive at the initial stages, with similar features to the simulation shown in Fig. 2-a. Fig 3-b corresponds to the PFP-I device [6], operating at 20 kV, in hydrogen/argon mixture, at 270 mTorr, in self breakdown mode. In this case, a 4.2  $\Omega$ , 8.75 ns transmission line, is used after the bank spark-gap. In this particular device, efficient initial breakdown has been found to be improved as a result of the high voltage oscillation, thus extending the operating voltage and pressure range of the plasma focus.

### CONCLUSIONS

The circuit simulations in Fig. 1 show clearly that a small circuit modification can result in a major change in voltage waveform at breakdown time. In particular, it is shown that the

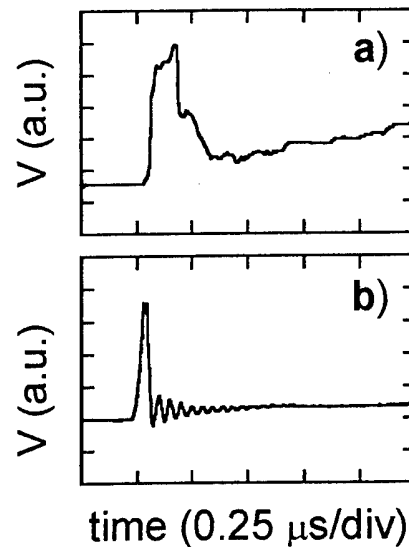


**Figure 3:** voltage traces at initial breakdown in operational devices.

Characteristic voltage signals at initial breakdown from two different operational small plasma focus devices are shown in figure 3. Fig. 3-a corresponds to the UNU/ICTP PFF device [7] operating at 14 kV applied voltage, in air at 15 mTorr. Due to the low operational pressure, initial breakdown is assisted by plasma injection 80 ns after the bank switch closes, using a set of

addition of a parallel capacity, a transmission line or a combination of both, produces a high frequency oscillating waveform superimposed on the applied voltage, with peak voltage exceeding the initial capacitor bank voltage. This combination of enhanced voltage and high frequency oscillation favors initial breakdown across the insulator surface, providing a favorable condition for sheath formation at low pressure, as it is shown in Fig. 3-b. After breakdown, a high rate of rise of current will facilitate the detachment of the sheath from the insulator. A local capacitor, close to the load will minimize the inductance in the current circuit at this stage. For practical applications, the geometrical layout will dictate the physical separation between the energy storage section of the load and thus the minimum length of coaxial cable that could be used. A suitable selection, based on realistic circuit simulation, of transmission line length and/or additional capacity, can easily be implemented to enhance the amplitude of the voltage delivered to the plasma focus chamber at early time. In order to improve breakdown and sheath formation, thus extending the operating pressure range of existing devices.

#### ACKNOWLEDGMENTS

This work has been partially funded by a doctoral research grant from FONDECYT. P. Silva acknowledges a scholarship from CONICYT.

#### REFERENCES

- [1] N.V. Filippov et al., Nucl. Fusion Suppl. 2, p. 577, 1962.
- [2] J.W. Mather, Phys. Fluids Suppl. 5, p. 5, 1964.
- [3] D.C. Gates, *Proc. Int. Conf. Energy Storage, Compression & Switching* (Plenum Press), V 2, p. 329, 1978.
- [4] A. Bernard et al., J. Physique Colloque, Supp. No. 5, p. 39, 1978.
- [5] H. Herold et al., Nucl. Fusion 29, p. 1255, 1989.
- [6] M. Favre et al., *Proc. BEAMS'96* (Prague, Czech Republic), this volume, 1996.
- [7] C.S. Wong et al., *Proc. BEAMS'96* (Prague, Czech Republic), this volume, 1996.



## STUDIES OF CURRENT SHEATH EVOLUTION IN A SMALL PLASMA FOCUS DEVICE

P. Silva, M. Favre, H. Chuaqui, E. Wyndham, and P. Choi\*

*Facultad de Física, Pontificia Universidad Católica de Chile  
Casilla 306, Santiago 22, Chile*

*\*LPMI, Ecole Polytechnique, Palaiseau 91128, France*

### ABSTRACT

We present preliminary time and space resolved studies of current sheath formation in Plasma Focus discharges, using a novel array of non invasive magnetic field probes. The experiments are performed in a Mather type plasma focus, which is powered by a 9  $\mu\text{f}$  capacitor bank, operating at 30 kV. The discharge is formed between a hollowed anode and six symmetrically arranged cathode rods. The array of small magnetic probes is located along the cathode rods. The probes are of millimeter size. They are shielded behind the rods, as to minimize capacitive coupling to the anode electrode, and allow non-perturbing measurements to be made. The array probe signals are recorded simultaneously, with 2 ns time resolution. Other available diagnostics include voltage and current probes in the external circuit, filtered PIN diodes located side and end on, and a multi-pinhole x-ray camera. A simple analytical model of current sheath evolution is used to interpret the probe signals. The experiments have been performed in pure Hydrogen and Hydrogen with Argon mixture, at pressures from below 0.2 Torr upwards. The effect of the Argon mixture on the current sheath structure is investigated with the probe array. It is found that at constant mass density operation, the increase in the percentage of Argon results in a thinner sheath, with steeper current profile.

### INTRODUCTION

It has been long recognized that overall performance in plasma focus operation depends critically on initial breakdown and current sheet formation. Although, several studies on initial breakdown or current sheath formation and evolution have been reported [1,2], most of the measurements rely on invasive probes or time integrated optical observations [3,4], which, as a whole, do not provide accurate enough information for quantitative studies. In particular, signals from mm size probes inserted into the plasma are difficult to interpret due to plasma shielding and skin depth effects. The structure of the current sheath depends strongly on the operating pressure and the presence of impurities. In this work we present preliminary time and space resolved studies of current sheath formation in Plasma Focus discharges in Hydrogen-Argon mixtures, using an array of non invasive magnetic field probes.

### EXPERIMENTAL APPARATUS

The experiments are performed in a Mather type plasma focus, which is powered by a 9  $\mu\text{f}$  capacitor bank, operating at 20 kV. The discharge is formed between a hollowed anode and six symmetrically arranged cathode rods. Further details on the experimental set-up are presented in a companion paper in these proceedings [5]. The array of small magnetic probes is located along the cathode rods. The probes are of millimeter size. They are electrostatically shielded and located behind the rods, away from the centre anode, as to minimize capacitive coupling to the anode electrode and plasma effects. Such arrangement allows non-perturbing measurements to be made. The probes have been used in two different configurations: as a symmetric array at a given height along the focus electrodes, to study sheath uniformity and

symmetry, and arranged in a row of up to six probes along one of the cathode rods, to study space and time evolution of the current sheath during the run down phase of the focus discharge. The array probe signals are recorded simultaneously, with 2 ns time resolution. The experiments have been performed in pure Hydrogen and Hydrogen with Argon admission, at pressures from below 0.2 Torr upwards. Other available diagnostics include voltage and current probes in the external circuit, filtered PIN diodes located side and end on, and a multi-pinhole x-ray camera.

A simple analytical model has been used to interpret the probe signals. The model assumes a zero thickness sheath, which is perpendicular to the anode and cathode. The magnetic fields due to the anode, cathode and sheath currents are calculated analytically, for different positions along the axial direction. A typical current sheath velocity, which is inferred from the actual probe array data, is used to obtain a time dependent magnetic field, at a given probe location. A sinusoidally rising current is assumed. A moving finite thickness sheath is obtained by superposition of several axially displaced zero thickness sheaths. Actual probes signals are compared with the time derivative of the magnetic field signal obtained with the model. Figure 1 shows the magnetic field for a zero thickness sheath, the magnetic field due to a sheath of 2 mm thickness, and the time derivative of the magnetic field at a characteristic probe position. The calculated signals allows to correlate the peak of the probe signal with the passage of the central part of the sheath and the width at the base with the actual thickness of the sheath.

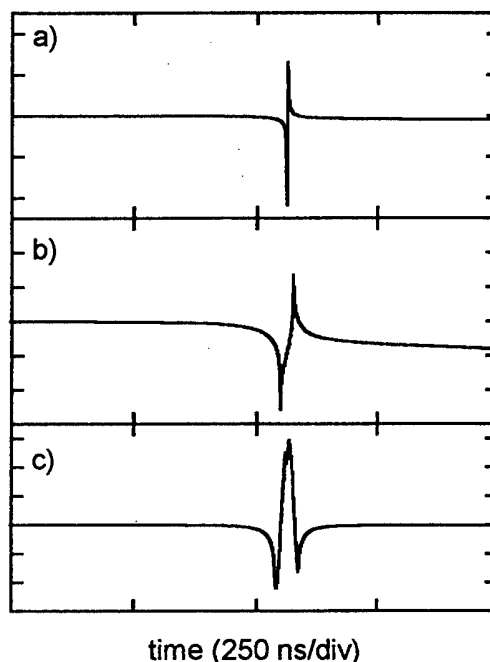


Figure 1: a) magnetic field signal due to a zero thickness sheath, b) magnetic field signal due to a finite thickness sheath, c) time derivative of magnetic field due to finite thickness sheath.

### EXPERIMENTAL RESULTS

Figure 2 shows characteristic signals obtained with shots at 1.3 Torr, pure Hydrogen (Fig. 2-a), and 0.27 Torr, with a mixture of 80% Hydrogen/ 20% Argon (Fig. 2-b), which corresponds to the same mass density than in the pure Hydrogen case.  $V$  is the voltage,  $dI/dt$  is the time derivative of the discharge current, PIN-A is a PIN diode located axially, at 40 cm from the focus region, with a 2  $\mu\text{m}$  Cu filter, and B1 to B5 are signals from the Bdot probe array, with individual probes located along a single cathode rod, at different axial positions, starting at 4.5 cm from the base plate, with each one separated by 1.0 cm. Superimposed on all traces, on an enlarged vertical scale, is the discharge current. Maximum current is  $\sim 140$  kA. The current trace indicates that at this mass density, focus occurs at peak current. Strong focus action at both pressures is inferred from the current dip, voltage spike and x-ray signal in the PIN diode.

Table I shows characteristic sheath thickness and velocity for different Hydrogen-Argon mixing ratios, at constant gas mass density.  $V_{B1 \rightarrow B3}$  and  $V_{B3 \rightarrow B5}$  are the mean sheath velocity

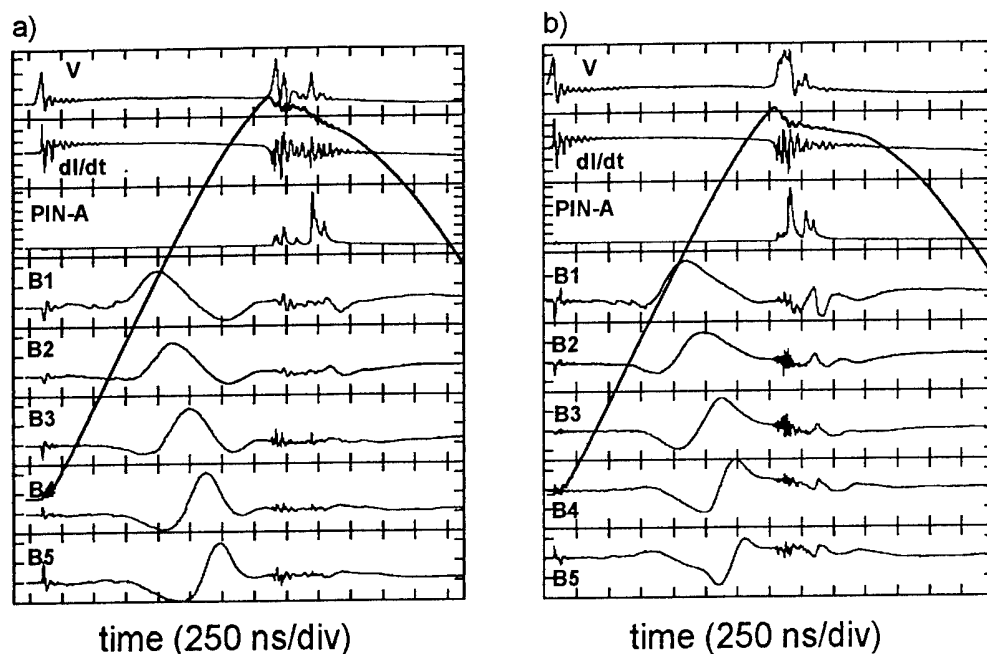


Figure 2: electric, X-ray and Bdot signals at: a) 1.3 Torr, pure H<sub>2</sub>, and b) 0.27 Torr, 80% H<sub>2</sub> + 20% Ar.

between positions of probes B1 and B3, and probes B3 and B5.  $\Delta B1$  and  $\Delta B5$  are the sheath thickness at probes B1 and B5.

TABLE I

Characteristic sheath velocity and thickness at different H<sub>2</sub>/Ar ratios.

GAS	$V_{B1 \rightarrow B3}$ (cm/ $\mu$ s)	$V_{B3 \rightarrow B5}$ (cm/ $\mu$ s)	$\Delta B1$ (mm)	$\Delta B5$ (mm)
H <sub>2</sub> , 0% Ar 1.3 Torr	7.9	8.3	7.3	4.8
H <sub>2</sub> , 5% Ar 0.66 Torr	7.9	8.7	7.3	3.8
H <sub>2</sub> , 10% Ar 0.45 Torr	6.4	10.2	5.9	4.2
H <sub>2</sub> , 20% Ar 0.27 Torr	6.4	12.4	5.8	4.3

## DISCUSSION

Three condition on the current sheath should be satisfied in order to achieve an efficient high energy density pinch at the compression stage: i) uniform initial breakdown across the insulator surface, ii) formation of a thin, axially symmetric and uniform sheath which propagates axially during the rundown phase, with high snowplough efficiency, and iii) current sheath reaching the axis at the time when the discharge current is maximum. Condition (i) is determined mainly by the geometric features of the electrode-insulator arrangement and the electrical characteristics of the electric circuit associated with the focus device. In particular, efficient breakdown is found to be enhanced if an initial high frequency, high voltage oscillation waveform is applied. Further discussions on the effect of initial high frequency, high voltage oscillation are presented elsewhere [6]. If the condition (i) is accomplished, condition (ii) depends on the ionization and radiation properties of the particular gas or gas mixture being

used and the applied voltage. Conditions (iii) depends on the electrode geometry, mass density of the working gas and rate of rise of the discharge current. The voltage and  $dI/dt$  signals shown in Fig. 2 exhibit a high frequency oscillation which is a result of the design features of the electric circuit of the device. Under these conditions, uniform initial breakdown and current sheath initiation are achieved, as it is inferred from the regular, single humped time evolving Bdot signals. Further confirmation of efficient initial breakdown has been obtained with observations using three symmetrically arranged Bdot probes, which show identical signals. Fig. 2 also shows that keeping the mass density constant at an optimized value for a given applied voltage, the formation of the dense pinch at focus compression can take place at peak current, regardless of the mass mixture ratio and gas pressure. This has been observed over a wide  $H_2/Ar$  mixing ratio, up to pressures below 0.2 Torr.

The simple model of Bdot probe signals presented above allows some particular characteristics of the axial evolution of the current sheaths at different  $H_2/Ar$  to be extracted from the experimental data. Despite the limitations of the model, which assumes a flat current sheath, perpendicular to the electrodes, instead of a curved structure due to the  $1/r$  dependence in the magnetic field, the main features of the Bdot probe signals are reproduced by the model, as it can be seen when comparing Fig. 1-c with B3 in Fig. 2-a. The peak in the probe signal corresponds to the center of the current sheath, whereas the two minima observed at each side of the central peak define the width of the sheath. Mean sheath velocities shown in Table I indicate that at low Ar content, the initial velocity tends to be lower than at higher Ar content, whereas at the final stages, before radial collapse, the characteristic axial velocity increases with increasing Ar content. On the other hand, the initial sheath thickness is found to be smaller at higher Ar content, becoming more or less independent of the gas composition near the end of the axial phase. Although the time from initial breakdown to axial pinch formation is the same for both conditions in Fig. 2, the Bdot probe array signals show clear differences in the shape and time evolution of the corresponding current sheaths. Besides an increase in sheath velocity and a decrease in sheath thickness as the sheath propagates axially, the Bdot probe signals in Fig. 2-a exhibit a clear time symmetry around B3. This is not observed in Fig. 2-b, where the signal evolves continuously, with a changing time dependent profile. To first approximation, this signal behavior can be interpreted as an indication of a transition from a near constant sheath current density profile when operating in pure hydrogen, to a time dependent, increasingly steeper sheath current density profile, as a result of the enhanced ionization due to the argon admixture. Further interpretation of the Bdot probe data will require an improved analytic model of the probe signals, which includes more realistic finite thickness effects and curvature.

#### ACKNOWLEDGMENTS

This work has been partially funded by a doctoral research grant from FONDECYT. P. Silva acknowledges a scholarship from CONICYT.

#### REFERENCES

- [1] A. Donges et al., *Phys. Letters* 76 A, p. 391, 1980.
- [2] S.I. Ananin et al., *Sov. J. Plasma Phys.* 4, p. 175, 1978.
- [3] K.H. Kwek et al., *IEEE Trans. Plasma Sci.* 18, p. 826, 1990.
- [4] H. Bruzzone et al., *Meas. Sci. & Tech.* 2, p. 1195, 1991.
- [5] M. Favre et al., *Proc. BEAMS'96* (Prague, Czech Republic), this volume, 1996.
- [6] P. Choi et al., *Proc. BEAMS'96* (Prague, Czech Republic), this volume, 1996.

# CHARACTERISTICS OF A SMALL PLASMA FOCUS DEVICE

M. Favre, P. Silva, H. Chuaqui, and E. Wyndham

*Pontificia Universidad Católica de Chile, Facultad de Física  
Casilla 306, Santiago 22, Chile*

P. Choi and C. Dumitrescu-Zoita

*Laboratoire de Physique des Milieux Ionisés, Ecole Polytechnique  
Palaiseau 91128, France*

## ABSTRACT

We report on experimental observations in PFP-I, a small 3.8 kJ plasma focus, which is operated in Hydrogen-Argon mixtures to investigate the effect of parameter modifications on the overall performance of the device. An extensive array of diagnostics is been used, which includes voltage and current probes in the external circuit, a novel small magnetic probes array located along the cathode rods, filtered PIN diodes located side and end on, and multi-pinhole X-ray camera. Extended operated range from below 0.2 Torr upwards has been achieved with the implementation of the auxiliary discharge circuit. Despite the low voltage and low energy operation, energetic beam formation has been observed at the time of the final compression, prior to disruption. Current sheath formation and evolution has been characterised using the magnetic probes array, in correlation with beam formation and plasma emission. Time integrated visible plasma spectroscopy is performed to investigate impurity effects on focus performance and plasma dynamics at the collapse phase.

## INTRODUCTION

Plasmas of ultra-high energy density can be easily produced in a small plasma focus device, at very modest costs [1,2]. This type of small device allows easy modification, combined with wide parameter range at high repetition rate operation. Much of the scaling parameters on the plasma focus has been evaluated, though many questions still remain. Extensive studies on the neutron production efficiency with device parameters have been reported in different experiments, although the underlying plasma properties have not been characterised to the same extent [3,4,5]. Further experimental studies are required in order to fully characterise small plasma focus device performance, mainly in view of potential applications as bright soft x-ray sources or charged particle beams generators. It is known that the basic parameters that affect the efficient operational regime in Plasma Foci are initial sheath formation, snowplough efficiency, and the presence of impurities. In this work we report on the operational capabilities of PFP-I, a small 3.8 kJ Plasma Focus device. The device has been designed to address the above parameters. A comprehensive set of diagnostics has been implemented, which include voltage and current measurements, multi pinhole x-ray photography, filtered PIN diode array, a novel Bdot probe array and space resolved optical spectroscopy. Preliminary results are presented, which highlight the operational capabilities of the device. Operation at constant mass density in Hydrogen-Argon mixtures allows effects due to Argon admission on the current sheath evolution and pinch performance, to be clearly identified. The presence of Copper impurities during the collapse phase, which arise from evaporated electrode material has been identified with the visible spectroscopy diagnostics. In general, the

results show that most of the phenomena observed on plasma focus devices covering a wide range of machine parameters, can be successfully investigated in a small device.

### EXPERIMENTAL APPARATUS

The experiments have been performed in PFP-I, a Mather type plasma focus, which is powered by a 9  $\mu\text{f}$  capacitor bank, operating up to 30 kV. A low inductance, 9 channel triggered spark-gap is used to transfer the charge from the capacitor bank to the focus. 10 ns transmission lines, with an effective impedance of 4.2  $\Omega$ , connect the spark-gap to the bank and focus. The electric circuit design has been optimized to enhance high frequency oscillation of the voltage at initial breakdown, in order to improve breakdown efficiency and uniform current sheath initiation. The discharge is formed between a

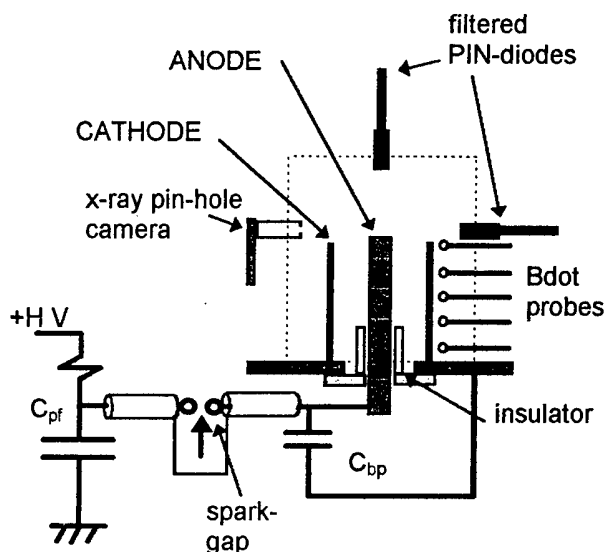


Figure 1: schematics of the plasma focus device.

hollowed anode, 1.2 cm radius and 14 cm length, and six cathode rods, symmetrically arranged in a 3.2 cm radius circle. The insulator is a Pyrex sleeve, 5 cm long. The focus is operated in Hydrogen-Argon mixtures, at pressures from below 0.2 Torr upwards. An array of small magnetic probes located along the cathode rods is used to study the current sheath structure during the run down phase of the discharge. The probes are electrostatically shielded and placed behind the cathode rods, allowing non-perturbing measurements to be made. Further details of the magnetic probes are presented elsewhere [6]. An array of filtered PIN diodes located side and end on, is used to study the electron beam formation and the plasma emission. These time resolved observations are correlated with space resolved measurements, using a multi-pinhole X-ray camera. A schematic of the experimental set-up is shown in figure 1. Time integrated space resolved spectroscopy is also applied. Light emission from the focus region is imaged onto a linear array of optical fibres. Individual fibres are 0.3 mm diameter. The other end of the fibber array is fed into a monochomator (68 cm focal length, 1800 ln/mm grating). Spectra are recorded on TMAX 3200 film.

### RESULTS AND DISCUSSION

Figure 2 shows characteristic signals for operation in 92% Hydrogen plus 8% Argon, at 1.4 Torr. The signals correspond to the voltage at the base of the focus, the time derivative of the current, and five PIN diodes: D-A, positioned axially, at 40 cm from the focus region, with 5  $\mu\text{m}$  Cu + 2  $\mu\text{m}$  Mylar filtering, D-L1 to D-L4, located side on, at 18 cm from the focus region, with 3  $\mu\text{m}$  Ag + 1  $\mu\text{m}$  Mylar, 4  $\mu\text{m}$  Mylar, 5  $\mu\text{m}$  Cu, and 7.5  $\mu\text{m}$  Ni + 2  $\mu\text{m}$  Mylar filtering respectively. The trace superimposed on the graphs corresponds to the discharge current. Focus action is seen to occur at peak current. The sharp increase in the associated voltage spike indicates efficient compression. When comparing the axial and lateral PIN diode signals, several features of the x-ray emission can be identified. The first x-ray pulse is due to a high

energy electron beam hitting the anode, as it coincides with the voltage spike. A second x-ray pulse is also associated with electron beams, as it coincides with a second voltage spike. However, at this time the x-ray emission has a contribution from the focus plasma, as it can be inferred when the relative heights of the first and second pulse in the axial and lateral PIN diodes are compared. A third period of x-ray emission is strongly dominated by plasma emission. Further discrimination of electron beam induced and plasma emission can not be established, as the side-on PIN diodes are not collimated as to exclude anode radiation. Companion time integrated pinhole x-ray photographs show emission from the anode surface and localized hot spots. These observations are in general agreement with previous investigations of x-ray emission in plasma focus operating with Hydrogen-Argon mixtures [7].

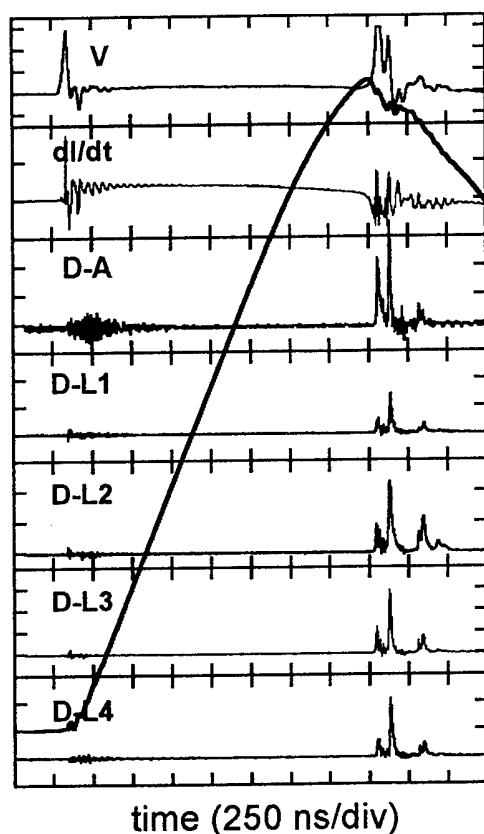


Figure 2: electric and PIN diode signals at 1.4 Torr

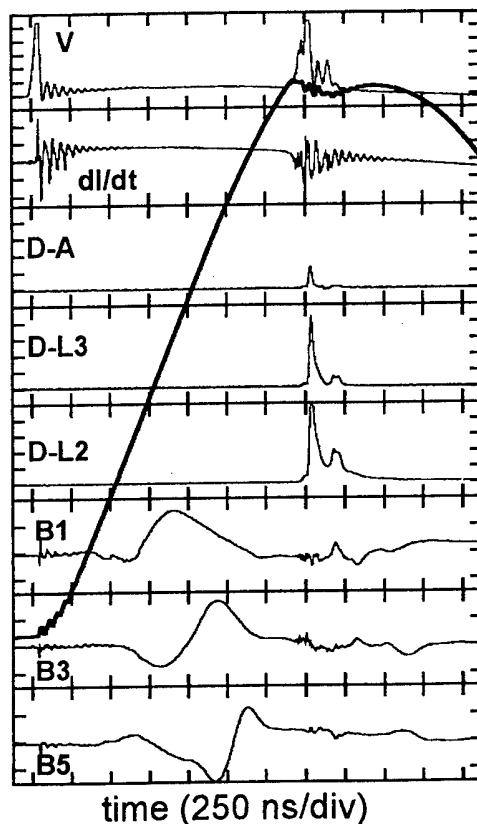


Figure 3: electric, PIN diode and Bdot signals at 0.24 Torr

Figure 3 shows time correlated, single shot data from the electric signals, PIN diodes and Bdot probes, for a shot in 90% Hydrogen plus 10% Argon, at 0.24 Torr. PIN diode identification and filtering is the same as that in figure 2. Despite the low operating pressure, significant focus action is seen to occur.

Two periods of x-ray emission are

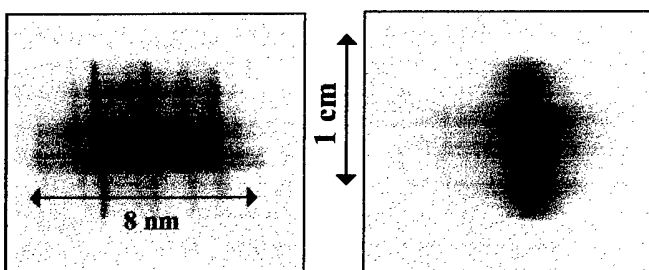


Figure 4: neutral copper lines at 510 nm (left) and  $H_{\beta}$  at 486 nm (right).

observed. The first one is clearly dominated by anode radiation due to electron beam hitting, whereas the second one has an important contribution from plasma radiation. The Bdot probe array signals show that as the sheath propagates axially the thickness decreases and the leading edge becomes more steep. Further discussion on the properties of the current sheath are presented in a companion paper in these proceedings [6].

Preliminary spectra of visible light emission have been recorded. Figure 4 shows characteristic time integrated  $H\beta$  and Copper neutral lines. Emission along the lines corresponds to a 0.3 mm slice across the axis of the discharge, at 2 mm from the anode edge. Each spectrum in fig. 4 is 8 nm wide. As the recorded spectra are time integrated, a suitable selection of particular lines which only appear at collapse time should be identified in order to apply this diagnostic. Nevertheless, the identification of Copper lines is important in order to evaluate the effect of impurities in focus performance.

### CONCLUSION

The operational capabilities of the small Plasma Focus are demonstrated. Improved initial breakdown efficiency is achieved due to an electric circuit which enhances initial  $dI/dt$ . This allows the focus to be operated at pressures below 0.2 Torr, with sharp focus collapse as a result of current sheath quality. The Bdot probes array allows quantitative investigations of current sheath properties, in correlation with focus performance. Preliminary results highlight the effect of impurities on sheath structure. The combined space and time resolved and x-ray diagnostics allows plasma and electron beam induced x-ray emission to be clearly identified. The time integrated visual spectroscopy provides an efficient diagnostic tool to investigate the effect of impurities on focus performance and dynamic effects associated with radial collapse. A comprehensive research programme is currently under development, in order to exploit the capability of this small device to address basic and yet not fully understood features of plasma focus physics.

### ACKNOWLEDGEMENTS

This work has been partially funded by a doctoral research grant from FONDECYT. P. Silva acknowledges a scholarship from CONICYT.

### REFERENCES

- [1] J.R. Smith et al., *Phys. Fluids* **28**, p. 2305, 1985.
- [2] S. Lee et al., *Amer. J. Phys.* **56**, p. 62, 1988.
- [3] G. Decker et al., *Phys Fluids* **26**, p. 571, 1983.
- [4] P. Choi et al., *Laser Part. Beams* **8**, p. 469, 1990.
- [5] K.N. Koshelev et al., *J. Phys. D: Appl. Phys.* **21**, p. 1827, 1988.
- [6] P. Silva et al., *Proc. BEAMS'96* (Prague, Czech Republic), this volume, 1996.
- [7] M. Favre et al., *Plasma Sources. Sci. & Tech.* **2**, p. 122, 1992.



# INFLUENCE OF STUB ANODE ON PLASMA MOTION AND NEUTRON YIELD IN AN 18-kJ PLASMA FOCUS

Ming-fang Lu<sup>\*</sup>, Tsin-chi Yang<sup>\*\*</sup>, Min Han<sup>\*\*</sup> and Si-ze Yang<sup>\*\*\*</sup>

<sup>\*,\*\*\*</sup>*Institute of Physics, Chinese Academy of Sciences, Beijing, 100080, P.R. China*

<sup>\*\*</sup>*Department of Electrical Engineering, Tsinghua University, Beijing, 100084, P.R. China*

## Abstract

Influences of stub anode on current sheath (CS) implosion and pinching as well as on neutron yield have been investigated on the DPF-40 Mather-type plasma focus device (20 kV, 18 kJ). The results show that the stub stabilizes the imploding CS and localizes the plasma pinch, which can be attributed to the azimuthal magnetic field introduced in front of the CS by an anode end discharge induced by the "needle point"-like stub. A centered single stub deteriorates the pinch dynamics and causes the neutron yield to be low and to have large shot-to-shot deviation. Three cases of effects on the plasma motion by the single stub can be distinguished according to the relative height of the stub ( $l_s$ ) to the axial height of the CS ( $z_{cs}$ ):  $l_s > z_{cs}$ ,  $l_s \sim z_{cs}$  and  $l_s < z_{cs}$ . The higher the stub the worse the pinch and neutron yield. When  $l_s \geq z_{cs}$ , the CS front moves along the stub and greatly changes the configuration and status of motion of the CS. The CS and pinch can also be stabilized and localized by a non-centered multi-stub anode. It is advantageous to the pinch dynamics and produces a higher mean neutron yield with less deviation ( $Y_n = (2.9 \pm 0.5) \times 10^8$  per shot,  $\Delta Y_n / Y_n = \pm 17\%$ ).

## Introduction

The plasma focus is considered to be prospective intensive impulse neutron, soft X-ray and ion beam sources<sup>[1,2]</sup>. It is known that anode (center electrode) end structure influences plasma motion, i.e. the implosion and pinching, in a plasma focus. J.W. Mather found that a stub anode can localize the pinch plasma and eliminate the  $m=1$  mode MHD instability caused by an asymmetrical pinch<sup>[3]</sup>. But the influence of the stub anode on the plasma motion has still not been systematically investigated<sup>[4,5, etc.]</sup>. In this paper, this problem has been investigated on the DPF-40 Mather-type plasma focus device<sup>[6]</sup>.

## Experimental apparatus and the stub anodes

The plasma focus device is shown schematically in Fig. 1. The anode (C.E.) is made of oxygen-free copper and of 64-mm diameter. It has a small transition arc of  $R=10$  mm on the anode edge. The charging voltage of the capacitor bank is 20 kV, the stored energy is about 18 kJ. Deuterium gas was filled to a pressure of 333 Pa for neutron emission. The plasma motion was observed by a single-frame double-Wollaston-prism laser differential interferometer (LDI) with an exposure time of about 10 ns<sup>[6]</sup>. Neutron yield was measured by a silver activation counter with a relative standard error of 20%<sup>[7]</sup>.

The centered single-stub anode is shown schematically in Fig. 2 (a). The stub is made of stainless steel and of  $\phi_s=10$  mm diameter, and of  $l_s=30, 20$  and  $10$  mm high respectively. When  $l_s=0$  mm, it transforms to a flat-ended solid anode. Figure 2 (b) shows the non-centered

This work was done in the Department of Electrical Engineering of Tsinghua University.

\*He is with the Institute of Electrostatics of Hebei University, and is now doing post-doctoral research in the Institute of Physics of Chinese Academy of Sciences.

multi-stub anode. Eight stubs (each of 6-mm diameter and 5-mm high, Ti) were symmetrically mounted in a circle of 30-mm diameter around the axis.

## Results and discussions

### A. The single-stub anodes

The LDI results of the imploding and pinching plasmas for the single-stub anodes are shown in Fig. 3 (a) to (c). It can be seen from Fig. 3 (a2) to (a3), (b1) to (b2) and (c1) to (c2) that all of the imploding CSs take the azimuthally symmetric and "funnel"-shaped configuration, namely the "stable mode", and forms the pinch at the stub end. It demonstrated good stabilization and localization effects on the plasma motion by the stub in comparison with both the stable mode and the unstable mode of CS implosion which occurred randomly with respect to each other in consecutive shots with roughly equal probability (Fig. 3 (d1) and (d2)), and the asymmetrical plasma motion in the unstable mode (Fig. 3 (d2) and (d3)) under a flat-ended solid anode<sup>[6]</sup>. The mechanism of these effects can be attributed to the azimuthal magnetic field introduced in front of the CS by an anode end discharge induced by the "needle point"-like stub. In Fig. 3 (a1) to (a4), one can find that the anode end discharge occurring at the stub end started from the earlier stage of the main discharge and lasted to the implosion phase. The magnetic field was firstly compressed by the rundown CS<sup>[8]</sup> (up to factor of about 170<sup>[6]</sup>) and exerted the stabilization and localization effects on the imploding CS.

Three cases of effects on the plasma motion by the single stub can be distinguished according to the relative height of the stub ( $l_s$ ) to the axial height of the CS ( $z_{cs}$ ) at the time the CS front implodes on the stub ( $r=0.5$  cm):

- (1)  $l_s > z_{cs}$ ; for the  $l_s = 30$  mm stub,  $z_{cs} \sim 1.6$  cm (Fig. 3 (a3));
- (2)  $l_s \sim z_{cs}$ ; for the  $l_s = 20$  mm stub,  $z_{cs} \sim 2.0$  cm (Fig. 3 (b2));
- (3)  $l_s < z_{cs}$ ; for the  $l_s = 10$  mm stub,  $z_{cs} \sim 1.8-2.0$  cm (Fig. 3 (c2)).

In case (1), the CS front moves axially along the stub with a larger velocity of  $v_z \sim 3.3 \times 10^7$  cm  $\cdot$  s<sup>-1</sup>, and catches up with the sheath apex some time later ( $\Delta t \sim 105$  ns, Fig. 3 (a3) to (a5) and Fig. 4). The configuration and status of motion of the CS then returns to those in the rundown phase (Fig. 1 (2)), and the CS re-accelerates along a "stub anode" of small diameter. When the sliding front reaches the stub end ( $t \sim -20$  ns), the CS returns to implosion again. The axial motion of the CS is shown in Fig. 4. Under this condition, the stub functions to extend the anode by a "stub anode" of small diameter, and greatly changes the configuration and status of motion of the CS just before the pinching. The radial motion of the CS is shown in Fig. 5. The net radial motion of the CS is stagnated to zero when it moves along the stub.

In case (2), the CS moves similarly to that in case (1) except for the weaker axial motion of the CS front along the stub and the less changes in the configuration and status of the CS.

Under the above two cases, the pinch formed is of worse status with disordered filamented structures (Fig. 3 (a6) and (b3)).

In case (3), the bottom part of the CS equivalent to the stub height is gradually "cut off" by the stub during the following implosion of the CS. The CS above the stub continues to implode and forms the pinch at the stub end. No obvious axial motion of the sheath front along the stub is observed. According to the "T"-type configuration of the CS and pinch, the pinch will be shortened by the "cut off" effect. And the higher the stub the shorter the pinch. But the stub has less influences on the configuration and status of the CS. It still forms a pinch of relatively better structure (Fig. 3 (c3)).

Neutron yields produced by the single-stub anodes are shown in Table 1. In comparison with that of the stable mode under the flat-ended solid anode, the neutron yield of the stub anodes decreased to about 27 to 56 percent. Also, it has large shot-to-shot deviation. The higher the stub the lower the neutron yield, which demonstrated the negative influences of the stub on the pinch dynamics, and is consistent with the results obtained by the interference images. For the flat-ended solid anode, the lower neutron yield with large deviation is due to the two randomly occurring modes of plasma motion.

In addition, the single stub is always strongly eroded by the pinch plasma, and a "crater"-like erosion hole is soon formed at the stub end with many "needle point"-like small protrusions, which further enhanced the discharge at the stub end.

### B. The non-centered multi-stub anode

To take advantage of the single-stub anode to stabilize and localize the imploding and pinching plasmas and, at the same time, to avoid its negative influences on the pinch dynamics and neutron yield, a non-centered multi-stub anode was designed (Fig. 2 (b)) and tested. The results of plasma motion for this anode are shown in Fig. 3 (e1) to (e3). The multi-stub anode also stabilized and localized the imploding and pinching plasmas. When the CS crosses the stub, its sliding front is stagnated to fall behind the mid part of the CS. The pinch is firstly formed at this part of the CS and then develops in both directions along the axis. It forms a symmetric and uniform pinch of good status (Fig. 3 (e3)), which is similar to the pinching process for a hollow or cavity anode<sup>[6]</sup>. The neutron yield is higher and has less shot-to-shot deviation ( $Y_n = (2.9 \pm 0.5) \times 10^8$  per shot,  $\Delta Y_n / Y_n = \pm 17\%$ , total 33 shots). The highest ones reached  $Y_{n,max} = 5.1 \times 10^8$  per shot. The multi-stub anode improved the pinch dynamics and neutron yield by avoiding direct interactions between the pinch plasma and the stub.

### Conclusion

The investigations on the stub anodes in plasma focus can be summarized as follows:

- (1) The stub anodes help to stabilize and localize the imploding and pinching plasmas. The mechanism can be attributed to the azimuthal magnetic field introduced in front of the CS by the anode end discharge induced by the "needle point"-like stub.
- (2) The centered single-stub anodes deteriorate the pinch dynamics and neutron yield by influencing the imploding current sheath and pinch status. Neutron yield is low and has large shot-to-shot deviation. The higher the stub, the stronger the negative influence it on the plasmas.
- (3) The non-centered multi-stub anode helps to improve the pinch dynamics and neutron yield. The neutron yield is higher and less deviated. It is one of the ideal anode end structures in plasma focus, and also helps to eliminate the spatial uncertainty of the sources for neutron and X-ray emission.

- [1] Jassby, D.L., Trans. Am. Nucl. Soc., 30 (1978) 61
- [2] Howells, M., Kirz, J., Sayre, D., et al. Phys. Today, 39 (1985) 22
- [3] Mather, J.W., Bottoms, P.J., Carpenter, J.P., et al. 4th Int. Conf. on Plasma Phys. and Contr. Fusion Res., (Madison, 1971), (Vienna:IAEA, 1971) 561-572
- [4] Wainwright, T. E., Pickles, W. L., Sahlin, H. L., et al. 2nd Int. Conf. on Energy Storage, Compression, and Switching (Venice, 1978), (New York:Plenum Press, 1983) 317-323
- [5] Wang, X.X. and Yang, T.C., IEEE Trans. Plasma Sci., 21 (1993) 175-180
- [6] Lu, M.F., J. Phys. 29D (1996) 660-680
- [7] Lu, M.F., Han, M. and Wang, X.X., Nucl. Electronics and Detection Tech., 14(1994) 212-217 (in Chinese)
- [8] Mather, J.W., In: Lovberg, R.H., Griem, H.R., eds, Methods of Experimental Phys. Vol. 9B, Plasma Physics, (New York:Academic Press, 1971) 187

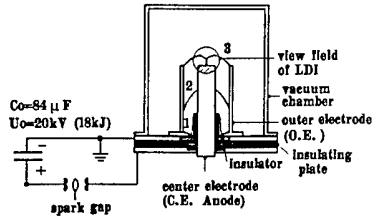


Fig. 1 The schematic diagram of the DPF-40 plasma focus  
1. CS formation in the breakdown phase; 2. CS in the rundown phase; 3. CS in the implosion and pinch phases.

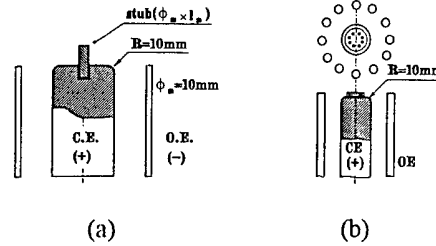


Fig. 2 (a) The centered single-stub anode;  
(b) the non-centered multi-stub anode.

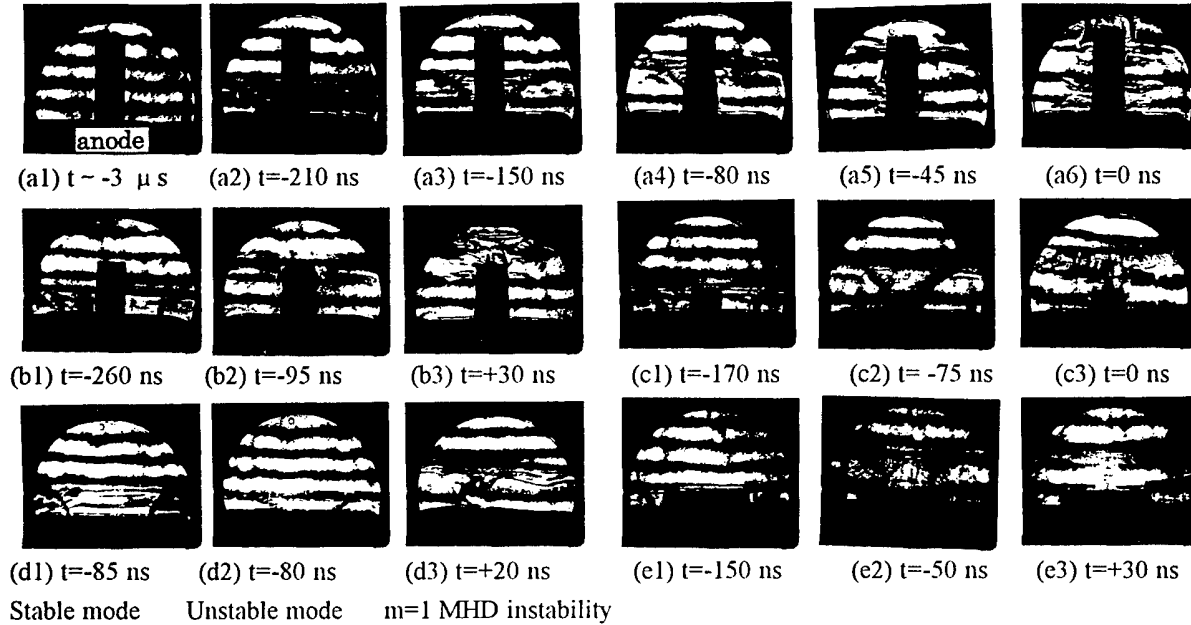


Fig. 3 LDI results of plasma motion. (a)-(c) for the single-stub anodes; (a)  $l_s = 30$  mm, (b)  $l_s = 20$  mm, (c)  $l_s = 10$  mm; (d) for the solid anode ( $l_s = 0$  mm); (e) for the multi-stub anode.

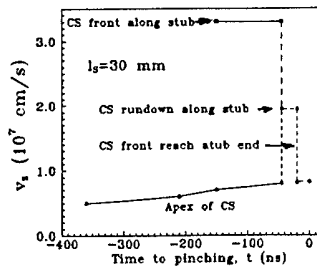


Fig. 4 Axial motion of the CS.

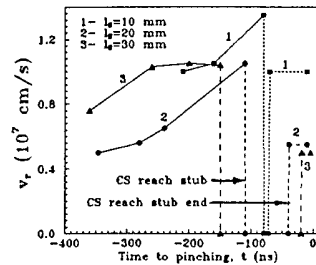


Fig. 5 Radial motion of the CS.

Table 1. Neutron yield versus stub height for the single-stub anodes

Stub height, $l_s$ / mm		Mean yield, $Y_n / 10^8$ per shot	Deviation, $\Delta Y_n / Y_n$ (%)	Counted shots
10		$1.53 \pm 1.03$	$\pm 67$	153
20		$0.93 \pm 0.65$	$\pm 70$	32
30		$1.05 \pm 0.50$	$\pm 48$	29
Solid anode ( $l_s = 0$ ) <sup>[6]</sup>	Stable mode	$2.1 \pm 0.4$	$\pm 20$	25
	Unstable mode	$0.4 \pm 0.16$	$\pm 40$	23
	Mean yield	$1.3 \pm 0.9$	$\pm 69$	(total 48)

# COMPUTER SIMULATION OF A PLASMA FOCUS DEVICE DRIVEN BY A MAGNETIC PULSER

N. Georgescu, V. Zoita

*Institute of Physics and Technology of Radiation Devices,  
Plasma Physics and Nuclear Fusion Laboratory  
P.O. Box 5206, Magurele, Bucharest, R-76900, ROMANIA*

J. Larour

*École Polytechnique,  
Laboratoire de Physique des Milieux Ionisés,  
91128 Palaiseau, FRANCE*

## Abstract

A plasma focus device, driven by a magnetic pulse compression circuit, is simulated by using a PSPICE program. The elaborated program is much simpler than the other existing ones, which analyse the circuit by directly solving a system of integral-differential equations. The pre-pulse voltage and the high-voltage rise-times are obtained for a set of values of the bypass impedance (R or L). The optimum bypass impedance turns out to be an inductance. During the discharge period, the plasma load is considered as an LR impedance, each component being time dependent. A method is presented for giving us the possibility to introduce the time varying impedances in a PSPICE program. Finally, a set of simulation results (plasma current and voltage, plasma magnetic energy, plasma sheath mechanical energy, pinch voltage) is shown. The results are in good agreement with the classical experimental data.

## Introduction

At the Institute of Physics and Technology of Radiation Devices, Plasma Physics and Nuclear Fusion Laboratory, a plasma focus device (PFD) is being developed as an intense soft X-ray source. The main application we have in mind is the X-ray micro-lithography. In order to fulfill this application requirements, PFD needs to be driven by a pulser with a high average output power. The only method to reach the desired average output power level is the magnetic pulse compression, which is used in a large number of applications, including high-power particle beams, high-power lasers, intense X-ray sources. The method is extendible up to average power levels of 100 - 1000 kW [1].

A 200 J/pulse, 100 Hz magnetic pulse compression circuit (MPCC) has been designed [2, 3] to supply the plasma-focus soft-X-ray source. The circuit has a 25 kV working voltage, and compresses a 29.5  $\mu$ s / 1 kA initial pulse into a 560 ns / 100 kA plasma current pulse.

In order to predict and optimize the circuit and the plasma focus performance, a PSPICE circuit analysis program is used. The PSPICE program is very simple and takes no much time to write it. All the circuit voltages and currents are stored in the computer memory, and we can obtain any arithmetical combination between them.

While a PSPICE program is simple and powerful, it has not straightforward models for the non-linear magnetic switches from MPCC, and for the complex, time-varying plasma focus impedance. This paper describes the technique to overcome these difficulties.

### The simulation of the pre-breakdown phase

The last stage of the 200 J/pulse MPCC [3] has been analyzed. Its PSPICE equivalent circuit is shown in Fig. 1. For the simulation of the real operation three voltage controlled switches have been introduced. At  $t = 0$ , S1 is ON, and S2, S3 are OFF. During the pre-breakdown phase ( $t < 1.6 \mu\text{s}$ ), C3 capacitor is charged from the previous compression stage of the circuit. When C3 charging is finished ( $t = 1.5 \mu\text{s}$ ), S1 switch turns OFF. Just after the C3 charging completion ( $t = 1.54 \mu\text{s}$ ), L3 magnetic switch turns into its saturated state. This change is simulated by turning S2 switch ON. The final breakdown phase begins at  $t = 1.6 \mu\text{s}$ , when S3 switch turns ON.

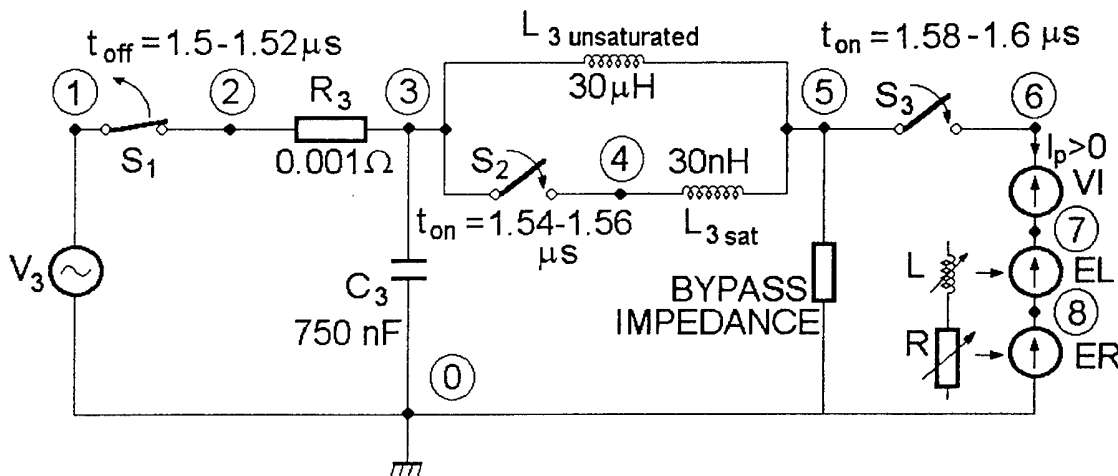


**Fig. 1.**

The PSPICE equivalent circuit for the MPCC last stage,  
having the plasma focus device as a load

The controlling voltage for S1, S2, S3 is represented by VS independent voltage source (see PSPICE program). Its voltage has fast transitions between 0-5 V, 5-10 V, 10 -15 V. Each of the three switches changes its state at one of the three transition moments.

In the MPCC circuit, the C3 capacitor voltage is given by:

$$v_3(t) = \frac{V_0}{2} \left( 1 - \cos \frac{\pi}{\tau_2} t \right),$$

where  $V_0 = 25 \text{ kV}$ ,  $\tau_2 = 1.5 \mu\text{s}$ . For a PSPICE representation,  $v_3(t)$  is written as:

$$v_3(t) = 12500 + 12500 \sin(2 \pi 333000 t - \pi/2) \text{ [V]},$$

and the corresponding PSPICE line is:

$$\text{V3 1 0 SIN}(12500 \text{ 12500 333E3 -90)$$

In the pre-breakdown phase, the plasma impedance is very large. In order to conduct the magnetisation current of the last magnetic switch (L3), a "bypass impedance" (parallel with the load) is needed. The magnetization current produces a pre-pulse voltage, before the high voltage ( $\sim 25 \text{ kV}$ ) appears on the load.

### The simulation of the discharge phase

During the discharge phase (breakdown + pinch) the main problem to be solved is the introducing of the time-varying plasma impedance into the PSPICE program.

The two plasma impedance components ( $L$ ,  $R$ ) are supposed to have a piece-wise linear temporal variation (Fig. 2a). The plasma inductance increases with time. During the pinch phase (1.9 - 2.0  $\mu$ s), the inductance rises much more rapidly. The plasma resistance reaches a peak of 20 m $\Omega$ . These variations are typical for a plasma focus discharge, and their purpose is only to test the correctness of the PSPICE program. Any other type of the temporal variation can be introduced using the piece-wise linear approximation.

The general technique for simulating time varying impedances involves synthesizing their components from dependent voltage and current sources. Thus, in Fig. 1, EL, ER sources represent the voltages across the plasma inductance, and the plasma resistance respectively. The corresponding voltage on the PFD load is obtained by adding the EL and ER voltages, which means V(7) voltage. The plasma discharge current is the current through the VI source (a "dead" voltage source, serving as an Amper-meter).

In the PSPICE program, an independent voltage source (VL), varying in the same manner as  $L(t)$ , is created. This source provides on an 1  $\Omega$  resistor, a voltage (V(25)), numerically equal with  $L(t)$ .

The voltage across  $L(t)$  is given by:

$$V_L(t) = L(t) \frac{di}{dt} + i(t) \frac{dL}{dt}.$$

For getting the derivative of  $i(t)$  (multiplied by  $10^{-6}$ ), a *Current-Controlled-Current-Source* (CCCS), named FI, supplies a current equal with the load one, into a 1  $\mu$ H inductance. (The attempt to introduce a 1 H inductance in the circuit, leads to convergence problems.) The output voltage (V(45)) will be equal with  $10^{-6} di/dt$ .

The derivative  $dL/dt$  is obtained by using the *Voltage-Controlled-Current-Source* (VCCS) named GL, which supply a current numerically equal with V(25) (i. e.  $L(t)$ ) into  $L90 = 1 \mu$ H. In this way, V(90) voltage represents  $10^{-6} dL/dt$ .

In our previous PSPICE programs, polynomial dependent sources were used to implement  $V_L(t)$  voltage. In this paper, the Analog Behavioral Modeling Module of newer versions of PSPICE [4] is used. This technique makes the modeling process easier and more straightforward. We can have now dependent sources whose values are given by any mathematical expression containing voltages and currents from the circuit. In the  $V_L(t)$  case, the PSPICE instruction for creating the EL source is simply:

EL 7 8 Value = { V(25)\*V(45)\*1E6 + I(VI)\*V(90)\*1E6 }

Plasma resistance simulation is much more simple. A voltage (V(110)) modeling the time-varying resistance values is created. Then, the ER source is defined as:

ER 8 0 Value = { V(110)\*I(VI) }

The Analog Behavioral Modeling Module can be used to provide other useful plasma focus time-varying parameters: plasma magnetic energy ( $L(t) i^2(t)/2$ ), pinch voltage ( $i(t)dL/dt$ ).

In order to obtain the plasma sheath mechanical energy, we have to model the relation:

$$E_{\text{mech}} = \frac{1}{2} \int_0^t \frac{dL}{dt} i^2(t) dt.$$

The PSPICE program contains the G3 current source with value  $\{i^2(t) dL/dt\}$ . This current charges a 2 F artificial capacitor. The capacitor voltage (V(100)) is numerically equal with  $E_{\text{mechanical}}$ .

# **PSPICE program**

PFLR.cir

V3 1 0 SIN(12500 12500 333E3 0 0 -90)

R3 2 3 0.001

C3 3 0 750N IC=0

L3UNSAT 3 5 30U IC=0

L3SAT 4 5 30N IC=0

LBYPASS 5 0 1U IC=0

VI 6 7 0

\* The three voltage-controlled switches:

\* (Controlling voltage = V(20))

S1 1 2 20 0 SOURCE

.MODEL SOURCE VSWITCH RON=0.001

+ ROFF=1E9 VON=2 VOFF=3

S2 3 4 20 0 SAT

.MODEL SAT VSWITCH RON=0.001

+ ROFF=1E9 VON=8 VOFF=7

S3 5 6 20 0 LOAD

.MODEL LOAD VSWITCH RON=0.001

+ ROFF=1E9 VON=13 VOFF=12

VS 20 0 PWL(0 0, 1.5U 0, 1.52U 5,

+ 1.54U 5, 1.56U 10, 1.58U 10, 1.6U 15)

R20 20 0 1

\* L(t) <=> V(25):

VL 25 0 PWL(0 10N, 1.6U 10N, 1.9U 20N,

+ 1.95U 50N, 2.3U 60N)

R25 25 0 1

\* dL/dt <=> V(90)\*1E6 :

GL 0 90 25 0 1

L90 90 0 1E-6 IC=0

\* i(t) <=> I(VI)

\* di/dt <=> V(45)\*1E6 :

FI 0 45 VI 1

L45 45 0 1E-6 IC=0

\* EL voltage <=> L(t)\*di/dt + i(t)\*dL/dt :

EL 7 8 Value = {V(25)\*V(45)\*1E6 +

+ I(VI)\*V(90)\*1E6}

\* R(t) <=> V(110) :

VR 110 0 PWL(0 0, 1.9U 0, 1.95U 20M, 2.0U 0)

R110 110 0 1

\* ER voltage <=> R(t)\*i(t) :

ER 8 0 Value = {V(110)\*I(VI)}

\* Plasma sheath mechanical energy =

\* = (1/2) Integral{i(t)\*i(t)\*dL/dt\*dt}:

G3 0 100 Value = {I(VI)\*I(VI)\*V(90)\*1E6}

CMEC 100 0 2 IC=0

RMEC 100 0 1E9

\* Plasma magnetic energy = L(t)\*i(t)\*i(t)/2:

EMAG 120 0 Value = {V(25)\*I(VI)\*I(VI)/2}

R120 120 0 1

\* Pinch voltage = i(t)\*dL/dt:

EPINCH 130 0 Value = {I(VI)\*V(90)\*1E6}

R130 130 0 1

\* Instruction for the transient analysis:

.TRAN 2N 2.3U 1.2U 2N UIC

.PROBE

.END

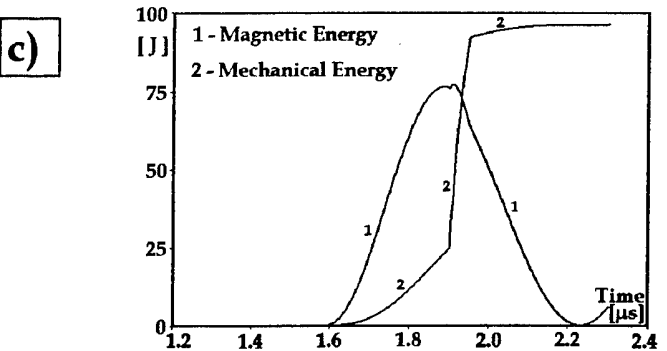
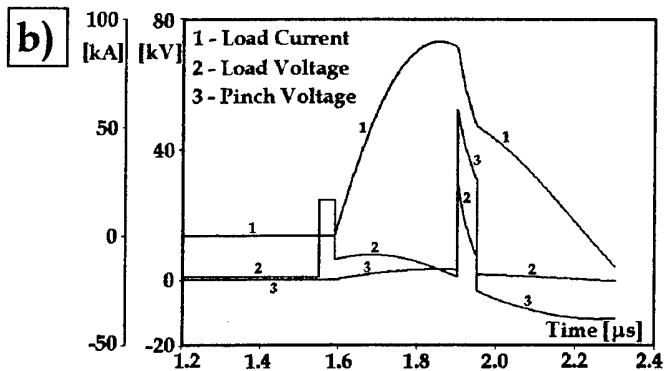
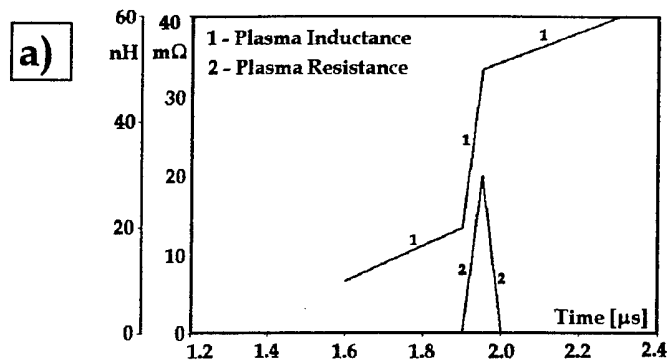


**Fig. 2.**

a) The supposed L(t), R(t) components of the plasma impedance.

b) , c) : **The computed results:**

b) load current, load voltage, pinch voltage;

c) plasma magnetic energy, plasma sheath mechanical energy.



### The simulation results

The PSPICE pre-breakdown transient analysis was made up to  $1.6 \mu\text{s}$ , for  $R = 1 - 10 \Omega$ , and  $L = 1 - 10 \mu\text{H}$ . For the  $R$  values, the pre-pulse voltages are from 660 up to 5800 V. After  $L3$  saturates ( $S2$  turns ON), the high-voltage rise-times are from 100 ns (for  $R = 1 \Omega$ ), down to 20 ns (if  $R = 10 \Omega$ ). Unfortunately, the shortest rise-time means the highest pre-pulse voltage.

For an  $L$  bypass impedance, the pre-pulse voltages are from 800 V to 6200 V. But the great advantage of the  $L$  impedance is the very short rise-time of the high-voltage: 1.5 - 2 ns for all the inductance values. A short high-voltage rise-time is a good condition for an optimum plasma-focus discharge. Another advantage of the  $L$  bypass impedance is that the top of the voltage does not decrease very much before breakdown.

The breakdown (acceleration + pinch) phase was analysed for an  $1 \mu\text{H}$  bypass inductance.

The simulated plasma current (Fig. 2b) has the typical variation for a plasma focus discharge: a sinusoidal shape before the pinch, and an important decrease during the pinch phase. The load and the pinch voltages (Fig. 2b) show also a good agreement with the classical experimental data. The data shown in Fig. 2c can be used to determine the partition of the energy in the discharge system.

### Conclusions

The elaborated PSPICE program has analyzed the transient phenomena in the MPCC last stage, having a plasma-focus device as a load.

The bypass impedance was a  $1 - 10 \Omega$  resistance or a  $1 - 10 \mu\text{H}$  inductance. For an optimum plasma-focus discharge, an  $L$  bypass impedance will be needed.

During the discharge time, the plasma impedance is represented as a series LR circuit, each component being a function of time. By using an original method, the time varying plasma impedance have been introduced in the PSPICE program. The technique involves synthesizing impedance components from dependent voltage and current sources. The Analog Behavioral Modeling Module of newer versions of PSPICE is used. A set of simulation results shows the good agreement between the theoretical simulation and experimental data.

The PSPICE method helps us to obtain a better understanding of the MPCC-driven plasma-focus device. The circuit and device optimisations can be achieved by using the simulation program instead of working on the experimental workbench. These computer simulations will be used to design a plasma-focus soft X-ray source for the future X-ray microlithography applications.

### References

- [1] Harjes, H.C., Penn, K.J., Reed, K.W., Mc Clenahan, C.R., Laderach, G.E., Wavrik, R.W., Adcock, J., Butler, M., Mann, G.A., Martinez, L., Morgan, F.A., Weber, G.J., Neau, E.L., "Status of the Repetitive High Energy Pulsed Power Project", Proc. of the 8-th IEEE Int. Pulsed Power Conf., San Diego, California, USA, 1991, pp. 543 -548.
- [2] Georgescu, N., Zoita, V., "Magnetic Pulse Compression Driver for a Plasma Focus X-Ray Source", Romanian Journal of Physics, 39, 3-4, 1994, pp. 253 - 263.
- [3] Georgescu, N., Zoita, V., Presura, R., "Magnetic Pulse Compression Circuits for Plasma Devices", 11th International Conf. on High Power Particle Beams (BEAMS '96), Prague, Czech Republic, paper P-2-35.
- [4] Banzhof, W., "Computer-Aided Circuit Analysis Using PSPICE" - Second Edition, Regents/Prentice Hall, NJ, USA, 1992, pp. 273-283.

# HIGHLY IONIZED COPPER CONTRIBUTION TO THE SOFT X-RAY EMISSION IN A PLASMA FOCUS DEVICE

V. Zoita, A. Patran and J. Larour\*

*Institute of Physics and Technology of Radiation Devices,  
Plasma Physics and Nuclear Fusion Laboratory  
P.O. Box 5206, Magurele, Bucharest, R-76900, Romania  
\*Ecole Polytechnique, Palaiseau, France*

## Abstract

In order to discriminate between the contributions of the gas plasma and of the anode (solid or plasma) to the soft X-ray emission in a plasma focus device, a series of experiments was carried out using the following combinations of experimental conditions: various gases, different absorption filters and viewing different regions in front of the centre electrode. The experiments were performed on the IPF-2/20 plasma focus device using the following working gases: helium, neon and helium-argon mixtures. The diagnostics used: magnetic probe for current derivative, PIN diode for the minimum pinch radius detection, PIN diodes for the soft X-ray emission, scintillator-photomultiplier detector for the hard X-ray emission.

From the analysis of the various diagnostics data recorded with very good time correlation, it followed that the soft X-ray signals had a strong contribution from optical transitions of the highly ionised Cu (CuXX to XXII) emitting in the range 0.8-1.3 nm.

## Introduction

The plasma-anode interaction represents one aspect of particular importance in the development of a hot plasma soft X-ray source based on the plasma focus device [1, 2]. This regards both the effects on the electrode (determining its life-time) and the contribution of the (usually undesired) radiation emitted by the anode material to the soft X-ray yield of a plasma focus machine. The X radiation emitted from the near-anode region has been recorded by various means [3-6]:

- a non-filtered pinhole camera (even time-resolved) provides information about the radiation coming from that region, but it would not reveal the spectral feature (and thus the nature of the radiating object);

- a filtered pinhole image needs an image intensifier camera to obtain time resolution and it does not detect the higher energy component of the radiation;

- a crystal spectrometer provides only the softer energy spectrum which is usually space and time integrated.

The experiments presented in this paper benefited from the following experimental conditions: a satisfactory broad-band spectral resolution, with the possibility of "seeing" widely different photon energy bands; good space resolution (about one mm); good (a few nanoseconds) time resolution and synchronization between detecting channels; a plasma focus machine that worked efficiently over a very wide range of gas parameters (pressure and composition).

All these made it possible to identify certain features of the X-ray emission of the near-anode region and especially to point out the contribution of the metal (copper) plasma.

### Experimental setup

The experiments were performed on the IPF-2/20 plasma focus device [7] at 16 kV voltage (about 10 kJ energy) and 385 kA peak current. The centre electrode (anode) had a W/Cu/Ni alloy insert with a 15 mm hole on the axis. As working gases were used helium (pressures: 3.2-7.0 torr), neon (pressures: 2.6-7.3 torr) and helium-argon mixtures (pressures: 0.2-0.5 torr argon, for total pressures in the range of 4.0-4.8 torr).

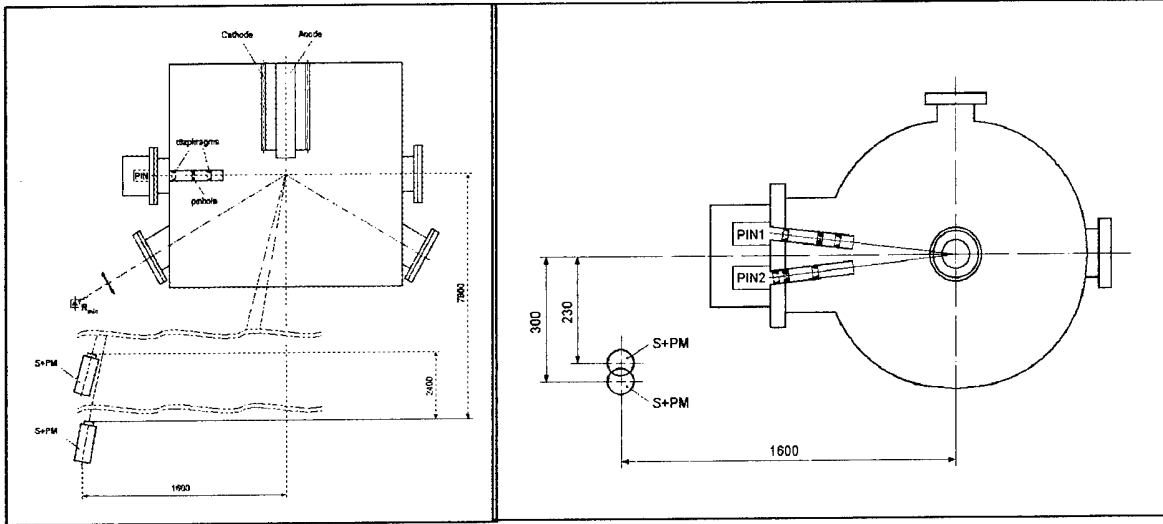


Fig. 1: Experimental setup

The following diagnostics were used: magnetic probe for current derivative, visible PIN diode for the minimum pinch radius detection and synchronisation of the detection channels, PIN diodes (Quantrad type) for the soft X-ray emission, scintillator-photomultiplier detector (S+PM) for the hard X-ray emission. The experimental setup is shown in Fig. 1.

The PIN Quantrad diodes were used with Al 75  $\mu\text{m}$  and Al 15  $\mu\text{m}$  absorption filters. The detectivities for a Quantrad PIN diode with and without filters are shown in Fig. 2.

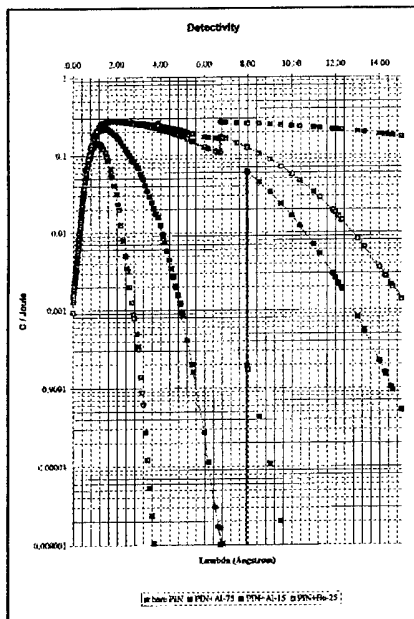


Fig. 2: PIN detectivity

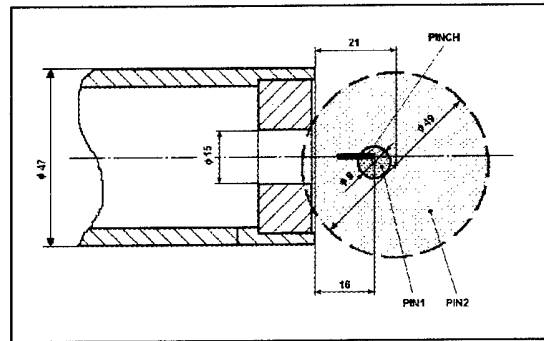


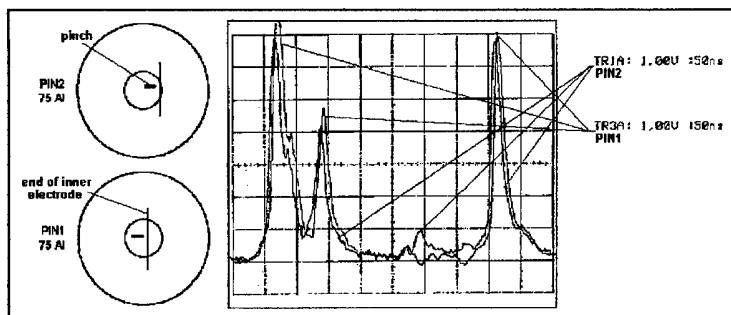
Fig. 3: Areas seen by the PIN detectors

The areas seen by the two PIN detectors were changed using the collimating system. The projected field of view of the two PIN diode detection channels on a plane containing the electrode axis is shown in Fig. 3.

## Results and analysis

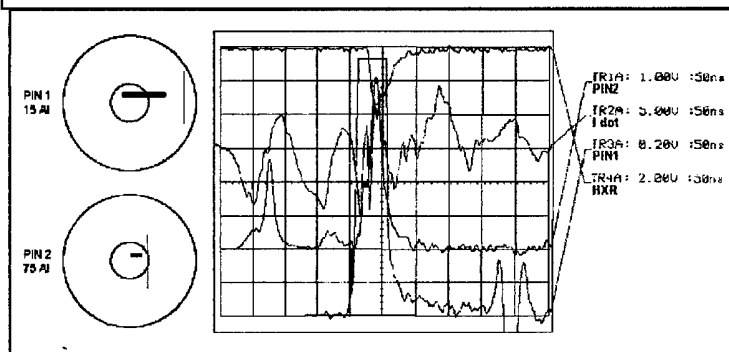
Neon discharges were used to test the response and time relationship between various detection channels. Typical ("standard") PIN diode signals obtained in neon discharges are shown in Fig. 4 displaying the internal structure for the X-ray pulses and the time correlation between the two detectors. A time delay of 5 ns between the two channels was due to a difference in cable length. The different sensitivities of the two diodes was explained by the difference in the construction parameters.

Fig. 4: PIN signals for a 3.4 torr neon discharge



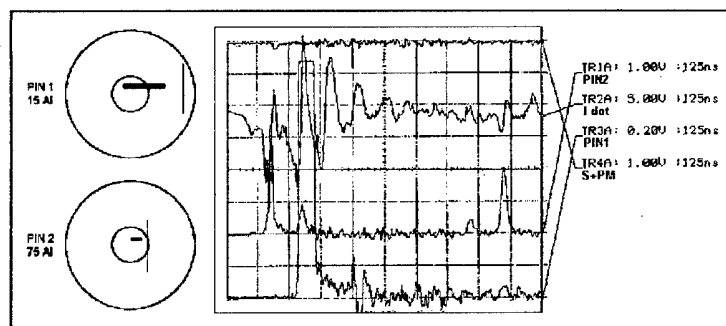
In helium discharges, the signal coming from the diode seeing the end of the centre electrode (PIN2) has a standard structure with three emission periods (Fig. 5).

Fig. 5: Diagnostics signals of a 4.8 torr helium discharge



In the other channel (PIN1) a very strong signal appeared, coincident with the third emission period of the PIN2 channel. The large PIN1 signal corresponds to a hard X-ray pulse and to a fast change in the I-dot trace. The correlation of the information provided by the four waveforms shown in Fig. 5 pointed out the existence of a strong electron beam that would produce both the hard X-rays in the S+PM channel and characteristic X radiation from the end of centre electrode in the PIN2 channel. Then a possible explanation for the PIN1 signal could be that it is characteristic line radiation induced by the electron beam in a cold (metal?) plasma situated at about 10 mm from the electrode end. However, a similar strong PIN1 signal is obtained in a helium-argon mixture discharge under different conditions: no hard X-ray signal, only a slight change in the I-dot waveform, and a rather small simultaneous pulse in the PIN2 channel (Fig. 6). A hard X-ray signal (with the corresponding change in the I-dot) can be seen but it is about 100 ns before the PIN1 one. It follows that one does not have a beam induced radiation.

Fig. 6: Signals from a helium-argon mixture discharge (4.3 torr total pressure, 0.2 torr argon pressure)

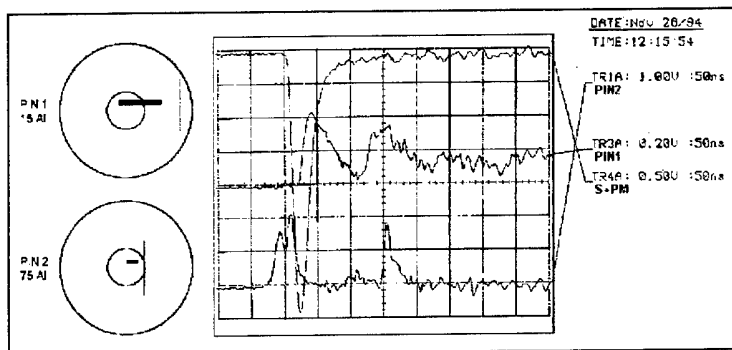


From the estimated amplitude ratio for this signal and the simultaneous peak of the

PIN2 channel, taking into account the geometrical and filtering conditions it was calculated that the signal could be either in the 0.3-0.4 nm spectral band or just over 0.8 nm.

Discharges made in pure neon provided supplementary information that helped to identify the source of the radiation seen by detector PIN1 in Fig. 5 and 6. The PIN1 channel in Fig. 7 sees H- and He-like neon ion emission in the 1.2-1.3 nm region. The line spectrum was recorded in such discharges and presented in a paper [8].

Fig. 7 Signals from a 4.2 torr neon discharge



From the analysis of the information presented above as well as from the spectral data given in reference tables [9], it follows that copper is the most probable candidate for the X-ray

emission seen by the PIN1 channel in He and He-Ar discharges. The radiation cannot be from the Cu L-characteristic lines because that would correspond to a very strong K-characteristic radiation signal in PIN1 that cannot be seen in the neon discharges.

The explanation put forward is that the PIN1 channel detected optical radiation from highly ionized copper: the CuXX to CuXXII ions have a lot of powerful lines in the 0.8-1.3 nm band.

### Conclusion

The analysis of the various diagnostics data (especially those provided by the PIN diodes and the scintillator-photomultiplier detector) recorded with very good time correlation in focus discharges produced in various gas fillings lead to the conclusion that the soft X-ray signals had a strong contribution from optical transitions of the highly ionized Cu (CuXX to XXII) emitting in the range 0.8-1.3 nm.

- [1] Kato, Y., Ochiai, I., Watanabe, Y., Murayama, S.: J.Vac.Sci.Technol., **B6** (1988) 195
- [2] Richter, F., Eberle, J., Holz, R., Neff, W., Lebert, R.: 2nd Intern. Conf. on Dense Z-Pinches, Laguna Beach, Ca., April 1989, (N.R. Pereira et al., eds), AIP, N.Y., p. 515
- [3] Burnett, J.C., Meyer, J., Rankin, G.: Can. J. Phys., **55** (1977) 194
- [4] Shimoda, K., Yamamoto, T., Takada, S., Sone, H., Hirano, K.: Jap.J. Appl.Phys. **26** 3 (1987) 451
- [5] Herold, H., Kaeppler, H.J., Schmidt, H., Shakhatre, M., Wong, C.S., Deeney, C., Choi, P.: Proc. 12th Int. Conf. on Plasma Phys. and Controlled Nuclear Fusion Research, Nice, 1988, paper CN-50/C-4-5-3
- [6] Bayley, J.M., Decker, G., Kies, W., Mälzig, M., Müller, F., Röwekamp, P., Westheide, J., Sidelnikov, Y.V.: J.Appl.Phys. **69** 2 (1991) 613
- [7] Mandache, N., Tisceanu, I., Zambreanu, V., Zoita, V., Serban, A., Doloc, C.: Proc. 18th Europ. Conf on Plasma Phys. and Controlled Nucl. Fusion, Berlin (1991) 333
- [8] Presura, R., Zoita, V., Paraschiv, I.: Proc. 11th Int. Conf. on High Power Particle Beams, Prague, June 1996
- [9] Kelly, R.L.: J. Phys. and Chem. Ref. Data, **16**, Suppl. No. 1, (1987)

## MAGNETIC PULSE COMPRESSION CIRCUITS FOR PLASMA DEVICES

N. Georgescu, V. Zoita, R. Presura

*Institute of Physics and Technology of Radiation Devices,  
Plasma Physics and Nuclear Fusion Laboratory  
P.O. Box 5206, Măgurele, Bucharest, R-76900, ROMANIA*

### Abstract

Two magnetic pulse compression circuits (MPCC), for two different plasma devices, are presented. The first is a 20 J/pulse, 3-stage circuit designed to trigger a low pressure discharge. The circuit has 16-18 kV working voltage, and 200 nF in each stage. The saturable inductors are realized with toroidal 25  $\mu\text{m}$  strip-wound cores, made of a Fe-Ni alloy, with 1.5 T saturation induction. The total magnetic volume is around 290  $\text{cm}^3$ . By using a 25 kV/1 A thyatron as a primary switch, the time compression is from 3.5  $\mu\text{s}$  to 450 ns, in a short-circuit load.

The second magnetic pulser is a 200 J/pulse circuit, designed to drive a high average power plasma focus soft X-ray source, for X-ray microlithography as the main application. The 3-stage pulser should supply a maximum load current of 100 kA, with a rise-time of 250 - 300 ns. The maximum pulse voltage applied on the plasma discharge chamber is around 20 - 25 kV. The three saturable inductors in the circuit are made of toroidal strip-wound cores with METGLAS 2605 CO amorphous alloy as the magnetic material. The total, optimized mass of the magnetic material is 34 kg. The maximum repetition rate is limited at 100 Hz by the thyatron used in the first stage of the circuit, the driver supplying to the load about 20 kW average power.

### Introduction

At the Institute of Physics and Technology of Radiation Devices, Plasma Physics and Nuclear Fusion Laboratory, the plasma devices research and applications have been developed for about 25 years. For the near future, our main goal is to obtain high average electromagnetic power delivered to the pulsed plasma loads. The classical solution for the pulser (condenser discharged through a spark-gap switch into the load) cannot be applied, because there is no spark-gap switch capable of discharging pulse currents of 10-100 kA or higher at more than 10 Hz repetition rate. The only method to reach the desired average output power levels is the magnetic pulse compression. In the magnetic pulse compression circuit (MPCC), a slow "energy package" is first generated in a primary circuit, by using a classical repetitive switch (thyatron, thyristor). Hereafter, this "low power" pulse is transmitted through a chain of condensers and saturable inductors (magnetic switches), which reshapes it to the short rise and duration time and to the higher power level required. Because the "low power" pulse can be switched by thyatrons or thyristors with the required pulse repetition frequency (PRF), we can have at the output very high power pulses, at repetition rates of 10-100 Hz or more.

Beginning in 1980, a lot of MPCC were constructed all over the world, for applications as high-power particle beams, high-power lasers, intense X-ray sources. Up to now, the magnetic pulse compression method was used for up to 100's kW output average-power [1].

### MPCC for triggering a low pressure discharge

Low pressure discharges are interesting from the point of view of plasma radiation sources (e.g. lasers, electron sources, flash X-ray sources). For such radiation sources, it is important to have very reproducible breakdown, plasma development and emission parameters. A high-power low-pressure discharge can be also used as fast switch or as triggering means for more powerful discharge configurations.

The schematic of the three-stage magnetic pulse compression circuit used to power a low pressure discharge is presented in Fig. 1. The circuit [2] compresses voltage pulses of up to 16 kV from 3.6  $\mu$ s to 450 ns when coupled to a short-circuit load. The measured intensity of the short-circuit current is about 10 ÷ 15 kA. The maximum transferred energy is 20 J per pulse. The temporal compression is accomplished by using as magnetic switches three toroidal saturable inductors made of 25  $\mu$ m Fe-Ni alloy ribbon (Telcon HCR type). The total magnetic volume of the saturable inductors is around 290 cm<sup>3</sup>. Manufacture data show that in the given conditions, the hysteresis losses are less than 15 - 20 W for each saturable inductor, at 100 Hz pulse repetition frequency. As a primary switch, a thyatron TGI 1000/25 (Russia), which has a 1 kA maximum allowed pulse current and 25 kV maximum anode voltage was used. The capacitors (200 nF/20 kV - Condenser Products - USA) limited the maximum charging voltage at 16 kV. This pulser can operate at repetition frequencies up to 100 Hz. At maximum repetition rate, the average power supplied to the load reaches 2 kW.

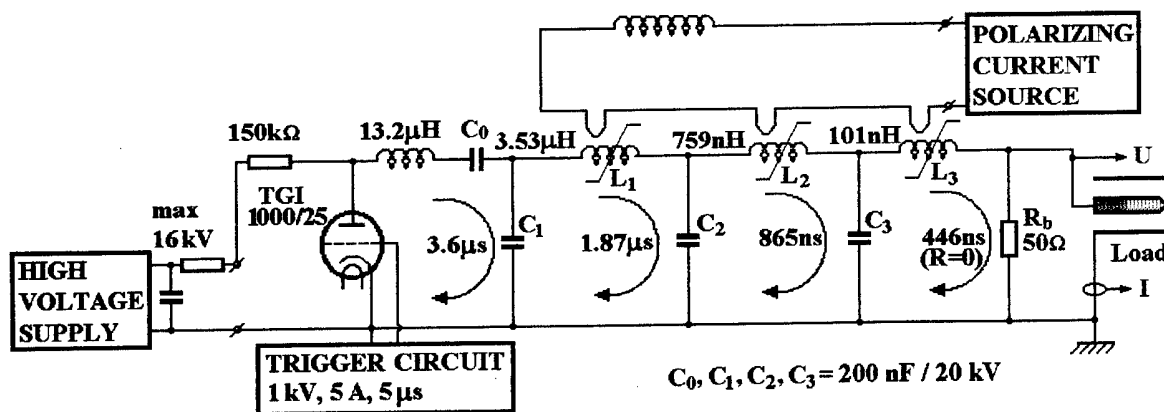


Fig. 1. Schematic of the magnetic pulse compression circuit with the coaxial discharge load. The measuring points for the discharge voltage and current are shown.

The high voltage pulse (either positive or negative) was applied through a low inductance path to a load consisting of two coaxial electrodes as shown schematically in Fig. 1. The outer electrode was a collar-shaped copper piece mounted on a brass tube. It had an outer diameter of 20 mm and the inner diameter of the front hole was 6.5 mm. The inner electrode was a tungsten rod 4 mm in diameter. Two geometries of the rod were employed, namely a pointed-end rod with 90° angle, and a flat-end rod with sharp edges. The top of the inner electrode was placed 3 mm behind the surface of the outer one. The discharges, performed in air, were observed for pressures in a range from about 50 Pa down to 2.5 mPa [3].

The best results were obtained by using the flat-end rod inner electrode as a cathode. In this case the breakdown voltage, the discharge current, the time lag between the moments of the peak voltage and current onset, as well as the location of a very bright discharge inside the

interelectrode gap were very reproducible. Besides, in this configuration the lowest pressure, 2.5 mPa, and the highest discharge current, up to 4.5 kA, were attained. A typical set of voltage and discharge current oscillograms is shown in Fig. 2. The fact that the breakdown voltage becomes independent on the working pressure for values below about 0.1 Pa can be explained considering that phenomena other than charge multiplication in the gas participated in the discharge onset. The field effect may be taken into account for the initiation of the discharge, while a more detailed study is necessary to identify the processes active at the lowest working pressures.

### MPCC for driving a repetitive plasma-focus soft-X-ray source

The second magnetic pulser is a 200 J/pulse MPCC, designed to drive a high-average-power plasma-focus soft-X-ray source, for X-ray micro-lithography as the main application. The 3 stage pulser should supply a maximum load current of 100 kA, with a rise-time of 250-300 ns. The maximum pulse voltage applied on the plasma discharge chamber must be around 20-25 kV. The pulse repetition frequency must be as high as possible, in order to reach a high average output power.

The design was made taking into account some available components: thyratrons for 25 kV and maximum 1 kA pulse current and pulse capacitors of 1.5  $\mu\text{F}$ /15 kV each. In these conditions, a 3 stage MPCC (Fig. 3) with  $C = 750 \text{ nF}$ /30 kV in each stage was designed.

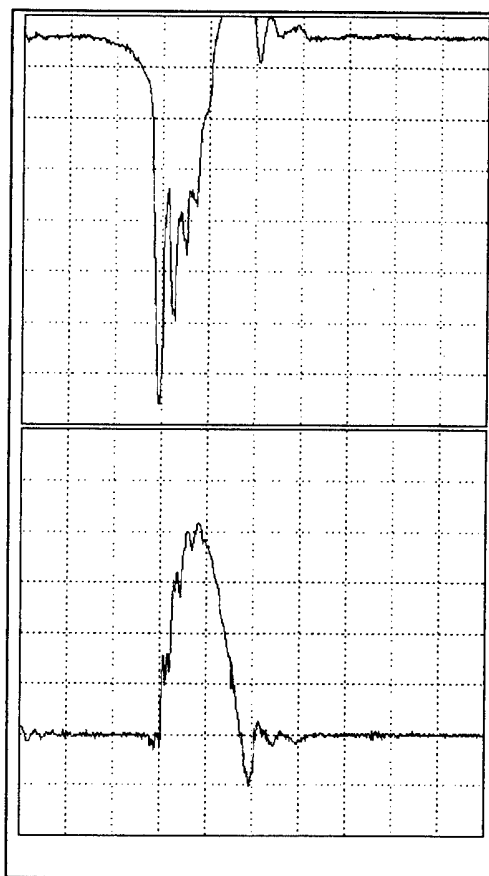


**Fig. 2.**

Voltage (upper trace) and discharge current (lower trace) oscillograms for a discharge at 10 mPa (Horizontal: 1  $\mu\text{s}$  / div.; Vertical: 2 kV / div., respectively 1 kA / div.)

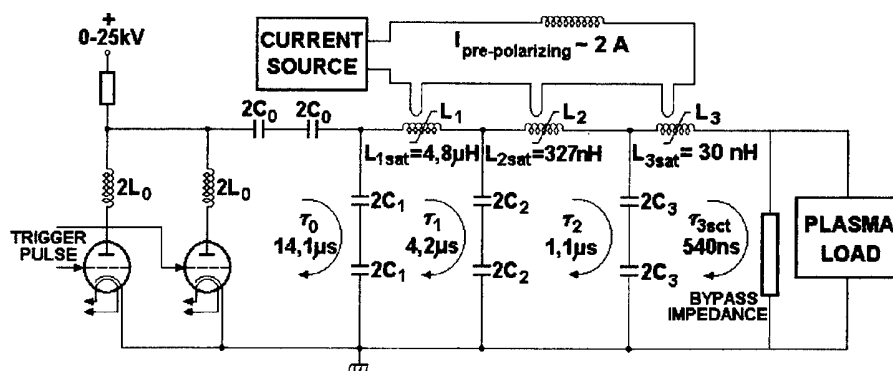


**Fig. 3.** Schematic of the magnetic pulse compression circuit (200 J/pulse) for driving a plasma-focus soft-X-ray source. ( $C_0 = C_1 = C_2 = C_3 = 750 \text{ nF}$ ;  $L_0 = 54 \mu\text{H}$ .)



For the saturable inductors  $L_1$ ,  $L_2$ ,  $L_3$ , the material Metglas 2605 CO, produced by Allied Signal Inc. USA is used. This is a Fe-based amorphous alloy with 3.4 T maximum flux density swing. For the first two stages, the toroidal strip-wound magnetic cores are made from 23  $\mu\text{m}$  ribbon, with 4  $\mu\text{m}$  interlaminar insulation. The last magnetic switch will be made with 15  $\mu\text{m}$  ribbon, because of the necessity to have a greater value for the short pulse permeability.

The MPCC compression ratio (or "gain") is given by:

$$G = (I_{\text{load max}}) / (2 I_{\text{primary switch max}}).$$

For the minimizing of the total mass of the magnetic material (200 \$/kg),  $G$  must be as low as possible. From this reason, two parallel coupled thyratrons have been considered as the primary switch. In this way  $G = 25$  and the necessary magnetic mass has been reduced from 77 kg (the case of one thyatron as the primary switch) down to 34 kg.

**TABLE 1**

The main parameters of the saturable inductors in 200 J/pulse MPCC

		$L_1$	$L_2$	$L_3$
Inner Diameter	[mm]	110	110	64
Outer Diameter	[mm]	160	160	93
Height	[mm]	141	141	400
Turns Number		20	6	1
Magnetic Losses / Pulse	[J/pulse]	1.2	1.8	3.1
Dissipated Power at 100 Hz	[W]	120	180	310

The main parameters of the saturable inductors are given in Table 1. The maximum allowed average current of the thyratrons (1 A) limits the pulse repetition frequency at 100 Hz. Thus the average output power is 20 kW.

### Conclusions

The magnetic pulse compression is the only method to drive the repetitive plasma focus devices.

A 20 J/pulse MPCC was used to drive a low pressure spark discharge. The influence of the electrode geometry and polarity on the discharge onset was studied. The best results (2.5 mPa, 4.5 kA) were obtained by using the flat-end rod inner electrode as a cathode.

A second, 200 J/pulse MPCC was designed for driving a plasma-focus soft-X-ray source, for X-ray micro-lithography as the main application. The saturable inductors are made from toroidal strip wound cores with METGLAS 2605 CO as the magnetic material (total mass: 34 kg.). The thyratrons limit the pulse repetition rate at 100 Hz.

### References

- [1] Johnson, D. L., et al., "Results of Initial Testing of the Four Stage RHEPP Accelerator", Proc. IX-th IEEE International Pulsed Power Conference, Albuquerque, NM, USA, 1993, pp. 437 - 440.
- [2] Georgescu, N., Zoita, V., "An Experimental Model of a Magnetic Pulse Compression Driver for a Plasma Focus X-Ray Source", Romanian Journal of Physics, 40, 1, 1995, pp. 17 - 24.
- [3] Presura, R., Georgescu, N., Cengher, M., Zoita, V., "Vacuum Discharge Driven by a Magnetic Pulse Compression Circuit", Proc. XVII-th International Symposium on Discharges and Electrical Insulation in Vacuum, Berkeley, CA, USA, 1996, paper 01C10.

# SOFT X-RAY SPECTROSCOPIC INVESTIGATION OF A PLASMA FOCUS OPERATED IN PURE NEON

R. Presura, V. Zoita, I. Paraschiv

*Institute of Physics and Technology of Radiation Devices,  
Plasma Physics and Nuclear Fusion Laboratory  
P.O. Box 5206, Magurele, R-76900, Bucharest, ROMANIA*

## Abstract

The soft X-ray emission of the medium-energy plasma focus device IPF-2/20 operated in pure neon was studied with spectral resolution. The spectra of H- and He-like Ne ions were recorded by means of a de Broglie spectrograph for initial filling pressures in the range  $1.3 \div 7$  torr. Both the soft X-ray emission characteristics and the plasma parameters are strongly dependent on the working gas pressure. The intensity of the He-like neon ions lines increases when the working gas pressure is raised, while for the H-like ions it has a maximum for about 5 torr filling. The electron density has values of the order of  $10^{20} \text{ cm}^{-3}$ . The electron temperature ranges between 300 and 350 eV. Both the plasma density and the plasma temperature decrease when the initial gas pressure is increased.

## Introduction

The spectral characteristics of the soft X-rays emitted by plasma focus discharges in pure Ne have been studied having in view both plasma diagnostics and atomic physics [1], and applications of the plasma focus as X-ray source [2].

The use of a plasma focus as soft X-ray source for a given application requires simple means of monitoring the X-ray emission spectrum. On the other hand, to optimise the operation of a plasma source, spectroscopic diagnostic is necessary for establishing relationships between the emission parameters and the functional parameters of the device. The plasma focus proved to be appropriate as X-ray source for microlithography, when operated in neon, since the H- and He-like Ne ions emission lines cover the spectral range 0.9 up to 1.4 nm, and the H-like ions radiative recombination continuum is very intense below 1 nm.

In this paper, a convex curved crystal spectrograph is used to record the highly-stripped Ne ions spectra produced by discharges in the IPF-2/20 plasma focus device. The aim of the investigation is to characterise the emission of the soft X-ray plasma source.

## Experimental set-up

The measurements were performed on the medium-energy plasma focus device IPF-2/20 [3]. In these experiments the energy stored in the capacitor bank was 10 kJ for 16 kV charging voltage. The maximum value of the current reaches 400 kA and the current rise time is 3.5  $\mu\text{s}$ . Pure Ne was employed as working gas, in a pressure range from 1.3 to 7 torr.

The spectroscopic measurements were performed by means of a de Broglie configuration [4] spectrograph [5] which is the most appropriate to record a wide spectral range while keeping high resolving power and sensitivity. For the spectral range mentioned, a

mica crystal {002} with the lattice spacing  $d \approx 0.99$  nm was chosen. The geometric parameters of the device were calculated using a ray-tracing code [6] to optimally satisfy the spectral and geometrical requirements of the experiments. For a 600 mm source-to-crystal distance, the following values resulted: the crystal curvature radius  $r_c = 70$  mm, the curvature radius of the film  $r_f = 120$  mm, and the size of the entrance aperture in the diffraction plane  $d_a \approx 20$  mm. The spectrograph was placed to view the source in radial direction (Fig. 1). For these values, the useful spectral range of the spectrograph is approximately  $0.1 \div 1.6$  nm. The functional parameters of the device, corresponding to these geometric parameters were: the inverse linear dispersion  $d\lambda / d\theta \approx 0.008$  nm / mm, and the resolving power  $\lambda / \Delta\lambda \approx 500 \div 1000$  for a source of 1 mm size in the diffraction plane. The resolving power is strongly limited by the source size since the spectrograph produces line broadening proportional with this parameter. On the other hand, this effect can be used to estimate the source size from the line widths, when this is the major broadening mechanism. The entrance aperture of the spectrograph was covered with an Al foil 9  $\mu$ m thick. The spectra were recorded on Kodak DEF (Direct Exposure Film) [7].

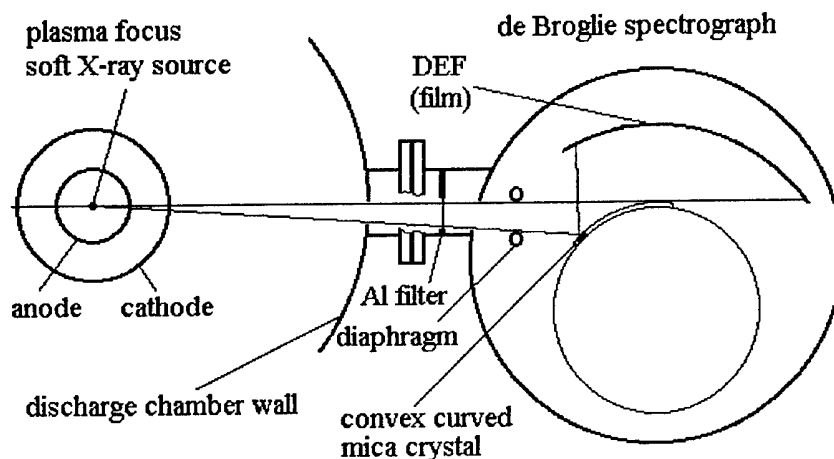


Fig. 1. The convex curved crystal spectrograph (de Broglie geometry). The connection to the plasma focus discharge chamber is indicated

The sensitivity of the spectrograph is high enough to allow for single-shot spectra recording in the conditions of the intense X-ray emission of the plasma focus. In certain cases, the spectra arising from more shots were recorded on the same film to increase the signal-to-noise ratio. The integration over more shots allows one also to study the reproducibility of the emission from the point of view of both the spectral intensity, and the source position and size. All records presented are time-integrated over 5 plasma focus discharges performed in the same initial conditions. As mentioned, the main limitation of the de Broglie spectrograph resolving power is due to the dimension of the X-ray source. Although the plasma focus device operated reproducibly, the small variations in the source position from one shot to another led to additional broadening of the spectral lines.

The X-ray emission rate in the spectral range 0.03 to 0.4 nm was measured with a surface barrier detector positioned at  $90^\circ$  with respect to the plasma focus axis. The discharge current was monitored by means of a Rogowski belt mounted in the collector of the device.

## Experimental results

The plasma focus device functioned well and reproducible for each value of the pressure from the point of view of both sheath and pinch formation, and soft X-ray emission. However, the filling pressure strongly influences the discharge dynamics, as shown both by the discharge current and the X-ray emission rate signals. The timing of the pinch phase is significantly delayed with respect to the peak value of the current as the pressure is increased. The surface barrier detector signals show that the X-rays are emitted in more bursts of about 100 ns duration. The total duration of the emission decreases from approximately 900 ns for 1.3 torr to about 300 ns for 7 torr discharges. The amplitude of the signals decreases by a factor of two when increasing the pressure.

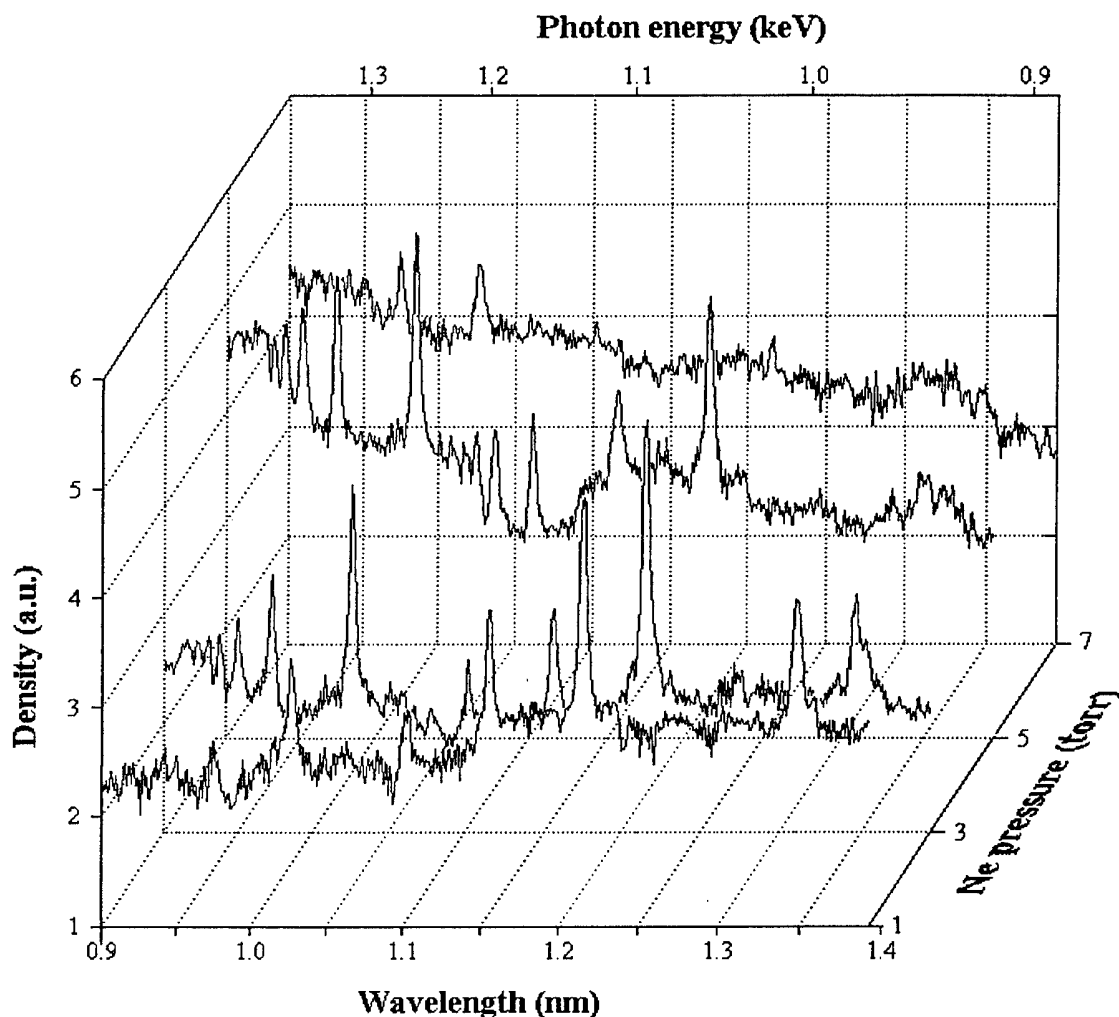


Fig. 2. The dependence of the highly-ionised Ne spectra on the initial filling pressure

Typical spectra of the highly-stripped Ne ions are presented in Fig. 2. Besides the changes in the discharge dynamics, the appearance of the spectra depends on the pressure due to the absorption in the working gas on the ray paths from the source to the detector. This effect is stronger at longer wavelengths.

The main features evidenced in the soft X-ray emission spectra (Fig. 2) of the Ne pinch plasma are, for all working pressures, several members of the principal series of the H- and He-like Ne ions and the recombination continuum. A blend of satellites to the resonance line of the H-like Ne ions and the intercombination line of the He-like ions can be, generally, observed in the spectra. The lines were identified using the ray-tracing code [6] and by comparison with published data [1, 8]. The resonance lines are affected by self-absorption due to plasma optical thickness for all initial Ne pressures. The line intensity for the He-like neon ions increases when the working gas pressure is raised, while for the H-like ions it has a maximum for 5.3 torr filling. The intensity of the intercombination line relative to the He-like ions resonance line increases with the pressure. The radiative recombination continuum spectrum is well featured in the case of 5.3 torr neon discharges.

An analysis of the spectra allows one to determine the parameters of the emitting pinch. Due to the space- and time- integration, the resulting values are averaged over the source size, emission duration, and emission fluctuations from discharge to discharge.

An estimation of the plasma density on the basis of the Inglis-Teller relationship [9] gives values of the order of  $10^{20} \text{ cm}^{-3}$ . When the working gas pressure increases the electron density decreases, as suggested by the increase of the quantum number of the last visible member in the principal series, by the increase of the intensity ratio of the intercombination to the resonance lines of the He-like Ne ions, and by the decrease in the effect of self-absorption.

The fact that the intensities of the H-like Ne ions lines are comparable or stronger than those of the He-like Ne ions lines indicates a relatively higher population of the H-like ionisation stage, pointing to electron temperatures higher than  $300 \div 350 \text{ eV}$  [9]. The shift of the maximum of the continuum emission towards longer wavelengths and the increase of the intensity ratio of the He-like to H-like Ne ions resonance lines indicate that the plasma temperature decreases too when the initial Ne pressure is increased.

The observed trends of the plasma density and temperature can be correlated with the decreasing signals of the surface barrier detector and can be justified by the fact that the delay between the current maximum and pinch formation moments increases when the heavy gas pressure increases.

## Conclusions

The IPF-2/20 plasma focus device operated in pure neon emits intense H- and He-like ions line and continuum spectra. The plasma parameters were estimated from the spectral records. When increasing the working gas pressure, the spectral elements change in relative intensity, and both the plasma density and temperature show a lowering tendency. These observations are correlated with the delayed pinch formation, characteristic for higher filling pressures.

- [1] Peacock, N.J., Spear, R.J., and Hobby, M.G., *J. Phys. B: Atom. Molec. Phys.*, **2** (1969) 798
- [2] Neff, W., Eberle, J., Holz, R., Lebert, R., and Richter, F., *Proc. SPIE*, **1140** (1989) 13
- [3] Cebanu, A., et al., *Plasma Phys. Contr. Nuclear Fusion Res.*, IAEA, Vienna, Vol. II, (1981) 197
- [4] Birks, L.S., *Rev. Sci. Instrum.*, **41** (1970) 1129
- [5] Presura, R., Paraschiv, I., Zoita, V., to appear in *Rom. Rep. Phys.* (1996)
- [6] Presura, R., *Proc. IX-th Conf. Plasma Physics and Applications*, Bucharest, (1996) - in preparation
- [7] Henke, B.L., Uejio, J.Y., Stone, G.F., Dittmore, C.H., Fujiwara, F.G., *J. Opt. Soc. Am. B*, **3** (1986) 1540
- [8] Kelly, R.L., *J. Phys. Chem. Ref. Data* **16**, suppl. 1, (1987) 1
- [9] Griem, H.R., *Plasma Spectroscopy*, McGraw-Hill, New York (1964)

# WORKING GAS EFFECTS ON THE X-RAY EMISSION OF A PLASMA FOCUS DEVICE

M.Cengher, R.Presura, V.Zoita

*Institute of Physics and Technology of Radiation Devices,  
P.O. Box 5206, Magurele, Bucharest, R-76900, ROMANIA*

## ABSTRACT

Experiments on the plasma focus device IPF-2/20 operating with argon, neon and mixtures of argon with deuterium were performed and some X-ray emission parameters measured. The time evolution of the X-ray emission and dependence of the X-ray yield on the working gas composition was analyzed. The softer X radiation was measured with time resolution in the energy bands from 4 to 40 keV, and the hard X-rays for energies above 200 keV. In deuterium-argon mixtures the soft X-ray yield increases both with pressure (for the same ratio of argon) and with the quantity of argon added to deuterium at the same total pressure. For argon or neon the hard X-ray yield is lower than for deuterium-heavy gas mixtures. The softer X-ray yield decreases with pressure both for neon and for argon.

## 1. Introduction

The plasma focus device is a source of intense electromagnetic radiation in a wide range of energies, including the X-ray region of spectrum. Experimental studies (as [1][2][3][4]) were made on the subject of X-ray emission when working in pure gases ( $N_2$ , Ne, Ar) and in gas mixtures.

The main goal of the investigations presented in this paper is to study the temporal evolution of the X-ray signals to compare the softer X-ray yield for deuterium-argon mixtures and for pure argon and neon and to reduce the hard component of the plasma focus X-ray emission. The argon ratios in mixtures was from 2.0 to 6.1% by volume, static filling regime. The gas mixture total pressure was in the range 2.4 torr to 6.5 torr. The pure argon pressure was 2.0 - 3.1 torr and the neon pressure ranged from 1.3 to 7 torr.

## 2. Experimental set-up

The experiments have been performed on the IPF-2/20 plasma focus device, whose capacitor bank is 80  $\mu$ F and was operated at 16 kV (10.25 kJ stored bank energy). The working

gases were Ar, and Ar-D<sub>2</sub> mixtures with Ar proportions from 2.0 to 6.1% by volume, static filling regime. The gas mixture total pressure was in the range 2.4 torr to 6.5 torr. The pure argon pressure was 2.0 - 3.1 torr and the neon pressure ranged from 1.3 to 7 torr.

The diagnostics used were: magnetic probe for current derivative, Rogowski belt for (integrated) current, PIN diode and surface barrier detector (SBD) for the softer X-ray emission rate, photomultiplier and scintillator detector for hard X-ray and neutron emission rates. Each of the semiconductor X-ray detectors was positioned side-on; was used in combination with a 25 µm thick Al filter, and the sensitivity was over 1% of the maximum in the spectral range from 4 keV to 40 keV as it resulted from the SBD [5] sensitivity curve. The time response of SBD was found to be is similar with that of the PIN diode.

The scintillator-photomultiplier is positioned end-on, outside the discharge chamber, at about 15° with respect to the electrode axis. The lower energy limit of the the radiation arriving at the scintillator-photomultiplier is 200 keV and is defined by the 2cm thick steel wall of the discharge chamber.

### 3. Experimental results

The typical time evolution in the softer X-ray range can be observed in fig. 1 where is presented the SBD signal for two different discharges at total pressure 5.9 torr and Ar volumetric ratio 2.3% . The reproducibility of the time evolution of the signal is rather low. The first discharge in fig.2 has two main periods of emission separated by 50 ns, each of them presenting in turn several peaks. The total duration of emission is 250 ns. The second discharge has only one period of emission with four peaks and the duration of emission is 150ns.

As a rule, comparing several sets of discharges at different pressures and gas compositions, there are one or two main periods of emission the total duration being from 150 to 600 ns depending on the gas conditions. The first period lasts for about 100 ns and features several (two or three) shorter pulses. The second period of emission (if it exists) is separated from the first one by a time interval of about 50 ns. The second period lasts for about 100-150 ns. The duration of emission averaged on a several discharges increases slowly with the pressure as well as with the ratio of Ar.

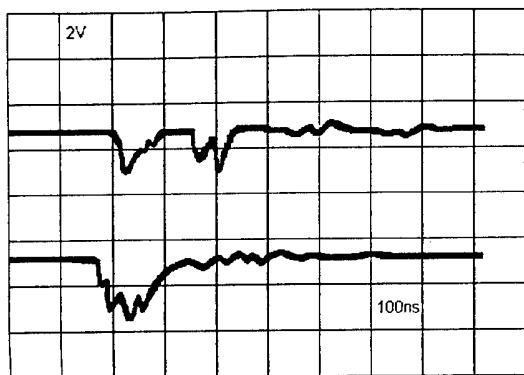


**Fig.1 :** Time evolution of the softer X-ray emission obtained with SBD at volumetric ratio of Ar 2.3% at a total Ar-D<sub>2</sub> mixture pressure of 5.9 torr.

The time scale is 100 ns/division and the amplitude is 2V per division.

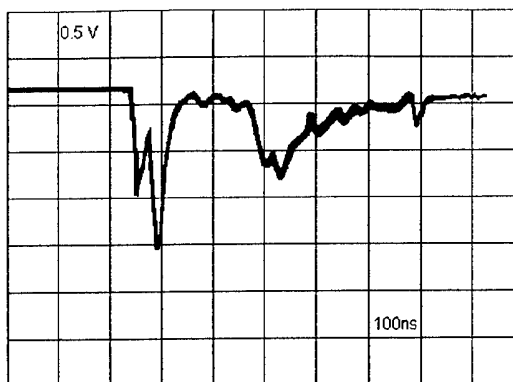


**Fig.2 :** The hard X-ray signal corresponding to a volumetric ratio of Ar 2.3% at a total Ar-D<sub>2</sub> mixture pressure of 5.9 torr.

The time scale is 100 ns/division and the amplitude is 0.5V per division.

The hard X-ray signal for the D<sub>2</sub>-Ar mixtures presents a much shorter period of emission than the softer X-ray signal of the same discharge and has one or two peaks. The first peak presents a fast rise, and is often coincident in time with the second peak of the first period of the softer X-ray signal. A typical scintillator-photomultiplier signal corresponding to the second discharge of fig. 1 is

shown in fig. 2: two narrow hard X-ray peaks of 100 ns duration are followed after 100 ns by a signal at the moment of the arrival of the neutrons at the detector.

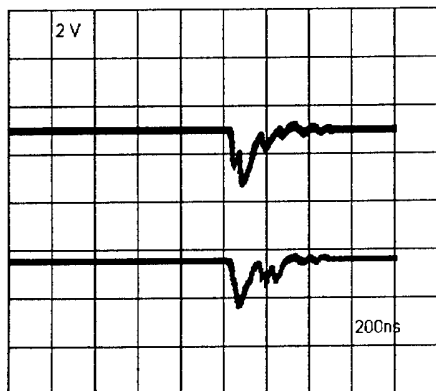


**Fig.3 :** The softer X-ray signal obtained with SBD when working in pure Ar at a 2.4 torr

The time scale is 200 ns/division and the amplitude is 2V per division.

An analyze of the hard X-ray signals for different ratios of Ar in the D<sub>2</sub>-Ar mixture was made and it was found that the signal amplitude is decreasing with the increasing ratio of argon. When working in pure Ar at a 2.4 torr pressure the hard X-ray signal is even smaller than for mixtures.

The time evolution of the softer X-ray signal in pure argon presents only one main



period featuring several (2-4) peaks of emission with duration of 200-600 ns as can be seen in fig.3 where the Ar pressure is 2.4 torr. The duration of emission decreases with pressure. The ratio of softer X-ray yield to hard X-ray yield was also found to decrease with pressure in argon.

The time evolution of the softer X-ray signal in pure neon is similar with that of pure argon, presenting one period of emission of about 300 ns, featuring several peaks.

In fig. 4 is presented the variation with the total pressure of the time integrated energy emitted in the 4-40keV energy range for argon (rhombic points), neon(triangles) and deuterium-argon mixture with 3% argon (round points). The emitted energy decreases in pure argon and in pure neon with the increasing pressure. For a mixture of deuterium and argon with 3% volumetric ratio of argon, the softer X-ray yield has a different behaviour: is increasing slowly with the total pressure.

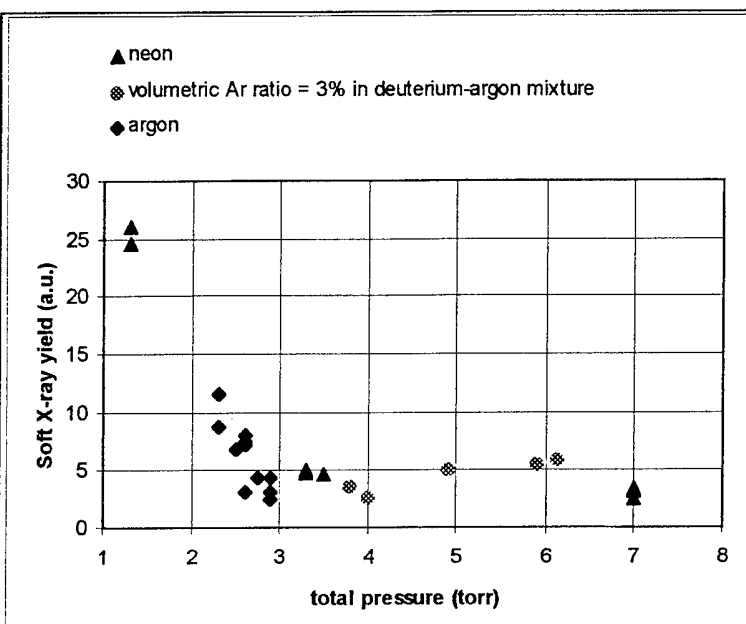


**Fig.4** : The softer X-ray yield dependence with the total pressure in argon (rhombic points), neon(triangles) and deuterium-argon mixture with 3% argon (round points)

#### 4. Conclusions

For a D<sub>2</sub>-Ar mixture with small volumetric proportions of Ar the softer X-ray yield increases with the quantity of added heavier gas and with the total pressure at a constant ratio of argon. The ratio of soft to hard X-ray yield increases with pressure, too. For the use of pure argon or neon as working gas the softer X-ray yield decreases with the increasing pressure.

#### References

1. W. Neff, J. Eberle, R. Holz et.al., SPIE, vol.1140, *X-Ray Instrumentation*, (1989)13
2. Y. Kato, S.H. Be, *Appl.Phys.Lett.*, **48** 11 (1986) 686
3. Y. Kato, I. Ochiai, Y. Watanabe, S. Murayama, *J.Vac.Sci.Technol.*, **B6** (1988) 195
4. R. Lebert, R. Holz, D. Rothweiler, et.al., *X-Ray Microscopy III*, Springer, 1990
5. N.Bogatu, D.Falie et.al., Internal Report LOP-53-1985, Central Institute of Physics, Bucharest, 1985

## PSEUDOSPARK SWITCHES (PSS) FOR PULSED POWER APPLICATIONS

F. Heine, U. Prucker, K. Frank, A. Görtler, A. Schwandner, R. Tkotz, D.H.H. Hoffmann  
and J. Christiansen

*Physics Department I, University of Erlangen, Erwin-Rommel-Str. 1, Erlangen, D-91058, Germany*  
Funded by the BMBF, Germany

### ABSTRACT

Basing on the pseudospark discharge, a low pressure gas discharge in a special geometry, fast closing switches for different pulsed power applications have been designed. Medium power PSS ( $\leq 30$  kA peak current) were used in laser circuits whereas high current PSS are tested successfully in high current pulsed power applications ( $\leq 200$  kA). For currents of a few kA the discharge is supported by cathode spots on the cold cathode surface. For higher currents anode activity is observed too. Inserting semiconductor material seems not only to suppress high erosive spot formation but support diffuse large-area electrode emission. A different approach to solve the problem of lowering the erosion rate is the multichannel PSS (MUPS). In order to distribute the discharge current to more than one single channel three or more discharge channels are radial or coaxial arranged. With regard to high voltage applications the maximum hold-off voltage was increased by adding an intermediate electrode.

### INTRODUCTION

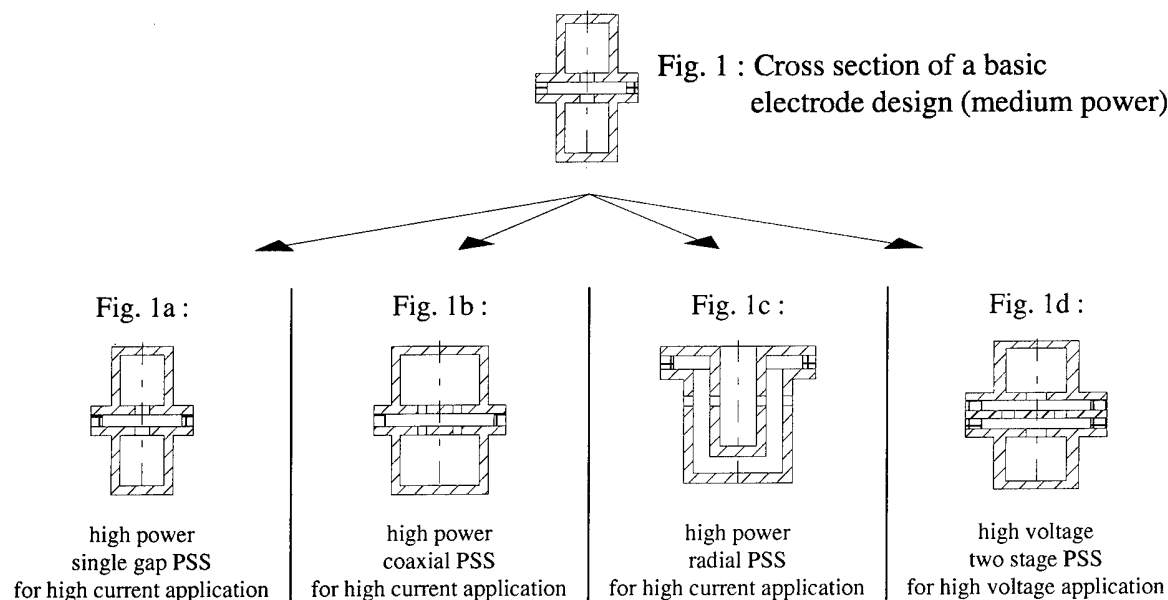
The pseudospark discharge is a low pressure gas discharge on the left hand side of a breakdown characteristic comparable to the paschen curve [1]. The pseudospark is based on a special geometry shown in figure 1. In this basic set-up electrodes with a central aperture are separated a few millimetres by an insulator. The back of the electrodes are arranged as hollow electrodes. The PSS can be run in the self breakdown or triggered mode. In the last one the discharge is initiated by the injection of electrons into the hollow cathode due to a surface flashover [2] or a pulsed glow discharge behind the hollow cathode [3], but also other trigger methods like ferroelectric trigger [4] or triggering with an UV-light pulse [5] are used. The reliable trigger ability with a low jitter, the fast current rise up to  $10^{12}$  A/s and the 100% current reversal led to the application as high power switch. Different discharge modes must be distinguished during the discharge development [6]. In the selfbreakdown mode the discharge starts as a Townsend-discharge on the axis of the discharge chamber. With increasing current a positive space charge builds up near the cathode bore hole which leads to field enhancement in the hollow cathode. At a critical positive space charge density the breakdown of the hollow cathode is initiated. In the triggered mode the critical space charge density develops due to the trigger discharge. As soon as the hollow cathode discharge breaks down the voltage over the gap drops for a first time and the current rises up to several hundreds of ampere. After this phase a further drop of the anode voltage can be observed depending on the discharge parameters. In this phase the discharge is located at the inside of the cathode bore hole. The mechanism of this mode is still under discussion [7,8]. After this the discharge turns to the high current mode correlated with a further decrease of the voltage

drop due to the appearance of cathode spots around the central aperture. Now the electron emission process has changed to field-enhanced thermionic emission. The discharge seems to be homogeneously distributed around the bore hole for peak currents of a few kA and microsecond pulses. For greater currents the discharge constricts and is located on the plane electrode surface. Anode activity can be observed for currents above 50 kA using molybdenum electrodes [9]. A real anode spot builds up on Mo-electrodes at 90 kA, correlated with the strong deposition of anode material on the cathode surface and a kink in the current voltage characteristic [9,10]. The temporal development of the discharge is strongly dependent on the external parameters of the electrical circuit. For instance not all discharge phases mentioned above are detectable for a fast current rise and high switching voltage.

### PSS DEVELOPMENT AT ERLANGEN PHYSICS DEPARTMENT

In recent years at Erlangen university multiple PSS have also been developed as sealed off systems in metal ceramic technology and an integrated hydrogen reservoir. They are used for medium power applications as pulsed gas lasers and are for some little time under investigation for high power devices i.e. power modulators driving high energy accelerators, recycling facilities using EMP and EMP generators. According to the corresponding pulsed power application the electrode design varies. Fig. 1 shows the used basic electrode design. The usual working gas pressure is in-between 10 and 50 Pa for hydrogen, deuterium or helium. Electrodes can be cooled by oil or demineralized water. Shielding structures protect the alumina insulator against metal vapour.

The principal goal of the development consists in constructing long-life low-pressure high power switches which can replace ignitrons and spark gaps in a certain power range.



For electric circuits with hold-off voltages up to 30 kV the *one-gap/one-channel PSS* (Fig. 1) dominate. These *medium power PSS* (<30 kA) are mainly used for fast circuits with a short pulse duration (some 100 ns) and a high requirement in trigger delay (200 ns) and jitter time (< 5 ns), i.e. excimer lasers and pulsed CO<sub>2</sub> lasers.

For peak currents in the range of 30 - 120 kA and for pulse lengths of some  $\mu$ s the *high power PSS* were developed. With regard to the pulse length and the maximum peak current the

number and the arrangement of the electrode holes differ. Besides a special one channel high power basic design shown in fig. 1a (similar to basic design) also *multichannel PSS* exist up to now only in two basic forms. The radial and the coaxial type are shown in Fig. 1b and 1c. The symmetrical arrangement and the simultaneous ignition of the channels provide a reduced erosion and a higher life time. In order to safely operate at a low erosion rate the peak current per channel should not exceed 45 kA. Multichannel PSS show excellent performance not only in high current applications. For a further decrease of the erosion rate, semiconductor electrodes such as SiC are now in use [11].

To increase the hold-off voltage of the switch, *multigap PSS* (Fig. 1d) with plane electrodes have been tested successfully. Two or three stages nearly double or triple the hold-off voltage.

### **MEDIUM POWER PSS**

Sealed off versions of medium power switches have already been tested in many industrial applications, mainly in power supply circuits for lasers. A lifetime test of a sealed off system was performed under conditions typical for excimer lasers (anode voltage 22 kV, anode current 9.1 kA, reverse current 10%, charge transfer per pulse 1.69 mC, halfwave duration 100 ns). The switch was still working at the end of the test with an obtained lifetime of 129 million discharges (total charge transfer 220 kC) [10]. Furthermore parallel operation in a gas laser power supply of two switches was performed successfully with an output gain of 20% instead the use of common thyratrons [10].

### **HIGH CURRENT PSS**

#### **One-channel/one-gap PSS**

This switch is developed for currents up to 100 kA and hold off voltages up to 30 kV. The typical gap distance of this switch is 3 mm, the hole diameter and electrode thickness are 5 mm. The switch is triggered by a surface flashover arranged behind the hollow cathode. Life time tests with different electrode materials were performed [10]. The main erosion occurs around the bore hole. Depending on material and discharge parameters the bore hole widens up or narrows by molten material pushed into the hole. In the first case the hold-off voltage decreases because of a higher field penetration into the hollow cathode in the second case the trigger ability of the PSS is worse because of a lower field penetration into the hollow cathode.

The best results considering lifetime were obtained with high melting, high refractory materials like W. As mentioned above the discharge contracts to about 6mm in diameter and moves away from the bore hole onto the plane surface. To avoid this high erosive constricted arc mode semiconducting electrode materials are investigated. The central aperture and gap distance were 3 mm each. At the outer molybdenum electrodes the gap distance was 5 mm. In contrast to metal electrodes the discharge appears homogeneously distributed over the entire SiC-electrode surface [11]. No significant electrode erosion could be observed, neither at the bore hole nor on the plane SiC-electrode. The PSS provided with semiconducting electrodes suffer from a lower hold-off voltage in comparison to metal electrodes, because of a higher current emission at the triple point gas-metal-semiconductor.

#### **Multichannel PSS (MUPS)**

A different approach to lower the erosion rate is to divide up the total current to numerous channels. There are two basic designs to arrange the discharge channels in parallel: coaxial (fig. 1b) and radial (fig. 1c). Both systems are triggered with a pulsed glow discharge in the back of the hollow cathode [10,3]. The bore holes of the coaxial design are arranged on a

circle of 25 mm diameter in our latest experiments. Best results for a simultaneous triggering of all channels are achieved using a pulsed hollow cathode discharge in combination with a common hollow cathode for all channels. A jitter less than 5 ns is achieved. For microsecond pulses the plasma columns attract each other due to magnetic forces and pinch at the axis. So the coaxial MUPS isn't well suited for high current application and plus lengths longer than the pinchtime, because pinching causes greater electrode erosion.

In the case of the radial MUPS best results are achieved with three channels with a gap distance and a hole diameter of 3 mm and an electrode thickness of 4 mm. The hollow cathode has an inner diameter of 30 mm and is common for all channels. Equal to the coaxial design the plasma columns start moving due to magnetic forces and are pinching on the bottom of the electrodes for pulses longer than the pinch-time. For pulses of a few microseconds pinching can be avoided by increasing the length of the electrodes. A lifetime test of the 3-channel device was provided with a charge transfer of 3.6 C per shot. The test was stopped after 25000 discharges. The main erosions occurs at the bottom of the electrodes, where the discharge channels pinch. The electrode bore hole erosion was negligible. To avoid high erosion at the bottom of the switch Sic-electrodes are inserted at the bottom. A performance test in a plasma accelerator with a peak current of 500 kA resulted in nearly no erosion on the SiC surface. A long term test with this electrode design showed no considerable electrode erosion at the bottom.

### HIGH VOLTAGE PSS

These multiple stage switches were developed in order to handle applications with high applied voltages (up to 60 kV) and medium connected currents ( $< 20$  kA), i.e. waste gas detoxification. Present problems in the reliable trigger behaviour should be solved in the near future [10]. Different designs with an intermediate electrode or two or more separated gaps were tested. Also high current versions ( $\leq 120$  kA) are still under investigation, but up to now they are limited in the maximum hold-off voltage ( $\leq 45$  kV) [12].

### OUTLOOK

Besides the systems described above now also less power designs are under construction in order to switch applied voltages in-between 500 V and 20 kV. It could be driven alternatively by positive or negative applied voltages. Furthermore a new *high power concept* with a lifetime of  $10^6$  is to be tested, to make switching possible for hold-off voltages up to 40 kV and peak currents in the range of 200 kA.

### REFERENCES

- [1] J. Christiansen, C. Schultheiß, Z. Phys., vol. A 290, pp. 35-41, 1977.
- [2] A. Görtler, et al., IEEE Trans. Plasma Sci., vol. 17, pp. 762-765, 1989.
- [3] T. Mehr, et al., IEEE Trans. Plasma Sci., vol. 23, no. 3, pp. 324-329, 1995.
- [4] H. Gundel, et al., Appl. Phys. Lett., vol. 54, p.2071, 1989.
- [5] G. Kirkmann, et al., Appl. Phys. Lett., vol. 52, no. 8, pp. 613-615, 1988.
- [6] M. Stetter, et al., IEEE Trans. Plasma Sci., vol. 23, no. 3, pp. 283-293, 1995.
- [7] T. Mehr, et al., J.Appl. Phys. 79 (2), 15 Jan. 1996.
- [8] M. Stetter, et al., J.Appl. Phys. 79 (2), 15 Jan. 1996.
- [9] U. Prucker, et al., Proc. XVII ISDEIV, Berkley, July 21-26, 1996.
- [10] R. Tkotz, et al., IEEE Trans. Plasma Sci., vol. 23, no. 3, pp. 309-317, 1995.
- [11] A. Schwandner, et al., Proc. XVII ISDEIV, Berkley, July 21-26, 1996.
- [12] A. Görtler, A. Schwandner et al., IEEE Trans. Plasma Sci., vol. 42, no.10, 1995.

# NANOSECOND BREAKDOWN OF LIQUID DIELECTRICS

J. Mankowski, M. Kristiansen, and L. Hatfield

*Texas Tech University  
Pulsed Power Laboratory  
Department of Electrical Engineering  
Lubbock, TX 79409-3102, USA*

## ABSTRACT

Breakdown characteristics of various liquids are investigated. Electric field strengths recorded are over 4 MV/cm and at breakdown times ranging from 1 to 4 nanoseconds. Liquids examined are filtered and unfiltered transformer oil, castor oil, and freon 12.

## INTRODUCTION

Ultrawideband radiation source designs are continually being improved to produce shorter pulses (hundreds of picoseconds) at higher voltages (megavolts). Empirical data on breakdown of high pressure gases and liquids at these short time lengths and high electric field strengths are limited. In this paper, experimental results of the breakdown characteristics of several liquid dielectrics are presented. These liquids are filtered and unfiltered transformer oil, castor oil, and freon-12. Electric field strengths attained are over 4 MV/cm. Breakdown times recorded are 1 to 4 nanoseconds. By varying gap distance, a relation between electric field strength and time to breakdown can be determined.

## EXPERIMENTAL SETUP

The voltage source used for this experiment is the Russian-built, SEF303A pulser. This source produces a 250 kV, 1 ns risetime, 4 ns wide, negative pulse into a matched load. A schematic of the experimental setup including the pulser and a typical output voltage waveform are shown in Figures 1 and 2, respectively. The voltage pulse is created from a Tesla coil through a Blumlein generator into a 45 ohm output.

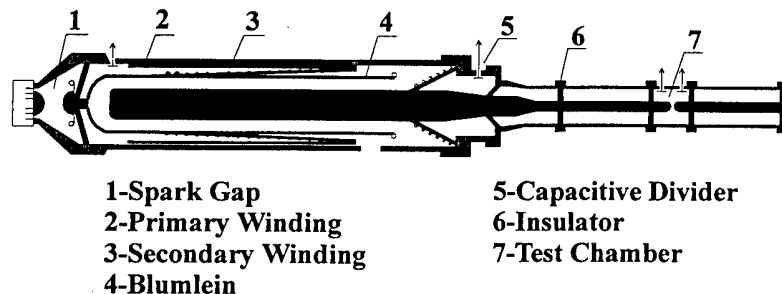


Figure 1. The SEF 303A pulser.

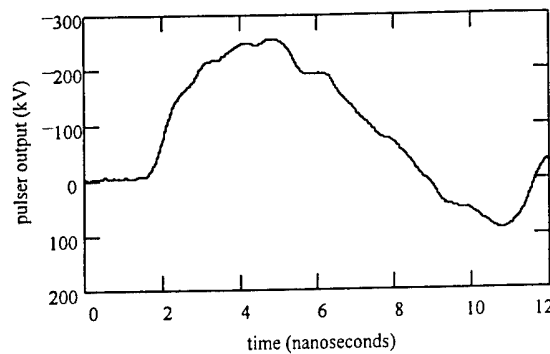


Figure 2. Typical output voltage of the SEF 303A pulser into a 45 ohm load

The coaxial lines before and after the test chamber are each 45 ohm. The reason for the lines before and after the test chamber is to delay the return of the reflected pulse to the gap. The lines are made long enough so that events in the gap will have been recorded before the reflections return. Physical dimensions of the load lines are 1 m long, 7.9 cm outer diameter, and 2 cm inner conductor diameter. The test chamber itself is 20 cm long and rated to contain pressures at over 2000 psi. The transformer oil is filtered to remove down to 1 micron particles. Inside the chamber are two, 1 cm radius, hemispherical, polished brass electrodes.

Also located inside the test chamber are the capacitive dividers. The dividers may also be considered self-integrating D-dot probes. The capacitance of the divider is chosen to provide the necessary attenuation of the pulse and large enough to drive the 50 ohm load of the cable. The divider is composed of a 2.4 cm by 10.1 cm strip of deposited aluminum foil on top of 25 micron thick kapton. The transit time along the divider is significantly shorter than the duration of the pulse to be measured.

Each of the dividers is directly above one of the electrodes. By recording the voltage from each divider during a single shot, the potential difference across the gap during breakdown can be recorded. From the dividers, the voltage signal is carried by 24 GHz bandwidth cable through 18 GHz bandwidth attenuators to a Tektronix SCD-5000 transient digitizer.

The exact attenuation of the dividers is calculated by use of a calibration pulse from a Spire line pulser. This pulser is capable of delivering a 1 kV amplitude pulse with a 0.8 nanosecond risetime. This pulse was also used to determine the transfer function of the entire system in order to compensate for any distortions of the pulse. However, it was deemed unnecessary to apply the software compensation due to the relatively high bandwidth of the system and good response of the probes.

## EXPERIMENTAL RESULTS

Liquids examined are filtered and unfiltered transformer oil, castor oil, and freon-12. The oils were pressurized to 500 psi to minimize possible effects due to air bubbles. The freon-12 pressure was approximately 120 psi. A typical breakdown waveform at each electrode is shown in Figure 3. This shot was taken with castor oil at 500 psi and a gap spacing of 1.14 mm. The first coaxial line before breakdown is an open circuit therefore, voltage doubling occurs. During the time it takes for breakdown to occur, the line after the gap is being charged capacitively from the first line across the gap. It is the difference between these two voltages that is used to calculate the time average electric field and peak electric field across the gap before breakdown occurs.

Several plots are presented for each of the liquids. Figure 4 shows the relation between time average electric field strength and time to breakdown.

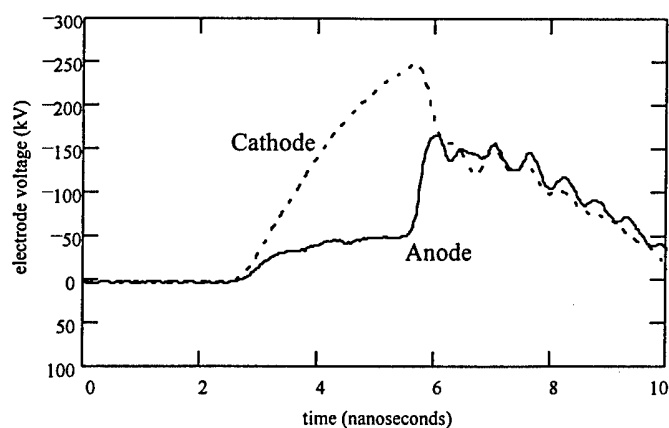


Figure 3. Voltage waveforms at the cathode and anode for Castor oil at 500 psi and 1.11 mm gap spacing.

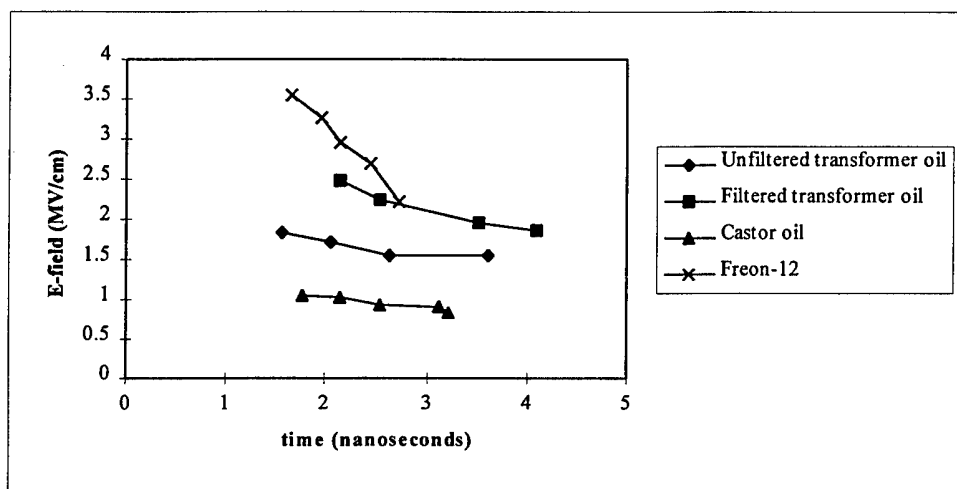


Figure 4. Time average E-field vs time to breakdown for various liquid dielectrics.

Note from Figure 4 that as the applied electric field is decreased by increasing the gap distance the time to breakdown increases, which is to be expected. Freon seems to be more sensitive than the oils when the gap spacing is varied. Also note the higher breakdown strength of the filtered transformer oil compared to the unfiltered.

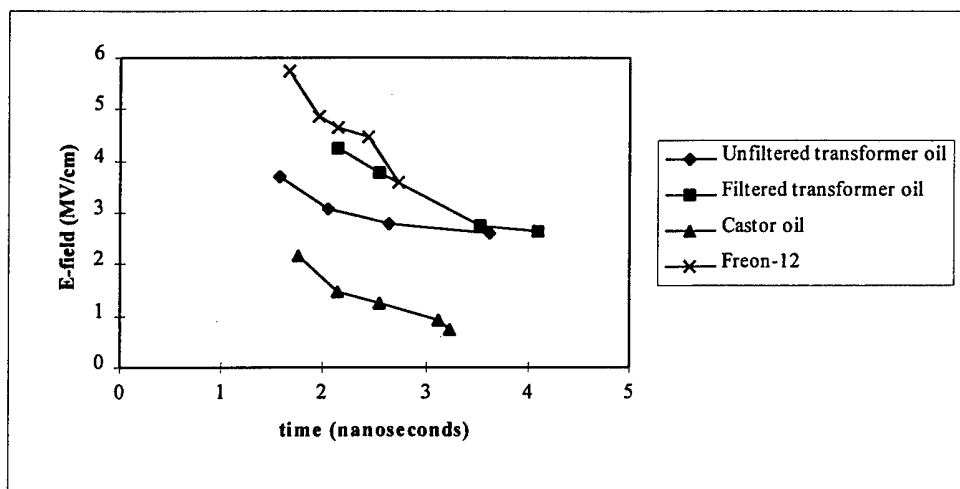


Figure 5. Peak E-field vs time to breakdown for various liquid dielectrics.



Figure 5 shows the relationship between peak electric field and time to breakdown. Vorobyov et al<sup>1</sup> have reported transformer oil electric field breakdown strengths of over 4 MV/cm at breakdown times of approximately 1 ns. These data appear to correspond well with their findings.

This work was supported by AFOSR/DOD MURI.

## REFERENCES

1. Vorobyov A.A., Ushakov V. Ya., and Bagin V.V., Electrical strength of liquid dielectrics at voltage pulses of a nanosecond duration, *Electrotechnika*, 1971

# The EMP Excitation of Radiation by the Pulsed Relativistic Electron Beam

V.A. Balakirev, G.L. Sidel'nikov

National Science Center "Kharkov Institute of Physics and Technology"

Academicheskaya St. 1, Kharkov, 310108, Ukraine

e-mail: kfti@rocket.kharkov.ua

**Abstract.** The mechanisms of the excitation of ultra-wideband electromagnetic pulses (EMP) by short pulses of high-current relativistic electron beams are proposed and investigated. It is shown that the transformation efficiency of the bunch kinetic energy to the excited energy of the EMP may be very significant.

## Introduction

By now, on the base of high-current relativistic electron beams (HCREB) the generators and amplifiers of various types (carcinotrons, magnetrons, gyrotrons, vircators and other) with a power level of  $(10^8-10^{10})$ W and a pulse duration of  $(10^{-8}-10^{-6})$ s were developed.

However, these high-power generators are intended for generation of narrow-band pulse signals, with pulse duration  $\tau_p$  significantly exceeding the period of high-frequency electromagnetic oscillations ( $\tau_p/T \gg 1$ ). These generators are not suitable for generation of powerful electromagnetic pulses (EMP), with  $\tau_p \lesssim T$ .

This is caused by a resonant character of the process of energetic exchange between electrons and those of excited electromagnetic field. Therefore, it is clear that for the effective EMP generation by high-current bunches it is necessary to use the non-resonant (impact) mechanism of radiation, for example, such, as spontaneous coherent transition radiation or bremsstrahlung radiation in the external magnetic field. Short electron bunches with a duration of  $(0.1-10)$ ns, an energy of  $(0.5-1)$ MeV and peak currents of  $(10-100)$ kA can be obtained either by transformation of the continuous electron bunches to a sequence of electron pulses (modulated beams) [1], or by direct HCREB generation of a short and ultra-short duration in high-current devices [2].

## 1. The transition radiation of EMP during the crossing of the conducting screen by the electron bunch

Consider model of a radiating device represented in Fig.1. From the drift chamber 1 through the foil 2 the electron bunch goes out in the free space. When the electron bunch crosses the conducting plane, including the foil 2 and the conducting screen 3, the EMP is formed. Consider the radius of the screen to be unlimitedly large to provide simplicity. Besides, we neglect by the change of the form pulsed current during its propagation.

In the far zone the pulse of electromagnetic radiation is described by the term [3]

$$H_\varphi = -\frac{2}{cR} I(t - R/c) \frac{\beta \sin \theta}{1 - \beta^2 \cos^2 \theta}, \quad (1)$$

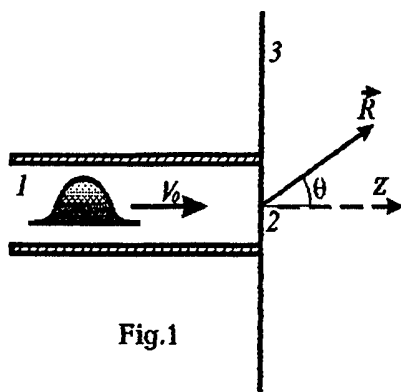


Fig.1

$\beta = V_0/c$ ,  $V_0$  is the speed of the beam,  $c$  is the speed of the light in vacuum,  $R$  is the distance between the coordinates origin and the observation point,  $\theta$  is the angle between the longitudinal axis of symmetry and the vector  $\vec{R}$ ,  $I(t)$  is the total current of the bunch,  $t$  is the time. Expression (1) is valid for the electron bunches of small cross size

$$r_b/ct_b\gamma \ll 1,$$

where  $r_b$  is the bunch radius,  $t_b$  it is duration,  $\gamma$  is the relativistic factor. This condition, as a rule, is satisfied.

Important conclusion follows from the expression (1), namely, that the radiation pulse precisely copies the current pulse, i.e. the beam antenna on the transition radiation has the wideband properties. The complete radiated energy may be calculated by the expression

$$W_{rad} = (1/c)F(\beta) \int_{-\infty}^{\infty} I^2(t) dt, \quad (2)$$

where

$$F(\beta) = \frac{1}{2(\gamma-1)} \left( \frac{1+\beta^2}{\beta} \ln \frac{1+\beta}{1-\beta} - 2 \right).$$

Let us determine the efficiency of the beam radiator as the ratio of the radiated energy (2) to the beam kinetic energy

$$\eta = W_{rad}/W_{kin}, \quad (3)$$

where  $W_{kin} = Qmc^2(\gamma-1)/e$ ,  $Q = \int_{-\infty}^{\infty} I(t) dt$  is the complete bunch charge,  $e$  is the charge of the electron. For the Gauss bunch  $I(t) = I_b \exp(-t^2/t_b^2)$  the efficiency of a beam radiator dictates by expression

$$\eta = \sqrt{2}F(\beta)I_b/I_A,$$

where  $I_b$  is the peak current of the bunch,  $I_A = mc^3/e = 17\text{kA}$ . For the electron beam with the maximum current 8kA and the energy 1MeV about 40% of the kinetic energy is transformed to the EMP energy.

## 2. Transition Excitation of EMP by a High Current Electron Beams in the Coaxial Line

The transformation of the energy of the relativistic electron beam to the EMP energy may be accomplished by the special device—converter. The possible schematic diagram of such device is represented in Fig.2. From drift chamber, made in the form of the circular

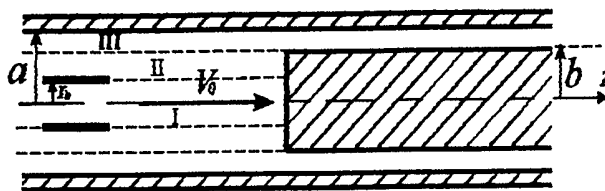


Fig.2

waveguide, the pulse electron bunch falls on the central cylindrical conductor, positioned coaxially with the waveguide. The TEM pulsed field excites, as the result of the transition radiation of the beam in the coaxial line. Let us consider the electron bunch of the tubular form

$$\vec{j} = -I_b \frac{\delta(r-r_b)}{2\pi r_b} T(t-z/V_0) \vec{e}_z, \quad (4)$$

where  $\vec{j}$  is a current density,  $\delta(r)$  is the delta-function. The function  $T(t)$  describes a longitudinal structure of the bunch. The bunch radius is less than the radius of the internal conductor. We calculate pulsed radiation by using the method of Hilbert boundary problem. Let us find the solution in the form of an integral on the longitudinal wave numbers of the cylindrical waves. In the domains I— $\{r < r_b, z < 0\}$ , II— $\{b > r > r_b, z < 0\}$  and III— $\{a > r > b, -\infty < z < \infty\}$  the amplitudes of the field may be written in the form

$$\begin{aligned} E_{z\omega}^I &= \int_{-\infty}^{\infty} e_1(k) J_0(vr) e^{ikz} dk, \\ H_{\varphi\omega}^I &= -ik_0 \int_{-\infty}^{\infty} v^{-1} e_1(k) J_1(vr) e^{ikz} dk, \\ E_{z\omega}^{II} &= \int_{-\infty}^{\infty} [e_2(k) J_0(vr) + e_3(k) \Delta_0(vr, vb)] e^{ikz} dk, \\ H_{\varphi\omega}^{II} &= -ik_0 \int_{-\infty}^{\infty} v^{-1} [e_2(k) J_1(vr) + e_3(k) \Delta_1(vr, vb)] e^{ikz} dk, \\ E_{z\omega}^{III} &= \int_{-\infty}^{\infty} e_4(k) \Delta_0(vr, vb) e^{ikz} dk, \\ H_{\varphi\omega}^{III} &= -ik_0 \int_{-\infty}^{\infty} v^{-1} e_4(k) \Delta_1(vr, vb) e^{ikz} dk, \end{aligned} \quad (5)$$

where  $\Delta_n(vr, vb) = J_n(vr) N_0(vb) - J_0(vb) N_n(vr)$ ,  $n = 0, 1$ .

Having used the boundary conditions for the fields, we will obtain the system of a functional equations, which may be reduced to the singular integral equation for the function  $\varkappa = \varkappa^+ - \varkappa^-$ ,  $\varkappa^+$  is analytical function in the upper half-plane,  $\varkappa^-$  is analytical function in the lower half-plane

$$2Z_1 \hat{L} \varkappa - Z_2 \hat{L} \varkappa - \hat{L} (Z_2 \varkappa) = -\frac{4I_\omega}{ca} \frac{h}{\pi(k^2 - h^2)} \frac{J_0(vr_b)}{J_0(va)}, \quad Z_2 = \frac{k_0 \Delta_1(va, vb)}{v \Delta_0(va, vb)}. \quad (6)$$

Here  $\hat{L}$  is integral dyadic with the Cauchy kernel. Let us find the solution of the integral equation (6) in the quasistatic approximation  $k_0 a \ll 1$ . This case is most interesting because the contribution of the waveguide modes in the radiation field is negligibly small. The main expenses of the bunch kinetic energy will be used to the TEM field excitation in the coaxial waveguide. The solution of the integral equation (6) makes find the magnetic field in the coaxial line

$$H_{\varphi\omega}^{III} = -i \frac{2I_\omega}{ca} \int_{-\infty}^{\infty} \frac{X^-(h) \Delta_1(va, vb)}{X^+(k) \Delta_0(va, vb)} \sqrt{\frac{k_0 - h}{k_0 - k}} \frac{e^{ikz}}{2\pi(k - h)} dk. \quad (7)$$

The expressions for the functions  $X^\pm(k)$  have the form [4]

$$X^+ = \sqrt{\frac{i}{\ln(a/b)}} \frac{1}{\sqrt{(k_0 + k)a}}, \quad X^- = \sqrt{\frac{\ln(a/b)}{i}} \sqrt{(k_0 - k)a}, \quad (8)$$

The residue in the pole  $k = k_0$  of the integrated function (7) gives the field of the coaxial TEM wave

$$H_{\varphi\omega}^{III} = -(2I_\omega/cR) \exp(ik_0 z).$$

We will receive a simple expression for the excited TEM pulse executing the inverse Fourier transformation

$$H_{\varphi}^{III} = -\frac{2I(t - z/c)}{cR}. \quad (9)$$

It follows from this formula that the form and the amplitude of the TEM pulse is determined only by the bunch current. For the efficiency of the radiator (3) we have the simple formula

$$\eta = \frac{2 \ln(a/b)}{(\gamma - 1)I_A} \left( \int_{-\infty}^{\infty} I^2(t) dt \right) / \left( \int_{-\infty}^{\infty} I(t) dt \right). \quad (10)$$

For the Gauss beam we find from (10) that

$$\eta = \frac{\sqrt{2} \ln(a/b)}{\gamma - 1} \frac{I_b}{I_A}.$$

In particular, the transformation efficiency of the bunch energy to the TEM pulse energy for  $a \approx 2.7b$ , the of bunch energy 1MeV, of the current 10kA is 40%.

## Conclusions

The results of theoretical researches of powerful EMP generation by high-current relativistic electron bunches of the short duration on the basis of transition radiation is presented. The schemes of beam radiators are proposed as well. It is shown that the transition radiation is effective mechanism of the powerful EMP excitation with the pulse duration (0.1–10)ns. The frequency spectrum of the EMP is close to the frequency spectrum of the HCREB and can be changed by varying the current pulse parameters. The advantages of the EMP generators based on the transition radiation of HCREB, are their high efficiency and constructive simplicity, as well as the possibility to regulate the spectrum of excited EMP. Generation process of EMP by the electron bunch in a coaxial line is investigated. A efficiency of beam radiators, using beams with a current (5 – 20)kA and energy (0.5 – 1)MeV, may reach (30 – 60)%.

The perspective mechanism of EMP excitation is the radiation, formed by the short-pulse HCREB under formation of a virtual cathode.

## References

- [1] Friedman M., Serlin V., Lau Y.Y., Krall J. Proc. of 8 Int. Conf. on High-Power Particle Beams. (BEAMS'90). 1990. Novosibirsk. V.1. P.53.
- [2] Chaika V.E., Goncharuk I.M. Materials Conf. "SHF-engineering and space communication". Sevastopol. Ukraine. 26–28 September. 1994. V.2. P.393. (in Russian).
- [3] V.A. Balakirev, G.L. Sidel'nikov Transition radiation of modulated electron beams in an inhomogeneous plasma. Survey. Kharkov. 1994. 104p. (in Russian).
- [4] Vainshtein L.A. Theory of diffraction and method factorisation. M.: "Soviet radio". 1966. 431p. (in Russian).

# HIGH POWER PULSED NEUTRON SOURCE FOR ELECTRONUCLEAR INSTALLATION

S.A. Korenev, I.V. Puzynin, V.N. Samoilov, A.N. Sissakian

*Joint Institute for Nuclear Research,  
141980, Dubna, Moscow region, Russia*

**Abstract.** The pulsed neutron source on the basis of reaction  $T(d,n)He$  is described in the report. The source consists of pulsed Arkad'ev-Marx generator and vacuum diode with explosive ion emission.

## INTRODUCTION

The research in the field of electronuclear power generation [1] and surface modification of materials by neutron [2] has been of practical interest. The small neutron sources can be used for test experiments and investigations of surface modification of materials. The development of neutron sources on the basis of reaction  $T(d,n)He$  [3,4] allows to design new small pulsed neutron sources. The small neutron source on the basis this reaction in the vacuum diode with explosive ion emission is considered.

## THE GENERAL STRUCTURE OF NEUTRON SOURCE.

The main idea of this pulsed neutron source consists in the next. The deuteron ion beams from anode plasma in the ion source with explosive ion emission irradiate tritium target and as a result of the reaction  $T(D,n)He$  we have neutron beams. The motivation of using explosive ion emission is increasing of neutron yield because explosive ion emission allows to have high current of ion beam.

The pulsed neutron source consists of a high voltage generator for deuteron ion beam, acceleration, vacuum diode and vacuum chamber with target unit. A schematic block-diagram of pulsed neutron source is given in Fig. 1.

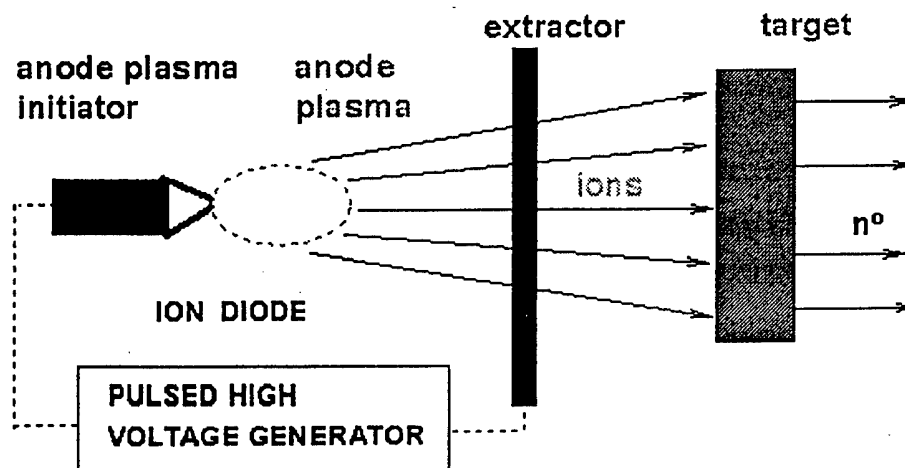


Fig.1. The general block-diagram of pulsed neutron source

The pulsed high voltage generator is a Arkad'ev-Marx generator with five capacitors steps. The polarity is set on the high voltage rectifier. The vacuum diode is very simple in design and comprises a stainless steel chamber 350 mm long and 400 mm in diameter, high voltage insulator from Capralon on which is mounted the anode plasma initiator, a cathode ( extractor electrode), and various diagnostic devices for measurements of ion and neutron beams, total current ( integrating Rogovski transformer and Faraday cup), and the pulsed voltage on the anode ( a high resistance divider).

The deuthrone polymer initiator of anode plasma of 10 mm diameter is used for production of deuterone beams. Distance between anode and cathode is 7 mm.

#### MAIN PARAMETERS OF NEUTRON SOURCE.

The pulsed high voltage generator operates in the following main parameters range:

- voltage 100- 700 kV;
- pulse duration 300 - 1000 nsec;
- pulse repetition 1-5 Hz.

The Current-Voltage characteristic for the ion source for deuterons is shown in Fig.2.

The neutron generation target is the 2 mm thick copper-zirconium alloy substrate onto which with tritium. The results of measurement of 14 MeV neutrons yield is shown in Fig.3. These measurements are shown possibilities of using of neutron source for different applications.

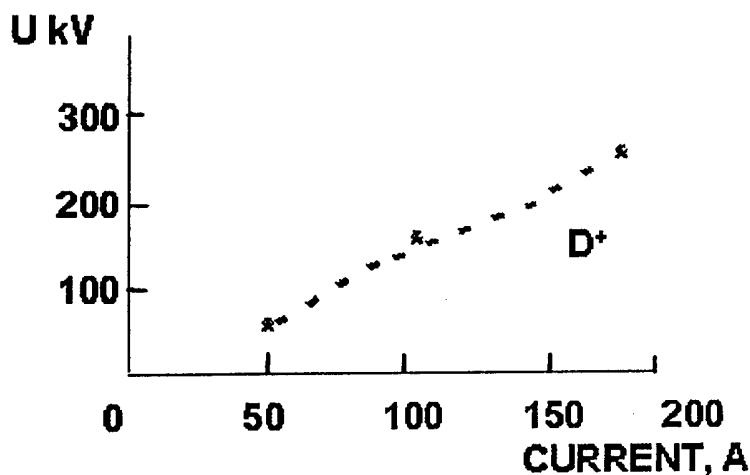


Fig.2. The Current-Voltage characteristics of ion source.

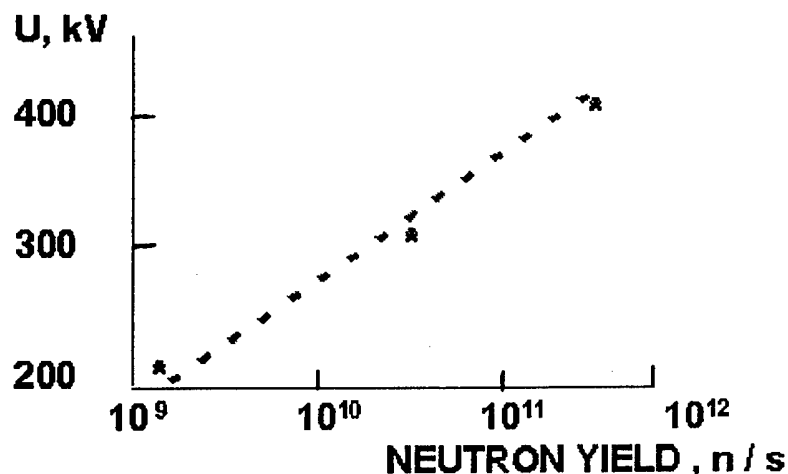


Fig.3. Neutron yield from voltage on the ion source.

#### EXPLOSIVE ION EMISSION

A detailed discussion of pulsed explosive emission is reviewed in detail in refs. [5,6] only the main principles are considered here. Referring to the schematics shows in Fig.1, a plasma is formed on the surface of the anode (on the plasma initiator) and then to extract ions from by applying a single positive voltage pulse.

For a planar ion source the electric field  $E$  must exceed the threshold value needed to form anode plasma:

$$E = KU/d > 10^7 \text{ V/cm}, \quad (1)$$

where:  $U$  is the voltage applied to the diode,  $K$  is the amplification factor of the electrical field on the initiator determining its geometry, and  $d$  is the distance between anode and cathode.

The kind of ion beams can be selected from among all metals and conducting and dielectric materials [7].

#### DISCUSSION

The main problem of pulsed neutron sources on the basis standard reaction is ion source for production of deuteron. The using duaplasmatron, ECR type sources allow to work in continuous regimes [4] and vacuum arc [8] - in the pulsed regime. Explosive ion emission permits to production more high current ion beams and its properties are interesting for design simply neutron source. The results of measurements are shown its. The pulsed neutron source can be used in the surface modification of different materials in the combine with pulsed electron/ion source with explosive emission [9]. The future development of this kind of neutron source consists in the study of stable regimes of forming pulsed neutron beam.



## CONCLUSION

1. New variant of pulsed neutron source on the basis of ion source with explosive ion emission is considered.
2. Parameters of pulsed neutron source allow to use in the different experiments.
3. The operation of this pulsed neutron source is more simple.

## REFERENCES

- [1] Carminati F., Geles C., Klapisch R., Revol J.P., Roche Ch., Rubio J.A., Rubbia C. "An Energy Amplifier for Cleaner and Inexhaustible Nuclear Energy Production Driven by Particle Beam Accelerator" CERN/AT/93-47(ET) (1993)
- [2] Rej D.J., Pickrell M.M., Wroblewski D.A. Appl. Phys. Lett. 68 (18), (1996), p. 2517.
- [3] Hunt S.E. "Nuclear Physics for Engineering and Scientists", John Wiley & Sons, (1987).
- [4] Voronin G.G. and e.a. 3rd European Confr. Particle Accelerator (EPAC'92), V.2, (1992), p.2678.
- [5] Korenev S. 3rd International Conf. "Energy Pulse and Particle Beam Modification of Materials", Drezden, Germany, Proc., (1989), p. 448.
- [6] Korenev S. Nuclear Instruments and Methods in Physics Research B80/81 (1993), p. 242.
- [7] Korenev S. Review Scientific Instruments, April (1994), p.147
- [8] Bessrabsky Yu.G. and e. al. Priboru and Technika Experimenta (Russia), No 5, (1994), p. 206.
- [9] Korenev S., Perry A. X Intern. School on Vacuum Ion and Electron Technology, Sozopol, Bulgaria, (1994), p.25, Vacuum , (1996) ( in pres).

□

# INTENSIVE NEUTRON SOURCE BASED ON POWERFUL ELECTRON LINEAR ACCELERATOR LIA-30 AND PULSED NUCLEAR REACTOR FR-1

V.S.Bossamykin, A.S.Koshelev, A.I.Gerasimov,  
V.S.Gordeev, A.V.Grishin, V.Ya.Averchenkov,  
S.A.Lazarev, G.N.Maslov, Yu.M.Odintsov.

*RFNC-VNIIEF, Mira pr.37, Sarov(Arzamas-16)  
Nizhni Novgorod region, 607190, Russia*

## Abstract

Some results of investigations on joint operation modes of linear induction electron accelerator LIA-30 (~40 MeV, ~100kA, ~20 ns) and pulse reactor FR-1 with compact metal core with the aim of high intensive neutron fluxes receipt are given. Multiplication Q factor for prompt neutrons in FR-1 booster mode operation changed from 100 to 4500. Total output of prompt neutrons from FR-1 at  $Q=2570$  was  $1.4 \cdot 10^{16}$  1/puls with pulse half width ~25  $\mu$ s.

## Introduction

Availability in VNIIEF of high power pulse electron accelerator LIA-30 put into operation in 1988 [1] and fast reactor FR-1 with compact metal core [2] (1979) allowed on their base to create high intensive neutron source. Lower, there is briefly given characteristics of neutron radiation from LIA target, FR operation as neutron autonomous source, data on joint operation of LIA and FR, and FR operation as booster-breeder in pulse mode.

## LIA and FR main design and operation parameters

LIA and FR arrangement scheme is shown in fig.1; shielding wall between them is not depicted. LIA accelerating system is formed by 4 injectors and 32 accelerating units. 288 water

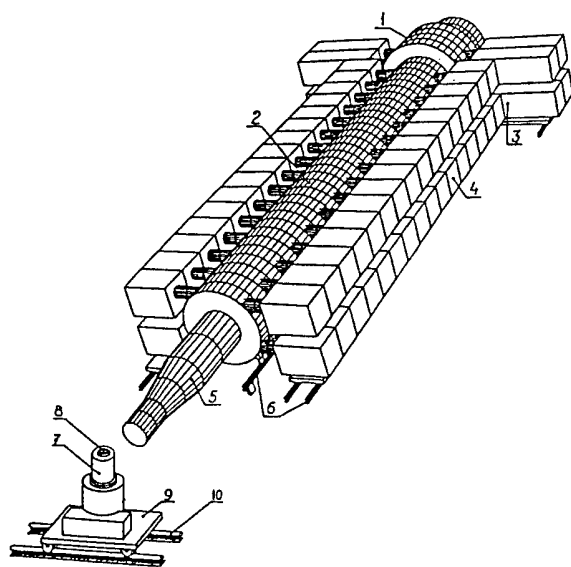


Fig.1. Scheme of LIA accelerating system and FR reactor arrangement. 1 and 2 - injector and accelerator units, correspondingly; 3 and 4 - generators for injector and accelerating radial lines charging; 5 - electron beams output device; 6 - LIA transport rails; 7 - FR core; 8 - central channel in FR core; 9 - trolley; 10 - rails.

insulated radial lines (RL) serve as accumulators and formers of accelerating voltage in units; each pair of RL are switched by gas-filled trigatrons with nanosecond accuracy (their total number is 2432). RL are charged from Marx generators at  $\sim 0.75 \mu\text{s}$  up to 500 kV. Formation, acceleration and electron beam transportation are executed in longitudinal magnetic field  $\sim 0.5 \text{ T}$ . The accelerating systems dimensions are: length - 25 m, width - 9.5 m, height - 4 m. The maximum accelerating rate - 1.7 MeV/m. LIA generates the electron beam with the following parameters: energy  $\sim 40 \text{ MeV}$ , current  $\sim 100 \text{ kA}$ , pulse duration  $\sim 20 \text{ ns}$ . At that, there is created bremsstrahlung radiation (BR) at the distance of 1 m from the target with maximum exposure dose  $\sim 10^4 \text{ rad}$  and exposure power  $\sim 5 \cdot 10^{11} \text{ rad/s}$ . In the similar less intensive operation modes the dose is approximately twice smaller. The interval between LIA triggering  $\geq 5 \text{ min}$ .

High enriched uranium ( $\sim 90 \% \text{ U}^{235}$ ) as Mo alloy ( $\sim 9 \%$ ) served as fissile material in FR core. The core arrangement axis cutting is presented in fig.2. Thin-walled ( $\leq 15 \text{ mm}$ ) ring

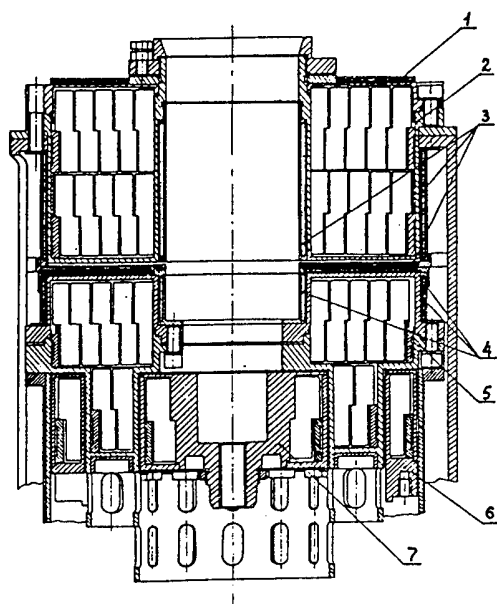


Fig.2. Core axis section. 1, 3, 4 - boron screens; 2 - stable upper unit; 5 - movable low unit; 6 - controlling unit; 7 - pulse unit.

elements core construction supplies specific energy release increase at the account of thermal tension lowering in it, connected with pulse character and non-equilibrium space distribution of field temperature. Such structure of the core supplies the FR boosted operation mode as autonomously and as the booster-breeder at the joint operation with LIA. The fissile material core has the outer diameter - 286 mm, height - 266 mm.

#### Neutron detectors

A set of 16 integral detectors with threshold sensitivity to neutrons is given. They are: filter-free and with 1 mm thick Cd filter neutron activation detectors with the use of  $\text{Al}^{27} (n, \alpha)$ ,  $\text{S}^{32} (n, p)$ ,  $\text{Ni}^{58} (n, p)$ ,  $\text{In}^{115} (n, n')$ ,  $\text{Au}^{197} (n, \gamma)$ ,  $\text{Cu}^{63} (n, \gamma)$  reactions; filter-free and in 1 mm thick Cd filter and in  $0.58 \text{ g/cm}^2 \text{ B}$  filter on  $\text{B}^{10}$  fission detectors with  $\text{U}^{235} (n, f)$ ,  $\text{Pu}^{239} (n, f)$  reactions; in 1 mm thick Cd filter detectors with  $\text{Np}^{237} (n, f)$ ,

$U^{238}$  (n, f) reactions. As a direct measurement of neutrons spectrum from LIA-30 target unit there was used time-of-flight method with plastic scintillator SPS detector with photomultiplier CNFT-3. Transit base was 60 m, while measurements were performed at  $180^\circ$  angle to the direction of electrons hit the target, that's why the base part shared the length ( $\sim 28$  m) of beam vacuum path in LIA. BEB - the detectors in the shape of polyethylene ball with 107 mm in diameter with Mn and Au activation detectors in the centers served as the detectors with the small sensitivity dependence on neutrons energy. There was performed a calibration of these detectors but in experiments on LIA the small influence ( $<20\%$ ) of  $\gamma$ , n reactions on Au detector indications was received. FR neutron pulse shape was measured by KNK-15 or KNVK2-5 fission vacuum chamber, placed in the core central channel in order to exclude the influence of the slow background neutrons of the room on its indications.

#### Main results.

LIA target design was consisted of a composite disc on the basis of W powder  $\sim 3$  mm in thickness and 430 mm in diameter, creating bremsstrahlung radiation, and the  $U^{238}$  dioxide of natural isotope composition disc adjoint to it, 40 mm in thickness and 300 mm in diameter in stainless steel thin wall shell. Neutrons output from the target made up  $1 \cdot 10^{14}$  n/puls which spectrum is closed up to  $U^{238}$  spectrum of HERMES III. [3] (fig.3), except its hard part, and may be presented as:

$$Y(E) = 8.52E \cdot \exp(-5E) + 0.518 \cdot \sqrt{E} \cdot \exp(-0.786E) \quad (1)$$

at Y normalization = 1; E - neutron energy (MeV).

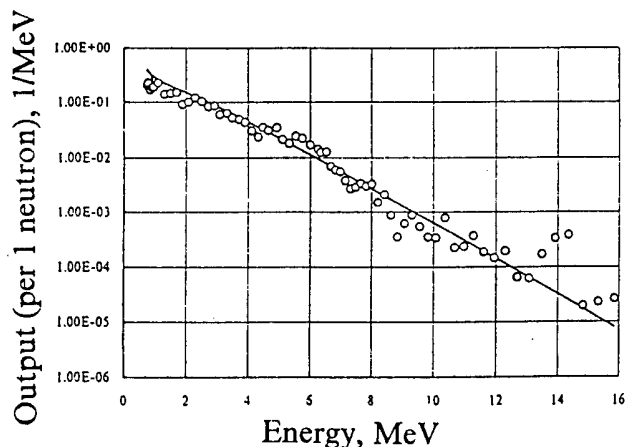


Fig.3. Neutron spectra from uranium targets of LIA (o) accelerators and HERMES III (-).

At LIA and FR joint operation and core arrangement along the acceleration path axis at 0.9 m of the core center from LIA target there is supplied the stable operation of the assemblies with their maximum autonomous parameters output and their controlled synchronic triggering. At that, FR creates neutron pulse as in the autonomous mode of  $\sim 60 \mu s$  (at half height) with  $3.6 \cdot 10^{17}$  maximum fission of energy release used in practice in the core ( $5.0 \cdot 10^{17}$  leakage neutrons). Leakage neutrons spectrum satisfies

$$Y(E)=13.18E \cdot \exp(-5E)+0.372 \cdot \sqrt{E} \cdot \exp(-0.786E). \quad (2)$$

Additional information about these operation mode is in [4].

In FR booster mode (fig.4) the distance from LIA target for bremsstrahlung

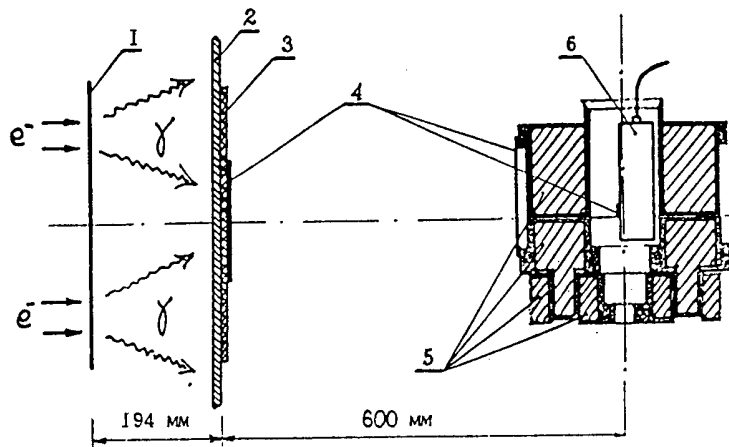


Fig.4. LIA target unit and FR arrangement scheme. 1 - LIA bremsstrahlung target; 2 - Al disc, 10 mm in thickness; 3 - plexiglas disc (20 mm); 4 - Ni detectors; 5 - pieces of fissile materials core; 6 - fission vacuum chamber.

radiation generation served composite disc on the basis of W powder 430 mm in diameter and 3.6 mm in thickness.  $UO_2$  disc was absent. Al and plexiglas screens, 10 and 20 mm in thickness were arranged for accompanying radiation filtration. FR operation at Q multiplication factor change of reactor system on prompt neutrons from 100 to 4500 is researched. In this range Y neutron output per pulse seemed to be satisfied to  $Y \approx 5 \cdot 10^{12} \cdot Q$  ratio, and pulse half width  $\tau \approx 10^{-2} \cdot Q$ ,  $\mu s$ . For example,  $\tau = 5 \mu s$  pulse duration at Q and Y of correspondingly 500 and  $0.25 \cdot 10^{16}$ ,  $\tau = 10 \mu s$  at Q and Y of correspondingly 1000 and  $0.5 \cdot 10^{16}$ ,  $\tau = 25 \mu s$  at Q and Y of correspondingly 2570 and  $1.4 \cdot 10^{16}$  were experimentally recieved.

The combined radiation of LIA-FR complex was used for performing some physical researches.

### Conclusion

A more detailed study of neutron pulsed formation processes in FR booster mode including the facilities possibilities expanding for more effective use of bremsstrahlung radiation from LIA target and combined neutron source power increase are planning.

The similar complex facilities are necessary for researches to create the safe nuclear energy in electron accelerator - subcritical blanket systems.

[1] Pavlovskii A.I., Bossamykin V.S., Gerasimov A.I. et al. : BEAMS 92. 9-th Intern. Conf. on High-Power Particle Beams, 1(1992)273.

[2] Pavlovskii A.I., Malinkin A.A., Kolesov V.F et al. : Voprosy atomnoj nauki i tekhniki. Series. Impulsnye reaktory i prostye kriticheskie sborki, № 1(1985)3.

[3] Sanford T.W.L., Lorence L.J., Halblieb J.A. et al : Nucl.Sci.Eng., 114 (1993)190.

[4] Bossamykin V.S., Koshelev A.S., Gerasimov A.I. et al. : PANS II. Phys. Advanced Puls. Neutron, (1995)114.

# MONTE CARLO SIMULATION OF HIGH-FLUX 14 MeV NEUTRON SOURCE BASED ON MUON CATALYZED FUSION USING A HIGH-POWER 50 MW DEUTERON BEAM

M. Vecchi<sup>1</sup>, F.I. Karmanov<sup>2</sup>, L.N. Latysheva<sup>3</sup>, I.A. Pshenichnov<sup>3</sup>

1 ENEA, via Martiri di Monte Sole 4, 40129 Bologna, Italy

2 INSTITUTE OF NUCLEAR POWER ENGINEERING 249020 Obninsk, Russia

3 INSTITUTE FOR NUCLEAR RESEARCH, RUSSIAN ACADEMY OF SCIENCES, 117312 Moscow, Russia

As it has been mentioned in /1-4/ there is an interest to build a 14-MeV high-intensity neutron source in order to study the behaviour of materials under an intense irradiation by 14-MeV neutrons. The main purpose of the present work is to present Monte Carlo simulation of an intense neutron source based on muon catalyzed fusion process mCF-INS /1/.

The layout of the setup is presented on Fig.1. A deuteron beam (12mA,  $E_d$ ) is directed onto a cylindrical carbon target (primary target  $L_t$ ,  $R_t$ ), located in vacuum chamber (converter  $L_c$ ,  $R_c$ ) with a strong solenoidal magnetic field ( $H_{max}$ ,  $H_0$ ) to produce negative pions. The direction of the d-beam is  $180^\circ$  (back pion production). The pions and muons which originate from pion decay are guided along magnetic field lines to a DT-cell (synthesizer). We assume that the synthesizer has the shape of a cylinder and the material of the front  $d_{fr}$ , lateral  $d_{lat}$  and back  $d_b$  walls is titanium. Assuming  $X_c=100$  fusion per muon, mCF-INS produces 14-MeV neutrons with a source strength of up to  $10^{17}$  n/s.

It is interesting to note that the neutron intensity depends directly on the deuteron current.

The range for the basic parameters of the setup specified on Fig1. is as follows:

$L_c = 500 - 1300$  cm,  $R_c = 20 - 50$  cm,  $H_0 = 7 - 10$  T,  $E_d = 1 - 2$  GeV/N,  
 $L_t = 30 - 100$  cm,  $R_t = 0.4 - 10$  cm,  $d_{fr} = 0.25$  cm,  $d_{lat} = 0.5$  cm,  
 $d_b = 0.25$  cm, DTdensity = 0.5 (LHD),  $H_{max}/H_0 = 1.3 - 1.5$ ,  $q_{back} = 120^\circ - 143^\circ$ ,  
 $L_s = 5 - 50$  cm,  $R_s = 4$  cm, SR=single reflection, DR=double reflection,

Pion production in the primary target is simulated by means of Intranuclear and Internuclear cascade codes created in the Institute for Nuclear Research of Russian Academy of Sciences while pion and muon transport process is studied by a Monte Carlo code based on GEANT3.21 created at CERN /6/.

Two important problems coexist: the correct efficiency estimation of the pion production and utilisation processes and the problem of optimal choice of the parameters of the setup in order to obtain the highest intensity of the neutron flux. An opportunity which discussed in /1,3/ deals with the deuteron beam of the energy about 1 GeV/N and with 30 cm carbon cylinder as the primary target.

In a paper /5/ we tried to expand the region of optimisation of the efficiency of negative pion production by deuterons /5/ respect to the region considered previously /1,3/ both for the deuteron energy and primary target geometry. Dependencies of the pion yield on the target size and deuteron energy have been investigated in detail. However, the calculations /5/ of the pion yield have been done without taking into account a loss of pions in the primary target due to the influence of the magnetic field during the pion and muon transportation to the fusion target (pions can re-enter the primary target by spiral trajectories).

The main purpose of the present work is to calculate the pion and muon utilisation efficiency taking into account the above-mentioned of pion absorption in the primary

target as well as all the other losses of pions and muons in the walls of converter and DT-cell.

#### 1. Pion production and absorption in the primary target.

Initial distributions of pions leaving the primary target in space and momentum ( $x, y, z, P_x, P_y, P_z$ ) were calculated by means of Intranuclear and Internuclear Cascade Codes /5/ created in INR. It is well known fact that the outgoing pions have a wide angular and energy distribution. An example of momentum, angle and longitudinal momentum distributions presented on Fig.2.

Table1 presents the integral characteristics of negative pions and deuterons leaving the primary target. As it was already noted /5/, the length of the target of 30 cm seems to be not sufficient "to consume" all the deuterons for pion production and one can conclude that an essential part of beam particles goes out of the target. For the targets listed in the Table 1, the integral absorption rate due to re-entering into the primary target in the magnetic field (with the values specified above) turns out to be at the level of 13% for T8 case and 35% for T2 case.

#### 2. Pion and muon transport to DT-cell.

Pion and muon transport to DT-cell is simulated by GEANT3.21.

Some trajectory calculations is shown on Fig.1. For the case of homogeneous magnetic field in setup and in assumption of quasi-continuous slowing down approximation there are exist some simple analytical solutions of the motion equations of pions and muons. Comparison of z-coordinate and cyclotron radius dependencies on energy demonstrates a good agreement between analytical solutions and results obtained by means of GEANT3.21.

In order to confine pions which travel backward a simple model of a magnetic mirror has been employed with mirror ratio  $H_{\max}/H_0 = 1.3 - 1.5$ . According to this model each particle is reflected at its starting point in P-Z plane if its momentum direction angle belongs to the range  $[90^\circ, \theta_{\text{back}}]$ . One can see the influence of magnetic trap on the spectrum of outgoing pions on Fig. 3.

Preliminary results of simulation are presented in Tab.1- Tab.3 and on Fig.2, Fig.3-4.

It seems to be necessary to test our program by means of calculation of the setup variants which have been considered by other groups before /3,7/. Unfortunately it is difficult or even impossible to reproduce each that situation entirely but as one can see from Tab.2 our results have the same order of magnitude as the results of above-mentioned groups. In the Tab.3 we present detailed description of the several most encouraging variants of neutron source setup.

#### 4. Conclusion

Preliminary estimations demonstrate the possibility to reach the level of  $10^{14}$  n/s/cm<sup>2</sup> for the neutron flux. This flux can be used to study the behaviour of materials of fusion reactors /1/ or to drive into operation a hybrid nuclear reactor /8/.

#### References

1. C.Petitjean, F.Atchison, G.Heidenreich et. al., " A 14-MeV High-Flux Neutron Source based on Muon Catalyzed Fusion - A Design Study". Fusion Technology, v.25,July 1994,p.437-450
2. Yu.V.Petrov, E.G.Sakhnovsky, "Production of 14-MeV Neutrons based on Muon Catalyzed Fusion", Preprint 1833, SPNPI (1992)
3. G.Heidenreich, C.Petitjean, H.K.Walter, V.E.Markushin, "A High-Flux 14-MeV Neutron Source Based on Muon Catalyzed Fusion: Progress in a Realistic Design", PSI, Internal report, 1994
4. Yu.V.Petrov, E.G.Sakhnovsky, " On a 14-MeV Neutron Source Based on MCF for Fusion Materials Research", Preprint SPNPI 2064, Gatchina, 1995
5. L.N.Latysheva, I.A.Pshenichnov, M.Vecchi, " Negative pion production by deuterons", the talk presented at mCF-95, Dubna, Russia,1995
6. GEANT Detector Description and Simulation Tool , CERN Program Library Long Writeup W5013, 437p

7. F.I.Karnanov "Calculation of the Muon Fraction Stopped in the target of an 14-MeV Neutron Source". Hyperfine Interactions, 82,439 (1993)

8. S.S.Gershtein, Yu.V.Petrov, L.I.Ponomarev, "Muon catalysis and nuclear breeding", Sov.Phys.Usp.,33(8)(1990)591.

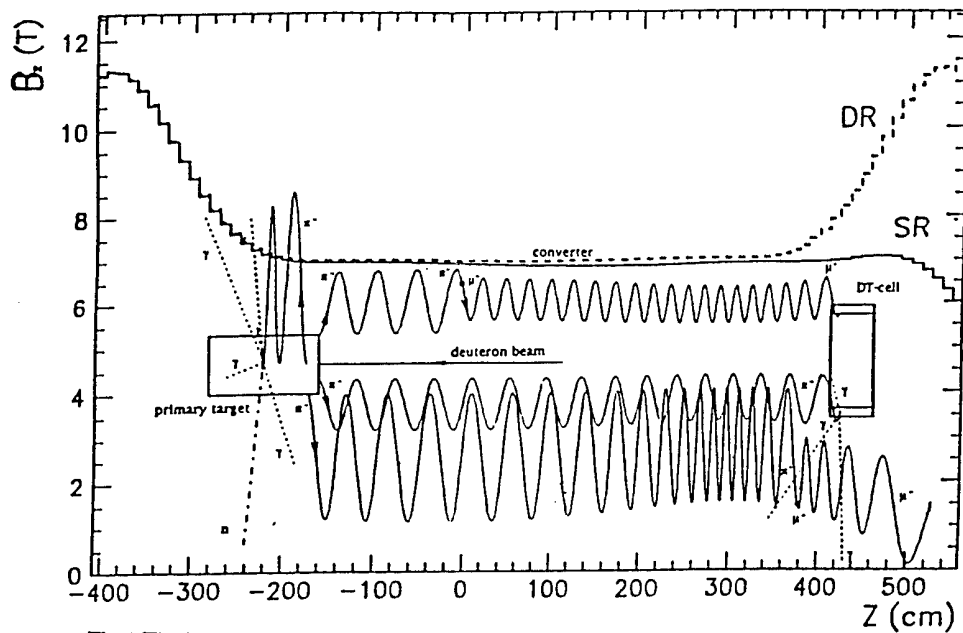


Fig.1 The layout of the setup

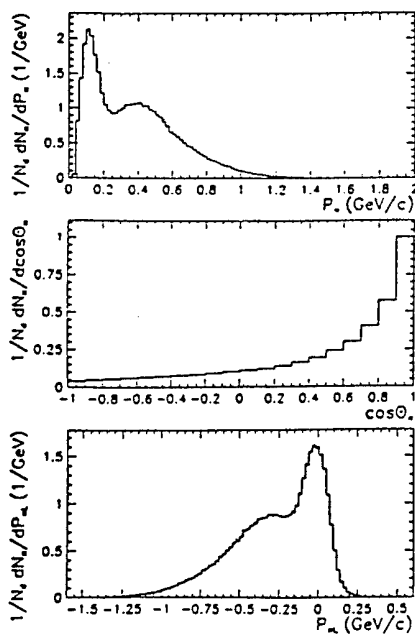


Fig.2 The initial momentum and angular distributions obtained by means of INR codes

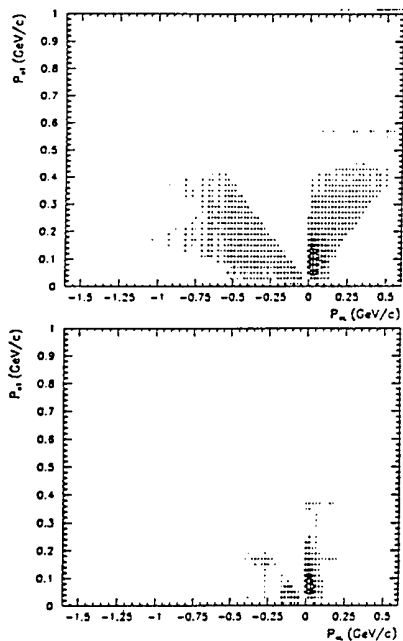


Fig.3, up Two-dimensional momentum distributions of outgoing pions after the trap impact  
Fig.3, down two-dimensional initial momentum distributions for the pions stopped in the primary target

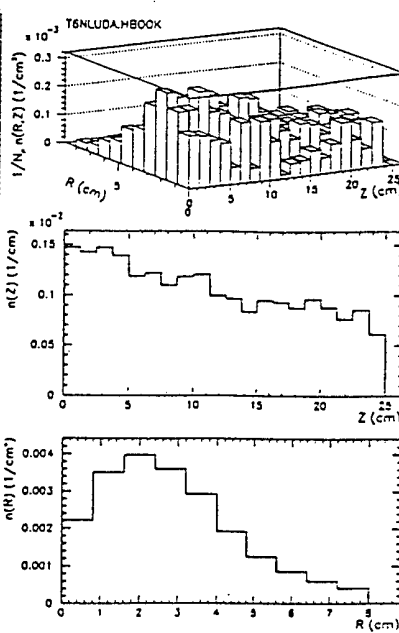


Fig.4 Two-dimensional distributions for muons stopped in the DT-cell



Table 3. Conversion coefficients and fraction of stopped pions and muons for different components of set-up. Dimensions are in cm.

run name	T8MARKU	T8MARKU2	T6NMARCE	T6NLUIDA
primary beam	T8N	T8N	T6N	T6N
converter	180°	180°	180°	180°
	50	50	50	50
	700	700	1000	1300
	8	8	8	8
	40	40	25	25
DT-cell	1.6	1.6	0.5	0.5
	0.8	0.8	0.3	0.3
	2	2	2	2
magnetic field (T)	9	10	7	9
	15	10	10	15
	28.25	54.18	41.42	34.15
	10.49	12.77	15.77	18.52
	43.33	30.08	33.44	38.24
pion statistics (% per pion)	0.0	0.0	1.39	0.1
	12.30	2.76	1.89	1.84
	2.68	1.21	0.54	0.47
	7.92	0.47	8.17	10.06
	6.32	14.37	5.07	3.90
	0.93	0.98	1.30	1.29
	0.0	0.0	0.02	0.0
	11.33	6.69	2.43	2.33
	9.39	2.00	4.09	3.22
	5.95	0.68	13.47	17.89
	1.39	0.93	1.12	1.39
	2.78	1.48	3.02	4.61
	5.24	2.95	2.92	3.62
estimated neutron flux 10 <sup>14</sup> (n/s/cm <sup>2</sup> )	0.2	0.1	0.5	0.6

Table 1. Integral characteristics of particles leaving primary graphite target.

run name	T (GeV/N)	d <sub>beam</sub> (cm)	d <sub>target</sub> (cm)	L <sub>target</sub> (m)	N <sub>K<sup>+</sup></sub>	<E <sub>K<sup>+</sup></sub> > (MeV)	N <sub>d</sub>
T0	1	0.8	0.8	0.3	0.117	157.17	0.424
T1	1	10	10	0.3	0.107	166.97	0.354
T2	2	10	10	0.3	0.254	285.50	0.355
T3	2	10	10	1	0.457	273.33	0.071
T4	2	0.6	10	1	0.478	272.90	0.040
T5	2	0.6	0.6	1	0.318	273.91	0.270
T6	2	2	2	1	0.395	274.48	0.172
T7	2	2	2	0.6	0.366	276.21	0.216
T8	1	0.6	0.8	0.3	0.120	157.57	0.417

Table 2. Comparison with results of other groups. Dimensions are in cm, muon stops in % per one pion.

run	name or ref.	[7]	[3]	T8MARKU2	[3]	T8MARKU1
beam	energy direction	1 GeV/N 0°	1 GeV/N 180°	1 GeV/N 180°	1 GeV/N 180°	1 GeV/N 180°
target	material	Be	C	C	C	C
	diameter	point	0.8	0.8	0.8	0.8
	length	like	30	30	30	30
converter	R	20	50	50	50	50
	L	4000	4000	7000	8000	7000
DT-cell	R	10	10	8	8	8
	L	30	30	40	40	40
	d lateral wall	5	5	1.6	1.6	1.6
	d front wall	0.8	0.8	0.8	0.8	0.8
	d back wall	2	2	2	2	2
magnetic field (T)	H <sub>0</sub>	10	10	10	9	9
	H <sub>max</sub>	12	12	10	15	15
pion decays (%)		71	80	30.08		43.33
muon stops	in walls of DT-cell	35	30.6	6.8	18	20.7
	in DT-mixture	4.3	6.2	2.1	2.95	3.2
						5.24

# THE NIKE ELECTRON BEAM-PUMPED KrF LASER AMPLIFIERS

V. Serlin, J.D. Sethian, C.J. Pawley, S.P. Obenschain, and K.A. Gerber

*Plasma Physics Division, Naval Research Laboratory, Washington D.C. 20375, USA*

A.V. Deniz and T. Lehecka

*Science Applications International Corporation, McLean, VA, USA*

W. Webster

*Research Support Instruments, Inc., Alexandria, VA, USA*

## Abstract

The NIKE laser is a 56-beam angularly-multiplexed KrF laser system designed for inertial confinement fusion experiments. The last two amplifiers of the laser are both electron beam pumped systems. The smaller of the two has a 20cm x 20cm aperture. It uses a single 18 kJ Marx generator to produce two 300 kV, 75 kA, 120 nsec flat top electron beams that are injected into the opposite sides of the laser cell.

Various diagnostics, including Faraday cups, pressure jump sensors, and dosimetry media, showed that the energy deposition and pumping uniformity meet the laser requirements, and that the transmission efficiency, from cathode to laser cell is about 50 %. Laser kinetics codes accurately predict the observed gain of the laser pulse, based on the measured electron beam deposition.

The larger amplifier in NIKE has a 60 cm x 60 cm aperture. It has two independent electron beam systems, each powered by a 170 kJ Marx generator that produces a 670 kV, 500 kA, 240 nsec flat top electron beam. Faraday Cup measurements show that the electron beam current varies by less than 10 % across the 200 cm x 60 cm laser cell aperture. In order to fully characterize and optimize this amplifier, various diagnostics are used to monitor the high voltage pulses. The most challenging environments are the 200 cm x 60 cm electron beam diodes.

Several time resolved diagnostics have been developed to monitor the total current evolution, current density and uniformity of the electron beam in the diodes. Operation and performance of the diodes will be monitored and analyzed with these diagnostics. In particular, the total current will be directly measured by an array of dB/dt probes.

At full operating voltage the system deposits more than 70 kJ into the laser gas mixture. All of these parameters meet the NIKE design requirements of 5 kJ of laser energy in 240 nsec. At peak performance NIKE produces 5 kJ of laser light, typically it generates 3-4 kJ.

This work is supported by the U. S. Department of Energy

(The full text has not been supplied.)

## AIRIX AT CESTA

P.ANTHOUARD, J.BARDY, C.BONNAFOND, P.DELSART, A.DEVIN, P.EYHARTS,  
P.EYL, D.GUILHEM, J.LABROUCHE, J.LAUNSPACH, J. de MASCUREAU,  
E.MERLE, J.C.PICON, A.ROQUES, M.THEVENOT, D.VILLATE, L. VOISIN

*Commissariat à l'Energie Atomique  
Centre d'Etudes Scientifiques et Techniques d'Aquitaine  
BP N°2 - 33114 LE BARP - FRANCE*

**Abstract**

AIRIX Flash X-ray Radiographic facility is based on a 4 MeV - 3,5 kA pulsed electron injector and a 16 MeV induction accelerator; it is scheduled to be commissioned in 1999. The accelerator will consist of 64 induction cells powered by 32 H.V. generators operated at 250 kV. The final 20 MeV electron beam will be focused on a target designed for X-ray conversion.

At CESTA, PIVAIR is a testbed designed as a validation step of AIRIX up to 8 MeV. The injector, operating since March 94, has been connected with 8 accelerating cells, increasing electron beam energy to 5,8 MeV. Two kinds of induction cells have been successfully tested and beam diagnostics have been developed (time resolved spectrometer, emittancemeter, BPM,...). A Tickler experiment is planned from March to June 96 in order to study BBU instabilities. Then, the 16 cells PIVAIR accelerator will be completed for beam dynamic studies and focusing on a target for X-ray source characterization.

**Introduction**

AIRIX facility is designed to produce a 16-20 MeV, 3.5 kA, 60 ns high brightness electron beam for Flash X-ray Radiography application [1]. The first studies and experiments began in 1992 with the development of a 250 kV pulsed generator and a versatile induction prototype cell.

PIVAIR milestone, which is a validation step of AIRIX up to 8 MeV, started with the 4 MeV, 3.5 kA Injector assembly at CESTA in february 1994. After acceptance test, the first accelerating module was aligned and coupled to the injector. By the end of 1995 two kinds of induction cells have been tested at 250 kV ; a BBU experiment is planned this year with 8 accelerating cells set up, in order to validate numerical calculations.

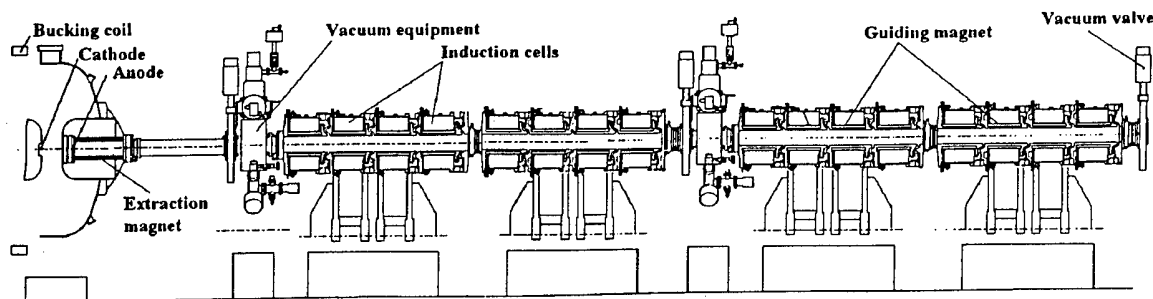


Figure 1: PIVAIR final accelerator set up

### Injector

The injector, very close to the one used at Los Alamos on the ITS facility for the DARHT program, was build by PSI [2]; it comprises a 4 MV good flatness pulse generator developed by PSI and a vacuum diode designed by LANL. Acceptance tests have demonstrated a 4 MeV-3.5 kA electron beam with a low energy spread ( $\pm 1\%$  over 60 ns). The beam emittance was measured at  $1600 \pm 300 \pi \cdot \text{mm} \cdot \text{mrad}$  with the pepper-pot method.

### Pulsed generators

A high voltage pulsed generator has been designed to drive two induction cells with 250 kV nominal, 75 ns pulses with  $\pm 1\%$  flat top deviation [3].

Nine generators have been assembled and successfully tested on resistive loads; 6 of them are currently operating on PIVAIR induction LINAC. Last improvements are going to be tested with solid state switching in the trigger circuit.

### Induction cell design and testing

Each induction cell comprises ferrite cores (250 mm I.D., 500 mm O.D., 25 mm thick) housed in a non magnetic stainless steel body, a 4 layers bifilar wound solenoid magnet and 2 printed circuit dipole trim coils. The 19 mm width accelerating gap has been shaped in order to obtain good voltage holdoff and minimize the beam coupling with the gap cavity to reduce BBU instability.

The prototype HV pulse generator was operated to test the prototype induction cell with different set up in order to experiment several solutions:

a) *gap insulator*: the first experiments began with brazed alumina (successfully used at 120 kv on another induction accelerator at CESTA: LELIA) but flashovers in the 200 kV range made this way too uncertain to succeed on the schedule. An alternative solution, using Rexolite (as on DARHT induction cells), was tested; flashovers occurred at 150 kV and we had to change the gap geometry in order to maintain the right angle ( $\approx 40^\circ$ ) between insulator surface and E-field. In this configuration, the induction cell supported 300 kV pulses and we decided to construct the first 4 PIVAIR cells.

b) *ferrite under vacuum*: dielectric oil surrounding ferrite cores was replaced by vacuum so gap insulator could be suppressed. In this configuration vacuum interface and high voltage insulation are transferred on H.V.cable heads which is more convenient for induction cell maintenance in case of flashover. Moreover BBU calculations shows that transverse impedance is better for this configuration. The first H.V. tests exhibited current leakage between ferrite cores and the internal diameter of the metallic housing. This led to increase the ferrite core internal diameter to 270 mm in order to improve H.V. insulation but meant to lower the ferrite section and the available flux swing. This was partly balanced by adding a 12<sup>th</sup> ferrite core (only 12 mm thick). The prototype cell was then successfully tested at 300 kV and 4 cells with ferrite under vacuum were constructed for PIVAIR.

*Ferrite studies*: the first tests began with TDK 11 B and we observed that 11 cores were not able to maintain a 75 ns flat top at 250 kV range because ferrite saturation occurred too early. Available flux swing had to be increased so we tested TDK PE 16 ferrite while CEA-LR was developing a specific composition for AIRIX; these studies resulted in a 15 % flux swing gain and CEA-LR was chosen to furnish next PIVAIR and AIRIX ferrite cores.

## Diagnostics

As low energy spread and small emittance are essential to optimize beam transport and final focus, accurate and time resolved diagnostics have been developed[4].

*Spectrometer:* a magnetic spectrometer, using Cerenkov radiation (produced by electron beam interaction with a 100 optical fiber sheet ) and a streak camera, allows a continuous time analysis with a 1 nsec resolution and an energy resolution  $\Delta E/E = 0.1\%$  over a 0.1 E energy range.

*Emittance measurements:* using the pepper pot technique, with a plastic film scintillator and a CCD gated camera, this diagnostic measures time resolved electron beam transverse emittance.

*Beam position and current monitors:* located every 4 accelerating cells, these diagnostics have 2 main functions:

- coupled with analogic summers and integrators on a medium range oscilloscope ( $\Delta f = 500$  MHz), they measure beam current and position for beam transport and centering.
- connected directly on a high resolution analyser ( $\Delta f > \text{GHz}$ ) they will be involved in BBU studies.

The first operating mode is facing with fast transition time problems, while the second is difficult to calibrate and needs FFT analyses.

## PIVAIR experiments and results

*Alignment:* mechanical and magnetic alignment are key topic for beam transport and emittance conservation along the accelerator. The initial procedure, using a laser beam, aborted. We then used a theodolite to align a 4 cell block on the reference axis normal to the cathode. For the next step we will install a HLS and WPS network [5] successfully developed and used at ESRF .

*Beam transport:* an envelope code called ENV has been developed at CESTA and experimentally validated on LELIA induction accelerator. On PIVAIR, the magnetic fields were measured along the reference axis with a Hall probe. Then an optical diagnostic (Cerenkov or OTR) was used at the injector output to measure the beam mean quadratic radius for different sets of extraction magnet; a numerical optimization determined then initial beam characteristics in order to be used as data entry for beam transport along the accelerator.

An other code is under development to tune trim coils for beam centering.

*Induction cell characterization:* by the end of 1994, the first 4 induction cells using TDK PE 11 ferrites and Rexolite insulator were installed on PIVAIR testbed. The "routine" level was 210 kV per cell, confirmed by a spectrometer measurement of 4.8 MeV at the 4 cell output for a 4 MeV-3.5 kA injected beam. For higher accelerating voltages, a reverse peak voltage appears across cell gap 440 ns after the main pulse and leads to a flashover. We think this phenomenon is caused by ferrite saturation.

During 1995, 8 new cells using CEA ferrites have been tested with beam. Four of them comprised a Rexolite insulator, the others used ferrite under vacuum. To obtain the same vacuum level in beam pipe, the second technology needs 2 days heating at 70 °C in order to dehydrate ferrites. High voltage tests with beam exhibited similar results: energy gain was 1 MeV for each 4 cells block, and we noticed some spread in accelerating pulse width involving certainly ferrite premagnetization spread. With the rexolite cell, a flashover on

reverse voltage occurs often above 230 kV; with the other technology, reverse voltages up to 250 kV have not generated any flashover but the voltage flat top was 7% shorter and we had to carefully synchronize injector and pulse generators. We decided then to construct the 4 last induction cells for PIVAIR with the "ferrite under vacuum" technology, just changing the gap shape according to the last transverse impedance calculations.

This year 12 induction cells have been operated with the injector, increasing the beam energy to 6.7 MeV (cf Figure 2); flashovers across Rexolite insulator led us to disassemble Rexolite cell blocks in order to refurbish accelerating gap and insulator (cleaning, polishing).

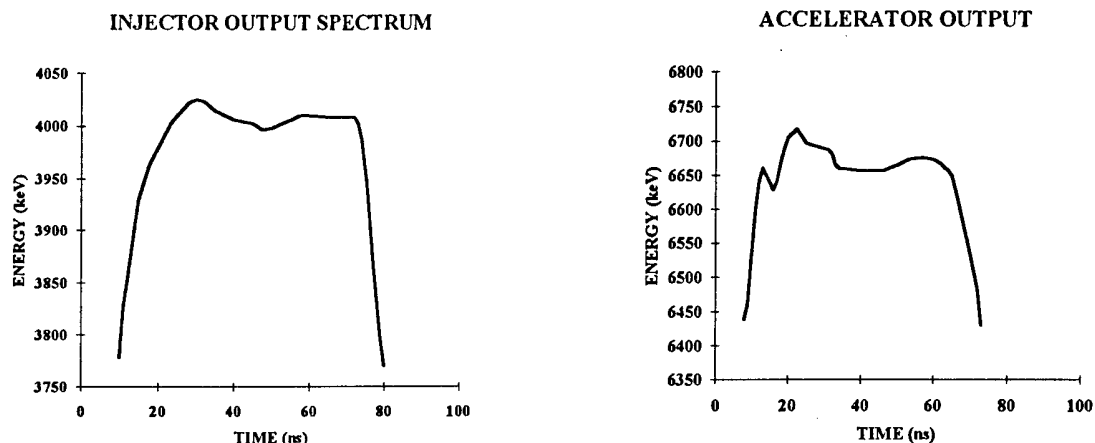


Figure 2: beam spectrum before and after 12 cells acceleration

### Beam Break Up studies

BBU instability studies have first been conducted in order to minimize the beam coupling with the induction cell accelerating cavity; this implies to lower induction cell transverse impedance. Transverse impedance depends on gap geometry and material dielectric constant; measurements have been performed with a two wires method and agree with PALAS numerical calculations. The next step will involve beam dynamic studies.

*Tickler experiment:* in this experiment, a resonant cavity (possibly feeded with an external HF source for reproducibility) placed at the injector output, is excited by the electron beam. The cavity mode is going to excite electron beam transverse motion. The aim of this experiment is to measure how much the coupling between accelerating gaps and beam is going to enhance the magnitude of this transverse motion. By the middle of June 96 the "tikler cavity" will be coupled with the injector and the first accelerating module (8 Rexolite cells). Comparisons with numerical calculations would lead to choice the final AIRIX induction cell technology

### Conclusion

The final PIVAIR set up is planned by the end of the year in order to begin beam transport and focusing at 8 MeV. The first radiography experiment could start next year.

- [1] J.LAUNSPACH, et al: 10<sup>th</sup> BEAM'S Proc., (94) p 515
- [2] Pulse Science Inc, 600 Mc Cormick street-San Leandro, CA 94577, USA
- [3] P.ANTHOUARD, et al, 4<sup>th</sup> EPAC Proc., (94) p 722
- [4] D.VILLATE, et al, PAC Proc., (95) to be published
- [5] C.BONNAFOND, et al, 5<sup>th</sup> EPAC Proc, (96) to be published

## SPACE POWER DISTRIBUTION OF SOFT X - RAY SOURCE "ANGARA-5-1".

K. S. Dyabilin, V. E. Fortov, E. V. Grabovskij  
M. E. Lebedev, V. P. Smirnov

*High Energy Density Research Center, Izhorskaya 13/19, Moscow  
127412, Russia  
Troitsk Institute of Innovative and Fusion Research, Troitsk,  
142092, Russia*

One of the effective ways to solve the problem of the spatial nonuniformity of the power is to use the x-ray emission from a plasma with an approximately thermal spectrum. The high density and temperature Z-pinch plasmas are rather good candidates for that. The report presents the results of the study of the shock waves in condensed targets formed by applying intense pulses of soft x-radiation (SXR). The attention is paid on the spatial distribution of the SXR power because of its strong influence on the shock wave front uniformity.

For the plasma generation, the double liner scheme was used: the internal liner as a low density agar-agar cylinder with the implanted Mo was used (the density is less than  $1 \text{ mg/cm}^3$ , cylinder mass about  $200 \text{ } \mu\text{g}$ ). The external liner diameter was  $4 \text{ mm}$ , wall thickness -  $0.2 \text{ mm}$  and height  $10 \text{ mm}$ . As the external liner, the supersonic annular Xe jet with mass about  $150 \text{ } \mu\text{g}$  was used. The value of the pinch current was about  $3.5 \text{ MA}$ . Z-pinch plasma radiated SXR with the typical temperatures about  $60\text{-}100 \text{ eV}$  [1]. This radiation was coming on the planar target which was positioned under the internal liner  $1 \text{ mm}$  apart and caused the intense shock wave.

The targets were made as step  $16\text{...}30 \text{ } \mu\text{m}$  Al and  $80\text{-}200 \text{ } \mu\text{m}$  Pb, or pure  $180 \text{ } \mu\text{m}$  Pb, or stepped  $16 \text{ } \mu\text{m}$  Sn and  $180 \text{ } \mu\text{m}$  Pb plates being connected together. Such large thickness allowed to eliminate the thermal heating of the target. The velocity of the shock wave was defined by the optical base method as the difference between the moments in the flashes of light emitted upon the shock waves break out at the rear surface of a sample. The sample was imaged by the a SNFT-2 streak camera. Spatial resolution corresponds to  $20 \text{ lp/mm}$  in sample plane, temporal resolution less than  $0.3 \text{ ns}$  was provided.

The averaged (over the target volume) shock wave velocity for Al plus Pb stepped target is  $(7.3 \pm 0.6) \cdot 10^3 \text{ m/s}$  for  $80 \text{ mm}$  Pb thickness, and  $(4.6 \pm 0.3) \cdot 10^3 \text{ m/s}$  for  $200 \text{ mm}$  [1]. In accordance with the lead Hugoniot [2], this means that the shock compression pressures were  $300 \text{ GPa}$  and  $90 \text{ GPa}$  correspondingly.

Typical streak camera records are shown in Fig. 1.



Fig.1 Streak camera records (positive) of shock break out from sample obtained in ANGARA-5-1 experiments: lead-180  $\mu\text{m}$ ; Between bench-marks - 13 ns.

An important question was the spatial uniformity of the irradiated power. Let us define the nonuniformity as:

$$\xi = \frac{\Delta q}{q}$$

where  $q$  is radiative flux.

Supposing that the velocity of the shock wave  $u$  is function of pressure  $P$  which depends on  $q$ , one can write for the spatial derivative of  $q$ :

$$\frac{\partial q}{\partial x} = \frac{\frac{\partial u}{\partial x}}{\frac{\partial u}{\partial P} * \frac{\partial P}{\partial q}}$$

Also, using the connection  $P \sim u^2$  one can express  $\xi$ :

$$\xi = \frac{\Delta q}{q} = \frac{\Delta t}{t} * \left\{ \frac{2}{\frac{\partial \ln P}{\partial \ln q}} \right\}$$



Here  $t$  is time of shock front arriving at the free surface. On the diameter 4 mm the measured  $\frac{\Delta t}{t}$  is about 2% . So the value  $\frac{\partial \ln P}{\partial \ln q}$  is to be about unity.

Theoretical simulations predict the value of the nonuniformity about 3% within the liner size: Fig. 2 shows the calculated space distribution of the radiative power on the target. Two curves correspond sources with the surface and volume radiative mechanisms. One can see that on the distance 2 mm (liner radius) the uniformity is good enough. One should note that direct measurements of the shock wave arriving on free surface give some confirmations of this fact (Fig. 1).

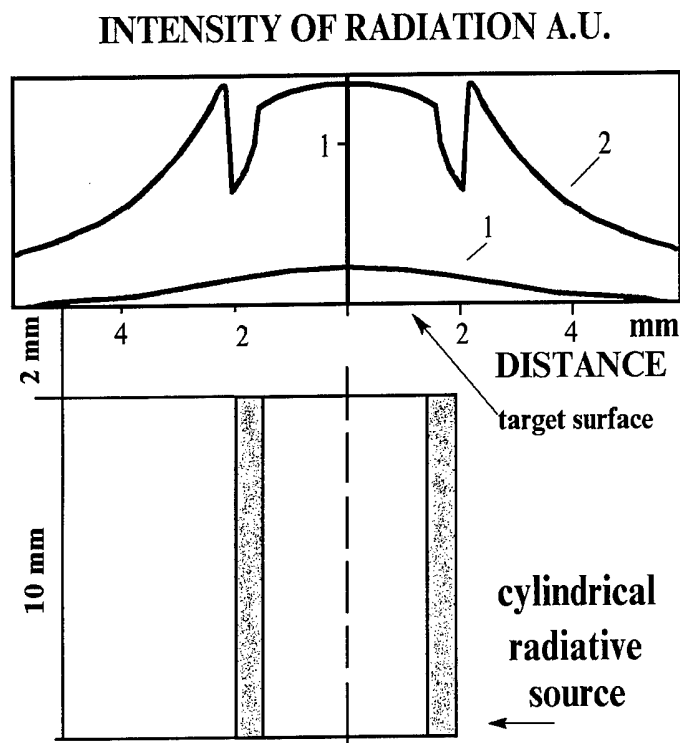


Fig. 2 Simulations of space distribution of the radiative power on the target: 1- volume radiation, 2- surface radiation.

Besides the measurements of the shock-wave velocities, the direct estimations of the shock compression size region were carried out. In these experiments, the regimes without the internal liner were used. As it is known, in iron under the pressures more than 13 GPa there exists a phase transition, which can be visible on the metallic surface. Fig. 3 shows such an imagination of the phase transition induced by the shock wave in our experiments. The pure iron target was positioned on the cathode, so the possible influence of the electron beams was excluded. One can see that in this experimental scheme, when only the external liner was compressed on itself, the typical radial radiative region size is

about 2 mm. One should note that in a standard double-liner scheme, this size is to be somewhat more. But the direct measurements in a standard scheme are impossible because of the target damage due to the strong radiative flux.

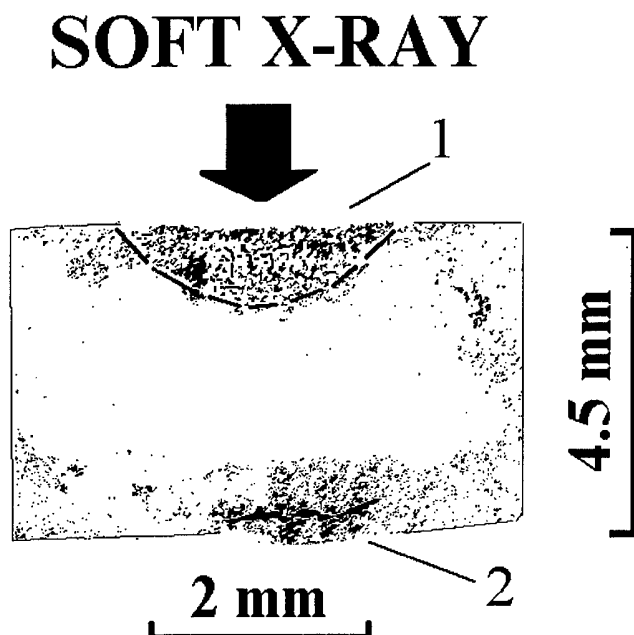


Fig. 3 Microphotography of polish section of pure iron target after intensive soft x-radiation interaction (power level  $0.5 \cdot 10^{12} \text{ W/cm}^2$ ) : 1- phase (a - e) transition region, pressure more than 13 GPa; 2 - split

### Conclusion

The results presented above show that uniform intense shock waves can be generated by Z-pinch soft x-ray plasma radiation. The uniformity of shock wave is very high. At a flux power about some  $\text{TW/cm}^2$ , a shock pressure of some hundreds GPa was achieved.

### REFERENCES

1. E. Grabovskij et al., JETP Lett., 60,3 (1994)
2. A. Bushman, V. Fortov. Sov. Tech. Rev. B Term.Phys., 1, 219, (1987)

## Dielectric-filled Radiofrequency Linacs

Rickey J. Faehl, Rhonald K. Keinigs, Edward W. Pogue  
*Los Alamos National Laboratory*

### ABSTRACT

High current, high brightness electron beam accelerators promise to open up dramatic new applications. Linear induction accelerators are currently viewed as the appropriate technology for these applications. A concept by Humphries and Hwang may permit radiofrequency accelerators to fulfill the same functions with greater simplicity and enhanced flexibility. This concept involves the replacement of vacuum *rf* cavities with dielectric filled ones. Simple analysis indicates that the resonant frequencies are reduced by a factor of  $(\epsilon_o / \epsilon)^{1/2}$  while the stored energy is increased by  $\epsilon / \epsilon_o$ . For a high dielectric constant like water ( $H_2O$ ), this factor, can approach 80. We have performed a series of numerical calculations of simple pill-box cavities. Eigenfunctions and resonant frequencies for a full system configuration, including dielectric material, vacuum beamline, and a ceramic window separating the two have been computed. These calculations are compared with the results of a small experimental cavity which we have constructed and operated. Low power tests show excellent agreement.

### Introduction

Radiofrequency linear accelerators (*rf* linacs) have long been the source for high energy, high brightness electron beams.<sup>(1,2)</sup> Such accelerators have generally been dismissed for intense, high current applications; high current beams can deplete the stored energy on time scales short compared with cavity filling times. Linear induction accelerators are usually the choice for high current applications. Humphries and Hwang<sup>(3)</sup> have suggested that *rf* linacs can be suitable for high current applications if the vacuum cavities of a conventional *rf* linac are replaced with dielectric-filled cavities. A small vacuum beamline is still required for electron transport, but the overwhelming volume of the cavity is composed of high dielectric constant material. Simple analysis indicated that the stored energy in the cavity will be greatly increased if  $\epsilon / \epsilon_o \gg 1$ . This concept was studied by Maggiore, et.al.<sup>(4)</sup> The lossy nature of most dielectrics suggests that steady operation will lead to severe heat management issues. For pulsed operation, however, we find that even moderately high gradients (1-10 MV/m) do not present major difficulties. In the present study we have conducted numerical studies to examine electromagnetic and beam loading issues and have constructed a small, low power cavity to test our models.

The analysis of a simple dielectric-filled pill-box cavity reveals the dominant characteristics of this concept. A circular cavity with radius  $R$ , length  $L$ , filled with a dielectric material which has a complex permittivity  $\epsilon = \epsilon_r + i\epsilon_i$  will resonate in  $TM_{mnp}$  mode. The frequency of these modes, in the limit that  $\epsilon_i \ll \epsilon_r$  is

$$\omega_{mnp} = \frac{K}{\sqrt{\epsilon_r \mu_o}} \left( \frac{1}{1 + (\epsilon_i / \epsilon_r)^2} \right)^{1/2} \quad (1)$$

where  $K = \left( \frac{X_{mn}^2}{R^2} + \frac{\pi^2 p^2}{L^2} \right)^{1/2}$ ,  $p = 0, 1, 2, \dots$  and  $X_{mn}$  is the zero of the Bessel function

of  $J_m(X_{mn}r)$  at  $r = R$ . The effect of dissipation in the dielectric is to reduce the cavity resonance by a frequency on the order of  $\delta\omega = \frac{1}{2}(\epsilon_i / \epsilon_r)^2$ . The portion of the  $Q$  due to losses in the dielectric is given by

$$Q_d = \frac{\epsilon_i}{\epsilon_r}. \quad (2)$$

There are other sources of electromagnetic energy loss, including wall losses, energy which couples back out the feed line, and energy dissipation due to beam loading. The total  $Q$  can be computed from  $Q^{-1} = \sum_{i=1}^N Q_i^{-1}$  if the component  $Q_i$ 's are known. The total energy stored in such a cavity is approximately  $\epsilon_r / \epsilon_0$  times that of a vacuum cavity. Total  $Q$  can be reduced by a factor as much as  $(\epsilon_i / \epsilon_r Q)$  over that of the same vacuum cavity, with  $Q_0$ .

For sustained high power operation, this low  $Q$  will present severe heat management problems. Temperature increase in the dielectric will result in time-dependent shifts in the cavity resonances. Eventually this temperature rise can lead to dielectric breakdown, phase change of the dielectric, or decomposition. Any of these effects will lead to system failure. These issues can be greatly mitigated if the cavity is limited to pulsed mode operation. This pulsed mode is the one that we feel offers significant advantages for high current, high gradient operations.

### **Numerical Methods**

The basic cavity analysis in this study was conducted numerically with a PC-based version of the SUPERFISH code,<sup>(5)</sup> CFISH. The basic cavity used was a pillbox cavity, filled with de-ionized water ( $H_2O$ ). The outer radius,  $R$ , is 0.178 m and the length is 0.178 m. In the initial set of calculations, the entire volume of the cavity was filled with water. The feed antenna was near the outer radius. All cavity wall material was taken to be aluminum.

A modification on the basic configuration which is felt to be closer to that of an actual accelerator was also studied. In this variant, a 0.01 m radius vacuum beam line was included along the z-axis. A 0.01 m thick ceramic window was added to separate the water and vacuum regions. Beam loading was not used in the CFISH calculations, because we have studied such effects in a series of a particle-in-cell calculations, which we describe below. The variant geometry is shown in Figure 1.

The dielectric properties of water, were extracted from Hasted.<sup>(6)</sup> Both temperature and frequency dependence for the complex permittivity were used. We did not account for nonlinear shifts in the permittivity.

Self-consistent loading and parasitic mode growth were studied in a series of calculations with our 2 1/2-D fully electromagnetic, relativistic particle-in-cell code.<sup>(7,8)</sup> In these axisymmetric calculations, the nonsymmetric portions of the cavity resonance spectrum were automatically excluded. Our initial calculations were very similar to the variant CFISH configuration, except that the outer radius is 0.1781 m and the beam line radius is 0.009 m. The cavity is pumped through an axisymmetric feed in the outer wall. This feed consists of a very low impedance coaxial line ( $Z_l = 1.4\Omega$ ) connecting to a radial line. This is a very low  $Q$  configuration, so a "fuse" is switched on after the cavity has reached steady state oscillation. This "fuse"

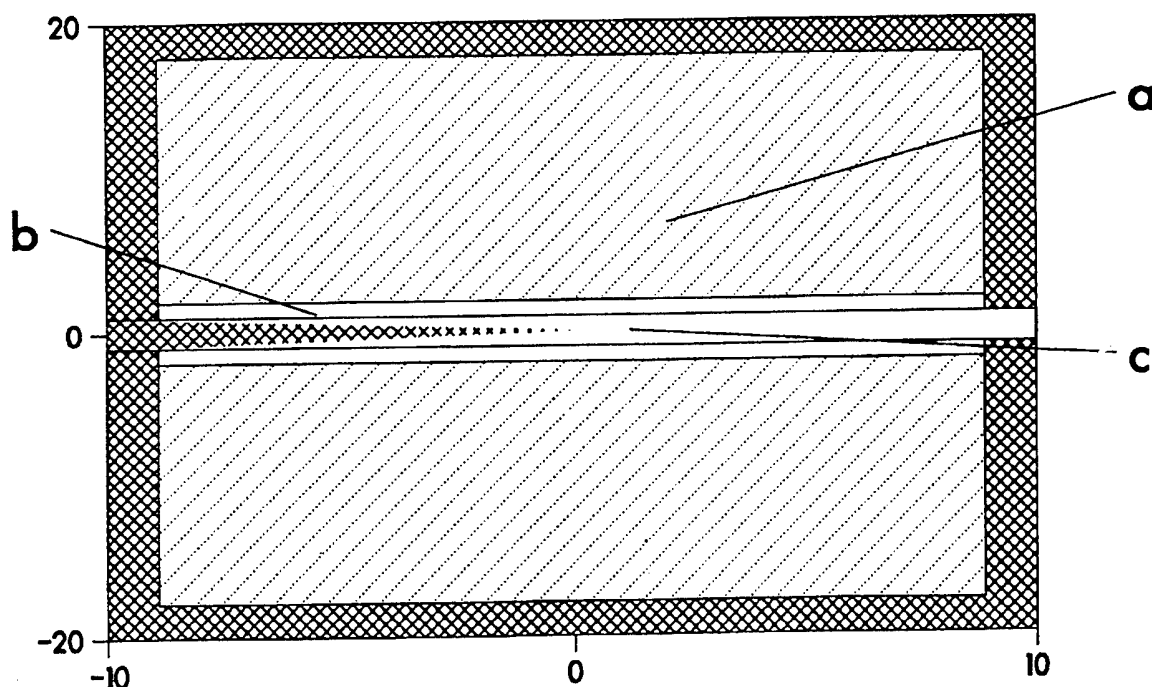


Figure 1. Configuration used for CFISH calculations; (a) dielectric (b) ceramic window, (c) vacuum beamline.

decouples the feed from the cavity. This resulting numerical cavity, with water at 20° C, has a  $Q$  of approximately 1100.

After the cavity has been rung up, an electron beam is injected into the system. Electron energy has been arbitrarily chosen so that  $\beta_z \gamma = 1.0$  (211. keV). Current in the beam has been varied from 1.0 Amperes to over 1.0 kiloamperes. No guiding magnetic field has been used in these initial calculations.

### Numerical Results

The CFISH calculations are summarized in Figure 2. Eq (1) is an excellent fit to the  $TM_{010}$  frequency. Inclusion of the vacuum line and ceramic window increases the resonant frequency, but only by about 1 Mhz for these conditions.

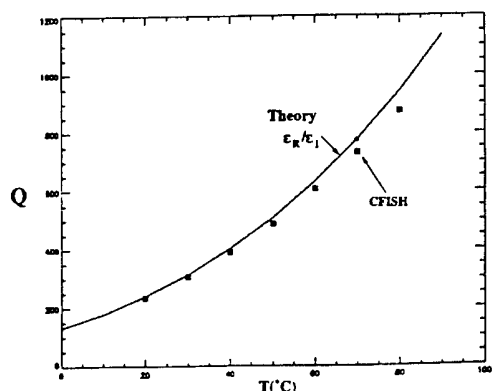


Figure 2. Comparison of cavity  $Q$  evaluated with CFISH (solid) and simple theory ( $\square$ ).

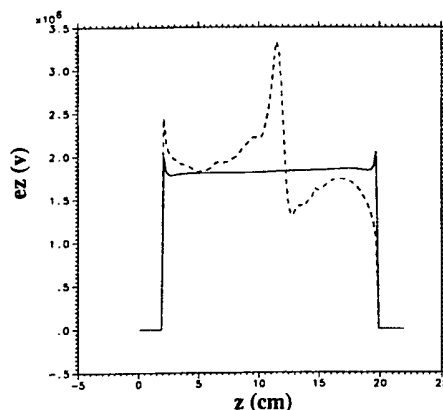


Fig 3 Comparison of electric field profile along the inner edge of the ceramics window before (solid) and after (dash) electron beam injection

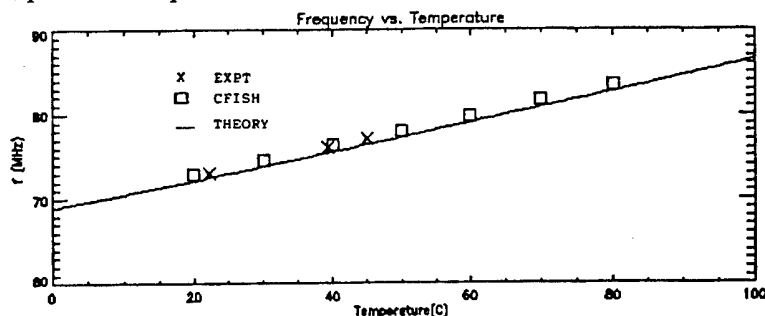
Figure 2 shows the comparison between the computed  $Q$  in CFISH, including wall losses with the simple assumption that  $Q$  is given by  $\epsilon_r / \epsilon_i$  of the dielectric material. At low temperatures, the  $Q$  is clearly dominated by losses in the water. By 80°C, these losses still comprise a major part of the total, but wall losses can no longer be neglected.

A solid dielectric window is needed to separate the vacuum beamline from the liquid dielectric medium. There are several potential issues associated with this window. Electrical breakdown, impedance mismatching, and charge build-up from stray beam impact can all severely effect cavity performance. PIC calculations illustrate the importance of charge build-up on the dielectric window, even for relatively low beam current. Figure 3 shows the difference in axial profiles of the  $z$ -component of electric field on the inner window surface after 0.83  $\mu$ s of electron beam injection (1.0A). The non-oscillatory component of  $E_z$  due to spacecharge, localized near  $z = 0.15$  m, has already reached magnitudes comparable to the cavity field at this time in the simulation. This calculation did not employ a magnetic field for beam transport, so beam loss to the window was exaggerated. High current beam transport can be afflicted with tenuous halos. We intend to obtain more quantitative bounds on this problem as we conduct further studies on beam loading effects.

Initial experiments have been conducted in a simple pillbox cavity. We used a 10 Watt variable frequency power supply to drive a loop antenna in a cavity with the same dimensions as are used in the CFISH calculations. A spectrum analyzer was employed to obtain the low order cavity resonances. The fundamental  $TM_{010}$  is of special interest because we wish operate the accelerator in this mode. Figure 4 shows the agreement between experimental data and CFISH calculations, as function of water temperature.

The present experimental and numerical studies are still at a preliminary phase. Numerically, we will explore beam transport and cavity loading issues. These calculations will continue to be conducted in close collaboration with the experimental effort. The experimental studies will concentrate on high power drivers, power dissipation in the dielectrics and breakdown issues.

**Figure 4.**  $TM_{010}$  frequency calculated in CFISH (solid) and measured in the experiment as a function of water temperature.



## REFERENCES:

1. Helmut Wiedemann, **Particle Acceleration Physics**, Springer-Verlag (Berlin) 1993.
2. Stanley Humphries, Jr, **Principles of Charged Particle Acceleration**, John Wiley and Sons (New York) 1986.
3. S. Humphries and C. S. Hwang, IEEE Trans. Nuc. Sci., NS-39, 2986 (1983).
4. C. J. Maggiore, A. M. Clogston, G. Spalek, W. C. Sailor, and F. M. Mueller, APL **64**, 1453 (1994).
5. K. Halbach and R. F. Holsinger, "SUPERFISH-A Computer Program for Evaluation of RF Cavities with Cylindrical Symmetry, Part. Accel. **7**, 213 (1976).
6. J. B. Hasted, **Aqueous Dielectrics**, Chapman and Hall, Ltd. (1973) London.
7. G. Gisler and M. E. Jones, Proc. 11th Int. Conf. on the Numerical Simulation of Plasmas, 1985 (Unpublished)
8. R. J. Faehl, B. DeVolder, and B. Wood, J. Vac. Sci. Technol. B, **12**, 884 (1994).

# OPERATION OF LIA-30 LINEAR INDUCTION ACCELERATOR IN THE MODE OF GENERATION OF TWO BREMSSTRAHLUNG PULSES

V.S.Bossamykin, A.I.Gerasimov, V.S.Gordeev, A.V.Grishin,  
V.P.Gritsina, A.D.Tarasov, A.S.Fedotkin, S.A.Lazarev, A.Ya.Averchenkov.

*RFNC-VNIIEF, Mira pr.37, Sarov (Arzamas-16),  
Nizhni Novgorod region, 607190, Russia*

## Abstract

For possibilities broadening of physical researches at LIA-30 linear induction accelerator ( $\sim 40$  MeV,  $\sim 100$  kA,  $\sim 30$  ns) there was studied a mode of its operation with the generation of two bremsstrahlung pulses separated by specified time interval from 0 to 5  $\mu$ s. In accelerating channel there was installed an additional tube cathode and a synchronization system for two accelerating modules groups triggering for the formation and acceleration in different initial time moment of two annular electron beams with different outer diameters was changed. A boundary energy of each beam electrons acceleration may be regulated and the boundary energy sum is  $\leq 40$  MeV.

## Introduction

LIA-30 - ironfree linear induction electron accelerator with  $\sim 40$  MeV energy,  $\sim 100$  kA beam current in  $\sim 30$  ns pulse duration [1]. LIA acceleration system is consisted of 36 modules with 4 inductors in each. Pulse high voltage of each two inductors is concentrated in accelerating gap formed by thin-walled hollow drift tubes. The tubes simultaneously serve as solenoid coils screens creating in vacuum channel the longitudinal magnetic field with  $\sim 0.5$  T intensity. At  $\sim 1$  ms field rise time the screens thickness doesn't interfere with the field pass through them. The screens aperture (except 4 screens at the beginning of acceleration system) is 0.43 m, the accelerating system length is  $\sim 23$  m (without the beam output device). Some results of transport and acceleration of high current electron beam research in LIA-30 in uni-pulse mode of bremsstrahlung generation are presented in [2].

## Design of accelerating system

For operating in two bremsstrahlung pulsed generation mode the accelerating system (AS) is separated into two parts; in each of them there take place the formation and acceleration of the annular electron beams of different diameters along the single longitudinal axis. The AS configuration version where the first part contains 15 modules together with the injector modules (# 1...4) and the second - 21 modules is given in fig.1. In the other version it is convenient to separate the AS into parts in 6:30, 10:26, 15:21, 26:10 modules ratio under the synchronization system operation optimum conditions [3]. The diode of first part is produced by the voltage adder from 4 injector modules and by the diode accelerating gap between the tube end of the stainless steel adder with 0.5 mm wall thickness and anode with diaphragm at 4 and 5 modules joint.

In AS second part the voltage from 3 modules is added; the diode gap is produced between the similar adder end and the anode diaphragm between 18 and 19 modules. Metal diaphragms are transparent for longitudinal magnetic field and serve for the beams collimation and protection of gaps between drift tubes from the scattered electrons. The

accelerated electron beams were transported behind the AS through the output device at the distance of 4.4 m up to a composite material on W powder basis 6 mm in thickness target, further bremsstrahlung passed through Plexiglas disc 70 mm in thickness and through Al 15 mm in thickness flange, separating the atmosphere air and vacuum volume.

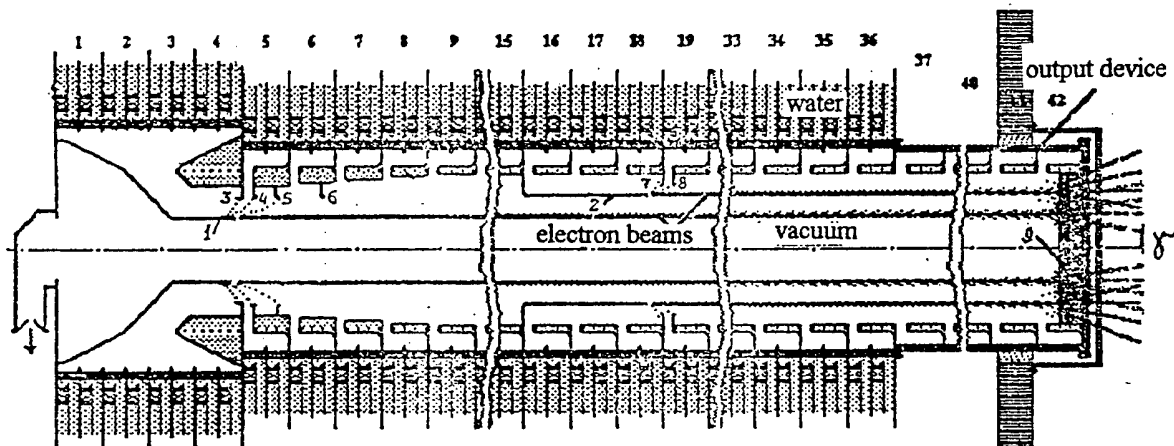


Fig.1. LIA-30 acceleration system scheme in two bremsstrahlung pulses generation mode. Numerals in the upper part of the figure means the ordinal numbers of the injector (1...4) and acceleration modules (5...36) as well as the modules along the axis extent of the beam output device solenoids (37...42). 1 - the first cathode; 2 - the second cathode; 3...6 - diaphragms in the AS first part; 7, 8 - diaphragms in the AS second part; 9 - target.

### The researches main results

Correspondingly 15 and 25 cm diameters of the first and the second tube cathodes for all the mentioned ratio of modules amounts in AS both parts appeared to be optima for maximum current pass of electron beams. For example, the use of the first cathode with diameter less than 15 cm reduced the first bremsstrahlung pulse dose characteristics. The use of 30 cm in diameter second cathode revealed the lower efficiency of the beam charge transportation to the target equal 70 %. The reduction of this cathode diameter up to 20 cm limits the current pass of the first beam at its diameter 15 cm. The diaphragms arrangements along the beamline and the holes diameters in them were experimentally found, based on the electrons minimum losses by the both beams and the bremsstrahlung maximum doses provision. In the first part of AS the holes diameters were 21 cm and in the second part - 30 cm.

The change range of  $\tau$  time interval between bremsstrahlung pulses from 0 to 5  $\mu$ s was evaluated. The electron acceleration was performed during the first voltage pulse durations generated by the modules of accelerating voltage. It is established that the second bremsstrahlung pulse is reproduced consistently at  $\tau \leq 1 \mu$ s. At  $\tau > 1 \mu$ s there begin to show the breakdowns of accelerated gaps in the AS modules second part; this is connected with the increase in channel operating rarefaction of  $\sim 1.3 \cdot 10^{-2}$  Pa of residual gases, released from the target under the action of the first beam and breakdowns of gaps in the first part of AS during the duration of the third and further pulses considerably reduced on amplitude of alternating



voltage. The typical parameters of the injected electron beams are: in the AS first part - 4 MeV, 75 kA, 32 ns (FWHM) in the second part - 3 MeV, 65 kA, 28 ns.  $D_1$  and  $D_2$  doses of the first and the second bremsstrahlung pulses measured at 1 meter from the target depending on K ratio of acceleration modules in the AS first and second parts at autonomous triggering each of AS parts are given in Table 1. Relatively low  $D_1$  values are explained by electron energy losses at their drift through the second part of AS [2]. The availability of cavity between the drift tubes and water isolation boundary in inductors leads to inductances excitation on them retarding the pulse potentials achieving the amplitude values from 40 to 160 kV in each module.

The results of two pulse operation mode of LIA at  $K=15:21$  for some  $\tau$  values are given in Table 2. One can see that at  $\tau \geq 1 \mu s$   $D_2$  dose begins to decrease essentially. Bremsstrahlung pulses oscillograms in LIA two pulses operation mode are shown in fig.2.

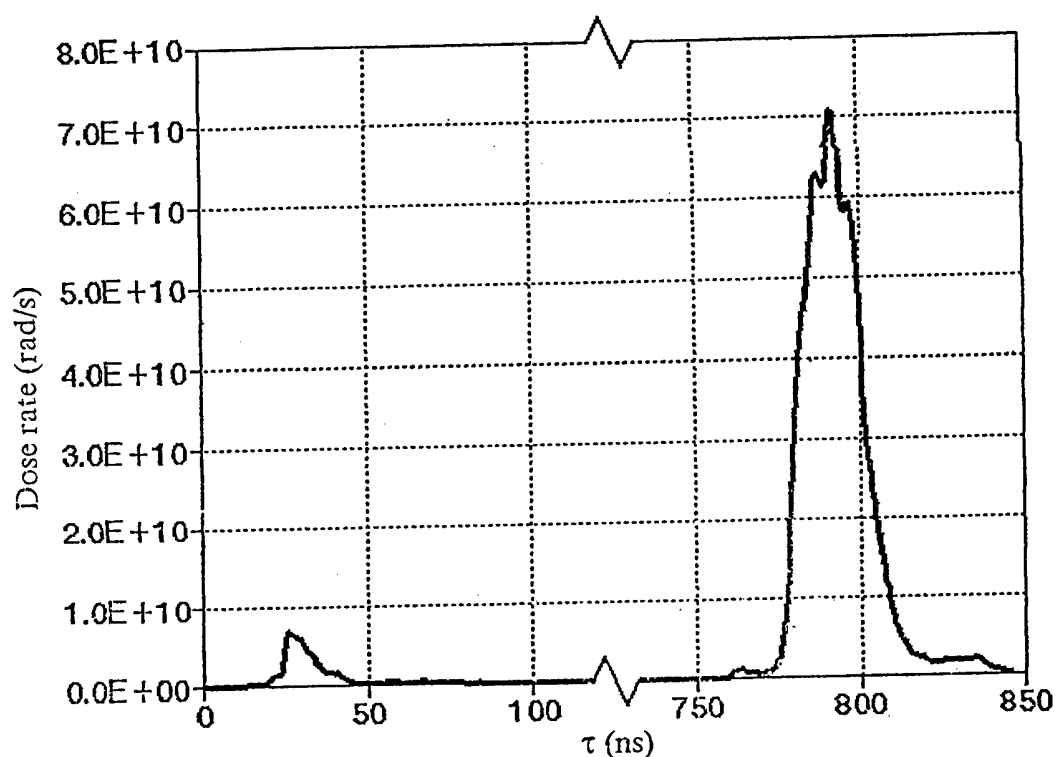


Fig.2 Bremsstrahlung pulses shapes at  $K=15:21$ .

Table 1

K	$D_1$ , rad	$D_2$ , rad
6:30	25	3200
10:26	100	2900
15:21	350	2600

Table 2

$\tau$ , $\mu s$	0.3	0.6	0.9	1.8	5
$D_1$ , rad	350	350	350	350	350
$D_1/t \cdot 10^{11}$ , rad/s	0.35	0.35	0.35	0.35	0.35
$D_2$ , rad	1300	2200	1300	500	200
$D_2/t \cdot 10^{11}$ , rad/s	0.6	1.2	0.6	0.2	0.1

## Conclusion

The obtain in LIA-30 accelerator of two coaxial beams of accelerated electrons separated by the controlled time interval with the possibilities to change the electrons energy in beams and the corresponding generation of two separated bremsstrahlung pulses broadening the accelerator possibilities and it is used for of physical researches performance. Bremsstrahlung pulses shape may be modified by time program of mutual operation of acceleration modules in AS parts. In should be mentioned that the given method of LIA operation allows to obtain three or more separated bremsstrahlung pulses.

[1] Pavlovskii A.I., Bossamykin V.S., Gerasimov A.I. et al. :BEAMS 92. 9-th Intern. Conf. on High - Power Particle Beams, 1 (1992) 273

[2] Bossamykin V.S., Veresov V.P., Gerasimov A.I. et al. : VEAMS 96. 11-th Intern. Conf. on High - Power Particle Beams, (1996)

[3] Pavlovskii A.I., Tananakin V.A., Grishin A.V. et al. : 9-th IEEE Intern. Pulsed Power Conf., 2 (1993) 913

## X-RAY RADIATION SOURCE BASED ON PLASMA FILLED DIODE

N.F. Popkov, V.I. Kargin, E.A. Ryaslov, A.S. Pikar'

*All-Russia research institute of experimental physics (VNIIEF), Arzamas-16, Nizhni Novgorod region, 607190, RUSSIA*

*The paper gives the results of studies on a plasma X-ray source, which enables one obtain 2.5 krad of a radiation dose per pulse over an area of 100 cm<sup>2</sup> in the quantum energy range from 20 to 500 keV. Pulse duration is 100 ns. Spectral radiation distribution under various operation conditions of plasma a diode are obtained. A Marx generator served as an initial energy source of 120 kJ and discharge time of  $T/4=10^{-6}$  s. A short electromagnetic pulse ( $10^{-7}$  s) was shaped using plasma erosion opening switches.*

1. The most easy and reliable method to sharpen an electromagnetic pulse is to use plasma erosion opening switches (PEOS). This method does not require a "fast operating" capacitor bank [1]. In this method the energy stored in a "slow operating" capacitor bank is converted into a magnetic inductance energy, which is switched to a load. When an inductive storage circuit of breaks, a short electromagnetic pulse is generated which is delivered into a load. PEOS operation is based on the property of a high-current discharge in a plasma to increase resistance sharply, when the current reaches a critical current [2]. Because of the fact that power increase is followed by significant voltage increase, the generators based on PEOS have found wide application in accelerator engineering aimed at generating electron beams and X-ray bremsstrahlung pulses. The work presents the results of studies on the "PLASMA X-RAY" pulse generator. The parameters of the generator are:  $V=1$  MV,  $I=250$  kA,  $W=120$  kJ.

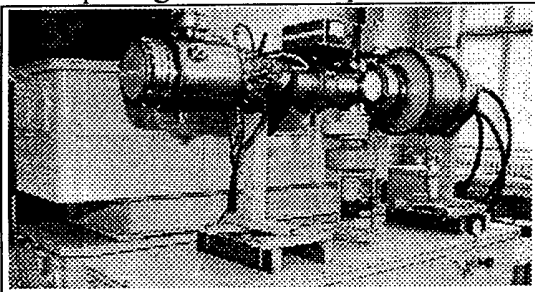


Fig. 1. The general view of the radiation source.

2. The radiation source is shown in Fig. 2. Three Marx generators served as initial energy storage connected in parallel. The total capacity of the generators is 0.96  $\mu$ F, inductance is 0.25  $\mu$ H. The stored energy with 100 kV of the charging voltage is 120 kJ [3]. The output voltage of five cascades generator is 500 kV. When a circuit of an inductive storage breaks, a pulse of 1 MV amplitude is generated. The output of Marx generator is connected to a

collector 2 of inductive storage using transmission line. The transmission line included three KVI-500 cables, its total inductance is 0.25  $\mu$ H. The inductance of a transmission line up to PEOS is 0.72  $\mu$ H. Time for discharge current in line is 6  $\mu$ s, the current amplitude is 400 kA. With nine cables the period for discharge current is 4  $\mu$ s. The vacuum portion of a storage is separated from a collector by a polyethylene insulator 3 with a diameter of 45 cm. Six coaxial plasma guns 4 of a surface-erosion type are located at a distance of 120 cm from an insulator. The radial velocity and the density of plasma created by this gun are 7cm/ $\mu$ s and  $10^{13}$  cm<sup>-3</sup> respectively. The discharge current amplitude in gun's circuit is 20 kA. The vacuum line is a coaxial one. It consists of a number of sections 5, connected by adapting rings 6, where inductive current probes 7 are located. The external coaxial diameter is 214 mm, internal one is 80 mm. At the end of the line a target 8 and a voltage divider 9 are located. To prevent the

insulator from being illuminated by PEOS plasma and to protect it from target evaporation products it is shielded by a dielectric disk 10 and a set of metal washers 11.

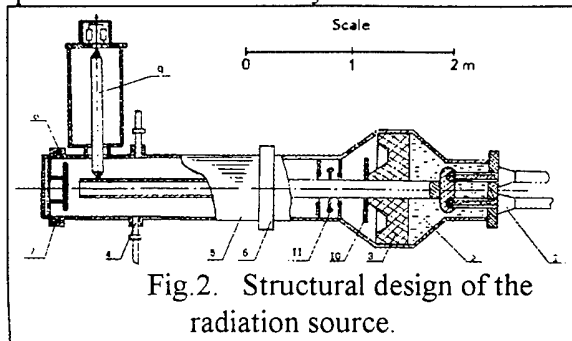


Fig. 2. Structural design of the radiation source.

The facility operates the following way. After the Marx generator and capacitor bank, which powers plasma guns, have been charged, the capacitor bank is triggered and plasma is injected into the gap of the vacuum inductive storage line. After a delay time  $t_d$ , which is necessary to fill a gap with plasma and create the necessary density, the Marx generator fires and the inductive storage contour is closed via PEOS. When the critical current is reached, a

sharp increase of plasma resistance takes place and the energy is transferred into a load. The source can work in regime one pulse per minute.

3. In the first experiments we used a vacuum diode as a load. The distance from a PEOS to diode is 90 cm, a cathode radius  $r_k$  is 20 mm, the cathode-anode gap changes from 5 to 30 mm. Voltage on a diode measured by a resistive voltage divider is 1.4 MV. The maximum beam current does not exceed 50 kA. The beam is formed by hollow cathode, the structure of which has been retained. In order to measure X-ray radiation, thermoluminescent dosimeters (TLD) were used. They were located at the distance of 50 mm from a tantalum target with the thickness of 100  $\mu\text{m}$ . The maximum X-ray dose reached 3 krad per pulse. X-ray pulse duration recorded by p-i-n diodes is 100 ns. The average quantum energy in the radiation spectrum of a vacuum diode is 400 keV. At the absence PEOS the voltage on the vacuum diode is 500 kV, current is 25 kA and X-ray dose is 300 rad.

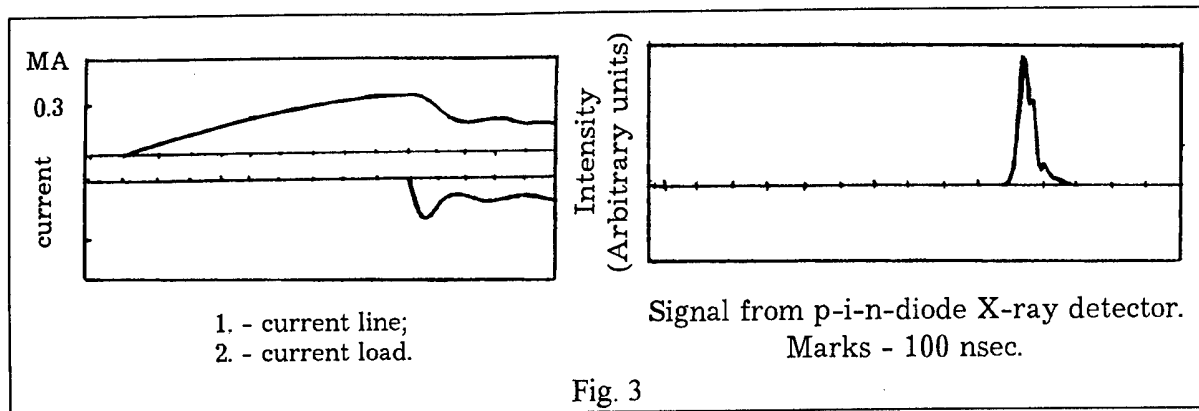
An erosion track, left on the center electrode of the vacuum inductive storage section when plasma is shifted by the effect of the force  $\vec{F} = [\vec{j} \times \vec{B}]$ , had the length about 70 cm. This value agrees with the calculated value, when PEOS critical current  $I_c$  is 300 kA given by [2]

$$I_c = \sqrt{M_i / Z m_e} n_i Z e V_F 2 \pi r_k l, \text{ here} \quad (1)$$

$M_i$ ,  $m_e$ -ion and electron mass,  $Z$ - ion charge,  $n_i$ -plasma density,  $V_F$ -flow velocity,  $2 \pi r_k l$ - switch area. The ion species is composed mostly of doubly ionized carbon ions  $C^{++}$  and its velocity was defined in preliminary experiments  $V_F \approx 6 \cdot 10^6$  cm/s. From (1) can be obtained the value of entire plasma mass per length unit  $m_p = M_i n_i 2 \pi r_k l$ . We solved the plasma motion equation under the force  $\vec{F} = [\vec{j} \times \vec{B}]$  and the shift length  $L_{\text{shift}} \approx 70$  cm was obtained. It is consistent with observed value.

In the following experiments one portion of an inductive storage was disassembled and the distance from the PEOS to a load was reduced to 45 cm. During the time required to power the inductive storage (1.4  $\mu\text{s}$ ) plasma reached the load, filled the interelectrode gap and plasma diode was formed.

In this case diode current increased and reached the value 70-80% of storage current (Fig. 3). The presence of hard X-ray bremsstrahlung confirms that there is an electron beam in plasma. Cathode diameter change did not significantly effect the diode current. At the same time the change of the gap length between a cathode and anode leads to current and X-ray yield. Table 1 gives the results of the experiments for two values of the cathode-anode gap with various delay times and voltages of PEOS powering.



In all pulses, when time delay or PEOS voltage increases, the moment of current transfer into a load is shifted to later times. When  $t_d \approx 9.5 \mu s$  and  $V_{PEOS} \approx 80 \text{ kV}$  the current transfer moment comes far beyond maximum of the storage current. It is associated with plasma density increase and hence PEOS critical current. As storage current does not increase any more, the moment of transfer comes only when plasma disperses. In doing so X-ray dose drops sharply. The maximum X-ray dose, measured using TLD at the distance of 50 mm from a target, reached 2.5 krad.

Gap (cathode-anode), mm	8	8	27	27
$U_{PEOS}$ , kV	60	60	80	80
Time delay $t_d$ , $\mu s$	4.5	6.0	4.5	6.0
Storage current, kA	225	290	275	310
Load current, kA	205	220	205	255
Time of current transfer, $\mu s$	1.1	1.3	1.4	1.7
Radiation energy, J	90	270	230	55

To define spectral X-ray composition we used TLD spectrometer, comprising seven detectors based on aluminum phosphate glass with copper filters of various thickness. Detectors were located in an aluminum casing of the spectrometer at a radius

of 45 mm. The spectrometer was calibrated by choosing a spectrum and comparing an absorption line, obtained on the basis of this spectrum, with the experimental curve. Fig. 4 gives spectral X-ray distributions with various time delay. Energy estimation in the range from 50 to 500 keV is 90 J for  $t_d = 4.5 \mu s$  and 270 J for  $t_d = 6 \mu s$ . In other case, when the plasma is injected to a gap of a diode, the radiation energy (5 keV) is 1 kJ.

4. When measuring the soft X-radiation, we used one Marx generator and slightly changed the target design. The hollow cylindrical anode was attached to the metal hollow cone connected to the reverse current conductor. In the end of the line the dielectric flange was installed. The hole in the anode was shielded by the tantalum foil with the thickness of 20  $\mu m$ .

In the first pulse the line current amplitude reached 160 kA, while that of the load current-140 kA. In further pulses the foil evaporated, the hole was formed and with its increase the load current was rising. In Fig. 5 the set of oscillograms is given as to three sequential pulses, as well as the signal from the X-ray detector with the titanium filter (30  $\mu m$ ). In distinction from Fig. 3 the above mentioned signal duration is 200 ns and the long attenuation is observed. In this case the load current was increased more than twice and the line current at that moment rose insignificantly 10-15% of its amplitude.

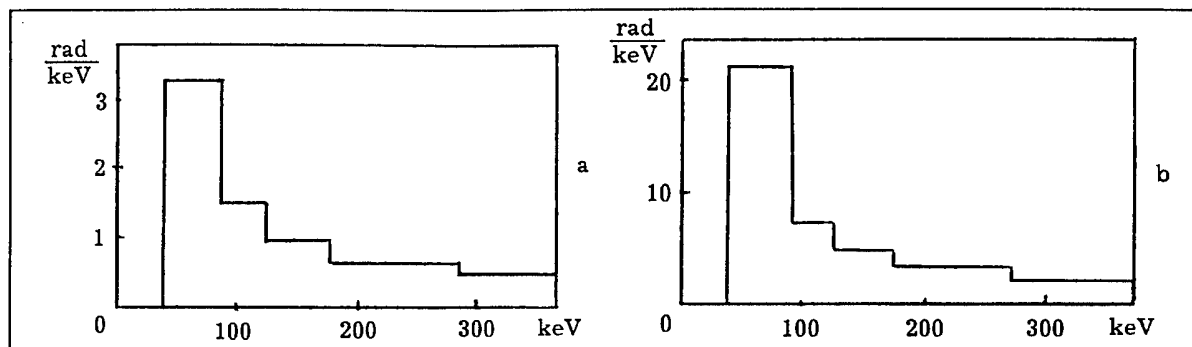


Fig. 4. Spectral X-ray distribution with various time-delays:

a -  $t_d = 4.5 \mu s$ ,  $V_{PEOS} = 60 kV$ ; b -  $t_d = 6 \mu s$ ,  $V_{PEOS} = 60 kV$ .

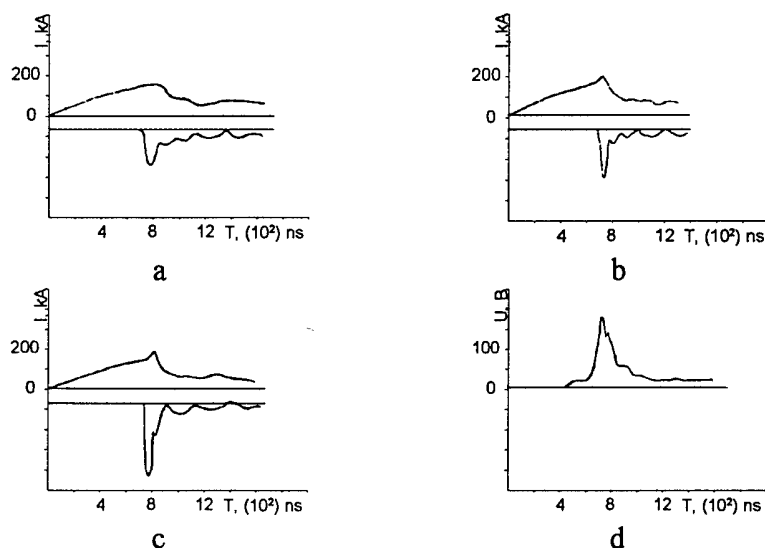


Fig. 5 Current pulses (a, b, c) and X-Ray pulse (d).

We believe that the load current increase is associated with the magnetic field topology change and formation in plasma of metastable current layer accumulating excessive magnetic field energy. In the course of this layer explosive damaging the magnetic fluxes are compressed in the contours, resulting in the current increase there. The line circuit inductance is much higher than that of the load circuit and changes rather slightly. So, the line current changes insignificantly. Formation and disintegration of such current layers in plasma are described in the article by A. G. Frank [4].

- [1]. Meger R.A. et al, Appl. Phys. Lett, v. 42, p. 943, (1983).
- [2]. Ottinger P.F. et al, J. Appl. Phys., v. 56(3), p. 774, (1984).
- [3]. V.S. Bossamykin, A. I. Gerasimov, A.I. Pavlovskii et al, "System of 500 kV Marx generators for LIA-30 radial line charging", 9-th IEEE Int. Pulse Power Conference, Albuquerque, NM (USA) 21-23 June 1993, Springfield, VA, NTIS, 1993, v. 1 pp. 993-995
- [4]. A.G. Frank, J. "Plasma Physics and Plasma Electronic Engineering, v. 160, p.93, Works of FIAN, M, "Nauka" Publisher, 1985.



## AUTHOR INDEX



NNNN - First Author  
NNNN - Presenting Author  
NNNN - Co-author 1-48

Abdallah Jr., J.	687				Bondarenko, G.G.	840				
Abdallah, C.T.	433				Bonnafond, C.	628				
Abubakirov, E.B.	410				Borisov, V.V.	526				
Adachi, T.	52				Borovina, D.L.	928				
Adams, R.G.	1	48			Borovkov, V.V.	296				
Afonin, V.I.	691	697	701		Bossamykin, V.S.	619	640	938		
Agafonov, M.A.	182	213			Bowman, C.D.	139				
Agalakov, V.P.	301				Branitski, A.V.	140	292	526	530	534
Agee, F.J.	928				Bratman, Vi.L.	401				542
Alberts, T.E.	37				Breeze, S.F.	150				
Alfverov, D.F.	999				Breeze, S.P.	37				
Aliaga-Rossel, R.	762				Bruns, C.	753				
Alley, W.E.	753				Bryunetkin, B.A.	1075				
Allshouse, G.A.	37				Brzosko, J.S.	131				
Allshouse, G.O.	146				Bugaev, S.P.	905				
Anderson, D.E.	1171				Bulan, V.V.	942				
Anderson, J.	238				Bulgakov, T.	917				
Ando, R.	331	339	351	393	Burdakov, A.V.	182				
Andreiev, A.	267	793	809		Burenkov, O.M.	1084				
Andronov, A.N.	485				Burkov, P.V.	1221				
Anfinogentov, V.G.	381				Burmasov, V.S.	335	1046			
Anthouard, P.	628				Butenko, V.I.	64				
Aoki, T.	501				Buth, L.	1123	1127	1155	1257	
Appartaim, R.K.	111				Buzin, V.N.	538	558			
Apruzese, J.P.	146	749			Bystrickii, Vit.	127	917	1217	1221	
Arad, R.	41	1039	1216		Bystricky, V.	917				
Aranchuk, L.	276				Bystruckii, V.M.	886				
Arkhipov, A.V.	319	371	789		Campbell, M.M.	882				
Arzhannikov, A.V.	182	213	367	1127	Carlson, A.L.	37	48			
Astrelin, V.T.	182				Carlson, R.L.	188				
Attelan-Langlet, S.	1064				Carmel, Y.	405				
Aubert, J.H.	37				Caryotakis, G.	406				
Aurass, H.	1031				Cassany, B.	276				
Auvray, P.	276				Castle, M.	238				
Averchenkov, V.Ya.	296	619	640		Cengher, M.	599				
Avrillaud, G.	276				Chagin, M.N.	182				
Azharonok, V.V.	797				Chaikovski, S.	917				
Babineau, M.A.	121				Chamdani, E.P.A.	898				
Baca, P.	37				Chandler, G.A.	1	37			
Baca, P.M.	37				Chedia, O.V.	1035				
Bachmann, H.	1123				Chen, Ch.	1018				
Bailey, J.E.	1	37	48		Cheng, D.	924				
Bailey, V.L.	60				Cheng, J.	238				
Bakshaev, Yu.L.	962				Chernenko, A.S.	154	962			
Bakst, R.B.	522				Chernikov, E.V.	873				
Balakirev, V.A.	426	611			Chernykh, E.V.	457				
Bangerter, R.O.	91				Chernyshev, V.K.	7	538	558	1008	1084
Baranowski, J.	737				Chernyshev, V.V.	158				
Barber, T.L.	37				Chigrinov, S.	921				
Bardy, J.	628				Childers, K.	1003				
Barinov, N.U.	301				Ching, C.H.	48				
Barnard, J.J.	91				Chishiro, E.	27	1163			
Bauer, W.	1123	1155			Chittenden, J.P.	741				
Baumung, K.	72				Chlenov, A.M.	671	675			
Bayol, F.	276	1203			Chmielewski, A.G.	824				
Belenki, G.S.	301				Cho, S.O.	453				
Benattar, R.	771				Choi, P.	276	305	505	509	566

Cohn, D.	249					Faenov, A. Ya.	683	687	1075	
Collier, J.	271					Fainberg, Ya.B.	229			
Collins, C.B.	928					Farny, J.	271			
Colombant, D.	206					Favre, M.	305	<u>505</u>	566	<u>570</u> <u>574</u> <u>679</u>
Commisso, R.J.	121	749					762			
Cook, D.L.	1	37				Fedotkin, A.S.	640			
Cooperstein, G.	115	<u>1147</u> <u>1151</u>				Fedulov, M.V.	140	542		
Corcoran, P.	150	989				Fedyunin, A.V.	522			
Csanak, G.	687					Fehl, D.L.	37			
Cuneo, M.E.	1	101	1054			Fernsler, R.	206			
Dan'ko, S.	550					Fessenden, T.J.	91			
Danilenko, K.N.	292					Filatov, A.L.	<u>909</u>			
Danilenko, K.V.	140					Filatova, I.I.	<u>797</u>			
Danilov, V.V.	<u>1027</u>					Filius, P.G.	121	284		
Darzneĳ, S.A.	<u>1241</u>					Filipowicz, M.	917			
Datsko, I.M.	522					Filuk, A.B.	1	<u>48</u> <u>1115</u>		
Davanloo, F.	<u>928</u>					Fink, Y.	1018			
Davara, G.	41	1058	<u>1063</u>			Fisher, A.	749			
Davidson, R.C.	1018					Fisher, R.C.	115			
Davis, H.A.	<u>263</u>	890	894			Fisher, V.	1063			
Davis, J.	705	<u>709</u>	757			Foerster, E.	733			
Davlatjan, T.A.	<u>832</u> <u>836</u>					Fortov, V.E.	140	<u>292</u>	449	457 632 653
De Groot, J.S.	721	753					<u>1119</u> 1269			
De Mascureau, J.	628					Frank, K.	603			
Decker, G.	174	659				Frescaline, L.	276			
Deeney, C.	1	150				Friart, D.	550			
Degnan, J.H.	131	158	558			Friedman, M.	<u>206</u>			
DeGroot, J.S.	146					Frolov, I.N.	140	<u>526</u>	534	542
Deichuly, M.F.	<u>221</u>					Frolov, V.	276	<u>1211</u>		
Delsart, P.	628					Fruchtman, A.	1229			
Demidov, B.A.	1269					Fuchs, M.I.	<u>410</u>			
Demin, A.N.	1084					Funatsu, M.	52			
Dempsey, J.	1003					Furukawa, H.	1103			
Denisenko, P.V.	182					Gahl, J.M.	433			
Denisov, Yu.A.	817					Galakhov, I.V.	<u>946</u>	<u>950</u>	977	<u>981</u>
Deniz, A.V.	627					Gale, D.G.	131			
Deryugin, Yu.N.	<u>192</u>					Garafov, A.M.	691			
Derzon, M.S.	1	37				Garanin, S.F.	558	1084		
Desjarlais, M.P.	1	48	<u>101</u>			Gasheev, A.S.	946	950	977	
Destler, W.W.	405					Gasque, A.M.	<u>550</u>			
Deulin, Yu.I.	182					Gass, V.G.	473			
Deutsch, C.	<u>1103</u>					Gavrilov, N.W.	<u>844</u>			
Devin, A.	628					Georgescu, N.	<u>582</u> <u>591</u>			
Devlin, D.J.	993					Gerasimov, A.I.	<u>619</u> 640			
Didenko, A.N.	<u>445</u> <u>449</u>					Gerber, K.A.	627			
Diyankov, O.V.	697	<u>713</u>	717	725	<u>775</u>	Gerusov, A.V.	140			
Diyankov, V.S.	<u>309</u>	958	969			Giese, H.	95	1107	1111	
Dolgachev, G.I.	301	<u>1207</u>				Gilgenbach, R.	<u>347</u>			
Doroshkin, A.A.	1195					Gilliland, T.L.	37	146	753	
Douglas, M.R.	37	146	150			Ginzburg, N.S.	213	<u>242</u>	<u>245</u>	<u>496</u>
Dudin, I.F.	1084					Girka, I.O.	323			
Dukart, R.J.	1	37				Girka, V.O.	<u>323</u>			
Dumitrescu-Zoita, C.	276	305	574	679		Giuliani Jr., J.L.	709	<u>757</u>		
Dyabilin, K.E.	140					Glazyrin, I.V.	697	713	<u>717</u>	725 775
Dyabilin, K.S.	292	<u>632</u>	<u>653</u>			Glidden, S.C.	1171			
Ebine, T.	52					Goel, B.	<u>23</u>	1253		
Eddleman, J.L.	146	721	753			Goertler, A.	603			
Efremov, V.P.	<u>1269</u>					Gofman, Yu.I.	<u>801</u> <u>805</u>			
Emic, J.	753					Gogolewski, P.	737			
Emlin, D.R.	844					Golubev, A.	271			
Endou, T.	1265					Gomberoff, K.	<u>1215</u>	1216		
Engelko, V.	<u>95</u>	267	<u>793</u>	809	<u>1107</u> <u>1111</u>	Gondarenko, N.A.	<u>745</u>			
Ermakov, A.E.	473					Gonzales, A.	886			
Etllicher, B.	<u>276</u>	758	<u>1064</u>	1199	1203 1211	Gorbachev, K.V.	445	449	457	
	1237					Gorbics, S.G.	1071			
Eyharts, P.	628					Gorbulin, Yu.M.	154	550		
Eyl, P.	628					Gordeev, A.V.	<u>1131</u> <u>1135</u>			
Eylon, S.	91					Gordeev, V.S.	619	640	<u>938</u>	
Faehl, R.J.	275	<u>636</u>				Goyer, J.R.	121	1003		

Grabovskii, E.V.	140	292	526	<u>534</u>	542	<u>546</u>	Igarashi, H.	351											
	632	653	942				Ikeda, A.	339											
Grabowski, C.T.	433						Ilyin, V.N.	485											
Graham, J.D.	131						Imada, G.	27											
Granatstein, V.L.	238	405					Imanari, K.	27	<u>1167</u>										
Grebenyuk, V.	917						Ionov, A.I.	558											
Grechikha, A.V.	<u>1139</u>						Ishihara, O.	481											
Greenly, J.B.	81	<u>111</u>	263	1054	1143	<u>1171</u>	Ivanov, B.I.	64											
Greenly, J.M.	115						Ivanov, V.A.	1008											
Gregorian, L.	41	<u>1058</u>	1063				Ivanov, Yu.F.	873											
Grekhov, I.V.	981						Ives, H.	989											
Gribov, A.N.	<u>942</u>						Ivonin, I.A.	1269											
Grigor'ev, S.V.	1217	1221					Ivonin, I.V.	1068											
Grigoriu, C.	27	<u>898</u>					Iwasaki, H.	1179											
Grigoryev, V.P.	1221						Jacquet, L.	550											
Grinevich, B.Ye.	<u>538</u>	558					Jayness, R.	347											
Grishin, A.V.	619	<u>640</u>					Jeong, Y.-U.	453											
Gritsina, V.P.	640						Jiang, W.	27	<u>477</u>	<u>890</u>	894	1167							
Grua, P.	550						Jobe, D.O.	37	146	150	753								
Grushin, I.I.	869	873					Johan, A.	276											
Grusin, I.A.	<u>946</u>	950	977	981			Johnson, D.J.	1	37	101									
Gryaznov, V.K.	23						Jones, T.G.	115											
Gubanov, V.P.	<u>965</u>						Jongewaard, E.	406											
Gudov, S.N.	946	<u>950</u>	977	981			Kahniashvili, T.A.	1035											
Guilhelm, D.	628						Kalachnikov, V.V.	832	836										
Gula, A.	917						Kalashnikov, M.P.	1075											
Gullickson, R.L.	284						Kalinin, Yu.G.	154	550	<u>1050</u>	1207								
Gurashvili, V.A.	797						Kalynov, Yu.K.	<u>401</u>											
Gurin, V.E.	158						Kamada, K.	331	339	<u>351</u>	393								
Gurko, V.F.	327						Kaminski, A.A.	245											
Guth, H.	1155						Kaminski, A.K.	245											
Haill, T.A.	1						Kamiya, T.	52											
Hakoda, M.	355						Kandaurov, I.V.	<u>327</u>	335										
Hammer, D.A.	81	683	687	1054	1143	1171	Kanel, G.I.	72											
Hammer, J.H.	146	<u>178</u>	<u>554</u>	<u>721</u>	753		Kargin, V.I.	158	192	296	<u>644</u>	656	663						
Han, M.	578							667											
Hanamori, S.	355						Karlický, M.	<u>1031</u>											
Hanson, D.L.	1	1115					Karlykhanov, N.G.	717	<u>725</u>	775									
Hasegawa, D.	351						Karmanov, F.I.	623											
Hasegawa, J.	<u>1179</u>						Karpova, I.G.	844											
Haserath, H.	271						Kasuya, K.	<u>52</u>											
Hashimoto, Y.	<u>848</u>						Kataev, V.N.	158											
Hatfield, L.L.	469	607					Kato, S.	355											
Hebert, M.P.	284						Kaufman, Y.	<u>509</u>											
Hebron, D.E.	37						Kawada, M.	339											
Heine, F.	<u>603</u>						Kawakita, Y.	355											
Hellmann, A.	1155						Kawasaki, S.	1179											
Henins, I.	275						Kawata, S.	<u>355</u>	<u>781</u>	<u>1245</u>	<u>1249</u>								
Herleb, U.	<u>68</u>	<u>1191</u>					Kazakova, I.F.	192											
Hernandez, J.	753						Keeler, N.	1269											
Hinshelwood, D.D.	<u>115</u>						Keinigs, R.K.	636											
Hiraoka, K.	<u>1022</u>						Kekez, M.M.	<u>954</u>											
Hirota, K.	1245	1249					Kellogg, J.C.	749											
Hochman, J.M.	347						Kellogg, J.W.	37											
Hoebel, W.	23	1253					Kharlov, A.V.	<u>1217</u>	1221										
Hoffman, D.	1119						Khilchenko, A.D.	182											
Hoffman, D.H.H.	603						Khmara, V.A.	485											
Hogan, B.	238						Khryapov, P.A.	905											
Holmberg, C.D.	131						Kiefer, M.L.	1											
Hoppé, P.	72	1123	1127	<u>1155</u>	1257		Kies, W.	174	659										
Horioka, K.	501	1022	1179	1265			Kievitskaya, A.	921											
Hosokai, T.	<u>501</u>						Kim, A.A.	127	276	1203									
Hotta, T.	1095						Kingsep, A.S.	154	550	<u>729</u>	1207	<u>1225</u>							
Hubbard, R.	206						Kingsley, L.E.	928											
Huetner, R.	1257						Kirillov, G.A.	977											
Hunt, J.W.	263						Kiuttu, G.F.	<u>131</u>	158	558									
Hurst, M.J.	37						Klyachkin, Yu.	<u>852</u>	<u>853</u>										
Hussey, T.W.	558						Knyazev, B.A.	<u>1054</u>	1143	<u>1195</u>									
Ido, D.	52						Koba, Yu.V.	154											



Maenchen, J.E. 882  
 Magda, I.I. 422  
 Mahrin, V. 917  
 Makarov, A.G. 182  
 Makartsev, G.F. 158 296  
 Mako, F. 437  
 Mankowski, J. 607  
 Mann, G. 1031  
 Manuilov, V.N. 385 401 485  
 Marder, B.M. 1 146 753  
 Markov, P.I. 426  
 Maron, Y. 41 48 146 1039 1058 1063  
 1215 1216 1229  
 Marshall, T.C. 397  
 Marten, H. 23 1253  
 Martin, T.H. 150 989  
 Martinez, C. 37  
 Martynenko, V.A. 981  
 Maslov, G.N. 619  
 Massier, H. 1123 1155  
 Masuda, W. 27  
 Masugata, K. 27 477 898 1010 1163 1167  
 Masuzaki, M. 196 331 339 351 393  
 Matsubara, H. 973  
 Matsushita, A. 973  
 Matsuzawa, H. 973  
 Matveenko, A.N. 1195 1127  
 Matvienko, V.M. 873  
 Matzen, M.K. 1 37 150  
 Maxon, S. 753  
 McDaniel, D.H. 1 37 150  
 McGuire, E.J. 1 37 48  
 McGurn, J.S. 37 146 150 753  
 McNamara, W.F. 37  
 Medovshikov, S.F. 542  
 Mehlhorn, T.A. 1 37 48 101  
 Meisel, G. 1257  
 Mekler, K.I. 182  
 Melkozerov, A.V. 663 667  
 Melnikov, G.V. 489  
 Melnikov, P.I. 182 1195  
 Mendel Jr., C.W. 1 56  
 Menge, P.R. 1  
 Merle, E. 628  
 Meshkov, O.I. 327 335  
 Messina, G. 453  
 Mesyats, G.A. 135 828 909 917 1241  
 Meyers, J.W. 131  
 Mikhailov, S.G. 1076  
 Mikhailov, V.M. 445  
 Milyavskii, V.V. 389  
 Mima, K. 1113  
 Mintsev, V.B. 1109  
 Mirnov, V.V. 1027  
 Mironenko, V.D. 649  
 Mironychev, P.V. 158 192  
 Mischin, M. 1107  
 Mishenski, V.O. 140 542 1064 1080  
 Mitchell, I. 762  
 Mitin, L.A. 229 430  
 Mitterauer, J. 1183  
 Miu, D. 898  
 Miyamoto, S. 52  
 Mizhiritskii, V.I. 154 962  
 Moats, A.R. 37  
 Mocek, T. 271  
 Mock, R.C. 146 753  
 Moir, D.C. 993  
 Mokhov, V.N. 558 1084

Monjaux, P. 276  
 Moo, S.P. 1233  
 Morell, A. 1203  
 Moreno, J. 305 505  
 Mori, M. 355  
 Morozov, I.V. 1084  
 Mosher, D. 115 146 749 753 1147 1151  
 Mostrom, M. 150 989  
 Motovilov, V.A. 909  
 Moya, S.S. 188  
 Mróz, W. 271  
 Mueller, G. 267 809  
 Munier, A. 1225  
 Munz, C.-D. 1159  
 Murakami, H. 1099  
 Murakami, M. 1103  
 Muron, D.J. 37  
 Murug, V.M. 701 946 950 977 981  
 Nagovitsin, A.Yu. 985  
 Naito, K. 355  
 Nakagawa, Y. 1155  
 Nakai, H. 1179  
 Nakai, S. 52  
 Nakajima, M. 501 1022 1179 1265  
 Nakayama, M. 481  
 Nanobashvili, I.S. 1035  
 Nash, T.J. 37 146 146 150 753  
 Nastasi, M. 275  
 Nastarenko, S.T. 158 296  
 Nazarov, D.S. 359  
 Neau, E. 255  
 Nedoseev, S.L. 140 534 542 546  
 Neri, J.M. 115  
 Nesterov, E.V. 445 449 457 461  
 Neuner, U. 1265  
 Ney, P. 771  
 Nichipor, H. 824  
 Nickles, P.V. 1075  
 Niimi, G. 52  
 Nikiforov, A.F. 140  
 Nikiforov, V.G. 140  
 Nikolaev, V.S. 182  
 Nikolov, N.A. 453  
 Nishigori, K. 52  
 Nishihara, K. 1103  
 Nishimoto, H. 60  
 Nishiyama, S. 355  
 Nishihinski, M.S. 1207  
 Niu, K. 1091 1261  
 Noack, D.D. 37  
 Nobuhara, S. 465 481  
 Nochnaya, N.A. 813 844 878  
 Noonan, W.A. 115  
 Nudikov, V.N. 158  
 Obenschein, S.P. 627  
 Odintsov, Yu.M. 619  
 Ofitserov, M.M. 401  
 Ogawa, M. 501 1265  
 Ognivenko, V.V. 64  
 Oguri, Y. 1265  
 Okada, T. 1095 1099  
 Okayama, H. 52  
 Oleinik, G.M. 140 526 530 534 542 546  
 Oliver, B.V. 115  
 Olsen, R.W. 37  
 Olson, C.L. 115 1115  
 Olson, J.C. 111 263 890 894  
 Olson, R.E. 37  
 Olson, T. 886

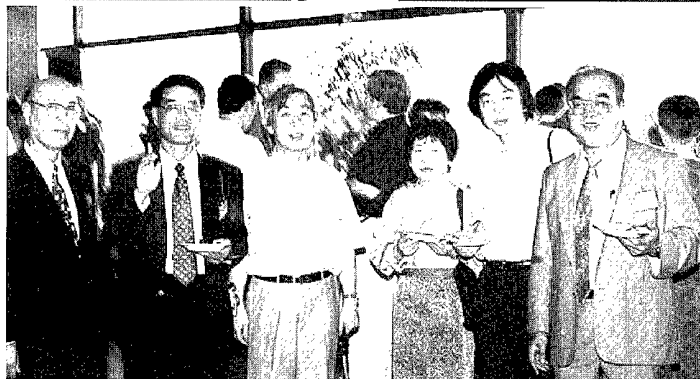
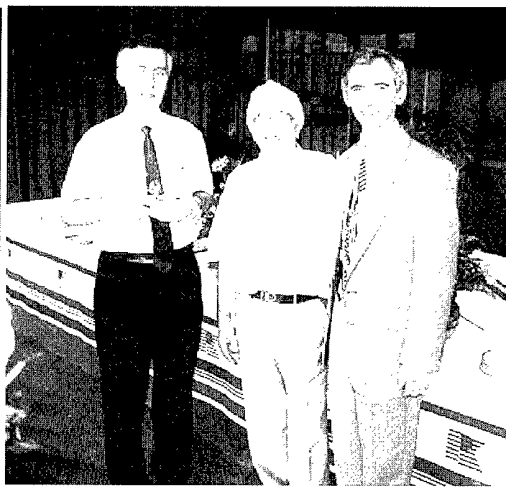
Omelchenko, Yu.A.	81	1171	1175	Prokopenko, Yu.V.	422			
Onishchenko, I.N.	64	<u>426</u>		Proskurovsky, D.I.	<u>259</u>	359	813	
Opekounov, M.S.	<u>817</u>	<u>1068</u>		Prucker, U.	603			
Osin, V.A.	946	950	977 981	Pshenichnov, I.A.	623			
Osipov, V.V.	<u>1076</u>			Puchkarev, V.	886			
Ostashev, V.I.	691			Pulsifer, P.E.	146			
Otochin, A.A.	140			Putnam, S.D.	<u>60</u>			
Ottinger, P.F.	115	121		Puzynin, I.V.	<u>615</u>	785	854	
Oucherenko, D.A.	817			Qian, Q.	1018			
Outten, C.A.	131			Qiu, A.C.	301			
Ozur, G.E.	259	<u>359</u>		Quintenz, J.P.	<u>1</u>	37		
Paduch, M.	162	<u>737</u>		Raacke, J.	<u>659</u>			
Pak, S.V.	1008			Radjuk, E.	824			
Panesh, A.M.	<u>864</u>			Ratakhin, N.	917			
Pankratov, V.I.	946	950		Razilov, R.V.	182			
Papazian, Yu.V.	1064			Razinkova, T.J.	140			
Paraschiv, I.	595			Razorenov, S.V.	72			
Parys, P.	271			Reass, W.A.	263			
Parzhitskii, S.	917			Reed, K.W.	255			
Patran, A.	<u>587</u>			Reginato, L.	91			
Pavlov, S.S.	985			Reiser, M.	238			
Pavlov, V.S.	158			Rej, D.J.	<u>275</u>	894		
Pavlovskii, A.P.	<u>649</u>			Remnev, G.E.	817	<u>869</u>	<u>873</u>	878 <u>902</u> 1068
Pavlovsky, E.S.	1084			Renk, T.J.	1	882		
Pawley, C.J.	627			Renner, O.	<u>733</u>			
Pechenkin, S.A.	1068			Ridlon, R.N.	188			
Pegel, I.V.	913			Riege, H.	<u>68</u>	1191		
Pegoev, I.N.	946	950		Rintamaki, J.I.	347			
Peng, X.	924			Řipa, M.	343			
Pereira, N.R.	<u>745</u>	<u>1071</u>		Robozarov, S.V.	485			
Perevodchikov, V.I.	229	<u>430</u>		Rodgers, J.	405			
Perin, S.S.	182			Roewekamp, P.	<u>174</u>	659		
Persiansev, I.V.	292			Rogerson, J.	709	757		
Peskov, N.Yu.	213	<u>245</u>		Rohlana, K.	<u>271</u>			
Peter, B.	1063			Romanov, I.G.	<u>821</u>			
Peter, W.	437			Romanova, G.M.	821			
Peters, C.	91			Romanova, V.M.	<u>683</u>	<u>687</u>		
Peterson, D.L.	146	150		Romary, P.	<u>550</u>			
Peterson, G.G.	<u>749</u>			Roques, A.	628			
Petkun, A.A.	221			Roschupkin, S.A.	445	449		
Petlytski, V.	921			Rose, D.V.	115	1147		
Petrakov, V.N.	977	981		Rosenthal, S.E.	1			
Petrov, S.I.	691			Rosmej, F.B.	<u>1075</u>			
Petrukhin, A.A.	538			Rosocha, I.	886			
Pfeifer, M.	271	733		Roth, I.	1003			
Phillips, R.	406			Roth, P.	<u>363</u>			
Pichugin, V.E.	140	542	<u>546</u>	Rothstein, V.P.	813	259		
Picon, J.C.	628			Rouille, C.	276	758	1203	
Piekoszewski, J.	860			Rous, J.	305			
Pikar', A.S.	<u>158</u>	192	296 644 <u>656</u> 663	Rousskikh, A.G.	522			
	667			Rovenskikh, A.F.	182			
Pikuz, S.A.	<u>683</u>	687		Rowley, J.E.	121	284		
Pikuz, T.A.	683			Rudakov, L.I.	<u>154</u>	729	<u>776</u>	<u>780</u> 1199
Podulka, W.J.	81	1171		Ruden, E.L.	131			
Pogue, E.W.	636			Ruggles, L.E.	37	150		
Pointon, T.D.	48	101		Ruiz, C.L.	1	37		
Ponomarev, A.V.	225			Rukhadze, A.A.	225	<u>431</u>		
Ponomarev, S.V.	701			Rukin, S.N.	<u>135</u>	1241		
Popkov, N.F.	<u>158</u>	192	<u>296</u> 644 656 663	Rusch, D.	72	1123	1127	1155 1257
	<u>667</u>	985		Ruskov, A.S.	158			
Pornet, J.	550			Rutkovskaia, K.	921			
Porter, J.L.	37	150		Ryaslov, E.A.	158	192	296	644 656 <u>663</u>
Postnikova, A.S.	485				<u>667</u>			
Postupaev, V.V.	182			Ryutov, D.D.	<u>178</u>	<u>554</u>		
Potarov, A.V.	691			Ryzhackova, E.G.	192			
Potyomkin, A.V.	873			Ryzhkov, V.A.	<u>869</u>	873		
Presura, R.	591	<u>595</u>	599	Saavedra, R.	679	762		
Price, D.	217			Sabirov, B.	917			
Prishchepov, V.P.	64			Sadowski, M.	<u>170</u>			

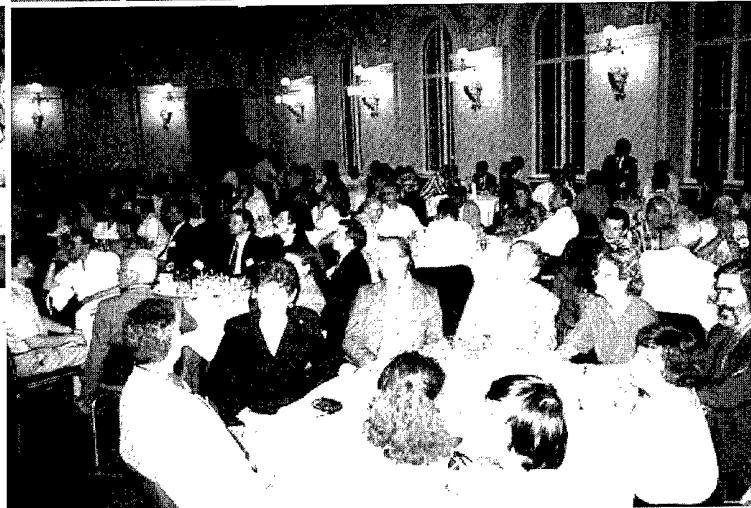
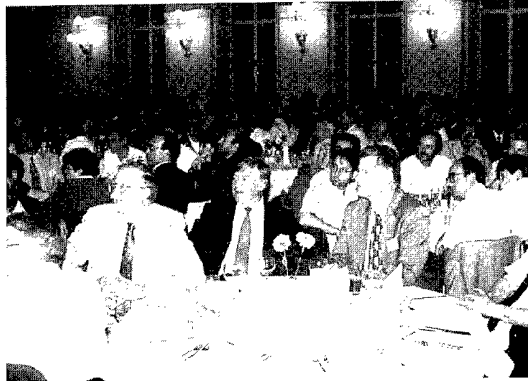
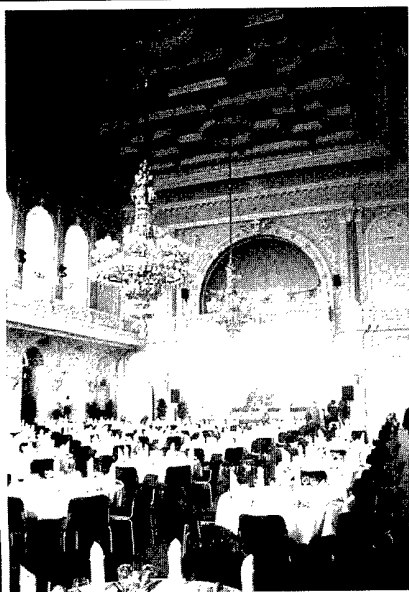
Saenger, E. 1257  
 Sajer, J.M. 550  
 Salnikov, L.I. **824**  
 Samoilov, V.N. 615 785 854  
 Samsonov, S.V. 401  
 Sanford, T.W.L. 1 **146** 150 **753**  
 Sanin, A.L. 327 335  
 Saraph, G. 238  
 Saratov, A.F. 158  
 Sarfaty, M. 41 1216 **1229**  
 Sasorov, P.V. 140 542  
 Sawyer, P.S. 37  
 Schalk, S. 95 1107 1111  
 Schamiloglu, E. **433**  
 Schegolikhin, N. 267  
 Scheitrum, G. 406  
 Scheuer, J.T. 275  
 Schleinitz, H.M. 263  
 Schlitt, L. 1003  
 Schmitz, F. 174  
 Schneider, L.X. 255  
 Schneider, Ralph F. 284 757  
 Schneider, Rud. **1159**  
 Schnuerer, M. 1075  
 Schoen, T. 1257  
 Schumacher, G. 267 809  
 Schwandner, A. 603  
 Scotnikov, V.A. 909  
 Seamen, J.F. 1 37 146 150 753  
 Sedykh, S.N. 245  
 Seidel, D.B. 1  
 Seitz, G.J. 188  
 Semenov, E.P. 182  
 Semushin, S. 276 758 1211  
 Semyonov, S.I. 158  
 Senikh, A.V. 701  
 Sergeev, A.P. 245  
 Sergeev, A.S. 242 245 496  
 Serlin, V. 206 **627**  
 Sevastianov, A.A. 776  
 Shaidullin, V.Sh. 558  
 Shapiro, A.L. 229 430  
 Sharkov, B. 271  
 Sharp, W.M. 91  
 Shashkov, A. Yu. 1050  
 Shelkovenko, T.A. 683 687  
 Shen, Zh.K. 301  
 Shijan, V.D. 671 675  
 Shiloh, J. **437**  
 Shimanovich, V.D. 797  
 Shkvarunets, A.G. 225 **405**  
 Shlapakovskii, A. S. **441**  
 Shlenov, Yu.V. 840  
 Shoup, R.W. 150 **989**  
 Shpak, V.G. 242 **473** **913**  
 Shpitalnik, R.R. 41 1215 **1216**  
 Shulov, V.A. 813 **878**  
 Shumilin, V.P. 445 449 457 461  
 Shumshurov, A. 271  
 Shunailov, S.A. 242 473 913  
 Shurter, R.P. 188 **993**  
 Sidel'nikov, G.L. 611  
 Sidorenko, D. Yu. 426  
 Sidorov, V.A. 999  
 Silva, P. 566 **570** 574  
 Simanovskii, D.M. 174  
 Šimek, M. 343  
 Sincerny, P. **1003**  
 Sinebryukhov, A.A. 127 917 1217 1221

Sinebryukhov, V.A. 127 917  
 Singer, J. 72 1127 1257  
 Singh, J.P. 1233  
 Singleton, C. 1127  
 Sinitisky, S.L. 182 213 367  
 Sissakian, A.N. 615 785 854  
 Skála, J. 271  
 Skladnik-Sadowska, E. 737  
 Skobelev, A.N. 1008  
 Skobelev, I. Yu. 1075  
 Skvortsov, V.A. 389 **513**  
 Slavnov, Yu.K. 526  
 Slinker, S. 206  
 Slovikovskii, B.G. 135  
 Slut, S.A. 1 101  
 Smirnov, V.P. 140 292 526 534 542 546  
 632 653 1064  
 Smith, I. 60 150 989  
 Sochugov, N.S. 905  
 Sokolova, O.V. 558  
 Sokovnin, S. Yu. **828**  
 Solomonov, V.I. **1076**  
 Sominski, G.G. 319 371 418 789 485  
 Sonegawa, T. 27  
 Sorokin, S. 917  
 Sotnikov, G.V. 426  
 Soto, L. 679 762  
 Spassovski, I.P. **453**  
 Spencer, T.A. 347  
 Spielman, R.B. 1 37 146 150 753 989  
 Springer, P.T. 753  
 Stallings, C. 1003  
 Stambulchik, E. 48  
 Stanislawski, J. 860  
 Stark, M.A. 37  
 Stein, E. 1123 1159  
 Stepchenko, A.S. 965  
 Stephanakis, S.J. 115 749 1151  
 Stinnett, R.W. **882**  
 Stoltz, O. 72 1123 1127 1155 1257  
 Stolupin, V. 917  
 Straka, P. 271  
 Strauss, D. 267 809  
 Strelkov, P.S. 225  
 Stroganov, V.A. 445 449 457 461  
 Struts, V.K. 902  
 Struve, K.W. 146 150 753 882 989  
 Stygar, W.A. 1 146 150 989  
 Sudan, R.N. **81** 780 1171 1175  
 Suganomata, S. 973  
 Summa, W.J. 158 284  
 Sun, F.J. 301  
 Sunami, H. 52  
 Suvorov, V.N. 649  
 Swanekamp, S.B. 1147 1151  
 Sweeney, M.A. 1  
 Tabak, M. 721  
 Takahata, S. 331  
 Tantawi, S. 406  
 Tarakanov, V.P. 913  
 Tarasov, A.D. 640  
 Tarasov, A.V. 182 213  
 Tauschwitz, A. 91 1127 1155  
 Tereshatova, E. 853  
 Thevenot, M. 628  
 Thoe, R.S. 753  
 Thomas, J. 60  
 Thompson, J. 121  
 Thornhill, J.W. 146 709 749



[illegible]





Invitation to the next conference

**Welcome to Haifa**  
**ברוכים הבאים לחיפה**

We look forward to the continued success of the BEAMS meetings at

# **BEAMS'98**

**in Haifa, Israel.**

Conference date: **June 8-12, 1998**

Host organization: **Rafael, Haifa**

*For more information please contact*

**Dr. Joseph Shiloh, Conference Chair**

Dept. 23, Rafael

Haifa, ISRAEL

E-mail: [beams98@plasma-gate.weizmann.ac.il](mailto:beams98@plasma-gate.weizmann.ac.il)

[jshiloh@rafael.co.il](mailto:jshiloh@rafael.co.il) or [shilo@eng.tau.ac.il](mailto:shilo@eng.tau.ac.il)

*WWW home page BEAMS'98:*

<http://plasma-gate.weizmann.ac.il/~peter/beams98.html>

